NASA/CP-1999-208982/PART2

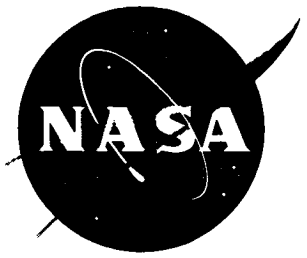

The Second Joint NASA/FAA/DoD Conference on Aging Aircraft

Charles E. Harris, Editor
Langley Research Center, Hampton, Virginia

January 1999

The NASA STI Program Office ... in Profile

Since its founding, NASA has been dedicated to the advancement of aeronautics and space science. The NASA Scientific and Technical Information (STI) Program Office plays a key part in helping NASA maintain this important role.

The NASA STI Program Office is operated by Langley Research Center, the lead center for NASA's scientific and technical information. The NASA STI Program Office provides access to the NASA STI Database, the largest collection of aeronautical and space science STI in the world. The Program Office is also NASA's institutional mechanism for disseminating the results of its research and development activities. These results are published by NASA in the NASA STI Report Series, which includes the following report types:

- TECHNICAL PUBLICATION. Reports of completed research or a major significant phase of research that present the results of NASA programs and include extensive data or theoretical analysis. Includes compilations of significant scientific and technical data and information deemed to be of continuing reference value. NASA counterpart of peer-reviewed formal professional papers, but having less stringent limitations on manuscript length and extent of graphic presentations.

- TECHNICAL MEMORANDUM. Scientific and technical findings that are preliminary or of specialized interest, e.g., quick release reports, working papers, and bibliographies that contain minimal annotation. Does not contain extensive analysis.

- CONTRACTOR REPORT. Scientific and technical findings by NASA-sponsored contractors and grantees.

- CONFERENCE PUBLICATION. Collected papers from scientific and technical conferences, symposia, seminars, or other meetings sponsored or co-sponsored by NASA.

- SPECIAL PUBLICATION. Scientific, technical, or historical information from NASA programs, projects, and missions, often concerned with subjects having substantial public interest.

- TECHNICAL TRANSLATION. English-language translations of foreign scientific and technical material pertinent to NASA's mission.

Specialized services that complement the STI Program Office's diverse offerings include creating custom thesauri, building customized databases, organizing and publishing research results ... even providing videos.

For more information about the NASA STI Program Office, see the following:

- Access the NASA STI Program Home Page at ***http://www.sti.nasa.gov***

- E-mail your question via the Internet to help@sti.nasa.gov

- Fax your question to the NASA STI Help Desk at (301) 621-0134

- Phone the NASA STI Help Desk at (301) 621-0390

- Write to:
  NASA STI Help Desk
  NASA Center for AeroSpace Information
  7121 Standard Drive
  Hanover, MD 21076-1320

NASA/CP-1999-208982/PART2

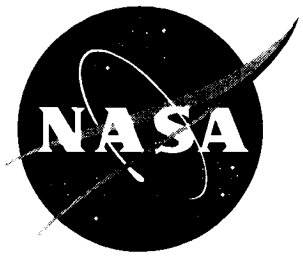

The Second Joint NASA/FAA/DoD Conference on Aging Aircraft

Charles E. Harris, Editor
Langley Research Center, Hampton, Virginia

Proceedings of a conference sponsored by the National Aeronautics and Space Administration, Federal Aviation Administration, U.S. Air Force Materiel Command, U.S. Naval Air Warfare Center, and U.S. Army Research Laboratory, and held in Williamsburg, Virginia
August 31 - September 3, 1998

National Aeronautics and
Space Administration

Langley Research Center
Hampton, Virginia 23681-2199

January 1999

Available from:

NASA Center for AeroSpace Information (CASI)
7121 Standard Drive
Hanover, MD 21076-1320
(301) 621-0390

National Technical Information Service (NTIS)
5285 Port Royal Road
Springfield, VA 22161-2171
(703) 605-6000

Preface

The purpose of the conference was to bring together world leaders in aviation safety research, aircraft design and manufacturing, fleet operation and aviation maintenance to disseminate information on current practices and advanced technologies that will assure the continued airworthiness of the aging aircraft in the military and commercial fleets. The conference included reviews of current industry practices, assessments of future technology requirements, and status of aviation safety research. The conference provided an opportunity for interactions among the key personnel in the research and technology development community, the original equipment manufacturers, commercial airline operators, military fleet operators, aviation maintenance, and aircraft certification and regulatory authorities. Conference participation was unrestricted, with 623 participants from the international aviation community.

Conference Organizing Committee:

Charles E. Harris, General Chairman, NASA Langley Research Center
James C. Newman, Jr., NASA Langley Research Center
William P. Winfree, NASA Langley Research Center
William R. Elliott, WR-ALC/TIED, Robins Air Force Base
John W. Lincoln, ASC/EN, Wright Patterson Air Force Base
Joseph P. Gallagher, WL/CCI, Wright Patterson Air Force Base
Chris C. Seher, FAA, William J. Hughes Technical Center
Alfred L. Broz, FAA, Chief Scientist/Technical Advisor for Nondestructive Evaluation
Robert G. Eastin, FAA, Chief Scientist/Technical Advisor for Fracture Mechanics/Metallurgy
Aubrey E. Carter, Technical Operations Center, Delta Air Lines, Inc.
Ulf G. Goranson, Boeing Commercial Airplane Group, The Boeing Company
Amos W. Hoggard, Jr., Douglas Products Division, The Boeing Company
Paul C. Hoffman, NAWCAD, Patuxent River
Feldon D. Bartlett, Jr., Vehicle Structures Directorate, Army Research Laboratory
Sonya Herrin, Conference Administrative Manager, Science and Technology Corporation

Sponsoring Organizations:

National Aeronautics and Space Administration, Langley Research Center
Federal Aviation Administration, William J. Hughes Technical Center
United States Air Force, Air Materiel Command
United States Naval Air Warfare Center, Aircraft Division
Unites States Army Research Laboratory

- TABLE OF CONTENTS -

PART 1

APPROACHES TO FLEET MANAGEMENT

PART 2

STRUCTURAL ANALYSIS METHODS

POSTERS

STRUCTURAL ANALYSIS METHODS

ON THE ASSESSMENT OF THE CRITICALITY OF CRACK SCENARIOS WITH RESPECT TO WIDESPREAD FATIGUE DAMAGE

Peter Horst
Institute of Aircraft Design and Lightweight Structures
Technical University of Braunschweig
Langer Kamp 19
D-38106 Braunschweig, Germany
phone: +49 531 391 2685
fax: +49 531 391 2695
e-mail: p.horst@TU-BS.de

ABSTRACT

The main question in the assessment of Widespread Fatigue Damage (WFD) criticality is the question how critical certain crack and crack initiation scenarios are, with or without combination with the residual strength problem. This paper deals with methods for the assessment of the criticality of crack scenarios. Emphasis is put on the question of deteriorating effects.

1. INTRODUCTION

Different sources, like e.g. the AAWG (Aging Aircraft Working Group) defined some basic wording with respect to aging aircraft [1]. One of the essential diagrams shows the drop of the residual strength due to single and multiple site damage, as shown in figure 1. The main concern is the rapid drop of the residual strength in the case of Multiple Site Damage (MSD). This drop mainly occurs, if the MSD scenario consists of equal cracks at all sites. From all cases known from practice it can be concluded that the equal size crack scenario is very unlikely to occur. It would therefore lead to some very conservative results, if such a scenario is taken into account.

The problem seems not so crucial, if the crack scenario is more realistic. This is visualized in figure 1, too. There seems to be a certain probability to find residual strength curves. The question mainly is: What is the scenario like, which may be called "MSD"-like, and what is the right way to assess this. One information can be concluded from all reports on the WFD/MSD problem, this is the fact that a well-designed joint will not show a distinct trend for MSD-like scenarios. Therefore, either some kind of real mistake in the design, or some kind of a deteriorating effect must occur in order to yield such an effect.

In trying to assess what kind of scenario is MSD-like – in the sense that the residual strength drops dramatically – the most promising way seems to be a Monte-Carlo Simulation. This kind of approach has been published by Horst et al. In [2]. A typical result is illustrated in figure 2. The axes are the number of cycles up to the detection of the first initiated crack and the other one indicates the "inspection interval", i.e. the number of cycles up to criticality of the crack scenario.

In the paper [2] and others, the problem of assessing the behavior of aging aircraft structures has mainly been focussed on the initiation, crack growth and residual strength of structures under pure fatigue loading. The main result from the investigations dealing purely with fatigue was that the probability to find multiple site damage (MSD) or widespread fatigue damage (WFD) like scenarios is very limited. If the original joint design has been made according to today's design rules.

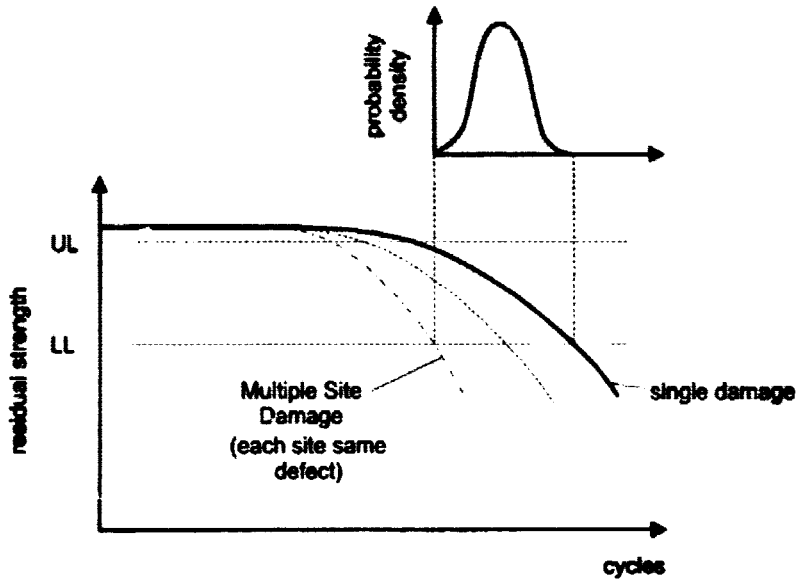

Figure 1: Drop of residual strength due to single and multiple defect

The criterion for a MSD-like scenario illustrated in figure 2 is a very small interval in this figure. It is very hard to find a better way to assess the probability to find MSD just by criteria, which need less effort to be predicted. Different ways have been checked by the author, but none was absolutely convincing. This means that a Monte-Carlo Simulation is needed to predict such probabilities. On the other hand it has been found that the criterion 3 to find 3 adjacent cracks is e.g. at least a good hint. This is the reason, why this

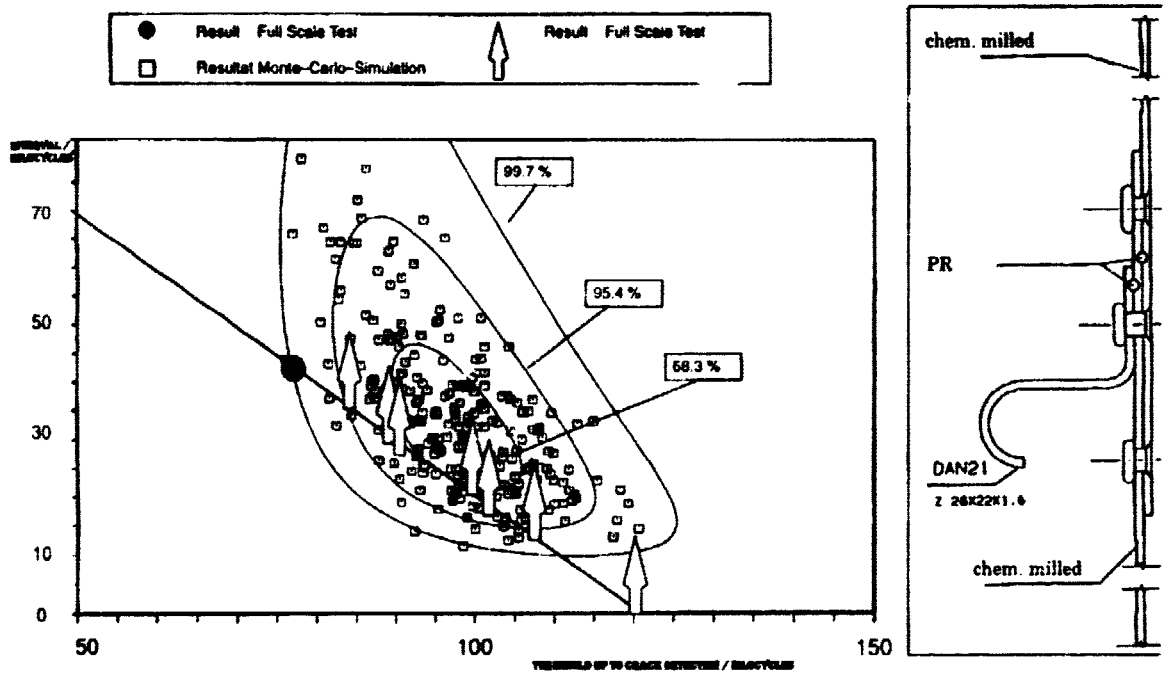

Figure 2: Results of a Monte-Carlo Simulation (after [2])

criterion is used in this paper for further investigations. Other criteria may also be found, but they are not even so attractive.

One main reason why MSD may occur (or that the probability to find MSD-like scenarios is significantly high) seems to be that, due to some kind of deterioration of the joint, the performance changes drastically. This paper tries to discuss a model for such a deteriorating effect in order to find out, what could be the limits for the size (etc.) of such an effect to be worried.

2. THE PROBLEM

Up to now the behavior of structures with respect to MSD has been investigated by means of a Monte-Carlo Simulation. It therefore seems to be right to follow this way again in the case of the investigation of the influence of deteriorating effects on MSD.

Since the former employer of the author mainly deals with fuselage structures and therefore mainly uses 2024 T3xx as skin material, it seems to be reasonable to stick to the main effects found for such a material. One of the main deteriorating effects surely may be corrosion. From the different sources it is quite obvious that corrosion may influence the fatigue behavior of the material, but the crack growth rate widely seems to be unchanged (as long as there is no major loss of material and thickness). This is the reason to focus the work described in this report mainly on the fatigue behavior, i.e. on the initiation problem.

Due to the reasons mentioned the question arises how to model the effect, where it is not sure that the model may only deal with corrosion; other deteriorating effects on the fatigue behavior may as well be represented by the model (e.g. debonding of doublers etc.).

2.1 The original fatigue model

Within the original fatigue model, fatigue is represented by a log-normal distribution, i.e. two parameters N_{mean} and S_{dev} fully represent the fatigue behavior, as indicated by the following figure 3.

The scatter is represented by the equation

$$T_{FN} = N_{90} / N_{10} \qquad (1)$$

Where N_{90} is the number of cycles for a probability of survival of 90% of the specimen and N_{10} is the one for 10%, respectively. The standard deviation s_{dev} is liked to T_{FN} by

$$S_{dev} = - 0.3906 \log(T_{FN}) \qquad (2)$$

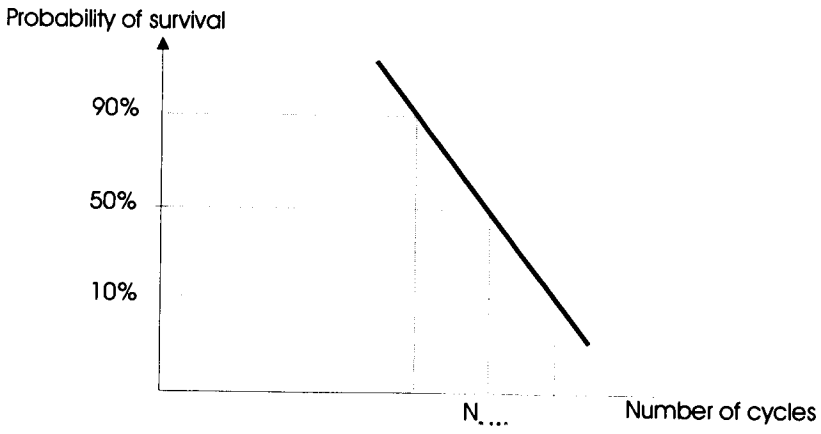

Figure 3 : Probability of survival in the case without deteriorating effect (ordinate in probabilistic scale)

This scatter in fatigue may be valid for the case without any deteriorating effect. The fatigue behavior is illustrated for one single stress level.

2.2 The case of a deteriorating effect

If a deteriorating effect occurs, it is assumed that the fatigue behavior drops instantaneously by a factor, both in N_{mean} and s_{dev}. This is surely not totally true. It is a clear simplification, but it will not violate the truth too much. The situation is illustrated in figure 4.

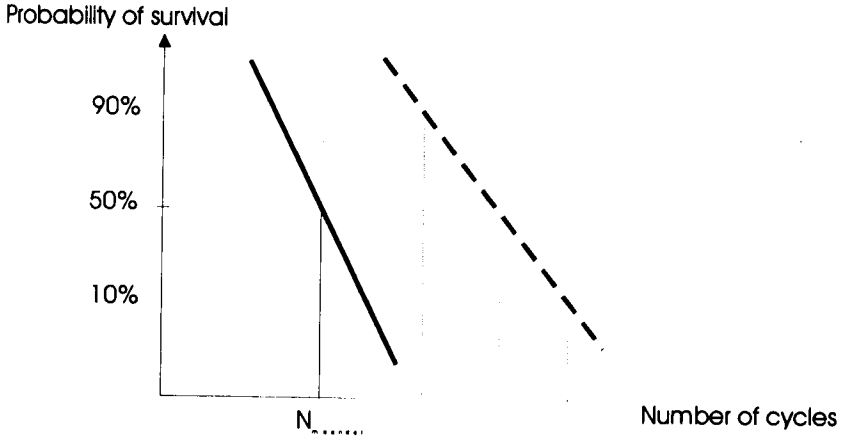

Figure 4: The probability of survival in the case of a deteriorating effect (ordinate in probabilistic scale)

The newly defined values of the deteriorated fatigue problem are $N_{meandet}$ and s_{devdet}

It is the question how to define the combined problem of a specimen, which initially shows no deteriorating effect and a deterioration after some time. It seems to be reasonable to define that the combined fatigue problem is governed by the same simple law as in the case of a change in the stress level, i.e. it is governed by Palmgren-Miner's law.

$$1 = \frac{N_{un\,det}}{N_{fat}} + \frac{N_x}{N_{fat\,det}}$$

Where N_{undet} is the number of cycles accumulated before the deteriorating effect occurred. N_{fat} is the randomly assigned fatigue life of the fatigue critical location without deteriorating effect. N_x is the number of cycles needed to find a damage in a deteriorating state and N_{fatdet} is the pendant to the number N_{fat}, but in the deteriorated state.

The total life of one fatigue critical location adds up to

$$N_{fat} = N_{un\,det} + N_x$$

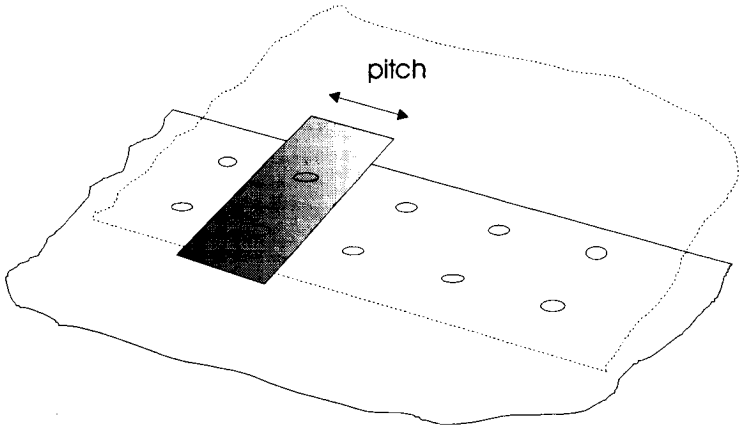

Figure 5 : The definition of the "pitch parameter"

2.3 Further Parameters involved

There are of course some more parameters, which will govern the problem.

Firstly, it has to be specified, when the deteriorating effect occurs. This is again a probabilistic problem. Therefore, a log-normal distribution will be appropriate here again. The two involved parameters are:

- N_{dave}
- s_{dave}

The number of cycles which are found without a deteriorating effect Nun det is of course determined via the combination of N_{dave} and s_{dave}, as well as a random process, which gives the probabilistic aspect of this process. Furthermore, it has been decided to use a fixed extension of the deteriorated zone. This is of course again a simplification, but it has some benefits with respect to the problem, which is investigated in this report later on. Surely, it would be possible to use some kind of probabilistic approach here too, but this would also be linked to detectability questions etc., which would make it quite sophisticated. This is not done here.

The additional parameter is "n x pitch" which is the number of adjacent rivet pitches, which are deteriorated in one instance. Figure 5 tries to illustrate this assumption.

3. AN EXAMPLE FOR THE EFFECTS OF DETERIORATION

An example to test the effects of deterioration of the fatigue life due to the model given in section 2 will be discussed in this section.

3.1 The basic problem

The basic problem consists of

- a set of 20 fatigue critical locations, e.g. rivets etc.
- the mean fatigue life per fatigue critical location is $N_{mean} = 4$ in a log-scale
- the standard deviation (log-scale) is 0.15

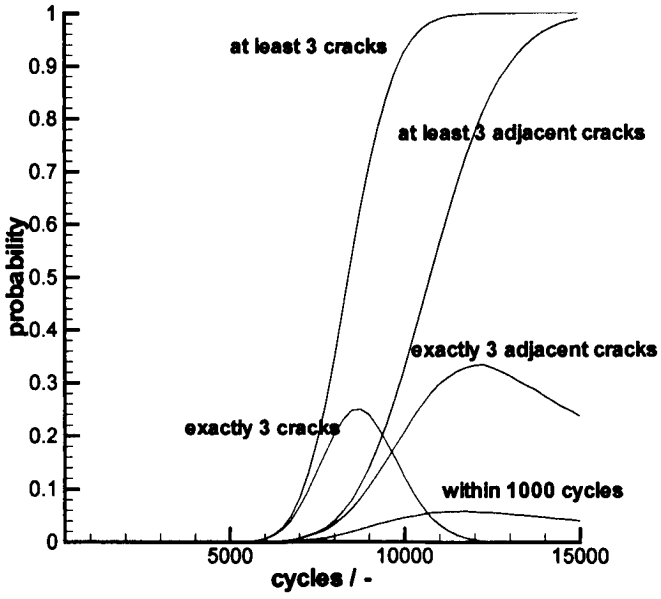

Figure 6 : Results in the case with no deteriorating effects

Different criteria are checked in this case, which may serve as indications for MSD-like scenarios. All are probabilities to find certain scenarios within the 20 fatigue critical locations:

- the probability that at least 3 cracks initiated
- the probability that exactly 3 cracks initiated
- the probability that at least 3 adjacent cracks initiated
- the probability that exactly 3 adjacent cracks initiated
- the probability that at least 3 adjacent cracks initiated within 1000 load cycles.

It is quite clear that this example is not perfect, but it may be assumed that criterion number 3 and 5 may be seen as one typical example which may be interesting with respect to the initiation of MSD-scenarios. The results for this basic example are given in figure 6.

3.2 Deteriorating effects

The same example has now been checked adding the possibility of deterioration of the fatigue life. This has been done by using different parameters for the onset and the fatigue life due to the deteriorating effect.

Namely,

- the mean value for the probability to find a deteriorating effect has been varied between 1 and 5 in log-scale
- the drop in the fatigue behavior after onset of the deteriorating effect has been set to 1 in a log-scale.
- the extent of the deteriorating effect has been varied between 1 and 3 pitches

The other parameters have been kept constant. This is especially true for the standard deviation of both, the drop in fatigue under the deterioration and the life up to the deterioration. This may be interesting to some extent, but it surely is not the parameter of major interest.

All results have been found by simulating 25,000 different MSD scenarios. This is not an extremely high number of simulations, but it seems to result in a relatively stable curve. Very small probabilities can only be found by simulating a much higher number of scenarios. But it becomes obvious from the results that this is not essential for the discussion here.

Results are given in the following figures 7 to 11. The cases are as follows

- case 1 : mean value for the deteriorating effect : 2 (log-scale)
  extent of deterioration : 1 pitch
- case 2 : mean value for the deteriorating effect : 5
  extent of deterioration : 2 pitches
- case 3 : mean value for the deteriorating effect : 2
  extent of deterioration : 2 pitches
- case 4: mean value for the deteriorating effect : 4
  extent of deterioration : 3 pitches
- case 5 : mean value for the deteriorating effects : 2
  extent of deterioration : 3 pitches

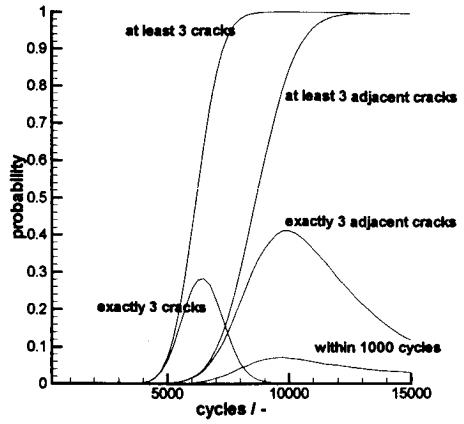

Figure 7 : Probability in case 1

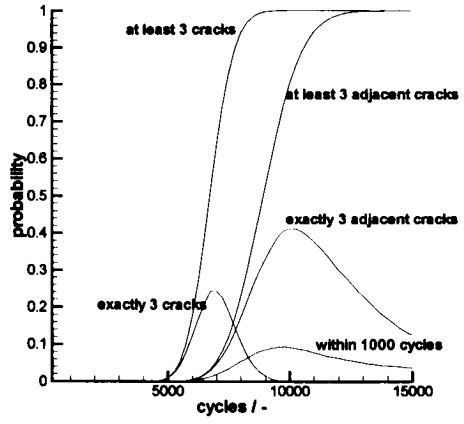

Figure 8 : Probability in case 2

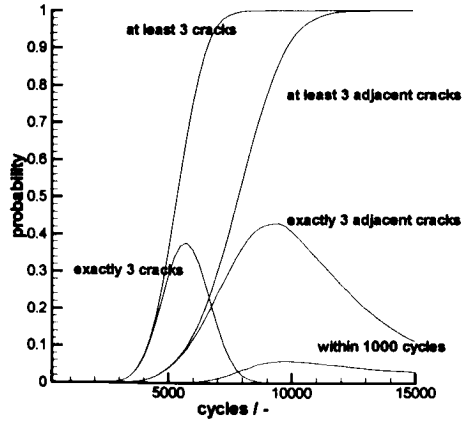

Figure 9 : Probability in case 3

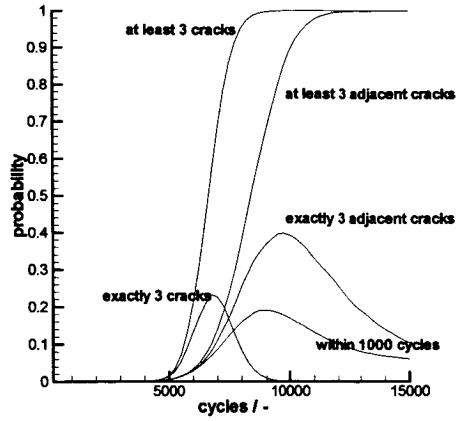

Figure 10: Probability in the case 4

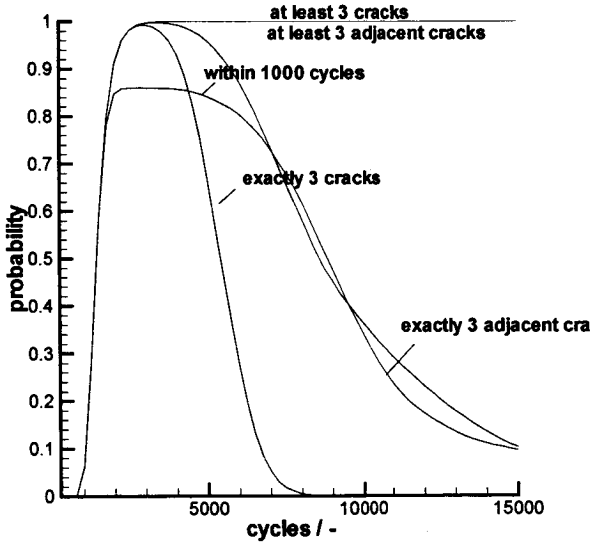

Figure 11: case 5

4. CONCLUSIONS

Some essential conclusions can be drawn from the results of this example.

By assuming that the criteria for the probability to have 3 adjacent cracks and to initiate 3 cracks within a very small period of time are essential as criteria to find some kind of MSD-like scenario, the results are very interesting.

By looking at figure 7 , i.e. a curve which reflects the cases, where only one pitch is deteriorated in width, one finds the followings clues

- Although, many fatigue critical locations face some deteriorating effect within the life of the specimen, the changes in the essential curves for at least 3 adjacent cracks and cracks initiated within 1000 cycles do not change too much.

- This same conclusion is found by figures 8 and 9, where the size of the deteriorating effect is 2 pitches wide.

This situation changes completely, if the width of the deteriorating effect reaches the size of 3 x pitch. Figures 10 and 11 illustrate this case.

- While in figure 10, where the mean value of N_{dave} is equal to 4 (log-scale), which is exactly the mean value of the ordinary fatigue life of the specimen, nearly nothing is changed,

- in figure 11 all curves really changed completely (and this is actually also the case for a mean value of 3, too).

This result is very interesting by saying that it suggests that deteriorating effects are possibly essential for the building of MSD-like scenarios, but this will only happen,

- MSD-like scenarios will be more likely to occur, if the size of the deteriorating effect is of the size, which seems to define the MSD scenario

- And the mean value of the initiation of a deteriorating effect is not larger than the one for the fatigue life

The deteriorating effects are not essential, if

- The mean life for the initiation of the deterioration is much larger than the one for the normal fatigue life

- And if the size of the defect is smaller than the one assessed to be essential for the MSD-scenario.

Surely, more discussions are possible, but this result seems to be the most essential one.

ACKNOWLEDGMENTS

The author gratefully acknowledges the fact that some of the work reported in this paper has been funded by the CEC (European Community) in the frame of the Brite/EuRam project „Structural Maintenance of Aging Aircraft" during the period when he was working for Daimler-Benz Aerospace Airbus.

REFERENCES

[1] AAWG Final Report

[2] Horst, P. and Schmidt, H.-J., *A Concept for the evaluation of MSD based on probabilistic assumptions* , paper presented at the 80th AGARD Structures and Materials Panel, held in Rotterdam, The Netherlands, 10-11 May 1995, published AGRAD CP-568

THE GROWTH OF MULTI-SITE FATIGUE DAMAGE IN FUSELAGE LAP JOINTS

Robert S. Piascik
NASA Langley Research Center
Hampton, VA, 23681 USA.
Tel: (757) 864-3483
Fax: (757) 864-8911
E-Mail: r.s.piascik@larc.nasa.gov

Scott. A. Willard
Lockheed Engineering and Sciences Co.
Hampton, VA, 23681 USA.

ABSTRACT

Destructive examinations were performed to document the progression of multi-site damage (MSD) in three lap joint panels that were removed from a full scale fuselage test article that was tested to 60,000 full pressurization cycles. Similar fatigue crack growth characteristics were observed for small cracks (50 μm to 10mm) emanating from counter bore rivets, straight shank rivets, and 100° counter sink rivets. Good correlation of the fatigue crack growth data base obtained in this study and FASTRAN Code predictions show that the growth of MSD in the fuselage lap joint structure can be predicted by fracture mechanics based methods.

1. INTRODUCTION

To predict the growth of multi-site fatigue damage in fuselage structures, it is essential to thoroughly understand the processes that govern fatigue crack initiation and growth. The objective of this research is to:

- develop a fatigue crack database that completely describes the initiation and growth of small cracks in the riveted lap joint fuselage structure,
- provide a basis for comparing the crack growth behavior simulated in laboratory test specimens to the behavior in actual aircraft components, and
- serve as a benchmark to verify fatigue crack growth analytical methodology.

This research will assist in developing engineering tools that predict the onset of widespread fatigue damage (WFD), assist in setting damage inspection intervals, and quantify non-detectable damage prior to repair.

Multi-site damage (MSD) is defined as the simultaneous presence of multiple fatigue cracks in the same structural element (1). For MSD to occur, it is likely that the same damage process takes place at multiple locations within the same structural element. For the lap joint, similar damage processes occur at multiple rivet locations along the same rivet row. The thorough understanding of the MSD processes is required to develop deterministic methods for predicting the onset and growth of fatigue cracks. From this study, the detailed characterization of crack initiation sites at rivet holes will assist in the development of probabilistic and/or equivalent initial flaw size (EIFS) methods used to model crack nucleation. Fractographic analysis is used to catalog crack front morphologies that are essential for developing crack-tip stress intensity factor expressions for MSD. In addition, a comprehensive database is developed to validate fatigue crack growth predictions.

2. RESULTS AND DISCUSSION

A comprehensive destructive examination was conducted on three lap joint panels (panels 1, 3, and 6) removed from a full-scale test article pressurized to 60,000 cycles (2-4). During full-scale fatigue testing, visible outer skin cracks were noted in lap joints located at three isolated regions of the test article depicted in Figure 1. The regions that exhibited cracks were removed for detailed fractographic examinations. Panel 1 was removed from the bottom region of the test article and panels 3 and 6 were removed from two different locations along the side of the test article. The destructive examinations summarized herein describe the initiation and growth characteristics of small cracks emanating from counter bore, straight shank, and 100° countersink riveted lap joints. A brief description of each panel is summarized in Table 1. A detailed description is provided in references 2-4. These data are compared to independent small crack laboratory test results and are used to benchmark MSD crack growth predictions.

TABLE 1 PANEL DESCRIPTION

Panel #	No. of Rivet Rows	No. of Bays*	Rivet Type	Comments
1		6	Counter Bore	Visible cracks in bays 2-6
3	3	5	Straight Shank & 100° Countersink	Visible cracks in bay 2
6	4	5	Counter Bore	Visible cracks in bays 1-3, & 5

* A bay is the portion of lap joint (≈ 1.5 ft. long) located between adjacent tear straps.

2.1 DESTRUCTIVE EXAMINATIONS

Table 2 summarizes the results of the destructive examinations (2-4). A total of 419 rivet holes were examined for the presence of fatigue cracks by performing detailed optical and scanning electron microscopy (SEM) on approximately 2500 specimens. The precise location of the crack relative to the structure was documented and all fracture surfaces were characterized to document the site of crack initiation, crack front morphology, and fracture surface marker band details (discussed later). The examinations revealed that 45%, 77%, and 33% of the rivet holes examined in panels 1, 3, and 6, respectively, contained fatigue cracks.

TABLE 2 DESTRUCTUVE EXAMINATION SUMMARY

	Panel #1	Panel #3	Panel #6
No. of Bays Examined	3*	3	½
No. of Rivet Holes Examined	256	133	30
No. of Rivet Holes with Cracks	126	103	10
Percentage of Holes with Cracks	45%	77%	33%
No. of Fatigue Cracks Found	188	136	16

* Tear strap regions were examined in panel #1.

2.2 FATIGUE CRACK INITIATION

MSD in the fuselage lap joint is a likely result of cracks nucleating from fretting damage and regions of high stress concentration. The majority of fatigue cracks found in the counter bore riveted lap joint initiated along the faying surface (the interface between the outer and inner skins) of the outer skin

shown in Figure 2. Here, clad layer fretting along the faying surface was caused by repeated relative movement of the inner and outer skin in a highly localized contact area around the rivet hole. A black aluminum oxide on the faying surface marked the fretted region that containing debris and microcracks shown in Figures 2c and 2d. From this highly localized damaged region, fatigue cracks grew initially in a near semicircular manner (Figure 2a). As fatigue crack length increased, the crack front became elliptical in shape (Figure 2b). Many outer skin fatigue cracks propagated to a length of nearly two skin thicknesses prior to breaking through the outboard surface of the outer skin. A likely cause for subsurface cracking is lap joint bending loads and/or compressive residual stress produced from rivet head expansion into the counter bore region of the rivet hole. Figure 3 shows a typical region of crack initiation for the straight shank rivet. Figure 3a shows the fretting damage area (region A in Figure 3c) along the inboard surface of the straight shank hole. Figure 3c shows the fatigue crack and rivet hole region at an oblique angle. The micrograph shown in Figure 3b reveals an abraded surface containing microcracks similar to that observed in Figure 2d. Examination of the rivet shank mating surface (directly opposite of the abraded hole surface) revealed a black aluminum oxide region characteristic of fretting. The elliptical crack front shape shown in Figure 3d suggests the presence of lap joint bending loads (similar to that observed for the counter bore rivet (Figure 2)). The three examples shown in Figure 4a are typical examples of cracking observed in the 100°-countersink lap joint. Inboard corner cracks and shank/countersink corner cracks are located in regions of high stress concentration. These regions also exhibited some evidence of rivet/hole contact suggesting that fretting may have contributed to crack initiation. The third small fatigue crack shown in Figure 4a is located along the rivet hole surface in the rivet shank region; here, fretting is a likely cause for crack initiation. The dashed lines in Figures 4a and 4b mark the crack fronts and show that the small cracks in Figure 4a are circular in shape and at longer crack lengths, shown in Figure 4b, the crack front is somewhat circular in shape.

2.3 FATIGUE CRACK GROWTH DATA BASE

The growth rate of fatigue cracks 50 μm to 10 mm in length contained in panels 1, 3, and 6 was determined by performing detailed fractographic examinations (2-4). The examinations quantitatively determined the rate of crack propagation by tracking the progression of the fatigue crack front determined by the precise location of crack surface marker bands. During full-scale pressure testing, the pressure load was altered to form coded markings (marker bands) on fatigue crack surfaces contained in the lap joint. Figure 5 is an SEM micrograph showing an example of a fatigue crack surface marker band. Here, a six band code is used to mark the exact location of the crack front for a fatigue crack in panel 1 at 30,000 pressure cycles. Knowing the exact location the crack front at a known load cycle, a comprehensive fatigue crack growth database was developed.

The data shown in Figures 6 and 7 show that upper rivet row fatigue cracks contained in panels 1, 3, and 6 exhibit identical crack growth characteristics. Figures 6a, 6b, and 6c are plots showing marker band based fatigue crack growth rate (da/dN) data for cracks propagating from counter bore rivet holes, straight shank rivet holes, and 100° counter sink rivet holes, respectively. A comparison of the linear regression analysis (dashed and dotted lines) in Figures 6a and 6b reveal that:

- all counter bore cracks in panel 1 (bays 2, 3, and 4) exhibit the same crack growth characteristics, and
- all straight shank cracks in Panel 3 (bays 1 and 2) and Panel 6 (bay 4) exhibit the same crack growth characteristics.

A minimal amount of data from 100° counter sink rivet holes is shown in Figure 6c for panel 3 (bay 3). The excellent agreement of 100° counter sink crack growth rate data with the linear regression

analysis from Figures 6a and 6b (dashed line in Figure 6c) suggests that all fatigue cracks contained in the three different rivet configurations exhibit similar crack growth rate characteristics. A summary of all marker band based da/dN data is presented in Figure 7. This plot reveals that fatigue crack growth in riveted lap joint fuselage structure is well behaved; here, no appreciable difference is observed for data obtained from three rivet configurations, seven lap joint bays, and three different fuselage locations. The quantitative data in Figure 7 strongly suggest that the fatigue crack growth behavior of lap joint cracks ranging in size from 50 μm to 10 mm is deterministic and predictable.

Quantifying the fatigue crack growth rates for cracks of length less than 100 μm is problematic. Within the microstructural small crack regime (crack lengths < 50 to 100 μm), marker band analysis becomes extremely difficult and little data was obtained from the riveted structure. To estimate the growth rate behavior of microstructural small fatigue cracks in the lap joint, laboratory test results were used. The local stress at the rivet hole was estimated using the same procedure used for previous predictions of fatigue crack growth in panel 1 (5). Here, a neat pin (rivet) was assumed and a local stress of 143 MPa was estimated from the following parameters: S_{remote} = 90 MPa (remote stress in based on test article operational pressure) (6), 29% of the load is carried by the upper rivet in a four rivet row lap joint, and bending is $S_{bending} = \gamma S_{remote}$ where $\gamma = 0.5$ (7,8). A large body of small crack growth data for aluminum alloy 2024-T3 was generated by a "round robin program" conducted by thirteen laboratories (9). Each laboratory used a single edge (blunt) notch specimen and a replica technique for monitoring the growth of surface and corner fatigue cracks propagating from the blunt notch tested at a local stress level of 145 MPa. Because the small crack growth data were generated at a local stress level similar to the estimated local stress in the lap joint rivet hole, a comparison of laboratory and lap joint fatigue crack growth characteristics can be made. The laboratory microstructural small crack data are compared to the marker band data from panels 1, 3, and 6 in Figure 8 with the general assumption that local stresses due to rivet expansion are second order (neat pin assumption). The results shown in Figure 8 reveal the typical large scatter in microstructural small crack growth data; here, wide variations in small crack growth data are a result of crack front / microstructure interactions (10). A comparison of the linear regression analysis for the lap splice panel data (thick line) with the laboratory small crack data (thin line) suggests a strong correlation between the two data sets. Assuming that rivet fit-up effects are second order, the combined data base shown in Figure 8 represents the fatigue crack growth characteristics for riveted lap joint fuselage structure for crack lengths ranging from the microstructural small regime to 10 mm.

2.4 FATIGUE CRACK GROWTH PREDICTION

Fatigue crack growth predictions made by FASTRAN, a plasticity-induced crack closure based code, are in excellent agreement with lap joint marker band derived crack growth data. Compared in Figure 9 are the fatigue crack growth data and linear regression analysis results (dashed and dotted lines) from the destructive examinations conducted on panels 1, 3, and 6 and the results of two FRASTRAN predictions (5). The combined remote and bending load prediction is in good agreement with the panel data for crack lengths of less than one skin thickness and nearly duplicate the linear regression results. The prediction, using only remote stress, under predicts crack growth rates in the short crack regime (<1 mm). The abrupt transition in the predicted results at crack lengths equal to the skin thickness is due to the change in the crack-tip stress intensity factor expression as the subsurface crack emerges through the outer skin thickness. The results shown in Figure 9 demonstrate that fracture mechanics based analytical methods accurately predict the fatigue crack growth rate behavior in lap joints from distinctly different fuselage locations and containing different rivet configurations (counter bore, straight shank, and 100° counter sink rivets).

The FASTRAN prediction using remote and bending lap joint loads is compared to the marker band based crack length versus load cycle data in Figure 10. Two distinct populations are noted in Figure 10, the open circle data are those cracks that initiated first and grew to longer lengths and the solid data points are cracks that initiated later in life. The straight hole / neat pin prediction shown in Figure 10 assumes an EIFS of 50 μm. The EIFS was based on early destructive examination results suggesting that faying surface fretting in the clad layer (nominal thickness of 50 μm) initiated most upper rivet row lap splice fatigue cracks (2). These assumed parameters resulted in predictions that are in good agreement with most of the counter bore riveted lap joint data (solid data points) in Figure 10a and straight bore riveted lap joint data (solid data points) in Figure 10b. A twenty-percent error is observed between the predicted crack length and the measured crack length (open data points) at 60,000 pressure cycles. It is speculated that the life prediction did not approximate crack (a versus N) behavior (open data points) because fit up stresses may have been significant for those cracks that initiated earlier in life. As these first fatigue cracks grew, fit up forces at neighbor rivet locations decreased. More rigorous predictions are required; they should include, (1) accurate crack-tip stress intensity expressions for observed crack configurations, (2) accurate local stress concentration factor for the rivet hole configuration, (3) understanding of lap splice rivet hole local stress relaxation as a function of fatigue life, and (4) an appropriate EIFS for each fatigue crack initiation type.

SUMMARY

This research has established a comprehensive data-base that fully characterizes fuselage riveted lap joint multi-site fatigue damage. After 60,000 pressure cycles, the fuselage exhibits isolated regions of lap joint MSD that is characterized by small fatigue cracks contained in 50 to 80 percent of the rivet holes. Crack initiation is linked to mating surface fretting damage and regions of high stress concentration. The upper rivet row is most prone to subsurface outer skin crack growth; here, cracks can grow to two thicknesses in crack length before penetrating the outer skin outboard surface. No appreciable difference in fatigue crack growth characteristics was observed for cracks emanating from three rivet configurations, seven lap joint bays, and three different fuselage locations. These quantitative data strongly suggest that the fatigue crack growth behavior of lap joint cracks ranging in size from 50 μm to 10 mm is deterministic and predictable. Excellent correlation between marker band based lap joint fatigue crack growth rates and laboratory data suggest that microstructural small crack data can be used to verify predictions. FASTRAN code predictions of fatigue crack growth correlate with the destructive examination data base, thus showing that fracture mechanics based methods predict the growth of multi-site fatigue damage in the lap joint.

ACKNOWLEDGEMENT

The authors wish to gratefully acknowledge Mr. Michael L. Gruber and Ms. Anastasia Arseniev of the Boeing Co. for their technical guidance.

REFERENCES

1. Swift, T., "Widespread Fatigue Damage Monitoring – Issues and Concerns", Proc. of Intn'l. Symposium on Advanced Structural Integrity Methods for Airframe Durability and Damage Tolerance, Edited by C.E. Harris, NASA Conf. Pub. 3274, Hampton, VA, 1994, pp. 829-870.

2. Piascik, R.S. and Willard, S.A., "The Characterization of Fatigue Damage in the Fuselage Riveted Lap Splice Joint", NASA/TP-97-206257, National Aeronautics and Space Administration, Washington, D.C., 1997.
3. Piascik, R.S., Panel #3 Destructive Examination Results, to be published.
4. Piascik, R.S., Panel #6 Destructive Examination Results, to be published.
5. Piascik, R.S. and Willard, S.A., "The Characterization of Multi-Site Fatigue Damage in the Fuselage Riveted Lap Splice Joint", ICAF 97 Fatigue in New and Aging Aircraft, EMAS Publishing, 339 Halesowen Rd., Cradley Heath, West Midlands, UK, 1997, pp.93-114.
6. Gruber, M.L., Mazur, C.J., Wilkins, K.E., and Worden, R.E., "Investigation of Fuselage Structure Subjected to Widespread Fatigue Damage", DOT/FAA/Ar-95/47, National Technical Information Service, Springfield, VA, Feb. 1996.
7. Hartman, A. and Schijve, J., "The Effect of Secondary Bending on the Fatigue Strength of 2024-T3 Alclad Riveted Joints", NLR TR 69116U, Nat. Aerospace Lab. of the Netherlands, 1972.
8. Schijve, J., "Some Elementary Calculations on Secondary Bending in Simple Lap Joints", NLR TR 72036, Nat. Aerospace Lab. of the Netherlands, 1972.
9. Newman, J.C., Jr., and Edwards, P.R., "Short-Crack Growth Behavior in an Aluminum Alloy – An AGARD Cooperative Test Programme", AGARD Report No. 732, 1988.
10. Small Fatigue Cracks, Edited by R.O. Ritchie and J. Lankford, TMS-AIME, Warrendale, PA., 1986.

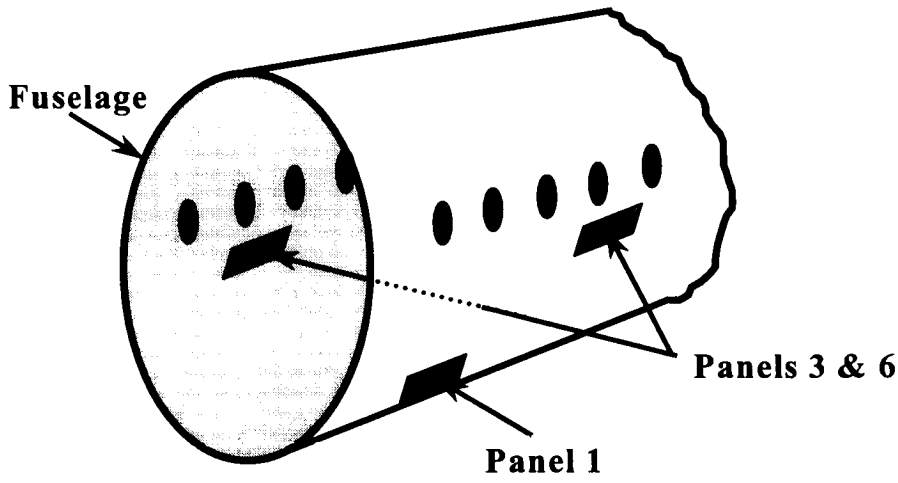

Figure 1. Schematic showing the location of the tear down panels.

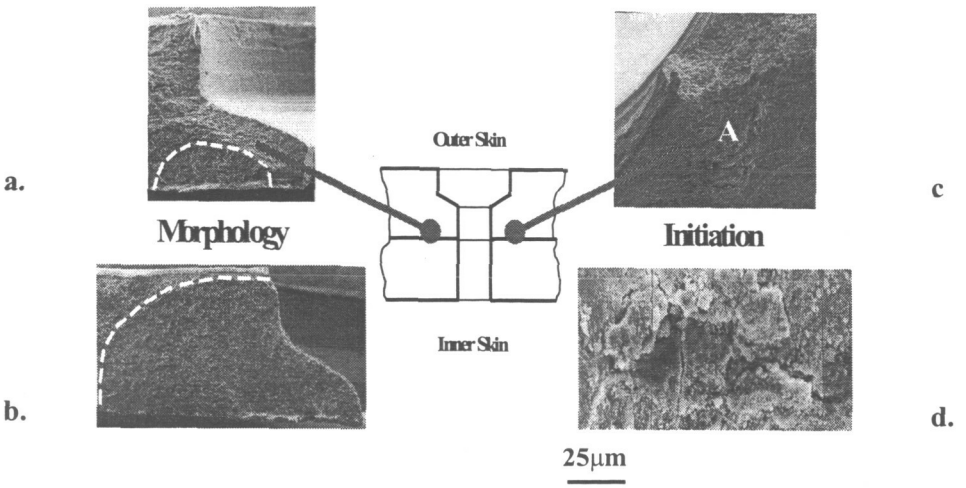

Figure 2. Counterbore rivet outer skin cracking: a) and b) SEM micrographs showing the progression of fatigue cracks (dashed lines mark the crack front), c) micrograph shows the rivet hole at an oblique angle and the location of fretting damage (region A) along the faying surface (site of crack initiation), and d) high magnification micrograph showing fretting debris and microcracks in " region A of Figure 2c".

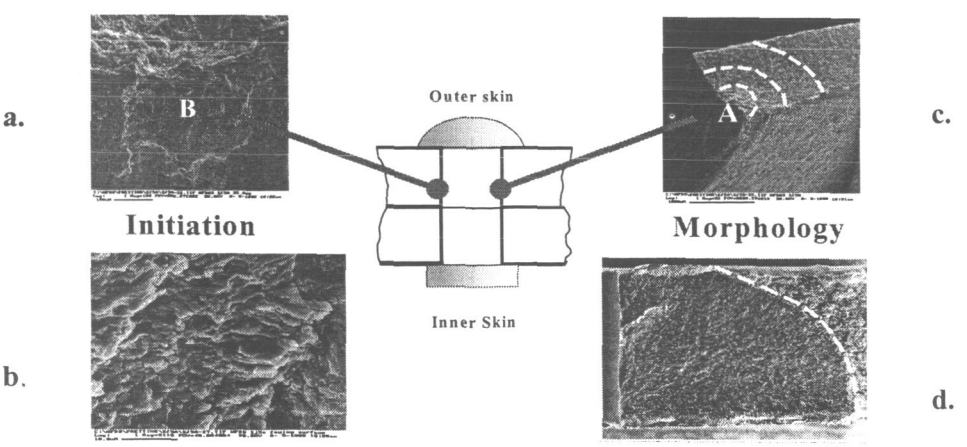

Figure 3. Straight shank rivet outer skin cracking: a) Micrograph of the crack initiation site (region A in "c"), b) high magnification micrograph of fretting surface at region B, c) the micrograph shows the region of crack initiation (region A) along the inside surface of the rivet hole near the inboard corner (dashed lines depict the progression of the fatigue crack), and d) micrograph showing a fatigue crack with multiple initiation sites (arrows) along the surface of the rivet hole (dashed line marks the crack front).

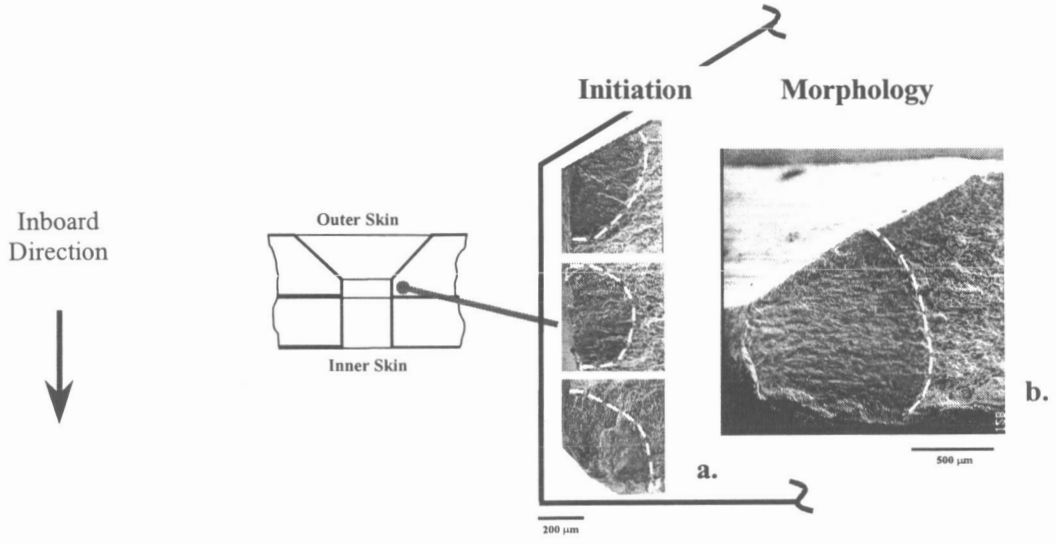

Figure 4. 100° countersink rivet outer skin fatigue cracking: a) Depicted is the outline of the rivet hole and the micrographs show the typical crack initiation sites along the rivet hole surface and crack morphology (dashed lines mark the crack front) and b) shows the typical crack front shape of a fatigue crack that has propagated nearly one-half the length of the counter sink.

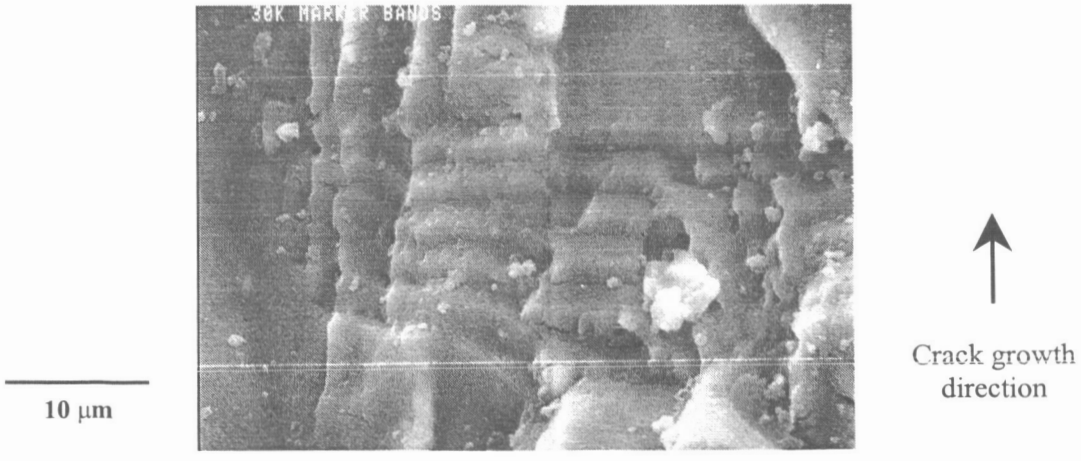

Figure 5 The micrograph shows a markerband from a fatigue crack surface in panel 1. This markerband locates the crack front at 30,000 pressure cycles.

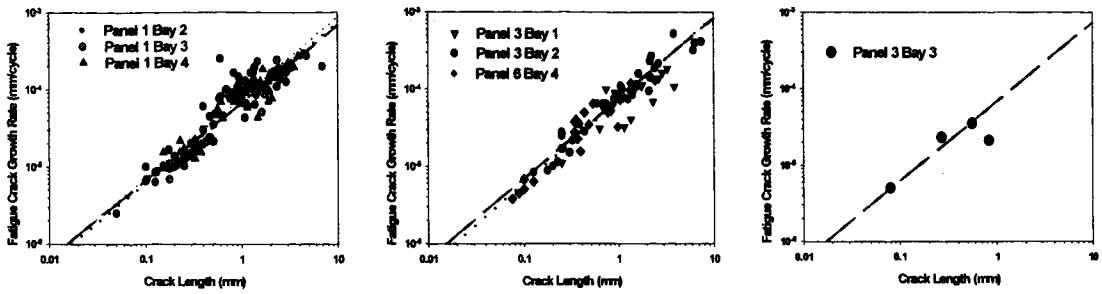

Figure 6. Plots of fatigue crack growth rate versus crack length for the a) counter bore rivet, b) straight shank rivet, and c) 100° counter sink rivet.

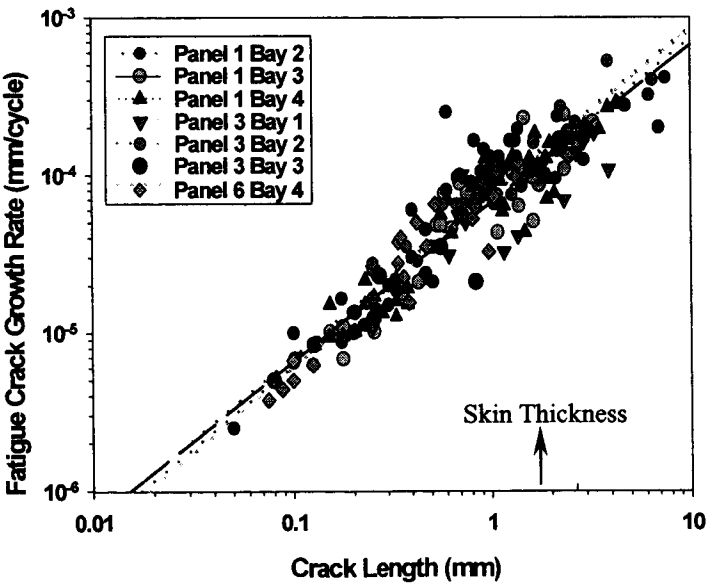

Figure 7. Summary of marker band based fatigue crack growth data from panels 1, 3, and 6.

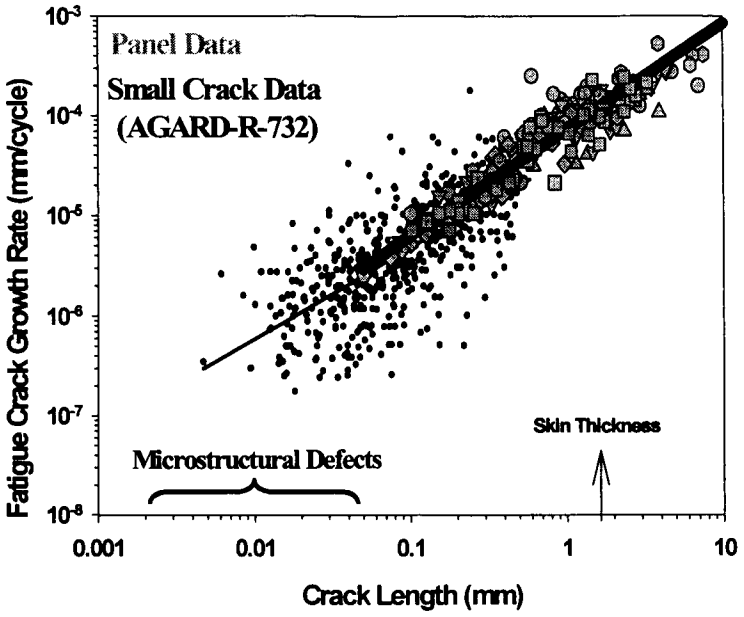

Figure 8. Comparison of small crack growth laboratory data and lap joint marker band based crack growth data from panels 1, 3, and 6.

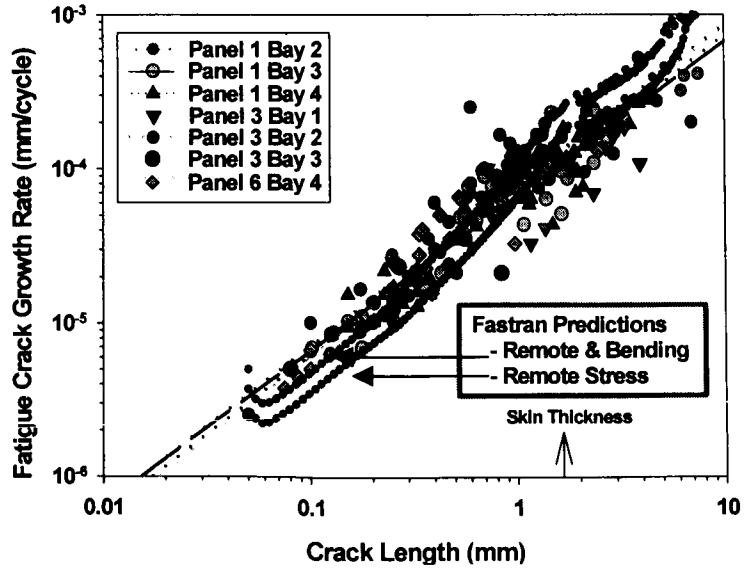

Figure 9. Comparison of two FASTRAN Code predictions (remote plus bending stress and bending stress) and crack growth rate data obtained from real aircraft lap joint structure.

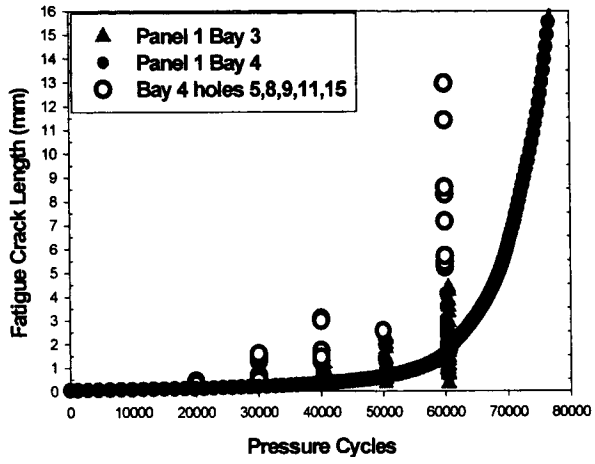

a.

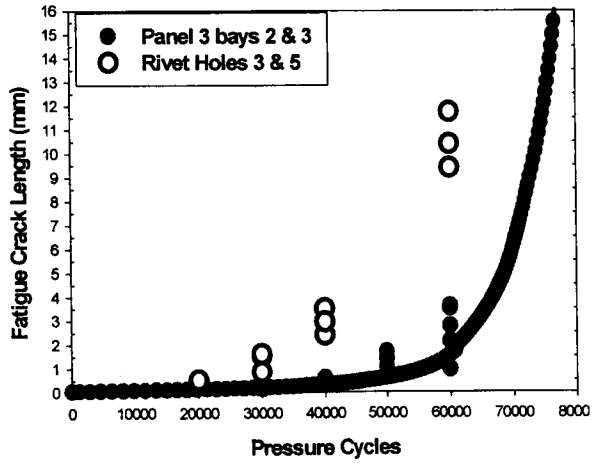

b.

FASTRAN Prediction

Figure 10. Comparison of FASTRAN Code prediction and marker band based crack length versus load cycle data obtained from) counterbore riveted and b) straight shank riveted structure.

RESIDUAL STRENGTH PRESSURE TESTS AND NONLINEAR ANALYSES OF STRINGER- AND FRAME-STIFFENED ALUMINUM FUSELAGE PANELS WITH LONGITUDINAL CRACKS

Richard D. Young, Marshall Rouse, Damodar R. Ambur, and James H. Starnes, Jr.
NASA Langley Research Center
Hampton, VA 23381
Tel: 757-864-2894
Fax: 757-864-7791
r.d.young@larc.nasa.gov

ABSTRACT

The results of residual strength pressure tests and nonlinear analyses of stringer- and frame-stiffened aluminum fuselage panels with longitudinal cracks are presented. Two types of damage are considered: a longitudinal crack located midway between stringers, and a longitudinal crack adjacent to a stringer and along a row of fasteners in a lap joint that has multiple-site damage (MSD). In both cases, the longitudinal crack is centered on a severed frame. The panels are subjected to internal pressure plus axial tension loads. The axial tension loads are equivalent to a bulkhead pressure load. Nonlinear elastic-plastic residual strength analyses of the fuselage panels are conducted using a finite element program and the crack-tip-opening-angle (CTOA) fracture criterion. Predicted crack growth and residual strength results from nonlinear analyses of the stiffened fuselage panels are compared with experimental measurements and observations. Both the test and analysis results indicate that the presence of MSD affects crack growth stability and reduces the residual strength of stiffened fuselage shells with long cracks.

1. INTRODUCTION

The fail-safe design philosophy applied to transport aircraft fuselage structures requires that the structures retain adequate structural integrity in the presence of discrete source damage or fatigue cracks. As economic factors encourage the use of commercial and military transport aircraft well beyond their original design requirement, it has become increasingly important to develop methods to predict accurately the residual strength of structures with cracks. The goal of NASA's Aircraft Structural Integrity Program is to develop a verified nonlinear structural analysis methodology for stiffened structures with damage and subjected to combined internal pressure and mechanical loads. The approach to accomplish this goal has been to: develop hierarchical modeling strategies required to represent the multi-dimensional length scales present in fuselage shells with cracks and multiple-site damage (MSD); develop material and geometric nonlinear shell analysis capabilities and conduct nonlinear analyses of stiffened shells subjected to internal pressure and mechanical loads; and conduct experiments to verify analyses and to identify critical behavioral characteristics.

The present paper presents recent results of residual strength pressure tests and nonlinear analyses of stringer- and frame-stiffened aluminum fuselage panels with longitudinal cracks. The tests and analyses, performed by the Structural Mechanics Branch at the NASA Langley Research Center, were intended to verify the analyses methods and to identify critical behavioral characteristics of the crack growth in generic wide-

body fuselage panels with long cracks. Two damage conditions are considered: a longitudinal crack located midway between stringers, and a longitudinal crack adjacent to a stringer and along a row of fasteners in a lap joint that has multiple-site damage (MSD). The loading condition for the panels is internal pressure plus axial tension loads. The axial tension loads are equivalent to a bulkhead pressure load. The fuselage panel tests are described and experimental results are reported. Then, analysis and finite element modeling methods using the STructural Analysis of General Shells (STAGS) program[1] are described. A description of the crack-tip-opening-angle (CTOA) skin fracture criterion[2,3] and the procedure for defining fracture parameters based on small laboratory specimens are presented. Predicted crack growth and residual strength results from nonlinear analyses on the stiffened fuselage panels are then compared with experimental measurements and observations.

2. EXPERIMENTS

Two stringer- and frame-stiffened aluminum fuselage panels with longitudinal cracks were tested in the pressure-box test machine at NASA Langley Research Center. The test specimens, the test machine, and the test method, are described. Then, the test results are presented.

2.1 TEST SPECIMENS

The first fuselage panel tested in this study, ASIP1, has six stringers and three frames, and is shown in Fig. 1 prior to testing. The overall dimensions of the panel include a 122-in. radius, a 72-in. length, and a 63-in. arc width. The skin is 0.063-in.-thick 2024-T3 aluminum with the sheet rolling direction parallel to the stringers. The stringers are 7075-T6 aluminum Z-section stringers with a stringer spacing of 8.1 in. The frames are 7075-T6 aluminum I-section frames with a frame spacing of 22 in. There are 0.063-in.-thick 2024-T3 aluminum circumferential tear straps, bonded to the skin, and located midway between the frames. The stringers and frames are riveted to the skin, and the frames are connected to the stringers by riveted stringer clips. Aluminum doublers are fastened to the curved ends of the panel between the stringers and along the sides of the panel between the frames. These doublers distribute the loads from the axial and hoop load plates into the panel skin, and they are slotted to be flexible in the direction parallel to the panel edges. The initial damage for panel ASIP1 was a 10-in.-long longitudinal crack, located midway between stringers and centered on a severed frame, as indicated in Fig. 1.

The second fuselage panel tested in this study, ASIP2, has four stringers and three frames, and is shown prior to testing in Fig. 2(a). The overall dimensions of this panel are the same as for ASIP1: a 122-in. radius, a 72-in. length, and a 63-in. arc width. The skin is 0.063-in.-thick 2024-T3 aluminum with the sheet rolling direction parallel to the stringers. The stringers are 2024-T3 aluminum inverted hat-section stringers with a stringer spacing of 14 in. The frames are 2024-T3 aluminum Z-section frames with a frame spacing of 22 in. There are 0.040-in.-thick 2024-T3 aluminum waffle tear straps, bonded to the skin, and located under the stringers and frames, but there are no tear straps midway between the frames. The stringers and frames are riveted to the skin and tear straps, and the frames are connected to the stringers by riveted stringer clips. Aluminum doublers are fastened to the curved ends of the panel between the stringers and along the sides of the panel between the frames to distribute the loads from the axial and hoop load introduction plates into the panel skin. There is a lap joint in this panel under the second stringer from the left as the panel is shown in Fig. 2(a). In the lap joint, the skin from the right side of the panel is the outer skin and overlaps at a greater radius over the inner skin from the left side of the panel. The layers of the lap joint are connected with three rows of 0.125-in.-diameter countersunk fasteners. The fastener pitch in the longitudinal direction is 1.0 in., and the three rows of fasteners are spaced 1.33 in. in the circumferential direction with the middle row of fasteners centered on a hat-section stringer. The initial damage for panel ASIP2 consisted of a 10-in.-long longitudinal lead crack and MSD cracks along the edge of the lap joint. The 10-in.-long lead crack was located adjacent to the second stringer and centered on a severed frame, as indicated in Fig. 2(a). A schematic

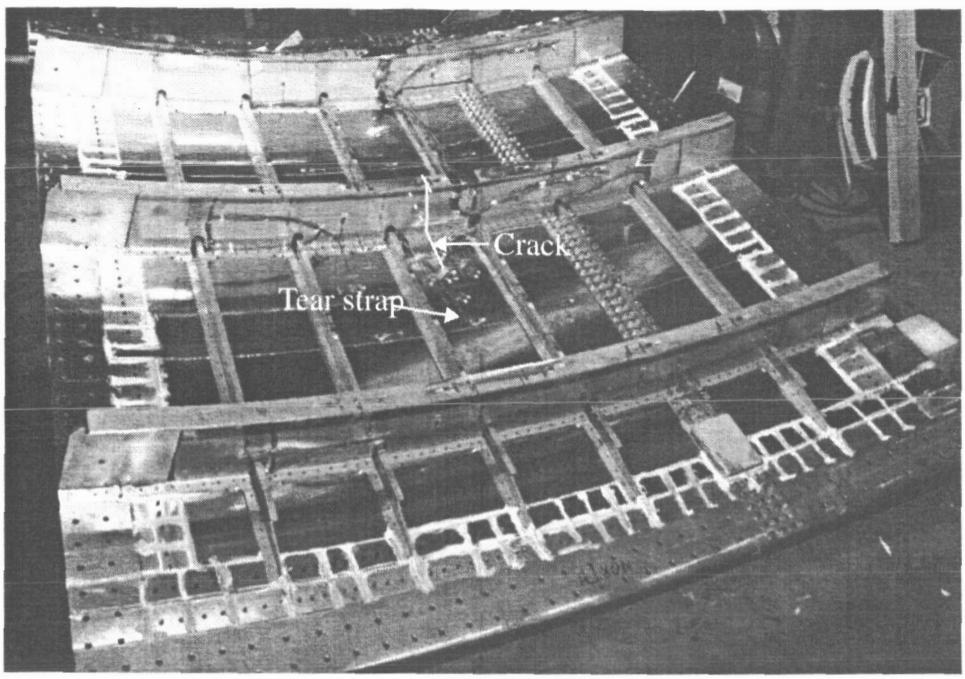

Figure 1. Panel ASIP1 prior to testing.

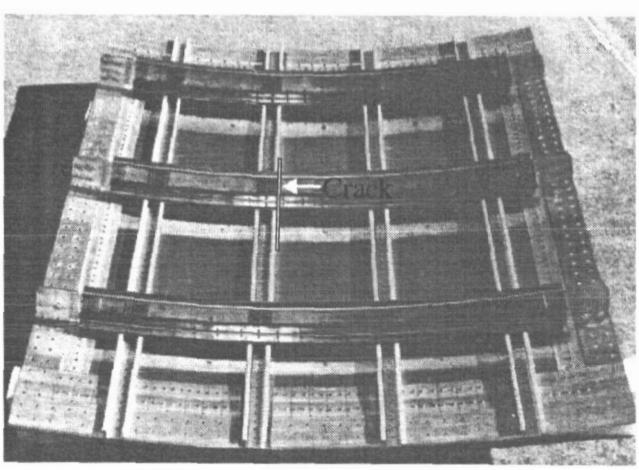

(a) Photograph of panel ASIP2

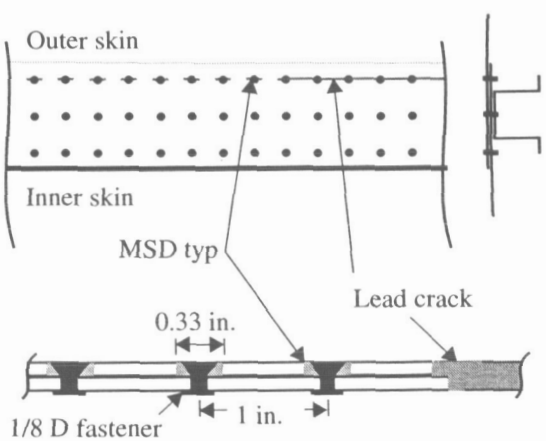

(b) Lap joint detail with lead crack and MSD cracks

Figure 2. Panel ASIP2 prior to testing.

of the lap joint, shown in Fig. 2(b), indicates that the lead crack was along the third row of fasteners in the lap joint. The MSD cracks were introduced prior to panel assembly by making small longitudinal cuts in the outer skin of the lap joint that extend 0.05 in. on each side of the fastener countersink for each fastener in the third row of fasteners. The resulting initial damage state was a 10-in.-long longitudinal lead crack with 0.33-in.-long MSD cracks in the outer skin, spaced ahead of the lead crack with a 1 in. pitch. The lead crack and MSD cracks were defined to be along the 'critical third row of fasteners' which is where lap joint eccentricity, pressure pillowing of the skin, and the fastener countersink combine to promote crack growth in the outer skin.

2.2 PRESSURE-BOX TEST MACHINE AND TEST METHOD

A schematic of the pressure-box test machine is shown in Fig. 3. The pressure-box test machine is capable of applying axial tensile loads of up to 7,000 lb/in. and internal pressure loads of up to 20 psi. Axial loads are applied at each end of the panel by two 225-kip hydraulic actuators connected to curved steel load introduction plates. Pressure is applied to the concave side of the panel using a 100 psi air supply source and a pneumatic control system. Circumferential or hoop loads that develop in the skin of the panel are reacted by flat steel load introduction plates attached to the straight edges of the panel, and two steel rods that connect each load introduction plate to the rigid steel frame of the pressure-box test machine. Hoop loads that develop in the frames of the panel are reacted by steel rods that connect each end of the panel frames to the rigid steel frame of the test machine. Each steel rod that reacts the hoop loads includes a turnbuckle device that can be adjusted to ensure that hoop loads of proper magnitudes are introduced in the panel frames and skin for a given loading condition. The reaction loads in the hoop rods are measured by load cells built into the rods. A continuous rubber seal is connected to the bottom of the axial and hoop load plates and to the top of the steel pressure containment box to permit the panel to float freely when pressurized and to minimize air leakage. A detailed description of this test machine is provided in Ref. 4. The loading condition for the two fuselage panels that were tested was a combination of internal pressure plus axial tension loads. The axial load was prescribed to be equivalent to the bulkhead pressure load in a closed pressurized cylinder, and was applied during the test in proportion to the internal pressure load. Strain gages, linear variable displacement transducers, and video cameras were used to measure the panel response.

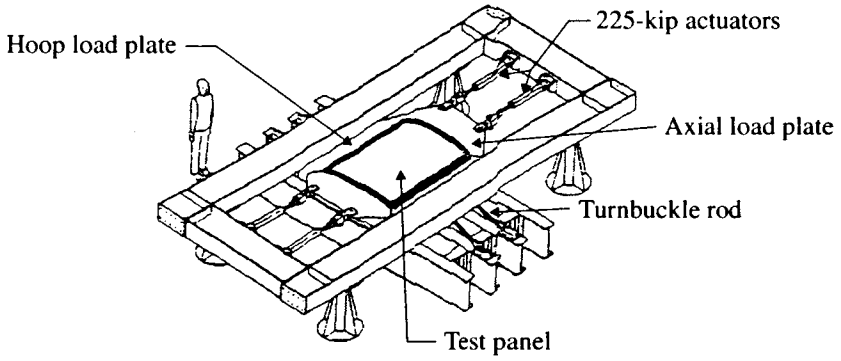

Figure 3. Pressure-box test machine.

2.3 TEST RESULTS

The test results for ASIP1 are summarized in Fig. 4. As the internal pressure was increased, each end of the skin crack extended in the longitudinal direction until it intercepted the adjacent tear strap. The crack growth behavior was symmetric with respect to the central severed frame. A photograph of the entire panel after testing is shown in Fig. 4(a), and a close-up of the crack trajectory on one end of the initial crack is shown in Fig. 4(b). From the video record of the test, it was determined that the crack growth behavior was as indicated on the right side of Fig. 4(b). The initial crack tip location is identified at the bottom of this figure. When the pressure was increased to 14.6 psig, the crack had extended approximately 0.85 in. on each end. At a pressure of 15.9 psig, the crack had extended by 1.95 in. from the initial crack tip location. Then, as the pressure was increased from 15.9 psig to 16.1 psig, the skin crack extended an additional 3.15 in. on each end and then stopped growing when the crack tip propagated to the edge of the adjacent bonded tear strap. The first 1.95 in. of crack growth displayed stable tearing, while the final tearing was marginally stable, extending more than 3 in. over a five second time interval with only a 1.3% increase in load. When the crack growth stopped at the tear straps, the initial 10-in.-long crack had extended to a total length of 20.2 in. and the test was terminated.

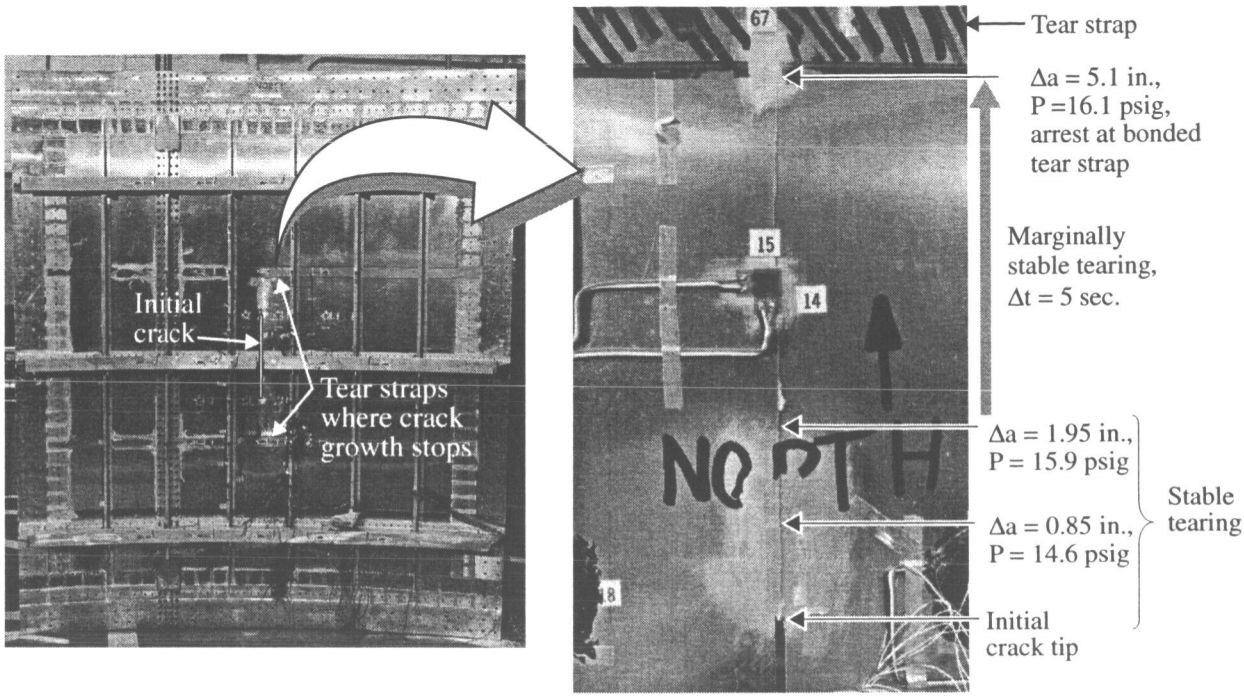

(a) Panel after testing, crack length increased from 10 in. to 20.2 in.

(b) Crack trajectory on one end of the crack

Figure 4. Panel ASIP1 test results.

When panel ASIP2 was tested in the pressure-box test machine, the video record did not show any visible crack growth for pressure levels less than 9.95 psig. When the pressure reached 9.95 psig, the lead crack suddenly extended on each end of the crack, and linked up with the series of MSD cracks ahead of the lead crack. The crack extended in the longitudinal direction in a fast fracture mode, and extended over the entire panel length in an instant. The crack growth behavior was symmetric with respect to the central severed frame. Photographs which characterize the failure of panel ASIP2 are shown in Fig. 5. A view of the outer surface of the panel is shown in Fig. 5(a) which shows that the skin crack has extended the full length of the panel. A view of the inner surface of the panel is shown in Fig. 5(b) which shows that the skin crack has extended past the adjacent frame and tear strap, failing each of these components at fastener hole locations. A close-up of the crack trajectory is shown in Fig. 5(c) which shows the link-up of the MSD cracks along the row of fasteners with the lead crack growing to the right, and the MSD cracks growing to the left and right so that link-up occurs midway between the fasteners.

3. ANALYSES

The analysis method used in the present study to predict the residual strength of stringer- and frame-stiffened aluminum fuselage panels with longitudinal cracks is described in this section. All analyses were conducted using the STAGS (STructural Analysis of General Shells) nonlinear shell analysis code.[1] An overview of the STAGS code and a description of the finite element modeling used are presented. A skin fracture criterion and a method of determining the fracture parameters from small laboratory tests are described. Then, the results of nonlinear analyses of the fuselage panels with damage are presented and compared to the experimental results.

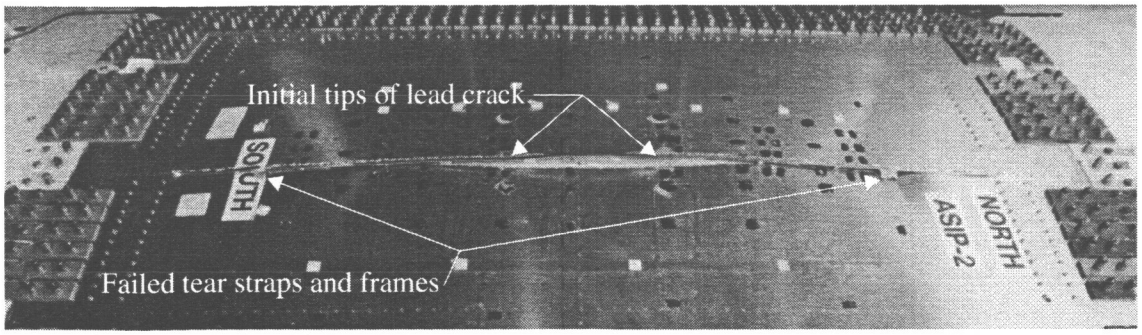

(a) Self-similar crack growth over the entire length of panel, failing adjacent tear straps and frames

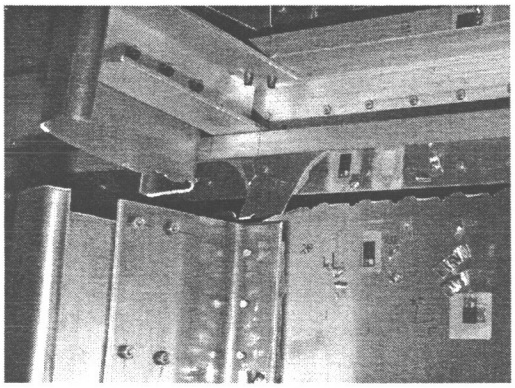

(b) Failed tear strap and frame

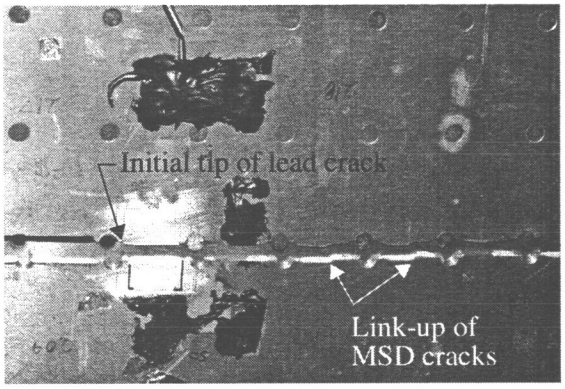

(c) Crack trajectory with link-up of MSD cracks

Figure 5. Panel ASIP2 after testing.

3.1 NONLINEAR ANALYSIS CODE AND FINITE ELEMENT MODELING

STAGS is a finite element code for analyzing general shells and includes the effects of geometric and material nonlinearities in the analysis. The code uses both the modified and full Newton methods for its nonlinear solution algorithms, and accounts for large rotations in a shell by using a co-rotational algorithm at the element level. The Riks pseudo arc-length path following method[5] is used to continue a solution past the limit points of a nonlinear response. The plasticity model in STAGS applies a mechanical sublayer distortional energy plasticity theory. Nonlinear material properties are defined by prescribing a piecewise linear representation of the elastic-plastic stress-strain curve. The material properties of 2024-T3 and 7075-T6 aluminum alloys are given in Fig. 6. The material properties for 2024-T3 are for the T-L orientation since the fuselage test panels have both the sheet rolling direction and the skin cracks parallel to the longitudinal direction.

STAGS can perform crack-propagation analyses, and can represent the effects of crack growth on nonlinear shell response. A nodal release method and a load relaxation technique are used to extend a crack while the shell is in a nonlinear equilibrium state. The changes in the stiffness matrix and the internal load distribution that occur during crack growth are accounted for in the analysis, and the nonlinear coupling between internal forces and in-plane and out-of-plane displacement gradients that occurs in a shell are properly represented. In addition to the nonlinear equilibrium solution, output from STAGS calculations includes the following crack-tip fracture parameters: strain-energy-release rates (used to predict crack growth rates for fatigue loading conditions and residual strength crack extension from an elastic analysis) and the crack-tip-opening angle (CTOA, used to determine residual strength crack extension from an elastic-plastic analysis).

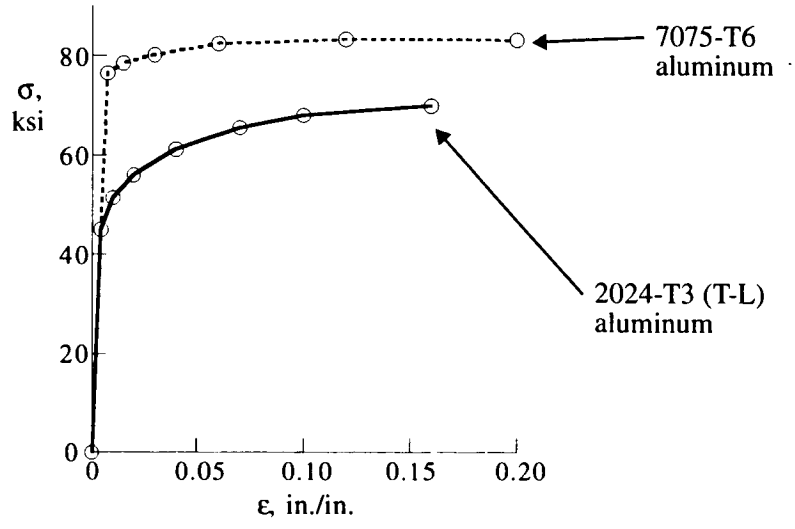

σ, ksi	ε, in./in.
0.00	0.00
76.5	0.0074
78.5	0.015
80.0	0.03
82.3	0.06
83.3	0.12
83.4	0.20

σ, ksi	ε, in./in.
0.0	0.00
45.0	0.0043
51.5	0.01
56.0	0.02
61.0	0.04
65.5	0.07
68.0	0.10
70.0	0.16

Figure 6. Piecewise linear stress-strain curves for 7075-T6 and 2024-T3 (T-L) aluminum alloys.

Procedures for computing the strain-energy-release rates using the modified crack closure integral method, and computing the linear elastic fracture mechanics stress-intensity factors from the strain-energy-release rates are described in Refs. 6-8.

Finite element models are constructed using a collection of two-node beam elements, two-node fastener elements, and four-node plate elements.[9] In addition, five- and seven-node mesh-transition elements which provide 2:1 mesh refinement are used to develop a mesh that has a high level of mesh refinement near the crack and a coarse mesh far away from the crack. Each node of the model has six degrees of freedom. Structural components including skins, stringers, frames, tear straps, and stringer clips are modeled by plate elements to represent accurately the cross sectional shapes of all components.

Riveted connections between structural components are modeled using beam elements, or fastener elements in the region close to a crack, where fastener flexibility is thought to affect load transfer. The fastener elements represent the offsets of the joined components with rigid links that are connected by spring elements with six degrees of freedom. The spring elements can model elastic-plastic behavior, and fastener breakage if a prescribed fastener strength is exceeded. In the fuselage panels considered in the present paper, the fastener loads are relatively low. Thus, in the analyses conducted for the present paper, the fastener elements are assumed to be linear elastic and fastener failure is not considered. The axial, flexural, and torsional stiffnesses of the spring elements are estimated by assuming that the fastener behaves like a simple elastic rod with a diameter equal to the fastener diameter. The elastic shear stiffness of the fastener is computed using the empirical relation developed by Swift,[10]

$$K_s = \frac{ED}{\left[A + C\left(\frac{D}{B_1} + \frac{D}{B_2}\right)\right]}$$

where E is the elastic modulus of the sheet material, D is the fastener diameter, B_1 and B_2 are the thicknesses of the joined sheets, and A and C are empirical factors, equal to 5.0 and 0.8, respectively, for aluminum rivets. This empirical stiffness represents the net shear stiffness of the fastener-sheet connection and accounts for bearing deformations, thus the finite element models do not include modeling of the fastener hole or the countersink details. Also, if the fastener element is joining surfaces with fine meshes, then the fastener load should be distributed to over an area on the surface so that local surface deformations do not reduce the ef-

fective stiffness of the fastener-sheet connection. Load distribution can be accomplished by defining rigid links, beam elements, or a least-squares loading condition to connect the fastener node to the surrounding shell nodes.[11] The area in the shell over which the fastener load is distributed should be of the order of the fastener cross-sectional area, since distributing the load over a larger area may inadvertently stiffen the shell. The bonded tear straps and the skin are modeled as stacked layers in a single shell with the appropriate eccentricity included, thus ignoring any flexibility in the adhesive bond. For conditions where deformation of the model would cause interpenetration of elements, the general contact capability in STAGS is invoked to prevent such penetration.

To simulate the experimental conditions, the finite element models include the load introduction hardware and replicate the loading conditions as applied in the experiments. Symmetry conditions are applied in the model whenever possible to increase the computational efficiency.

3.2 FRACTURE CRITERION

The fracture criterion currently implemented in the STAGS code is the crack-tip-opening-angle (CTOA) criterion. The CTOA criterion is supported by experimental measurements of the critical angle during stable crack growth, and has been shown to be well suited for modeling stable crack growth in ductile materials and predicting the onset of unstable crack growth in fracture analyses conducted using elastic-plastic finite element methods.[2,3] The CTOA is defined as the angle made by the upper crack surface, the crack tip, and the lower crack surface, evaluated at a fixed distance from the moving crack tip, as illustrated in Fig. 7. The CTOA criterion assumes that crack extension will occur when the CTOA reaches a critical value, $CTOA_{cr}$, and that the $CTOA_{cr}$ will remain constant as the crack extends. In a finite element analysis which typically uses two-dimensional plane stress elements, plane strain elements are used in a region on each side of the crack line to simulate the three-dimensional constraint effects developed at the local crack tip.[12] The width of the plane strain region on each side of the crack line is commonly referred to as the plane strain core height, h_c, and is approximately equal to the thickness of the specimen. The parameters $CTOA_{cr}$ and h_c are shown schematically in Fig. 7. The values of $CTOA_{cr}$ and h_c depend on the sheet material, the orientation of the crack relative to the sheet rolling direction, and the sheet thickness, and are determined by correlating elastic-plastic finite element analyses and experimental results for small laboratory specimens.

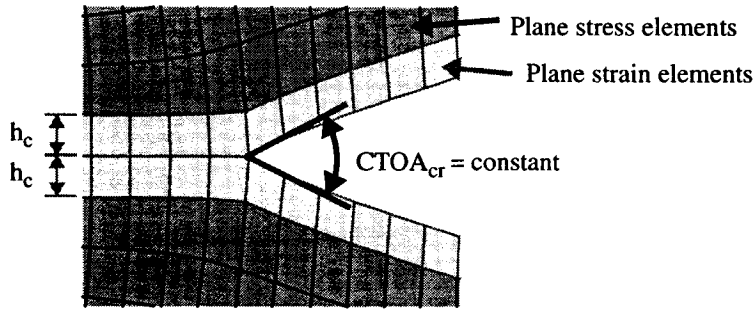

Figure 7. Critical crack-tip-opening angle, $CTOA_{cr}$, and plane strain core height, h_c.

3.3 DETERMINATION OF FRACTURE PARAMETERS

The procedure for determining the values of $CTOA_{cr}$ and h_c from small laboratory specimens for use in the residual strength analyses of the fuselage panels is described. It is assumed that the fracture parameters are a function of the material, sheet thickness, and crack orientation relative to the sheet rolling direction, but are independent of the structural configuration or loading. For the two fuselage panel tests described in the present paper, the skins were 0.063-in.-thick 2024-T3 aluminum alloy with the sheet rolling direction parallel to the panel's longitudinal axis. The skin cracks in each panel are longitudinal cracks, and the principal

stress and yielding in the skin near the crack is in the direction perpendicular to the crack. Thus, the principal stress and yielding in the skin is perpendicular to the sheet rolling direction, which is referred to as the T-L orientation of the material. To determine the fracture parameters for this material and crack orientation, the Mechanics of Materials Branch at NASA Langley Research Center conducted compact tension (C(T)) and middle-crack-tension (M(T)) laboratory tests on 0.063-in.-thick sheets of 2024-T3 aluminum with the cracks parallel to the sheet rolling direction. The compact-tension test was conducted with a 6-in.-wide specimen with an initial crack length a = 2.4 in. Middle-crack-tension tests were conducted for 12-in.-wide and 24-in.-wide specimens with initial crack lengths 2a = 4 in. and 8 in., respectively. These tests included tests where the sheet was constrained against buckling and tests where buckling of the sheet was allowed. Personnel from the Mechanics of Materials Branch then conducted geometrically linear elastic-plastic analyses of the compact-tension test and the middle-crack-tension tests with buckling constrained. Analyses were conducted using three-dimensional elements in the ZIP3D code[13,14] to determine the value of $CTOA_{cr}$ so that ZIP3D analysis results were consistent with the test results. Using three-dimensional elements eliminates the plane stress and plane strain elements required in a two-dimensional analysis, which allows an independent determination of $CTOA_{cr}$. Then, analyses were conducted using two-dimensional elements in the ZIP2D code[15,16] to determine the value of h_c so that ZIP2D analysis results were consistent with ZIP3D results. By following this procedure, personnel of the Mechanics of Materials Branch determined that $CTOA_{cr}$ = 5.0 deg. and h_c = 0.04 in. for 0.063.in.-thick 2024-T3 aluminum for fracture in the T-L orientation.

To confirm that these fracture parameters could be applied in the STAGS analyses, geometrically nonlinear elastic-plastic analyses were conducted to predict the response of the compact-tension and middle-crack-tension panels, with and without buckling constraints. A typical finite element mesh used for analyzing the M(T) panels is shown in Fig. 8. The finite element models utilize mesh refinement to provide an element size of 0.04 in. along the crack line, and utilize symmetry when possible. The experimental and predicted crack extension results for the C(T) and M(T) panels are shown in Fig. 9 as a function of the applied load. These results verify the selection of $CTOA_{cr}$ = 5.0 deg. and h_c = 0.04 in. and indicate that the analyses with STAGS accurately predict the reduction in strength of the panels caused by the geometrically nonlinear effect of panel buckling.

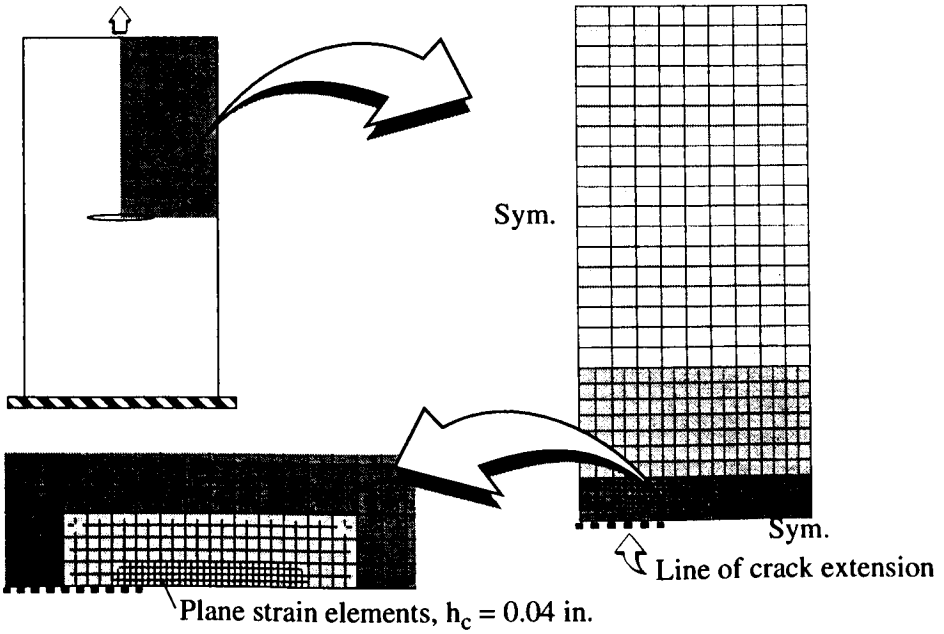

Figure 8. Typical finite element mesh for STAGS analysis of M(T) specimens.

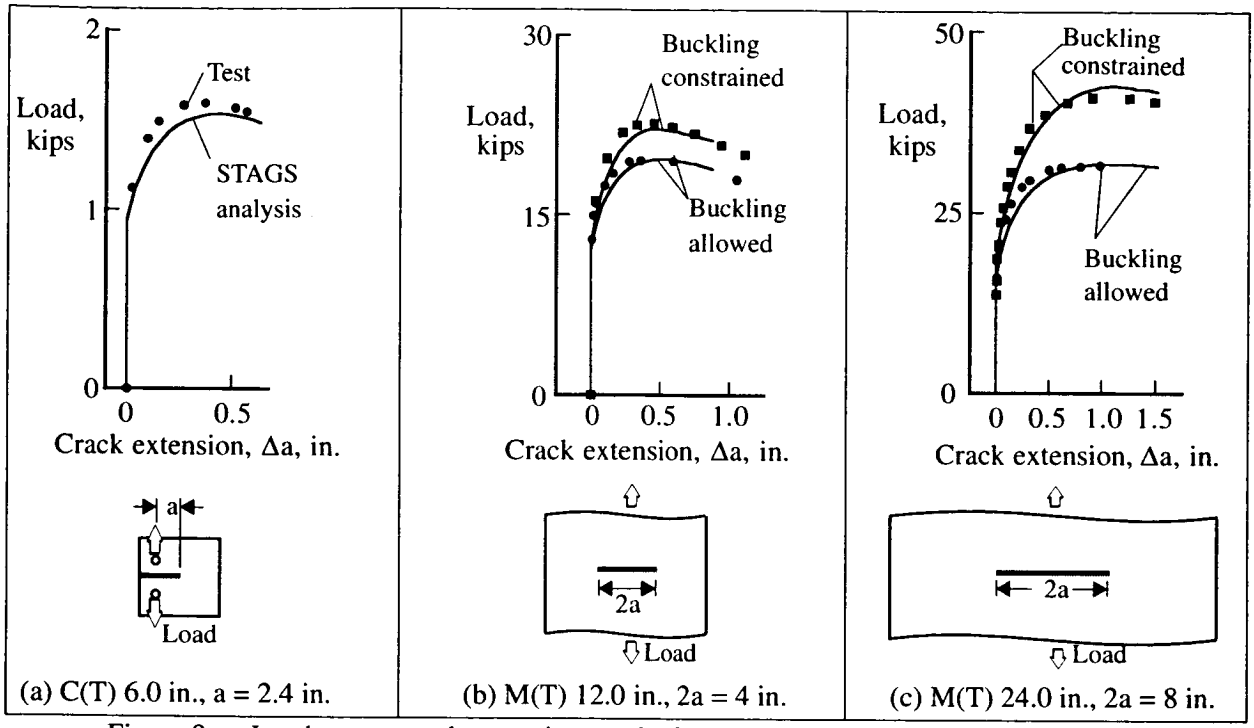

Figure 9. Load versus crack extension results from C(T) and M(T) tests, and nonlinear STAGS analyses with $CTOA_{cr}$ = 5.0 deg. and h_c = 0.04 in.

3.4 FRACTURE ANALYSES OF FUSELAGE PANELS

Geometrically nonlinear elastic-plastic analyses were conducted to predict the residual strength of the two fuselage panels that were tested. In all cases, the element length along the crack is approximately 0.04 in., the region of plane strain elements is defined by h_c = 0.04, and the tearing criterion is $CTOA_{cr}$ = 5.0 deg. The finite element models used for the analyses and results from a typical solution are described. Then, the results of the analyses are compared to the experimental results, with emphasis on the far-field load introduction, the strains in the local region around the crack tip, and the crack extension response as a function of internal pressure.

3.4.1 Fuselage Panel ASIP1

The finite element model for panel ASIP1 has 4,950 elements and 29,300 degrees of freedom, and is shown in Fig. 10. Since this panel has a longitudinal crack that is midway between stringers and is centered on the middle frame, a quarter symmetry model is used for the analysis. The plane of symmetry about the axial direction is located at the center of the middle frame so that only one half of the middle frame cross section is modeled. The plane of symmetry about the hoop direction is located midway between stringers. The asymmetry of the Z-section stringers with respect to this plane is considered to be a small effect and is ignored in the analysis.

A typical solution with 1.0 in. of stable tearing crack extension is shown in Fig. 11. The contour plot of the hoop stress in the region around the crack tip region, shown in Fig. 11(a), indicates a high stress region near the crack tip. A contour plot of the plastic strains in the hoop direction is shown in Fig. 11(b) which indicates the size of the plastic zone around the crack tip, and the existence of a plastic wake which forms behind the moving crack tip as the crack extends.

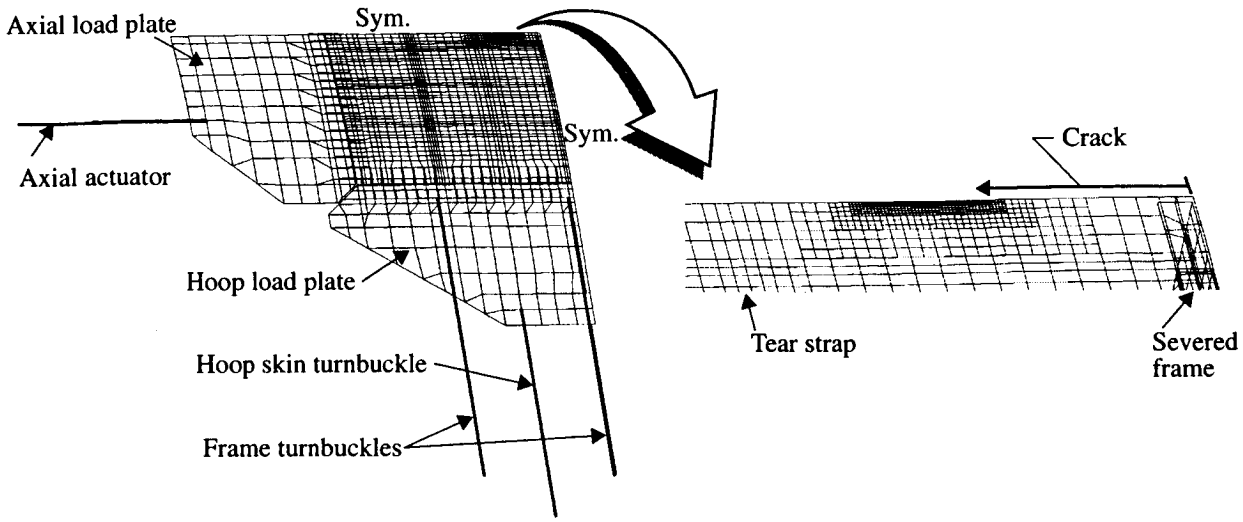

Figure 10. Quarter symmetry finite element model for panel ASIP1.

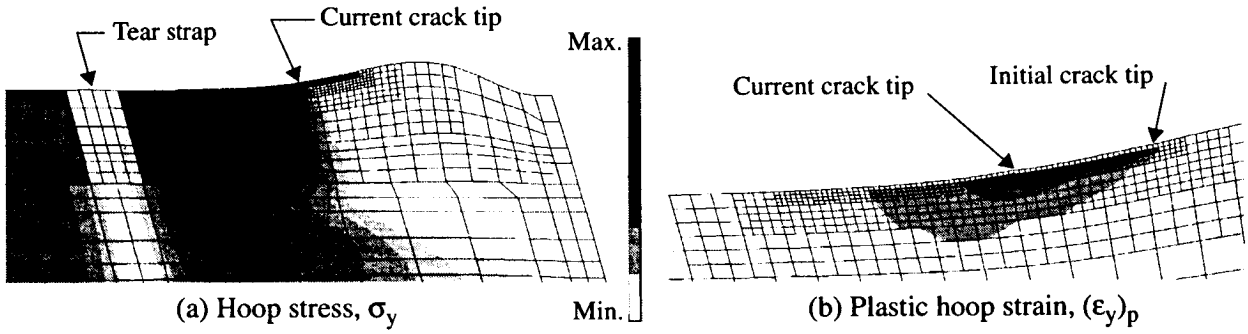

Figure 11. Typical stable tearing analysis results for panel ASIP1 with $\Delta a = 1.0$ in.

The far-field load introduction results predicted by the analysis and measured in the experiment are compared in Fig. 12. The plots of the frame hoop reaction loads and skin hoop reaction loads shown in Figs. 12(a) and 12(b), respectively, indicate good agreement of the results. The predicted and experimental strains in the skin at two locations near the initial crack tip are compared in Fig. 13. The correlation between the predicted and measured skin axial strains and the skin hoop strains shown in Figs. 13(a) and 13(b), respectively, indicates that the finite element model accurately simulates the stress state around the crack tip region.

The crack extension response from the analysis and the experiment is compared in Fig. 14 as a function of pressure. The crack extension data from the experiment were extracted from the video record which did not provide data for crack extension shorter than 0.85 in. These results indicate good agreement in the pressure corresponding to crack extension values of 0.85 in. to 1.0 in., but a discrepancy in the predicted and observed responses occurs for crack extension greater than 1.0 in. In the experiment, after 1.0 in. of crack extension, very small increases in pressure cause significant amounts of crack extension, while the analysis indicates that larger increases in pressure are required for additional crack extension. The values of the pressure for the test and the analysis differ by only 1% for 1 in. of crack extension, but differ by 14% for 2 in. of crack extension. The discrepancy in the nature of the crack growth for crack extension greater than 1.0 in. is consistent with discrepancies that have been observed in test and analysis results of wide unstiffened sheets.

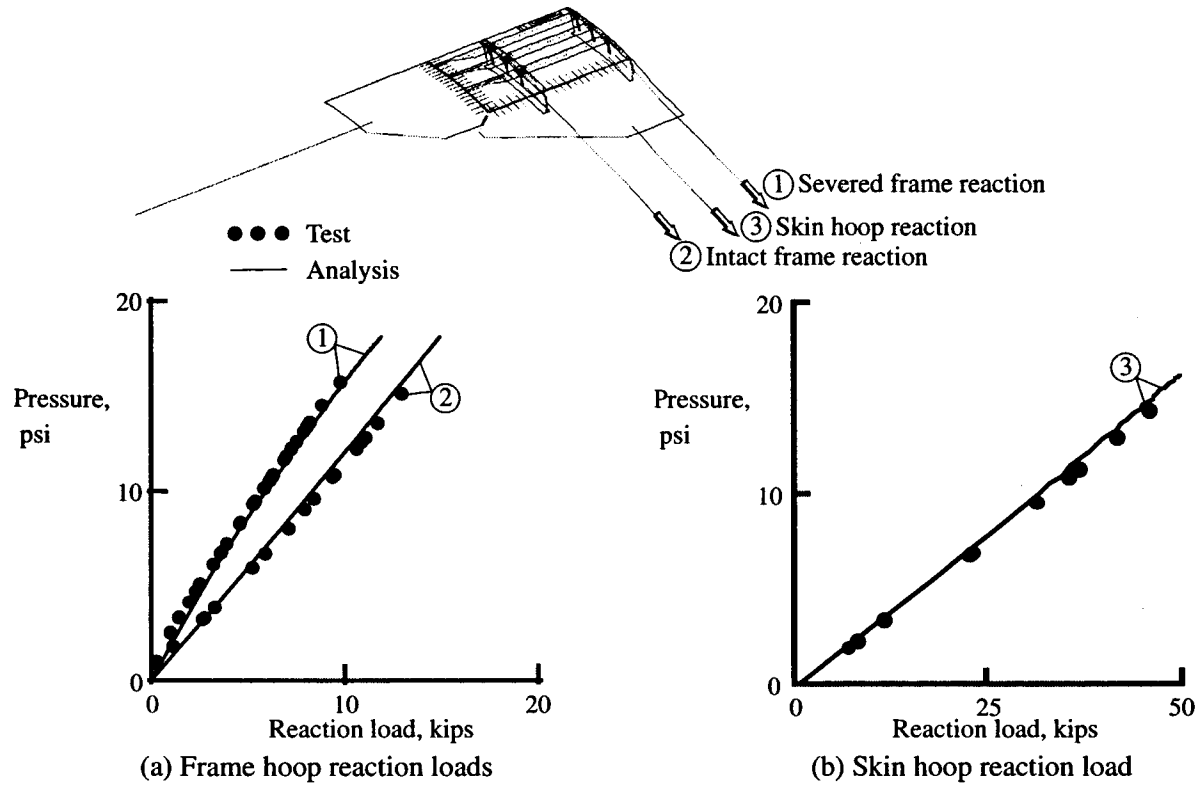

Figure 12. Panel ASIP1 test-analysis correlation of far-field load introduction results.

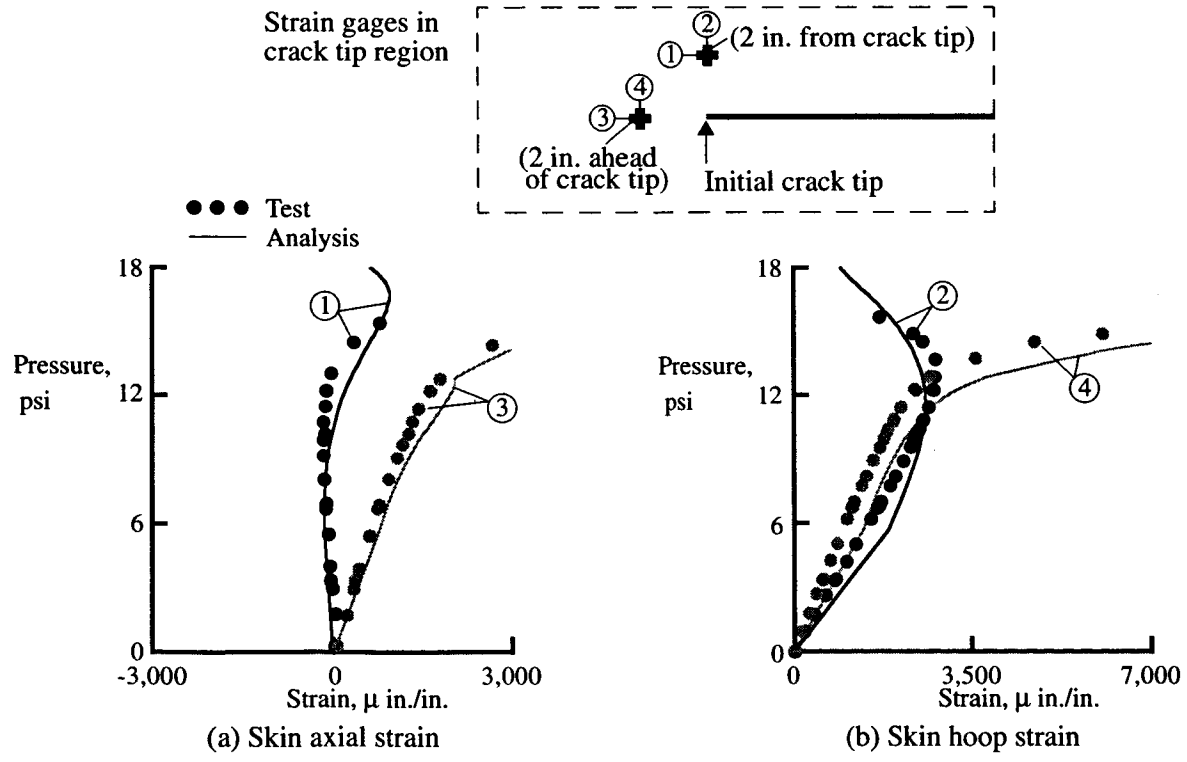

Figure 13. Panel ASIP1 test-analysis correlation of strain results in a crack tip region.

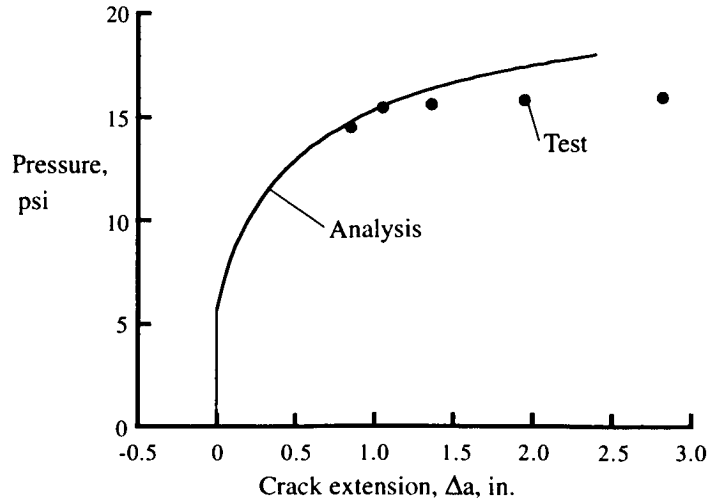

Figure 14. Panel ASIP1 test-analysis correlation of crack extension results as a function of pressure.

3.4.2 Fuselage Panel ASIP2

The finite element model for panel ASIP2 has 11,000 elements and 63,500 degrees of freedom, and is shown in Fig. 15. Since this panel has a longitudinal crack that is adjacent to a stringer and is centered on the middle frame, a half-length symmetry model is used for the analysis. The assumed plane of symmetry about the axial direction is located at the center of the middle frame. To represent the Z-section middle frame, the entire frame cross section is modeled, symmetry conditions are applied to the frame web, and a half thickness is assigned to the frame components. The inner and outer skins of the lap joint are modeled as discrete layered shells connected with fastener elements. Anticipating that panel failure will correspond to link-up of the first few MSD cracks, the MSD cracks are modeled by introducing small cracks in the outer skin at the three fasteners directly ahead of the initial lead crack. In these locations, the fasteners are attached to the side of the crack where compression bearing will occur, and rigid links are used to distribute the fastener connection over a region equal to the rivet cross-sectional area. The general contact capability in STAGS is utilized to prevent penetration of the inner and outer skin layers of the lap joint when the pressure load is applied to the inner skin.

A typical solution with crack growth in the lead crack and the MSD cracks is shown in Fig. 16. The contour plot of the hoop stress in the region around the crack tip region, shown in Fig. 16(a), indicates the high stress regions near the crack tips of the lead crack and the MSD cracks. A contour plot of the plastic strains in the hoop direction is shown in Fig. 16(b) which indicates that there are regions of plastic deformation emanating from the lead crack and from the MSD crack tips, and that for the solution shown, the plastic zones from the lead crack and the first MSD crack have coalesced. The deformed shape shown in these plots indicates that the deformation on the side of the crack attached to the stiffener is much smaller than the deformation on the other side of the crack, demonstrating that the crack is not tearing due to a symmetric loading condition. The asymmetric loading could promote curvilinear crack growth, but it is assumed in the analysis that interaction between the lead crack and the MSD cracks will cause self-similar crack growth. The opening of the MSD cracks is also evident in the deformed shapes.

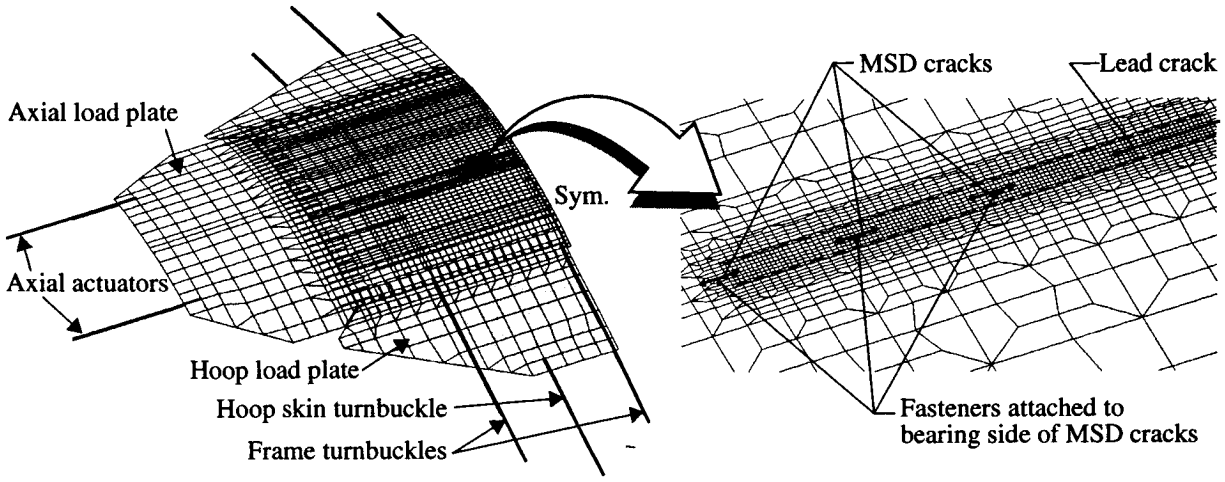

Figure 15. Half-length symmetry finite element model for panel ASIP2.

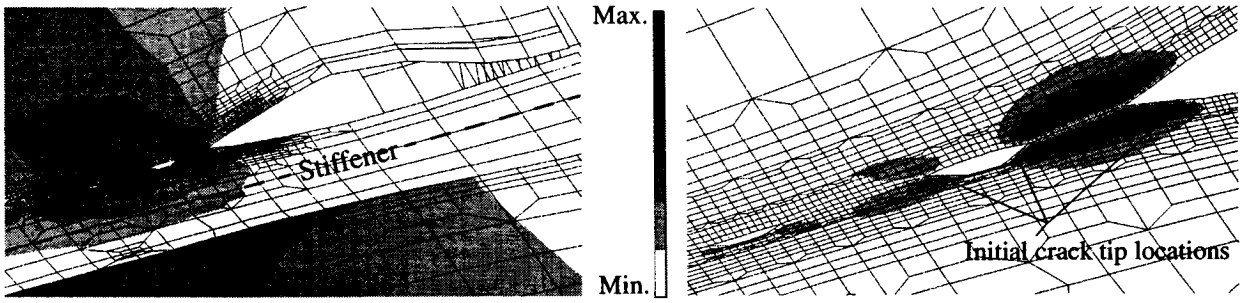

(a) Hoop stress, σ_y

(b) Plastic hoop strain, $(\varepsilon_y)_p$

Figure 16. Typical analysis results for panel ASIP2 showing crack growth in the lead crack and MSD cracks.

The far-field load introduction results predicted by the analysis and measured in the experiment are compared in Fig. 17. The plots of the frame hoop reaction loads and skin hoop reaction loads shown in Figs. 17(a) and 17(b), respectively, indicate good agreement of the results. The asymmetry in the frame hoop reactions due to the crack not being in the center of the panel was accurately predicted by the analysis. The predicted and experimental strains in the skin at three locations near the initial crack tip are compared in Fig. 18. The correlation between the skin axial strains and the skin hoop strains shown in Figs. 18(a) and 18(b), respectively, indicates that the finite element model accurately simulates the stress state around the crack tip region.

The crack extension response from the analysis and the experiment are compared in Fig. 19 as a function of pressure. The crack extension data from the experiment are represented by a horizontal line at a pressure of 9.95 psi. The analysis results indicate that a small amount of stable tearing occurs, with a transition to fast fracture occurring at a pressure of 11.01 psi. The breaks in the solid curve indicate locations where the lead crack links up with the MSD cracks to create a discontinuity in the length of the lead crack. Thus, the analysis predicts fast fracture and link-up at a pressure that is 11% greater than what was observed in the experiment. For comparison purposes, the predicted response of panel ASIP1 is also included in Fig. 19. The difference in the predicted stability of the tearing response of these two panels is caused by the interaction of the lead crack and the MSD cracks in panel ASIP2.

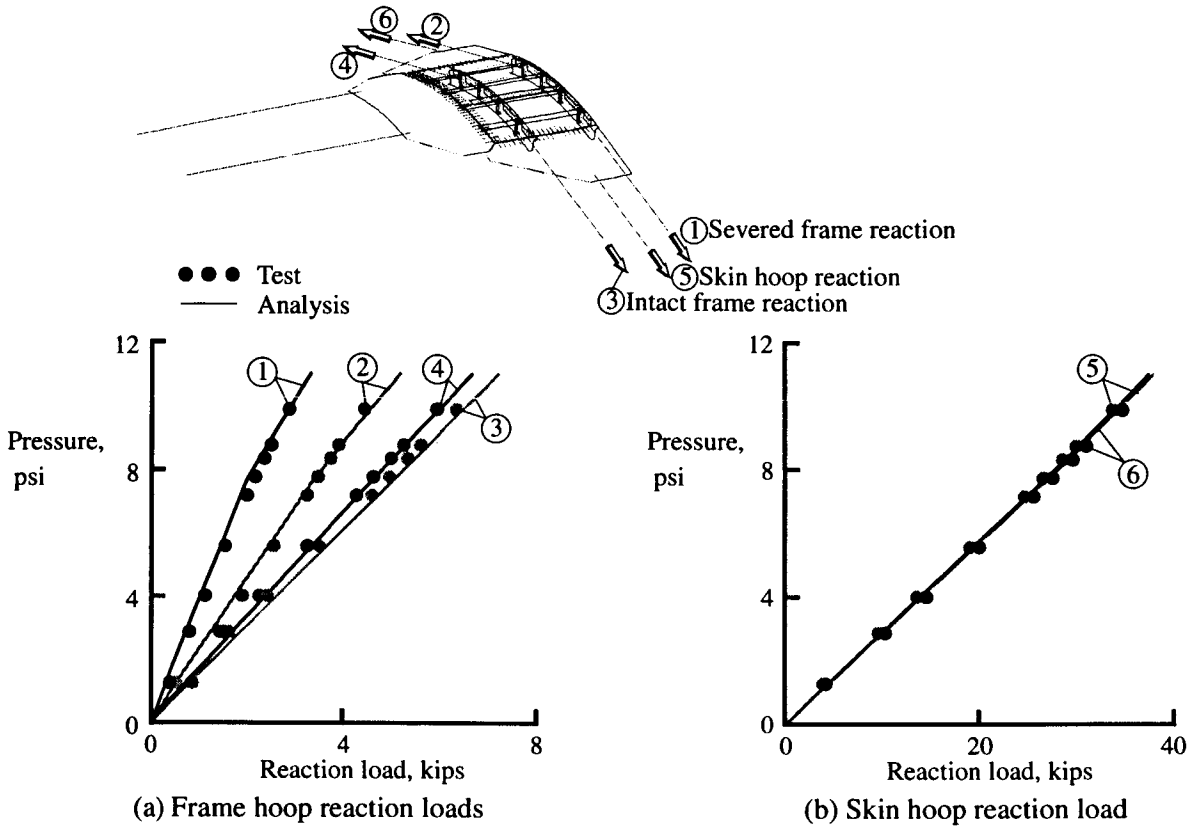

Figure 17. Panel ASIP2 test-analysis correlation of far-field load introduction results.

To illustrate the effect of the MSD cracks on the stable tearing response, additional analysis results are presented which isolate the crack extension behavior of the lead crack and the MSD cracks. The extensions of crack tips 1, 2, and 3 are plotted as a function of pressure in Fig. 20, where crack tip 1 is the crack tip of the lead crack, crack tip 2 is the crack tip of the first MSD crack on the end closest to the lead crack, and crack tip 3 is the crack tip on the other end of the first MSD crack. At a point in the solution corresponding to Point (A) in the plot, the pressure is 9.28 psi and stable tearing has initiated at the lead crack, crack tip 1. The plastic strain in the hoop direction that corresponds to Point (A) is shown in Fig. 20(b), and indicates that plastic strains are most apparent at the tip of the lead crack, but a small region of yielding exists at crack tip 2 in the MSD crack. At Point (B) in the solution, the pressure is 10.68 psi, and stable tearing occurs at crack tip 1 and crack tip 2. The plot of the plastic strains at Point (B) indicates that the plastic zones at crack tip 1 and crack tip 2 have coalesced, and that yielding has initiated at crack tip 3. At Point (C) in the solution, the pressure is 11.01 psi, and the tearing at crack tip 1 and crack tip 2 has become unstable as the two crack tips grow toward each other at a constant pressure. The plot of the plastic strains at Point (C) indicates that a large amount of yielding has occurred between crack tip 1 and crack tip 2, and additional yielding has occurred at crack tip 3. At Point (D) in the solution, the pressure remains at 11.01 psi, crack tip 1 and crack tip 2 have coalesced, and the lead crack has suddenly extended from crack tip 1 to crack tip 3. At this point, crack tip 3 is also displaying unstable crack growth toward the next MSD crack, which is also growing toward crack tip 3. At a constant pressure of 11.01 psi, the MSD cracks will continue to grow toward each other and the panel will tear along the row of MSD cracks until the crack intersects a tear strap or frame which may, or may not, arrest the propagating crack. In the experiment, the running crack caused the tear straps and frames to overload and fail, and the skin crack propagated to the ends of the panel.

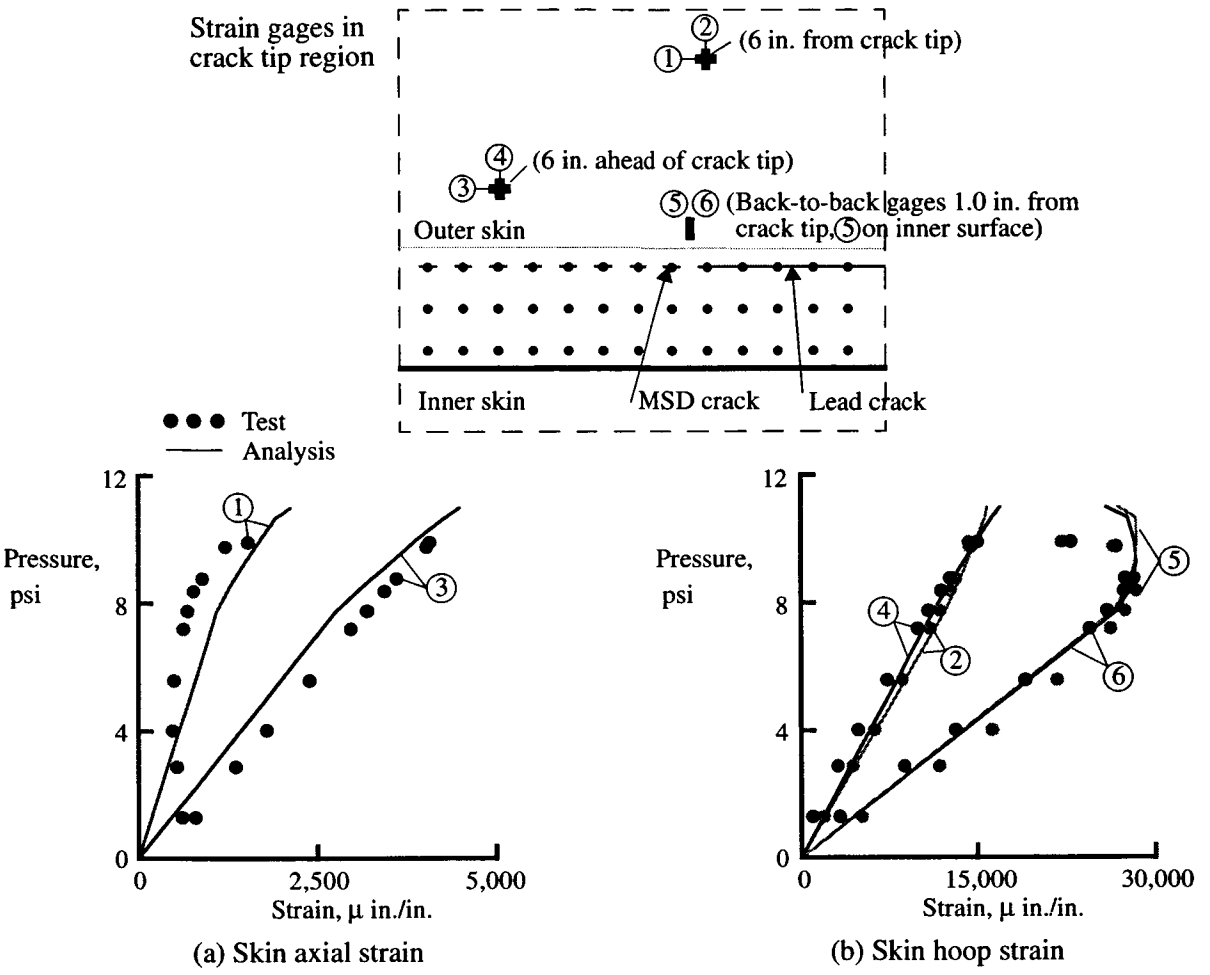

Figure 18. Panel ASIP2 test-analysis correlation of strain results in a crack tip region.

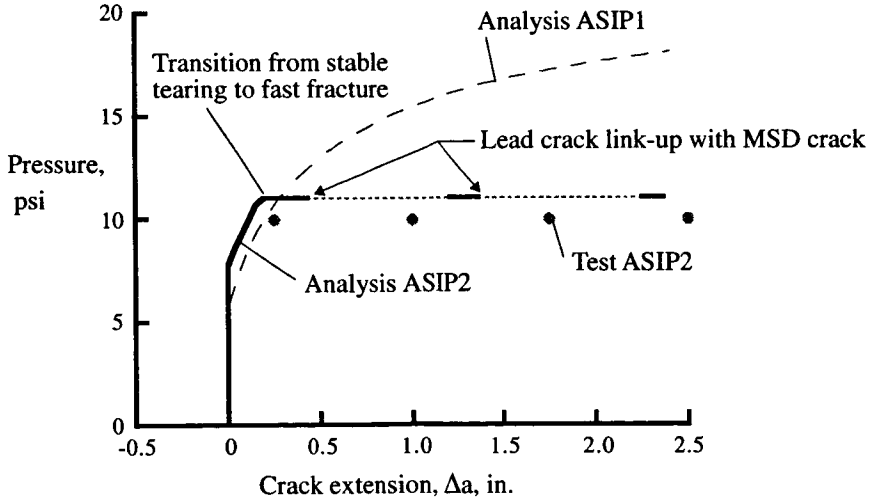

Figure 19. Panel ASIP2 test-analysis correlation of crack extension results as a function of pressure.

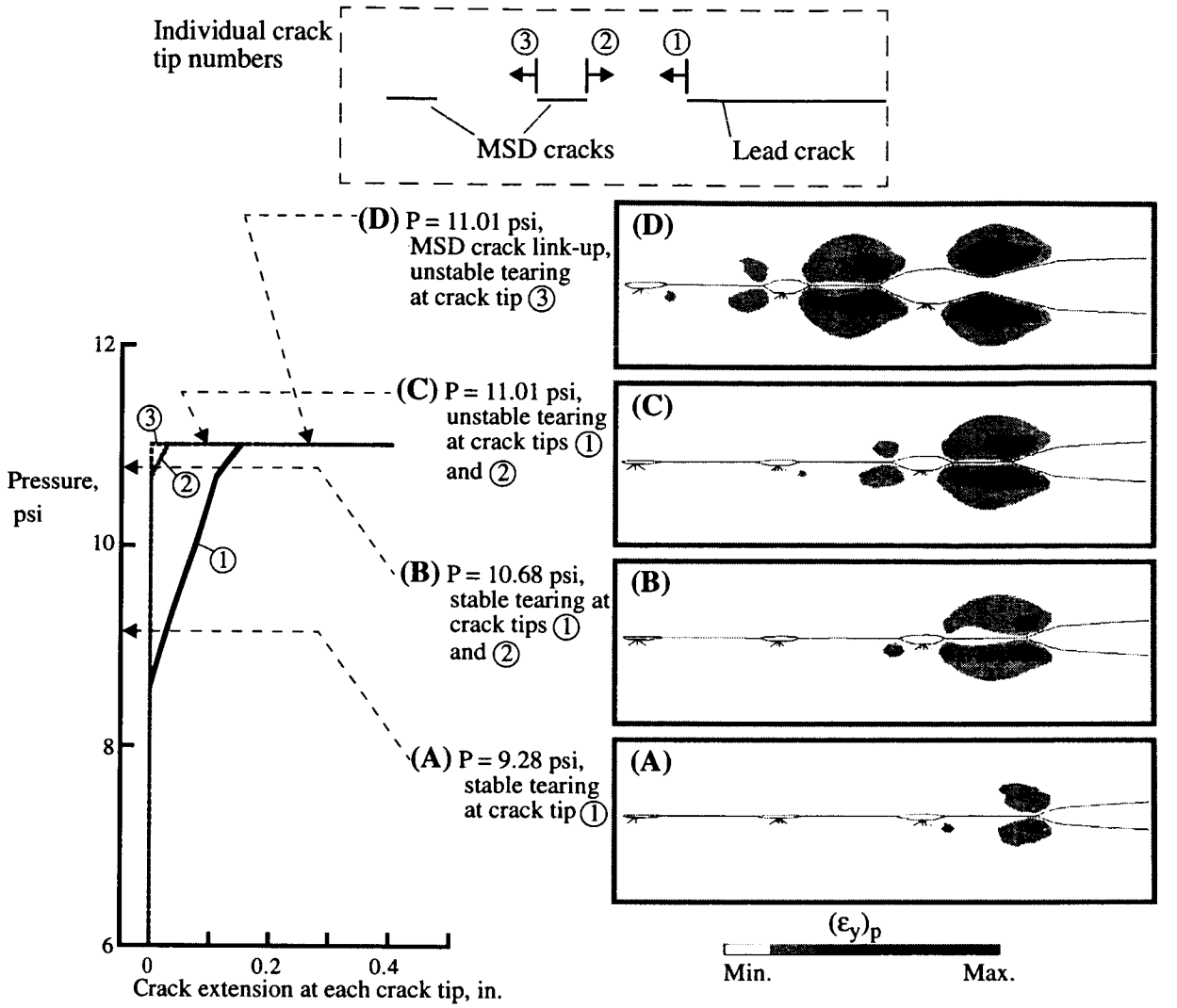

(a) Crack extension as a function of pressure

(b) Plastic strain in the hoop direction at solutions corresponding to points (A), (B), (C), and (D)

Figure 20. Crack extension behavior of the lead crack and the MSD cracks.

CONCLUDING REMARKS

Results of residual strength pressure tests and nonlinear analyses of two stringer- and frame-stiffened aluminum fuselage panels with longitudinal cracks have been presented. Both fuselage panels were generic wide-body fuselage panels with 0.063-in.-thick 2024-T3 aluminum skins. The first fuselage panel had six stringers and three frames, and circumferential tear straps located midway between the frames. The initial damage for this panel was a 10-in.-long longitudinal crack, located midway between stringers and centered on a severed frame. The second fuselage panel had four stringers and three frames, and waffle tear straps located under the stringers and frames. The initial damage for the second fuselage panel consisted of a 10-in.-long longitudinal lead crack and multiple-site damage (MSD) cracks, located adjacent to a stringer, along the edge of a lap joint, and centered on a severed frame.

For the fuselage panel with the lead crack located midway between stringers and no MSD cracks, a substantial amount of stable tearing occurred, and the tear straps located midway between the frames arrested the crack growth in the skin. For the panel with the lead crack and MSD cracks adjacent to a stringer and along a lap joint, very little stable tearing occurred. Interaction between the lead crack and the MSD cracks caused unstable crack growth that could not be arrested by the panel to occur at a relatively low pressure load. For both panels considered, there was significant out-of-plane deformation along the crack, indicating a geometrically nonlinear response. For the case with the lead crack adjacent to a stringer, the deformations were not symmetric across the crack, indicating a mixed-mode loading condition at the crack tip. The numerical and experimental results presented in the paper support the following general remarks. The difference in the crack growth behavior and the residual strength of the two panels implies that the presence of MSD cracks affects the crack growth stability and reduces the residual strength of stiffened fuselage shells with long cracks. Also, the arrest of the crack growth at the tear strap in the first panel, and the failure of the tear straps and frames at fastener hole locations in the second panel, suggest that the tear strap location and sizing, and methods of attaching the skins, tear straps, and stiffening structure may affect the ability to arrest crack growth.

The results presented in the paper show that geometric and material nonlinear structural analyses can accurately represent the internal load distributions, local stress and displacement gradients, and crack growth behavior in stiffened fuselage shells with long cracks and subjected to internal pressure loads. The nonlinear structural analysis methods provide higher fidelity results than traditional linear-elastic engineering analysis approximations for these panel configurations which display significant plastic yielding and nonlinear out-of-plane deformations. To obtain good correlation of test and analysis results for built-up fuselage shell structures, it may be necessary to include all structural detail features and nonlinear response characteristics (e.g., element or component buckling, contact, and fastener yielding or failure) in the numerical models. The numerical models and structural analysis methods must be able to represent accurately the multiple length scales involved in simulating the global response of a large stiffened panel, the local fracture behavior of thin sheets, and the interaction between structural components and load redistribution in a stiffened structure as the damage propagates.

ACKNOWLEDGMENTS

The authors would like to express their thanks to Mr. David F. Moore, Analytical Services and Materials, Inc., and Mr. Roland F. Vause, NYMA, Inc., for their technical support.

REFERENCES

[1]Rankin, C. C., Brogan, F. A., Loden, W. A., Cabiness, H. D., "STAGS User Manual, Version 3.0," Lockheed Martin Missiles and Space Co., Inc., Advanced Technology Center, Report LMMS P032594, June, 1998.

[2]Newman, J.C., Jr., "An Elastic-Plastic Finite Element Analysis of Crack Initiation, Stable Crack Growth, and Instability," ASTM STP 833, 1984, pp. 93-117.

[3]Dawicke, D. S., Sutton, M. A., Newman, J. C., Jr., and Bigelow, C. A., "Measurement and Analysis of Critical CTOA for an Aluminum Alloy Sheet," NASA TM-109024, September 1993.

[4]Ilcewicz, L. B., Smith, P. J., and Horton, R. E., "Advanced Composite Fuselage Technology," NASA CP-3178, 1992, pp. 97-156.

[5]Riks, E., "Some Computational Aspects of the Stability Analysis of Nonlinear Structures," Computational Methods in Applied Mechanics and Engineering, Vol. 47, 1984, pp. 219-259.

[6]Rankin, C. C., Brogan, F. A., and Riks, E., "Some Computational Tools for the Analysis of Through Cracks in Stiffened Fuselage Shells," Computational Mechanics, Springer International, Vol. 13, No. 3, December 1993, pp. 143-156.

[7]Potyondy, D. O., "A Software Framework for Simulating Curvilinear Crack Growth in Pressurized Thin Shells," Ph.D. Thesis, Cornell University, Ithaca, NY, 1991.

[8]Potyondy, D. O., Wawrzynek, P. A., and Ingraffea, A. R., "Discrete Crack Growth Analysis Methodology for Through Cracks in Pressurized Fuselage Structures," International Journal for Numerical Methods in Engineering, Vol. 38, 1995, pp. 1611-1633.

[9]Rankin, C. C., and Brogan, F. A., "The Computational Structural Mechanics Testbed Structural Element Processor ES5: STAGS Shell Element," NASA CR-4358, 1991.

[10]Swift, T., "Fracture Analysis of Stiffened Structure," In Damage Tolerance of Metallic Structures: Analysis Methods and Application, ASTM STP 842, 1984, pp. 69-107.

[11]Young, R. D., Rose, C. A., Dávila, C. G., Starnes, J. H., Jr., and Rankin, C. C., "Crack Growth and Residual Strength Characteristics of Selected Flat Stiffened Aluminum Panels," Proceedings of the First Joint DoD/FAA/NASA Conference on Aging Aircraft, Ogden, UT, July, 1997.

[12]Dawicke, D. S., Newman, J.C., Jr., and Bigelow, C. A., "Three-Dimensional CTOA and Constraint Effects During Stable Tearing in a Thin-Sheet Material," In Fracture Mechanics: 26th Volume, ASTM STP 1256, 1995, pp. 223-242.

[13]Shivakumar, K. N. and Newman, J. C., Jr., "ZIP3D - An Elastic-Plastic Finite-Element Analysis Program for Cracked Bodies," NASA TM-102753, 1990.

[14]Dawicke, D. S. and Newman, J. C., Jr., "Residual Strength Predictions for Multiple Site Damage Cracking Using a Three-Dimensional Finite Element Analysis and a CTOA Criterion," Fatigue and Fracture Mechanics: 29th Volume, ASTM STP 1332, T. L. Panontin and S. D. Sheppard, Eds., American Society for Testing and Materials, 1998.

[15]Newman, J. C., Jr., "Finite Element Analyses of Fatigue Crack Propagation -- Including the Effects of Crack Closure," Ph.D. Thesis, Virginia Polytechnic institute and State University, Blacksburg, VA, May 1974.

[16]Dawicke, D. S., "Residual Strength Predictions Using a Crack Tip Opening Angle Criterion," FAA-NASA Symposium on the Continued Airworthiness of Aircraft Structures, DOT/FAA/AR-97/2, Vol. II, July 1997, pp. 555-566.

RESIDUAL STRENGTH ANALYSIS OF SKIN SPLICES WITH MULTIPLE SITE DAMAGE

J. E. Ingram, Y. S. Kwon, K. J. Duffié and W. D. Irby
Lockheed Martin Aeronautical Systems Company
Marietta, GA 30063

Abstract

The widespread fatigue damage (WFD) assessment of the L-1011 aircraft has necessitated a significant update to the damage tolerance analysis methods at Lockheed Martin Aeronautical Systems (LMAS). This paper describes the methods of analysis, which will be used to predict the effect of multiple site damage (MSD) cracks on the residual strength of WFD-susceptible locations of the airframe. The STAGS finite element code is used to develop an enhanced engineering approach for calculating the lead crack and MSD crack link-up stresses in ductile alloys. This approach involves using the crack tip opening angle (CTOA) as a criteria for crack extension in STAGS models of various multiple-crack configurations. To study the fastener load redistribution in lap splices containing lead and MSD cracks, detailed nonlinear solid element models were constructed using the Lockheed Martin DIAL finite element code. These lap joint models were run for numerous configurations of lead and MSD cracks, and show the effect of fastener load peaking and shedding as the lead crack approaches and emerges from MSD-cracked fastener holes. The results of these nonlinear calculations are used to develop a code for residual strength, based on crack link-up (using the enhanced engineering approach) when the linear-elastic stress intensity solution is known from detailed models of more complex wing and fuselage structure.

Background

The analysis methods for durability and damage tolerance at Lockheed Martin have been based on fracture mechanics principles since the late 1960s – beginning with the C-5A. Since then, the other Lockheed Martin aircraft in the Air Force fleet have been included in the fracture-based analysis system. Because of this total reliance on crack growth and fracture-based residual strength, and because of the constant updating of these methods in the three decades since the C-5A analyses, a comprehensive library of stress intensity solutions has evolved. These solutions, together with refinements in the crack growth and loads system, have proven to be accurate when compared to test and service experience. The accumulated data, analysis tools and experience represent a strong motivation for us to apply as much of this analysis system as possible to the WFD Assessment of the L-1011.

The L-1011 is obviously a large transport type aircraft, but has a significant difference in construction from the Air Force aircraft. The fuselage of the L-1011 is primarily 2024-T3, whereas the military transports are 7000-series alloys. The ductility of the 2024-T3 material, and the need to evaluate the possible condition of multiple cracks resulting from WFD, have necessitated the update to our analysis methods described herein.

The Link-up Model

An engineering model for link-up has been investigated by numerous researchers, and has usually involved a calculation of the plastic zone sizes at the tips of the lead and MSD crack tips as

shown in Figure 1. In this procedure, the stress intensities for the two interacting cracks are determined from linear elastic analyses, and the load level at which the two plastic zones touch is the link-up load. Broek [1] showed that equating the sum of the plastic zone dimensions, r_{p1} and r_{p2}, to the ligament length, L, would result in the following expression for the stress at link-up:

$$\sigma_{LU} = \sqrt{2} F_{col} \left[L \Big/ \left(a_1 \beta_1^2 + a_2 \beta_2^2 \right) \right]^{1/2} \tag{1}$$

Where β_1 and β_2 are the total geometric correction factors for the lead crack (a_1) and MSD crack (a_2) respectively; and include the effects of interaction and finite width. F_{col} is the collapse stress, determined by Broek to be 37.5 ksi for 2024-T3 Clad material. After comparison of predictions using this equation to the test results [1], Broek determined that the agreement between analysis and test could be significantly improved by modifying the link-up equation as follows:

$$\sigma_{LU} = C F_{col} \left[L \Big/ \left(a_1 \beta_1^2 + a_2 \beta_2^2 \right) \right]^{1/2} \tag{2}$$

where:

$$C = 0.5 + .9 \left[\frac{1}{1 + L/a_1} \right] \tag{3}$$

The function, C, is described as a transition model that results in better agreement between the plastic zone touch model and test data across the entire range of ligament lengths; effectively "tuning" the model to the behavior of the 2024-T3 material.

Equations 2 and 3 were incorporated into a Lockheed Martin residual strength code to evaluate how well this method of "tuning" the plastic zone touch method would agree with the Foster Miller Tests. In this code, the interaction between the two cracks is calculated using the method of Kamei and Yokoburi [2], and the finite width correction is by Isida [3]. Figure 2(a) shows a comparison of the link-up predictions using these methods to the Foster Miller test data [4]. In Figure 2(b), the function *C* (equation 3) is compared to the values that would have resulted in perfect agreement between analysis and test (by substituting the test link-up stress for σ_{LU} and solving for *C*).

At the time of this first investigation, the Foster Miller tests were the only data points available with which to evaluate the engineering link-up model. The lead and MSD cracks in these tests were line cracks. Since then, additional MSD tests have been conducted, including 2024-T3 specimens containing larger lead cracks, thicker material, and MSD cracks from open holes. The first attempt to evaluate whether or not an engineering model can be sufficiently accurate across a broad range of sizes, geometries and thicknesses, was to analyze these additional tests using Broek's model. A second set of 2024-T3 specimens [5], tested for the FAA by the National Institute of Standards (NIST), were 90 inches wide and contained central lead cracks ranging up to 20 inches (tip to tip). The material was .040 inch thick bare 2024-T3. Ten panels were tested – four without MSD cracks, and six with MSD cracks of varying size and spacing. Dr. Bert Smith, at Wichita State University, conducted a third MSD test

program [6] which included 22 specimens, all of which were .063 inch thick, 24 inch wide 2024-T3 clad material.

The link-up prediction methods described above were used to analyze the NIST and Wichita State Tests. The MSD cracks from open holes in these tests were converted to equivalent line cracks before calculating the interaction. The equivalency was based on equal stress intensity (K), and equal crack separation (or ligament length, L). Bowie correction factors [7] for symmetric double cracks from an open hole, were used along with the interaction and finite width factors to calculate K for the open hole MSD test specimens.

The comparison of the calculated link-up stress to the measured values for all three test series are presented in Figure 3(a), and indicate an average difference of 13.4%. The test-derived values of the transition function, C, are shown in Figure 3(b), along with the graphical representation of C (equation 3). The wider range of a_1/L values in the later series of MSD tests indicate some adjustment in the transition function would give better correlation of analysis to test. A modified transition function, C' was obtained by best fit to the test-indicated points:

$$C' = 1.83 - e^{-.057 a_1/L}$$

In Figure 4(b), the test-derived C values are again presented along with the modified transition function, C', and, for comparison, the original transition function, C. Note that in this comparison, the collapse stress, F_{col}, was replaced by the yield stress, F_{ty}. This was done to facilitate including the additional test results, and to allow the modified transition function to be based on properties readily available in material handbooks. Thus, the comparison of the original transition funtion, C, to the test values has been slightly distorted. The comparison of analysis to test using this new transition function, C', is shown in Figure 4(a). The average error for all 48 tests, using C', is 7%. This is close to the average error obtained using the original transition function, C, when comparing the Foster-Miller test series alone.

The error associated with using these (tuned) link-up models is most likely acceptable for analysis of the airframe, given other inaccuracies in the calculations of loads and stresses. However, the fact that the size of the MSD crack, a_2, is not present in the expressions for C or C' would seem to indicate that better precision could be obtained if this effect were quantified. An attempt was made to determine if a parametric set of transition functions existed that would account for a_2, as shown schematically in Figure 5, where a separate function is hypothesized for different values of a_2 or a_2/L. When the test-derived C values shown in Figure 4(b), were examined individually, it became apparent that some of the test-derived points above the best-fit line were small a_2/L values, and some were large. The same was true for test points below the line. No trend could be observed in the test values regarding a_2 or a_2/L. At this point, it was not clear if scatter in the link-up behavior or inadequate analysis was the reason for the inability to discern the effect of a_2.

In order to gain some insight into the true degree of scatter, as well as the influence of the MSD crack size on σ_{LU}, a full elastic-plastic analysis of the interacting cracks was needed. After review of several possible analysis tools to use for this, the STAGS code [8] was selected. The critical crack tip opening angle, ψ_{cr}, was selected as the criteria for tearing in the STAGS analysis. To determine the best

modeling scheme to use in the STAGS models, the first analysis attempted to simulate the stable tearing from an R-curve test [9]. The values of ψ_{cr} and the width of the plane strain strip, h, (along the crack path) were obtained, which (together with the nonlinear stress strain curve), best fit the K_R-curve behavior for the 2024-T3 material. The parameters ψ and h are defined in Figure 6, which is a sketch of a STAGS model near the crack tip. A comparison of the STAGS-calculated K_R curve and the test curve are shown in Figure 7. Once ψ_{cr} and h were determined, a series of STAGS models were constructed to simulate the Foster Miller MSD test specimens. Figures 8(a) and 8(b) show a typical MSD test panel and model – in this example, test panel P-8. Figure 8(c) shows the results of the STAGS analysis in terms of applied (far field) stress vs. crack length. The thick, horizontal lines at the bottom of the plot represent the lead and MSD crack lengths at the beginning of the analysis. The curve extending up from the tips of each crack represent the stable tearing in terms of far field stress vs. crack length (extension). Where the tearing curve peaks, and skips to the next crack tip, is the point at which link-up occurs. In other words, the calculated link-up stresses are obtained as the peak value of each of these curve segments. In the case of test P8, two link-up calculations and one final panel rupture stress are calculated. Also shown in Figure 8(c) are the test link-up stresses, which are indicated by the solid (dot) symbols. All of the Foster Miller test panels were analyzed in this manner, and the average difference between the STAGS-calculated link-up stresses and the 15 measured values was 2.3%.

Based on the good agreement between STAGS and the test results, an effort was initiated to determine if an engineering model could be further refined by using STAGS to calculate the influence of the MSD crack size along with lead crack size and ligament length. The three crack geometry parameters, a_1, a_2 and L, were evaluated in a STAGS analysis matrix in which each parameter was analyzed for three values (to obtain the nonlinear relationship). This resulted in 27 ($3a_1$ x $3a_2$ x 3L) nonlinear STAGS tearing analyses. The results of the analyses indicated that, as in the test results, no trend regarding a_2 could be determined – at least not with the data presented as in Figure 5. For given a_1/L values, the STAGS-derived C values for small a_2 crack lengths fell above as well as below the line; as did the larger a_2 values. At the same time, it was observed that interpolation (nonlinear, by curve fitting) between the STAGS link-up values gave excellent agreement with tests when the interpolation was based directly on geometry and link-up stress. In other words, the STAGS results showed that the link-up stress is unique for all three geometry terms – a_1, a_2, and L, but not for the normalized (a/L) terms. Thus, the appropriate way to present the parametric STAGS link-up stress calculations is in terms of link-up "surfaces" as shown schematically in Figure 9(a). This sketch also shows how the interpolation is accomplished to obtain the link-up stress for a given geometry.

To incorporate these results into an engineering model requires only that a surface (expanded look-up table) be obtained that fits the nine ($3a_1$ x $3a_2$) STAGS calculations for each ligament (L) surface; and that some curve fitting procedure be included to perform the interpolation shown in Figure 9(a). The procedure used in the Lockheed Martin code is a least squares approach to fit a second order equation to the STAGS results and generate the link-up "surfaces." The analyses of the Foster Miller and Wichita State MSD link-up tests were repeated using the updated code, and compared to test results in Figure 9(b). The STAGS-based link-up model resulted in an average error of 4.0%. The NIST tests were not included, as these 90 inch wide specimens would have required much larger STAGS models for the parametric analysis. The smaller models were used first to determine the viability of this method. Larger STAGS models are in progress – both for further verification of the method for the longer crack lengths, and because the eventual use in analysis of the airframe will require them.

The difference in accuracy between the 2.3%, when each Foster-Miller specimen was explicitly modeled with STAGS, and the 4% from the curve-fit model is due to two factors. First, the cracks in the Foster-Miller specimens were line cracks, installed with a jeweler's saw, while the cracks in the Wichita State tests were Electrical Discharge Machine (EDM) cracks from open holes. This difference may result in some difference in link-up stress, which is not accounted for in the STAGS-based curve fit model (the same curves were used for both test series). Second, there is likely some additional error due simply to the least-squares approximation to the 27 STAGS calculations. A separate set of STAGS calculations for the same matrix of crack lengths could be developed for the Wichita State test results, and this would likely further improve the accuracy, but this has not yet been done.

Fastener Load Effects

To use the enhanced (STAGS-based) link-up model in an analysis of realistic aircraft structure, the influence of the fastener loads on the lead and MSD cracks will have to be calculated. Historically, when crack growth and residual strength calculations were made for lead cracks in rows of attachments such as lap joints, the load transfer at the initiation site would be accounted for in the stress intensity solution, but not in subsequent fastener holes (in the crack path). These (next) fastener holes were treated as open holes. In addition, the load transfer was held constant on the first fastener until ligament failure, and then assumed to be zero thereafter - due to an intuitive expectation that the cracked hole was too "soft or weakened" to transfer load.

In the MSD problem, the link-up stress, and ultimately the residual strength, is a function of the damage condition and state of stress at each "next" hole in the crack path. To improve the accuracy of the link-up predictions, a series of detailed, solid element models were constructed for multiple crack configurations in a lap splice. The purpose of the models was to obtain both the stress intensities at the multiple crack tips, and to calculate the redistribution of the fastener forces in the cracked lap joint. The Lockheed Martin DIAL finite element code was used to conduct this analysis, for two primary reasons: 1) it uses a method of input, called syntactic input, which allows the model to be easily re-meshed with different dimensions; 2) the availability of the interface elements permit simulation of the contact behavior at all the bearing surfaces. Figure 10 is a deflected shape for one of the crack configurations of this model, which shows the bearing/sliding behavior of the fasteners in each hole, and gives an indication of the mesh density used in the model. The stress intensities K_1 (lead crack tip) and K_2 (MSD crack tip) calculated from the DIAL models are shown in Figure 11.

The effect of the lead and MSD cracks on the redistribution of fastener forces is presented in Figure 12 for the first four fasteners in the path of the crack. At very short crack lengths, the fastener forces are equal. As the lead crack extends, the force on fastener number 1 begins to decrease in a manner resembling exponential decay. The other fasteners (2, 3, and 4) ahead of the lead crack tip are increasing as the first fastener unloads. When the lead crack extends to the next MSD crack (at fastener hole 2), the "force decay" process begins for fastener 2. This predictable pattern of peaking and shedding of fastener loads provides a way to estimate the stress intensities at lead and MSD cracks in lap joint configurations other than the two-row lap modeled here. In turn, this enables the calculation of the equivalent crack lengths for use in the link-up model. The conversion to equivalent line cracks is based, as it was for the analyses of the open hole tests described earlier, on equal stress intensities and equal ligament lengths.

Summary

Enhancements to our fracture-based analysis system were developed to address the new problems presented by the widespread fatigue damage assessment of the L-1011. First, a link-up model was derived, that accounts for all three crack-geometry terms (a_1, a_2 and L), and is based on the elastic-plastic analysis using the crack tip opening angle and the STAGS program. This model accurately predicts link-up of cracks from open holes when the equivalent line cracks are determined. Second, to be able to apply the STAGS-based interpolation link-up model to lap joints, new stress intensity solutions were obtained for a lap joint which contained multiple combinations of lead and MSD cracks, and accounted for fastener force redistribution within the cracked joint.

References:

1. Broek, D., "The Effects of Multi-Site Damage on the Arrest Capability of Aircraft Fuselage Structures," FractuResearch TR 9302, June, 1993.

2. Kamei, A., and Yoloburi, T., "Two Collinear Asymmetrical Elastic Cracks," Report of the Research Institute for Strength and Fracture of Materials, Tohoku University, Vol. 10, Section 1-4, pp. 41-42, December 1974.

3. Isida, M. "Stress Intensity Factors for the Tension of an Eccentrically Cracked Strip," Journal of Applied Mechanics Series E, September 1966, p. 674-675.

4. Thomson, D., Hoadley, D., and McHatton, J., "Load Tests of Flat and Curved Panels with Multiple Cracks," Foster Miller Draft Final Report, September, 1993

5. DeWit, R., Fields, R., Low, S., Harne, D., and Foecke, T., "Fracture Testing of Large-Scale Thin Sheet Aluminum Alloy," DOT/FAA/AR-95/11, February, 1996.

6. Smith, B., Movak, A., Saville, P., Myose, R., and Horn, W., "Improved Engineering Methods for Determining the Critical Strengths of Aluminum Panels with Multiple Site Damage in Aging Aircraft," Proceedings of the 2nd Annual NASA/FAA/DOD Conference on Aging Aircraft, Williamsburg, VA., Aug. 31-Sept. 3, 1998.

7. Bowie, O. L., "Analysis of an Infinite Plate Containing Radial Cracks Originating from a Circular Hole," Journal of Mathematics and Physics, Vol. 23, No. 1, April 1956, pp. 60-71.

8. STAGS (STructural Analysis of General Shells) Structural Analysis Program, Version 3.0, User Manual, February, 1998, Lockheed Martin Advanced Technology Center.

9. 2024-T3 Aluminum K_R-Curve Data From Tests Conducted at NASA-LaRC, 1997

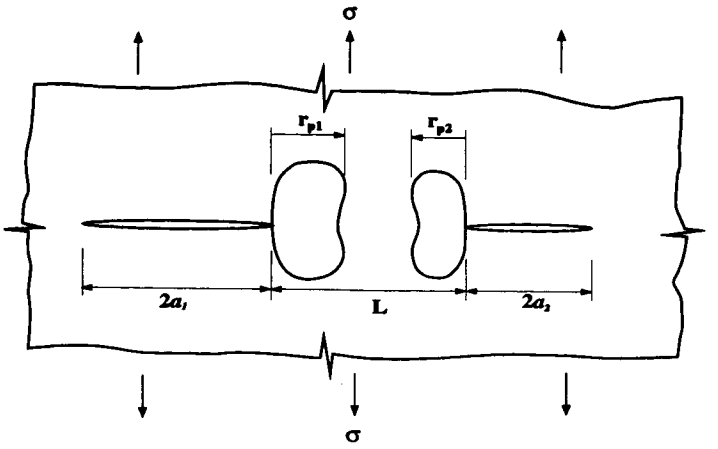

Figure 1 Geometry of Lead and MSD Cracks with Plastic Zones.

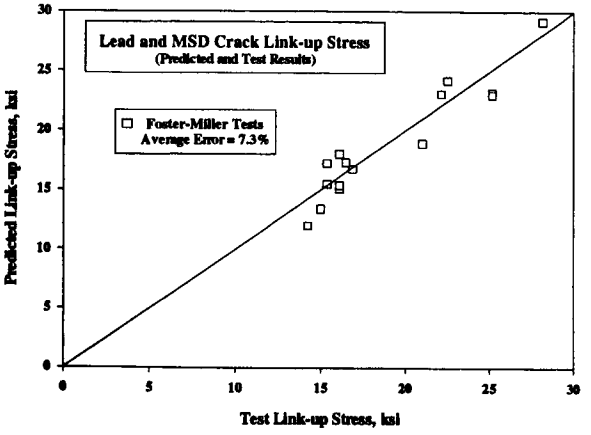

(a) Test vs. Calculated Link-up Stress

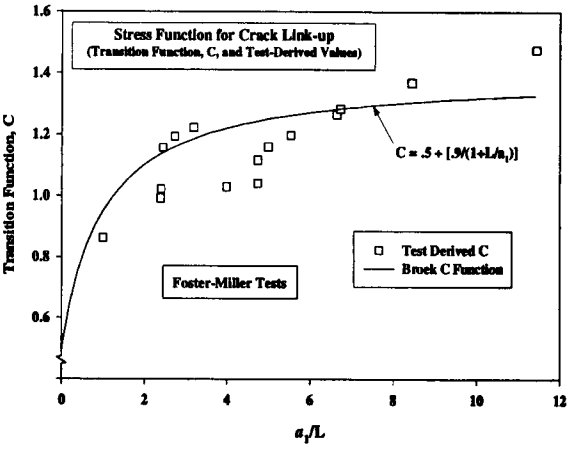

(b) Comparison of Transition Function, C, to Test-indicated Values

Figure 2 Foster-Miller MSD Test and Analysis Results

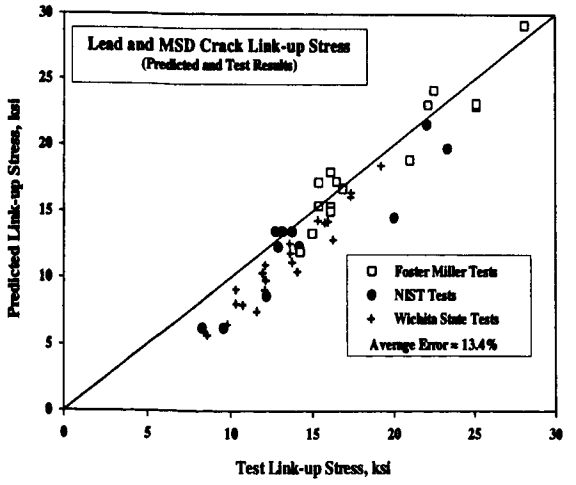

(a) Test vs. Calculated Link-up Stress

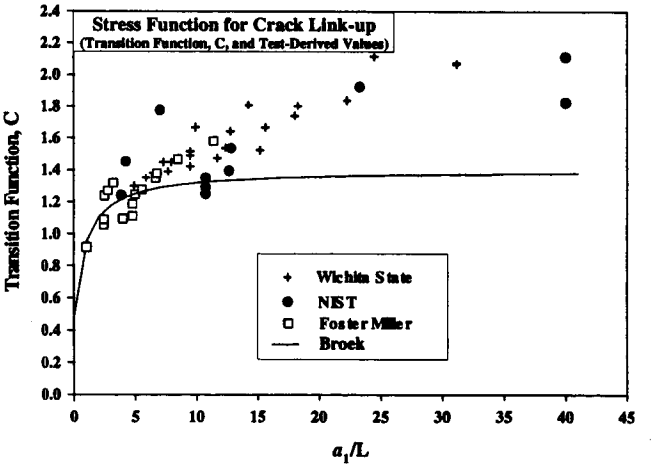

(b) Comparison of Transition Function, C, to Test-indicated Values

Figure 3 Test and Analysis Results – All MSD Tests

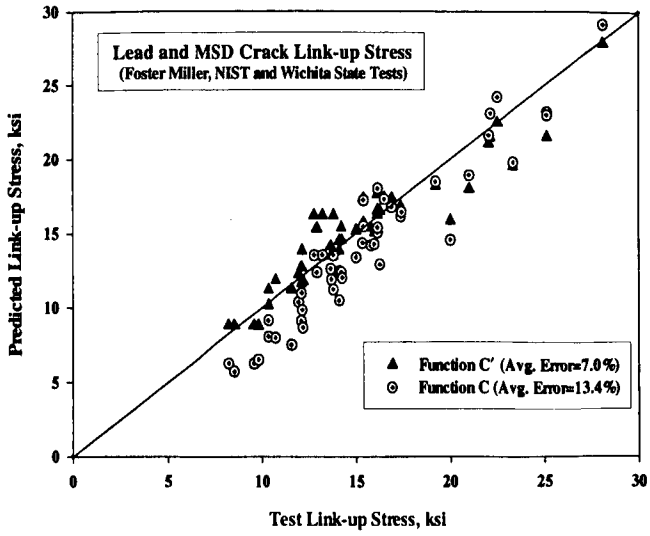

(a) Test vs. Calculated Link-up Stress

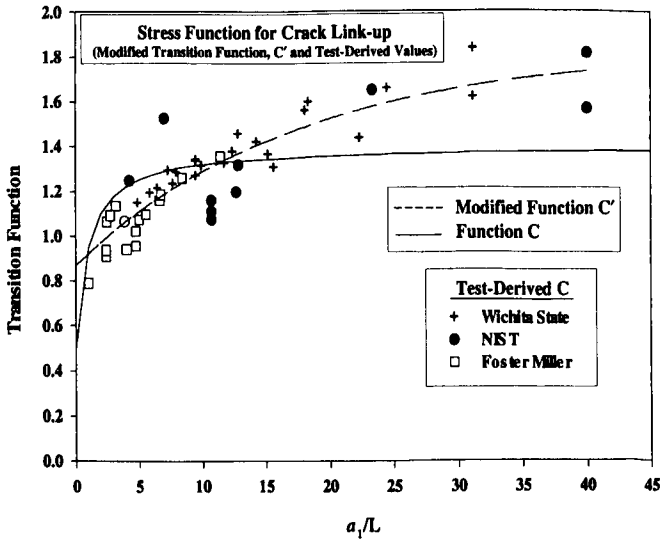

(b) Transition Functions and Test-indicated Values

Figure 4 Effect of Modified Transition Function, C', on Prediction Capability

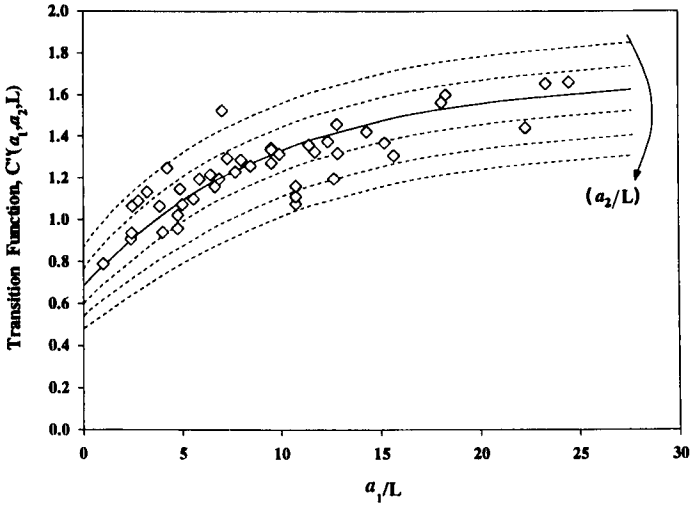

Figure 5 Hypothesized Parametric Transition Function C''

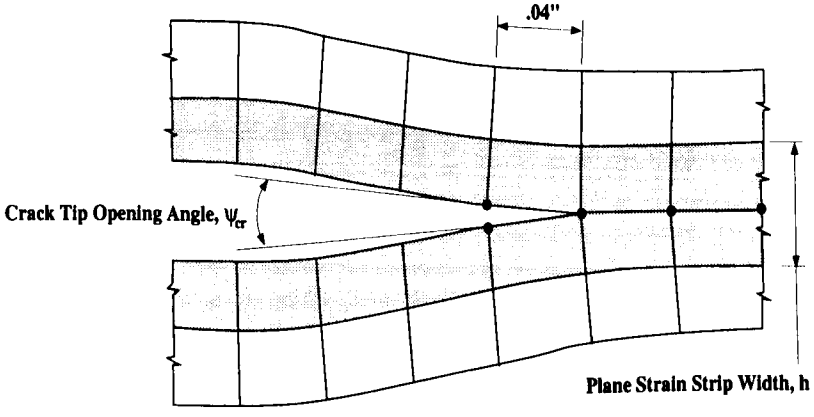

Figure 6 Crack Tearing Parameters in STAGS Link-up Models.

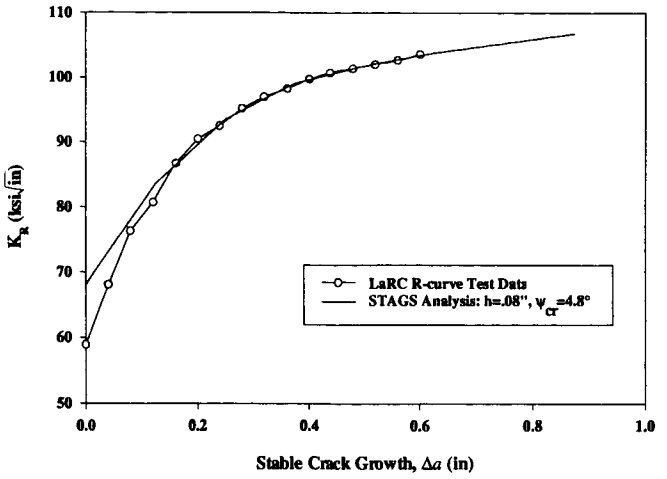

Figure 7 Comparison of Stable Tearing Results (K_R) from Test [9] and STAGS Analysis Result.

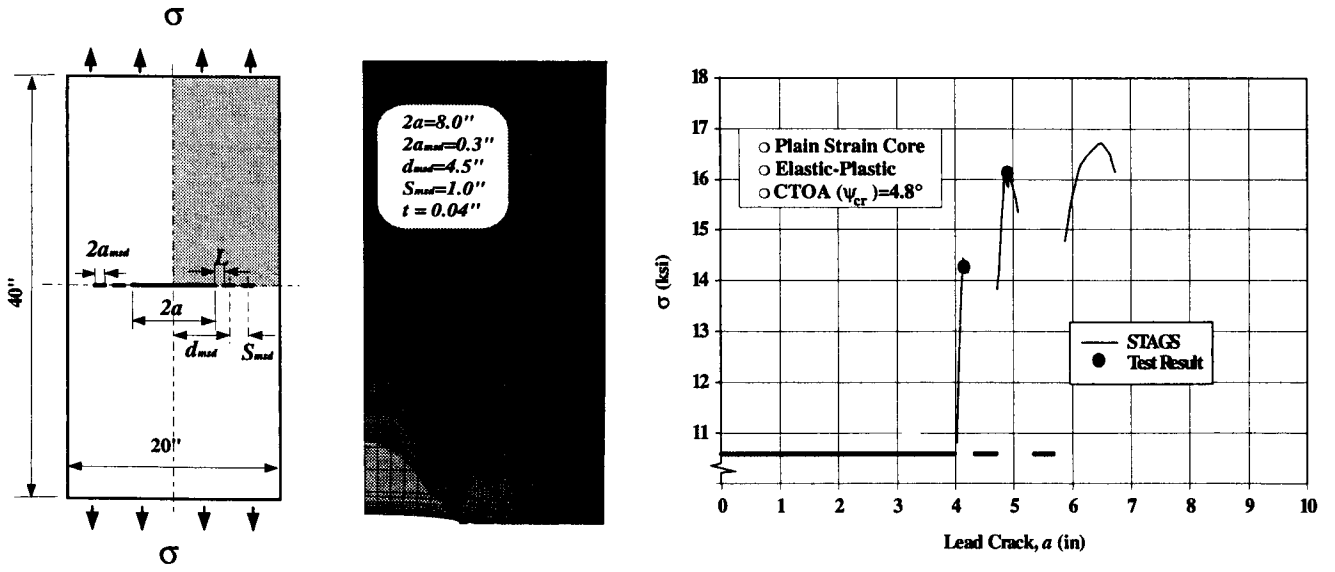

(a) Test Specimen (b) STAGS Model (c) STAGS Tearing/Link-up Calculations

Figure 8 STAGS Analysis of Foster Miller MSD Test Specimen Number P8

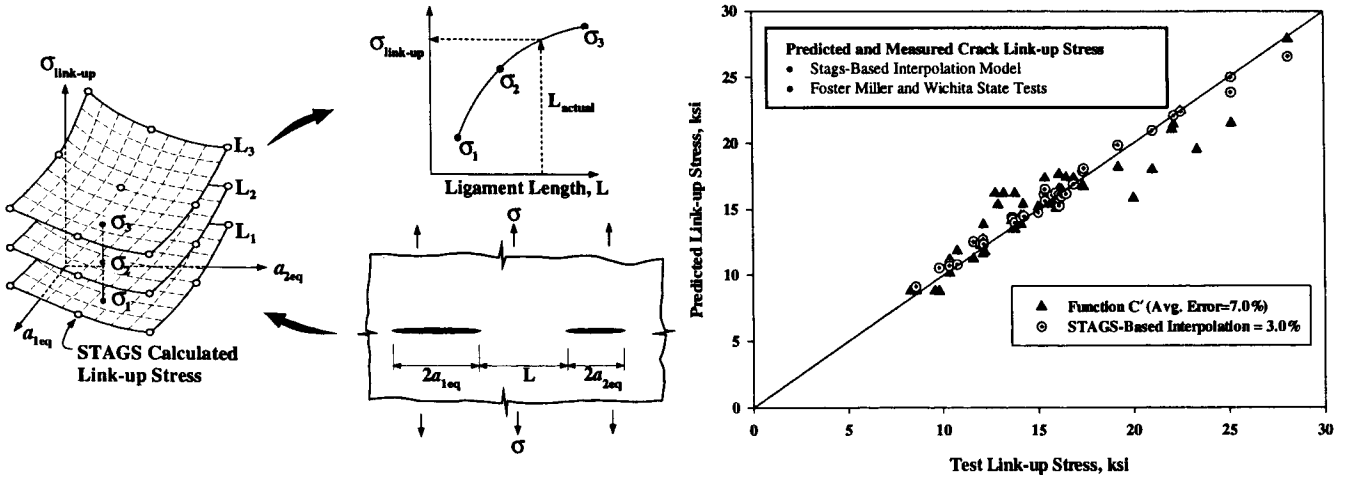

(a) Scheme for Crack Link-up by Interpolation (b) Comparison of Link-up Calculations and and Test Results

Figure 9 STAGS-based Interpolation Link-up Model

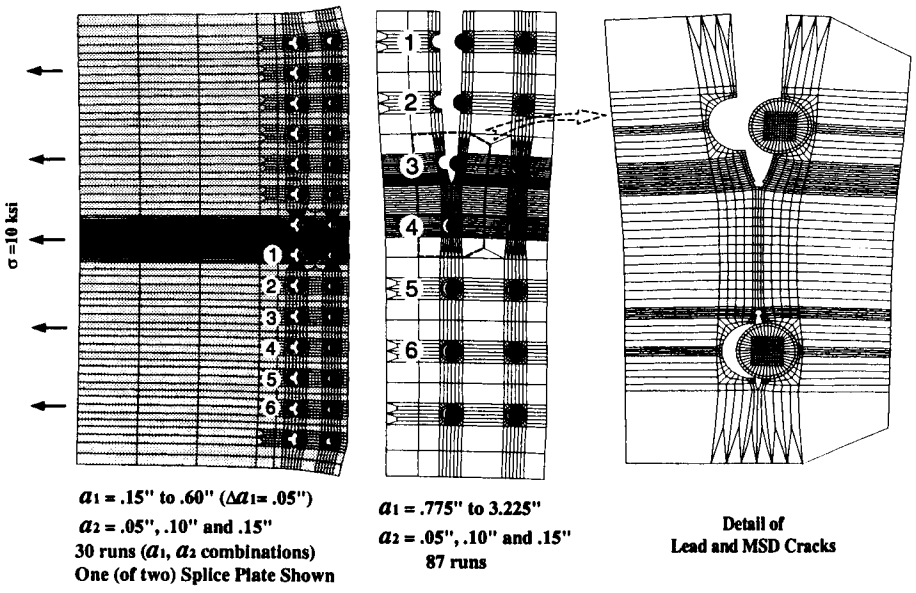

Figure 10 DIAL Lap Joint MSD Model.

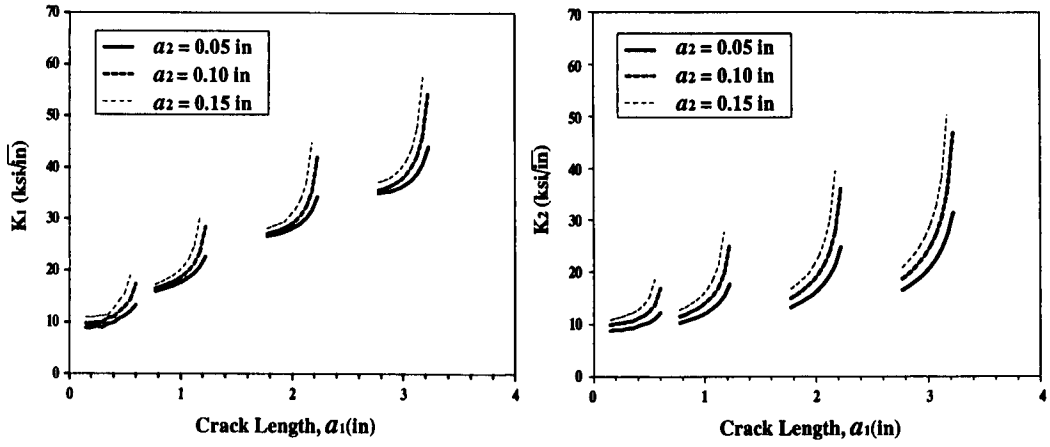

Figure 11 Stress Intensity Calculations from DIAL Lap Joint MSD Model.

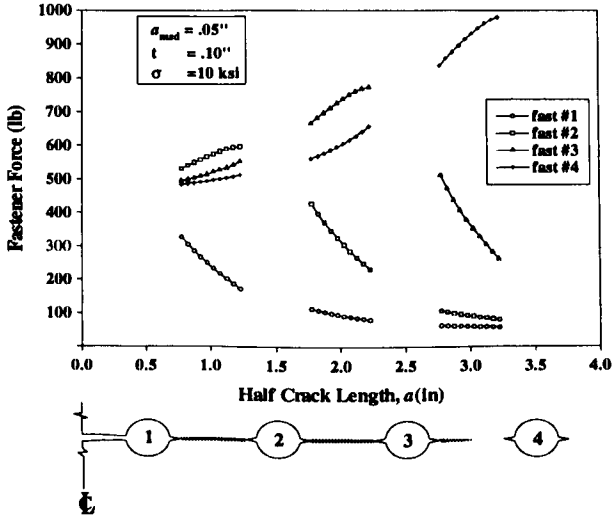

Figure 12 Fastener Force Redistribution from DIAL Lap Joint Model.

FATIGUE CRACK GROWTH PREDICTIONS IN RIVETED JOINTS

S. A. Fawaz
Air Force Research Laboratory
Wright-Patterson AFB, OH 45433, USA
(937) 255-6104 ext. 239
(937) 656-4999
scott.fawaz@flight.wpafb.af.mil

J. Schijve
Faculty of Aerospace Engineering, Delft University of Technology
Kluyverweg 3, 2629 HS Delft, The Netherlands

ABSTRACT

A characteristic aspect of fatigue of riveted lap joints is the occurrence of crack growth under a complex stress system, which in its simplest form consists of cyclic tension with superimposed cyclic bending due to the eccentricity in the lap joint. In reality, rivet squeezing leads to hole expansion and built-in residual stresses. In the empirical part of the investigation a simpler problem was analyzed first, i.e. fatigue crack growth in a multiple-hole sheet specimen loaded under combined tension and bending stress. Crack growth development for small part-through cracks could be followed by fractographic observations employing marker load cycles in between constant-amplitude loading. The same marking technique was employed for a simple lap joint having two rivet rows with four rivets in each row. The crack growth history could be reconstructed from a crack length of 75 μm to final fracture at 12 mm.

In the analytical part, the well-known Newman-Raju K-solutions are available for part-through cracks. After through cracks are obtained they continue to grow with oblique crack fronts due to the combined tension and bending. Since no K-solutions are available for these cracks, the finite-element method and a three dimensional virtual crack closure technique (3D VCCT) were adopted. K-solutions for the crack shapes obtained in the open hole sheet specimen lap joint experiments are then calculated and adopted for the prediction of the growth of these cracks. A satisfactory agreement has been obtained. K-values have been calculated for a range of crack depth to crack length ratios, crack depth to sheet thickness ratios, and hole radius to sheet thickness ratios.

The Newman/Raju K-solutions and newly calculated K-solutions for the through cracks have been incorporated into a crack growth prediction scheme. The prediction algorithm not only predicts the fatigue life within 6% of the actual life, but also accurately predicts the crack growth history until just prior to final fracture.

1. Introduction

The crack growth prediction model developed here does not use a new crack growth law or incorporate any new phenomenological behavior witnessed during the experimental investigation. Simply stated, the crack growth model predicts crack growth of part through and through cracks with crack shapes typically found in longitudinal lap-splice joints of pressurized fuselage structure. Results of fatigue crack growth experiments on different types of specimens are used for the validation of the prediction model. It covers, center cracked tension specimens, center cracked tension/bending specimens, specimens with a single open hole with edge cracks, and riveted lap joint specimens. In view of the aims of the present research program on fatigue of riveted lap joints of fuselage lap splices, the predictions are restricted to constant-amplitude (CA) loading, but it includes part through cracks with a quarter elliptical crack front

as well as through cracks with an oblique crack front. Moreover, combined tension and bending is addressed.

The predictions are compared to results obtained in the experimental investigation. Stress intensity factors are partly borrowed from the literature. For the part through crack growth, the well-known Newman/Raju stress intensity factor equations are used. The through crack portion of the fatigue life is modeled using the newly developed stress intensity solutions for a part elliptical through crack shown in Figure 1 which was first presented in reference [1]. A question that immediately comes to mind is how to address the transition from a part through to through crack? The transition is supposed to occur at the moment that K at the deepest point along the bore of the hole exceeds 1.4 times K_{Ic}, which is the criterion used in the NASGRO Crack Growth Computer Program[3]. The crack depth then becomes equal to the sheet thickness. The smallest a/t ratio of a through crack for which K values became available from the FEA results is 1.05. This value is then used for calculating the first growth increment of the through crack after break through to the other sheet surface.

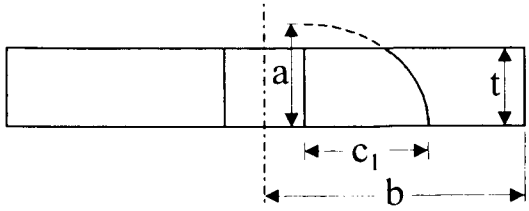

Figure 1 Part-Elliptical Through Crack Geometry

The sheet material considered is 2024-T3 Alclad. The basic da/dN - ΔK crack growth data used for predictions are presented first (section 2), followed by predictions for part through cracks in section 3 and oblique through cracks in section 4. Both types of cracks are considered under different types of loading. The investigation is summarized in a number of conclusions in section 5.

2. Basic da /dN -ΔK Relation Adopted for Crack Growth Predictions

The Forman-Newman-de Koning, FNK, crack growth equation is used to describe the basic da/dN - ΔK relation applicable to 2024-T3 thin sheet material. The FNK equation, Eqn. (1) is an extension of the Forman equation with added parameters, p and q, to better fit the material data in the extremal regions of the da/dN vs. ΔK curve.[2-4]

$$\frac{da}{dN} = C\left(\frac{1-f}{1-R}\Delta K\right)^{n} \frac{\left(1-\frac{\Delta K_{th}}{\Delta K}\right)^{p}}{\left(1-\frac{K_{max}}{K_c}\right)^{q}} \tag{1}$$

where a = crack length, N = number of applied fatigue cycles, R = stress ratio, ΔK = stress intensity factor range, C, n, p, q = empirically derived material constants, f = crack opening function, ΔK_{th} = threshold stress intensity factor, K_c = critical stress intensity factor. The crack opening function, f, for plasticity induced crack closure, is defined by Newman as[5]

$$f = \frac{K_{op}}{K_{max}} = \begin{cases} \text{maximum of } R \text{ or } A_0 + A_1 R + A_2 R^2 + A_3 R^3 & R \geq 0 \\ A_0 + A_1 R & -2 \leq R < 0 \end{cases} \tag{2}$$

with the A_i coefficients given below.

The plane stress/plane strain constraint factor is α and σ_{max} and σ_0 are the maximum applied stress and flow stress, respectively. For the predictions where the crack opening function is included, α is set to 1.5, as recommended in reference [3], and the ratio of σ_{max}/σ_0 to 0.3.[1,5] Although the equations appear overly complicated for constant amplitude loading, it degenerates to the closure corrected Paris equation

$$A_0 = (0.825 - 0.34\alpha + 0.05\alpha^2)\left[\cos\left(\frac{\pi}{2}\frac{\sigma_{max}}{\sigma_0}\right)\right]^{\frac{1}{\alpha}}$$

$$A_1 = (0.415 - 0.071\alpha)\frac{\sigma_{max}}{\sigma_0}$$

$$A_2 = 1 - A_0 - A_1 - A_3$$

$$A_3 = 2A_0 + A_1 - 1$$

by setting p = q = 0. If the material does not exhibit significant crack closure, the crack opening function can be bypassed by setting f equal to R; i.e., $K_{op} = K_{min}$. In addition, if p and q are again set to zero, Eqn. (1) reverts to the Paris equation, $da/dN = C\Delta K^n$. A more in depth review of the FNK equation is presented in references [2-5]. The full equation has been coded in the computer program to give the user a choice of the three crack growth relations. For most predictions here, the Paris equation is used unless otherwise stated. From constant amplitude fatigue test data of center crack tension specimens, shown in Figure 2, the da/dN - ΔK relation is established, from which the Paris constants, C and n, are calculated to be 1.67×10^{-12} and 3.07, respectively.

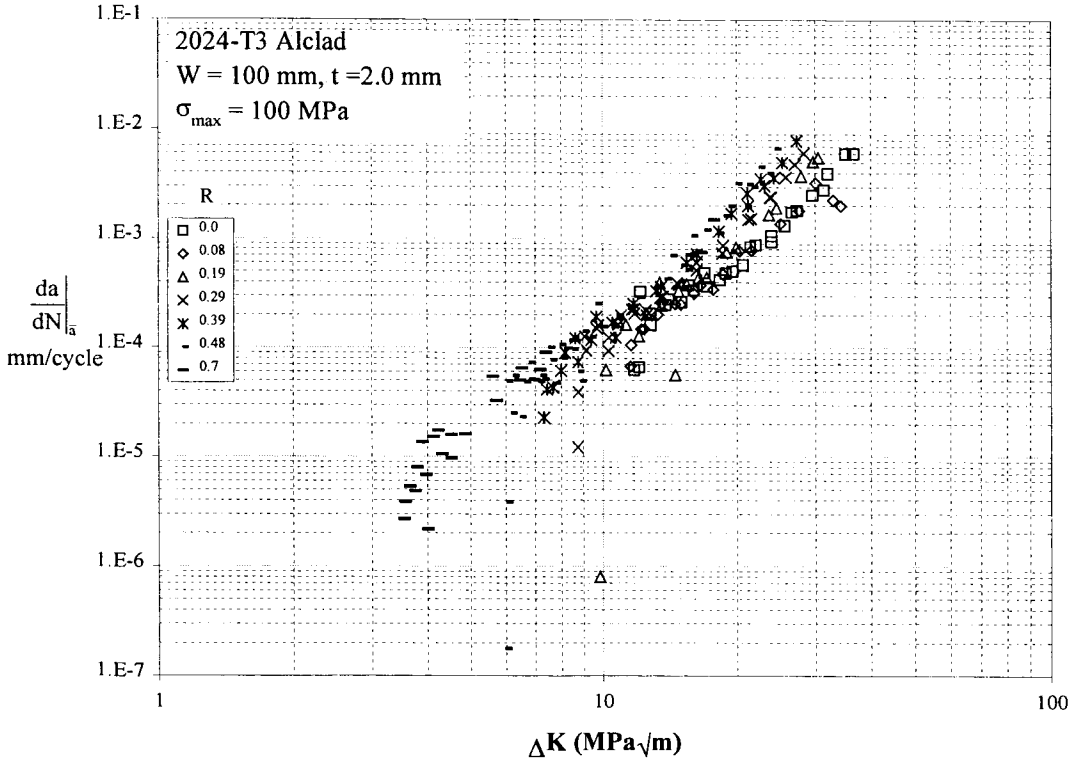

Figure 2 Crack Growth Rate Data Used for Predictions

3. The Growth of Part Through Cracks

Part through cracks initiated at the bore of a hole are generally supposed to have a quarter elliptical crack front. The size is then determined by the two semi-axis, the crack length "c_1" and the crack depth "a", see Figure 3. For the prediction of the fatigue crack growth life, an initial flaw assumption must be made, not only for the crack size, but also for the crack shape. For example, if the initial crack length "c_1" is assumed to be 1.27 mm (0.05 in., an initial crack size adopted by the USAF Damage Tolerance Requirements), an initial crack depth "a" must also be assumed. A parametric study is completed in section 3.1 to investigate the dependence of the part through crack growth on the assumed shape of the initial flaw. Predictions are made for the same value of "a" but three values of a/c_1 of the initial flaw.

The predictions are based on calculating da/dN and dc_1/dN in order to find the new locations of the semi-axis of the quarter elliptical crack. It thus is assumed that the crack front remains quarter elliptical and that the prediction can be restricted to two points of the crack front. This is the approach generally adopted in the literature. Predictions for crack extension are made in for a large number of points distributed along the crack front. A quarter ellipse is then drawn through the predicted new points of the crack front. For that purpose a regression analysis is used. In sections 3.1 and 3.2, sensitivity studies are completed to determine the effect of the initial flaw shape assumption and the bending factor, respectively. A comparison between predicted and observed crack shapes is made in section 3.3. It should be noted that the predictions in sections 3.1 – 3.3 are made for combined tension and bending.

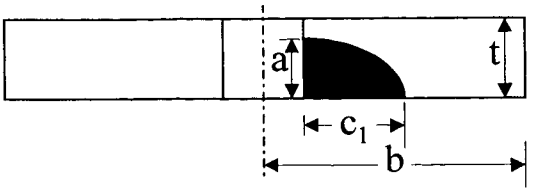

Figure 3 Part Through Crack Geometry

3.1 The Effect of the Initial Flaw Shape a/c_1

The Newman/Raju corner crack solutions for K-values remain as the primary reference for crack growth predictions of part elliptical crack geometries. For this reason, not to mention the ease of programming the numerous polynomial equations, the Newman/Raju solutions are the only solutions used for part through crack growth.[6] For the predictions that are completed here, the same initial crack depth is a = 0.01 mm, but there are three values of the a/c_1 ratio: 0.5, 1.0, and 2.0, i.e. c_1 = 0.02, 0.01, and 0.005 mm, respectively. The calculations are for a 100 mm wide specimen of 2024-T3, thickness 1.0 mm with a 2.0 mm hole in the center. The remote stress is 100 MPa of both tension and bending (bending factor k = 1.0). Obviously, the bending should affect the fatigue crack shape development. Results are shown in Figure 4 - Figure 6 for the three a/c_1 ratios, respectively. The figures show crack fronts obtained at intervals of approximately 20% of the fatigue life defined by the last crack front to static break through of the remaining ligament.

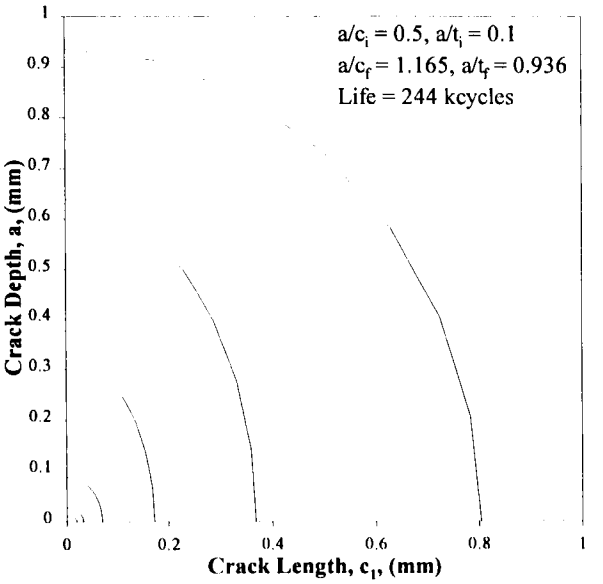

Figure 4 Crack Shape Development with Initial a/c_1 = 0.5

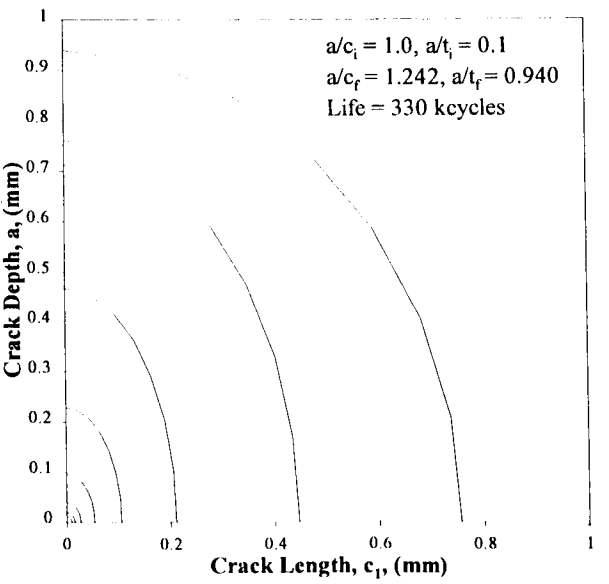

Figure 5 Crack Shape Development with Initial a/c_1 = 1.0

Although the initial a/c_1 ratios are highly different in the three figures, the final a/c_1 are similar but slightly increasing ($1.165 \le a/c_1 \le 1.338$) with the initial a/c_1 ratios. In [1], the final a/c_1 ratios calculated were constant at $a/c_1 \approx 0.575$. Since then, modifications to the Newman/Raju equations for a double corner crack at a hole have resulted in more continuous solutions for $a/t < 0.2$ and $a/t > 0.8$.[7,8] The figures show that the crack shape is always changing. The change in crack shape, a/c_1, is also evident in Figure 7 for each of the initial crack shapes, $a/c_1 = 0.5$, 1.0, and 2.0. Crack growth appears to be very much similar during the fatigue life, as should be expected, although the shape is changing. The final crack shape is converging to an $a/c_1 \approx 1.25$. The large difference in fatigue lives until break through may suggest a strong dependence on the initial flaw shape assumption. However, in Table 1, the life is split into an initial part until $c_1 = 0.25$ mm and a second part from $c_1 = 0.25$ to break through. It then turns out that the relatively large initial part of the life is strongly depending on the initial crack shape. A t the end of this initial part, the crack shapes for the three initial a/c_1 values are no longer that much different. As a consequence, the second part is practically independent on the initial crack shape. It has also been noted in the literature that semi-elliptical surface cracks with highly different a/c_1 values of the initial flaw show a tendency to grow to crack shapes with approximately the same a/c_1 ratio. Ichsan recently discussed this.[9] However, the results of the semi-elliptical surface cracks were grown under cyclical tension, which resulted in stabilized a/c_1 ratios close to 1.0. The present observation of a continually changing a/c_1 ratio for different initial flaw shapes is related to the occurrence of combined tension and bending.

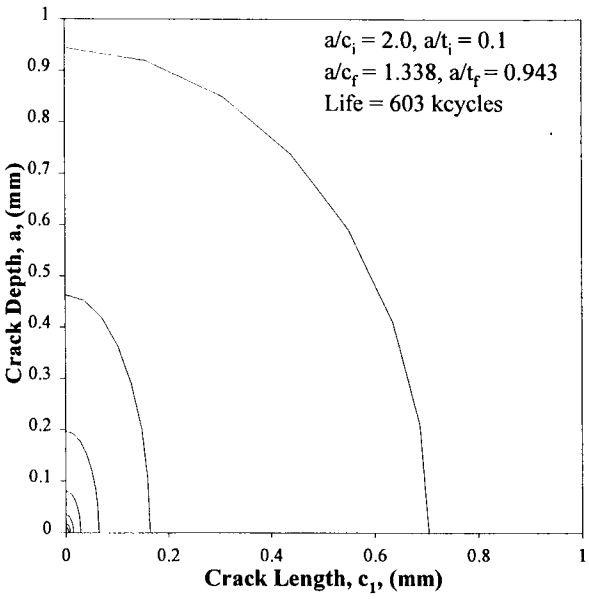

Figure 6 Crack Shape Development with Initial $a/c_1 = 2.0$

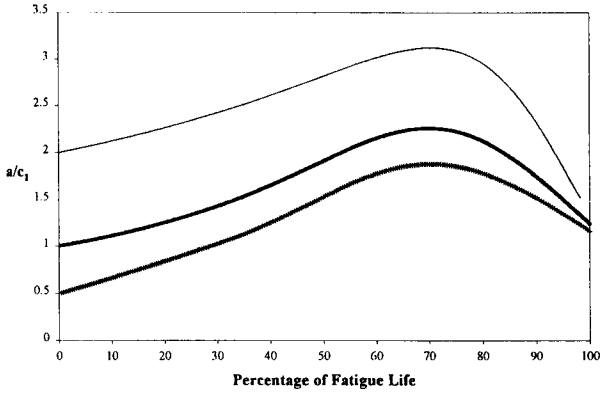

Figure 7 Crack Shape Development during the Fatigue Life

The effect of the applied stress, specifically the ratio between the tension and bending stress, should be important. A similar parametric study was conducted using the same specimen dimensions as before except the initial flaw shape and size is fixed, $a_i = 0.2$, $c_i = 0.2$, and the bending factor, k ($=\sigma_b/\sigma_t$) is

TABLE 1. Crack Growth of Initial Small Corner Flaws of Different Shapes until Break Through

Initial Flaw Data							Final Flaw Data						Crack Growth Life (kcycles)	
r/t	$a/c_1\|_i$	$a/t\|_i$	a_i (mm)	c_{1i} (mm)	$K_i(a)$ MPa$\sqrt{m}$	$K_i(c_1)$ MPa$\sqrt{m}$	$a/c_1\|_f$	$a/t\|_f$	a_f (mm)	c_{1f} (mm)	$K_f(a)$ MPa$\sqrt{m}$	$K_f(c_1)$ MPa$\sqrt{m}$	Life from initial flaw to $c_1 = 0.25$ mm	Life from $c_1 = 0.25$ mm to break through
1	0.5	0.01	0.01	0.02	2.389	2.125	1.165	0.936	0.936	0.804	7.306	9.926	176	68.0
1	1	0.01	0.01	0.01	1.951	1.752	1.242	0.940	0.940	0.756	7.114	9.579	262	67.9
1	2	0.01	0.01	0.005	1.538	1.151	1.338	0.943	0.943	0.705	6.888	9.207	535	67.8

varied from 0 to ∞. As can be seen from Figure 8 and Table 2, as the bending factor increases, the a/c$_1$ ratio at break through decreases. This behavior is expected because increasing bending is increasing the stress at one side of the sheet and decreasing the stress at the opposing surface. In addition, the effect of the bending stress is also seen when comparing the fatigue lives of two cases where the maximum stress is the same. For example, for a σ_{max} = 150 MPa, the larger k (more bending) the longer the life, ≈305 compared to ≈116 kcycles.

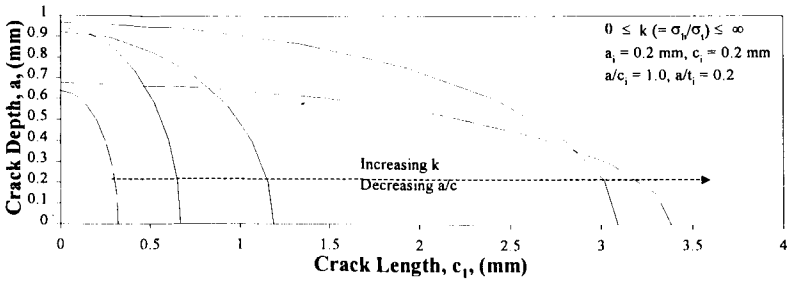

Figure 8 Crack Shape Development as a Function of the Bending Factor, k

TABLE 2 Dependence of Crack Shape on Bending Factor, k

k	σ_t (MPa)	σ_b (MPa)	σ_{max} (MPa)	$a/c_1\|_f$	$a/t\|_f$	life (kcycles)
0	100	0	100	2.000	0.640	120.923
0.5	100	50	150	1.411	0.943	116.494
1	100	100	200	0.775	0.920	75.277
2	50	100	150	0.312	0.965	304.515
∞	0	100	100	0.200	0.677	2086.260
	= a/c out of limits					

3.2 Crack Extension Predictions along the Entire Crack Front

In the previous section, the crack extension was predicted for the ends of the two semi-axis, a and c$_1$, to arrive at the new crack front, assuming that it would remain quarter-elliptical. The Newman/Raju K-solution allows a calculation of K along the entire crack front. It implies that crack extension can be predicted for many points of the crack front. It leads to many new points of the moving crack front, which then can not be expected to be accurately a quarter elliptical curve with the same axes. However, it is possible to draw such a quarter ellipse through the new data points by adopting a regression analysis. The Newman/Raju equations can then be applied again for predicting the next crack extension. Ichsan adopted this procedure for a semi-elliptical surface crack loaded under remote tension only. He found that fitting an elliptical crack front for 32 points leads to a slightly longer fatigue life than predicted by the method of the previous section, i.e. predictingΔa and Δc_1 for the axes and assuming that the crack front remains elliptical. The difference was on the order of 10%. A similar comparison is made in [1] for two corner cracks at a hole under remote tension and bending (bending factor, k = 1) with similar results. Using more than 32 calculation points along the crack front results in a negligible effect on the fatigue life. However using fewer calculation points results in a slightly larger difference between the curve fit and non-curve fit prediction. The crack growth for the fit data is less than the unfit since the linear regression is decreasing the a or c$_1$ dimension by a small amount after each cycle. As can be expected, the small systemic decrease in crack size has a cumulative effect. As a result, a prediction with a small initial flaw assumption will undergo more regression calculations thereby having a larger effect on the fatigue life. To eliminate the systemic error due to curve fitting, at least 32 calculation points should be used.

3.3 Comparison between Predicted and Observed Crack Shapes

Since in situ crack shape measurement is not currently possible, the only method of verifying the K solutions is by using the fatigue life or crack front shape after failure. For the 7-open hole tests, shown in Figure 9, several specimens were statically loaded to failure prior to failure by fatigue, and the crack shapes were measured. Thus for a given number of cycles, the crack shape is known and comparisons can be made with the analytical predictions. Such a comparison is shown in Figure 10 for five separate cracks in the same specimen. The predictions are completed assuming each hole is located in a finite

width strip with no interaction with adjacent cracks. Since the cracks are still small, this procedure should be allowed. The five cracks do not have the same dimension because the initiation has taken different numbers of cycles. The shapes are predicted for the crack length "c_1" as observed, starting from a quarter elliptical crack with $a/c_1 = 1.0$. The initial a/c_1 value is not very important for the present size of the crack as discussed in section 3.1. Figure 10 shows a very good agreement with the crack shape development as observed from the specimen fracture surface. Similar satisfactory results were obtained for specimens with a single open hole also loaded by combined tension and bending.

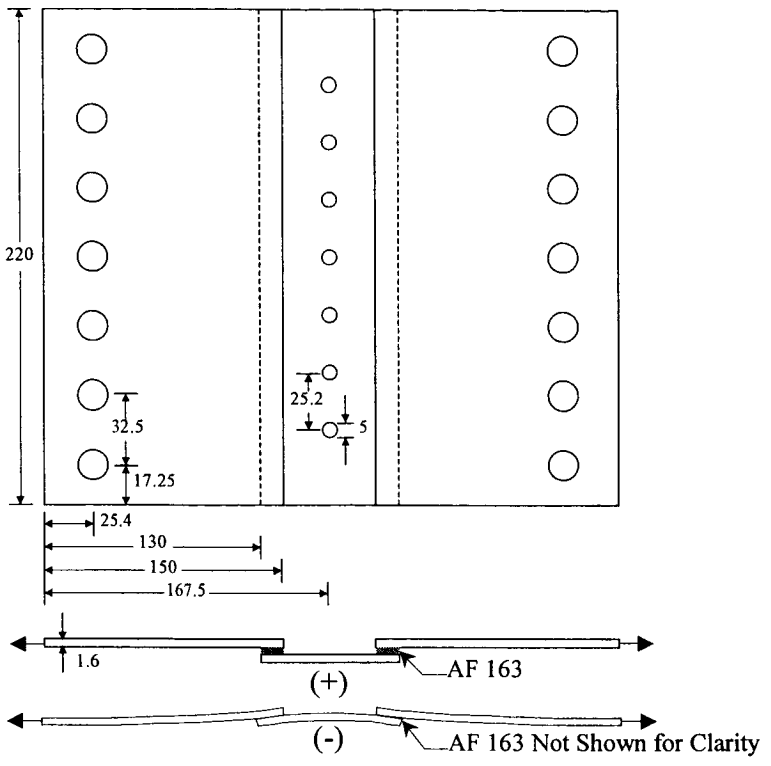

Figure 9. Measured vs. Predicted Crack Shape

4. The Growth of Through Cracks

The only K-solution for through cracks under combined loading conditions now available is the library of the NASGRO Fatigue Crack Growth Computer Program.[3] It applies to the loading cases shown in Figure 11. It assumes that the crack has a crack front perpendicular to the sheet surface. Predictions with these K-solutions are compared in section 4.1 to the test results presented in [1]. The effect of the initial flaw shape assumption and the bending factor on oblique through crack growth are discussed in section 4.2. In sections 4.3 and 4.4, the K-solutions developed in [1] are used.

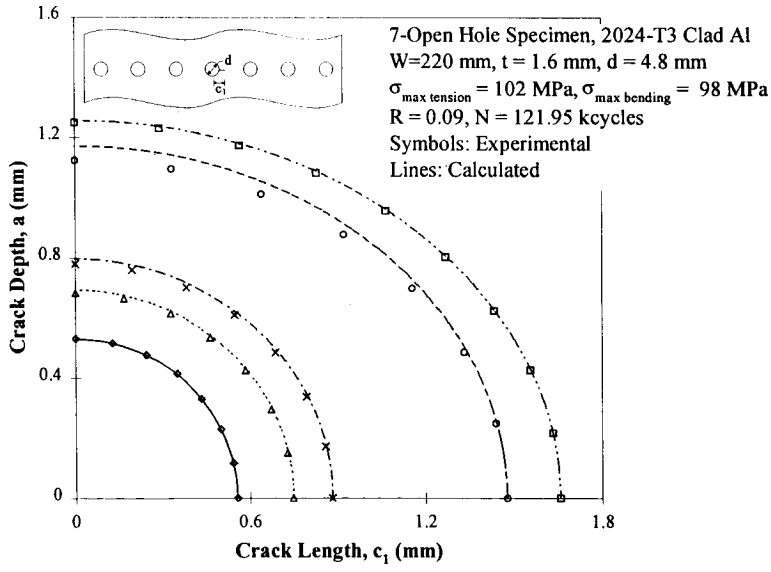

Figure 10. Measured vs. Predicted Crack Shape

4.1 Through Crack Growth: Published Stress Intensity Solutions

First predictions with the NASGRO K-solutions are made for through cracks starting from an open hole in a specimen loaded under tension only. An assumption had to be made about the crack initiation life, which was made to predict not only the fatigue life, but also the entire crack history. To do so an initial flaw size is assumed for which a prediction is made. A comparison is then made between the actual and predicted crack histories. If the prediction is underestimating the crack growth, the initial flaw size is increased; conversely, if the

prediction is overestimating the crack growth, the initial flaw size is decreased. An example of the comparison between prediction and tests results is shown in Figure 12, which shows a good agreement. Similar correlation was obtained for all open hole specimens loaded by remote tension only.

Unfortunately, the correlation is not as good for specimens subject to combined remote tension and bending shown in Figure 13. Crack growth rates for cracks larger than 2 mm are highly overestimated. Although some aspects of the theoretical background of the NASGRO K-solutions may be questioned, there is one obvious reason for disagreement. In the NASGRO concept, the crack is supposed to be a through crack with a straight crack front perpendicular to the plate surface. In reality, under combined tension and bending such cracks grow with an oblique part-elliptical front. In Figure 13, the crack length plotted is c_1 (see Figures 1 and 3), which is the largest length of the crack at the material surface where the bending stress has its maximum. Since the crack through the thickness is lagging behind this point the cracked area is smaller than assumed in the NASGRO solution. An overestimation of the crack growth should then be expected.

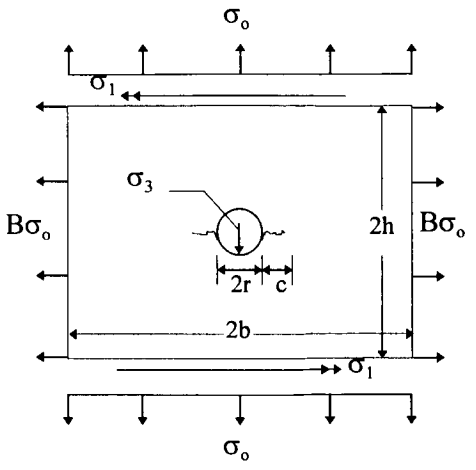

Figure 11 NASGRO TC09 Crack Case

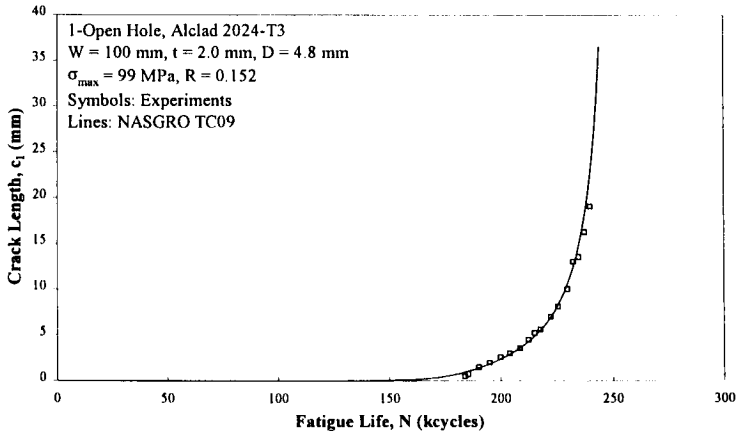

Figure 12 TC09 Verification Remote Tension

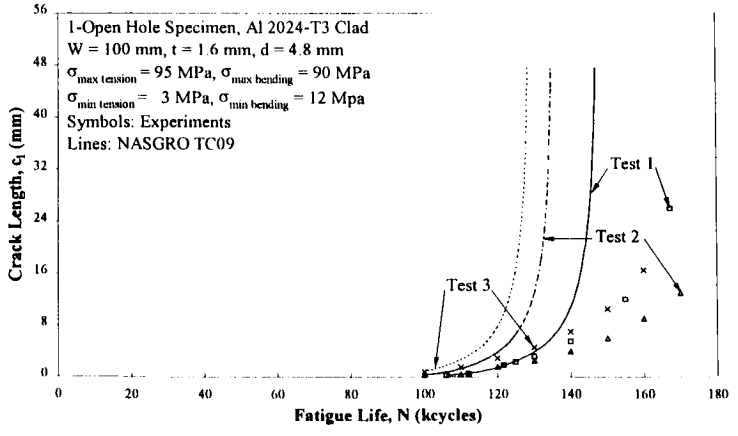

Figure 13 TC09 Verification Remote Tension and Secondary Bending

4.2 The Effect of the Initial Flaw Shape a/c_1

A similar parametric study conducted for the part-through cracks is done for the oblique through cracks (OTC). For the predictions that are completed here, an initial crack length, $c_1 = 2.1$ mm, has been used with four values of the a/c_1 ratio: 0.5, 1.0, 1.5, and 2.0, i.e. a = 1.05, 2.1, 3.15, and 4.2 mm, respectively. The calculations are for a 100 mm wide specimen of 2024-T3, thickness 1.0 mm with a 2.0 mm hole in the center. The remote stress is 100 MPa of both tension and bending (bending factor k = 1.0). Results are shown in Figure 14 - Figure 17 for the four a/c_1 ratios, respectively. The figures show crack fronts obtained at intervals of approximately 20% of the fatigue life. The last crack front applies to net section yield or $K_{applied(c_1)} > K_{Ic}$.

Although the initial a/c_1 ratios are highly different in the four cases, the final a/c_1(=0.435) are exactly the same. Similarly, the final a/t (=2.175) ratios are the same for all four predictions. Generally, the magnitude of K for a straight through crack from a hole is larger than an OTC of the same c_1 length. This behavior is manifest in the slightly larger fatigue life for the crack, Figure 14, with initially high a/c_1 and a/t ratios. Figures 14 – 17 as well as Figure 18 shows that the crack shape quickly stabilizes regardless of the initial shape. In view of the difficulties in accounting for the crack shape during the transition between a part through crack to OTC, it appears that assuming an "incorrect" shape for the first cycle as an OTC is of little consequence. Recall, when the part through crack breaks through the thickness there is an instantaneous increase in the crack depth and most likely no noticeable increase in the crack length; thus a crack shape must be assumed for the beginning of the OTC portion of the prediction.

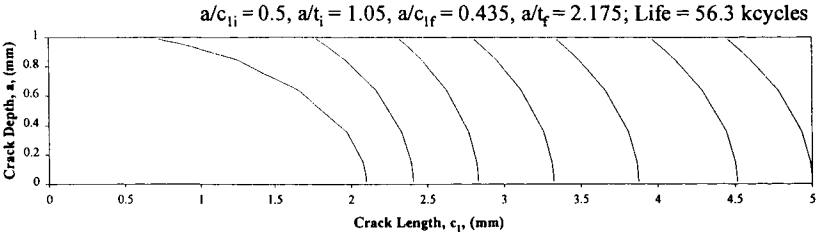

Figure 14 Crack Shape Development with Initial a/c_1 = 0.5, a/t = 1.05

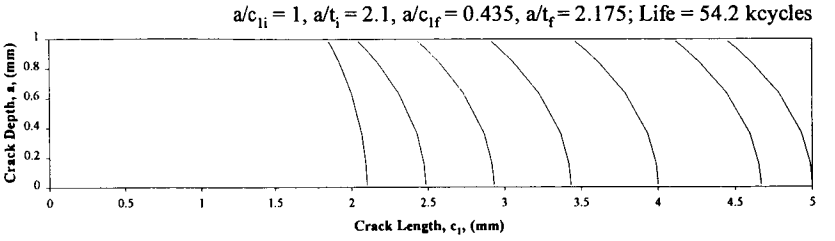

Figure 15 Crack Shape Development with Initial a/c_1 = 1, a/t = 2.1

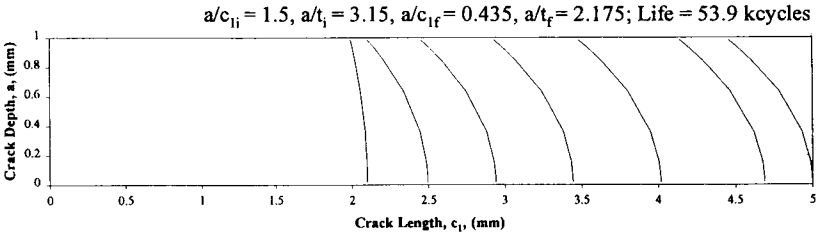

Figure 16 Crack Shape Development with Initial a/c_1 = 1.5, a/t = 3.15

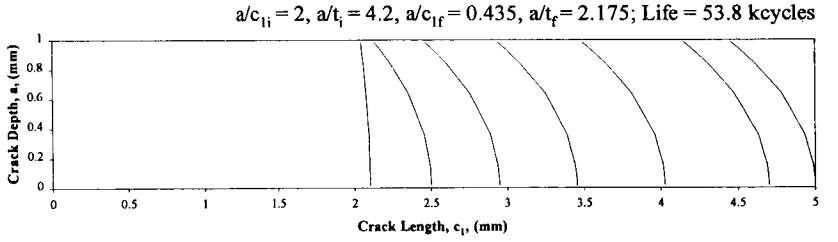

Figure 17 Crack Shape Development with Initial a/c_1 = 2, a/t = 4.2

In the parametric study above, it was shown that the initial flaw shape assumption is of little consequence in fatigue life predictions. Furthermore, the effect of the applied stress, specifically the ratio between the tension and bending stress, should be important. A similar parametric study was conducted using the same specimen dimensions as before except the initial flaw shape and size is fixed, a_i = 1.05, c_{1i} = 1.05, and the bending factor, k ($=\sigma_b/\sigma_t$) is varied from 0.5 to 2.0. As can be seen from Figure 19 and Table 3, as the bending factor increases, the a/c_1 ratio decreases. This

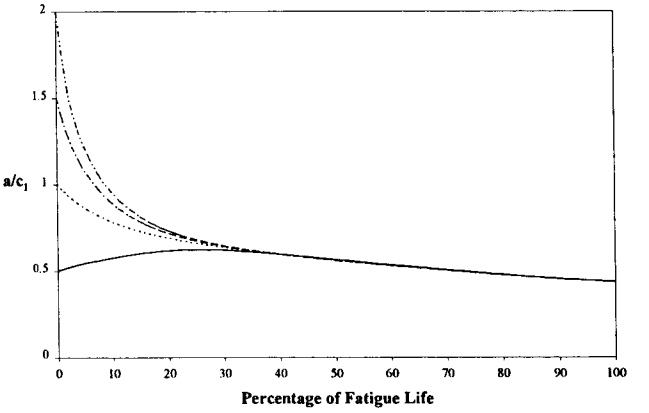

Figure 18 Effect of Initial Flaw Shape on Flaw Shape Development

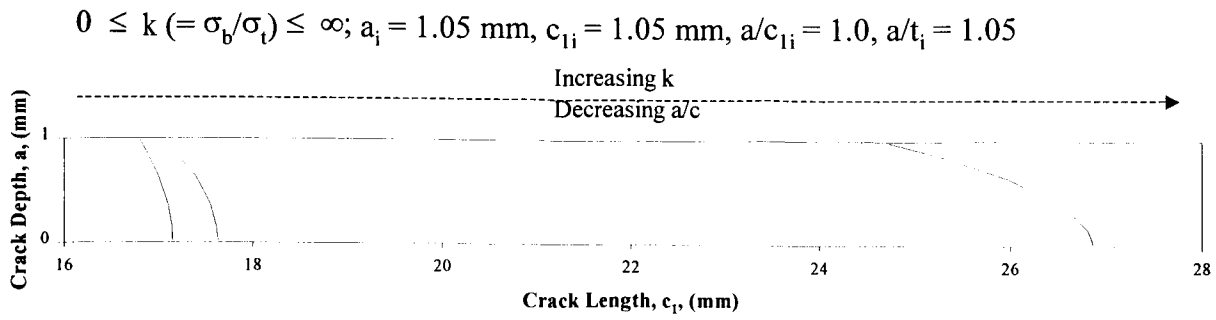

Figure 19 Effect of the Bending Factor, k on Flaw Shape Development

behavior is expected for the same reason as stated for the part through cracks, the larger k (more bending) the smaller the a/c_1 and longer the life, ≈754 compared to ≈205 kcycles.

TABLE 3 Dependence of Crack Shape on Bending Factor, k

k	σ_t (MPa)	σ_b (MPa)	σ_{max} (MPa)	$a/c_1\|_f$	$a/t\|_f$	Life (kcycles)
0.5	100	50	150	0.280	4.809	204.685
1	100	100	200	0.216	3.810	131.932
2	50	100	150	0.094	2.527	754.256

4.3 Through Crack Growth Predictions with the New K-Solutions: Open Hole Specimens

K-solutions for oblique through cracks at a hole were obtained from finite elementanalyses for a range of crack depth to crack length ratios (a/c_1 = 0.2, 0.3, 0.4, 0.6, 1.0, 2.0), crack depth to sheet thickness ratios (a/t = 1.05, 1.09, 1.13, 1.17, 1.21, 2.0, 5.0, 10.0) and hole radius to sheet thickness ratios (r/t = 0.5, 1.0, 2.0).[1] The results were presented in tabular format. These values could be converted to a polynomial description of the results. However, with the computational power of current desktop personal computers, there is no need for the time consuming derivation of such polynomial equations. A computer program has been developed, which by interpolation obtains the K-values for the applicable crack shape and size, defined by values of a/c_1, a/t, and r/t. The interpolation is handled by a choice of three different interpolation routines; linear, higher order polynomial, or cubic spline. Although the linear interpolation is attractive in it's simplicity, it is not well suited for interpolating between the large ranges in the a/c_1 and a/t values. Both the higher order polynomial and cubic spline routines are used with no distinguishable difference. However, the cubic spline appears to be more stable than the higher order polynomial in extrapolating K's from a table. Extrapolation may be required in a/c_1 in the latter stage of the fatigue life where the crack is growing quite rapidly, and the crack front is straightening out resulting in large a/c_1 ratio.

The new K solutions have been used to predict the fatigue life of an open hole specimen subject to tension and bending ($k \approx 1.0$). The cracks nucleate and grow naturally as corner cracks; thus, the Newman/Raju K-solution is used until the crack grows through the thickness of the sheet. Once the crack is a through crack, the new solutions are used until final fracture.

The transition from a part through to through crack is difficult to examine experimentally; therefore an assumption of the transition behavior was made as explained previously in section 1. Examination of the fracture surfaces of the fatigue specimens that were statically overloaded to failure when the crack was close to the transition area did not show a detectable change in the crack shape. As mentioned previously, since the fracture surfaces must be viewed by destructive inspection, the comparison is made of cracks from different specimens of the same geometry tested at the same remote stress level. Thus, the factor of 1.05 does not alter the crack shape significantly, but does account for the instantaneous increase in the crack depth at the moment of break through. Additional assumptions that must be made in the prediction calculation are the initial flaw size and shape. Based on fractographic observations, the initial

crack shape is assumed to be quarter circular, $a/c_1 = 1.0$. The initial flaw size is estimated. The prediction algorithm iterates by varying the initial flaw size (quarter circular shape) until the crack length and number of cycles at failure is achieved.

The prediction of the open hole specimen subject to combined tension and bending shown in Figure 20 does not exactly follow the entire crack growth history. The transition from a part through to a through crack is seen at approximately 112 kcycles where the crack length and depth (the latter not shown in the figure) is about 1.8 mm. The predictions previously reported in [1], showed a slight cusp in the prediction curve during the transition from a part through to a through crack. This was attributed to not accurately calculating K in the transition region. Specifically, the front surface K calculated for the last cycle as a part through crack is higher than the first K calculated for the through crack, implying a higher crack growth rate just before break through. The ligament width in the thickness direction is going to zero and such a behavior might occur in view of the questionable K-values at the moment of the transition. Grandt et al. reported a nearly constant crack growth rate for the c_1 crack length during the transition from a part through to through crack.[10] As seen in Figure 20, the cusp in the transition region has disappeared which is attributed to using the modified Newman/Raju equations.[7,8]

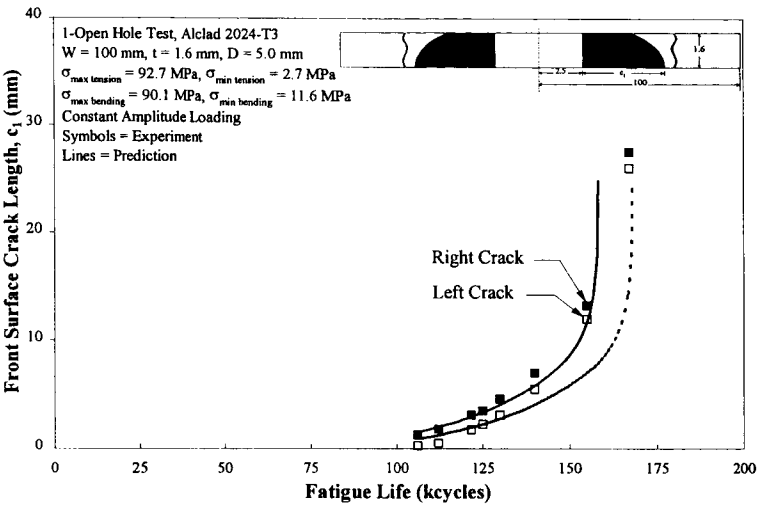

Figure 20 Crack Growth Prediction in 1-Open Hole Specimen Subject to Combined Tension and Bending

The new K's do not account for a changing stress field, which occurs as the crack becomes quite long. A long crack implies a reduction in the bending stiffness of the sheet; thus, the crack is experiencing a more tensile stress field. In a tension dominant stress field, it was shown in [1] for a center cracked sheet with a part elliptical oblique crack subject to pure tension and separately combined tension and bending that the K's for the pure tension case are higher than that for the combined loading assuming the same applied remote stress. From the correlation between actual and predicted crack histories in Figure 20, the K solutions used for this complex crack shape subject to combined tension and bending loading are reliable. Within the scope of linear elastic fracture mechanics, K remains to be a good similitude parameter when the crack geometry and loading condition are well characterized.

4.4 Through Crack Growth Predictions with the New K-Solutions: Asymmetric Lap-Splice Joint Specimens

The asymmetric lap-splice joint shown in Figure 21 was fatigue tested using a program loading spectrum that creates marks, groups of fatigue striations, on the fracture surface which can be clearly seen at low magnification (typically less than 5000X) in the scanning electron microscope. The spectrum is composed of blocks of constant amplitude loading followed by smaller blocks of constant amplitude loading at a lower K_{max} and was successfully used by Piascik[11] and Fawaz[1]. The joint offers several simplifying features when compared to lap-splice joints used in transport aircraft in that the load transfer in each rivet row is known, 50%, and the joint has a point of symmetry at its centroid. The K-calculations include tension, bending, and hole loading.

Predictions for the asymmetric lap splice joint are shown in Figure 22 and 23. As was discussed in section 3.1, the initial flaw size and shape strongly affect the fatigue behavior of small cracks. Attempts have been made to try and predict the small crack history when the crack is still a corner crack using the Newman/Raju solution. However, since the flaw shape at these small crack lengths cannot be determined from the marker bands, predictions are made for several initial flaw shapes (a/c_1 = 0.2, 1.0, 1.5, and 2.0) using the known c_1 crack length. From these predictions, the initial flaw shape did not affect the crack shape at break through which was previously shown in Figure 4 - 6. Even though the life to break through slightly increases with a larger initial a/c_1, the Newman/Raju solutions do adequately predict crack growth of an initial crack to break through. Note Figure 22 is for a crack that has not grown through the thickness. It is worth noting that the Newman/Raju solutions do not account for rivet interference or load transmission by friction between the sheets at the faying surface, both of which can result in decreasing the load available for crack extension. Since a low squeeze force was used to install the rivets, the hole expansion and clamping

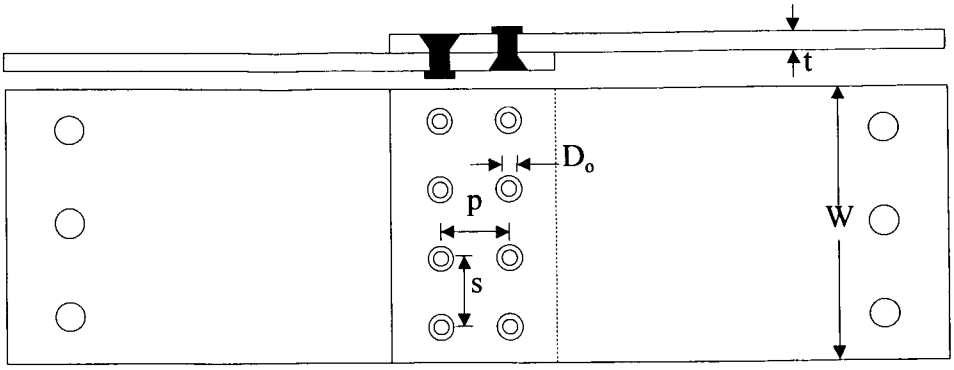

Figure 21 Asymmetric Lap Splice Joint

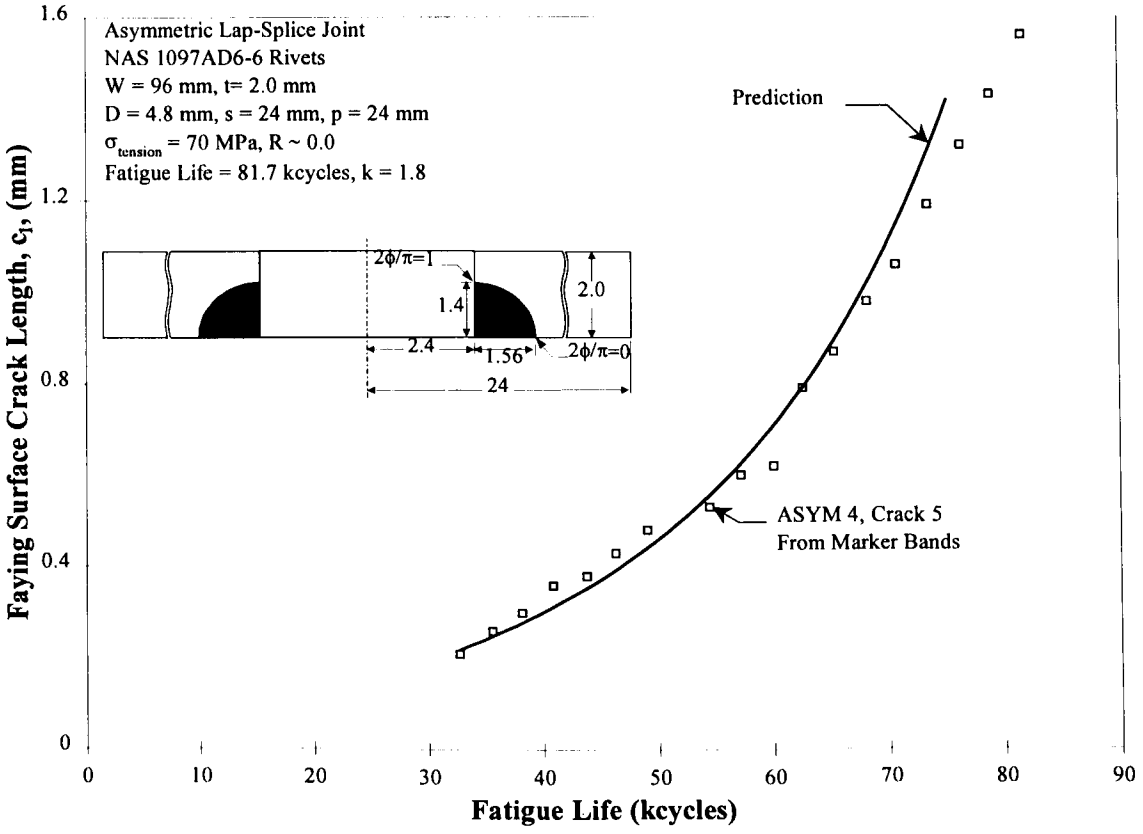

Figure 22 Crack Growth Prediction for Asymmetric Lap Splice Joint, Part Through Crack

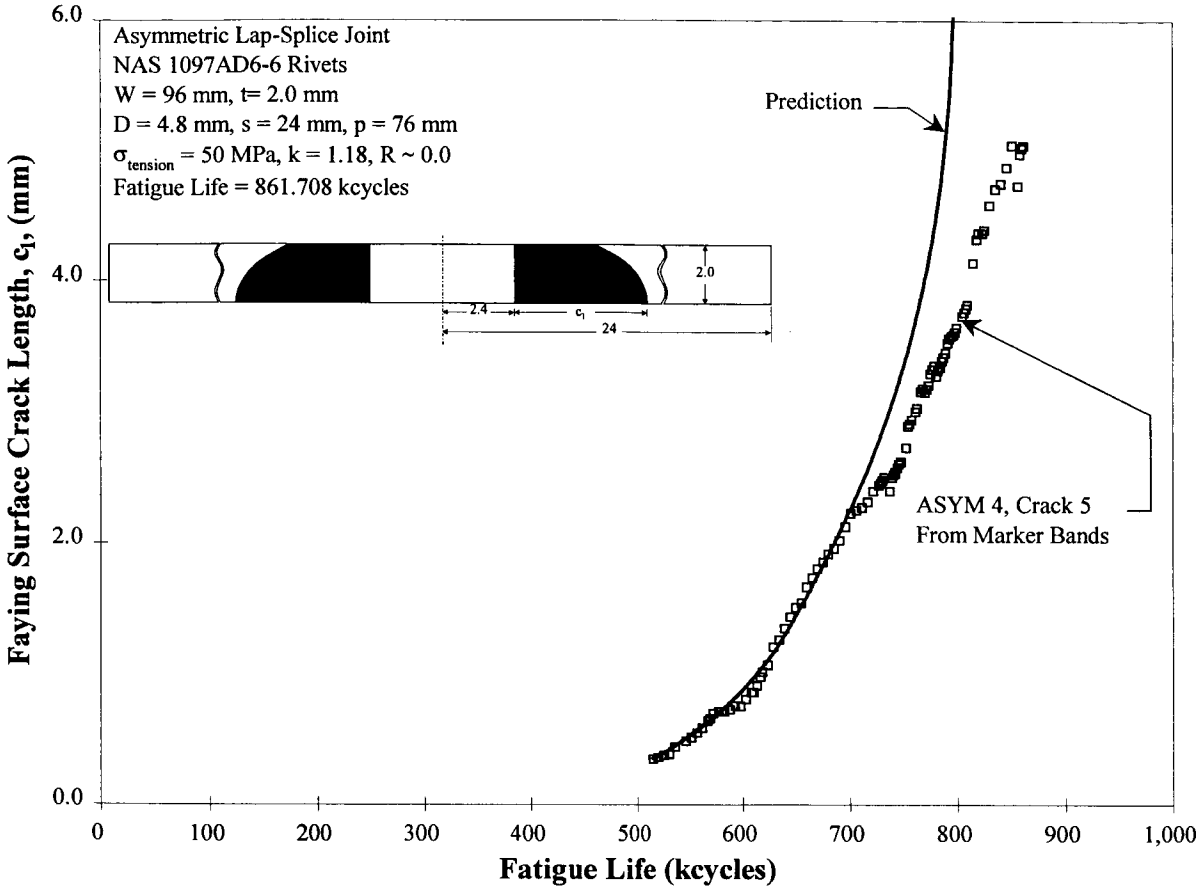

Figure 23 Crack Growth Prediction for Asymmetric Lap Splice Joint, Through Crack

force are low diminishing the residual stresses near the rivet hole. In a joint with highly squeezed rivets, the predictions may not correlate to the test data as well. In that case then, a shortcoming in the prediction model would be the inability to account for interference and load transmission by friction. The prediction in Figure 23 as well as that shown in Figure 22 shows the new K solutions are performing reasonably well. In Figure 23, the prediction underestimates the fatigue life by approximately 10% resulting from a slight overestimation of K during the through crack portion. Examination of the fracture surface of both critical rows showed extensive cracking. As adjacent cracks grow, the rivet is less effective in transferring the load; thus, the load is redistributed to the remaining rivets. Not accounting for load shedding is another weakness of the model. By the rather steep slope of the through crack region, the crack is growing quite fast with slightly more than 10% of the fatigue life remaining. Assuming the crack is growing from a rivet hole in a finite width sheet with no other cracks at other rivets is an oversimplification of the cracking scenario.

5. Conclusions

- Crack Growth Prediction Methodology: da/dN - ΔK Relation
  - In general, the same crack growth prediction methodology developed and used in the NASGRO Crack Growth Computer Program is adopted. The Forman-Newman-de Koning crack growth law is available in the crack growth prediction computer program, but due to the simplicity of the load spectrum (CA) and the well characterized sheet material (2024-T3), the FNK equation is degenerated to the closure corrected Paris Law for all predictions.

- Crack Growth Predictions Using Published K Solutions
  - Double Corner Cracks at a Hole Subject to Tension and Bending, Newman/Raju
    - The Newman/Raju solutions accurately predicted both the crack shape and fatigue life for open hole specimens subject to remote tension and bending, (Figure 10).
    - The initial flaw shape assumption has a negligible effect once the crack length at the material surface, "c_1" exceeds 0.25 mm in a 1.0 mm thick sheet. However, due to the dependence of the K-value at the material surface, $K(c_1)$, on the "c_1" crack length, crack growth in the small crack regime ($c_1 \leq 0.25$ mm) is affected.
    - For studying the K variation along the crack front, a regression analysis must be preformed after each crack growth increment to fit the crack front back to an elliptical shape. To avoid regression analysis errors with the N/R solutions, 32 calculation points along the crack front must be used. Otherwise systematic errors occur in the crack shape (either in the crack depth or crack length) ultimately affecting the fatigue life.
  - Double Through Cracks at a Hole Subject to Tension and Bending (NASGRO TC09)
    - The TC09 solution accurately predicted crack growth in open hole specimens loaded in pure tension (Figure 12), but underestimated the fatigue life consistently by at least 30% for combined tension and bending (Figure 13).
- Crack Growth Predictions with Newly Developed K Solutions
  - The new K solutions for two part-elliptical, oblique through cracks at a hole have been used to predict the fatigue life of an open hole specimen subject to combined tension and bending ($k \approx 1.0$). In addition, predictions have been completed for an asymmetric lap splice joint.
  - Predictions of the *open hole* specimens subject to combined tension and bending ($k \approx 1$) show good agreement for a majority of the crack history. The predicted crack size is underestimated in the last 6% of the fatigue life.
  - Predictions of the *asymmetric lap-splice joint* are also adequate with the fatigue life being underestimated for both reconstructed crack histories, Figure 22 and 23. If crack growth in riveted joints is to be predicted more accurately, consideration of the effects of friction and residual stresses on the part through crack growth and crack interaction on the through crack growth is required.

REFERENCES

[1] Fawaz, Scott Anthony. Fatigue Crack Growth in Riveted Joints. Diss. Delft University of Technology, 1997. Delft, NL.

[2] Forman, Royce G., Vankataraman Shivakumar, James C. Newman Jr., Susan M. Piotrowski, and Leonard C. Williams. Development of the NASA/FLAGRO Computer Program. Fracture Mechanics: Eighteenth Symposium ASTM STP 945. D. T. Read and R. P. Reed, Eds., American Society for Testing and Materials, Philadelphia, 1988. 781-803.

[3] NASGRO Fatigue Crack Growth Computer Program, Version 2.01, NASA JSC-22267A, 1994.

[4] Forman, R. G., and S. R. Mettu. Behavior of Surface and Corner Cracks Subjected to Tensile and Bending Loads in Ti-6Al-4V Alloy. Fracture Mechanics: Twenty-Second Symposium, Vol. 1, ASTM STP 1131, H. A. Ernst, A. Saxena, and D. L. McDowell, Eds., American Society for Testing and Materials, Philadelphia, 1992. 519-546.

[5] Newman Jr., J. C. "Crack Opening Stress Equation for Fatigue Crack Growth," International Journal of Fracture. 24 (1984): R131-R135.

[6] Newman, Jr., J. C. and I. S. Raju. Stress Intensity Factor Equations for Cracks in Three-Dimensional Finite Bodies Subjected to Tension and Bending Loads. NASA-TP-85793, 1985.

[7] Zhao, W., J. C. Newman, Jr., M. A. Sutton, X. R. Wu, and K. N. Shivakumar, "Analysis of Corner Cracks at Hole by a 3-D Weight Function Method with Stresses from Finite Element Method," NASA Technical Memorandum 110144, July 1995.

[8] Zhao, W. and Newman, Jr., J. C., Electronic Communication, Unpublished NASA Langley Research Center Results, 24 February 1998.

[9] Putra, Ichsan, S. Fatigue Crack Growth Predicitons of Surface Cracks Under Constant-Amplitude and Variable-Amplitude Loading. Diss. Delft University of Technology, 1994. Delft:NL.

[10] Grandt, Jr., A. F., J. A. Harter, and B. J. Heath, "Transition of Part-Through Cracks at Holes into Through-the - Thickness Flaws," Fracture Mechanics: Fifteenth Symposium, ASTM STP 833, R. J. Sanford, Ed., American Society for Testing and Materials, Philadelphia, 1984, pp. 7-23.

[11] Piascik, Robert S. and Scott A. Willard. The Characterization of WideSpread Fatigue Damage in the Fuselage Riveted Lap Splice Joint. NASA-TP-97-206257, 1997.

NONPLANAR FATIGUE CRACK GROWTH IN 7075-T73 ALUMINUM

Second Joint NASA/FAA/DoD Conference on Aging Aircraft

Scott C. Forth and Leroy H. Favrow
United Technologies Research Center
Product Integrity, M/S 129-73, East Hartford, CT 06108 USA
Phone: (757) 864-8937
Fax: (757) 864-8911
forthsc@utrc.utc.com

William D. Keat
Union College
Mechanical Engineering Dept., Schenectady, NY 12308 USA

ABSTRACT

A specimen geometry and experimental procedure have been designed for characterizing the fatigue crack growth behavior of 7075-T73 aluminum under mixed-mode loading conditions. Specimens were prepared with semi-circular EDM flaws oriented at angles of 30, 45 and 60-degrees with respect to the applied tensile loading to induce nonplanar crack growth. Multiple tests run at each crack geometry/loading condition indicate that an acceptable level of repeatability has been attained. The experimental results were used to assess analytical models of crack growth, ranging from a projection technique to a fully three-dimensional simulator of nonplanar crack growth based on the surface integral method.

1. INTRODUCTION

Mixed-mode crack growth has been a factor in fracture analysis for some time. The first two-dimensional models yielded accurate results for anything that could be simplified to a through crack. This allowed for two-dimensional experiments [1 2 3 4 5 6] that yielded a significant amount of data that is used today. However, with the increasing complexity of parts, modeling three-dimensional cracks accurately is more important than ever.

Experimental techniques defined by ASTM and other standards organizations are mostly used for well-behaved two-dimensional or planar three-dimensional crack growth analysis. The effects of out of plane cracking are still limited to two-dimensional test procedures that have yielded excellent data, yet neglect a dimension. Therefore, modifying the ASTM standards to produce a three-dimensional nonplanar experimental technique was necessary.

The analytical capability to model a nonplanar three-dimensional crack has been developing rapidly in the last few years. The finite element method[7 8], the boundary element method[9 10 11 12], the weight function method[13], and the surface integral method[14 15 16] have all been developed and implemented to predict crack behavior in parts. However, there is very little experimental data in the literature to verify that 3D simulations of mixed-mode crack growth are accurate. A comparison to 3D planar results will give one confidence that the algorithm is accurate for those cases, but the extension to mixed-mode is still an unproven science. Hence, a fully three-dimensional mixed-mode experimental test procedure is needed to verify the assumptions that the nonplanar analytical models are based upon.

In this paper, an experimental technique was developed to model mixed-mode crack growth. Using the data from these experiments, the projection technique for life prediction was evaluated using the NASGRO and FASTRAN computer codes. The three-dimensional fatigue crack growth code, Safe, was used to explicitly model the nonplanar surface crack and predict fatigue life and crack growth trajectory.

2. EXPERIMENTAL TECHNIQUE

A typical aerospace material, 7075-T73 aluminum, was chosen due to its wide use in commercial and military applications. It is also a well-characterized material in respect to the heat treat, crack growth, and grain boundary effects. Therefore, any crack growth studies performed would have a solid base of data for reference. The fatigue crack growth specimens were taken from actual parts such that the L-T grain direction would be under investigation. During testing, the elongated grains were aligned parallel to the applied tensile loading to minimize grain boundary effects on fatigue crack growth.

The initial specimen geometry was chosen to adhere to ASTM E740 suggested specimen geometry type, with the exception that the surface EDM flaw was to be at an angle θ (30°, 45°, 60°) with respect to the applied tensile load (see Figure 4 for definition of θ). This geometry, however, failed in the grips. The specimen design was modified to lower the stress concentration at the radii blend areas and reduce the required grip holding force, which lessened the damage to the specimen tab areas. The resultant K_{tt} specimen is defined in Figure 1. These modifications proved to be sufficient to produce failures associated with the EDM surface flaws and not grip or radius areas in all subsequent tests performed.

The test systems employed are commercially available servo-hydraulic types, which employ hydraulically actuated wedge grips. The wedge grips are equipped with serrated jaws for positive specimen location and anti-slip control. Strain gauged test bars of similar geometry to the actual test specimens were used to check for grip alignment. Maintaining maximum bending strain amplitudes of $\pm$ 15$\mu\varepsilon$ are easily attainable in the specimen ligament areas by means of grip positioning within the limits of the threaded connections and bevel lock washers used for locking of grip assemblies. For example, using a Young's Modulus of Elasticity of 6.895×10^4 MPa for aluminum, one can obtain an approximate $\pm$1.03425 MPa of bending stress in the specimen ligament.

Visualization of the EDM flaws was performed using commercially available CCD cameras, incandescent lights, automated VCR and a computer equipped with the necessary PC driver card for VCR control. VCR control allows for frequency and duration of taping to be determined *a priori* to test start, so as to enable the capture of the entire crack growth sequence on a typical two hour video tape.

Marker banding was used to highlight the nonplanar crack front throughout the test. The maximum load applied was kept constant, and the minimum load was dropped to zero to create the bands. This procedure yielded excellent results using a marker to regular load cycle ratio of 100 to 1, as can be seen in Figure 2. The effect of these marker bands on the life of the specimen is shown to be negligible in Figure 3.

3. ANALYTICAL MODELS

Several analytical tools were used to model crack growth in the specimens. The surface integral finite element hybrid code, Safe[15] [16], was used to explicitly model the nonplanar crack path. The FASTRAN[3] code, a weight function technique using a plasticity induced closure model based on local incremental yielding, and the NASGRO[17] code, a weight function method implementing the Dugdale strip yield model for plasticity induced crack closure, were implemented to model the crack as a planar fracture using the projection technique.

The projection technique is commonly used to simplify a 3D mixed-mode analysis to an equivalent mode I problem so that it can be handled by any of a number of fracture codes which are available for performing a mode I growth analysis. An equivalent mode I initial flaw is generated by projecting the actual crack geometry onto a plane that is oriented perpendicular to the applied tensile loading. In Figure 4, the length $2c$, which represents the length of the line of intersection of the actual crack with the free surface, is projected to form an equivalent $2c'$, where c' becomes the radius of an assumed semi-circular initial flaw. This equivalent crack can then be grown in mode I with the aid of a code such as FASTRAN or NASGRO.

The surface integral method (Safe), also known as the body force or displacement discontinuity method, has been used to efficiently model 3D nonplanar fractures in infinite regions[15 16]. The governing integral equation is obtained by summing the effects of displacement discontinuities that have been distributed over the nonplanar fracture surface to model the crack:

$$t_k = \iint_A \Gamma_{kmn} n_m \delta_n dA \tag{1}$$

where t_k are known traction components at a collocation point on the crack surface, Γ_{kmn} are the stress influence functions for displacement discontinuities in an infinite region, n_m is the normal to the crack plane at the collocation point and δ_n represents the variation of crack opening/shear. A planar free surface in close proximity to the crack can be modeled by substituting for Γ_{kmn} the bimaterial stress influence functions derived in Keat, et al (1997)[14]. In addition, multiple free surfaces can be modeled by deploying multiple sets of these bimaterial stress influence functions as defined below:

$$t_k = \iint_A \left[\Gamma_{kmn} + \sum_{i=1}^{I} \Phi^i_{kmn} \right] n_m \delta_n dA \tag{2}$$

in which I is the number of free surfaces, and Φ^i_{kmn} are nonsingular functions that modify Γ_{kmn} to account for the presence of the free surfaces. An important advantage of this approach is that only the surface of the fracture has to be discretized. To grow the crack, criteria governing both the rate (Forman equation[17]) and direction (maximum circumferential stress theory[18]) of crack growth were applied locally at the mid-sides of the elements bordering the crack front. An automatic remesher then used this information to add a ring of crack elements to the mesh of the previous time step (see Figures 8, 9 and 10).

4. RESULTS

The specimen machining and actual testing were conducted at both United Technologies Research Center and NASA Langley Research Center over a span of six months. This allowed for an assessment of the repeatability of the technique. The consistent specimen geometry and cross-sectional stresses in the tests facilitated a direct comparison of crack geometry effects on fatigue life, as illustrated in Figures 5, 6 and 7. An R ratio of 0.7 was chosen to minimize the effects of plasticity induced closure in the experiment and thus simplify the analysis. The marker banding procedure may have induced a closure effect in the fatigue calculations. However, this is not evident in the data as shown in Figure 3.

Using the projection technique, analytical fatigue crack growth analyses were performed with both FASTRAN and NASGRO. The results are shown in Figures 5, 6 and 7. It can be implied from these figures that as the angle, θ, increases, the accuracy of the projection method decreases. The approximate error ranges from 37% at 30-degrees to 50% at 60-degrees. However, in every case the projection technique led to a conservative estimate of fatigue life.

Results were also generated using the nonplanar fatigue crack growth code, Safe. The fatigue life calculated is depicted as a vs. N in Figures 5, 6 and 7, where a is the projected crack depth and N represents fatigue cycles. The crack growth trajectories are compared to the experimental data in Figures

8, 9 and 10. It is apparent that the maximum circumferential stress theory, used to predict crack growth trajectory, applies well to these experimental tests. However, the fatigue life calculations based on the Forman equation do not. This is most likely due to the fact that the Forman equation does not consider the effects of K_{II} and K_{III} on crack growth.

5. CONCLUSIONS

The experimental procedure described in this paper has proven to be a reliable and repeatable method for measuring nonplanar fatigue crack growth in 7075-T73 aluminum. The specimen design is very straightforward, and requires little or no additional tooling to generate. The tests were all performed in an apparatus that is readily available and no special augmentations were needed for the machines.

The development of a 3D growth law based upon experimental data is necessary. The projection technique, a procedure based upon treating a mixed-mode problem as simply mode I, loses accuracy as the off-axis stresses increase at the crack. Nevertheless, the projection technique always yielded conservative fatigue life estimates for the cases studied. The analysis of the mixed-mode crack using a fully three-dimensional model should have yielded the most accurate results. However, failure to consider mode II and III effects when determining the rate of crack extension led to nonconservative estimates of crack depth. A modification of the fatigue algorithms using an energy equivalence technique may yield more accurate results.

6. ACKNOWLEDGEMENTS

The authors would like to thank the United Technologies Research Center machine shop for their work in translating parts into specimens; Ron Holland for experimental testing, data reduction, and contribution to the specimen design; Ron Brown for metalography work, sample preparation, and testing documentation; Al Ivaldi for specimen documentation and data reduction; and Jim Newman, Jr. for insight into specimen design and analytical modeling.

7. REFERENCES

[1] Lam, Y.C., 1993, "Mixed mode fatigue crack growth with a sudden change in loading direction", *Theo. And App. Frac. Mech.*, Vol. 19, pp. 69-74.

[2] Cruse, T.A., Meyers, G.J. and R.B. Wilson, 1977, "Fatigue growth of surface cracks", *Flaw Growth & Fracture*, ASTM STP 631, pp. 174-189.

[3] Newman, J.C., Jr., Wu, X.R., Venneri, S.L. and C.G. Li, 1994, "Small-crack effects in high-strength aluminum alloys", *NASA Ref. Pub. 1309.*

[4] Sih, G.C. and B.M. Barthelemy, 1980, "Mixed mode fatigue crack growth predictions", *Eng. Fracture Mech.*, Vol. 13, pp. 439-451.

[5] Toor, P.M., 1975, "A unified engineering approach to the prediction of multiaxial fatigue fracture of aircraft structures", *Eng. Fracture Mech.*, Vol. 7, pp. 731-741.

[6] Cruse, T.A. and P.M. Besuner, 1975, "Residual life prediction for surface cracks in complex structural details", *J. of Aircraft*, Vol. 12, No. 4, pp. 369-375.

[7] Nakamura, T. and D.M. Parks, 1988, "Three-dimensional stress field near the crack front of a thin elastic plate", *J. of App. Mech.*, Vol. 55, No. 4, pp. 805-813.

[8] Newman, J.C., Jr. and I.S. Raju, 1981, "Stress intensity factor equations for cracks in three-dimensional finite bodies", *NASA Technical Memorandum 83200*, pp. 1-49.

[9] Aliabadi, M.H., 1997, "Boundary element formulations in fracture mechanics", *ASME App. Mech. Rev.*, Vol. 502, pp. 83-96.
[10] Guanshui, X., Argon, A.S., Ortiz, M. and A. Bower, 1995, "Development of a variational boundary integral method for analysis of fully three dimensional crack advance problems", *Comp. Mech. '95*, Vol. 2, pp. 2874-2889.
[11] Selcuk, S., Hurd, D.S., Crouch, S.L. and W.W. Gerberich, 1994, "Prediction of interfacial crack path: a direct boundary integral approach and experimental study", *Int. J. of Fracture*, Vol. 67, pp. 1-20.
[12] Li, S., Xiao, L. and M.E. Mear, 1997, "Boundary element method for three dimensional fracture analysis", *Proc. Of 3rd NASGRO IWG.*
[13] Zhao, W., Newman, J.C., Jr., and M.A. Sutton, 1997, "A three-dimensional weight function method - evaluation and applications", *Fatigue & Fracture Mech.*, 27th Vol., ASTM STP 1296, pp. 563-579.
[14] Keat, W.D., Erguven, M.E. and J.F. Dwyer, 1997, "Modeling of 3D mixed-mode fractures near planar bimaterial interfaces using surface integrals", *Int. J. for Num. Meth.*, Vol. 39, pp.3679-3703.
[15] Forth, S.C. and W.D. Keat, 1996, "Three-dimensional nonplanar fracture model using the surface integral method", *Int. J. of Fracture*, Vol. 77, No.3, pp. 243-262.
[16] Forth, S.C. and W.D. Keat, 1997, "Nonplanar crack growth using the surface integral method", *ASME Gas Turbines & Power*, Vol. 119, No. 4, pp. 964-968.
[17] Forman, R.G., and Mettu, S.R., 1992, "Behavior of surface and corner cracks subjected to tensile and bending loads in Ti-6Al-4V alloy", *Fracture Mech.*, 22nd Symposium, Vol. 1, ASTM STP 1131, pp. 519-546.
[18] Erdogan, F. and G.H. Sih, 1963, *ASME J. of Basic Eng.*, Vol. 89, pp. 159-525.

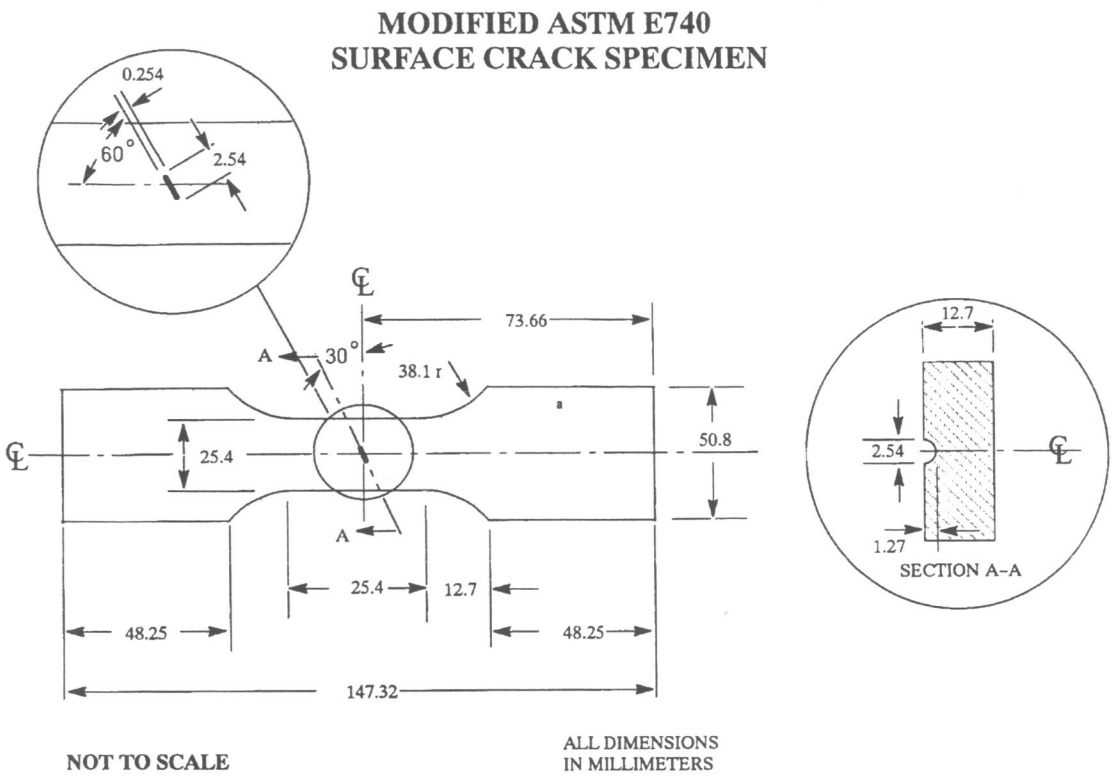

Figure 1: Mixed-mode crack growth specimen design.

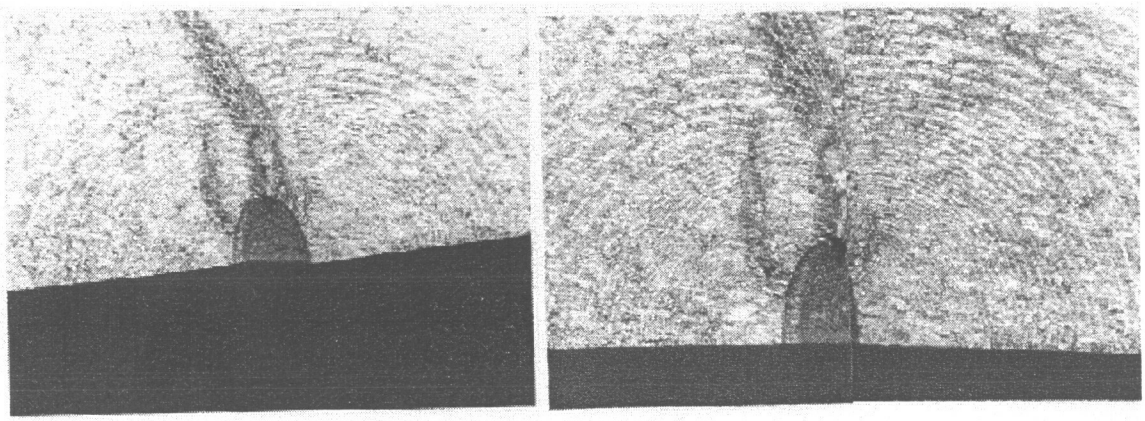

Figure 2: Marker bands at 60 degree EDM notch at 10x and 30x magnification.

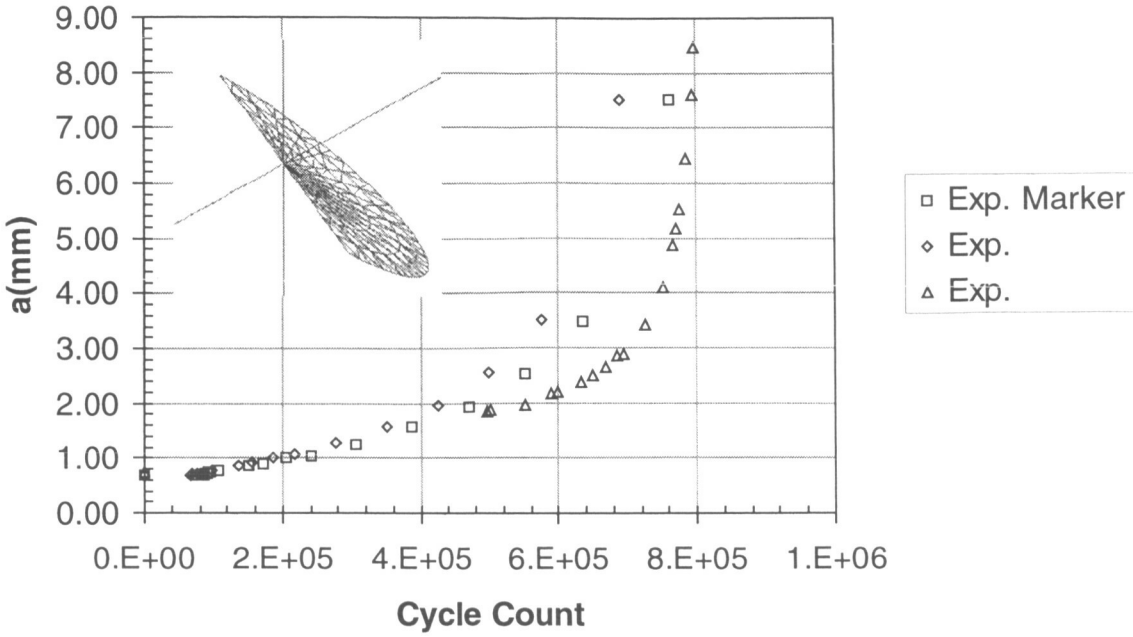

Figure 3: Effects of marker bands on specimen fatigue life for 60-degree case.

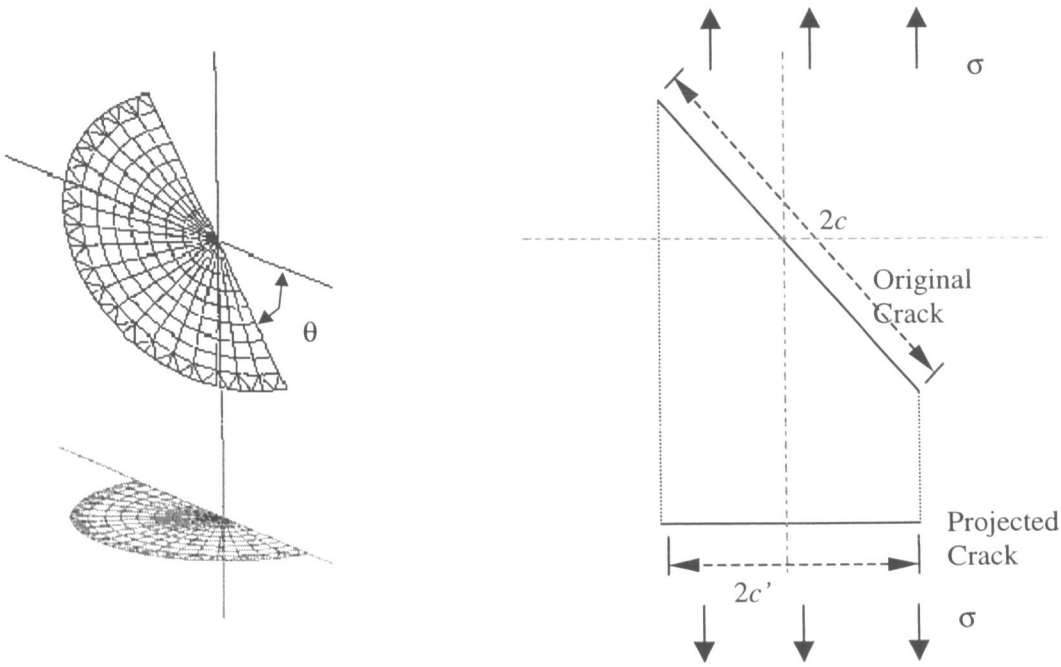

Figure 4: Projection of crack based on surface dimensions.

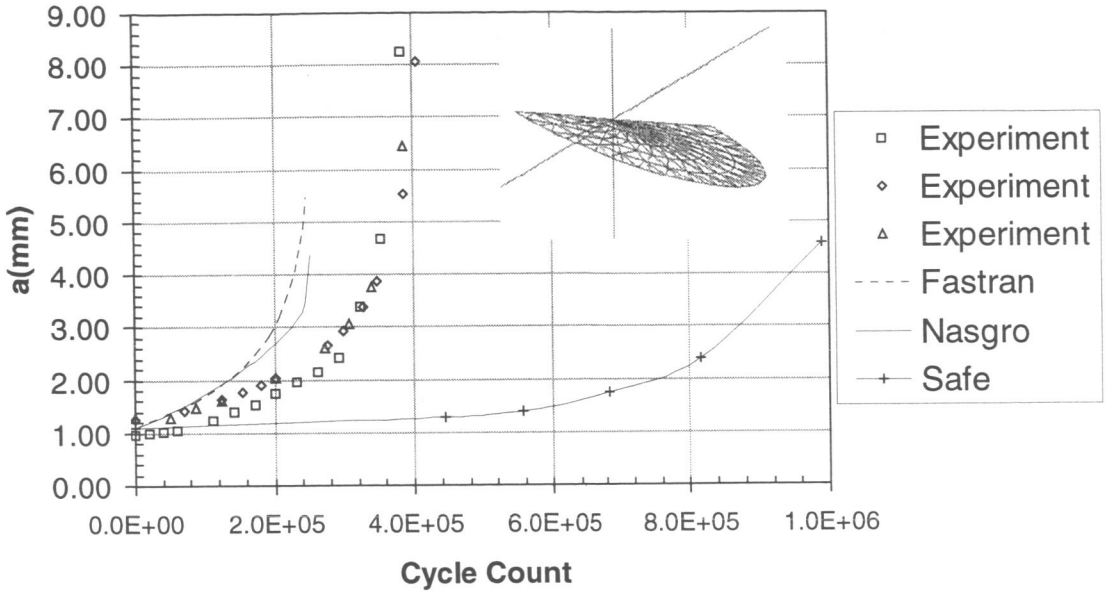

Figure 5: Crack depth vs. cycle count for 30-degree crack.

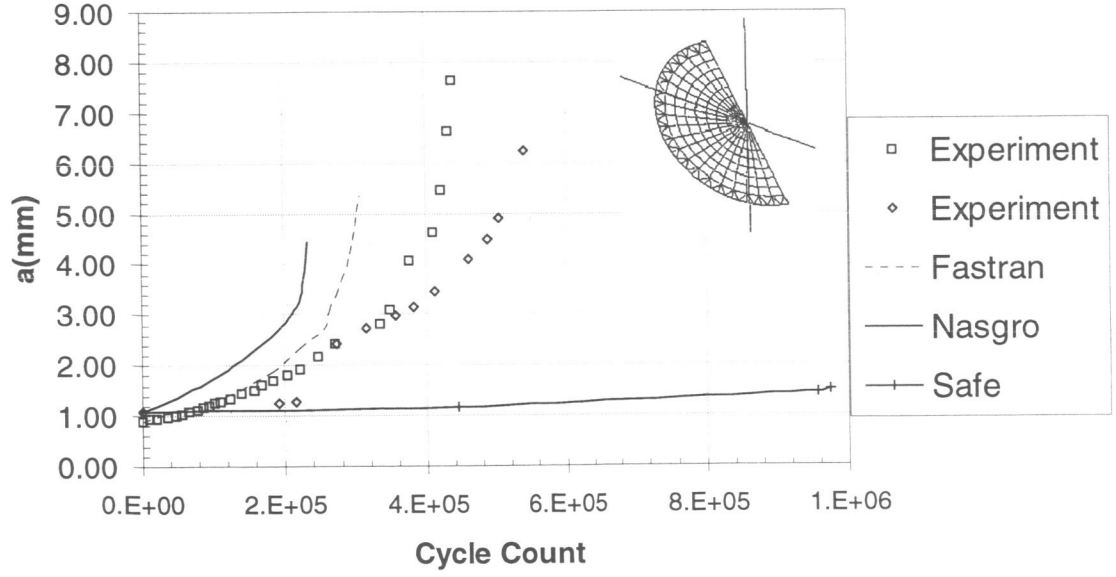

Figure 6: Crack depth vs. cycle count for 45-degree crack.

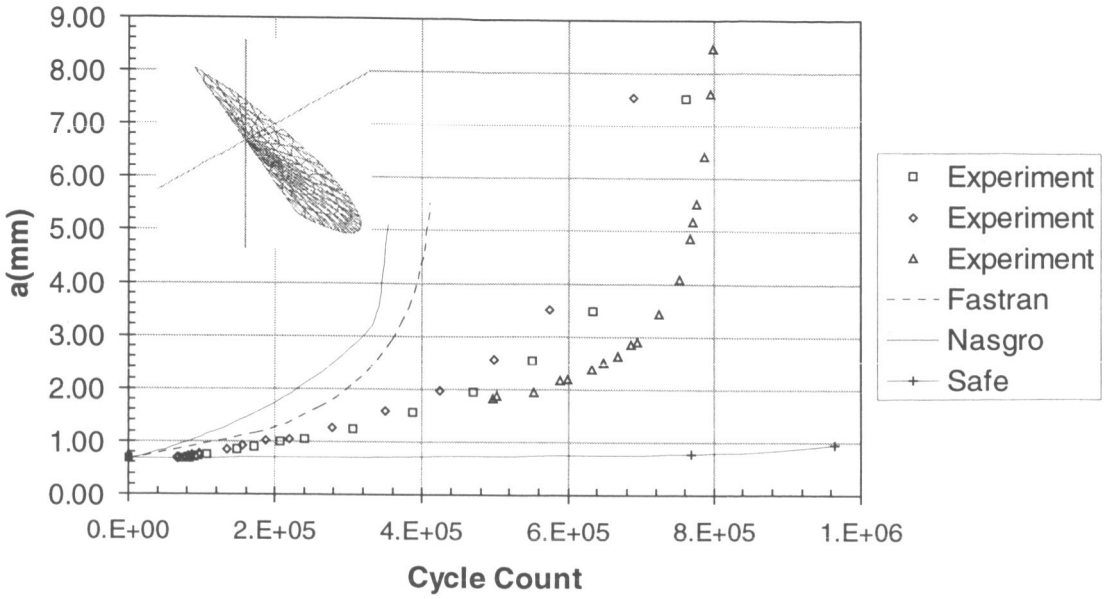

Figure 7: Crack depth vs. cycle count for 60-degree crack.

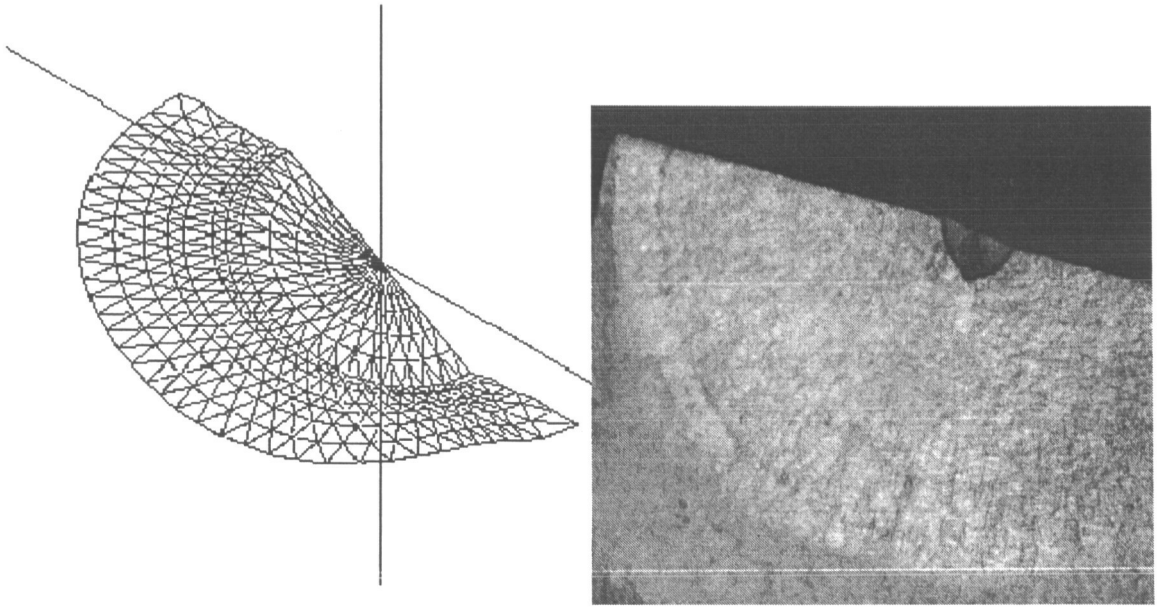

Figure 8: Mixed-mode crack growth for 30-degree case (mesh and photo).

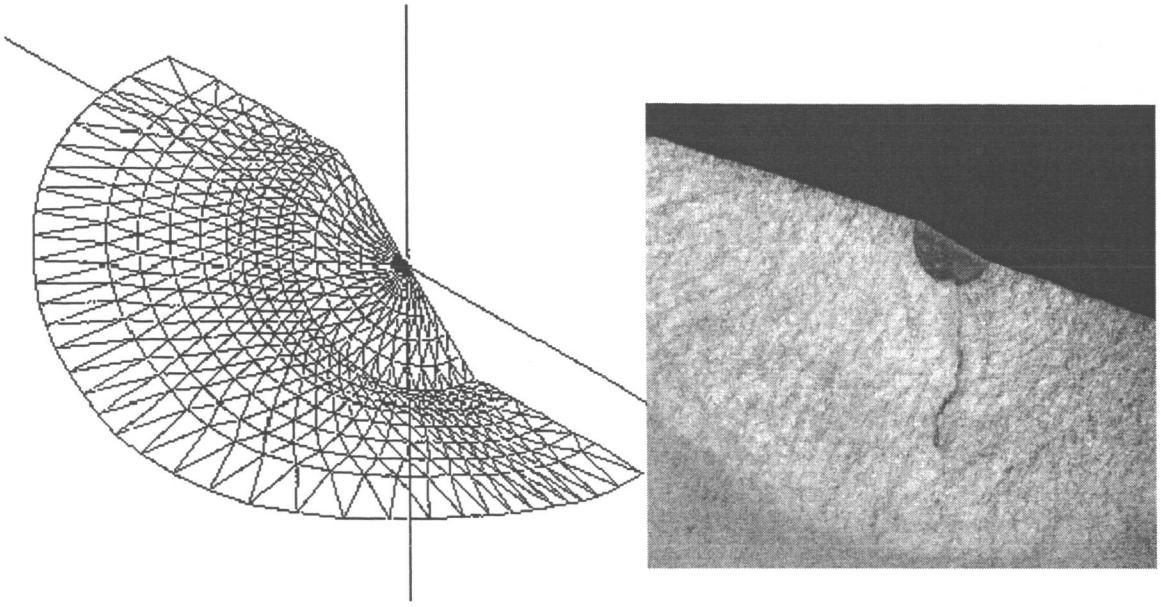

Figure 9: Mixed-mode crack growth for 45-degree case (mesh and photo).

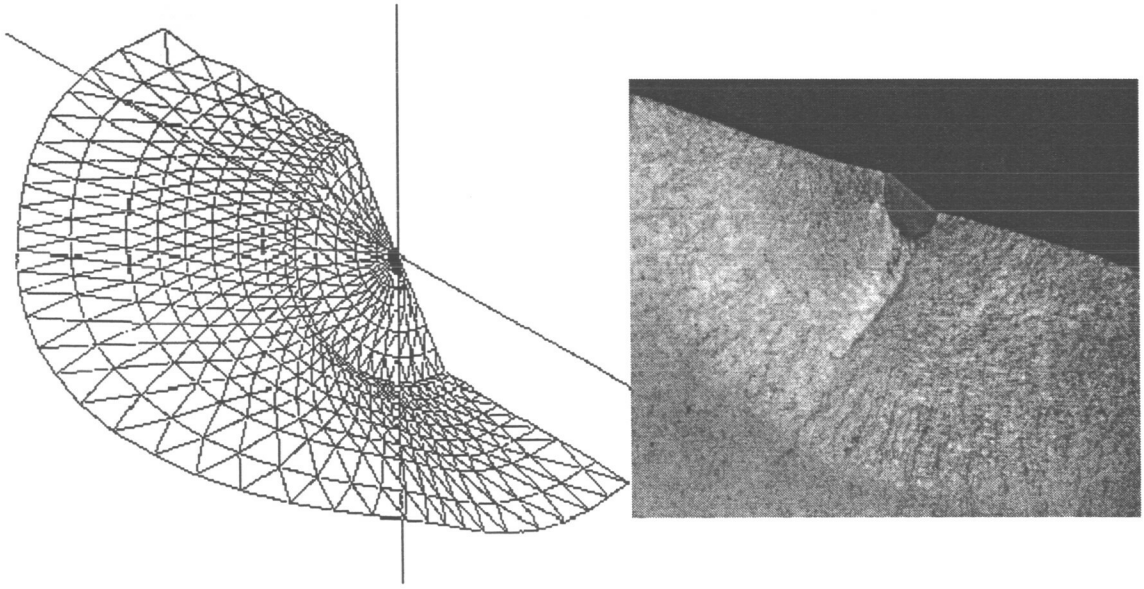

Figure 10: Mixed-mode crack growth for 60-degree case (mesh and photo).

QUANTIFYING SPECTRUM LOADING EFFECTS on FATIGUE CRACK GROWTH

H. Lewis Zion
Georgia Tech Research Institute
Smyrna, GA, 30080, USA
770-528-4906
770-528-3271 (Fax)
lew.zion@gtri.gatech.edu

W. Steven Johnson
Georgia Institute of Technology
Atlanta, GA, 30332, USA

Dale L. Ball
Lockheed Martin Tactical Aircraft Systems
Fort Worth, TX, 76101-0748, USA

Richard A. Everett, Jr.
U.S. Army Vehicle Structures Directorate
Hampton, VA, 23681-0001, USA

ABSTRACT

The combined effects of four variables on calculated spectrum fatigue crack growth (FCG) were compared using an experimental design approach (NASGRO 3.0 adaptation). The four parameters which were considered were: (1) load interaction, (2) load sequence (rainflow counted low-to-high, rainflow counted and randomized, and rainflow counted high-to-low), (3) crack tip stress state (plane stress versus plane strain) and (4) spectrum type (FELIX-28 helicopter rotor blade spectrum versus F-16 wing root bending moment spectrum). Each of the three load interaction models available in NASGRO 3.0 was used to compute load interaction effects. The investigation concluded that the order of cycles and crack tip constraint play relatively minor roles in computed FCG for problems involving repeated application of either of the given spectra, while the effects of the spectrum type itself, inclusion of load interaction effects and the synergy of spectrum with load interaction are highly significant.

INTRODUCTION

In order to insure aircraft structural integrity using damage tolerance analysis (DTA) engineers are required to predict, with reasonable accuracy, both accumulated fatigue crack growth (FCG) as well as the rate at which it takes place at those structural locations which are fatigue-critical. These predictions are important since they serve as the basis for scheduling periodic inspection and/or corrective maintenance. As such from a safety perspective it is important that they be conservative enough to prevent a significant loss of structural integrity (load-carrying capability and/or stiffness) from occurring between inspections. At the same time, from an economic perspective it is also important that these predictions not be overly conservative such that the inspections become too frequent while revealing no evidence of structural damage.

It has been well established that during linear elastic fracture mechanics (LEFM) analysis of a metal structure it is necessary to account for the localized zone of plasticity that exists in front of, as well as in the wake of, a growing fatigue crack. Given that there is sufficient surrounding elastic constraint,

this plastically-deformed material will be in a state of residual compression as a condition of equilibrium. This phenomenon known as plasticity-induced closure causes the *effective* stress intensity range to be lower than the value that would be associated with the range of stress intensity calculated from a given maximum and minimum stress pairing particularly at lower *R*-ratios. Under an aircraft spectrum loading scenario FCG prediction becomes considerably more difficult due to the variation in both the vibratory amplitude as well as mean stress components of the loading cycles. It is this variation in cyclic loading which requires that *load interactions* be considered. Simply stated: the plastic zone size and associated residual stresses of the current cycle affect the growth rate of the subsequent cycle and so on. In capturing these load interaction effects several semi-empirical mathematical models have been developed. In general all load interaction models can be described as addressing the plasticity and associated residual stresses ahead of the growing crack or in its wake or in both locations.

In addition to accounting for load interaction when making variable-amplitude FCG predictions, the *order* in which the constituent regimes of the spectrum block occur is generally thought to be important and was considered in this investigation.

A third factor which was considered in this investigation was the level of *constraint* at the crack tip which falls somewhere between the two idealized extremes of plane stress or plane strain behavior. The effect of crack tip constraint on FCG is thought to be significant by many researchers and has been the focus of much of the more recent investigative work done in the field of fracture mechanics (e.g. [1]).

The final aspect to be considered was the *type* of the loading contained within the mission spectrum which is a function of the degree of variability in both the mean and vibratory stress components which comprise its constituent flight regimes. This was accomplished by comparing the spectrum loading of fixed wing versus rotary wing aircraft.

It is worth noting that while there is a general qualitative consensus among aircraft industry practitioners that changes in fatigue crack growth rate (FCGR) do occur because of load interaction effects along with these three additional factors, the quantitative methods of analytically accounting for their individual as well as collective effect(s) vary considerably. Moreover, some analysts would argue that after many repetitions of a given spectrum loading some or all of these effects will be averaged out so that the net effect on FCGR and accumulated FCG will be minimal. Thus, it is only slightly conservative to simplify the analysis by ignoring them altogether. In addition, there is still widespread skepticism in the rotorcraft structural community with regard to the viability of implementing on-condition replacement of fatigue-critical components based on DTA. With this and the previously-highlighted thoughts in mind an investigation was conducted using a statistical *experimental design* approach along with the NASGRO 3.0 crack growth code [2] to sort out the relative importance of four effects (factors) and/or their interactions on FCGR which by designation are: (A) the ordering of the cycles in the spectrum (i.e. rainflow counted low-to-high, randomized load levels or rainflow counted high-to-low); (B) whether or not a load interaction model is included (i.e. none versus one of three load interaction models which include generalized Willenborg, strip yield closure or multiple parameter yield zone); (C) whether or not the constraint is plane strain or plane stress and (D) two types of loading spectra; namely either an F-16 fighter (wing root bending) spectrum or a FELIX-28 (semi-rigid hingeless rotor) helicopter spectrum. Details of the investigative procedure follow.

INVESTIGATIVE PROCEDURE

As mentioned in the previous section an experimental design was constructed to investigate the effects of four factors. This experimental design, which is summarized in Table 1, enables one to sort out the (main) effect of each of these factors (i.e. *order*, *load interaction*, *constraint*, and *spectrum type*) as well interactions among factors on two different FCG times: (1) elapsed flight time in going from a

flaw size of .030" to .1" and (2) elapsed flight time in going from a flaw size of .030" to critical length, a_c. Additionally the NASGRO 3.0 (March 1997 beta-test version) FCG code [2] served as the basic analysis tool for this investigation. The model geometry used was a rotationally-constrained single edge notched tension (SENT) standardized specimen (SS06 in the NASGRO model library) which was 8" by 8" with thickness of 1" in the case of plane strain or .125" in the case of plane stress. The material used was 7075-T73 aluminum oriented in the longitudinal (L-T) direction with properties drawn directly from the NASGRO 3.0 material library.

The two aircraft fatigue loading spectra used in the investigation, herein referred to as FELIX-28 and F-16, will now be described. FELIX-28 is a truncated version of the larger standardized spectrum known as FELIX which along with HELIX was developed through the collaborative efforts of three European countries. [3] In particular FELIX addresses the spectrum loading associated with *semi-rigid* (hingeless) rotors while HELIX addresses *articulated* (hinged) rotors. In generating the FELIX the recorded flight data from four different missions were considered which include: (1) training, (2) transport, (3) anti-submarine warfare and (4) search and rescue. In all 140 flights representing 190.5 flight hours were considered. While the full FELIX contains over two million cycles, the truncated FELIX-28 contains only 161,034 cycles. The full FELIX is scaled such that the maximum load in the spectrum is 100 units. The ground minimum load (i.e. rotor drooped) is -28 units. In arriving at the final version of the full FELIX vibratory loads below 16 units were omitted. In arriving at the final version of FELIX-28 vibratory loads below 28 units were further omitted. The maximum and minimum stress levels in the FELIX-28 spectrum as furnished for this investigation were respectively 70.44 ksi and -21.08 ksi. The need to address actual stress magnitudes as furnished for both spectra will become apparent when the scaling procedures used are discussed shortly.

TABLE 1 FACTORS AND ASSIGNMENTS FOR FCG INVESTIGATION

Factor (Designation)	Low Level (-1)	Center Level (0)	High Level (+1)
Order (A)	Rainflow Low-to-High	Randomized Load Levels	Rainflow High-to-Low
Load Interaction (B)	None		Willenborg or Closure*
Constraint (C)	Plane Strain		Plane Stress
Spectrum Type (D)	FELIX-28		F-16

* Load interaction model was either Generalized Willenborg or Strip-Yield Closure

The F-16 (wing root bending) spectrum used in this investigation was furnished by the Lockheed Martin Tactical Air Systems Division of the Lockheed Martin Corporation located in Fort Worth, TX. It is a tension-dominated spectrum based on actual flight-recorded data. It is comprised of 377 individual flights which include a total of 42,476 cycles encompassing 454.8 flight hours. Its maximum and minimum load levels are 100 and -21.96 units respectively. The maximum and minimum stress levels in the F-16 spectrum as furnished for this investigation are respectively 22.63 ksi and -4.97 ksi. It is also worth noting that the as-furnished stress in level flight is 5.63 ksi. Unlike the FELIX-28 helicopter spectrum which, in addition to low-frequency, large-amplitude cycles generated by entering and recovering from maneuvers, contains additional low-amplitude, high-frequency cycles as a natural consequence of the periodic rotor aerodynamics and dynamics; the F-16 spectrum contains *only* cycles generated as a direct consequence of entry into and recovery from maneuvering flight. After processing the F-16 spectrum using a rainflow processor truncation of vibratory load levels at or below approximately 2.5 units further reduced the total number of cycles to 27,822.

As is evident from the previous two paragraphs the two spectra differed significantly in their absolute maximum and minimum stress levels. Thus, in order to logically compare the two individual scale factors had to be developed. Additionally practical considerations dictated that the FCG times should be long enough to allow a significant number of passes through the respective spectra as well as

be consistent with the material and SENT geometry. The end result of these considerations was a decision to scale the F-16 spectrum by a factor of 0.849 which effectively lowered its maximum stress to 19.22 ksi and its level flight stress to 4.78 ksi. In order to form a reasonable basis of comparison of FCG between the two spectra it was then decided to scale the FELIX-28 spectrum by a factor of 0.146 such that the mean stress at its statistical mode (i.e. a cruise condition load level which contained 71,072 of the 161,034 total cycles) would be 4.78 ksi. The results of scaling the respective spectra are most visible when viewed in the form of exceedence curves. As such, Figure 1 shows the resulting maximum and minimum exceedence curves for the scaled FELIX-28 spectrum while Figure 2 shows the corresponding exceedence curves for the scaled F-16 (wing root bending) spectrum. One notes from these figures that the F-16 is considerably more severe than the FELIX-28 in terms of the amount of load excursion. However, in examining the respective horizontal axes of Figures 1 and 2 one notes that the rate of exceedence is much higher for the FELIX-28 than for the F-16. It was also noted that the F-16 exceedence curves strongly resemble the exceedence curves for a typical fighter spectrum (e.g. [4]). From a practical perspective it should be kept in mind that these exceedence curves do not portray the associativity of any individual cyclic maximum-minimum pairing. In the case of the F-16 where all the cycles come from maneuvering this is much less of an issue than for the FELIX-28 where a large share of the cycles come from periodic aerodynamic and dynamic rotor loads.

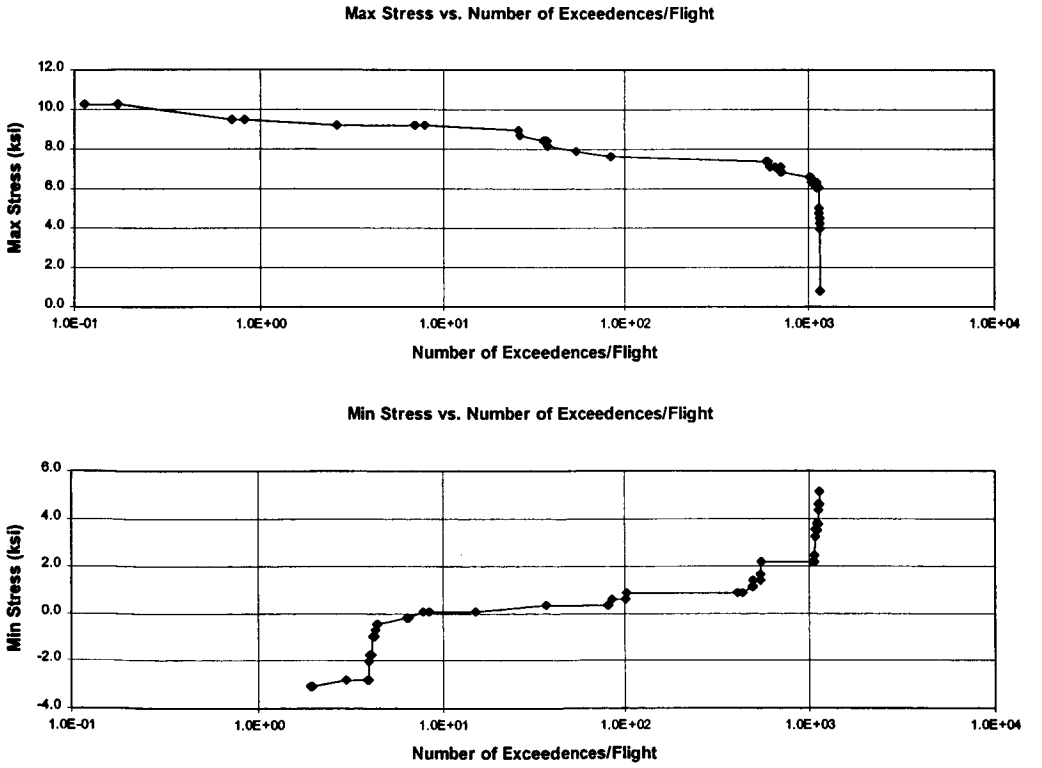

Figure 1 Exceedence Curve for FELIX-28 Spectrum

As mentioned earlier both the generalized Willenborg and strip yield (closure) models were used to generate load interaction results in this investigation. Additionally, the multiple parameter yield zone (MPYZ) model [5] was also run later in the investigation in order to provide an additional sanity check on certain unexpected results. The (Generalized) Willenborg model as implemented in NASGRO 3.0 is based on the original semi-empirical model developed by Willenborg *et al.* [6] As such it is only intended to include effects of load interaction insofar as they would result in FCG retardation. Specifically, it is not intended to include the effects of acceleration, underloads or multiple overloads which are included in the more elaborate MPYZ model.

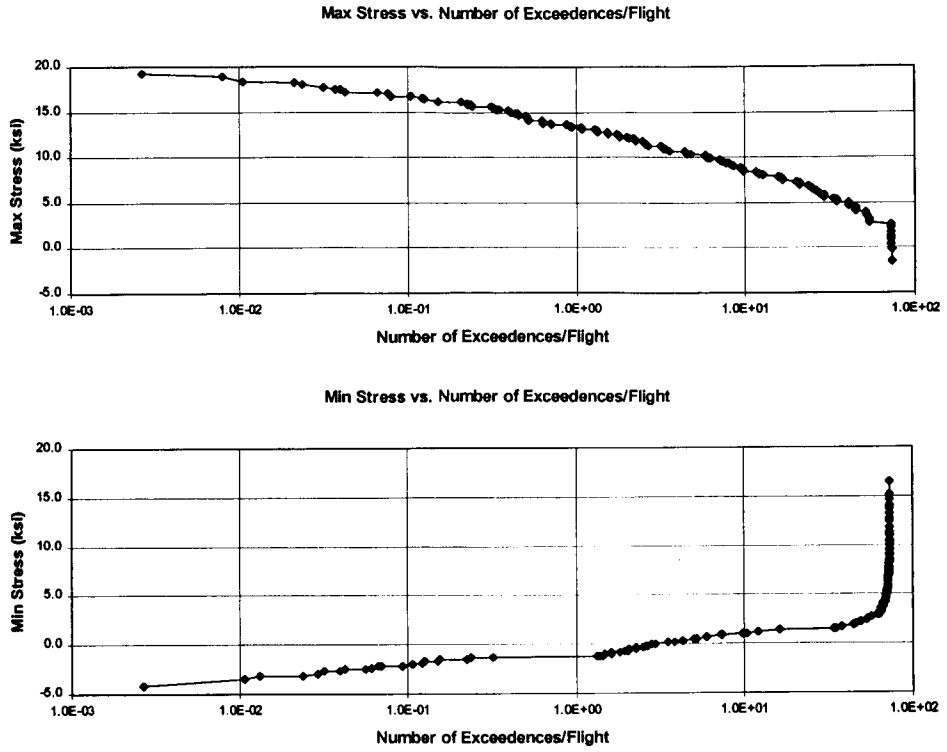

Figure 2 Exceedence Curve for F-16 Wing Root Bending Spectrum

The mechanics of the Generalized Willenborg model can generally be described as conditionally controlling FCG depending on how the growth increment and size of the plastic zone at the crack tip (idealized as circular) associated with the *current* load cycle compares to the plastic zone size associated with *previous* load cycles. The model is intended to only address FCG retardation, but does include provision for no growth when the ratio of current-to-previous plastic zone size reaches a specified *shutoff* value. However, the model is specifically not intended to account for accelerated crack growth (e.g. due to underloads). Details of the model are discussed extensively in [2].

The strip yield model as implemented in NASGRO 3.0 is based on a crack-closure adaptation of Dugdale's original strip yield model [7]. The details of the model which are presented in [2] are rather involved, however, a few of the more important attributes of the model will be briefly presented here. Essentially the model tracks the movement of plastic material both ahead of, and in the wake of the crack in order to come up with an *effective opening stress* and its associated stress intensity factor. Here the basic concept of *crack closure* is evidenced by the fact that plastically-deformed material associated with the growing crack must be compensated by residual compressive stresses as a condition of equilibrium. The net effect of the plastic strains along the crack faces and their compensating compressive residual stresses cause the crack faces to remain in contact during a portion of the tensile loading associated with an ensuing load cycle. Since FCG can only occur when the crack is open this effectively reduces the range of stress intensity.

As implemented in NASGRO 3.0 the *basic* (strip yield) solution is accomplished by progressively releasing rigid perfectly-plastic bar finite elements along the crack faces to simulate FCG. With each load step an effective opening stress is calculated which depends both on the enjoined (intact) elements ahead of the crack as well as the separated elements left in its wake. However, unlike the (generalized) Willenborg which addresses only FCG retardation, the strip yield closure model *addresses*

all aspects of load interaction (i.e. effects of underload, multiple overloads, etc. which can result in FCG acceleration, hold-time or retardation). Unfortunately the numerical finite element solution in the strip yield model comes at the price of significantly more computer run time than does either the Willenborg or the MPYZ algorithms. This additional run time can be significantly reduced with minimal loss of accuracy by invoking the *fast* option at run time. The *fast* option essentially comes up with an average opening stress value over two complete passes of the loading spectrum which is then used in the remaining FCG calculations. In this investigation it was noted that the fast strip yield option resulted in less than 0.5% difference in FCG times when compared with the basic strip yield results while reducing the CPU time by more than a factor of 10 (i.e. basic strip yield CPU time was 13,672 seconds while the fast strip yield was 1,245 seconds). However, the corresponding cases using the Willenborg and MPYZ load interaction models ran in 7 and 5 CPU seconds respectively.

Recall that one of the principal reasons for conducting this investigation centered on the effect of the *order* that cycles occur within the respective load spectra (i.e. factor A in Table 1). Therefore before concluding this section it is appropriate that some brief comments be made in this regard. Specifically, a rainflow cycle counting processor algorithm similar to the one described in [8] (also used in [9]) was used to segregate cycles into bins according to their mean and range stress values. In order to generate the low-to-high sequence the bins were then sorted in ascending order with range as the primary criteria and mean as the secondary criteria. In the case of the FELIX-28 this resulted in 50 discrete load levels. In the case of the F-16 wing root bending spectrum this resulted in 130 discrete load levels (once the respective spectra had been truncated as described previously). The high-to-low sequence essentially inverted the low-to-high sort. Note: both were accomplished with the aid of a spreadsheet. In the case of the randomized load level sequence the discrete load levels from the respective spectra were assigned a random number. The random numbers which served to identify each load level (i.e. range, vib, min, max, number of cycles, etc.) were then sorted in ascending order. Here it is important to point out that the concept of randomized load levels is somewhat controversial in the sense that the cycles at a given load level are forced to occur sequentially in the spectrum of loads whereas in flight this would not necessarily (and more likely not) be the case. As such this may, in and of itself, disrupt the natural progression of FCG when load interactions are considered. Specifically, the randomized load level sequence should more properly be considered to be *pseudo-random* due to the fact that, although the sequence of load levels themselves is random, the cycles at a given load level proceed till completion. A discussion of the investigative results follows.

RESULTS

Using the experimental design given in Table 1 two crack growth times (i.e. from .030" to .1" and from .030" to critical length, a_c) for each experimental block were generated. The results for the FELIX-28 spectrum with the Willenborg load interaction model are given in Figure 3. In reviewing these results it is surprising to note that the FCG times are less when the Willenborg load interaction model was turned on versus the corresponding experimental blocks where there was no load interaction. This immediately suggested that the Willenborg model was not working as intended since it is only supposed to address the retardation effects of load interaction. However, in examining the corresponding results for the F16 (wing root bending) spectrum in Figure 4 it appears that the Willenborg model *is* acting properly. Specifically, the FCG times are higher with Willenborg as expected for the tension-dominated F-16 spectrum.

FELIX-28 Crack Growth Resuls (Factor D = -1 in all cases)

Block	Factor A Order	Factor B Load Interaction	Factor C Constraint	Cycs (.030-.1)	Flt-hrs (.030-.1)	Cycs (.030-.ac)	Flt-hrs (.030-.ac)
1	Low-High (-1)	None (-1)	Pln Strain (-1)	3,941,857	4,663	4,301,775	5,089
2	Low-High (-1)	None (-1)	Pln Stress (+1)	4,192,589	4,960	4,598,309	5,440
3	Low-High (-1)	Willenborg (+1)	Pln Strain (-1)	2,664,555	3,152	3,025,618	3,579
4	Low-High (-1)	Willenborg (+1)	Pln Stress (+1)	2,741,043	3,243	3,146,254	3,722
5	Random (0)	None (-1)	Pln Strain (-1)	3,884,887	4,596	4,214,836	4,986
6	Random (0)	None (-1)	Pln Stress (+1)	4,099,044	4,849	4,507,533	5,332
7	Random (0)	Willenborg (+1)	Pln Strain (-1)	2,226,735	2,634	2,559,388	3,028
8	Random (0)	Willenborg (+1)	Pln Stress (+1)	2,264,639	2,679	2,655,091	3,141
9	High-Low (+1)	None (-1)	Pln Strain (-1)	3,819,505	4,518	4,147,953	4,907
10	High-Low (+1)	None (-1)	Pln Stress (+1)	4,042,338	4,782	4,432,410	5,243
11	High-Low (+1)	Willenborg (+1)	Pln Strain (-1)	2,567,699	3,038	2,890,756	3,420
12	High-Low (+1)	Willenborg (+1)	Pln Stress (+1)	2,623,030	3,103	3,019,880	3,572

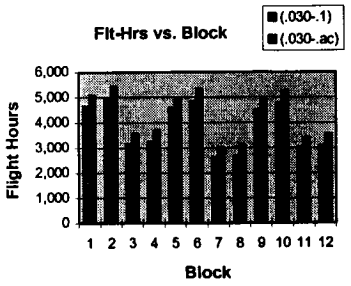

Figure 3 Results with FELIX-28 Spectrum and Generalized Willenborg Model

F-16 Crack Growth Results (Factor D = +1 in all cases)

Block	Factor A Order	Factor B Load Interaction	Factor C Constraint	Cycs (.030-.1)	Flt-hrs (.030-.1)	Cycs (.030-.ac)	Flt-hrs (.030-.ac)
1	Low-High (-1)	None (-1)	Pln Strain (-1)	776,273	8,312	1,029,060	11,018
2	Low-High (-1)	None (-1)	Pln Stress (+1)	862,482	9,235	1,223,243	13,098
3	Low-High (-1)	Willenborg (+1)	Pln Strain (-1)	849,669	9,098	1,168,458	12,511
4	Low-High (-1)	Willenborg (+1)	Pln Stress (+1)	978,050	10,472	1,502,326	16,086
5	Random (0)	None (-1)	Pln Strain (-1)	772,910	8,276	1,008,176	10,795
6	Random (0)	None (-1)	Pln Stress (+1)	855,571	9,161	1,202,904	12,880
7	Random (0)	Willenborg (+1)	Pln Strain (-1)	903,942	9,679	1,243,213	13,311
8	Random (0)	Willenborg (+1)	Pln Stress (+1)	1,027,777	11,005	1,586,279	16,985
9	High-Low (+1)	None (-1)	Pln Strain (-1)	769,681	8,241	1,001,624	10,725
10	High-Low (+1)	None (-1)	Pln Stress (+1)	852,221	9,125	1,196,378	12,810
11	High-Low (+1)	Willenborg (+1)	Pln Strain (-1)	740,658	7,930	1,001,592	10,724
12	High-Low (+1)	Willenborg (+1)	Pln Stress (+1)	843,880	9,036	1,253,011	13,416

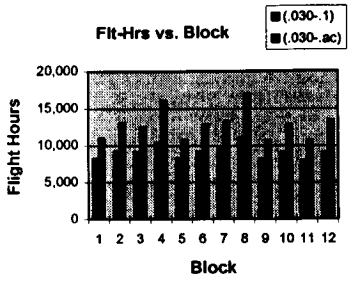

Figure 4 Results with F-16 Spectrum and Generalized Willenborg Model

Results using strip yield (closure) as the operative load interaction model are given in Figure 5 for the FELIX-28 spectrum and Figure 6 for the F-16 spectrum. Here the FELIX-28 FCG times are very close to those generated with Willenborg as the load interaction model shown in Figure 3. However, a similar comparison of the corresponding F-16 strip yield FCG times of Figure 6 with the earlier Willenborg results of Figure 4 show considerably more retardation (by a factor of two or more).

FELIX-28 Crack Growth Resuls (Factor D = -1 in all cases)

Block	Factor A Order	Factor B Load Interaction	Factor C Constraint	Cycs (.030-.1)	Flt-hrs (.030-.1)	Cycs (.030-.ac)	Flt-hrs (.030-.ac)
1	Low-High (-1)	None (-1)	Pln Strain (-1)	3,941,857	4,663	4,301,775	5,089
2	Low-High (-1)	None (-1)	Pln Stress (+1)	4,192,589	4,960	4,598,309	5,440
3	Low-High (-1)	Closure (+1)	Pln Strain (-1)	2,577,680	3,049	2,964,064	3,506
4	Low-High (-1)	Closure (+1)	Pln Stress (+1)	2,681,170	3,172	3,154,375	3,732
5	Random (0)	None (-1)	Pln Strain (-1)	3,884,887	4,596	4,214,836	4,986
6	Random (0)	None (-1)	Pln Stress (+1)	4,099,044	4,849	4,507,533	5,332
7	Random (0)	Closure (+1)	Pln Strain (-1)	2,520,856	2,982	2,899,595	3,430
8	Random (0)	Closure (+1)	Pln Stress (+1)	2,607,890	3,085	3,059,645	3,619
9	High-Low (+1)	None (-1)	Pln Strain (-1)	3,819,505	4,518	4,147,953	4,907
10	High-Low (+1)	None (-1)	Pln Stress (+1)	4,042,338	4,782	4,432,410	5,243
11	High-Low (+1)	Closure (+1)	Pln Strain (-1)	2,736,032	3,237	3,095,209	3,662
12	High-Low (+1)	Closure (+1)	Pln Stress (+1)	2,833,956	3,353	3,282,528	3,883

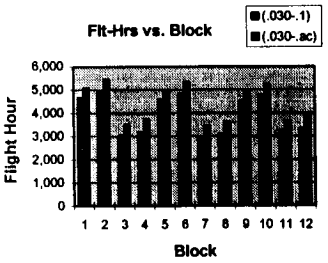

Figure 5 Results with FELIX-28 Spectrum and Strip Yield Model

F-16 Crack Growth Resuls (Factor D = +1 in all cases)

Block	Factor A Order	Factor B Load Interaction	Factor C Constraint	Cycs (.030-.1)	Flt-hrs (.030-.1)	Cycs (.030-.ac)	Flt-hrs (.030-.ac)
1	Low-High (-1)	None (-1)	Pln Strain (-1)	776,273	8,312	1,029,060	11,018
2	Low-High (-1)	None (-1)	Pln Stress (+1)	862,482	9,235	1,223,243	13,098
3	Low-High (-1)	Closure (+1)	Pln Strain (-1)	1,406,883	15,064	1,975,330	21,150
4	Low-High (-1)	Closure (+1)	Pln Stress (+1)	1,572,030	16,832	2,476,093	26,512
5	Random (0)	None (-1)	Pln Strain (-1)	772,910	8,276	1,008,176	10,795
6	Random (0)	None (-1)	Pln Stress (+1)	855,571	9,161	1,202,904	12,880
7	Random (0)	Closure (+1)	Pln Strain (-1)	1,397,298	14,961	1,981,946	21,221
8	Random (0)	Closure (+1)	Pln Stress (+1)	1,571,595	16,827	2,495,205	26,717
9	High-Low (+1)	None (-1)	Pln Strain (-1)	769,681	8,241	1,001,624	10,725
10	High-Low (+1)	None (-1)	Pln Stress (+1)	852,221	9,125	1,196,378	12,810
11	High-Low (+1)	Closure (+1)	Pln Strain (-1)	1,609,808	17,237	2,152,253	23,045
12	High-Low (+1)	Closure (+1)	Pln Stress (+1)	1,863,528	19,953	2,727,678	29,206

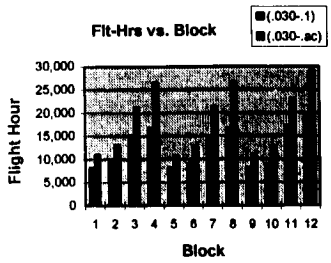

Figure 6 Results with F-16 Spectrum and Strip Yield Model

The conflicting results associated with the Willenborg model findings suggested that the Willenborg model used in this study seems to address the full compliment of load interaction effects whereas it is portended to only address the retardation aspect of load interaction. In order to provide a basis for investigating this hypothesis the MPYZ load interaction model was run as factor B for the same experimental design as the Willenborg and strip yield models. Note that in making these runs the default MPYZ values (i.e. A=1.0, B=3.0, Y=0.0 and Z=1.0) were accepted (described in [2] and [5]). In these additional MPYZ cases the FELIX-28 spectrum results were nearly identical to the corresponding earlier Willenborg and strip yield results. In the case of the F-16 spectrum the MPYZ model showed slightly less FCG retardation when compared with the Willenborg model while both the Willenborg and MPYZ models showed considerably less retardation than when strip yield was the operative load interaction model. Figure 7 illustrates at a glance the effect of all three load interaction models on calculated FCG time in going from .030" to a_c. Although not listed (or depicted) the FCG times from .030" to .1" showed a similar trend.

Block	Spectrum	Other Factors (A, B, C)	Willenborg (.030-.a_c)	Strip Yield (.030-.a_c)	MPYZ (.030-.a_c)
1	FELIX-28	(-1, +1, -1)	3579	3506	3575
2	FELIX-28	(-1, +1, +1)	3722	3732	3724
3	FELIX-28	(0, +1, -1)	3028	3430	3041
4	FELIX-28	(0, +1, +1)	3141	3619	3153
5	FELIX-28	(+1, +1, -1)	3420	3662	3432
6	FELIX-28	(+1, +1, +1)	3572	3883	3584
7	F-16	(-1, +1, -1)	12511	21160	11022
8	F-16	(-1, +1, +1)	16086	26512	14290
9	F-16	(0, +1, -1)	13311	21221	13077
10	F-16	(0, +1, +1)	16985	26717	16666
11	F-16	(+1, +1, -1)	10724	23045	9631
12	F-16	(+1, +1, +1)	13416	29206	12022

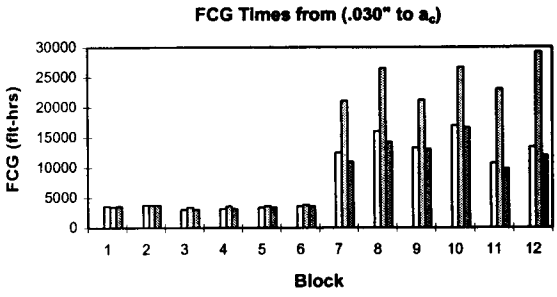

Figure 7 Effect of Respective Load Interaction Model on .030" - a_c FCG

Having gone to considerable length in describing the effect of load interaction on FCGR. A few comments are in order with regard to the other factors. Specifically, this investigation sought most to assess the effect of the *order* (Factor A) of cycles within a given spectrum. As such, a review of Figures 3 thru 6 show that in the case of both spectra the ordering of cycles played a relatively minor role in the resulting FCG times. It is worth noting in these results that there *is* a slight drop off in FCG time as one moves from the low-high (-1) to random (0) to high-low (+1) sequencing of load cycles while holding the other factors fixed (i.e. factors B, C and D the same). This behavior is a necessary result due to the large number of cycles which are included in both the FELIX-28 and F-16 spectra (i.e. 161,034 and 27,822 cycles respectively). Specifically, the final pass through the spectrum made in reaching the respective FCG targets is a partial one, therefore if the larger cycles occur earlier on this final pass the target is reached slightly sooner. The effect of *constraint* (factor C) is also small in comparison to the effect of load interaction, yet more significant in causing retardation than the effect of order. The constraint effect is expected due to the larger plastic zone size associated with plane stress versus plane strain. Finally, the effect of the two different *type* of spectra (factor D) is quite significant as one would expect with FCG times differing by a factor of two or more.

At the outset of this paper the *experimental design* concept was introduced which uses statistics (i.e. analysis of variance or ANOVA in tandem with *orthogonal arrays*; see [10]) to capture the effect, or lack thereof, of several factors and/or their interactions in a compact *factorial design* arrangement. As such, the overall FCG results from Figures 3 and 4 were examined to see if they agreed with the observations. These experimental design results are displayed in the form of an *effects plot* in Figure 8.

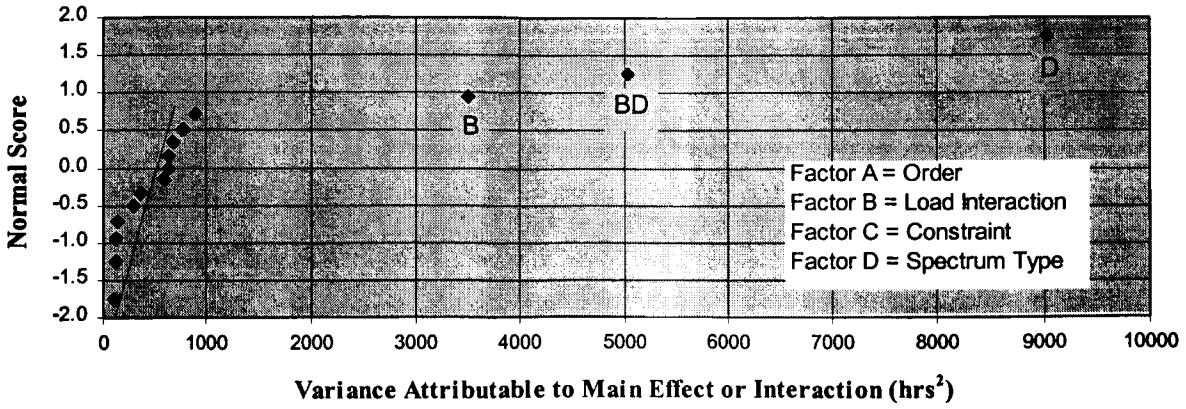

Figure 8 Effects (Normality) Plot Generated from Figure 3 and 4 Results

The *effects plot* uses an algorithm developed by Yates (also described in [10]) to graphically display information as to which *main effects* or *interaction(s)* are responsible for the variation in a response variable; in this case (.030" to .1") FCG time. Examination of this figure quickly confirms that the points assigned to the main effects of factors B and D (i.e. load interaction and spectrum type) along with their interaction (BD) lie far off of the line of normality and are therefore, the ones causing most of the variation in FCG. This result is not unexpected since the results indicated significantly retarded FCG for the F-16 while indicating accelerated FCG for the FELIX-28.

Finally, while the FCG results for the F-16 are more or less in keeping with expectation insofar as the evidenced retardation in cases where load interaction was considered, the accelerated FCG seen in corresponding cases for the FELIX-28 requires some elaboration. In this regard it is important to realize that the fatigue cycles contained in the FELIX-28 spectrum come from a variety of sources. First consider that a typical helicopter maneuver consists of an entry phase caused by collective and/or cyclic control input, a steady state phase where the rotor blade experiences periodic loads as a natural consequence of the aerodynamics and dynamics associated with flapping and a recovery phase caused by collective and/or cyclic control input. Thus, there is a half cycle increase in load (i.e. steady shift upward in absolute load from entry control input) followed by a periodic vibratory load sequence followed by a corresponding half cycle decrease in load (i.e. steady shift downward from recovery control input). This type of maneuvering suggests that the spectrum is tension dominated. However, prior to takeoff the rotor blade assumes a negative (drooped) load in the at-rest state. Thus the spectrum does contain occasional high amplitude ground-air-ground cycles with a negative R-ratio which are quite large when compared to the much lower amplitude high R-ratio periodic rotor loads that comprise a large portion of the total cycles, thereby accounting for the acceleration.

CONCLUSIONS

The results of this investigation indicate that, for the experimental design arrangements considered herein (Table 1), FCG was largely dominated by *load interaction* (factor B) and spectrum *type* (factor D) along with their synergistic effect (interaction of factors B and D). In particular analytical predictions for the F-16 wing root bending fighter spectrum, which is tension-dominated, consistently resulted in retarded crack growth when load interaction effects were considered. Conversely the FELIX-28 (hingeless rotor) helicopter spectrum predictions, which is also tension-dominated but does contain periodic underloads due to rotor droop, consistently resulted in accelerated crack growth when load interaction effects were considered. By comparison the effect of *constraint* (factor C) was small but measurable as expected owing to the larger plastic zone size and higher fracture toughness of

plane stress versus plane strain with no apparent interaction with the other factors. Finally the effect of *order* (factor A) was only slight. Moreover, the small effect associated with order was directly attributable to the final pass through the spectrum (i.e. high-to-low resulted in reaching the FCG goal sooner than low-to-high). These results suggest that, from an analytical prediction perspective, repetitive application of a given loading spectrum can be characterized as containing retardation or acceleration when load interaction effects are included regardless of the order in which its constituent load cycles are applied.

Quantitatively FCG time was consistently augmented (by a factor of 1.1 to 2.3) for the F-16 spectrum when load interaction was included, while diminishing by 40% or more in corresponding cases (i.e. otherwise same combination of factors A, B, and C) involving the FELIX-28 spectrum. There was good agreement among all three load interaction models available in NASGR0 3.0 (i.e. Generalized Willenborg, Strip Yield Closure and MPYZ) in cases involving the FELIX-28 spectrum. However, while the corresponding load interaction cases involving the F-16 showed good agreement between the generalized Willenborg and MPYZ load interaction models, there was somewhat greater retardation (approximately a factor of 2) evident in the results using the strip yield closure model (i.e. strip yield closure F-16 predicted FCG times were less conservative compared to those of Willenborg and MPYZ).

REFERENCES

1. *Constraint Effects in Fracture, ASTM STP 1171*, Hackett, E. M., Schwalbe, K. H., Dodds, R. H., Eds., American Society for Testing Materials, Philadelphia, 1993.

2. Forman, R.G., Shivakumar, V., Mettu, S. R., Newman, J. C., "Fatigue Crack Growth Computer Program - NASGRO Version 3.00: Theoretical and Operational Manual", NASA Johnson Space Center, JSC-22267B, March 1997.

3. Edwards, P. R., Darts, J., "Standardized Fatigue Loading Sequences for Helicopter Rotors (HELIX and FELIX) Part 1: Background and Fatigue Evaluation", Royal Aircraft Establishment, TR 84044.

4. ten Have, A. A., "European Approaches in Standard Spectrum Development", *Development of Fatigue Loading Spectra, ASTM STP 1006*, Potter, J. M., Wantanabe, R. T., Eds, American Society for Testing Materials, Philadelphia, 1989, pp. 17-35.

5. Johnson, W. S., "Multiple Parameter Yield Zone Model for Predicting Spectrum Crack Growth", *Methods for Predicting Fatigue Crack Growth Under Random Loading, ASTM STP 748*, American Society for Testing Materials, Philadelphia, 1981, pp. 85-102.

6. Willenborg, J., Engle, R. M. Jr., Wood, R. A., "A Crack Growth Retardation Model Using an Effective Stress Concept", Air Force Flight Dynamics Laboratory Report AFFDL-TM-71-1-FBR, January, 1971.

7. Dugdale, D. S., "Yielding of Steel Sheets Containing Slits", Journal of Mechanics and Physics of Solids, Vol. 8, 1960, pp. 100-104.

8. Khosrovaneh, A. K., Dowling, N. E., Berens, A. P., Gallagher, J. P., "Fatigue Life Estimates for Helicopter Loading Spectra", *Journal of the American Helicopter Society*, July, 1990.

9. Everett, R.A. Jr., Bartlett, F. D. Jr., Elber, W., "Probabilistic Fatigue Methodology for Six Nines Reliability", *Journal of the American Helicopter Society*, April, 1992.

10. Box, G. E. P., Hunter, W. G., Hunter, J. S., *Statistics for Experimenters*, Wiley, New York, 1978.

ANALYTICAL FRAMEWORK FOR ASSESSMENT OF CORROSION AND FATIGUE IN FUSELAGE LAP JOINT

Dale A. Cope, Patrick S. Johnson, Angela Trego, and J. Doug West
Boeing Information, Space, and Defense Systems
Wichita, Kansas 67277 USA
(316) 526-9873 Fax: (316) 523-3130
dale.a.cope@boeing.com

ABSTRACT

This paper discusses the development and demonstration of the Corrosion Damage Assessment Framework (CDAF). Two specific concerns that could affect safety limits for aging aircraft are the effects of corrosion damage and widespread fatigue damage (WFD) on structural integrity. This project evaluated the capabilities of several advanced analysis tools for assessing these effects on the structural integrity of riveted lap joints. In constructing the framework, Boeing evaluated existing structural analysis tools capable of performing stress analysis, fatigue crack propagation analysis, and structural failure risk assessment. To validate the tools, analyses were conducted on and compared to experimental test data from a previous research effort. This paper summarizes the tools and procedures used in the analytical framework and the analysis results of the experimental test.

Under the CDAF project, the advanced structural analysis tools that were evaluated included:

- Finite-element code, FRANC2D/L for determining stress distributions and stress intensity factors of cracks,
- Crack growth analysis code, AFGROW, for estimating fatigue crack growth life, and
- Risk analysis code, PROF, for determining the probability of fracture.

The framework outlines the approaches used to provide the input data for each analytical tool, the procedures required to accomplish the analyses, and the processes to transfer data between the various analytical tools.

These existing structural analysis tools were evaluated for their capabilities to address crevice corrosion and multiple site damage (MSD) associated with WFD in fuselage lap joints. To validate the analysis tools, one of the case studies performed compared analysis results to experimental test data on lap joint coupon specimens with and without corrosion. The evaluations investigated the tools' capabilities to account for two primary effects of crevice corrosion - material thinning and corrosion pillowing- and for two primary effects of WFD – MSD cracks and small cracks (cracks less than 0.05-in). The tools demonstrated the capabilities to perform stress analysis, crack growth analysis, and risk analysis on thin structural components with multiple layers of material and multiple cracks. Analysis results showed good agreement between predicted and experimental fatigue life for both the baseline and corroded configurations. Evaluations showed that analysis tools could account for material thinning and MSD cracks, but limitations in some of the tools prevented a complete evaluation that accounted for corrosion pillowing or small cracks. With further improvements in analysis tools and techniques, the analytical framework would be useful in assessing the impact of corrosion damage and MSD on the integrity of an aircraft structural component.

1. INTRODUCTION

The extended use of many aircraft results in increased maintenance and repair costs because of structural cracking and corrosion problems. In most cases, older aircraft spend longer times undergoing depot maintenance, resulting in a severe impact on readiness. Furthermore, extended aircraft service places increased importance on forecasting when the system must be replaced. The U.S. Air Force must be able to accurately determine the expected structural life and evaluate the structural integrity of aircraft systems. Two primary mechanisms that can affect the longevity and structural health of the metallic structures are corrosion and fatigue cracking, including the onset of widespread fatigue damage (WFD). Overall, improvements in the predictions and estimations of the effects of corrosion damage and WFD can help reduce costs, extend service life, and enhance aircraft readiness.

This paper discusses a portion of the development and demonstration of the Corrosion Damage Assessment Framework (CDAF). This project evaluated the capabilities of several advanced analysis tools for assessing the effects of corrosion damage and WFD on the structural life and strength of riveted lap joints. In constructing the framework, Boeing evaluated advanced structural analysis tools capable of performing stress analysis, fatigue crack propagation analysis, and structural failure risk assessment. As part of validating the tools, analyses were conducted

on and compared to experimental test data on lap joint specimens from a previous research effort. This paper summarizes some of the tools and procedures used in the analytical framework and the analysis results of the experimental test.

2. ANALYTICAL FRAMEWORK

The analytical framework incorporated several existing structural analysis tools to address crevice corrosion and fatigue cracks associated with WFD in fuselage lap joints. Analyses investigated the tools' capabilities to account for two primary effects of crevice corrosion - material thinning and corrosion pillowing- and for two primary effects of WFD – cracks from multiple site damage (MSD) and small cracks (cracks less than 0.05-in). The following structural analysis tools were evaluated in context of this analytical framework.

a. A finite-element analysis tool, FRANC2D/L, which gages the effects of corrosion damage and MSD on structural parameters such as stress level and stress intensity factor (SIF). (Swenson and James, 1997)
b. A crack growth analysis tool, AFGROW, which estimates the crack growth life for an assumed crack geometry when various levels of corrosion damage are present. (Harter, 1998)
c. A structural failure risk assessment tool, PROF, which defines the relative risk of structural failure for assumed levels of corrosion damage. (Berens and Papp, 1995)

A brief description of each analysis tool is provided below. The overall analysis approach is discussed in detail in Cope et al. (1998), which identifies the input data required by each tool, outlines the procedures required to accomplish the analyses, and identifies the data that is transferred between the various analytical tools.

2.1 Finite-Element Analysis Tool, FRANC2D/L

FRANC2D/L (FRacture ANalysis Code) is a finite element analysis program for the simulation of crack growth in two-dimensional layered structures. The strength of FRANC2D/L lies in its ability to perform the following tasks in an automated fashion: (1) calculate stress intensity factors for cracks through the thickness at multiple crack tips; (2) determine the trajectory and magnitude of crack growth under fatigue loading for each crack tip; and (3) implement crack growth at each crack through local remeshing around the crack tip. The program can represent layered structures, such as lap joints or bonded repairs, where each layer is modeled by a separate mesh. The layers can be connected in overlap regions with rivet or adhesive elements. The code is limited to considering planar geometry only. Plane stress or plane strain elements are available. In addition, a linear bending option is also available, which allows out-of-plane displacements and accounts for the off-set distances which may exist between layers. When the bending option is used, bending stresses/strains and out-of-plane displacements are automatically calculated in addition to the standard in-plane stress, strain and displacement distributions. However, since the bending option is limited to linear behavior (not accounting for geometric nonlinearity), this option could greatly overestimate the bending effects due to pillowing or load eccentricity in fuselage lap joints. Furthermore, the presence of linear bending does not significantly affect the SIF calculation in FRANC2D/L. The SIF values are calculated based on stress distributions at the element mid-plane where the stresses due to bending are zero.

2.2 Crack Growth Life Analysis Tool, AFGROW

The crack growth life analysis tool estimates crack propagation for an assumed crack geometry when defined damage conditions from corrosion and/or MSD are present. AFGROW calculates fatigue crack growth life. It has the capability to account for the effect of corrosion damage and/or MSD using the appropriate SIF (or stress level) which characterizes the physical and/or geometrical effect associated with the damage scenario. This tool was used to predict the behavior of cracks that were generally larger than 0.05 inches long in airframe alloys. Inputs include: choice of 21 crack cases - including user defined through crack and part through crack configurations, initial flaw size, choice of several materials - including user defined tabular data input, and a load schedule. Outputs include a graphical or text version of crack size vs. cycle directly viewed in the analysis code or it may be exported into Excel via a pull down menu option in AFGROW. Material da/dN vs. ΔK tabular data may also be plotted and viewed in the software to check material properties. AFGROW also provides a simple procedure for editing individual elements in the model.

2.3 Structural Failure Risk Assessment Tool, PROF

The structural failure risk assessment tool (PROF) is a risk analysis computer program. The acronym PROF stands for PRobability Of Fracture. PROF evaluates structural safety and life in terms of fracture probabilities of equivalent details in any airframe in a fleet. The inputs for a PROF run consist of the following: (1) table of crack size versus

the number of cycles, (2) stress intensity factor versus the crack length, (3) initial crack size distribution, (4) fracture toughness, (5) stress distribution profile, (6) constants related to the number of locations, (7) inspection intervals, (8) a probability of detection function for inspections, and (9) crack size distribution of the repaired crack sites. With these inputs, the fracture probabilities are calculated for single flights as a function of spectrum hours and for entire intervals between maintenance actions. PROF evaluates durability by calculating the expected number of cracks to be detected at each inspection cycle. This information can be used to estimate the cost effectiveness of planned maintenance scenarios. PROF can define the relative risk of structural failure when various levels of corrosion damage are postulated to exist in the structural locations of interest. This tool has the capability for analyzing the effect of different damage scenarios.

3. VALIDATION OF ANALYTICAL FRAMEWORK

The analysis methods are validated with results from experimental coupon-level tests. These test coupons contained material and geometric features representative of typical lap joint structure; however, they were not components of a full-scale fuselage structure. Specific objectives in these tests included the study of corrosion and MSD effects on fatigue crack growth. The tests consisted of lap joint specimens, both corroded and uncorroded, that were fatigue tested at the National Research Council (NRC) of Canada. Where applicable, the results of these experimental coupon tests are summarized and discussed relative to the impact that corrosion damage and MSD had on fatigue life and risk of failure of the test coupons. Analytical predictions of the test conditions are compared to the test results and summarized along with the assumptions used to make the predictions.

3.1 Corrosion and Fatigue Testing

Several fatigue tests have been completed at NRC on lap joint specimens, which included lap joint specimens with no corrosion (8 specimens) and specimens corroded prior to testing (6 specimens). Scott (1997) and Eastaugh et al. (1995) discuss in detail the testing of these lap joint specimens. Figure 1 shows the geometry and configuration for a lap joint specimen. It is constructed of two 0.040 inch sheets of 2024-T3 clad aluminum with three rows of 5/32 inch 2117-T4 rivets. The test specimens were 10 inches wide with 8 fasteners in each row across the width.

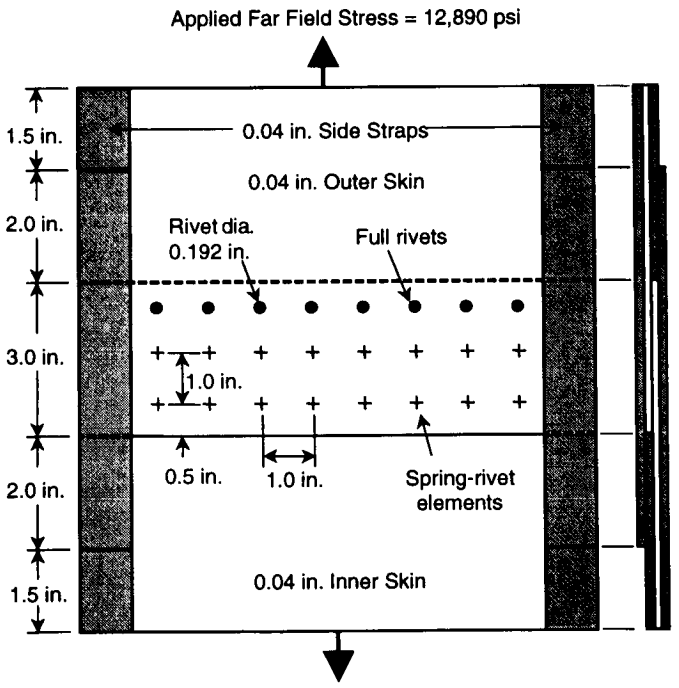

Figure 1. NRC Lap Joint Specimen Configuration.

Test data included crack growth measurements (c vs. N) during fatigue testing of both uncorroded and corroded specimens along with measurements of pillowing distortion and thickness loss on corroded specimens (Scott, 1997). Crack growth measurements of naturally occurring cracks were visually recorded when the crack had grown through the skin thickness from underneath the rivet head. The pillowing distortion is due to the buildup of corrosion byproducts in the lap joint, and the thickness loss estimated in the corroded specimens was about 2% (Scott, 1997). In analyzing the crack growth test data, it was observed that 95% or more of the joint life was controlled by the lead crack (first observed crack) behavior. The joint life was defined as a single crack spanning all eight rivets in the upper row of fasteners (Scott, 1997). The lead crack occurrences ranged from a single crack on one side of a rivet to double cracks of equal length on each side of a rivet. 50% of the occurrences were a single crack (Scenario 1), 10% were double cracks of equal length on each side of a rivet (Scenario 2), and the remaining 40% were double cracks with different lengths on each side of a rivet (Scenario 3) (Cope et al., 1998).

3.2 Analysis of MSD Lap Joint Specimens

The framework's analysis tools are used to model and analyze these lap joint specimens to validate the analysis approach in the framework. A stress analysis was performed to determine crack tip SIF values; a fatigue crack

growth analysis was performed to predict the life of the lap joint; and risk analysis was performed to determine the probability of fracture. Analysis was only performed for the lead crack using three different scenarios, as observed in the test data. The stress analysis was performed to investigate capabilities for analyzing straight-front cracks outside the rivet head. From the stress analysis, SIF values were generated as a function of crack length. Crack growth analysis was then performed to determine the fatigue life of the lap joint (crack length versus cycles). These analyses were performed for specimens with no corrosion and specimens with 2% thickness loss, the estimated level in the corroded specimens. Results from the stress and SIF analyses along with the fatigue crack growth analyses were used in a risk analysis. For the risk analysis, crack growth analyses were also performed for scenarios that simulated 5%, 8%, and 10% thickness loss.

3.2.1 FRANC2D/L Model and Analyses

The first step in the analysis procedure was to perform a stress analysis of the lap joint. The crack was assumed to be through the thickness of the plate and have a straight front perpendicular to the plate surface. No countersink geometry was modeled, straight shank rivets and holes were used, and no plastic yielding was considered. The effect of the countersunk hole on SIF was approximated by a two-dimensional analysis of a straight shank hole, whose radius is the radius of the countersink at mid-thickness. Dawicke et al. (1992) showed that this approximation compared well (within 0.2%) with three-dimensional SIF solution of a countersunk hole with a 0.175-inch crack. Under these assumptions, the problem could be adequately modeled using two-dimensional geometry.

The FRANC2D/L model configuration was based on the geometry, materials, and loading of the experimental specimens (Figure 1). The model consisted of six-noded triangular plate elements. The inner and outer skins, modeled as discrete layers, were attached only at the rivet locations and along the side straps (which were adhesively bonded on the test specimen).

Rivets were modeled using two methods. In the first method, the rivets were modeled as circular, elastic plugs in both layers, and the plugs were attached to the surrounding structure using gap elements. The plugs were then attached from layer to layer using the adhesive element available in FRANC2D/L. This method was applied to the uppermost row of rivets as indicated in Figure 1, which was shown to be critical in the experimental test results. The second method of modeling rivets used a two-noded spring element. Each node of the element was attached to one of the two skin layers. This method was used to model each rivet in the lower two rivet rows, where the detailed stress distribution surrounding each rivet was less important.

Gap elements were also used at the rivet/skin interface for the upper rivet row to model rivet interference. The interface condition that governed the relative displacement between the rivet and skin was defined to generate nonzero stresses for a zero displacement. This technique modeled the effect of a slightly oversized rivet bearing against the rivet hole. The radial rivet interference level used in the finite element analysis was 0.00075-in (0.8% of the rivet radius), as measured in previous experimental testing (Dawicke et al., 1992).

Load eccentricity inherent to the single lap joint problem was introduced by offsetting the two skin layers. The offset produced bending in the lap joint. The bending stresses that resulted from this load eccentricity were compared with experimental strain gage data. The offset dimension was then adjusted to produce model bending stresses which generally agreed with the experimental data.

Two aspects of corrosion were considered in the FRANC2D/L analysis: material thinning and pillowing. The effect of material thinning was modeled through a uniform thickness reduction over the corroded region (faying surfaces of the lap joint). The presence of pillowing was modeled by introducing a transverse pressure acting against the faying surfaces of the lap joint in accordance with the NRC procedure for simulating pillowing (Bellinger et al., 1994).

Cracks were introduced into the outer skin in the upper rivet row according to three different scenarios. In Scenario 1, a single radial crack was located at the right hand edge of rivet hole number 4. In Scenario 2, cracks were located at both edges of rivet hole number 4. The initial crack lengths in this case were equal. In Scenario 3, cracks were once again located at both edges of rivet hole number 4. In this case, the initial crack length on the left side of the hole was one half of the initial crack length on the right side. The cracks were incrementally grown using the automated crack propagation routine. The crack tip SIFs were recorded at each propagation step.

The plots in Figure 2 summarize the results of the FRANC2D/L finite element analysis. These plots contain K-solutions for a range of crack configurations, corrosion conditions, and rivet interference levels. In each case, the K-solution is plotted for the lead crack which grows from 0.01 inches to 0.35 inches. The vertical axis in each plot

contains ΔK which is given by, $\Delta K = K_{max} - K_{res}$, where K_{max} is the crack tip SIF for the lap joint under maximum hoop load and K_{res} is the crack tip SIF under no hoop load. For the cases of no rivet interference, K_{res} is zero, but for nonzero rivet interference, K_{res} is nonzero.

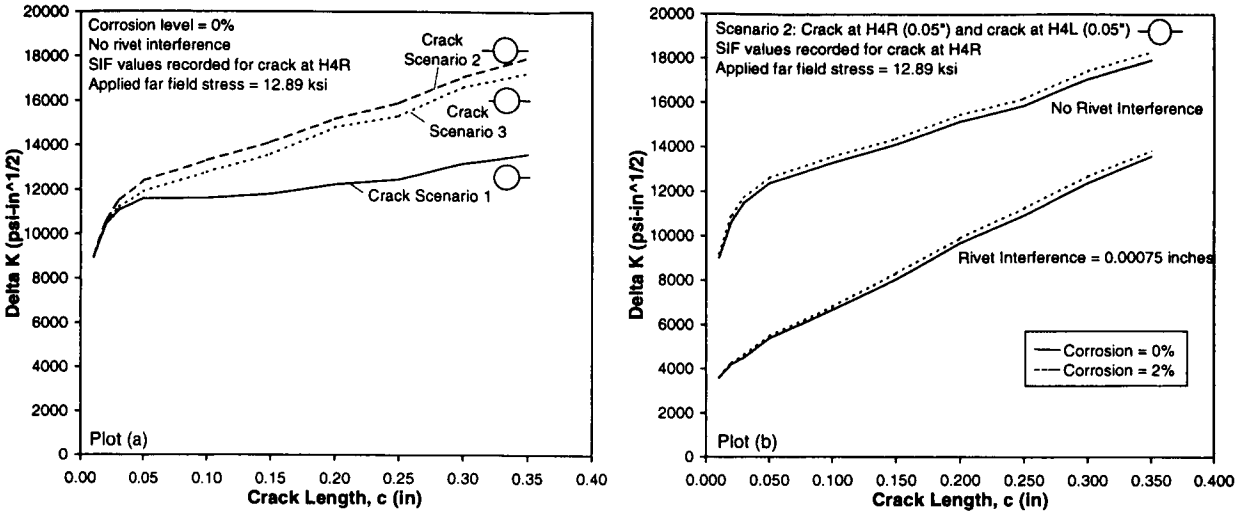

(a) (b)

Figure 2. FRANC2D/L SIF Predictions for (a) Different Crack Scenarios and (b) Different Interference and Corrosion Levels

Based on these results, several observations can be made regarding the effects of crack configuration, corrosion conditions, and rivet interference level on crack tip SIF. Figure 2a compares the SIF results for the three crack configurations corresponding to Scenarios 1 through 3. The plot shows a significant increase in SIF for the case of diametrically opposed cracks compared to that of a single crack, as observed in previous studies. Results for Scenarios 2 and 3 show very similar SIF values, which indicates that SIF values for the longer crack in Scenario 3 are not very sensitive to the length of the shorter crack on the opposite side of the hole. Scenario 2 provides an upper bound to SIF values in Scenario 3 if the shorter cracks were to increase in length to match the longer crack. Since Scenarios 2 and 3 yielded such close results, Scenario 3 was omitted from subsequent analyses.

Figure 2b compares K-solutions for two levels of rivet interference and two levels of corrosion. The effect of rivet interference was to increase substantially the residual SIF value under no applied hoop load (K_{res}), and to increase slightly the SIF value at maximum applied hoop load (K_{max}). The result was a large drop in ΔK over the entire range of crack growth. These results indicate how sensitive the ΔK-solution is to the level of rivet interference, which confirms similar results in previous studies (Dawicke et al., 1992).

The effect of corrosion was modeled through uniform thinning of the material in the corroded region. In this case, one would expect the average stresses in the corroded region, and therefore the SIF values, to increase by a factor of approximately t/t_{corr}, where t is the original thickness, and t_{corr} is the corroded panel thickness. The FRANC2D/L prediction yielded the expected result, as the SIF values for the 2% corrosion case were about 1.02 times higher than for the case with no corrosion. This result was consistently obtained for all analysis cases that had no interference. For the analysis cases that included rivet interference, the effect of uniform material thinning was slightly different. For small crack lengths (less than 0.05 inches), the material thinning had a reduced impact on the SIF values, yielding an average increase of approximately 1% in ΔK. For crack lengths greater than 0.05 inches, the average increase in ΔK was back to the 2% level observed in the zero rivet interference case.

Initially, the effects of pillowing corrosion were also included in the analysis by applying a transverse pressure to the faying surfaces of the lap joint (Bellinger et al., 1994). The effect of the transverse pressure was to induce local bending stresses in the skins around each rivet, thereby producing non-uniform stresses through the thickness of the skin. However, SIF values calculated in FRANC2D/L were based on stresses at the mid-plane of each layer. The mid-plane stresses were, of course, unaffected by bending stresses, and therefore, the calculated SIF values saw no contribution from the pillowing pressure. Moreover, even if a method was used which captured the effect of bending

on SIF, the resulting SIF distribution along the crack front would obviously become non-uniform. It follows that crack growth rate and crack length would also become non-uniform along the crack front. These conditions represent a complicated three-dimensional crack growth problem beyond the scope of this investigation. Therefore, pillowing corrosion effects were not considered further. In all the results presented herein, the effect of corrosion was accounted for solely through the method of thinning the material uniformly in the corroded region, a method commonly employed in previous studies to account for corrosion damage. Bellinger and Komorowski (1998) propose a nonlinear finite element analysis approach for investigating corrosion pillowing in fuselage lap joints.

The K-solutions obtained from the FRANC2D/L analysis were recorded and converted to beta factors for use in AFGROW. The conversion equation is given below:

$$\beta = \frac{K_{max} - K_{res}}{\sigma_{ref}\sqrt{\pi c}}$$

where σ_{ref} is the reference stress set at 12.89 ksi based on experimental load level (Scott, 1997). Since $\Delta K = K_{max} - K_{res}$, variation in the load ratio, R, was implicitly accounted for by the variation of K_{res} as a function of crack length. R varied from about 0.6 to 0.3 as the crack length increased. The use of K_{res} rather than a residual stress is dependent on the analysis tool. Other crack growth programs may account for residual stresses differently, but they should provide the same or similar results. The resulting stress intensity factors and beta factors are tabulated in Cope et al. (1998) for each crack scenario, rivet interference level, and corrosion level considered.

3.2.2 Crack Growth Analyses

Next, analysis was performed using the crack growth code AFGROW. Inputs included a constant amplitude of 12.89 ksi with an R ratio of 0.02. Since the SIF solutions used the far field stress of 12.89 ksi, this same load was used for the crack growth analysis. The material properties were for 2024–T3 clad aluminum with a da/dN lower limit of 10^{-9} inches/cycle. This lower limit was chosen as a first-order approximation of small crack effects.

To account for the different R ratios, the K_{res} was separated out of the K_{max} and K_{min} data for each crack length. The appropriate beta value was then calculated for the applied stresses and K values as discussed in Section 3.2.1. Each crack length had a corresponding beta and a K_{res} value, which was entered as a function of crack length in the residual K table (an option in AFGROW). Since the K_{res} was caused by an interference fit fastener that remains in the hole, this method only works for a constant amplitude loading scenario. The assumption is that the relationship between K_{res} and crack length is unique, which is only true for a given applied stress. A different input stress at a given crack length would result in a different K_{res}. The residual stress capability currently in AFGROW is designed to work for cases where you have pre-existing residual stresses (from machining or coldworking, etc). In general, an interference fit fastener must be handled differently - the K_{res} due to the interference fit fastener must be calculated real time as the crack grows for a variable applied stress spectrum.

The predictive analysis of cracks without interference grossly under predicted the normalized test data while the interference predictive analysis over predicted the test data, as shown in Table 1. Percent errors were calculated as

$$\left| \frac{\text{Predictive Results - Normalized Test Data}}{\text{Normalized Test Data}} \right| \text{X } 100$$

where the normalized test data used was the single case which best represented the appropriate scenario. As this analysis was only a proof of concept analysis, the published amount of rivet interference was presumed close enough to show it had an effect on the life prediction of the crack, as shown in previous studies (Dawicke et al., 1992; Newman et al., 1997). A lengthy iterative process would be required to find a rivet interference value that would enable a closer prediction of the crack growth life.

TABLE 1. Prediction Estimation Errors.

		Specimen Crack Location	No Interference	Interference 0.00075-in
Scenario 1:	Fatigue	F1-4R	38% less	22% more
	2% Corrosion	CF4-4R	28% less	42% more
Scenario 2:	Fatigue	F6-5L	43% less	36% more
	2% Corrosion	CF3-4R	51% less	18% more

The next results (Figure 3) plot scenario 1 and scenario 2 (solid lines) with an interference of 0.00075 inches against all the fatigued and corroded normalized test data. The lead cracks' test data are identified in the figures by specimen number and crack location, i.e., F0-6L is the lead crack on the left side of rivet 6 in the fatigued specimen 0. (F = fatigue (no corrosion), CF = fatigue with prior corrosion, L = left, R = right). Comparing these two plots shows a definite loss in life when corrosion was present, as has been found in previous studies. Both the normalized test data points and the predictive analysis have a decrease in life of about 10% or more as a result of 2% thinning.

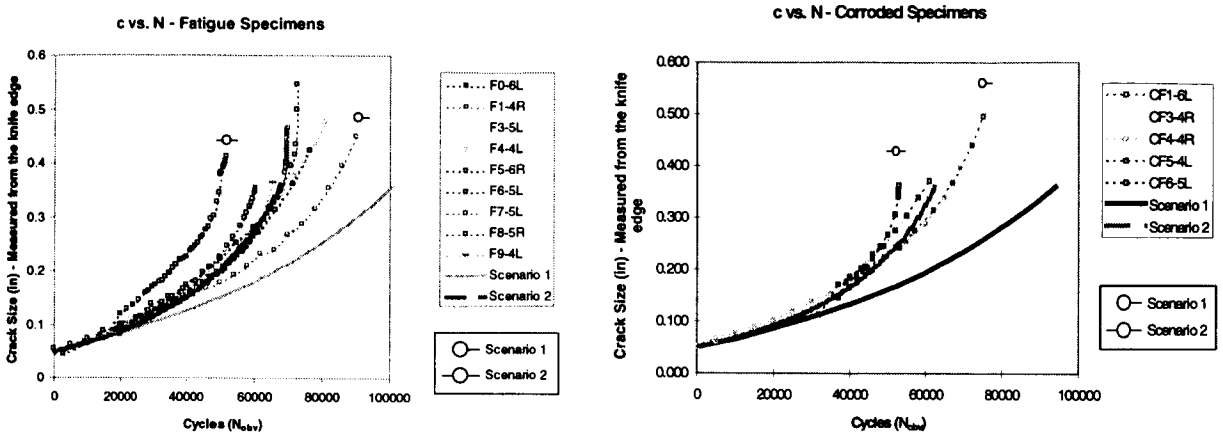

(a) (b)

Figure 3. Predicted Crack Growth for NRC Lap Joint Specimens with (a) No Corrosion and (b) Prior Corrosion.

Analysis was then performed for the risk analysis using an initial short crack of 0.010 inches. Shown in Figure 4, crack growth curves were calculated for five corrosion levels (0%, 2%, 5%, 8%, and 10%) for both Scenario 1 and 2 using the 0.00075-in rivet interference. As discussed in Cope et al. (1998), the risk analysis also used these analysis curves to extrapolate the first observed cracks to an estimated length at 50,000 cycles.

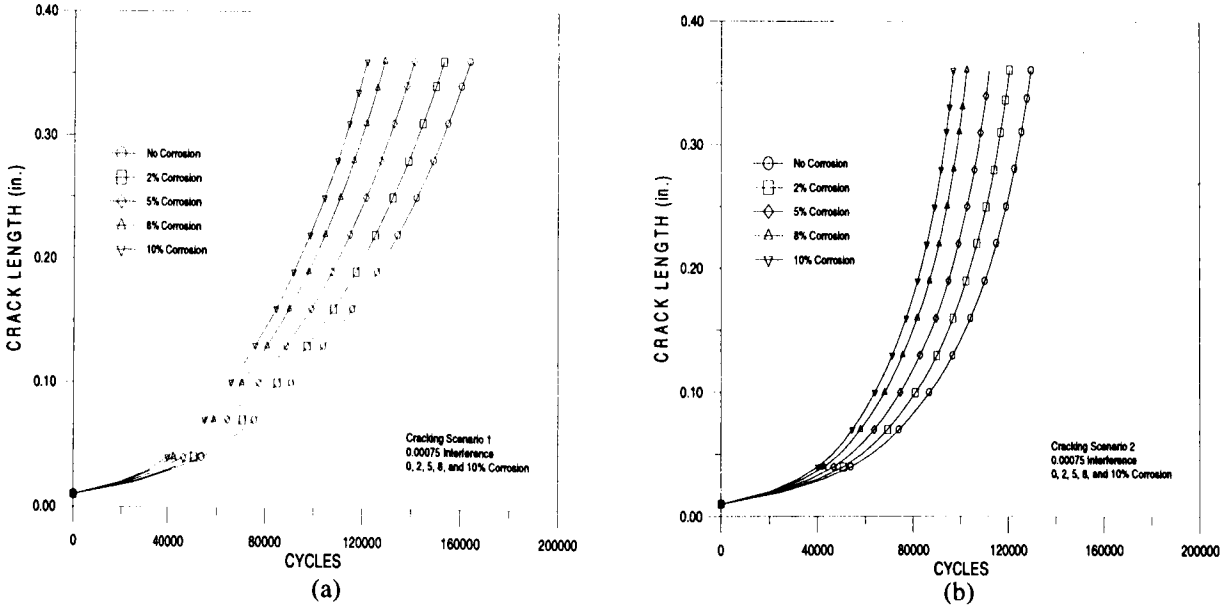

(a) (b)

Figure 4. Crack Size versus Cycles at 5 Corrosion Levels for (a) Scenario 1 and (b) Scenario 2

3.2.3 Risk Assessment

The risk assessment of the lap joints is based on the fracture probability of a randomly selected lap joint from the population being analyzed. One run of PROF produces a time history of fracture probability for an initial crack population with a fixed geometry and stress history. However, the population of lap joints to be modeled will not have a fixed geometry when the possibility of MSD is permitted. Further, the introduction of corrosive thinning will change the expected stress history and crack growth projections of a lap joint. If the distribution of these factors is known, the fracture probability can be evaluated from multiple PROF runs at conditions representative of percentiles of the distributions. The conditional fracture probabilities can then be combined or interpreted in terms of their relative frequencies of occurrence.

To perform the risk analyses that correspond to 0%, 2%, 5%, 8%, and 10% thinning, ten individual runs of PROF were required – five levels of stress (corrosion severity) for each of two MSD scenarios. Probability of fracture as a function of cycles was calculated for each of the ten combinations of cracking scenario and corrosion severity. These calculations do not account for any additional corrosive thinning after the start of the analysis. Fracture of the lap joint specimens was defined as the lead crack exceeding 0.35 inch. Figure 5 presents the conditional fracture probabilities for Scenarios 1 and 2. Time zero in the PROF analyses corresponds to 50,000 cycles in the test data. The fracture probabilities behave as expected - Scenario 2 increased risk of fracture over Scenario 1, and the risk of fracture increased as stress levels increased due to corrosion material loss.

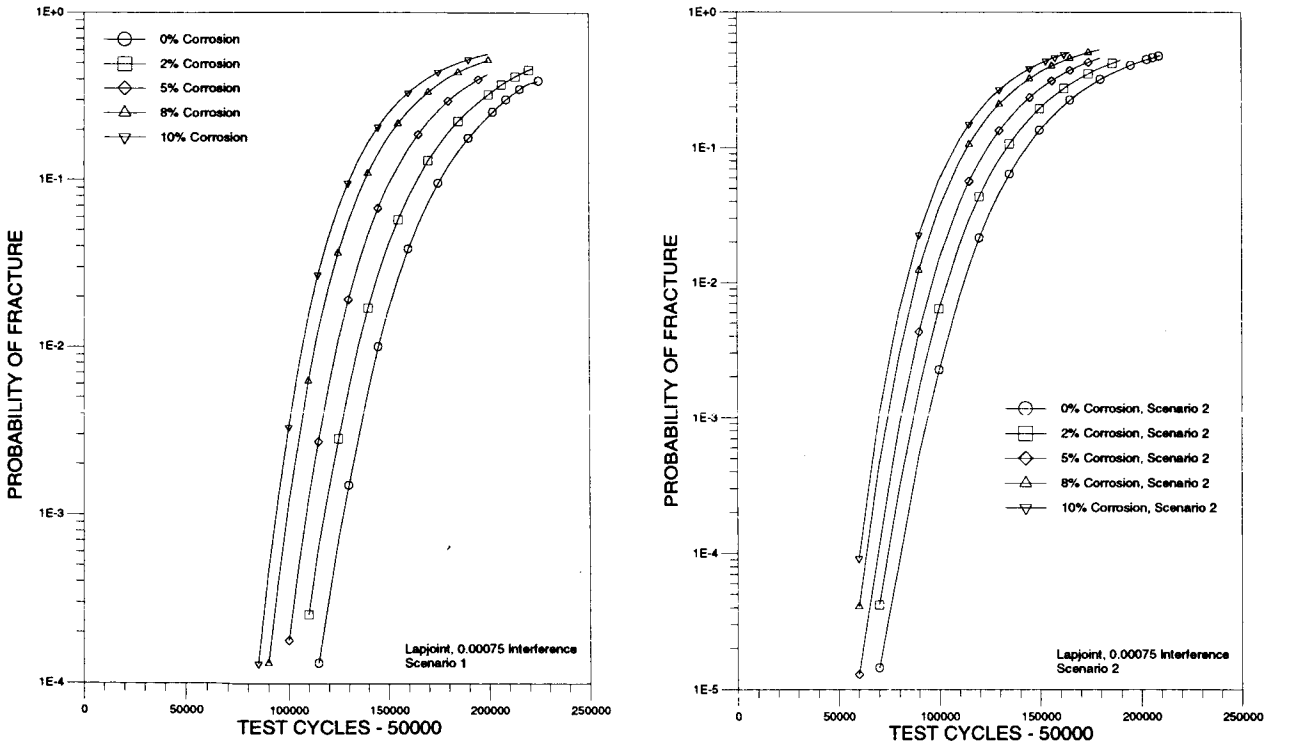

(a) (b)

Figure 5. POF versus Cycles for for (a) Scenario 1 and (b) Scenario 2

4. RESULTS AND CONCLUSIONS

This project evaluated advanced structural analysis tools for addressing the effects of corrosion damage and MSD cracks on stress distributions, stress intensity factors, fatigue life, and risk of fracture of a skin lap joint. The analysis tools included:

- Finite-element code, FRANC2D/L, for determining stress distributions and stress intensity factors of cracks,
- Crack growth analysis code, AFGROW, for estimating the fatigue crack growth life, and
- Risk analysis code, PROF, for determining the probability of fracture with a defined damage scenario.

4.1 Summary of Analysis Results

The analysis of the skin lap joint was based on the lap joint specimens tested with no corrosion and with 2% corrosion. These specimens were fatigue tested, allowing multiple cracks to form naturally in the joint. A finite element analysis was performed to determine crack tip SIF values, and a fatigue crack growth analysis was performed to predict the life of the lap joint. Analysis was performed for the lead crack using the three different cracking scenarios experimentally observed. Then, results from the finite element analysis and fatigue crack growth analysis were used in a risk analysis. Analysis of the MSD lap joint specimens showed several conclusions.

First, two-dimensional analysis was sufficient to generate results which generally followed the long crack growth test data (i.e., crack length greater than 0.05 inches) for both the baseline and corroded configurations. However, due to the fact that only 2% corrosion was exhibited, the bending stresses associated with pillowing were not as significant as corrosion levels seen in typical aircraft lap joints. Therefore, in the more extreme case of, say 10% corrosion, the bending stresses due to pillowing may be high enough to render a two-dimensional analysis inaccurate. Although analyses attempted to account for both pillowing and thinning effects in the joint, only the thinning effects of corrosion damage were successfully accounted for.

Second, the presence of rivet interference produced a significant impact on the SIF and crack growth predictions. Rivet interference could be manipulated to match the test data, but would require a time-consuming iterative process. Without rivet interference, crack growth analysis was conservative, but with rivet interference of 0.00075-in., the crack growth analysis overestimated the life. These results highlight the apparent sensitivity of fatigue crack growth rate to rivet interference.

Third, the risk assessment showed the relative impact of thinning on the probability of fracture. The lap joint fracture probability for the severity characterized by ten percent thinning can be 70 times greater than that of an uncorroded lap joint. If maintenance scheduling were based on keeping the fracture probability below 0.0001 to 0.001 when compared with an uncorroded lap joint, a lap joint with ten percent corrosion thinning would have a 25 to 50 times greater chance of resulting in fracture. Risk assessments require not only test data, but also historical corrosion data to generate meaningful results. The more data collected in the future at various corrosion levels and initial crack distributions, the more realistic the predicted results will be.

4.2 Assessment of Structural Analysis Tools

This project developed and demonstrated an analytical framework for estimating the effects of corrosion damage and WFD on structural integrity. The analytical framework incorporated a number of advanced analysis tools that, when taken together, have the capabilities to perform stress analysis, crack growth analysis, and risk analysis on thin structural components with multiple layers of material. Accounting for the thinning effect of corrosion and multiple cracks in these analyses were straight forward. However, the modeling and analysis of corrosion pillowing and small cracks demonstrated some of the limitations of the tools. With further improvements in analysis tools and techniques, the analytical framework would be useful in assessing the impact of corrosion damage and MSD on the integrity of an aircraft structural component.

Based on characterization of corrosion damage and fatigue cracking, the deterministic structural analysis tools can determine stress intensity factors and fatigue crack growth life of structural components with damage conditions from uniform material thinning due to corrosion and from multiple cracks in multi-layered structure. With defined initial quality or crack size distributions and deterministic information, the probabilistic structural analysis tool can predict the risk of failure while accounting for the probability of detecting the damage condition. This capability allows the reliability of inspections to be assessed along with analysis methods to determine the probability of fracture in a structural component.

From this study, it was concluded that the finite element analyses and risk assessment analyses were labor intensive and could not easily be streamlined. Minimal automation from the output of FRANC2D/L to the input of AFGROW and from the output of AFGROW to the input of PROF could be achieved. However, it is recommended that each module be kept separate since distinct modules would allow greater flexibility for the engineers. The separate analyses also create individual checkpoints for the application of engineering judgement.

REFERENCES

Bellinger, N. C. and J. P. Komorowski (1998). "Finite Element Analysis Approach for Cracks at Countersunk Holes in Fuselage Lap Joints With and Without Corrosion Pillowing", LM-ST-823, Institute for Aerospace Research, National Research Council of Canada, 27 April 1998.

Bellinger, S. Krishnakumar, and J.P. Komorowski (1994). "Modeling of Pillowing Due to Corrosion in Fuselage Lap Joints", Canadian Aeronautics and Space Journal, Vol. 40, No. 3, September 1994.

Berens, A.P. and M.L. Papp (1995). "WINPROF Version 1.0 User's Guide", Report UDR-TR-94-83, UDRL.

Cope, D. A., P.S. Johnson, J.J. Luzar, A. Trego, and J.D. West (1998). "Corrosion Damage Assessment Framework", Final Report on Corrosion/Fatigue Effects on Structural Integrity Contract, D500-13008-1, The Boeing Company, Boeing Information, Space, and Defense Systems, August 1998.

Dawicke, D.S., S. Gondhalekar, E.P. Phillips, and D.V. Swenson (1992). "Crack Growth from Loaded Rivet Holes", Structural Integrity of Aging Airplanes, NASA / FAA, Atlanta, GA, April 1992.

Eastaugh, G.F., D.L. Simpson, P.V. Straznicky and R.B. Wakeman (1995). "A Special Uniaxial Coupon Test Specimen For The Simulation Of Multiple Site Fatigue Crack Growth And Link-Up In Fuselage Skin Splices", National Research Council of Canada and Carleton University, AGARD-CP-568, December 1995.

Harter, J. A. (1998). "AFGROW User's Manual Version 3.1.1", #WL-TR-97-3053, Wright-Patterson AFB, OH, February 1998.

MIL-HDBK-5G (1994). Military Handbook, "Metallic Materials and Elements for Aerospace Vehicle Structures", Department of Defense, 1 November 1994.

Newman, J.C., Jr., C.E. Harris, M.A. James, and K.N. Shivakumar (1997). "Fatigue-Life Prediction of Riveted Lap-Splice Joints Using Small Crack Theory", International Committee on Aeronautical Fatigue, 19th Symposium, Edinburgh Scotland, 18-20 June 1997.

Scott, J.P. (1997). "Corrosion and Multiple Site Damage in Riveted Fuselage Lap Joints", Master's Thesis, Carleton University, March 1997.

Swenson, D. and M. James (1997). "FRANC2D/L: A Crack Propagation Simulator for Plane Layered Structures", Version 1.4 User's Guide, Kansas State University, December 1997.

MATHEMATICAL MODEL TO PREDICT FATIGUE CRACK INITIATION IN CORRODED LAP JOINTS

Gerhardus H. Koch
CC Technologies Laboratories, Inc.
Dublin, OH 43016, U.S.A.
Telephone: 614-761-1214
Telefax: 614-761-1633
E-Mail: kochg@cctlabs.com

Le Yu and Noriko Katsube
The Ohio State University
Columbus, OH 43210, U.S.A.

Clare A. Paul
AFRL/VASE
Wright Patterson AFB, OH 45433, U.S.A.

ABSTRACT

There is increasing concern about the possible detrimental effects of corrosion on the structural integrity of fuselage lap joints. Corrosion in lap joints can lead to a decrease in strength because of loss in skin thickness, early fatigue crack initiation caused by the formation of stress risers, and increased fatigue crack growth rates. The mode of corrosion in lap joints has generally been considered to be uniform loss of material. Based on the concept of general thickness loss and the formation of voluminous corrosion products as a result of exfoliation corrosion, models to predict the stress distribution and fatigue crack initiation sites have been previously developed. These models indicate that that the combination of loss in skin thickness and the build up of voluminous corrosion products inside the lap joint will lead to high stresses in the joint where fatigue cracks are likely to initiate. However, these calculations are not based on the actual morphology of corrosion in the lap joint.

In this paper, detailed metallography of a KC-135 lap-joint section describes the complex nature of corrosion on the contact or faying surface, with barely detectable corrosion penetrating deep into the skin. A finite element model was developed, based on the actual corrosion morphology of the lap joint. The finite element program ABAQUS was used to model the strain/stress distribution in a corroded lap-joint section. The corrosion was simulated by decreasing the skin thickness and applying a uniform pressure to represent the build up of corrosion by-products. A small hemisphere was introduced to simulate the localized intergranular corrosion. The results of the finite element analysis demonstrated that even a small hemispherical indent superimposed on uniform type corrosion near a fastener hole resulted in significant increase in elastic strain such that early fatigue crack initiation could be anticipated.

INTRODUCTION

Over the past several years, much attention has been given to the phenomenon of multi-site damage (MSD), particularly of fuselage lap joints. The concern about MSD of lap joints was triggered by the infamous incident on April 28, 1988 where an Aloha Airlines Boeing 737 flying at 24,000 ft (7,300 m) suffered a structural failure in which an 18 ft (5.5 m) section of the fuselage crown was torn. The aircraft landed safely; however, one life was lost.

An accident/failure investigation by the National Transport and Safety Board (NTSB) concluded that the failure resulted from rapid and catastrophic crack growth caused by lap joint multiple site damage.[1] It is important to know, however, that this aircraft had operated its entire life in a tropical marine environment. Thus, severe corrosion due to exposure to this environment could have contributed to the formation of fatigue crack nucleation sites, which could have eventually lead to MSD and catastrophic failure. Extensive studies have been conducted to analyze and model MSD.[2-5] In these studies, MSD was generally considered to consist of small flaws, such as fatigue cracks originating from fastener holes, which could barely be detected by standard NDI techniques. Generally, these detectable cracks are greater than 0.05 inches. Again, environmental factors and corrosion must be taken into consideration. Although corrosion was considered to be a costly economic problem, it was not deemed to be an adverse factor in the structural integrity of critical airframe structures, such as fuselage lap joints.[6]

Recently, much attention has been given to the phenomenon of pillowing of lap joints, where voluminous corrosion products at the contact or faying surfaces of a lap joint cause deformation of the skin, see Figure 1. Work by Komorowski and coworkers[7-9] indicated that the volume increase associated with the corrosion products is approximately 6.5 times the volume of the corroded parent aluminum alloy. The large volume increase and resulting deformation of the skin likely results in high stresses near the fasteners, which can have a definite detrimental effect on the structural integrity of the lap joint by lowering the strength and providing preferential sites for fatigue crack initiation. Mathematical and finite element modeling by Komorowski[7-9] were used to simulate the presence of the voluminous corrosion products within the fuselage lap joint. The stresses in the skin, which result from the internal pressure by the corrosion product build-up, from the fasteners, and from the reduction in thickness caused by material loss were all taken into account. The results of the calculations indicated that the pillowing significantly increases the stress in a fuselage lap joint, particularly in the vicinity of the fastener holes.

Moreover, fracture mechanics analyses conducted by Bellinger and Komorowski[9], and Welch[10] revealed troubling cracking behavior in lap joints subject to pillowing. The analyses suggested that cracks would form on the faying surface, forming a semi-elliptical crack front with a high aspect ratio without breaking through the outer surface of the skin. This would make visual inspection of the crack difficult. Also, analyses by Welch suggested that these cracks would propagate in directions other than perpendicular to the hoop stress.

1. APPROACH

2.1 CORROSION CHARACTERIZATION

While the above-discussed analyses were based on uniform loss of metal thickness as a result of crevice or exfoliation corrosion, no attempt was made to consider the actual lap joint corrosion morphology. It

is reasonable to assume that localized corrosion, such as pitting or intergranular corrosion, could have an adverse effect on the stress distribution in the lap joint, and are a further detriment to the structural integrity of the joint.

A detailed characterization of the corrosion in a fuselage lap joint was performed using conventional metallographic techniques. A section of corroded fuselage lap joint was recovered from a KC-135 aircraft fuselage. This fuselage skin was made of aluminum alloy 2024-T3 sheet, and the original thickness of the lap joint section shown in Figure 2 was 1 mm (40 mils). After extensive visual inspection, areas for metallographic sectioning were selected. The selection of these areas was based on the appearance of corrosion both on the contact or faying surface and the outside surface. Generally, there was no evidence of corrosion on the outside surface of the skin, unless the corrosion had completely penetrated. The lap joint section was cut in different directions, longitudinally, transversely, and diagonally, so that the effect of orientation on the corrosion morphology could be examined.

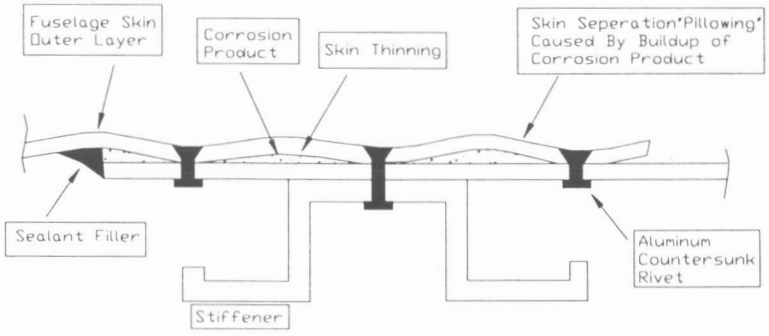

Figure 1. Cross Section Through Lap Joint

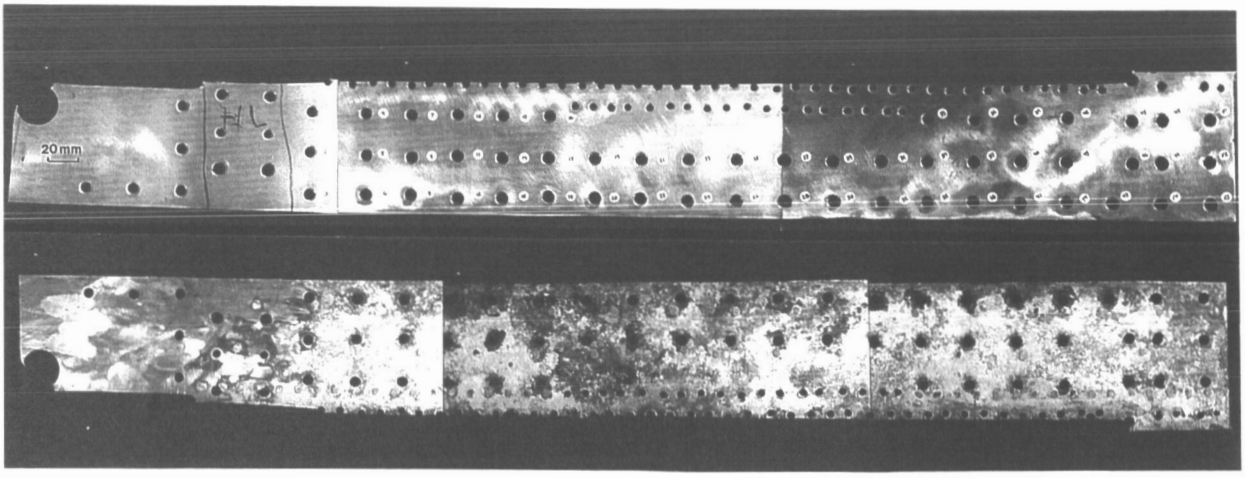

Figure 2. Contact (Top) and Outside (Bottom) Surface of KC-135 Fuselage Lap Joint

The cut sections were mounted in epoxy, which was cured under vacuum. The metallographic cross sections were ground and polished with colloidal silica and magnesium oxide to 2 μm finish. In order to be able to study the corrosion morphology in three dimensions, several parallel and perpendicular cross sections were made.

2.2 FINITE ELEMENT ANALYSIS

Finite element analyses (FEA) were carried out using ABAQUS and I-DEAS. The I-DEAS program has the capability to automatically generate both two- and three-dimensional meshes, and is designed to interface with ABAQUS. In order to address the complex geometry of the type of corrosion in the fuselage lap joints, 10-node tetrahedron elements were used. The mesh of tetrahedron elements was automatically generated by I-DEAS and imported to ABAQUS for finite element calculation and post-processing.

The finite element analyses were performed on a 38 square mm (1.5 square inch), 10 mm (0.04 inch) thick sheet, which was reduced in thickness to 0.9 mm (0.036 inches) to simulate a 10 percent loss in thickness due to uniform corrosion attack. The distance between the four fastener holes in the coupon was 25.4 mm (1 inch), and the dimensions of the holes were modeled after those of the fuselage lap joint section examined in this study, tapered holes with a 3.5 mm (0.14 inch) inner radius and 4.5 mm (0.18 inch) outer radius. A hemispherical pocket representing a region of localized corrosion was superimposed onto the uniformly corroded area. The material properties used for the finite element analyses were those for aluminum alloy 2024-T3 with the Young's modulus 73,776 MPa of (10,700 ksi) and the Poisson's ratio of 0.33. Finally, linear elastic deformation was assumed in the analysis.

The strain distribution on the lap joint section were calculated, based on a 6.895 x 10^3 Pa (1psi) uniform hydrostatic pressure, which simulates the pressure produced by the corrosion by-product. The 1 psi pressure was arbitrarily selected in order to simplify the calculations. Since elastic conditions are assumed, linear extrapolation to any value of pressure and resulting vertical displacement and strain can be carried out. Throughout the analysis, the symmetry condition was applied, so that one quarter of the boundary value problems could be analyzed. When necessary, the macro-micro analysis was used to improve the accuracy and efficiency of the model. Macro models based on a relatively coarse mesh were used first, and the calculated displacement fields were then used as boundary conditions for the fine-meshed micro models, which were used to represent the regions of localized corrosion.

3. RESULTS

3.1 CORROSION CHARACTERIZATION

As shown in Figure 2, the outside of the lap joint showed little or no evidence of corrosion, but on the contact or faying surface of the lap joint, voluminous corrosion products (hydrated Al_2O_3 or Al $(OH)_3$), which are characteristic of exfoliation corrosion, can be observed.

Metallographic cross sections through the lap joint section, such as in Figure 3, show extensive corrosion of the aluminum alloy skin, including pitting, exfoliation corrosion and intergranular corrosion. The figures show that exfoliation corrosion can either start from the faying surface or from a fastener hole. In the latter case, exfoliation can propagate over long distances before sufficient corrosion product is build up to create the pillowing effect. Once sufficient corrosion product has

formed, lifting of the grains is observed, which is characteristic for severe exfoliation corrosion. When the grains are lifted off, and surrounded by the hydrated aluminum hydroxide, corrosion of the alloy grains continues by an apparent form of dealloying corrosion. The optical micrographs of exfoliated grains, shown in Figure 4, clearly demonstrate the dissolution of the grains. Specifically, the micrograph shows remnants of the corroded grains indicating selective dissolution.

Further examination of several metallographic cross sections through the lap joint section demonstrated the presence of localized regions of intergranular corrosion in the aluminum alloy skin under the exfoliated regions. The intergranular attack, which occurs along grain boundaries and subgrain boundaries, is very tight suggesting that the voluminous aluminum hydroxide corrosion byproducts has

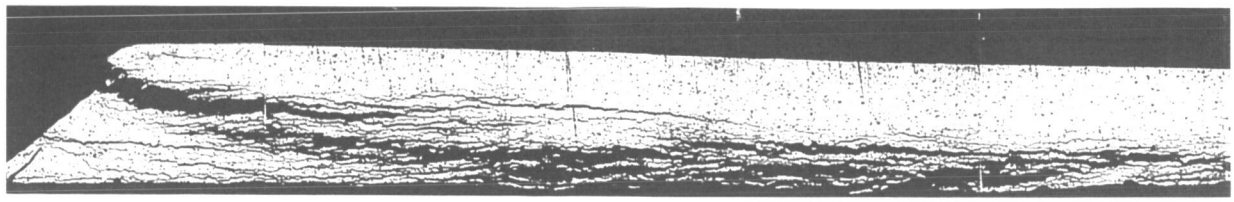

Figure 3. Metallographic Cross Section Through Area Adjacent To Fastener Hole. Outside Surface Is Facing Up.

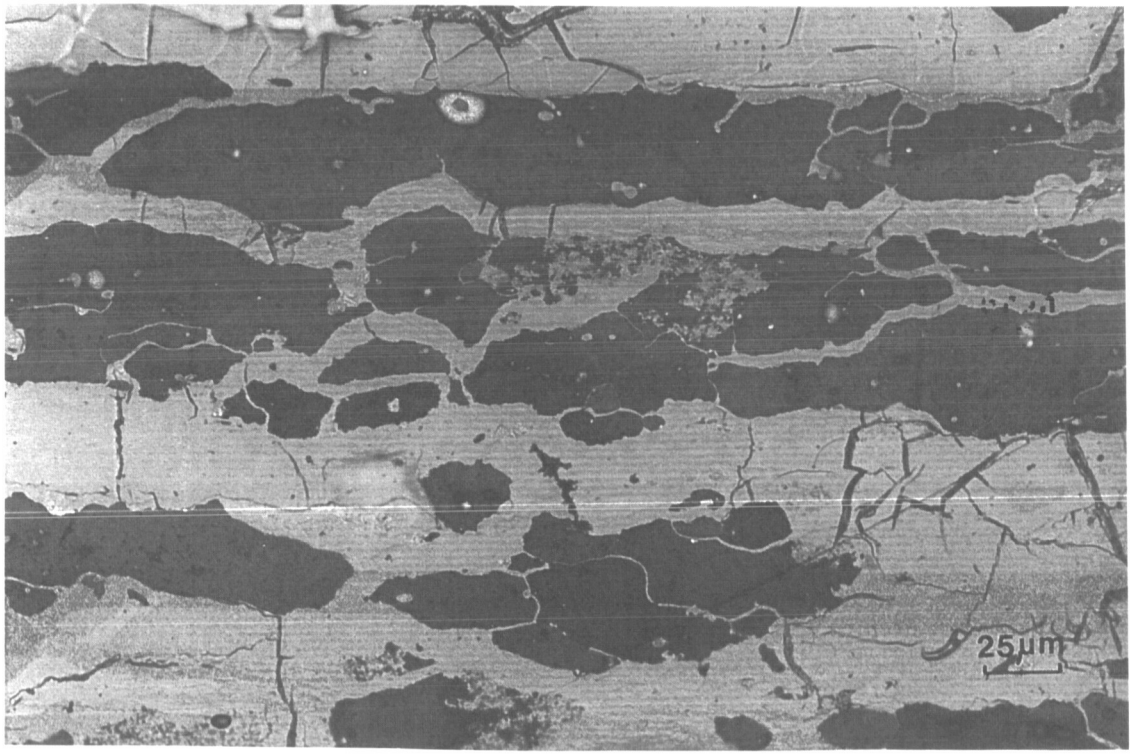

Figure 4. Metallographic Cross Section Of Exfoliated Grain, Showing Preferential Dissolution Of Aluminum From The Grains.

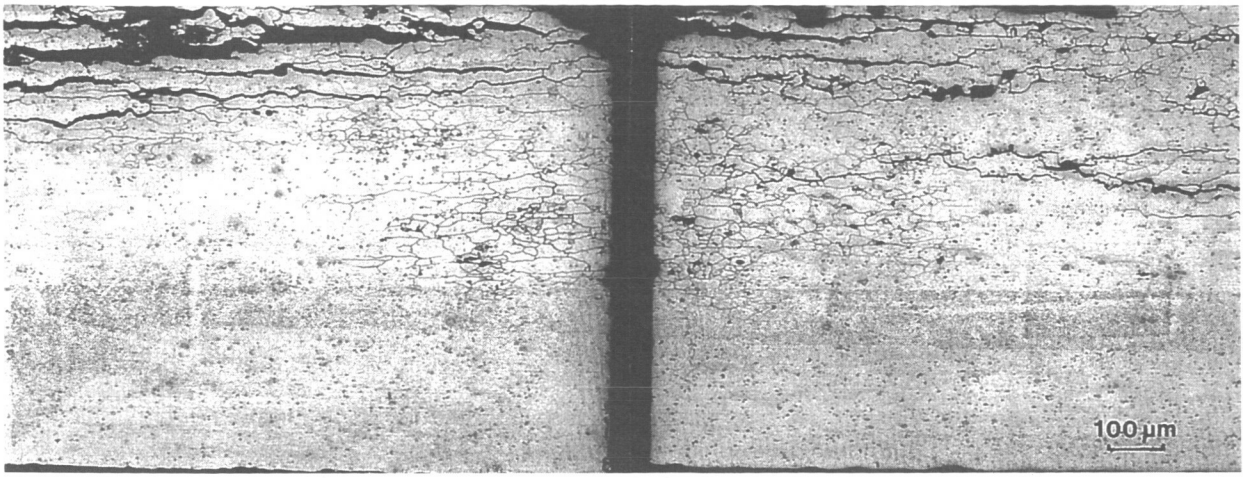

Figure 5. Optical Micrographs Of Perpendicular Cross Sections Showing A Pocket Of Fine Intergranular Corrosion.

not yet formed. Perpendicular cross sections such as shown in Figure 5 suggest that these regions of intergranular attack occur in the form of approximate hemispheres, and can propagate deep into the skin. In some cases, it was found that the intergranular attack has occurred along a single path, which is characteristic of intergranular stress-corrosion cracking.

3.2 FINITE ELEMENT ANALYSIS

The finite element modeling was conducted on a 38 square mm (1.5 square inch) plate section, 0.9 mm (0.036 inch) thick. The dimensions of the fastener holes, with an inner radius of 3.5 mm (0.14 inch) and outer radius of 4.5 mm (0.18 inch), were similar to those of the fastener holes in the fuselage lap joint. Because of the symmetry of the plate, one quarter of the plate was modeled using 3420 10-node tetrahedron elements. The displacement components of the fastener hole were assumed to be zero. When a uniform pressure of 1 psi was applied, the maximum normal strain in the diagonal direction of the plate was found to be 0.029 on the diagonal 0.198 inches from the center of the fastener hole.

In order to examine the effects of localized corrosion on the stress and strain distribution on the plate, a small hemisphere with a radius of 0.46 mm (0.018 inches) was placed on the diagonal 5 mm (0.198 inch) away from the center of the fastener hole. The location of the hemisphere was selected to coincide with the point where the normal strain in diagonal direction was the highest. With the 0.46 mm (0.018 inch) radius hemisphere, the maximum normal strain in diagonal direction is 0.0498, which occurs on the side where the hemisphere is located, see Figures 6 and 7. The strain at the location of the hemisphere is approximately 72% higher than the strain at the same location without the hemisphere. It is important to note that the calculations are based on the assumption of linear elasticity, and thus the magnitude of the maximum normal strain is well beyond the elastic range of the material.

After determining the effect of a 0.46 mm (0.018-inch) radius hemisphere on the strain distribution near a fastener hole, the effect of size of the hemisphere was investigated. When the 0.46 mm (0.018-inch) radius hemisphere was reduced by a factor of two, it was found that upon application of the 1 psi lateral pressure, the maximum normal strain was 0.053. This strain is 6.6% larger than the strain calculated for the larger hemisphere. The results of these calculations indicate that the size of the hemisphere has a significant effect on the stress-strain distribution around the hemisphere, and that there is likely to be an

optimal size at which the strain is at a maximum. Preliminary study indicates that a hemisphere with a radius of about a quarter of the plate thickness seems to cause the highest localized strain.

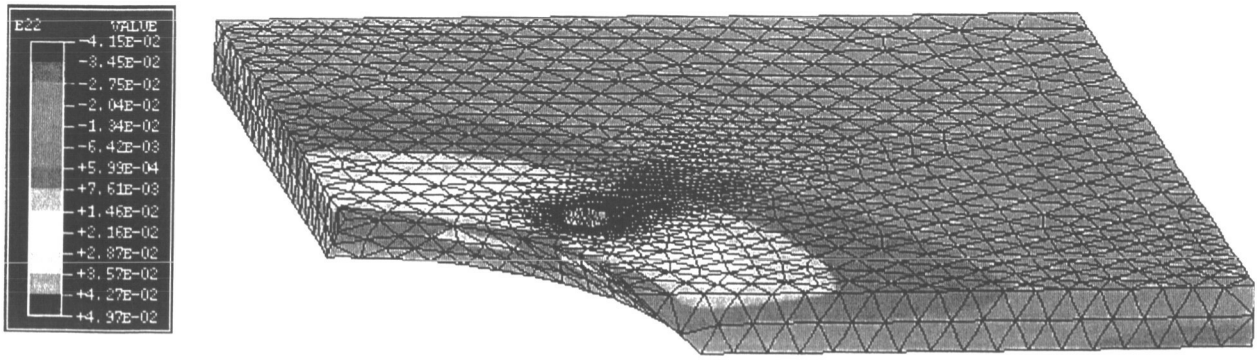

Figure 6. Finite Element Mesh of Quarter Sheet with Fastener Hole and Hemisphere with 0.46 mm (0.018 Inch) Radius and Located 5 mm (0.198 Inch) from Center of Fastener Hole.

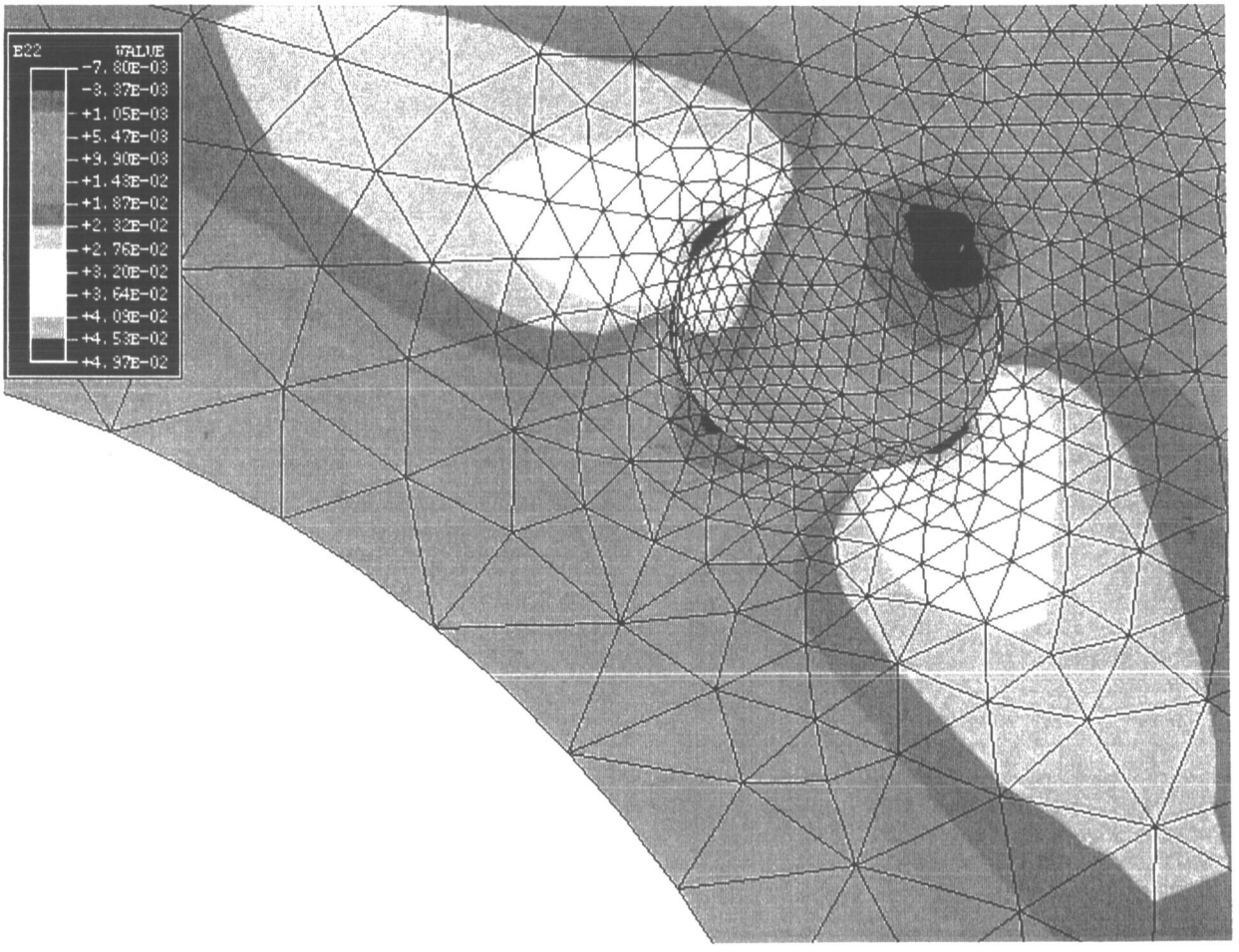

Figure 7. Local view of Strain Distribution Around the Hemisphere Shown in Figure 6.

3.3 IMPACT ON FATIGUE LIFE

A first-order approximation of the reduction in crack nucleation associated with the increase in local stresses caused by the faying surface corrosion can be accomplished using strain-based fatigue analysis. The increase in local stresses caused by the build-up of corrosion product can be thought of as creating a constant residual stress around the fastener hole. The increase in local stresses caused by the localized corrosion geometry may be accounted for by multiplying the stress concentration of the baseline geometry with a stress concentration associated with the corrosion geometry. The trends depicted in Figure 8 show the sensitivity in life prediction as a function of material data parameters (Dowling[11] versus ASM[12]), residual stresses, and stress concentration factors.

Previous studies by Komorowski, et. al. [7-9] have shown that local stresses near the edge of a fastener hole due to faying surface corrosion product build-up can exceed the yield strength of aluminum alloy 2024. Results of another study by Perez, et al., [13] indicate that multiplying the stress concentration of a specimen with a hole (K_t=3.18) by 1.21 can generally quantify the effect of a surface etchant in Al 2124-T951. Further study of the data generated by Harmsworth [14] and Perez [13] indicate that the stress concentration due to corrosion is a function of stress level. A power law regression was used to calculate the maximum stress as a function of cycles for the uncorroded and corroded specimens. An effective stress concentration due to the corrosion was then found as a function of cycles to crack nucleation. The results of this calculation are shown in Table 1, where S_u and S_c are maximum nominal stresses for the uncorroded and corroded specimens, respectively. This type of analysis forms the underpinnings of a method to account for the effect of surface finish on life [13]

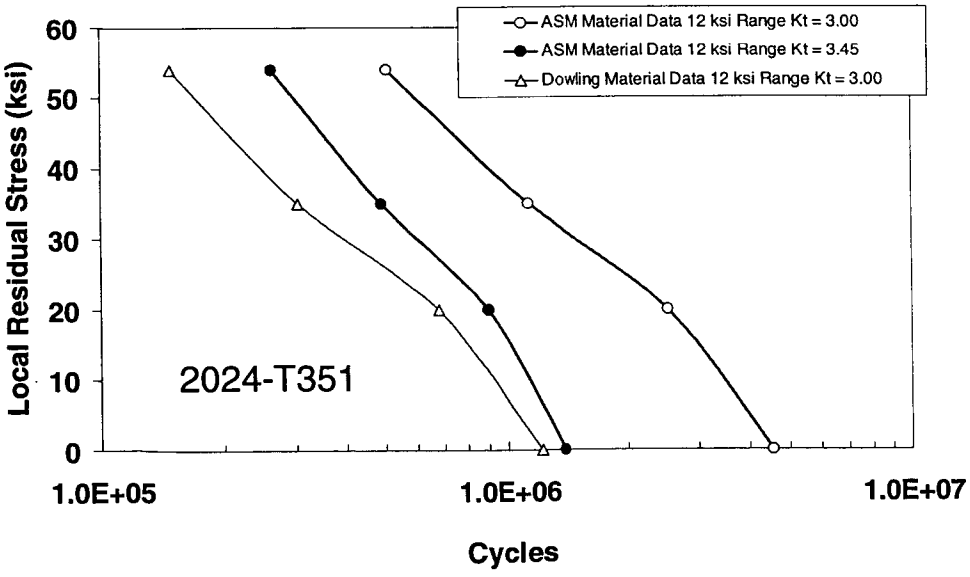

Figure 8 Local Residual Stress As A Function Of Fatigue Cycles For Different Material Parameters

Table 1. Stress Ratio's For Uncorroded (S_u) And Corroded (S_c) Specimens As A Function Of Cycles To Crack Nucleation.

Cycles	S_u/S_c [12]	S_u/S_c [13]
100	0.90	
1000	1.04	
10000	1.20	1.07
100000	1.39	1.18
1000000	1.61	1.29

4. DISCUSSION AND CONCLUSIONS

The results of this research strongly suggests that corrosion on the contact or faying surfaces of a fuselage lap joint can have a detrimental effect on the structural integrity of the joint. Contrary to the general assumption that corrosion in lap joints is uniform in nature, the metallographic results demonstrate that lap joint corrosion is complex and a combination of various forms of corrosion. The most obvious is exfoliation corrosion, which is a special form of intergranular corrosion common in the 2024-T3 aluminum alloy. Initially, the grain boundaries are attacked and hydrated aluminum oxide, $Al_2O_3.3H_2O$, or aluminum hydroxide, $Al(OH)_3$ corrosion byproducts form at the grain boundaries. Since the volume of the corrosion byproducts is approximately six times that of the aluminum it replaces, the surface of the skin tends to swell. Once the exfoliated grains are surrounded by the corrosion byproduct, the grains will continue to corrode by preferential dissolution of aluminum, forming aluminum hydroxide. When these voluminous aluminum hydroxide corrosion byproducts form in the confined space between the two contacting skins of a lap joint, considerable pressure is exerted on to the skins. Since in the case of the KC-135 fuselage lap joint, the inside skin of the lap joint is supported by a longeron, the pressure inside the joint will push out the outer skin. This will result in bulging between the fasteners, also known as pillowing.

It was demonstrated in the literature, and confirmed in the present FEA work that the pillowing resulting from the corrosion byproducts causes high stresses and strains in regions adjacent to the fastener holes. These regions could then become preferential sites for fatigue crack initiation. Moreover, it was found by Komorowski et al.[9] and Welch[10] that once cracks form, they develop semi-elliptical crack fronts with high aspect ratio's. These cracks do not break the surface and are therefore difficult to detect. Also, it was pointed out by Welch[10] that these cracks can propagate in directions other than perpendicular to the hoop stress, which could potentially lead to rapid loss of the lap joint function.

Detailed metallographic analysis of the lap joint section revealed that underneath the exfoliated grains regions of fine intergranular attack exist. These regions can be approximated by a hemisphere, which can deeply penetrate into the skin. Due to the tightness of the intergranular corrosion, it will be very difficult to detect and recognize these regions of corrosion with the common NDI techniques, until they have completely penetrated the skin. The hemispheric envelopes of the intergranular corrosion were simulated with FEA in order to determine their effects on the stress and strain distribution of a pillowing skin between four fasteners. The FEA indicated that under conditions of uniform loss of plate thickness, the maximum strain of the plate as a result of pillowing is already high near the fastener holes. When hemispheres are introduced at those locations of high strain, the resulting maximum strain increases significantly without affecting the vertical displacement of the plate. It was further found that the size of the hemisphere has a significant effect on the local maximum strain level. If the hemisphere is very

small, its effect on the strain distribution is also small. If the hemisphere is relatively large (half the thickness of the plate), then the effect of uniform thinning and pillowing overwhelms the effect of the hemisphere. Thus, the localized high strain near the fastener hole depends on both the pillowing and the formation of areas of localized corrosion, and preliminary calculations indicate that a hemisphere with a radius of a quarter plate thickness results in the highest local strain.

The results presented in this paper, lead to the conclusion that corrosion inside lap joints of aluminum alloy 2024-T3 is very complex. Some forms of corrosion observed are exfoliation corrosion, pitting, preferential dissolution, and intergranular corrosion. Due to the formation of voluminous corrosion byproducts inside the joint, the outer skin of the joint is pushed out, which results in high stresses around the fastener holes. The presence of local regions of intergranular corrosion under the exfoliated grains weakens the joint further by lowering the residual strength, and by creating possible sites for fatigue crack nucleation. Based on the FEA Results, stress analyses can be performed to account for the effect of corrosion fatigue life. While this type of analysis is useful in understanding the magnitude of the various contributing factors on the reduction of fatigue life, it will not be used to assess the life in U.S. Air Force aircraft. The U.S. Air Force requires the use of Damage Tolerance methodology to help assure the safe operation of its aircraft. The authors, and others, continue to develop corrosion metrics and transformations that will be used to assess the impact of corrosion on structural life using approaches based in fracture mechanics.

5. ACKNOWLEDGEMENTS

This work was performed under STTR Phase I Contract F33615-97-C-3215, which was administered under the technical direction of Mr. Clare A. Paul, AFRL/VASE.

6. REFERENCES

1. "Aircraft Accident Report – Aloha Airlines, Flight 243, Boeing 737-200, N737111, near Maui, Hawaii, April 28, 1988", NTSB/AAR-89/03, National Transportation Safety Board Bureau of Accident Investigation, Washington, D.C., June 4, 1989.

2. Structural Integrity of Aging Airplanes, Eds. S. N. Atluri, S. G. Sampath, and P. Tong, Springer-Verlag, New York, 1990.

3. Durability of Metal Aircraft Structures, Proc. of International Workshop on Structural Integrity of Aging Airplanes, March 31-April 2, 1992 Atlanta, Eds, S. N. Atluri, C.E. Harris, A. Hoggard, N. J. Miller, and S. G. Sampath.

4. FAA/NASA International Symposium on Advanced Structural Methods for Airframe Durability and Damage Tolerance, Hampton, VA, May 4-6,1994, Ed. C.E. Harris.

5. FAA/NASA Sixth International Conference on the Continued Airworthiness of Aircraft Structures, Atlantic City, NJ, June 27-28, 1995.

6. Lincoln, J.W. *The USAF Approach to Attaining Structural Integrity of Aging Aircraft,* Structural Integrity in Aging Aircraft, AD-Vol. 47, ASME 1995, pp. 9 – 19.

7. Bellinger N.C., S. Krishnakumar, and J. P. Komorowski, *Modelling of Pillowing Due to Corrosion in Fuselage Lap Joints,* Canadian Aeronautics and Space Journal, Vol. 40, No. 3, September 1994, pp. 125-130.

8. Bellinger, N.C., and J. P. Komorowski, and S. Krisnakumar, *Numerical Modelling of Pillowing Due to Corrosion in Fuselage Lap Joints,* LTR-ST-2005, National Research Council Canada, April 1995.

9. Bellinger, N. C., and J. P. Komorowski, *Implications of Corrosion Pillowing on the Structural Integrity of Fuselage Lap Joints,* Proceedings of the NASA-FAA Symposium on the Continues Airworthiness of Aircraft Structures, July 1997, pp. 391-401.

10. Welch, D. W., *Fracture Mechanics Analysis of a Corroded Aircraft Fuselage Lap Joint,* Master of Science Thesis, The University of Oklahoma, Norman OK, 1997.

11. Dowling, N. E., *Mechanical Behavior of Materials*, Prentice Hall, New Jersey, 1993

12. ASM Handbook, *Fatigue and Fracture* Vol 19, pp. 231, ASM International, Ohio, 1996

13. Perez, R., and C. Brook, et.. al., *Metrics Exploration and Transformation Development For Corrosion/Fatigue,* WL/FIBEC Control No. F33615-95-D-3216

14. Harmsworth, C., L., *Effect of Corrosion On The Fatigue Behavior of 2024-T4 Aluminum Alloy*, ASD Technical Report 61-121, July 1961

15. Juvinall, R. C., Engineering Considerations of Stress, Strain, and Strength, McGraw-Hill Book Company, 1967

ANALYTICAL AND TEST EVALUATIONS ON THE LINKUP OF MULTIPLE CRACKING IN STIFFENED FUSELAGE PANELS

David Y. Jeong
U.S. Department of Transportation
Volpe National Transportation Systems Center
Cambridge, MA 02142 USA
Telephone (617) 494-3654
Telefax (617) 494-3096

John G. Bakuckas, Jr.
Federal Aviation Administration
William J. Hughes Technical Center
Atlantic City International Airport, NJ 08405 USA

Gopal Samavedam
Foster-Miller, Inc.
Waltham, MA 02154 USA

ABSTRACT

This paper describes testing and analysis of stiffened curved fuselage panels containing multiple cracks. Testing was conducted on a fabricated panel with various cracking configurations. The typical cracking scenario was a main lead crack with multiple smaller collinear cracks. Engineering analyses were conducted to predict the remote stress at linkup. These analyses were carried out with a displacement compatibility model in conjunction with analytically derived expressions for the bulging factor. The expression for the bulging factor included empirical constants which were determined from curve fitting of finite element results. Estimates for linkup are based on assuming that linkup occurs from plastic collapse of ligaments between adjacent crack-tips. The engineering analyses provided reasonable but conservative estimates for the remote stress at linkup, in most cases (i.e., the predicted values were lower than the experimental values). In general, the predicted linkup stresses are within 25% of the experimentally measured values. Further work is needed to improve the accuracy of the approach used in this paper, particularly in validating the effect of bulging in pressurized stiffened curved panels.

1.0 INTRODUCTION

Widespread fatigue damage (WFD) in the form of small cracks emanating from multiple rivet holes in a fuselage lap joint can degrade the load carrying capacity of an aircraft. The reduction in residual strength of flat panels due to multiple cracking has been demonstrated experimentally in previous work.[1] Research is currently ongoing to develop and validate analytical and computational models to predict the reduction in residual strength of stiffened curved structures with multiple cracks.

As part of model validation, a task sponsored by the Federal Aviation Administration (FAA) William J. Hughes Technical Center was undertaken to conduct testing on full-scale, stiffened, curved panels using the FAA Aging Aircraft Test Fixture designed and operated by Foster-Miller, Inc. (FMI) under contract with the U.S. Department of Transportation. The test fixture applies axial and pressurization loading simultaneously, and in the proper proportion, to simulate service loading in an actual airplane. The test articles for this fixture contain structural details resembling those found in a commercial transport aircraft. In the present work, residual strength tests were performed on a panel with two different multiple cracking configurations. The first configuration consisted of a two-bay skin lead crack with multiple smaller collinear cracks spanning an intact central strap. The second configuration consisted of a two-bay lead crack in the upper row of an unbonded longitudinal lap splice with multiple smaller collinear cracks spanning a broken central strap. The data obtained from these tests can be used to validate the analytical and computational models now under development to predict the residual strength of aircraft panels.

In addition to testing, engineering analyses were performed to predict the remote stress at linkup. In these analyses, linkup was assumed to occur when the ligament between adjacent crack tips becomes completely plastic. Curvature was taken into account by applying a bulging factor. Mathematical expressions for bulging factor as a function of applied stress, crack length, and other parameters were derived by Broek[2] from solid mechanics principles. These expressions contained unknown constants that were determined from curve fitting of geometric nonlinear finite element (FE) results conducted by Bakuckas, *et al.*[1] The derived expressions for the bulging factor were used in conjunction with a displacement compatibility analysis[4] which was applied to include the effect loads carried by rivets that attach the frames and the tear straps to the skins. The actual test panel, however, contained bonded tear straps. Infinite rivet stiffness and a relatively small spacing between rivets were assumed in the analysis to model a perfect and continuous bond between the skins and the tear straps.

2.0 DESCRIPTION OF TEST PANEL AND DAMAGE CONFIGURATIONS

In the present work, static strength tests were conducted to determine linkup stresses in fuselage panels with two different cracking configurations which are briefly described as follows.

(1) ***A two-bay skin lead crack with multiple collinear cracks and an intact central tear strap.*** Figure 1 shows a schematic of the first damage configuration which consists of a 13-inch lead crack with multiple small cracks on both sides of the lead crack. The small cracks are 0.55 inches with a center-to-center spacing of 1 inch.

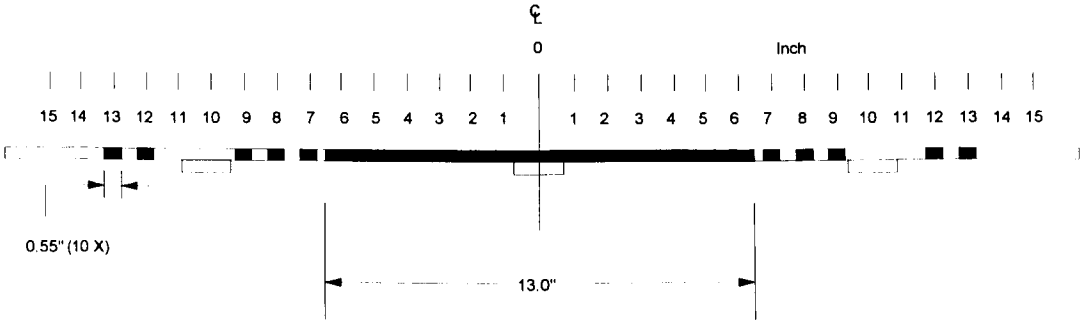

Figure 1. Two-bay skin crack with multiple collinear cracks and an intact central strap.

(2) ***A two-bay lap-splice lead crack with multiple collinear cracks and a broken central tear strap.*** Figure 2 shows a schematic of the damage configuration in the lap-splice of the test panel. The lead crack is 11.5 inches in length. The three small cracks on each side of the lead crack are 0.35 inches measured tip to tip and centered over the 1-inch fastener spacing.

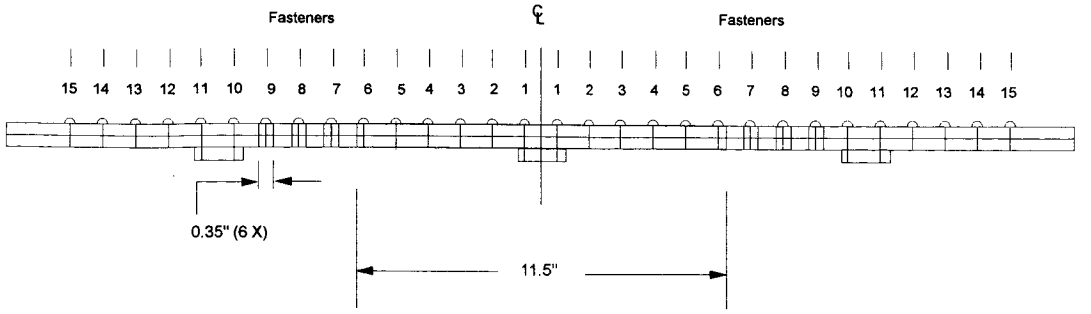

Figure 2. Two-bay lap-splice crack with multiple collinear cracks and a broken central tear strap.

The test panel was constructed with stringer ties, aluminum tear straps, and an unbonded longitudinal lap splice. The tear straps were bonded to the skin, but not riveted. Also, the panel had a radius of curvature of 75 inches and a skin thickness of 0.040 inch. The relevant geometric details and materials for the test panel are summarized in Table 1.

TABLE 1. DESCRIPTION OF PANEL DETAILS

Detail	*Material*	*Cross-Sectional Dimensions*
Skin	Al. 2024-T3	0.040 inch thickness
Rivets	Al. 2117-T4	BACR15CE5D 100° countersunk head, 5/32 inch shank diameter
Stringer	Al. 2024-T3	0.050 in. thick a. 1.0 in. b. 1.25 in. c. 1.0 in. 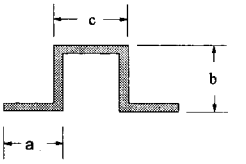
Tear Strap	Al. 2024-T3	0.040 in. thick × 1.25 in.
Frame	Al. 7075-T6	0.050 in. thick a. 1.0 in. b. 2.5 in. c. 1.0 in. 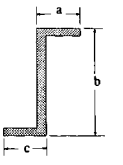

One test panel was used in the experimental phase of this work. Each crack configuration was tested separately and monitored with high-speed video equipment to capture the linkup events. The two-bay skin crack configuration (Figure 1) was tested first. After the linkup stresses were measured, the

damaged area was repaired with a riveted aluminum patch. Then, the two-bay lap-splice crack configuration (Figure 2) was tested. An analysis software program called RAPID (Repair Assessment Procedure and Integrated Design)[5] was used to verify that the distance between the repair patch and the cracked lap-splice region was sufficient for interaction effects to be negligible. Specific details of the testing procedures are described in a report written by Warren and McHatton.[6]

2.0 BULGING FACTORS

The bulging factor is defined as the ratio of the stress-intensity factor of a curved panel to that of a flat panel:

$$\beta_B = \frac{K_{curved}}{K_{flat}} \tag{1}$$

Bulging cracks have been examined by using geometric nonlinear finite element (FE) analyses to calculate stress intensity factors in pressurized stiffened curved panels.[7] The effects of an intact and a broken central strap on the bulging factor were studied. Figure 3 shows the FE results for normalized stress-intensity factors in curved panels with an 80-inch radius and 0.048-inch skin thickness. Also, these results apply to panels with aluminum tear straps that are 1 inch wide, 0.048 inch in thickness, and spaced 10 inches apart. The solid symbols in the figure represent cases for an intact central strap, and the open symbols refer to cases for a broken central tear strap. Moreover, the results indicate that the stress-intensity factor is significantly reduced in the case of an intact central strap compared to the case of a broken central strap.

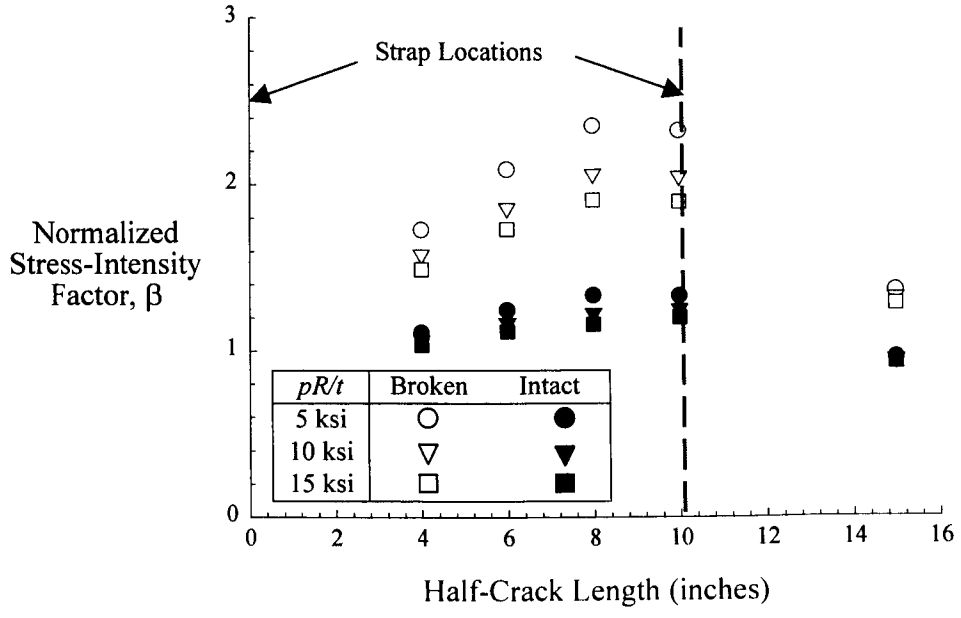

Figure 3. FE results for normalized stress-intensity factors in stiffened curved panels with intact and broken central straps.

However, the normalized stress intensity factors shown in Figure 3 are considered as the product of two separate effects

$$\beta = \beta_S \times \beta_B \tag{2}$$

where β_s is a factor accounting for stiffening only and β_B is the bulging factor. In the present work, the effect of stiffening due to tear straps was examined with a displacement compatibility analysis[4] and a hybrid finite element analysis.[7] These analyses were conducted for flat panels with the same dimensions and structural details as the finite element results. Figure 4 shows reasonable agreement between the two different approaches in calculating the stiffening factors for a flat panel with a broken central strap.

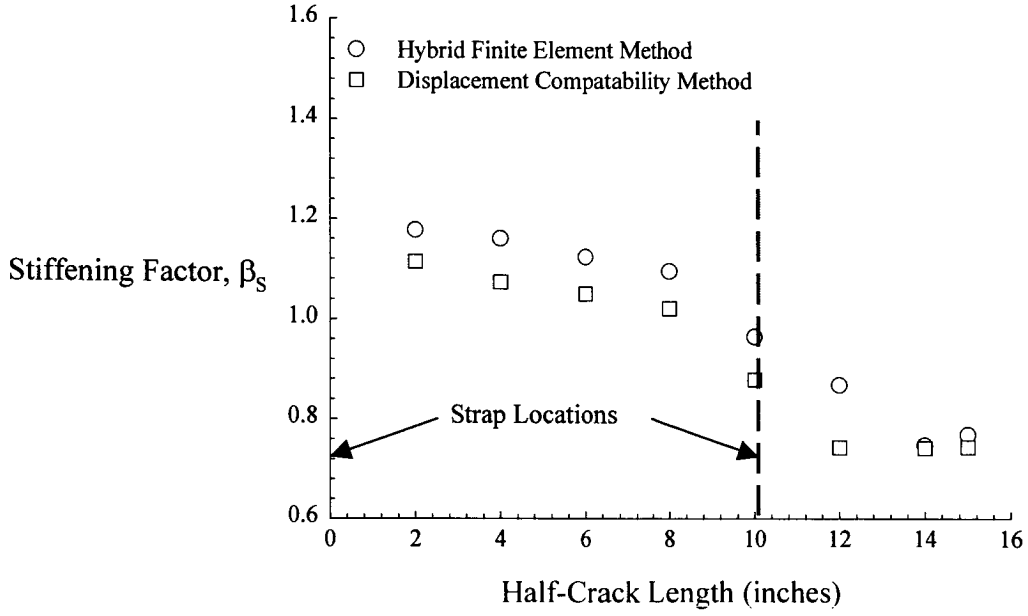

Figure 4. Comparison between hybrid finite element and displacement compatibility analyses for stiffening factor in a flat panel with a broken central strap.

A mathematical expression for bulging factors in stiffened curved panels based upon structural mechanics and dimensional analyses has been derived by Broek.[2] A similar expression to the one developed by Broek is used in the present study, and is given as follows:

$$\beta_B = \begin{cases} 1 + 0.775\left(\frac{E}{\sigma}\right)^{1/3}\left(\frac{a}{R}\right)^{5/6}\left[1 - \alpha\left(\frac{t_{st}}{R}\right)^2\sqrt{\frac{s}{a}}\frac{E_{st}A}{Ets + E_{st}A}\right] \times f \text{ if } a \le s \\ 1 + \left(\frac{s}{a}\right)^2\left[0.775\left(\frac{E}{\sigma}\right)^{1/3}\left(\frac{a}{R}\right)^{5/6}\right] \times \left[1 - \alpha\left(\frac{t_{st}}{R}\right)^2\sqrt{\frac{s}{a}}\frac{E_{st}A}{Ets + E_{st}A}\right] \times f \text{ if } a > s \end{cases} \tag{3}$$

where s is the tear strap spacing, t is the skin thickness, t_{st} is the tear strap thickness, A is the tear strap cross-sectional area, E is Young's modulus for the skin material, E_{st} is Young's modulus for the tear strap material, and

$$f = \begin{cases} 1 & \text{for a skin crack} \\ \left(1 - c_1 \dfrac{w_{lap} t_{lap}}{st}\right) \times \left(1 - c_2 \dfrac{E_{string} I_{string}}{Est^3}\right) & \text{for a lap splice crack} \end{cases} \quad (4)$$

where w_{lap} is the width of the lap splice, t_{lap} is the thickness of the lap splice, E_{string} is Young's modulus for the stringer material, I_{string} is the moment of inertia of the stringer about the radial axis. In the present work, c_1 and c_2 are assumed to be 0.01 and 0.001, respectively. Equation (3) also contains an empirical constant, α, which is determined by a least squares regression of the finite element results with the stiffening effect removed (effectively, results from Figure 3 with results from Figure 4 extracted). The value of this empirical constant depends on applied stress and on whether the central tear strap is intact or broken (Table 2).

TABLE 2. VALUES FOR CONSTANT α IN BULGING FACTOR

Applied stress (ksi)	*INTACT central strap*	*BROKEN central strap*
5	1.16×10^7	-1.26×10^6
10	1.05×10^7	-1.72×10^6
15	1.01×10^7	-1.52×10^6

Figure 5 compares results for a skin crack from finite element (FE) analyses (with the stiffening effect stiffening removed) with the mathematical expression for bulging factor as given by equation (3). In this figure, the symbols refer to the FE results with the stiffening effect extracted, and the lines represent the values from equation (3). In general, the agreement between the finite element analyses and the mathematical expression for bulging factor is within 8%. It is assumed that the mathematical expression for bulging factor from equation (3) can be used to predict residual strength and multiple-crack linkup in panels with dimensions differing from those considered in the finite element analyses.

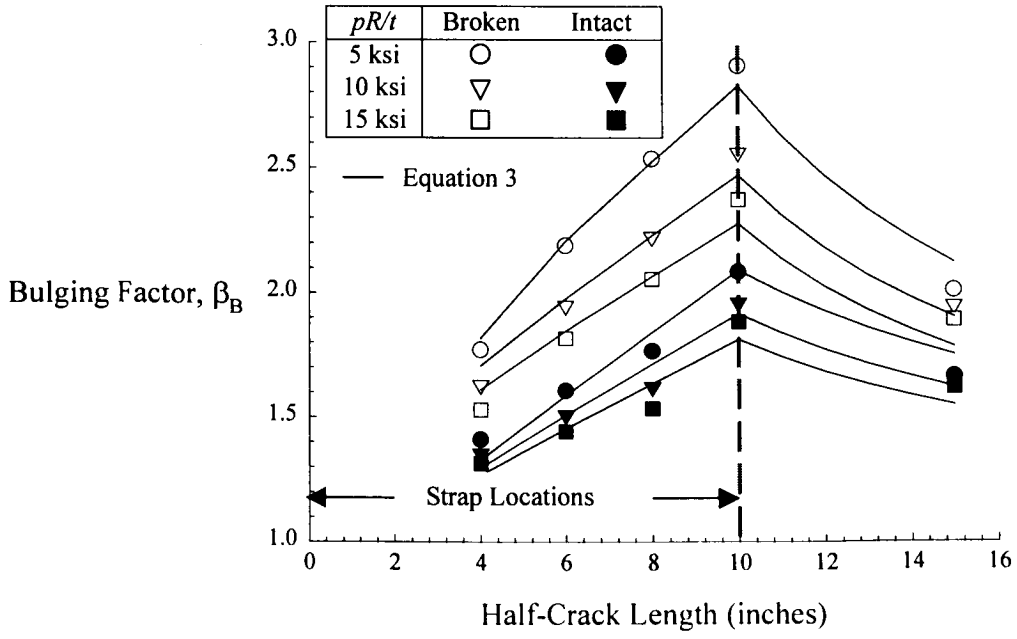

Figure 5. Comparison between FE results and bulging factor equations for stiffened curved panels with intact and broken central straps.

3.0 ANALYSIS OF MULTIPLE CRACK LINKUP

Linkup of a main lead crack with adjacent smaller cracks is assumed to occur when the plastic zones from adjacent crack tips join together. This concept is shown schematically in Figure 6 in which the circles represent the plastic zones ahead of the crack tips. In other words, linkup is assumed to occur when the ligament between crack tips becomes completely plastic.

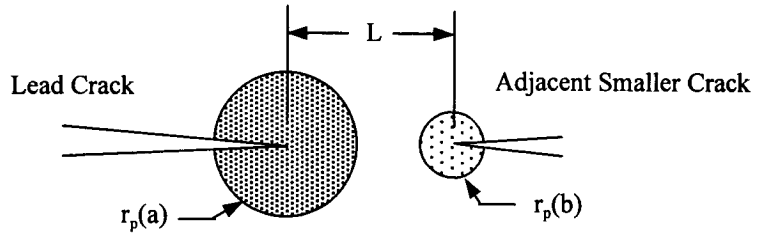

Figure 6. Schematic of plastic zones at the tips of a lead crack and an adjacent smaller crack.

Thus, the formulation of a mathematical expression for linkup stresses based on this plastic collapse criterion relies on an estimate of the plastic zone size. An equation to calculate the remote stress at linkup based on the plastic collapse of ligaments was derived by Tong, *et al.*[8]

$$\sigma_o^2\left[\frac{(\beta_S\beta_B\beta_a)^2 a}{\sigma_p-\sigma_o(1-\beta_S\beta_B\beta_a)}+\frac{(\beta_H\beta_b)^2 b}{\sigma_p-\sigma_o(1-\beta_H\beta_b)}\right]=2L(\sigma_p-\sigma_o) \tag{5}$$

In equation (5), σ_o is the remote stress, σ_p is the yield strength of the skin material, a is the half-length of the lead crack, b is the half-length of the adjacent crack, L is the ligament length (or distance between crack tips), β_B is the bulging factor, and β_S is the stiffening factor. Also, β_a and β_b are factors accounting for the interaction of adjacent cracks, and are defined as[9]

$$\beta_a=\sqrt{1+\left(\frac{2b}{L}\right)\left\{1-\left[1+\left(\frac{L}{2a}\right)\right]\left[1-\left(\frac{E(k)}{K(k)}\right)\right]\right\}}$$

$$\beta_b=\sqrt{1+\left(\frac{2a}{L}\right)\left\{1-\left[1+\left(\frac{L}{2b}\right)\right]\left[1-\left(\frac{E(k)}{K(k)}\right)\right]\right\}} \tag{6}$$

In these equations, $K(k)$ and $E(k)$ are the complete elliptic integrals of the first and second kind respectively, and

$$k=\sqrt{\frac{4ab}{(L+2a)(L+2b)}} \tag{7}$$

Equation (5) includes a correction factor to account for the stress concentration at the edge of an open hole produced by the remote loading[10]

$$\beta_H = \begin{cases} 1 & \text{for a skin crack} \\ 1 + \dfrac{1}{2\left(\dfrac{2b}{d}\right) + 1.93\left(\dfrac{2b}{d}\right) + 0.539} + \dfrac{1}{2\left(\dfrac{2b}{d}\right) + 2} & \text{for a lap splice crack} \end{cases} \tag{8}$$

where b is the length of the crack emanating from edge of the rivet hole and d is the rivet hole diameter.

Equation (5) can be modified to include the effect of stable crack extension:

$$\sigma_o^2 \left[\frac{(\beta_S \beta_B \beta_a)^2 a}{\sigma_p - \sigma_o(1 - \beta_S \beta_B \beta_a)} + \frac{(\beta_H \beta_b)^2 b}{\sigma_p - \sigma_o(1 - \beta_H \beta_b)} \right] = 2(L - \Delta a)(\sigma_p - \sigma_o) \tag{9}$$

where Δa is the stable crack extension. The present analysis assumes that the R-curve for stable extension in 2024-T3 aluminum obeys a power law:[11]

$$K_R = K_o \Delta a^n \tag{10}$$

where K_o is 103.4 ksi-in$^{1/2}$ and n is 0.14.

An alternative formulation to calculate linkup stresses can be derived by estimating the plastic-zone size from Irwin's model,[12] which gives the following expression for linkup stress:

$$\sigma_o = \sigma_p \sqrt{\frac{2L}{(\beta_S \beta_B \beta_a)^2 a + (\beta_H \beta_b)^2 b}} \tag{11}$$

The effect of stable tearing can be included in this formulation by replacing L in equation (11) with L-Δa.

4.0 RESULTS AND DISCUSSION

The displacement compatibility analysis used in this present work was originally developed to analyze panels with riveted tear straps. Since the actual test panel contained adhesively bonded tear straps, two assumptions were made in the displacement compatibility analysis. First, the rivet flexibility was assumed to be zero (i.e., infinite rivet stiffness) to approximate a perfect bond. Second, the rivet pitch (i.e., spacing between rivets) was assumed to be relatively small to approximate a continuous bond. Values of 1 inch, ½ inch, ¼ inch, and ⅛ inch for the rivet pitch were assumed in the analysis. The stiffening factors approached limiting values as the rivet pitch decreased. Thus, a rivet pitch of ⅛ was assumed in the displacement compatibility analysis. Moreover, the linkup stresses calculated from this engineering approach were considered as upper bound estimates because of these assumptions.

Table 3 compares the calculated linkup stresses to the values measured during the full-scale tests. The table shows that the calculated linkup stresses in most cases were less than those measured during the tests, indicating conservatism of the analyses. The 2nd linkup in the first cracking configuration was overestimated by the analysis. Estimates based on the Tong plastic zone model were more conservative than those based on the Irwin model for the two-bay skin crack with an intact central strap, but the trend was reversed for the other damage configuration. The calculations for the two-bay lap-splice crack in

both plastic-zone (PZ) models predicted that the 1st and 2nd linkups should have occurred simultaneously, which was verified in the tests. Approximate values for the internal pressure to create linkup (in psi) can be calculated by dividing the linkup stresses in Table 3 by a factor of 2000. Thus, for the damage configurations in these tests, the pressures at linkup varied between 3.4 and 5.5 psi which are much less than the nominal operating pressures for typical commercial aircraft.

TABLE 3. LINKUP STRESSES IN KSI

Damage Configuration		*Calculated Linkup Stresses**		*Test Result*
		Tong PZ Model	*Irwin PZ Model*	
Two-bay skin crack with INTACT central strap	*1st linkup*	8.2 (-19.6%)	8.5 (-16.7 %)	10.2
	2nd linkup	10.4 (-1.0%)	10.9 (+3.8%)	10.5
Two-bay lap-spice crack with BROKEN central strap	*1st linkup*	7.0 (-20.5%)	6.9 (-21.6%)	8.8
	2nd linkup	6.8 (-23.6%)	6.7 (-24.7%)	8.9

* Numbers in parentheses refer to percent error compared to test result.

Some of the assumptions in calculating linkup stresses for stiffened fuselage panels were examined in the present analysis. These assumptions include the estimation of the plastic-zone size (Tong versus Irwin) and the effect of stable tearing. The results in Table 3 were calculated with the effect of stable tearing included. While both of these assumptions had a strong to moderate effect on predicting linkup stresses in unstiffened flat panels,[11] they were found to have a weak effect on calculating linkup stresses in stiffened curved panels. An additional assumption made that could have a more profound effect on the predicted linkup stress is that a fuselage radius of 80 inches was used to obtain the empirical constants in equation (3) due to available FE results whereas the actual radius of the panel tested was 75 inches.

Other predictions for linkup stresses were calculated using an analysis software program called STOPMSD.[13] This software program applies an analysis procedure that is similar to the approach adopted in the present study. Differences in the analysis procedures are in the bulging factor. Similar parametric studies were conducted with the software program to examine the effects of rivet flexibility and rivet pitch, as in the analyses described previously. The upper bound values for the 1st and 2nd linkups in the case of the two-bay skin crack were estimated as 7.5 ksi and 11.0 ksi, respectively. These predictions are within 27% and 5% of the respective experimental results. These differences are similar to those listed in Table 3. In the case of the two-bay lap-splice crack, the software program calculated a linkup stress of 9.1 ksi for both the 1st and 2nd linkups. These predictions are within 3% of the experimental values.

5.0 CONCLUSIONS

The present work entailed testing and analysis of laboratory panels resembling a commercial transport-category aircraft. The engineering analyses described in this paper gave reasonable estimates for the remote stresses at linkup in pressurized stiffened curved panels. Although the calculated linkup stresses were considered as upper bond estimates, the predicted values were conservative in comparison with test data in most cases. In general, the predicted linkup stresses are within 25% of the experimental values. Stable tearing had a relatively weak effect on the calculation of linkup stresses. The Tong and Irwin plastic zone models produced approximately equivalent predictions for multiple-crack linkup. Bulging factor has a significant effect on predicting linkup stresses. Additional work is needed to address this issue.

ACKNOWLEDGMENTS

Dr. Peter Warren, Mr. John McHatton, Ms. Susan MacPherson, and Mr. Mike Winter are acknowledged for their technical support during the testing phase of this work. The authors would also like to acknowledge the support of Dr. Thomas H. Flournoy, Program Manager of the FAA William J. Hughes Technical Center's National Aging Aircraft Research Program, and Mr. George Neat, Program Manager of aging aircraft research at the Volpe National Transportation Systems Center.

REFERENCES

1. J.R. Maclin, "Performance of fuselage pressure structure." *1991 International Conference on Aging Aircraft and Structural Airworthiness*, NASA Conference Publication 3160, pp. 67-74, 1992.
2. D. Broek, "Analysis of Residual Strength and Fracture Arrest in Aircraft Fuselages with Arresters and Widespread Fatigue Damage (WFD), Part III Geometry Factors for Panels with Straps." FractuREsearch Report No. TR9706, 1997.
3. J.G. Bakuckas, Jr., P.V. Nguyen, C.A. Bigelow, and D. Broek, "Bulging factors for predicting residual strength of fuselage panels." *ICAF97, Proceedings of the 19th Symposium of the International Conference on Aeronautical Fatigue*, pp. 179-196, 1997.
4. T. Swift, "The effects of fastener flexibility an stiffener geometry on the stress intensity in stiffened crack sheet," *Prospects of Fracture Mechanics*. Leyden, The Netherlands: Noordhoff International Publishing, pp. 419-436, 1974.
5. Repair Assessment Procedure and Integrated Design (RAPID) Analysis Methods Document, Version 2.1, May 1998.
6. P. Warren and J. McHatton, "Experimental Methodology and Test Results for Evaluation of Residual Strength of Curved Aircraft Fuselage Skin Panels with Multiple Site Damage." Foster-Miller, Inc. Report, 1998.
7. P. Tong, "A hybrid finite element method for damage tolerance analysis," *Computers & Structures 19*, pp. 263-269, 1984.
8. P. Tong, R. Greif, L. Chen, and D.Y. Jeong, "Damage tolerance of fuselage panels with widespread fatigue damage," *17th Symposium of the International Committee on Aeronautical Fatigue*, Stockholm, Sweden, 1993.
9. H. Tada, P. Paris, and G. Irwin, *The Stress Analysis of Cracks Handbook*, Second Edition, Paris Productions, Inc., 1985.
10. J. Schijve, "Stress intensity factors of hole edge cracks, comparison between one crack and two symmetric cracks," *International Journal of Fracture 23*, pp. R111-R115, 1983.
11. D.Y. Jeong, "Analyses of Residual Strength and Multiple Crack Linkup Based on Plastic Collapse," Volpe Center Report, 1994.
12. G.R. Irwin, "Analysis of stresses and strains near the end of a crack traversing a plate," *Journal of Applied Mechanics 24*, pp. 361-364, 1957.
13. D. Broek, "Analysis of Residual Strength and Fracture Arrest in Aircraft Fuselages With Arresters and Widespread Fatigue Damage (WFD), Part I - Software Operation and Manual." FractuREsearch Report No. TR9706, 1997.

BENEFITS OF IMPROVED FUSELAGE SKIN SHEET ALLOY 2524-T3 IN MULTI-SITE DAMAGE SCENARIOS

Gary H. Bray, Robert J. Bucci, Michael Kulak and Charles J. Warren
Aluminum Company of America
Alcoa Center, PA 15069 USA
Telephone: (724) 337-5727
FAX: (724) 337-5436
gary.bray@alcoa.com

Alten F. Grandt, Jr., Patrick J. Golden and Darren G. Sexton
School of Aeronautics and Astronautics
Purdue University
West Lafayette, IN 47907 USA

ABSTRACT

This paper quantifies the improved resistance to the consequences of multi-site damage (MSD) that can develop in older aircraft provided by new Alcoa aluminum fuselage skin sheet alloy 2524-T3. Results from three types of tests are presented for 2524-T3 and the incumbent fuselage skin sheet alloy 2024-T3: (1) residual strength tests to assess the effect of multi-site damage on residual strength of unstiffened and stiffened flat panels; (2) fatigue tests on unstiffened flat panels to assess the effects of multi-site damage on fatigue life; and (3) fatigue tests on multi-hole coupons with and without prior corrosion to evaluate the resistance of each alloy to naturally occurring MSD. The results indicate that alloy 2524 offers improved structural damage tolerance in the presence of MSD due to its superior fatigue crack growth resistance and fracture toughness and is more resistant to MSD from corrosion in bare sheet form. The residual strength of 2524 panels containing a lead crack with MSD at adjacent holes was 8.8 to 10.4% higher than 2024 panels and the average fatigue life 27 to 45% longer depending on MSD flaw size. The two alloys had equivalent resistance to MSD from fatigue alone but the mean flaw areas following corrosion and fatigue were 18% smaller in bare 2524 than in bare 2024 and the corroded area alone 32% smaller. Potential advantages of the improved damage tolerance of 2524-T3 to aircraft manufacturer/operators are weight savings, lower operating costs, easier inspectability and increased safety.

1. INTRODUCTION

The service life of an airframe can potentially introduce multi-site damage (MSD) states such as widespread fatigue and/or corrosion that may imperil the structural integrity of the aircraft. The inspection intervals set by standard residual strength and damage tolerant design are normally directed at the presence of a single crack, but may be inadequate in the presence of MSD. It is well known, for example, that small fatigue cracks ahead of a larger lead crack can significantly reduce the residual strength and fatigue life normally associated with the lead crack [1-5]. This realization and the desire for reliable, longer lasting aircraft with lower maintenance costs have given rise to requirements that non-pristine or aging structure be accounted for in design and maintenance strategies. This philosophical shift has created demand for affordable replacement materials that cannot only resist the occurrence of multi-site damage, but which offer improved structural damage tolerance when MSD is present.

An excellent example of one such material is new aluminum alloy 2524-T3 (formerly C188-T3) developed by Alcoa. Currently used in the Boeing 777 aircraft, 2524-T3 was designed for fuselage skin sheet as a replacement for 2024-T3, the industry standard since the DC-3. As shown in Table 1, 2524-T3 has superior fatigue crack growth resistance and plane stress fracture toughness (Kc) in comparison to 2024-T3 while maintaining equivalent tensile properties. Boeing utilized the improvements of 2524 in fracture toughness and fatigue crack growth resistance to obtain weight savings and reduced manufacturing costs in new structure over incumbent alloy 2024 design [6-8]. The goal of the present study described in this paper is to quantify the beneficial effects of the improved damage tolerance provided by 2524-T3 over 2024-T3 once MSD is already present and to compare the resistance of both alloys to the onset of MSD from fatigue alone and in combination with corrosion.

TABLE 1. TYPICAL MECHANICAL PROPERTIES 0F ALCLAD 2524-T3 AND 2024-T3 ALUMINUM ALLOYS (LT DIRECTION)

Alloy	Thickness (inch)	TYS (ksi)	UTS (ksi)	Kc[a] (ksi√in)	da/dN@ ΔK=30 (inch/cycle)[b]
2524-T3	0.032-0.062	44	61	158	9.0E-05
	0.063-0.128	45	64		
	0.129-0.249	44	64		
2024-T3	0.032-0.062	43	62	128	2.7E-04
	0.063-0.128	45	65		
	0.129-0.249	45	65		

[a] M(T) specimen, T-L orientation, W=16 in., 2ao= 4 in.

[b] T-L orientation, R=0.1, relative humidity > 90%

2. EXPERIMENTAL PROCEDURES

2.1 TEST MATERIALS

The 2024-T3 and 2524-T3 materials used in this study were purchased commercially in the form of 0.050-inch thick alclad and 0.100-inch thick bare sheet. The strength and plane stress fracture toughness (Kc) properties measured in these materials are shown in Table 2. Fatigue crack growth curves for the 0.050-inch alclad sheet are shown in Figure 1.

TABLE 2. MECHANICAL PROPERTIES OF MATERIALS IN THIS STUDY (LT DIRECTION)

Alloy	Thickness (in.)	TYS (ksi)	UTS (ksi)	Elong. (%)	Kc (ksi√inch)[a]
Alclad 2524-T3	0.050	43.6	60.3	20.5	150
Alclad 2024-T3	0.050	43.6	61.9	18.5	136
Bare 2524-T3	0.100	44.9	68.0	24.0	149
Bare 2024-T3	0.100	45.8	69.5	21.2	136

a M(T) specimen, T-L orientation, W=16 in., 2ao= 4 in.

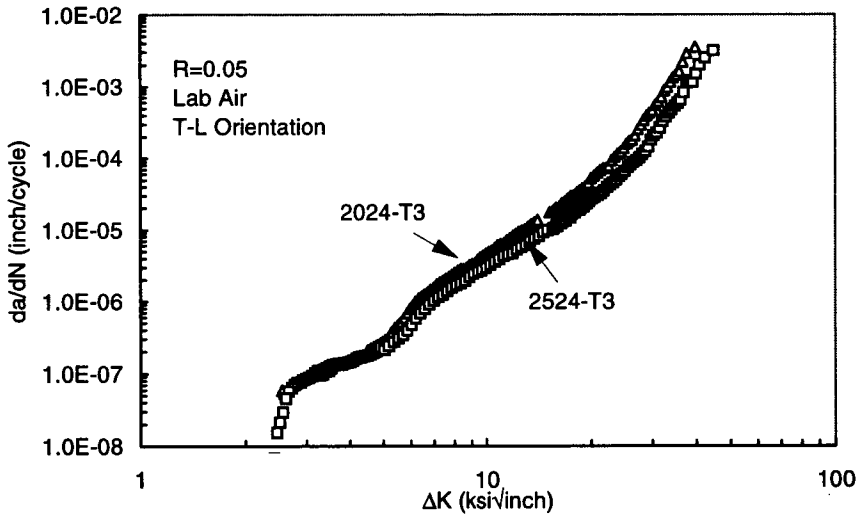

Figure 1. Fatigue crack growth curves for alclad 2524-T3 and 2024-T3 sheet in this study.

2.2 MSD RESIDUAL STRENGTH TESTS

The goal of these tests was to determine how the residual strength of each alloy is influenced by small flaws (MSD) ahead of a lead crack. The lead crack is intended to model accidental damage or a large fatigue crack from a rogue flaw, while the small MSD is representative of widespread fatigue or corrosion which could develop in older aircraft. Tests were performed on both unstiffened and stiffened flat panels of 0.050-inch alclad sheet. The unstiffened panels were 16 inches wide by 40 inches long with a 21-inch long uniform-width test section. The panels contained a central row of open holes oriented perpendicular to the applied tensile stress. The holes were 5/32 inch diameter and were spaced 1.0 inch apart on center. A 4.4-inch long lead crack was formed by sawing the ligament between the five central holes and then introducing 0.10-inch long EDM notches at the end of this slot. The configuration of the stiffened panels was identical except that two stiffeners 0.080 thick by 1.25 wide by 26.25 inches long of 7050-T76 sheet were attached to the panel by 3/16 diameter rivets spaced 0.75 inch apart. The stiffeners were attached parallel to the panel length and spaced 9 inches apart with the lead crack centrally located between them. Small through-thickness MSD flaws were introduced by EDM on each side of the remaining open holes in the plane of the lead crack. The unstiffened panels contained MSD flaw sizes of either zero, 0.05, 0.10, or 0.15 inch and the stiffened panels contained flaw sizes of either 0.05 or 0.10 inch. All cracks were oriented in the T-L orientation relative to the parent sheet. The panels were pulled to failure in remote tension under displacement control. Extension of the lead crack was obtained as a function of applied load during stable crack growth. Link-ups between the lead crack and the cracks emanating from the MSD flaws were also recorded visually with the aid of an optical microscope.

2.3 MSD PANEL FATIGUE TESTS

The goal of these tests was to determine how fatigue life of each alloy is influenced by small flaws (MSD) ahead of a lead crack. Tests were performed on unstiffened panels of 0.050-inch alclad sheet. The panels were 9 inches wide by 21 inches long with a 14-inch long uniform-width test section. These panels also contained a single row of 5/32-inch diameter holes spaced 1.0 inch apart oriented

perpendicular to the applied tensile stress. A 1.36-inch long lead crack was created by sawing the ligament between the two central holes and introducing a 0.10 inch long EDM slot at the end of the two holes. Small through-thickness MSD flaws of either zero, 0.05 or 0.10 inch were introduced by EDM on each side of the remaining open holes in the plane of the lead crack. All cracks were again oriented in the T-L orientation. The panels were cycled to failure using a maximum gross stress of 8.56 ksi and a stress ratio of R=0.05. The position of each crack tip including the lead and MSD flaws was recorded as a function of elapsed cycles with a traveling microscope.

2.3 MULTI-HOLE FATIGUE COUPON TESTS

The goal of these tests was to compare the size and frequency of naturally occurring MSD in 2524 and 2024 sheet resulting from fatigue alone or in combination with corrosion. Multi-hole fatigue tests were conducted on three material/conditions; (1) pristine 0.050-inch thick alclad sheet; (2) pristine 0.100-inch thick bare sheet; and (3) 0.100-inch thick bare sheet with prior corrosion. The multi-hole coupons were 6.25 inches wide by 24 inches long and contained four rows of six holes (24 total) at mid-length. The length dimension was in the long transverse (LT) direction of the parent sheet. The hole diameter was 5/32 inch and the hole spacing was 1.0 inch on center. The holes were drilled and deburred but not reamed. The pristine alclad and pristine bare coupons were then fatigue tested without any additional preparation. Three pristine alclad coupons of each alloy were fatigued 150000 cycles at maximum remote stress of 14.9 ksi and two pristine bare coupons 200000 cycles at a maximum remote stress of 14 ksi. Coupons for the bare corroded condition were exposed 24 h in sodium chloride/hydrogen peroxide solution prepared in accordance with ASTM G110. Previous work on 2024 indicates the fatigue performance following this method of corrosion is similar to that following one year seacoast exposure. Three coupons of each alloy were then fatigued 100000 cycles at a maximum stress of 10 ksi. The stress ratio in all tests was R=0.05. The specific number of cycles applied to each condition was approximately two-thirds to three-fourths of the lifetime of specimens tested to failures.

Following fatigue cycling to the specified number of cycles, each hole (24 per coupon) was broken open and examined for possible fatigue cracks and in the case of the bare corroded coupons for corrosion damage. To break open each hole, a 1-inch square coupon of material containing the hole was excised from the panel. Notches were cut in the square piece perpendicular to the direction of loading in the plane of likely crack growth. Then each specimen was pulled to failure in a tensile test machine to expose any cracks. The total number of potential cracks in each alloy was 96 for the pristine bare condition (2 specimens x 2 per hole) and 144 (3 specimens) for the pristine alclad and corroded bare condition. All holes were examined using an optical microscope at magnifications up to 70x. Depth and area measurements were made of all observed cracks. The accuracy of the optical measurement technique was verified by examining a portion of the fracture surfaces in a scanning electron microscope. For the pristine conditions, the observed crack shapes were converted to an equivalent quarter-circular corner crack using a stress intensity matching method similar to Luzar and Hug [9]. This enabled cracks of various aspect ratios to be fairly compared. For the bare corroded condition, this method was not practical due to the complexity and irregularity of the combined corrosion and fatigue damage. Instead the area of corrosion, area of fatigue and total damage area were measured and compared.

3. EXPERIMENTAL RESULTS AND DISCUSSION

3.1 RESIDUAL STRENGTH WITH MSD

The results of the residual strength tests on unstiffened and stiffened panels with MSD are given in Table 3. In the unstiffened panels, rapid failure occurred upon link-up of the lead crack and MSD at the

adjacent fastener hole with the exception of the panels with no MSD which exhibited first link-up while exhibiting stable crack extension. In the stiffened panels, rapid failure was preceded by link-up between the lead crack and MSD at the adjacent fastener hole and link-up between the resulting crack and MSD at the second fastener hole. In both cases the lead cracks were observed to extend stably at approximately 70% to 80% of the maximum load while the MSD cracks did not extend until very close to specimen failure at approximately 95% of maximum load. A comparison of stiffened panel behavior in the two alloys is illustrated by plots of applied remote stress versus lead crack length for the 0.05-inch MSD flaw size in Figure 2. Residual strength as a function of MSD flaw size for the stiffened and unstiffened panels are shown graphically in Figure 3. While the presence of small MSD in the holes ahead of a lead crack reduced the residual strength in both alloys, 2524 continues to have superior residual strength relative to 2024 when MSD is present. The percentage improvement in 2524 over 2024 was 8.8 to 10.4% in the unstiffened panels and 9.3 to 10% in the stiffened panels depending on MSD flaw size. Thus, when viewed as a replacement for 2024-T3, alloy 2524-T3 gives a significant increase in the margin of safety for multi-site damage scenarios.

TABLE 3. RESIDUAL STRENGTH TEST RESULTS FROM UNSTIFFENED AND STIFFENED 2524-T3 AND 2024-T3 PANELS WITH MSD

Specimen Type	MSD Size (inch)	Event	Remote Stress (ksi) 2024-T3	Remote Stress (ksi) 2524-T3	Improvement (%)
Unstiffened	None	Failure	26.83	29.19	8.8
	0.05	Failure	23.47	25.80	9.9
	0.10	Failure	21.96	24.04	9.5
	0.15	Failure	19.47	21.50	10.4
Stiffened	0.05	1st Link Up	22.20	25.00	11.2
		2nd Link Up	21.63	24.87	13.0
		Failure	26.81	29.57	9.3
	0.10	1st Link Up	21.38	23.79	10.1
		2nd Link Up	21.13	23.24	9.1
		Failure	25.25	28.05	10.0

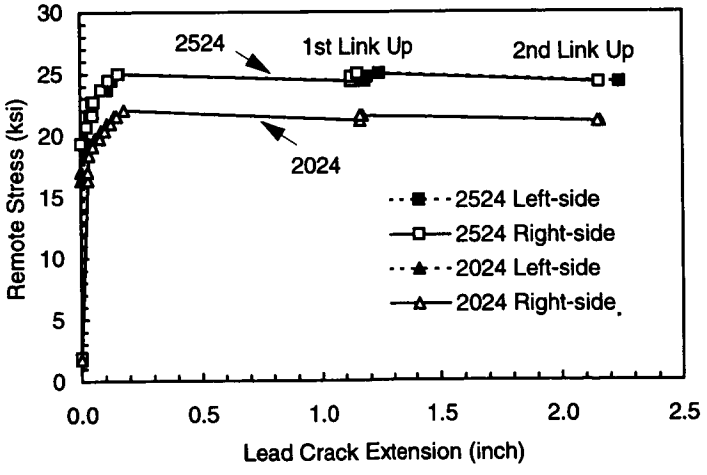

Figure 2. Results of residual strength tests on stiffened panels comparing response of 2524-T3 and 2024-T3 alclad sheet with 0.05 inch MSD.

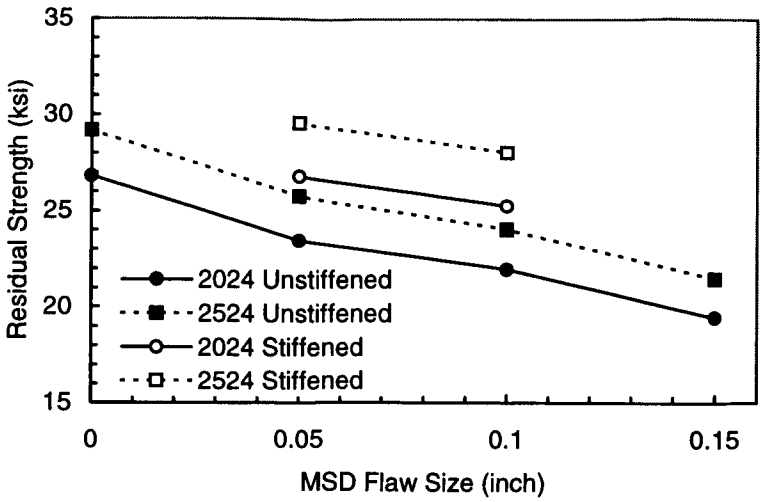

Figure 3. Comparison of residual strengths for 2524-T3 and 2024-T3 alclad sheet in unstiffened and stiffened panels versus MSD flaw size.

3.2 FATIGUE LIFE WITH MSD

The results of the fatigue tests on unstiffened panels are summarized in Table 4. In the two panels of each alloy with no MSD, fatigue cracks quickly formed at the tips of the lead crack and propagated to failure. Fatigue cracks were not observed to initiate in the row of open holes until these holes were intersected by the lead crack. The lead crack stopped momentarily at the open holes until fatigue initiated on the opposite side. In the three panels of each alloy with MSD, fatigue cracks initiated from the MSD flaws in the row of open holes after 20 to 25% of the total lifetime and propagated until overtaken by the lead crack. A crack propagation diagram comparing the position of the lead and MSD cracks as a function of elapsed cycles in 2524 and 2024 is shown in Figure 4 for the 0.05-inch MSD flaw size. Fatigue life for each alloy as a function of MSD flaw size is shown graphically in Figure 5. As anticipated, the fatigue life decreases with increasing MSD flaw size in both alloys. However, for any given flaw size, the lives of the 2524 panels are 27 to 45% longer than corresponding 2024 panel as a consequence of the superior fatigue crack growth resistance of alloy 2524.

TABLE 4. FATIGUE TESTS RESULTS FROM UNSTIFFENED 2524-T3 AND 2024-T3 PANELS WITH MSD

MSD Size (inch)	Lifetime to Failure (cycles)		Average Improvement (%)
	2024-T3	2524-T3	
None	90141	115392	28.6
	75725	97980	
0.05	38379	47577	26.9
	38256	49693	
0.10	26616	38593	45.0

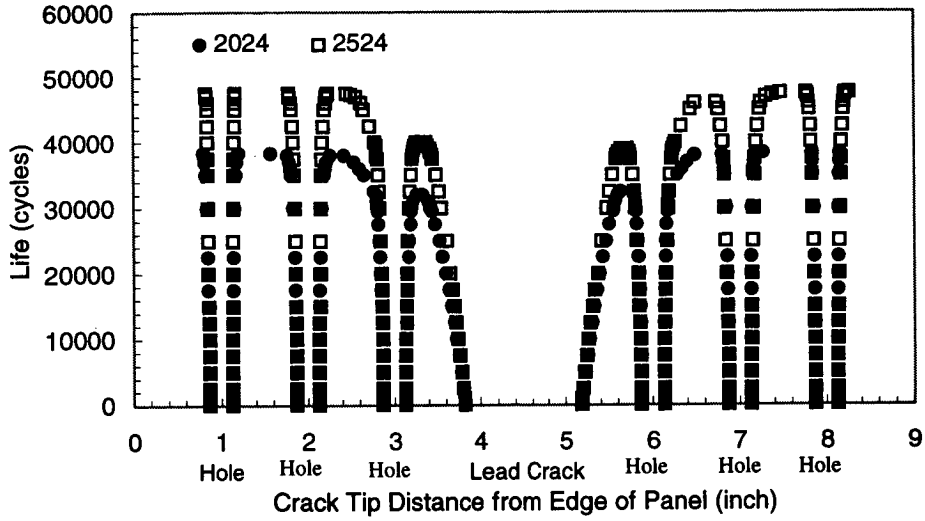

Figure 4. Comparison of fatigue crack propagation diagrams for unstiffened panels of 2524-T3 and 2024-T3 alclad sheet with 0.05 inch MSD.

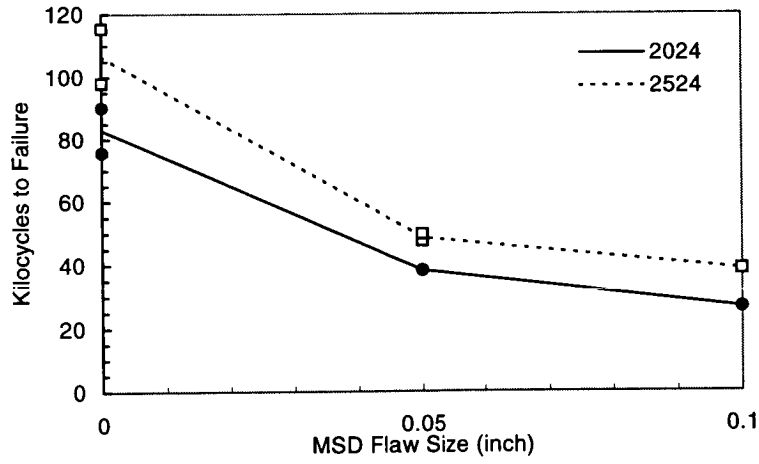

Figure 5. Comparison of fatigue life for 2524-T3 and 2024-T3 alclad sheet in unstiffened panels versus MSD flaw size.

3.3 MSD FROM FATIGUE AND CORROSION

Descriptive statistics from the pristine alclad and pristine bare multi-hole coupons are given in Table 5. In the pristine alclad condition, about 20% of the potential 144 sites exhibited fatigue cracks in both alloys. Typical of alclad sheet, nearly all the fatigue cracks initiated in the softer clad layer instead of the core material. In the pristine bare condition, only about 3% of the potential 96 sites exhibited fatigue cracks. The far greater percentage of initiating sites in the clad material than in the bare material indicates that clad material is more prone to the formation of MSD from fatigue alone. However, the purpose of the clad layer is to protect the core material from corrosion. Therefore, it is likely that any advantage bare material provides with respect to resistance to MSD from fatigue may be lost in the presence of corrosion which is prevalent on aging aircraft. The mean of the equivalent quarter circular

corner crack sizes obtained by stress intensity matching was about 13% greater in 2524 than in 2024. The means include only those sites containing a crack. Confidence intervals at the 95% level were calculated for the difference in means between alclad 2524 and 2024 and this difference was determined to be statistically insignificant [10]. The scarcity of initiation sites in the bare material made such a calculation meaningless. It was initially expected that 2524 would have smaller equivalent crack sizes due to its improved fatigue crack growth resistance. However, the advantage of 2524 over 2024 is typically greater at medium and high ΔK than it is at low ΔK present at the early stage of crack growth. For the specific lots of 2524 and 2024 used in this study there was very little difference in fatigue crack growth (FCG) resistance at low ΔK (see Figure 2). The results of the panel fatigue tests and multi-hole coupon tests taken together indicate that while the improved FCG resistance in 2524 relative to 2024 yields a significant improvement in fatigue life when MSD flaws are already present, it does not significantly effect the resistance to the formation of MSD from fatigue because of the different portions of the FCG curve involved in the early and later stages of crack growth.

TABLE 5. DESCRIPTIVE STATISTICS FOR PRISTINE MULTI-HOLE FATIGUE COUPONS OF ALCLAD AND BARE 2524-T3 AND 2024-T3 SHEET

	Clad 0.050 inch thick Fatigued 150000 cycles at 14.9 ksi			Bare 0.100 inch thick Fatigued 200000 cycles at 14.0 ksi		
	2024-T3	2524-T3	Diff.	2024-T3	2524-T3	Diff.
No. Cracks/No. Sites	33/144	31/144	-2/144	2/96	3/96	+1/96
Mean (inch)[a]	0.0113	0.0128	+13.2%	0.0107	0.0121	+13.1%
St. Dev. (inch)	0.0089	0.0074	-16.8%	0.006	0.0052	-13.3%

[a] Mean crack size for equivalent quarter circular corner crack.

Descriptive statistics from the bare corroded multi-hole specimens are given in Table 6. Of the potential 144 sites, corrosion was observed at 99% of the sites and fatigue at 97% of the sites in the 2024 specimens compared to 92% and 83% of the sites, respectively, in the 2524 specimens. Typically, fatigue emanated at corrosion pits along the bore of the hole. The mean values of the areas from corrosion, fatigue and total damage for each alloy and 95% confidence intervals for the mean are shown in Figure 6. On average, the area of corrosion was 32% less in 2524 than in 2024. This was a consequence of the pits in 2524 being, in general, less deep and separated by uncorroded material while those in 2024 were deeper and partially or fully coalesced. These same characteristics were observed in a previous study by Bray et al. [11]comparing the smooth fatigue performance of bare 2524 and 2024 with prior corrosion. In that study, these characteristics were attributed to the much lower number density of constituent particles in 2524 relative to 2024. Pitting at the smaller constituent particles abundant in 2024 is believed to link up or coalesce the larger pits formed at the larger particles. The mean area of fatigue was 5% greater in 2524. Again, it was expected that the fatigue area would be less in 2524 because of its improved FCG resistance and because the starting flaw (i.e., the area of corrosion) was smaller. However, as already discussed the FCG resistance at low ΔK in the specific lots used in this study were not significantly different. Also, most of the fatigue area in 2524 is between the non-coalesced pits while in 2024 this material has already been corroded away. Since the pits in 2524 are not coalesced and not as deep the fatigue cracks may be experiencing greater stress intensification from the hole than in 2024. On average, the total area of corrosion plus fatigue at each hole was 18% less and the maximum depth of attack 16% less in 2524 than in 2024. Confidence intervals at the 95% level were calculated for the difference in means for corrosion, fatigue and total damage areas [10]. The difference in means between

2524 and 2024 was statistically significant for corrosion area and total damage area but not for fatigue area.

TABLE 6. DESCRIPTIVE STATISTICS FOR CORRODED MULTI-HOLE FATIGUE COUPONS OF BARE 2524-T3 AND 2024-T3 SHEET

Metric	2024-T3	2524-T3	% Difference
Number of Sites (144 possible)			
With Corrosion	142	133	-6%
With Fatigue	140	127	-9%
With Corrosion and Fatigue	138	120	-1%
Mean Value			
Maximum Depth (mm)	0.81	0.68	-16%
Corrosion Area (sq. mm)	0.94	0.64	-32%
Fatigue Area (sq. mm)	0.56	0.59	+5%
Total Area (sq mm)	1.50	1.23	-18%

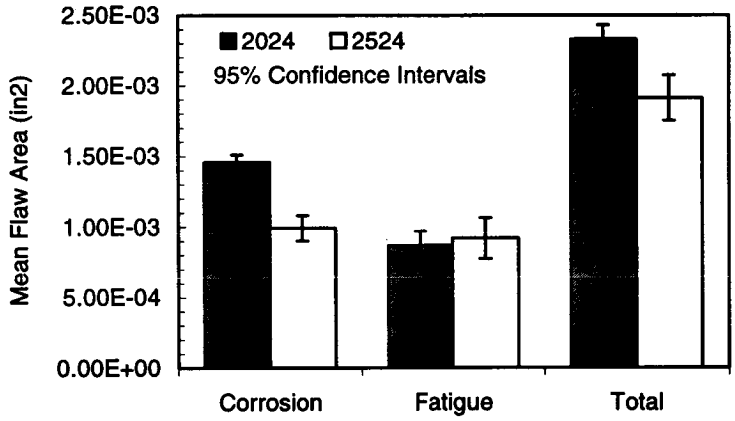

Figure 6. Comparison of mean values of area from corrosion, fatigue and total damage in corroded 2524-T3 and 2024-T3 bare sheet.

CONCLUSIONS

The results of this study indicate that alloy 2524-T3 sheet offers significant advantages in structural damage tolerance relative to incumbent alloy 2024-T3 in fuselage skin sheet applications, both in new aircraft and in multi-site damage scenarios that might be found in aging aircraft. The results show that 2524 offers not only improved structural damage tolerance relative to 2024 due to its superior fatigue crack growth resistance and fracture toughness but is also more resistant to MSD from corrosion in bare sheet form. Potential advantages of 2524-T3 to aircraft manufacturer/operators are an increase in allowable stress (weight savings), increase in inspection interval (lower operating costs), easier inspectability (larger crack sizes can be tolerated) and increase in safety (reduced risk of failure).

ACKNOWLEDGMENTS

The residual strength tests were conducted at the USAF Wright Laboratory Flight Dynamics Directorate in Dayton, Ohio. The assistance of D. Conley and M. Derriso in providing access to the Flight Dynamics Directorate Fatigue and Fracture Test Facility is greatly appreciated.

REFERENCES

1. Mar, J.W., "Structural Integrity of Aging Airplanes: A Perspective," Structural Integrity of Aging Airplanes, S.N. Atluri, S.G. Sampath, P. Tong, Eds. Springer-Verlag, 1991, pp. 241-273.

2. Swift, T., "Widespread Fatigue Damage Monitoring Issues and Concerns," FAA/NASA International Symposium on Advanced Structural Integrity Methods for Airframe Durability and Damage Tolerance, NASA Conference Publication 3274, Part 2, C.E. Harris, Ed., Sept. 1994, pp. 829-870.

3. Moukawsher, E.J., Heinimann, M.B, and Grandt, A.F., Jr., "Residual Strength of Panels with Multiple Site Damage," Journal of Aircraft, Vol. 33, No. 5, 1996, pp. 1014-1021.

4. Moukawsher, E.J., Grandt, A.F., Jr., and Neussl, M.A., Fatigue Life of Panels with Multiple Site Damage," Journal of Aircraft, Vol. 33, No. 5, 1996, pp. 1003-1013.

5. Heinimann, M.B., and Grandt, A.F., Jr., "Analysis of Stiffened Panels with Multiple Site Damage," Proc. Of 1996 USAF Structural Integrity Program Conference, San Antonio, TX, Dec. 3-5, 1996.

6. Hyatt, M.V. and Axter, S.E., "Aluminum Alloy Development for Subsonic and Supersonic Aircraft," Science and Engineering of Light Metals (RASELM '91), Japan Institute of Light Metals, October 1991, pp. 273-280.

7. Staley, J.T., "Aluminum Alloys for Subsonic Aircraft," Aerospace Thermal Structures and Materials for a New Era, University of Virginia Thermal Structures Conference (2nd), Charlottesville, VA, Oct. 19, 1994, pp. 343-358.

8. McGuire, J. and Varanasi, R., "Boeing Structural Design and Technology Improvements," Airliner, April-June 1996, pp. 12-19.

9. Luzar, J., Hug, A., "Lower Wing Disassembly and Inspection Results of Two High Time USAF B707 Aircraft," presented at USAF Structural Integrity Program Conference, San Antonio, TX, Dec. 1996.

10. Golden, P.J., A Comparison of Fatigue Crack Initiation at Holes in 2024-T3 and 2524-T3 Aluminum Alloys," M.S. Thesis, School of Aeronautics and Astronautics, Purdue University, 1997.

11. Bray, G.H., Bucci, R.J., Colvin, E.L., and Kulak, M., "Effect of Prior Corrosion on the S/N Fatigue Performance of Aluminum Sheet Alloys," Effects of the Environment on the Initiation of Crack Growth, ASTM STP 1298, W.A. Van der Sluys, R.S. Piascik, and R. Zawierucha, Eds., American Society for Testing and Materials, 1997.

FRACTURE ANALYSIS OF THE FAA/NASA WIDE STIFFENED PANELS

B. R. Seshadri
National Research Council Associate
NASA Langley Research Center
Hampton, Virginia, 23681-2199 USA
Tel: 757-864-3478
Fax: 757-864-8911
b.r.seshadri@larc.nasa.gov

J. C. Newman, Jr., D. S. Dawicke and R. D. Young
NASA Langley Research Center
Hampton, Virginia, 23681-2199 USA

ABSTRACT

This paper presents the fracture analyses conducted on the FAA/NASA stiffened and unstiffened panels using the STAGS (STructural Analysis of General Shells) code with the critical crack-tip-opening angle (CTOA) fracture criterion. The STAGS code with the "plane-strain" core option was used in all analyses. Previous analyses of wide, flat panels have shown that the high-constraint conditions around a crack front, like plane strain, has to be modeled in order for the critical CTOA fracture criterion to predict wide panel failures from small laboratory tests. In the present study, the critical CTOA value was determined from a wide (unstiffened) panel with anti-buckling guides. The plane-strain core size was estimated from previous fracture analyses and was equal to about the sheet thickness. Rivet flexibility and stiffener failure was based on methods and criteria, like that currently used in industry. STAGS and the CTOA criterion were used to predict load-against-crack extension for the wide panels with a single crack and multiple-site damage cracking at many adjacent rivet holes. Analyses were able to predict stable crack growth and residual strength within a few percent (5%) of stiffened panel tests results but over predicted the buckling failure load on an unstiffened panel with a single crack by 10%.

1. INTRODUCTION

Widespread fatigue damage is of great concern to the aging commercial transport fleets because the residual strength of a stiffened structure with a single long crack may be significantly reduced by the existence of adjacent smaller cracks as postulated by Swift [1]. Whereas a single long crack in a fuselage structure may produce flapping, a process by which a cracked fuselage would peel open in a small local region and lead to safe decompression, a fuselage with a long lead crack and multiple-site or multiple-element damage (MSD or MED) cracking may not flap. Tests on panels with long lead cracks and MSD have shown that the presence of an array of small adjacent cracks strongly degrade residual strengths [2,3]. One of the objectives in the NASA Aging Aircraft Research Program [4] is to develop the methodology to predict flapping or failure in damaged fuselage structures in the presence of widespread fatigue damage. The approach is to use a finite-element shell code with global-local, adaptive mesh capabilities and appropriate local fracture criteria to predict progressive failure in complex structures. In the future, fuselage structures may be designed by analysis, and verified by tests, to produce flapping or improved crack arresting capability under MSD or MED conditions.

In an effort to develop the methodologies required to predict the residual strength of complex fuselage structures with MSD, a series of tests and analyses have been performed from the coupon level to

subscale fuselage simulation tests [5,6]. These series of tests were used to verify the residual strength methodology based on the critical crack tip-opening angle (CTOA) failure criterion. NASA and the FAA have designed a series of wide, stiffened panels with single and multiple-site damage cracking at many simulated rivet holes [7,8]. These panels had "fatigue" MSD cracks instead of sawcuts. The panels were made of 2024-T3 sheet material (thickness of 1.6 mm) with five 7075-T6 stiffeners (thickness of 2.2 mm). Stiffeners were placed symmetrical about the thickness of the sheet. The central stiffeners were cut and the panels were allowed to buckle during the stable tearing and crack linkup process. Load-crack extension, load-strain records and out-of-plane displacement measurements were made during all tests.

Stable crack growth in metallic materials has been studied extensively using elastic-plastic finite-element methods, see reference 9. These studies were performed to investigate various fracture criteria. Of these, the crack-tip-opening angle (CTOA) or displacement (CTOD) criterion was shown to be the most suited for modeling stable crack growth and instability during the fracture process. Numerous investigators have also experimentally measured CTOA (or CTOD) during fracture. Dawicke et al. [10], using a high-resolution photographic camera with a video system, has shown that the critical angles during stable crack growth in thin-sheet aluminum alloys were nearly constant after a small amount of tearing. The non-constant CTOA region (measured at the free surface) was shown to be associated with severe tunneling during the initiation of stable tearing. Newman and Dawicke [11] and Dawicke et al. [12] have extensively applied the CTOA fracture criterion and the finite-element method to analyze stable crack growth and fracture of many complex crack configurations made of aluminum alloys. Seshadri and Newman [13] have also used the finite-element method and the CTOA criterion to predict stable tearing in the presence of severe out-of-plane buckling for both aluminum alloys and steels.

This paper presents the fracture analyses conducted on the FAA/NASA stiffened panels using the STAGS (STructural Analysis of General Shells) code [14,15] with the critical crack-tip-opening angle (CTOA) fracture criterion. The STAGS code, with the "plane-strain" core option, was used in all analyses. Previous analyses of wide, flat panels have shown that the high-constraint conditions around a crack front, like plane strain, has to be modeled in order for the critical CTOA fracture criterion to predict wide panel failures from small laboratory tests [16]. In the present study, the critical CTOA value was determined from a wide (unstiffened) panel with anti buckling guides. The plane-strain core size was estimated from previous fracture analyses and was about equal to the sheet thickness. Rivet flexibility and stringer failure were based on methods and criteria, like that currently used in industry [1]. Comparisons were made between load-crack extension on stiffened and unstiffened panels with single cracks and MSD. An assessment of the capability of the STAGS code with the critical CTOA failure criterion to predict residual strength was made.

2. EXPERIMENTS

NASA Langley Research Center (LARC) and the FAA William J. Hughes Technical Center have jointly designed and sponsored fracture tests on 1016-mm wide sheets made of 1.6-mm thick 2024-T3 aluminum alloy with and without stiffeners [7,8]. Ten wide panel fracture tests were conducted at LARC. Half of the specimens had five 7075-T6 aluminum alloy stiffeners (41 mm wide, 2.2-mm thick) riveted on each side of the sheet with a spacing of 203 mm, as shown in Figure 1(a). The stiffeners were orientated in the direction of loading and perpendicular to the direction of the crack(s). The rivets were 2017-T4 aluminum alloy button head with a 25.4-mm rivet spacing (d_r). The 7075/2024/7075 lay-up was bonded only in the grip area but riveted over the remainder of the sheet. The central stiffeners were cut along the crack line. Open holes were machined into the sheet at the required rivet spacing along the crack line but rivets were not installed. Holes were not machined into the stiffeners along the crack-line location. Five

different crack configurations were tested: a single center crack, a single center crack with an array of 12 holes (4.8-mm diameter) on either side of the lead crack, and a single center crack with three different equal multiple-site damage (MSD) cracking (0.25, 0.76 and 1.3-mm) at the edge of each hole. The MSD cracks were introduced into the test specimen by fatigue precracking at a low applied cyclic stress level [8]. Figure 1(b) shows the details of the crack configuration along the crack line. The lead crack half-length (c_i) in all of the specimens was 101.5 mm. For each crack configuration, identical specimens were tested with and without riveted stringers. All tests were conducted under stroke control. During the tests, measurements were made of load, crack extension, applied end displacement, strain field in the crack-tip region, strains in the intact and broken stiffeners, and displacement fields (local and global).

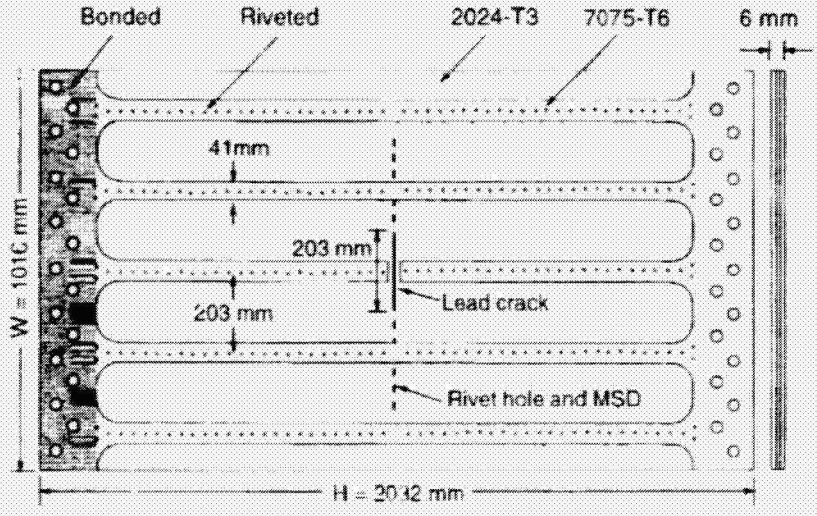

(a) Stiffened panel

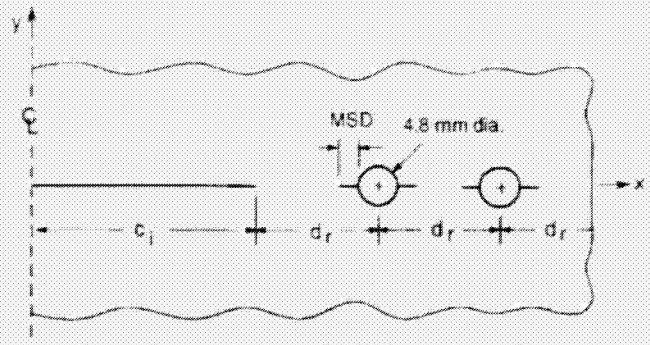

(b) Typical open-hole and MSD crack configuration

Figure 1. Stiffened panel and typical crack configuration analyzed.

Test results on load-against-crack extension measured on the five stiffened panels [7,8] are shown in Figure 2. The first intact stringer was located at about 100 mm from the initial crack-tip location (see dashed line). Circular symbols show the results for the single crack. The large gap in the data was when the crack was underneath the stiffener. Once the crack emerged from under the stiffener, the panel failed (solid symbol). Square symbols show the results from the single crack with 12 open holes on each side of the crack. The vertical steps in the data (with no crack extension) was when the crack linked with an open hole, and additional load was required to fracture the material at edge of the hole. Again, the solid symbol denotes the maximum failure load on the panel. Results show that even a panel with a single

crack and only open holes fail at a significantly lower load than that of a specimen with a single crack. The three tests with different size MSD all behaved in a similar manner. After the lead crack linked with the MSD cracks and grew pass the stiffener, the sheet failed and all 24 MSD cracks linked. Panel failure then occurred at about a 10% higher load than sheet failure. These results show that MSD at open holes reduce the residual strength about 30% from that of a panel with only a single crack.

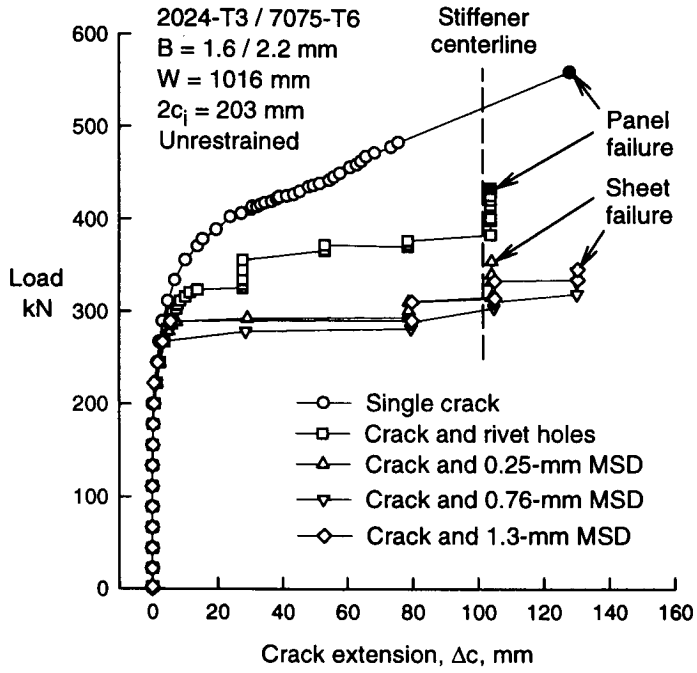

Figure 2. Load-against-crack extension from stiffened panel test program [7,8].

Large middle-crack tension panels (restrained against buckling) were tested to measure the critical crack-tip-opening angle (CTOA) on the 1.6-mm thick sheet 2024-T3 material during stable tearing and fracture. The critical CTOA is plotted against crack extension in Figure 3. The 610-mm wide specimen had an initial sawcut (254 mm in length) and the 1016-wide specimen had a large fatigue crack. During the fracture tests, a high-resolution camera and video system [10] was used to record the tearing crack. At each video image, corresponding to a given amount of crack extension, four to six measurements of the critical angle were measured from 0.5 to 1.5 mm from the crack tip. The average values are shown in Figure 3. The test measurements show an average angle of 5.15 degrees with a ±1 degree of scatter. The critical CTOA was nearly constant over nearly two orders of magnitude in crack extension. For small amounts of crack extension (less than sheet thickness), larger CTOA values are generally measured on the surface of the specimen, possibly due to severe crack tunneling (see ref. 12).

3. ANALYSES

The STAGS finite-element shell code [14,15] and the critical crack-tip-opening angle (CTOA) failure criterion were used to model stable tearing of cracks and residual strength behavior of wide, flat-unstiffened and flat-stiffened panels made of 2024-T3 aluminum alloy sheet and 7075-T6 stiffeners. Rivet connectivity, rivet yielding, stiffener yielding, out-of-plane buckling and stiffener-sheet contact behavior were modeled during the stable tearing process. Single cracks and multiple-site-damage (MSD) cracks at simulated rivet holes were considered. The holes, used to produce the MSD cracks, were only open holes.

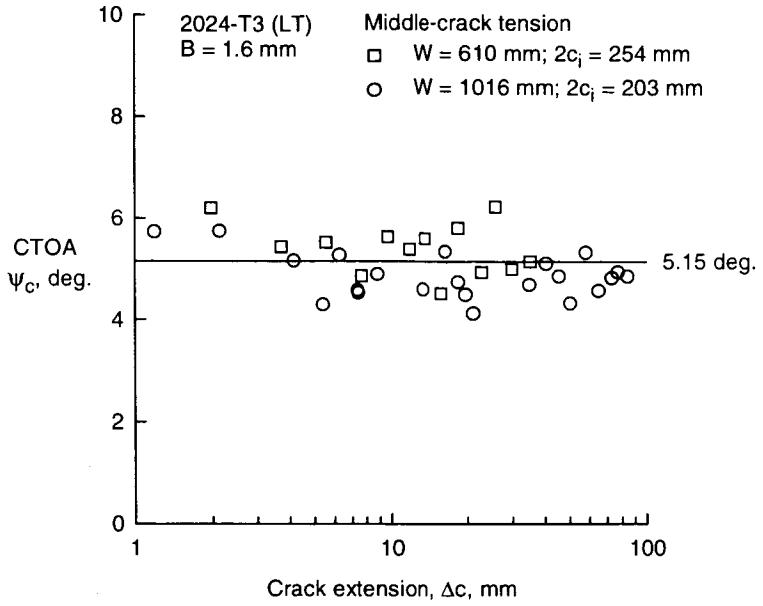

Figure 3. Measured critical CTOA for thin aluminum alloy sheet material.

3.1 STAGS FINITE-ELEMENT ANALYSES

STAGS is a finite element program for the analysis of general shell-type structures [14,15]. The program has several types of analysis capabilities (static, dynamic, buckling, crack extension, material nonlinear and geometric nonlinear behavior). STAGS has crack extension capability based on the critical crack-tip-opening angle or displacement (CTOA or CTOD) criterion, the T*-integral [17] and the traditional K_R-curve. In the current study, quadrilateral shell elements with 6 degrees-of-freedom per node (three displacements and three rotations) were used in all model. The quadrilateral shell element was under "plane-stress" conditions everywhere in the model except for a "core" of elements along the crack plane that were under "plane strain" conditions [16]. Elastic-plastic material behavior of the sheet and stiffener were approximated by multi-linear stress-strain curves. The White-Besseling plasticity theory with a form of kinematic hardening was used to account for yielding and reverse yielding during unloading [14].

In this section, the procedures used in modeling the stiffened panels and the crucial issues related to rivet flexibility are discussed. Before analyzing these wide stiffened panels, a preliminary study (both experimental and numerical) was carried out to understand the basic concepts of load transfer in built-up structure using a laboratory coupon specimen. For this purpose, 305-mm wide center-cracked panels with a single central stiffener was tested and analyzed. Both cut and intact stiffener situations were considered. The specimens were strain-gaged to measure sheet and stiffener strains (and load transfer) as a function of remote load and crack extension. This particular study helped in understanding the important issues involved in modeling rivet flexibility and sheet-stiffener contact during buckling of the specimen. Comparison between the experiments and the analysis were made at both global and local levels. Load transfer through the rivets near to the crack-tip region were compared with test results. Further details on these tests are given in references 7 and 8.

The specimen configuration and a typical finite-element model for the stiffened panel are shown in Figures 1(a) and 4, respectively. Because the configuration and loading were symmetric, only a quarter of the sheet and stiffeners was modeled. Figure 4 shows only the lower part of the mesh pattern used to model the lead crack and MSD. The mesh pattern to model the upper part of the specimen (not shown) is

similar to that shown in the upper part of Figure 4. The remote loading was applied as uniform displacement. Symmetry boundary conditions were applied along the specimen centerlines except for the crack surfaces that were free. This model contained 13,145 shell elements, 17,287 nodes, 97,254 degree-of-freedoms (DOF) and 82,372 active DOF.

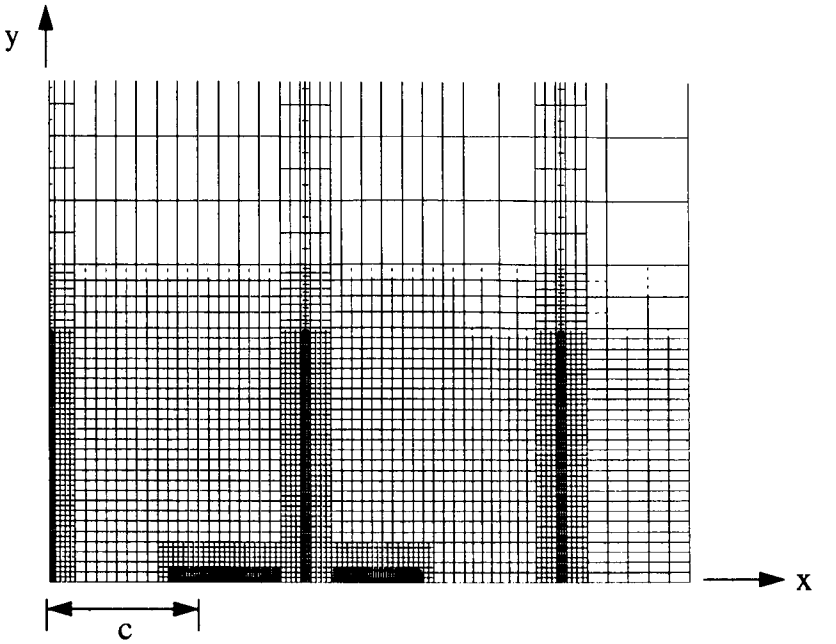

Figure 4. Typical finite-element model of flat, stiffened panel with single and MSD cracks.

3.1.1 Modeling of Sheet and MSD Cracking

To model the fracture process with the CTOA failure criterion, a model with an array of small elements were positioned along the crack plane. A minimum crack-tip element size (d) of 1 mm, along the line of crack extension, was chosen to be the same for all meshes generated for the different crack configurations. From previous parametric and convergence studies, it was found that a minimum crack-tip element size of 1 mm (linear-strain element) was sufficient to model stable tearing under elastic-plastic conditions [18]. Crack growth was governed by monitoring the critical CTOA (ψ_c) at a distance of 1 mm (one element) behind the crack tip. In general, the critical value (ψ_c) was determined by matching the average failure load measured on several tests of M(T) specimens (restrained from buckling), as will be discussed later.

The MSD crack sizes in the tests were 0.0 (no crack), 0.25, 0.76 and 1.3-mm in length from the open holes, see Figure 1(b). Because the MSD crack sizes were smaller than the 1-mm crack-tip element size, the circular holes were not modeled. To model MSD cracks, the displacement conditions for the nodes along the symmetric plane over the diameter of the hole and MSD cracks were set free. The total crack lengths for the four MSD cases were: 4.8 (hole diameter), 5.3, 6.3 and 7.4-mm, respectively. In the analyses, the corresponding crack lengths were set at: 5, 5, 6 and 7-mm, respectively. For the single crack and open hole only configurations, the "crack" which was used to simulate the unsupported hole region had a critical CTOA (24 degs.) large enough to prevent crack growth. Whereas, the lead crack had a constant tearing CTOA from initiation to failure. Crack linkup occurred under constant CTOA conditions for all crack tips. An option to have a crack-initiation displacement, δ_i, or CTOA, ψ_i,

different than the tearing CTOA, ψ_c, has recently been added to the STAGS code [15]. This option is used to simulate fracture of "sawcuts" and stable tearing of cracks [19]. This option was not used in the current study to simulate fracture of open holes connected by a crack (sharp-notch configuration). Only stable tearing until the crack linked up with the first open hole was considered.

3.1.2 Modeling of Stiffeners and Rivets

Analyses of cracked-stiffened panels by Newman and Dawicke [11] indicated that a refined mesh was required in the region of the rivet connection to maintain proper load transfer. In the 1016-mm wide stiffened panels, the elements in the rivet-connection region were 2 mm by 2 mm. Larger elements were used away from the rivet connection and away from the crack plane to help reduce the number of degrees-of-freedom. The stiffeners were modeled separately and overlapped the sheet with an offset equal to the sheet thickness. Rivet holes were not modeled.

Rivet connections between the stiffener and sheet were modeled with fastener elements in STAGS. The fastener elements are non-linear spring elements with six degrees-of-freedom (three translations and three rotations). For each degree-of-freedom, the user has to input the non-linear load-displacement curve. Rigid links were used at the end of each fastener to distribute the load transferred across each rivet. Rivet holes were again not modeled (a tight fit between the rivet and hole was assumed). For more information on the fastener element capability in STAGS, refer to references 14 and 15.

3.1.3 Modeling Buckling and Stiffener-Sheet Contact

Seshadri and Newman [13] have demonstrated that stable tearing in the presence of buckling can be predict with STAGS and the CTOA fracture criterion. In order to simulate buckling of both the stiffened and unstiffened panels, a bifurcation analysis was conducted to determine the first buckling mode shape. This out-of-plane displacement shape (about 10% of the sheet thickness) was then introduced as an imperfection in the sheet for the non-linear analysis. The sheet and stiffener surfaces penetrated each other as they deformed out-of-plane. To prevent penetration, contact elements and multi-point constraint conditions were used to allow the sheet and stiffener surfaces to contact or separate during buckling.

3.1.4 Modeling of Crack-Tip Constraint

A concept of defining plane-strain elements around the crack-front region was adopted to simulate three-dimensional constraint conditions around a crack front [16]. Previous analyses of wide flat panels [12] have shown that the high constraint conditions around a crack front, like plane strain, has to be modeled in order for the critical CTOA criterion to predict wide panel failure from small laboratory tests. The plane-strain core capability has recently been added to the STAGS code [15]. The plane-strain core is defined as a strip of elements (h_c is half-height) parallel to the crack plane. In the present analyses, the core height was selected as 2 mm to help fit the failure loads on various width M(T) specimens.

3.2 DETERMINATION OF THE CRITICAL CTOA

A critical CTOA (ψ_c) value was used to model the onset of crack growth and the stable tearing process. This criterion is equivalent to a critical CTOD (δ_c) value at a specified distance behind the crack tip. At each load increment, the CTOA was calculated and compared to a critical value ψ_c. When the CTOA exceeded the critical value, the crack-tip node was released and the crack was advanced to the next node. This process was continued until crack growth became unstable under load control or until the desired

crack length had been reached under displacement control. For multiple-site-damage cracking analyses, all cracks were controlled by the same critical CTOA at each crack tip.

The load-crack-extension results on the single crack in the 1016-mm wide panel was used to determine the critical CTOA (ψ_c) by trial-and-error. Figure 5(a) shows the measured load-against-crack extension results (symbols) from only one-side ($x > 0$) of the wide panel. The use of the digital-image correlation system to measure out-of-plane displacements prevented crack-extension measurements from the other side ($x < 0$) of the panel, thus crack extension was assumed to be symmetric. A value of $\psi_c = 5.4$ degrees was found to fit the maximum load quite well. The calculated results from the analysis tended to over predict crack extension after crack initiation. This behavior has been a general trend that has been observed on many other tests and analyses [10-13]. At first glance, a higher CTOA at initiation than during stable tearing would fit the test data better. However, the plastic history generated during fatigue pre-cracking was not modeled because this capability has not been incorporated into STAGS. It was estimated that fatigue pre-cracking would raise the initial portion of the predicted curve by about 10 kN. Also, a crack in the thin-sheet material severely tunnels at crack initiation, as much as two times the sheet thickness, so the surface measurement of crack extension is low compared to the interior [12]. These two issues would tend to make the predicted results with a constant CTOA in better agreement with the test data. A comparison of the measured and calculated load-against-crack-opening displacements at the center of the crack are shown in Figure 5(b). Here the calculated results agreed well with the test measurements.

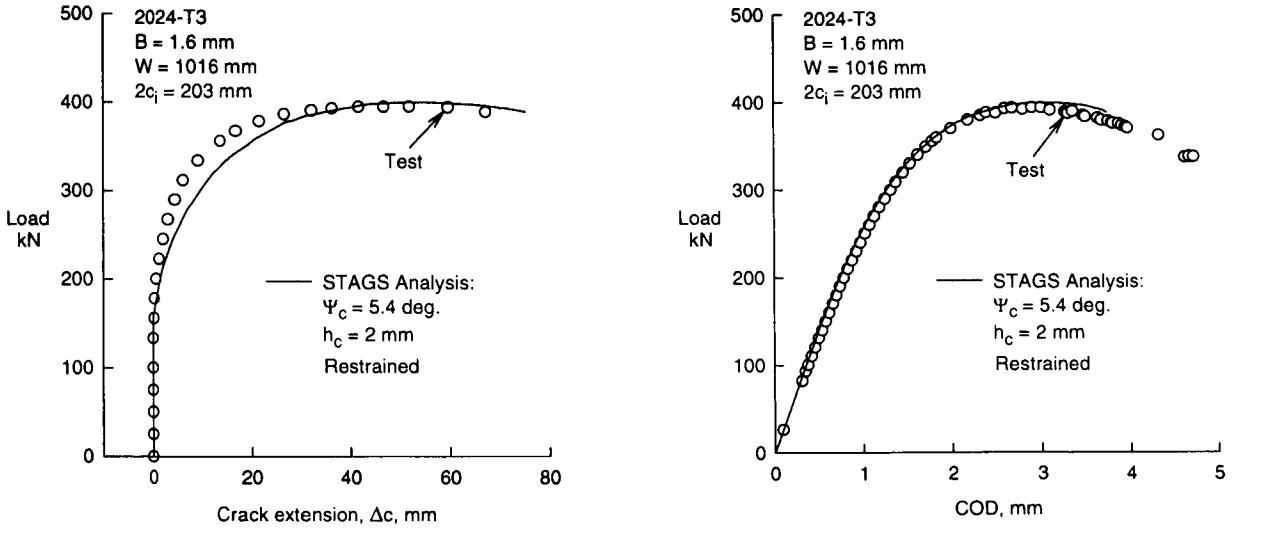

(a) Load-against-crack extension

(b) Load-against-crack-opening displacement

Figure 5. Measured and calculated load-against-crack extension and displacements using CTOA.

The value of CTOA (5.4 deg.) needed to fit the wide panel test results using the finite-element analyses was slightly larger than the average value (5.15 deg.) measured on the same wide panel (Fig. 3). There could be numerous reasons why these values do not agree. First, the measurements are made on the surface of the specimen and fracture is controlled by the deformation state in the interior. To minimize the number of degrees-of-freedom in structural analyses, the crack-tip element size has been selected to be about 1-mm in size. Smaller element sizes will support larger strains and leave larger residual plastic deformations and, possibility, smaller CTOA values. The finite-element analyses assume small strain

and crack-tip deformations occur under large-strain conditions. However, measurements and analyses tend to indicate that the critical CTOA is nearly constant for large amounts of stable tearing and for conditions of extreme plastic deformations.

Fracture tests conducted on smaller middle-crack tension M(T) and compact tension C(T) specimens were analyzed with the STAGS code and the critical CTOA of 5.4 degrees with the same plane-strain core size. Predicted failure loads on tests conducted on 305 and 610-mm wide M(T) specimens, restrained and un-restrained from buckling, were within ±5% of the test failure loads, but the predicted failure load on a 152-mm wide C(T) specimen was 8% lower than the average test failure load from several tests.

3.3 FRACTURE ANALYSIS OF UNSTIFFENED PANELS

STAGS and the critical CTOA determined from restrained wide panel tests were used to predict stable crack growth behavior of wide unstiffened panels with a single crack, a single crack with multiple open holes, and a single crack with MSD at each open hole. These panels were allowed to buckling. These predictions (curves) are compared with the test results (symbols) in Figure 6. The predicted results for a single crack agreed well with test data up to about 15 mm of crack extension. Here the test data reached a plateau and failed after a crack extension of about 35 mm. The predicted failure load was about 10% higher than the test load. For the single crack and open holes, the predicted stable tearing behavior as the

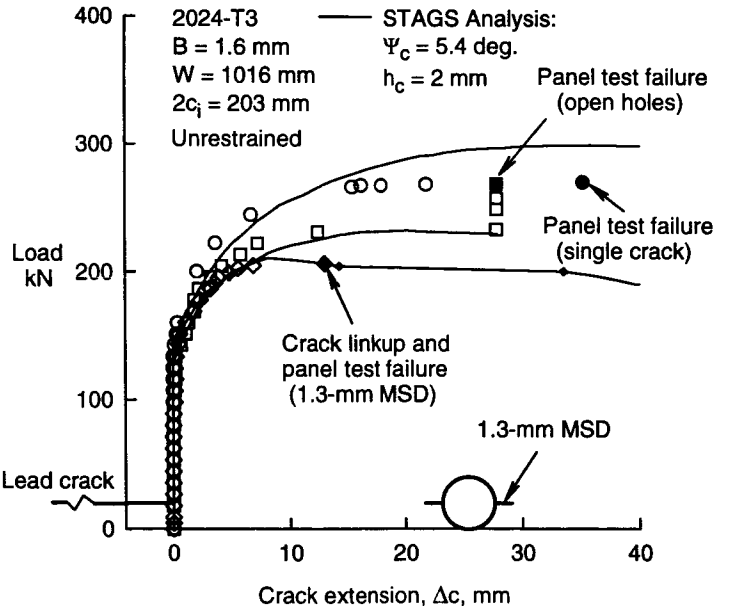

Figure 6. Measured and predicted load-against-crack extension for unstiffened panels.

crack linked up with the first open hole agreed well with test measurements. The insert shows the lead crack and location of the first hole. The panel failed at a load (15%) higher than the crack-hole linkup load, but no attempt was made to model the fracture of a sharp-notch configuration (crack connecting two holes). For the single crack with the 1.3-mm MSD, the lead crack and the MSD crack both grew and linked up when the lead crack had grown about 13 mm. The panel failed at the first linkup of the lead crack and the MSD crack (large solid diamond symbol). The small solid symbols show the calculated MSD crack size at linkup. The predicted maximum load, at about 8 mm of crack extension, agreed well with the test failure load. The remaining curve is the predicted behavior under displacement control.

3.4 FRACTURE ANALYSIS OF STIFFENED PANELS

The stable crack growth behavior of wide stiffened panels with a single crack and a single crack with MSD at each open hole was predicted using STAGS and the critical CTOA value. Again, these panels were allowed to buckle. Figure 7 shows the test measurements (symbols) made on the panel with a single crack. The insert shows the relative location of the stiffener. Crack extension was measured until the crack went underneath the stiffener. Once the crack grew outside of the stiffener, the panel failed (solid symbols). Whether failure of the panel was due to sheet failure or stiffener failure could not be determined. Failure of either would immediately result in panel failure because the stiffeners were carrying about one-half of the applied load.

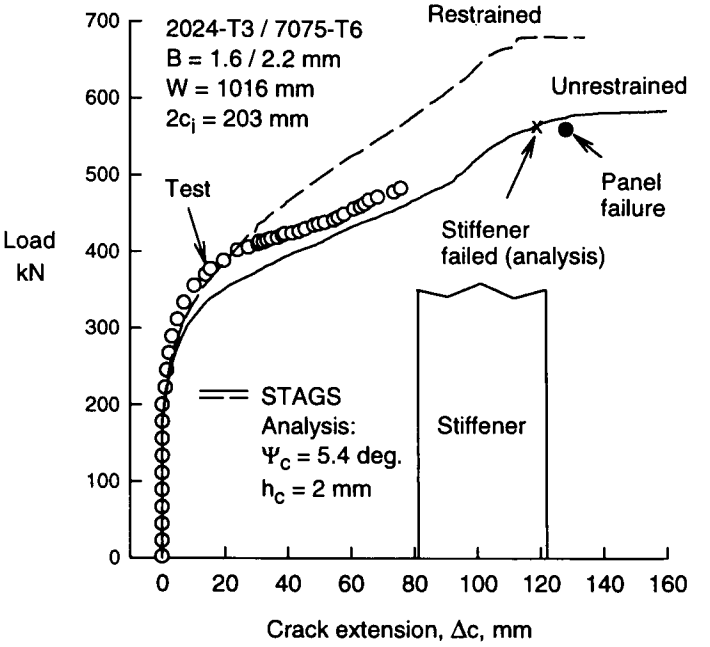

Figure 7. Measured and predicted load-against-crack extension for stiffened panel with single crack.

Two predictions were made using STAGS. First, the panel was restrained against buckling and the predicted results are shown by the dashed curve in Figure 7. After 20 mm of crack extension the restrained analysis tended to significantly over predict the test data and the predicted failure load was much higher than the test failure load. However, the unrestrained analysis (buckling allowed) under predicted the early stages of stable tearing but agreed well after about 30 mm of crack extension, similar to the results shown in Figure 5(a). The predicted failure load from the fracture of the sheet was 4% higher than the test failure load. The calculated stiffener failure load (x symbol) was extremely close to the actual test failure load. (Stiffener failure load was based on fracture tests conducted on the 305-mm wide specimens with a single intact stiffener at x = 0 [7,8].)

A comparison of the measured and predicted load-against-crack extension for the wide stiffened panel with a lead crack and the 1.3-mm MSD is shown in Figure 8. The insert shows the relative location of the lead crack, open holes, MSD, and the intact stiffener. The measured load-crack extension values for the data underneath the stiffener were inferred from the load-time trace recorded on this specimen. As the crack linked up with the open hole at about 125 mm, the sheet failed with all 24 MSD cracks linking. Panel failure then occurred at about a 10% higher load to break the stiffeners. The predicted load-crack extension behavior matched the test results very well. These results indicated that the STAGS code and

the CTOA failure criterion could predict stable tearing in the presence of MSD in a stiffened structure with severe out-of-plane deformations, typical of what may occur in an aircraft fuselage under pressure.

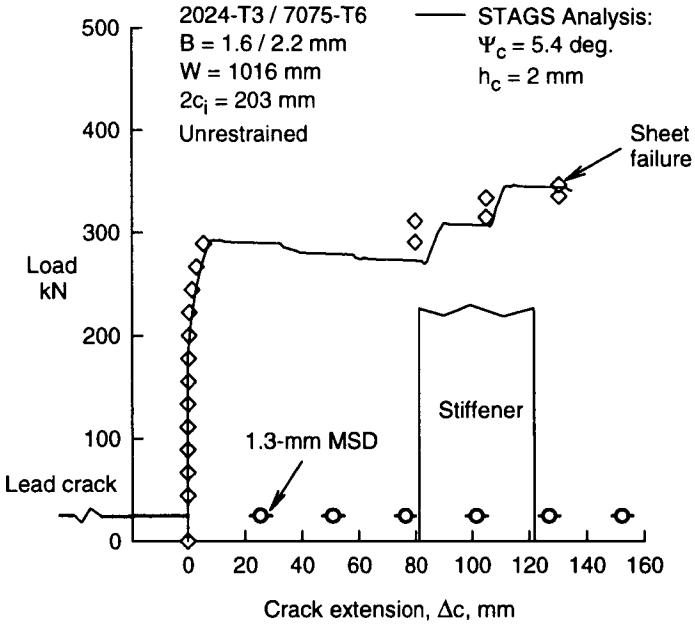

Figure 8. Measured and predicted load-crack extension for stiffened panel with crack and 1.3-mm MSD.

4. CONCLUSIONS

The STAGS finite-element code and the CTOA fracture criterion were used to predict stable tearing and residual strength of 1016-mm wide stiffened panels made of 2024-T3 aluminum alloy sheet with 7075-T6 stiffeners. The panels had a single crack, a single crack with 12 open holes, and a single crack with 12 equal-size and equally-spaced multiple-site damage (MSD) cracks. A similar series of tests were also conducted on unstiffened panels. This work supports the following conclusions:

(1) The measured critical crack-tip-opening angle (CTOA) was nearly constant over two orders of magnitude of crack extension for the thin-sheet 2024-T3 aluminum alloy.

(2) A constant critical crack-tip-opening angle (CTOA), ψ_c = 5.4 degrees, with the plane-strain core and STAGS were able to predict stable tearing behavior and residual strength of 152 to 1016-mm wide specimens within ±10%.

(3) A constant critical crack-tip-opening angle (CTOA), ψ_c = 5.4 degrees, with the plane-strain core and STAGS were able to predict stable tearing behavior and residual strength of wide stiffened panels with single cracks and MSD under severe buckling within 5%.

5. ACKNOWLEDGMENTS

The authors wish to thank Mr. Tom Swift, FAA Retired, for guidance in designing the stiffened panels and Dr. Charles Rankin, Lockheed Palo Alto Research Laboratory, for incorporating the plane-strain core and the CTOA options into the STAGS code.

6. REFERENCES

[1] Swift, T., "Damage Tolerance in Pressurized Fuselages", New Materials and Fatigue Resistant Aircraft Design, D. L. Simpson, ed., EMAS Ltd., 1987, pp. 1-77.

[2] Maclin, J., "Performance of Fuselage Pressure Structure," International Conference on Aging Aircraft and Structural Airworthiness, C. E. Harris, ed., NASA CP-3160, Washington, D.C., 1992, pp. 67-75.

[3] McGuire, J. F. and Goranson, U. G., "Structural Integrity of Future Aging Airplanes", 1991 International Conference on Aging Aircraft and Structural Airworthiness, C. E. Harris, ed., NASA CP-3160, Washington, D.C., 1992, pp. 33-48.

[4] Harris, C. E.; Newman, J. C., Jr.; Piascik, R. and Starnes, J. H., Jr., "Analytical Methodology for Predicting the Onset of Widespread Fatigue Damage in Fuselage Structure", Journal of Aircraft, Vol. 35, No. 2, 1998, pp. 307-317.

[5] Dawicke, D. S.; Gullerud, A. S.; Dodds, R. H. and Hampton, R., "Residual Strength Predictions with Crack Bulging," 2nd Joint NASA/FAA/DoD Conference on Aging Aircraft, Williamsburg, VA, 1998.

[6] Young, R. D.; Rouse, M.; Ambur, D. R. and Starnes, J. H., Jr., "Residual Strength Pressure Tests and Nonlinear Analyses of Stringer- and Frame-Stiffened Aluminum Fuselage Panels with Longitudinal Cracks," Second Joint NASA/FAA/DoD Conference on Aging Aircraft, Williamsburg, VA., 1998.

[7] Dawicke, D. S.; Newman, J. C., Jr. and Tan, P. W., "FAA/NASA Wide Panel Fracture Tests - Part I Executive Summary," NASA TM (in progress), 1998.

[8] Johnston, W. M. and Helm, J. D., "FAA/NASA Wide Panel Fracture Tests - Part II Experimental Test Program," NASA CR (in progress), 1998.

[9] Kanninen, M.; Rybicki, E.; Stonesifer, R.; Broek, D.; Rosenfield, A. and Nalin, G., "Elastic-Plastic Fracture Mechanics for Two-Dimensional Stable Crack Growth and Instability Problems", ASTM STP 668, 1979, pp. 121-150.

[10] Dawicke, D. S.; Sutton, M. A.; Newman, J. C., Jr. and Bigelow, C. A., "Measurement and Analysis of Critical CTOA for Thin-Sheet Aluminum Alloy Materials", Fracture Mechanics: 25th Volume, ASTM STP 1220, F. Erdogan, ed., 1995, pp. 358-379.

[11] Newman, J. C., Jr. and Dawicke, D. S., "Fracture Analysis of Stiffened Panels under Biaxial Loading with Widespread Cracking," AGARD CP-568, 1995, pp. 3.1-3.16.

[12] Dawicke, D. S.; Newman, J. C., Jr. and Bigelow, C. A., "Three-Dimensional CTOA and Constraint Effects during Stable Tearing in a Thin-Sheet Material," Fracture Mechanics: 26th Volume, ASTM STP 1256, W. G. Reuter, J. H. Underwood and J. C. Newman, Jr., eds., 1995, pp. 223-242.

[13] Seshadri, B. R. and Newman, J. C., Jr., "Analyses of Buckling and Stable Tearing in Thin-Sheet Materials," Fatigue and Fracture Mechanics: 29th Volume, ASTM STP 1332, T. L. Panontin and S. D. Sheppard, eds., 1998.

[14] Almroth, B.; Brogan, F. and Stanley, G., "User's Manual for STAGS", NASA CR 165670, 1978.

[15] Rankin, C. C.; Brogan, F. A.; Loden, W. A. and Cabiness, H. D., "STAGS User Manual - Version 2.4," Lockheed Martin Advanced Technology Center, Report LMSC P032594, 1997.

[16] Newman, J. C., Jr.; Booth, B. C. and Shivakumar, K. N., "An Elastic-Plastic Finite-Element Analysis of the J-Resistance Curve using a CTOD Criterion", Fracture Mechanics: 18th Volume, ASTM STP 945, D. T. Read and R. P. Reed, eds., 1988, pp. 665-685.

[17] Atluri, S. N. and Tong, P., "Computational Schemes for Integrity Analyses of Fuselage Panels in Aging Airplanes," Structural Integrity of Aging Airplanes, Springer-Verlag, 1991, pp. 33.

[18] Dawicke, D. S. and Newman, J. C., Jr., "Residual Strength Predictions for Multiple-Site Damage Cracking using a CTOA Criterion," Fatigue and Fracture Mechanics: 29th Volume, ASTM STP 1332, T. L. Panontin and S. D. Sheppard, eds., 1998.

[19] Newman, J. C., Jr., Dawicke, D. S., Sutton, M. A. and Bigelow, C. A., "A Fracture Criterion for Widespread Cracking in Thin-Sheet Aluminum Alloys," Durability and Structural Integrity of Airplanes, Vol. I, A. F. Blom, ed., EMAS Ltd., 1993, pp. 443-468.

IMPROVED ENGINEERING METHODS FOR DETERMINING THE CRITICAL STRENGTHS OF ALUMINIUM PANELS WITH MULTIPLE SITE DAMAGE IN AGING AIRCRAFT

Bert Smith, Adil Mouak, Perry Saville, Roy Myose, and Walter Horn
Department of Aerospace Engineering
Wichita State University
Wichita, Kansas 67260-0044, USA
Phone: (316) 978-5938
Fax: (316) 978-3307
Email: bsmith@ae.twsu.edu

ABSTRACT

An aging aircraft accumulates widespread fatigue damage commonly referred to as multiple site damage (MSD). For ductile materials such as 2024-T3 aluminum, MSD may lower the critical (residual) strength below that which is predicted by conventional fracture mechanics. An analytical model generally referred to as the linkup model (or the plastic zone touch model) has previously been used to describe this phenomenon. However, the linkup model has been shown to produce inaccurate results for many configurations. This paper describes two modifications of the linkup model that have been shown to predict accurate results over a wide range of configurations for both unstiffened and stiffened flat 2024-T3 panels with MSD at open holes.

INTRODUCTION

An aging aircraft accumulates widespread fatigue damage in the form of small scale cracking at places of high stress concentration. This type of damage is commonly referred to as multiple site damage (MSD). Panels with major cracks exhibit a loss in strength. However panels with MSD in addition to major cracks may exhibit further loss in strength, especially panels of ductile materials such as 2024-T3 aluminum. In an attempt to explain this phenomenon, Swift[1] described an analytical model called the linkup model or the plastic zone touch model. The linkup model clearly shows this additional loss in strength from MSD. However, it does not predict the magnitude of the loss accurately over a wide range of configurations. This paper describes investigations[2,3] of the linkup model that resulted in the development of two improved models, referred to herein as linkup-mod1 and linkup-mod2 (or simply Mod1 and Mod2). Both of these modified linkup models were developed empirically from test data for 40 different flat unstiffened 2024-T3 aluminum panels with MSD, and additionally have been validated with test data from 12 different stiffened panels. Both of these modified linkup models are easy to use and give accurate results for a large range of parameters including panel thickness and width, lead crack length, MSD crack length, and ligament length. This investigation should add to the understanding of the degree to which nonlinear behavior can be described with a simplified engineering model.

ANALYTICAL MODELS

A schematic diagram of a panel with multiple site damage is shown in Figure 1. It has a lead crack of length 2a and collinear cracks, called MSD cracks, emerging from each hole. The linkup model is based on the concept that ligament failure will occur when the remote stress σ reaches a level that causes the surfaces of the lead crack tip plastic zone and the adjacent MSD crack tip plastic zone (Figure 1) to touch. When this happens, the crack extends from a to a' (Figure 1). The remote stress corresponding to this

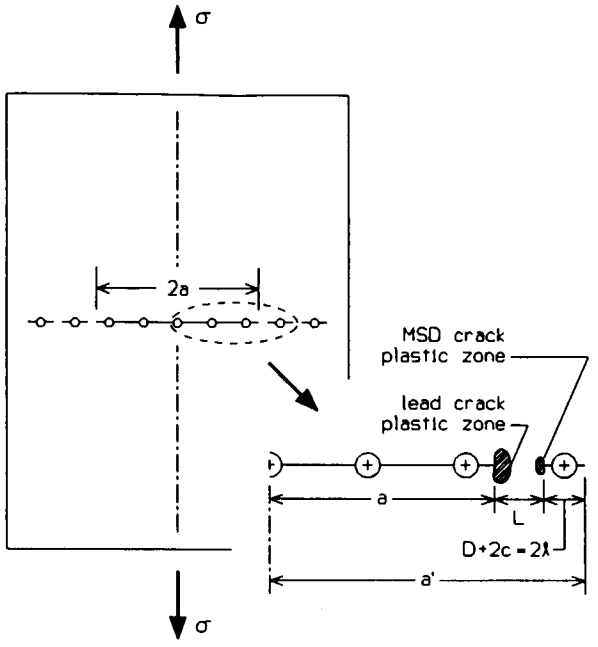

Figure 1. Panel configuration.

condition is denoted by σ_{LU} and is given by Equation 1, where β_a and β_ℓ are the geometric corrections to stress intensity for the lead crack and the adjacent MSD crack, respectively.

$$\sigma_{LU} = \sigma_{ys}\sqrt{\frac{2L}{a\beta_a^2 + \ell\beta_\ell^2}} \quad \text{where } \beta_a = \beta_{a/\ell}\beta_w\beta_S \text{ and } \beta_\ell = \beta_{\ell/a}\beta_B \tag{1}$$

In this equation, σ_{ys} is the yield strength; the terms $\beta_{a/\ell}$ and $\beta_{\ell/a}$ are the corrections resulting from two collinear cracks of unequal length (the lead crack and the adjacent MSD crack)[4]; β_W is the finite width correction; β_S is the correction for stiffeners[5]; $\beta_B=\beta_b(c/\ell)^{1/2}$ where β_b is the Bowie correction for open holes.

Two other stresses are of importance in the development of the improved model. These two stresses are the critical stresses as determined from brittle fracture and from net section yielding, and are given as follows:

$$\sigma_{LEFM} = \frac{K_c}{\sqrt{\pi a}\beta_a} \quad \text{and} \quad \sigma_{NSY} = \sigma_{ys}\frac{A_N}{A_G}$$

The quantities K_C, A_N, and A_G are the fracture toughness, the net cross sectional area at the cross section with the holes and cracks, and the gross cross sectional area, respectively. Another stress that needs to be defined is σ^*, which is the lower of the two stresses σ_{LEFM} and σ_{NSY}. The critical stress from testing is denoted as σ_{Test}. The modification referred to previously as linkup-mod1, or Mod1, is determined by displaying the previously defined stresses as shown in Figure 2. The plotted data shown in the figure have little scatter and can be represented by a single curve. The curve that fits the data is a power form of least squares from which the critical stress for Mod 1 can be expressed. When the data are represented by a single curve, the stress σ_{Test} becomes the critical stress for Mod 1, as given in Equation 2.

$$\frac{\sigma_c}{\sigma_{LU}} = 0.75\left[\frac{\sigma_{LU}}{\sigma^*}\right]^{-0.5} \quad \text{or} \quad \sigma_c = \frac{3}{4}\sqrt{\sigma_{LU}\sigma^*} \tag{2}$$

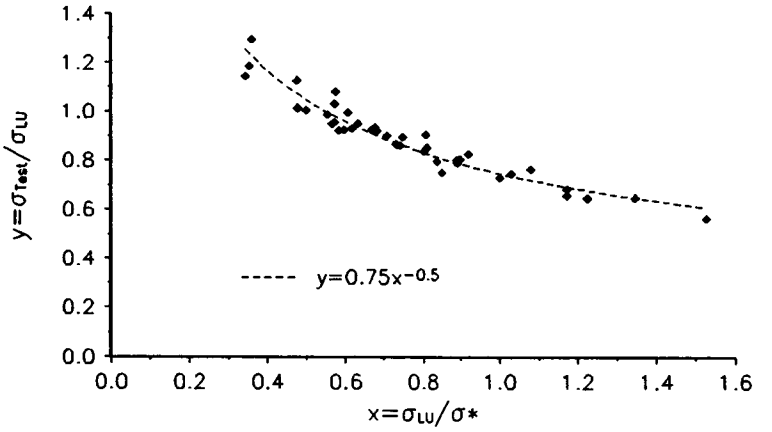

Figure 2. Power form correction used for Mod1.

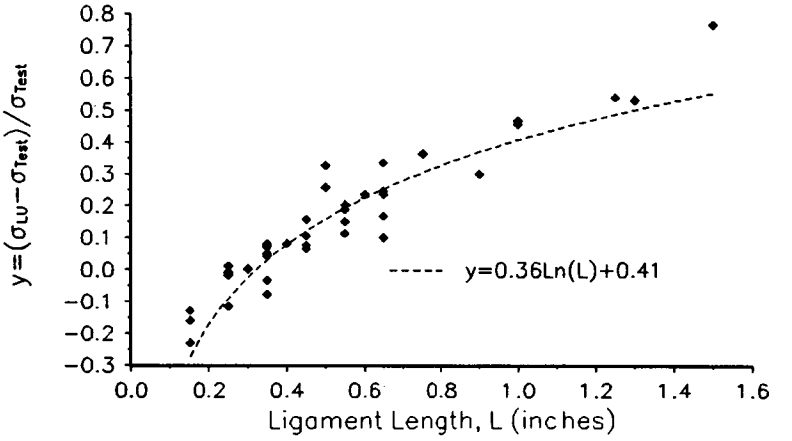

Figure 3. Natural log form correction used for Mod2.

After investigating a large amount of test data, it became apparent that the ligament size strongly influenced the linkup stress σ_{LU}. Therefore the data was displayed as illustrated in Figure 3, with the ligament size plotted on the horizontal axis, and the error between linkup stress and test value plotted on the vertical axis. This plot has more scatter when represented with a single curve than the previous plot shown in Figure 2. However, it was decided to represent this data with a single equation of the natural log form. When the data are represented by a single curve, the stress σ_{Test} becomes the critical stress for Mod 2, as given in Equation 3.

$$\frac{\sigma_{LU}-\sigma_C}{\sigma_C} = A\left[\ln(L)\right]+B \quad \text{or} \quad \sigma_C = \frac{\sigma_{LU}}{A\left[\ln(L)\right]+(B+1)} \tag{3}$$

If the stresses σ_c and σ_{LU} are in units of ksi and the ligament size is in inches, the values of the constants A and B are 0.36 and 0.41, respectively. Both of these models were developed from test values for a total of 40 different configurations of flat unstiffened panels with MSD cracks. The details for these panels are given in Table 1. Test values for nine of these configurations were obtained from the National Institute of Standards and Technology (NIST)[6], and nine more were obtained from Foster-Miller, Inc. (F-M)[7]. Test data for the other 22 configurations were obtained from testing at Wichita State University (WSU). The NIST panels were 90 inches wide, the Foster-Miller panels were 20 inches wide, while the Wichita State University panels were 24 inches wide. Both of the models (Mod1 and Mod2) were additionally validated with test data from 12 different stiffened panels. Details of the stiffened panels are given in Table 2.

TABLE 1. UNSTIFFENED PANEL CONFIGURATION

Panel ID	Source	MSD Type	Crack Type	W (inches)	t (inches)	D (inches)	a (inches)	c (inches)	L (inches)
1	NIST	hole	saw cut	90	0.04	0.221	10.00	0.14	0.25
2	NIST	hole	saw cut	90	0.04	0.221	7.00	0.09	0.30
3	NIST	hole	saw cut	90	0.04	0.221	2.80	0.19	0.40
4	NIST	hole	saw cut	90	0.04	0.221	7.70	0.09	0.60
5	NIST	hole	saw cut	90	0.04	0.221	9.50	0.14	0.75
6	NIST	hole	saw cut	90	0.04	0.221	3.80	0.19	0.90
7	NIST	hole	saw cut	90	0.04	0.221	10.75	0.14	1.00
8	NIST	hole	saw cut	90	0.04	0.221	10.75	0.14	1.00
9	NIST	hole	saw cut	90	0.04	0.221	5.00	0.09	1.30
10	WSU	hole	EDM	24	0.063	0.25	3.675	0.05	0.15
11	WSU	hole	EDM	24	0.063	0.25	3.575	0.05	0.25
12	WSU	hole	EDM	24	0.063	0.25	3.475	0.05	0.35
13	WSU	hole	EDM	24	0.063	0.25	3.325	0.20	0.35
14	WSU	hole	EDM	24	0.063	0.25	3.275	0.15	0.45
15	WSU	hole	EDM	24	0.063	0.25	3.225	0.10	0.55
16	WSU	hole	EDM	24	0.063	0.25	3.175	0.05	0.65
17	WSU	hole	EDM	24	0.063	0.25	4.675	0.05	0.15
18	WSU	hole	EDM	24	0.063	0.25	4.575	0.05	0.25
19	WSU	hole	EDM	24	0.063	0.25	4.475	0.05	0.35
20	WSU	hole	EDM	24	0.063	0.25	4.325	0.20	0.35
21	WSU	hole	EDM	24	0.063	0.25	4.275	0.15	0.45
22	WSU	hole	EDM	24	0.063	0.25	4.225	0.10	0.55
23	WSU	hole	EDM	24	0.063	0.25	4.175	0.05	0.65
24	WSU	hole	EDM	24	0.063	0.25	5.675	0.05	0.15
25	WSU	hole	EDM	24	0.063	0.25	5.575	0.05	0.25
26	WSU	hole	EDM	24	0.063	0.25	5.475	0.05	0.35
27	WSU	hole	EDM	24	0.063	0.25	5.325	0.20	0.35
28	WSU	hole	EDM	24	0.063	0.25	5.275	0.15	0.45
29	WSU	hole	EDM	24	0.063	0.25	5.225	0.10	0.55
30	WSU	hole	EDM	24	0.063	0.25	5.175	0.05	0.65
31	WSU	hole	EDM	24	0.063	0.25	6.325	0.20	0.35
32	F-M	slit	saw cut	20	0.04	-	4.00	-	0.35
33	F-M	slit	saw cut	20	0.04	-	3.80	-	0.45
34	F-M	slit	saw cut	20	0.04	-	1.60	-	0.50
35	F-M	slit	saw cut	20	0.04	-	2.50	-	0.50
36	F-M	slit	saw cut	20	0.04	-	3.70	-	0.55
37	F-M	slit	saw cut	20	0.04	-	1.60	-	0.65
38	F-M	slit	saw cut	20	0.04	-	3.60	-	0.65
39	F-M	slit	saw cut	20	0.04	-	3.00	-	1.25
40	F-M	slit	saw cut	20	0.04	-	1.50	-	1.50

W=panel width t=panel thickness D=hole diameter
a=lead crack half length c=MSD crack length L=ligament length

TABLE 2. STIFFENED PANEL CONFIGURATION

Panel ID	Source	MSD Type	Crack Type	W (inches)	t (inches)	D (inches)	a (inches)	c (inches)	L (inches)
1	WSU	hole	EDM	24	0.063	0.25	4.675	0.05	0.15
2	WSU	hole	EDM	24	0.063	0.25	4.575	0.05	0.25
3	WSU	hole	EDM	24	0.063	0.25	4.475	0.05	0.35
4	WSU	hole	EDM	24	0.063	0.25	4.275	0.15	0.45
5	WSU	hole	EDM	24	0.063	0.25	4.225	0.10	0.55
6	WSU	hole	EDM	24	0.063	0.25	4.175	0.05	0.65
7	WSU	hole	EDM	24	0.063	0.25	5.675	0.05	0.15
8	WSU	hole	EDM	24	0.063	0.25	5.575	0.05	0.25
9	WSU	hole	EDM	24	0.063	0.25	5.475	0.05	0.35
10	WSU	hole	EDM	24	0.063	0.25	5.275	0.15	0.45
11	WSU	hole	EDM	24	0.063	0.25	5.225	0.10	0.55
12	WSU	hole	EDM	24	0.063	0.25	5.175	0.05	0.65

μ = ratio of stiffener area to total area = 0.3 (ref. 5)

TEST DATA

A servo-hydraulic MTS testing machine was used to determine the linkup stresses for the 22 unstiffened panel configurations and the 12 stiffened configurations tested at WSU. Figure 4 shows an unstiffened test panel with test fixturing, and Figure 5 shows a stiffened panel. These 24-inch wide panels were 0.063 inches thick (2024-T3 clad) and 36 inches between test fixtures. Midspan fixtures were used to prevent buckling along the crack line, and heavy fixtures were used at each end to help distribute the load evenly across the width. The panels in figure 5 were stiffened on both sides of the panel with aluminum strips of 1.05 inches by 0.155 inches, resulting in μ=0.3 (ref. 5). The bay width was 12 inches and the 0.25-inch diameter steel stiffener bolts were centered one inch apart.

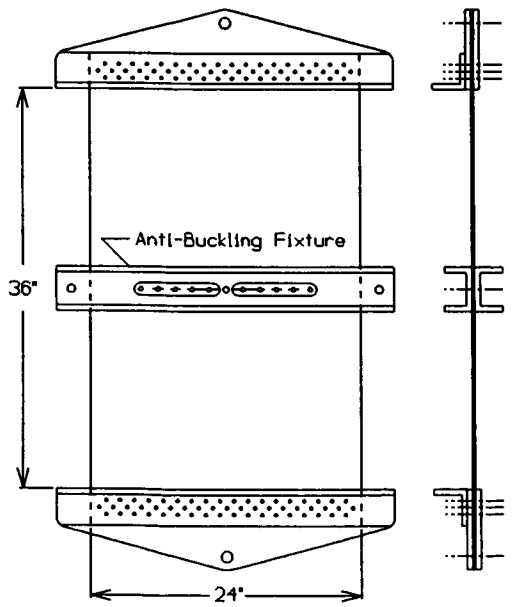

Figure 4. Unstiffened test panel.

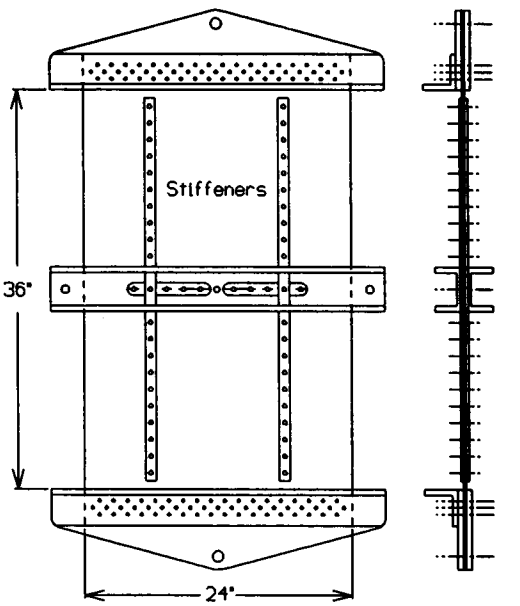

Figure 5. Stiffened test panel.

During the early stages of testing, both stroke control and load control were used, producing identical results. Thus, stroke control was used thereafter at a rate of 0.01 inches per minute. The man-made MSD cracks were produced by Electro Discharge Machine (EDM) with a 0.004 inch diameter wire resulting in actual crack widths of 0.005 inches. The saw cuts in the NIST[6] panels were 0.003 inches in width and those in the Foster-Miller[7] panels were 0.006 inches in width. Initially it was decided to test three panels of each configuration, however, the results were so consistent that this procedure was abandoned and each of the remaining panels was used for a different crack configuration. Tables 1 and 2 contain pertinent information for each panel, and Tables 3 and 4 include the test results and calculated stresses. Where duplicates were tested, the test value in Tables 3 and 4 represent the average value, however, the variation was less than one percent. Each panel was cut from an oversized aluminum sheet so that the tensile strength could be obtained from the excess material. Details of the information for the panels tested by NIST and Foster-Miller are in References 6 and 7, respectively.

RESULTS

The stresses for the unstiffened panels are given in Table 3 and illustrated in Figures 6 and 7. Figures 6 is a plot of panel identification number versus the linkup stress from physical testing, the stress calculated from the linkup model and the stress calculated from the linkup-mod1 model. Figure 7 is the same except the stress is calculated from the Mod2 model rather than the Mod1 model. In each figure the first nine ID's are the 90-inch panels tested by NIST, the next 22 ID's are the 24-inch panels from WSU, while the final nine ID's are the 20-inch panels from Foster-Miller. The NIST and the Foster-Miller panels are arranged in order of increasing ligament length. The WSU panels are arranged in groups of nominal lead crack length $2a_n$, and within each of these groups they are arranged in order of increasing ligament length. The symbol x represents the test values, the circles represents analytical results predicted by the linkup model, while the triangles represent analytical results determined from the Mod1 model in Figure 6 and the Mod2 model in Figure 7. The average difference between the test results and the results from the linkup model is 19.2%. The average differences between the test results and the results from the modified linkup models are 3.65% for the Mod1 model and 4.87% for the Mod2 model.

The stresses for the stiffened panels are given in Table 4 and illustrated similarly in Figure 8 for Mod1 and Figure 9 for Mod2. Again, the ID's are arranged first in groups of nominal lead crack length and within each of these two groups they are arranged in order of increasing ligament length. The average difference between the test results and the results from the linkup model is 14.4%. The average differences between the test results and the results from the modified linkup models are 4.39% for the Mod1 model and 2.65% for the Mod2 model. While the modified linkup models give excellent results for most all configurations, the linkup model is unconservative ($\sigma_{LU} > \sigma_{Test}$) for configurations with longer ligaments and is often conservative ($\sigma_{LU} < \sigma_{Test}$) for cases with shorter ligaments. For the Mod1 model, the stress σ^* is the lower of the two stresses σ_{LEFM} and σ_{NSY}. The fracture toughness of the material must be known to determine σ_{LEFM} and the yield strength must be known to determine σ_{NSY}. Because of the large width of the NIST panels (ID's 1 through 9), σ_{LEFM} was the lower of the two stresses. Because of the narrower widths of the other panels (24 inches and 20 inches), σ_{NSY} was either lower than or very close to σ_{LEFM}. For determining σ_{NSY}, yield strength testing was done in all cases, and 0.2% offset yield strength was used. The Mod2 model does not require a fracture toughness value, and is most likely only applicable for the material used in its development (2024-T3 aluminum). The stresses for panel ID's 13 through 16, 20 through 23, and 27 through 30 represent critical stresses as well as linkup stresses. It is significant to observe that the linkup model predicts unconservative values for these panels while the modified models are much more accurate and usually slightly conservative if anything.

TABLE 3. UNSTIFFENED PANEL STRESSES

Panel ID	σ_{ys} (ksi)	K_c (ksi $\sqrt{i\ n}$)	σ_{LEFM} (ksi)	σ_{NSY} (ksi)	σ^* (ksi)	σ_{LU} (ksi)	Mod1 σ_c (ksi)	Mod2 σ_c (ksi)	σ_{Test} (ksi)
1	50.0	101	16.32	36.13	16.32	9.03	9.11	9.44	8.92
2	50.0	101	20.20	40.91	20.20	12.24	11.80	12.07	12.20
3	50.0	101	31.84	44.91	31.84	21.68	19.70	19.59	20.00
4	50.0	101	19.75	40.58	19.75	17.59	13.98	14.23	14.20
5	50.0	101	17.61	33.91	17.61	17.62	13.21	13.47	12.90
6	50.0	101	28.25	44.47	28.25	30.47	22.00	22.30	23.40
7	50.0	101	16.56	33.07	16.56	19.40	13.45	13.86	13.20
8	50.0	101	16.56	35.85	16.56	19.40	13.45	13.86	13.30
9	50.0	101	25.11	40.02	25.11	33.79	21.85	22.77	22.00
10	47.7	104	25.73	27.72	25.73	9.74	12.33	12.29	11.58
11	47.7	104	27.55	28.09	27.55	13.97	14.86	14.61	14.09
12	47.5	104	28.57	28.37	28.37	17.45	16.69	16.40	16.27
13	42.5	100	27.01	24.77	24.77	14.75	14.33	13.86	13.67
14	41.9	100	28.27	24.97	24.97	17.66	15.75	15.43	15.96
15	42.4	100	28.97	25.88	25.88	20.71	17.36	17.13	17.41
16	42.5	100	29.78	26.50	26.50	23.79	18.83	18.85	19.22
17	42.2	100	21.08	23.32	21.08	7.56	9.47	9.53	9.80
18	42.2	100	22.62	23.71	22.62	10.71	11.68	11.20	12.09
19	42.2	100	23.37	24.04	23.37	13.34	13.24	12.54	13.77
20	41.9	100	22.91	21.83	21.83	12.48	12.38	11.73	11.94
21	41.6	100	23.95	22.22	22.22	15.03	13.71	13.13	14.09
22	42.2	100	24.59	24.18	24.18	17.66	15.50	14.61	15.33
23	42.6	100	25.15	25.31	25.15	20.30	16.93	16.08	17.37
24	47.9	104	18.87	21.82	18.87	7.47	9.58	9.42	8.56
25	47.9	104	20.23	22.20	20.23	10.56	11.48	11.04	10.73
26	47.7	104	20.93	22.55	20.93	13.15	12.91	12.36	12.14
27	41.8	100	19.74	19.21	19.21	10.86	10.84	10.21	10.33
28	41.6	100	20.63	19.63	19.63	13.07	12.02	11.42	12.11
29	42.0	100	21.02	20.34	20.34	15.18	13.18	12.56	13.62
30	42.2	100	21.60	22.81	21.60	17.39	14.53	13.78	15.77
31	41.8	100	17.08	16.63	16.63	9.54	9.45	8.97	10.33
32	43.7	103	25.50	23.57	23.57	14.85	14.03	13.95	14.13
33	43.7	103	25.99	22.70	22.70	16.79	14.64	14.67	14.50
34	43.7	103	41.98	29.68	29.68	26.45	21.02	22.45	21.00
35	43.7	103	32.20	24.01	24.01	20.42	16.61	17.33	15.38
36	43.7	103	26.74	20.95	20.95	19.28	15.08	15.95	16.00
37	43.7	103	43.60	32.30	32.30	33.26	24.58	26.35	24.88
38	43.7	103	27.27	25.75	25.75	21.55	17.67	17.07	17.25
39	43.7	103	31.14	28.37	28.37	34.72	23.54	23.60	22.50
40	43.7	103	45.25	32.74	32.74	49.99	30.34	32.68	28.25

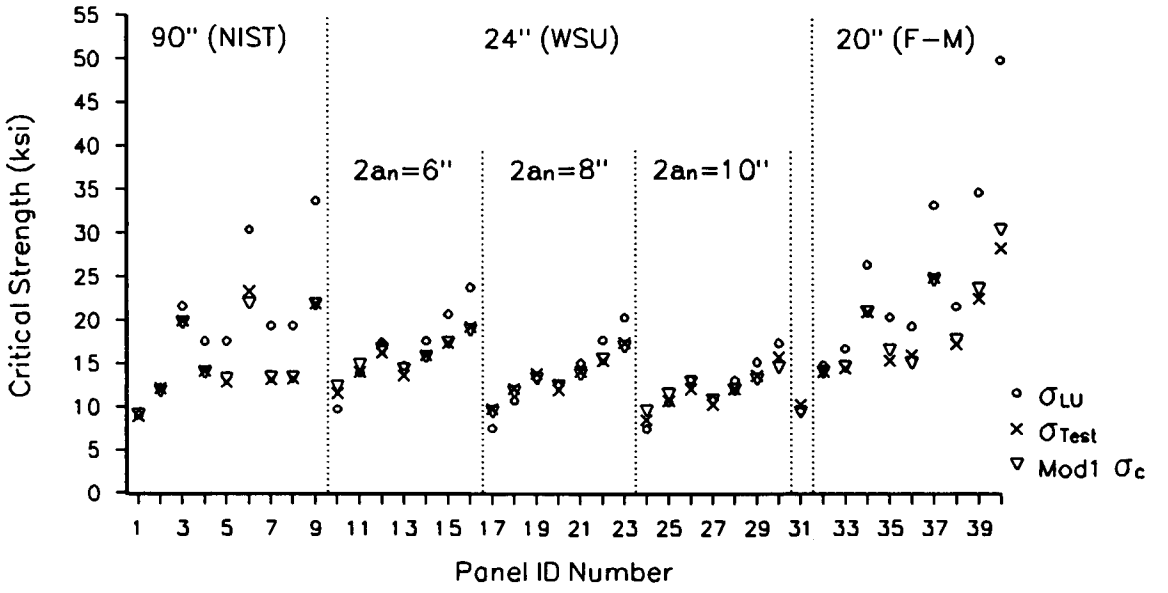

Figure 6. Unstiffened panel stresses compared to Mod1.

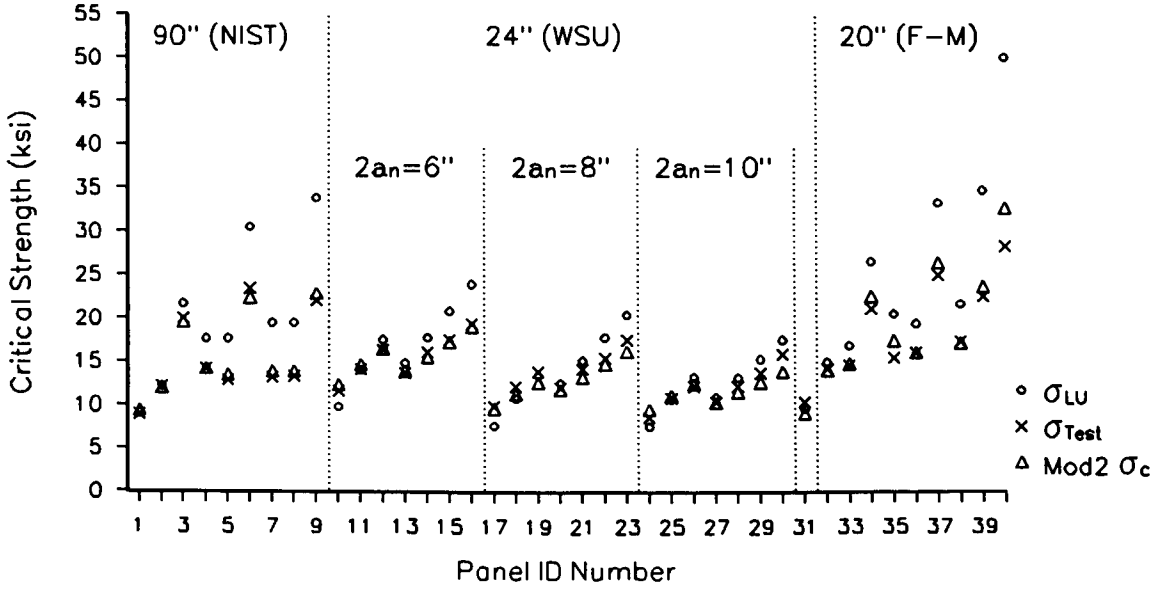

Figure 7. Unstiffened panel stresses compared Mod2.

TABLE 4. STIFFENED PANEL STRESSES

Panel ID	σ_{ys} (ksi)	K_c (ksi $\sqrt{in}$)	σ_{LEFM} (ksi)	σ_{NSY} (ksi)	σ^* (ksi)	σ_{LU} (ksi)	Mod1 σ_c (ksi)	Mod2 σ_c (ksi)	σ_{Test} (ksi)
1	43.0	100	24.24	26.83	24.24	8.50	10.76	10.72	10.60
2	43.0	100	25.51	27.24	25.51	12.02	13.13	12.57	12.61
3	43.0	100	26.19	27.58	26.19	14.96	14.84	14.06	14.49
4	43.0	100	26.38	27.29	26.38	16.81	15.79	14.69	13.84
5	43.0	100	26.97	27.98	26.97	19.50	17.20	16.13	16.05
6	43.0	100	27.45	28.65	27.45	22.12	18.48	17.53	17.72
7	43.0	100	25.88	22.88	22.88	8.62	10.53	10.87	10.83
8	43.0	100	26.54	23.34	23.34	12.09	12.60	12.64	12.86
9	43.0	100	26.57	23.80	23.80	14.84	14.10	13.95	14.08
10	43.0	100	25.80	23.89	23.89	16.19	14.75	14.14	13.96
11	43.0	100	26.09	24.51	24.51	18.67	16.04	15.44	16.34
12	43.0	100	26.37	25.27	25.27	21.11	17.32	16.73	18.54

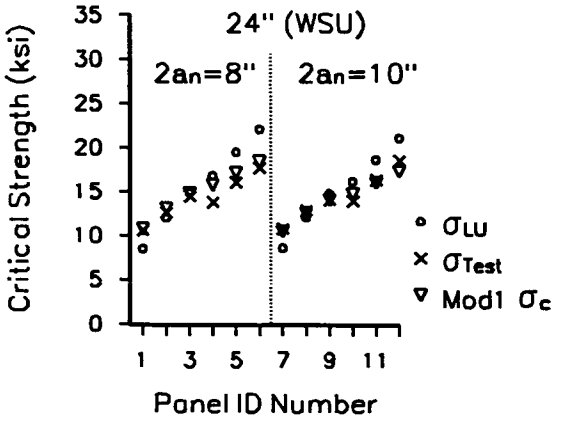

Figure 8. Stiffened panel stresses compared to Mod1.

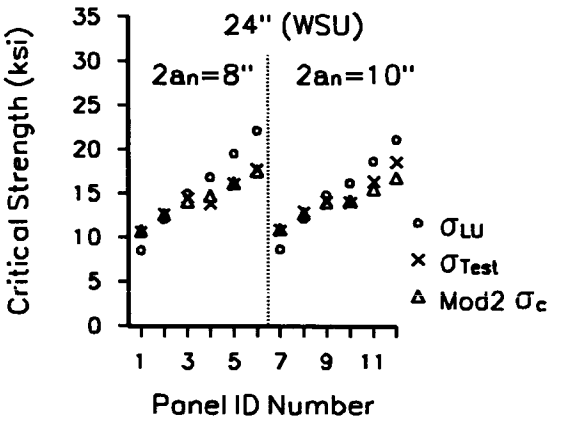

Figure 9. Stiffened panel stresses compared to Mod2.

CONCLUSIONS

The original linkup model is accurate for predicting the critical strength for certain crack configurations, but highly inaccurate for others. It appears to give conservative results for configurations with short ligaments and unconservative results for configurations with long ligaments. However, the improved models of Equations 2 and 3 give accurate results for a large envelope of configurations covering a variety of panel widths and thicknesses, lead crack lengths, MSD crack lengths, and ligament lengths for both unstiffened and stiffened panels.

ACKNOWLEDGEMENTS

This work was sponsored by the industry members of the Aircraft Design and Manufacturing Research Center of Wichita State University, Wichita, Kansas. The material for the aluminum panels was donated by Alcoa Aerospace Center, Hutchinson, Kansas, and EDM cracks were produced by the Materials Testing Laboratory of the Boeing Company, Wichita, Kansas. Their support is greatly appreciated.

REFERENCES

[1]T. Swift, "Widespread Fatigue Damage Monitoring Issues and Concerns," 5th International Conference on Structural Airworthiness of New and Aging Aircraft, Hamburg, Germany, June 1993.

[2]B. Smith, J. Camenzind, R. Myose, P. Saville, A. Mouak, W. Horn, "The Effect of Multiple Site Damage on the Critical Strength of Aluminum Panels," Proceedings of the 19th Southeastern Conference on Theoretical and Applied Mechanics, Deerfield Beach, FL, May 1998.

[3]B. Smith, P. Saville, A. Mouak, R. Myose, W. Horn, "A Further Study on the Effect of Multiple Site Damage on the Critical Strength of Aluminum Panels," Proceedings of the 12th Engineering Mechanics Division Conference of ASCE, La Jolla, CA, May 1998.

[4]D.P. Rooke and D.J. Cartwright, "Compendium of Stress Intensity Factors," London, Her Majesty's Stationary Office, 1976.

[5]C.C. Poe, Jr., "Stress Intensity Factor for a Cracked Sheet with Riveted and Uniformly Spaced Stringers," NASA Langley Research Center, NASA TR-T-356, May 1971.

[6]R. Fields, S. Low III, D. Harne, T. Froecke, "Fracture Testing of Large-Scale Thin-Sheet aluminum Alloy," National Institute of Standards and Technology, NISTIR 5661, May 1995.

[7]D. Thompson, D. Hoadley, J. McHatton, "Load Tests of Flat and Curved Panels with Multiple Cracks," Foster-Miller, Inc. (prepared for FAA), September 1993.

CORROSION PILLOWING CRACKS IN FUSELAGE JOINTS

Nicholas C. Bellinger, Jerzy P. Komorowski and Ron W. Gould
National Research Council Canada
Institute for Aerospace Research
Structures, Materials and Propulsion Laboratory
Bldg. M-14, Montreal Road
Ottawa, Ontario, Canada K1A 0R6
Tele : (613)993-2410
Fax: (613)952-7136
E-mail: nick.bellinger@nrc.ca

ABSTRACT

In a previous study carried out at the National Research Council Canada, pillowing in a fuselage lap joint caused by the presence of corrosion products was shown to result in a stress gradient through the skin thickness. This gradient led to a very high stress along the faying surface of the outer skin and a decreased stress on the outer surface. Consequently, it was shown that corrosion pillowing could cause the formation of semi-elliptical cracks with a high aspect ratio. In recent tear-down inspections, these types of cracks have been found on the faying surfaces of disassembled corroded circumferential and longitudinal lap joints. These joints were obtained from both retired and operational aircraft. The majority of the cracks discovered had not penetrated through to the surface, although some had lengths in excess of 6.35 mm (0.25 in.). All the fracture surfaces showed extensive intergranular cracking with numerous secondary cracks. Fatigue striations were observed on some of the crack surfaces. None of the cracks were found using conventional nondestructive inspection techniques typically used for lap splice inspection.

1. INTRODUCTION

Over the past few years, the National Research Council Canada (NRCC) has been carrying out research to determine the effect that corrosion pillowing has on the structural integrity of fuselage lap joints. Pillowing is the term used to describe the out-of-plane deformations that occur when corrosion products build-up between lap joint skins. A chemical analysis of the corrosion products found a mix of oxides, primarily aluminum oxide trihydrate[1] with a molecular volume ratio relative to the alloy from which it originated of 6.45. It is this high molecular volume ratio that is responsible for the out-of-plane deformations of riveted skins. Numerical studies have shown that pillowing can significantly alter the stress state in joints[2,3,4] and depending on its distribution and severity, the maximum stress could shift to other locations. These locations could include second or third skin layers and previously non-critical rivet rows which are typically not subject to regular inspections for cracks. In a preliminary fracture mechanics study carried out at NRCC using finite element techniques, stress intensity factors were calculated for straight fronted through-the-thickness cracks of different lengths[5]. Cracks under the rivet head were not examined in this study. The results indicated that corrosion pillowing can significantly increase the stress intensity factor for the crack edge along the skin faying surface with a concurrent decrease on the opposite side. This suggests that a crack could grow more rapidly along the faying surface than through the skin thickness resulting in a semi-elliptical crack front with a high aspect ratio[5]. Although these types of cracks could initiate due to fatigue, given the presence of a corrosive medium in a high-sustained stress area, environmentally assisted cracking may be the dominant mechanism in this situation[6]. Based on typical design stresses in a lap joint, corrosion with as little as 4% thickness loss

could cause local stress increases that would result in very early crack initiation. Also, high aspect ratio cracks would make detection difficult because they do not break through the exterior surface until late in the growth phase. Since these types of cracks are difficult to detect, the risk of in-service failure increases. This increased risk is particularly significant if corrosion pillowing occurs in an area previously considered non-critical, where inspections are not carried out on a regular basis.

This paper presents the preliminary results of a fractographic investigation of cracks found in corroded lap joints. The fracture surfaces of all the cracks examined thus far consisted mainly of intergranular cracking with numerous secondary cracks and all showed evidence of corrosion. The majority of the cracks found had not penetrated through the thickness, although some had lengths greater than 6.35 mm (0.25 in.).

2. PILLOWING CRACKS

NRCC has a large collection of corroded and non-corroded fuselage lap joints from both retired and operational aircraft. A number of joints were inspected using D Sight™, an enhanced optical nondestructive inspection technique[7] and then disassembled to quantify the level of corrosion detected. During specimen disassembly, a number of corroded joints were found to contain cracks where corrosion pillowing was the highest. These cracks have been found in the first and second layer skins, in longitudinal and circumferential joints and in both retired and operational aircraft. The majority of the cracks, which will be referred to "pillowing cracks", had not penetrated through the thickness and were not detected using conventional nondestructive inspection (NDI) techniques, such as eddy current. Table 1 lists the types of aircraft in which cracks have been found thus far, along with the number of hours/cycles for each aircraft. Also included in the table are the locations of the cracks and the approximate date when the aircraft was withdrawn from use (WFU) as well as the date when the joint was cut out (CUT).

TABLE 1. RECORDED INCIDENCES OF PILLOWING CRACKS

Type of Aircraft	Hours / Cycles	Location of crack	Layer	WFU / CUT
L1011	38,040 / 31,370	33R / BS589-609	First	Dec. 93 / Sept. 93
B727-235	55,640 / 48,660	4R / BS1100	Second	Sept. 92 / May 93
B727-200	D Check	S30 / BS1090	First	In service / Aug 95
B727-100	61,890 / 54,150	S19R / BS600-640	Second	July 94 / July 96
B727-90C	72,400 / 56,700	S19-26L / BS440	First	In service / Oct 95
B727-235	56,870 / 49,530	S19R / BS700-720	First	Mar 92 / Feb 93
A300[8]	10,400 / 6,940	S31L / FR26-31	First	In service / Oct 81
B727-295	61,854 / 55,465	S19R / BS660-680	First	Jan 90 / Feb 98
B727-295	63,349 / 55,676	S19R / BS720A-720B	First	Aug 89 / Feb 98

As can be seen from Table 1, cracks have been found in a number of different locations on various aircraft with diverse operating lives. The A300 cracking incident was found from a service bulletin issued in 1982 by Airbus Industrie[8]. This bulletin reported the existence of severe corrosion in a lap joint, which after being removed from the aircraft was found to contain a number of small cracks around the rivet holes. To give an overview of the locations where pillowing cracks have been found, the contents of Table 1 were mapped onto the generic fuselage diagram (turtle diagram) shown in Figure 1. This figure demonstrates that these cracks are randomly distributed throughout a fuselage.

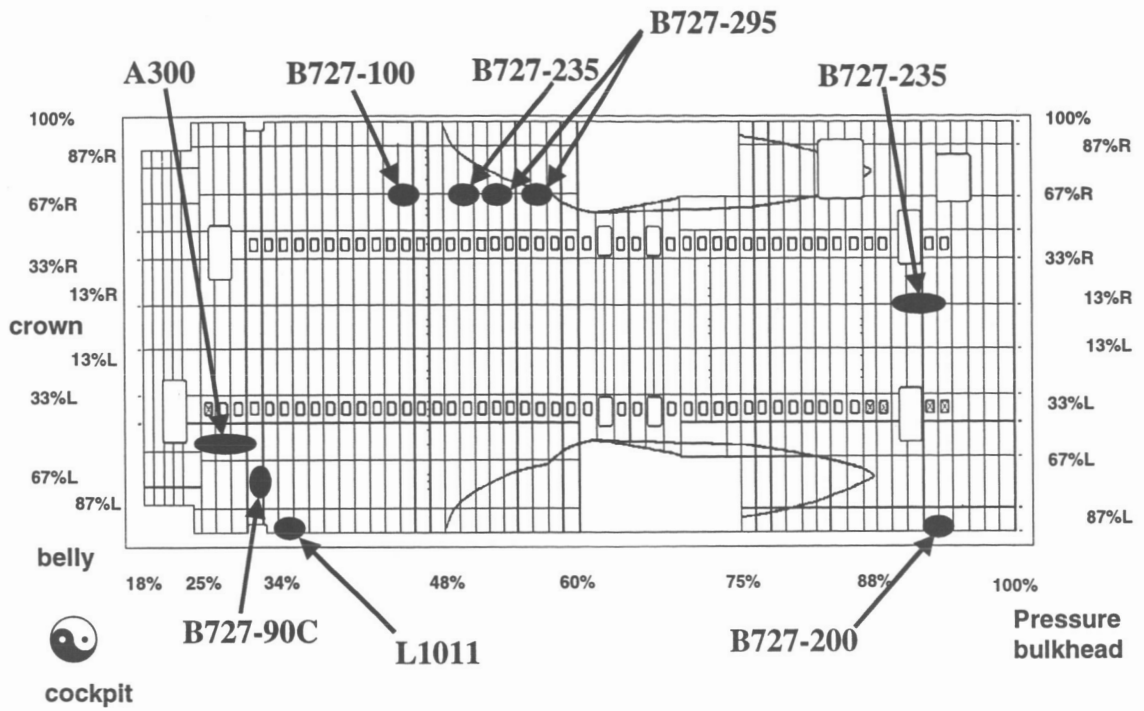

Figure 1. Turtle diagram of a generic fuselage showing locations of pillowing cracks.

An example of pillowing cracks contained within a corroded lap joint is shown in Figure 2. This figure shows the presence of multiple cracks at each rivet hole that is located in the area of maximum pillowing, which is characteristic of these types of cracks. Only one crack in this joint had penetrated the skin thickness, which was due to the fact that it had grown to the edge of the sheet.

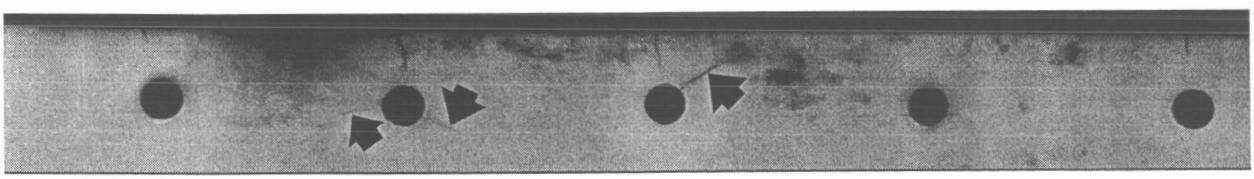

Figure 2. X-ray image of a retired B727-200 lap joint showing cracks in the area of maximum pillowing (second layer cracking). Darker regions indicate thickness loss due to corrosion.

2.1 STRESS STATE IN A CORRODED LAP JOINT

Finite element analysis indicated that corrosion pillowing alters the stress state in lap joints[3,5]. A plot of the principal stress in a lap joint subjected to both hoop stress and rivet interference is shown in Figure 3. As can be seen from this figure, the outer surface of the countersunk skin is subjected to tensile stresses. However, when corrosion is introduced, the resulting pillowing significantly decreases the stress on the outer surface while increasing the stress on the faying surface, Figure 4. In fact, for the amount of corrosion simulated for this analysis (10% thickness loss in the outer skin), a compressive stress is predicted in the immediate vicinity of the rivet hole on the outer surface[9]. Included in this figure is the approximate location of the neutral axis. It should be pointed out that the maximum depth to which a faying surface crack can grow would be limited to some level below this axis due to the fact that small positive stress intensity factors would not be sufficient to propagate a crack[4].

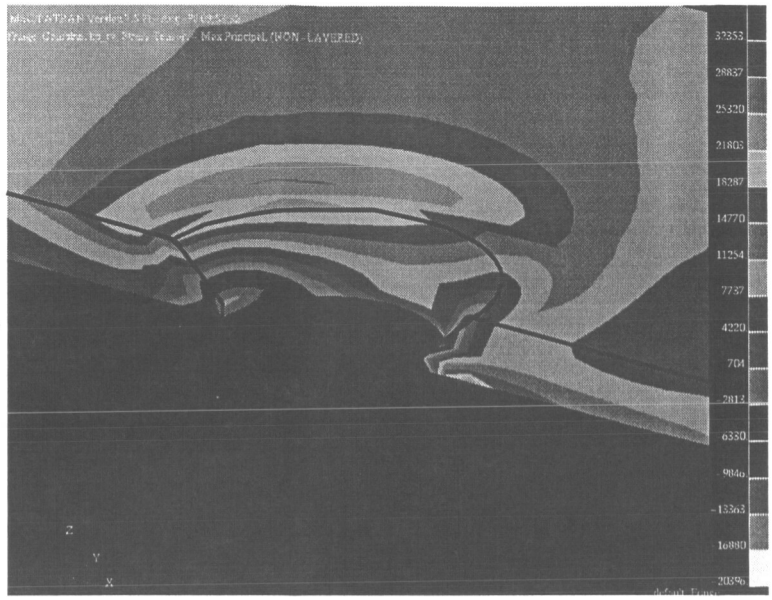

Figure 3. Stress plot of non-corroded lap joint. Loading includes hoop stress and rivet interference.

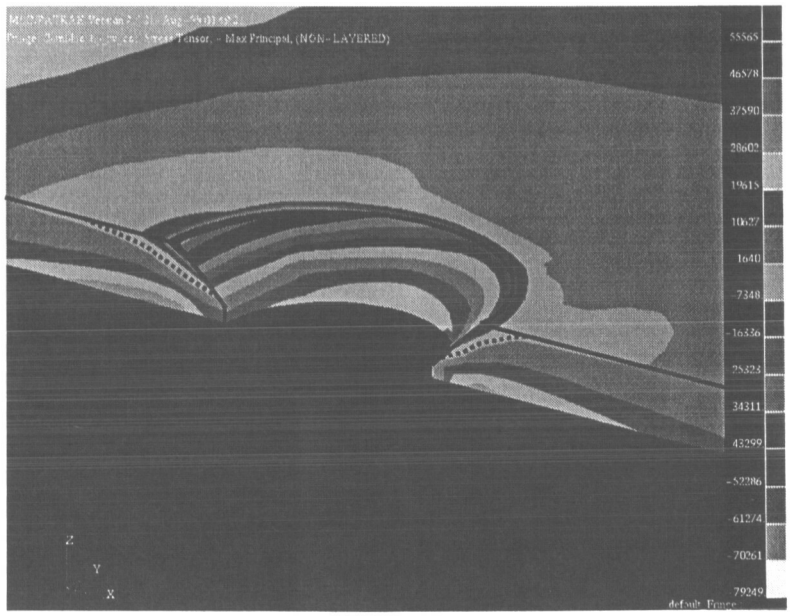

Figure 4. Stress plot of corroded lap joint. Dotted lines indicate approximate location of neutral axis (10% thickness loss in outer skin). Loading includes hoop stress, rivet interference and corrosion pillowing.

2.2 FAILURE INVESTIGATION

An investigation is being carried out to determine the fracture mode for pillowing cracks. In this investigation some of the corroded lap joints from Table 1 are being disassembled, cleaned and the cracks pried open. The cleaning process was specifically developed by NRCC to remove the corrosion products from the joint without damaging the parent material (Al 2024-T3). So far, five cracks from two aircraft have been examined using scanning electron microscopy, three from B727-90C, one of which was

through the thickness and two from an L1011. The dimensions of the cracks along the faying surface, a, and through the thickness, b, are given in Table 2 along with the approximate crack shape. The average thickness loss for the B727-90C joint was less than 8% in a 0.991 mm (0.039 inch) thick skin whereas for the L1011, it was 14% in a 1.65 mm (0.065 inch) thick skin. It should be noted that the corrosion in the L1011 joint was confined to a very localized area and it is unlikely that this damage would have been detected under normal maintenance procedures.

TABLE 2. DIMENSIONS OF PILLOWING CRACKS

Aircraft Type	Faying surface, a, mm (in.)	Through the thickness, b, mm (in.)	Ratio (a/b)	Approximate crack shape
B727-90C	7.125 (0.281)	0.991 (0.039)	7.16	
	2.692 (0.106)	0.891 (.035)	3.02	
	5.876 (0.231)	0.336 (0.013)	17.5	
L1011	10.5 (0.413)	0.432 (.017)	24.3	
	6.431 (0.253)	0.574 (.023)	11.2	

As can be seen from Table 2, the majority of the cracks have very high aspect ratios as was predicted by finite element analysis[5]. The cracks in the B727-90C joint were all located at a single hole while the ones from the L1011 joint came from two of the holes that surrounded the maximum pillowing. It should be pointed out that very little corrosion damage (such as pitting) or fretting damage was present around the rivet holes as shown in Figure 5. This is understandable since the amount of corrosion products in the two joints was small and thus unable to sufficiently overcome the clamping force under the rivet heads to allow a large amount of the corrosive medium to penetrate. This restriction would limit the corrosion damage around the rivets. There was no fretting damage because the joints contained an adhesive layer that prevented the two faying surfaces from contacting.

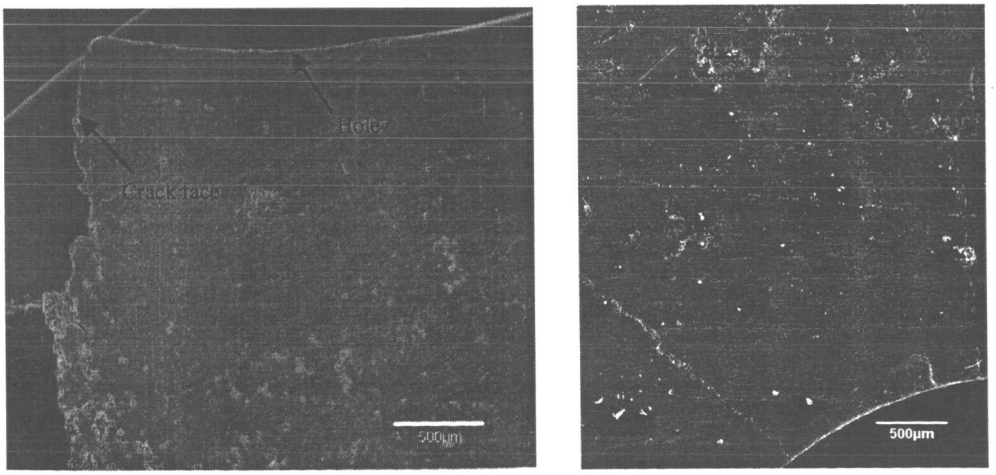

a) B727-90C faying surface

b) L1011 faying surface

Figure 5. Scanning electron micrograph showing little corrosion and fretting damage around rivet holes.

2.2.1 B727-90C Cracks

The pillowing cracks in the B727-90C aircraft occurred in a circumferential butt joint that consisted of two adjacent skins 1.02 mm (0.04 inch) thick with 0.51 mm (0.02 inch) thick shim strips located between

the skins and the frame as shown in Figure 6a. The cracks were discovered when an unexpected link-up of two adjacent tunneling cracks occurred while the panel was being wedged open to locate corrosion damage during a routine maintenance activity. The location of these two cracks, along with the cracks that were pried open are shown on the x-ray thickness map in Figure 6b. This thickness map gives an indication of the severity of the corrosion that was present in the skin. The darker areas indicate where thickness loss occurred due to corrosion damage. Although this skin only had an average thickness loss of less than 3%, the shim strip was very corroded and thus was the main contributor to the corrosion pillowing that occurred in the joint (second layer corrosion) and consequently the cause of the increased stress. The actual percentage thickness loss was not determined for the shim because the operator inadvertently discarded it.

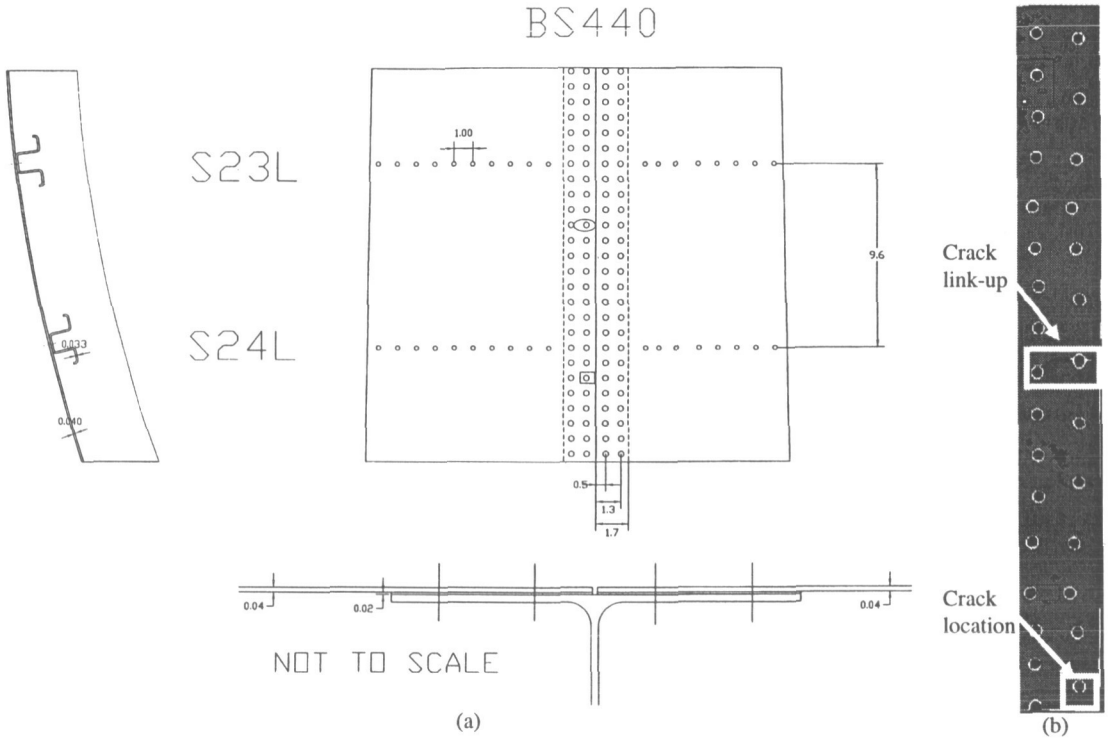

Figure 6. B727 fuselage butt joint; a) Schematic showing joint configuration and b) X-ray thickness map showing thickness loss and crack locations (Average thickness loss in outer skin <3%).

An optical image of the cracks that were pried open is shown in Figure 7a. This figure clearly shows the characteristic multiple cracks, which have formed a star shape pattern suggesting that corrosion pillowing was present around the entire hole. The crack growth through the thickness was not perpendicular to the surfaces but occurred at an angle as shown in Figure 7b. These angles ranged from 11.3° to 32° from the perpendicular for the three cracks. A scanning electron micrograph of the crack that has an aspect ratio of 17.5 is shown in Figure 7c. This crack has the highest aspect ratio of all the cracks at this hole. As can been seen in this figure, there are three distinct regions on the fracture surface. Regions i and ii occur on different fracture planes, which suggests two initiation sites, while Region iii was on the same plane as Region ii but contained exfoliation. This exfoliation appears to follow the approximate boundary between the clad layer and the parent material. The presence of the clad layer on the faying surface was verified using electron dispersive spectroscopy (EDS). Exfoliation is not unique to this particular crack and has been observed in other lap joints as shown in Figure 8.

All the surfaces showed extensive intergranular cracking with numerous secondary cracks as shown in Figures 9a and 9b. Upon closer examination of the fracture surfaces, fatigue striations were found (Figure

9c), which suggests that the cracks were growing under fatigue loading. However, striations were found only along the crack front where very little corrosion was present.

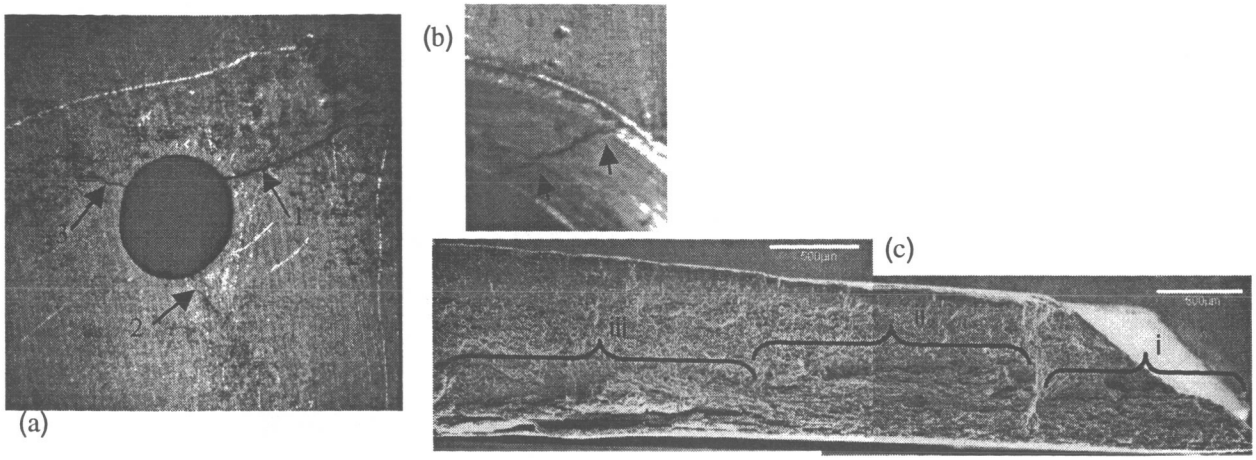

Figure 7. Images of the pillowing cracks found in the B727-90C joint. a) Optical image showing all 3 cracks, b) Optical image of crack 2 showing typical angled crack growth, that is not perpendicular to hoop stress loading and c) Scanning electron micrograph of crack 3 showing three distinct fracture regions.

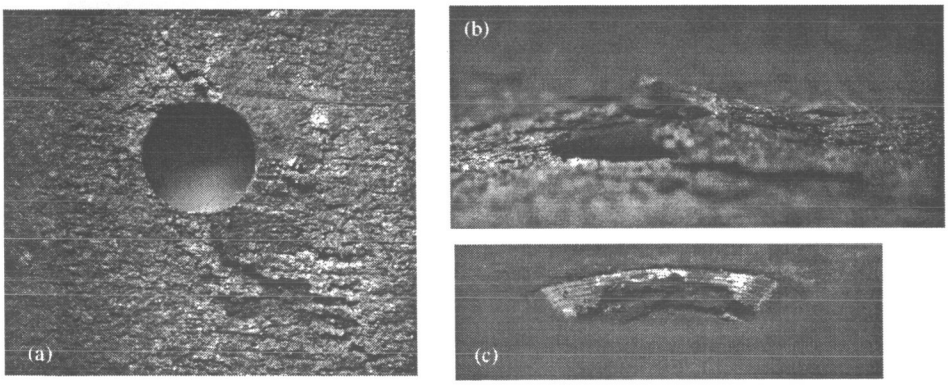

Figure 8. Optical image showing exfoliation around rivet hole in the B727-295 joint; a) Top view of exfoliated hole, b) Angled view showing exfoliation and c) View of countersink showing significant damage.

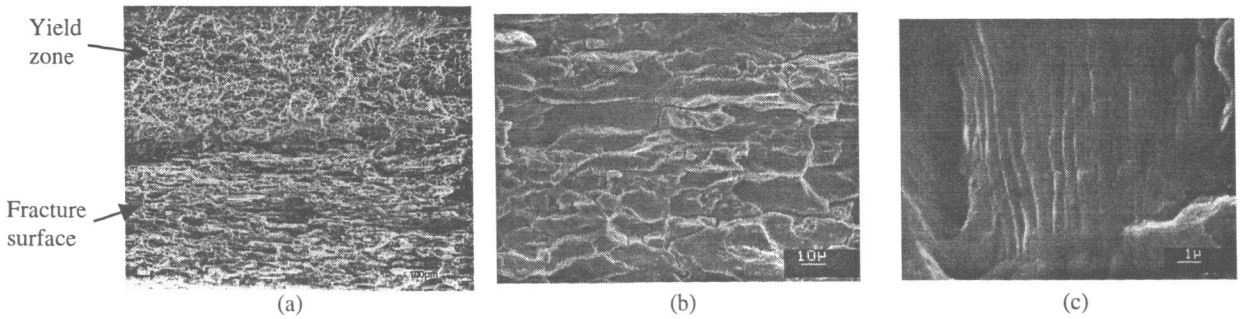

Figure 9. Scanning electron micrographs of fracture features from the B727-90C joint; a) Typical intergranular fracture, b) Close-up of intergranular fracture with secondary cracking common to all fracture surfaces, c) Typical fatigue striations that were found in cracks 2 and 3 (refer to Figure 7a).

2.2.2. L1011 Cracks

The pillowing cracks in the L1011 aircraft were found adjacent to a longitudinal butt joint, which consisted of two skins approximately 1.651 mm (0.065 inch) thick with a beauty strip on top as shown in Figure 10a. The pillowing cracks occurred outside of the "beauty" strip. Two cracks were pried open, which were located at two separate holes as shown in Figure 10b. As can be seen from Figure 10b, the star shape pattern cracks only occurred at one of the rivet holes. All the other holes contained cracks only on one side indicating that the increased stress caused by the pillowing only affected the region between these four holes.

Given the skin thickness and the fact that the first crack examined, crack 1 in Figure 10b, had not penetrated into the countersink, it was decided to grind some of the material away from the outer surface of the skin (countersink side). Although this grinding was necessary to make prying open of the crack easier, it was feared that since these types of cracks appear to initiate due to environmentally assisted cracking, the crack depth could increase away from the rivet hole given the longer exposure time to the corrosive medium. This increase in depth was confirmed after the crack was pried open, as shown in Figure 11. As can be seen from this figure, a small portion of the crack front may have been lost due to the grinding action in Region ii. Included in this figure is an indication of the location of the countersink and the thickness of the skin (black line). The possibility of an increase in crack depth away from the rivet hole is the reason why not as much material was removed for the second crack, which resulted in the entire crack front being exposed. It should be noted that the depth of the second crack did not vary as much as the first one (that is the crack depth was relatively constant).

The crack labeled 1 in Figure 10b had four distinct regions, each having a different crack depth as shown in Figure 11. These regions suggest the presence of four initiation sites, which could not be easily identified. The fracture surface of crack 2, on the other hand, contained only one fracture plane. However, there was a large secondary crack present half way through the crack depth, which suggests that crack branching had occurred.

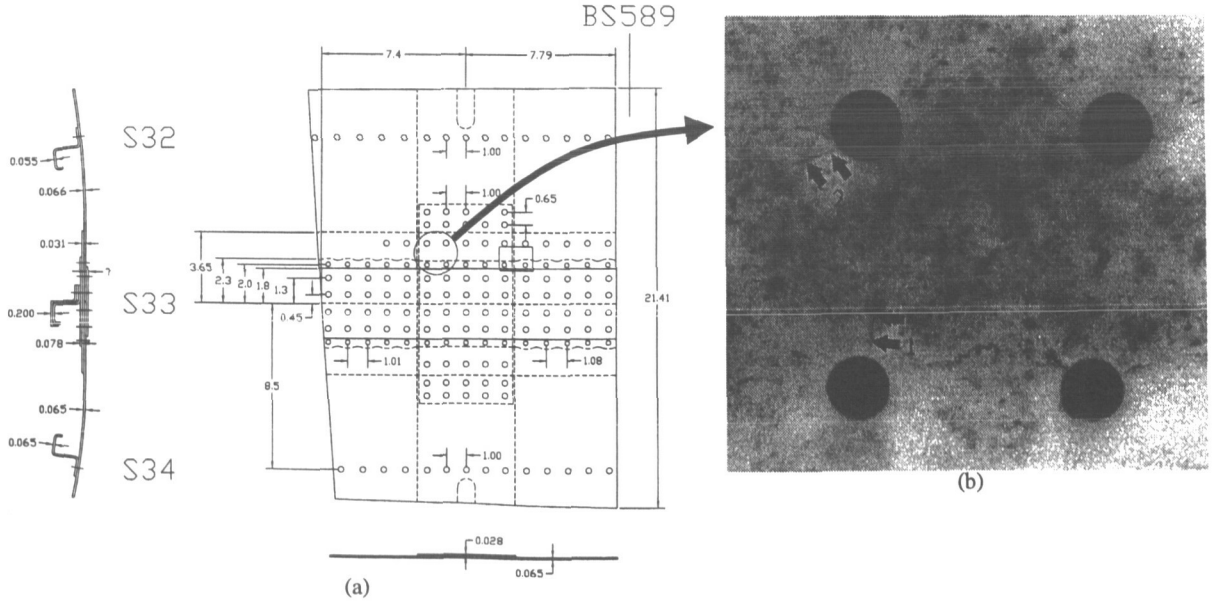

Figure 10. L1011 longitudinal butt joint; a) Schematic showing joint configuration, b) X-ray image showing location of cracks that were pried open.

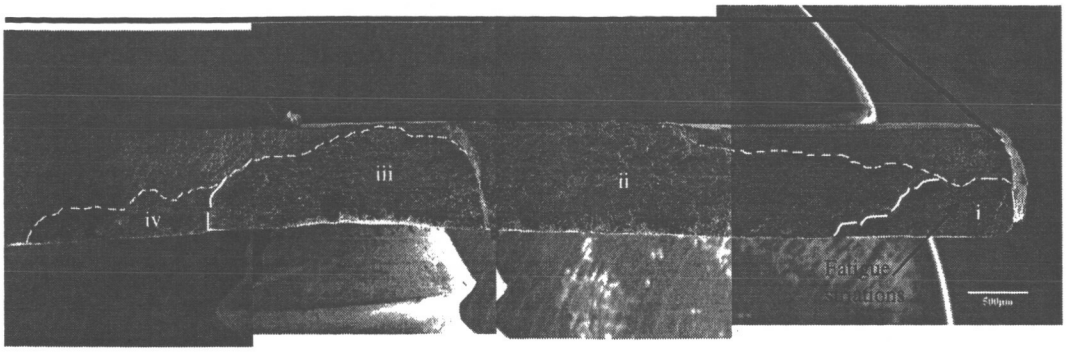

Figure 11. Scanning electron micrograph of fracture surface of crack 1 from Figure 10b. The black line indicates the full thickness of the sheet. The white dashed lines indicate the crack fronts.

The fracture characteristics were similar to those from the B727-90C joint in that the through-the-thickness penetration was angled, Figure 12a, and all fracture surfaces showed extensive intergranular cracking, Figure 12b. The penetration angle was 36° for the first crack and 21° for the second. The first crack also showed the presence of fatigue striations, Figure 12c, particularly for that portion of the crack under the countersink. The second crack did not contain any fatigue striations but again showed intergranular cracking. A possible explanation for the absence of fatigue striations is the close proximity of a longer, more pronounced crack, which may have been the dominant crack.

An EDS examination of the skin surfaces revealed that cladding was not present on the faying surface. This joint was bonded and it has been assumed that the cladding layer was either removed or was not initially present in order to enhance the bond quality. It should also be pointed out that this joint was more difficult to disassemble than the one from the B727 because the bond was still strong.

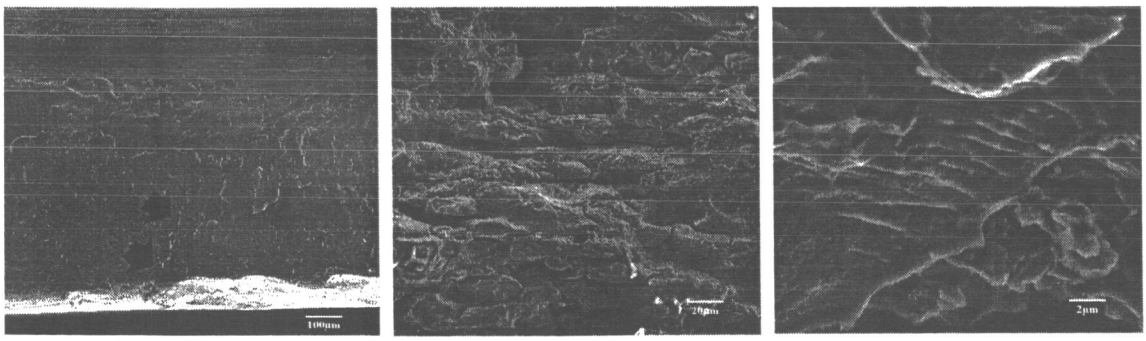

(a) (b) (c)

Figure 12. Scanning electron micrographs of fracture features from the L1011 joint; a) Angled crack growth through the thickness, b) Intergranular cracking with numerous secondary cracking and c) Fatigue striations under the countersink.

3. CONCLUSIONS

The high aspect ratio cracks predicted in a previous numerical study have been found in both retired and operational circumferential and longitudinal lap joints containing corrosion. The results from this investigation thus far can be summarized as follows:

- Pillowing cracks have a tendency to occur in groups (that is, star shape pattern cracks at more than one hole) and do not normally penetrate through-the-thickness. Some of the crack lengths were

greater than 6.35 mm (0.25 in.). The cracks normally occur on the side of the hole that is affected by the increased stress due to the pillowing and the cracks tend to propagate into the pillowed region.

- All the cracks that have been pried open were corroded and showed extensive intergranular fracture with numerous secondary cracking.
- The crack growth through the skin thickness was not perpendicular to the faying and outer skin surfaces but occurred at an angle.
- A number of cracks had multiple initiation sites. Although these sites could not be determined, they were evident due to the different crack planes that were present.
- Some of the fracture surfaces contained fatigue striations near the crack edge where corrosion was light. More cracks from different joints will be pried open to obtain further evidence for possible corrosion fatigue interaction.

Although this investigation is continuing, support is evolving to explain the presence of these types of cracks. Given that these cracks have only been found in areas where corrosion pillowing is present and that they propagate into the pillowed region, it is highly unlikely that they have initiated and grown due to fatigue loading. A more likely explanation is that they initiated and grew due to environmentally assisted cracking, since there is a corrosive medium present in a high-sustained stress region. Proof for this scenario is shown in the fracture characteristics; intergranular cracking and angled crack growth through the thickness. The presence of striations along some of the crack fronts suggests that once these cracks initiate, they could grow under fatigue loading.

4. ACKNOWLEDGEMENTS

The authors would like to thank Mr. A. Marincak and Mr. A. Othman for their technical assistance on joint disassembly and specimen preparation. They would also like to thank Mr. T. Chapman for his technical assistance on the x-ray mapping procedure. This work is being carried out under partial funding from the Department of National Defence through AVRD and the United States Air Force Corrosion Program Office through NCI Information Systems, Inc.

5. REFERENCES

1. S. Krishnakumar, J.P. Komorowski and I. Sproule, "Chemical Characterization of Corrosion Products in Fuselage Lap Joints", NRC LTR-ST-1952, November 1993.
2. N.C. Bellinger, S. Krishnakumar and J.P. Komorowski, "Modelling of Pillowing Due to Corrosion in Fuselage Lap Joints", CAS Journal, Vol. 40, No. 3, 1994, pp. 125-130.
3. N.C. Bellinger, and J.P. Komorowski, "Corrosion Pillowing Stresses in Fuselage Lap Joints", AIAA Journal, Vol. 35, No. 2, February 1997, pp. 317-320.
4. Douglas W. Welch, "Fracture Mechanics Analysis of a Corroded Aircraft Fuselage Lap Joint", Master of Science Thesis, University of Oklahoma, 1997.
5. N.C. Bellinger, J.P. Komorowski and R.W. Gould, "Damage Tolerance Implications of Corrosion Pillowing on Fuselage Lap Joints", Journal of Aircraft, Vol. 35, No. 3, May-June 1998, pp. 487-491.
6. J.P. Komorowski, N.C. Bellinger and R.W. Gould, "The Role of Corrosion Pillowing in NDI and in the Structural Integrity of Fuselage Joints", Published in the proceedings of the 19th Symposium of the International Committee on Aeronautical Fatigue, Edinburgh, 16-20, June 1997.
7. J.P. Komorowski, S. Krishnakumar, R.W. Gould, N.C. Bellinger, F. Karpala and O.L. Hageniers, "Double Pass Retroreflection for Corrosion Detection in Aircraft Structures", Materials Evaluation, Vol. 54, No. 1, January 1996, pp. 80-86.
8. Airbus Service Bulletin, A300-53-178, revision September 19, 1988.
9. N.C. Bellinger and J.P. Komorowski, "Finite Element Analysis Approach for Cracks at Countersunk Holes in Fuselage Lap Joints With and Without Corrosion Pillowing", NRC LM-ST-823, April 1998.

Towards a Predictive Design Methodology for Composite Laminate Patches Based on Physical Modeling of Failure Processes

Peter W. R. Beaumont
Cambridge University Engineering Department
Trumpington Street, Cambridge CB2 1PQ, UK
Tel: +44 01223 332 600
Fax: +44 01223 332 662
pwrb@eng.cam.ac.uk

James M. Greer, Jr.
Center for Aircraft Structural Life Extension
Department of Engineering Mechanics
United States Air Force Academy, Colorado, 80840

ABSTRACT

A predictive design methodology has been developed for composite materials and structures based explicitly on analytical models of the physical processes (phenomena) by which damage accumulates. This methodology has been successfully applied to a variety of advanced strategic composite material systems. The effects of environment, temperature, and moisture, for instance, are also included in this modeling strategy. It would be desirable to reformulate this phenomena-based micromechanics model for application to composite-bonded repairs of metallic structures. This reformulation would allow the model to be applied to (1) empirical models of composite patch behavior (to provide a predictive capability), (2) existing finite element models (to ensure the widest possible utility to the design and application of composite patches to cracked aircraft structures), and (3) the design of software, including existing material and patch optimization codes (to aid implementation at all stages of the predictive design process and application). The major objective is to successfully apply this physical model of damage growth in a format suitable for the predictive design of notch-insensitive, damage tolerant composite-metal patch systems for application in hostile environments, including extremes of temperature. It is the intent that the form of these models will be suitable for incorporating into existing design software, e.g., as a constitutive law sub-routine for a finite element code and a sub-routine of an optimization code for patch design. This paper describes and assesses this design methodology as it has been applied to composites, and suggests how it might be applied to the technology of composite repairs to metallic structures.

1. INTRODUCTION

A gap exists in our knowledge of the differences in behavior between material and structure that can be explained in terms of a size of scale or "sizescale" (microscopic vs. macroscopic vs. macroshape). As the sizescale moves from lamina to test coupon to component, the nature of failure exhibits this knowledge gap as well. This sizescale, which spans several orders of magnitude, provides a framework for trying to understand the differences in failure behavior of material on the one hand and large scale structure on the other.

Frequently, the composites industry experiences hardware development problems due to design oversights that lead to matrix-dominated load paths and to the formation of a multitude of matrix cracks, splits and delaminations. Consequently, by far the largest number of development and in-service problems with composite hardware are associated with interlaminar shear and out-of-plane tension (peel stress). One approach is to assess, in sequence, the effect of cyclic stress on the residual strength and life-time

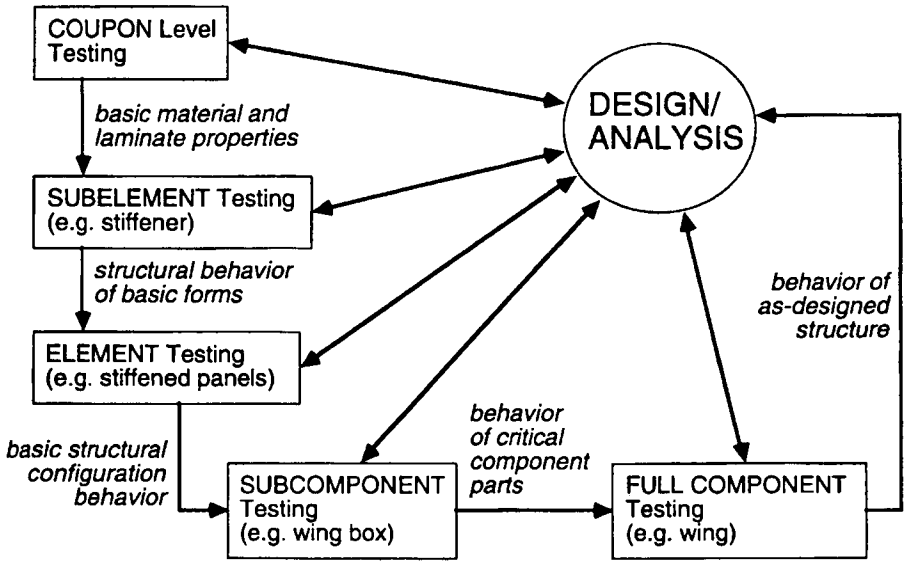

Figure 1: The building-block approach, after Lagace, et al.[1]

of a test coupon, substructural element, component and, finally, large-scale structure by a progression of experiments. This process of development testing has been termed the "building block" approach. It is used during the design and analysis phase wherein critical areas of the structure are selected for test verification. This "building block" method, as described by Lagace, et al.[1] is depicted in Figure 1. Any critical strength features are subsequently identified and isolated in the form of test articles of progressively increasing complexity and size. The "building block" methodology is based on transferring empirical information and relating experimental data from one point on the sizescale to another. Empirical methods, however, do have serious limitations and shortcomings.

An alternative and innovative approach is to begin the design process at the constituent level with physical model-informed selection of fiber and its surface treatment, matrix and its processing conditions, and architecture (geometry) of laminate construction[1-4]. As the shift of information both ways along the sizescale proceeds, the design process at each level of size has to include the identification of the principal failure mechanisms.

Differences in the nature of behavior as the "size" of the problem varies creates a gap between where "design" changes hands from being a materials issue to being a structural one. In this regime no one has really taken responsibility for bridging the void. If we take the materials issues as encompassing the establishment of and understanding of micro-level material behavioral characteristics (fiber, matrix, and interface characteristics), we might say that we characterize the properties of the material at that particular scale by reference to the fiber direction. There is no real consideration of the effects of geometry or architecture of the laminate. Initial material tests are usually of unidirectional specimens. A notch is considered as a geometrical aberration. Conversely, at the structural design size, we tend to look at the overall geometry of a component. But we tend to look on the material properties as being set (in a geometric sense) at a global level. Bridging this gap appears to be a key source of difficulty.

We often fail to look at the geometry within the component. By looking at the geometry we gain an important link between both sides. If we say that a component carries various loads from loading points to attachment points, we can also say that this could be expressed as a stress field. That stress field would have some geometric pattern to it, generally a curving one. Now if we look at this pattern and lay

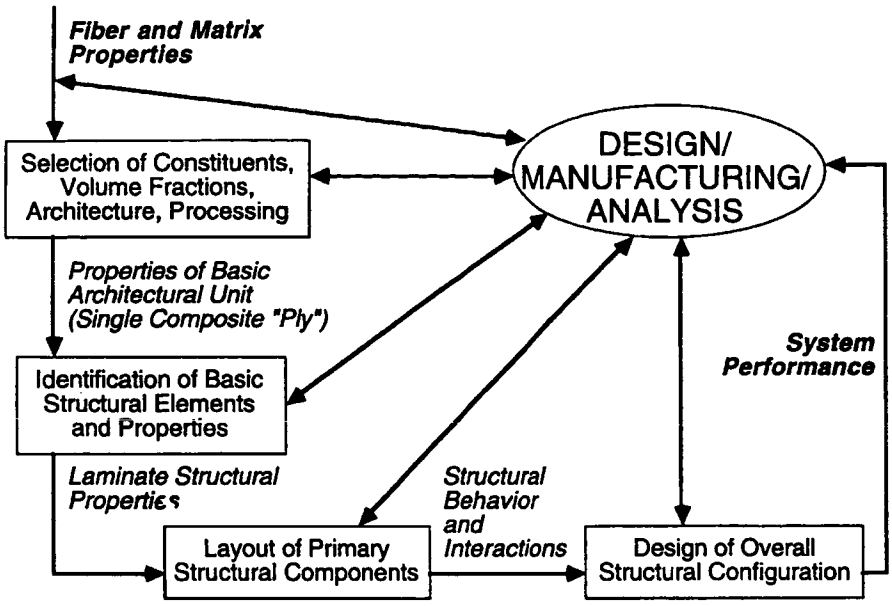

Figure 2: The Model-Informed approach, after Lagace, et al.[1]

our fibers to follow the force-flow lines in the structure, then the directional properties of the fibers have something approximating the proper directional reference frame we used at the material level. That is, the stresses are well referred to the fiber directions, and we can use our sequence of sizescales well. But what is normally done is to define a global set of fiber orientations. This global set is then, in general, not in the right micro directions when we look at a particular point within the structure. At this point, the logic in the sizescale sequence is broken. It is easy to think in terms of big sheets of fiber, but we also know that ideas such as individual tow placement by embroidery techniques to answer internal architecture needs are being considered (Jim Platt, private communication, 1997). Moving the starting point of design down to the constituent (fiber, matrix, process) level promises a more efficient and cost-effective design process[1], provided the tools can be developed to understand the macro-level effect of these constituent-level changes. The framework for such a model is depicted in Figure 2.

2. A BRIEF OVERVIEW OF CERTIFICATION METHODOLOGIES

A basic element of any certification or qualification procedure is design development and verification testing which assesses and validates the design of critical hardware features [5]. All too frequently, the effect of local details are identified very late in the design cycle. Unfortunate experiences of this kind contribute to early over-optimism in the material's initial performance figures and design rating. Furthermore, any structural analysis performed at this stage is rarely of sufficient detail to adequately evaluate the effect of interlaminar stresses on potential failure modes and margins-of-safety. Broadly speaking, three certification approaches have been considered at one time or another, and all need to be underpinned by research in order to enhance the status of composite structure design, development and certification of flight hardware: (1) Damage Tolerance, (2) Safe Life/Reliability, and (3) Wearout Model. To implement one or more of these approaches demands that analysis procedures, material characterization, and component testing are addressed in detail to provide an assessment and awareness of their applicability to the development and certification of composite flight hardware. For the purposes of this paper, only the damage-tolerance approach will be briefly summarized.

2.1 DAMAGE TOLERANCE METHODOLOGY

The damage-tolerance philosophy assumes that the largest flaw exists at the most critical location in the structure and that structural integrity can be maintained even though the flaw may grow until detected by periodic inspection. In this approach, "damage-tolerance capability", which covers both flaw growth potential and residual strength of the damaged part, is verified by analysis and test. The assessment of each component would include issues of high strain, strain concentrations, minimum margin of safety details, major load paths, damage-prone areas, and special inspection areas. That part of the structure selected as critical would be included in the experimental and test validation of the substantiation procedures for damage tolerance. Those critical structural areas would then form the basis for the subcomponent and full-scale component level of evaluation, whichever is applicable, and would be developed (or be available). Potential damage-initiation sites are free edges, bolt holes, ply terminations, and, with respect to bonded repair of structures, at a composite patch interface. Hence, a technique for the evaluation of the conditions for growth/no growth of delaminations and cracks is an essential tool for the determination of the damage tolerance of composite structures. Prerequisites for an evaluation include: a structural analysis to indicate locations where critical interlaminar stresses exist, and an empirical assessment of critical interlaminar strain energy release rates for failure modes I and II combined with a subcritical fatigue crack growth law for both modes of failure. While a fracture mechanics approach is not considered sufficiently mature at present to warrant a recommendation for general application to the certification of developmental composite hardware, nevertheless, we will consider the merits of fracture and damage mechanics principles.

3. A BRIEF CONSIDERATION OF FRACTURE AND DAMAGE MECHANICS

In most advanced composites, an array of matrix cracks in the individual transverse plies comprise the earliest signs of damage, often referred to as first ply failure. Following transverse ply cracking, delamination cracks accompanied by splits frequently form, including fiber breaks, precipitated by these transverse ply cracks[6-9]. Individual cracks of these kinds can be treated using the principles of fracture mechanics; collectively, their effects on the properties of the material can be quantified using relationships based on damage mechanics principles. Damage and fracture mechanics principles are based on quantitative relationships between microscopic and macroscopic parameters that attempt to bridge the gap on the sizescale between classical materials science (single-fiber reinforcement models at the microstructural level), and structural engineering and hardware development (at the one meter level and above). It is precisely at this gap that "design" normally changes hands from being a materials issue to being a structural one, for which neither group has taken responsibility. At the micron level, basic research seeks a detailed understanding of a problem through elegant analysis or experimentation with conspicuous absence of immediate need for solution or time constraints. Solutions to applied problems at the other end of the sizescale need not necessarily be complete and, in fact, a complete understanding of the problem is rarely required. The solutions require synthesis, optimization, approximation and "feel", and generally have a time constraint. In the strictest sense, "damage mechanics" refers to the physical mechanisms of multiple cracking by which damage forms and propagates in the material. Very few systematic attempts have been made to apply damage mechanics to advanced composites. One example goes back fifteen years to the pioneering work of Poursartip, Beaumont and Ashby[6]. In this and other reported work on fatigue damage accumulation[7,9], a fatigue damage mechanics approach is developed which is based on the assumption of a relationship between the extent of damage accumulation and changes in stiffness (or strength) of a family of carbon fiber-epoxy laminates. In these studies, delamination induced by in-plane tension loading is the principal damage mechanism, with translaminar cracking and decohesion occurring behind the advancing delamination crack front.

Another key aspect of design is the manner in which a material under stress reacts to the presence of stress concentrators such as holes or notches. At General Dynamics, more than twenty-five years ago, a paper was published on the macroscopic fracture mechanics and the fracture stress of advanced composites containing small holes or slits[10]. Numerous adaptations and variations embracing similar concepts have appeared since then[11-13]. While these macroscopic empirical models offer the potential of working models they are considerably restricted in their application. For example, they do not provide insight into the

mechanisms or causes of damage, or the mechanics of ultimate failure. Neither do they predict a fracture stress for different intrinsic material variables or extrinsic (environmental and thermal) conditions other than those of the test. They provide no insight into the connection between data at the laminate and microstructural levels, or even the reasoning behind the selection of fiber and matrix and process route in the first place. Such a design approach imposes a heavy burden of testing and data collection which is time-consuming and uneconomical in this current cost-conscious climate.

4. THE NEEDS AND REQUIREMENTS OF A PREDICTIVE DESIGN METHODOLOGY

As mentioned earlier, current design processes for aerospace composite structures are empirical. "Allowable stresses" in design and other material parameters are determined through extensive (and often statistical) test programs which are then transferred to progressively higher levels of structural complexity. This "building block" approach is favored because the overall design can be built up carefully and systematically from the results of individual tests conducted at various levels of size to meet the specific needs of the complete structural design. Such methodology lacks flexibility and is becoming uneconomical in today's cost-conscious operating climate[1-4]. It would be desirable to reduce the dependence on large test programs to generate design data or to justify the introduction of a new or alternative material system. This need is particularly acute at the early stages of the design process, when irreversible decisions are made on the choice of material system and composite architecture. On the other hand, the physical modeling approach enables us to gain understanding of the origin of failure processes; to capture the material's response in an equation or code of design; to predict material behavior under conditions not easily simulated in the laboratory (for example, extremely long duration fatigue tests); and to guide the optimization of micro- and macro-structure of the material for longevity and durability[1-4].

5. DEVELOPING A PHYSICAL MODEL OF COMPOSITE FRACTURE

A model is a gross simplification of the mechanism that contains its essential elements[14]. At the heart of the model lies the physical mechanism(s), which can best be identified by direct observation using, for instance, optical or in-situ scanning electron microscopy. Other indirect techniques include C-scan and X-radiography of damaged material. In constructing a model, use is made of the tools of engineering and materials science: the equations and principles of mechanics, thermodynamics, kinetics, and so on. Many of the models have an empirical component which requires a more subtle approach or "fine tuning". An element of empiricism introduces unknown constants into the equation. Often, they simply multiply to produce only one, perhaps two, unknown constants. A calibration procedure is then required to set values on them; one experimental measurement for each constant. The design of critical experiments is a vital element to this process. When the model is combined with experimental data of (say) fatigue strength, this approach leads to a design methodology having the power of prediction which comes from an understanding of the relevant (dominant) mechanisms. At best, the model encapsulates the physical basis of the problem in mathematical form; it summaries what has been observed and predicts behavior under conditions that have not been investigated. The need to model the dominant mechanism(s) and to incorporate the model in the design process itself need only be pertinent in the first instance at the "microscopic" size level.

At the beginning of the modeling process, we start by identifying the purpose of the model. It might, for example, require a predictive capability, as far as possible *a priori*, of the fracture and fatigue behavior of new composite material systems with a minimum of calibration or "fine tuning" of the model. To begin with, this necessitates the identification of the elements essential to such a model[4].

5.1 DESIRED INPUTS AND OUTPUTS OF A DAMAGE MODEL

To be useful in structural design, material system optimization and selection, and performance prediction, a damage-based model of fracture stress or fatigue strength would utilize material property data and information that would be routinely available as part of the overall design process. In the case of the fracture stress of cross-ply panels this would equate to the following inputs: (1) geometry, (including hole

size and shape); lay-up (of the $[(0_i/90_j)_N]_S$ family), (2) matrix and fiber properties; laminate/ply elastic properties, (3) delamination resistance (interlaminar toughness), (4) environment, temperature; stress-state, cyclic load spectra, rate (or time). The desired output would be a prediction of fracture stress, fatigue life-time, or post-fatigue (residual) strength (or stiffness) as a function of the inputs listed above.

Our observations show that failure involves similar components of damage in a variety of systems: carbon fibers in thermosetting and in thermoplastic matrices; Kevlar fibers in epoxy resin; and glass fibers in epoxy resin. Primarily, the common features of interacting matrix cracks within the notch tip damage zone include[9]: (1) splitting in the 0° plies, (2) transverse ply cracking in the 90° plies, and (3) delamination cracking (of approximately triangular shape) at the 0/90 interfaces.

In the carbon-fiber/epoxy family of laminates, under increasing stress the damage zone simply grows in size without changing its characteristic shape. Consequently, the extent of damage growth can be completely quantified in a straightforward manner. Under monotonic loading, the extent of damage simply increases in size until catastrophic (unstable) failure of the composite occurs by the simultaneous tensile fracture of the localized load bearing fibers adjacent to the notch tip. From experimental evidence we postulate that two interrelated phenomena govern the failure of notched cross-ply laminates: firstly, that localized interlaminar (delamination) and intralaminar (splitting and transverse) cracks grow by either a quasi-static fracture mechanism or a fatigue (or a time-dependent) mechanism; and secondly, that these cracks modify the notch tip stress distribution that leads to notch tip blunting. Catastrophic failure of the composite occurs, therefore, when the local tensile strength of the 0° ply at the notch tip is exceeded by the local tensile stress. It is important to consider, however, that the local tensile strength of the 0° ply may be affected by the presence of matrix-dominated transverse ply cracks in the damage zone. There is convincing evidence widely documented that composite strength is a stochastic quantity which depends on the volume of material under stress.

6. AN EXAMPLE: A DAMAGE AND FRACTURE STRESS MODEL

Following identification of the dominant failure mechanisms, the model is set up in two parts: (1) a quantitative assessment of sub-critical damage growth-rate, and (2) determination of the localized stress and 0° ply fracture stress at the notch. The former would be determined by direct observation; the latter by finite element analysis and in-situ tensile strength measurement of the 0° ply. Details have been described extensively elsewhere[8,9]. A brief synopsis follows here.

6.1 THE DAMAGE GROWTH AND DAMAGE-MODIFIED FRACTURE STRESS

Initially, the global strain energy release-rate can be calculated solely on the applied tensile loading. These calculations utilize a crude finite element representation of the notched specimen combined with the idealized damage zone. Subsequently, the analysis could be extended to include the effects of elevated temperature and residual (thermal) stress. In the example of quasi-static loading, the global strain energy release-rate can be equated, via a Griffith-type energy balance, to the appropriate fracture energies of the splitting and delamination mechanisms. In the case of fatigue loading, an empirical cyclic crack growth-rate power law (or "Paris" law) is compared to the observed damage (split) growth-rate per cycle and to the calculated cyclic global strain energy release-rate.

The second part of the model would be to relate the fracture stress of the laminate to the actual damage-state at the notch tip. It would be reasonable to assume that catastrophic failure occurs when the localized tensile stress in the 0° plies exceed its local strength. Given that the strength of the 0° ply is dependent on the size of the damage zone and also on the equivalent volume of ply under stress at the notch tip, then, not surprisingly, the localized tensile strength of the 0° ply follows a Weibull weakest link statistics model. We observe that the net effect of competition between the damage-growth mechanisms that can simultaneously blunt notches and reduce the 0° ply strength is to increase the residual fracture stress of the laminate.

Table 1: Sizescales and factors associated with bonded repair failure.

Failure Mode	Approx. Sizescale	Dominant Factors
1 - K not reduced	mm-m	struct. geom, matl. prop.
2 - Patch fails in tension	μm-mm	mfg. proc., matl. prop., flaws
3 - Skin fails due to load attraction	nm	matl. prop.
4 - Disbond due to peel	nm-μm-mm	surface prep., matl. prop., flaws
5 - Disbond due to shear	nm-μm-mm	surface prep., matl. prop., flaws

6.2 MODEL INTEGRATION

In monotonic loading, the two parts of the model would act in synergy. As the applied stress increases, the damage zone grows, reducing the stress concentration at the notch tip, while simultaneously increasing the effective volume of the 0° ply under stress. The latter would result in a reduction in the 0° ply strength. To predict failure, then, would require an evaluation of the current state of damage and a knowledge of the local notch tip stress concentration factor and the current volume of 0° ply under stress at the tip. This would establish whether the specimen survives or fails at that particular applied stress. Such coupling between damage growth and the volumetric dependence of strength of the 0° ply would appear to be the origin of the so-called "hole size effect" frequently observed in composite materials and reported by Waddoups[10] and Whitney and Nuismer[11].

7. APPLICATION TO BONDED REPAIR

The use of adhesively bonded composite (including fiber-metal laminates) patches to metal aircraft structures for crack patching purposes has become the method of choice for several scenarios. In areas where riveted repairs are impractical (or even prohibitive) and replacement of aircraft skin or other parts is uneconomical, bonded repairs are often employed. The failure modes associated with bonded repairs to aircraft skin generally fall into five categories[15]: (1) failure to sufficiently reduce the stress intensity factor, resulting in continued crack growth, (2) failure of the patch by exceeding patch tensile strength, (3) failure of the aircraft skin near the patch due to load attraction by the stiffer patch, (4) failure at bondline due to peeling stress, and (5) failure at bondline due to shear stress.

The lengthscales and dominant factors associated with these various modes failure are depicted in Table 1. Some of these factors are well understood, intrinsic to the material, and easily modeled. For example, if the stresses in the aircraft skin near the patch are known, the intrinsic property (yield strength) of the skin allows for failure prediction (a limit-load criterion). On the other hand, consider a Mode 4 failure, which is primarily driven by surface preparation (including the bonding/curing process), the material properties, and any pre-existing flaws (or flaws generated in during the bonding process). These factors, in general, are much less well-understood and more difficult to model. Moreover, the current (non-destructive) state-of-the-art does not permit finding extant flaws to the degree such that accurate failure prediction can be made. Because of this, high-fidelity, three-dimensional, nonlinear finite element analyses, accompanied (when practical) by experimental verification, are used in the design of a bonded repair. Much work is on-going in the development of less expensive design-tools, including both analytical[16] and numerical-based[17] software, but there are not yet any "simple" tools of high enough fidelity to give the repair designer sufficient confidence to abandon the expensive and time-consuming methods currently used.

As an example of how this model-informed experimental approach might be applied to bonded repair, consider Figure 3. It depicts the fatigue results of tests using GLARE™ (a fiber-metal laminate) and boron-epoxy patches on 2024 aluminum panels[18]. The panels were pre-cracked in the center ($2a_0 = 25\,\text{mm}$), and the GLARE™ and boron-epoxy patches were chosen to be of equivalent stiffness. Armed with the

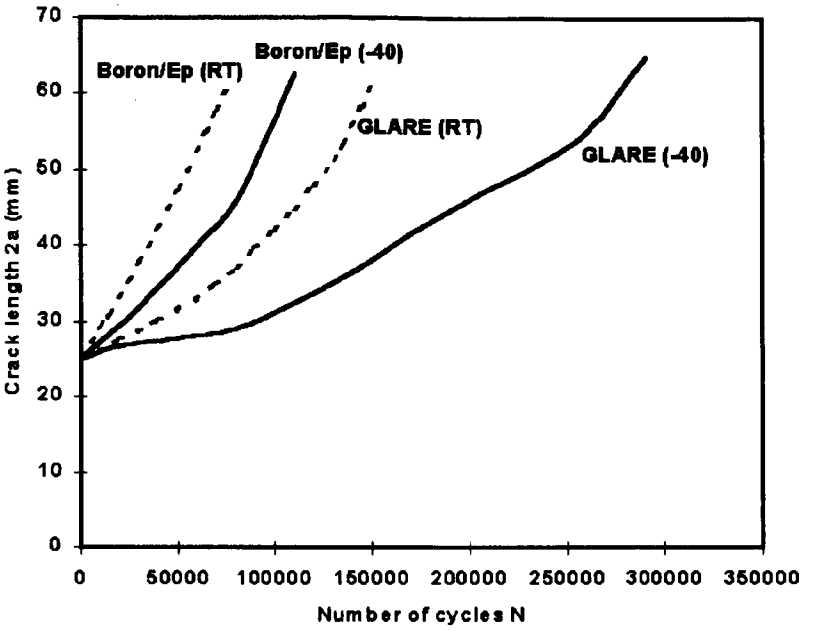

Figure 3: GLARE^{TM} vs. Boron-Epoxy, cold vs. room temperature, after Verhoeven[18].

appropriate material property data (e.g., adhesive modulus vs. temperature), the data of Figure 3 could be used to predict the behavior of, say, the GLARE^{TM} repair at some intermediate temperature. But it tells us nothing about how the repair would behave in a humid environment, or with a poorly prepared surface, or with a damaged patch. This is where the goals of model-informed empiricism could be applied. An entirely empirical approach to understanding all of these effects would require a prohibitively large matrix of test points. Model-informed empiricism, on the other hand, takes the approach of modeling the physical processes of damage and combining these with appropriate experimental verification ("fine tuning") to developing a predictive tool.

Building on the example of section 6, a possible path for developing a failure prediction capability for, say, a notched (flawed) composite patch failure could include the following steps:

1. Perform at least one quasi-static tensile test on a patch to failure to obtain X-radiographs (or images from another NDI technique) of the damage zone shape vs. increasing stress. Check to see if the notch tip damage grows in a self-similar manner (or not). Certain carbon fiber-epoxy laminates under increasing stress and temperature exhibit changes in the shape of the damage zone. If this occurs, then further calibration steps would be required.

2. Construct a finite element representation of the damage zone. (Re-call that the finite element model is used to obtain a global strain energy release-rate for the combined growth of a split and delamination crack).

3. Essentially, split energy, G_s, and delamination energy, G_d, (units of J/m^2) are found by comparing the model to the experimental data of split length vs. stress. G_s is obtained from the stress to initiate splitting, while G_d is determined from the rate of split growth with increasing stress.

4. The in-situ strength of the 0° ply within the laminate is determined by performing a series of tensile tests on waisted specimens. This data is fitted by a two parameter Weibull weakest link statistics model in order to determine the Weibull modulus.

5. The finite element model of Step 2 is used to obtain the notch tip stress-volume integral (i.e., the effective volume of the 0° ply under localized stress at the notch tip) as a function of damage zone size which is characterized by split length.

6. The model is now in a form that can be used to predict correctly the fracture stress as a function of hole size, ply thickness, and laminate stacking sequence (for the particular family of laminates) and its dependence on the extent of damage growth.

For cyclic loading, there is an intermediate step, Step 1a, in which damage is monitored for a given loading waveform up to a particular number of cycles. Such observations and measurements are necessary in order to determine the empirical parameters of the fatigue crack growth power law. Given this calibration sequence, then the fatigue version of the model now predicts correctly fatigue damage growth and post-fatigue residual strength for a range of flaw sizes, ply thickness, stacking sequences, and fatigue history.

Clearly, this analysis assumed knowledge of the stress field in the patch—a non-trivial problem when it is bonded to an aircraft skin. But including the effects of bonding would similarly involve a combination of analytical tools and "fine tuning" with selected experiments.

CONCLUSIONS

Lagace, et al.[1] have called for a design and analysis approach that begins at the constituent/process level (one level below the "coupon" level) and that allows for prediction of the response of the complete structure. They stress that this goal is not ***attainable***, but is ***realistic***, in the sense that striving toward this goal will result in substantial improvements over current processes. Modeling the mechanisms of damage and relating them to experimental data and empirical correlations provides a first attempt at achieving a predictive capability in design, particularly with regard to issues of strength, durability and longevity[1-4]. It has the potential to provide a cost-effective alternative to the present largely empirical approach which takes an excessive amount of time and money. Current mechanistic models can be used to bound problems, identify critical material properties, and map likely failure modes. This will lead to improved test programs which concentrate on critical issues at the important sizescale(s). In the longer term, improved modeling will allow the design process to begin with an intelligent choice of constituent materials and interfaces and to proceed with the prediction of performance at the various sizescales[1-4]. Existing design methodologies at the higher structural sizescales will be supported and justified by a fundamental understanding at lower sizescales. The added benefits of this approach include more options to the designer, a reduced need for extensive and costly testing, and more efficient and shorter design iteration cycles.

ACKNOWLEDGEMENTS

We gratefully acknowledge the support of the Air Force Research Laboratory (AFRL/VASE) for this work. The first author wishes to acknowledge the financial support of the U. S. Air Force Academy and the European Office of Aerospace Research and Development (EOARD) (SPC 98-4004). In addition, thanks are due to Major Rob Fredell of the Air Force Academy for the encouragement and support during various aspects of this work in Colorado Springs.

REFERENCES

[1]P. A. Lagace, S. Mark Spearing, and Hugh L. McManus (1996), "A Proposed Design Methodology for the Failure and Durability of Composite Structures", Proceedings of the 11th DoD/NASA/FAA Conference on Fibrous Composites in Structural Design, Fort Worth.

[2]S. M. Spearing, P. A. Lagace and H. L. N. McManus (1995): "On the Role of Lengthscale in the Prediction of Failure of Composite Structures: Assessment and Needs", Proceedings of the 10th International Conference on Composite Materials, Whistler, BC, Canada, IV-49. Published by Woodhead Publishers.

[3]S. M. Spearing, P. A. Lagace and H. L. N. McManus (1997): "On the Role of Lengthscale in the Prediction of Failure of Composite Structures: Assessment and Needs". Accepted for publication in *Applied Composite Materials.*

[4]S. M. Spearing and P. W. R. Beaumont (1997): "Towards a Predictive Design Methodology of Fibre Composite Materials". Accepted for publication in *Applied Composite Materials.*

[5]K. T. Kedward and P. W. R. Beaumont (1992): "The Treatment of Fatigue and Damage Accumulation in Composite Design", *Intl. J. Fatigue, 14*, (5) 283-294.

[6]A. Poursartip, M. F. Ashby and P. W. R. Beaumont (1982) : "Damage Accumulation during Fatigue of Composites", *Scripta Metallurgica, 16*, 601-606.

[7]A. Poursartip, M. F. Ashby, P. W. R. Beaumont (1986): "Fatigue Damage Mechanics of a Carbon Fibre Composite Laminate: Parts 1,2", *Composites Science and Technology, 25*, 193-218, 283-299.

[8]M. T. Kortschot and P. W. R. Beaumont (1990): "Damage Mechanics of Composite Materials 1-4," *Composite Sci. and Tech., 39*, 289-326; *40*, 147-180.

[9]S. M. Spearing, P. W. R. Beaumont (1992): "Fatigue Damage Mechanics of Composite Materials 1-4," *Comp. Sci. Tech. 44*, 159-177, 299-307, 309-317.

[10]M. E. Waddoups, J. R. Eisenmann and B. E. Kaminski (1971): "Macroscopic Fracture Mechanics of Advanced Composite Materials", *J. Composite Materials, 5*, 446-454.

[11]J. M. Whitney and R. J. Nuismer (1974): "Stress Fracture Criteria for Laminated Composites Containing Stress Concentrations", *J. Comp. Materials, 8*, 253-265.

[12]J. Awerbuch and M. S. Madhukar (1985): "Notched Strength of Composite Laminates: Predictions and Experiments - A Review", *J. Reinf. Plas. Comp. 4*, 3-159.

[13]J. K. Wells and P. W. R. Beaumont (1982): "Correlations for the Fracture of Composite Materials", *Scripta Metallurgica, 16*, 99-103.

[14]M. F. Ashby (1992): "Physical Modeling of Material Problems", *Mat. Sci. & Tech., 8*, 102-111.

[15]R. S. Fredell and C. B. Guijt (1998), "GLARE™ Patching Efficiency Studies," in A. A. Baker et al., Eds., *Bonded Repair of Aircraft Structures*, 2nd Ed., accepted for publication, Nijhoff Publishers, Dordrecht.

[16]R. Fredell, J. Marr, and A. Vlot, "An Engineering Approach to the Design and Analysis of Fuselage Crack Patching with CalcuRep for Windows", Specialists' Conference on Composite Repair, Vancouver.

[17]James, Mark and Swenson, Daniel, *FRANC2D/L: A Crack Propagation Simulator for Plane Layered Structures.* Available from `http://www.mne.ksu.edu/~franc2d/`.

[18]S. Verhoeven (1998), "In-Service Effects on Crack Growth Under Bonded Composite Repairs", M. S. Thesis, Faculty of Aerospace Engineering, Delft University of Technology.

A CTOD APPROACH TO ASSESS STABLE TEARING UNDER COMPLEX LOADING CONDITIONS

Claudio Dalle Donne
German Aerospace Center DLR, Institute of Materials Research
D-51170 Cologne, Germany
Tel: +49-2203-601-4608
Fax: +49-2203-696480
e-mail: Claudio.Dalle-Donne@dlr.de

ABSTRACT

An engineering approach for assessing the ductile fracture of cracked thin structure based on the δ_5 crack tip opening displacement (ctod) is presented. Standard laboratory tests and experiments with biaxially loaded cruciform specimens of 6 mm thick 2024-T3 sheets showed that the δ_5-R-curves were reasonably independent of specimen geometry and applied loading conditions over almost the entire testing range. This was also found for inclined pre-cracks (mixed-mode I/II) and small cracks emanating from notches under biaxial loading. Only negative biaxial loading ratios, which lowered dramatically the constraint of plastic deformation ahead of the crack tip, led to an apparent increase of crack resistance. These constraint effects could however be quantified through a second parameter based on the linear elastic T-stress. The driving force was estimated with the Engineering Treatment Method (ETM), which required only the stress intensity factor and plastic limit load solutions of the considered structure as well as the material stress and strain power law as input parameters. The ETM predictions of δ_5-driving force were compared to the experimentally measured ctod values.

INTRODUCTION

The prediction of the residual strength of a cracked aircraft fuselage structure requires an assessment method that accounts for large amounts of stable tearing in thin sheet materials. The material characterisation side of such an approach is usually expressed through a crack resistance curve (R-curves). It is well known that crack resistance curves obtained with the standardised ASTM-methodologies on the basis of J-integral or stress intensity factor are geometry dependent, if the material is sufficiently ductile [1, 2]. Therefore the usefulness of such R-curves for a residual strength assessment of aircraft fuselage structures is questionable, especially when the loading conditions of the structure are different from the loading conditions of the standardised specimens. Typical examples are the biaxial loading conditions experienced in the fuselage or small cracks emanating from notches and rivet holes. Further, the fatigue cracks may not be perpendicular to the main loading axis. This would lead to a mixed-mode I/II loading condition.

To overcome the problem of transferability of R-curves from laboratory specimens to real structures, several new fracture parameters were developed ([3, 4] and overview in [5]). Unfortunately the measurement of parameters which deliver geometry independent R-curves is often sophisticated and so are the finite element calculations which are usually required for the driving force estimation in the structural assessment. Typical examples of such fracture criterion are the T^*-integral and the crack tip opening angle ctoa, which have been recently presented as candidate parameters for the assessment of stable crack growth in fuselage structures [6, 7].

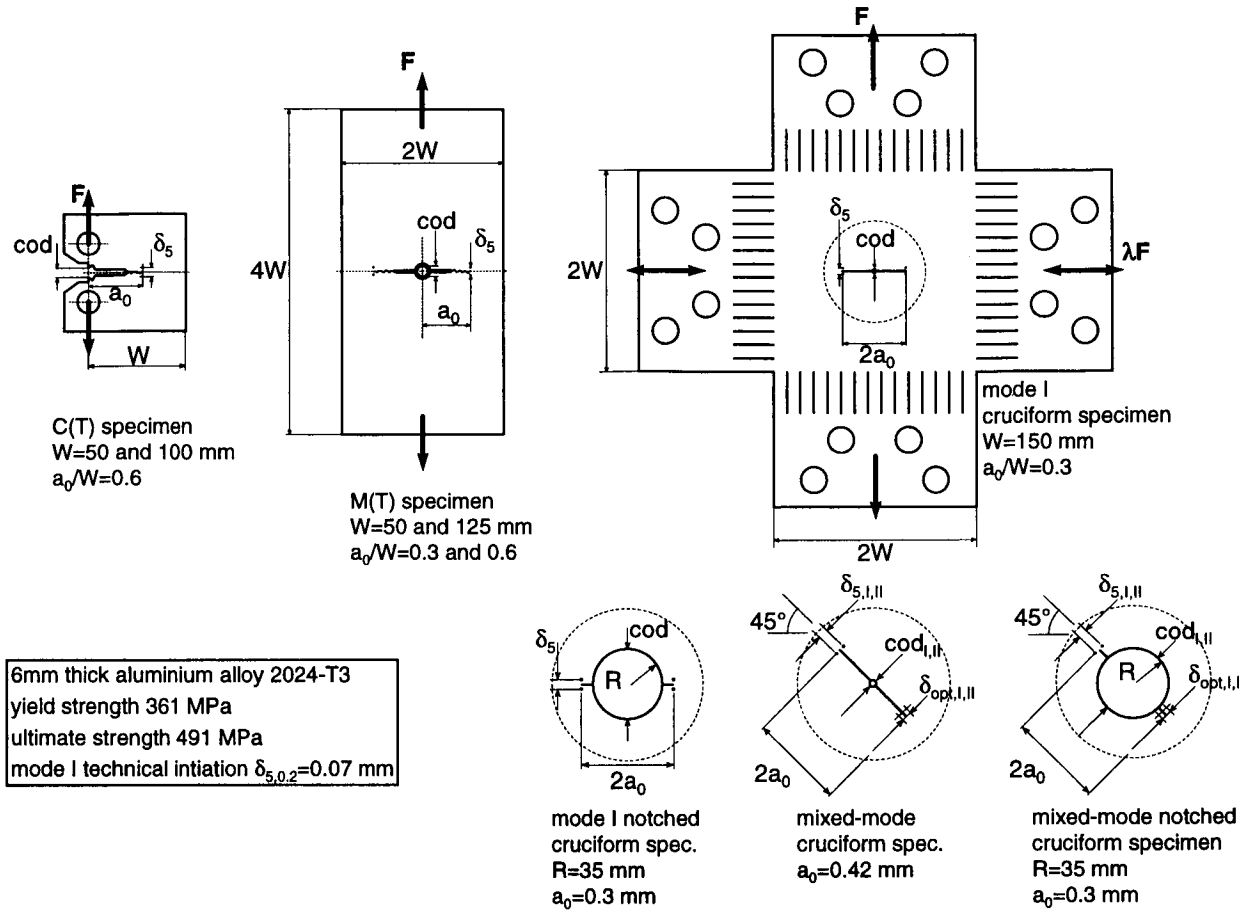

Figure 1. Specimen configurations, tensile properties and the mode I initiation value of 2024-T3. The drawings in the lower right part of the figure show the cracked central part of the cruciform specimens.

In this paper a simple engineering approach based on the δ_5 crack tip opening displacement [8] is presented. The crack tip opening measurement is straightforward, because it is based on a stationary clip gage positioned on the tip of the fatigue pre-crack. No finite element calculations are needed for the δ_5 driving force, which is estimated with the Engineering Treatment Model (ETM) [9, 10]. The analytical ETM requires only the stress intensity factor and plastic limit load solutions of the considered structure as well as the material stress and strain power law as input parameters. The approach is validated by experiments carried out on standard and cruciform specimens of 2024-T3 under biaxial loading.

EXPERIMENTAL PROCEDURE

Standard C(T) and M(T) specimens were fabricated in different sizes from 6 mm thick 2024-T3 sheet material, Figure 1. The tensile properties of the slightly anisotropic 2024-T3 sheets were averaged over the results of several tensile specimens machined in different orientations [11]. The C(T) and M(T) specimens were tested in the directions parallel and perpendicular to the sheet rolling direction. The main loading axis of the cruciform specimens always coincided with the rolling direction.

The mode I cruciform specimens contained simple through thickness fatigue cracks and the notched cruciform specimens were characterised by short cracks emanating from a hole, Figure 1. In both the mixed mode cruciform specimens the fatigue cracks were inclined by an angle of 45°. The experiments were carried out in a biaxial load rig under displacement control [12]. The load biaxiality λ was varied between –1 and +0.5. This induced different ratios of mixed-mode loading in the cruciform specimens with inclined

pre-cracks. A load ratio of $\lambda = -1$ corresponded to pure mode II loading in both mixed-mode specimens. The mode I loading component increased with increasing load ratio [13].
The δ_5 crack tip opening displacement was measured with a clip gage at the original fatigue crack tip [8]. In case of mixed mode loading a specially designed support [13] was used, which allowed a decomposition of the measured displacements in the sliding and opening mode ($\delta_{5,I}$ and $\delta_{5,II}$). These measurements were equivalent to the much simpler optical evaluation of the mode I ($\delta_{opt,I}$) and mode II ($\delta_{opt,II}$) components carried out on some specimens [13].
Stable crack growth during the experiments was monitored with the potential drop technique. Further experimental details are found in [12, 13].

R-CURVES

In this chapter the materials characterisation side of the ctod approach is addressed. Some of the results were published previously by the author [12, 13].
Independently of specimen orientation and size, all R-curves of the standard specimens fall in a common scatterband, Figure 2. The C(T) specimens formed the lower bond, the M(T) specimens the upper bond of this scatterband. The averaged mode I technical initiation value (stable crack growth of $\Delta a = 0.2$ mm) is given in Figure 1. The R-curves of the mode I cruciform specimens loaded uniaxially ($\lambda = 0$) or with a positive load ratio ($\lambda = +0.5$) delivered approximately the same $\delta 5$-Δa-curve as the standard specimens, Figure 2 left side. This was also valid for the R-curves of the notched cruciform specimens tested uniaxially and with compressive stresses parallel to the crack, Figure 2 right side, which lie on the lower bond of the scatterband (like the C(T) specimens). In case of the cruciform specimen without a hole, compressive loading parallel to the crack led to an apparent increase of fracture toughness in terms of δ_5.
Unfortunately the δ_5-Δa-curves showed a certain degree of dependency from the loading or specimen configuration. Because of the fixed δ_5 clip-gage location, local crack tip opening measurements were only possible at the onset of stable crack propagation. With increasing crack growth, i.e. increasing distance between the crack tip and the δ_5-identations, the global deformation characteristics of the specimen influenced more and more the δ_5-output. R-curves measured with specimens exerting high plastic

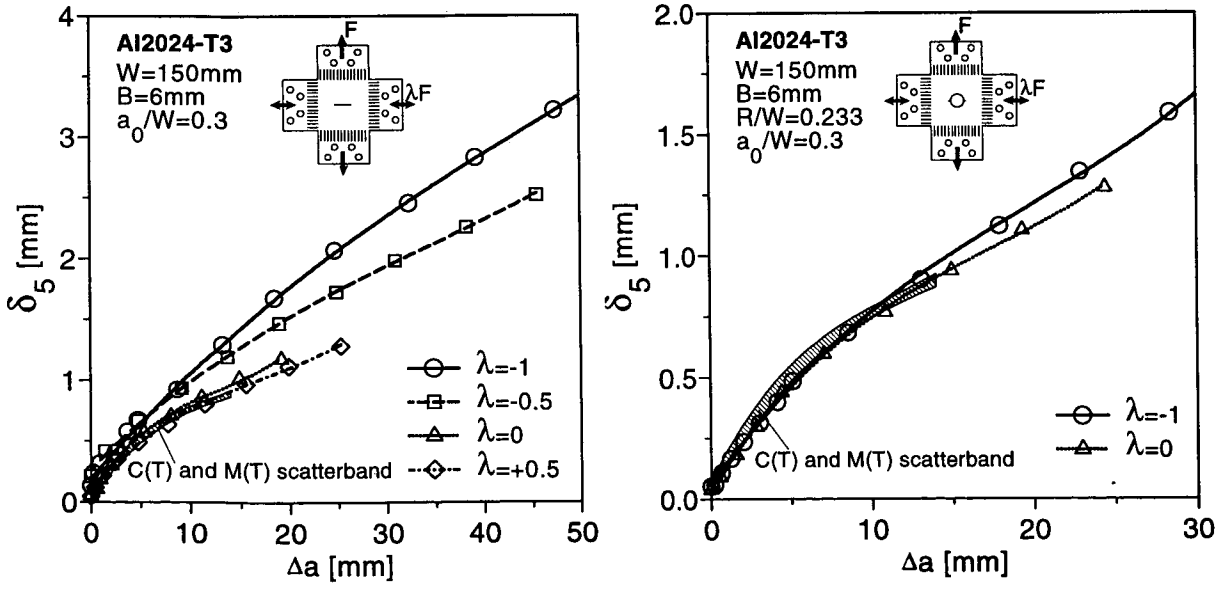

Figure 2. Mode I crack resistance curves of the biaxially loaded cruciform specimens with central crack (left) and with small cracks emanating from a hole (right) compared to the R-curves evaluated with standardised specimens.

constraint on plastic deformation generally are lower than R-curves of low-constraint geometries, in which the crack flanks are wide opened because of the extended plastic zones ahead of the crack. For a given thickness the amount of (in-plane) constraint can be quantified with a second parameter [1, 2]. In this approach the linear elastic T-stress is chosen as a second parameter because of its simplicity. It relies on the constant term in the series expansion of the crack parallel stresses in the elastic field near a crack tip [14]. Solutions for the T-stress are available for a wide variety of geometries and loading cases [15, 16]. As an elastic term, T can be readily evaluated with analytical methods (such as the weight function method [16, 17]) if a suitable T-value is not available. Since the T-stress depends on loading, Leevers and Radon [18] introduced the dimensionless local or inherent biaxiality B

$$B = \frac{T\sqrt{\pi a}}{K_I} \tag{1}$$

which depends only an the geometry and loading conditions. Figure 3 shows the comparison of the B-values of the investigated specimens at the initial crack length a_0. The B-values of the simple cruciform, the C(T) and M(T) specimen remain approximately constant over almost the entire testing range. In the notched cruciform specimens the influence of the central notch on the crack tip field decreases with increasing crack length. Therefore at lager stable crack extensions ($\Delta a > 15$ mm), the B-values decrease and gradually tend towards the B-values of the cruciform specimen without a hole loaded at the same λ.
Cruciform specimens under negative loading ratios are characterised by low B-values and therefore yield the highest R-curves. Highly constrained geometries, like the C(T)-specimen or the notched cruciform specimen with small cracks, deliver lower δ_5-Δa-curves. The independence of B from the global biaxiality λ for short cracks in the notched cruciform specimens is also clearly reflected in the slopes of the R-curves on the right side of Figure 2.
The family of resistance curves can now by plotted as a function of $T/R_{p0.2}$ ($R_{p0.2}$ = yield strength) for constant crack extensions, Figure 4 left side. This diagram gives the complete information on the resistance to stable crack growth in terms of δ_5 of 6 mm thick 2024-T3 sheets. Similar curves for steel were first produced by Hancock et al. [20]. When the difference in load level of the specimens and structures (or equivalently the difference in size) is not too big, also the B value can be used as a second parameter, Figure 4 right side. It was shown in [11] that especially for steels, where the constraint effects are more pronounced than in aluminium alloys, the representation of the R-curves in function of B gives more

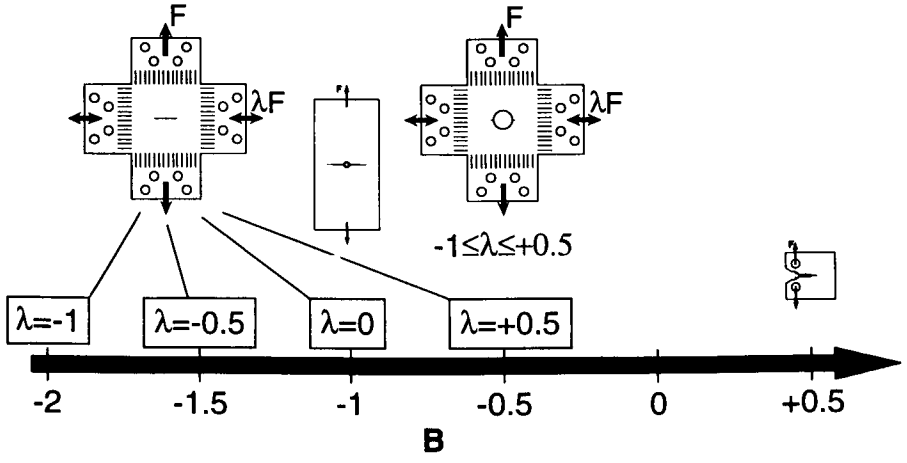

Figure 3. Comparison of the local biaxiality parameter B of the investigated specimens at the initial crack lengths (B taken from [15, 18, 19]).

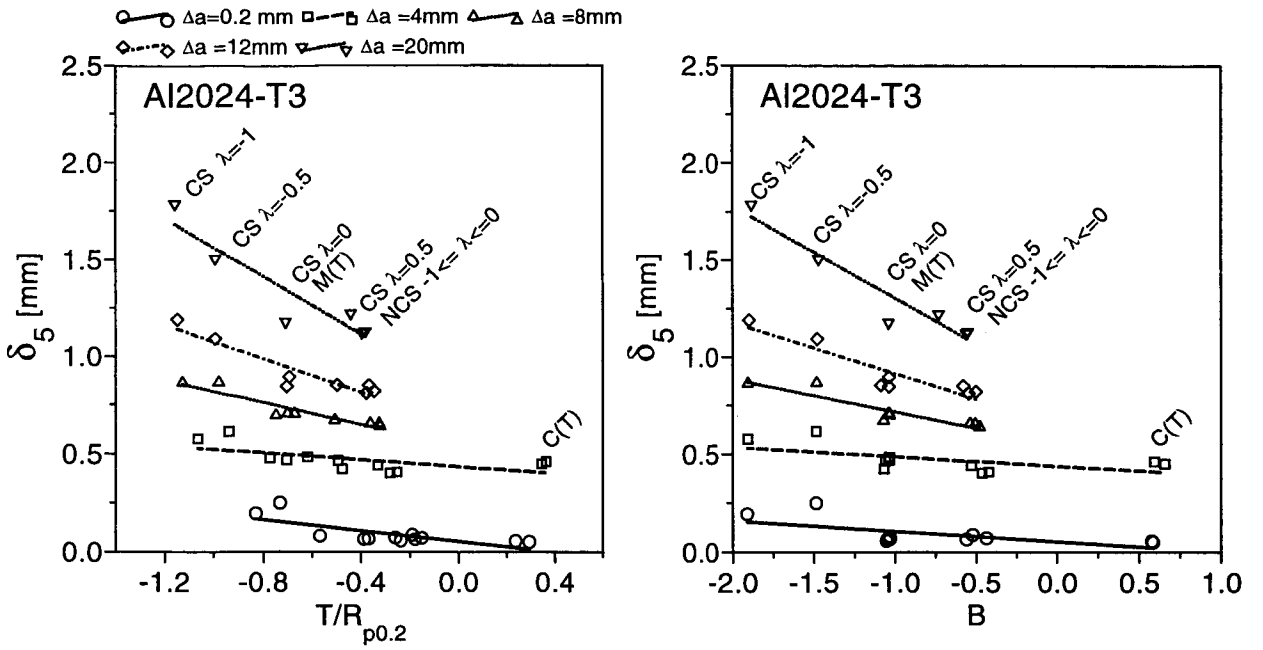

Figure 4. Mode I crack resistance curves parameterized by $T/R_{p0.2}$ (left) and by B (right). CS = cruciform specimen, NCS = notched cruciform specimen.

consistent results.

In the framework of the ctod approach the $T/R_{p0.2}$ or B parameter can be used to choose or design a specimen which matches the constraint parameters of the considered structures, in order to obtain a laboratory δ_5-Δa-curve very close to the one expected in the real structure. Similarly the conservativeness of the laboratory R-curve can be estimated through a comparison of the B-values of the specimen and the cracked structure. Finally, as shown in [11, 21] for steels, the curves in Figure 4 can be used to predict the resistance curves for any other geometry from the knowledge of its crack tip constraint characteristics through a simple interpolation.

The problem of crack growth direction in the mixed mode experiments was discussed in [13, 22]. So far it is important to know, that under predominant mode II loading ($\lambda < 0$) cracks due to shear type fracture grew approximately in the maximum shear strain direction in both types of mixed mode specimens. This means that the stable cracks remained almost parallel to the original fatigue pre-crack. Moderate mode I crack tip opening components ($\lambda \geq 0$ or more precisely $K_I/K_{II} \geq 0.7$ [22]) caused a crack path deviation, i.e. the stable crack grew normal to the maximum tensile stress or the main loading axis as a mode I crack. Figure 5 shows the crack resistance curves of the cruciform specimens without (left side) and with a central notch (right side) in terms of the magnitude of the crack tip displacement vector

$$\delta_v = \sqrt{\delta_I^2 + \delta_{II}^2} \tag{2}$$

versus the amount of stable crack growth Δa. Since some data was gathered optically and not with the δ_5 clip-gage, the subscript „5" for δ_v is omitted (see chapter „Experimental Procedure"). The background of the crack tip displacement vector as a mixed mode fracture parameter was outlined in [13, 22, 23].

The crack resistance curves of the mixed mode cruciform displaying tensile or mode I crack growth ($\lambda \geq 0$) lie in the common scatterband of the standard C(T) and M(T) specimens just as the R-curves of the mode I cruciform specimens tested at the same load ratio, Figure 5 left side. High mode II loading components ($\lambda < 0$) drove the shear crack in its original direction and led to an apparent increase of fracture toughness. For a given Δa, the δ_v values were raised into the area of the δ_5-Δa curves of mode I

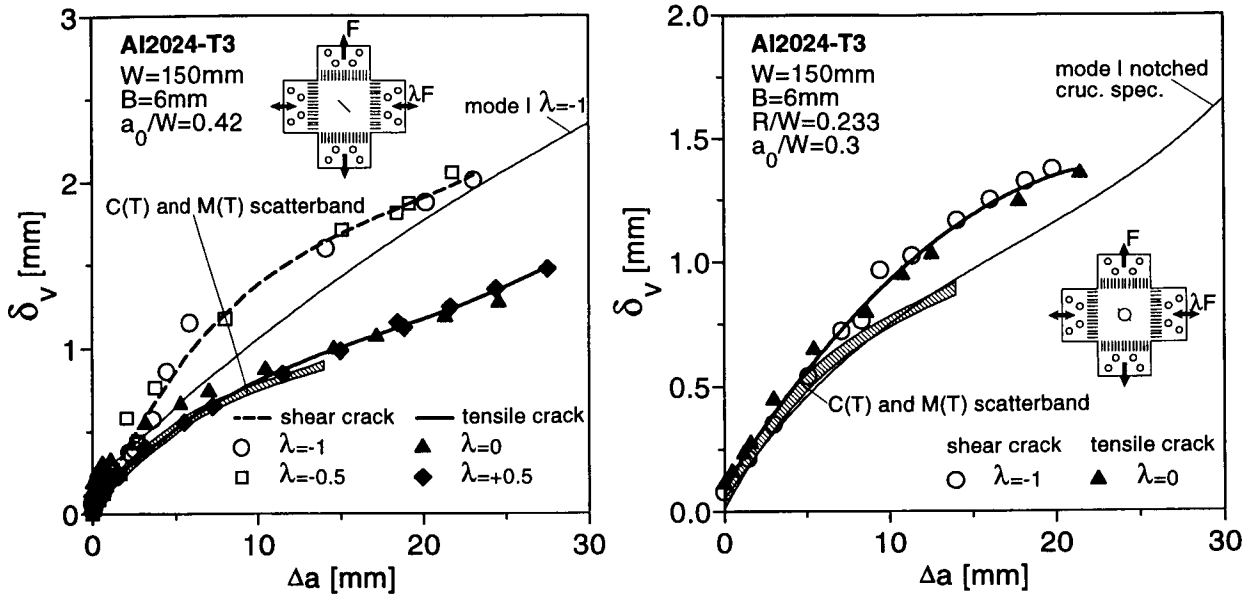

Figure 5. Crack tip displacement vector δ_v versus stable crack growth of the experiments carried out with the mixed mode cruciform specimen (left) and the notched mixed mode cruciform specimen (right).

cracked cruciform specimen tested at the same λ. The crack parallel T-stress of the mixed mode cruciform specimen with an 45° inclined pre-crack is approximately equal to zero independently of the applied load ratio λ [24] and therefore much higher than in the respective mode I specimens. The reason for the increase of mode II fracture toughness in terms of δ_v-Δa is the constraint reduction due to the predominant shear loading components. As indicated in [25] mode II components reduce the triaxial stress state ahead of the crack tip compared to mode I cracks under the same loading. Hancock at al. [26] showed that the loss of constraint due to shear loading can be correlated with the constraint of low-constraint mode I fields. For example pure mode II loading in a medium to low work hardening material is related with a loss of constraint comparable to $T/R_{p0.2} = -1.3$ in mode I at a fixed load level. With this value the mode II crack resistance curve on the left side of Figure 5 fits in the family of mode I δ_5-$T/R_{p0.2}$-curves of Figure 4 (left side).

The δ_v-Δa curves of the notched mixed mode specimens, Figure 5 right side, show virtually no effect of mixed-mode ratio, even if the two loading ratios caused two different crack propagation mechanisms. The higher resistance curves of the mixed-mode experiments compared to the mode I tests with notched cruciform specimen can be explained through the finite element analysis of Kfouri et al. [27]. They demonstrated that the constraint conditions in the crack tip region decrease in severity as the pre-crack inclination angle increases. In the case of the shear crack R-curve the T-stress or the constraint exerted by the notch dominates over the constraint reduction due to mode II loading.

CRACK DRIVING FORCE ESTIMATION

The Engineering Treatment Model was developed by Schwalbe and co-workers to provide a framework for a quick estimation of the mode I δ_5 driving force in function of the applied load. The basic version of ETM [9] has been validated for a number practical mode I loading cases [28] and was extended to mixed-mode I/II loading conditions recently [22]. For sake of simplicity the new, more sophisticated ETM-procedures published in [10] are not considered here.

The basic principle is presented in Figure 6. The cracked structure is assumed to deform in a state of prevailing plane stress and the material's engineering stress and strain curve is approximated with a piecewise power law:

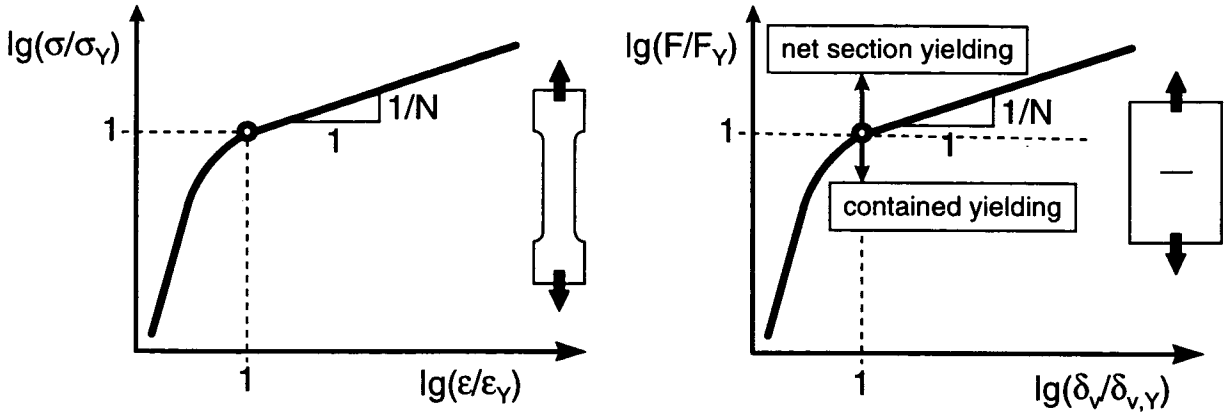

Figure 6. Determination of the driving force in terms of crack tip opening displacement δ_5 with the ETM formalism. In mode I situations δ_v is replaced by δ_5.

$$\frac{\varepsilon}{\varepsilon_Y}=\left(\frac{\sigma}{\sigma_Y}\right)^N \qquad \sigma>\sigma_Y, \quad N>1 \tag{3}$$

where the yield strength σ_Y is set equal to $R_{p0.2}$. Under contained yielding the crack tip opening displacement is given by small scale yielding, non-hardening solution for plane stress developed in [22]

$$\delta_v=\frac{\sqrt{K_{I,eff}^2+K_{II,eff}^2}\sqrt{K_{I,eff}^2+3K_{II,eff}^2}}{E\sigma_Y} \tag{4}$$

where $K_{I,eff}$ and $K_{II,eff}$ are the plasticity corrected stress intensity factors evaluated with

$$a_{eff}=a+\frac{1}{2\pi\sigma_Y^2}\left(K_I^2+3K_{II}^2\right) \tag{5}$$

In case of mode I loading (K_{II} = 0) the well known small scale yielding solution is obtained. In the author's opinion the closed form solution of the mixed-mode Dugdale crack [29], which includes also the effects of global biaxial loading, should be preferred to equation (4) when applicable (for example in center cracked structures).

Under net section yielding conditions ($F > F_Y$) the material's strain hardening law (3) is transferred to the yielding net section so that

$$\frac{\delta_v}{\delta_{v,Y}}=\left(\frac{F}{F_Y}\right)^N \tag{6}$$

where $\delta_{v,Y}$ is constant in (6) and evaluated with equation (4) at the plastic limit load F_Y. More information on the mixed-mode ETM as well as the fitting procedure of the material's stress and strain power law is found in [22].

In Figure 7 the ETM prediction (lines) is compared the measured δ_5 values (points) of a mode I notched cruciform specimen loaded at a negative biaxiality ratio. The contained yielding solution (4) was calculated with Newman's [30] K_I-function for short cracks emanating from a hole in an infinite plate

under biaxial loading. The limit load F_Y was approximated assuming constant v. Mises equivalent stresses in the remaining ligament:

$$F_Y = \frac{2BW\sigma_Y}{\sqrt{\lambda^2 + \frac{1}{\left(1-\frac{a}{W}\right)^2} + \frac{\lambda}{\left(1-\frac{a}{W}\right)}}} \tag{7}$$

In the contained yielding region the ETM predictions are very close to the experimental results. On the basis of the $\delta_{5,02}$-value of the standard specimens the crack initiation of the notched specimen is predicted exactly. At higher loads and extensive stable crack growth the ETM estimation is less accurate. This is probably connected with the inaccuracy of the contained yielding and limit load solution, which for long cracks do not rate the finite dimensions of the specimen correctly. The simple limit load solution (7) clearly overestimates the real limit load of the two mixed mode specimens in Figure 8. The error in the ETM-prediction is reduced, if the fully plastic ETM line is shifted to the plastic limit load value measured with strain gages positioned in the remaining ligament (broken line in Figure 8). This argument is corroborated by the improved correlation between the ETM and the δ_v-F/F_Y behaviour of steel cruciform specimens, where the amount of stable crack growth is reduced compared to the aluminium alloy specimens [22]. Since no solution for kinking cracks was available, K_{II} was set zero in equations (4) and (5). The pre-crack length a_0 was projected in the crack propagation direction and K_I was then evaluated with the formula for mode I cracked cruciform specimen [31].

It should be noted here, that in mixed-mode loading case the direction of crack propagation is not known a priori. Even if some advances in predicting the stable crack growth direction have been made recently [32, 33], it is recommended to perform two analyses, assuming shear crack growth and tensile crack growth and to opt for the conservative result.

In Figure 9 the ETM predictions are compared with the measured crack tip displacement vectors of two cruciform specimens loaded at a negative λ and thus displaying shear controlled fracture. The small scale

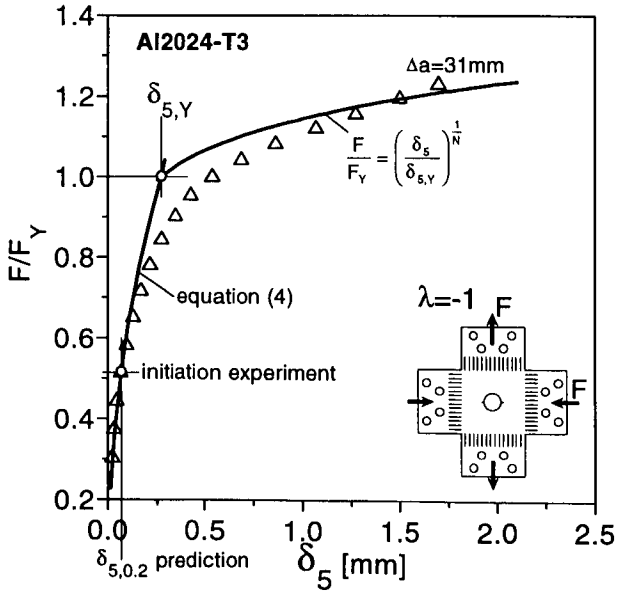

Figure 7. Comparison of the ETM prediction with an experiment on mode I notched cruciform specimen.

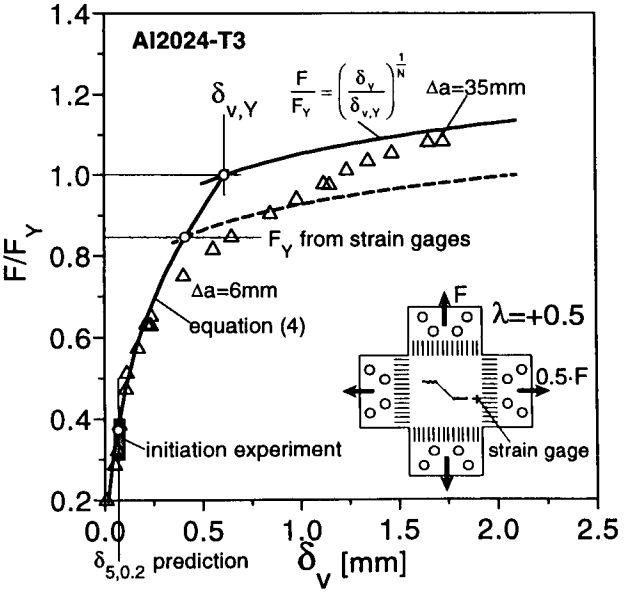

Figure 8. Comparison of the ETM prediction with two mixed mode experiments on cruciform specimens having tensile crack growth.

yielding δ_v was calculated with the mixed-mode Dugdale model mentioned above. The limit load solution was obtained assuming constant v. Mises equivalent stresses in the slanted ligament [22].
The ETM prediction is very close to the experimental results. The technical initiation load is apparently slightly underestimated.
So far the amount of stable crack propagation was extracted directly from the experimental results to suppress unwanted geometry effects on the R-curve. In the ETM prediction of the load displacement behaviour of a mode II loaded cruciform specimen in Figure 10, the stable crack growth was accounted through a single step iteration procedure [10]. Therefore the R-curve of the standard specimens had to be extrapolated linearly for $\Delta a > 14$mm. Alike δ_v in Figure 9 the displacement vector in the center of the crack (cod_v) was calculated with the mixed mode Dugdale solution. The fully plastic part of the load displacement relation was assessed using the usual ETM formalism. More examples are found in [22].

CONCLUSION

A simple engineering approach for assessing ductile failure in thin structures containing arbitrarily oriented cracks was presented. It is based on a stationary crack tip displacement measurement at the fatigue crack tip δ_5. Mode I R-curves of C(T)-specimens gave a conservative estimate of crack initiation and resistance to stable crack growth. The experimental simplicity of measuring the crack tip displacements at a fixed position has the disadvantage of introducing some geometry and loading dependence in the R-curves at great Δa-values, where δ_5 and δ_v are more and more influenced by the global deformation behaviour of the specimen. The introduction of a second parameter based on the linear elastic T-stress quantifies the loading and geometry effects quantitatively in mode I and qualitatively in mixed mode loading cases. The interaction of constraint effects due to geometry and to mixed mode loading needs however some more clarification.
The driving force or load displacement behaviour of cracked structures was estimated with the Engineering Treatment Model (ETM). The analytical ETM requires only the stress intensity factor and plastic limit load solutions of the considered structure as well as the material stress and strain power law as input parameters. The quality of this approach strongly depends on the accuracy of the limit load solution.

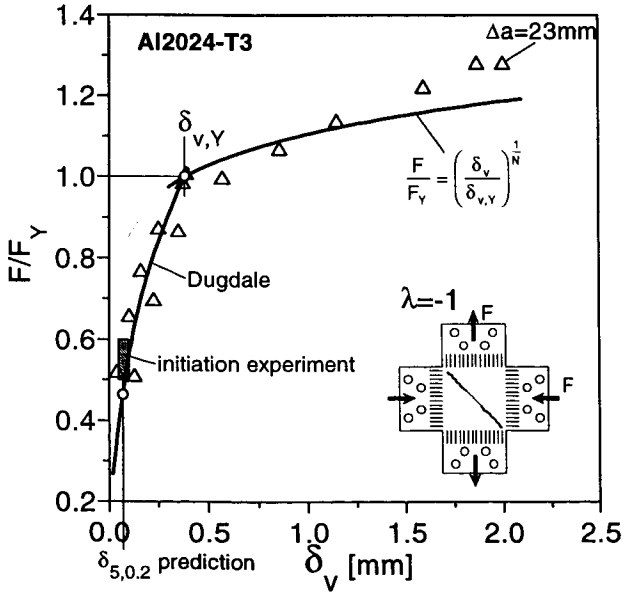

Figure 9. Comparison of the ETM prediction with two experiments on mixed mode cruciform specimens that failed under shear crack growth.

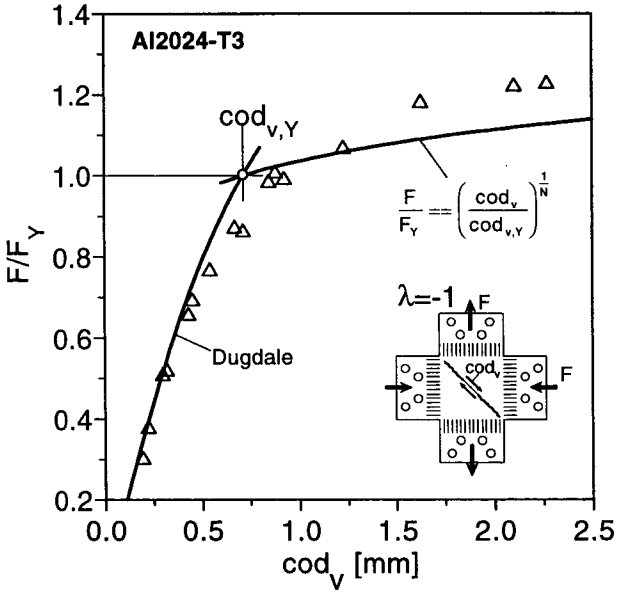

Figure 10. Prediction of the load displacement curve of two experiments with mode II loaded cruciform specimens having shear crack growth.

REFERENCES

[1] Hackett, E.M., Schwalbe, K.-H. and Dodds, R.H, Editors: Constraint Effects in Fracture, ASTM STP 1171, Philadelphia, ASTM, 1993.

[2] Kirk, M.T. and Bakker, A., Editors: Constraint Effects in Fracture Theory and Applications: Second Volume, ASTM STP 1244, Philadelphia, ASTM, 1995.

[3] Newman, J.C.: Fracture Mechanics: Fifteenth Symposium, ASTM STP 833, 1984, 93-117.

[4] Atluri, S.N., Nishioka, T. and Nakagaki, M.: Engng. Fracture Mech., 20, 2, 1984, 209-244.

[5] Brocks, W. and Schmitt, W.: in [2], 209-231.

[6] Newman, J.C.: Fracture Analysis of Stiffened Panels Under Biaxial Loading with Widespread Cracking, NASA TM 110197, 1995.

[7] Lam, P.W., Kobayashi, A.S., Atluri, S.N. and Tan, P.: Mixed-Mode Crack Behaviour, ASTM STP 1359, ASTM, to be published 1998.

[8] Hellmann, D. and Schwalbe, K.-H.: Fracture Mechanics: Fifteenth Symposium, ASTM STP 833, ASTM, 1984, 577-605.

[9] Schwalbe, K.-H. and Cornec, A.: Fatigue Fract. Engn. Mater. Struct., 14, 1991, 405-412.

[10] Schwalbe, K.-H., Zerbst, U., Kim, Y.-J., Brocks, W., Cornec, A., Heerens, J. and Amstutz, H.: EFAM ETM 97– the ETM Method for Assessing the Significance of Crack-Like Defects in Engineering Structures, GKSS-Research Center, Germany, GKSS 98/E/6, 1998.

[11] Dalle Donne, C.: Übertragbarkeit von Rißwiderstandskurven von Standardproben auf biaxial belastete, bauteilähnliche Kreuzproben, Düsseldorf, VDI Verlag, Düsseldorf, Germany 1997.

[12] Dalle Donne, C. and Döker, H.: Proc. of the 10th European Conf. on Fract. ECF 10, Vol. 2, EMAS, 1994, 891-900.

[13] Dalle Donne, C. and Döker, H.: Multiaxial Fatigue and Deformation Testing Techniques, ASTM STP 1280, ASTM, Philadelphia, 1997, 243-263.

[14] Williams, M.L.: J. Appl. Mech., 24, 1957, 109-114.

[15] Sherry, A.H., France, C.C and Goldthorpe, M.R.: Fatigue Fract. Engn. Mater. Struct., 18, 1, 1995, 141-155.

[16] Fett, T.: A Compendium of T-Stress Solutions, FZK Karlsruhe, Germany, FZKA 6057, 1998.

[17] Sham, T.-L.: Int. J. of Fracture, 48, 1991, 81-102.

[18] Leevers, P.S. and Radon, J.C.: Int. J. of Fracture, 19, 1982, 311-325.

[19] Seed, G.M.: Cracks at Elliptical Notches, Ph.D Thesis, University of Sheffield, 1988.

[20] Hancock, J.W., Reuter, W.G. and Parks, D.M.: in [1], 21-40.

[21] Burtsow, M. C. and Howard, I.C.: Fatigue Fract. Engn. Mater. Struct., 19, 4, 1996, 461-474.

[22] Dalle Donne, C.: Mixed-Mode Crack Behavior, ASTM STP 1359, ASTM, submitted 1998, .

[23] Dalle Donne, C. and Pirondi, A.: to be presented at the 12th European Conf. on Fract. ECF 12, May 14.-18. 1998 in Sheffield, U.K.,1998.

[24] Westergaard, H.M.: J. Appl. Mech., 6, 1939, A49-83.

[25] Aoki, S., Kishimoto, K., Yoshida, T. and Sakata, M.: J. Mech. Phys. Solids, 35, 4, 1987, 431-455.

[26] Hancock, J.W., Nekkal, A. and Karstensen, A.D.: Proc. of the 9th Int. Conf. on Fract. ICF 9, Vol. 4, Pergamon Press, 1997, 2015-2022.

[27] Kfouri, A.P., Wong, H.D. and Miller, K. J.: Fatigue Fract. Engn. Mater. Struct., 15, 8, 1992, 743-762.

[28] Schwalbe, K.-H.: Fracture Mechnics: 26th Volume, ASTM STP 1256, ASTM, 1995, 763-778.

[29] Becker, W. and Gross, D.: Int. J. of Fracture, 37, 1988, 163-170.

[30] Newman, J.C.: An Improved Method of Collocation for the Stress Analysis of Cracked Plates with Various Shaped Boundaries, NASA, TN D-6376, 1971.

[31] Amstutz, H., unpublished finite element calculations.

[32] Sutton, M. A., Zhao, W., Boone, M. L., Reynolds, A. P. and Dawicke, D. S.: Int. J. of Fracture, 83, 3, 1997, 275-290.

[33] Chao, Y.J. and Liu, S.: Int. J. of Fracture, 87, 3, 1998, 201-223.

Residual Strength Predictions with Crack Buckling

D. S. Dawicke
NASA LaRC
Hampton, VA 23681, USA
Tel: (757)864-4577
Fax: (757)864-8911
d.s.dawicke@larc.nasa.gov

A. S. Gullerud and
R. H. Dodds, Jr.
University of Illinois
Urbana, Illinois 61801, USA

R. W. Hampton
NASA ARC
Moffett Field, CA 94035, USA

ABSTRACT

Fracture tests were conducted on middle crack tension, M(T), and compact tension, C(T), specimens of varying widths, constructed from 0.063 inch thick sheets of 2024-T3 aluminum alloy. Guide plates were used to restrict out-of-plane displacements in about half of the tests. Analyses using the three-dimensional, elastic-plastic finite element code WARP3D simulated the tests with and without guide plates using a critical CTOA fracture criterion. The experimental results indicate that crack buckling reduced the failure loads by up to 40%. Using a critical CTOA value of 5.5°, the WARP3D analyses predicted the failure loads for the tests with guide plates within ± 10% of the experimentally measured values. For the M(T) tests without guide plates, the WARP3D analyses predicted the failure loads for the 12 and 24 inch tests within 10%, while over predicting the failure loads for the 40 inch wide tests by about 20%.

1. INTRODUCTION

Commercial transport aircraft are designed with a damage tolerant philosophy that permits the aircraft to maintain structural integrity in the presence of long cracks. Continued aircraft safety is obtained through inspections that locate cracks before they reach a size that can lead to the loss of the aircraft. The determination of inspection intervals and locations requires accurate analytical fracture mechanics tools. An important requirement of these analytical tools is the ability to determine the amount of load (residual strength) that a structure can endure for a given crack size. This requires an analytical tool that can predict stable crack growth in a thin ductile material. Additionally, since the fuselage is a pressurized thin-skin structure, crack bulging may be present, detrimentally affecting fracture behavior. An effective analytical tool should provide accurate modeling of crack growth in cases with crack bulging.

Crack bulging is the out-of-plane deformation of the crack faces and surrounding material. In an aircraft fuselage structure, crack bulging results from internal pressure acting in the out-of-plane direction and in-plane compressive stresses along the crack faces. Local crack buckling is likely to occur in thin structures (i.e., if the crack half-length to thickness ratio, a/B, is large) and when the crack face stresses (σ_x) are in compression.

Development of pressure induced crack bulging is difficult in flat laboratory specimens, but local crack buckling occurs naturally in thin, wide specimens. Forman [1] examined the effect of crack buckling on the failure stress of three aluminum alloys and two steels. Identical fracture tests were conducted on flat sheets, with and without guide plates. Figure 1 plots the resulting buckling ratio (the ratio of failure stress without guide plates to failure stress with guide plates) against the ratio of crack length to specimen

thickness. Buckling reduced the failure stress by up to 40%; furthermore, the magnitude of the reduction increased with the ratio of crack half-length to thickness ratio (a/B).

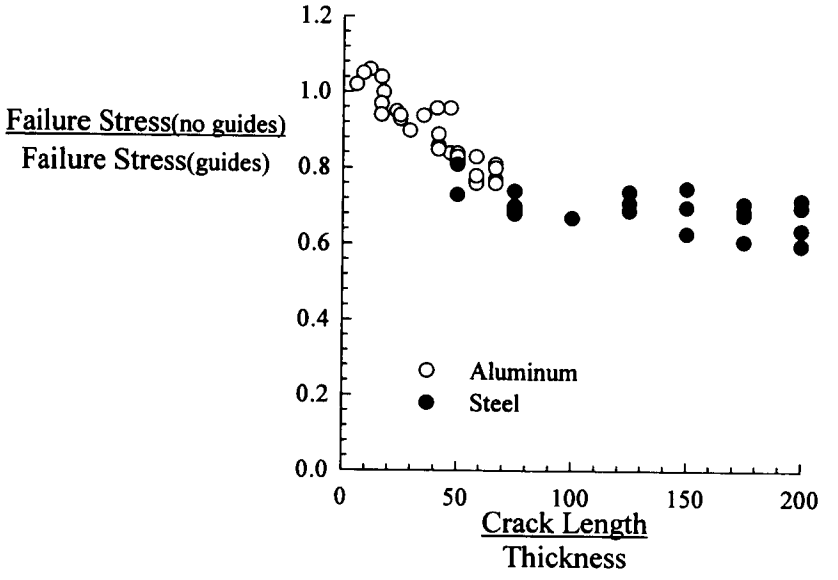

Figure 1. Experimental measurements of the reduction in failure stress due to crack buckling [1].

Finite element predictions of thin aluminum fuselage structures with crack buckling require both an elastic-plastic fracture criterion and a geometrically nonlinear analysis. Thin aluminum structures experience large-scale plastic deformation and extensive stable tearing prior to reaching critical load. Linear elastic fracture mechanics (LEFM) tools do not account for large scale plasticity, thus tend to be structural size dependent [2,3]. Approaches based on elastic-plastic fracture mechanics (EPFM), such as the J-integral resistance curve [4,5], T*-integral resistance curve [6-8], or the critical crack tip opening angle (CTOA) [9-11], are less specimen size dependent [12]. Crack buckling results in local out-of-plane crack displacements that are large relative to the thickness of the material, amplifying crack tip stresses. Modeling the coupling of the membrane stress resultants and out-of-plane displacements requires a geometrically nonlinear analysis [13].

The objective of this paper is to examine the crack tip opening angle (CTOA) fracture criteria, using middle crack tension (M(T)) and compact tension (C(T)) specimens constructed from 0.063 inch thick 2024-T3 aluminum alloy. Fracture experiments using these specimens were conducted with and without guide plates to restrain out-of-plane displacements along the crack face. For cracked thin sheets without guide plates, in-plane compressive stresses along the crack surfaces cause the crack to buckle and exhibit out-of-plane displacements, producing behavior similar to pressure induced crack bulging. To evaluate the effectiveness of the CTOA criterion, analyses using the three-dimensional, elastic-plastic finite element code WARP3D [14] modeled the fracture behavior of the tests. Simulation of the C(T) specimens provided a critical CTOA value that was then used to predict the M(T) tests with and without guide plates. The analyses of the unconstrained (without guide plates) tests employed a geometrically nonlinear formulation to accurately model the large buckling deformations.

2. EXPERIMENTAL PROCEDURE

Fracture tests were conducted on 0.063 inch thick 2024-T3 aluminum alloy M(T) and C(T) specimens. Several different specimen sizes were tested for each of the two specimen types, as summarized in the test matrix shown in Table 1. All of the specimens were precracked at a stress intensity factor range of $\Delta K = 8$ ksi $\sqrt{\text{inch}}$ and a stress ratio of $R = 0.1$. Each specimen was fractured under displacement control at a ramp rate in the range of 0.02 – 0.04 inch/min. Measurements of load, crack extension, crack opening displacement, and out-of-plane displacements were made during the tests. The out-of-plane displacement measurements were performed using a digital image correlation technique [15].

TABLE 1
TEST MATRIX OF THE FRACTURE EXPERIMENTS

C(T)			M(T)		
Width, W (inch)	a/W	Guides	Width, W (inch)	a/W	Guides
2	1/3	yes	3	1/3	no
4	1/3	yes	12	1/3	yes, no
6	1/3	yes	24	1/3	yes, no
			40	1/5	yes, no, p*
			40	1/3	yes, no

* partially constrained, initial guide plates not 100% effective

Guide plates were used to constrain the out-of-plane buckling on some of the M(T) and all of the C(T) specimens. The purpose for the guide plate tests was to decouple the crack growth from the buckling and in the case of the M(T) specimens, to quantify the influence of buckling on the residual strength. The guide plates for the C(T) specimens consisted of two sheets of 1/8 inch thick steel that sandwiched the specimen. Thin strips of Teflon tape were used to reduce friction between specimen and guide plates, while bolts along the edges of the guide plates restricted separation. The guide plates for the M(T) specimens consisted of four sheets of 3/8 inch thick aluminum that formed two "sandwiches" above and below the crack plane, as shown in Figure 2. A pair of 0.5 inch spacer blocks were used to physically separate the top and bottom guide plates, preventing tensile load from being transferred through the guides. This type of guide plate configuration appeared to restrict buckling in specimens as large as 24 inches wide. However, buckling was visible at the center of the crack during the fracture of the 40 inch wide panels. To increase the out-of-plane stiffness of the 40 inch wide guide plates, three sets of 3 inch steel I-beams were placed on both the upper and lower sets of guide plates, as shown in Figure 2.

3. ANALYTICAL PROCEDURE

The elastic-plastic finite element code WARP3D [14] was used to model the fracture behavior of the C(T) and M(T) tests. Simulation of the fracture process employed the crack tip opening angle (CTOA) criterion. This criterion assumes that stable crack extension occurs when the angle made by the upper crack surface, the crack tip, and the lower crack surface reaches a critical value. The measurement of the CTOA on the upper and lower crack surfaces is made at a fixed distance behind the crack tip, taken here to be 0.04 inches [11]. For a buckling crack, where the crack tip region experiences significant deformation, measurement of the CTOA involves tracing an arc along the center of the deformed specimen for a distance of 0.04 inches, then calculating the angle at that location. Linear interpolation between nodes, enables measurement of the CTOA at the correct position. See Figure 3 for a schematic of this process.

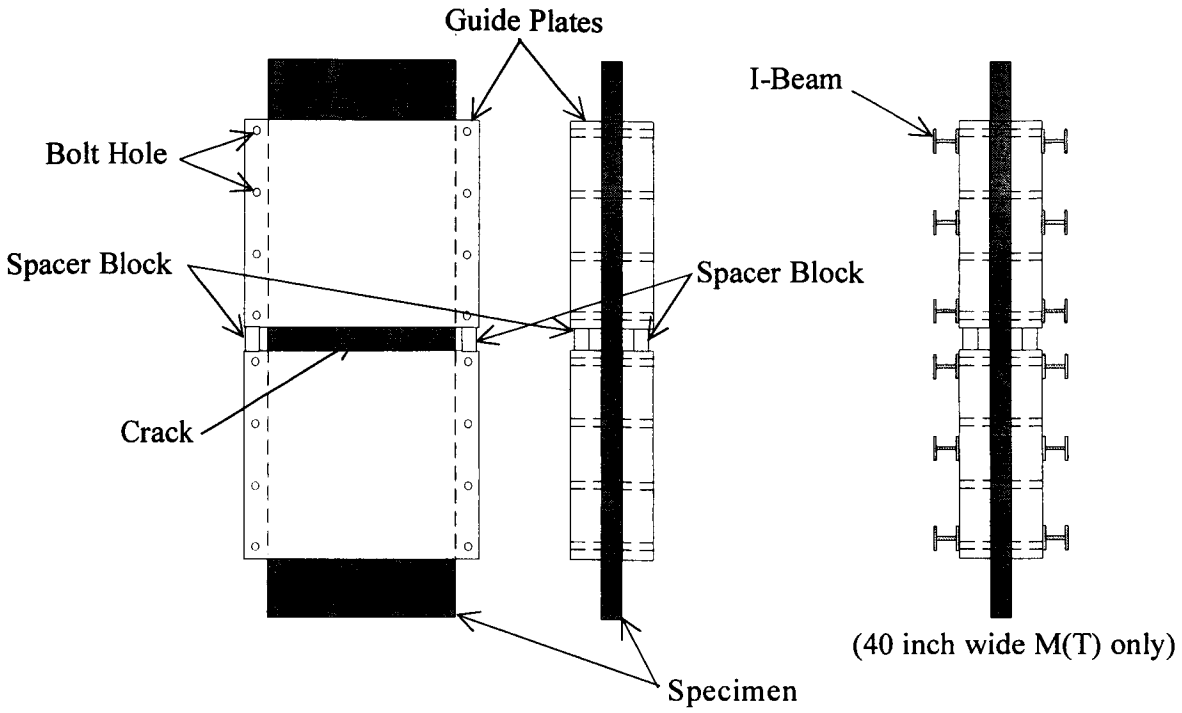

Figure 2. Schematic of M(T) guide plates.

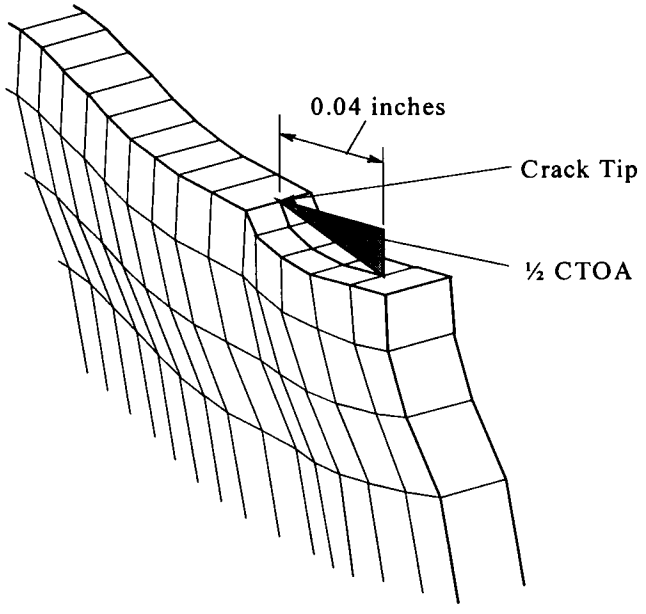

Figure 3 Definition of the critical CTOA for a buckling crack.

To eliminate dependence of the results on mesh resolution, the analyses used multiple elements over the 0.04 inch distance. Simulation of each test used several meshes with increasing refinement, until further refinement produced no significant change in the results; typically, analyses converged using 0.02 or 0.01 inch elements. When the CTOA reached its critical value, all nodes within the 0.04 inch distance released

simultaneously, thereby growing the crack by a 0.04 inch increment. The WARP3D analyses restricted the crack to maintain a straight front through the thickness.

The analyses of the tests with guide plates employed 8-node fully integrated brick elements. The meshes for the unconstrained models primarily utilized 20 node bricks with reduced integration, one element through the thickness. The crack plane, however, consisted of 8-noded elements with four elements through the thickness to support crack growth. Figure 4 shows a typical mesh. Transition elements and rapid geometric transitions served as a bridge between the crack plane elements and the remainder of the mesh. To initiate buckling, the meshes for the unconstrained tests included an initial out-of-plane perturbation, corresponding to either the first buckling mode shape or three-quarters of a cosine wave. The maximum magnitude of the perturbation corresponded to ten percent or less of the specimen thickness. Modal shell analyses conducted in ABAQUS, that utilized the same mesh profile and material description as the WARP3D analyses, provided the buckling mode shapes. Furthermore, the element formulation in WARP3D included the $\bar{B}$ method for alleviating locking in fully integrated elements, as developed by Hughes [17].

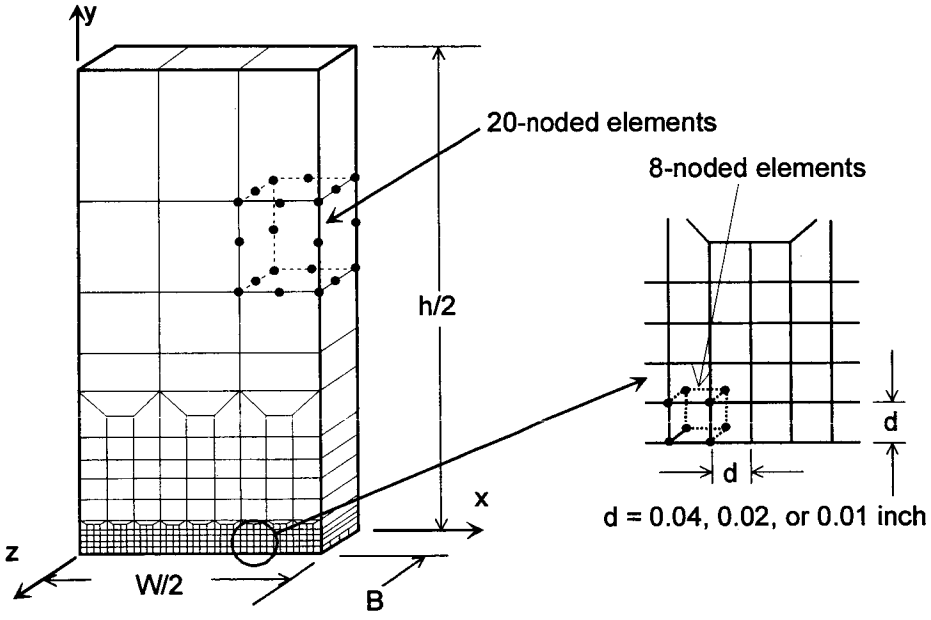

Figure 4. Finite element mesh used to model the 3 inch wide M(T) specimens.

4. RESULTS AND DISCUSSION

The following section contains a summary of all of the experimental fracture results and the WARP3D analyses. The critical CTOA value for the 0.063 inch thick, 2024-T3 aluminum alloy was determined by conducting WARP3D analyses of the C(T) fracture tests. Tables 2 and 3 contains summaries of the test results and analytical predictions for the C(T) and M(T) fracture tests, respectively.

Fracture tests were conducted for 2, 4, and 6 inch wide C(T) specimens. Figure 5 contains the failure load for each of the C(T) tests. At least two identical tests were conducted for each specimen width, producing a maximum difference in failure load of about 6%. Elastic-plastic finite element analyses were

conducted for each test condition using WARP3D. A critical CTOA value of 5.5° provided the best fit for the failure load for all conditions. The maximum difference between the experimental measurements and the WARP3D finite element simulations was 10%. The average difference between the experiments and the predictions, for all of the C(T) tests, was 4%.

TABLE 2
SUMMARY OF EXPERIMENTAL AND PREDICTED FAILURE LOADS FOR THE C(T) FRACTURE TESTS (A/W = 0.4)

Width, W (inch)	Measured Failure Load (kips)	WARP3D Failure Load (kips)	WARP3D $\frac{P_{prediction}}{P_{test}}$
2	0.71	0.64	0.90
4	1.28	1.20	1.02
6	1.79	1.73	0.97

TABLE 3
SUMMARY OF EXPERIMENTAL AND PREDICTED FAILURE LOADS FOR THE M(T) FRACTURE TESTS

Width (inch)	2a/W	Measured Failure Load (kips)	WARP3D Failure Load (kips)	WARP3D $\frac{P_{prediction}}{P_{test}}$
3*	1/3	6.85	6.37	0.93
12*	1/3	24.28	23.74	0.98
24*	1/3	43.73	46.27	1.06
40*	1/3	66.78	74.09	1.11
40*	1/5	88.78	92.45	1.04
12**	1/3	20.90	21.24	1.02
24**	1/3	32.21	34.62	1.07
40**	1/3	44.35	53.68	1.21
40**	1/5	60.80	72.37	1.19

* Guide Plates ** No Guide Plates

Fracture tests were conducted on 3, 12, 24, and 40 inch wide M(T) specimens for the 0.063 inch thick 2024-T3 aluminum alloy. The 3 inch wide M(T) specimens were tested without guide plates and no crack buckling was observed. The larger M(T) specimens were tested with and without guide plates and substantial crack buckling was observed for the tests conducted without guide plates.

Elastic-plastic finite element analyses using WARP3D were conducted for each of the specimens tested with guide plates. The critical CTOA value used in the predictions was the same 5.5° obtained from the C(T) analyses. Figure 6 contains the failure stresses for each of the M(T) tests and the corresponding WARP3D analyses. The maximum difference between the experimental measurements and the finite element predictions was 11%. The average difference between the experiments and the predictions, for all of the tests, was 2%. While the average error for all of the WARP3D predictions looks excellent, the analyses increasingly over-predict the failure stress for larger specimen widths. This trend has three possible explanations: (1) the finite element model of the larger specimens may be too stiff, (2) the critical CTOA may be a mild function of specimen width, or (3) the guide plates may not have completely eliminated crack buckling.

To investigate the stiffness of the finite element models, select analyses were duplicated using different mesh resolutions to conduct convergence studies. The convergence studies explored reducing the element size along the crack plane (keeping the distance for measuring the CTOA constant), increasing the number of element layers through the thickness, and increasing the volume, around the crack growth region, modeled with the smallest size elements. These analyses confirmed that the meshes in this study produced converged results. Furthermore, the $\overline{B}$ formulation in WARP3D alleviates the effect of element locking; therefore, neither mesh resolution nor locking appear to have influenced the stiffness of the finite element meshes.

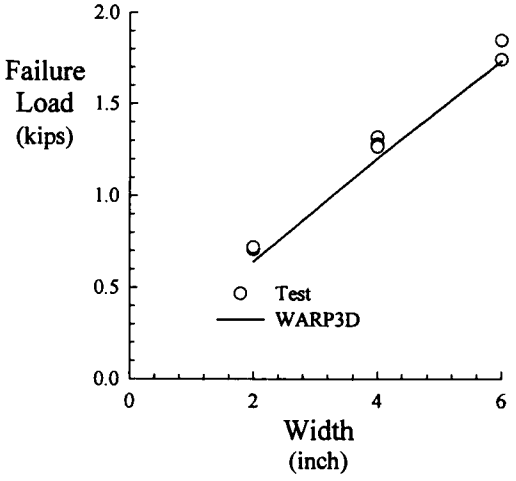

Figure 5. Measurements of failure load against specimen width for C(T) fracture tests (a/W=0.4) and the WARP3D finite element simulations with a critical CTOA of 5.5°.

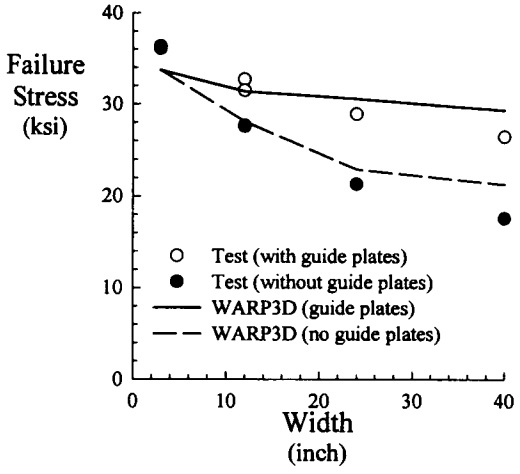

Figure 6 Measurements of failure stress against specimen width for M(T) fracture tests (2a/W=1/3) and the WARP finite element simulations with a critical CTOA of 5.5°.

The critical CTOA value of 5.5° results in an almost exact prediction of the behavior of the 12 inch wide M(T) fracture tests using WARP3D. The critical CTOA values required to "exactly" match the 24 and 40 inch wide M(T) fracture tests would be about 5.3° and 5.1°, respectively. This indicates that the CTOA fracture criterion is at worst, a mild function of specimen width.

The use of guide plates was intended to decouple the crack growth from the buckling behavior, allowing geometrically linear analyses to effectively model the crack growth. The guide plates shown in Figure 2 were sufficient to prevent buckling in the 12 inch and 24 inch wide panels, but the guide plates alone did not prevent buckling in the 40 inch wide panel. The initial 40 inch wide guide plates consisted of four 3/8 inch thick sheets of aluminum that sandwiched the specimen. Teflon sheets were placed between the guide plates and the specimen to reduce the friction between the specimen and guides. The 40 inch wide M(T) specimen tested with the guide plates experienced a 24% increase in failure stress over the unconstrained test, as shown in Figure 7. However, the guide plates were observed to deform out-of-plane about 0.1 inches, indicating that the stiffness of the guide plates was not sufficient to prevent buckling. The out-of-plane stiffness of the guide plates was increased by attaching six pairs of I-beams to the outside of the plates, as shown in Figure 2. A third, identical specimen was tested with the modified guide plate configuration and the measured failure stress was 46% larger than the unconstrained test, as shown in Figure 7.

The unconstrained, partially constrained, and I-beam constrained tests illustrate the difficulty in obtaining completely constrained conditions for wide, thin panels and the strong influence of even a small amount of crack buckling on residual strength. The guide plates that partially constrained the specimen greatly restricted the out-of-plane displacements (from about 1.0 inch in the unconstrained test to about 0.1 inches in the partially constrained test), yet the failure load was 18% lower than the test with the more effective guide plates. It is possible that the I-beam guide plates did not entirely restrict the buckling effects on the fracture behavior, indicating a lower failure stress than would be present in a completely constrained test.

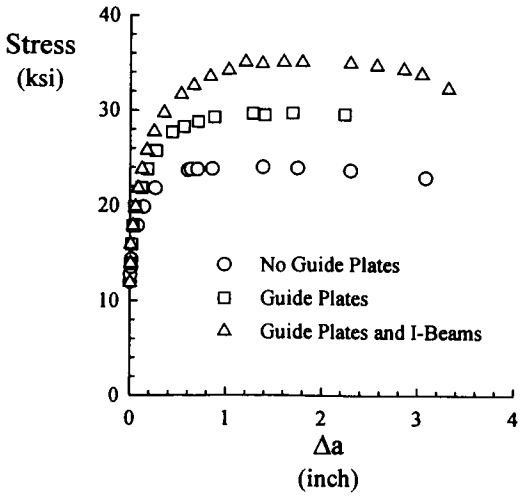

Figure 7. Measurements of stress against crack extension for the 40 inch wide M(T) test with an initial crack length to width ratio of 2a/W = 0.2.

The fracture tests conducted without guide plates experienced significant out-of-plane displacements and exhibited reductions in residual strength of up to 40% compared to identical constrained tests. In all tests, both the upper and lower crack surfaces buckled in the same direction. Reference 15 provides details on out-of-plane displacement measurements made for these tests. Figure 8 plots out-of-plane displacement measurements against the distance from the center of the specimen for 12 inch, 24 inch, and 40 inch wide M(T) fracture tests. The out-of-plane displacement measurements were made 0.5 inches above the crack plane, for a load condition near the failure load of each test. The maximum displacement at the center of the specimen was about 1.0, 0.5, and 0.25 inches for the 40, 24, and 12 inch wide M(T) specimens, respectively. To illustrate the differences in the shapes of the curves, the out-of-plane displacement (w) for each specimen was normalized by the maximum displacement (w_{max}), while the distance from the center of the specimen (x) was normalized by the half width of the specimen (W/2), as shown in Figure 9. The normalized displacements indicate that the 24 and 40 inch wide specimens exhibit considerable secondary buckling at about 2x/W = 0.5 and -0.5. The secondary buckling was almost nonexistent in the 12 inch wide specimen.

Geometrically nonlinear, elastic-plastic finite element analyses using WARP3D were performed for each of the tests conducted without guide plates; Figure 6 displays the results. The critical CTOA value used in the predictions was the same 5.5° used in the other analyses. The WARP3D analyses predicted within 7% the fracture behavior of the 12 inch and 24 inch wide specimens with crack buckling, but over-predicted the failure stress of the 40 inch wide specimen by 21%. As with the guide plate tests, the analyses over-predict the failure stress for larger specimens. Again, the trend has three possible explanations: (1) the finite element models for the larger specimens may not capture the buckling behavior properly, (2) the critical CTOA may be a mild function of specimen size, or (3) the critical CTOA may be influenced by the large out-of-plane deformations associated with crack buckling. The out-of-plane displacements and secondary buckling of the 40 inch wide M(T) fracture test was much more severe than either the 12 inch or 24 inch wide tests. Additional studies are required to demonstrate that the finite element mesh refinement, sufficient to obtain convergence in the constrained tests, is also sufficient to obtain convergence in the unconstrained tests.

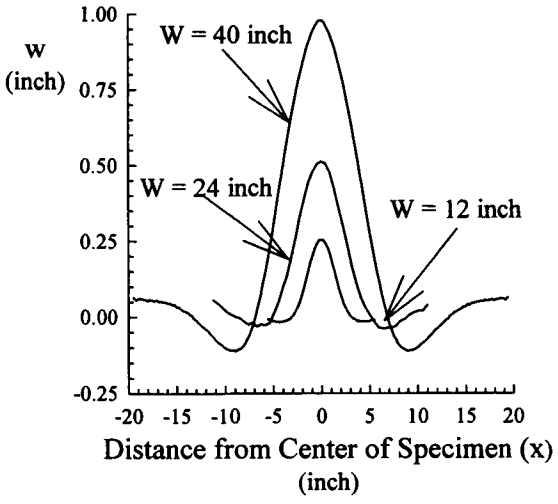

Figure 8. Out-of-plane displacements (w) measured 0.5 inches above the crack plane, at a load near the failure load for three different size M(T) specimens (2a/W = 1/3).

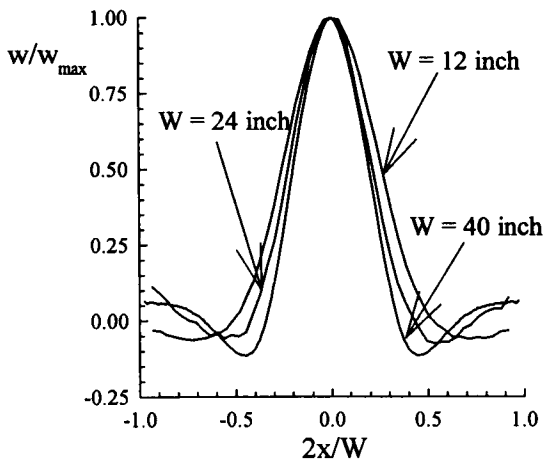

Figure 9. Out-of-plane displacements normalized by the maximum displacement against the distance from the centerline normalized by the half-width for the measurements shown in Figure 8.

5. CONCLUDING REMARKS

Tests were conducted on middle crack tension (M(T)) and compact tension (C(T)) specimens constructed using 0.063 inch thick 2024-T3 aluminum alloy. The C(T) specimens were tested with guide plates to restrict out-of-plane crack buckling, while the M(T) specimens were tested with and without guide plates. The C(T) tests were simulated with WARP3D to determine the critical CTOA value. Using this same CTOA value, the M(T) tests, conducted with and without guide plates, were predicted with WARP3D. The results from this study indicate:

1. Crack face buckling was experimentally shown to reduce the residual strength by as much as 40%.
2. The WARP3D analyses required a critical CTOA value of 5.5° to model the 0.063 inch thick material.
3. The WARP3D analyses predicted the failure load for all of the tests with guide plates to within 10% of the experimental measurements. The average error for all of the tests was small, however, a slight trend in the data indicated that the analyses were increasingly unconservative for larger panels.
4. The WARP3D analyses were able to predict the behavior of the 12 inch and 24 inch wide tests conducted without guide plates within 10%, but overpredicted the behavior of the 40 inch wide test without guide plates by about 20%.

6. REFERENCES

1. Forman, R. G. "Experimental Program to Determine Effect of Crack Buckling and Specimen Dimensions on Fracture Toughness of Thin Sheet Materials", AFFDL-TR-65-146, January 1966.

2. Feddersen, C. E., "Evaluation and Prediction of the Residual Strength of Center Cracked Tension Panels", ASTM STP 486, 1971, pp. 50-79.
3. Wang, D. W., "Plane-Stress Fracture Toughness and Fatigue-Crack Propagation of Aluminum Alloy Wide Panels" Sixth National Symposium on Fracture Mechanics, 1973, p. 334-349.
4. Gudas, J. P. and Davis, D. A., "Evaluation of the Tentative J(I)-R Curve Testing Procedure by Round Robin Tests of HY-130 Steel," Journal of Testing and Evaluation, Vol. 10, No. 6, Nov. 1982, pp. 252-262.
5. Newman, J. C., Jr., Booth, B. C., and Shivakumar, K. N., "An Elastic-Plastic Finite-Element Analysis of the J-Resistance Curve Using a CTOD Criterion," ASTM STP 945, 1988, pp. 665-685.
6. Atluri, S. N., "Energetic Approaches and Path-Independent Integrals," Computational Methods in the Mechanics of Fracture, 1986, pp. 123-165.
7. Brust, F. W., McGowan, J. J., and Atluri, S. N., "A Combined Numerical-Experimental Study of Ductile Crack Growth after a Large Unloading, Using T*, J and CTOA Criteria," Engineering Fracture Mechanics, Vol. 23, 1986, pp. 537-550.
8. Wang, L., Brust, F. W., and Atluri, S. N., "The Elastic-Plastic Finite Element Alternating Method (EPFEAM) and the Predictions of Fracture Under WFD Conditions in Aircraft Structures, Part II: Fracture and the T*-Integral Parameter," FAA Center of Excellence for Computational Modeling of Aircraft Structures, Georgina Institute of Technology, 1995.
9. Kanninen, M. F., "The Analysis of Stable Crack Growth in Type 304 Stainless Steel," International Conference of Fracture, 1980, pp. 1759-1768.
10. Newman, J. C., Jr., "An Elastic-Plastic Finite Element Analysis of Crack Initiation, Stable Crack Growth, and Instability," ASTM STP 833, 1984, pp. 93-117.
11. Dawicke, D. S. and Newman, J. C., Jr., "Residual Strength Predictions for Multiple Site Damage Cracking Using a Three-Dimensional Finite Element Analysis and a CTOA Criterion," Submitted for Publication in Fatigue and Fracture Mechanics: 29th Volume, ASTM STP 1321, 1998.
12. Dawicke, D. S. and Newman, J. C., Jr., "Evaluation of Various Fracture Parameters for Predictions of Residual Strength in Sheets with Multi-Site Damage," Proccedings from the First Joint DoD/NASA/FAA Conference on Aging Aircraft, 1998.
13. Starnes, J. H., Jr., Rose, C. A., and Rankin, C. C., "Effects of Combined Loads on the Nonlinear Response and Residual Strength of Damaged Stiffened Shells," Proceedings of the FAA-NASA Symposium on the Continued Airworthiness of Aircraft Structures, 1996, pp. 183-196.
14. Koppenhoefer, K. C., Gullerud, A. S., Ruggieri, C. and Dodds, R. H., Jr., "WARP3D: Dynamic Nonlinear Analysis of Solids Using a Preconditioned Conjugate Gradient Software Architecture", Structural Research Series (SRS) 596, UILU-ENG-94-2017, University of Illinois at Urbana-Champaign, 1994.
15. Johnston, W. M. and Helm, J. D., "Experimental Results from the FAA/NASA Wide Panel Fracture Tests," Second Joint NASA/FAA/DoD Conference on Aging Aircraft, Williamsburg, VA, 1998..
16. Dawicke, D. S., "Residual Strength Predictions Using a CTOA Criterion," DOT/FAA/AR-97/2, Proceedings of the FAA-NASA Symposium on Continued Airworthiness of Aircraft Structures, July 1997, pp. 555-566.
17. Hughes, T. J., "Generalization of Selective Integration Procedures to Anisotropic and Nonlinear Media," International Journal for Numerical Methods in Engineering, Vol. 15, 1980, pp. 1413-1418.

A MIXED-MODE I/II FRACTURE CRITERION AND ITS APPLICATION IN CRACK GROWTH PREDICTIONS

Michael A. Sutton, Xiaomin Deng, and Fashang Ma
Department of Mechanical Engineering, University of South Carolina
Columbia, SC 29208, USA
Telephone: (803) 777-7158
E-Mail: sutton@engr.sc.edu

James S. Newman, Jr.
NASA Langley Research Center, Mechanics of Materials Branch
Hampton, VA 23681, USA

ABSTRACT

A crack tip opening displacement (CTOD)-based, mixed mode fracture criterion is developed for predicting the onset and direction of crack growth. The criterion postulates that crack growth occurs in either the Mode I or Mode II direction, depending on whether the maximum in either the opening or the shear component of CTOD, measured at a specified distance behind the crack tip, attains a critical value.

For crack growth direction prediction, the proposed CTOD criterion is shown to be equivalent to seven commonly used crack growth criteria under linearly elastic and asymptotic conditions. Under elastic-plastic conditions the CTOD criterion's prediction of the dependence of the crack growth direction on the crack-up mode mixity is in excellent agreement with the Arcan test results. Furthermore, the CTOD criterion correctly predicts the existence of a crack growth transition from mode I to mode II as the mode mixity approaches the mode II loading condition.

The proposed CTOD criterion has been implemented in finite element crack growth simulation codes Z1P2DL and FRANC2DL to predict the crack growth paths in (a) a modified Arcan test specimen and fixture made of AL 2024-T34 and (b) a double cantilever beam (DCB) specimen made of AL 7050. A series of crack growth simulations have been carried out for the crack growth tests in the Arcan and DCB specimens and the results further demonstrate the applicability of the mixed mode CTOD fracture criterion crack growth predictions and residual strength analyses for airframe materials.

1. INTRODUCTION

Among the various fracture parameters that have been proposed over the years, crack tip opening displacement (CTOD) has been shown to have potential in quantifying crack tip deformations during stable crack growth. Computational studies of stable crack growth under Mode I loading were performed by Newman et al.[1-3] to assess the viability of a CTOA-based fracture criterion for numerical simulation. In addition, Dawicke and Sutton[4] conducted a series of tests to obtain the critical CTOA value for an aluminum alloy (2024 T#). They found that the measured CTOA approached a constant value after an initial amount of crack growth approximately equal to the specimen thickness. Dawicke et al.[5] then used the CTOA criterion in two-dimensional finite element analyses and successfully predicted the crack-growth behavior of these test specimens.

Previous studies of CTOD-based fracture criterion were confined to Mode I crack extension along a fixed direction which closely approximated the initial crack line, which do not answer the important questions, "In what direction and at what loading will a stationary crack or a stable growing crack propagate under mixed mode loading?" Over the years, a variety of fracture criteria have been proposed to answer these questions, including among others the maximum circumferentical stress criterion, the maximum energy release rate criterion, the stationary strain energy density criterion, and the $K_{II} = 0$ criteria. In many cases, the theories proposed have adequately described the direction of crack growth for Mode I-type dominated fracture under mixed mode loading. However, the recent tests on Arcan specimens conducted by Amstutz et al.[6, 7] have shown that there is a sharp transition of crack growth behavior from predominantly Mode I type to Mode II type. In mode II, the crack grows under conditions that are locally shear-type in the crack tip region with the crack tip opening displacement (CTOD) dominated by the shear component parallel to the crack line.

Preliminary studies[8] have shown that the CTOD-based fracture criterion can predict the load-crack extension response when crack propagation is forced to follow the experimentally observed crack growth paths. In order to develop a CTOD based fracture criterion for general mixed mode loading conditions, the authors[9] have studied the fundamental basis for the CTOD fracture criterion under mixed mode loading through analysis of *initial* crack kinking along arbitrary directions. The work has shown that, along the *initial* crack growth direction, in-plane crack tip deformations and stresses are either nearly Mode I or Model II type. Furthermore, either the opening or the shearing CTOD component of the kinked crack is a maximum during the *initial* increment of crack propagation. Using this data, *initial* crack growth is predicted to occur in either locally Mode I or locally Mode II direction, depending upon whether the opening or the shear component of CTOD measured at a specified distance behind the crack tip attains the critical value. Transition from Mode I-dominated initial crack growth to Mode II-dominated initial crack growth is predicted to occur when the shear component of CTOD reaches the critical CTOD value first.

In this work, a mixed mode, CTOD-based fracture criterion for the prediction of ***both initial kinking and stable crack propagation*** is outlined and verified through successful predictions of experimentally observed crack growth behavior in Arcan specimens[6, 7] made of AL 2024-T3 and in double-cantilever beam (DCB) specimens[10] made of AL 7050.

2. RATIONALE FOR THE CTOD-BASED MIXED MODE FRACTURE CRITERION

Figures 1a and 1b provide a graphical description of the CTOD components for the main crack and for the kinked crack. The initial idea behind the proposed CTOD criterion is that crack growth occurs along the direction where CTOD for the kinked crack (defined as Δ, at a fixed distance behind the current crack tip) is a maximum. Under linearly elastic and asymptotic conditions, several important conclusions have been obtained. For crack kinking along the mode I direction (say along $\theta_0 = \theta_c^I$), quantities $\Delta, \delta_I, \sigma_\theta, k_1$, and G take their respective maximum values, while quantities $\delta_{II}, \sigma_{r\theta}$ and k_2 become zero, where k_1 and k_2 are the stress intensity factors for the kinked crack, $\sigma\theta$ and $\sigma_r\theta$ are the circumferential normal and shear stresses, and G is the strain energy release rate. Thus, using the maximum in δ_I or Δ as a fracture parameter for the prediction of crack growth is equivalent to using the maxima in commonly accepted fracture criteria (e.g, σ_θ, G, k_I). Similarly, for crack kinking along the mode II direction (say along $\theta_0 = \theta_c^{II}$), the quantities $\delta_{II}, \sigma_{r\theta}$ and k_2 are maxima and δ_I, σ_θ and k_1 approach zero. In this case, using the maximum in δ_{II} as a fracture parameter for prediction of the direction of crack growth is equivalent to using the maxima in commonly accepted fracture criteria (e.g,

$\sigma_{r\theta}, K_{II}$). These results suggest that the CTOD components, δ_I and δ_{II}, are viable fracture parameters for predicting crack growth under mixed mode loading conditions. Conceptually, the onset of crack growth can be assumed to occur in either the direction θ_I^c or θ_{II}^c, depending on whether $(\delta_I)_{\max} = \delta_I^c$ or $(\delta_{II})_{\max} = \delta_{II}^c$ is satisfied first, where δ_I^c and δ_{II}^c are the critical values for δ_I and δ_{II}, respectively, to be determined from Mode I and Mode II fracture experiments, respectively. It can be shown that $(\delta_I)_{\max}$ (if $\theta_0 = \theta_I^c$) and $(\delta_{II})_{\max}$ (if $\theta_0 = \theta_{II}^c$) are explicit functions of the crack tip opening displacement for the main crack, D, under linearly elastic and first-order asymptotic conditions. Thus, the

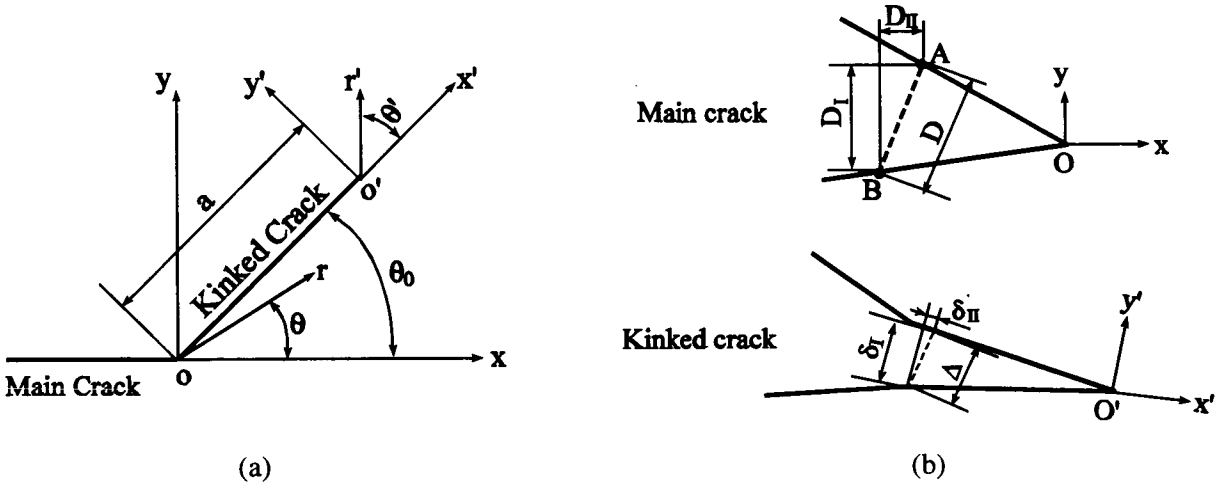

Figure 1 A geometrical representation of the relation between a main crack and a short kinked crack: (a) coordinate systems for the main and kinked cracks, and (b) definitions of crack tip opening displacements for the main and kinked cracks.

attainment of a critical value for $(\delta_I)_{\max}$, $(\delta_{II})_{\max}$ corresponds to a critical value for D. Hence, it is possible to use only the CTOD quantities at the main crack tip to assess the direction and onset of crack propagation.

For elastic-plastic crack growth, the finite element code ZIP2DL developed by Deng and Newman[11, 12] has been used with the mixed mode CTOD criterion and a small-scale yielding (SSY) model to predict the dependence of the crack growth direction in AL 20204-T3 on the crack-tip local mode mixity defined by α=arctan(D_{II}/D_I). This is achieved by simulating initial crack growth in twelve possible directions in the interval of $-90 < \theta_0 < 90^0$. A finite element mesh with focused elements around the main crack tip is developed to allow crack growth along each of the twelve directions ahead of the main crack tip. The applied load is increased gradually until the computed CTOD value at a specified distance behind the initial crack tip attains a critical value of $D = D_c$ (D_c is obtained in the Arcan tests by Amstutz et al.[6, 7]). The crack is then extended along the radial line by one element length by allowing the appropriate node pair to separate. This provides the mechanism for determining the critical kinking direction $\theta_0 = \theta_c$ that has the maximum in δ_I or δ_{II}.

The SSY simulations were performed for three values of the T-stress (normalized and represented by B=-1, 0, 1). Figure 2 presents the predicted crack kinking direction (assuming $\delta_I^c = \delta_{II}^c$) as a function of the local mode mixity, α. The experimental data are for the Arcan specimens. It can be seen that the effect of the T-stress on the predicted initial crack direction is quite small, suggesting that the CTOD criterion is not sensitive to specimen size and geometry based on the SSY analyses. Also, the CTOD

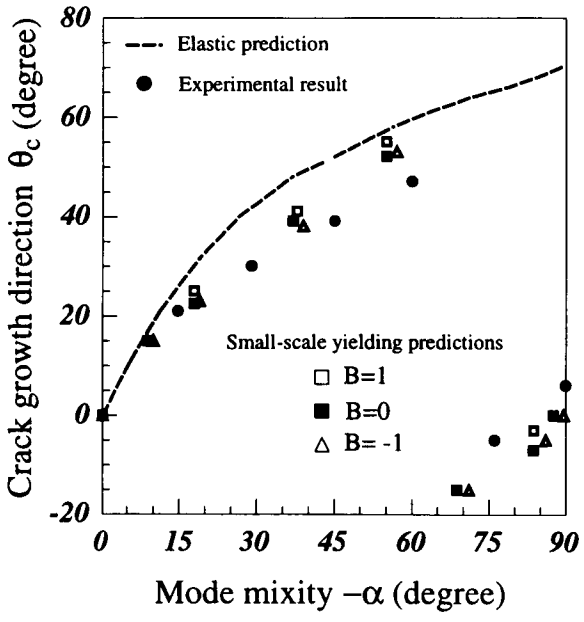

Figure 2 The crack growth direction θ_c as a function of the local mode mixity α, predicted under both linearly elastic and modified small-scale yielding conditions, and compared with the Arcan test results.

criterion predicts a transition of initial crack kinking mode from Mode I to Mode II as the mode mixity varies from Mode I values to Mode II values. This prediction is consistent with the recent experimental evidence of Amstutz et al for a 2024-T3 aluminum specimen, where a transition in fracture mode was observed during initial crack kinking for $\alpha \cong 70^0$. Finally, it is noted that the linear elastic prediction has the correct trends for predicting the initial kinking direction during Mode I crack growth, but it is not capable of predicting the transition to Mode II type crack growth.

The crack growth direction, θ_c, on the mode mixity, α, can be expressed in the following empirical expressions, which are to be used in the mixed mode CTOD criterion for the direct determination of crack growth directions under arbitrary mixed-mode loading conditions:

$$\left.\begin{aligned} \theta_c^I &= a_1 \arctan(b_1\alpha) \quad for \quad \alpha < \alpha_c \\ \theta_c^{II} &= a_2 \cos(b_2\alpha)\frac{\alpha}{|\alpha|} \quad for \quad \alpha \geq \alpha_c \end{aligned}\right\} \quad (1)$$

where α_c is the critical local mode mixity for the transition of Mode I to Mode II type fracture and a_1, b_1, a_2 and b_2 are the fitting parameters. For 2024-T3 aluminum, the fitting parameters have been obtained from the Arcan tests and they are

$$\alpha_c = 70^0, a_1 = -36.5, b_1 = 2.2, a_2 = 57.3, b_2 = 1.0 \quad (2)$$

3. NUMERICAL SIMULATION OF CRACK GROWTH USING THE CTOD CRITERION

The mixed mode CTOD fracture criterion has been implemented in the finite element code FRANC2DL[13, 14], which uses a mapping algorithm to re-mesh the crack-tip region and to transfer the state variables. Upon satisfaction of the fracture criterion, nodal release and load relaxation techniques are employed to advance the crack. In this manner, crack propagation can be simulated in arbitrary directions, as specified by the CTOD fracture criterion.

The CTOD criterion as implemented in FRANC2DL has been used to predict the crack growth paths and other features of crack growth behavior observed in the Arcan tests[6, 7] and in the DCB tests[10]. Six-node triangular elements are used for both the Arcan and DCB specimens. The near-crack-tip element size is 0.5 mm. When the CTOD value at the second node behind the crack tip (which is at a distance of 1 mm) attains the critical value D_c, the fracture criterion predicts the crack growth direction θ_c, and the crack is extended by two elements (1mm). Re-meshing is performed and equilibrium re-established after crack advance and the process is repeated throughout the crack propagation process until the desired crack propagation length is achieved.

3.1 Predictions of Crack Growth Behavior of the Arcan Specimens

Test data for the Arcan tests include the load-crack extension curves and the crack growth paths. The critical CTOD value has been measured and the average, D_c=0.089 mm, is used in this study. Actual material properties for AL 2024-T3 (including the strain hardening curve) are used as input to the finite element models. The only input related to the crack growth behavior is the critical CTOD value. The loading fixture and specimen geometries have been discussed by Amstutz et al.[6, 7]

Simulations for the Arcan tests have been carried out for the full spectrum of mixed-mode loading cases. Due to page limitation, comparisons of the measured and predicted crack growth paths for the Arcan specimens are presented here only four loading cases (denoted by the loading angle Φ, where $\Phi=0^0$ is for mode I and $\Phi=90^0$ is for mode II), as shown in Fig. 3. The comparison demonstrates that the crack growth path predictions using the CTOD-based mixed mode fracture criterion are in good agreement with the experimental observations throughout the crack propagation process. Predictions of the load-crack extension curves (not shown here) are also in excellent agreement with test data.

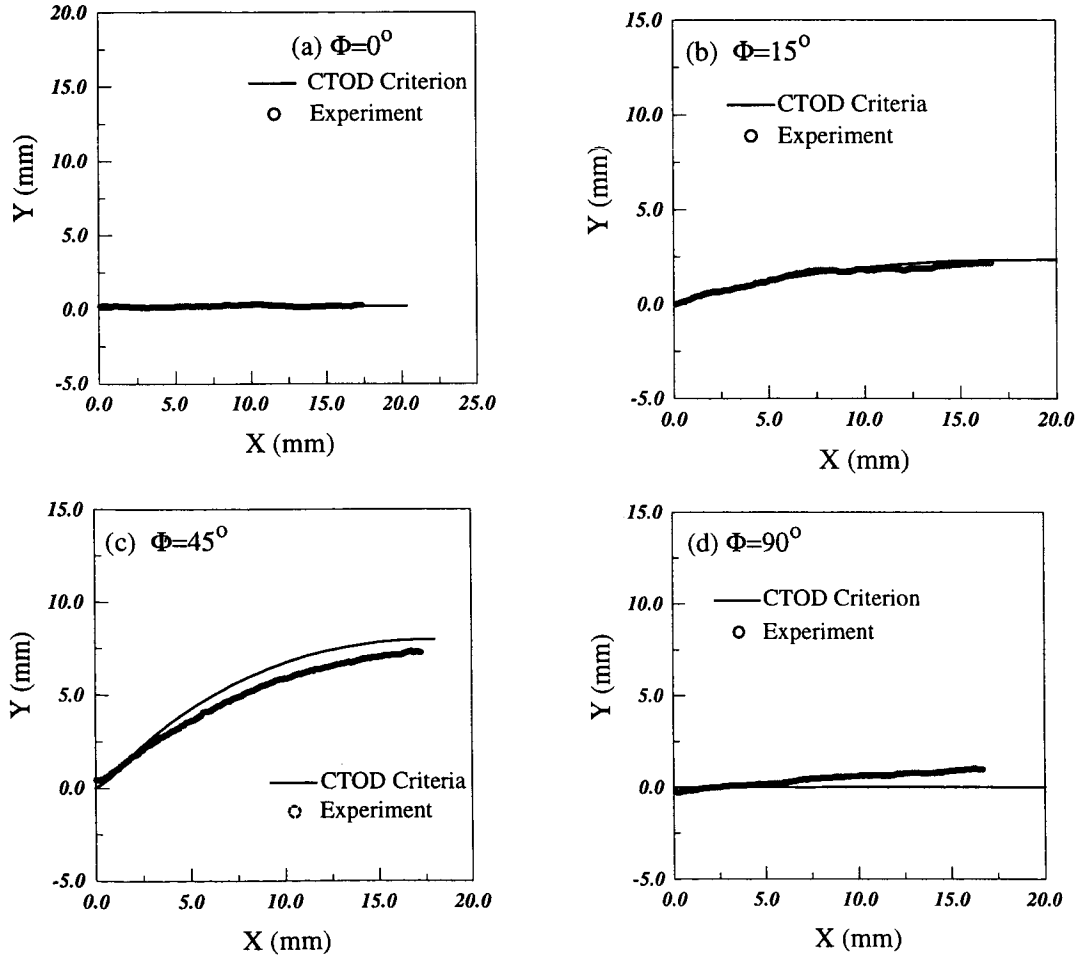

Figure 3 Predicted and measured crack growth paths for the Arcan tests for (a) $\Phi = 0^0$, (b) $\Phi = 15^0$, (c) $\Phi = 45^0$, (d) $\Phi = 90^0$.

3.2 Predictions of Crack Growth Behavior of the DCB Specimens

Mode I crack growth in DCB specimens is known to have an instability problem, in that the crack growth path is rarely along the expected straight line in the original crack direction. Depending on the particular built-in asymmetry in either the specimen geometry or the loading application, the crack growth path in a DCB test usually will curve away from the straight line either from one side or from the other. Without knowing the details of the built-in asymmetry, it is impossible to predict whether the crack will deviate from the straight line one way or another. In order for the CTOD criterion to predict the curved crack growth direction, details of the actual crack-surface geometry of the DCB specimens are modeled in the finite element meshes. These details provide the built-in geometrical asymmetry.

The database for the DCB specimens do not include the critical CTOD value nor the load-crack extension curves. As such, the measured load-load point displacement curve and the crack growth path for a particular DCB specimen are used in this study to estimate the critical CTOD value, D_c, for the material. Then the estimated critical CTOD value is used for all later predictions for this and other specimens made of the same material. The procedure used to estimate D_c is as follows.

Noting that for small α ($< 10^0$), the $\delta_c \sim \alpha$ relationship in Fig. 2 predicted by elastic and elastic-plastic analyses are nearly identical and that the elastic results are independent of material properties, it is expected that the $\delta_c \sim \alpha$ relation will depend only weakly on material properties for naturally growing cracks when the local mode mixity is dominantly mode I ($\alpha < 10^0$). Using the $\delta_c \sim \alpha$ relation for AL 2024-T3 ($a_1 = -36.5, b_1 = 2.2$) and assuming a value for D_c, the crack growth process in the DCB specimen with $a/w = 0.171$ is simulated, where a is the initial crack length and w is the width of the specimen in the crack direction. By comparing the measured and predicted load-load point displacement curves and the crack growth paths, a critical D_c value with the best overall fit can be chosen. As shown in Fig. 4a for the load-load point displacement (deflection) curve, and in Fig. 4b for the crack growth path, a

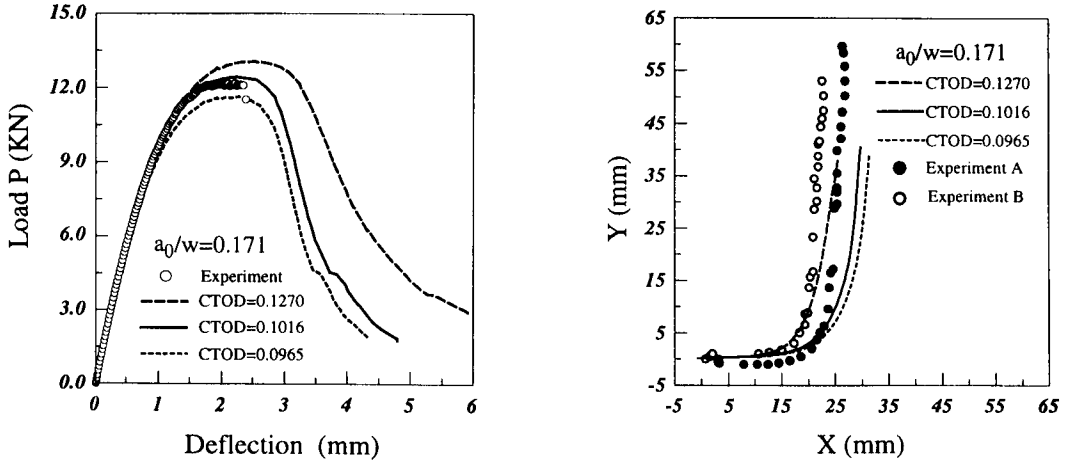

Figure 4 Predictions compared with tests for a DCB specimen with $a/w = 0.171$: (a) load-load-line displacement curve (b) crack growth path.

best overall fit is found when $D_c \cong 0.1016$ mm. It is noted that experimental measurements A and B in Fig. 4b refer to the crack growth paths measured from the two surfaces of the same DCB specimen. It is

also observed from Fig. 4b that the three predicted crack growth paths curve up on the same side of the original crack line and all can basically follow the measured crack growth trend.

To examine whether the chosen D_c value of 0.1016 mm can be used to produce reasonable predictions for other DCB specimens made of the same material, it is now used in finite element simulations of the crack growth tests in DCB specimens with $a/w = 0.404$ and 0.545. The results are presented in Figs. 5 and 6, where comparisons of the measured and predicted crack growth paths and load-load point displacement curves are shown, respectively. These comparisons shows that the CTOD criterion does a good job in predicting the rapid changes in the observed crack growth direction, with only slightly less curvature than what was measured, and that the predicted load-load point displacement curves are in excellent agreement with the measured response.

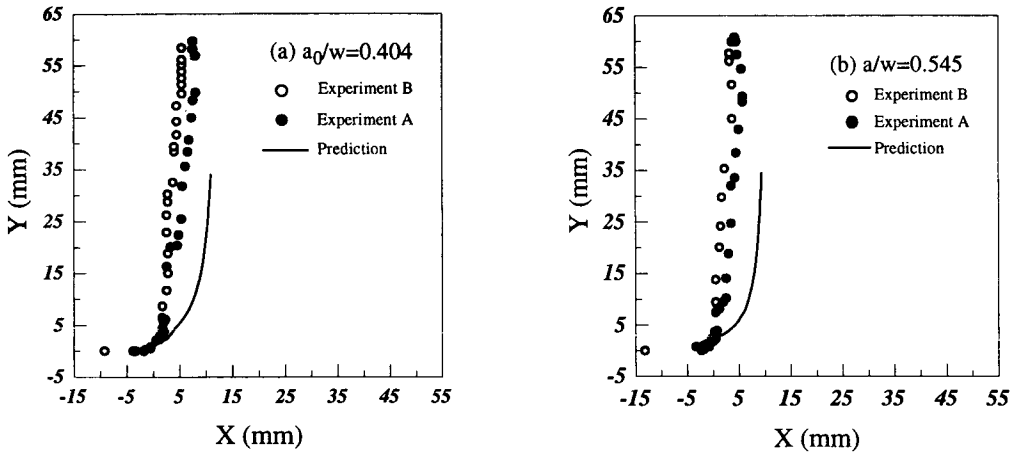

Figure 5 Predicted and measured crack growth paths for DCB specimens with (a) $a/w = 0.404$ and (b) $a/w = 0.545$, where the predictions are obtained using a critical CTOD of $0.1016mm$.

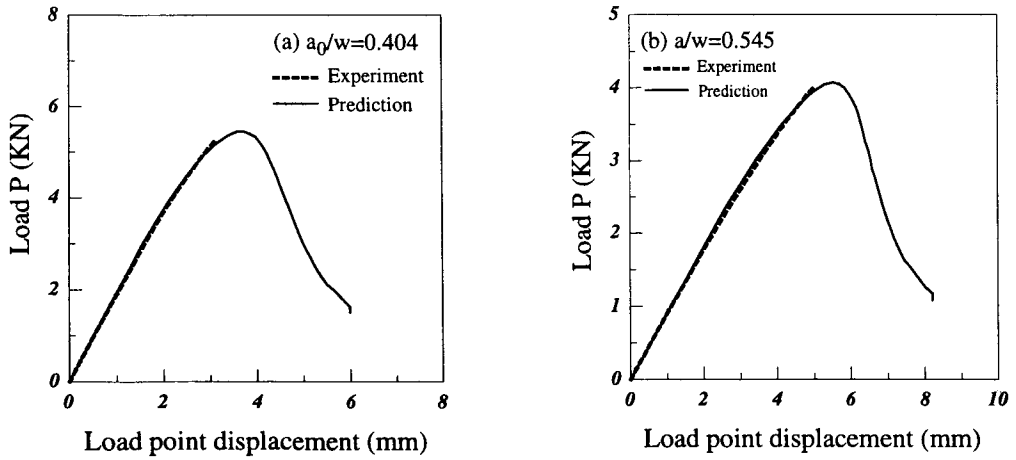

Figure 6 Predicted and measured load-load-line displacement curves for DCB specimens with (a) $a/w = 0.404$ and (b) $a/w = 0.545$, where the predictions are obtained using a critical CTOD of $0.1016mm$.

4. SUMMARY AND CONCLUSIONS

First, theoretical analyses and finite element simulations for crack growth in Arcan specimens indicate that crack growth occurs under either locally Mode I or locally Mode II conditions, which agree with experimental observations in the Arcan specimens. The mode of fracture which occurs depends on whether the tensile or shear component of CTOD first attains a critical value.

Second, the proposed mixed mode CTOD fracture criterion can adequately capture the mixed mode crack growth behavior (including the crack growth path, the load-crack extension curve and the load-load line displacement response) in ductile airframe materials. Results clearly show that predictions for both the Arcan-specimen and DCB are in good agreement with experimental data.

Third, since the fracture parameter is expected to be a material property, the CTOD criterion developed for 2024-T3 aluminum using the Arcan specimen data can be used for predicting crack growth for other specimen geometry. In fact, we have performed a range of crack growth simulations for both middle crack tension specimens and compact tension specimens machined from 2.3-mm thick, 2024-T3 aluminum. Results similar to those presented in this paper have been obtained for both specimens, with propagation occurring under locally Mode I conditions throughout the crack growth process.

Fourth, for the DCB specimen, due to the lack of a measured critical CTOD, the measured load-load point displacement curve and the crack growth path for a particular DCB specimen was used to estimate the critical CTOD value, D_c. By matching the measured and predicted load-load point displacement curves and also considering the prediction for the crack growth path, an estimate for D_c was determined and was used for later predictions for this and other DCB specimens made of the same material. The estimated critical value of CTOD for Al 7050 is approximately on the order of that obtained for Al-2024-T3, with both specimens nominally in the LT orientation (crack initially perpendicular to the rolling direction).

Finally, with regard to the crack growth paths shown in Figs. 4 and 5 for the DCB specimens, recent experimental observations[10] suggest that the fracture behavior of Al 7050 is highly anisotropic with $(K_{IC}^{TL}/\ K_{IC}^{LT}) \approx 0.60$ for Al-7050, which would imply that $(\delta_{IC}^{TL}/\ \delta_{IC}^{LT}) \approx 0.60$. Since our simulations used a constant CTOD value for all angles, the predicted crack paths would have less curvature than the actual crack growth paths, which is precisely what is shown in Figs. 4 and 5. It appears that the CTOD-based fracture criterion can be extended to include the effects of anisotropic material fracture behavior by including a functional form for critical CTOD as a function of direction. The functional form can be determined experimentally through a series of mixed mode tests. The specimens to be tested would have flaws at an initial angle to the material directions, and the effects of material direction on critical CTOD would be measured during crack growth.

ACKNOWLEDGMENTS

The authors wish to thank (a) Mr. Rick Pettit from Boeing, Inc. for both the use of his experimental data from several DCB crack growth tests and his timely discussions of key issues in the testing process, (b) Drs. Daniel Swenson and Mark James from the Kansas State University for their assistance in modifying and using FRANC2DL in our fracture simulations, and (c) Dr. David S. Dawicke at NASA Langley Research Center for his assistance in both fracture tests and fracture simulations. In addition, the financial support of NASA headquarters through an NASA EPSCoR grant is gratefully acknowledged.

REFERENCES

1. Newman, J. C., Jr., 1977. Finite Element Analysis of Crack Growth under Monotonic and Cyclic Loading. *ASTM STP* 637, 56-80.
2. Newman, J.C., Jr., 1984. An Elastic-Plastic Finite Element Analysis of Crack Initiation, Stable Crack Growth, and Instability. *Fracture Mechanics, ASTM STP* 833, 93-117.
3. Newman, J.C., Jr., Dawicke, D. S., and Bigelow, C. A., 1992. Finite Element Analyses and Fracture Simulation in Thin Sheet Aluminum Alloy. *NASA TM*-107662, NASA Langley Research Center, Hampton, Virginia.
4. Dawicke, D. S., Sutton, M. A., 1994. CTOA and Crack-Tunneling Measurements in Thin 2024-T3 Aluminum Alloy. *Experimental Mechanics* 34, 357-368.
5. Dawicke, D. S., Sutton, M. A., Newman, J. C., Jr., Bigelow, C. A., 1995. Measurement and Analysis of Critical CTOA for Aluminum Alloy Sheet. *Fracture Mechanics, ASTM STP* 1220, 358-379.
6. Amstutz, B. E., Sutton, M. A., Dawicke, D. S. and Newman, J. C., Jr., 1995. An Experimental Study of CTOD for Mode I/ II Stable Crack Growth in Thin 2024-T3 Aluminum Specimens. *Fracture Mechanics, ASTM STP* 1256, 256-271.
7. Amstutz, B. E., Sutton, M. A., Dawicke, D. S. and Boone, M. L., 1995. Effects of Mixed Mode I/II Loading and Grain Orientation on Crack Initiation and Stable Tearing in 2024-T3 aluminum. *Fatigue and Fracture, ASTM STP* 1296, 105-125.
8. Sutton, M. A., Zhao, W., Deng, X., Dawicke, D. S., and Newman, J. C., Jr., 1997. Numerical Investigations Into the Viability of CTOD as a Fracture Parameter for Mixed-Mode I/II Tearing of Thin Aluminum Sheets. *Proceedings of the FAA-NASA Symposium on Continued Airworthiness of Aircraft Structures (Atlanta, Georgia, August 28-30, 1996), DOT/FAA/AR*-97/2, Vol. II, 461-472.
9. Ma, F., Deng, X., Sutton, M. A. and Newman, J.C., Jr., 1998. A CTOD Based Mixed Mode Fracture Criterion. *Mixed Mode Crack Behavior, ASTM STP* 1359 (in press).
10. Pettit, R., 1998, Private Communication with M. A. Sutton.
11. Deng, X., Newman, J. C., Jr., 1997. Implementation and Application of a Large-Rotation Finite Element Formulation in NASA Code ZIP2DL. *FAA-NASA Symposium on Continued Airworthiness of Aircraft Structures (Atlanta, Georgia, August 28-30, 1996), DOT/FAA/AR*-97/2, Vol. II, 377-390.
12. Deng, X., Newman, J. C., Jr. 1997. ZIP2DL – An Elastic-Plastic, Large-Rotation Finite-Element Stress Analysis and Crack-Growth Simulation Program. *NASA Technical Memorandum* 110332, NASA Langley Research Center, Hampton, Virginia.
13. Swenson, D., James, J., 1997. FRANC2D/L: A Crack Propagation Simulator for Plane Layered Structures. User's Guide, Version 1.4.
14. James, M. A., Swenson, D., 1998. A Software Framework for Two-Dimensional Mixed Mode I/II Elastic-Plastic Fracture. *Mixed Mode Crack Behavior, ASTM STP* 1359 (in press).

YIELD-STRIP MODELS FOR RESIDUAL STRENGTH OF MSD DAMAGED CURVED AND FLAT PANELS

Karl-Fredrik Nilsson
Aeronautical Research Institute of Sweden
P.O. Box 110 21, S-161 11 Bromma Sweden

ABSTRACT

The paper presents a yield-strip model to compute the residual strength of structures damaged by multiple site damage (MSD) and two particular applications. The first presents a parameter study of a stiffened sheet where the influence of crack patterns, and crack sizes and crack growth resistance are investigated,. This study showed that the residual strength reduction was more pronounced for crack growth resistant materials, that also very small cracks may have a large impact and that cracking at tear straps is particularly deleterious. The second applications concerned an analysis of a cylindrical shell where nonlinear bulge-out is accounted for. The residual strength was compared with corresponding flat sheet results. The stress levels for the shell are two to three times lower due to bulge out, but the relative reduction due to MSD was very similar.

1. INTRODUCTION

Multiple-site damage (MSD) may substantially reduce the residual strength of aging aircraft structures[1-5]. Continued airworthiness of aging aircraft requires that we understand why and to what extent MSD may reduce the residual strength, in particular if it falls below the design limit (onset of MSD). Such knowledge can only be gained from relevant modelling along with testing. A complete analysis involves a complex and combined fracture and structural problem. It is therefore necessary to start with simple structures such as flat sheets and gradually increase the complexity to a fuselage structure, to understand the basic mechanisms and important modelling aspects.

It is well established that plastic effects must be accounted for in the fracture problem since plastic zones normally extend over several MSD cracks[6,7,8]. The crack tip opening angle (CTOA) criterion [6,9,10,11] and the T*-parameter[8] have been successfully adopted to predict residual strength in MSD situations. Since we are dealing with thin sheets, the plasticity modelling may be simplified by using yield-strip models[7,10-13]. For flat sheets the elasto-plastic residual strength problem may then be solved semi-analytically. In this paper a brief description of the yield-strip model adopted to MSD conditions will be given and exemplified by two applications.

Onset of MSD does not just involve the size of cracks but also the crack distribution and material properties. A study where the semi-analytical technique is adopted to flat stiffened sheets (Fig 1a) to assess the importance of crack size, crack distribution and crack growth resistance for the criticality of MSD will be first presented. The second application, Fig. 1b), deals with application of the yield-strip model to a cylindrical shell. The shell problem is considerably more complex since crack bulging requires a kinematically nonlinear analysis. An outline of the solution procedure will be given. The importance of kinematical nonlinearity will be quantified as well as a comparison of the relative effect of MSD for shells and flat sheets.

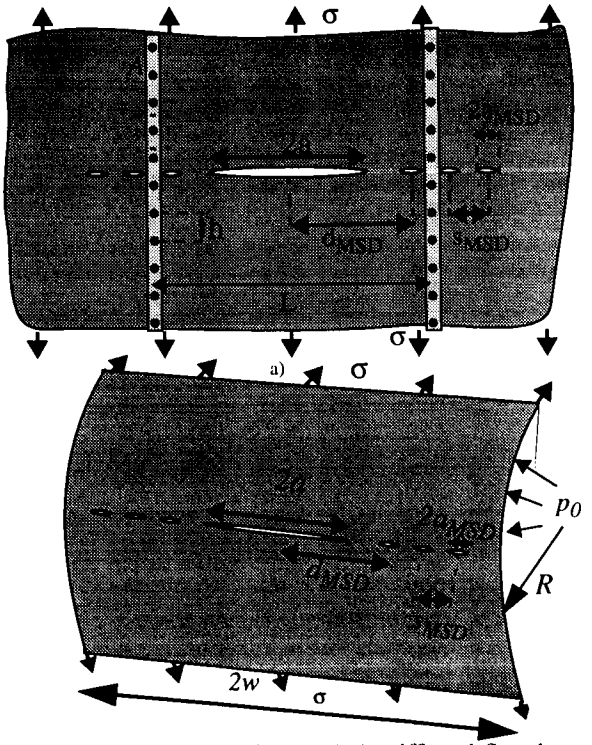

Fig. 1. The Model Problem. a) A stiffened flat sheet b) cylindrical shell with major crack, $2a$, and microcracks aligned on each side,

2. THE FRACTURE MODEL

The adopted elastic-plastic fracture model has been described previously at different stages of development [7,10-13], and we therefore only summarize the physical arguments and main features here.

2.1 Plastic Crack Interaction Model

In the yield-strip model plastic deformation is modelled by extending the physical crack with a fictitious length, s, where cohesive forces corresponding to yielding act [14, 15]. Fig. 2 shows the adopted yield-strip model when the plastic zone extends over three MSD cracks. Cracks embedded in the plastic zone are modelled as traction free entities whereas the yielded ligaments have a traction which is equal to the yield stress of the sheet material, σ_Y. The MSD cracks outside the plastic zone have a very small effect and can be neglected in applications[7]. In presence of MSD cracks, the *average* stress in the plastic zone, *s*, will be lower than yield stress of the material, thereby reducing the cohesive forces of the yield zone. This is one of the most important mechanisms for the MSD induced residual strength reduction and is here referred to as the *MSD reduced strength of the sheet material.*

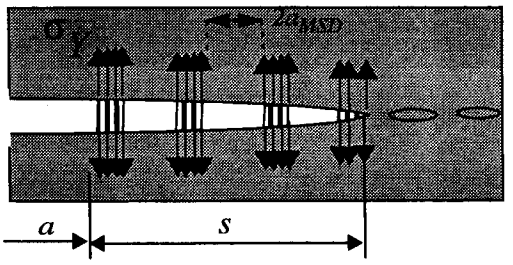

Fig. 2. Illustration of the yield strip model where the plastic zone extends over three MSD-cracks.

2.2 Crack Propagation Model

The fracture toughness of aircraft sheet material has usually a significant crack growth resistance, i.e. the crack driving force increases with crack growth. Experimentally determined crack growth resistance curves are often treated as a material parameter. The crack growth resistance is, however, *not* a simple material parameter, and will always be approximate when used for other geometries and loadings other than the ones used in the basic tests. The application of such an experimentally determined *R*-curve is particularly questionable for MSD damaged panels since it is very unclear how to apply the *R*-curve after link-up.

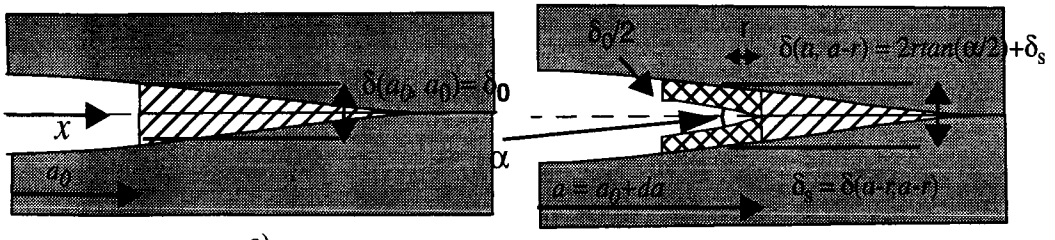

Fig. 3 The crack profile at initiation a) and b) at propagation with definition of crack growth parameters, α and δ_0. The hatched area depicts the plastic stretch behind the crack tip.

Deng and Hutchinson[10] realized this predicament and suggested a two-parameter crack propagation criterion for the MSD problem. Onset of crack growth is determined by a critical crack opening, δ_0, whereas continuous growth is governed by a constant crack opening angle, α, as displayed in Fig. 3a and 3b. The CTOA-criterion model has a very strong support in data from experiments of thin sheets, e.g. Newman *et al.*[6]. In the model, crack growth is initiated when the crack tip opening displacement reaches the critical value, δ_0. Subsequent growth is modelled by advancing the crack in small increments *r*, requiring that the standard Dugdale opening a distance *r* behind the current tip attains the opening associated with the near tip angle criterion plus the plastic stretch, δ_s, *viz*

$$\left.\begin{aligned} \delta_c(a_0, a_0) &= \delta_0 \qquad \text{initiation} \\ \delta_c(a, a-r) &= 2r\tan(\alpha/2)+\delta_s \qquad \text{propagation} \end{aligned}\right\}. \quad (1)$$

The first argument in the critical crack tip opening, δ_c, refers to the current crack position and the second to the point where the displacement is evaluated. The subscript *s* denotes the stretch. The plastic stretch,

$\delta_s = \delta(a-r, a-r)$, is the crack tip opening displacement at the crack tip of the previous increment and usually increases with crack growth and gives the crack growth resistance.

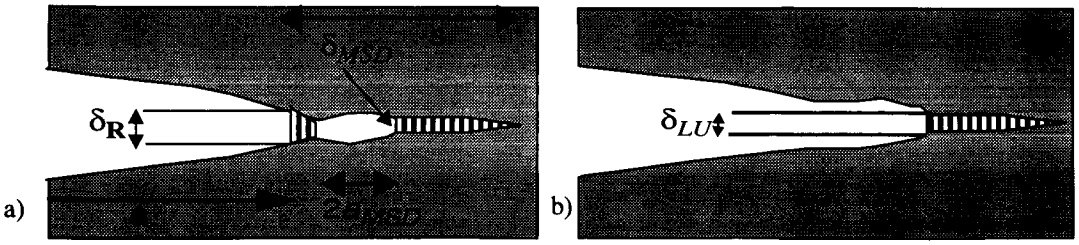

Fig. 4 The crack tip deformation with definition of crack opening displacements
a) just prior to crack link-up, the major crack has an opening δ_R and the right tip of the small crack δ_{MSD}
b) after crack link-up, the extended restarts with (1) with $\delta_c=\delta_{LU}$.

Due to the pronounced crack growth resistance effect, the smaller MSD cracks will usually (almost always in the numerical examples) attain the critical value, δ_0, prior to link-up and should therefore be allowed to propagate as well. In this paper each crack tip is assumed to be governed by the criterion (1) for onset and continuous growth. After link-up with the MSD crack, the new extended crack, $a+2a_{MSD}$, follows the propagation criterion (1) as outlined in Fig. 4, and where δ_{MSD} is the stretch of the right crack tip of the MSD crack just prior to link-up and δ_{LU} the critical value to restart growth after linkup. If the MSD crack has not propagated, i.e. $\delta_{MSD} < \delta_0$ then $\delta_{LU} = \delta_0$ otherwise $\delta_{LU} = 2r\tan(\alpha/2) + \delta_{MSD}$. The same procedure is repeated when two MSD cracks coalesce. Two effects that will reduce the residual strength associated with the growth of MSD cracks may now be identified. Growth of MSD cracks will *eat away the ligaments* and thereby accelerate the "reduced strength effect" we can call that *MSD induced ligament erosion.* At link-up, the plastic stretch of the MSD crack is smaller than that of the lead crack ($\delta_{MSD} < \delta_R$), and in accordance with the adopted propagation law (1) infers a *drop in the crack growth resistance after link-up.*

2.3 Computational Procedure

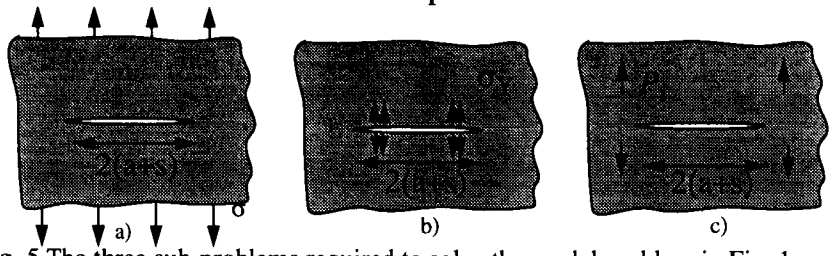

Fig. 5 The three sub-problems required to solve the model problem in Fig. 1

The residual strength problem in Fig 1a can then be derived by superposition of the three elastic subproblems illustrated in Fig. 5 which can be found in Handbooks[17] or derived by complex variable methods[16]. The condition that the total stress intensity at the tip of plastic zone, $x=a+s$, must vanish, provides the relation which relates the applied load, σ, with the plastic zone length, s. This relation is nonlinear in s but linear in σ and P_i. The procedure to generate numerical results takes a specified s and computes the associated σ and P_i from the condition that the stress intensity factor should vanish and displacement compatibility between sheet and strap of the modelled crack should be zero. Once these quantities have been determined all other quantities including the crack opening displacement can also be determined. The critical stress, σ_c, is then determined by an iterative procedure where s is updated until the crack growth condition (1) is satisfied as outlined in Fig. 6.

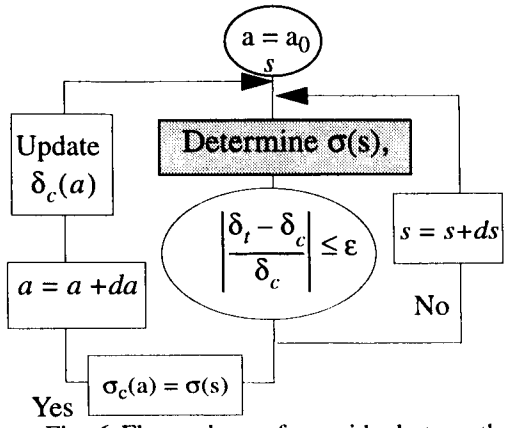

Fig. 6 Flow scheme for residual strength calculation

2.4. Comparison with Experiments for Flat Unstiffened Sheets

The fracture model embodied in Eq. (1) was adopted along with the three subproblems[11] to predict the values of crack link-up and maximum load for the three series of unstiffened flat panels tests described in[18-20]. These panels represented a large variety of panel widths, size and number of MSD cracks and major crack length. The two fracture parameters, α and δ_0, were first determined for each series of tests by fitting the curves for panels without MSD cracks.

The load at first link-up for all panels are shown in Fig. 7. Each set of results corresponds to one particular panel, and the four bars represent: computed values when there is no MSD; measured load with MSD; computed values with MSD. The mean value and standard deviation for the relative difference between test results and predictions was 0.8% and 6.3% only. These numbers should be compared with the overall reduction due to MSD which was 30%. Subsets of these experiments have also been analysed by full elasto-plastic FE analyses in conjunction with a CTOA criterion[6] as well as by the elasto-plastic FE alternating method and using the T*- integral as crack growth parameter[8]. The present predictions were very close to and consistent with the predictions[6] in particular but also to the ones in[8].

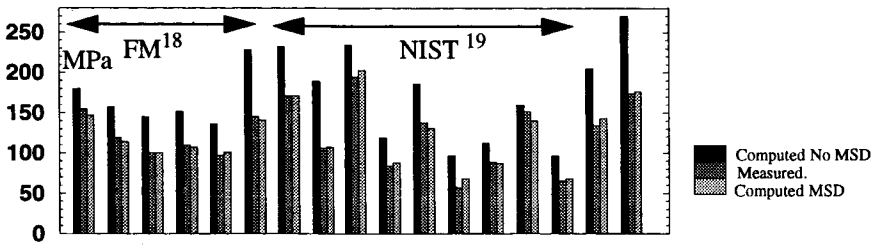

Fig. 7 Computed and Measured Load at first link-up.

3. INFLUENCE OF MSD CRACK PATTERNS AND CRACK GROWT RESISTANCE

We now proceed to the parameter study for the stiffened flat sheet shown in Fig 1a. A more comprehensive study than what is reported here can be found in[13]. Material data and geometries representative of a typical aircraft sheet material and geometry will be adopted in the examples to follow. The sheet is assumed infinitely wide, elastic-perfectly plastic with E = 70GPa, ν = 0.33 and $\sigma_Y = 350MPa$[a].The strap has the same E and ν but a higher yield stress; 482MPa. These yield stresses are representative for the 2024 and 7075 Al-Alloys. The sheet thickness, t, is $1mm$ and the cross section area of the strap, A, $50mm^2$. The strap spacing, L, is $475mm$, rivet spacing, h, and MSD crack spacing, s_{MSD}, are 25 mm.

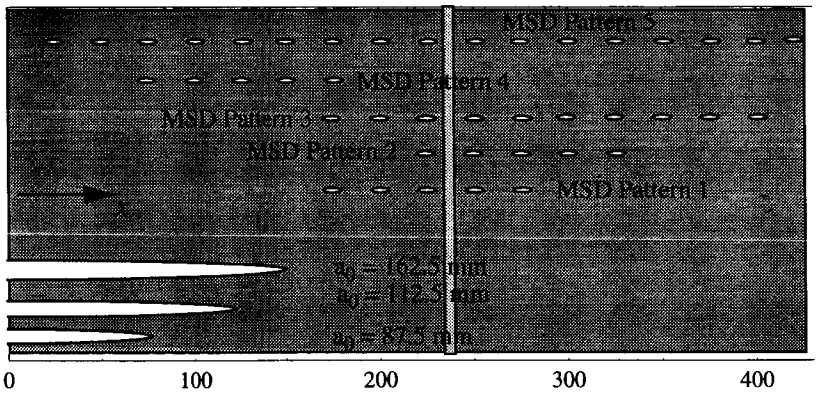

Fig. 8 The three initial crack lengths of the lead crack and the five MSD patterns used in the parameter study. The length of MSD cracks, $2a_{MSD}$ are 10 mm in the figure.

Two fracture criteria will be used:

- Crack propagation criteria 1: $\delta_0 = 0.24mm$, $\alpha = 0.047$ *rad*, $r = 1mm$
- Crack propagation criteria 2: $\delta_0 = 0.5mm$, $\alpha = 0$ *rad*, $r = 0$ *mm*

a. Aircraft sheet material have plastic hardening. The adopted value represents the mean value of initial yield and ultimate stress.

Three initial crack lengths, a_0 = *87.5, 112.5 and 162.5mm* and *five* different MSD crack patterns will be adopted:

- MSD Pattern 1: d_{MSD} = *175mm*, s_{MSD} = *25mm*, *No of MSD cracks = 5*
- MSD Pattern 2: d_{MSD} = *225mm*, s_{MSD} = *25mm*, *No of MSD cracks = 5*
- MSD Pattern 3: d_{MSD} = *175mm*, s_{MSD} = *25mm*, *No of MSD cracks = 10*
- MSD Pattern 4: d_{MSD} = *75mm*, s_{MSD} = *25mm*, *No of MSD cracks = 5*
- MSD Pattern 5: d_{MSD} = *25mm*, s_{MSD} = *25mm*, *No of MSD cracks = infinite*

For each MSD pattern, *five* different crack lengths, $2a_{MSD}$ = *0, 2, 5, 10 and 15mm* will be analysed. Thus in all 126 $(2 \cdot 3 \cdot [1 + 5 \cdot 4])$ different cases will be analysed. The lead crack lengths and the five MSD crack patterns for the case $2a_{MSD}$ = *10 mm* are shown in Fig. 8.

Before we proceed, we will briefly comment on the selection of parameters.

- Crack propagation criteria 1 is a representative value for the 2024-alloy and this particular set has been fitted to actual tests[19]. The second one has no crack growth resistance. The value of the crack opening displacement is, however, a representative value for aircraft sheet alloys[21].
- The lead crack can be formed by coalescence of MSD crack or by discrete source damage due to uncontained failure of engines, fan blades etc. The three values for a_0 are selected to represent a short, an intermediate and a long lead crack.
- MSD cracking in real structures is primarily located in the mid-bay region[2] as in MSD Pattern 4. MSD Pattern 5 represents the case where each rivet site is cracked. This is expected to be the pattern with the overall largest residual strength reduction, and should give a conservative estimate of residual strength for MSD damaged panels with a given MSD crack length. The remaining MSD patterns (Pattern 1,2 and 3) have the cracking concentrated at the stiffener. These patterns are selected since we anticipate that such MSD cracking may drastically reduce the crack arrest effect of the tear strap.
- Cracks emanating from the fastener hole will be at least of the order of a mm, probably more, before they are detectable whereas the rivet hole is typically 5mm. Thus, the length of the hole plus the cracks emanating from the hole is typically 5-10 mm before detection. There are reports that very small cracks may reduce the residual strength considerably, but that the reduction is a relatively weak function of the actual size of the MSD cracks[1,4,5]. This is sometimes referred to as the "knock-down" effect. The chosen MSD crack lengths are selected to cover the range from very short cracks to fairly long ones.

As a basis for the discussion of results the particular case: crack propagation criteria 1, a_0 = *87.5mm*, MSD Pattern 1, $2a_{MSD}$ = *10mm*, will be discussed in some more detail. Fig. 9a shows the residual strength for this case, or more precisely the applied load required to drive the *lead* crack, σ_c, as function of its half-length, a. For comparison the corresponding residual strength with no MSD is also plotted. At link-up with a smaller crack the length of the lead crack is increased by the length of the small crack. This crack extension is represented by the dotted lines in Fig. 9a. The numbers 1-7 correspond to particular events which take place sequentially and are illustrated pictorially in Fig. 9b.

At "1" the critical crack tip opening is attained and crack growth is initiated. Due to the crack growth resistance, crack propagation takes place under increasing load until the point "2" where the plastic zone engulfs the first MSD crack and with a resultant local drop in residual strength. At "3" the first MSD crack starts to propagate and at "4" two propagating MSD cracks link up to form a larger MSD crack, which is followed by another MSD crack linkup soon after. The lead crack links up with the "linked-up" MSD crack at "5" and this "extended" lead crack restarts at "6". The right tip of the linked-up MSD crack had not grown prior to linkup and it therefore restarts with crack tip opening δ_0. This is followed by link-up with remaining MSD cracks. At "7" all MSD cracks have coalesced with the lead crack but in this case the tip of

the extended crack has propagated prior to link-up and the crack opening displacement, δ_c is therefore higher than δ_0.

The particular sequence of events were rather different for the 126 cases. In particular, when the second crack growth criterion is adopted, MSD cracks do not propagate prior to link-up. The drop in the residual strength at first ligament yield (i.e. point "2"), is only a local minimum for many cases and should not be used as a criterion for crack linkup.

The residual strength curves for the initial MSD crack length $2a_{MSD}$ = *10mm*, are displayed in Fig. 10-13. Fig. 10 shows the result for the shortest initial lead crack length, crack growth resistant material for all five crack patterns. Fig. 11 show the results for MSD pattern 3 at the three initial lengths *87.5, 112.5* and *162.5 mm* respectively. In Fig. 12 the crack growth criterion 2 is adopted and results shown for MSD patterns 2, 4 and 5. For the second propagation criterion there is no "history dependence" and all three initial crack lengths can be presented in the same curve. It is obvious from these results that all parameters in the parameter study have significant effects and the interaction is intricate. Some general trends are however obvious:

- The "crack arrest bump" in the residual strength curve can be almost annihilated by MSD cracking located at the strap, and thereby disable its crack arrest capability.
- The MSD reduction in the residual strength is more pronounced for a crack growth resistant material (crack growth criterion 1). This could be expected since all three "reduction mechanisms" mentioned above are active.
- The case with MSD cracking only in the mid-bay (Pattern 4) is the least critical since the crack arrest capability of the strap is retained.
- The scenario "each rivet site cracked", i.e. MSD Pattern 5, gives a strongly conservative estimate of the residual strength if we assume MSD Pattern 4 to be the most prevalent one.

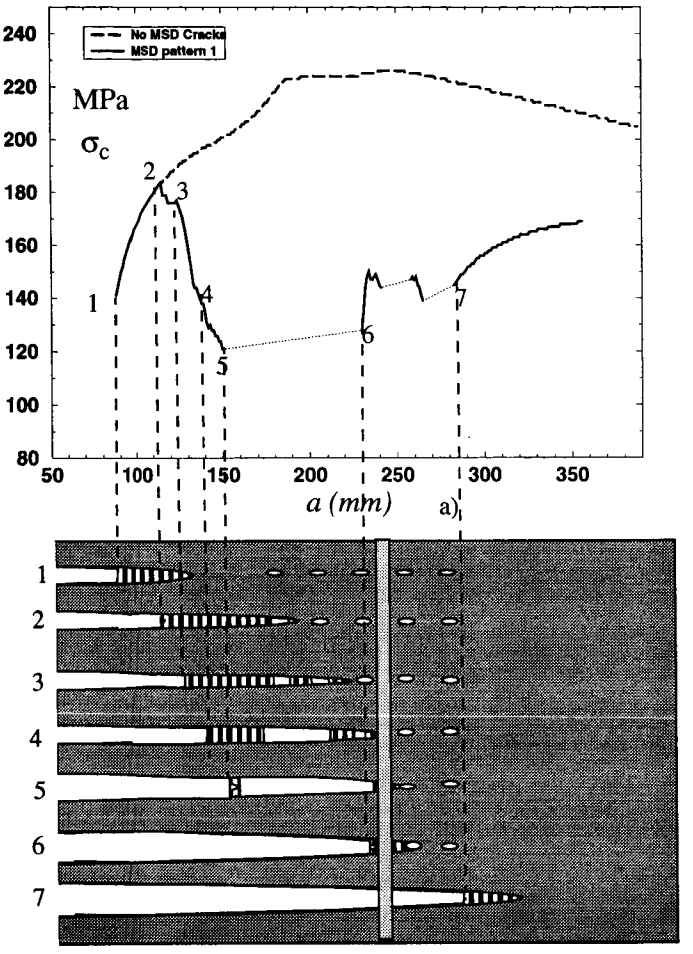

Fig. 9
a) Residual strength curve and b) sequence of events for case with a*0* = *87.5mm, MSD pattern 1, 2aMSD = 10mm,* d*0* = *0.24mm,* a = *4.7 rad*
Sequence of events:
1/ Onset of crack growth for lead cracks (δc = *0.24*)
2/ First ligament fully yielded (δc = *0.55*)
3/ Onset of crack growth for first MSD crack (δc = *0.65*)
4/ Linkup between MSD crack 1 and 2 (δc = *0.74*)
5/ Lead crack links up with MSD crack (δc = *1.12*)
6/ Continued growth of lead crack after link-up (δc = *0.24*)
7/ All MSD cracks linked up (δc = *0.36*)

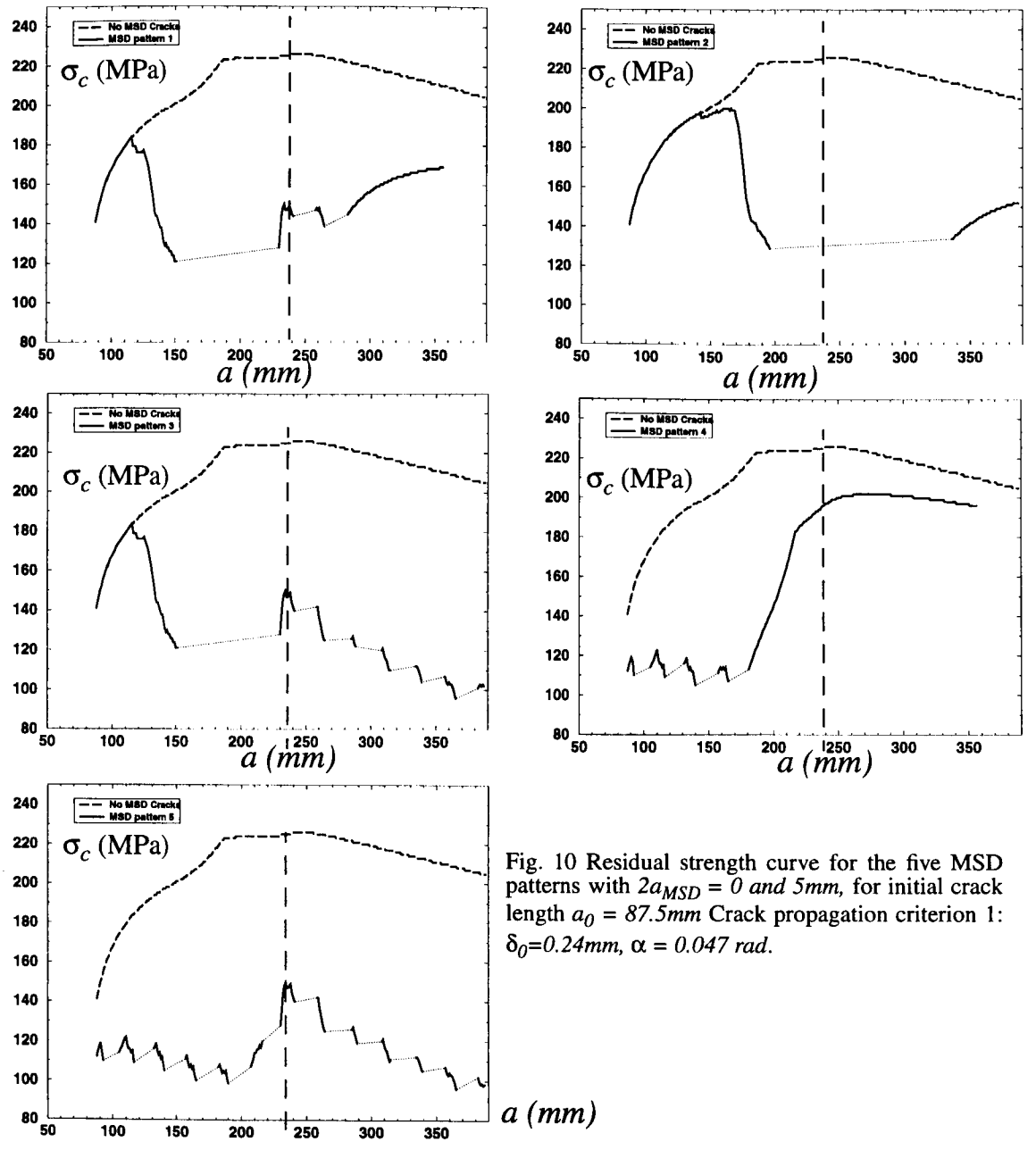

Fig. 10 Residual strength curve for the five MSD patterns with $2a_{MSD} = 0$ *and 5mm,* for initial crack length $a_0 = 87.5mm$ Crack propagation criterion 1: $\delta_0 = 0.24mm$, $\alpha = 0.047$ *rad.*

Figs. 13a and 13b show the maximum value of the stress, σ_c, in the interval $a_0 < a < 1.05L$, as function of the MSD crack length for MSD Pattern 1-5 and $a_0 = 112.5mm$ for the first and second crack growth criteria respectively. We see immediately a very distinct difference between the two crack growth criteria: In Fig. 13a, the crack growth resistant material, there is a very clear "knock-down" effect which cannot be found for the case with no crack growth resistance (Fig. 13b). The knock-down effect is due to growth of the small MSD cracks. For a crack growth resistant material MSD cracks engulfed by the plastic zone will start to propagate and thereby erode the strength of the sheet; for shorter MSD cracks this effect will only require a slightly higher load than for longer ones.

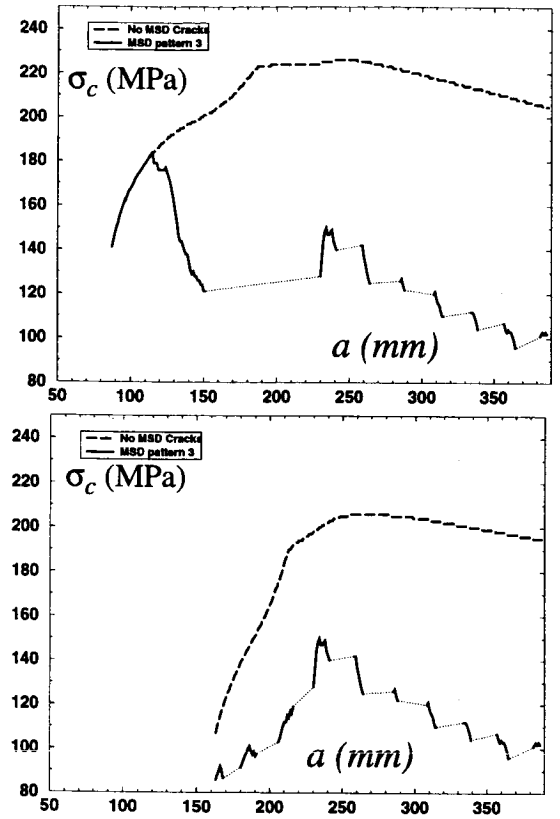

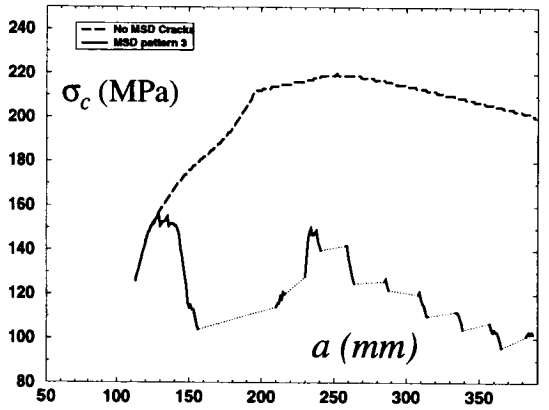

Fig. 11 Residual strength curve for three initial lengths of the lead crack, a0 = 87.5, 112.5 162.5 mm for MSD pattern 3 and with $2a_{MSD}$ = *0 and 5mm.* Crack propagation criterion 1: δ_0=*0.24mm,* α = *0.047 rad.*

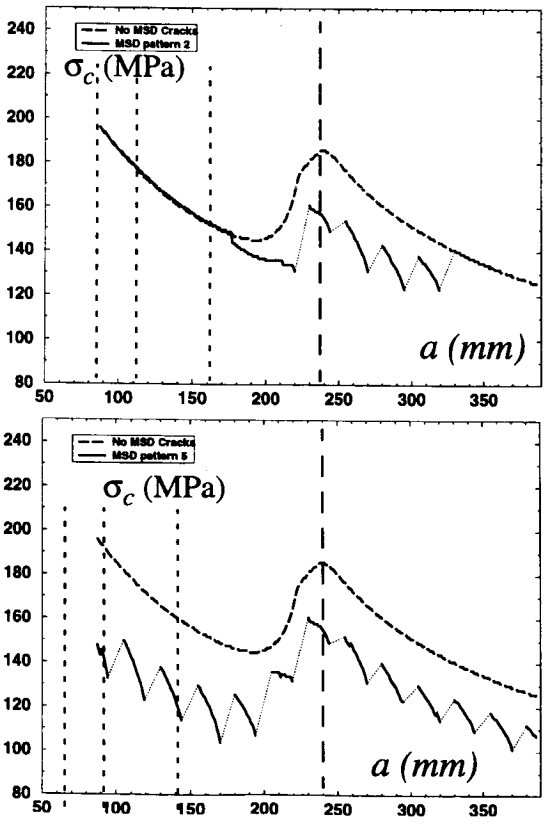

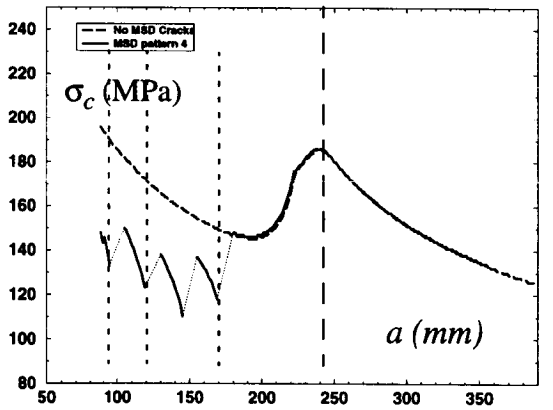

Fig. 12 Residual strength curve for the five MSD patterns with $2a_{MSD}$ = *0 and 5mm,* for initial crack length a_0 = *87.5, 112.5, 162.5 mm.* Crack propagation criterion 2: δ_0=*0.50mm,* α = *0 rad,*

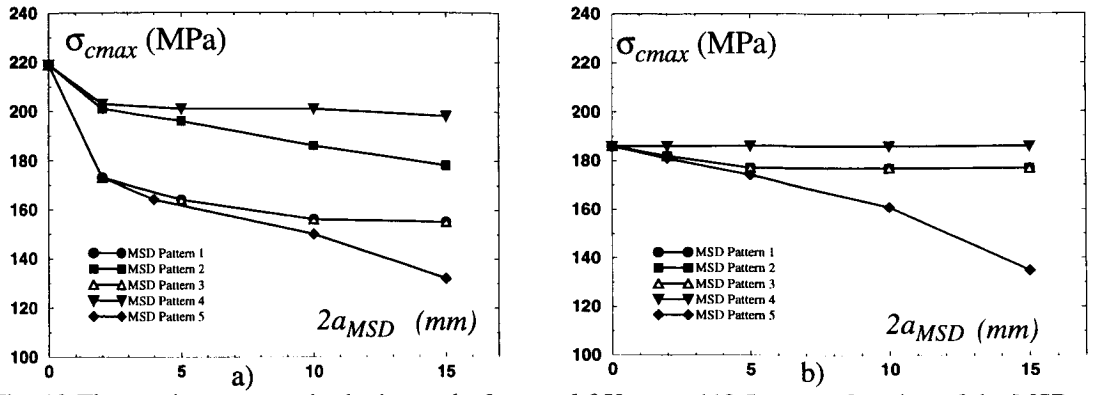

Fig. 13 The maximum stress in the interval $a0 < x < 1.05L$, a_0 = 112.5 mm as function of the MSD crack length, $2a_{MSD}$, for all 5 MSD patterns crack propagation criterion 1 a) and 2 b) respectively

Typical MSD cracking occurs mainly in the mid-bay where the skin stress is high. MSD Pattern 4, with cracking in the mid-bay only was less critical to MSD since the tear strap effect was intact. Although, one should expect less cracking at the tear straps, one should perhaps expect some cracking there as well, but then significantly shorter cracks. Due to the knock-down effect such small cracks may have a strong influence. In Fig. 13, the residual strength for MSD Pattern 4 with $2a_{MSD}$ = *10mm* is shown along with the reduction when there are 5 additional cracks which are only 2mm (Pattern 4b), which is shown in the Figure insert. The effect of the small cracks is drastic. The crack arrest capability of the tear strap is functioning, but at significantly reduced level.

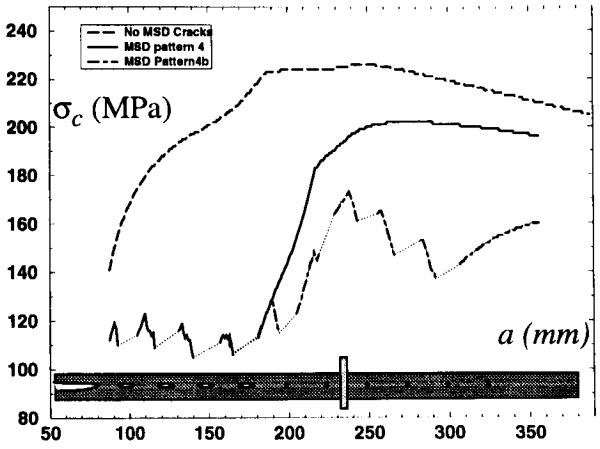

Fig. 14 The residual strength for MSD Pattern 4 with $2a_{MSD}$ = *5mm* and with 5 additional 2mm MSD cracks. Crack propagation law 1.

4. CURVED PANELS

Yield strip models are usually applied to plane problems, but applications to linear shell problems can also be found[22]. It is well-known that the stress intensity factor is increased by the bulge-out and that computation of stress intensity factor for shells requires a kinematically nonlinear analysis[23,24]. It must therefore be expected that a kinematically nonlinear analysis is required when the yield-strip model is applied to shells and this feature infers a modification in the yield strip computational procedure outlined for the flat sheet. Furthermore, the bulge-out will necessarily introduce some *bending* at the crack tip which violates the yield strip assumption since when a *constant* yield stress is applied along the yield strip zone, the stress field in front of the plastic tip cannot continuously merge through the thickness with the stress field behind the tip. A more detailed study than the one given here can be found in[12]. The model problem shown in Fig. 1b, with radius R = 1000 mm, skin thickness t = 1mm, and width w = 2000 mm is singled out as our benchmark problem. The small crack damage consists of 10 mm cracks with a centre-to-centre distance of 25 mm, i.e. $2a_{MSD}$ = 10mm and s_{MSD} = 25 mm.

4.1 Computational model

The computational procedure outlined in Fig. 6 is retained. The difference from the flat sheet case lies in the solution to the structural problem for a given plastic zone size, s, represented by the grey box in Fig. 6. Due to the kinematical nonlinearity, it is not possible to first separate the load cases and then add them. Instead an iterative procedure outlined in Fig. 15 is adopted. The procedure for this step is that the yield stress loading, σ_Y, is kept constant, while the internal pressure, p_0, is adjusted iteratively until the stress singularity has vanished. Since there is always some bending and the applied yield-strip loading is constant, the criterion is fulfilled in a weak sense.

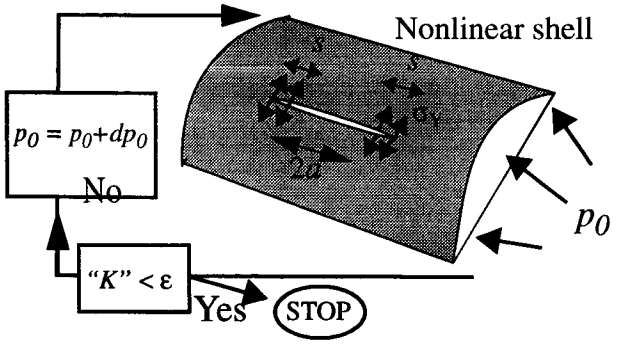

Fig. 15 K and δ_t are *nonlinear* functions of p_0 and σ_Y. p_0 is updated iteratively until $K < \varepsilon$ which determines p_0 and δ_t for given s.

The in-house p-version FE-code STRIPE was used to solve the structural problem. The analysis was a full three-dimensional one. In the p-version improved accuracy of results is achieved by increasing the polynomial order of the shape functions while keeping the number of the finite elements constant. The "p" feature can be used to efficiently obtain convergence and computational speed for the nonlinear shell problem[12]. Double symmetry was assumed in the FE modelling. The shell is subjected to a internal pressure load, p_0, and an axial load, $p_0R/2t$ along the edge $x_1 = w$, and the yield strip loading σ_Y applied along yielded ligaments analogous to the flat sheet case. The meshing for a given geometry is adjusted to the particular geometry such that the tips of the small cracks within the plastic zone coincide with an element corner with mesh refinement. The number of degrees of freedom of the FE-model depends on the geometry, but were in the order $2 \cdot 10^3$, $3.5 \cdot 10^3$ and $6 \cdot 10^3$ for $p = 2$, 3 and 4 respectively. In order to compare with flat sheet results, the applied load will be expressed in the skin hoop stress, $\sigma = p_0R/t$. One atmosphere internal pressure (p_0 = 0.1013MPa), thus corresponds to 101.3 MPa skin stress and this is roughly the stress level we should expect in a pressurized fuselage.

4.2 Convergence study and assessment of bending

A convergence study was first performed and results were found to have converged for the polynomial level, $p = 3$. This is the p-level used in all examples below and the numerical errors in the results can be considered negligible. It was mentioned above that the stress field could not merge continuously with the applied yield stress through the thickness when there is bending. Fig. 16 shows the through-thickness distribution of the hoop stress component, $\sigma_{\phi\phi}$, at 0.1 mm behind and ahead of the plastic tip for a 200 and 400 mm crack with 87 mm long plastic zone. If we measure the amount of bending by the maximum difference of the stress through the thickness divided by average stress, then the bending is 7% and 21% for 200 and 400 mm crack respectively. The amount of bending is, as expected, larger for the longer crack. These values are considered acceptable. The physical effect of bending is not clear. One consequence could be that the crack front would "tilt" a little bit. In the present paper this issue will not be further elaborated upon. However, it should be born in mind that the logic for the yield strip model may be questioned for longer cracks due to bending.

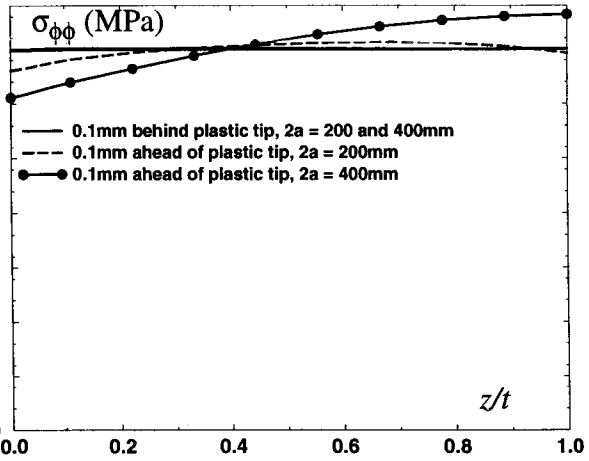

Fig. 16 Stress distribution through the thickness 0.1mm behind and in front of tip of plastic zone.

4.3 Comparison of between a kinematically linear and nonlinear analysis

The computational time can be significantly reduced if kinematically nonlinear effects are not accounted for. It is therefore of interest to quantify the effect of kinematical nonlinearity. The crack tip opening displacement as function of the applied skin stress is shown in Fig. 17 for a 200 mm lead crack based on a kinematically linear and nonlinear analysis. Assuming that crack propagation is governed by a critical crack opening, it follows that a linear analysis predicts *consistently and significantly* a lower critical load and that this effect increases slightly with increasing load. For crack tip opening displacements in the range 0.5 to 1 mm; this difference is about 30%. By coincidence the load displacement curve for the nonlinear MSD damaged panel follows very closely the undamaged linear one.

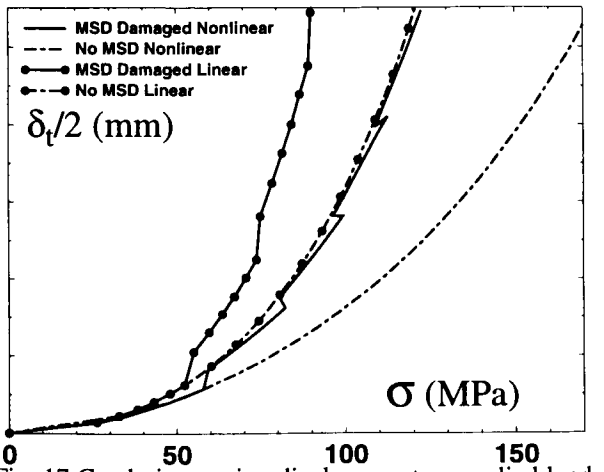

Fig. 17 Crack tip opening displacement vs applied load for cylindrical shell MSD damaged and no damage as given by kinematically linear and nonlinear analysis

4.4 Comparison between a cylindrical shell and a flat sheet

Fig. 18 shows the crack tip opening displacement versus the applied skin load derived for the nonlinear cylindrical shell and a corresponding flat sheet model with a 200 mm lead crack. The relative difference in crack opening between the flat sheet model and the cylindrical shell (i.e. bulge factor for yield strip model) is quite large and increases with crack length. The skin stress corresponding to a certain crack tip opening displacement for the cylindrical shell is typically one half for the 200 mm crack and a third for the 400mm crack of the flat sheet values.

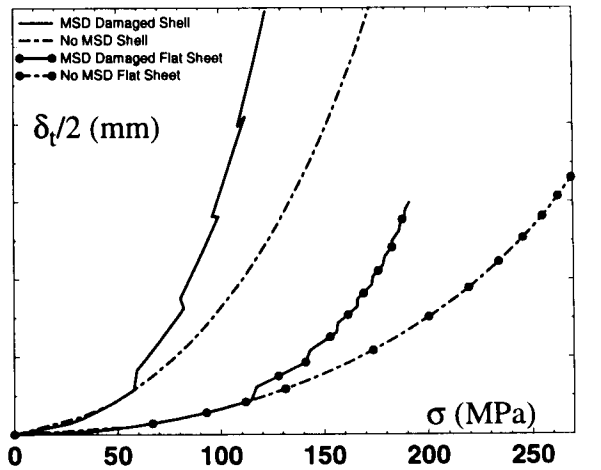

Fig. 18) Crack tip opening displacement vs applied load for MSD damaged and undamaged Flat Sheet and Cylindrical shell $2a$ = 200mm

The residual strength curve for a pressurized cylindrical shell and associated crack growth criterion may be computed following the outlined computational procedure. Fig. 19a and 19b show the residual strength of the cylinder and the corresponding flat sheet model problem using the crack growth criterion 1, i.e. $\delta_c = 0.5mm$ and no crack growth resistance. First of all it should be noted that the critical stress level is considerably lower for the shell than for the flat sheet and that this difference increases with the crack length. For a half crack length $a = 50, 100$ and 200 *mm*, the reduction factor in the residual strength is lowered by a factor of about 1.5, 2 and 3 respectively. The reduction factor due to MSD is, however, more or the same for the flat sheet and the cylinder and for the 12.5 *mm* case MSD cracks the MSD induced reduction is about 40%.

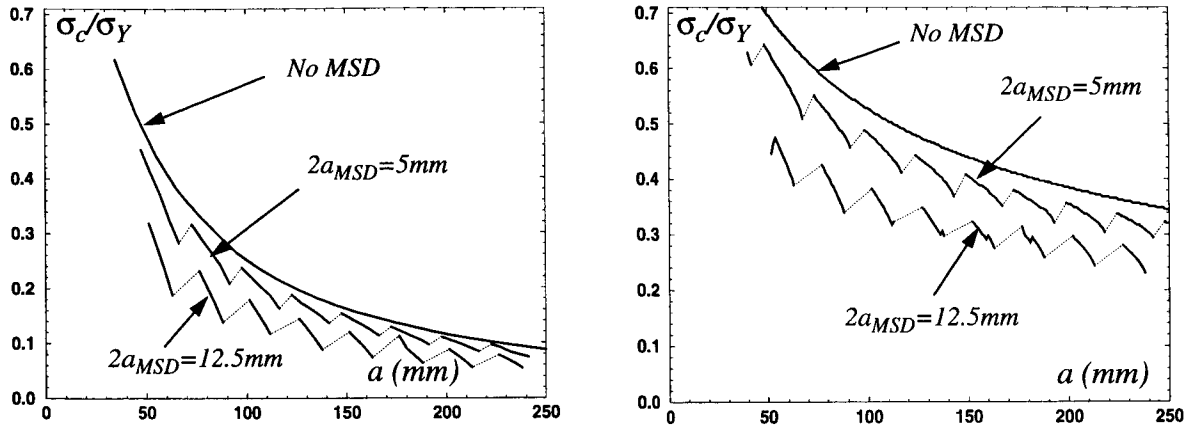

Fig. 19 The computed residual strength for a a) cylinder and b) flat sheet at different MSD levels. d_{MSD} = 45 mm, s_{MSD} = 25 mm, δ_c = 0.5 mm

5. CONCLUSIONS

The MSD-induced reduction in residual strength is caused by plastic crack interaction. The yield-strip model is particularly suitable for thin sheets. Crack growth is assumed to be governed by a constant crack opening angel (CTOA-criterion) and crack growth resistance is accounted for by the plastic stretch released by the advancing crack tip. The ultimate problem we want to analyse, the cracked fuselage, is structurally a very complex problem. It is therefore necessary to start out with simpler geometries and gradually increase the complexity to gain understanding of the basic mechanisms. For flat sheets, the residual strength problem can be solved semi-analytically resulting in very short modelling and computational times. In the parameter study of the flat stiffened sheet, three major mechanisms for residual strength reduction were identified:

- The *reduced strength effect* caused by the reduction in the average stress in the yield zone when the plastic zone engulfs at least one MSD crack
- *MSD induced ligament erosion* caused by simultaneous growth of lead crack and MSD cracks
- *Drop in the crack growth resistance after link-up*

The study also revealed that the reduction in residual strength caused by MSD was more pronounced for crack growth resistant materials, cracking located at the tear strap was particularly deleterious and that even very small cracks could reduce the residual strength substantially. A vital question is of course if these findings can be transferred to the complex structures similar to a fuselage. In particular the bulge-out effect in curved shells, the secondary bending effect for asymmetric joints, and the more complicated bolt-hole interaction problem at the local MSD-level may change the picture. In order to answer this question we need to model these effects. An attempt to model the bulge-out effect while using the yield strip model was presented in the second part of the paper. The bulge-out increases as expected the crack opening displacement considerably thereby lowering the residual strength significantly but for materials with no crack growth resistance the relative reduction due MSD was very similar for flat sheets and cylinders.

The function of a tear strap is not just to arrest a propagating axial crack by reducing the circumferential stresses (as in this paper), but also to deflect the crack in the circumferential direction. MSD-cracking works as a local weakening in the longitudinal direction and may therefore inhibit the crack deflection[25]. Incorporation of deflection criteria is therefore essential. For linear elastic fracture analyses there exist such criteria based on the mode mixity of the stress intensity factors and the T-stress[26]. Plastic effects are, as we have seen here, fundamental in the MSD problem and corresponding elasto-plastic deflection criteria are needed.

ACKNOWLEDGEMENT

The work has been funded by the European Commission under Contract BRPR-CT95-0079, by the Swedish National Board for Industrial and Technical Development (NUTEK) under contract 8525-96-01648 and by the Swedish Defence Material Administration, (FMV) under contract 50562-LB78548,

REFERENCES

[1] Swift, T., (1993), Widespread Fatigue Damage Monitoring-Issues and Concerns, Proc. of 5th Int. Conf. on Aging Aircraft, June 1993, Hamburg Germany.

[2] Mayville, R., and Sigelmann, M., (1993), *A Laboratory Study of Multiple Site Damage in Lap-Splices,* DOT/FAA/CT-93/74, FAA Technical Center, N.J., USA.

[3] Goranson, U.G., (1993), *Damage Tolerance - Facts and Fiction,* in Durability and Structural Reliability of Airframes, A.F. Blom (ed), 3-106, London, UK, Engineering Materials Advisory Services Ltd.

[4] Gruber, M.L., Wilkins, K.E., and Worden, R.E., (1996), Investigation of Fuselage Structure Subject to Widespread fatigue Damage, in Proceedings of the FAA-NASA Symposium on the Continued Airworthiness of Aircraft Structures, Bigelow, C. (ed), GA, USA, DOT/FAA/AR-97/2, pp. 439-460.

[5] Maclin, J. R., (1991), *Performance of Fuselage Pressure Structure*, in Proceedings 1991 Int. Conf. on Aging Aircraft and Structural Airworthiness, Harris C.E. (ed.), 67-74. NASA-CP-3160, USA

[6] Newman, J.C., Dawickie, D.S., Sutton, M.A. and Bigelow, C.A., (1993), in Durability and Structural Reliability of Airframes, Blom A,F. (ed.), 443-468, London, UK, Engineering Materials Advisory Services Ltd.

[7] Nilsson, K.-F. and Hutchinson, J.W.: Interaction Between a Major Crack and Small Crack Damage in Aircraft Sheet Material, *Int. J. Solids Structures*, 31, pp. 2331-2346., 1994.

[8] Wang, L., Brust, F.W. Atluri, S.N., (1997), The Elastic-Plastic Finite Element Alternating Method (EPFEAM) and the prediction of fracture under WFD conditions in Aircraft Structures, PartIII: Computational predictions of the NIST multiple site damage experimental results, *Computational Mechanics*, 20, pp.199-212.

[9] Harris, C. E., Newman, J.C., Piascik, R.S., Starnes, J. H., (1997), *Analytical Methodology for Predicting the Onset of Widespread Fatigue Damage in Fuselage Structure*, in Proceedings of the FAA-NASA Symposium on the Continued Airworthiness of Aircraft Structures, August 1996, GA, USA, Ed. (C. Bigelow) DOT/FAA/AR-97/2, pp. 63-88.

[10] Deng, X., and Hutchinson, J.W. (1996), *Approximate Methods for Analyzing the Growth of Large Cracks in Fatigue Damaged Aircraft Sheet Material and Lap-Joint*, Harvard Univ., MECH-277, Cambridge, MA, USA

[11] Nilsson K-F, (1996), *Elasto-Plastic Models for Interaction Between a Major Crack and Multiple Small Cracks*, in Proceedings of the FAA-NASA Symposium on the Continued Airworthiness of Aircraft Structures, (C. Bigelow, C. (ed), 197-225, August 1996, GA, USA, DOT/FAA/AR-97/2.

[12] Nilsson, K-F, (1997), *Application of Yield-Strip Models for Residual Strength Assessment of Flat and Curved MSD Damaged Panels*, FFA TN 1997-43, Sweden.

[13] Nilsson, K.F., (1998), Influence of MSD Crack Pattern on Residual Strength of Flat Stiffenned Sheets, FFA TN 1998-09 (to appear in *Computational Mechanics*)

[14] Dugdale, D. S., (1960), Yielding of Steel Sheets Containing Slits, *J. Mech. Phys.* Solids, 8, 100-104.

[15] Barenblatt, G.I., (1962), The Mathematical Theory of Equilibrium Cracks in Brittle Fracture, in *Advances in Applied Mechanics*, VII, eds: Dryden, H.L., and von Karman, Th., p. 55-130.

[16] Muskhelishvili, N.I. *Some Basic Problems of The Mathematical Theory of Elasticity,* Noordhoff Int. Publishing, Leyden, The Netherlands, 1977

[17] Tada, H, Paris, P., and Irwin, G., (1985), *The Stress Analysis of Cracks Handbook,* Del Research Corporation, 226 Woodburn Drive, St. Louis, Missouri, USA

[18] Thomson, D., Hoadley, D. and McHatton, J.: *Load Tests of Flat and Curved Panels with Multiple Cracks,* Foster-Miller, Waltham, MA Final Report, 1993.

[19] deWit, R., Fields, R.J., Low III, S.R., Harne, D.E. and Foecke, T.: *Fracture Testing of Large-Scale Thin Sheet Aluminium Alloy,* NISTIR 5661, US Dep. of Commerce, 1995.

[20] *Residual Strength in stiffened panels*, performed as part of GARTEUR Action Group SM 18, Assessment of Multiple Site Damage in Highly Loaded Joints, NLR, The Netherlands.

[21] Hoysan, S.F.,and Sinclair, G., B., (1993), On the variability of fracture toughness, *Int. J. Fracture*, 60, R43-R49.

[22] Erdogan, F., and Ratwani, M., (1972), Plasticity and the Crack Opening Displacement in Shells, *Int. J. Fracture Mech.*, 8, pp. 413-426.

[23] Ansell, H., (1988), *Bulging of Cracked Pressurized Aircraft Structure*, Thesis. NO. 138, Linköping Institute of Technology, Sweden.

[24] Riks, E. *Bulging Cracks in Pressurized Fuselages,* (1987), A numerical Study. NLR MP. 87058. The Netherlands.

[25] Kosai, M, and Kobayashi, A.S, (1991), *Axial Crack Propagation an Arrest in Pressurized Fuselage* in Structural Integrity of Aging Aircraft, Atluri, S.N. (ed), 225-239, Berlin, Germany, Springer Verlag

[26] Shimamoto, A., Kosai, M., Kobayashi, A.S. and Tan, P., (1993), *Dynamic Crack Curving at Tear Strap with MSD, Durability and Structural Integrity of Airframes,* pp. 239-257, Proceedings of the 17:th ICAF Symposia in Stockholm, Sweden, Ed: Blom, A.F.,

BOUNDARY CORRECTION FACTORS FOR ELLIPTICAL SURFACE CRACKS EMANATING FROM COUNTERSUNK RIVET HOLES

Anisur Rahman
Drexel University
FMRC, Dept of Materials Engineering
Philadelphia, PA 19104 USA
Telephone (215) 895-2382
Telefax (215) 895-6684

John G. Bakuckas, Jr., Catherine A. Bigelow, and Paul W. Tan
FAA William J. Hughes Technical Center
AAR-430
Atlantic City International Airport, NJ 08405 USA

ABSTRACT

To predict crack growth and residual strengths of riveted joints subjected to widespread fatigue damage (WFD), accurate stress and fracture analyses of corner and surface cracks at a rivet hole are needed. The results presented in this paper focus on the computation of stress-intensity factor (SIF) solutions for cracks at countersunk rivet holes for tension, bending, and wedge load conditions. A wide range of configurations was considered varying the crack size, crack shape, crack location, and the height of the straight-shank hole. A global-intermediate-local (GIL) hierarchical approach implementing the finite element method was used in this study. The GIL approach was used to determine the boundary correction factors, a nondimensional representation of the SIF, for a wide range of configurations representing typical countersunk holes in aircraft structural joints. The boundary correction factor was determined along the crack front in terms of the physical angle measured from the inner surface of the plate to the boundary of the countersunk rivet hole. In general, the values of boundary correction factors increased as the location along the crack front moves from the inner surface of the plate towards the hole boundary. For all the crack locations analyzed, the inner surface of the plate has less of an influence on the boundary correction factor than the hole and outer surface boundaries. The values of the boundary correction factor were highest for the crack fronts closest to the hole boundary. The trends in the solutions were the same for the three loading conditions.

INTRODUCTION

Ongoing aging aircraft research activities are aimed at developing and implementing advanced fatigue and fracture mechanics concepts into the damage tolerance analysis methodology for the aging, current, and next generation fleets. These activities include developing methods to predict the onset of widespread fatigue damage (WFD). One of the objectives of the Federal Aviation Administration's National Aging Aircraft Research Program is to develop the methodology to predict crack initiation,

crack growth rates, and residual strengths of aircraft structures susceptible to WFD. One of the fourteen possible locations susceptible to WFD identified by Industry Committee on WFD was the riveted lap splice joint. Multiple cracks can form in a riveted lap splice joint due to stress concentrations in the rivet holes. To reliably predict crack growth rates and fracture strengths of riveted joints susceptible to WFD, accurate stress-intensity factor (SIF) solutions of corner and surface cracks at a rivet hole are needed.

Exact closed-form SIF solutions for cracks in three-dimensional solids are often lacking for complex configurations such as countersunk rivet holes; therefore, approximate solutions must be used. Over the past two decades, considerable effort has been placed on developing computationally efficient methods to provide accurate SIF solutions for cracks in three-dimensional bodies. These methods include conventional finite element method (FEM) [1-4], the finite element alternating method (FEAM) [5-7], the boundary element method (BEM) [8-9], and the three-dimensional weight function method (WFM) [10-11]. With advances in pre and post processors, and computer hardware and the improvements in equation solvers, time savings are being realized in both geometry development and analysis of complex models. With the computational tools in place, much needed SIF solutions required for damage tolerance assessments of cracked rivet holes can be obtained.

A recent experimental study [12] provides extensive experimental data on the crack front shape and fatigue growth of cracks from rivet holes in fuselage lap joint regions. Fatigue damage in an actual fuselage lap joint removed from a full-scale test article was characterized. An extensive database was established cataloging the damage state of the fuselage lap region including crack initiation, growth rates, size, location, and fracture morphology. Hidden cracks from rivet holes in the inner skin, outer skin, and tear straps were found during fractographic examinations. In the outer skin, cracking typically initiated from the rivet hole at the faying surface between the inner and outer skins due to fretting. Marker band analysis showed that the cracks typically grew beneath the surface with elliptical fronts, remaining hidden for a portion of their growth. Penetration of the tunneling cracks to the outer surface occurred after growing to lengths of two to three times the skin thickness. To complement such experimental studies, SIF solutions would be useful in interpreting results as well as conducting damage tolerance assessments. However, few solutions exist for cracks at countersunk rivet holes. Some work has been done to generate SIF solutions for cracks in countersunk rivet holes [4,7]. However, many gaps exist in available SIF solutions and further work is required particularly for breakthrough crack configurations and solutions under bending and pin loading.

The objective of this project is to develop SIF solutions for cracks at countersunk rivet holes to expand on the currently available solution database. This paper provides a summary of the work conducted. A complete presentation of the results can be found in reference 13. Configurations representing typical countersunk holes in aircraft structural joints were analyzed under tension, bending, and wedge loading conditions. Selection of the crack size, crack shape, and crack location were varied to represent typical experimental observations. A global-intermediate-local (GIL) hierarchical approach based on the finite element method was used. Representative results for boundary correction factors calculated using the GIL approach are presented.

CONFIGURATION AND LOADINGS

The configuration analyzed in this study was of a countersunk rivet hole in a plate with a half-height to half-width ratio $H/W = 2$ as shown in Figure 1(a). The straight-shank hole radius to plate half-width (W/R) was 5. For all calculations, the total angle subtended by the countersunk hole was 100°. The ratio of the length of the straight-shank portion of the hole to the plate thickness (h/t) was varied to values of 0.05, 0.25, and 0.50. The plate modulus of elasticity was $E = 1$ psi, and Poisson's ratio was $\nu = 0.3$.

Three loading conditions were considered in this study, a remote tension (S_t), remote bending (S_b), and line loads (P_y) applied in the hole as shown in Figure 1(b), 1(c), and 1(d), respectively. A remote tension load was applied using a constant stress, S_t = 1.0 unit force per unit area. A remote bending load was applied using a linear stress distribution through the thickness. On the side of the countersunk bore (Z/t = 0.0), S_b = 1.0 unit force per unit area and on the side of the straight-shank hole (Z/t = 1.0), S_b = 0.0 unit force per unit area. This ensured an opening displacement of the crack surfaces. The line load (P_y), simulating a wedge load condition, was applied on the plane of symmetry of the countersunk hole. The line load, P_y, was defined as the vertical component of a traction line load, P_l, acting normal to the surface, Figure 1(e), where P_l = 1.0 unit force per unit length. The value for the applied line load in this study was the following:

$$P_y = \begin{cases} P_l \cos 50^\circ & 0 \le \dfrac{Z}{t} \le 1 - \dfrac{h}{t} \\ P_l & 1 - \dfrac{h}{t} < \dfrac{Z}{t} \le 1 \end{cases} \tag{1}$$

The five crack locations shown in Figure 1(f) were analyzed. All cracks were elliptical with the center of the ellipse at the intersection of the straight-shank portion of the rivet hole and the inner surface of the plate. The size and shape of each crack was defined by a and c, the two elliptical axis, where a is parallel to the Z-axis and c is parallel to the Y-axis. At crack location 1, Figure 1(f), the crack is a corner crack with the value of a set to $h/2$ where h/t was varied from 0.05, 0.25, and 0.5. At crack location 2, also a corner crack, a was set equal to h and h/t was varied as before. At crack location 3, a breakthrough crack, a was defined such that the crack would intersect the surface of the rivet hole at $Z/t = (h+t)/2t$; h/t was varied as before. At crack location 4, a through-the-thickness crack, a was defined such that the crack would intersect the surface of the rivet hole at Z/t = 1. For crack locations 1 through 4, a/c was varied from 1, 0.75, and 0.5. At crack location 5, only one crack was analyzed, a breakthrough crack having a/c = 1 with c/t = 3.125. These cracking configurations were selected to represent typical scenarios observed during fractographic examinations reported in reference 12. The full analysis matrix shown in Table 1 consists of 117 solutions.

DEFINITION OF STRESS-INTENSITY FACTOR

The mode I stress-intensity factor (K_I) at any location along the crack front under tensile loading is given as

$$K_I = S_t \sqrt{\frac{\pi a}{Q}} F_t\left(\frac{a}{t}, \frac{a}{c}, \frac{h}{t}, \frac{R}{t}, \theta\right) \tag{2}$$

for bending load:

$$K_I = S_b \sqrt{\frac{\pi a}{Q}} F_b\left(\frac{a}{t}, \frac{a}{c}, \frac{h}{t}, \frac{R}{t}, \theta\right) \tag{3}$$

and for wedge load:

$$K_I = S_w \sqrt{\frac{\pi a}{Q}} F_w\left(\frac{a}{t}, \frac{a}{c}, \frac{h}{t}, \frac{R}{t}, \theta\right) \tag{4}$$

where the wedge stress per unit area, S_w, is simulated using a normal line load P_l as

$$S_w = \frac{P_l}{t} \tag{5}$$

The boundary correction factors, F_t (tensile), F_b (bending), and F_w (wedge load) were calculated along the crack front for the various combinations of parameters (a/c, h/t, and crack location) shown in Table 1. The crack dimensions a and c, the parametric angle φ, and physical angle θ are defined in Figure 1(g). The parametric angle φ is the angle to the point on the crack front indicated by the solid circle in Figure 1(g) measured with reference to the circle contained within the ellipse. The physical angle θ is the angle to the point on the crack front indicated by the solid circle in Figure 1(g) measured with reference to the ellipse defining the crack front. The shape factor for an ellipse Q is given by the square of the complete elliptic integral of the second kind [14]:

$$\left.\begin{aligned} Q &= 1 + 1.464\left(\frac{a}{c}\right)^{1.65} \quad for\ \frac{a}{c} \le 1 \\ Q &= 1 + 1.464\left(\frac{c}{a}\right)^{1.65} \quad for\ \frac{a}{c} > 1 \end{aligned}\right\} \tag{6}$$

GLOBAL-INTERMEDIATE-LOCAL HIERARCHICAL APPROACH

The global-intermediate-local (GIL) hierarchical finite element approach illustrated in Figure 2, established and verified in reference 15, was used to obtain the boundary correction factors for countersunk rivet holes. The commercially available finite element program ABAQUS 5.6 [16] was used for the analysis. In the first step (global level) of the GIL approach, an analysis of the plate subjected to the prescribed loading conditions is conducted. For the cases analyzed here, due to symmetry in the geometry and loading, one quadrant of the plate was modeled. The global model typically contained 1200 20-noded brick elements.

In the next stage (intermediate level), an analysis is conducted of the area of interest, in these cases the higher stress gradient region near the hole, using a more refined mesh. The intermediate model typically consisted of 5000 20-noded brick elements. The boundary conditions for the intermediate model were taken from the global model using the submodelling features in ABAQUS.

In the final stage (local level), an analysis is conducted that was even more focused on the region of interest, in these cases the region around the crack front. A highly refined mesh with elements orthogonal to the crack front was used. The boundary conditions for the local model were taken from the global model using the submodelling features in ABAQUS.

From local models, the J-integral was calculated along the crack front using the equivalent domain integral method (EDIM). For cases where there is no mixed mode fracture and assuming a plane strain elastic material response, the mode I SIF at any point along the crack front can be calculated from the J-integral as

$$K_I = \sqrt{\frac{JE}{1-\nu^2}} \tag{7}$$

It should be noted that for small cracks at locations 1 and 2, Figure 1(f), the full GIL approach (three levels) was required. For larger crack sizes at locations 3, 4, and 5, a two-level global-local hierarchical approach was sufficient to obtain acceptable results. In the two-level approach, the global model had approximately 4500 20-noded brick elements and the local model had 5600 20-noded brick elements.

RESULTS AND DISCUSSIONS

The parameters in Table 1 were varied to the specified values yielding a total of 117 solutions. All results are reported in reference 13 with representative results presented as boundary correction factors, nondimensionalized form of the stress-intensity factor. The effect of the shape of the crack, the location the crack, the length of straight-shank hole, and the loading condition are illustrated.

EFFECT OF CRACK SHAPE ON BOUNDARY CORRECTION FACTOR

The boundary correction factors under tension F_t as a function of the physical angle θ for cracks at location 2 are shown in Figure 3 for $h/t = 0.5$. The shapes of the elliptical cracks was varied from $a/c = 1$, 0.75, and 0.5. The value of a was held constant and the values of c varied. In general, for all three a/c ratios, when moving along the crack front from the inner surface to the hole boundary (i.e. as the physical angle increases) the value of the boundary correction factor increased. As shown in Figure 3, for small values of θ, (near the inner surface of the plate) values of boundary correction factors increased with an increase in the value of a/c. Smaller a/c values mean a larger value c and therefore the influence of the hole boundary is less. With increasing values of θ, (towards the boundary of the hole), the solutions for the three values of a/c merge. At $\theta = 90°$ as expected, the values of the boundary correction factor were highest indicating the influence of the hole boundary is greatest there. Similar trends were observed at different crack locations and h/t ratios.

EFFECT OF CRACK LOCATION ON BOUNDARY CORRECTION FACTOR

The boundary correction factors under tension F_t as a function of the physical angle θ for $a/c = 1$ and $h/t = 0.25$ are shown in Figure 4. The figure shows F_t for all locations of the crack. In general, at each location, when moving along the crack front from the inner surface to the outer surface and hole boundaries (increasing θ) the value of the boundary correction factor increases. Thus, for all crack locations, the hole and outer surface boundaries have more of an effect on the boundary correction factor than the inner surface of the plate. Note, for crack fronts nearest the hole boundaries, crack locations 1 and 2, the values of the boundary correction factor are higher. For cracks at location 2, values of F_t near the hole boundary are highest due to the abrupt change in the hole boundary at the knee. The crack fronts further from the hole surface have lower boundary correction factors. Similar trends were observed at different a/c and h/t ratios.

The boundary correction factors under tension F_t as a function of the physical angle θ for $a/c = 1$ and $h/t = 0.05$ are shown in Figure 5. Similar trends are observed as for the case with $h/t = 0.25$ shown in Figure 4. That is, the boundary correction factors increase with an increase in the physical angle, and the values are highest for cracks at locations 1 and 2 which are nearest the hole. In comparing the results from Figures 4 and 5, the effect of changing h/t on the boundary correction factor is evident. For crack locations 3, 4, and 5 where the influence of the hole is lessened, the values of F_t are similar for the two values of h/t. However, at crack locations 1 and 2 the change in h/t results in a significant difference for the two values of h/t. For $h/t = 0.05$, Figure 5, a near knife edge condition exists resulting in a much higher stress

gradient region in the straight-shank portion of the hole compared with the case where h/t = 0.25. Consequently, the boundary correction factors for the crack fronts near the hole boundary at locations 1 and 2 are higher for h/t = 0.05 compared with h/t = 0.25.

EFFECT OF APPLIED LOADING ON BOUNDARY CORRECTION FACTORS

The boundary correction factors under bending F_b and wedge loading F_w as a function of the physical angle θ for h/t of 0.25 are shown in Figures 6 and 7, respectively. Each figure shows the results for values of a/c = 1, 0.75, and 0.5. Similar trends are observed for both the bending and wedge loadings as for the tension load case shown in Figure 3. The values of boundary correction factors increase with increases in the physical angle when moving along the crack front from the inner surface towards to hole boundary. In addition, for small values of θ, near the inner surface, the boundary correction factor was larger for larger values of a/c. At larger values of θ, points on the crack front nearest the hole boundary, the values of the solutions for each of the three a/c ratios merge.

CONCLUDING REMARKS

The expansion of the database of known stress-intensity factor (SIF) solutions of cracks emanating from countersunk rivet holes under tension, bending, and wedge load conditions has been undertaken in this study. Results were generated for 117 different configurations. The crack size, crack shape, and crack location were selected to represent typical experimental observations. The crack shape was selected using the ratio of the elliptical crack length in the thickness direction to that in the width direction a/c = 0.5, 0.75, and 1. In addition, the ratio of the length of the straight-shank portion of the hole to the plate thickness (h/t) was varied ranging from 0.05, 0.25, and 0.50. Cracks at five locations were analyzed: (1) corner cracks passing through the middle of straight shank portion of the rivet hole; (2) corner cracks passing though inner knee of the rivet hole; (3) breakthrough crack passing through the middle of the inclined surface of the rivet hole; (4) breakthrough crack passing through the upper knee of the rivet hole, and; (5) through-the-thickness crack passing through the inner and outer surfaces of the plate.

A global-intermediate-local (GIL) hierarchical submodeling technique was used to generate the stress-intensity factor solutions. Representative results generated using the GIL approach are presented in this paper in terms of the boundary correction factors. The effect of the shape of the crack, the location of the crack, the height of the straight-shank portion of the countersunk rivet hole, and applied loading are presented. The boundary correction factor was determined along the crack front in terms of the physical angle measured from the inner surface of the plate to the given point on the crack front.

In general, the values of boundary correction factors increased as the crack front moves from the inner surface of the plate towards the hole boundary. For points on the crack front near the inner surface of the plate, the value of the boundary correction factor increased with an increase in the value of a/c. When moving along the crack front from the inner surface to the hole boundary, boundary correction factor solutions for the three values of a/c merge. For the five crack locations considered, the inner surface of the plate has less of an influence on the boundary correction factor than the hole and outer surface boundaries. The values of the boundary correction factor were highest for the crack fronts closest to the hole boundary. The trends in the solutions were the same for the three loading conditions.

ACKNOWLEDGEMENTS

This research was supported in part by grant number 97-G-026 from the Federal Aviation Administration William J. Hughes Technical Center. The computational effort was partially supported by grant number MSS960013P from the Pittsburgh Supercomputing Center.

REFERENCES

1. Raju, I. S. and Newman, J. C., Jr., "Stress-Intensity Factors for a Wide Range of Semi-Elliptical Surface Cracks in Finite-Thickness Plates," *Engineering Fracture Mechanics*, Vol. 11, No. 4, 1979, pp. 817-829.

2. Pickard, A. C., "Stress-Intensity Factors for Cracks With Circular and Elliptic Crack Fronts - Determined by 3D Finite Element Methods," PNR-90035, Rolls Royce Limited, May 1980.

3. Tan, P. W., Raju, I. S., Shivakumar, K. N., and Newman, J. C., Jr., "Evaluation of Finite-Element Models and Stress-Intensity Factors for Surface Cracks Emanating from Stress Concentrations," *Surface-Crack Growth: Models, Experiments, and Structures, ASTM STP 1060,* American Society for Testing and Materials, 1990, pp. 34-48.

4. Gosz, M. and Moran, B. "Stress-Intensity Factors for Elliptical Cracks Emanating From Countersunk Rivet Holes," *DOT Report - DOT/FAA/AR-95/111,* April 1998.

5. Nishioka, T. and Atluri, S. N., "Analytical Solution for Embedded Elliptical Cracks and Finite Element-Alternating Method for Elliptical Surface Cracks Subjected to Arbitrary Loadings," *Engineering Fracture Mechanics*, Vol. 17, 1983, pp. 247-268.

6. Nishioka, T. and Atluri, S. N., "An Alternating Method for Analysis of Surface Flawed Aircraft Structural Components," *AIAA Journal*, Vol. 21, 1983, pp. 749-757.

7. Tan, P. W., Bigelow, C. A., O'Donoghue, P. E., and Atluri, S. N., "Stress-Intensity Factor Solutions for Cracks at Countersunk Rivet Holes Under Uniaxial Tension," *DOT Report - DOT/FAA/CT-93/68*, February 1994.

8. Cruse, T. A., "Application of Boundary-Integral Equation Method to Three-Dimensional Stress Analysis," *Computer and Structures*, Vol. 3, 1973, pp. 509-527.

9. Heliot, J., Labbens, R. C., and Pellissier-Tanon, A., "Semi-Elliptical Surface Cracks Subjected to Stress Gradients," *Fracture Mechanics, ASTM STP 677*, C.W. Smith (ed.), American Society for Testing and Materials, 1979, pp. 341-364

10. Zhao, W., Wu, X. R., and Yan, M. G., "Weight Function Method for Three-Dimensional Crack Problems," *Engineering Fracture Mechanics*, Vol. 34, No. 3, 1989, pp. 593-607.

11. Zhao, W., Newman, J. C., Jr., Sutton, M. A., Wu, X. R., and Shivakumar, K. N., "Analysis of Corner Cracks at Hole by a 3-D Weight Function Method with Stresses From Finite Element Method," *NASA Technical Memorandum 110144,* July 1995.

12. Piascik, R. S. and Willard, S. A., "The Characteristics of Fatigue Damage in the Fuselage Riveted Lap Splice Joint," *NASA/TP-97-206257*, November 1997.

13. Rahman, A., Bakuckas, J. G., Jr., Bigelow, C. A., and Tan, P. W., "Boundary Correction Factors for Cracks at Countersunk Rivet Holes for Tension, Bending, and Wedge Loading," *DOT Report - DOT/FAA/AR-98/37,* December 1998.

14. "Stress Intensity Factors Handbook", Volume 2, Appendix A, Editor-in-Chief, Y Murakami, Pergamon Press, 1987.

15. Bakuckas, J. G., Jr., "Comparison of Boundary Correction Factor Solutions for Two Symmetric Crack in a Straight Shank Hole," *DOT Report - DOT/FAA/AR-98/36,* December 1998.

16. ABAQUS Version 5.6, Hibbitt, Karlsson, and Sorensen (HKS), 1080 Main Street, Pawtucket, RI 02860, USA, 1996

TABLE 1: ANALYSIS MATRIX

h/t	0.05, 0.25, 0.5
a/c	1.0, 0.75, 0.5
Locations	1, 2, 3, 4, and 5
Loading Conditions	Tension, Bending, and Wedge Load

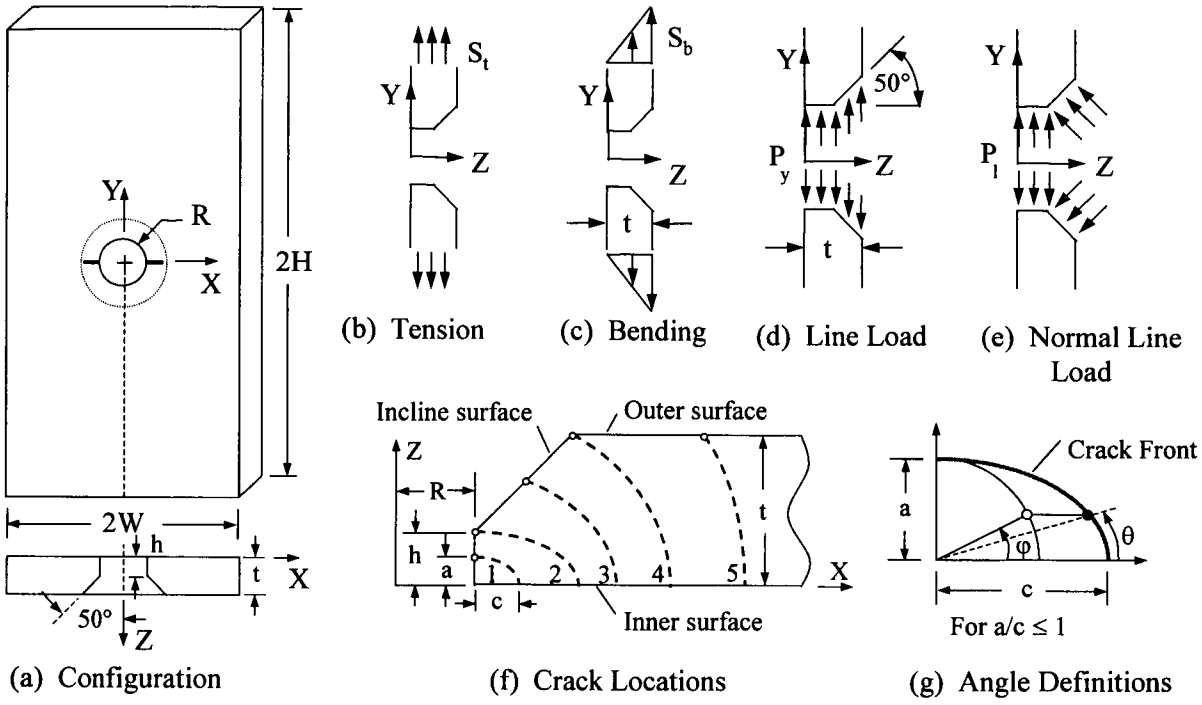

Figure 1. Problem description

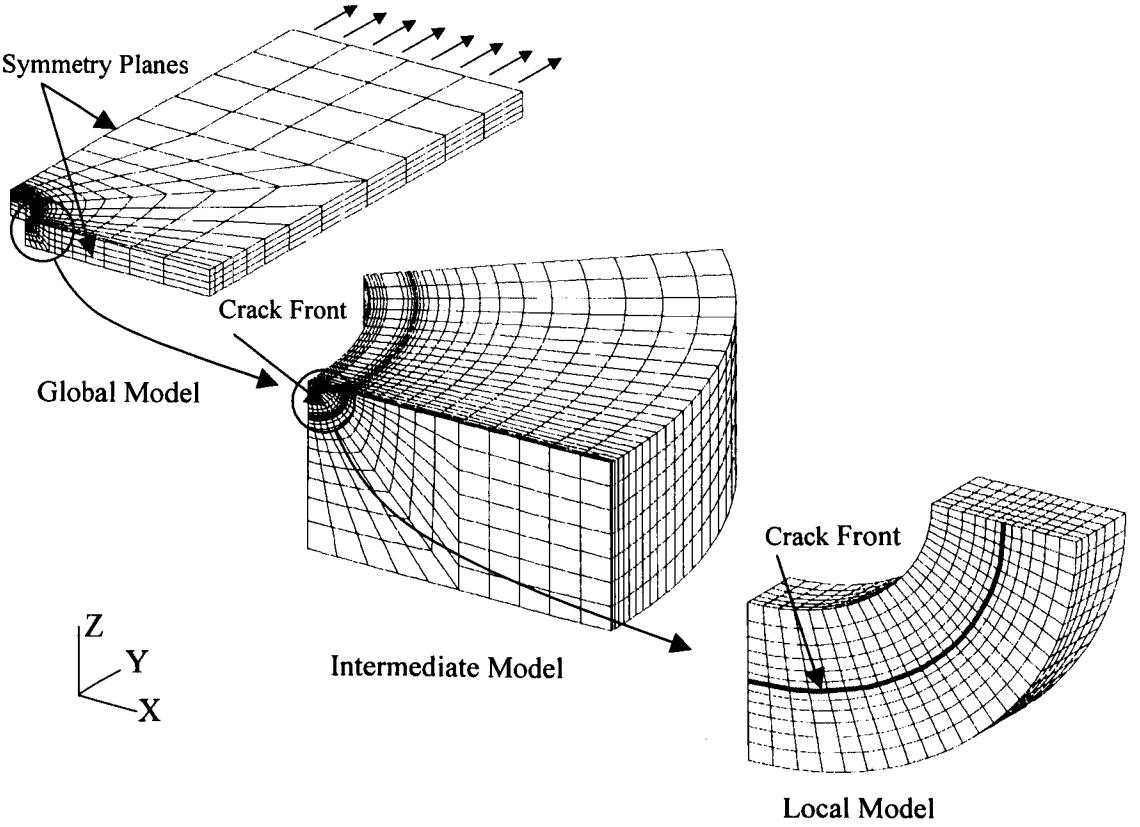

Figure 2. Global-intermediate-local (GIL) hierarchical approach

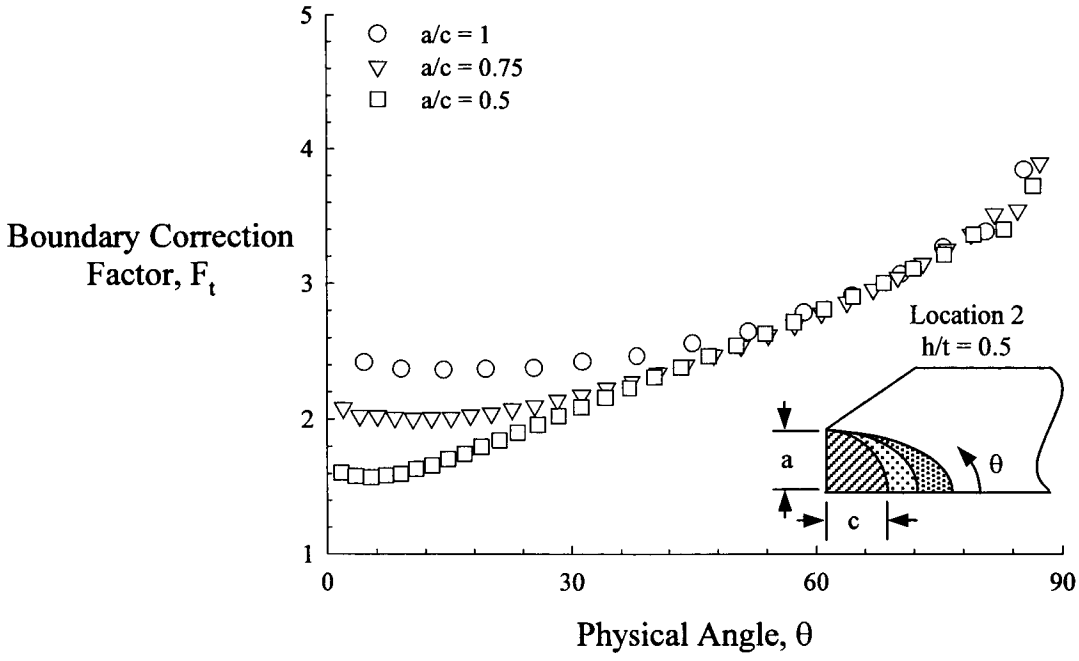

Figure 3. Effect of crack shape on boundary correction factors

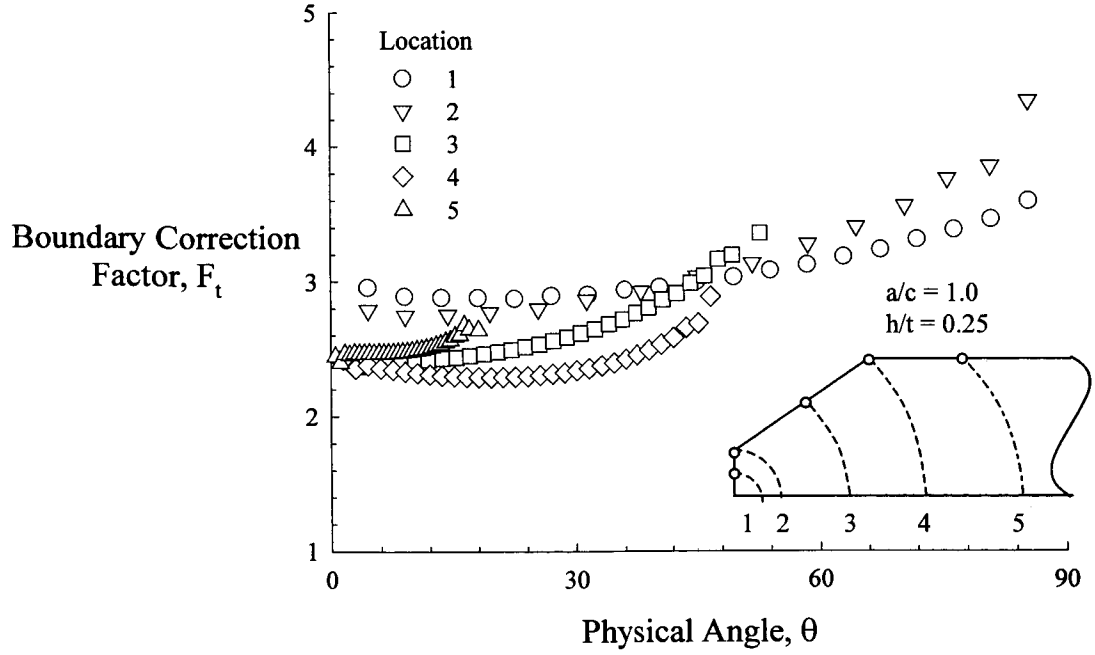

Figure 4. Effect of crack location on boundary correction factors

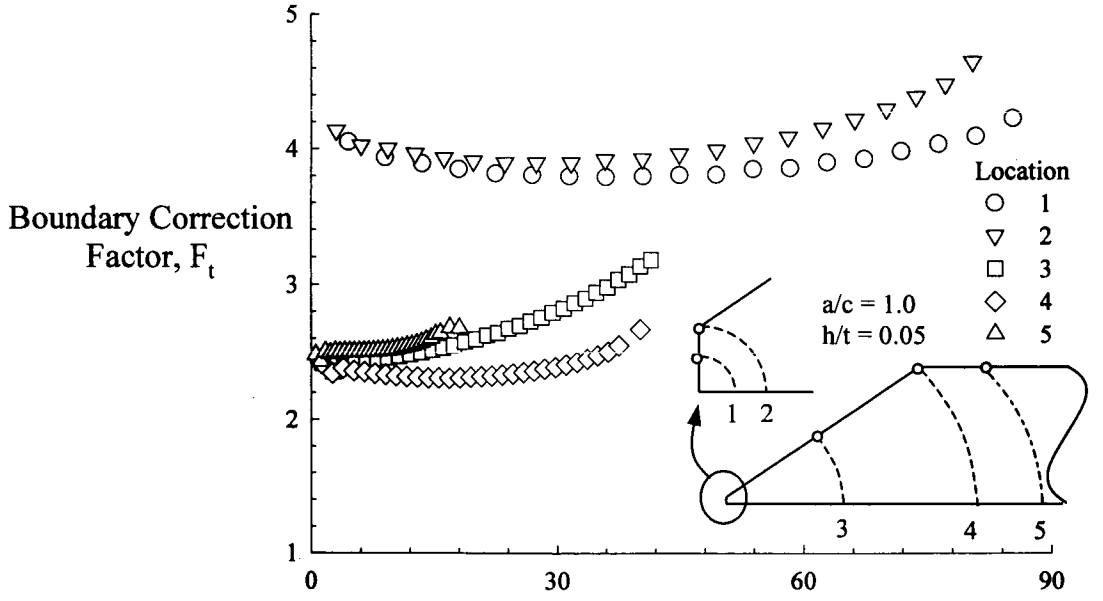

Figure 5. Effect of crack location on boundary correction factors

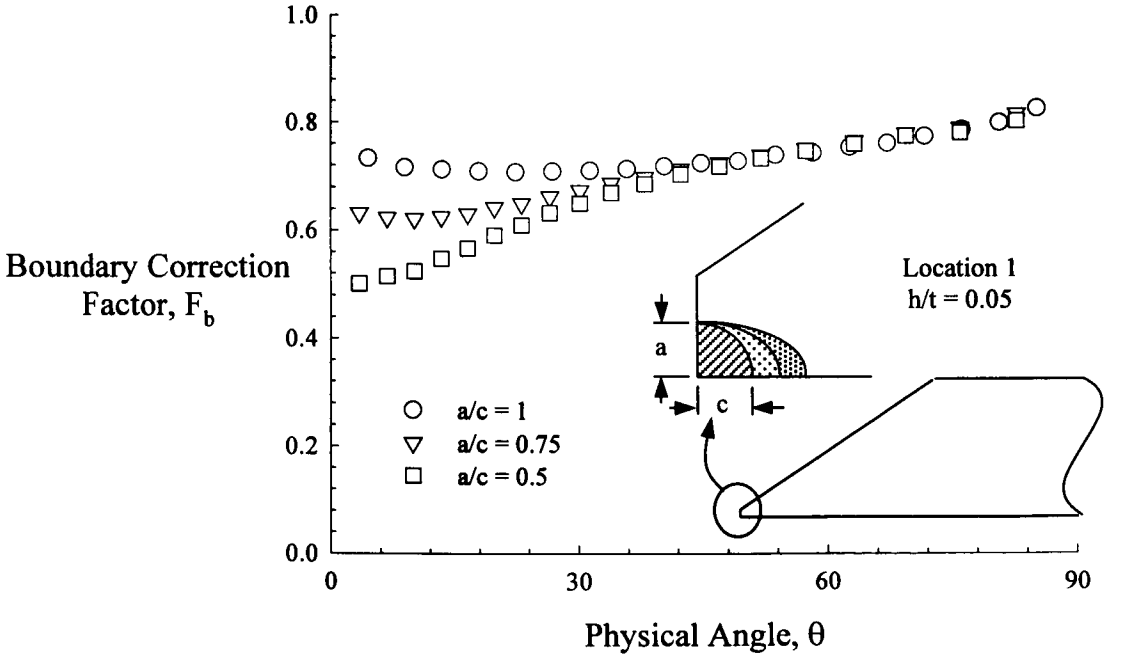

Figure 6. Boundary correction factors for bending loading conditions

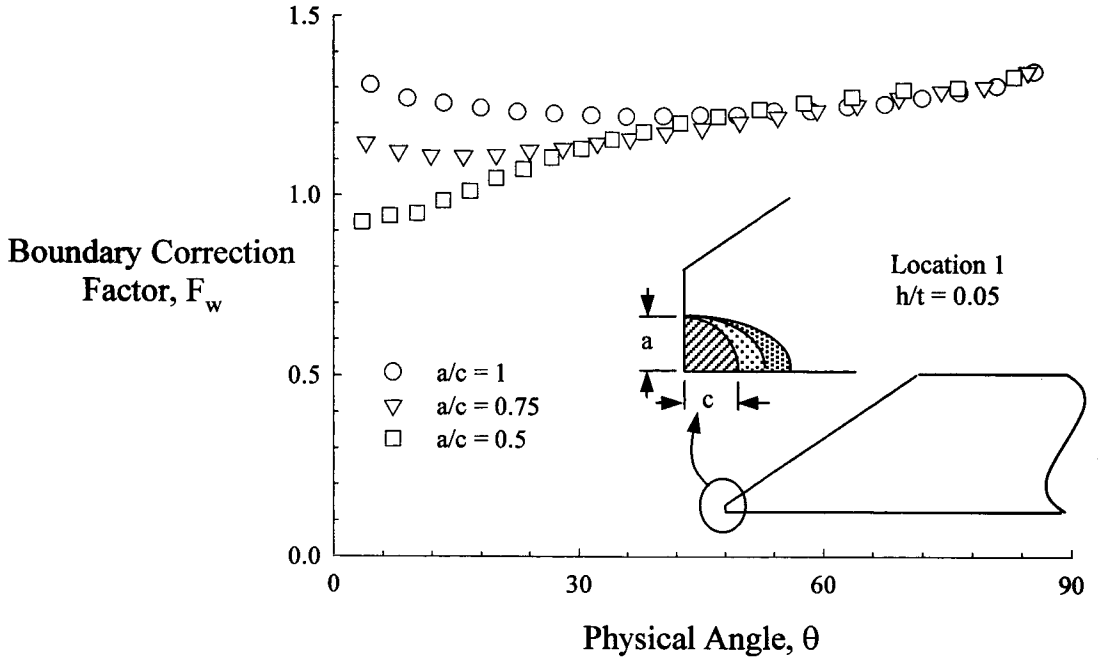

Figure 7. Boundary correction factors for wedge loading conditions

STABLE TEARING AND BUCKLING RESPONSES OF UNSTIFFENED ALUMINUM SHELLS WITH LONG CRACKS

James H. Starnes, Jr., and Cheryl A. Rose
NASA Langley Research Center
Hampton, VA 23681-0001, USA
Tel: (757) 864-3168
Fax: (757) 864-7791
j.h.starnes@larc.nasa.gov

ABSTRACT

The results of an analytical and experimental study of the nonlinear response of thin, unstiffened, aluminum cylindrical shells with a long longitudinal crack are presented. The shells are analyzed with a nonlinear shell analysis code that accurately accounts for global and local structural response phenomena. Results are presented for internal pressure and for axial compression loads. The effect of initial crack length on the initiation of stable crack growth and unstable crack growth in typical shells subjected to internal pressure loads is predicted using geometrically nonlinear elastic-plastic finite element analyses and the crack-tip-opening angle (CTOA) fracture criterion. The results of these analyses and of the experiments indicate that the pressure required to initiate stable crack growth and unstable crack growth in a shell subjected to internal pressure loads decreases as the initial crack length increases. The effects of crack length on the prebuckling, buckling and postbuckling responses of typical shells subjected to axial compression loads are also described. For this loading condition, the crack length was not allowed to increase as the load was increased. The results of the analyses and of the experiments indicate that the initial buckling load and collapse load for a shell subjected to axial compression loads decrease as the initial crack length increases. Initial buckling causes general instability or collapse of a shell for shorter initial crack lengths. Initial buckling is a stable local response mode for longer initial crack lengths. This stable local buckling response is followed by a stable postbuckling response, which is followed by general or overall instability of the shell.

1. INTRODUCTION

Transport fuselage shell structures are designed to support combinations of internal pressure and mechanical loads which can cause the structure to have a geometrically nonlinear structural response. These shell structures are required to have adequate structural integrity so that they do not fail if cracks develop during the service life of the aircraft. The structural response of a transport fuselage shell structure with a crack is influenced by the local stress and displacement gradients near the crack and by the internal load distribution in the shell. Local fuselage out-of-plane skin displacements near a crack can be large compared to the fuselage skin thickness, and these displacements can couple with the internal stress resultants in the shell to amplify the magnitudes of the local stresses and displacements near the crack. In addition, the stiffness and internal load distributions in a shell with a crack will change as the crack grows and when the skin buckles. This nonlinear response must be understood and accurately predicted in order to determine the structural integrity and residual strength of a fuselage structure with damage.

Fuselage shells are usually designed to allow the fuselage skin to buckle above a specified design load that can be less than the design limit load for the shell. During the design of the fuselage, it is assumed that the design limit load can occur anytime during the service life of the aircraft. As a result, a long crack could

exist in the fuselage shell after a considerable amount of flight service, and loading conditions could occur that cause the shell with the long crack to buckle. The results of a preliminary analytical study[1] of the effects of long cracks on the nonlinear response of unstiffened aluminum shells indicates that the behavior of a shell can be influenced significantly by the initial length of the crack.

The present paper describes the results of an analytical and experimental study of the effects of internal pressure and axial compression loads on the responses of thin, unstiffened, laboratory scale, aluminum cylindrical shells with a long longitudinal crack. Two wall thicknesses are considered in the analytical study to determine the effect of wall thickness on the shell response. The predicted effect of the initial crack length on the initiation of stable crack growth and on unstable crack growth is discussed for shells subjected to internal pressure loads. Stable crack growth is simulated using a geometrically nonlinear elastic-plastic finite element analysis and the crack-tip-opening angle (CTOA) fracture criterion. In addition, predicted prebuckling, buckling, and initial postbuckling results are presented and compared for cylindrical shells subjected to axial compression loads. The results presented illustrate the influence of the loading condition and initial crack length on shell crack-growth instabilities, and on shell buckling instabilities.

2. EXPERIMENTS

2.1 TEST SPECIMENS

The cylindrical shells tested in this investigation were fabricated from 0.040-inch-thick 2024-T3 bare aluminum alloy sheet, with the roll direction oriented circumferentially. All specimens were 39 inches long and 18 inches in diameter. Each specimen was fabricated with a 1.5-inch-wide double lap splice with 0.040-inch-thick splice plates and a single row of 0.1875-inch-diameter aluminum rivets on each side of the splice. The rivets were spaced 1.5 inches apart along the length of the specimens and were located five rivet diameters from the edges of the splice plates. A single longitudinal crack (0.010-inch-wide sawcut) was machined in each specimen at the specimen midlength, diametrically opposite to the lap splice. The initial cracks were either 2.0, 3.0 or 4.0 inches long. Specimens that were subjected to internal pressure loads had the crack tips sharpened with a razor blade to approximate a fatigue crack, and to insure some stable crack growth before the shells failed. To assure proper load introduction, and to assure that the ends of the cylinders remained circular during the tests, both ends of each specimen were potted in an aluminum-filled epoxy resin. The potting material extended 1.5 inches along the length from each end of the specimen, resulting in a test section length of 36 inches. The ends of the specimens subjected to compression loads were machined flat and parallel.

2.2 APPARATUS, INSTRUMENTATION AND TEST PROCEDURE

The specimens subjected to axial compression were loaded with a controlled end-shortening displacement using a 300-kip hydraulic test machine. Before each test a load balancing procedure was employed to assure that the load was applied to the specimens as uniformly as possible. All compression specimens were loaded to the point of global collapse. Specimens subjected to internal pressure loads were attached to end fittings, and slowly pressurized to failure with nitrogen gas. Details of the shell specimen and the end fittings are shown in Fig. 1. Two end plates with O-ring seals maintained internal pressure in the shell. A pressure line was attached to one end of the specimen and an instrumentation terminal block was attached to the other. One end ring of the specimens was clamped to rigid beams on the ground, and the other end was unconstrained in the axial direction to allow free expansion of the specimen.

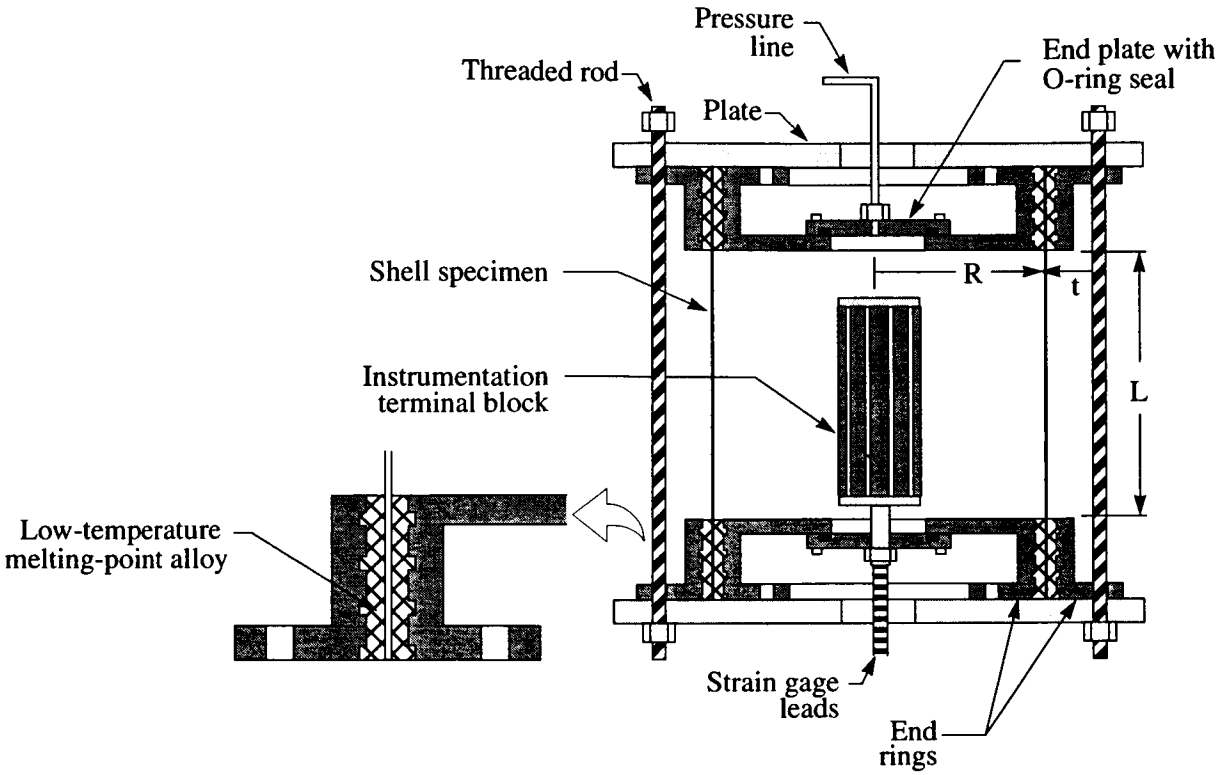

Figure 1. Schematic of pressure test shell specimen.

All specimens were instrumented with back-to-back electrical resistance strain gages mounted on the internal and external surfaces of the cylinder. Crack wire gages were applied at a crack tip of the specimens subjected to internal pressure loads to record the stable crack growth response of the crack. A moiré interferometry procedure was used with the compression-loaded specimens to observe the deformation patterns before and after buckling had occurred. Three non-collinear direct current differential transducers were used to measure the displacements of the loading platen for the compression loaded specimens. All data were recorded with a data acquisition system, and the response of all specimens was recorded on video tape.

3. SHELL MODELS AND ANALYSIS PROCEDURES

3.1 SHELL MODELS

The geometry of the shells analyzed in this study is defined in Fig. 2a. The shells have a 9.0-inch radius, R, a 0.040- or 0.020-inch-thick wall, t, and a 36.0-inch unsupported length, L. A longitudinal crack is located at $\theta = 0°$ and at shell mid length. The initial crack length, a, ranges from 1.0 to 4.0 inches. The shells are typical laboratory-scale cylindrical shells and are made of 2024-T3 bare aluminum alloy, with the sheet rolling direction oriented in the circumferential direction.

The finite element models used to simulate the response of the cracked shells subjected to internal pressure and axial compression loads are shown in Fig. 2b and Fig. 2c, respectively. For the internal pressure load case, advantage was taken of the symmetry of the problem, and only a quarter of the shell was modeled.

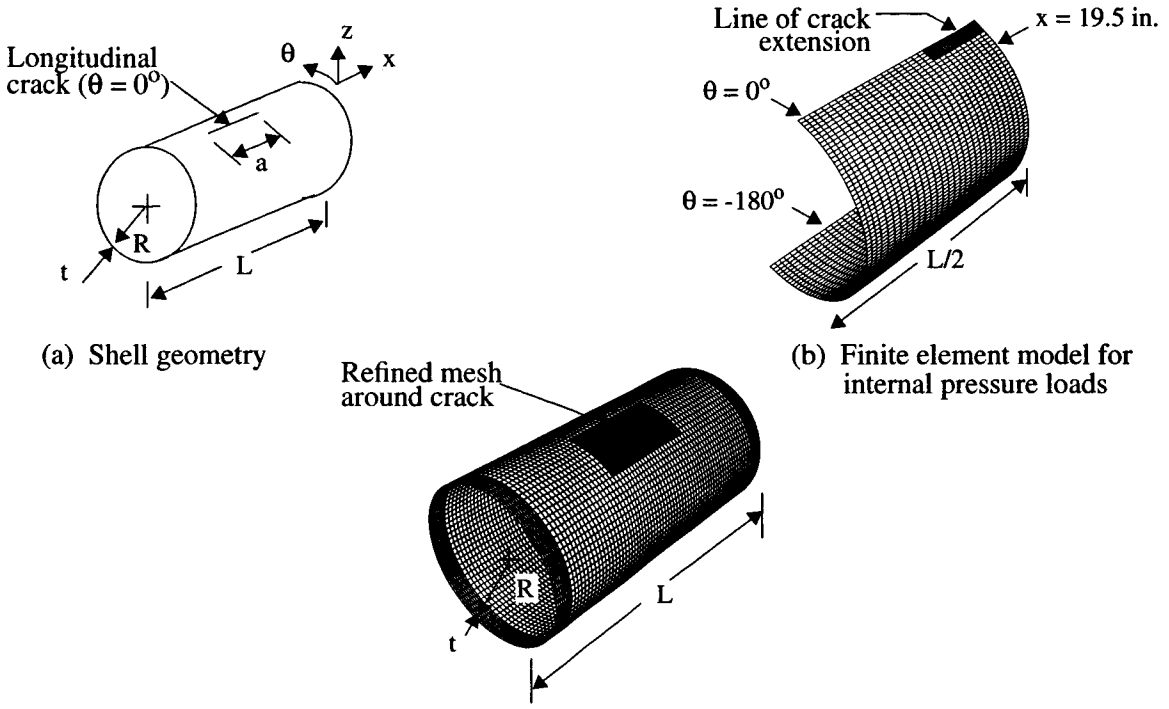

Figure 2. Shell geometry and finite element models.

Symmetry conditions were applied along the edges $\theta = 0°$ and $\theta = -180°$ and along the edge $x = 19.5$ inches. Self-similar crack growth was assumed; therefore, straight cracks with initial half-lengths of 0.5 to 2.0 inches were defined in the model along $\theta = 0°$ and extended from the symmetry boundary at the edge, $x = 19.5$ inches. Mesh refinement was used to provide elements with side lengths equal to 0.04 inches along the line of crack extension. This mesh density was required to predict accurately the crack extension using the CTOA criterion.[2] The shells were modeled using STAGS standard quadrilateral shell elements and mesh-transition elements, to transition from the very refined mesh around the crack to a course mesh remote from the crack. Each of the shell element nodes has six degrees of freedom, including three translational degrees of freedom, u, v, and w, and three rotational degrees of freedom, about the axes x, θ, and z. Internal pressure was simulated by applying a uniform lateral pressure to the shell wall and an axial tensile force to the end of the shell at $x = 0.0$ inches. Multi-point constraints were used to enforce a uniform end displacement. The circumferential and radial degrees of freedom, v and w, respectively, were constrained in regions of the cylinder 0.0 in. $\leq x \leq$ 1.5 in. to approximate the experimental end conditions.

The entire cylindrical shell was modeled for the axial compression load case. The finite element model for this load case is shown in Fig. 2c. Straight cracks with initial lengths of 1.0 to 4.0 inches were defined in the model along $\theta = 0°$ and at the shell midlength. The primary objective of the study for the axial compression load case was to continue the analysis beyond the critical buckling state, and to focus on the post-buckling response of the shell with a crack. Thus, the interaction between local buckling and crack extension was not specifically addressed; that is, the crack lengths were held constant throughout the analyses. Therefore, the mesh was not as refined in the vicinity of the crack for this load case as it was for the internal pressure load case. The compression load was applied to the ends of the shell by specifying a uniform end displacement. As in the pressure load case, the circumferential and radial degrees of freedom, v and w, respectively, were constrained in regions of the cylinder 0.0 in. $\leq x \leq$ 1.5 in. to approximate the experimental end conditions.

3.2 NONLINEAR ANALYSIS PROCEDURE

The shell responses were predicted numerically using the STAGS (STructural Analysis of General Shells) nonlinear shell analysis code.[3] STAGS is a finite element code for general-purpose analysis of shells of arbitrary shape and complexity. STAGS analysis capabilities include stress, stability, vibration and transient response analyses, with both material and geometric nonlinearities represented. The code uses both the modified and full Newton methods for its nonlinear solution algorithms, and accounts for large rotations in a shell by using a co-rotational algorithm at the element level. The Riks pseudo arc-length path following method[4,5] is used to continue a solution past the limit points of a nonlinear response.

STAGS can also perform crack-propagation analyses, and can represent the effects of crack growth on nonlinear shell response. A nodal release method and a load-relaxation technique are used to extend a crack while the shell is in a nonlinear equilibrium state.[6] The condition for crack extension is based upon a fracture criterion. When a crack is to be extended, the forces necessary to hold the current crack tip nodes together are calculated. The crack is extended by releasing the nodal compatibility condition at the crack tip, applying the equivalent crack-tip forces, and then releasing these forces to establish a new equilibrium state, which corresponds to the longer crack. The changes in the stiffness matrix and the internal load distribution that occur during crack growth are accounted for in the analysis, and the nonlinear coupling between internal forces and in-plane and out-of-plane displacement gradients that occurs in a shell is properly represented. Output from STAGS, associated with a crack, includes the strain-energy-release rate in an elastic analysis, and the crack-tip-opening angle (CTOA) in an elastic-plastic analysis. These quantities can then be used as part of a fracture criterion in an elastic analysis or an elastic-plastic analysis to predict stable crack growth and the residual strength of a damaged shell.

3.2.1 Internal Pressure Load

An elastic-plastic STAGS analysis, using the nodal release method and load relaxation technique described above to extend the crack, was used to predict the residual strength of the cracked pressurized cylinders. The material nonlinearity was represented by the White-Besseling mechanical sublayer distortional energy plasticity theory used in STAGS. A piecewise linear representation was used for the uniaxial stress strain curve for 2024-T3 aluminum (Fig. 3).[7]

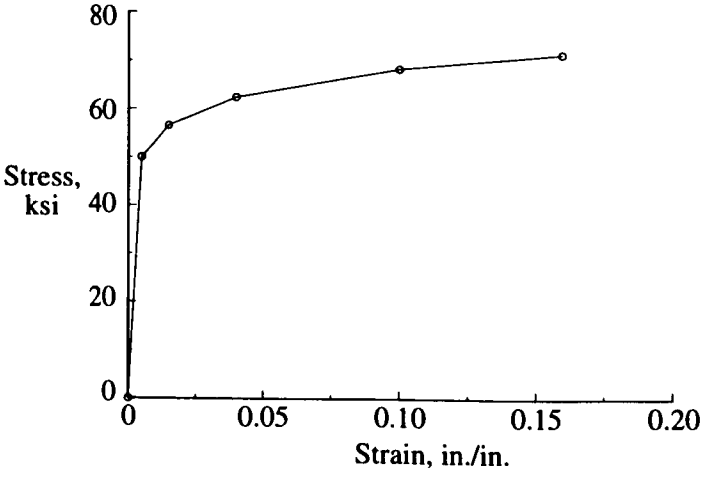

Stress (ksi)	Strain (in./in.)
0.00	0.00
50.0	0.0048
56.6	0.015
62.3	0.040
68.2	0.100
71.1	0.160

E = 10.35 Msi
ν = 0.3

Figure 3. Piecewise linear representation for the uniaxial stress-strain curve for 2024-T3 aluminum (L-T orientation).

The critical crack-tip-opening angle (CTOA) fracture criterion[2,7,8] was used to simulate stable crack growth. The CTOA fracture criterion uses the crack opening angle, shown schematically in Fig. 4, as the fracture parameter. The CTOA, evaluated at a fixed distance from the moving crack tip, is defined as the angle made by the upper crack surface, the crack tip, and the lower crack surface. In the present study, the CTOA was evaluated at a distance of 0.04 inches behind the crack tip. Newman[2] has shown this value to be adequate for analyzing stable crack growth in a wide variety of materials. The criterion assumes that crack growth will occur when the angle reaches a critical value, $CTOA_{cr}$, and that the critical value will remain constant as the crack extends. These assumptions are supported by experimental studies and numerical elastic-plastic finite element analyses that have shown that, in several metals, the CTOA is essentially constant after some initial crack growth.[7] The value of the critical angle is dependent on the sheet material, the sheet thickness and the crack orientation, and can be determined from three-dimensional, elastic-plastic, finite element simulations of the fracture behavior of small laboratory specimens. The determined angle can then be used to predict the fracture behavior of different structural configurations. In a two-dimensional, plane stress, elastic-plastic finite element analysis, the accuracy of residual strength predictions obtained using the $CTOA_{cr}$ determined as described above, is affected by the panel width. This dependence on panel width is postulated to be caused by three-dimensional constraint effects that develop near the crack tips.[9] To eliminate the dependence of the two-dimensional plane stress finite element analysis on the structural configuration, the three-dimensional constraint effects are approximated in the two-dimensional model by incorporating a "core" of plane strain elements on each side of the crack line (see Fig. 4). The dimension of the plane strain core region on each side of the crack line is referred to as the plane strain core height, h_c. The value of h_c can be determined by correlating two-dimensional, elastic-plastic finite element analysis results, that use the $CTOA_{cr}$ determined from three-dimensional finite element analysis, with experimental results for small laboratory specimens. The procedure used in the present study for determining the values of $CTOA_{cr}$ and h_c is described in more detail in Section 3.3.

The prebuckling, buckling and postbuckling responses of the shells for the axial compression loading condition were determined using the following analysis procedure. The prebuckling responses were determined using the geometrically nonlinear quasi-static analysis capability in STAGS. The initial, unstable, postbuckling response of the shell was predicted using the nonlinear transient analysis option of the code. The transient analysis was initiated from an unstable equilibrium state just beyond the buckling point by increasing the end-shortening displacement. The transient analysis was continued until the transient response damped out or decayed. Once the transient analysis converged to a steady-state solution, the load relaxation option of the code was used to establish a stable equilibrium state. The subsequent stable postbuckling response of the shell was computed using the standard nonlinear, static analysis option. For the parametric studies presented in Section 4.2, plasticity effects were not included in the analyses. However, elastic-plastic analyses were conducted to provide a preliminary assessment of the effects of plasticity on the shell buckling response, and for comparison with the experimental results.

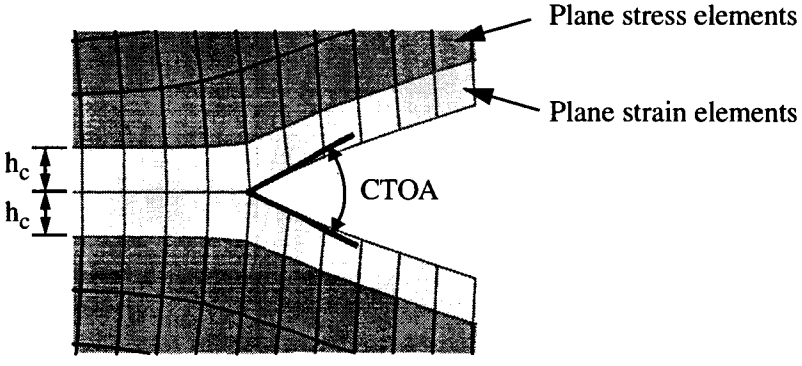

Figure 4. Schematic for fracture parameters, $CTOA_{cr}$ and h_c.

3.3 DETERMINATION OF $CTOA_{cr}$ AND h_c

Fracture tests of compact tension, C(T), and middle crack tension, M(T), specimens were conducted by the Mechanics of Materials Branch at NASA Langley Research Center. The test specimens were made of the same 0.040-inch-thick 2024-T3 aluminum sheet material that was used for the cylinders. The specimens were fatigue cracked, or notched, with the crack perpendicular to the sheet rolling direction. The C(T) specimens were 6 inches wide, with an initial crack length, a, equal to 2.4 inches. The M(T) specimens were 12 inches wide, with an initial crack length, a, equal to 4 inches. For the notched specimens, the tips were sharpened with a razor blade to produce crack tips similar to the crack tips in the pressurized cylinder test specimens. A residual strength test of each specimen was conducted under displacement control loading conditions. Guide plates, to constrain out-of-plane deformations, were used during the residual strength tests of all of the C(T) specimens and of one of the fatigue cracked M(T) specimens. Load, crack extension, and surface crack opening displacement measurements were made during the tests. The fracture behavior of the unconstrained M(T) panel with the razor blade sharpened notch was basically identical to the behavior of the unconstrained M(T) panels with fatigue cracks.

The fracture parameters that were used in the residual strength analysis of the pressurized cylinders were determined by simulating the fracture behavior of the C(T) and M(T) tests. Personnel from the Mechanics of Materials Branch conducted three-dimensional, geometrically linear, finite element simulations, with the ZIP3D code,[10,11] to determine the $CTOA_{cr}$ that best correlated the experimental results for the constrained C(T) and M(T) tests. In the three-dimensional analyses, the three dimensional constraint effects at the crack tip are directly modeled, and the core height parameter, h_c, is eliminated. The angle determined from the three-dimensional analyses was then used in a geometrically linear, two-dimensional simulation performed using the ZIP2D code[12,13] to determine the core height, h_c, that best correlated the experimental results for the constrained M(T) and C(T) tests. The fracture parameters determined in this manner for 0.040-inch-thick 2024-T3 bare aluminum, for fracture in the L-T orientation, had a $CTOA_{cr}$ equal to 5.6 degrees and a plane strain core height equal to 0.04 inches.

To verify application of these parameters in a STAGS analysis, elastic-plastic, geometrically nonlinear STAGS analyses were conducted for the C(T) tests, and for the constrained and unconstrained M(T) tests. The mesh used in the analysis was refined to provide elements along the line of crack extension with side lengths equal to 0.04 inches. Predicted and measured load results for the C(T) and M(T) panels are shown in Fig. 5 for increasing values of crack extension, Δa. These results indicate that the STAGS analysis accurately predicted the stable tearing and residual strength for the C(T) and for the M(T) panels with buckling constrained. The STAGS analysis for the unconstrained M(T) specimens predicted accurately the early portion of the crack extension. However, some discrepancy was observed in the analysis predictions and experimental results for the latter portion of crack extension, and the residual strength of these tests was overpredicted by approximately 9%. This discrepancy is consistent with the differences that have been observed in test and analysis results of wider and thicker, unstiffened sheets. Additional studies are required to resolve this issue.

4. RESULTS AND DISCUSSION

The nonlinear analysis and test results for thin unstiffened aluminum cylindrical shells with a longitudinal crack are presented in this section. Results have been generated for two loading conditions: internal pressure only, and axial compression only. Results for these loading conditions are presented for shells with a longitudinal crack at shell midlength and with initial crack lengths of 1.0, 2.0, 3.0 and 4.0 inches. The maximum value of the applied internal pressure considered is 143 psi. This pressure is the pressure required to cause a shell with a 1.0-inch-long initial crack and a 0.040-inch wall thickness to fail due to an internal pressure load. The axial compression loads are increased from zero to the maximum axial load that the shell can

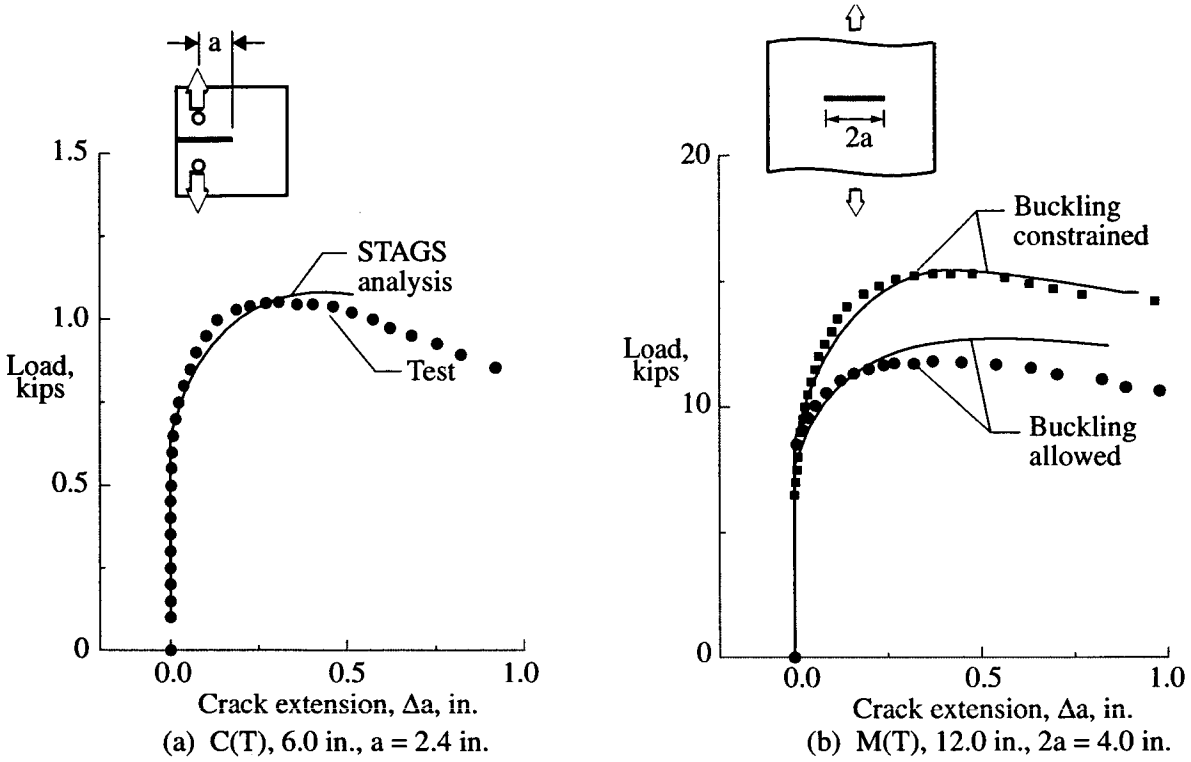

Figure 5. STAGS analysis predictions and test results for C(T) and M(T) panels.

support. Typical results are presented to illustrate the effects of crack length on the crack growth response of a shell subjected to internal pressure loads, and on the prebuckling, buckling and postbuckling responses of a shell subjected to axial compression loads. Shells with both 0.020- and 0.040-inch wall thicknesses are considered for the analysis results, but only shells with a 0.040-inch wall thickness are considered for the experimental results.

4.1 INTERNAL PRESSURE LOADS

The effect of increasing the internal pressure in a shell on the total crack growth or crack extension is shown in Fig. 6a and Fig. 6b for shells with initial crack lengths of 1.0, 2.0, 3.0, and 4.0 inches, and with wall thicknesses of 0.040 and 0.020 inches, respectively. These results were generated using the mesh shown in Fig. 2b, and a STAGS plane stress analysis, prior to determining the fracture parameters $CTOA_{cr}$ and h_c from the C(T) and M(T) tests. Therefore, a preliminary critical crack-tip-opening angle was determined by correlating the results of a STAGS plane stress analysis of a cylinder with an initial 4.0-inch-long longitudinal crack with the experimentally observed behavior of an aluminum shell of the same geometry. The critical crack-tip-opening angle determined in this manner, and used in all of the parametric studies, was 5.36^{o}. The results in Fig. 6 indicate that the internal pressure in the shell can be increased, and the cracked shell will remain in equilibrium, up to a pressure at which yielding occurs at the crack tips and the opening angle at the crack tips reaches a critical value. At this pressure, the crack will start to grow. The initial growth of the crack is stable and the crack will not extend unless the pressure is increased. Eventually, unstable crack growth occurs. Unstable growth occurs when the slope of the curves in Figs. 6a and 6b becomes zero, which means that a small increase in pressure causes a very large increment in crack extension.

The effect of increasing the initial crack length on the internal pressure required to initiate stable crack growth and on the pressure at which stable growth changes to unstable crack growth is summarized in Fig. 6c for the two shell wall thicknesses. The solid curve for each shell wall thickness represents the pressure

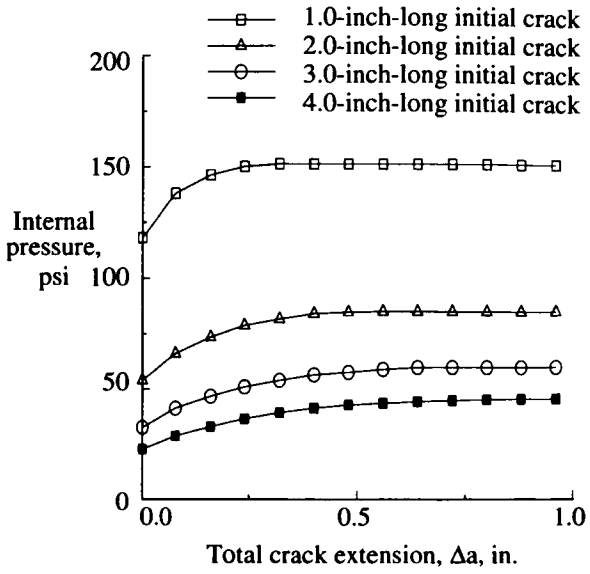

(a) Crack extension for 0.040-inch-thick shells

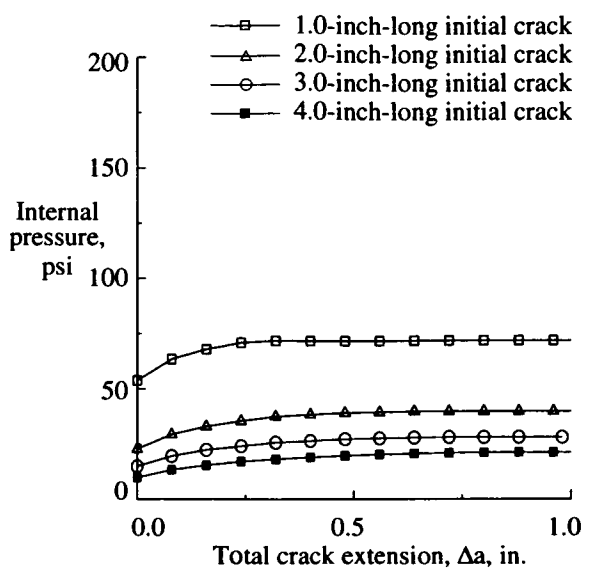

(b) Crack extension for 0.020-inch-thick shells

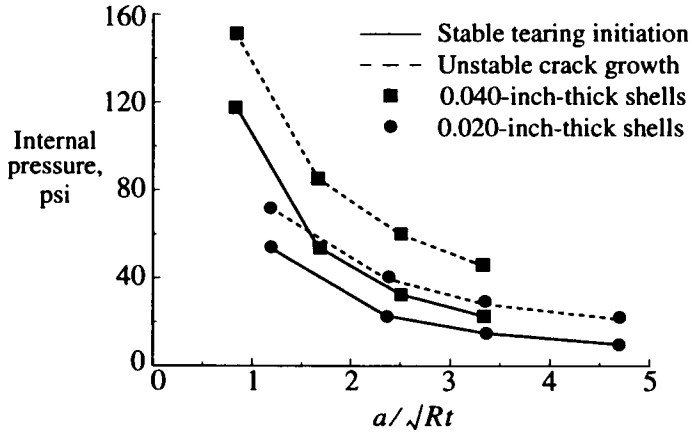

(c) Initial stable tearing and unstable crack growth

Figure 6. Effect of increasing internal pressure on initial stable crack growth and unstable crack growth for different initial crack lengths.

required to initiate stable crack growth as a function of normalized initial crack length, and the dashed curve for each shell wall thickness represents the pressure that causes the crack growth to become unstable. These results indicate that the internal pressure required to initiate stable crack growth and to cause unstable crack growth decreases as the initial crack length increases. The results shown in Fig. 6c also indicate that the difference between the internal pressure required to initiate stable crack growth and the internal pressure that causes unstable crack growth decreases as the initial crack length increases. For an initial crack length of 1.0 inch, stable crack growth initiates in the 0.040-inch-thick shell when the internal pressure is approximately 113 psi, and unstable crack growth occurs when the internal pressure is approximately 143 psi. The difference between the internal pressure required to initiate stable crack growth and the internal pressure that causes unstable crack growth is approximately 30 psi for the 1.0-inch initial crack length in the 0.040-inch-thick shell. The results for an initial crack length of 2.0 inches in the 0.040-inch-thick shell indicate that stable crack growth initiates when the internal pressure is approximately 51 psi, and unstable crack growth occurs when the internal pressure is approximately 79 psi. The difference between the internal pressure required to initiate stable crack growth and the internal pressure that causes unstable crack growth for

this initial crack length is 28 psi. The difference between the internal pressure required to initiate stable crack growth and the internal pressure that causes unstable crack growth for the 3.0- and 4.0-inch initial crack lengths in the 0.040-inch-thick shell is approximately 24 psi and 21 psi, respectively. The results for the 0.020-inch-thick shell are similar, but with lower values of internal pressure.

The results from the nonlinear analyses indicate that the internal pressure load induces large outward radial displacements in the neighborhood of the crack. The response associated with these radial displacements is often referred to as "crack bulging" in the literature and is the cause of the larger crack opening displacements and crack-tip stress-intensity factors in a shell, compared to those for a flat sheet under otherwise identical conditions.[14] Furthermore, the extent of crack bulging is a function of the nondimensional crack curvature parameter, $a/\sqrt{Rt}$. This observation is illustrated for the 0.040-inch-thick shell in Fig. 7, which shows the radial displacement response along the shell length at the circumferential location $\theta = 0°$, just before the initiation of stable crack growth, for each of the initial crack lengths. The radial displacement at the center of the crack normalized by the shell thickness, t, is w_o/t =1.00, 1.65, 2.38 and 3.23 for the 1.0-, 2.0-, 3.0- and 4.0-inch-long initial cracks, respectively. These displacements are greater than or equal to the shell wall thickness for all of the crack lengths considered, and represent large displacements in the context of nonlinear thin shell theory. The increase in crack bulging for the longer initial crack lengths is consistent with the observation that the pressure required to initiate stable crack growth decreases with the increase in initial crack length.

Experimental and analytical results for the 0.040-inch-thick shells are compared in Fig. 8 and Fig. 9. The analytical results were generated using the fracture parameters determined as described in Section 3.3. The experimental and predicted strains in the skin at three locations near the crack tip are compared in Fig. 8. The correlation between the predicted and experimentally determined strains indicates that the finite element model accurately simulates the stress state near the crack tip. The effect of internal pressure on the analytical and experimental crack growth results is shown in Fig. 9 for shells with initial crack lengths equal to 2.0, 3.0, and 4.0 inches. The analytical and experimental residual strength results correlate very well for all crack lengths. However, in all cases, the analysis overpredicts the initial portion of the crack growth response.

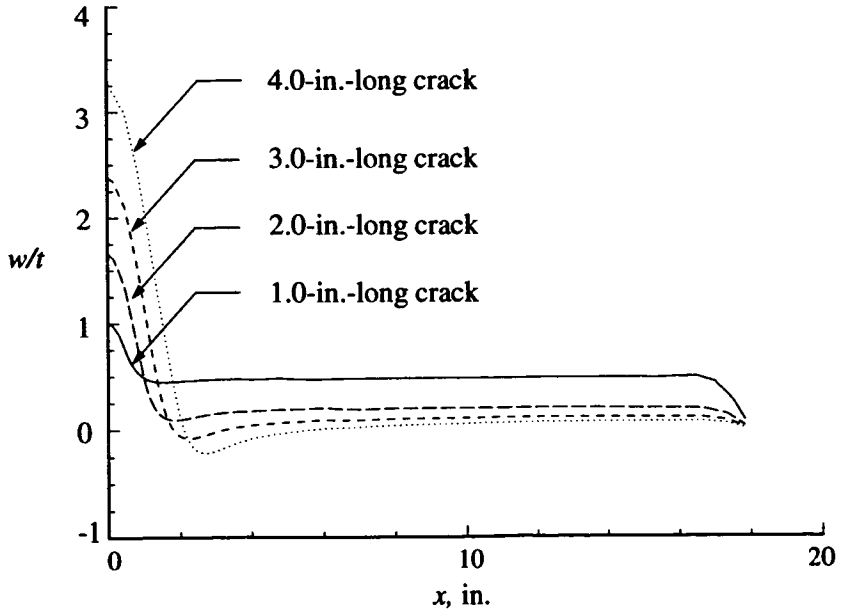

Figure 7. Radial displacement response along the shell length at the circumferential location θ = 0°, just before the initiation of stable crack growth for 0.040-inch-thick shells.

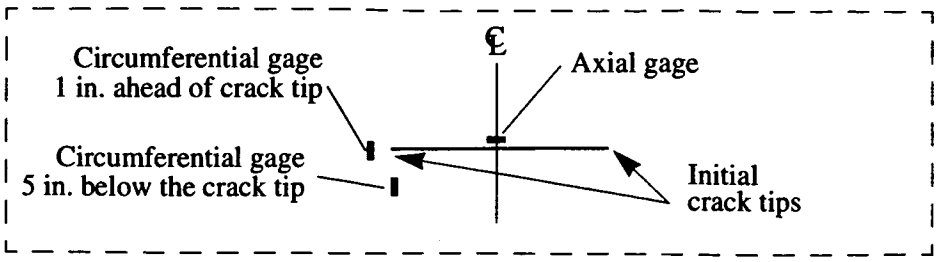

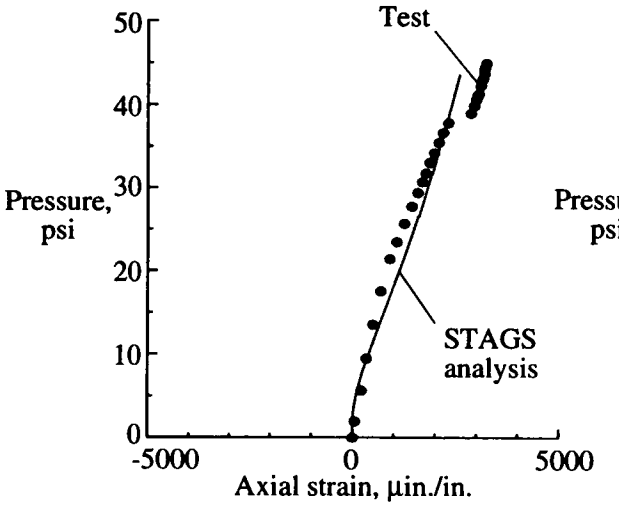

(a) Axial strain at the crack centerline

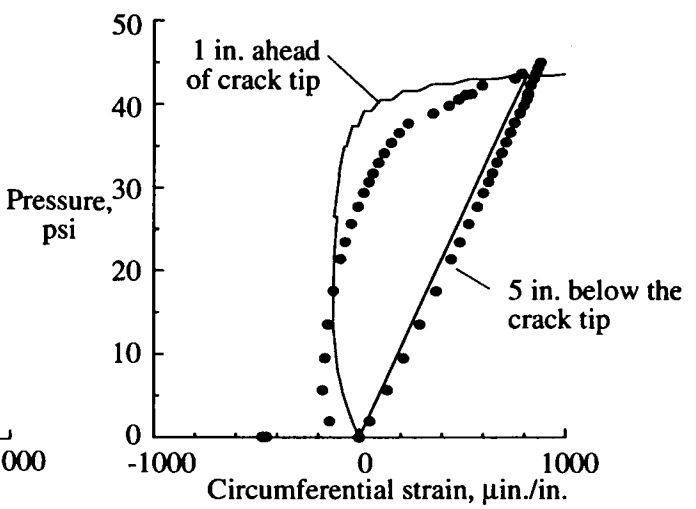

(b) Circumferential strain, below and ahead of the crack tip

Figure 8. Comparison of experimental and predicted strain response for a shell with a 4.0-inch-long initial crack.

4.2 AXIAL COMPRESSION LOADS

The predicted load-shortening responses for a 0.040-inch-thick shell and a 0.020-inch-thick shell with initial crack lengths of 1.0, 2.0, 3.0 and 4.0 inches and subjected to axial compression are shown in Figs. 10a and 10b, respectively. An initial outward geometric imperfection in the form of the lowest eigenmode was used in the nonlinear analyses to generate local deformations in the vicinity of the crack. The applied compression and end-shortening values are normalized by the corresponding classical buckling values for a shell without a crack. For the 0.040-inch-thick shell and the 0.020-inch-thick shell with a 1.0-inch-long crack, the crack introduces an effective imperfection that causes general instability to occur at the loads indicated by the X in Figs. 10a and 10b. These shells cannot support additional compression load after buckling. For a shell with a longer crack, local buckling near the crack precedes shell collapse. The filled symbols in Figs. 10a and 10b identify the loads that correspond to initial local buckling near the crack for the 0.040-inch-thick shell and the 0.020-inch-thick shell, respectively, with the 2.0-, 3.0-, and 4.0-inch-long initial cracks. Prior to buckling the radial displacement, w_o, at the center of the crack edges is nearly equal to zero. Once the critical load is reached, w_o increases rapidly as the load increases. Initial local buckling is followed by a stable postbuckling response, and the load can be further increased after local buckling has occurred near the crack edges.

As the load is increased after initial local buckling has occurred, the 0.040-inch-thick shells with the 3.0- and 4.0-inch-long cracks, and the 0.020-inch-thick shells with the 2.0-, 3.0-, and 4.0-inch-long cracks ex-

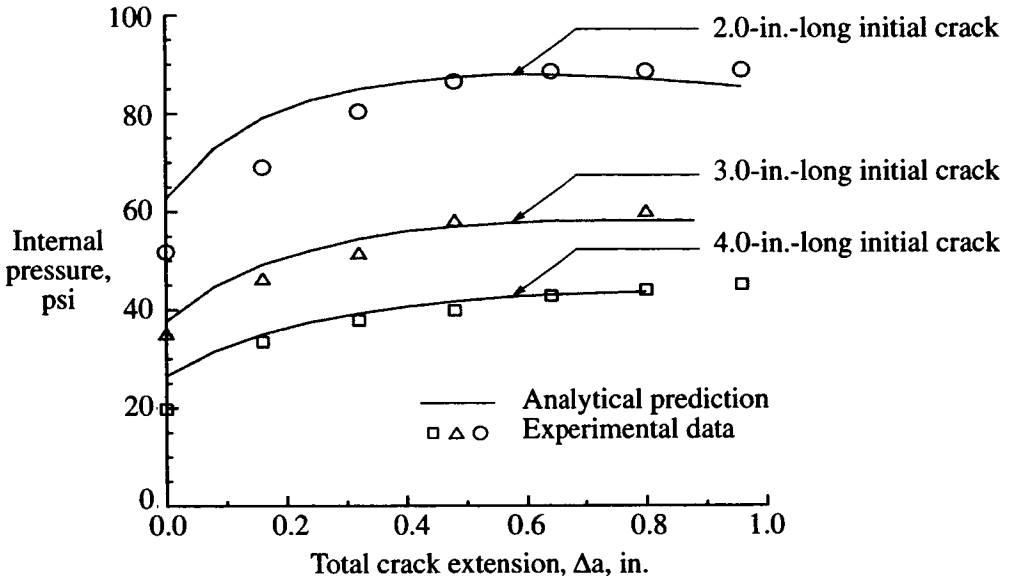

Figure 9. Comparison of analytical and experimental total crack extension results for 0.040-inch-thick internally pressurized shells.

perience a change in the local buckling mode. The initial postbuckling response of the shells after the mode change is unstable, and as a result, the axial load decreases after buckling occurs. The unstable transition region in the response predictions is indicated by the broken lines in Figs. 10a and 10b. The unstable transition from the stable initial buckled configuration to the stable postbuckling configuration was determined by using the transient analysis capability in STAGS. The transient analysis was continued until the kinetic energy in the system was small. A time history of the kinetic energy during the transient analysis of the 0.040-inch-thick shell with a 3.0-inch-long crack is shown in Fig. 11. The deformed shapes labeled A, B, C and D in Fig. 11 correspond to the points A, B, C and D on the load-end shortening and kinetic energy history curves, and show the development of the shell's postbuckled response. Point A corresponds to the initial buckling deformation, points B and C correspond to solutions obtained during the transient analysis, and point D represents the stable postbuckled equilibrium state. Once a stable equilibrium state was determined from the transient analysis, the nonlinear static analysis was resumed to compute the stable postbuckling equilibrium response results shown in Fig. 10a. The analysis was continued for the shells with the 3.0- and 4.0-inch-long cracks for the 0.040-inch-thick shells, and for the shells with the 2.0-, 3.0-, and 4.0-inch-long cracks for the 0.020-inch-thick shells until computational convergence problems were encountered. The load corresponding to the onset of these convergence difficulties is assumed to correspond to shell collapse. Collapse of the 0.040-inch-thick and of the 0.020-inch-thick shells with 2.0-, 3.0- and 4.0-inch-long cracks is identified by the open symbols in Figs. 10a and 10b, respectively.

The initial local buckling load predictions and qualitative approximations for the shell collapse load for the 0.020- and 0.040-inch-thick shells are summarized in Fig. 10c. The predicted collapse loads for the shells are only qualitative approximations because they were assumed to correspond to the point of onset of convergence difficulties in the elastic analyses, and, as will be shown subsequently, the collapse loads for the shells with the longer cracks may be affected by material nonlinear response. The values of the normalized initial buckling loads for the 0.040-inch-thick shells are P/P_{cr} = 0.88, 0.54, 0.39, and 0.32, and the qualitative approximate values of the normalized collapse loads are P/P_{cr} = 0.88, 0.59, 0.49, and 0.47 for the 1.0-, 2.0-, 3.0- and 4.0-inch-long cracks, respectively. The values of the normalized initial buckling loads for the 0.020-inch-thick shells are P/P_{cr} = 0.73, 0.41, 0.30, and 0.24, and the qualitative approximate values of the normalized collapse loads are P/P_{cr} = 0.73, 0.47, 0.43, and 0.41 for the 1.0-, 2.0-, 3.0- and 4.0-

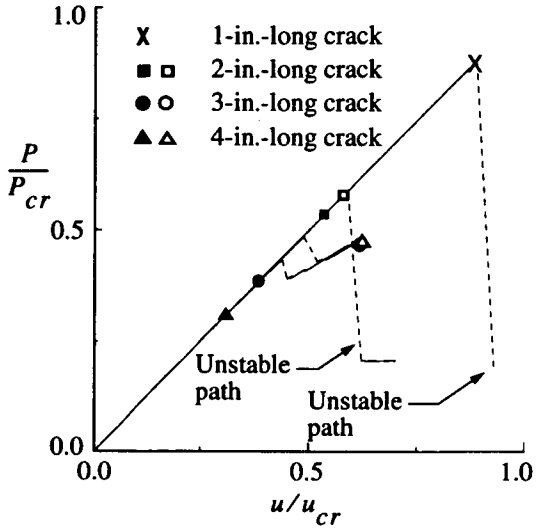

(a) Load-shortening response for 0.040-inch-thick shells

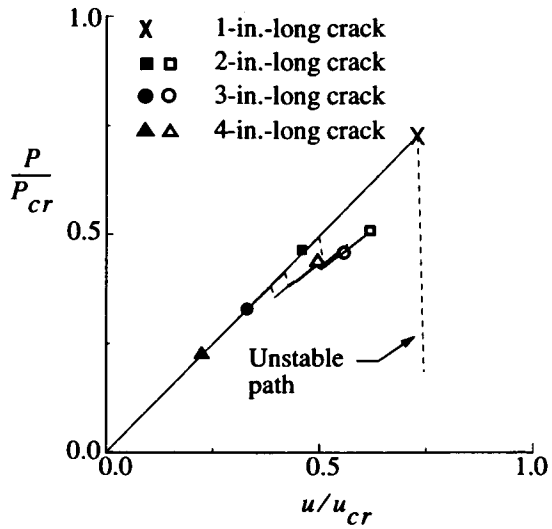

(b) Load-shortening response for 0.020-inch-thick shells

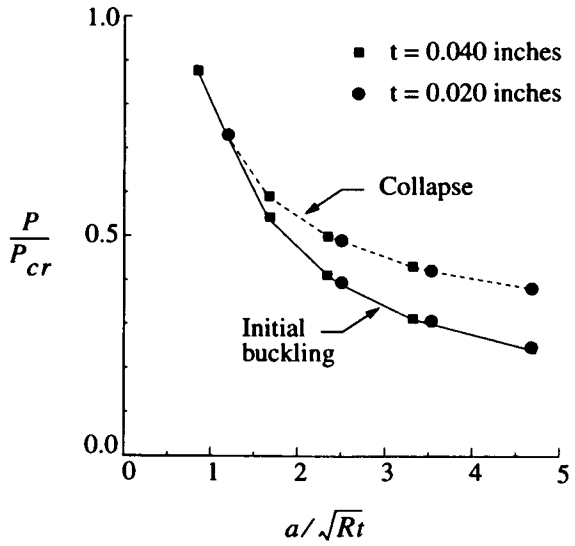

(c) Initial buckling and collapse loads

Figure 10. Effect of initial crack length on the response of cylindrical shells with longitudinal cracks and subjected to axial compression.

inch-long cracks, respectively. These results indicate that the magnitudes of the initial buckling loads and collapse loads for the shells decrease as the initial crack length increases. In addition, the difference between the load at initial buckling and the load at collapse is smaller for the shorter crack lengths. The initial local buckling load results for the 0.020- and 0.040-inch-thick shells are represented very well by a characteristic curve that is based on the curvature parameter $a/\sqrt{Rt}$.

The effects of material nonlinearities on the predicted load-shortening response and deformation patterns for a 0.040-inch-thick shell with a 3.0-inch-long crack are shown in Fig. 12. Initial plastic yielding occurs for an applied load corresponding to $P/P_{cr} = 0.43$, which is approximately 90 percent of the buckling load corresponding to the local mode change. The load-shortening predictions based upon an elastic analysis and an elastic-plastic analysis, and the deformation pattern prediction just prior to the local mode change, indicate that the shell response prior to the local mode change is adequately predicted by an elastic analysis

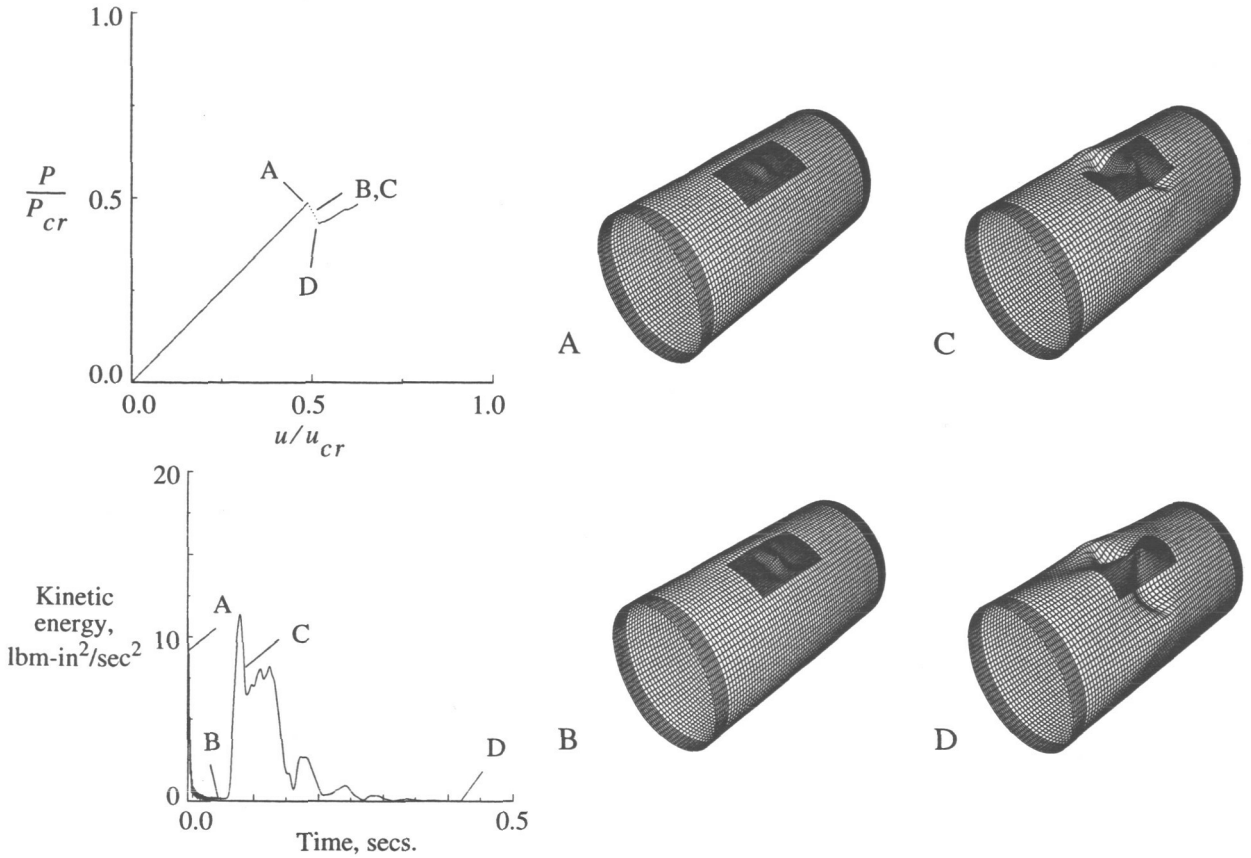

Figure 11. Transient analysis results for the unstable buckling response of a 0.040-inch-thick shell with a 3.0-inch-long crack and subjected to axial compression.

(Figs. 12a and 12b). The initial postbuckled response predictions of the two analyses are, however, significantly different. The initial postbuckled deformation pattern prediction from the elastic-plastic analysis, corresponding to Point B in Fig. 12a, is shown in Fig. 12c, and the initial postbuckled deformation pattern prediction from the elastic analysis, corresponding to Point C in Fig. 12a, is shown in Fig. 12d. Computational convergence problems were encountered in the elastic-plastic analysis at Point B, which prevented prediction of the response further into the postbuckling load range. The postbuckled deformation pattern predicted by the elastic-plastic analysis is very similar to the deformation pattern labeled **C** in the elastic, transient analysis shown in Fig. 11. These results suggest that for the cylinder studied, yielding of the aluminum will prevent the postbuckled deformation pattern predicted by the elastic analysis from developing. This suggestion is consistent with the experimentally observed behavior. The initial postbuckled deformation pattern for the 0.040-inch-thick cylinder with a 3.0-inch-long crack observed in the experiment and shown in Fig. 13a is very similar to the postbuckled deformation pattern predicted by the elastic-plastic analysis, and shown in Fig. 13b.

The predicted prebuckling and buckling analysis results and the measured results for the 0.040-inch-thick shells with crack lengths of 2.0, 3.0, and 4.0 inches are shown in Fig. 14. The analysis predictions were obtained using a material nonlinear analysis. Shell wall imperfections were not measured. An initial geometric imperfection in the form of the lowest eigenmode was used in the nonlinear analysis to generate local deformations in the vicinity of the crack. The measured loading-platen displacements were used to determine the amount of end rotations of the shell, and these data were used as input loading parameters for the nonlinear analysis. Buckling of each of the shells is identified by the symbols in Fig. 14. The filled symbols correspond to the analytical buckling predictions, and the open symbols correspond to the experimentally

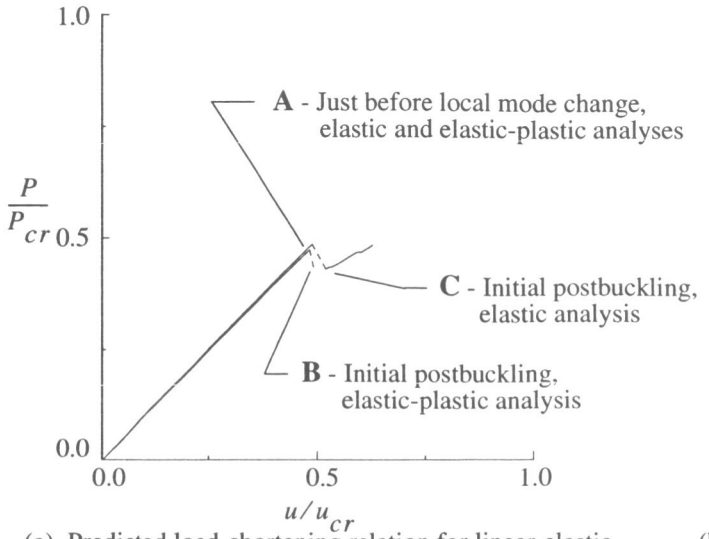

(a) Predicted load-shortening relation for linear-elastic response and material-nonlinear response

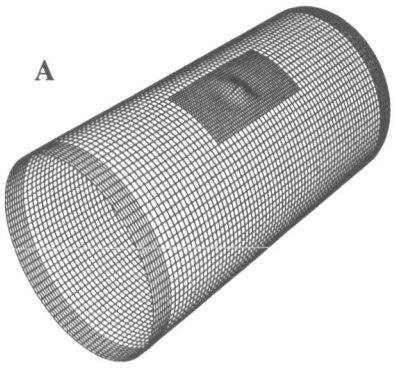

(b) Predicted deformation pattern just before local mode change, for linear-elastic response and material-nonlinear response (Point A)

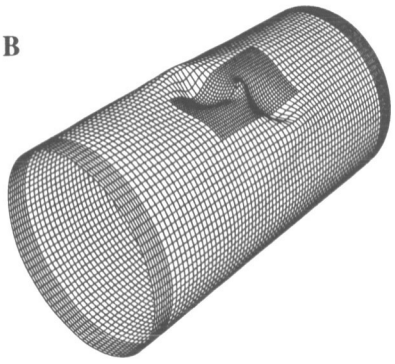

(c) Predicted initial postbuckling deformation pattern for material-nonlinear response (Point B)

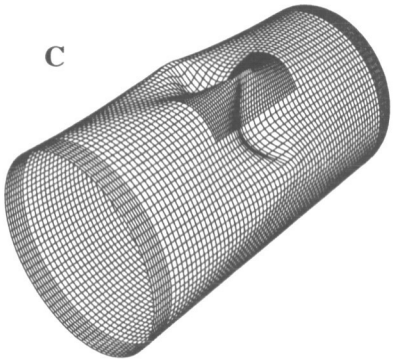

(d) Predicted initial postbuckling deformation pattern for linear-elastic response (Point C)

Figure 12. Comparison of linear-elastic and material-nonlinear responses of a 0.040-inch-thick shell with a 3.0-inch-long crack and subjected to axial compression.

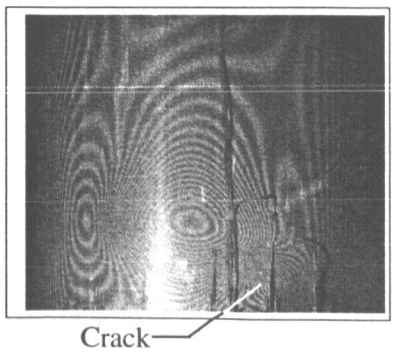

(a) Measured postbuckling deformation

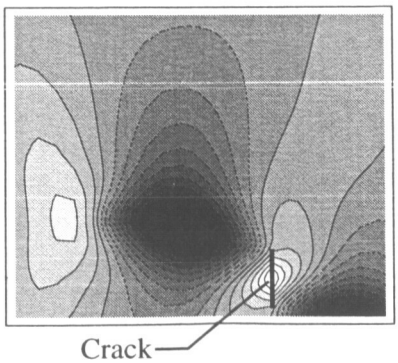

(b) Predicted postbuckling deformation

Figure 13. Comparison between measured and predicted postbuckling response at Point B, on Fig. 12a.

measured buckling loads. For the shell with the 2.0-inch-long crack, the predicted and measured general instability occurred at the loads indicated by the squares in Fig. 14. For the shells with the 3.0- and 4.0-inch-long cracks, the symbols indicate the load at which there was a change in the local buckling mode. The results shown in Fig. 14 indicate that the analytical results slightly overestimate the experimental results for the buckling loads, but slightly underestimate the shell stiffness. The discrepancies in the presented analytical and experimental results could be a result of uncertainties in the loading platen end rotations, shell wall imperfections, and other differences in the analytical model and the as-tested specimens.

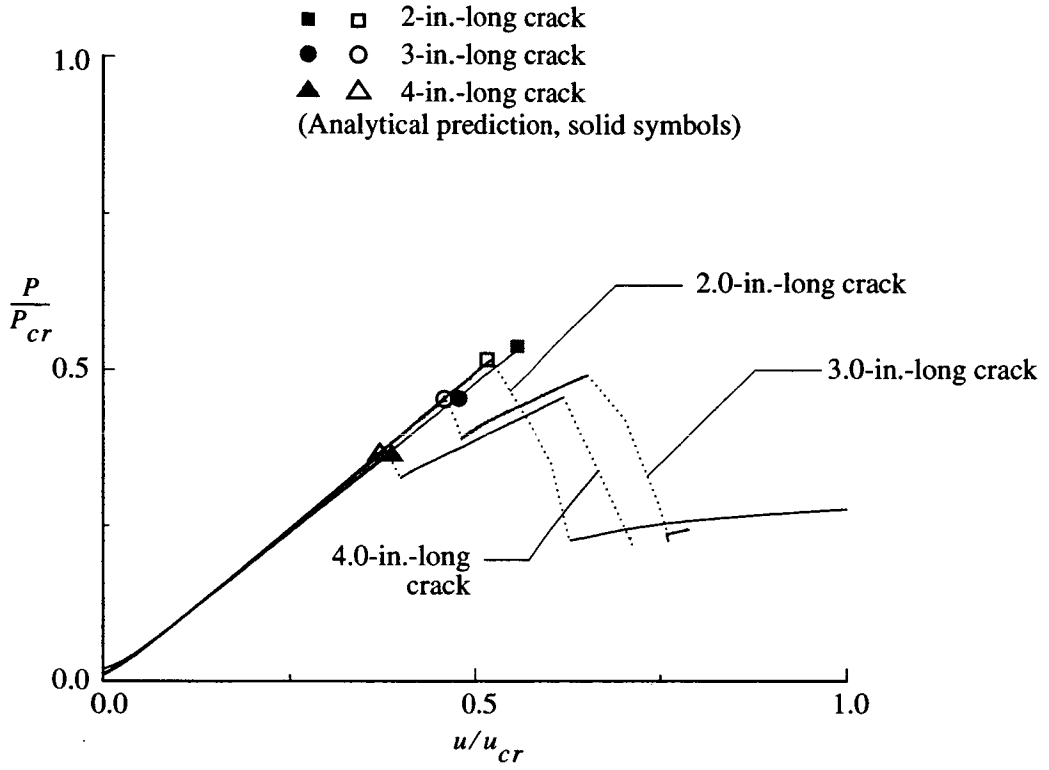

Figure 14. Summary of predicted and experimental load-shortening relations for 0.040-inch-thick shells subjected to axial compression.

CONCLUDING REMARKS

The results of an analytical and experimental study of the effects of a longitudinal crack on the nonlinear response of thin, unstiffened, aluminum cylindrical shells subjected to internal pressure and axial compression loads are presented. The results indicate that the nonlinear response of a shell depends on the loading condition applied to the shell and the initial crack length. The magnitude of the internal pressure required to initiate stable crack growth in a shell subjected to internal pressure decreases as the initial crack length increases. The magnitude of the internal pressure required to cause unstable crack growth in a shell also decreases as the initial crack length increases. The effects of crack length on the prebuckling, buckling and postbuckling responses of typical shells subjected to axial compression loads are also described. The initial buckling load of a shell subjected to axial compression decreases as the initial crack length increases. Initial buckling causes general instability or collapse of a shell for shorter initial crack lengths. Initial buckling is a stable local response mode for longer initial crack lengths. This stable local buckling response is followed by a stable postbuckling response, which is followed by general or overall instability of the shell.

REFERENCES

[1]Starnes, J., H., and Rose, C., A., "Nonlinear Response of Thin Cylindrical Shells with Longitudinal Cracks and Subjected to Internal Pressure and Axial Compression Loads," AIAA Paper No. 97-1144, April 1997.

[2]Newman, J. C., Jr., "An Elastic-Plastic Finite Element Analysis of Crack Initiation, Stable Crack Growth and Instability," ASTM STP 833, 1984, pp. 93-117.

[3]Brogan, F. A., Rankin, C. C., and Cabiness, H. D., "STAGS User Manual, Version 3.0," Lockheed Martin Missiles and Space Co., Inc., Advanced Technology Center, Report LMMS P032594, June, 1998.

[4]Riks, E., "Some Computational Aspects of the Stability Analysis of Nonlinear Structures," Computational Methods in Applied Mechanics and Engineering, Vol. 47, 1984, pp. 219-259.

[5]Riks, E., "Progress in Collapse Analysis," Journal of Pressure Vessel Technology, Vol. 109, 1987, pp. 27-41.

[6]Rankin, C. C., Brogan, F. A., and Riks, E., "Some Computational Tools for the Analysis of Through Cracks in Stiffened Fuselage Shells," Computational Mechanics, Springer International, Vol. 13, No. 3, December 1993, pp. 143-156.

[7]Dawicke, D. S., Sutton, M. A., Newman, J. C., Jr., and Bigelow, C. A., "Measurement and Analysis of Critical CTOA for an Aluminum Alloy Sheet," NASA TM-109024, September, 1993.

[8]Newman, J. C., Jr., Dawicke, D. S., Sutton, M. A. and Bigelow, C. A., "A Fracture Criterion for Widespread Cracking in Thin-Sheet Aluminum Alloys," Proceedings of the ICAF 17th Symposium, 1993.

[9]Dawicke, D. S., Newman, J. C., Sutton, M. A., and Amstutz, B. E., "Stable Tearing Behavior of a Thin-Sheet Material with Multiple Cracks," NASA TM-109131, July, 1994.

[10]Shivakumar, K. N., and Newman, J. C., Jr., "ZIP3D - An Elastic-Plastic Finite-Element Analysis Program for Cracked Bodies," NASA TM-102753, 1990.

[11]Dawicke, D. S., and Newman, J. C., Jr., "Residual Strength Predictions for Multiple Site Damage Cracking Using a Three-Dimensional Finite Element Analysis and a CTOA Criterion," Fatigue and Fracture Mechanics: 29th Volume, ASTM, STP 1332, T. L. Panontin, and S. D. Sheppard, Eds., American Society for Testing and Materials, 1998.

[12]Newman, J. C., Jr., "Finite Element Analyses of Fatigue Crack Propagation -- Including the Effects of Crack Closure," Ph.D. Thesis, Virginia Polytechnic Institute and State University, Blacksburg, VA, May 1974.

[13]Dawicke, D. S., "Residual Strength Predictions Using a Crack Tip Opening Angle Criterion," FAA-NASA Symposium on the Continued Airworthiness of Aircraft Structures, DOT/FAA/AR-97/2, Vol. II, July 1997, pp. 555-566.

[14]Riks, E., Brogan, F. A., and Rankin, C. C., "Bulging of Cracks in Pressurized Fuselages: A Procedure for Computation," in Analytical and Computational Models of Shells, Noor, A. K., Belytschko, T., and Simo, J. C., Eds., The American Society of Mechanical Engineers, ASME-CED Vol. 3, 1989.

FRACTURE MECHANICS OF THIN, CRACKED PLATES UNDER TENSION, BENDING AND OUT-OF-PLANE SHEAR LOADING

Alan T. Zehnder, C.-Y. Hui, Yogesh Potdar
Department of Theoretical and Applied Mechanics
Cornell University, Ithaca NY 14853
(607)255-9181, (607)255-2011 (fax), atz2@cornell.edu

Alberto Zucchini
ENEA
40128 Bologna, Italy

ABSTRACT

Cracks in the skin of aircraft fuselages or other shell structures can be subjected to very complex stress states, resulting in mixed-mode fracture conditions. For example, a crack running along a stringer in a pressurized fuselage will be subject to the usual in-plane tension stresses (Mode-I) along with out-of-plane tearing stresses (Mode-III like). Crack growth and initiation in this case is correlated not only with the tensile or Mode-I stress intensity factor, K_I, but depends on a combination of parameters and on the history of crack growth. The stresses at the tip of a crack in a plate or shell are typically described in terms of either the small deflection Kirchhoff plate theory. However, real applications involve large deflections. We show, using the von-Karman theory, that the crack tip stress field derived on the basis of the small deflection theory is still valid for large deflections. We then give examples demonstrating the exact calculation of energy release rates and stress intensity factors for cracked plates loaded to large deflections. The crack tip fields calculated using the plate theories are an approximation to the actual three dimensional fields. Using three dimensional finite element analyses we have explored the relationship between the three dimensional elasticity theory and two dimensional plate theory results. The results show that for out-of-plane shear loading the three dimensional and Kirchhoff theory results coincide at distance greater than h/2 from the crack tip, where h/2 is the plate thickness. Inside this region, the distribution of stresses through the thickness can be very different from the plate theory predictions. We have also explored how the energy release rate varies as a function of crack length to plate thickness using the different theories. This is important in the implementation of fracture prediction methods using finite element analysis. Our experiments show that under certain conditions, during fatigue crack growth, the presence on out-of-plane shear loads induces a great deal of contact and friction on the crack surfaces, dramatically reducing crack growth rate. A series of experiments and a proposed computational approach for accounting for the friction is discussed.

1. INTRODUCTION

The motivation for this work stems directly from concerns regarding fracture along a lap joint in a pressurized aircraft fuselage. As shown in Figure 1, in this scenario the side of the crack near the

stringer is much stiffer than the other, which is only a single sheet thick. This less stiff side bulges out further than the stiff side, resulting in out-of-plane tearing stresses as the crack tip. At the outset of our research little was known about fracture and fatigue in sheets under such loadings. Thus, to be able to answer practical questions regarding the integrity of pressurized shell structures, we have, over the past six years studied the fracture mechanics of sheets under tension and out-of-plane shear loading.

As defined in Figure 2, for general loadings of thin, cracked plates under membrane and out-of-plane loads, two fracture modes with corresponding stress intensity factors K_I, K_{II} can be identified with the membrane loads, and two fracture modes with stress intensity factors k_1, k_2 can be identified with the out-of-plane loads. Analyses such as the results in Figure 1 show that the two important fracture modes for the lap joint problem are the membrane K_I and the out-of-plane k_2. Thus, the discussion in this paper will emphasize problems combining K_I and k_2 loadings. The crack tip stress fields and energy release will be discussed first, followed by a discussion of effects of large deflections, and finally fatigue crack growth. Details of some of this work appear in earlier publications, [1-8], while other sections, namely the discussion of the three dimensional crack tip fields is new.

2. STRESS FIELD AND ENERGY RELEASE RATES

Crack growth is determined by the stress and strain fields in the immediate vicinity of the crack tip. Thus to understand the behavior of cracked plates and to correlate experimental data, the crack tip fields must be understood and described. The crack tip fields are inherently three dimensional, and in principal can be determined numerically for each particular situation. Such an approach, however is not only overwhelming from the engineering point of view, but gives little insight into the general nature of the crack tip fields. Our approach is to construct analytical models of the crack tip stress state using Kirchhoff plate theory superimposed with plane stress. In this construction the stresses on a plane ahead of the crack, in the coordinate system of Figure 3, are

$$\sigma_{yy} = \frac{K_I}{\sqrt{2\pi r}} + \frac{k_1}{\sqrt{2r}}\frac{2z}{h},$$

$$\sigma_{xy} = \frac{K_{II}}{\sqrt{2\pi r}} + \frac{k_2}{\sqrt{2r}}\frac{2z}{h}\left(\frac{1+\nu}{3+\nu}\right),$$

$$\sigma_{23} = \frac{-k_2 h}{2(2r)^{3/2}(3+\nu)}\left[1-\left(\frac{2z}{h}\right)^2\right],$$

where ν is the Poisson's ratio, h is the plate thickness, and the stress intensity factors, K_I, K_{II}, k_1, k_2 are defined in Figure 3.

The crack tip energy release rate is related to the stress intensity factors by [5,7]

$$G = \frac{K_I^2 + K_{II}^2}{E} + \frac{k_1^2 + k_2^2}{3E}\pi\left(\frac{1+\nu}{3+\nu}\right),$$

where E is the Young's modulus.

The Kirchhoff plate theory is restricted to small deflections, however in many practical problems involving fracture of thin plate the deflection will not be small. This leads to the question: Do the Kirchhoff theory fields still describe the crack tip stresses when the deflection is large? As proven in ref.[1] the answer is yes. Large deflections, however, couple the in-plane and out-of-plane fracture modes, and are non-linear functions of the applied loads. Several examples are given in ref.[1].

In reality the crack tip fields are three dimensional varying through the thickness of the plate with distributions that may differ from those in the above equations. For example, Figure 4 shows the out-of-plane shear stress for a thin cracked plate under uniform shear. Away from the crack tip the distribution is approximately parabolic as predicted by plate theory, but very close to the crack tip, $2r/h<0.3$ the stress is nearly constant through the thickness, going to zero in a boundary layer at the free surface. Further investigation of the relationship between the three dimensional fields and the plate theory fields is underway, using the finite element method.

3. FATIGUE CRACK GROWTH UNDER K_I, k_2 LOADING

To simulate fatigue crack growth of a lap joint crack experiments were performed using a double edge cracked sheet of 0.090" thick 2024-T3 aluminum alloy loaded in in-phase cyclic tension and torsion[6,8]. The test specimen is shown in Figure 5. Some of the results of these experiments are given in Figure 6 which plots fatigue crack growth rate versus the cyclic mode-I stress intensity factor only. Generally the crack initially grows faster than the rate for pure mode-I loading. However as the fatigue crack length increases the crack growth slows down, even stops for extended periods before jumping forward. The reason for this is the great amount of contact and friction that occurs behind the crack as the crack surfaces try to slide past one another to accomodate the out-of-plane shear loading. A second set of experiments were performed in which crack face contact was artificially eliminated. These experiments show that the rate of fatigue crack growth rate in the absence of contact is well above the pure mode-I rate.

These results led us to ask: Is there a way to quantify the effect of crack face contact in such situations? We take the point of view that the actual stress intensity factor seen at the crack tip is the K due to external loading minus the K due to crack face contact. To estimate the K due to contact a set of experiments keeping the K due to external loading was performed. In these constant nominal ΔK experiments, as shown in Figure 7, the rate of crack growth is initially greater than the pure mode-I rate then decreases steadily with increasing crack length. The experiments provide a data pool to aid in the construction of a modeling approach for crack face contact, friction and their effect on crack growth. We have proposed and approach for the development and implementation of such models. In the proposed study the wear and consequent evolution of friction of the crack faces will be measured directly with the results used to determine parameters of a state variable model of friction. This model would then be implemented in a finite element simulation of crack growth. If this approach is successful it will point the way to performing accurate engineering predictions of fatigue crack growth in thin sheets under tension and out-of-plane shear loading.

ACKNOWLEDGMENTS

This work was supported by NASA Langley Research Center, through grant NAG-1-1311.

REFERENCES

1. C.-Y. Hui, Alan T. Zehnder, and Yogesh Potdar, "Williams meets von Karman: Mode Coupling and Non-Linearity in the Fracture of Thin Plates," to appear in **International Journal of Fracture**, (1998).

2. M. Viz , D. Potyondy, A. Zehnder, C. Rankin, and E. Riks, "Computation of Membrane and Bending Stress Intensity Factors for Thin, Cracked Plates," **International Journal of Fracture, Vol. 72,** pp. 21-38 (1995).

3. Mark J. Viz, Alan T. Zehnder, and John-David Bamford, "Fatigue Fracture of Thin Plates Under Tensile and Transverse Shear Stresses," in **Fracture Mechanics: 26th Volume, ASTM STP 1256,** Reuter et al. (eds.) American Society for Testing and Materials, Philadelphia, PA, pp. 631-651, (1995).

4. Alan T. Zehnder, and Chung-Yuen Hui, "Stress Intensity Factors for Plate Bending and Shearing Problems," **Journal of Applied Mechanics, Vol. 61,** pp. 719-722, (1994).

5. C.Y. Hui and Alan.T. Zehnder, "A Theory for the Fracture of Thin Plates Subjected to Bending and Twisting Moments," **International Journal of Fracture, Vol. 61,** pp. 211-229, (1993).

6. Mark J. Viz, and Alan T. Zehnder, "Fatigue Crack Growth in 2024-T3 Aluminum Under Tensile and Transverse Shear Stresses", in **FAA/NASA International Symposium on Advanced Structural Integrity Methods for Airframe Durability and Damage Tolerance, NASA CP-3274**, C. Harris, (ed.) pp. 891-910 (1994).

7. Alan T. Zehnder, Mark J. Viz, and Anthony R. Ingraffea, "Fatigue Fracture in Thin Plates Subjected to Tensile and Shearing Loads: Crack Tip Fields, J Integral and Preliminary Experimental Results," Proceedings of the **VII International Congress on Experimental Mechanics,** pp. 44-50, Society for Experimental Mechanics, Bethel, CT, (1992).

8. Mark J. Viz, "Fatigue Fracture Under In-Plane Symmetric and Out-of-Plane Antisymmetric Mixed-Mode Deformations", Ph.D. Thesis, Cornell University, (1996).

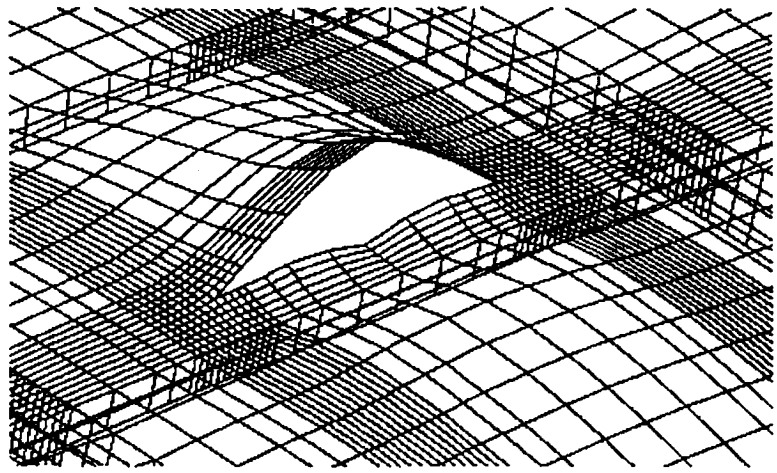

Figure 1, Deformed mesh from a finite element analysis of a one-bay fuselage section with a crack lying alongside a stringer. Bulging out of one side relative to the other is clearly seen. (from V.O. Britt, formerly of NASA Langley).

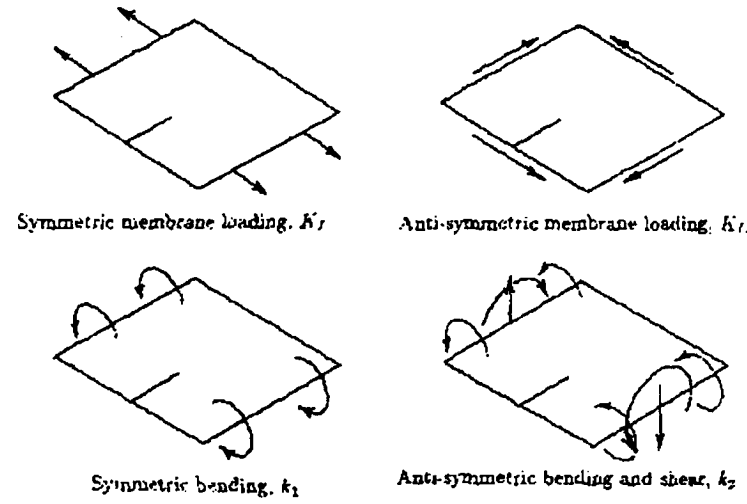

Figure 2, Membrane, bending and transverse shear fracture modes for a plate with a straight through crack. Stress intensity factors corresponding to each mode are shown.

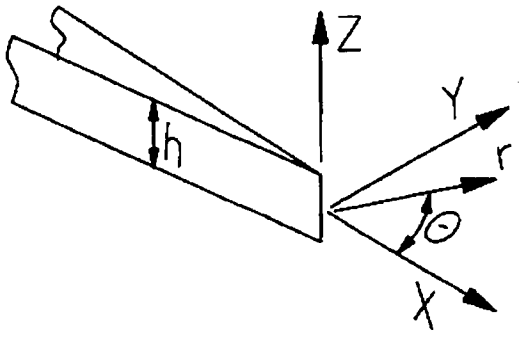

Figure 3, Crack tip coordinate system.

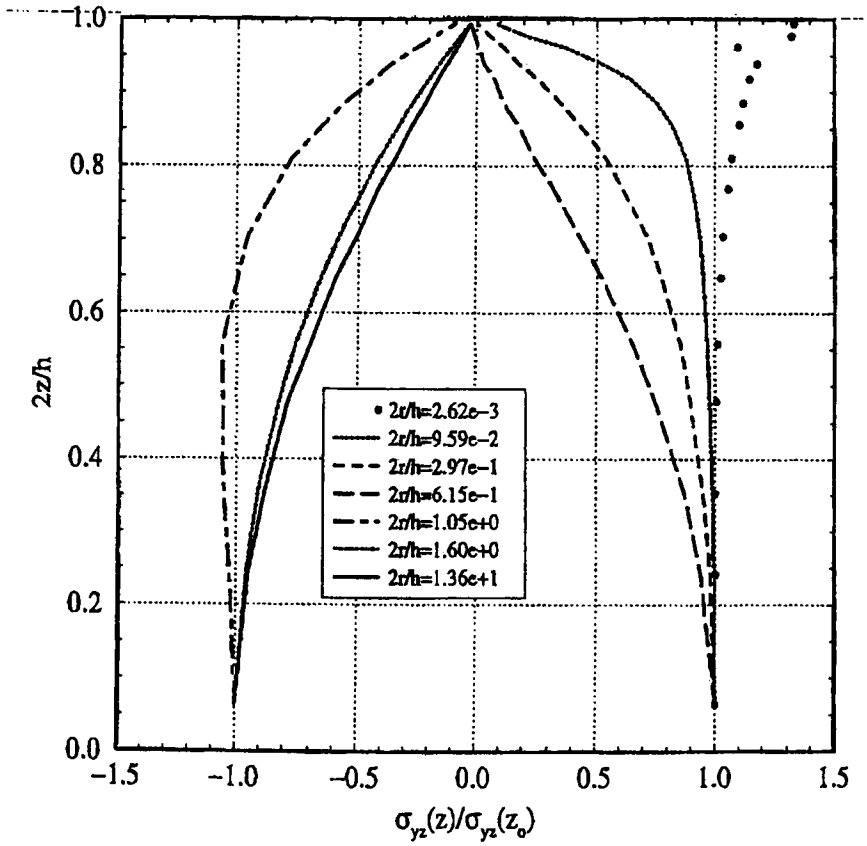

Figure 4, Thin cracked plate under uniform shear (h/a=0.02). Distributions of the out-of-plane shear stress through the thickness from a three dimensional finite element analysis at different radial distances from the crack tip. (z_0=0.065 h/2)

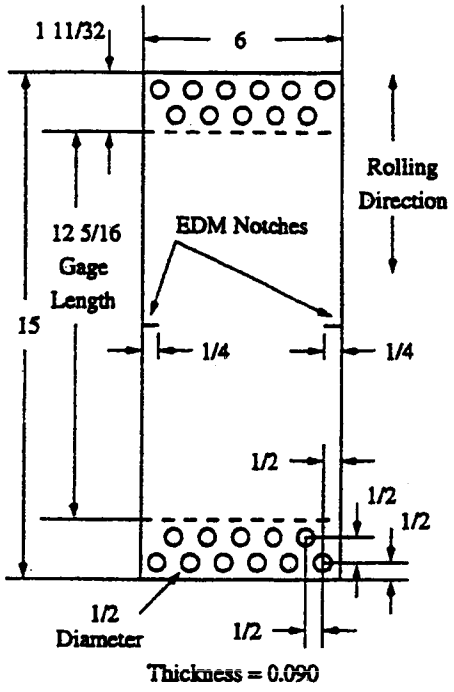

Figure 5, Double edge notched tension torsion fatigue crack growth test specimen.

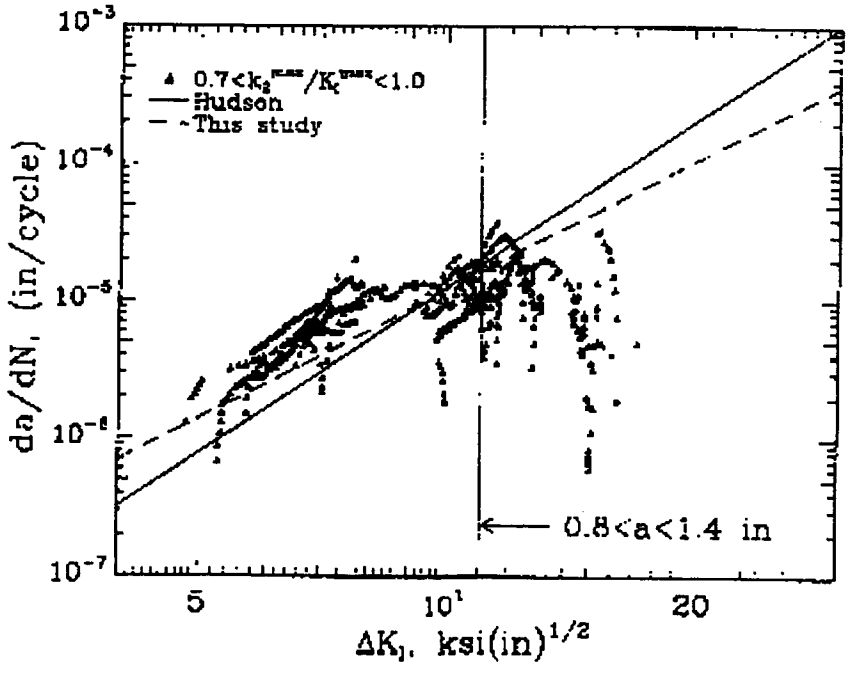

Figure 6, Mixed-mode fatigue crack growth rate results from relatively large values of Δk_2. The solid and dahed lines represent the crack growth rate for pure mode-I loading. The vertical line indicates the range of crack lengths present in this data when $\Delta K_I = 11$ *ksi* $in^{1/2}$.

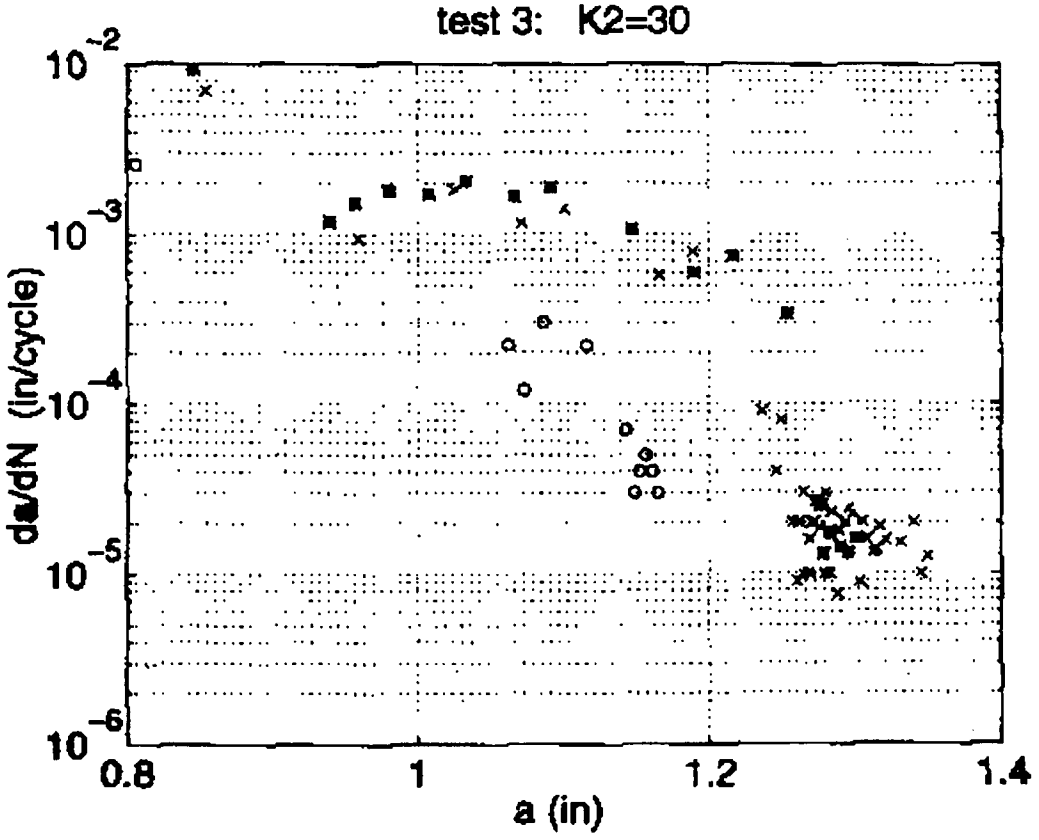

Figure 7, Mixed-mode fatigue crack growth rate vs. crack length from constant ΔK_I, Δk_2 tests. Initial crack length is 0.8 inches.

RESIDUAL STRENGTH PREDICTION OF FUSELAGE STRUCTURES WITH MULTIPLE SITE DAMAGE

Chuin-Shan Chen, Paul A. Wawrzynek, and Anthony R. Ingraffea

The Cornell University Fracture Group
641 Rhodes Hall, Cornell University
Ithaca, New York, 14853, USA

(607) 254-8815
www.cfg.cornell.edu

ABSTRACT

This paper summarizes recent results on simulating full-scale pressure tests of wide body, lap-jointed fuselage panels with multiple site damage (MSD). The crack tip opening angle (CTOA) fracture criterion and the FRANC3D/STAGS software program were used to analyze stable crack growth under conditions of general yielding. The link-up of multiple cracks and residual strength of damaged structures were predicted. Elastic-plastic finite element analysis based on the von Mises yield criterion and incremental flow theory with small strain assumption was used. A global-local modeling procedure was employed in the numerical analyses.

Stress distributions from the numerical simulations are compared with strain gage measurements. Analysis results show that accurate representation of the load transfer through the rivets is crucial for the model to predict the stress distribution accurately. Predicted crack growth and residual strength are compared with test data. Observed and predicted results both indicate that the occurrence of small MSD cracks substantially reduces the residual strength. Modeling fatigue closure is essential to capture the fracture behavior during the early stable crack growth. Breakage of a tear strap can have a major influence on residual strength prediction.

1 INTRODUCTION

Modern aircraft structures are designed using a damage tolerance philosophy. This design philosophy envisions sufficient strength and structural integrity of the aircraft to sustain major damage and to avoid catastrophic failure. However, structural aging of the aircraft may significantly reduce the residual strength, which raises many important safety issues.

One of the most notable problems in aging aircraft is widespread fatigue damage (WFD). WFD has two subsets, multiple site damage (MSD) and multiple element damage (MED). This paper presents recent results on simulating full-scale pressure tests of wide body, lap-jointed fuselage panels with MSD [1, 2]. The tests, funded by the Federal Aviation Administration (FAA), and performed by the Boeing Commercial Airplane Group, were intended to characterize crack growth in a generic wide body, lap-jointed fuselage configuration subjected to MSD. The FRANC3D/STAGS program [3, 4, 5, 6] was used to perform the numerical analyses. The

crack tip opening angle (CTOA) fracture criterion [7, 8, 9] was used to control stable crack advancement. Calculated stress distributions are compared with strain gage readings. Predicted crack growth and residual strength results are then compared with experimental measurements.

2 FULL-SCALE FUSELAGE PANEL TESTING

The full-scale fuselage panel tests investigated in this study were performed on a wide body pressure test fixture with a radius of curvature of 127 inches. A brief overview of the panel tests is presented below. More information about the fixtures and tests can be found in [10, 11, 1, 2].

Two identical curved lap-jointed panels were fabricated. The test panels were designed to simulate typical wide body fuselage crown structures consisting of bonded tear straps and floating frames connected to hat section stringers with stringer clips. Skins and tear straps were made of 0.063 inch thick, 2024-T3 clad aluminum alloy. Stringers, frames, and stringer clips were made of 7075-T6 aluminum clad. The skins were joined by the lap joints. The joint was a typical three row configuration assembled using standard 3/16 inch diameter, 100° countersunk-head rivets. The tear straps were hot bonded to the skins at each frame station. The outer and inner tear straps were overlapped above the lap joint. The detailed dimensions of panels, frames, stringers, and stringer clips can be found in [1, 2].

A five-inch initial saw cut was inserted along the upper rivet row in the outer skin. For the panel with MSD cracks, small sawcuts were inserted in the outer skin after the rivet holes had been drilled, but prior to the application of the fay sealant and rivet installation. The panels were subjected to pressure cycling until the length of the crack reached about two frame bays for the residual strength tests. The central frame was then cut prior to static loading to failure. Rosette strain gages were installed back-to-back on the skins and tear straps in the vicinity of the lap joint.

3 NUMERICAL MODEL

All structural components including skins, stringers, and frames were modeled by displacement-based four-noded or five-noded quadrilateral shell elements [12, 13]. Each node of the shell element has six degrees of freedom. To analyze the panel tests with reasonable computer resources and sufficient accuracy, a global-local approach was used. Figure 1 shows the typical finite element meshes for the two hierarchical modeling levels employed in the simulations. A 12-stringer bay wide and 5-frame bay long panel, which is about the size of the test panel, was modeled at the global level. A 1x1 bay stiffened panel was modeled at the local level. The local model differed from the global model in the finite element mesh density and the detailed geometric modeling of the cross sectional shapes of stringers and frames.

Pressure loading was applied on all the external skins. Symmetric boundary conditions were imposed on all the boundary edges of the global model to simulate a cylinder-like fuselage structure. Uniform axial expansion was allowed at one longitudinal end. On this boundary edge, an axial force equal to $(PR/2) \cdot L$ was assigned where P is the applied pressure, R is the radius of the panel, and L is the arc-length of the edge. The kinematic boundary conditions (displacements and rotations) applied along the boundaries of the local model were extracted from the global model results. In addition to these kinematic constraints, the local model was also subjected to internal pressure.

A piecewise linear representation was used for the uniaxial stress-strain curves for 2024-T3

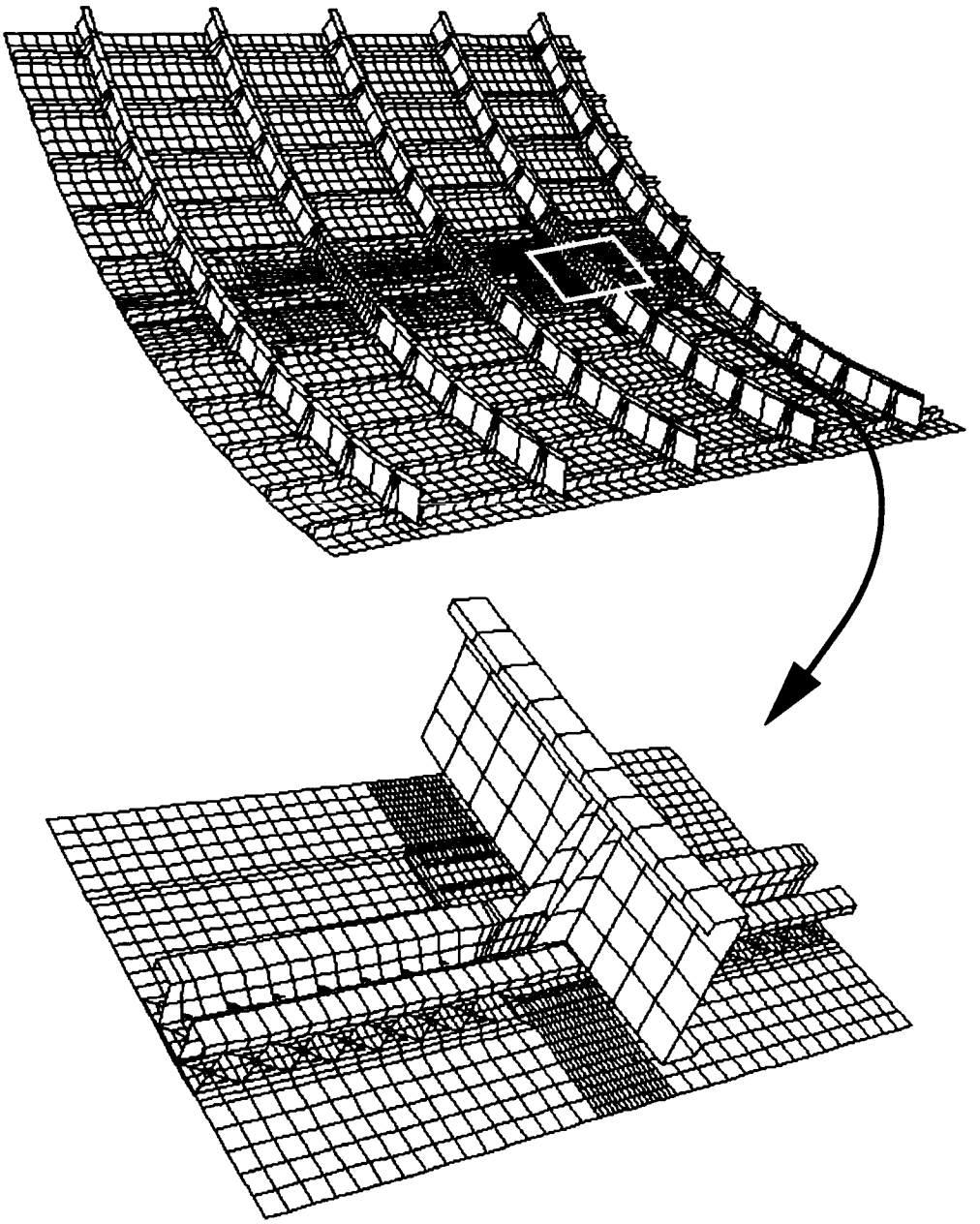

Figure 1: Global and local finite element models.

and 7075-T6 aluminum alloys (see Figures 2 and 3). Rivets were modeled by elastic-plastic spring elements that connect finite element nodes in the upper and lower skins and tear straps. Each rivet was modeled with six degrees of freedom, corresponding to extension, shearing, bending and twisting of the rivet. The stiffness of each degree of freedom was defined by prescribing a piecewise linear force-deflection curve. The axial, flexural, and torsional stiffnesses of the spring element were computed by assuming that the rivet behaves like a simple elastic rod with a diameter of 3/16 inch. The elastic shear stiffness of the rivet was computed by the following empirical relation developed by Swift [14]:

$$K_{rivet} = \frac{ED}{[A + C(D/t_1 + D/t_2)]} \tag{1}$$

where E is the elastic modulus of sheet material, D is the rivet diameter, t_1 and t_2 are thicknesses of joined sheets, and $A = 5.0$ and $C = 0.8$ for aluminum rivets. Initial shear yielding and ultimate shear strength of rivets were assumed to occur at load levels of 600 lb and 1080 lb, respectively. Once a rivet reaches its ultimate strength, it will *break* and lose its load carrying capacity. The force-deflection curve shown in Figure 4 for shearing is intended to represent, empirically, the net shear stiffness of a rivet-joined sheet connection, accounting for bearing deformations and local yielding around the rivet [14, 15].

The adhesive bond between skin and tear strap was also modeled with spring elements. The shear stiffness for the springs was computed based on an *effective* area of the adhesive with [16]:

$$K_{adhesive} = \frac{A_{eff}}{t_a/G_a + (3/8)(t_1/G + t_2/G))} \tag{2}$$

where A_{eff} is the bond area being lumped at the finite element nodal connection, G is the elastic shear modulus of sheet material, G_a is the elastic shear modulus of adhesive, t_1 and t_2 are the thicknesses of bonded sheets, and t_a is the thickness of adhesive bond. Because no adhesive tests were conducted, the material properties of adhesive, G_a and t_a, were obtained from the experimental results in [17]. The maximum shear deflection was assumed to be 0.001 inch. Similar to the rivet spring, once the adhesive spring reaches its ultimate strength, it will *break* and lose its load carrying capacity. The force-deflection curve for shearing is shown in Figure 5. The axial stiffness of the adhesive spring was derived from the shear stiffness. The torsional and flexural stiffnesses of adhesive were assumed to be negligible.

Both geometric and material nonlinearities were used in the analysis at the global and local modeling levels. The global shell model captures the overall nonlinear response of the stiffened, curved, pressurized structure. The local shell model provides the detailed deformation and stress field near the crack tips to compute the fracture parameters (*e.g.*, CTOA) that control crack growth.

4 DETERMINATION OF CTOA$_c$

Flat panel tests were conducted by the Boeing Commercial Airplane Group to obtain material properties for fatigue and fracture analysis of the curved fuselage panels. Four 48 inch wide, 80 inch long, 0.063 inch thick middle crack tension (MT) specimens were tested. The flat panel specimens were made from the same aluminum sheet used for the skin of the curved fuselage panels. A constant amplitude cyclic loading was applied to propagate an initial sawcut. After the fatigue crack growth, a residual strength test was conducted under a monotonically

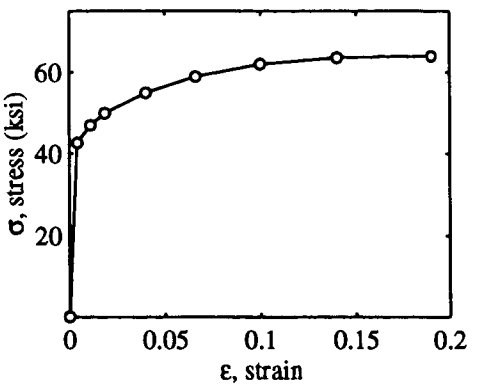

stress (ksi)	strain
0.0	0.0
42.7	0.0040667
47.0	0.011
50.0	0.0186
55.0	0.0399
59.0	0.066
62.0	0.1
63.6	0.14
64.0	0.19

E = 1.05e+04 ksi
ν = 0.33

Figure 2: Piecewise linear representation of the uniaxial stress-strain curve for 2024-T3 aluminum.

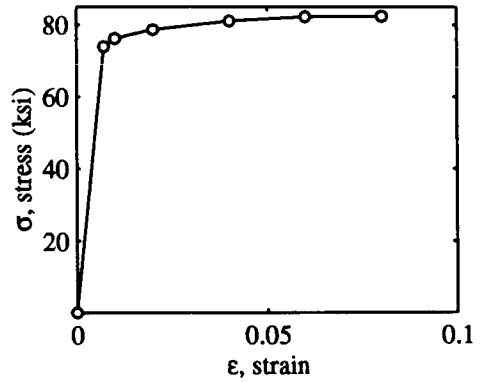

stress (ksi)	strain
0.0	0.0
74.0	0.00718
76.2	0.01
78.7	0.02
81.1	0.04
82.2	0.06
82.4	0.08

E = 1.03e+04 ksi
ν = 0.33

Figure 3: Piecewise linear representation of the uniaxial stress-strain curve for 7075-T6 aluminum.

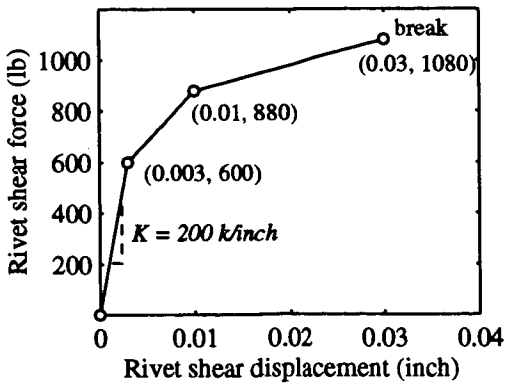

Figure 4: Shear stiffness and strength of rivet spring.

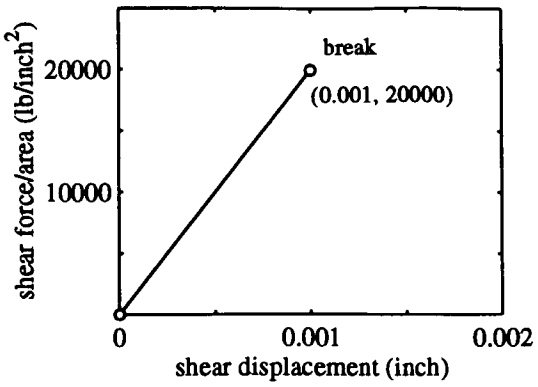

Figure 5: Shear stiffness and strength of adhesive spring.

TABLE 1: TEST MATRIX FOR MT SPECIMENS (AFTER [1])

Specimen ID	half initial crack (inch)	half final fatigue crack (inch)	$\sigma_{fatigue}$ (ksi)	R
2024_FAA_TL3	2.0	8.0	8.0	0.1
2024_FAA_TL4	2.0	5.5	16.0	0.1
	5.5	8.0	8.0	
2024_FAA_TL5	5.0	12.0	12.0	0.1
2024_FAA_TL6	2.0	8.0	7.0	0.5

increasing load. The test matrix prior to the residual strength test is summarized in Table 1. Visual crack extension measurements were taken. Surface $CTOA_c$ was measured for Specimen 2024_FAA_TL3 during the residual strength test. Nine values were obtained and the mean of the measured critical angles was about 5.5 degrees with a scatter band about $\pm 1.0°$.

The value of $CTOA_c$ used in the residual strength analysis of the fuselage panels was determined by finding an angle within the scatter band of the $CTOA_c$ measurements that best correlates with the observed crack growth and residual strength of the coupon tests. The FRANC3D/STAGS program was used to simulate fracture behavior of the MT specimens. A finite element mesh that models a quarter of the specimen with a crack tip element size of 0.04 inch and a half plane strain core height equal to 0.08 inch is shown in Figure 6. A plane strain core is used to capture the three-dimensional (3D) constraint effects developed at the local crack tip [18, 19, 20]. The half core height is about the thickness of the specimen.

Figure 7 compares the predicted crack growth results to the experimental measurements. The $CTOA_c$ of 4.5 degrees best correlates the predicted and measured residual strengths. However, it under-estimates the applied stress at the earlier stage of stable crack growth. The 5 and 5.5 degree critical angles give a better correlation for the earlier crack growth but over-predict the residual strength by 8.5% and 14.3%, respectively.

The discrepancy between predicted and measured crack growth at the earlier stage of tearing might relate to the residual plastic deformation left by the fatigue crack growth. This effectively increases the crack opening resistance during early stable crack growth [21]. The plastic wake

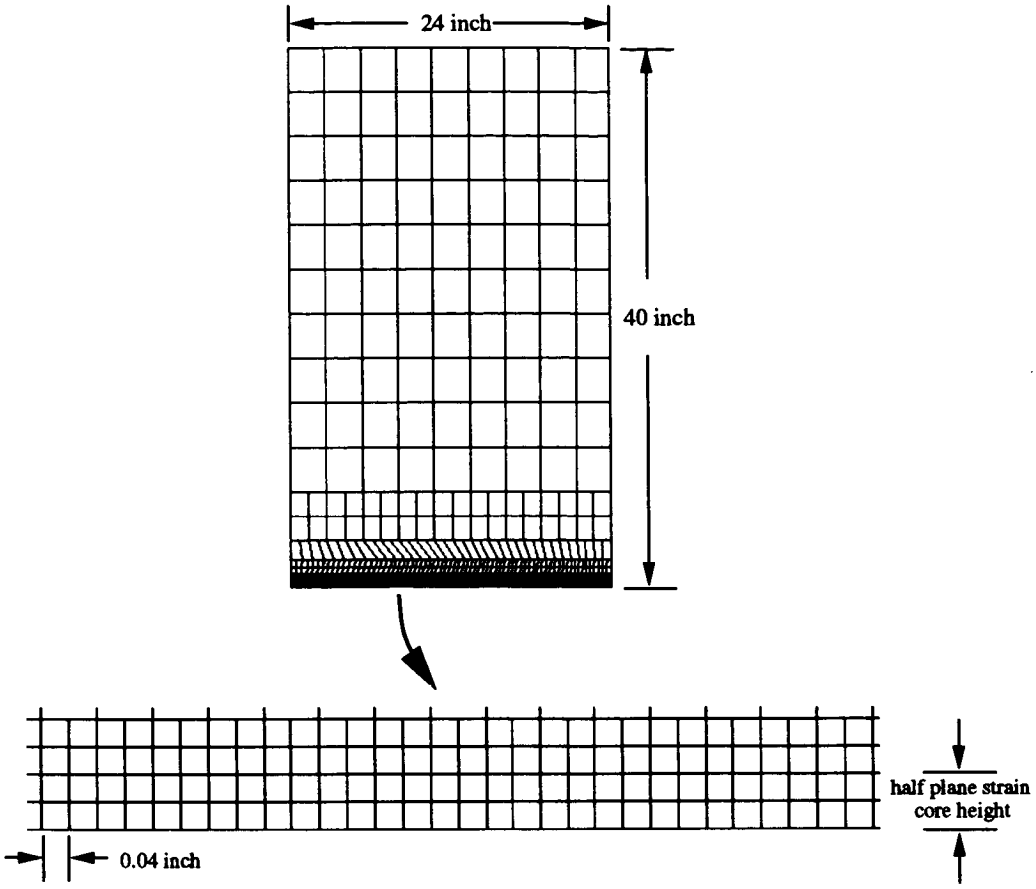

Figure 6: Finite element mesh for one quarter of 48x80 inch MT specimen.

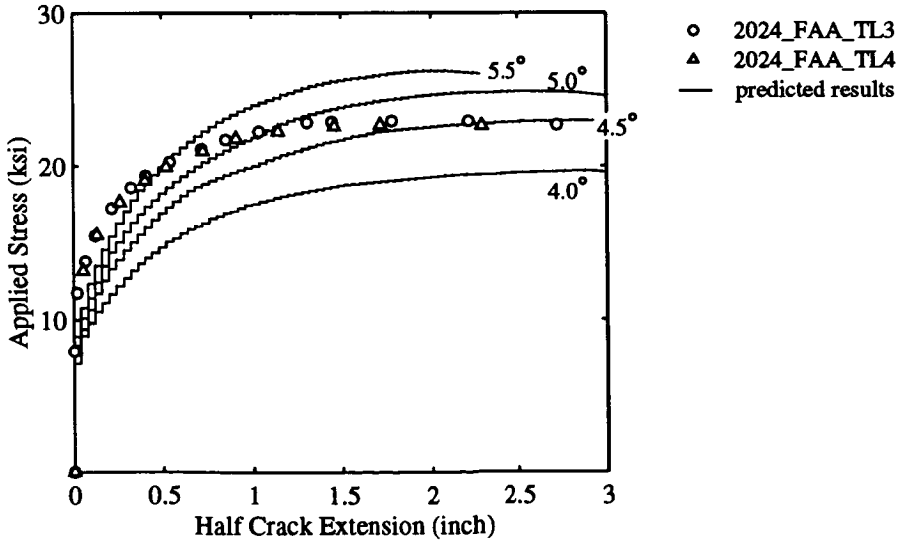

Figure 7: Predicted applied stress versus crack growth for 48 inch wide MT specimen (half plane strain core height = 0.08 inch).

effect on crack growth and residual strength analysis will be further discussed in Section 6.

5 NUMERICAL RESULTS: STRAIN GAGE COMPARISON

Strain gage comparisons were made to verify predicted stress distributions. Figure 8 shows the overall deformed structures for both the global and local models. Convergence studies were conducted to ensure accuracy of deformations and stress distributions. Major results from the studies are summarized below:

- For global models, the predicted results converged quickly. The predicted membrane hoop stresses agree well with experimental measurements. The predicted bending hoop stresses are comparable to experimental measurements as one refines the finite element meshes (Figure 9).
- Predicted results from a local model with about the same mesh density as the corresponding region in the global model agree well with global model predictions and experimental measurements. The agreement ensures the transition accuracy in the hierarchical modeling.
- Results with a much higher mesh density that is suitable for crack growth analysis disagree with the rest of the numerical predictions and experimental measurements. The discrepancy is related to the idealized representation of the two-noded spring element for the rivet connection in the finite element model [15, 22]. The single point connection results in unrealistic distortion of the surrounding shell elements. The local distortion causes premature yielding of the shell elements and reduces the load transfer from sheet to rivet. This artificial distortion of the shell elements is discretization-dependent [22, pp. 318–327]. Refining the mesh captures the local artificial distortion better, but makes the comparison to strain gage readings worse [15].

Two modeling idealizations are proposed to avoid this artificial effect. One is to faithfully represent the geometry of the rivets and their interference with the sheets. This would considerably increase the required computational resources and may not be simple to implement in thin-shell elastic-plastic crack growth analysis. The other approach is to generate distributed connections between the two-noded spring element and the surrounding shell elements [15]. The load distribution can be accomplished by defining rigid links, stiff spring elements, or a least-squares loading condition to connect the rivet-spring node to the surrounding shell-element nodes. Care must be taken while defining the area in the shell elements over which the rivet load is distributed. The area should be of the order of the rivet cross-sectional area, since distributing the load over a larger area may inadvertently stiffen the shell elements.

Figure 10 illustrates simulation of the distributed connection using stiff spring elements. Stiff spring elements with an order of magnitude higher stiffness than the rivet spring element are used to distribute the rivet load. For a rivet located on a prescribed tearing path, it is expected that the rivet stays intact on only one side of the crack as the crack propagates around the rivet. Thus, only the shell elements on this side of the crack are used to model the distributed rivet connection. Figure 11 shows the predicted hoop stress distributions with distributed connection simulations. A much better prediction is observed. The local mesh model with the distributed rivet connection was used for crack growth and residual strength analyses.

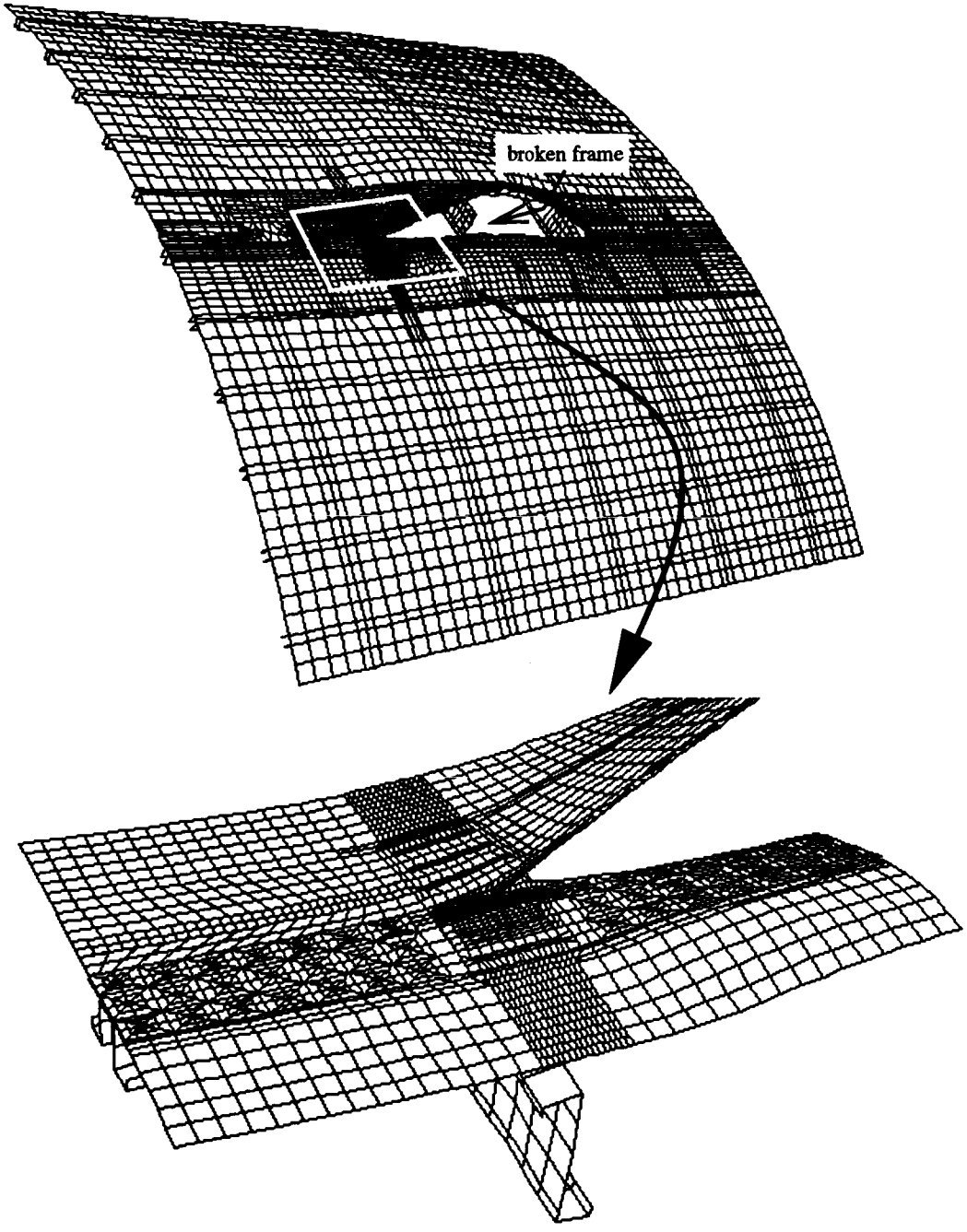

Figure 8: Deformed structures of the validation example at global and local modeling levels (pressure = 9.4 psi, crack length = 38.2 inch, magnification factor = 5.0).

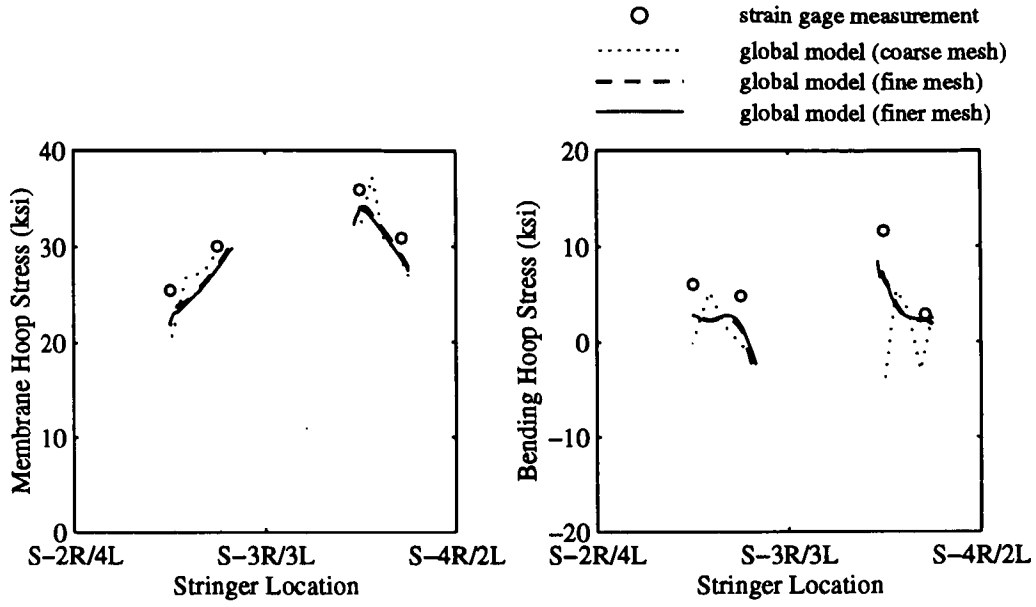

Figure 9: Global convergence study: comparison between computed and measured hoop stresses (pressure = 9.4 psi; crack length = 38.2 in.; frame cut; No MSD).

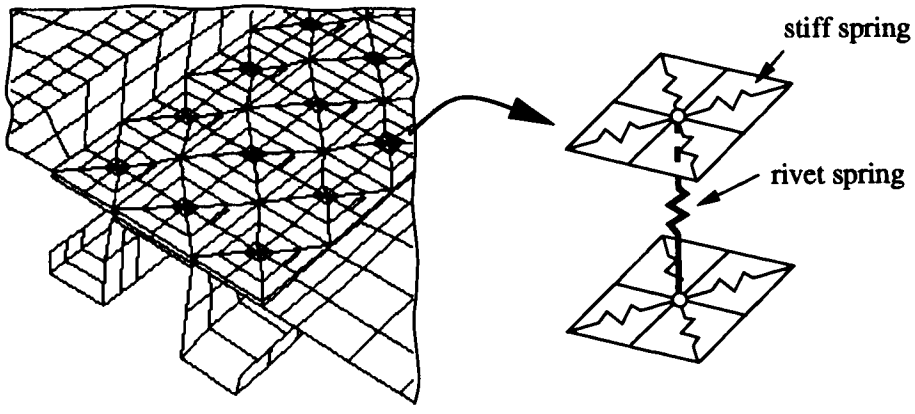

Figure 10: Illustration of distributed connection that connects a fastener node to surrounding shell nodes

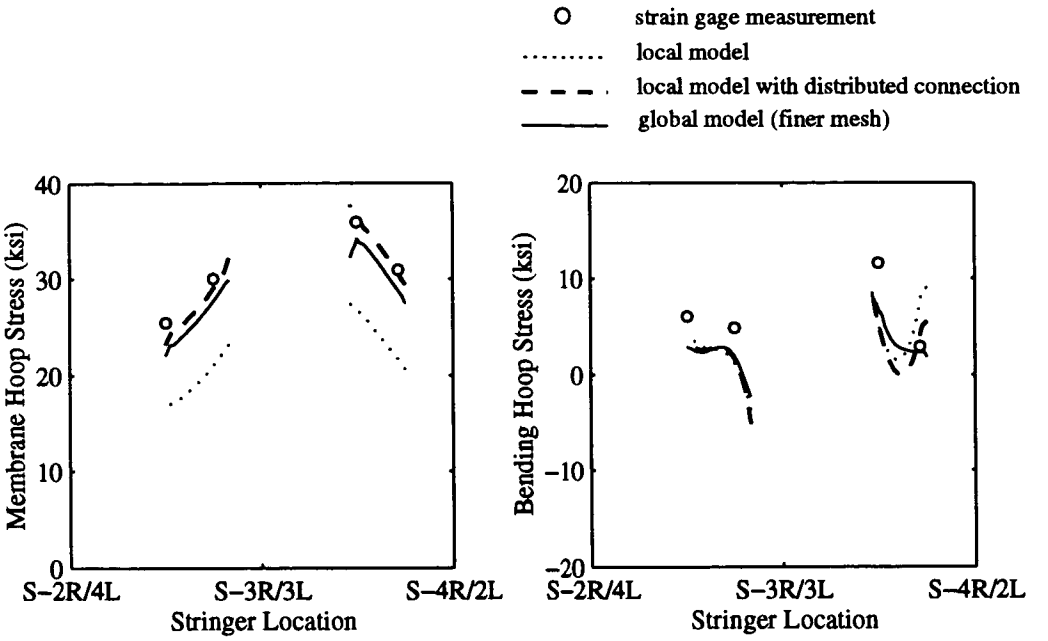

Figure 11: Effects of distributed rivet connection: comparison between computed and measured hoop stresses (pressure = 9.4 psi; crack length = 38.2 in.; frame cut; No MSD).

6 NUMERICAL RESULTS: CRACK GROWTH AND RESIDUAL STRENGTH ANALYSIS

Elastic-plastic crack growth and residual strength analyses were conducted using the local model. Both 4.5 and 5.5 degree critical angles computed at 0.04 inch behind the growing crack tip were used to investigate the sensitivity of $CTOA_c$ on crack growth and residual strength prediction. The 4.5° $CTOA_c$ is the angle that best correlates the predicted and observed residual strengths of the MT tests. The 5.5° angle is the mean from the surface $CTOA_c$ measurements in the MT tests. The plane strain core height was 0.16 inch along the prescribed tearing path.

Figure 12 shows predicted results from the first attempt at crack growth analysis. The change of the $CTOA_c$ from 4.5° to 5.5° increases predicted residual strength by about 33% and 22% for the cases without and with MSD cracks, respectively.

Although analysis results in Figure 12 clearly demonstrate the loss of residual strength due to the presence of MSD, all the predicted results (i) under-estimate the pressure loading to initiate the stable crack growth, and (ii) over-estimate the residual strength.

The much lower predicted pressure for tearing initiation is mainly caused by residual plastic deformation left by the fatigue crack growth. A possible cause for the lower residual strengths observed in the test may be related to the occurrence of tear strap failure. Both effects are discussed below.

6.1 RESIDUAL PLASTIC DEFORMATION EFFECTS

The test panels were subjected to pressure cycling prior to the residual strength test. To incorporate the residual plastic deformations due to the cyclic loading, the residual strength analyses were re-performed using an elastic-plastic cyclic loading simulation suggested by Newman [23].

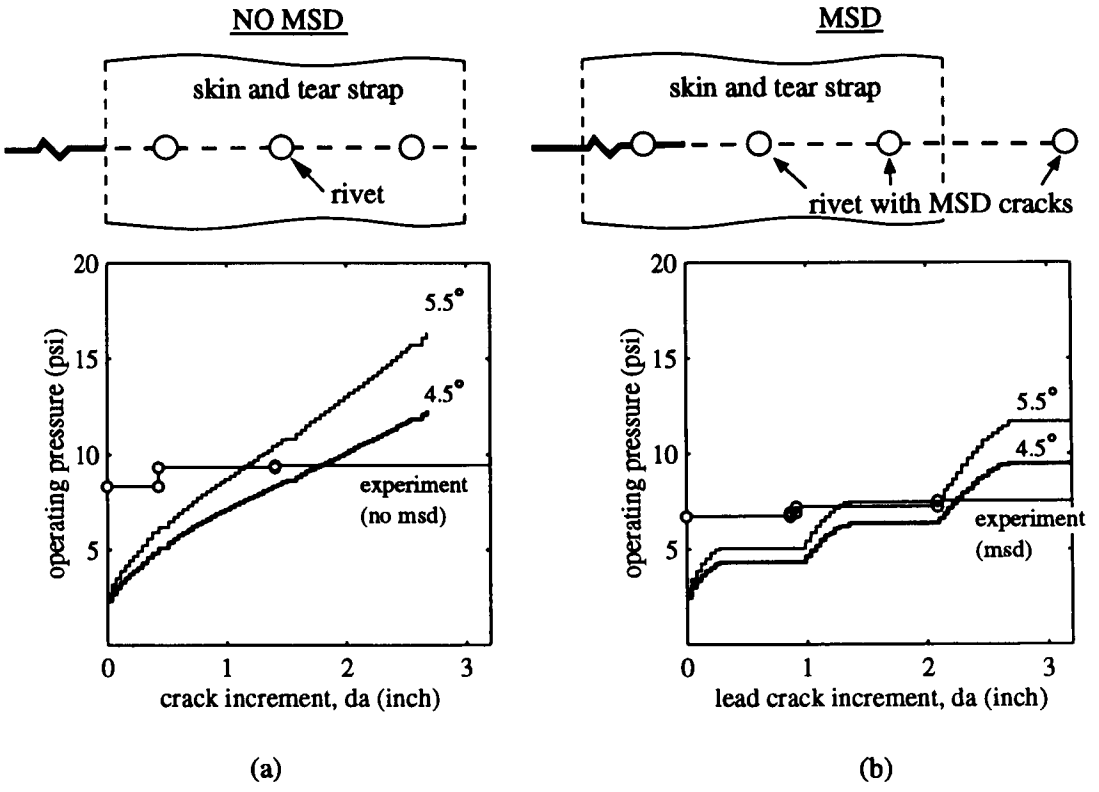

Figure 12: Comparison between the predicted crack growth and experimental measurements: (a) without MSD, and (b) with MSD.

The procedures consist of the following steps:

step 1 *Close* an appropriate length of fatigue crack.

step 2 Load the fuselage model to the maximum pressure loading conducted in fatigue tests.

step 3 Release the crack tip node and unload the model.

step 4 Repeat steps 2 and 3 until the crack tip reaches the initial position for stable tearing.

This procedure implies that the fatigue crack only propagates at the maximum pressure during the cyclic loading simulation. For Mode-I only deformations under constant-amplitude load cycling, crack surfaces close at a positive applied load (*i.e.*, step 3). The contact stresses cause the material to yield in compression. Crack face contact and reverse yielding were not modeled in the current simulations.

In subsequent analyses, the fuselage model is brought to the operating pressure level during fatigue tests without allowing the crack to advance. The crack is then allowed to advance one element, and the load is returned to zero. Figure 13 illustrates results for a 0.32 inch *length* of fatigue closure used in the analysis for the case without MSD cracks. The crack-opening and crack-closure pressures in the fuselage panel simulations follow similar trends observed in the MT flat panel simulations [23]. After two cycles of simulation, the crack-opening and crack-closure pressures quickly stabilize to 7.2 psi and 5.3 psi, respectively.

Figure 14 shows two predicted crack opening profiles when the pressure loading reaches 8.6 psi (no growth), one with fatigue closure effects and the other without. The effects of residual plastic deformations on the crack opening profile and consequently, the CTOA prediction, are clearly observed.

The 7.2 psi crack-opening pressure shown in Figure 13 seems to be too high in comparison with 2D plane stress results [23] and laboratory observations [24, 25]. This may be due to lack of modeling of contact conditions when the crack closes. That is, the crack faces pass each other so no compressive yielding is developed in the unloaded state. The compressive yielding stress will reduce residual tensile plastic deformation thus leading to a lower crack-opening pressure [23].

Figure 15 illustrates results for a 0.08 inch *length* of fatigue crack closure used for the case with MSD cracks. During cyclic loading simulation, the lead and MSD crack tips are released simultaneously. The crack-opening and crack-closure pressures at the second loading cycle for the lead crack are about 4.7 psi and 3.3 psi, respectively. We note that the *length* of fatigue crack closure is restrained by the *length* of MSD cracks. Further amount of fatigue crack closure simulation is possible but leads to somewhat ambiguous MSD fatigue crack propagation. The results after two cycles of simulation, however, is believed to essentially capture the residual plastic deformation effects based on those observed from the case without MSD cracks (Figure 13).

Figure 16 shows predicted crack growth that incorporates the closure effects. Table 2 summarizes the predicted and observed starting pressure to initiate the stable crack growth. The plasticity-induced closure increases the initiation pressure by about 150% to 210%. The predicted crack initiation loads are within 6% of experimental measurements for the cases that incorporate prior plastic residual deformations due to fatigue crack growth. However, the predicted residual strengths are still higher than those observed.

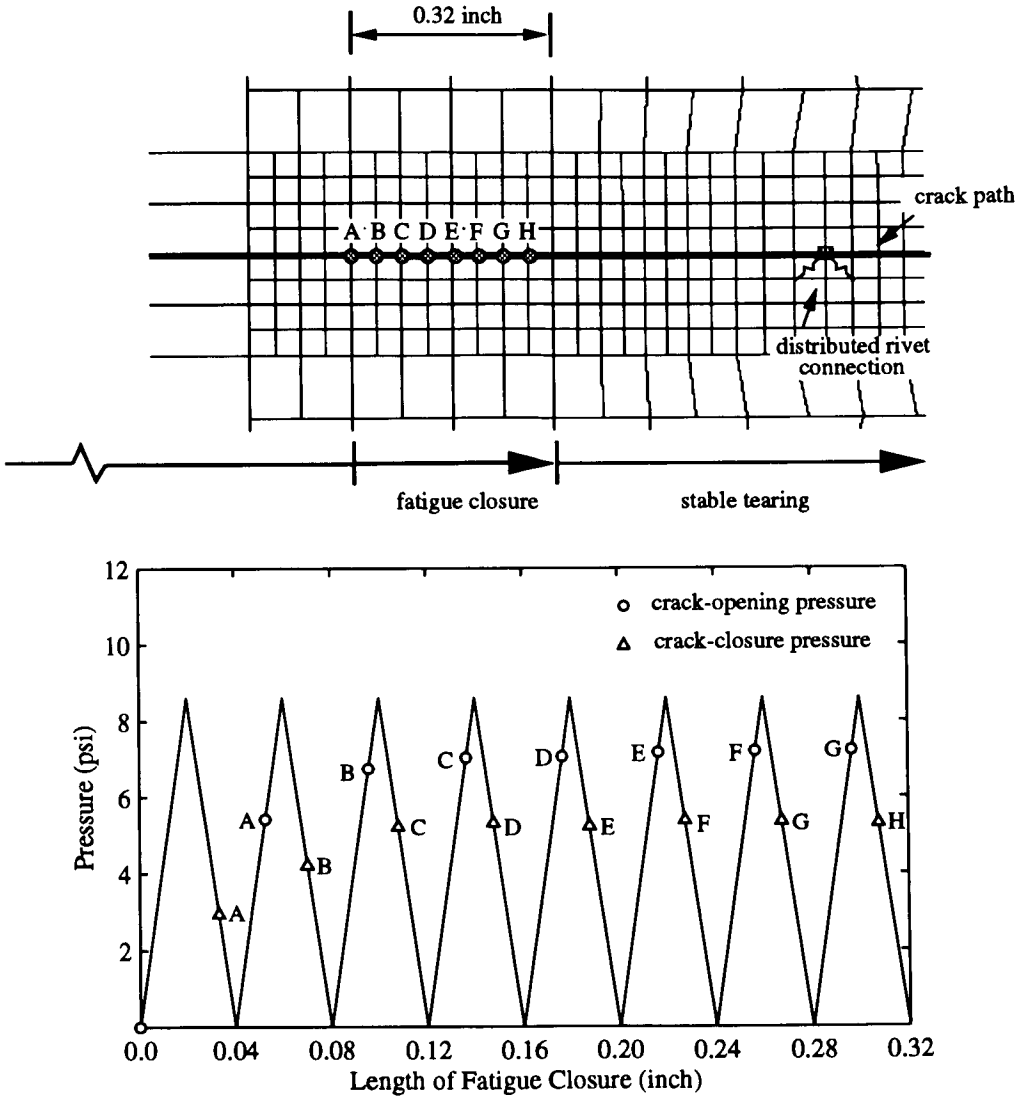

Figure 13: Predicted crack-opening and crack-closure pressure under cyclic loading (cyclic pressure = 8.6 psi, No MSD).

TABLE 2: PREDICTED AND OBSERVED LOADING FOR TEARING INITIATION

	predicted (psi)		observed (psi)
	$CTOA_c = 4.5°$	$CTOA_c = 5.5°$	
No MSD	2.3	2.7	8.3
No MSD (0.32 inch closure)	8.3	8.4	8.3
MSD	2.5	2.8	6.7
MSD (0.08 inch closure)	6.3	6.5	6.7

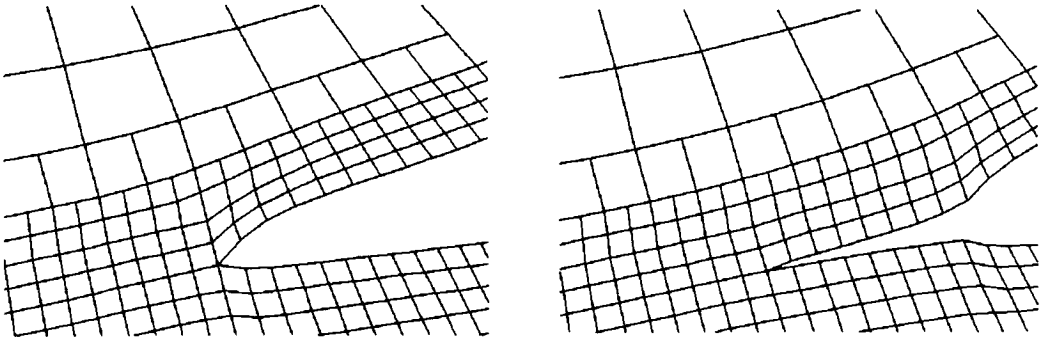

(a) (b)

Figure 14: Predicted crack opening profiles of outer skin at first tearing crack tip: (a) without fatigue closure, and (b) with 0.32 inch fatigue closure (magnification factor = 2.0).

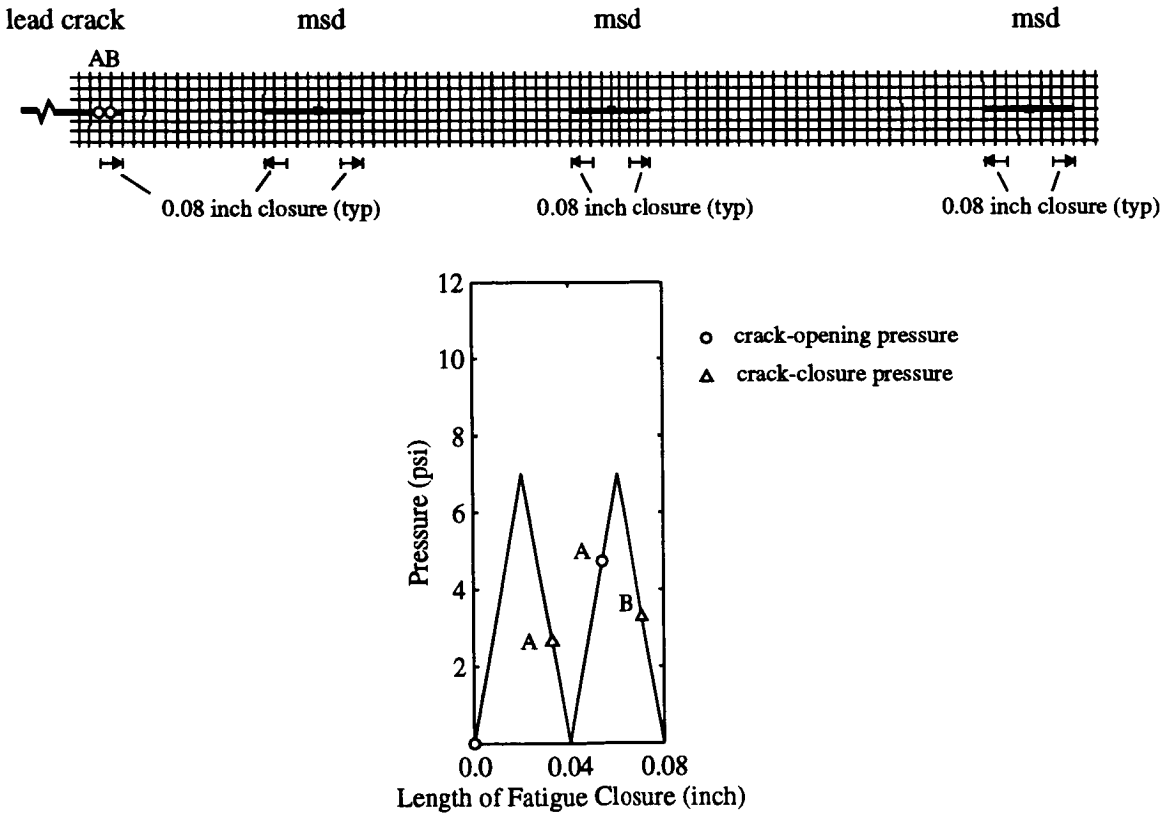

Figure 15: Predicted crack-opening and crack-closure pressure under cyclic loading (cyclic pressure = 7.0 psi, MSD).

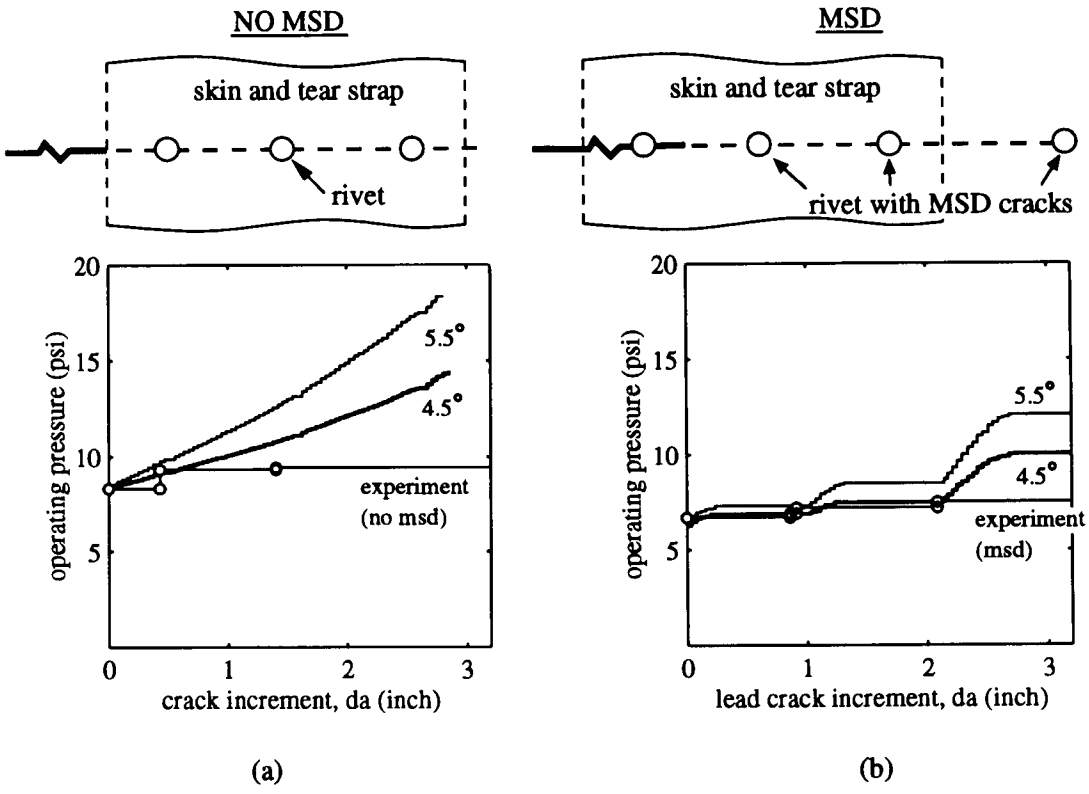

Figure 16: Comparison between predicted crack growth with fatigue closure effects and experimental measurements, (a) without MSD, and (b) with MSD.

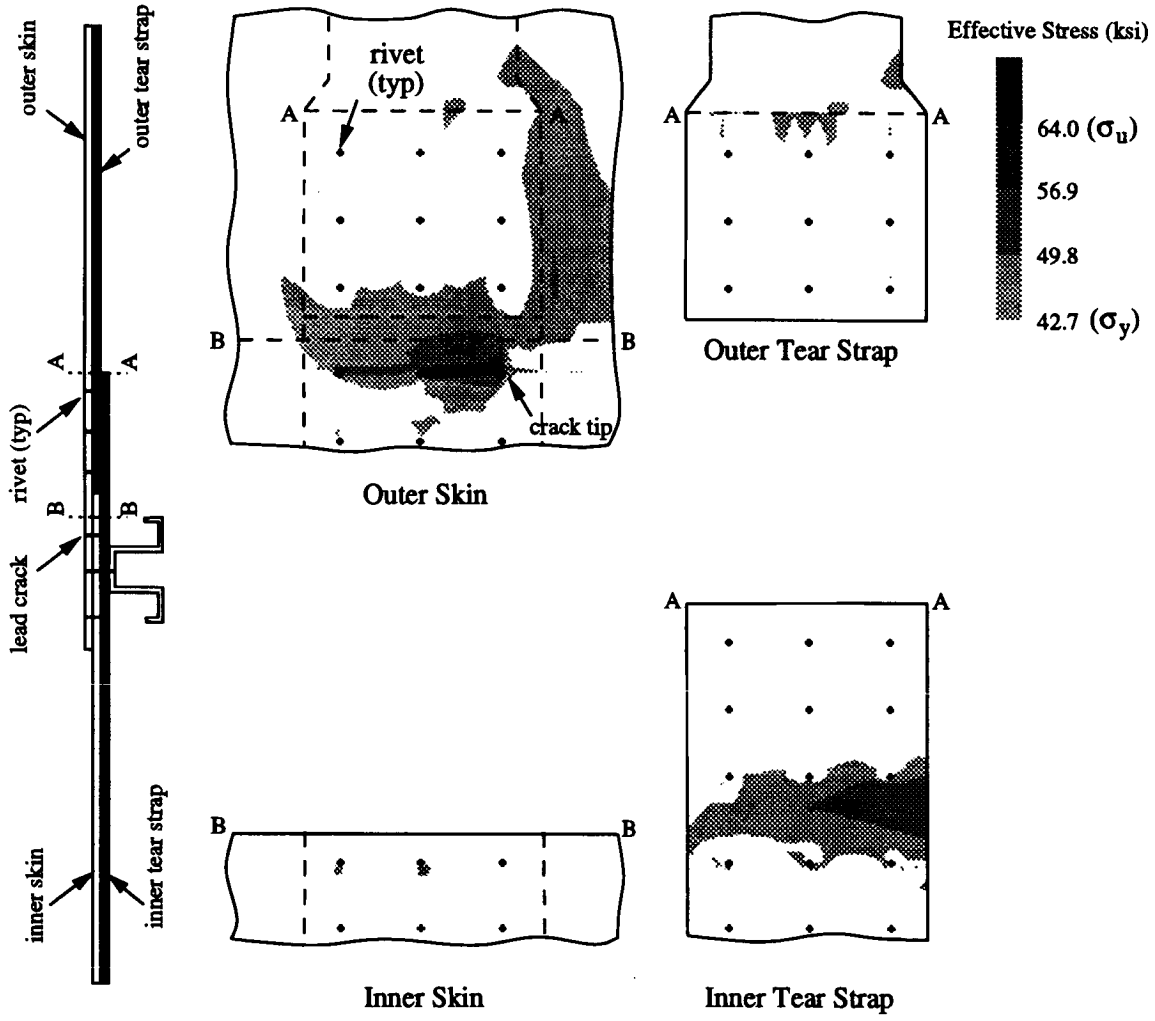

Figure 17: Predicted effective stress distribution (pressure = 9.86 psi, da = 0.5 inch, $CTOA_c$ = 5.5°).

6.2 EFFECTS OF TEAR STRAP FAILURE

A possible cause for the lower residual strengths observed in the test is the occurrence of failure of other structural elements. Figure 17 shows the predicted effective stress distribution in outer skin, inner skin, outer tear strap, and inner tear strap as the crack growth analysis reaches 9.86 psi pressure loading for the case without MSD cracks. Net section yielding is clearly shown in the inner tear strap.

The possible breakage of the inner tear strap during the residual strength test was also reported in [1]. To further investigate this possible MED scenario, a tear strap with rivet holes was modeled. By taking the kinematic boundary conditions from the local fuselage model, a stress concentration around the holes is observed (Figure 18). It is then postulated that the high stress concentration is likely to initiate new cracks from the rivet holes thus leading to breakage of the inner tear strap.

To incorporate the tear strap damage scenario into crack growth analysis, the inner tear strap is cut prior to crack growth analysis as illustrated in Figure 19. The predicted crack-

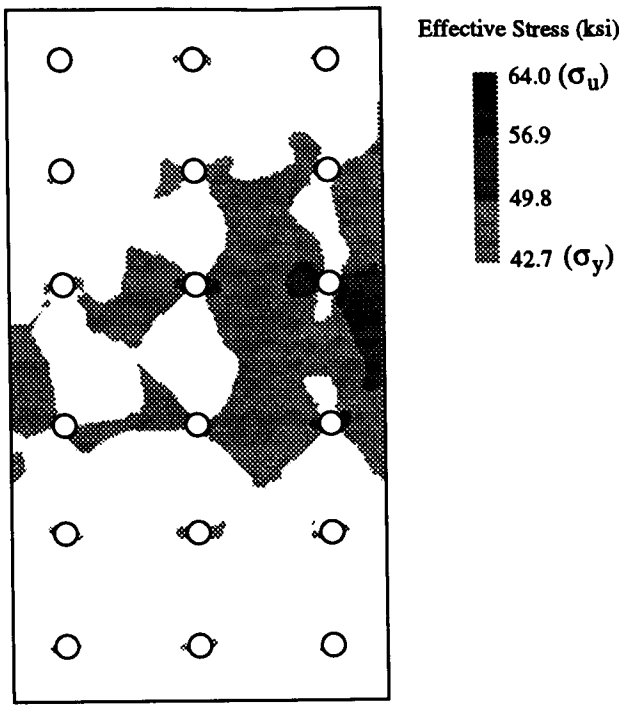

Figure 18: Predicted effective stress distribution of inner tear strap with rivet holes (pressure = 9.86 psi, da = 0.5 inch, $CTOA_c = 5.5°$).

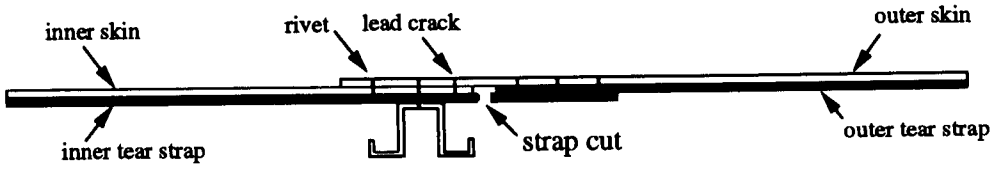

Figure 19: Illustration of broken inner tear strap.

opening pressures of the broken tear strap models with 0.32 and 0.08 inch fatigue closure are 7.0 psi and 3.1 psi for the cases without and with MSD cracks, respectively (*cf*: 7.2 psi and 4.7 psi for the models with the intact tear strap).

Figure 20 shows the predicted crack growth and residual strength for the fuselage models with a broken inner tear strap. The predicted residual strength using 4.5° $CTOA_c$ is within 13% of the experimental observation for the case without MSD cracks and within 1% of the experimental observation for the case with MSD cracks.

The higher predicted residual strength for the case without MSD may be related to the fact that the current model does not faithfully model the crack growth in the vicinity of rivets. In the panel test, the lead crack propagated into and re-initiated from a rivet hole as illustrated in Figure 21. Apparently, neither the CTOA fracture criterion for the lead crack propagation nor the idealized distributed rivet representation have sufficient accuracy in capturing this phenomenon. Further investigation is needed to quantify its effect on residual strength prediction.

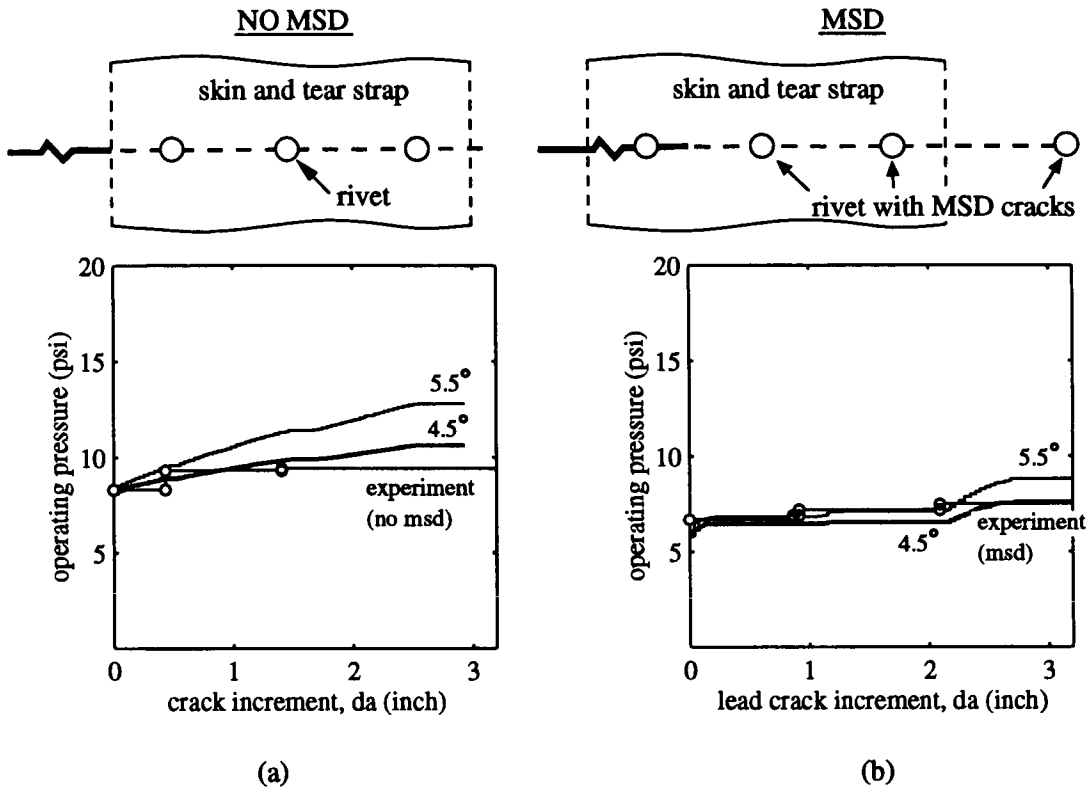

Figure 20: Comparison between predicted crack growth with broken tear strap and experimental measurements, (a) without MSD, and (b) with MSD.

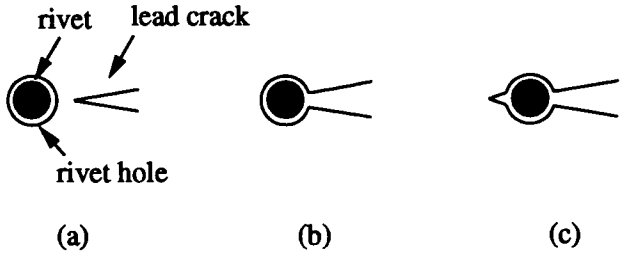

Figure 21: Illustration of crack propagation near rivet: (a) lead crack approaching rivet (b) lead crack growing into rivet hole, and (c) new crack initiating out of rivet hole.

7 CONCLUSIONS

The feasibility and validity of the analysis methodology to predict residual strength of pressurized fuselage structures subjected to MSD are examined. The major findings of this study are:

1. The distributed rivet load treatment of fasteners is crucial for the local crack growth model to accurately predict the stress distribution.

2. The occurrence of small MSD cracks substantially reduces the residual strength of pressurized fuselages. The reduction in residual strength prediction caused by MSD varies from 28% to 47%. A difference of 20% was observed in the tests.

3. The residual strength prediction is sensitive to changes in $CTOA_c$. Altering the $CTOA_c$ from 4.5° to 5.5° changes the predicted residual strength by 17% to 33% for the case without MSD cracks. It changes the predicted residual strength by 12% to 22% for the case with MSD.

4. The residual plastic deformation or the plastic wake from fatigue crack growth has a strong effect on stable crack initiation and a mild effect on residual strength prediction. For crack growth initiation, it is essential to incorporate the plastic wake to accurately predict the starting pressure loading. Neglecting plastic wake effect leads to a totally erroneous prediction of the earlier stable crack growth. For residual strength analysis, the plastic wake increases the predicted residual strength by 3% to 9%.

5. The breakage of the inner tear strap, categorized as possible failure of other structural elements during crack growth, is crucial to residual strength prediction. The occurrence of the broken tear strap reduces the predicted residual strength by 24% to 30%.

The CTOA fracture criterion together with the FRANC3D/STAGS program proves to be an effective tool to simulate: (1) lead crack growth, (2) MSD crack growth, (3) multiple crack interaction, (4) plastic wake from fatigue crack growth, and (5) tear strap failure in pressurized fuselages.

8 ACKNOWLEDGMENTS

The authors would like to thank Dr. James N. Newman, Jr., Dr. David S. Dawicke, Dr. Charles E. Harris, Dr. Charles C. Rankin, Dr. Richard D. Young, Mr. Keith E. Wilkins, Mr. Michael L. Gruber, Dr. Paul Tan, Mr. Richard G. Pettit and Dr. Bruce J. Carter for many helpful discussions. This work was performed with support from the NASA Langley Aircraft Structural Integrity Program under contract NAG-1-1184.

REFERENCES

[1] M. L. Gruber, C. J. Mazur, K. E. Wilkins, and R. E. Worden. Investigation of Fuselage Structure Subject to Widespread Fatigue Damage. Technical Report DOT/FAA/AR-95/47, FAA, February 1996.

[2] M. L. Gruber, K. E. Wilkins, and R. E. Worden. Investigation of Fuselage Structure Subject to Widespread Fatigue Damage. In *Proceedings of the FAA-NASA Symposium on the Continued Airworthiness of Aircraft Structures*, pages 439–460, Atlanta, Georgia, 1996.

[3] D. O. Potyondy, P. A. Wawrzynek, and A. R. Ingraffea. Discrete Crack Growth Analysis Methodology for Through Cracks in Pressurized Fuselage Structures. *International Journal for Numerical Methods in Engineering*, 38:1611–1633, 1995.

[4] C.-S. Chen, P. A. Wawrzynek, and A. R. Ingraffea. Methodology for Fatigue Crack Growth and Residual Strength Prediction with Applications to Aircraft Fuselages. *Computational Mechanics*, 19:527–532, 1997.

[5] C.-S. Chen, P. A. Wawrzynek, and A. R. Ingraffea. Simulation of Stable Tearing and Residual Strength Prediction with Applications to Aircraft Fuselages. In *Proceedings of the FAA-NASA Symposium on Continued Airworthiness of Aircraft Structures*, pages 605–618, 1996.

[6] B. J. Carter, C.-S. Chen, P. A. Wawrzynek, and A. R. Ingraffea. A Topology-Based System for Modeling 3D Crack Growth in Solid and Shell Structures. In *Proceedings of the Ninth International Congress on Fracture, ICF9*, pages 1923–1934, Sydney, Australia, 1997. Elsevior Science Publishers.

[7] J. C. Newman, Jr., D. S. Dawicke, and C. A. Bigelow. Finite-Element Analysis and Fracture SImulation in Thin-Sheet Aluminum Alloy. In *Proceedings of the International Workshop on Structural Integrity of Aging Airplanes*, 1992.

[8] D. S. Dawicke and J. C. Newman, Jr. Residual Strength Predictions for Multiple Site Damage Cracking Using a Three-Dimensional Analysis and a CTOA Criterion. In *Fatigue and Fracture Mechanics: 29th Volume, ASTM STP 1332*, 1998 (in press).

[9] C.-S. Chen, P. A. Wawrzynek, and A. R. Ingraffea. Elastic-Plastic Crack Growth Simulation and Residual Strength Prediction of Thin Plates with Single and Multiple Cracks. In *Fatigue and Fracture Mechanics: 29th Volume, ASTM STP 1332*, 1998 (in press).

[10] J. R. Maclin. Performance of Fuselage Pressure Structure. In *1991 International Conference on Aging Aircraft and Structural Airworthiness*, pages 67–74. NASA Conference Publication 3160, 1991.

[11] M. Miller, K. N. Kaelber, and R. E. Worden. Finite-Element Analysis of Pressure Vessel Panels. In *Proceedings of the International Workshop on Structural Integrity of Aging Airplanes*, 1992.

[12] C. C. Rankin, F. A. Brogan, W. A. Loden, and H. D. Cabiness. *STAGS User Manual Version 2.4*. Lockheed Martin Missiles & Space Co., Inc., Advanced Technology Center, 1997.

[13] C. C. Rankin and F. A. Brogan. *The Computational Structural Mechanics Testbed Structural Element Processor ES5: STAGS Shell Element*, 1991. NASA CR-4358.

[14] T. Swift. Fracture Analysis of Stiffened Structure. In *Damage Tolerance of Metallic Structures: Analysis Methods and Apllication, ASTM STP 842, Philadelphia*, pages 69–107, 1984.

[15] R. D. Young, C. A. Rose, C. G. Dávila, and J. H. Starnes, Jr. Crack Growth and Residual Strength Characteristics of Selected Flat Stiffened Aluminum Panels. Submitted for publication, the first joint DoD/FAA/NASA Conference on Aging Aircraft, Ogden, Utah, July 1997.

[16] R. Singh, J. H. Park, and S. N. Atluri. Growth of Multiple Cracks and Their Linkup in a Fuselage Lap Joint. *AIAA Journal*, 32(11):2260–2268, 1994.

[17] T. Swift. Fracture Analysis of Adhesively Bonded Cracked Panels. *Journal of Engineering Materials and Technology*, 100:10–15, 1978.

[18] J. C. Newman, Jr., D. S. Dawicke, M. A. Sutton, and C. A. Bigelow. A Fracture Criterion For Widespread Cracking in Thin-Sheet Aluminum Alloys. In *International Committee on Aeronautical Fatigue, 17th Symposium, Stockholm, Sweden*, 1993.

[19] D. S. Dawicke, J.C. Newman, Jr., and C. A. Bigelow. Three-Dimensional CTOA and Constraint Effects During Stable Tearing in a Thin-Sheet Material. In *Fracture Mechanics: 26th Volume, ASTM STP 1256, Philadelphia*, pages 223–242, 1995.

[20] C. L. Hom and R. M. McMeeking. Large Crack Tip Opening in Thin Elastic-Plastic Sheets. *International Journal of Fracture*, 45:103–122, 1990.

[21] D. S. Dawicke, J. C. Newman, Jr., M. A. Sutton, and B. E. Amstutz. Influence of Crack History on the Stable Tearing Behavior of a Thin-Sheet Material with Multiple Cracks. In *Proceedings of the FAA-NASA Sixth International Conference on the Continued Airworthiness of Aircraft Structures*, pages 193–212, Atlantic City, New Jersey, 1994.

[22] B.A. Szabó and I. Babuška. *Finite Element Analysis*. John Wiley & Sons, Inc., 1991.

[23] J. C. Newman, Jr. A Finite-Element Analysis of Fatigue Crack Closure. In *Mechanics of Crack Growth, ASTM STP 590, Philadelphia*, pages 281–301, 1976.

[24] W. Elber. Fatigue Crack Closure Under Cyclic Tension. *Engineering Fracture Mechanics*, 2:37–45, 1970.

[25] W. Elber. The Significance of Fatigue Crack Closure. In *Damage Tolerance in Aircraft Structures, ASTM STP 486, Philadelphia*, pages 230–242, 1971.

POSTER PRESENTATIONS

FATIGUE CRACK GROWTH SIMULTATION FOR COMPLEX THREE-DIMENSIONAL GEOMETRY AND LOADING

Thomas J. Curtin, Robert A. Adey, John M.W. Baynham, Philip Marais
Computational Mechanics Inc.
Billerica, Massachusetts, 01821, USA
978-667-5841
978-667-7582
cmina@ix.netcom.com

ABSTRACT

The focus of this paper is on the implementation of the boundary element method to investigate the impact of cracks in aerospace components. The theoretical background of the boundary element based fracture mechanics algorithms is discussed and the capability of the method is illustrated with applications pertinent to the aerospace industry. The methodology and applications discussed in this paper are based on the BEASY Fatigue and Crack Growth software developed by Computational Mechanics Inc. The boundary element method utilized in the software is well suited for simulating fracture and crack propagation. The BEASY fracture simulation tool can be easily incorporated in damage tolerance programs and serve to provide quantitative data in terms of the impact of fracture related damage.

1.INTRODUCTION

The high priority given to aging aircraft evaluation has resulted in a critical need for accurate and easy to use crack simulation software in the aerospace industry. Both military and commercial aircraft are aging and procurement of new aircraft is often restricted by budget limitations. Inventory assessment in the aircraft industry conducted during the early 1990s revealed that approximately 45 percent of the U.S. military and commercial aircraft fleet are over 15 years old. As a result of this aging fleet, airframe damage tolerance programs have been spawned to help predict residual life of aircraft and assess their continued airworthiness.

For damage tolerance program to be effective it is essential that fracture data can be evaluated in a quantitative manner. Fracture mechanics software provides the engineering community with this capability. Computer codes can be used to predict fatigue crack growth and residual strength in airframe structures. They can also be useful to determine in-service inspection intervals, time-to-onset of widespread fatigue damage and to design and certify structural repairs. Used in conjunction with damage tolerance programs fracture analysis codes can play an important role in extending the life of "high-time" aircraft.

2.0 FRACTURE MECHANICS USING THE BOUNDARY ELEMENT METHOD

2.1 Dual Boundary Element Method

The dual boundary element method is well suited to handle analysis of general embedded cracks and edge crack problems. The DBEM crack modeling strategy forms the basis of the dual

boundary element technology incorporated in the BEASY analysis algorithms. The dual boundary element method (DBEM) considers two independent equations, the displacement and traction boundary integral equations, within the same integration path for each pair of coincident source points [1, 10]. This crack modeling strategy allows a single-region boundary element analysis of a cracked body. The crack is represented by two elements occupying the same physical location, each element representing a face of the crack. The displacement and traction boundary integral equations are applied on the crack surfaces.

Because of the continuity requirements of the displacements and tractions for the existence of the traction BIE and the coplanar characteristics of crack surfaces, special consideration has to be taken for the discretization in the modeling. The introduction of discontinuous elements fulfils this continuity requirement for boundary variables while edge discontinuous elements give a necessary smooth transition from continuous to discontinuous elements on the boundary [2, 3].

2.2 Discontinuous Elements

Discontinuous elements play an important role in the boundary element method because the problem variables are not forced to be continuous across elements. The major benefit of discontinuous elements is their ability to model discontinuous stress results. They are therefore very useful in fracture mechanics analysis for modeling the stress behavior at a crack front.

A discontinuous element is represented as an element where the mesh point and node locations are not coincident. As a result of this formulation the nodes are not shared between elements. The geometry of the element is approximated by the mesh point location and shape functions. The variation of the traction and displacement boundary variables within the element is represented by values at the node location and interpolation functions [3].

2.3 Stress Intensity Factor Solution

In general the geometry and loading encountered in three-dimensional crack problems is too complex for the stress intensity factor (SIF) to be solved analytically. The SIF calculation is further complicated because it is a function of the position along the crack front, crack size and shape, type of loading, and the geometry of the structure.

Three-dimensional SIF solutions can be computed using a displacement extrapolation technique that involves correlation of the boundary element displacements on the crack surface with the theoretical values from Irwin's formula [2]. This extrapolation technique is illustrated in Figure 1. The SIF results are calculated at two locations remote from the crack tip using equations (1) and (2). These results are then extrapolated to the crack tip using equation (3). This method can be used for computing Modes I, II

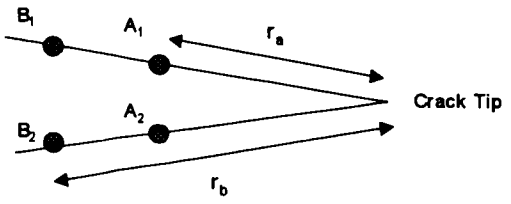

$$K_{I_A} = \frac{2\mu}{\kappa+1}\sqrt{\frac{2\pi}{r_A}}\left(\delta_{A_1} - \delta_{A_2}\right) \quad (1)$$

$$K_{I_B} = \frac{2\mu}{\kappa+1}\sqrt{\frac{2\pi}{r_B}}\left(\delta_{B_1} - \delta_{B_2}\right) \quad (2)$$

$$K_I = 2K_{I_A} - K_{I_B} \quad (3)$$

Figure 1. Schematic and equations illustrating implementation of displacement extrapolation technique used to compute stress intensity factors.

and III stress intensity factors for edge and embedded cracks.

2.4 Numerical Simulation of Crack Growth

Numerical simulation of crack growth provides a powerful predictive tool to use during the design phase as well as for evaluating the behavior of existing cracks. These simulations can be used to compliment experimental results and allow engineers to economically evaluate a large number of damage scenarios. Numerical methods are the most efficient way to simulate fatigue crack growth because crack growth is an incremental process where SIF values are needed at each increment as input to crack growth equations.

The boundary element method offers several advantages in crack growth simulation because high stress gradients at the crack front can be accurately modeled and the continuous re-meshing required to simulate crack growth is efficiently handled. The crack growth algorithm incorporated in the computer code allows the crack front to propagate as long as the effective SIF (K_{eff}) is between the lower bound of the threshold SIF (K_{th}) and the upper bound of the critical SIF (K_c). These bounding limits in the crack growth algorithm restrict the analysis to stable crack growth and subcritical crack growth.

In order to simulate mixed-mode crack growth an incremental type analysis is used where knowledge of both the direction and size of the crack increment extension are necessary. For each increment of crack extension, a stress analysis is performed using the DBEM, and the SIF are evaluated. The incremental direction and size along the crack front for the next extension are determined by fracture mechanics criteria involving SIF as the prime parameters. The crack front is re-meshed and the next stress analysis is carried out for the new configuration. The computational cycle used to simulate crack growth is illustrated in the flowchart shown in Figure 2.

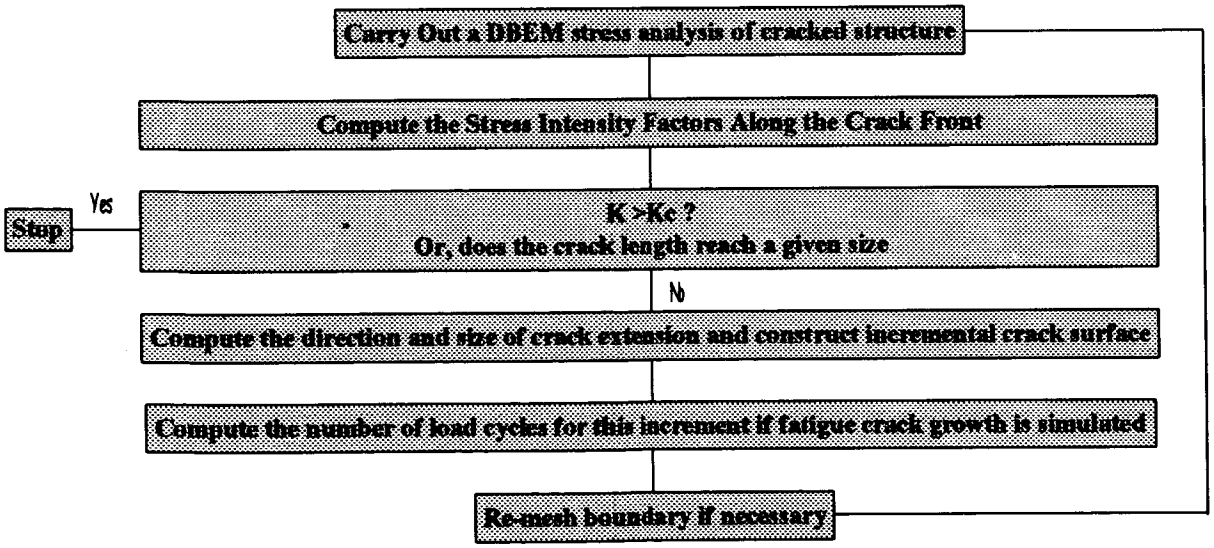

Figure 2. Computational cycle for numerical simulation of crack growth.

2.4.1 Incremental Direction Growth Criteria

Several criteria have been proposed to describe the direction of crack propagation for mixed mode crack growth [3]. Only the minimum strain energy density criterion is discussed in this paper. The strain energy density criterion is based on the postulate that the direction of crack propagation at any point along the crack front is toward the region where the strain energy density factor is a minimum. The strain energy density factor is shown in equation (4).

$$S(\theta) = a_{11}K_I^2 + 2\ a_{12}K_IK_{II} + a_{22}K_{II}^2 + a_{33}K_{III}^2 \tag{4}$$

The direction of crack growth is determined by minimizing this equation with respect to the angle theta (θ). The crack growth direction angle in the local coordinate plane perpendicular to the crack front can then be determined for each point along the crack front.

2.4.2 Incremental Crack Extension Distance

The maximum incremental distance that a crack would be expected to propagate can be determined using the strain energy density criterion or empirical methods. This paper discusses an empirical method based on experimental fatigue crack growth data. A method based on actual material behavior may better approximate crack propagation in engineering materials. The combined use of equations (5), (6), (7) and (8) illustrate the use of the Paris fatigue growth crack equation for determining both the maximum crack extension distance and the incremental crack extension distances for all the neighboring points along the crack front. A similar method could be adopted using the NASGRO 2.0 equation.

$$K_{eff} = \sqrt{(K_I + |K_{III}|)^2 + 2K_{II}^2} \tag{5}$$

$$\frac{da}{dN} = C\left(\Delta K_{eff}\right)^m \tag{6}$$

$$\Delta N = \frac{\Delta a_{max}}{(da\ /\ dN)_{max}} \tag{7}$$

$$\Delta a = \Delta N \frac{da}{dN} \tag{8}$$

The steps used to calculate the incremental crack extension distance are described below and intended to compliment the flowchart shown in Figure 2.

1. Conduct a stress analysis of the cracked structure using the DBEM.
2. Calculate ΔK_{eff} for each point along the crack front using equation (5).
3. Use a fatigue crack growth relationship (Paris or NASGRO 2.0) to calculate crack growth rate (da/dN) at each point along the crack front.
4. Determine the maximum value of da/dN along the crack front.
5. The maximum incremental crack distance (Δa_{max}) is a fixed value based on initial crack front element dimensions. (Δa_{max} is taken where ΔK_{eff} is a maximum and is equal to the length of the element side oriented perpendicular to the crack front).

6. Compute the number of cycles required to propagate the crack one increment using equation (7).
7. Scale the neighboring incremental crack extension distances along the crack front using equation (8).

3.0 APPLICATION IN THE AEROSPACE INDUSTRY

In order to demonstrate the accuracy and efficiency of the methodology discussed in the preceding sections two crack growth applications are described. The first application describes fatigue crack growth in a gear tooth and the second illustrates the use of the boundary element methodology to simulate repair of a cracked fuselage skin.

3.1 Fatigue Crack Growth in a Titanium Gear Tooth

The growth of a crack from the root of a gear tooth was simulated to determine the safe operating life of the component. The boundary element model of the gear tooth is shown in Figure 3. An embedded semi-circular crack was located near the root of the gear tooth. The crack was oriented normal to the surface of the root

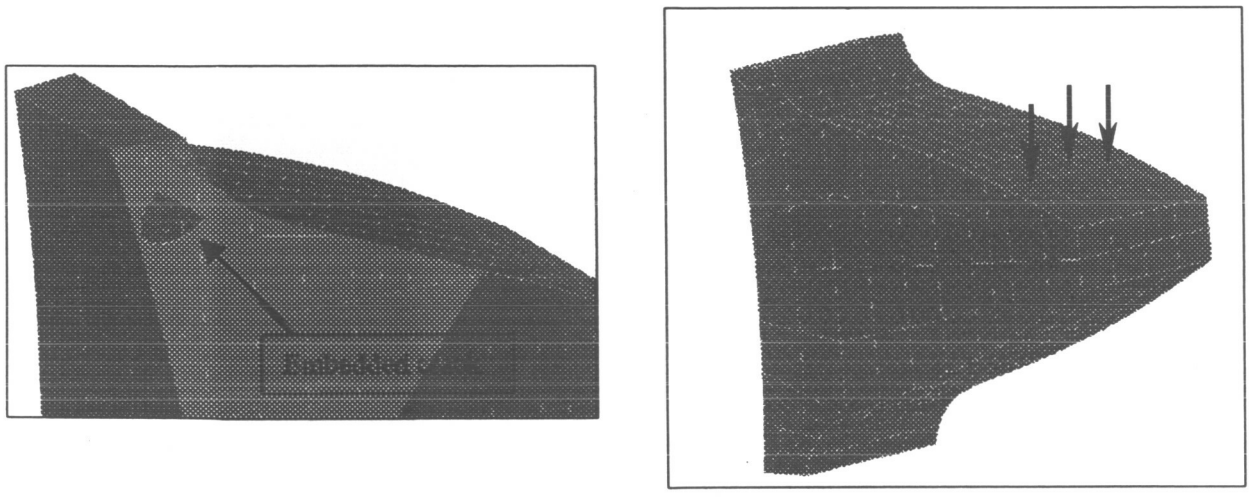

Figure 3. Boundary element model of titanium gear tooth. Embedded semi-circular crack shown located near root of gear tooth.

The gear tooth was made of titanium and material constants were elastic modulus E = 16,500 ksi and Poisson's ratio ν = 0.33. The fatigue crack growth curve fitting parameters were taken from the NASGRO 2.0 database where the material code P1CA13WA1 was selected. The gear tooth was loaded with uniform stress acting in a direction normal to the tooth surface. The load was applied near the end of the gear tooth in order to generate a tensile stress at the root. The fatigue crack analysis was conducted using constant amplitude cyclic loading with the stress ratio (R) equal to zero.

The fatigue crack growth analysis was conducted by using the minimum strain energy density criterion to determine incremental crack growth direction. The incremental crack propagation distance was determined using the relationship between crack size increment and number of cycles defined in the NASGRO 2.0 equation. The effective stress intensity factor (K_{eff}) was used in place of the maximum

stress intensity factor (K_{max}) in the NASGRO 2.0 equation. The formulation of K_{eff} is discussed in detail in references [3, 4].

Fatigue crack growth was simulated using two incremental steps. The initial crack front and the crack growth path for the semi-circular crack are shown in Figure 4. The deformed shape of the crack surface is indicative of mixed mode crack growth. The variation in the crack growth rate along the crack front for the two crack increment steps is shown in Figure 5. A large increase in the crack growth rate is observed at the edge of the crack (locations A and A` in Figure 4).

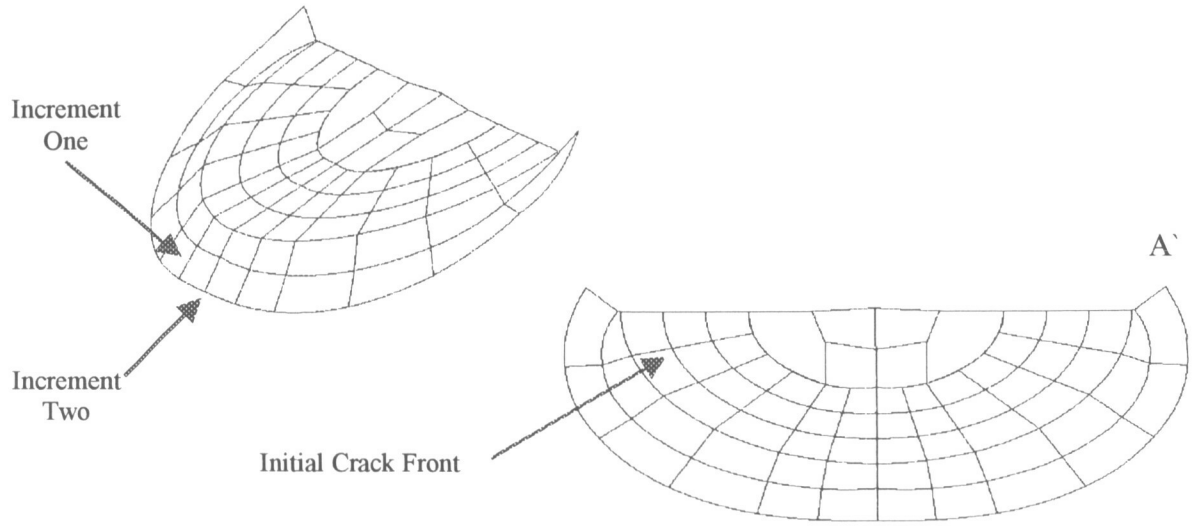

Figure 4. Two view of boundary element mesh showing deformed crack surface. Note "cupping" of crack which is typical for embedded crack subject to mixed mode loading.

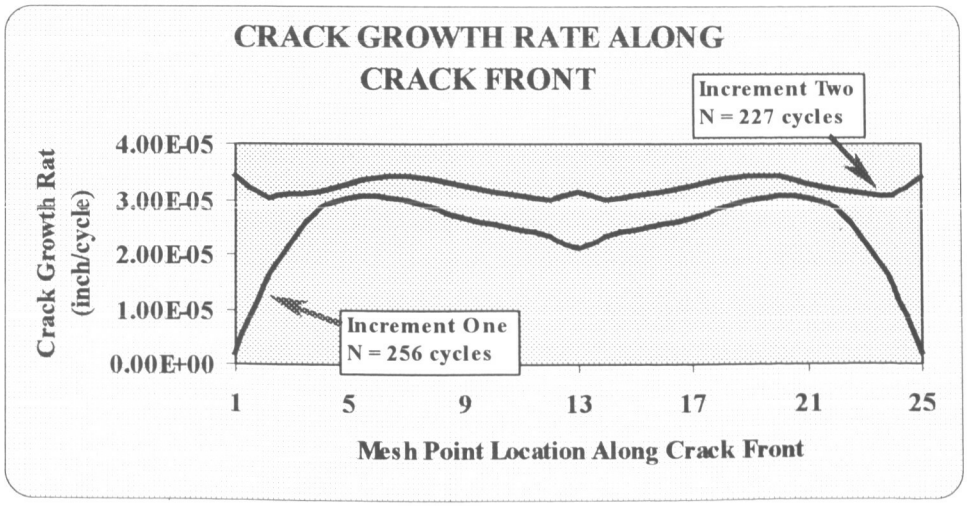

Figure 5. Plot of crack growth rate (da/dN) along crack front.

Figures 6 and 7 show Mode I and Mode II SIF values along the crack front. These plots suggest the cracked behavior of the gear tooth is governed primarily by Mode I crack growth which is consistent with the loading and geometry. The K_I value is also observed to become more uniform along the crack front as the crack propagates. The K_{II} value approaches zero along the center section of the crack front but tends to increase toward the outer edges of the crack front (location A and A shown in Figure 4). This suggests that there is an increasing component of shear stress acting at the edges of the crack. The K_{eff} reached a maximum value of 25.1 ksi $\sqrt{in}$ during the second increment. This is still well below K_c (50 ksi $\sqrt{in}$) and indicates that the crack would most likely have continued to propagate in a stable manner if additional crack extension increments were used in the analysis.

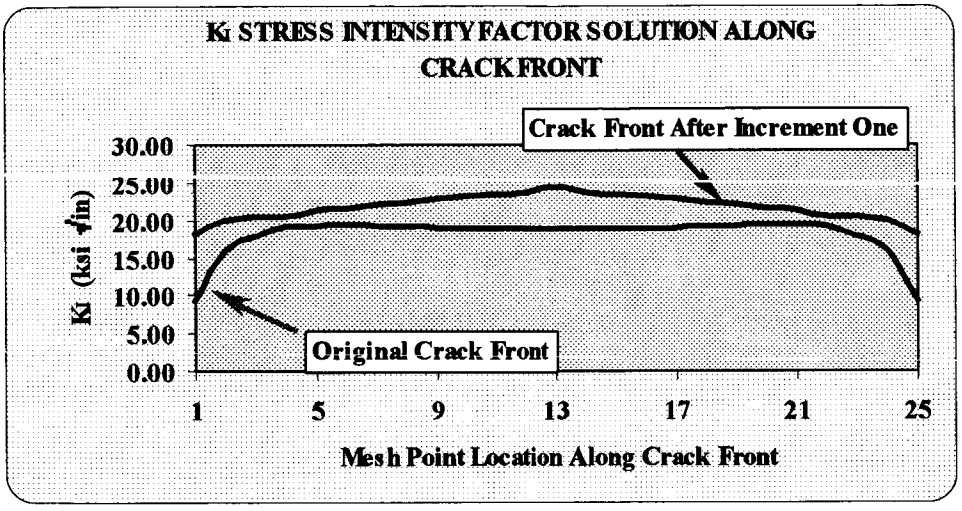

Figure 6. Plot of the Mode I stress intensity factor along the crack front at for the gear tooth model.

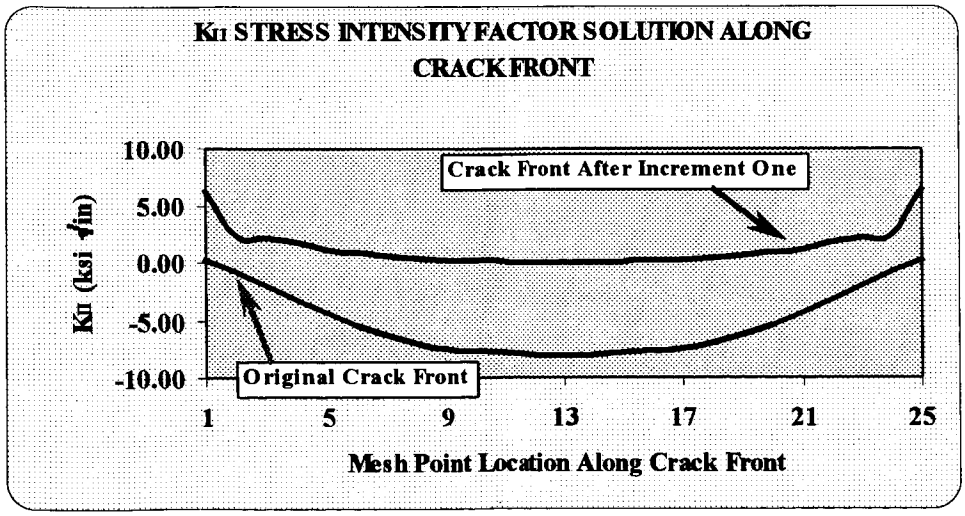

Figure 7. Plot of the Mode II stress intensity factor along the crack front at for the gear tooth model.

3.3 Simulation of a Patched Repair of a Cracked Fuselage Skin

The application discussed in the following section describes a simulated bonded patch repair of a crack in the stress-skin of an aircraft fuselage. This example is of interest given the recent endorsement of bonded repair techniques over some of the more common methods. The advantages of a bonded patch repair are that the creation of new damage near the repair site is less likely and the effectiveness of reducing crack growth is improved.

The first step in the analysis was to determine the SIF in a 0.0625-inch thick tension panel with a one-inch long center crack subject to a uniform tensile stress of 13,440 psi. The tensile panel was six inches wide by 15.6 inches long and made from 2024-T3 aluminum. The plate dimensions and loading were chosen so that the numerical results could be compared to experimental photoelastic work conducted by researchers in reference [5]. The numerical analysis produced a Mode I stress intensity factor of K_I = 18.2 ksi $\sqrt{in}$. This value is within less than 1% of the value obtained from the experimental study and slightly greater than the theoretical value for the two-dimensional plane strain case.

The second step in the analysis involved testing the same tensile panel with a 2x3 inch rectangular patch added above the damage site (Figure 8). The patch was also made from 2024-T3 aluminum and had the same thickness as that of the tensile panel. The structural adhesive used to bond the patch to the tensile panel was represented as a zone interface with internal spring boundary conditions. Spring stiffness values, applied in the three global coordinate directions, were derived using the elastic properties of the structural adhesive and an assumed glue line thickness.

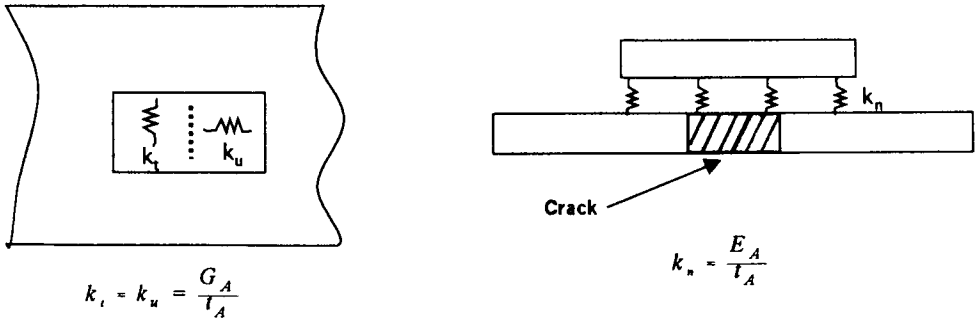

Figure 8. Boundary element model of aircraft skin with repair patch and schematic showing method to simulate structural adhesive properties (E_A = 560,000 psi, ν = 0.4, bond thickness = 0.005 inch).

Numerical results obtained for the stress distribution in the patch, and the redistribution of stresses in the tension panel under the patch, agree very well with experimental results. An enlarged view of the patched area showing the stress redistribution is shown in Figure 9. Numerical results indicate that the patch reinforced the cracked region and carried load over the crack opening with a corresponding decrease in

stresses in the damaged region and in the SIF at the repaired crack tips. The reduced SIF values result in a corresponding decrease in the rate of crack growth.

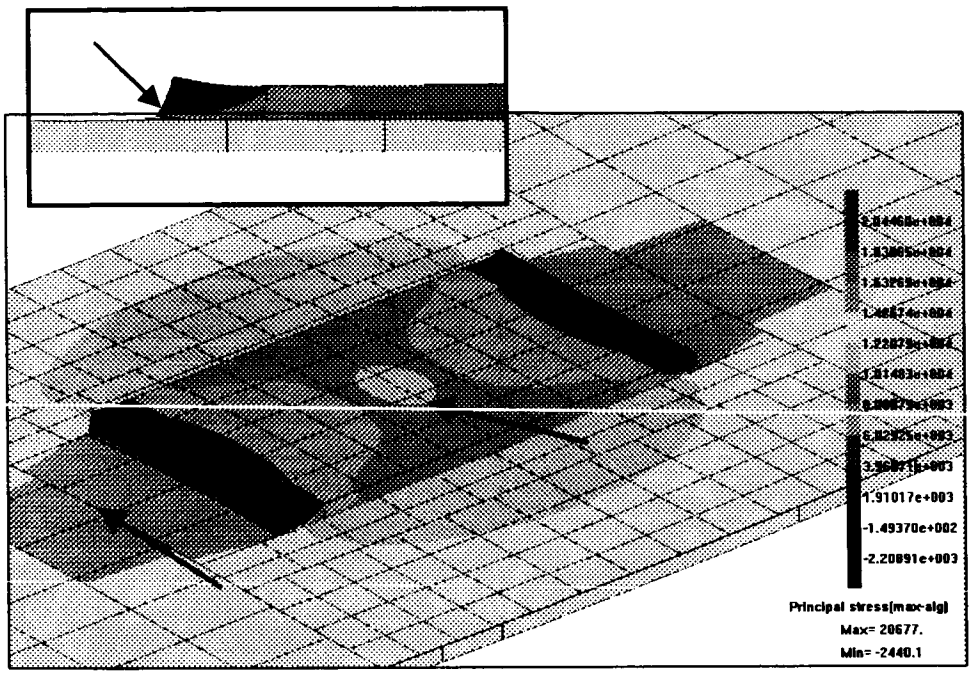

Figure 9. Principal stress results for patch repair simulation. Note stress transfer to plate and high tensile stress in patch above crack location. Also note "peeling" of patch edge.

The major difference between the numerical and experimental results was in the percent reduction in the SIF. The numerical model indicated a much greater reduction in the SIF. It is likely that this difference is a consequence of the method used to simulate the structural adhesive. It should also be noted that the experimental patch, although of similar dimensions, was elliptical in shape rather than rectangular and of slightly different material properties. These factors also limit the degree of comparison that can be made.

In order to investigate the sensitivity of K_I to the spring stiffness in the numerical model, a series of models were analyzed with varying spring stiffness. Better agreement with the results of the experimental model could be achieved as the spring stiffness was reduced from the initial values. In practice the numerical model would have to be calibrated using experimental results to better approximate the behavior of the adhesive before it could be used as an effective design tool.

No attempt was made to simulate the delamination observed, at higher loads, in the experimental model. However this behavior could be incorporated in the numerical model by adjusting the magnitude of the spring boundary conditions in the proper coordinate direction in accordance with the shear stress present at the patch/plate interface. Modeling of patch delamination would provide a more realistic understanding of the stress redistribution occurring in the repaired fuselage skin and facilitate assessment of the impact of the patch on arresting or reducing the crack growth rate.

CONCLUSIONS

The boundary element method is a robust and efficient technology that can be used to investigate the impact of cracks on the performance of structural components. The accuracy of the method, in the field of fracture mechanics, is well documented in the technical literature. Two applications were discussed in this paper to demonstrate the effectiveness of a boundary element based computer code in evaluating the impact of fatigue crack growth on structural components. The first application described a fatigue crack growth analysis of a three-dimensional gear tooth with complex geometry and loading. The second application demonstrated that the computer code was effectively used to simulate the bonded patch repair of a cracked fuselage skin. This application also illustrates that aircraft repair simulation, when combined with appropriate experimental data, can provide engineers with an economical and powerful remedial design tool.

REFERENCES

[1] Portela, A., Aliabadi, M.H. and Rooke D.P., "Dual Boundary Element incremental analysis of crack propagation", Int. Journal Computers and Structures, Vol. 46, pp 237-247, (1993).

[2] Aliabadi M.H. and Rooke D.P., Numerical Fracture Mechanics, Computational Mechanics Publications, Southampton UK / Boston MA, (1992).

[3] Mi, Yaoming, Three-Dimensional Analysis of Crack Growth, Computational Mechanics Publications, Southampton UK / Boston MA, (1996).

[4] Tanaka M. and Itoh, H., "New crack elements for boundary element analysis of elastostatics considering arbitrary stress singularities", Applied Mathematical Modeling, Vol. 11, 1987, p 357-363.

[5] Hastie, R.L. Fredell, R., Dally, J.W., "A photoelastic study of crack repair", Experimental Mechanics, Vol. 38, No.1, March 1998, pp 29-36.

[6] Hertzberg, R.W., Deformation and Fracture Mechanics of Engineering Materials, John Wiley & Sons, New York, New York, (1989).

[7] Anderson, T.L. Fracture Mechanics – Fundamentals and Applications, CRC Press, Boca Raton, FL, (1995).

[8] Cruse, T.A. and Meyers, G.J., "Three-Dimensional Fracture Mechanics Analysis", Journal of the Structural Division, ASCE, February 1977, pp 309-321.

[9] Newman, J.C. and Raju, I.S., "Stress-Intensity Factor Equations for Cracks in Three-Dimensional Finite Bodies Subjected to Tension and Bending Loads", NASA Technical Memorandum 85793, April 1984, pp 1-38.

[10] Brebbia, C.A., Telles, J.C.F. and Wrobel, L.C., Boundary Element Techniques, Springer-Verlag, Berlin, 1984.

[11] Tada, H., Paris, P. and Irwin, G., The Stress Analysis Cracks Handbook (2^{nd} edition), Paris Production Inc., St. Louis, Missouri, 1985.

A COMPARISON OF NUMERICAL METHODS OF FRACTURE ANALYSIS WITH HELICOPTER STRUCTURE

George V. Bauer
Airframe Structures
Sikorsky Aircraft Corporation
Stratford, CT, 06615
P (203) 386-7139
F (203) 386-3717
gbauer@sikorsky.com

ABSTRACT

This Paper provides the results of an investigation of two numerical methods for calculation of stress intensity and crack growth for through thickness cracks in complex structures. The two numerical methods are the NASTRAN two dimensional crack tip finite element CRAC2D and the Surface Integral and Finite Element (SAFE) hybrid analysis. The basis and applicability of each method is discussed, and comparison is made with standard through thickness crack handbook solutions. The application of these methods to crack growth analysis in a typical helicopter airframe structure is evaluated.

1. INTRODUCTION

Damage tolerant design using fracture mechanics or flaw tolerant methods is becoming the necessary and preferred methods for safe aircraft design. Military and FAR requirements specify that new aircraft design requires these types of analyses. This paper investigates two numerical computer methods of fracture mechanics stress intensity and crack growth analysis for through thickness cracks in metallic structure. It will first correlate each method with standard handbook solutions. It then presents the application of these methods to a typical helicopter airframe structure, involving redundant load paths, and the unique helicopter high cycle vibratory loading. Results will show recommended modeling techniques for each computational method.

Section 2 provides a review of the NASTRAN and SAFE-2D computational numerical methods of linear elastic fracture mechanics and correlation with standard handbook solutions. Four theoretical two-dimensional (2D) crack solutions will be evaluated with the two different computer methods. The first method, NASTRAN and the CRAC2D element, is a finite element based formulation. The second method, SAFE-2D, is a hybrid combination of finite element and surface integral theory. The correlation of these two methods with theory will prove their validity and provide techniques and capability for general fracture analysis use.

Section 3 provides a fracture analysis combining both techniques using a helicopter transmission support beam structure as an example. This involves the large and varying repeated forces and moments from the rotor and transmission. The structure consists of a left and right transmission support beam along with a fore and aft support frame. This structure was chosen due to the critical nature of its function, existence of history and field data on in-service cracking, and it being an example of airframe support structure with load-path redundancy.

2. CORRELATION OF COMPUTATIONAL METHODS WITH THEORY

The method of using finite elements to determine crack tip stress intensities is very versatile. It permits analysis of many different configurations of actual engineering geometries. This method determines solutions for 2-D structural problems, mechanically fastened assemblies, 3-D solid problems, and elastic-plastic elements accounting for crack tip plasticity.

The object of the Surface-integral And Finite Element hybrid (SAFE) method is to combine the best capability of each numerical method for evaluation of stress intensity and crack growth. Finite element analysis (FEA) is very effective in determining accurate stress and strain fields within various structures. It can help solve problems with material and geometric nonlinearites. FEA is also useful with inhomogeneities such as boundaries and interfaces. One problem with FEA is its difficulty in trying to model an elastic-plastic local stress region at the crack tip. Such problems include generating a sufficient mesh to capture the high stress/strain field gradients. The Surface integral method has been effectively used in problems with singularities and infinite domain. It can accurately model a crack in an infinite 2-D planar region by introducing a continuous distribution of dislocations to represent the crack in the structure.

2.1 Overview of NASTRAN FEM methods and the crack tip element

The two major types of fracture analysis methods using standard finite elements are direct and indirect solutions. The direct method allows the calculation of the stress intensity, K, by analyzing the stress field output from the finite elements. The indirect method solves for K by using other calculated quantities such as compliance, elastic energy, or the J integral.

One indirect method using NASTRAN to calculate K_I is the strain energy method. The strain energy is obtained from the model for a specific crack length either by direct program output or calculating the load/displacement energy at the crack tip. Incrementing the crack length and re-running the analysis will give the change in strain energy for the K_I calculation.

A direct method for mode I, for example, uses stress distribution equations for the stress intensity factor[1]. These equations are only valid for stress results immediately in front of the crack tip. Because of this constraint, the method requires many small elements or a very fine mesh in the crack vicinity. Also, the results from the elastic finite elements directly at the crack tip cannot be used because of the "real-life" plastic region. Stresses from the elements directly surrounding the crack tip must be used for distribution calculations. Some finite element codes (NASTRAN included) have developed a crack tip element that models the singularity in front of the crack tip and accounts for the fine mesh required in front of the crack.

Crack tip elements have been incorporated into MSC/NASTRAN so that mode I, II, and III stress intensity factors can be automatically calculated for a specific geometry and loading. Performing an analysis with these elements alleviates the fine meshing required at the crack tip to find displacement, stress, and strain fields. The CRAC2D element shown in Figure1 is a linear, isotropic, and homogeneous element that is compatible with any standard linear or quadratic isoparametric elements.

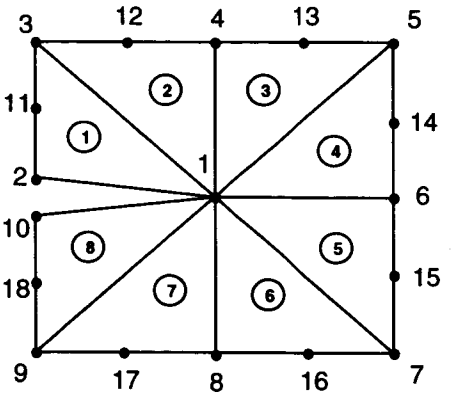

Figure 1. NASTRAN CRAC2D element

The theoretical development of the CRAC2D element is based on planar 2-D geometry but, can be used in 3-D space. It is built of 8-noded isoparametric elements degenerated by collapsing one side. Using a combination of 8 collapsed triangles, the shape functions of the crack element model the singular $1/\sqrt{r}$ stress and strain fields directly in front of a sharp linear elastic 2-D crack tip. The isoparametric map of material stiffness, displacements, and thermal/mechanical loading for the CRAC2D element can be combined directly with the whole finite element model to generate solutions. The stress intensity factors are then calculated based on displacements[2].

2.2 NASTRAN Model Correlation with Theory

A specific geometry from the transmission beam analysis in the next section was chosen for each of the correlation analyses. The .1 inch thick web of an aluminum I-beam is 7.68 inches in height between the upper and lower caps. A specific mesh of 4-noded quadrilateral elements was chosen as opposed to 8 noded elements for each correlation based on an initial error estimate comparison. This error check compared the calculated stress intensity factor from NASTRAN using a CRAC2D element in a specific mesh type and the handbook solution for a crack in a finite width plate. A mesh of 20 X 31 elements gave the most accurate results for this crack model.

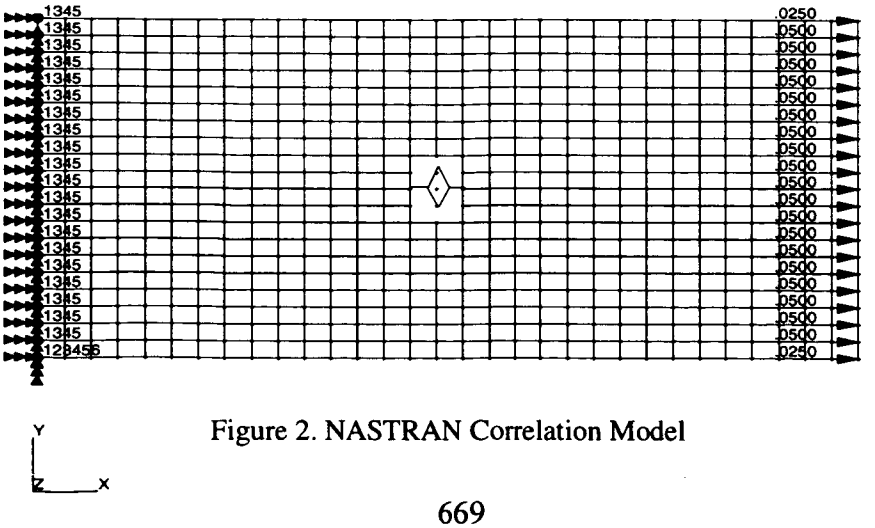

Figure 2. NASTRAN Correlation Model

With the general solution for finite width plates from Tada et. al.[3] being $K_I = \sigma\sqrt{\pi a}F(a/b)$ we get:

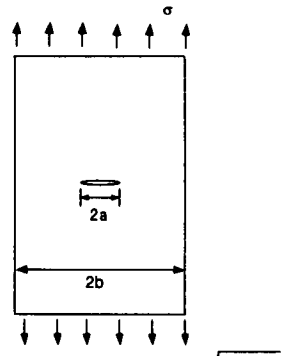

$$F(a/b) = \left\{1-.025(a/b)^2+.06(a/b)^4\right\}\sqrt{\sec\frac{\pi a}{2b}}$$

(a) Interior Crack in Tension

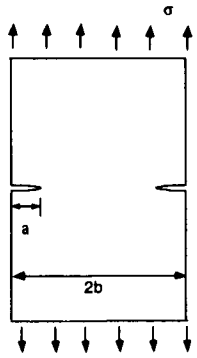

$$F(a/b) = \frac{1.122-.561(a/b)-.205(a/b)^2+.471(a/b)^3-.190(a/b)^4}{\sqrt{1-a/b}}$$

(b) Double Edge Crack in Tension

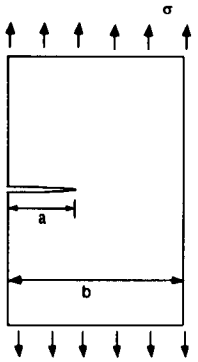

$$F(a/b) = \sqrt{\frac{2b}{\pi a}\tan\frac{\pi a}{2b}}\,\frac{.752+2.02(a/b)+.37(1-\sin{}^{\pi a}\!/_{2b})^3}{\cos{}^{\pi a}\!/_{2b}}$$

(c) Single Edge Crack in Tension

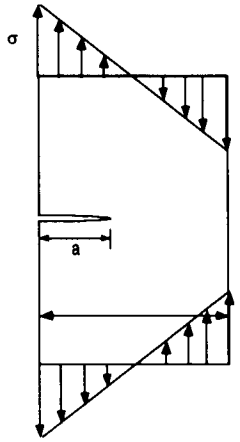

$$F(a/b) = \sqrt{\frac{2b}{\pi a}\tan\frac{\pi a}{2b}}\,\frac{.923+0.199(1-\sin{}^{\pi a}\!/_{2b})^4}{\cos{}^{\pi a}\!/_{2b}}$$

(d) Single Edge Crack in Pure Bending

Figure 3. Correlation Models

In each correlation case, multiple NASTRAN runs were made to re-mesh and grow the given crack in the Y direction to a new length. The accuracy was then compared with the standard handbook stress intensity solutions shown in Figure 3. For each case, the following tables show applied loads, crack length, resultant stress intensity factor from NASTRAN, and the theoretical calculation.

TABLE 1. NASTRAN CRACK PROPAGATION DATA

Model 40 - Interior Crack					Model 401 - Single Edge Crack				
σ	a	K-Calc	K-NAST	Δ %	σ	a	K-Calc	K-NAST	Δ %
1302	0.384	1439	1549	-7.7%	1302	0.384	1641	1602	2.4%
1302	0.768	2072	2140	-3.3%	1302	0.768	2418	2353	2.7%
1302	1.152	2619	2656	-1.4%	1302	1.152	3141	3064	2.5%
1302	1.536	3172	3185	-0.4%	1302	1.536	3909	3816	2.4%

Model 411 - Double Edge Crack					Model 421-Single Edge Crack, Pure Bending				
σ	a	K-Calc	K-NAST	Δ %	σ	a	K-Calc	K-NAST	Δ %
1302	0.384	1604	1573	2.0%	1302	0.384	1531	1492	2.6%
1302	0.768	2273	2211	2.7%	1302	0.768	2105	2049	2.7%
1302	1.152	2802	2723	2.8%	1302	1.152	2550	2495	2.2%
1302	1.536	3287	3196	2.8%	1302	1.536	2962	2905	1.9%
					1302	1.92	3384	3318	1.9%

Comparing K_I error percentages for the different crack models above, we get:

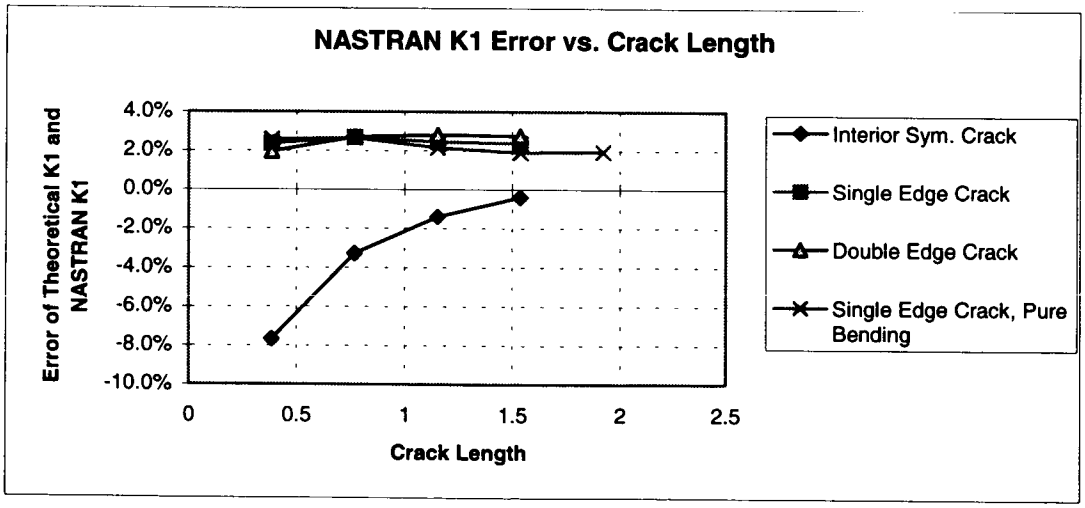

Figure 4. NASTRAN error comparison

2.3 Review of SAFE-2D

SAFE-2D integrates FEA and Surface Integral analysis of modeling structure in a two dimensional plane. Combining these two methods allows you to model and propagate a crack through the structure independent of the finite element mesh. It allows the crack to cross finite element boundaries and possibly different thicknesses, material, or geometry. It also allows the crack to propagate in any direction (depending on the loading) without re-meshing the new crack length region. The crack propagation is based on 2-D Linear Elastic Fracture Mechanics (LEFM) in the plane. The magnitude and direction is based on pure tensile loading mode I or the orientation which $K_{II} = 0$. This method also

allows the flexibility of modeling multiple cracks, multiple directions, and crack branching in quasi-static propagation.

The SAFE-2D formulation is the linear superposition of the finite element and surface integral models[4]. It determines the stress, strain, and displacement fields in the crack region by using the isoparametric mapping functions of the finite elements in the uncracked model. It then adds this information or uses this as boundary conditions into the surface integral model's distribution of dislocations in an "infinite medium" representing the crack. The numerical analysis for both methods are coupled due to this usage of boundary requirements.

As an example of the method, a problem shown in Figure 5 is broken into the two parts.

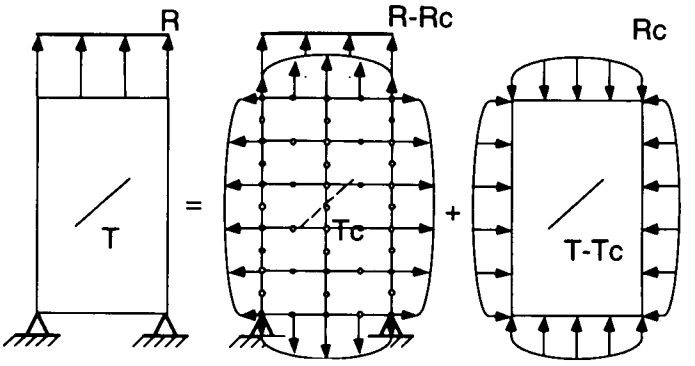

Figure 5. SAFE-2D Model Formulation

The aim is to calculate the stress intensity factor for the center-cracked plate under uniform tensile load R and traction T applied along the crack surface. First, the plate is meshed with 8-noded isoparametric plate elements to determine geometry, material stiffness, and reactions. Applying a correcting load, Rc, on the un-cracked finite element model accounts for the presence of the crack. The surface integral model is then loaded with Rc and the difference between traction load vectors. The applied loads on the surface integral model represents the finite boundary of the actual problem. Superimposing these two solutions will determine the stress intensity factors for the crack tip. It will also determine the stress state and conditions for crack propagation. Because the finite element part of the model does not have to be re-meshed, the solver only has to recalculate the surface integral equations for new crack propagation direction and length. A Paris Law, NASGRO 2.0, or other equations may be used to determine the progression of crack growth.

2.4 SAFE-2D Correlation With Theory

The same 4 crack models used in the NASTRAN correlation were analyzed in SAFE-2D. In this case, there was no re-meshing of the finite element model. Because the SAFE-2D code requires 8-noded quadrilateral elements, the same geometry and material were used but meshed with 20 X 31 quadratic elements. The surface integral crack calculations also required a surface be created about the perimeter of the mesh. (In this study only one rectangular surface is required) In each case, the crack center and number of wings were specified based on each theoretical model for comparison. To generate stress intensity factors as a function of crack length, an R ratio of 0.0 was used to propagate the crack. The tables below show each of the 4 model comparisons with standard handbook solutions. In each case the stress level, σ is 13020 psi.

TABLE 2. SAFE-2D CRACK PROPAGATION DATA

Centercrack				Single Edge Crack			
Crack Length, a	Safe-K1	K-Calc	Δ %	Crack Length, a	Safe-K1	K-Calc	Δ %
0.384000	14168	14386	1.5%	0.384	16084	16407	2.0%
0.422366	14953	15106	1.0%	0.422	17043	17264	1.3%
0.467718	15807	15923	0.7%	0.468	18078	18256	1.0%
0.521594	16760	16852	0.5%	0.524	19229	19405	0.9%
0.586187	17842	17917	0.4%	0.590	20559	20752	0.9%
0.664599	19091	19155	0.3%	0.672	22188	22359	0.8%
0.761322	20564	20620	0.3%	0.773	24328	24281	-0.2%
0.875519	22238	22287	0.2%	0.889	26376	26459	0.3%
1.006668	24108	24152	0.2%	1.022	28861	28956	0.3%
1.157486	26229	26271	0.2%	1.175	31717	31859	0.4%
1.330858	28682	28723	0.1%	1.351	35265	35298	0.1%
1.530382	31594	31636	0.1%				
1.759562	35158	35209	0.1%				

Double Edge Crack				Single Edge Crack, Pure Bending			
Crack Length, a	Safe-K1	K-Calc	Δ %	Crack Length, a	Safe-K1	K-Calc	Δ %
0.384000	15820	16043	1.4%	0.384	15105	15273	1.1%
0.422359	16701	16826	0.7%	0.422	15903	15960	0.4%
0.467734	17619	17708	0.5%	0.467	16724	16721	0.0%
0.521294	18600	18697	0.5%	0.520	17589	17559	-0.2%
0.584650	19676	19805	0.7%	0.582	18525	18481	-0.2%
0.660066	20908	21051	0.7%	0.654	19582	19498	-0.4%
0.751116	22434	22471	0.2%	0.740	20874	20632	-1.2%
0.863688	23932	24125	0.8%	0.844	22107	21933	-0.8%
0.993043	25658	25921	1.0%	0.969	23614	23399	-0.9%
1.141997	27537	27889	1.3%	1.115	25410	25022	-1.6%
1.313038	29710	30070	1.2%	1.282	27210	26826	-1.4%
1.509628	32060	32534	1.5%	1.474	29255	28871	-1.3%
1.735466	34929	35405	1.3%	1.694	31730	31240	-1.6%
				1.948	34773	34066	-2.1%

Now, a comparison of error percentages for all SAFE-2D models:

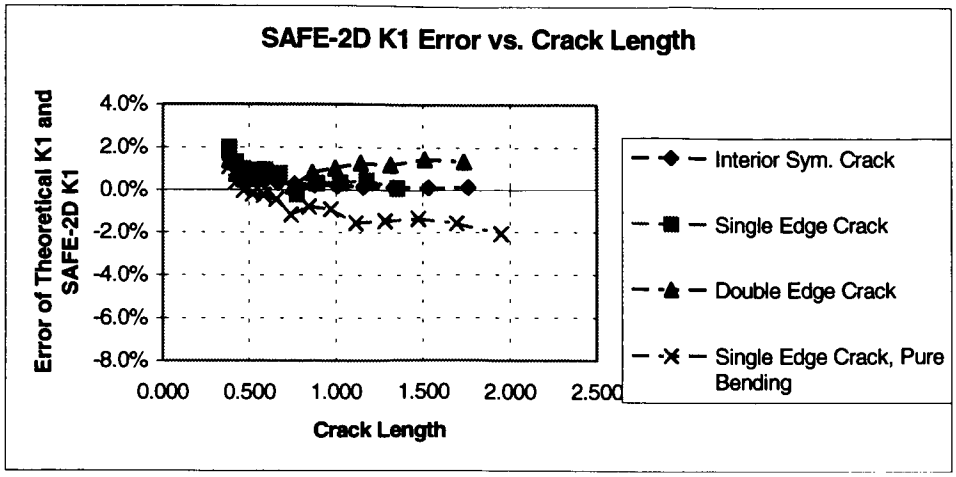

Figure 6. SAFE-2D error comparison

2.5 Method Summary

A comparison of stress intensity solution errors for each computational method is shown in Figure 7.

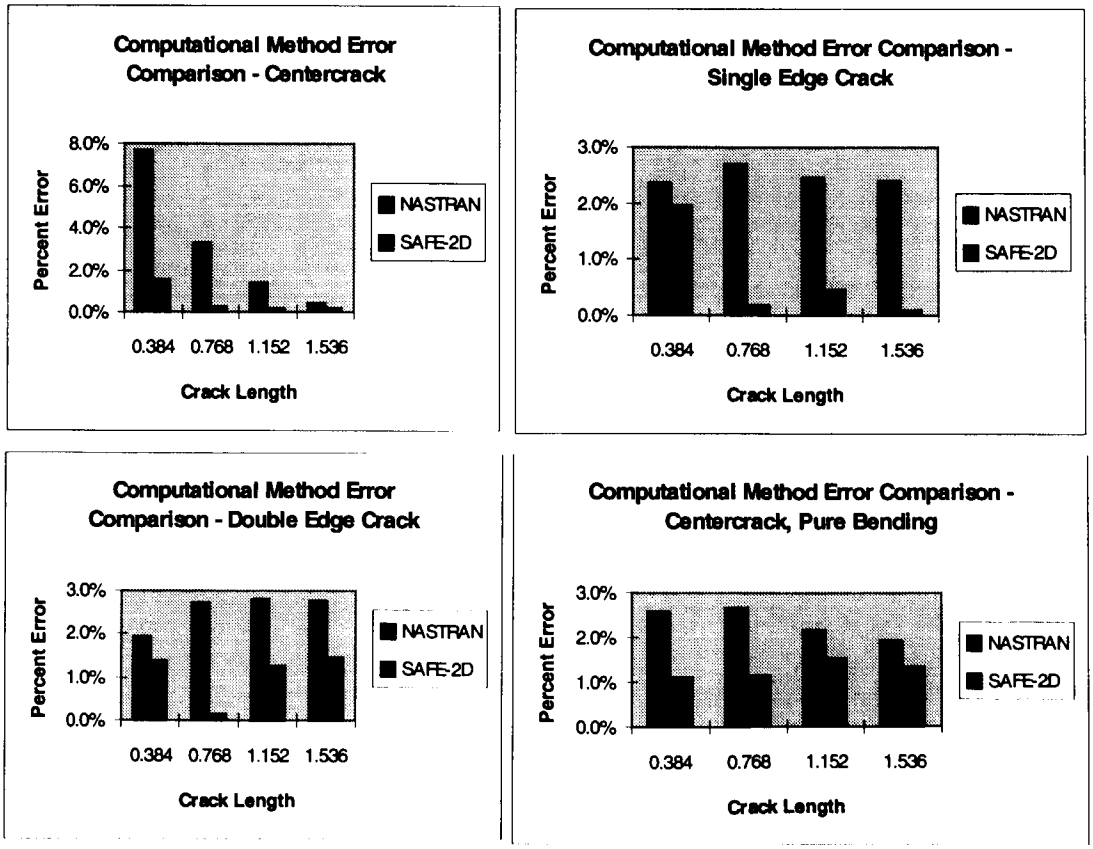

Figure 7. Computational methods error comparison

3. EXAMPLE AIRCRAFT STRUCTURE ANALYSIS

A 2-D crack growth analysis was performed on a helicopter transmission attachment beam. This structure was chosen because of its common occurrence in airframe structure. Typical of metallic airframes, this is part of an installation of built-up frames, beams, skins, and longerons. This design methodology provides a complex redundant load path structure. The cracked area for analysis is shown in Figure 8.

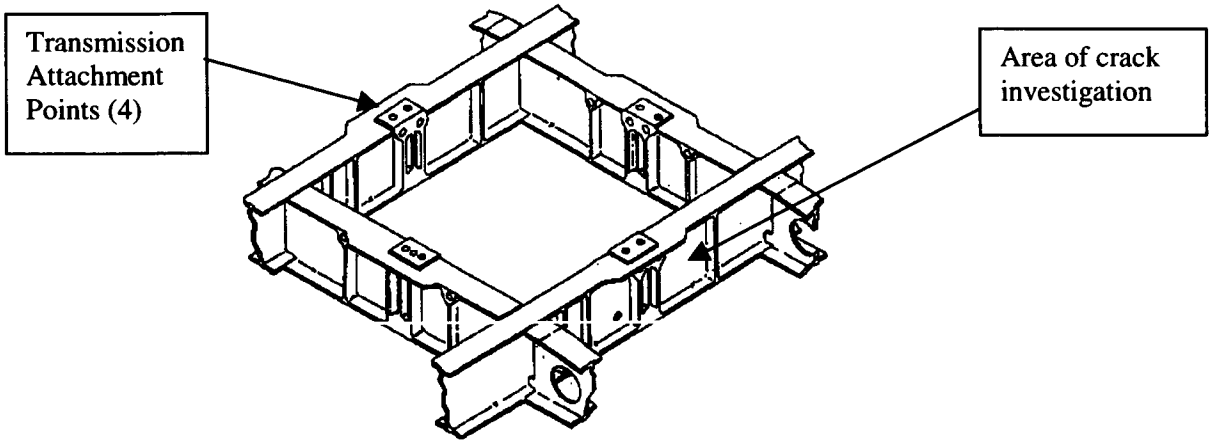

Figure 8. Example transmission attachment structure cut-away

3.1 Analysis

A full aircraft finite element model was analyzed to obtain the loads and deflections in the local structure. This method allows us to analyze a full range of maneuvers or loading spectrum to more accurately obtain local beam loads. Because of relatively thin gauge metal components, typical airframe structure is modeled and analyzed with 2D finite element plates. As introduced in Section 2, the CRAC2D element was meshed into the global aircraft finite element model to obtain local loads for different crack lengths. The cracked area was re-meshed four times to grow the crack to a specific length. The results of the load redistribution after crack growth for one maneuver (1g straight and level flight at Vh, cruising speed) is shown in Figure 9. The loads shown are freebody loads and were applied to the local SAFE-2D beam model.

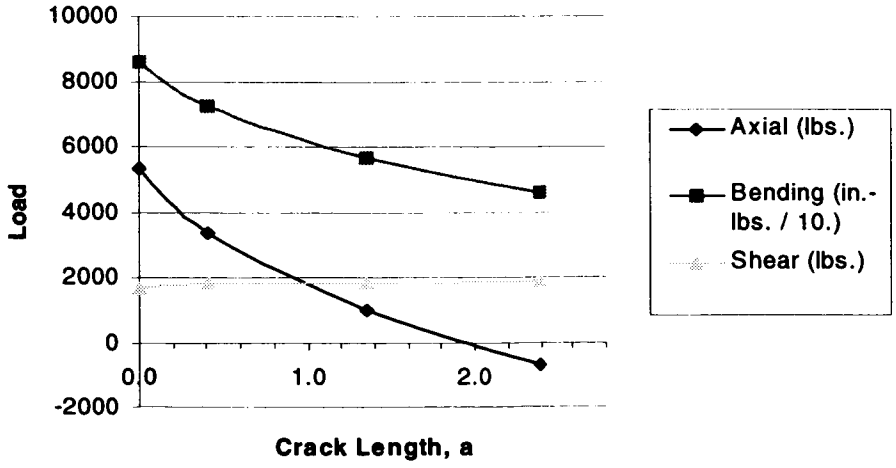

Figure 9. Load redistribution with crack propagation

As Figure 9 shows, as the beam deflects more with the crack growth, the other support structure resists the deflection and takes more loading. The final crack extension model is shown in Figure 10 in a deflected shape.

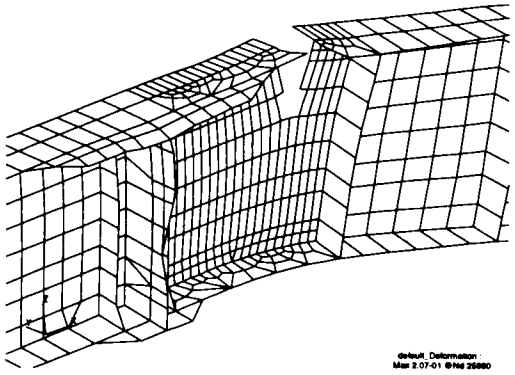

Figure 10. Deflected transmission beam with 2.4 inch crack

Field history has shown that the upper cap of the beam has fully cracked across the width before propagation through the web. This led us to a 2-D analysis of propagation through the 8 in. web. This beam is made from a 7075 T-73 aluminum forging. An R ratio of .69 was used in the analysis that was gathered from flight test data. The loads taken from the single level flight maneuver at the different crack lengths were applied to a SAFE2D model. Typically, the high frequency loading occurs at an interval of the main rotor revolution. In this case, a frequency of 17.19 Hz or 61,884 cycles per hour is used. To put the vibratory environment in perspective, the extremely high number of cycles also indicates the typical "endurance limit" of materials of 1. E+8 cycles is accumulated in only 1600 flight hours. The level flight maneuver used was chosen because of the high percentage of time spent in forward flight. The first SAFE-2D web model shown in Figure 11 is the crack propagation with only the un-cracked beam loads being used for the entire spectrum. (A conservative approach) The analysis of the second model incorporated reducing the load as the crack grows. The second model shows less crack growth and growth deceleration when the 4 step loading is applied at the different crack lengths.

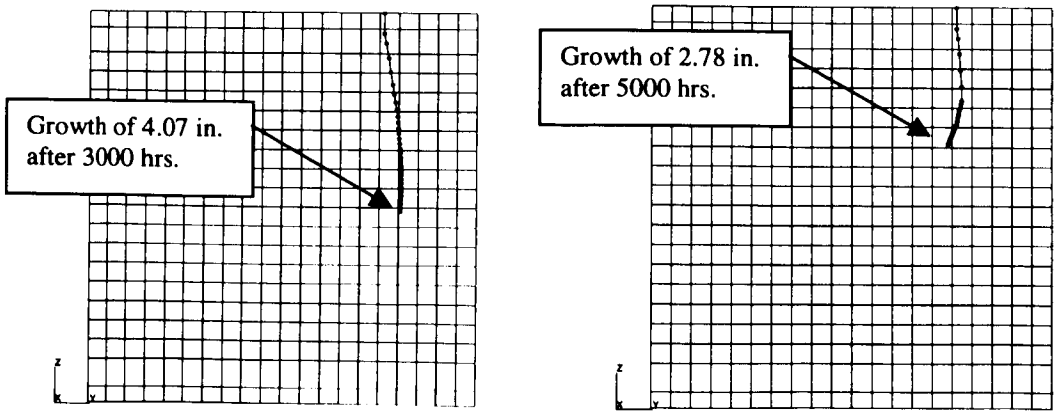

Single Load Level

Stepped Load Redistribution

Figure 11. SAFE2D crack growth plots through beam web

Figure 12 shows a close-up of the difference in crack paths for constant loading and stepped load redistribution. Each dot represents a 10 flight hour increment of growth.

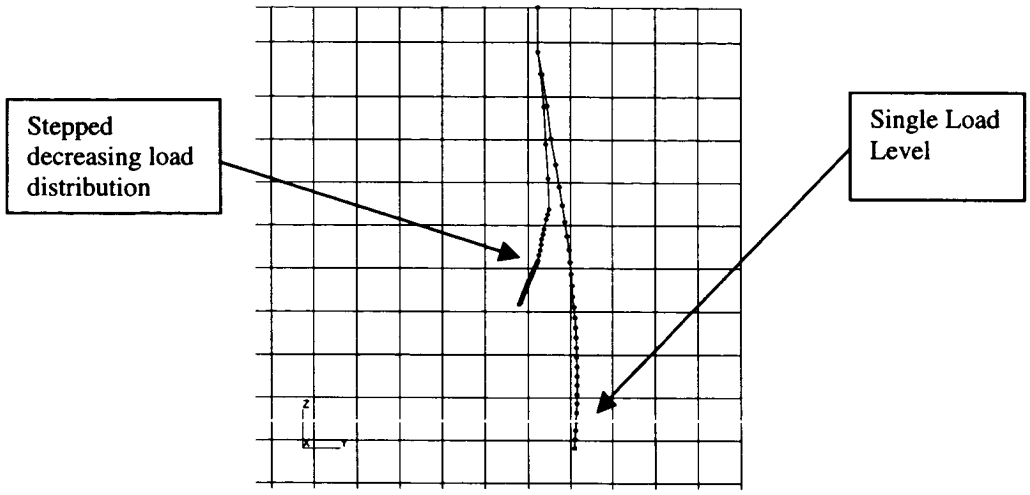

Figure 12. SAFE2D crack growth paths

CONCLUSIONS

Damage tolerant and residual strength analysis of airframe structure must take into account load redistribution after damage and growth. Widespread fatigue damage (WFD) is an emerging field of study that looks at a more global approach of damage tolerance. Figure 14 below shows a typical scenario of damage tolerant analysis. Using a combination of global FEA with SAFE-2D would facilitate analysis of airframe structure crack growth.

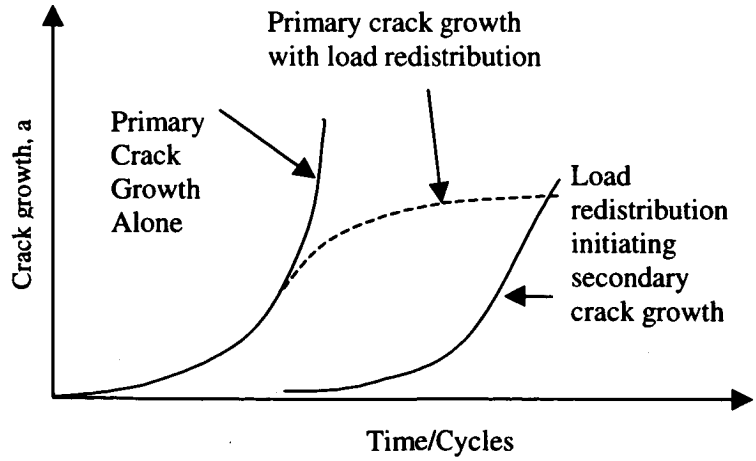

Figure 13. Global approach to damage tolerant structural analysis

One benefit for using the CRAC2D element in NASTRAN is the capability of modeling an in-plane 2-D crack with structures in 3-space. This allows for incrementing crack growth analysis in 3 dimensional structures with realistic applied loads and boundary conditions.

In the case of using NASTRAN for finding stress intensity factors, errors will undoubtedly become reduced when a fine mesh surrounding the crack tip element is used. Based on the initial correlation analysis, using very small elements also tends to increase error in long cracks. Case by case studies should be made for optimum crack element size. One drawback of using NASTRAN is constant re-meshing with the CRAC2D element to grow the crack through the structure.

One advantage SAFE-2D has is the capability to grow multiple cracks automatically through the structure without any re-meshing. It will calculate new directions and lengths for each crack. SAFE-2D also has the flexibility to grow the crack according to different laws (e.g. Paris, NASGRO, etc). The stress intensity factors from SAFE-2D are based on a proven dislocation density calculation with surface integrals. This combination of numerical techniques makes the answers more accurate. (As shown in this study by Figure 7)

Both methods have the advantage of using existing finite element models from previous analyses. Also, both methods can use standard pre and post-processing programs to generate models. For accurate crack growth analyses, obtaining the load levels and actual aircraft maneuver usage is critical.

ACKNOWLEDGEMENTS

The author would like to thank Dr. Bal Annigeri from the United Technologies Research Center for his help, instruction, and use of his resources. The author would also like to thank Mr. Paul Dufour, Sikorsky Aircraft for his technical and computer help. Also, thanks to Mr. Henry Konopka, Sikorsky Aircraft for providing a touch of reality: budget and valuable field history.

REFERENCES

1. D. Broek, "Elementary Engineering fracture Mechanics", Martinus Nijhoff Publishers 1986.

2. J. Parekh, R. Arnold, and P. Woytowitz, "A Modern Family of Crack Tip Elements for MSC/NASTRAN", MSC/NASTRAN Users' Conference, March 20-21, 1986.

3. H. Tada, P. Paris, G. Irwin, "The Stress Analysis of Cracks Handbook", Paris Productions Inc. and Del Research Corporation 1985 and other crack handbooks.

4. B. Annigeri and M. Cleary, "Surface Integral Finite Element Hybrid (SIFEH) Method for Fracture Mechanics, International Journal for Numerical Methods in Engineering, Vol. 20, 869-885 (1984).

5. NASTRAN On-line Computer Documentation, MacNeal-Schwendler Corporation, 1997.

6. Surface-Integral and Finite Element Hybrid Method User's Manual, United Technologies Research Center, September, 1993.

IMPORTANCE OF CHEMICALLY SHORT-CRACK-GROWTH ON FATIGUE LIFE

Evan J. Dolley and Robert P. Wei
Lehigh University
Department of Mechanical Engineering and Mechanics
19 Memorial Drive West
Bethlehem, PA 18015-3085 USA
610-758-3583
ejd2@lehigh.edu

ABSTRACT

Commercial and military aircraft are exposed to deleterious environments (such as atmospheric moisture and salt spray) that enhance the fatigue crack-growth (FCG) rates in aircraft structural components. This phenomenon, generically termed corrosion fatigue (CF) must be explicitly taken into account in the development of life prediction and management methodology. CFCG behavior may be separated into two regimes: a chemically long-crack regime and a chemically short-crack regime. Experimental data on aluminum alloys used in aircraft construction show that the CFCG rates are up to 10 times that in an inert environment in the long-crack regime. In the chemically short regime, the growth rates are further enhanced by up to a factor of three, with the effect extending out to crack lengths of up to 6 mm. The accelerated CFCG rates in the short-crack regime must be considered since they can affect crack-growth, for example, over nearly one-half of the inter-rivet distance in typical fuselage lap-splice joints. Crack-growth results on 2024-T3 and 7075-T6 aluminum alloys are presented and compared. The implication of the chemically short-crack-growth regime on fatigue life is discussed.

1. INTRODUCTION

Life management of existing aircraft and the design of future aircraft require that time dependent processes, such as corrosion and corrosion fatigue, be considered explicitly in life prediction methodologies. Corrosion and corrosion fatigue need to be considered especially in the life management of existing aircraft since the majority of aircraft in service are either approaching or have surpassed their initially planned usage of 20 years. Since the usage of many of these aircraft is being extended beyond 20 years, and some (for example, the C/KC 135) well beyond 20 years, corrosion and corrosion fatigue of the structure is an immediate issue to be addressed. Military and civilian aircraft are exposed to deleterious environments that include atmospheric moisture, acid rain and salt-spray. The deleterious environment can induce localized corrosion (such as, pitting) and enhance fatigue crack-growth (FCG) rates (corrosion fatigue) in aluminum alloys such as 2024-T3 and 7075-T6[1-6]. The purpose of this paper is to describe the chemically short FCG behavior of the 2024-T3 and 7075-T6 aluminum alloys and to discuss the implications of this behavior on fatigue life.

The corrosion and corrosion fatigue life of an aluminum alloy structure may be considered in terms of the contributions from three regimes: (1) formation of localized corrosion damage (such as, particle induced corrosion pits); (2) transition from the localized corrosion damage into fatigue cracks and subsequent growth in the chemically short regime; and (3) chemically long fatigue crack-growth. A chemically long fatigue crack exhibits enhanced FCG rates compared to those of a crack in a dry environment. For aluminum alloys, these rates are approximately 10 times faster than those in a dry environment[1]. The

long-crack-growth rate would be independent of crack length at a given stress intensity factor range (ΔK). The long-crack-growth response of 7075-T6 in water vapor and water, as compared to dry argon and oxygen, and vacuum, has been shown in Figure 1. The growth rates were enhanced by the presence of water vapor and water, with the greatest enhancement in water. The degree of enhancement depended upon the crack driving force (ΔK), being greater at the lower ΔK levels. Life prediction methodologies used for life management and new aircraft design must account for the range of environments that the aircraft is expected to encounter during service.

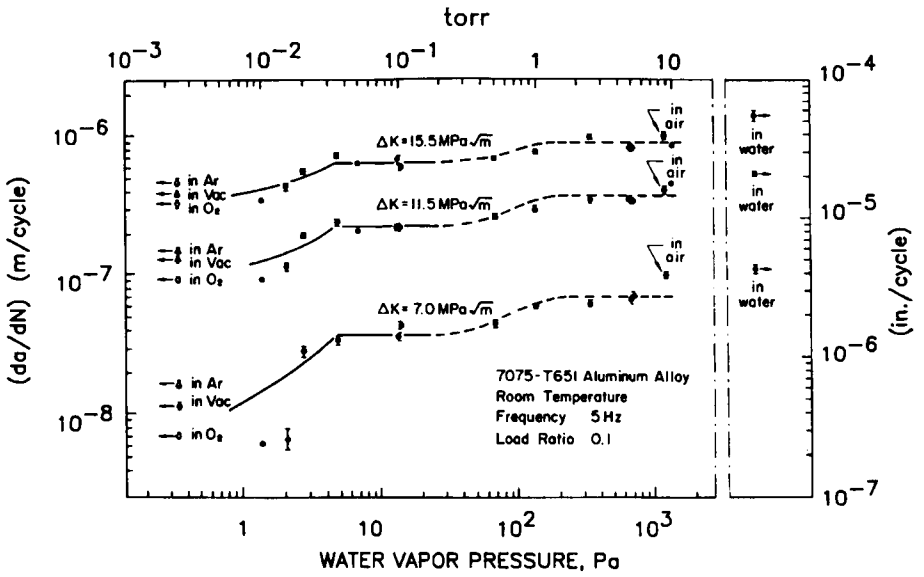

Figure 1. Enhancement of 7075-T6 FCG rates in water vapor and water as compared to those in dry and inert environments[1].

The FCG rates shown in Figure 1 represent the growth rates for a chemically long-crack. An increase over these growth rates can occur in ferrous and aluminum alloys at crack lengths between 0.5 and 6 mm under the same crack driving force in aqueous environments[7-12]. The increase between these crack lengths has been described as a chemically short-crack effect (SCE). Over this range of crack lengths, a chemically short-crack is microstructurally and mechanically long in that the crack length is considerably larger than the grain size of the material and linear elastic fracture mechanics applies. The chemically short FCG rate at a crack length of approximately 0.5 mm may be three times faster than that of a chemically long-crack in an aqueous NaCl environment for the same ΔK, reducing to that of the long-crack at about 6 mm. This change in the enhancement of FCG rates is attributed to the decrease in the concentration of dissolved oxygen at the crack-tip with increasing crack length[7,8]. The damage growth kinetics for all three regimes (localized corrosion, chemically short-crack-growth and chemically long-crack-growth) must be characterized and mechanistically modeled to provide an accurate estimate of the structure's fatigue life.

2. CHEMICALLY SHORT-CRACK EFFECT IN ALUMINUM ALLOYS

The impact of the chemically short-crack regime on the total fatigue life is of concern for aluminum alloys. The 2024-T3 and 7075-T6 aluminum alloys exhibited a chemically short-crack effect in an aerated 0.5M NaCl solution under constant ΔK control[7,8]. The results are summarized in Figures 2 to 4. The FCG experiments were performed under constant ΔK control on single edge crack specimens with rectangular gage sections at a test frequency of 10 Hz. and a stress ratio (R) of 0.1. The pH value of the

0.5M NaCl solution was approximately 6.2 during testing. The ΔK level and dissolved oxygen concentration of the aqueous solution were systematically varied from 4 to 10 MPa $m^{1/2}$ and 0 to 30 ppm, respectively.

The degree of FCG rate enhancement in the chemically short-crack regime depended upon the concentration of dissolved oxygen ($[O_2]$) in the aqueous environment and the ΔK level. The crack-growth response of the 2024-T3 aluminum alloy at several ΔK levels is shown as a function of crack length in Figure 2 for a dissolved oxygen concentration of 0 and 7 ppm. The FCG rates remained constant with increasing crack length in a deaerated solution ($[O_2]$ is near 0 ppm) at all ΔK levels tested[7,8,13]. A chemically short fatigue crack-growth effect was present at a dissolved oxygen concentration of 7 ppm. The FCG rate at a crack length of 0.5 mm was approximately 2 times greater than the growth rates when the crack length was greater than 4 mm at a ΔK of 4 and 5 MPa $m^{1/2}$. The chemically short-crack regime was considered to be between crack lengths from 0.5 mm to 5 mm at these ΔK levels. A crack length longer than 5 mm was considered to be a chemically long-crack. No evidence of a chemically short-crack effect was seen at ΔK levels above 5 MPa $m^{1/2}$ in the 7 ppm aqueous solution. The effect was seen, however, up to a ΔK level of 8 MPa $m^{1/2}$ when the solution was saturated with dissolved oxygen ($[O_2]$ = 30 ppm) as shown in Figure 3. The chemically short-crack effect does not exist at a ΔK level of 10 MPa $m^{1/2}$ or (higher) regardless of the dissolved oxygen concentration.

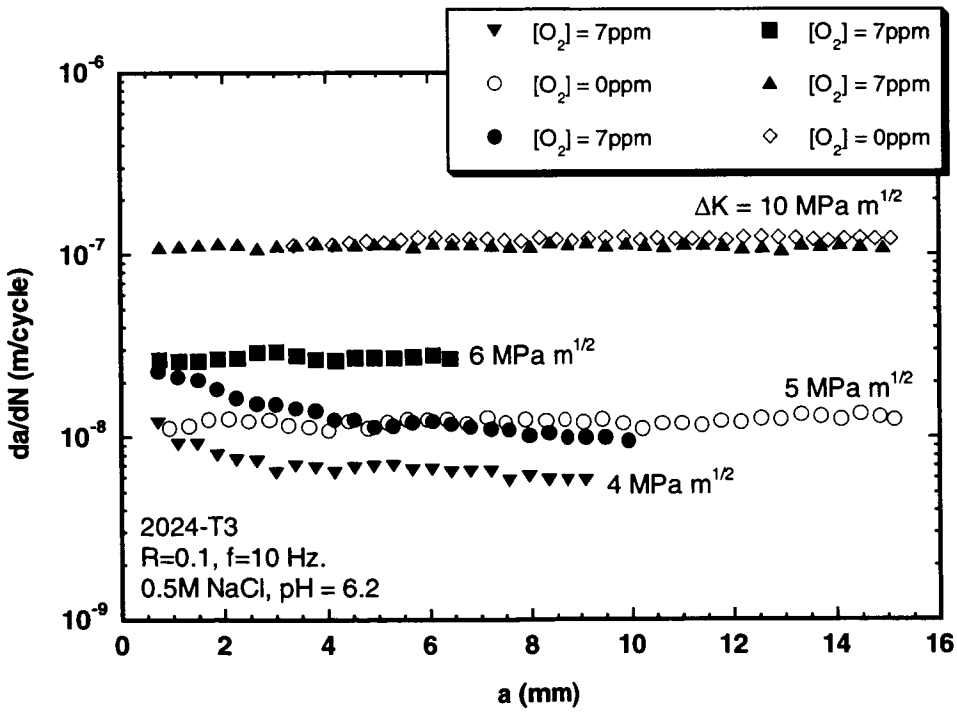

Figure 2. Chemically short-crack effect in the 2024-T3 aluminum alloy with a dissolved oxygen concentration of 0 and 7 ppm in the aqueous environment[7,8].

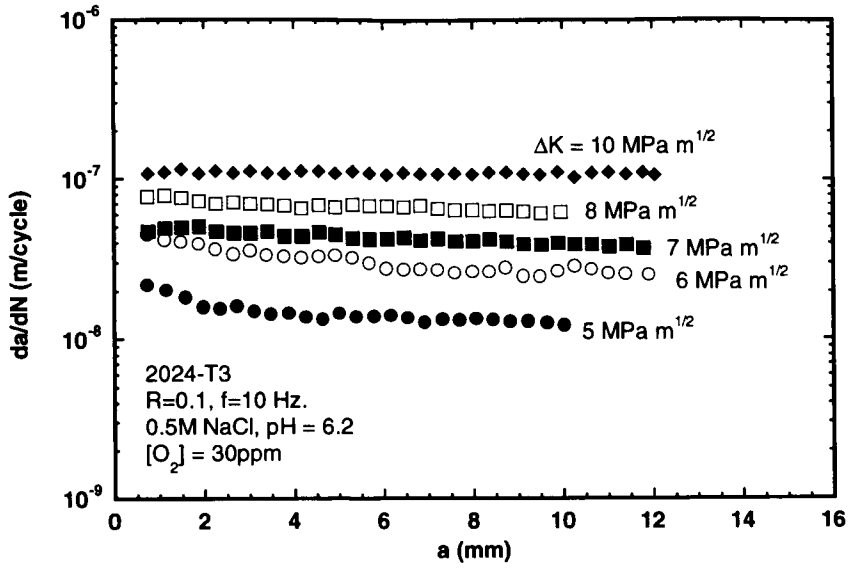

Figure 3. Chemically short-crack effect in the 2024-T3 aluminum alloy with a dissolved oxygen concentration of 30 ppm in the aqueous environment[7,8].

The 7075-T6 aluminum alloy also exhibited a chemically short-crack effect as shown in Figure 4. As with the 2024-T3 alloy, the chemically short-crack effect does not exist in the deaerated aqueous environment. The chemically short-crack effect was observed in the 7075-T6 aluminum alloy at all ΔK levels between 5 and 10 MPa $m^{1/2}$ with a dissolved oxygen concentration of 7 ppm. Increasing the dissolved oxygen concentration to 30 ppm did not produce an increase above the 7 ppm growth rates.

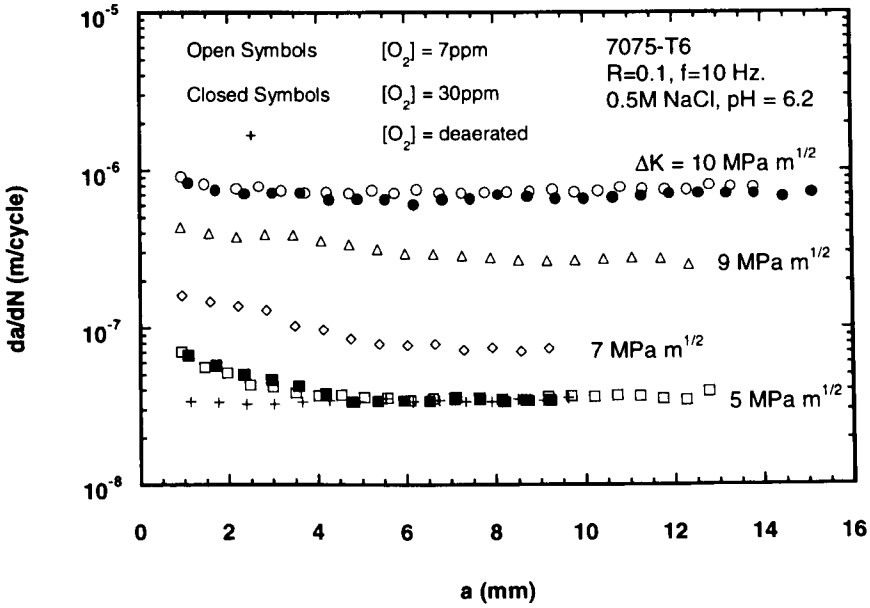

Figure 4. Chemically short-crack effect in the 7075-T6 aluminum alloy.

The results have shown the presence of a chemically short-crack phenomenon in two different aluminum alloys to varying degrees. The 7075-T6 aluminum alloy was more sensitive to the presence of dissolved oxygen in the aqueous environment. Figure 5 shows the ratio of the chemically short FCG rates to the chemically long FCG rates as a function of ΔK for the 7075-T6 and 2024-T3 aluminum alloys at a crack length of 0.5 mm. The ratio for the 7075-T6 alloy at an oxygen concentration of 7 ppm was greater than that for the 2024-T3 alloy at a higher concentration of dissolved oxygen. Chemically short FCG rates (at crack lengths near 0.5 mm or less) may be 3 times greater than chemically long-crack-growth rates depending upon the amount of dissolved oxygen in the aqueous environment, ΔK, and the aluminum alloy.

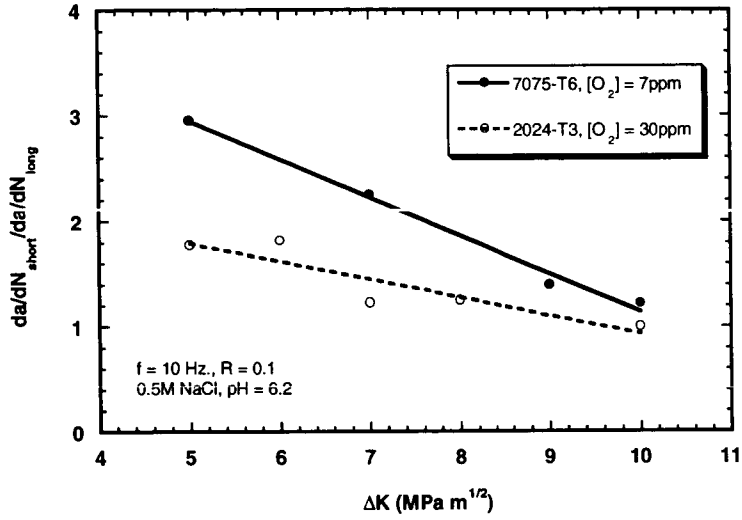

Figure 5. Ratio of chemically short to chemically long fatigue crack-growth rates for the 2024-T3 ([O_2] = 30 ppm) and 7075-T6 ([O_2] = 7 ppm) aluminum alloys.

3. EFFECT OF CHEMICALLY SHORT-CRACK EFFECT ON FATIGUE LIFE

Fatigue cracks will typically nucleate from localized corrosion damage (e.g., pits in aluminum) in structural components of the aircraft. The size of the corrosion damage at the transition to fatigue crack-growth (i.e., crack nucleation) would depend on the stress in the affected structural component. Assuming that the damage is a corrosion pit and that the pit size at transition may be considered as the initial crack size, then the initial crack size could range from 10 μm to 300 μm. The crack would then grow at the chemically short growth rates to a crack length of approximately 6 mm depending upon the ΔK level. The stress at the corrosion pit dictates not only the pit size for transition, or fatigue crack nucleation, but also influences the degree and extent of the chemically short-crack effect. Accurate estimations of fatigue life, therefore, require the use of FCG rates that properly reflect the crack length dependence as the crack grows from the initial corrosion damage.

To assess the impact of chemically short-crack-growth, fatigue life was estimated for growing a crack from a corrosion pit in a 1 mm-thick sheet of 2024-T3 and 7075-T6 aluminum alloys. For simplicity, the fatigue life was estimated by attributing the chemically short-crack behavior to the crack length interval from 30 μm to 1 mm and the chemically long-crack behavior from 1 to 6 mm. Since the crack was assumed to nucleate from a corrosion pit, the chemically short-crack life (30 μm to 1 mm) was determined by using a ΔK solution for a semi-circular surface crack in an infinite plate. Transition to long-crack-growth was assumed to occur when the semi-circular crack penetrated the sheet. The crack was then modeled as a through-thickness crack, with a starting length of 1 mm. The chemically long-

crack life (1 mm to 6 mm) was determined by using the ΔK solution for a through-thickness crack in an infinite plate. The fatigue life was then estimated by establishing a relationship of the FCG rates (da/dN) to ΔK and integrating over the given crack length intervals. The da/dN-ΔK relationship follows a power-law relationship such that

$$\frac{da}{dN} = C \bullet \Delta K^{n} \tag{1}$$

where

$$\Delta K = \beta \cdot \Delta\sigma \cdot \sqrt{\pi \cdot a} \tag{2}$$

and $\beta = 2.2/\pi$ for the semi-circular surface flaw (β_1), $\beta = 1$ for the through crack (β_2), $\Delta\sigma$ was the applied stress range at the pit, and a was the crack length. The chemically short-crack-growth rates were taken to be 2.0 and 1.5 times greater than the chemically long growth rates for the 7075-T6 and 2024-T3 alloys on average, respectively.

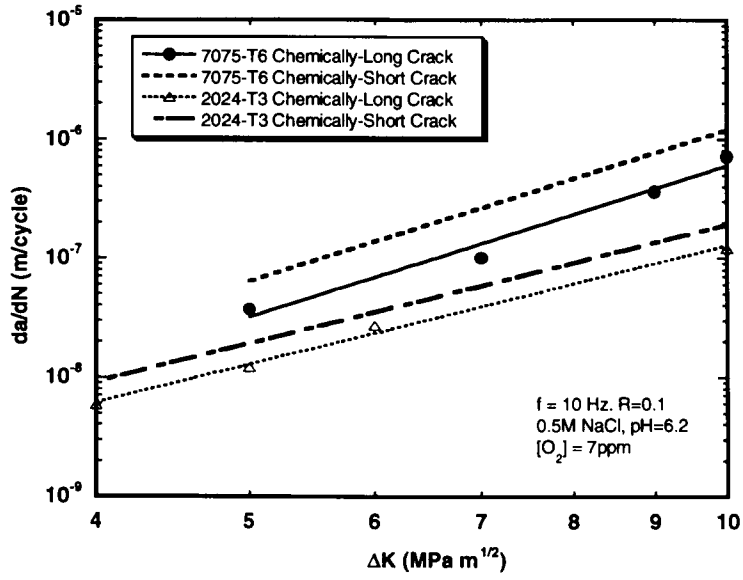

Figure 6. Power-law relationship for the 7075-T6 and 2024-T3 chemically long and short-crack regimes in a 0.5M NaCl solution.

The crack-growth rate coefficients (C) and exponents (n) were estimated from the FCG data in Figure 5. The power-law exponent (n) was assumed to be the same for the long and short-crack regimes. The growth rate coefficients were different for the long and short-crack regimes and are designated C_{LC} and C_{SC}, respectively. The coefficients and exponents for the 7075-T6 and 2024-T3 aluminum alloys are shown in Table 1.

TABLE 1. Crack-growth rate coefficients and exponents for the 7075-T6 and 2024-T3 aluminum alloys.

7075-T6			2024-T3		
C_{SC}(m cyc^{-1})((MPa$\sqrt{m}$)$^{-4.24}$)	C_{LC}	n	C_{SC}(m cyc^{-1})((MPa$\sqrt{m}$)$^{-3.32}$)	C_{LC}	n
3.48×10^{-11}	7.00×10^{-11}	4.24	9.17×10^{-11}	6.11×10^{-11}	3.32

The fatigue life, considering the long and short-crack behavior, was determined by substituting Equation (2) into Equation (1) and rearranging such that

$$N_f = \int_{a_{i\,SC}}^{a_{f\,SC}} \left[C_{SC}^{-1} \cdot \beta^{-n} \cdot \Delta\sigma^{-n} \cdot \pi^{-\frac{n}{2}} \cdot a^{-\frac{n}{2}} \right] da + \int_{a_{i\,LC}}^{a_{f\,LC}} \left[C_{LC}^{-1} \cdot \beta^{-n} \cdot \Delta\sigma^{-n} \cdot \pi^{-\frac{n}{2}} \cdot a^{-\frac{n}{2}} \right] da \,. \quad (3)$$

Integrating over the chemically short and long-crack-growth regimes produces

$$N_f = C_{SC}^{-1} \cdot \beta_1^{-n} \cdot \Delta\sigma^{-n} \cdot \pi^{-\frac{n}{2}} \cdot \left(\frac{n}{2} - 1 \right) \left[a_{iSC}^{\left(1-\frac{n}{2}\right)} - a_{fSC}^{\left(1-\frac{n}{2}\right)} \right] +$$

$$C_{LC}^{-1} \cdot \beta_2^{-n} \cdot \Delta\sigma^{-n} \cdot \pi^{-\frac{n}{2}} \cdot \left(\frac{n}{2} - 1 \right) \left[a_{iLC}^{\left(1-\frac{n}{2}\right)} - a_{fLC}^{\left(1-\frac{n}{2}\right)} \right] . \quad (4)$$

Equation (4) was then used to estimate fatigue life over the prescribed crack length intervals using two different stress ranges ($\Delta\sigma$ = 100 and 60 MPa). The estimated fatigue lives in Table 2 show that the chemically long fatigue life is approximately 4 percent of the total fatigue life for both alloys. The chemically long-crack regime (1 to 6 mm) was, therefore, neglected in the subsequent estimations of fatigue life.

TABLE 2. Estimated fatigue life for the chemically short and long-crack regimes.

	7075-T6			2024-T3		
Stress (MPa)	Chemically short (cycles) (a = 0.03-1 mm)	Chemically long (cycles) (a = 1-6 mm)	Total life (cycles)	Chemically short (cycles)	Chemically long (cycles)	Total life (cycles)
100	1.94×10^6	14,996	1.96×10^6	1.60×10^6	56,248	1.66×10^6
60	1.69×10^7	1.31×10^5	1.70×10^7	8.77×10^6	3.07×10^5	9.08×10^6

To further demonstrate the impact of the chemically short-crack regime, fatigue life estimates were made using the chemically short-crack-growth behavior from a crack length of 30 μm to 1 mm. The applied stress was systematically varied to produce resulting fatigue lives using the first term in Equation (4). The fatigue lives were then compared against lives estimated using only the chemically long-crack-growth rates. The impact of the chemically short-crack effect has been shown in Figures 7 and 8 as a reduction in estimated fatigue life by approximately one half. The cut off for the short-crack effect is due to the disappearance of the chemically short-crack effect at that ΔK level.

A factor of one-half reduction in fatigue life is substantial in terms of long-term design lives of approximately 20 years. A damage tolerance design and life management philosophy requires an accurate estimate of the fatigue crack-growth rates in a structure. As seen with the 2024-T3 and 7075-T6 aluminum alloys, the fatigue crack-growth rates were very different given changes in the environment,

crack length and crack driving force. The factor of one-half reduction in fatigue life corresponds to the doubling of chemically short FCG rates over those of a chemically long-crack.

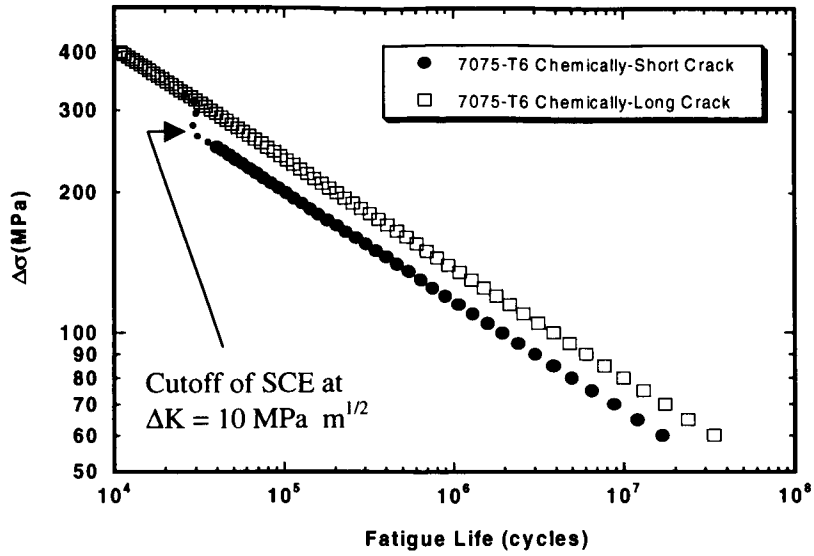

Figure 7. The reduction in the 7075-T6 fatigue life from a crack length of 0.03 mm to 1 mm when considering the chemically short-crack effect.

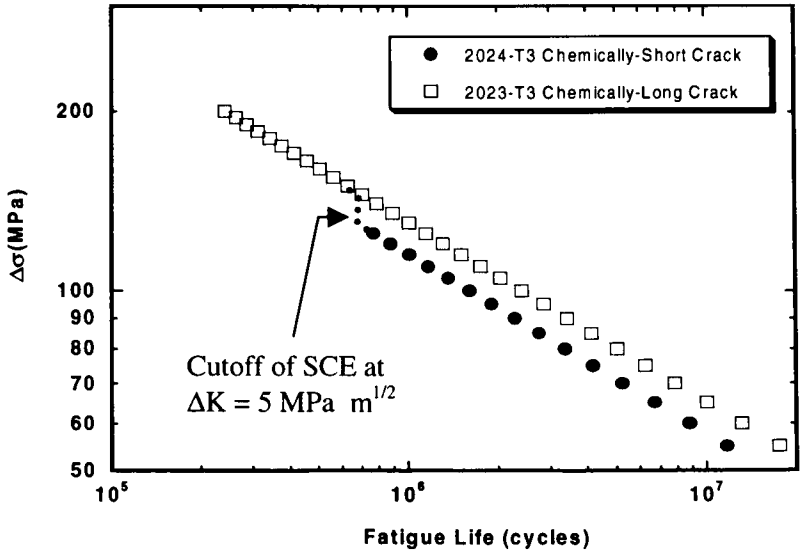

Figure 8. The reduction in the 2024-T3 fatigue life from a crack length of 0.03 mm to 1 mm when considering the chemically short-crack effect.

The finding would be different if the fatigue crack had nucleated at an open hole in the sheet material. The stress concentration effect of the hole may produce a sufficiently high ΔK where the chemically short-crack effect is not manifested. This is especially true for the 2024-T3 aluminum alloy where the effect is not seen at ΔK levels above 5 MPa $m^{1/2}$. Care must be exercised in characterizing the stresses and environments during aircraft operations so that accurate predictions of fatigue lives can be made.

CONCLUSIONS

A damage tolerance life management and design philosophy requires accurate information on the fatigue crack-growth rates in the environment in which the aircraft will operate. The 2024-T3 and 7075-T6 aluminum alloys exhibit a chemically short-crack effect where the FCG rate of a 0.5 mm-long-crack is faster than the FCG rate of a crack that is 6 mm long, depending upon the crack driving force. Overall the 7075-T6 alloy is more susceptible to the presence of salt water than the 2024-T3 alloy. The 7075-T6 alloy was also more sensitive to the chemically short-crack effect, exhibiting a factor of three increase in FCG rate at 0.5 mm over that of a long-crack at a ΔK of 5 MPa $m^{1/2}$, versus a factor of two for the 2024-T3 alloy. Fatigue life estimates were shown to rely on the proper characterization of the operating environment and applied loads on the aircraft structure. The chemically short-crack behavior in aluminum alloys can substantially reduce the fatigue life of a structure with respect to that based on chemically long-crack behavior alone. The reduction in fatigue life correlated well with the ratio of the chemically short and long-crack-growth rates. The estimated one-half reduction in fatigue life corresponded to the doubling of chemically short FCG rates relative to the chemically long FCG rates.

ACKNOWLEDGEMENTS

The research was funded by the Air Force Office of Scientific Research under Grants F49620-96-1-0245 and F49620-98-1-0198 and by the Federal Aviation Administration under Grant 92-G-0006. The authors would like to acknowledge Mr. Carl D. Miller for assistance with performing the fatigue experiments and Dr. Ming Gao for helpful discussions.

REFERENCES

1. Gao, M., and Wei, R.P., *Met. Trans. A*, Vol. 19A, pp. 1739-1750, 1988.
2. Wei, R.P., "Environmentally Assisted Fatigue Crack-growth", *Advances in Fatigue Science and Technology*, (eds.) Branco, C.M. and Rosa, L.G., pp. 221-252, 1989.
3. Tanaka, K., and Wei, R.P., *Engineering Fracture Mechanics*, Vol. 21, No. 2, pp. 293-305, 1985.
4. Lin, F-S, and Starke, Jr., E.A., "Mechanisms of Corrosion Fatigue Crack Propagation of 7XXX Aluminum Alloys in Aqueous Environments", *Hydrogen Effects in Metals*, Bernstein, I.M., and Thompson, A.W., Eds., AIME, pp. 485-492, 1981.
5. Mackay, T.L., *Engineering Fracture Mechanics*, Vol. 11, pp. 753-761, 1979.
6. Shim, G., and Wei, R.P., *Materials Science and Engineering*, Vol. 86, pp. 121-135, 1987.
7. Wan, K.C., Chen, G.S., Gao, M., and Wei, R.P., *International Journal of Fracture* 69, pp. R63-R67, 1994.
8. Wan, K.C., "Mechanical and Chemical Aspects of Corrosion Fatigue of a 2024-T3 Aluminum Alloy in the Short-crack Regime", Ph.D. Dissertation, Lehigh University, 1996.
9. Nakai, Y., Alavi, A., and Wei, R.P., *Met. Trans. A*, Vol. 19A, pp. 543-548, 1988.
10. Gangloff, R.P., and Wei, R.P., "Small Crack – Environment Interactions: The Hydrogen Embrittlement Perspective, *Small Fatigue Cracks*, Ritchie, R.O. and Lankford, J., Eds., TMS-AIME, pp. 239-264, 1986.
11. Doig, P., and Flewitt, R.E.J., *Met. Trans. A.*, Vol. 14A, pp. 978-983, 1983.
12. Gangloff, R.P., "The Criticality of Crack Size in Aqueous Corrosion Fatigue", *Res. Mechanica Letters*, pp. 299-306, 1981.
13. Piascik, R.S., and Willard, S.A., *Fatigue Fract. Engng, Struct.*, Vol. 17, No. 11, pp. 1247-1259, 1994.

COMPOSITE COATING OF JET ENGINE AIR INTAKE AS A PROTECTION AGAINST ACOUSTIC FATIGUE

Jiří Fidranský and Jiří Fiala
Aero Vodochody a.s.
Odolena Voda, 250 70, Czech Republic
+420-2-685 8041-9
+420-2-685 8243
jiri.fidransky@aero.cz

ABSTRACT

The Aero Vodochody L59 advanced jet trainer is powered by DV2 engine with the trust of 4900 lb. A significant damage of air intake was caused by sonic fatigue after a very short time of aircraft prototype testing. Original design of air intake was made as a sheet formed riveted aluminum structure. Initial damage, such as stiffener cracks and broken rivets, occurred after 50 hours of engine run. Acoustic loading was analyzed afterwards and significant load of almost 160 dB was found. Based on previous experience we assumed that existing structure was not able to withstand acoustic pressures of such level, mostly concentrated on frequency of 3 kHz. Having in mind natural fatigue limits of aluminum structures, removable part of air intake was replaced for modified one. Driving force of modification was an idea of durable and easy to change structure, with better damping. Engine inlet part was substituted for stiffer ring, made of high strength steel, cylindrical part of air passage was replaced by carbon fibre monolithic structure of outstanding durability, but bifurcated air duct as a part of the fuselage structure was hardly to change. This part is fully integrated into the fuselage load path and proposed material change to carbon fibre composite structure was not feasible. When structural response of fatigue critical areas was analyzed, existing metallic structure, coated with glass and carbon fibre composite as all surface doublers has been proposed as the most suitable solution. Main design goals were to lower stresses in existing fuselage structure, to improve structural damping, to reduce stress concentration and to use material with the best available fatigue characteristic. Final design consists of metal sheet with stacked layers of woven glass and carbon fibres in Epoxy matrix. Composite layers were impregnated, bonded to supporting structure and cured in single cycle. Sophisticated stacking up improved stiffness, structural damping and reduced thermal induced stresses between adjacent layers into acceptable level. Hybrid wall structure was designed so as to be tolerant to accidental damage or to interlaminar cracks. Therefore, a very extensive qualification process took place, but major problems, we were faced, concern environmental resistance of composite to metal bonding, resistance to thermal induced stresses and full scale verification of service efficiency. Several hundreds of coupons were tested during qualification process. Final proof of structure was given by in service measurement. The lot production of composite air intake coat required building up a special shop. At the beginning of nineties, about 70 air intakes of L59 aircraft were treated. Total covered surface was about 45 square feet per one aircraft. All aircraft have been in service for about 6 years. There have been no service reported difficulties regarding composite coat of air duct, their wear or damage. The same treatment seems to be effective for any acoustic loaded air passages or heavy loaded open surfaces.

1. INTRODUCTION

The airframe structure durability is a very important feature for both aircraft operator and producer. Reliable, cost effective product and durability required by operators is definitely one of the measures of cost effectiveness. Aircraft manufacturers are driven by market demands as well as by government

requirements to offer dependable and long lasting product. Many ways have been used, more or less efficiently, to manage airframe durability. Service life of military aircraft has been significantly extended during last forty years. Earlier „safe life" philosophy has been changed in many cases to more sophisticated „damage tolerant" one. The main effort has been concentrated on aircraft primary structure. Most probable failure modes have been evaluated and structure behavior under various load scenario was modeled, either by computer technology, or by applying realistic loading during tests. Failure modes were established describing actual damage by the most probable way. Regarding aircraft primary structure, such approach is more or less successful at the moment. Highly agile aircraft life strongly depends on type of usage, so it is rudimentary to have dependable knowledge about service load history. To manage the task, various types of health and usage monitoring systems are used. To keep primary structure failures under control is still important task, but our concentration on accustomed failure modes is sometimes not sufficient. There are a lot of cases, when we are faced to very different way of fatigue damage. If that happened, not only prediction method fails, but furthermore traditional design approach for fixing the problem does not work as well. The paper presents an example of unusual fatigue failure when formerly used design improvements did not solve the problem. It was because of serious acoustic damage of jet engine air intakes. Unconventional technology was required to modify existing structure but used solution has been working excellently so far.

2. DESCRIPTION OF THE STRUCTURE

The L59 aircraft is a subsonic single turbofan two seat advanced trainer developed and produced by Aero Vodochody, Czech Republic. It is a redesigned version of the well known L39 jet trainer, which has been in production since mid seventies and over 2,800 aircraft served in about 25 customer countries. Compare with its predecessor, designated L39, L59 is equipped with more powerful DV2 engine, strengthened airframe, redesigned cockpit and canopy, hydraulically actuated control surfaces and advanced avionics package, including weapon delivery system. First customer delivered aircraft has been operational since 1990. Up to now, over 70 aircraft have been build for four customer countries. Aircraft overall appearance is shown on Fig. 1.

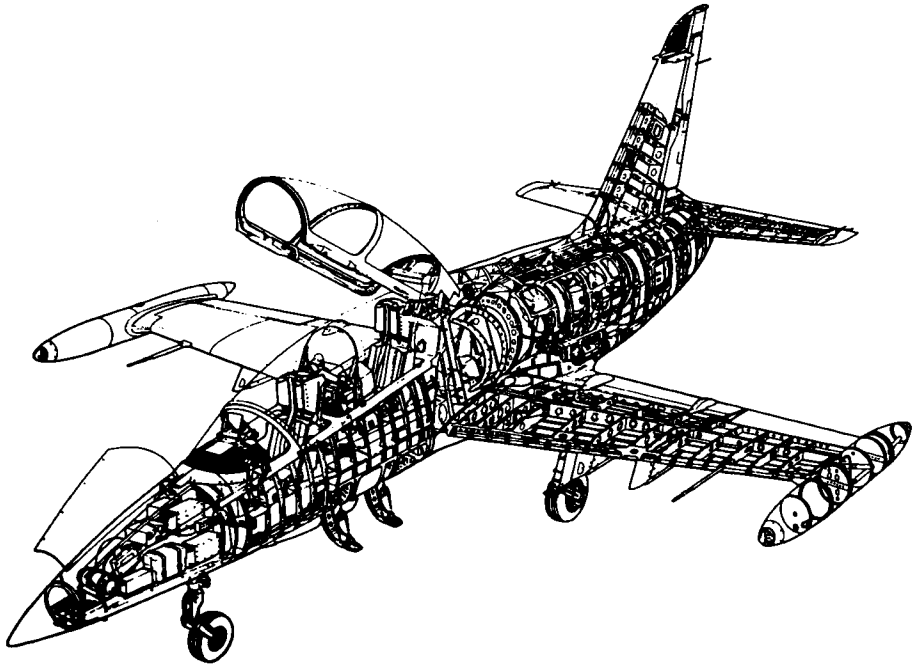

Figure 1 L 59 aircraft

The airframe structure is of a semimonocoque design, made mostly of aluminum alloys and steel. The aircraft was originally designed under safe-life criteria and proved by comprehensive full scale „flight by flight" tests. The service life of the L59 aircraft was qualified to 15,000 flight hours, or 30,000 missions. Loading spectrum for those figures corresponds to the advanced trainer utilization. Lifetime of the structure has been expected to be 30 years at least.

During airframe qualification, all load cases, expected as significant, were taken into consideration. But based on previous experience there was minimum attention paid to sonic fatigue of air intakes. There was never any evidence of their damage on L39 fleet, in spite of the fact, that more than 4 million flight hours had been accumulated. Unfortunately, after a short time of L59 prototype flight tests, our team was faced significant fatigue damage of that part.

The aircraft fuselage is a predominately semimonocoque structure, with bulkheads made of formed sheets and extruded stringers. Aircraft primary structure is made of 2024 and 2124 alloys. The bending load in the fuselage is carried out by extruded upper and lower longerons. The most loaded part of the fuselage is the central section, containing the fuel compartments and the engine air intake ducts. One piece wing is attached to the fuselage below the fuel tank floor and air intake ducts. There is a significant cut-out for the wing location in the fuselage structure. That is the reason, why central fuselage being extremely loaded part is the fatigue critical area. In spite of the fact, that air duct carries out minority of flight maneuver load, it is difficult to modify the structure.

The L59 air duct itself consists of several subcomponents. The original design was made of aluminum alloy sheets, made of 5052 alloy. The main part of bifurcated air duct, which is sheet formed and welded structure, was installed as an integral part of the center fuselage, riveted into the system of bulkheads and stringers. Wall thickness of the air duct was 2.0 mm. Adjoining part, closer to the engine, was rolled up cylinder, integrally stiffened. This part is connecting the embedded air duct with the engine inlet and it is removable, because of easy access during the engine dismantling. Figure 2 shows overall arrangement of the air duct system, including an illustrative information about composite coating layout.

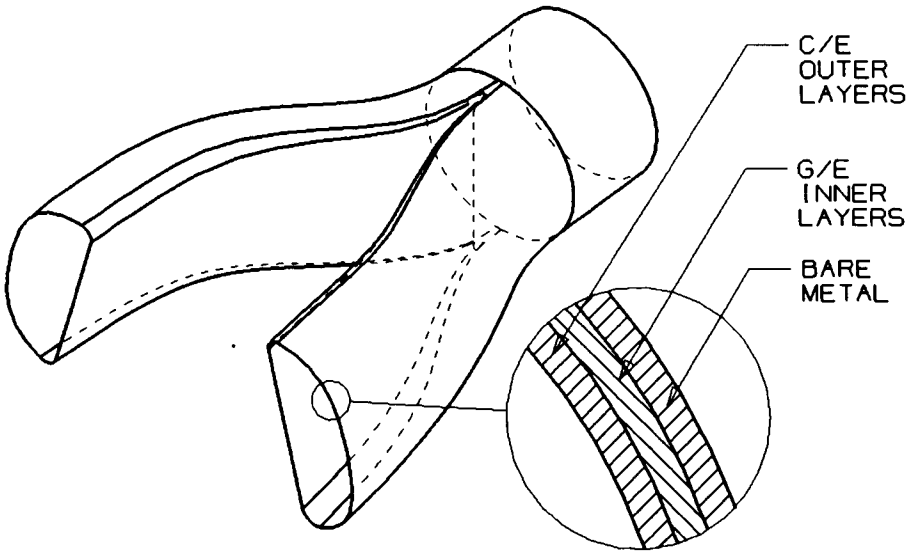

Figure 2 Air duct arrangement

The engine bay is housing DV2 engine, which is produced by PSPB, Slovakia. This two spool turbofan engine, having 22 kN (4,900 lbf) of trust, is of advanced, high efficient design. But high compression rate and fan efficiency has some disadvantages as well. The engine first-stage fan blade tip speed is

supersonic for the majority of power settings over the idle. This is why significant sonic load is generated by the fan and emitted in front of the fan disc. The acoustic energy of the shock waves is concentrated in a relatively narrow bandwidth of about 3 kHz. When initiation of structural damage was found, acoustic load along the air duct was measured. Very significant values of acoustic pressures were discovered, varying along the length of the air passage, but decreasing against direction of airflow. The engine intake in front of the rotor disc has to withstand the acoustic load of over 165 dB. Sonic load pattern is shown in Figure 3. Every part of the air duct has to be high-cycle fatigue durable.

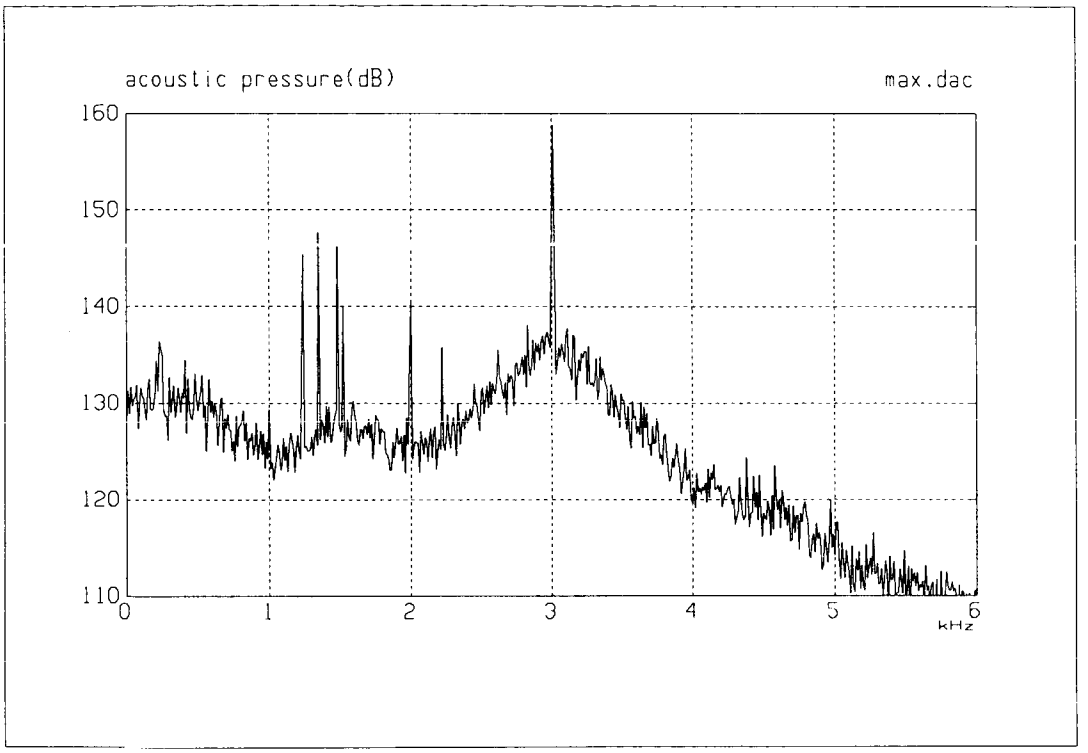

Figure 3 Acoustic pressure in air duct

3. AIR INTAKE DAMAGE

Even after initial stage of L59 flight tests, in late eighties, structural failures of the air duct were found. After about fifty hours of engine run, there were loose rivets, cracks in external air duct stiffeners, broken rivet heads and initial cracks from rivets countersink holes, [5]. As there is the biggest sonic load of the engine fan at zero aircraft velocity, the nominal stresses during the ground engine run on the air intake structure were measured. The maximum nominal stress was about 15 MPa, [2], pretty low compared with nominal stresses common in airframe structure due air maneuvers.

Some temporary provisions were done, to enable continuation of the flight tests, but more important was to analyze the problem and develop the high cycle fatigue durable structure.

4. SOLUTION OF THE PROBLEM

Acoustic load, generated by first-stage fan, has been calculated for various airflow and power setting conditions. Close to the engine fan, a computer model was based on 2D model of supersonic flow across the fan cascade. Farther the fan semiempirical model based on blade frequency and its combinative tones has been established, [1]. Dominant load was expected to be close to the 1st blade frequency. Possible decreasing of the load farther from the engine inlet was an important result of the analysis. Natural frequencies of the entire air passage were measured up to the range of several thousand of hertz. The main reason for initial analysis and measurement was to locate the most critical areas from the durability point of view. Coincidence of excitation and frequency response showed the zones, where stresses during service were repeatedly and precisely measured, [2].

Generally speaking, there are two ways of how to manage the appropriate response to the damaging acoustic load. Either to increase damping properties of the structure, or to enhance durability of the structure. Probably more effective is to enhance damping properties and even better is to lower the load by active damping. To apply active damping seems to be sometimes difficult, because of extra room needed for cellular damping, which is most common way of damping.

Having in mind all design aspects, different solution along the air passage has been applied. Most heavily loaded area close to the engine inlet was redesigned in a shape of cylindrical ring, made of high alloy steel. Removable air duct extension was modified as well and then fabricated as a monolithic carbon fibre reinforced plastic structure. Outstanding durability and good design of stiffeners reduced in service stresses to the acceptable level.

As mentioned above, main part of the air passage, bifurcated one, about 1.2 meter long, is build into the fuselage structure and it is hardly to change. This part is fully integrated into the fuselage load path and proposed material change to carbon fibre composite structure was not feasible. There were several options studied to improve durability of the structure. Solid aluminum rivets were replaced with tension type blind fasteners. Chemically milled sheets were used for strengthening the material of fastener rows. But more important was to reduce working stress either by increasing damping or by strengthening the wall structure. The simplest solution, to use thicker metal sheet, did not work, because excitation was to high and added mass did not allowed to reduce stresses significantly. Any commonly used damping materials were not efficient enough, moreover they were too heavy.

After analyzing the problem from structural dynamics point of view, the design goal was to find the structural modification to stiffen the structure, with minimum weight penalty and with additional damping capability. Endurance of added materials has to be better, than endurance of basic aluminum alloy structure. Hybrid fibre reinforced / metal structure seemed to be a good option, ref. [3].

Final design consists of metal sheet with glass and carbon fabrics layup in Epoxy resin matrix. Composite layers were impregnated and laid up on supporting structure and cured in a single cycle. The most important feature of the design was stack up of the composite layers. The overall thickness of composite is 2.1 mm.

4.1 DESIGN PRINCIPLES

Initial goal was to lower working stresses to about 30% of original value. Due to different reasons, final stress reduction was even higher. When the original air intake wall was coated, bending stiffness was about 5.3 times higher, than before. It was important, that this all surface composite doubler combined high bending stiffness with appropriate damping characteristic. To fulfill both needs, outer layers were of carbon fabric in Epoxy matrix and inner layers were made of glass fabric. Composite layup has been applied on inner surface of the air duct. Outer layers have had adequate stiffness and in conjunction with

original metal sheet have served as sandwich covers to inner layers. These have had lower modulus and appropriate damping. Interaction of both materials has been important for adjustment of damping and stiffening of the wall. As showed by coupon test of damping properties, coupons, coated with the same composite layup, have about 10 times higher damping, compared with uncoated coupons. More details are in [4].

Required characteristic were modeled on an analytical model and tested on specimens. Natural frequencies of the wall have been changed, but it was impossible to retune the structure to avoid having any frequency within the range of excitation. Although the stiffness of inner layers was due material limitation higher, than optimally required, the damping was still good enough. There is an example of FEM transient response analysis of the air duct shown on Figure 4.

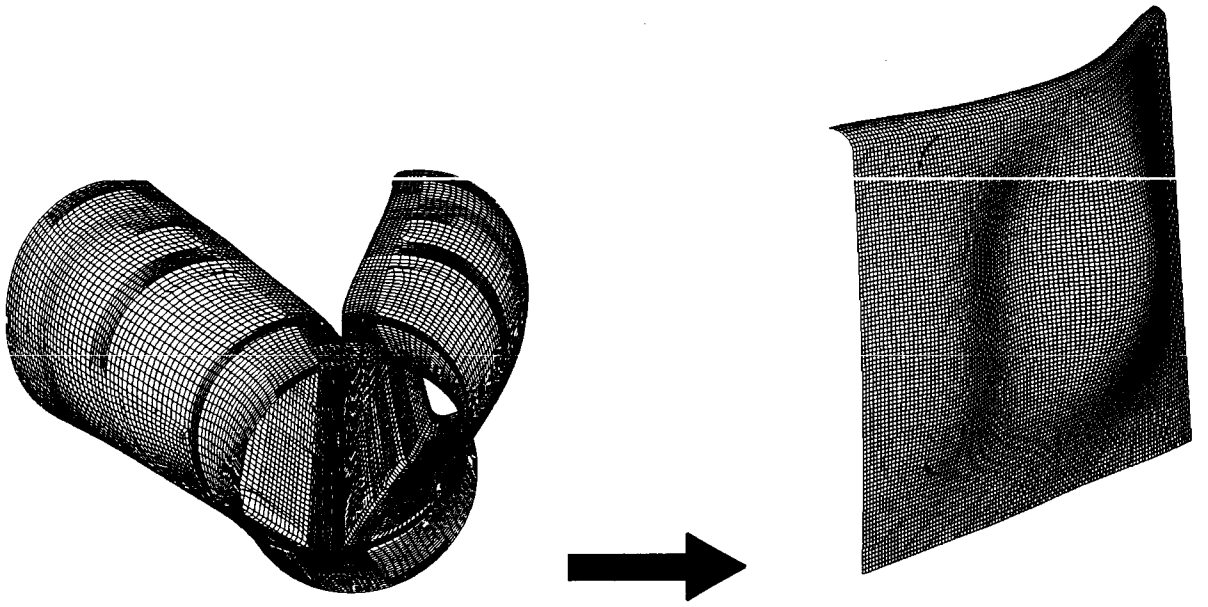

Figure 4 FEM analysis

The main design problem we faced up to was regarding the additional thermal stresses. Because of different thermal expansion coefficient of all materials used, e.g. carbon/Epoxy, glass/Epoxy and aluminum alloy, additional thermal stresses due temperature changes were significant. Based on the results of computational thermal analyses, maximum thermal stress was about 15 times higher, than the bending stress caused by acoustic loading. This stress has been acting on boundary between metal sheet and composite layup. The thermal stresses were both positive and negative, because of the curing process was applied at room temperature, with additional post curing at elevated temperature, but working temperature range has been expected from -55 °C (-67 °F) to 80 °C (176 °F). Temperature stress was important for two reasons. It was the highest stress acting on adhesive layer between metal and fibre reinforced plastic (FRP), so that layer became most critical area of the design. Second reason was that mean stress caused by thermal changes was added to alternating stresses caused by acoustic loading. Because life characteristic of any structure with mean stress above zero is degraded, composite coating has had some adversely effect on structure. Fortunately affect of mean stress has been much lower, compare with benefits of alternating stress reduction. It is also very important, that temperature cycling is not so frequent, at least compare with frequency of acoustic excitation.

Solution of stresses in adhesive layer was crucial for successful acoustic treatment. From design standpoint, the composite layup was optimized to reduce such type of stresses. Fortunately smooth stress pattern was beneficial for damping properties as well. As an effective solution, low modulus adhesive

layer with low stiffness fabric and tough Epoxy matrix was used. It was taken into consideration, that there is a significant risk of environmental degradation of strength and stiffness. Tensile or compression strength were not critical parameters of the design, but based on environmentally exposed coupon tests, a reduction of up to 60 % was anticipated. Biggest reduction concerns of values depending on matrix properties. Parameters driven by fabric properties were reduced much less, up to 80 - 90 % of original values. There was no problem to implement reduced parameters into design considerations, because strength margin was enormous. On the other hand, a special attention has been paid to environmental resistance of the adhesive layer. There were a hundreds of coupon tested with various bonding systems and matrixes. Shear and peel strength were tested on unexposed and environmentally exposed coupons. Finite element model predicted minimum level of bonding stress regarding to required cyclic and environmental endurance. It was necessary to develop special Epoxy based adhesive and matrix, to fulfill that requirement. Minimum strength reduction due to environmental degradation was a driving force for the development of an adhesive. It was important to develop an adhesive with long pot life, easy to work with, having good properties at elevated temperatures and minimum environmental degradation. Compromising of all needs was very difficult.

Composite coating has had excellent fatigue properties, when subjected to environmental and bending cycling. But as no manufacturing technique is perfect and there is a certain risk of in service damage, the design of composite coating has to be „damage tolerant". There were several damage modes predicted, but as a most probable and a most serious one, debonding at adhesive layer between composite and original metal skin was evaluated. To prove slow crack growth behavior, deformation energy rate has been measured by specimen test. As the statistically analyzed minimum the value of 0.5 N/mm was found. When maximum estimated value of interlaminar stresses (combination of thermal and bending stresses) was used for estimation of the critical crack length, it was proved, that the calculated critical length is even longer, than the air duct length. This result is valid, if elastic behavior is anticipated. As a conclusion, very little risk of unstable crack growth has been found under working conditions. Production defects of 10 mm have been anticipated as acceptable. All structure was tested by C-scan during quality assurance acceptance. Those relatively small defects were never exceeded during the production. It was difficult to predict flaw growth rate, especially when failure mode, like foreign object damage, is taken into consideration. That is why the structure is designed that way, that debonding up to the area of more than 300 mm x 300 mm is not a threat for structural integrity. Therefore, inspections in service are very easy, because by simple means like „coin tapping test" such delamination is easy to find. It is a good news, that during service so far, there was neither debonding nor other significant damage of composite coat, even though there were several incidents reported, like bird or runway debris impacts. Current fleet consists of about 70 aircraft and they are in service from four to six years.

Manufacturing of composite coating was a difficult task of engineering. Because of the inner air intake surface, which is about 4 square meters (45 square feet), the special clean shop was established. Composite inner coating was applied into the fully assembled structure, so there were areas difficult to access. After chromate anodizing and special surface treatment, the composite layers were laid up. To achieve optimal resin content glass and carbon fabrics were impregnated prior to installing on the surface. All surface was divided into several sections, manufactured one after another. Every section was cured separately. Pot life of matrix was limited, so good organization of process and skill workforce was essential. When coat was placed to proper position, stack up was vacuum bleed and cured by infralamp. After installation of all sections, entire coat was post cured at 80 °C (176 °F) to extend transient gel temperature. Because of necessity to go on with next coat section, when the previous one was completed, the whole coating of one individual aircraft took about ten working days. It was inevitable to solve many very difficult tasks during production and several unique procedures were developed, but it is out of the scope of this paper.

4.2 DESIGN VERIFICATION

Before entering the service, it was inevitable to verify design presumptions by full scale testing. It is hardly possible to do a full scale laboratory tests on structure subjected to heavy acoustic loading, because loading patterns are almost impossible to simulate. Frequency response of treated air intake was tested by ground vibration test, but as expected it was impossible to excite structure to higher modes, because of very high stiffness and damping. Most important verification was completed by in service strain gauges measurement. Based on previous experience, the same critical areas were measured without and with composite coat during ground engine run.

Measured response showed, that stress levels lowered to less than 30 % of original stresses, [7]. Stress reduction in measured areas differs from case to case. Comparison of stress levels at selected areas is shown on Table 1. Just for comparison, it can be mentioned, that analytically predicted value of stress reduction has been 17.4 %, [4].

TABLE 1: STRESS LEVELS WITH AND WITHOUT COMPOSITE COATING

strain gauge designation	**bare air intake** σ_{max} **[MPa]**	**air intake with coating** σ_{max} **[MPa]**	**stress reduced up to** **%**
C	12.7	0.3	2.4
G	14.4	4.0	27. 8
H	7.5	1.8	24.0
I	9.9	2.6	26. 3

Measured stresses were even lower than on L39 aircraft with AI25TL engine, [6]. That engine produces acoustic loading of about 20 dB lower, compared with DV2. There were never any evidence of cracking, or other failures on air duct of L39 aircraft. Thermal stresses are difficult to measure, but it was investigated during service, that temperature presumptions, regarding the maximum temperatures were too severe, even compare with hot climate in Africa. As air intakes are surrounded by fuel tanks, temperature of 80 °C was never reached. Also environmental degradation modes, applied during design, seem to be very conservative. After several years of service, when the majority of the fleet operates in African countries, the integrity of paint coat is still good and humidity effects seem to be less serious than anticipated. Final life analysis of the L59 air intakes, based on measured stresses, showed safe life far beyond the entire aircraft service life, [8].

5. CONCLUSIONS

The information described above shows that acoustic damage can be very serious phenomena in aircraft engineering. Although more common damage is regarding to the exhaust pipes and its surrounding, trans-sonic flow in engine fan may cause such an intensive excitation of air intakes, that conventional aluminum alloy structure can not withstand. That is why material change for material of better cyclic endurance was inevitable.

Composite doubles are commonly used for structural repairs of cracked or corroded aircraft skin. In some cases composite patches were used as structural reinforcement of beams as a weight effective and easy to install solution. As the authors know, the above described structure is the unique case, when composite doubler was used in large area as a surface protection against heavy loading. Special layup was used for increasing both stiffness and damping.

As the concept of the acoustic treatment of the jet engine air intake was very successful and as investigated not used before the application on the L59 aircraft, significant features of the solution were patented as the Czech Patent No. 280 188, [9].

Solution proved its efficiency during extensive testing and especially during long term service. First treated aircraft entered the service six years ago and about 70 aircraft were modified altogether. There were no service reported difficulties regarding composite coating and no significant wear or damage were found during periodical inspections. There have not been any failures of metallic structure reported as well. In service endurance of the air intake coating was also proved by undesirable way. One customer aircraft was written off due to extensive structural damage caused by heavy landing. Because of a cadet mistake, the aircraft landed on very high speed, ran over the end of the runway and stopped itself in a forest behind the runway. The fuselage was heavily deformed, outer wings were cut off and empennage was fully destroyed. Engine fan module was destroyed as well due to foreign object damage. Crew was injured, but survived. Central part of the fuselage had minor damages and air intakes, including its composite coat, were almost unaffected. There was no debonding or delamination found, in spite of the lot of foreign objects that went through it. It is strongly not recommended to prove production quality that way, but if it happens, it gives engineering satisfaction to the designers.

ACKNOWLEDGMENT

We would like to express our gratitude to the Aero Vodochody company for approval to reveal all valuable data and results of the research concerning the topic presented in the paper.

REFERENCES

[1] ŠULC, J., ŠAFAŘÍK,P., CEPNÍK, S.: Calculation of Pressure Fluctuation on Inner Wall of Air Duct of L39MS Aircraft, Equipped by DV2 Engine, Caused by Rotation of Fan During Supersonic Power Settings, (in Czech), Report ÚT ČSAV, Rep. No. T-421/90, 1990.

[2] ŠULC, J., BENEŠ, J., HŐSCHL, C., SMETANA, C., VESELÝ,E.: Measurement of Pressure Fluctuation and Dynamic Response on Inner Wall of Air Duct of Prototype L39MS Aircraft, Equipped by DV2 Engine, During Engine Ground Run, (in Czech), Report ÚT ČSAV, Rep. No. T-429/91, 1991.

[3] FIDRANSKÝ, J.: Development Study of Composite Air Duct Coating of L39MS Aircraft, (in Czech), Aero Vodochody, Rep. No. PP.3 - 15.91, 1991

[4] FIDRANSKÝ, J., HAUSMAN, J.: Final Report Concerning Structural Integrity Analysis of Composite Air Duct Coating of L59E Aircraft, (in Czech), Aero Vodochody, Rep. No. PP.3 - 11.92, 1992

[5] FEDERER, F., FIDRANSKÝ, J.: Evaluation of Strain Gauge Measurement and Air Duct Durability Analysis of L39MS Aircraft, (in Czech), Aero Vodochody, Rep. No. PP.3 - 13.91, 1991

[6] ŠULC, J.: Measurement of Pressure Fluctuation on Inner Wall of Air Duct of L39ZA Aircraft, Equipped by AI25TL Engine, During Engine Ground Run, (in Czech), Report Techson, Rep. No. T/Z-07/91, 1991

[7] SYMON, P., PŐSSNICKER, O.: Measurement of Dynamic Response of L59E Air Duct During Engine Run, (in Czech), SVÚSS, Rep. No.: 93-03101,1993

[8] FIDRANSKÝ, J.: Service Life Qualification of Air Duct Composite Coating of L59E Aircraft, Equipped with DV2 Engine, Aero Vodochody, (in Czech), Rep. No.: PP.3- 01.93, 1993

[9] Czech Patent No. 280 188, The Composite Coating Used for Damping of Acoustic Vibration, (in Czech), applied for patent March 20, 1992, patent administered since November 2, 1995

CF-18 INNER WING FRONT SPAR CRACKING

Yvan Francoeur
Bombardier Services, Defence
10,000 cargo road A-4
Mirabel International Airport
Mirabel (Quebec), J7N 1H3, Canada
Tel. (450) 476-4584
Fax. (450) 476-4451
Yvan.Francoeur@Services.Bombardier.com

Daniel Adam
Bombardier Services, Defence
10,000 cargo road A-4
Mirabel International Airport
Mirabel (Quebec), J7N 1H3, Canada
Tel. (450) 476-4879
Daniel.Adam@Services.Bombardier.com

ABSTRACT

Cracks at various holes on the Canadian CF-18 Inner Wing Front Spar (P/N 74A110604) near the Inboard Leading Edge Flap (ILEF) Drive Hinge were detected. The most cost effective modification for this location involve either coldwork, forcemate or IF bushing. The critical holes all located in a seal groove therefore the spar can only be reworked on 70% of its thickness. In addition, the holes are separated 1.0 inch apart so residual stresses of the coldwork and forcemate process super-impose at the center of the two hole. In this situation, available fatigue analysis produces highly questionable results. A fatigue coupon test is therefore required. The finite element analysis performed to evaluate the residual stress of each process and define the adequate test specimen geometry is presented. An experimental substantiation of the FE results will follow. Finally a brief discussion of the coupon test is provided.

INTRODUCTION

Premature cracking of the front spar (P/N 74A110604) inboard of the ILEF attachment (Figure 1) is an outstanding problem on the Canadian CF-18. This problem affects early spar configurations –2037 and -2037a that represent approximately 35% of the Canadian CF-18 fleet. The two configurations have similar cross-sections but they vary in terms of fastener patterns and size, and seal groove geometry.

The manufacturer's retrofit for this modification consisted in opening the hole, coldworking (CW) it and installing interference fit (IF) fastener. On many Canadian Forces' (CF) aircraft, the extent of cracking have exceeded the limits of the manufacturer's mod packages, so alternate repairs involving the installation of steel interference fit or forcemate bushings were developed.

The front spar of the International Follow-on Structural Test Program (IFOSTP) full-scale fatigue test (FT55) was recently found cracked at this location. The FT55 front spar configuration is –2039 that correspond to the improved configuration of the front spar (see STRUCTURAL DESCRIPTION). Since the FT55 test is aimed at testing the CF-18 center fuselage, the representativity of this failure for the CF-18 –2039 spars will need to be confirmed.

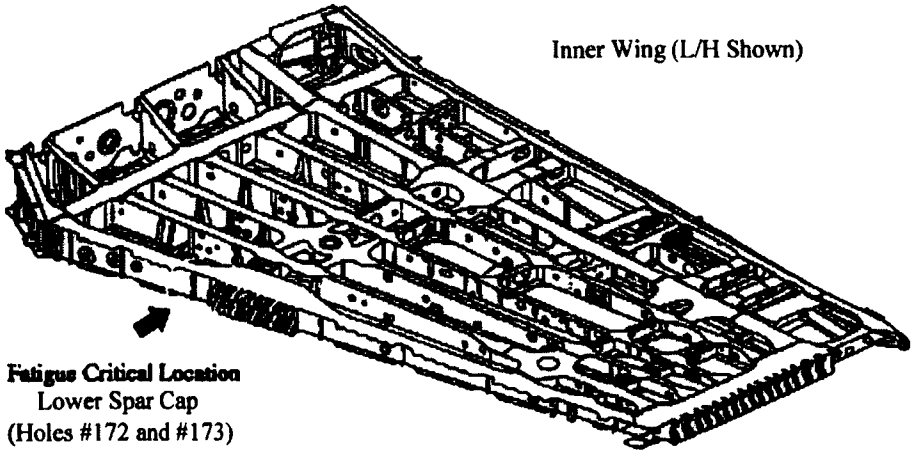

Figure 1. CF-18 Inner wing front spar and ILEF attachment

Based on Preliminary fatigue analysis it is believed that these modifications may not, provide a full service fatigue life. In particular, the effect of coldworking and forcemating has been severely questioned due to the onset of high residual stresses away from the edge of the holes. Normally, this usual secondary effect of coldworking and forcemating processes, is not a concern. However for the front spar, the situation is more complicated due to the rework of adjacent holes (see STRUCTURAL DESCRIPTION). As a result, the residual stresses are super-imposed and a stress peak is observed between the reworked holes. Last but not least, the holes are located in seal-grooves. Consequently, only 70% of the spar cap thickness is reworked.

Due to the presence of the residual stresses and plastic deformation current analytical tools are unable to provide reliable fatigue life estimates. A fatigue coupon test will therefore be performed to experimentally quantify the relative Life Improvement Factor (LIF) between each process (i.e. CW, FM & IF).

The finite element analysis performed to evaluate the residual stress of each process and define the adequate test specimen geometry is presented. An experimental substantiation of the FE results will follow. Finally a brief discussion of the coupon test is provided. Unfortunately, delays in the execution of the fatigue coupon test have prevented the presentation of final results.

Note: Through out this paper, when a rework is performed, either experimentally or analytically, the hole # 173 is always reworked before hole 172. This sequence is important because of the non-linearity nature of the problem (i.e. plastic deformation).

STRUCTURAL DESCRIPTION

The spar is made of die forging aluminum 7050-T7452 (formerly 7050-T73652). Its "C" channel form connects the upper and lower carbon epoxy wing skins (3/4" thick). The spar cap thickness varies between 0.190" (config 2037) to 0.270" (config 2039). As per blue prints, the critical hole diameters vary between 1/4" to 3/8" and are located 1.0" apart. The inner wings are "wet" fuel tanks. The sealing of the spar to skin interface is ensure by two 0.060" deep seal grooves (see Figure 2 un-shaded area). The groove width are between 0.470 (config 2037) to 0.530" (config 2039).

The failures are located on the lower spar cap just inboard of the ILEF (ILEF) drive attachment. In all cases, cracks were reported in at least one of hole 170 through 173. Fractographic analyses have confirmed initiation sites in the hole bore but also in the seal groove radius.

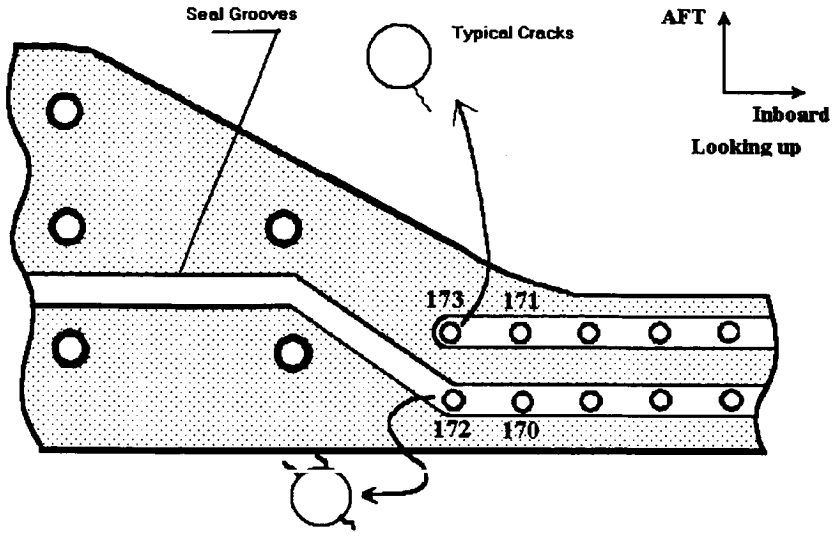

Although all four holes were reported with cracks, because of the similarity and also because preliminary analysis have suggested that holes 172 & 173 be more critical, the analysis will concentrated on those specific holes.

Figure 2 Spar Geometry

RESIDUAL STRESS ANALYSIS

In order to characterize the state of stresses produced by the different processes and also to define the geometry of a representative fatigue test specimen, non-linear Finite Element Analyses (FEA) for the three processes (i.e. CW, FM & IF) were performed. This section will present the details and results of these analyses.

First, a local model of the spar geometry (spar model) was analyzed. The spar model is similar to Figure 2 but only includes holes 172 & 173. In addition it was decided not to include the seal groove geometry to simplify the analysis. The description of each process characteristics is provided in TABLE 1. They were selected to represent the actual processes as normally implemented and not to produce equivalent residual stress/strain field.

TABLE 1 PROCESSES CHARACTERISTICS

Description	CW	FM	IF
Hole ID	7/16"	7/16"	7/16"
Interference	4.5% [1]	2.67% [2]	0.0025"
Bushing Material	N/A	Steel Cres	Steel Cres
Bushing Hole ID	N/A	5/16"	5/16"

The analysis showed that for the CW and FM processes, the entire section between the two holes exhibit plastic deformation. The CW plastic deformations and major stress contour plots are presented in Figures 3 and 4 respectively. In Figure 3, the area defined by the contour labeled "1" corresponds to 10 με and therefore can be seen as the limit of the plastically deformed zone. In Figure 4, approximately 15 and 20 ksi are observed between the holes and at the spar edge respectively.

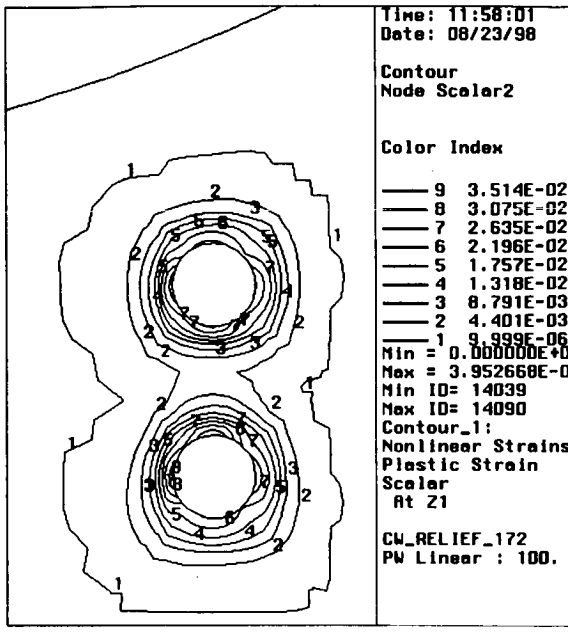

Figure 3 CW 4.5% plastic deformation

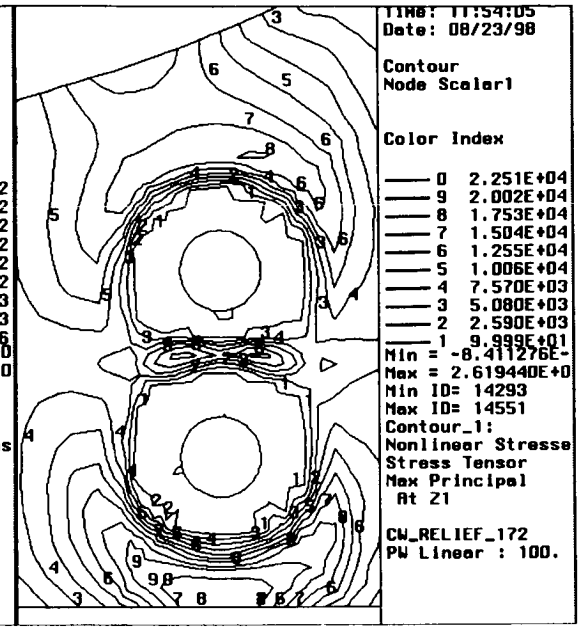

Figure 4 CW 4.5% Major residual stresses

In the Process of matching the spar model results, it was possible to demonstrate that a straight coupon 2.75" wide was able to adequately represent the spar geometry. This optimized test specimen geometry is presented in Figure 5.

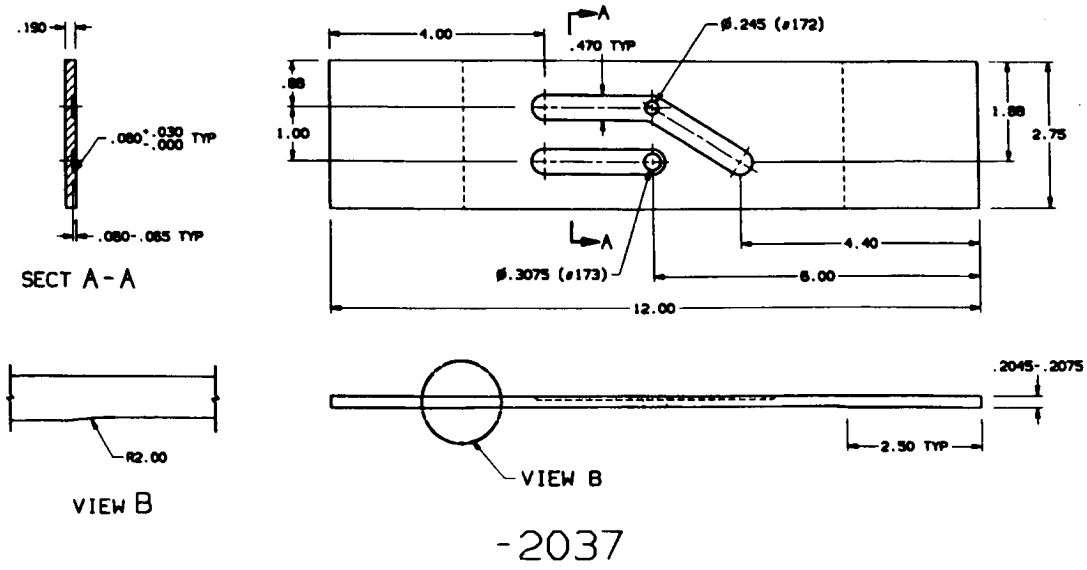

Figure 5 Coupon geometry

Comparative FE stress results for both the 2.75" coupon model and the spar model are presented in Table 2. Results are provided for seven characteristic locations defined on the axis formed by the center of the two critical holes, starting on the forward edge and ending on the aft spar cap edge. Note that "center" results do not exactly represent the maximum value because the maximum stress is usually shifted in direction of the first reworked hole. Table 2 refers to axial stresses in the spar cap.

TABLE 2 SPAR & COUPON FEM COMPARATIVE RESULTS

	Coldwork			Forcemate			Interference fit		
Locations	Coupon	Spar	Delta	Coupon	Spar	Delta	Coupon	Spar	Delta
Spar fwd edge	29	25.7	3.3	17.7	15.5	2.2	12.1	10.4	1.7
Hole 172 fwd edge	-44.3	-45.7	1.4	-3.6	-5	1.4	38.3	37.7	0.6
Hole 172 aft edge	-53	-54.7	1.7	-8.9	-10.5	1.6	36.7	35.7	1
Center	6.5	4.1	2.4	29.8	29.2	0.6	20.9	20.2	0.7
Hole 173 fwd edge	-37.1	-36.8	-0.3	-8.6	-10.5	1.9	36.7	36.6	0.1
Hole 173 aft edge	-40.1	-45.7	5.6	-3.3	-7.3	4	38.7	36.1	2.6
Spar aft edge	27.6	10	17.6	17.4	6.9	10.5	11.9	4.9	7

Except for the aft edge, Table 2 shows a fairly good correlation between the spar and coupon FEM's. However, considering the low probability for the aft edge location to develop cracks, the selected coupon geometry is considered adequate. In addition, the results of the coupon aft edge are very similar to those of the forward edge. This is beneficial because it will provide two test points for the forward edge where a higher possibility of crack is present.

The expected stress amplitudes of the coupon test were evaluated. From IFOSTP/FT55 strain readings, it was established that the operating gross stress of the spar cap should be between 15.0 to –6.0 ksi. These load conditions were applied to the coupon model. The resulting stress amplitude at all locations for each process is presented in Figure 6.

The location of crack initiation is only obvious for the IF process (i.e. at the hole edges). For the other processes, CW & FM, it is very difficult to confidently establish the potential crack initiation site(s). For the coldwork process, the edge of the coupon (and consequently the actual spar) operates at a high stress level compared to the rest of the section. Because of the Kt factor, the CW stress amplitude is larger at the edges of the hole than at the coupon edge. This large amplitude is absent in the other processes due to the hole propping under the bushing/fastener interference. For the FM process, the stress amplitude suggests that crack initiation might occur between the two holes.

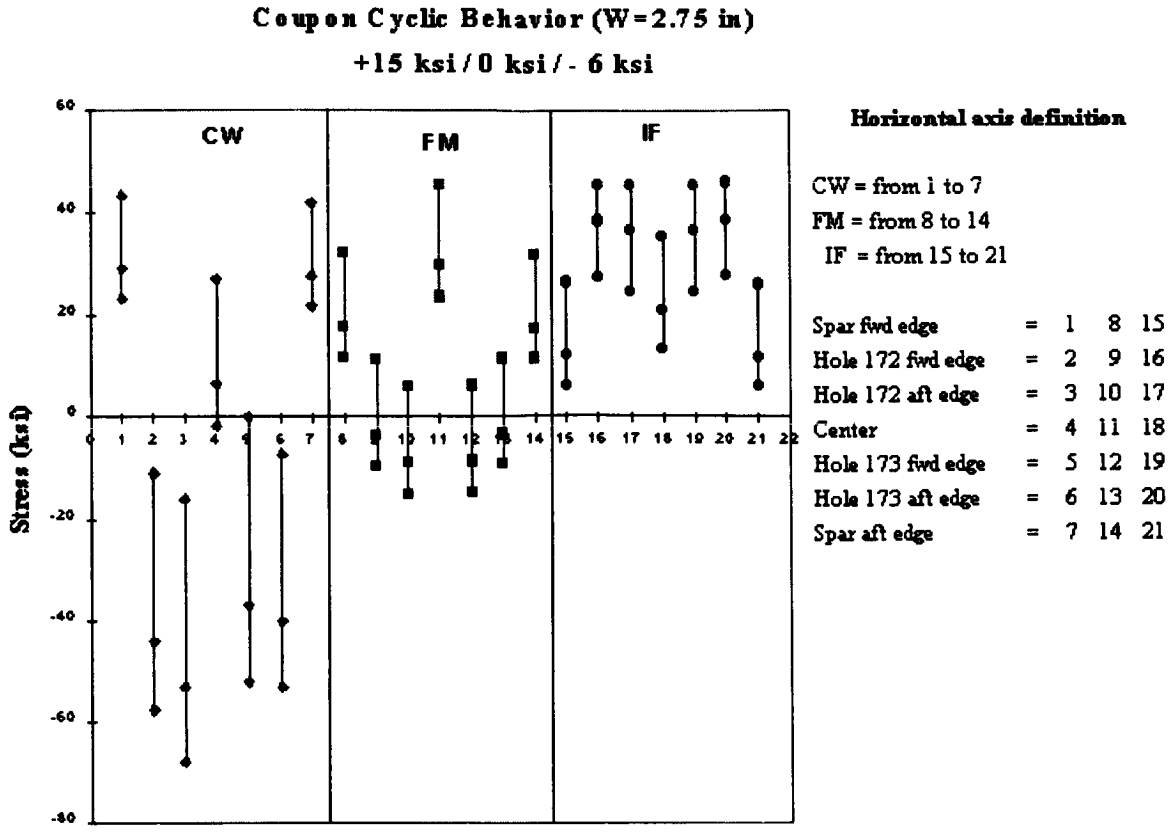

Figure 6 Comparative Stress Amplitude

EXPERIMENTAL VERIFICATION

For the CW configuration, the FEA has highlighted high residual stresses on the edge of the spar. In order to verify the FE results and evaluate the possibility of the fatigue coupon cracking on the edge, it was decided to experimentally evaluate the coldworking effects on a real wing. The experiment was performed on an unserviceable wing having the upper skin removed and therefore providing access to the upper surface of the spar cap.

In addition to the edge verification, it was decided to instrument the entire cross section of the lower spar cap to verify FE residual strain distribution. Also, the effect of reaming the holes on the residual strain/stress distribution was evaluated. Finally, since FEA was predicting large through the thickness stress gradient, attempts were made to confirm this effect but since only the side of the spar cap could be instrumented it appears that only a small gradient was recorded.

A total of 16 gauges were installed on this wing (see Figure 7): 12 on the upper surface, 2 on the forward edge (#1 & 2) and 2 on the aft edge (#15 & 16). As the access to the spar was only available from the top of the wing, the gauges could only be installed on the upper surface of the spar cap (CW entry side; opposite to the seal groove).

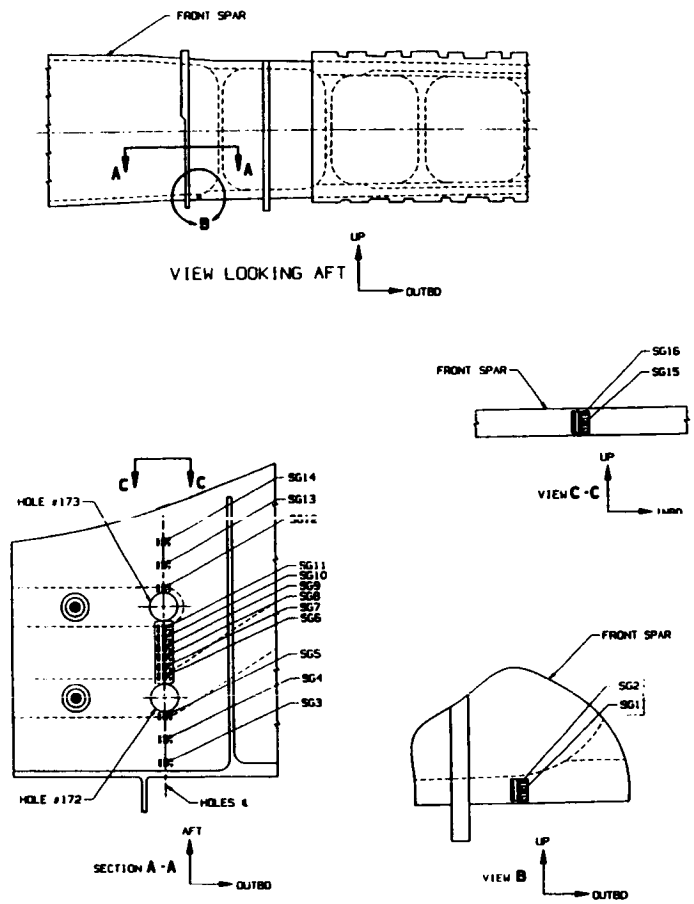

Figure 7 Instrumented Front Spar

Again, as for the FEA, hole diameters were reworked to 7/16". An interference of 3.91% was established from the diameters, mandrel and sleeve measurements. This is slightly less than the interference level used in previous FEA (4.5%). Corrections to the FEA were made to account for this variance.

To adequately compare experimental and FEA result, it was necessary to account for the stress gradient through the thickness of the spar cap because strain gauges were only installed on the upper surface of the spar cap. Therefore, the FE results were obtained from a 3D FEM of the spar (configuration 2037) where contrarily to the residual stress FEA, sealed groove were included.

Figure 8 shows the strain distribution throughout the lower spar cap for both the analytical results and the strain gauge readings. Although both sets of data present the same characteristic (shape), significant difference is observed between experimental and analytical strain readings; with the analytical results being considerably higher (maximum of 4.5% difference; Figure 8 entry side). It was thought that the effect of adjacent holes (170 & 171) could explain the differences but after verification it appears that this is not the case. Rather, the differences are attributed to modeling limitations because the CW process is strictly modeled on the FEA by radial expansion from the center of the hole. Therefore, the actual effect of pulling the mandrel through the hole is not simulated.

Figure 9 shows the CW FE stress distribution corresponding to the strain distribution shown in Figure 8. The shape difference between Figures 8 & 9 clearly highlight the non-linearity behavior of the phenomenon. At the holes' edges, the maximum compression stresses are obtained but for the strains, it is a maximum tensile strain that is observed. Because of this non-linearity, and the modeling limitations, it is not possible to extrapolate the stress levels on the actual wing from the strain differences provided in Figure 8.

One can also note on Figure 9 that the entry and exit stress distribution seem to be reversed compared to the usual CW behavior. Normally, compared to the entry side, the exit side exhibits higher compressive stress at the edge and higher tensile stress away from the hole. In Figure 9, the opposite is observed. This is a direct consequence of the seal groove effect because the spar cap is not reworked on it entire thickness. Therefore, when the holes are expanded, they pop-out because the neutral axis is not at the center of the cap, and this produces an effect opposite to what is normally observed.

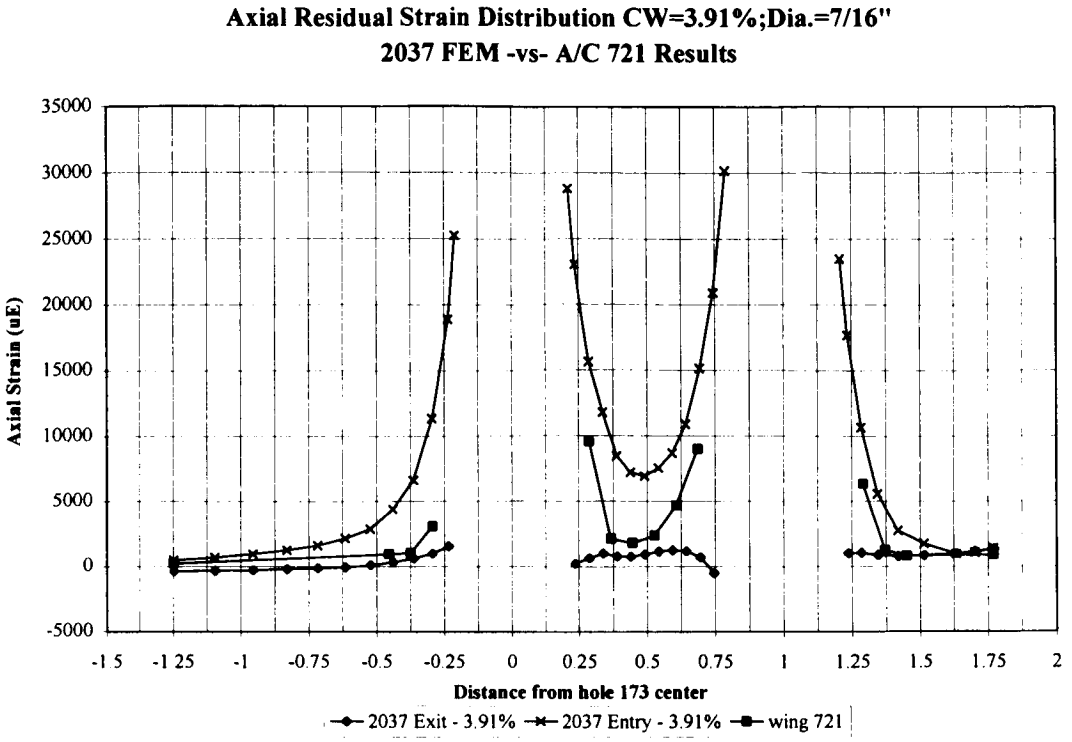

Figure 8 Experimental and Analytical Strain Deformations

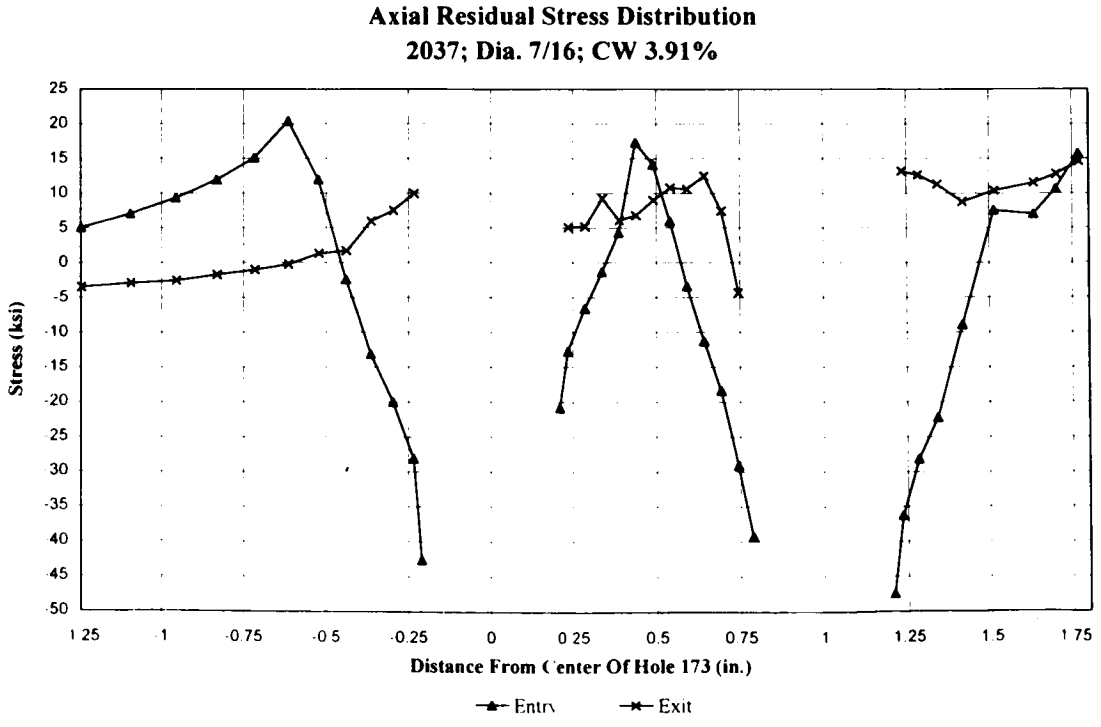

Figure 9 Axial Residual Stress - Entry & Exit

Initially, the aim of the experiment was to evaluate the possibility of the crack initiating on the edge of the actual spar in the CW configuration. From Figure 8, it can be noted that between 1.5" and 1.75"[3] (spar edge), experimental strain results tend to increase slightly. Also, analytical strain predictions are very close in this area to experimental measurements. Considering this situation, it is tempting to consider the FEA valid for the edge of the spar.

In fact, this might the case because the differences are attributed to the radial expansion of the hole rather than physically pulling on the mandrel. Therefore, away from the hole, this effect should be less significant. Moreover, there is minimal plastic deformation on the edge of the spar. If the FEA stress distributions are considered accurate close to the spar edge then, test failure on the coupon edges must be considered representative.

To confirm the effects of "stress-relieving", the effect of reaming the holes was evaluated by recording strain before and after reaming each hole. Results showed a strain reduction between 4% to 7% after both holes were reamed. In addition, readings taken one hour after the last reaming revealed an additional strains reduction of 3%.

DISCUSSION

Throughout this paper, we have focused on the residual stress analysis, experimental stress verification and strain distribution on the CF-18 front spar critical location inboard of the ILEF attachment. This discussion must be put in perspective within the scope of the project: to design the most efficient and cost effective repair for the CF-18 front spar.

The other alternative to reworking the holes by increasing the fatigue life will be to reduce the stress and deflection levels at the critical location. This may be achieved by inserting a fitting inside the "wet" wing cavity. However, access inside the wing cavity is cumbersome and certainly undesirable. All possible efforts must analyze the benefits from any possible rework that only requires access to the hole bores. Processes that meet this requirement are the CW, FM & IF. Unfortunately, available analytical tools to estimate the attainable fatigue life of these processes are unreliable. It is therefore required to rely on experiments to obtain the most accurate prediction.

The analysis presented in this paper contributed in defining representative test specimen geometry. Nonetheless, distinct issues remain to be resolved. As a minimum, it must be ensured that the strain induced onto the test specimens for the fatigue coupon test must closely match the unserviceable spar experimental strain results. Also, if excessive deformation occurs onto the specimen after the rework, an anti-buckling guide may have to be adapted to the testing fixture. It is expected that trial and error at the beginning of the fatigue test will provide the solution to these issues.

Early in the definition of the coupon test, two decisions were made in order to minimize the complexity and cost of the test.

1. The load transfer was omitted through the fasteners to reduce complexity and minimize scatter in result.
2. Surface etching of an actual spar cap in the area of interest revealed that the grain structure orientation is aligned with the spar axis. To reduce costs, the test specimens will be manufactured from aluminum plates instead of actual die forging. The plate thickness must however be approximately equal to the forging thickness at time of heat treatment.

Fractographic analysis revealed crack initiation sites in the seal groove radius. It is therefore important that the coupon test tries to replicate this phenomenon. Because the seal groove radius is never reworked, testing the specimen prior to the reworking will accumulate damage and simulate actual aircraft situation.

CONCLUSION

Based on preliminary analysis, it is believed that existing modification of the front spar may not, provide a full service fatigue life. Due to the presence of residual stresses and plastic deformation current analytical tools are unreliable. A fatigue coupon test was prepared to experimentally quantify the relative LIF between each process (i.e. CW, FM & IF).

To define the geometry of a representative fatigue test specimen, FEA for the three processes were performed. It was also established that a straight coupon 2.75" wide was able to adequately represent the spar geometry.

FEA having highlighted high residual stresses on the edge of the spar. To evaluate the possibility of crack initiation of the edge of the spar due to these high stresses, the FE results were verified by experiment on a real wing. The experiment revealed that although experimental and analytical strain results present the same characteristic (shape), close to the holes, significant difference in the result magnitude are observed and away from the holes, result difference is negligible. The phenomenon being highly non-linear, and also because of modeling limitations, it is not adequate (at least close to the holes) to extrapolate the stress levels on the actual wing from the experimental and analytical strain readings.

Unfortunately, delays in the coupon test prevent the presentation of the final result and consequently the most interesting conclusion remain to be establish.

END NOTES

1 Mandrel OD w.r.t. hole ID
2 Deformed bushing OD w.r.t. hole ID
3 Contrarily to FEA where edge results were taken directly on the surfaces, experimental edge results were obtained from gauge 1, 2, 15 & 16 located on the spar cap edge (Figure 7).

The Second Joint NASA/FAA/DOD Conference on Aging Aircraft
August 31 – September 3, 1998, Williamsburg, Virginia

Reduction in Fatigue Damage Incurred During Ground Operations on Rough Runways

Poster Presentation

Tony Gerardi, APR Consultants, Inc. Medway, OH. (937) 849-6795
Doug Tritsch, University of Dayton Research Institute, Dayton, OH (937) 229-4482
Robert Knarr, Consultant, Beavercreek, OH

EXECUTIVE SUMMARY:
The combination of expanded usage, extended service life, and fiscal constraints has led to a focus on the technologies which support the structural integrity of aging aircraft. The aim is to reduce the support and sustainment burdens of these aging aircraft. This includes safely extending the useful service life of an airframe by reducing the fatigue damage accumulation rates. Reducing the number of damaging events or the magnitude of some damaging events will mitigate the fatigue damage accumulation. The results from this DOD, STTR* Phase I funded effort offers a concept that involves altering the landing gear service procedures to increase the strut precharge pressure. This non-intrusive technique will significantly reduce the dynamic loads experienced by an aircraft during takeoff.

The fatigue life of an aircraft is based in part, on the number and magnitude of ground-air-ground (GAG) cycles the aircraft is expected to experience. Recall that the "ground" loads define the alternating portion of the GAG cycle. Fatigue crack initiation and growth rates are most influenced by changes in the alternating part of a damaging load cycle. Generally, the design has factored in dynamic loads experienced by the aircraft during takeoff, measured as accelerations at the center of gravity, (load factors). In particular, the negative load factors the overall GAG definition. It is important to recall that aircraft are designed for more positive g's than negative g's. However, it is not unusual to exceed 0.5 g on paved runways that have deteriorated with time and use. Consequently, operations on rough runways will reduce the life of the aircraft.

In Phase I of this STTR, the overall objective was to develop a practical method for estimating the extended airframe life by reducing loads due to ground operations on rough runways. The primary purpose of Phase I was to determine the feasibility of the concept that increasing the landing gear strut precharge pressure as an approach to achieving a reasonable reduction in the airframe loads. Phase I investigations have shown that ground loads can cause airframe structural damage and is more prevalent than previously suspected. One example was an L-1011 found with a 24- inch long crack in a rear wing spar web at the main landing gear trunnion attachment. The results of this effort included:

1) Establishing that a 30% reduction in the magnitude of the load was achieved by increasing strut precharge pressure.
2) Validation with hydraulic shaker tests.
3) A preliminary estimated fatigue life factor of 1.15, (15% life extension) achieved by reducing airframe loads due to rough runway ground loads.

This poster presentation covers the efforts and results from the Phase I STTR and describes the next step prior to implementation.

* Conducted for The AFRL at Wright Patterson AFB Ohio, Mr Mike Zieglar (937) 255-6104 ext 354

Objective

Extend Aircraft and Component Life by Reducing Ground Loads

Concept

Landing Gear Strut Servicing Modification

"Increase Strut Precharge Pressure "

Proof of Concept Test

Active Gear Experimental Test Setup

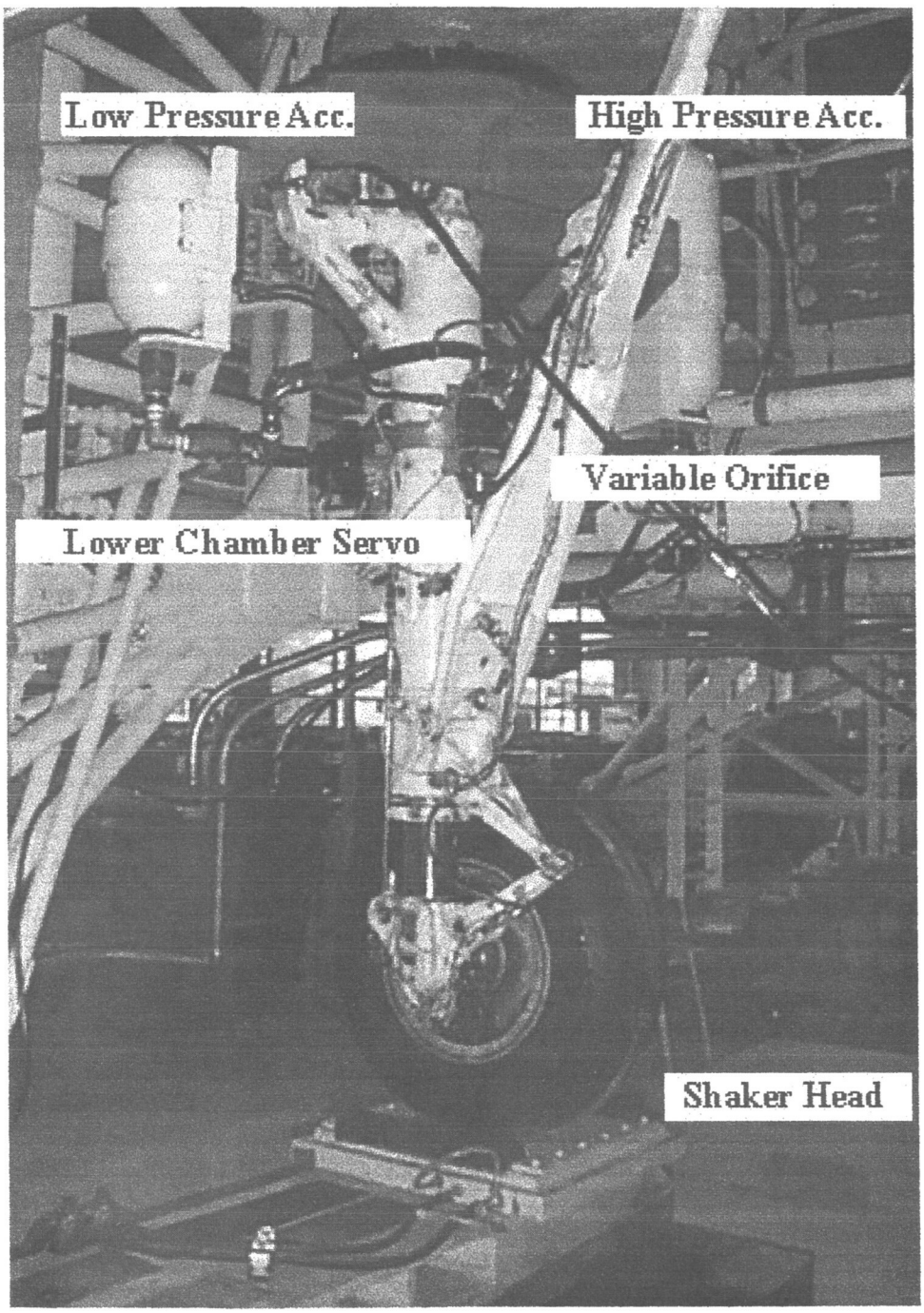

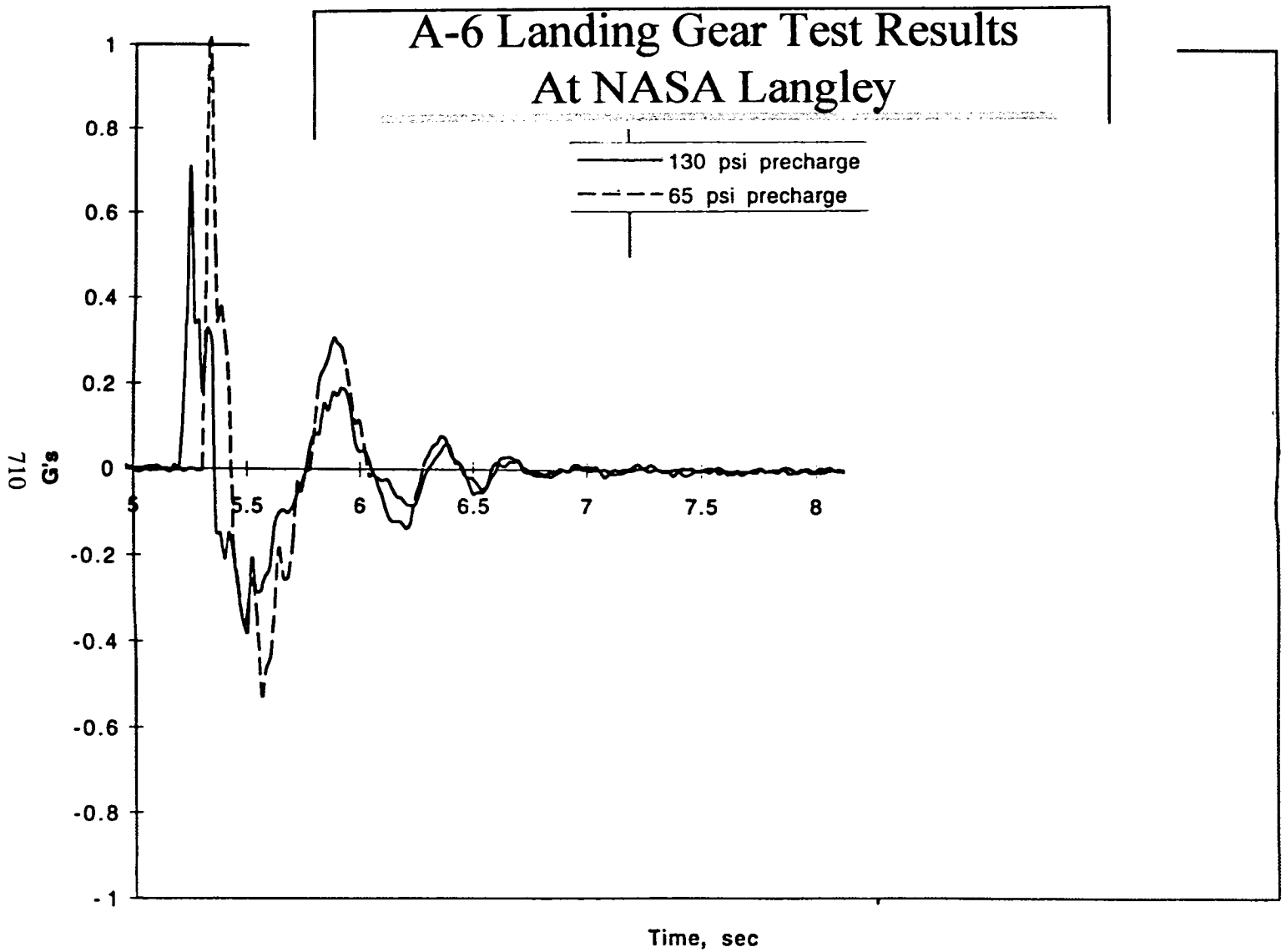
A-6 Landing Gear Test Results
At NASA Langley
130 psi precharge
65 psi precharge
710
G's
1
0.8
0.6
0.4
0.2
0
-0.2
-0.4
-0.6
-0.8
-1
5
5.5
6
6.5
7
7.5
8
Time, sec

Life Improvement

Cycle Counted Loads for B737, Predicted Nz for Normal Takeoff at Washington National + Measured Nz for Flight

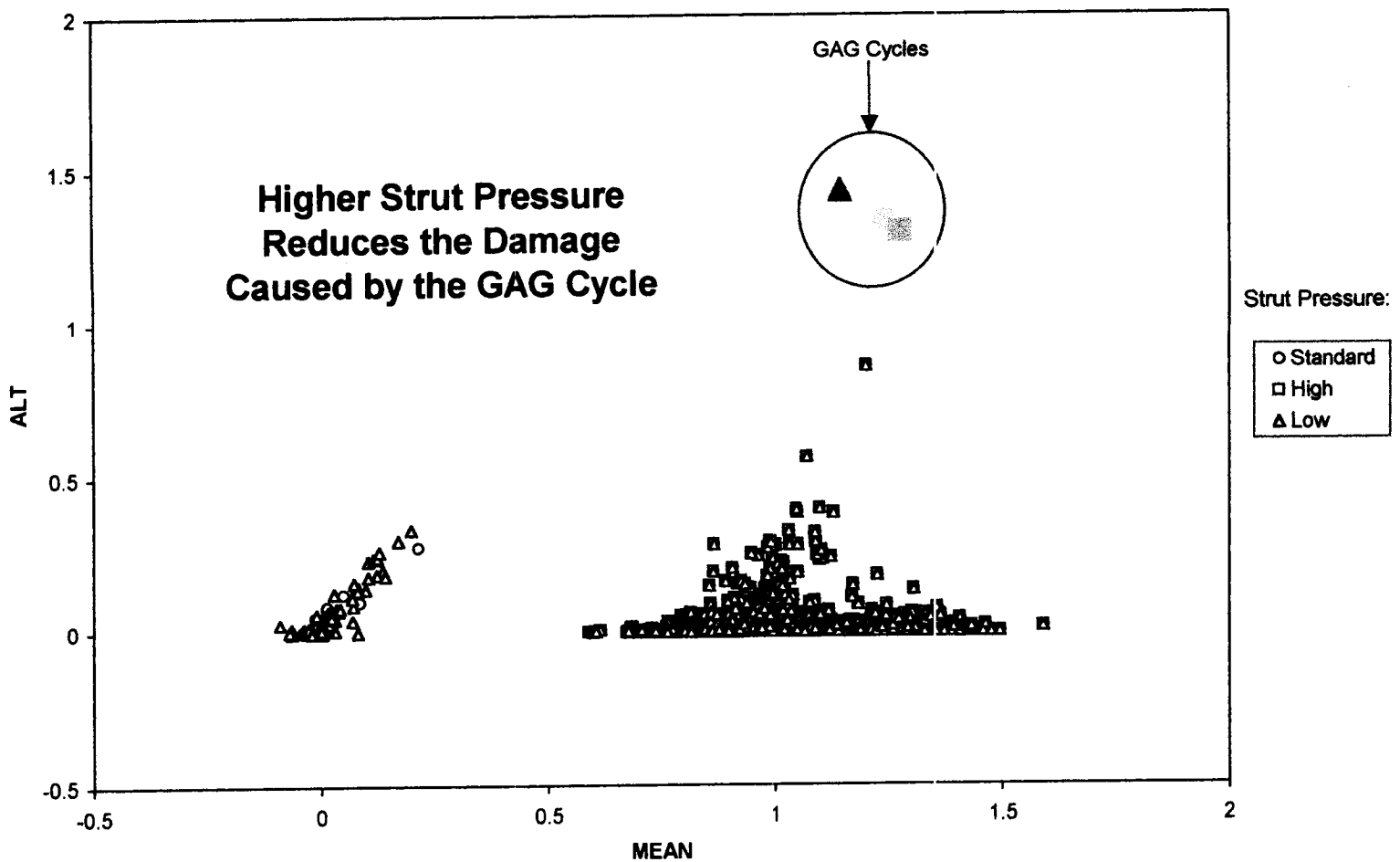

Advantages & Disadvantages

- Advantages
  - Workable/Practical
  - Across the Board Improvements
  - No "Mods" Required
  - Extended Life
  - Reduced Operating Costs
- Disadvantages
  - Modify Strut Servicing Procedures
  - Unique to Aircraft Type

Next Steps

1. Define the Loading Environment
2. "Try it": One - Two Year Operational Usage
3. Implementation: Develop New Strut Servicing Procedures for Each Aircraft Type

Define the Environment

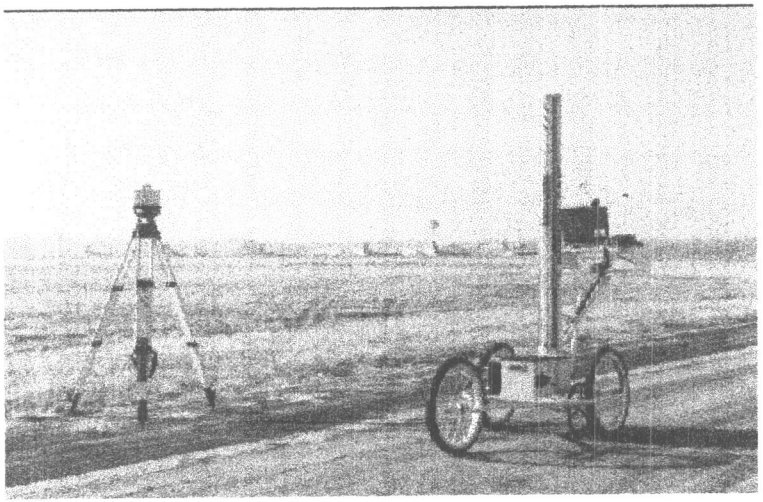

Multiple Lines of Survey
(Grade Removed)

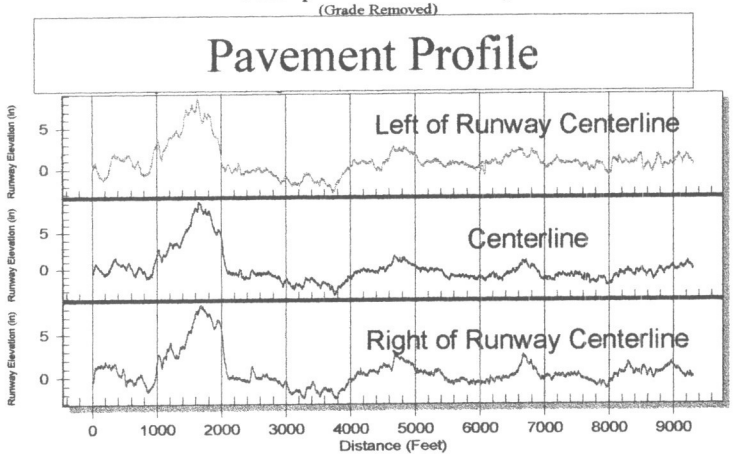

- Topographical Measurement Every Foot
- .01 Foot Accuracy
- Measures 10,000 Foot Runway in One Hour

Define the Environment

- Collect Profile Data on Many Runways
- Assess Dynamic Loads via Aircraft Simulations
- Based on the Above Results, Define the Loading Environment

Conclusions

- This Concept has Worked Better than Anticipated: 30-40% Reduction in Ground Loads
- Easy to Implement - No Structural Modifications
- Next Step - Define the Loading Environment

Next Step:

Defining the Aircraft/Runway Interaction Loading Environment

The design life of an aircraft is based in part on the magnitude and frequency of ground-air-ground (GAG) cycles over its life. Dynamic loads caused by runway roughness during taxi, takeoff, and landing rollout contribute to accumulated fatigue damage incurred during the GAG cycle. Although these loads are accounted for in the design, estimates of the ground loading environment are used because the actual loading is largely unknown. Better definitions of the loading environment would minimize risk in the design of new aircraft and provide a criterion for loads management as the aircraft age. A need exists to develop a better understanding of the ground loading environment. One way of accomplishing this consists of 4 parts:

- Collect and maintain a database of runway and taxiway profile data.
- Assess the dynamic loading potential of those runways and taxiways using aircraft simulation technology.
- Develop guidelines for using the database for defining loading environments.
- Use the loading spectra developed to minimize risk in design and life extension calculations.

Collection of data to support this concept from as many runways and taxiways as practical will result in building a large well defined set of loading criteria for ground events. This database can also be used to establish criteria for go/no go operations on rough runways and for scheduling pavement maintenance in order to control the loading environment.

- The anticipated benefits of this technology are as follows:
- A well defined loading environment of the runway roughness portion of the GAG cycle will reduce the risk in aircraft design and remaining life calculations.
- The established database will be applicable to military and commercial aircraft.
- This technology will also provide the information needed by an existing task group of the Air Transport Division of the American Society of Civil Engineers (ASCE) to establish an industrial standard for runway roughness criteria. A similar effort to establish runway roughness criteria based on aircraft dynamic response is underway by a study group in ICAO, (The International Civil Aviation Organization).

OPTICAL FIBER-BASED CORROSION SENSORS FOR AGING AIRCRAFT

Jennifer L. Elster, Jonathan A. Greene, Mark E. Jones, Tim A. Bailey, and Shannon M. Lenahan
F&S, Inc.
Blacksburg, VA 24060, USA
540-552-5128

Ignacio Perez
Naval Air Warfare Center
Patuxent River, MD 20670
301-342-8074

ABSTRACT

Optical fiber corrosion sensors are being developed to address the high service costs associated with current structural maintenance procedures of civilian and military assets. A distributed optical fiber sensor system will help reduce the costs associated with corrosion damage and extend the lifetime of existing structures. Annual national losses in time, labor, materials and systems has been estimated in the billions of dollars. Additional costs arise from system downtime that results from disassembly procedures necessary to locate corrosion damage in remote locations. Furthermore, the potential to damage other system parts during maintenance is increased when disassembly and reassembly occurs. The development of on-line optical fiber sensors capable of detecting corrosion would eliminate a significant portion of the maintenance costs. We present recent test results using optical fiber long-period grating (LPG) corrosion sensors. With the appropriate coating, the sensors can be designed to detect moisture, pH, metal-ions, nitrides, or sulfides in otherwise inaccessible regions of the aircraft. The LPG sensors can be rendered immune to temperature cross-sensitivity, multiplexed along a single fiber, and can be demodulated using a simple, low-cost spectrum analyzer.

KEY WORDS: optical fiber sensors, hydrogels, corrosion sensors, long period gratings, nondestructive evaluation, aging aircraft

INTRODUCTION

Optical fiber sensors are a novel and ideal approach for making chemical and physical measurements in a variety of harsh environments because they do not corrode and are resistant to attack by most chemicals, immune to electromagnetic interference, light weight, inherently small and have a flexible geometry. With the appropriate sensor configuration optical fiber sensors can be designed to be sensitive to a variety of environmental parameters including water vapor, chemicals, strain, temperature, and pressure. These sensors can be multiplexed in large numbers along a single optical fiber transmission cable, and can be used for either *in situ* or remote applications. These performance advantages make optical fiber sensors ideal for detection of corrosion in hidden and inaccessible regions of aircraft structures.

In current practice NDE techniques are employed to inspect suspect areas that have been already highlighted by either visual inspection or fleet experience on other aircraft. Techniques such as eddy current, ultrasonic, dye penetrates, and X-ray can be employed for further corrosion characterization,

but results are often ambiguous during early stages of corrosion and interpretation depends on the judgement of the inspector [1]. These methods also have difficulty determining corrosion in multi-layer structures and discriminating an old repair from a corrosion site. Because it is critical that corrosion is detected before structural integrity has been compromised, a cost effective method of corrosion monitoring is needed to determine corrosion in the early stages, when economical repair is still feasible. An onboard portable real-time fiber optic based detection system for corrosion by-products would eliminate many challenges associated with the early detection of corrosion in aging aircraft and other infrastructures. The presented results demonstrate the capability of long-period grating (LPG)-based corrosion sensors for measurement of corrosion precursors and by-products in hidden and inaccessible structural regions.

BACKGROUND

When water collect in crevices, it contains atmospheric contents such as acids, salts, and organics that provide the electrolytes that lead to aircraft corrosion damage. During the reduction–oxidation process (redox) corrosion by-products are produced. For aircraft aluminum alloys, the presence of dissolved Cl^-, NO_X and or SO_X anions catalyze the corrosion reactions which release Al^{3+} and Mg^{2+} ions from the aqueous-wet alloy surfaces. Thus, the advance of the corrosion process consists of two key events: failure of sealants at mated aluminum surfaces such as at joints and rivets which admit water and corrosive anions (Cl^-, NO_X , SO_X) and then the release of significant concentrations of divalent ions from corrosion reactions [2]. By monitoring for these corrosion precursors and by-products with an onboard system, early detection of corrosion is possible before structural integrity of the structure is compromised. With the appropriate coating, the LPG-based sensors can be designed to determine various corrosion precursors and by-products to detect corrosion levels in occluded structures.

SENSOR DESIGN

The LPG is a spectral loss element that scatters out light at a particular wavelength based on grating period, fiber refractive index, and the refractive index of the surrounding environment [3]. The presented LPG-based chemical sensors operate based on specially designed affinity coatings which cause a measurable change in the refractive index 'seen' by the LPG in the presence of target molecules. As the coating absorbs target molecules, the refractive index changes, causing a shift in the wavelength of the scattered light. A schematic of the optical fiber long-period grating (LPG) chemical sensor is shown in Figure 1.

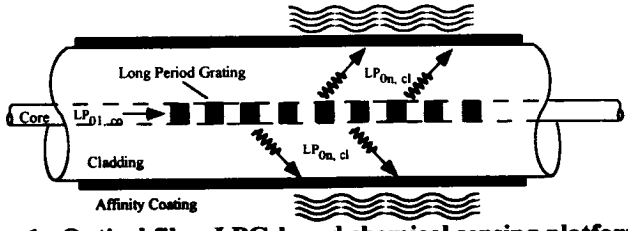

Figure 1. Optical fiber LPG-based chemical sensing platform for corrosion precursor and by-product detection.

The principle of the sensor operation is that light traveling through the optical fiber will be scattered out of the grating at different optical wavelengths as the index of refraction of the coating changes due to target molecule absorption. Figure 2 shows a representative spectrum shift with refractive index change for a LPG sensing element. The magnitude of the spectral shift can be tailored by adjusting LPG fabrication parameters.

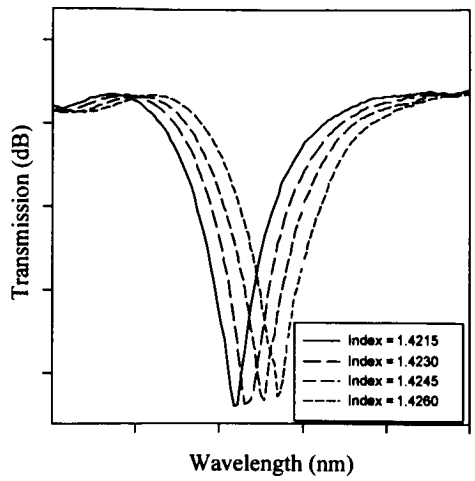

Figure 2. Long period grating (LPG) transmission spectrum.

The moisture sensor is fabricated by coating an LPG sensor element with poly(ethylene oxide) PEO, formed from the polymerization of ethylene oxide monomers [4]. This PEO derivative is a water absorbing hydrogel coating that swells in the presence of moisture and is easily applied to the long period grating. The coating thickness is optimized for high responsivity and reversibility. In the presence of water, the PEO hydrogel coating absorbs water and swells, leading to a decrease in the refractive index at the surface of the fiber, and a resulting shift in the LPG outcoupled wavelength.

Low profile arrays of LPG sensors that detect corrosion precursors and by-products such as moisture, pH, metal-ion levels, sulfides, and nitrides will be used along with the demodulation system to build a distributed corrosion health monitoring system for aging aircraft. Development and applications of the moisture sensors with demodulation techniques are presented below.

RESULTS

The transmission spectrum of a multiplexed dual PEO coated LPG sensor was monitored by using a broadband source and an optical spectrum analyzer. Figure 3 illustrates two LPG-based moisture sensors multiplexed serially on a single optical fiber and mounted on a simulated lapjoint. The transmission spectrum obtained from the dual sensor in a dry coating state is shown in Figure 4a as a relatively flat line. As shown, no loss dips were visible in the transmission spectrum, indicating that the index of refraction of the coating exceeds that of the fiber cladding. A higher coating index prevents coupling from the core mode into the higher-order cladding modes. However, once the sensor is submerged in water, the effective index is decreased and the familiar LPG loss dips returns to the spectrum. These sensors can be tailored to operate at various wavelengths to allow multiplexed operation, as shown in this sensor demonstration. The transmission spectrum of the hydrogel-coated LPG sensor element A submerged in a water bath is shown in Figure 4b. Figure 4c illustrates the transmission spectrum with both sensor element A and B submerged in the water bath. To demonstrate reversibility of the sensors, the sensors were removed from the water bath, and the original flat transmission spectrum was observed almost instantaneously, as shown in Figure 4d. Hence, the PEO coated LPG sensors display short response time, good reversibility and repeatability.

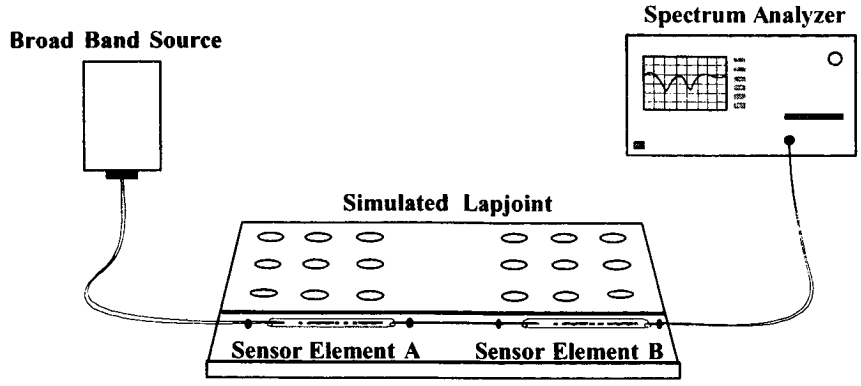

Figure 3. Dual multiplexed hydrogel-coated LPG moisture sensor element fabricated and tested.

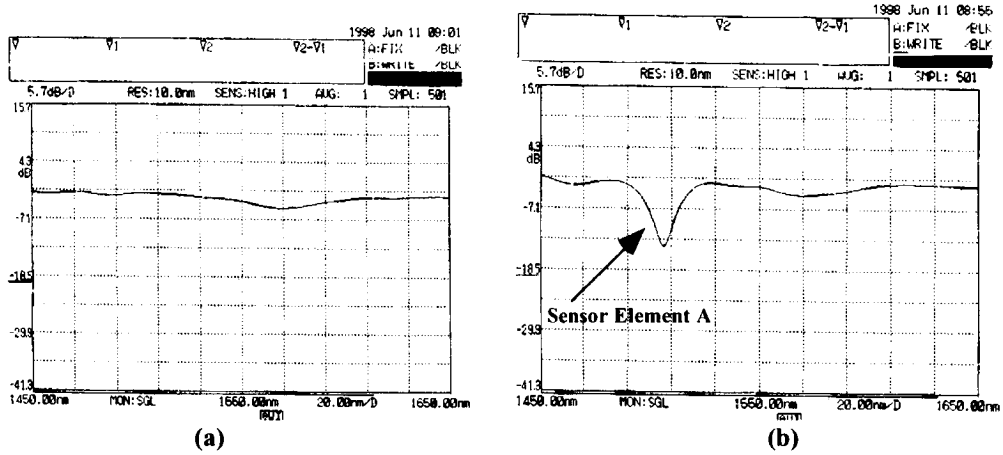

Figure 4a) Transmission spectrum of dual multiplexed moisture sensors in air
b) Transmission spectrum after sensor element A is submerged in water bath.

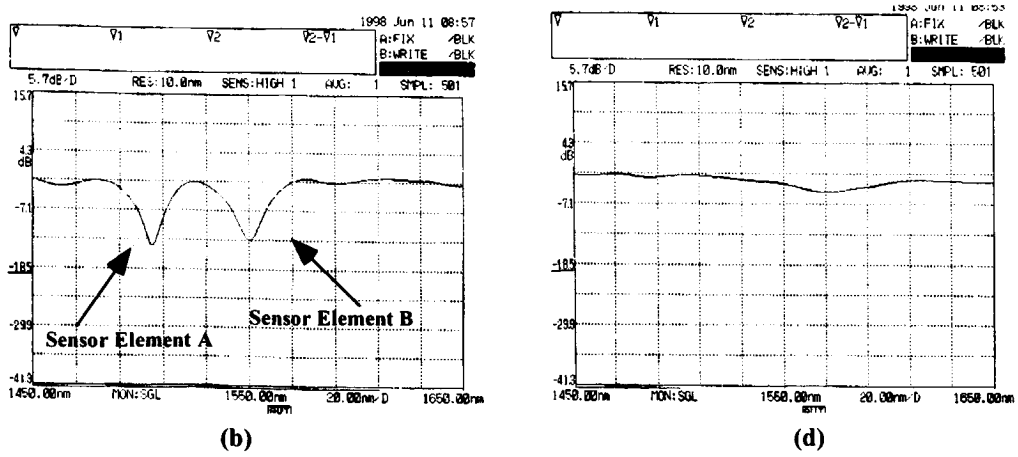

Figure 4c) Transmission spectrum with sensor element A and B submerged in water bath
d) Transmission spectrum returns to original flat base line spectrum when both sensor elements are removed from water bath.

For interrogation of the presented corrosion precursor and by-product sensors, a low cost demodulation system has been developed, fabricated and demonstrated. Figure 5 is a photograph of the sensor support system used for LPG-based corrosion and chemical sensors. The system consists of a demodulation box consisting of support optics, a laptop computer with application specific software, and an optical switch for multiplexing an array of sensors using a single demodulation system.

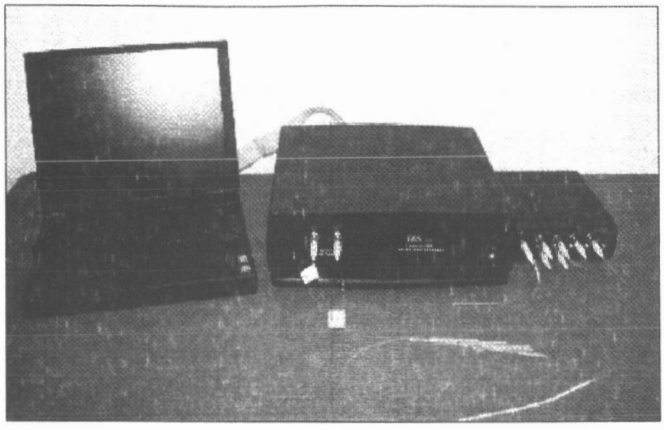

Figure 5. Photograph of LunaScan-3000 demodulation system with optical switch used for interrogation of LPG-based chemical sensors.

Figure 6 illustrates the graphical user interface developed for the corrosion sensor demonstration. This software can be used to interpret sensors and deliver appropriate information to the end user. As shown, a pop-up display will indicate a potentially corrosive environment in the presence of moisture. This software demonstrates the multiplexing capabilities of the LPG-based sensors by demonstrating two sensors on a single optical fiber. This capability can be expanded to numerous distributed sensors for embeddment in aging aircraft and other potentially corrosive infrastructure. When a specific sensor detects moisture a pop-up display warns the end user of a potentially corrosive environment at the detected location.

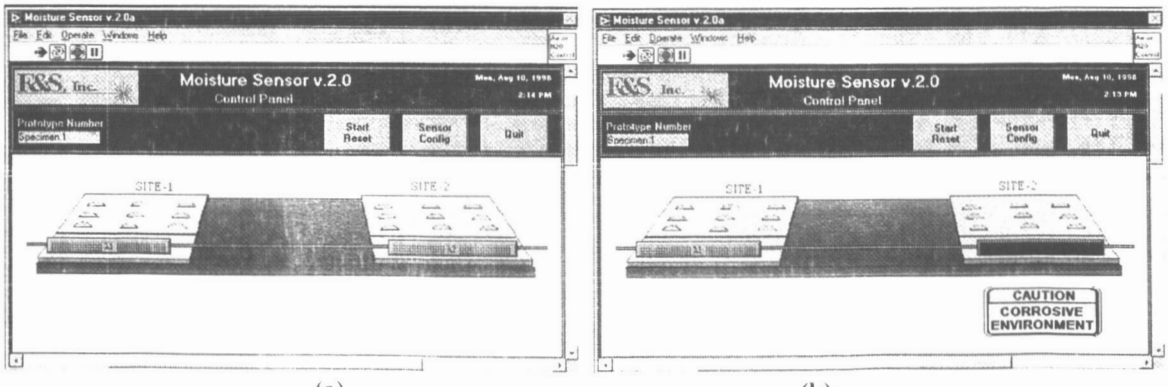

(a) (b)

Figure 6a) Graphical interface for moisture sensor demonstration in dry state
b) Pop-up display for corrosive environment when moisture is detected at site 2.

CONCLUSIONS

This paper presents recent long period grating-based sensor results that demonstrate the potential for not only corrosion detection in aging aircraft by monitoring moisture, pH, metal-ions, sulfides, and nitrides, but also for a variety of other chemical sensing applications. By coating the LPG sensor with specially designed affinity coatings that selectively absorb target molecules, selective, real-time monitoring of environmental conditions is possible. This sensing platform shows great promise for corrosion by-product detection in pipe networks, civil infrastructure, process control, and petroleum production operations and can be applied as biological sensors for in-vitro detection of pathogens, and chemical sensors for environmental and industrial process monitoring. These sensors can be highly multiplexed to produce multiple sensing sites for detecting various specific physical and chemical phenomenon along a single optical fiber. For each sensor and potential application, attachment and optical fiber routing issues need to be explored. Current research focuses on embeddable distributed sensor configurations for large area monitoring of corrosion in aging aircraft and ships.

ACKNOWLEDGEMENTS

This research has been performed under support from Patuxant Naval Air Warfare Center under contract N68335-97-C-0093. The authors acknowledge Dr. Craig Mitchie of Strathclyde University for providing samples of the hydrogel coating used for moisture sensor fabrication.

REFERENCES

1. D.A. Bruce, "Non-Destructive Detection of Corrosion for Life Management," 79th Meeting of the AGARD Structures and Materials Panel, Seville, Spain, Oct. 1994.
2. M.E. Inman, R.G. Kelly, S.A. Willard, R.S. Piascik, "Coordinated Metallographic, Chemical, and Electrochemical Analyses of Fuselage Lap Splice Joint Corrosion," Proc. of the FAA-NASA Symposium on Continued Airworthiness of Aircraft Structures (Atlanta, GA: 1996).
3. V. Bhatia and A.M. Vengsarkar, "Optical fiber long-period grating sensors," Optics Letters, vol. 21, no. 9, pp.692-694, 1996.
4. W.C. Mitchie et al., " Distributed sensor for water and pH measurement using fibre optics and swellable polymeric materials, " Opt. Lett., vol. 20 no.1, 1995.
5. J.A. Greene, M.E. Jones, P.G. Duncan, T.A. Bailey, F&S, Inc.;I.M. Perez, Naval Air Warfare Ctr., " Optical fiber corrosion sensors for aging aircraft,", SPIE Vol 3399, April 1998.

COMPOSITE PATCH REPAIR APPLICATIONS TO T-38 LOWER WING SKIN

James Helbling and Maro Heimerdinger
Northrop Grumman Corporation
Dept. 9B10/89, One Hornet Way, El Segundo, CA. 90245-2804, USA
Telephone- (310) 332-6004
Telefax- (310) 331-6648
E-Mail- James_Helbling@mail.northgrum.com

Mohan M. Ratwani
R-Tec
4 Latigo Lane, Rolling Hills Estates, CA. 90274, USA

ABSTRACT

A bonded composite reinforcement concept has been investigated for the T-38 aircraft as a means to retard crack initiation and crack growth occurring in a machined pocket area of the lower wing skin. A test program has been carried out to experimentally determine the crack growth life extension offered by the composite patch reinforcement and verify the patch design and analysis. Test specimens were designed to simulate the pocket area in the wing where cracking is occurring. Two specimens were tested under fighter spectrum loading. One specimen was tested without the reinforcement to obtain baseline crack growth data, and an identical specimen was tested with a 26 ply boron/epoxy patch bonded to one surface. The test specimens were strain gaged to obtain load distributions in the specimen and determine the amount of load transfer to the patch. The crack growth life of the specimen with the patch installed was found to be approximately twice that of the unreinforced specimen.

The crack growth data obtained from the tests showed considerably longer crack growth life compared to the analytical predictions. This anomaly was apparently the result of the initial flaw being placed near the corner of the machined pocket, thus causing the crack to be retarded in the direction of increased skin thickness. Adjustments were made to the analytical model which allowed for a good correlation between the predicted crack growth and the test data.

INTRODUCTION

Composite patch reinforcement is finding increasing use in the repair of metallic aircraft structure. This is due to several advantages the bonded reinforcement has over conventional mechanically fastened repairs. Aircraft structures which could not meet fail safety requirements with conventional doublers installed can be successfully repaired with the bonded repair concept. Some examples of this kind of repair in USAF aircraft include the T-38 lower wing skin "D" panel, C-141 weep holes, and F-16 lower wing skin fuel access hole.

T-38 lower wing skin machined lands between the 39% and 44% spars at W.S. 78 have developed cracks during field usage which result in the removal of the wing from service. A conventional mechanically fastened repair will degrade the structural integrity of the lower wing skin and jeopardize the fail safety of the component. Hence, there is a need to develop a reinforcement concept which will reduce stresses

in the pocket area and thereby reduce the tendency toward crack initiation and retard crack growth. Preliminary studies indicate that a boron/epoxy reinforcement concept provides the best load transfer and life extension prospect. A detailed design and analysis of the boron/epoxy bonded concept has been performed. A damage tolerance approach was used to design and analyze the reinforcement concept. Due to the complexity of the structural configuration (a pocket area with variable skin thickness) it was considered necessary to conduct a test program to verify the design and analysis and increase confidence in the repair concept.

A test program was devised in two parts. In the first part of the test program, coupon testing was performed to simulate the exact structural configuration and load environment in the wing. Two test specimens - one unreinforced and the other with a 26 ply boron/epoxy composite reinforcement installed (see Figure 1)- were considered necessary for testing to allow for a direct comparison of crack growth life between a baseline and reinforced specimen. The second portion of the test program involved the bonding of the reinforcement to a T-38 wing (Figure 2) being subjected to durability testing at Wright Patterson Air Force Base (WPAFB), Ohio, as a part of Air Force Contract F33615-90-C-3201, entitled "Advanced Technology Redesign of Highly Loaded Structures (ATROHS)". Both the coupon testing and the durability testing are being carried out under Lead-in-Fighter spectrum loading. The details of coupon tests are discussed here.

VALIDATION TESTING

A test validation program was performed to verify the composite patch design and verify by test the predicted life extension obtained through reinforcement.

TEST SPECIMEN DESCRIPTION

The test specimen configuration is shown in Figure 3. The pocket areas in the test specimen are designed to represent the cracking location in the T-38 lower wing skin between the 39% and 44% spars at W.S. 78. The thickness and pocket dimensions are representative of the actual dimensions in the wing skin. Each specimen has two pockets so that two sets of data can be obtained from each specimen. The cracks in the two pockets were placed sufficiently apart to ensure no interaction between the cracks in each pocket. Two specimen were fabricated, one to be used as a baseline and other to be reinforced with the composite patch.

Initial flaws were introduced in the test specimens in the pocket area on the side representing the inner moldline of the wing. The length of the flaw on the specimen surface was 0.25 inch with a flaw depth of 0.125 inch. This flaw size was chosen in accordance with AFGS 87221A requirements for an initial surface flaw away from a fastener hole. The flaws were introduced by an Electric Discharge Machining (EDM) process to produce a flaw 0.005 inch thick. Figure 4 shows a photomicrograph (7.5X) of the EDM machined area from the tested specimen.

COMPOSITE REINFORCEMENT FABRICATION AND BONDING

One of the requirements for the T-38 lower wing skin reinforcement program was to provide access to the fastener holes along the 44% and 39% spars near the cracking location which require recurring inspections. This necessitated holes being placed in the reinforcement at the exact location of the holes in the wing skin. The ply orientations and configuration are shown in Figure 1. During the cure process, Teflon plugs were installed in the holes in the laminate to control resin bleed and maintain the hole

dimensions. The plugs were installed to the thickness of the laminate in order to maintain uniform pressure over the laminate surface during the cure process. The laminate was cured in an autoclave at a pressure of 90 psi and a temperature of 240^{o}F for 60 minutes. Non-destructive inspection (NDI) using through transmission was performed on each laminate. The NDI showed the laminate to be of good quality and free of defects.

The patch area of the validation test specimen was anodized using the phosphoric acid non-tank anodize (PANTA) process. The bond surface was primed with Cytec BR127 primer and cured at 200^{0}F for one hour. The bond surface of the boron patch was prepared for bonding by abrading the surface with 240 grit silicon carbide abrasive sheet. The surface was then solvent wiped with MEK and wiped dry with a clean dry cloth. One ply of Cytec FM73 film adhesive was applied to the boron patch and the patch was installed on the bond surface of the test specimen. The assembly was vacuum bagged, placed in an oven and cured at 210^{0}F for 120 minutes under a vacuum pressure of 12 to 15 inches of mercury. The bonded assembly was ultrasonically inspected for disbonds and the "C" scans showed no defects.

STRAIN GAGE INSTALLATION

Nine strain gages were installed on the baseline specimen and twenty four gages were installed on the reinforced test specimen at the locations shown in Figure 5.

TEST SPECTRUM AND EQUIPMENT

All the specimens were tested to a stress spectrum representing the T-38 Lead-in-Fighter usage. One pass through the test spectrum represented 1000 flight hours. The maximum spectrum stress was 34.675 ksi.

The tests were conducted on two-post MTS servohydraulic test frames using 442 console controllers. All crack measurements were made visually on the surfaces of the specimens using a Bausch & Lomb stereo microscope.

TEST RESULTS

STRAIN GAGE RESULTS

The observed strains at 29% of the maximum spectrum load in the baseline test specimen are shown in Figure 6. The figure shows that the strains in the center of test specimen are almost the same on both surfaces (the surfaces representing the inner and outer moldline of the wing skin) indicating no bending in the center of the specimen. Also, the back to back gages in the center of the pocket area show identical strains, indicating no local bending in the center of the pocket. The gage near the grip area on the surface of the specimen representing the inner moldline shows lower strains than the gage installed on the back side due its proximity to the machined pocket. This strain gage on the inner moldline experiences a reduced stress field compared to the far field stress, as the location of the strain gage is closer to the end of the thicker section. The skin strain gradually reduces to zero at the end of the thicker section where the pocket starts.

The strains in the reinforced test specimen are shown in Figure 7. These strains are shown at 29% of maximum spectrum load. The strain gage data shows that the strain in the center of specimen is not the same on both surfaces. The strain gage on the composite reinforcement side shows strains which are 60% higher than those on the side without reinforcement. This indicates a significant amount of bending caused by the reinforcement.

A comparison of metal strains in the pocket at locations where there is no reinforcement (9 inches from specimen centerline) and at the reinforced locations (5.5 inches from specimen centerline) indicates that the metal strain is reduced from 1065 micro inch/inch to 848 micro inch/inch, or approximately 20%. Thus, the composite reinforcement causes a significant reduction in strain in the pocket. Figure 6 shows relatively small strains in the composite reinforcement compared to the skin strains. It may be noted that the elastic modulus of the composite reinforcement in the loading direction is $20.5X10^6$ psi compared to $10X10^6$ psi for aluminum.

CRACK GROWTH RESULTS

During the testing it was observed that the crack tips in both test specimens were growing at almost the same rate for approximately 1500 flight hours of spectrum testing. However, as the crack tip adjacent to the end of the machined pocket grew closer to the pocket edge, it grew at much slower rate than the tip which was away from the edge. The crack growth rate was found to be significantly different at the crack tips in both the pockets of the test specimen. This behavior was observed for the specimen with and without the composite reinforcement installed.

Crack Growth in Baseline Specimen

The half crack length as a function of flight hours for the left and right crack tips is shown in Figure 8 for upper pocket. The half crack length is measured from the centerline of the EDM flaw. The figure also shows average crack length. It is seen that after approximately 1,200 flight hours, the right crack tip is growing considerably slower as compared to left crack tip. At 7,000 flight hours, the half crack length at the left tip is 50% longer than that at the right tip. The slower crack growth of the crack tip adjacent to the edge of machined pocket is attributed to the stiffening provided by the thicker skin outside of the pocket, thereby reducing the stress intensity factors ahead of the crack tip. A similar crack growth behavior was observed for the lower pocket.

Crack Growth in Reinforced Specimen

The crack growth in the upper pocket of the reinforced specimen is shown in Figure 9. The figure also shows crack growth in the baseline specimen for comparison. It is seen that once again, the right crack tip closer to the machined pocket edge grows considerably slower as compared to the crack tip away from the pocket edge. Each of the crack tips in the reinforced specimen grows slower as compared to the crack tips in baseline specimen. The presence of the reinforcement significantly increases crack growth life.

The crack growth in the lower pocket for the specimens with and without reinforcement is shown in Figure 10. The figure shows a significant increase in crack growth life. It is seen that at 8,000 flight hours, the average crack length in the reinforced specimen is about half of that in the baseline specimen, even though the starting crack length in both the specimen was the same.

COMPARISON BETWEEN TEST RESULTS AND ANALYTICAL PREDICTIONS

The analytical predictions of crack growth in specimens with and without composite reinforcement were not straight forward due to the initial flaw being introduced at a radius in the pocket area. The crack tips experience stiffening due to thicker section on one side of the crack surface. In addition, the crack growth predictions become complex due to only one crack tip experiencing the stiffening effect, resulting in one crack tip growing at roughly half the rate of the other. All existing crack growth models assume the same crack growth rate at both the crack tips. Considering the complexity of the crack growth, no attempt was made to predict crack growth at individual crack tips of the specimens. However, techniques were developed to predict average crack length.

Crack Growth Correlation for Baseline Specimen

To account for the presence of the machined pocket radius along the crack plane, the stress intensity factors for a through crack geometry were modified using the analytical techniques developed in Reference 1. The influence of one crack tip experiencing the stiffening effect of pocket edge was accounted for by using stress intensity factors from Reference 2. The modified stress intensity factors were used in the Forman equation to make crack growth predictions under spectrum loading. The unequal crack growth at the crack tips was accounted for by modifying the crack growth constant, c, in the Forman equation. As the test data indicated the crack growth rate at one crack tip to be one half of that at other tip, an average value of c equal to 0.75 times the normal value was used in the Forman equation for crack growth predictions.

A comparison of predicted crack growth and observed crack growth is shown in Figure 11 for the upper pocket. The figure shows a good correlation between predicted and observed average crack length.

Crack Growth Correlation for Reinforced Specimen

To make crack growth predictions for the reinforced specimen, the stress intensity factors for the baseline specimen were modified to account for the influence of the reinforcement. The modification was performed using the analytical techniques developed in Reference 3 and incorporated in the Air Force computer code AFGROW (Reference 4). The AFGROW code was used to obtain stress intensity factors for a cracked sheet with a bonded repair. These stress intensity factors were multiplied by the stress intensity factors for the pocket area with no reinforcement. The stress intensity factors thus obtained were used in the Forman equation to predict crack growth life. The constant, c, in the Forman equation was taken as 0.75 times the normal value for 7075-T73 aluminum to compensate for unequal crack growth at the two crack tips. The predicted and observed average crack growth in the upper pocket of the reinforced specimen is shown in Figure 12. The figure also shows predicted and observed crack growth in the baseline specimen for comparison. The comparison between predicted and observed crack growth shows excellent correlation. The results indicate that the composite reinforcement doubles the crack growth life.

The comparison of predicted and observed crack growth behavior in the lower pocket is shown in Figure 13 for specimens with and without the composite reinforcement. Once again, the comparison between predicted and observed crack growth for the reinforced specimen shows excellent correlation. These results indicate that the analysis of References 3-4 can be used with confidence for damage tolerance analysis of metallic structures bonded with a composite reinforcement.

CONCLUSIONS

The following conclusions are drawn from the afore mentioned studies:

1. The composite patch reinforcement concept can be effectively used to retard crack growth at complex structural details such as skins with variable thickness (pockets).

2. Crack growth in skins pocket areas is influenced by variation in skin thickness, resulting in significantly different crack growth rates at the crack tips. This behavior can be accounted for in crack growth life predictions by modifying stress intensity factors and crack growth rate constants.

3. The composite patch repair analysis methodology incorporated into the AFGROW program can predict crack growth behavior in repaired structure with reasonable accuracy.

ACKNOWLEDGEMENT

The work reported here was sponsored by San Antonio Air Logistic Center, Kelly Air Force Base, San Antonio, Texas. Mr. Paul Piper was the Air Force project engineer.

REFERENCES

1. Ratwani M. M, " Stress Intensity Factors for Cracks at Root Radii in Skins With Lands" NOR 81-58, July 1981.

2. Tada, Paris, and Irwin, "Stress Intensity Factors Handbook"

3. Ratwani M. M, " Analysis of Cracked Metallic Layer Bonded to an Orthotropic (Composite) Layer ", NOR 78-32, March 1978.

4. "AFGROW" Computer Code Developed by Wright Patterson Air Force Base, Ohio.

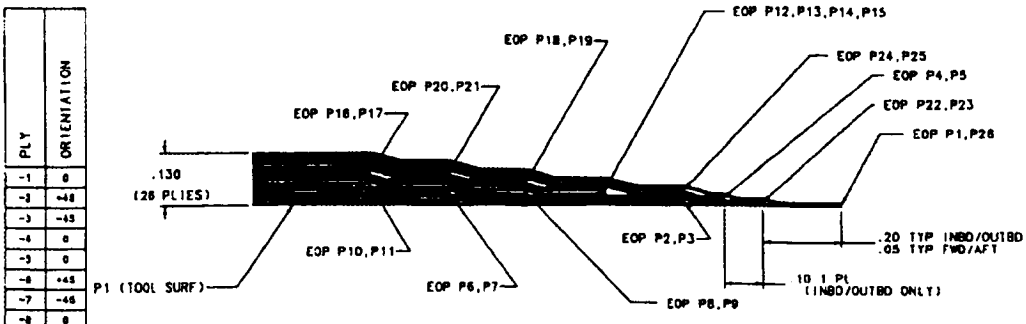

Figure 1. Composite Patch Repair Definition

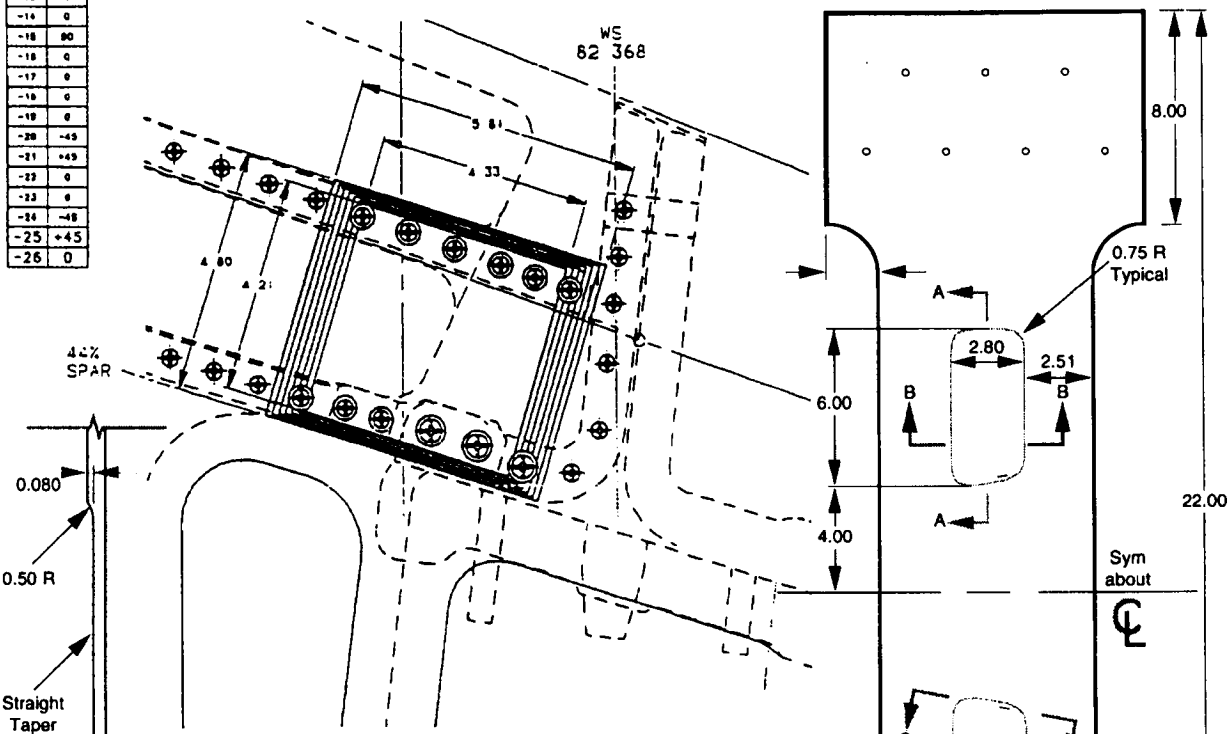

Figure 2. Composite Patch Repair On the T-38 Wing Structure

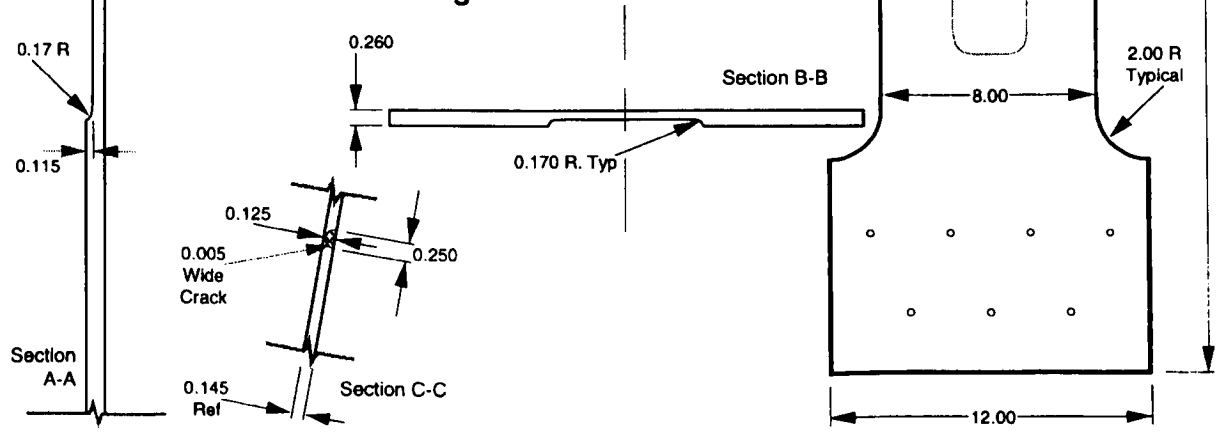

Figure 3. Wing Skin Test Specimen Configuration

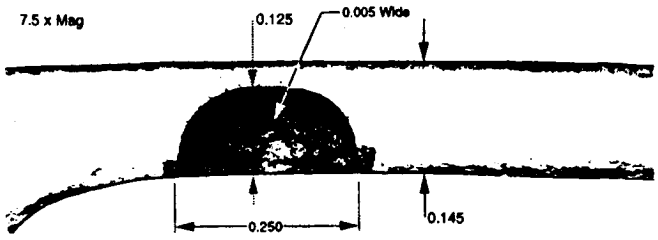

Figure 4. Photomicrograph of EDM Area In Failed Test Specimen

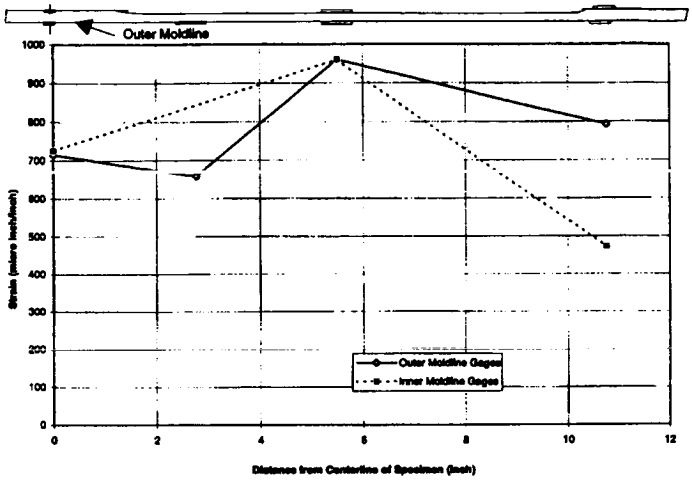

Figure 6. Strains In Baseline Specimen Without Composite Reinforcement

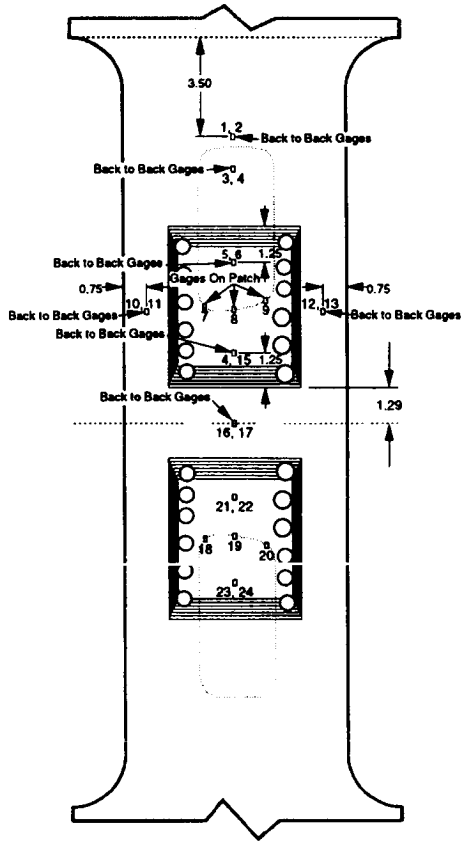

Figure 5. Patch Installation and Strain Gage Location On Test Specimen

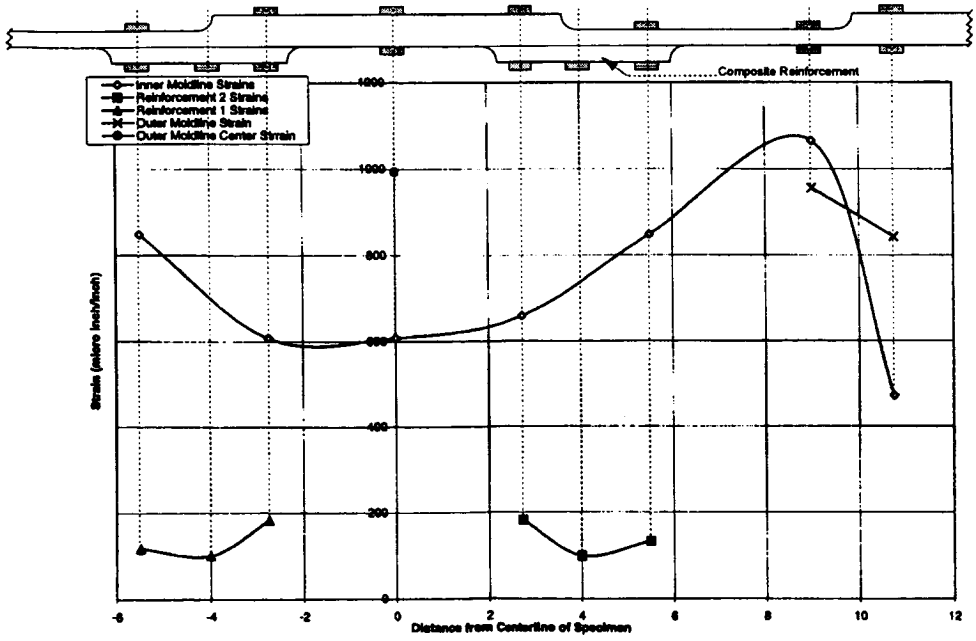

Figure 7. Strains In Specimen With Composite Reinforcement

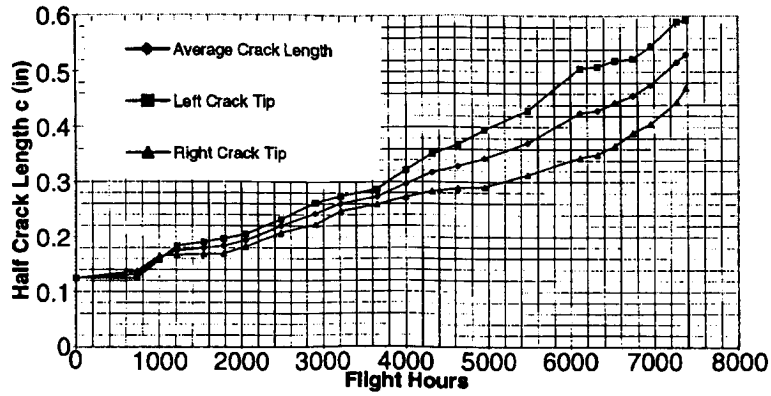

Figure 8. Crack Growth In Baseline Test Specimen Without Composite Reinforcement (Upper Pocket)

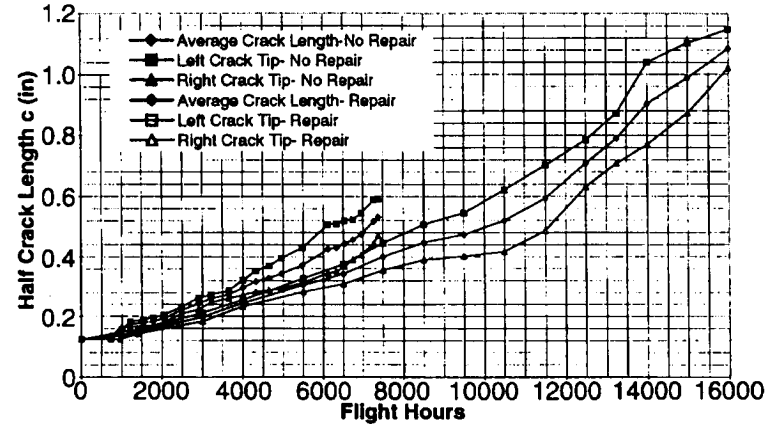

Figure 9. Comparison of Crack Growth In Test Specimens With and Without Composite Reinforcement (Upper Pocket)

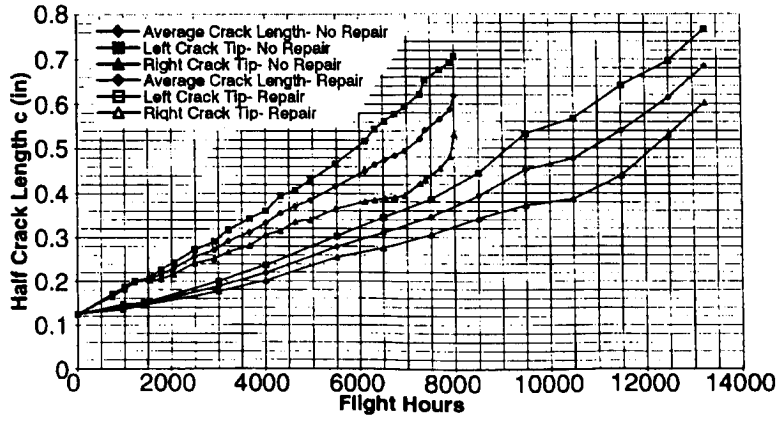

Figure 10. Comparison of Crack Growth In Test Specimens With and Without Composite Reinforcement (Lower Pocket)

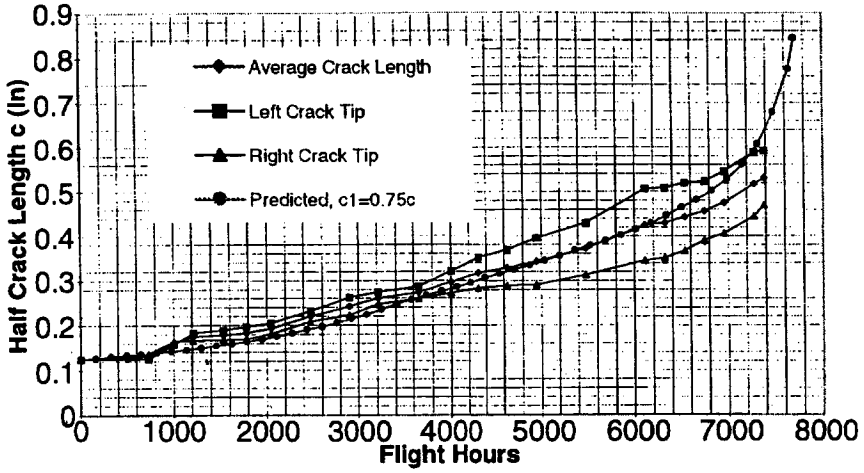

Figure 11. Comparison of Test and Predicted Crack Growth In Specimens Without Composite Reinforcement (Upper Pocket)

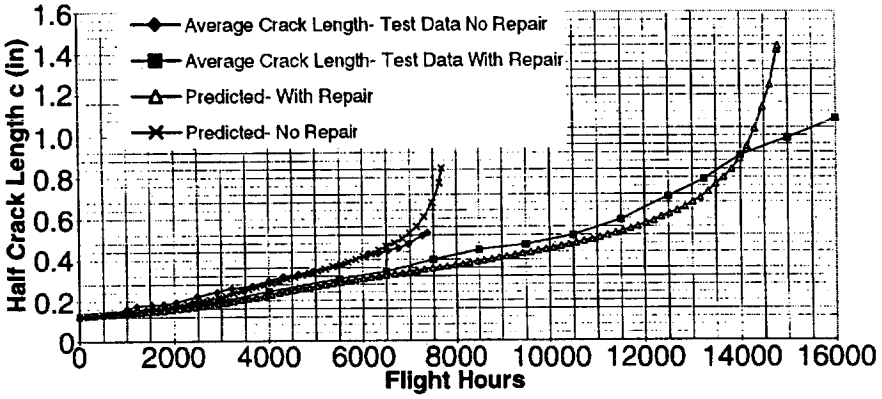

Figure 12. Comparison of Test and Predicted Crack Growth In Specimens With and Without Repair (Upper Pocket)

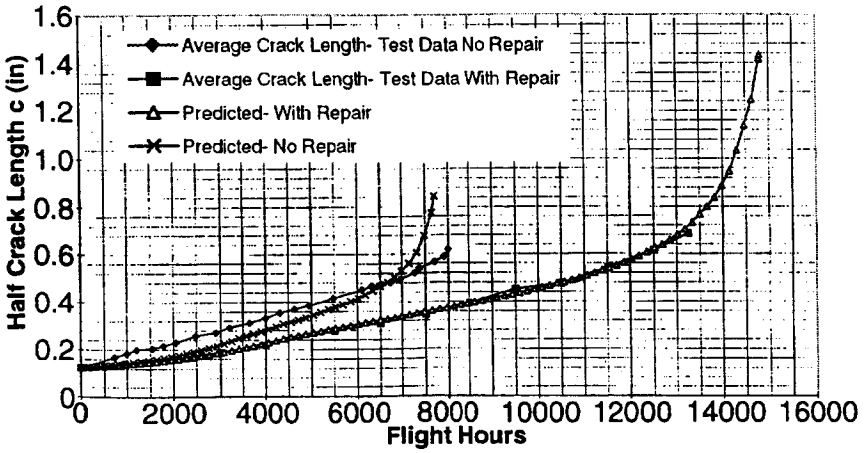

Figure 13. Comparison of Test and Predicted Crack Growth In Specimens With and Without Composite Reinforcement (Lower Pocket)

LAMB WAVE TOMOGRAPHY FOR CORROSION MAPPING

Mark K. Hinders and James C.P. McKeon[1]
Department of Applied Science
The College of William & Mary, Williamsburg, VA 23187-8795
phone: (757) 221-1519, fax: (757) 221-2050, email: hinders@as.wm.edu

ABSTRACT

As the world-wide civil aviation fleet continues to age, methods for accurately predicting the presence of structural flaws–such as hidden corrosion–that compromise airworthiness become increasingly necessary. Ultrasonic guided waves, Lamb waves, allow large sections of aircraft structures to be rapidly inspected. However, extracting quantitative information from Lamb wave data has always involved highly trained personnel with a detailed knowledge of mechanical-waveguide physics. Our work focuses on using a variety of different tomographic reconstruction techniques to graphically represent the Lamb wave data in images that can be easily interpreted by technicians. Because the velocity of Lamb waves depends on thickness, we can convert the travel times of the fundamental Lamb modes into a thickness map of the inspection region. In this paper we show results for the identification of single or multiple back-surface corrosion areas in typical aluminum aircraft skin structures.

INTRODUCTION

After nearly thirty years of clinical use, x-ray computerized tomography has become a routine medical imaging procedure, quickly providing invaluable information to physicians for both diagnosis and treatment planning. By electronically recording the x-rays which pass through the same region of the body in a number of different orientations, convolution-type reconstruction algorithms allow rapid computer reconstructions of internal structures [1]. Seismologists have developed different tomographic techniques to map subsurface structures for development of oil and mineral deposits, which have overcome the inherent geometric limitations not present in medical imaging by employing iterative reconstruction algorithms. We are interested in mapping hidden corrosion in the skins of aging aircraft. Corrosion alters the velocity of Lamb waves as they propagate through the thinned regions, and by monitoring the change in arrival time of Lamb waves traveling between two contact transducers at known separation we are able to detect areas of only a few percent thickness reduction. Although this has allowed us to locate areas of structural deterioration, it does not allow us to quantify the extent of the thinning. Tomographic reconstruction with Lamb waves allows accurate reconstruction of the variation of quantities of interest–such as thickness–throughout the region of interest without the need for highly-trained personnel to interpret Lamb wave signals.

[1]Current address: Sonix, Inc., 8700 Morrissette Drive, Springfield, VA 22152.

Previous tomographic Lamb wave work by Hutchins et al. [2] – [6] Achenbach [7] and Degertekin [8] used a parallel projection technique with the velocity and attenuation of Lamb waves as input for the reconstructions. For comparison to this earlier work, the results of a parallel projection technique for reconstruction using Lamb Wave velocity data on an aluminum plate with a thinned region are presented here. This is followed by a "crosshole" tomographic reconstruction from Lamb wave data shown for the same sample. Although the parallel projection tomographic scans give better reconstructions, the crosshole technique is a much more practical technique for aging aircraft applications. In our laboratory apparatus we are able to compare directly these two Lamb wave tomographic scanning techniques, and have begun to explore the capabilities and limitations of each.

LAMB WAVE TOMOGRAPHIC SCANNING SYSTEM

Our measurements are typically performed at a frequency-thickness of $fd \approx 2$ MHz-mm where only the lowest order symmetric and antisymmetric ($S0$ and $A0$) modes propagate appreciably. We use contact transducers excited by toneburst and then allow the Lamb wave modes to develop as the ultrasonic energy propagates. This is in contrast to other researchers who use angle-block transducers to select particular Lamb wave modes. We find that for automated scanning the careful coupling required to select particular waveguide modes via Snell's law is not practical. Instead we drive the transducers at a high enough frequency that the $S0$ mode has sufficient dispersion to give sensitivity to thickness variations, but low enough that all higher-order modes are cut off or negligible. The $S0$ mode at $fd \approx 2$ MHz-mm is appreciably faster than the $A0$ mode so that in our pitch-catch measurements the $S0$ signal will be distinct from the $A0$ signal. For corrosion detection we find it convenient to monitor changes in arrival time of the $S0$ signals, but depending on the flaws of interest we can monitor any combination of changes in arrival time or amplitude of the $S0$ and $A0$ modes. Although amplitude measurements are often most sensitive to the presence of flaws, the received signals are often more strongly affected by the variations in coupling inherent in automated scanning with contact transducers. Since tomographic reconstructions require many individual measurements to develop the projection data, we have concentrated our efforts on those measurements schemes which have the most promise for being fully automated.

Figure 1A shows schematically the geometry for parallel-projection tomography. The transducers are scanned along parallel lines with the Lamb waves propagating between them. At each position in the scan a measurement of some property of the Lamb waves, which are assumed to propagate along the straight rays shown, is recorded. Once the measurement has been done along each of the rays for that orientation, the sample is rotated by a fixed amount and the measurement is repeated. Projections consisting of seven parallel rays (transducer-pair positions) for four orientations (0, 45, 90 and 135 degrees) are shown. The "ray density" is critical to the quality of reconstruction. Note that the ray density is uniform for parallel projection tomography; this will not be the case for crosshole tomography. Having the rays pass through the region of interest from many orientations is also important to the quality of the reconstruction. The rays for parallel projection tomography cover all angles since projections must be evenly spaced over 180 degrees. This can be a disadvantage for contact scanning because a fairly large ring surrounding the region of interest (shown shaded in A) must be free of obstructions.

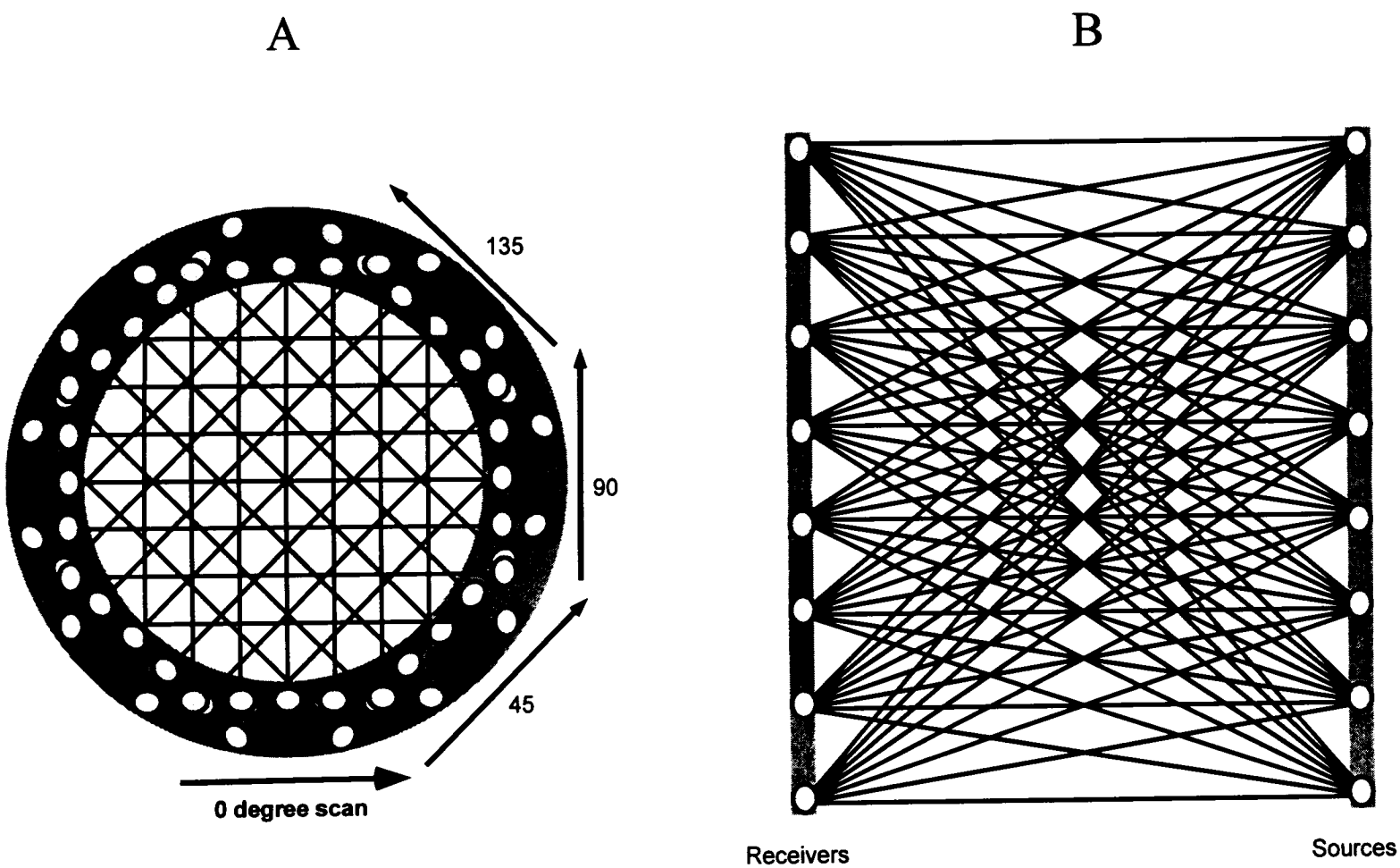

Figure 1: The scanning geometry and ray paths for parallel-projection tomography is shown (A) for the case of seven parallel rays at four orientations. Note that the ray density is uniform, and a fairly large obstruction free ring (shaded area) is necessary for contact scanning. The scanning geometry and raypaths for crosshole tomography are shown (B) for the case of eight sources and eight receivers. Note that the sixty-four raypaths produced do not provide a uniform ray density, but only two narrow obstruction free strips (shaded) are necessary for contact scanning.

Figure 1B shows the scanning geometry and ray paths for crosshole tomography for eight combinations of sources and receivers. Note how the ray density varies and that the rays do not pass through the region of interest from all orientations. These drawbacks in the reconstruction quality are offset by the increased practicality of the measurement. Namely, only two narrow strips (shaded in B) need to be free of obstructions for contact scanning. This can be especially important in aircraft applications where one wants to scan a long line of rivets or a lap joint. Since a complete scan of any large structure will be done via a "composite" of many smaller scans, the rectangular scanning of the crosshole tomography is inherently superior to the circular scanning region of the parallel projection scheme.

In our laboratory we have assembled an ultrasonic system that allows us to perform Lamb wave scans in both parallel projection and crosshole geometries. Schematics of the parallel projection and crosshole scanners are shown in Figures 2A and 2B. Broad banded contact piezoelectric transducers generate and receive the Lamb waves in a pitch-catch arrangement. For the parallel projection configuration, where the two transducers are always in the same relative orientation, shear contact transducers are automatically scanned in the direction perpendicular to the Lamb wave propagation. Two predominant signals, the lowest-order symmetric (S0 mode is first arrival) and antisymmetric (A0 is second arrival) can be observed at a frequency in the range 0.7 to 1.5 MHz. At each location of the transducer pair, the phase shift of the S0 mode is acquired through pulsed-phase-locked-loop (P2L2) circuitry. This instrument compares the phase of its pulsed output signal, which is sent to the transmitting transducer, with that of the amplified and low-pass filtered returned signal from the receiving transducer. A frequency counter is connected to the output of the P2L2, which gives information on the phase difference of the two signals in terms of frequency. The value of this reference frequency can be used to calculate both the time of flight and, because the distance between the two transducers is fixed, the integrated velocity of the Lamb waves. A normalized reference frequency provides the percentage change in these quantities, and allows us to detect changes in material properties. In our setup the sample is rotated by a fixed amount between each scan by a computer-controlled rotary table in order to obtain data from the different orientations necessary for tomographic measurements.

For the cross-borehole method, longitudinal contact transducers are scanned independently so that measurements are recorded at all of the necessary sender/receiver positions. Since the relative orientation of the transducers is constantly changing during the scan, the highly directional shear transducers can not be used even though they give a better signal in contact scanning. Instead, longitudinal contact transducers are used so that signals could be received from any angle. The received signal is sent to a digital oscilloscope, and the digitized waveform is sent to a personal computer and saved for later analysis.

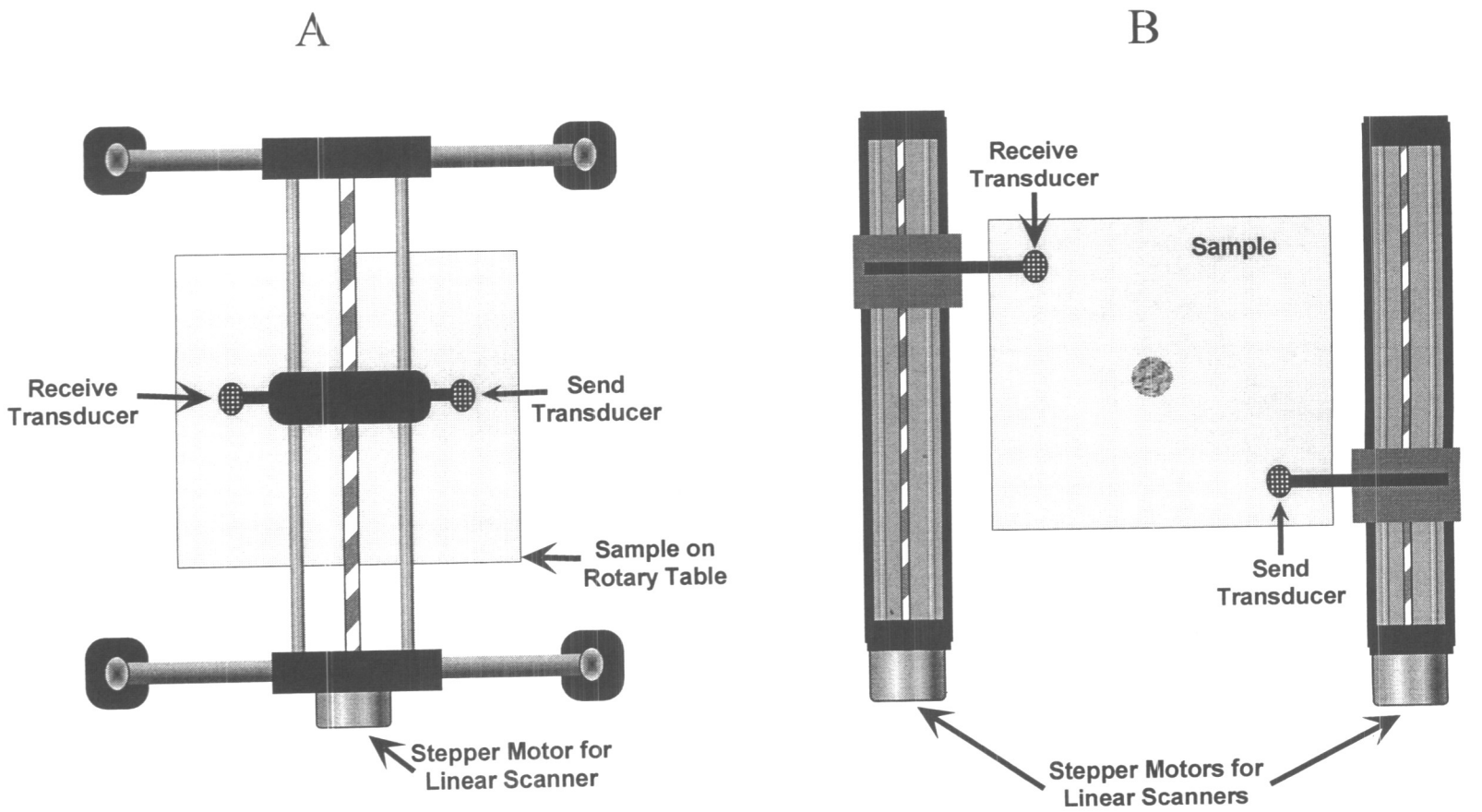

Figure 2: The parallel projection (A) and crosshole (B) scanning systems are shown here schematically. For parallel projection tomography, a pair of shear contact transducers in pitch-catch arrangement are scanned perpendicular to the direction of Lamb wave propagation. Measurements are taken at each point in the scan, and the sample is rotated by a computer controlled rotary table after each scan in order to obtain data from the different orientations. For crosshole tomography, two longitudinal contact transducers are scanned independently to the various sender/receiver positions by two computer controlled linear scanners. At each sender/receiver position, the received waveform is digitized and saved on a personal computer for later analysis.

RESULTS AND DISCUSSION

Figure 3A shows a parallel projection tomographic reconstruction contour plot of Lamb wave contact scanning data taken on a 2.45 mm thick aluminum plate with a 20 cm^2 region of 50% thickness reduction. The image covers 100 × 100 mm and was reconstructed from 18 projections of 100 rays each. The thinned region is shown clearly as the white region in the center of the image. Figure 3B shows a crosshole tomographic reconstruction of the same 100 × 100 mm region of the aluminum sample. This image was produced using the ART algorithm and 400 rays. Note that although the much lower ray density in the flaw region decreases the accuracy of the reconstruction, the location and size of the thinned region are accurately reproduced. The crosshole image is inherently lower resolution because the number of pixels corresponds to a much coarser computational grid.

One of the disadvantages of the parallel projection technique is that it requires measurements to be made from all sides of the region of interest. This is clearly impractical in any number of materials testing situations. The crosshole technique requires access to only two sides of the region, although better reconstructions will be possible with transducers scanned along a third (or even fourth) side of the region of interest. This corresponds to having a line of receivers along the surface of the ground in addition to down the two boreholes. It increases the ray density and gives a larger number of ray directions through the region of interest. Both of these increase the accuracy of the reconstruction. In the development of a practical scanning technique we have opted for a two-leg system, but the algorithms and instrumentation developed here can easily be extended. In the parallel projection tomographic scanner the travel distance of the Lamb waves is fixed, so that we can use the P2L2 to detect very small changes in arrival time due to thickness changes. This is not possible for the crosshole tomography because the path length is different for each of the rays. Instead we digitized the entire received waveform for subsequent processing to extract the arrival times of the $S0$ modes needed for input to the ART code. In our initial studies we merely identified the peaks of interest manually, but with hundreds or even thousands of such waveforms required for input to the tomographic reconstruction algorithm this was not practical. To automate this portion of the procedure, we have developed a rudimentary "expert system" which searches through the waveforms for a portion which corresponds to the characteristic $S0$ signal. It then records the time of arrival of that signal for each waveform and passes that to the tomographic code for the corresponding ray. The image shown in Figure 6 used this automated procedure without other signal or image processing.

There are a number of issues yet to be addressed in this work. Many are practical issues associated with developing rapid and operator-independent tomographic Lamb wave images. Scanning with contact transducers is slow and prone to errors from variations in coupling of the ultrasonic energy in and out of the plate. Neither of these are concerns in the laboratory, but are serious drawbacks in service. Both can be overcome by using arrays of transducers which are "electronically" scanned through all the various combinations. A ring of transducers could be used with standard fan-beam reconstructions and two or more linear arrays of transducers could be used with the crosshole algorithms. This would eliminate coupling problems, and would recover the speed inherent in Lamb wave techniques. The reconstruction algorithms run in near real time on modern PCs so there appears to be no inherent limits on implementation of this technique in the field. Although the Lamb wave physics is fairly complicated, an expert system which automatically extracts the tomographic inputs from the received waveforms will make measurements possible by technicians who neither know or care about those subtleties.

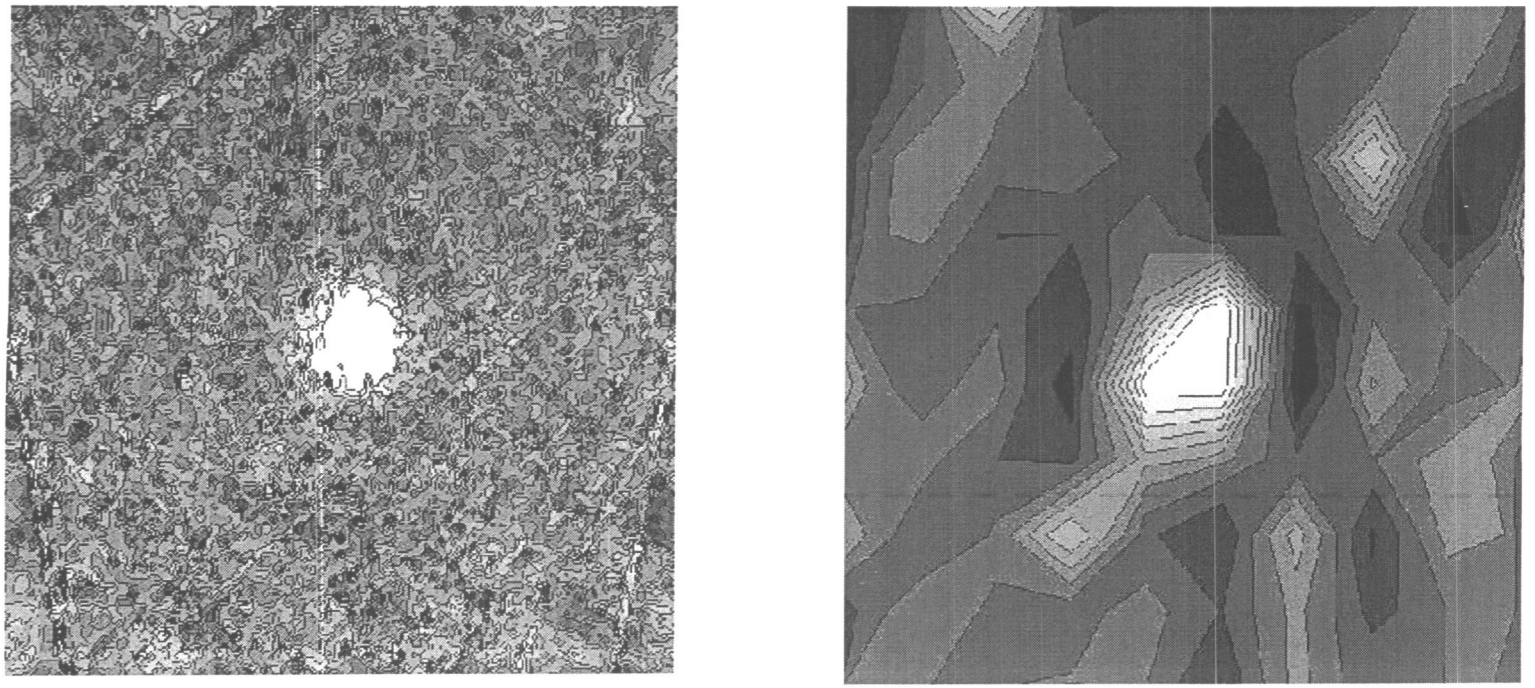

A B

Figure 3: Parallel projection (A) and cross-borehole (B) tomographic reconstruction contour plots of Lamb wave contact scanning data taken on a 2.45 mm thick aluminum plate with a 20 cm^2 region of 50% thickness reduction. The left image covers 100 mm $\times$100 mm and was reconstructed from 18 projections of 100 rays each. The thinned region (higher velocity) is shown clearly as the white region in the center of the image. The right image was produced using the ART algorithm and 400 "crosshole" rays. Note that although the much lower ray density in the flaw region decreases the accuracy of the reconstruction, both the location and size of the thinned region are accurately reproduced. The crosshole image is inherently lower resolution because the number of pixels corresponds to a much coarser computational grid.

The most serious limitation in the tomographic reconstruction algorithms that we have used in this work is that we have neglected diffraction effects. We have assumed that the thinning only caused the Lamb wave velocity to change, but that there was no scattering of the Lamb waves. For slight changes in thickness this is a reasonable assumption, but for general flaws there will always be scattering. Figure 4 shows parallel projection reconstructions of aluminum plates with small (A) and large (B) isolated through holes. Note in particular the scalloped edge and star-burst pattern around the large hole. Clearly the assumption of straight rays breaks down in this case. Incorporation of scattering effects into a Lamb wave diffraction tomography theory is the next step in our work. Mindlin's higher-order plate theory and classical scattering theory can be combined for this purpose. This will allow us to accurately map severe corrosion, as well as cracks, disbonds and other flaws which strongly scatter the Lamb waves. We also hope to be able to image subtle flaws in the presence of disruptive features such as lap joints and rivets in aircraft structures.

CONCLUSIONS

Lamb wave contact scanning is a promising technique for detecting hidden corrosion damage in aging aircraft strutures. Tomographic techniques allow the extent and severity of corrosion to be accurately mapped, without the need for highly trained personnel knowledgeable about waveguide physics. Cross-borehole Lamb wave scans have inherent advantages over parallel-projection methods, when practical implementation for aging aircraft structures is considered.

ACKNOWLEDGMENTS

The authors would like to thank Drs. Pat Johnston and Bill Winfree of NASA Langley NESB for financial and equipment support, as well as many helpful discussions. Additional support has been provided by the Office of Naval Research and by the Virginia Space Grant Consortium.

REFERENCES

1. A.C. Kak and M. Slaney: "Principles of Computerized Tomographic Imaging" (IEEE Press, New York, 1988).
2. W. Wright, D. Hutchins, D. Jansen, D. Schindel "Air- coupled Lamb wave tomography" IEEE Trans. Ultrason., Ferroelect., and Freq. Contr. 44(1) 1997 p. 53.
3. D. P. Jansen, D.A. Hutchins and J.T. Mottram, "Lamb Wave Tomography of Advanced Composite Laminates Containing Damage", Ultrasonics, Vol. 32, No. 2, p.83, (1994).
4. D.A. Hutchins, D.P. Jansen and C. Edwards, "Lamb Wave Tomography Using Non-Contact Transduction", Ultrasonics, Vol. 31, No. 2, p. 97, (1993).
5. D. P. Jansen, D. A. Hutchins "Immersion tomography using Rayleigh and Lamb waves" Ultrasonics 30(4) 1992 p. 245.
6. D. P. Jansen, D. A. Hutchins "Lamb wave tomography" 1990 Ultrasonics Symposium p. 1017.
7. Y. Nagata, J. Huang, J.D. Achenbach and S. Krishnaswamy, "Lamb Wave Tomography Using Laser-Based Ultrasonics", in Review of Progress in QNDE, Vol. 14, Edited by D.O. Thompson and D.E. Chimenti, Plenum Press, p. 561, (1995).
8. F.L. Degertekin, J. Pei, B.T. Khuri-Yakub, K.C. Saraswat "Insitu acoustic temperature tomography of semiconductor wafers" Appl. Phys. Lett. 64 (11) p. 1338 (1994).

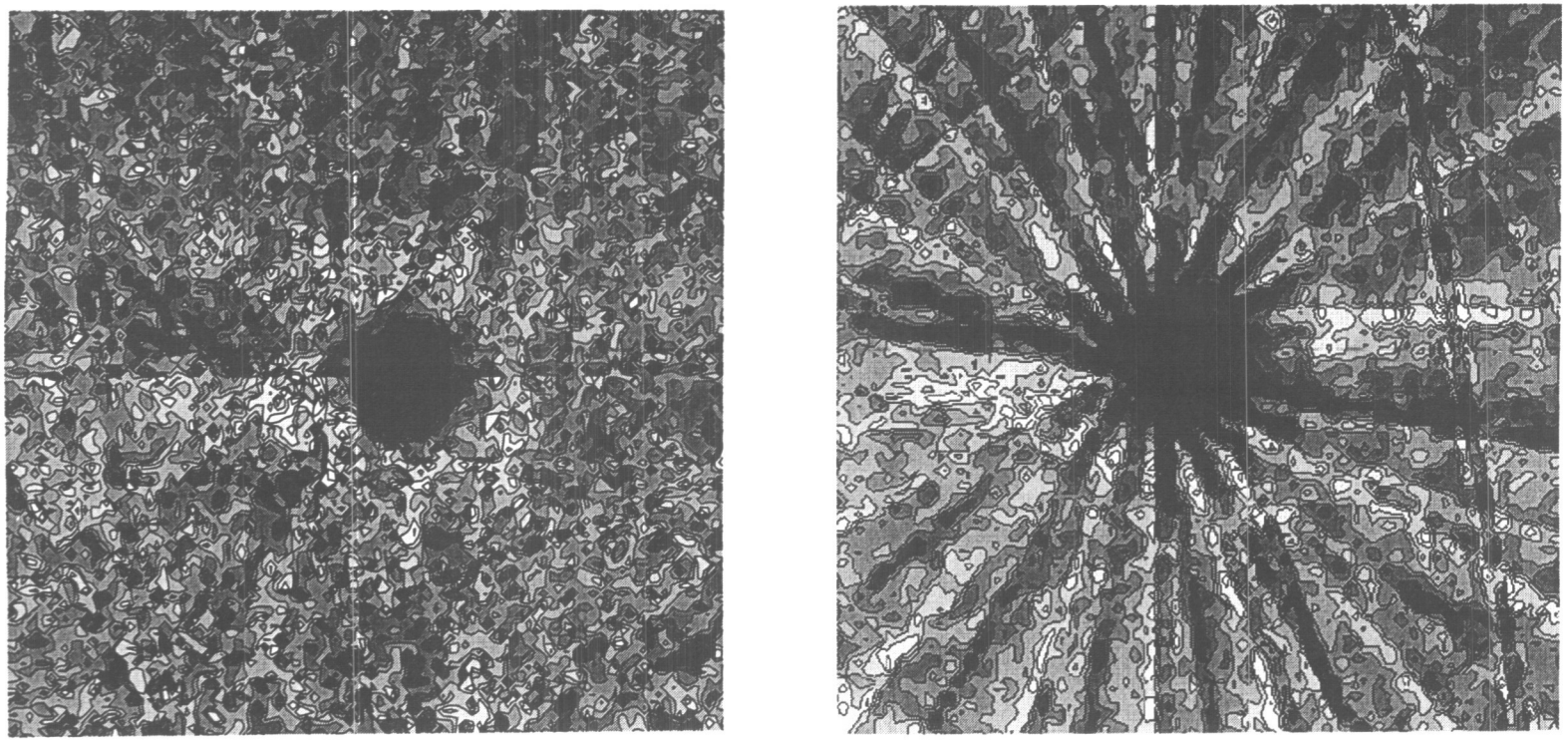

A B

Figure 4: Parallel projection tomographic reconstructions of aluminum plate with small (A) and large (B) isolated through holes. Note that the holes are reproduced as dark circles, indicating increased Lamb wave travel time. The image of the large hole has scalloped edges and starburst artifacts due to scattering effects.

EXPERIMENTAL RESULTS FROM THE FAA/NASA WIDE PANEL FRACTURE TESTS

William M. Johnston
Analytical Services and Materials Inc.
Hampton, Virginia 23666, USA
(757) 864-3472 (Office)
(757) 864-8911 (Fax)
w.m.johnston@larc.nasa.gov

Jeffery D. Helm
University of South Carolina
Columbia, South Carolina 29208, USA

ABSTRACT

The objective of the FAA/NASA wide panel test program was to determine the influence of multiple-site damage (MSD) on the residual strength of stiffened and unstiffened panels and to develop a body of experimental data that can be used to verify any fracture criterion for structures with MSD cracking. To simulate an aircraft skin, tests were conducted on 40-inch wide panels of 0.063-inch thick 2024-T3 aluminum alloy with stiffeners that were made of 0.090-inch thick 7075-T6 aluminum alloy. The FAA/NASA wide panel tests were performed on panels with and without riveted stiffeners for five different crack configurations. The riveted stiffened panels were designed to provide a configuration similar to a riveted curved aircraft structure. The crack configurations tested were single crack, single crack growing into a line of open holes, and single crack growing into a line of open holes with MSD cracks. These test configurations simulated a long crack in the presence of a row of holes with and without MSD. Experimental results of the linkup, maximum load, local and global strain fields, deformation field and load crack extension behavior are presented in this paper. The MSD cause a 20% and 30% reduction in strength for the unstiffened and stiffened panels respectively when compared to the center crack case. The MSD size (0.01 to 0.05 inch) did not significantly effect the reduction in strength caused by the MSD.

1. INTRODUCTION

As the existing commercial air transport fleet continues to age, research has been directed toward developing improved predictive methodologies to ensure structural integrity. One damage scenario that has caused great concern is the development of multiple-site damage (MSD). MSD is the development of multiple, interacting cracks, that individually have a negligible effect on the structure, but together can cause a significant reduction in the residual strength of the aircraft [1].

The materials used in aircraft fuselage structures are typically very ductile. This quality, while promoting the damage tolerance of the structure, also increases the complexity of the analyses required to model the fracture behavior. Linear elastic fracture mechanics (LEFM) based fracture criteria have structural size dependencies that limit their usefulness. Elastic plastic fracture mechanics (EPFM) based fracture criteria have been developed to overcome the shortcomings of LEFM. Experimental verification is required to confidently use any criterion to predict fracture behavior. For complete verification, a valid fracture criterion should be able to obtain fracture parameters from laboratory specimens and predict the behavior of full-scale structures. The objectives of the FAA/NASA wide panel test program were to determine the influence of multiple-site damage (MSD) on the residual strength of stiffened and unstiffened panels and to develop a body of experimental data that can be used to verify any fracture criterion for structures with

MSD cracking. The complete results from the FAA/NASA wide panel test program are given in References 2 and 3.

The wide panel tests were designed to provide an intermediary step between laboratory coupons and a full-scale structure. Tests were conducted on 40-inch wide flat panels, with and without riveted stiffeners. The riveted stiffened panels were designed to provide a flat approximation to a curved aircraft structure. The stiffeners add structural complexity to the flat panels, while maintaining the well defined boundary conditions of a simple laboratory coupon. Identical tests were conducted with and without the stiffeners, for five crack configurations (with and without MSD). These tests allow the effects of MSD and the stiffeners to be quantified. Measurements of crack growth, local strain, and full field in plane (u, v), and out-of-plane (w) displacements permit verification of any fracture analysis.

The material examined in the FAA/NASA wide panel test program was 0.063-inch thick 2024-T3 aluminum alloy. The test program consisted of a series of material characterization tests, a set of single stiffener tests, and a series of stiffened and unstiffened panels with MSD. The material characterization tests were conducted on middle-crack tension (M(T)) specimens ranging in width from 3 to 40 inches wide and compact tension (C(T)) specimens ranging in width from 2 to 6 inches. The stiffened and unstiffened panel tests with MSD were conducted on 40-inch wide panels with five different crack configurations: single crack, single crack with open holes, and single crack with open holes and 0.01, 0.03, and 0.05 inch MSD cracks emanating from both sides of each hole. These test configurations simulated a long crack in the presence of a row of holes with and without MSD. Identical tests were conducted with and without stiffeners for each crack configuration. A significant detail of these tests was that the equal length MSD cracks were fatigue cracks rather than the saw-cuts that have been typically used in MSD testing.

2. EXPERIMENTAL PROGRAM

The test program for the FAA/NASA wide panel fracture tests consisted of four sets of tests: (1) baseline static and fracture tests, (2) tests on 12-inch M(T) specimens with a single central stiffener, (3) unstiffened 40-inch wide panel fracture tests and (4) stiffened 40-inch wide panel fracture tests. The baseline material and fracture tests were conducted to determine the stress-strain behavior and the fracture behavior. Baseline tests were conducted on different specimen configurations and widths to establish a database that could verify the specimen configuration independence of any fracture criteria. The single stiffener tests provided a simpler structural configuration to determine panel/stiffener interaction. The 40-inch wide panels provided data on a geometrically nonlinear problem with known MSD cracking and well-defined boundary conditions. The stiffened wide panels added the complexity of a riveted structure. Although only a portion of the results are presented, the entire test program is discussed for completeness.

2.1 Material Characterization

Baseline material characterization tests were conducted on the 0.063-inch thick 2024-T3 aluminum alloy used in the wide panels and the 0.09-inch thick 7075-T6 aluminum alloy used in the stiffeners. Static tests were conducted on both materials to determine the stress-strain curve. Fracture tests were conducted on M(T) and C(T) specimens and are summarized in Table 1. Failure load presented represent the average failure load of 1 to 4 tests. Measurements of applied load, crack extension, and remote displacement were made for each test. The C(T) specimens were restrained with guide plates to prevent out-of-plane displacement. The M(T) specimens were tested with and without guide plates to evaluate the effect of crack buckling on the fracture behavior. Measurements of out-of-plane displacement were made on the M(T) specimens tested without guide plates using the video image correlation system, VIC_3D [4]. A complete summary of the fracture test results is given in Reference 5 while the static test results are presented in Reference 3.

2.2 Middle Crack Tension Specimen with a Single Stiffener.

Tests were conducted on four 12-inch wide M(T) specimens with single stiffeners to aid in testing and modeling the 40-inch specimens. The M(T) specimens were 12 by 36 inches with a 1.6 inch wide stiffener riveted to each side of the specimen as shown in Figure 1. The stiffeners were made of 0.090 inch thick 7075-T6 aluminum riveted on 1-inch centers from the crack line and bonded in the grip region. These tests presented a simpler structure to test and to model than the wide panels because the specimens had a single center crack and were tested with a single broken or unbroken stiffener bridging the crack line. Strain gages were applied to these specimens to assist in determining the load transfer from the panel through the rivets to the stiffener. Specimens with three different crack lengths and one with the stiffener cut were tested, as summarized in Table 2. The complete details from the experimental results are presented in Reference 3.

2.3 Wide Panel Tests

Wide panel tests were conducted on 40-inch wide panels of 0.063 inch thick 2024-T3 aluminum alloy. Two identical sets of five different crack configurations were tested with and without riveted stiffeners. The five crack configurations (Fig. 3) consisted of:

1. Single 8.0 inch center crack
2. Single 8.0 inch center crack with a row of twelve (12), 0.187-inch diameter holes on both sides of the long crack
3. Single 8.0 inch center crack with a row of twelve (12), 0.187-inch diameter holes on both sides of the long crack with 0.01-inch cracks emanating from both sides of each of the holes.
4. Single 8.0 inch center crack with a row of twelve (12), 0.187-inch diameter holes on both sides of the long crack 0.03-inch cracks emanating from both sides of each of the holes.
5. Single 8.0 inch center crack with a row of twelve (12), 0.187-inch diameter holes on both sides of the long crack 0.05-inch cracks emanating from both sides of each of the holes.

The precracking of the specimens with MSD was performed using a multi-step process. First, undersized holes with electrical-discharge machine (EDM) notches were machined into the panel. The EDM notches were less than the desired length of the small MSD cracks. The specimens were fatigue precracked at a load range that results in a stress-intensity factor range of 8-10 ksi(in)$^{1/2}$ for the MSD cracks. Each MSD crack was monitored during precracking. Once the cracks at a hole were precracked to the desired length, a small bolt with washers and a nut was placed into the hole. The bolts were torqued to a specific value causing the washers to transfer some load around the crack, reducing the stress intensity factor range, and thus also reducing the crack growth. This precracking procedure was continued until all 24 cracks reached the desired length [6]. The second step was to drill holes to the required diameter. This removed the undersized hole and left two cracks on each side of the 0.187-inch diameter hole (Fig. 2). A center EDM notch was cut onto the center of the specimen that was 0.5-inches less in length than the desired crack length. Again, the specimen was fatigue precracked at a stress-intensity factor range of 8-10 ksi(in)$^{1/2}$ for the large lead crack. Because the stress-intensity factor of the lead crack was significantly greater than those of the smaller cracks at the holes, the lead crack grew and the smaller MSD cracks remained stationary. This produced the final crack configurations shown in Figure 3.

The fatigue precracking procedure provided 24 sites of equal length MSD as shown in Table 3. In Table 3 the desired length (hole diameter plus two times MSD length) is shown along with the average precracked length of the 24 holes for the different MSD tests. The average length was within .0015 inches of the desired length and the standard deviation in crack length was .002 inches. Only the unstiffened case with 0.05-inch MSD had a standard deviation in crack length over .002 inches. This

results was caused by the crack at single hole that exceeded its desired length. Since, this hole was located away from the center crack, it did not adversely affect the test results.

The stiffened wide panels were constructed as shown in Figure 4. The panels had five 1.6-inch wide, 0.90-inch thick 7075-T6 stiffeners. The stiffeners were separated 8 inches (on centers), and placed symmetrically on the front and back of the specimen. The plate and stiffener were connected with MS20470AD6-8 button head rivets spaced 1 inch apart (on center) from the crack line (but not on the crack line). The stiffeners were bonded to the cracked panel in the grip region to facilitate load transfer. The center stiffener was cut, along the crack line of the 8-inch center crack, allowing the center of the specimen to buckle freely.

Because panels of thin aluminum alloy with a pre-existing crack experience large out-of-plane deformation (buckling) under tensile loading, the full-field displacement data was essential for developing a complete record of the experiments. To provide sufficient data for model verification in-plane and out-of-plane displacements were measured over an area of 21.7 inch wide by 9.8 inches high near the initial crack location using a two-camera stereo vision system, VIC_3D [4], as shown in Figure 4 as the Video-Image-Correlation (VIC) area. Displacement measurements were also made using this video image correlation system in a small region of the crack tip to determine the strain field. Load-displacement and load-crack extension data were recorded for each test and 58 strain gages were mounted on the stiffened panels to provide information on the strain in the stiffeners and in the sheet.

3. EXPERIMENTAL PROCEDURE

The specimens were tested in a 300 kip servo hydraulic test stand, using displacement control with a ramp rate of 0.005-0.015 inch/min. Crosshead displacement, load and strain gage output was recorded every five seconds by an automated data acquisition system. The movement of the crosshead was held constant after each 2-5 kips increment in load (depending on the expected failure load). At each of these intervals both local and global deformation fields were recorded using the VIC_3D systems. These loading intervals were continued until crack growth initiated, then the displacement was increased until the center crack extended in increments of about 0.050 inch. Crack length, load and the deformation field were recorded and loading was continued until failure. The maximum load and crack link up loads were recorded for each test.

3.1 Strain gage Locations

The five stiffened wide panels were instrumented with 58 strain gages (24 back to back pairs) to provide information on the strain field in the panel (Fig. 5). Gages were placed on both the 2024 sheet and on the 7075 stiffeners. Gages were placed in three locations on the 2024 panel. Far field gages were placed between the stiffeners 20 inches from the crack plane (gages 1-8 of Fig. 5) to provide information on load transfer into the sheets. Gages located 3.5 inches from the crack plane provided load transfer information between the stiffeners (gages 9-12 of Fig. 5). Local crack tip gages provided a point to confirm local strain fields for all configurations. Gages on the stiffener helped to determine load transfer from the panel to the stiffeners (gages 21-58 of Fig. 5).

3.2 Video Image Correlation Measurements

While the theoretical development for stereo imaging is well-documented [4,7-12], experimental measurements in solid mechanics using computer vision concepts are relatively recent [9,10,11]. The projection/back-projection method developed recently by Helm et al. [4], known as VIC_3D, is capable of true, point-to-point, surface displacement measurements for both curved and flat surfaces.

Two VIC_3D systems (shown in Fig. 6) were used to make global and local crack tip measurements (details of these systems are discussed in the Appendix). The surface displacements in a 21.7 inch by 9.8 inches area (shown in Figure 4) near the initial crack location were measured. This displacement data provides both out-of-plane and in-plane displacements for a given load and crack extension. In addition, local crack tip measurements were made using two different sized image areas. For the specimens without MSD, a small 0.24 by 0.16 inch area was examined for the determination of the crack tip opening angle (CTOA). For the cases with MSD, a larger 0.39 by 0.59 inch area was used to determine the strain field and plastic zones between crack tips. The ligament region between the lead crack and the first MSD site and between the first three MSD holes were also examined.

4. RESULTS AND DISCUSSION

Due to the large amount of information generated from these tests, only selected results from these tests are contained within this report. Maximum failure load and linkup loads are presented in Table 4. Load against crack extension results for the unstiffened panels are shown in Figures 7 and 8. Load crack extension results for the stiffened panels are presented in Reference 13. Sample data from the global and local VIC systems is shown in Figures 9-11. The load crosshead displacement, strain gage data and remaining VIC results are presented in Reference 3. A summary for these tests is provided in Reference 13, while the experimental procedure and results for these tests is explained in more detail in Reference 4 and 6.

4.1 Load-Crack Extension Data for Unstiffened Panels

The load-crack-extension results for the unstiffened panels are summarized in Figures 7 and 8. Figure 7 shows the results from the center crack test and the test with the crack growing into a row of rivet holes. For the test with the row of holes, at 52.5 kips the crack linked up with the first hole and the load continued to increase, without crack growth, until the specimen failed at about the same load as the specimen without holes. This behavior is indicated as the vertical section of open symbols on the graph. Figure 8 shows that all of the MSD cases had very similar crack extension behavior leading up to the first link-up.

4.2 Failure and Linkup Loads

Failure of the unstiffened panels with MSD was dominated by the first linkup between the lead crack and the first MSD site. The 0.01, 0.03, and 0.05 inch MSD cases failed at 48.3, 47.4, and 46.44 kips, respectively. The linkup load for the MSD cases was about 10% lower than the case where the center crack grew into holes without the MSD. The failure loads for the unstiffened panels with MSD were 20% lower than the failure load for the unrestrained center crack case (or the center crack case with holes and no MSD).

Failure of the stiffened panels was governed by the failure of the inner set of intact stiffeners. For the MSD cases after first linkup the crack grew to a point under the first intact stiffener. There the crack arrested until the load peaked. Since the test was conducted in displacement control, the crack continued to extend at lower loads until all MSD holes were linked up. The load then continued to increase until the first set of stiffeners fractured. For the stiffened panels the link up load was still about 10% lower for the cases with MSD when compared to the case with holes. The failure load for the specimens with MSD was 30% lower than the center crack case.

4.3 VIC Displacement and Strain Data

Displacement data from the VIC systems provided full field displacements and local strain fields. A local strain field for the unstiffened panel with 0.05-inch MSD is presented in Figure 9. The area between the center crack and the first MSD crack is shown for a load just prior to link up. The magnitude of strain values between crack tips varies from 2.5% at the center of the ligament to more than 10% strain at the crack tip. Data from the displacement fields for the unstiffened middle crack case are shown in Figures 10 and 11. The displacement field just prior to failure (54 kip) is shown in Figure 10, where the center of the crack is located at (0,0,0) and the crack tip is located at (8,0,0). The progression of the buckling through the test can be seen in Figure 11. This figure shows the out-of-plane displacement of a line 1-inch from the crack for 6 different load levels. The progression of the buckling shape can be seen from a flat sheet through maximum load until just prior to failure.

5. CONCLUDING REMARKS

The wide panel tests were designed to determine the influence of multiple-site damage (MSD) on the residual strength of stiffened and unstiffened panels and to develop a body of experimental data that can be used to verify any fracture criterion for structures with MSD. Tests were conducted on 40-inch wide flat panels, with and without riveted stiffeners. Identical tests were conducted with and without the stiffeners, for five crack configurations (with and without MSD). These tests allow the effects of the three sizes of MSD (0.01, 0.03, and 0.05 inch) and the stiffeners to be quantified.

The presence of MSD caused a drop in the linkup load, and failure load for both the stiffened and unstiffened wide panels. For both the stiffened and unstiffened cases the linkup load for the MSD cases was about 10% lower than the case where the center crack grew into holes without the MSD. The failure loads for the unstiffened panels with MSD was 20% lower than the failure load for the center crack case, while for the stiffened specimens the failure load with MSD was 30% lower than the center crack case. For both the stiffened and the unstiffened panels the varying the size of MSD less caused than a 3% change in the reduction of strength.

The FAA/NASA wide panel fracture tests demonstrated the effect of different sized MSD fatigue cracks (not sawcuts) on the failure of stiffened and unstiffened wide panels. These results, along with all the baseline tests provide a database for the validation of numerical methods of predicting fracture. The combinations of center crack, center crack with holes and MSD panels complete a set of well-defined problems.

6. REFERENCES

[1] Swift, T., "Damage Tolerance in Pressurized Fuselages", New Materials and Fatigue Resistant Aircraft Design, D. L. Simpson Ed., EMAS ltd., 1987, pp. 1-77.

[2] Dawicke, D. S., Newman, J. C., Jr. and Tan, P. W., "FAA/NASA Wide Panel Fracture Tests – Part I Executive Summary," NASA TM (In Progress), 1998.

[3] Johnston W.M., and Helm, J. D., "FAA/NASA Wide Panel Fracture Tests – Part II Experimental Test Program," NASA CR (In Progress), 1998.

[4]. Helm, J. D., McNeill, S. R., and Sutton, M. A., "Improved Three Dimensional Image Correlation for Surface Displacement Measurement", Optical. Engineering, Vol. 35, No. 7, 1996, pp. 1911-1920.

[5] Johnston W. M., "Fracture Tests on 0.063 inch Thick 2024-T3 Aluminum Alloy," NASA CR (In Progress), 1998.

[6] Johnston W. M., "FAA/NASA Wide Panel Fracture Tests – Part IV Experimental Procedure," NASA CR (In Progress), 1998.

[7] Tsai, R. Y., "An Efficient and Accurate Camera Calibration Technique for 3D Machine Vision", Proceedings of the IEEE Intl. Conference on Computer Vision and Pattern Recognition, 1986, pp. 364-374.
[8] Weng, J., Cohen, P. and Herniou, M., "Camera Calibration with Distortion Models and Accuracy Evaluation", IEEE Transactions of Pattern Analysis and Machine Intelligence, Vol. 14, No 10, 1992, pp. 965-980.
[9]. Luo, P. F., Chao, Y. J. and Sutton, M. A., "Application of Stereo Vision to 3-D Deformation Analyses in Fracture Experiments", Optical. Engineering, Vol. 33, No. 3, 1994, pp. 981-990.
[10] Luo, P. F., Chao, Y. J., Sutton, M. A. and Peters, W. H. III, "Accurate Measurement of Three-Dimensional Deformations in Deformable and Rigid Bodies Using Computer Vision", Experimental Mechanics, Vol. 30, No. 2, 1993, pp. 123-132.
[11] Kahn-Jetter, Z. L. and Chu, T. C., "3-D Displacement Measurements Using Digital Image Correlation and Photogrammetry Techniques", Experimental Mechanics, Vol. 30, No. 1, 1990, pp. 10-16.
[12] Born, M. and Wolf, E., "Principles of Optics", Pergamon Press, Third Edition, 1964, pp. 203- 233.
[13] Seshadri, B. R., Newman, J.C., Jr., Dawicke, D. S., and Young, R. D., "Fracture Analysis of the FAA/NASA Wide Stiffened Panels," Second NASA/FAA/DoD Conference on Aging Aircraft, Williamsburg, VA, August 31 – September 3, 1998.

APPENDIX
VIDEO IMAGE CORRELATION SYSTEM

While the theoretical development for stereo imaging is well-documented [4,7-11], experimental measurements in solid mechanics using computer vision concepts are relatively recent [9,10,11]. The projection/back-projection method developed recently by Helm et al. [4], known as VIC_3D, is capable of true, point-to-point, surface displacement measurements for both curved and flat surfaces.

The VIC_3D system used for this study can be divided into two main parts. The first part is the calibration of the camera system and the second is measurement of three-dimensional surface displacement field using image correlation methods. A schematic of the system is presented in Figure 6(a). Brief descriptions of both the calibration and measurement components are presented in the following sections.

A.1 System Calibration

Calibration of the two-camera computer vision system, VIC_3D, determines the relative positions and operating characteristics of both cameras. The calibration system is based on a series of images of a grid with known line spacing. Each camera is calibrated to the grid individually but, because the positions of the cameras are both known relative to the same grid, their relative position to each other is also known.

The camera and lens system is modeled as a pinhole device, as shown in Figure 6(b). To increase accuracy, the model is modified to correct for Seidel lens distortion [12]. The pin-hole camera projection governing equations have been described in previous publications [7,8]. The imaging characteristics of a camera modeled in this manner can be described by five parameters. The pinhole distance (phd) is the perpendicular distance from the pinhole to the sensor plane of the camera and can be considered the magnification factor of the lens. The location of the center of the image (C_x, C_y) is defined as the point on the sensor whose normal passes through the pinhole. These parameters are important because lens distortion is proportional to the cube of the distance from the center of the image. The lens distortion factor, κ, is a correction for Seidel lens distortion. The final parameter is the aspect ratio, λ, of the sensors. The value of λ is the ratio of the size of a pixel in the Y direction to its size in the X direction.

Six parameters X_o, Y_o, Z_o, α, β and γ are required to describe the relationship between a camera and the coordinate system of the calibration grid. The parameters, X_o, Y_o and Z_o describe the position in space of the grid relative to the camera and α, β and γ describe the angular orientation of the grid relative to the camera. To calibrate a camera, an image of the grid is taken. The camera is then moved perpendicular to its sensor plane and a second image is taken. Using (a) the known spacing of the grid, (b) the known movement of the camera and (c) the location of the grid intersections, as extracted from the calibration images, non-linear optimization can be used to find the parameters that best describe the position and operating characteristics of the camera. The process is then repeated, without moving the grid, for the second camera.

A.2 VIC_3D Measurements

Once calibration is completed, the VIC_3D stereo vision system can be used to measure object shape (profiling) or full field, three-dimensional displacements. VIC_3D uses a random pattern bonded to the surface to provide a unique set of features to map from one camera to the other. If the surface has a naturally occurring pattern, it may be used for the measurement.

A.3.1 Profile Measurements

The projection method used for profile measurements is shown schematically in Figure 6(c). The analysis uses a pair of images taken of the surface of the object by camera 1 and camera 2 at the same point in time. A small square section of the image taken by camera 1 is projected onto the candidate plane in space. Assuming that the surface of an object can be modeled using a series of small planar patches, each candidate plane is described relative to camera 1 by two of the plane's direction angles Θ, Φ and the variable Z_p denoting the location of the intersection of the plane and the optic axis for camera 1.

The initial position of the candidate plane is established through an interactive first guess generator. Because the operating characteristics of camera 1 are known, the gray levels of the subset can be projected onto the candidate plane, creating a virtual gray level pattern in space. The virtual gray level pattern is then projected into camera 2. This creates a second virtual gray level pattern at the sensor of the second camera. A cross-correlation error function between the recorded gray level pattern from camera 2 and the virtual gray level pattern projected onto the second camera's sensor is used to obtain optimal estimates for the candidate plane variables. Once the system has been optimized, the three dimensional position of that point on the surface of the object can be calculated from the camera 1 parameters and the position of the candidate plane.

A.3.2 Displacement Measurement

The displacement measurement system requires a set of images taken before the object is loaded (undeformed images) and a second set taken after the load was applied to the specimen (deformed images). The first part of the displacement measurement system is the same as that of the profile measurement system. An initial candidate plane is chosen and a virtual gray level pattern in space is established. As with the profile system, the virtual pattern is projected back into camera 2. At this point, the virtual gray level pattern in space is allowed to translate and rotate in a rigid-body manner to a second position as shown in Figure 6(d). The displaced virtual gray level pattern is then projected back to the sensor planes in cameras 1 and 2. As with the profile system, a cross-correlation error function is established between the virtual gray level patterns at the sensor planes of cameras 1 and 2 and the recorded gray level patterns from the deformed images recorded by those cameras. All three error functions are simultaneously optimized establishing both the position and displacement of that point on the surface of the object. By continuing the analysis on other portions of the undeformed camera 1 image, the profile and three-dimensional displacement of the surface of the object, for the entire field of view shared by both cameras is measured.

TABLE 1. BASELINE FRACTURE TESTS

C(T) Specimens B= 0.063 inch, a/W = 0.4			M(T) Specimens B= 0.063 inch, 2a/W = 1/3		
Width, W (in.)	Buckling Guides	Max Load (lbs)	Width, W (in.)	Buckling Guides	Max Stress (kips)
2	Yes	711	3	Yes	6.82
4	Yes	1268	12	Yes, No	24.3, 20.9
6	Yes	1736	24	Yes, No	43.7, 32.7
-	-	-	40	Yes, No	66.9, 44.4

TABLE 2. TEST MATRIX FOR BASELINE STIFFENER TESTS

12 in. Stiffened M(T) Specimens			
Crack Length 2a (in.)	2a/W	Stiffener Cut	Maximum Load (kips)
2	1/6	No	52.04
4	1/3	Yes, No	19.66, 43.40
6	1/2	No	34.00

TABLE 3. PRECRACKING RESULTS

Test Configuration	Desired Length (in)	Average Length (in)	Standard Deviation (in)	Range (max-min) (in)
0.01 MSD	0.2075	0.207	0.002	0.007
0.03 MSD	0.2475	0.247	0.002	0.006
0.05 MSD	0.2875	0.289	0.004	0.020
Stiffened 0.01 MSD	0.2075	0.209	0.002	0.007
Stiffened 0.03 MSD	0.2475	0.248	0.002	0.009
Stiffened 0.05 MSD	0.2875	0.287	0.002	0.010

TABLE 4. WIDE PANEL LINKUP AND MAXIMUM LOADS

Wide Panel Crack Configuration (2a/W = 1/5)	Stiffened	Buckling Guides	Linkup Load (kips)	Maximum Load (kips)
M(T) Constrained	No	Yes	-	88.78
M(T)	No	No	-	60.8
M(T) with 24 Holes	No	No	52.5	60.5
M(T) with 24 holes and 0.01 in. MSD	No	No	48.3	48.3
M(T) with 24 holes and 0.03 in. MSD	No	No	47.4	47.4
M(T) with 24 holes and 0.05 in. MSD	No	No	46.44	46.44
M(T)	Yes	No	-	126.2
M(T) with 24 Holes	Yes	No	73.12	97.82
M(T) with 24 holes and 0.01 in. MSD	Yes	No	65.74	89.00
M(T) with 24 holes and 0.03 in. MSD	Yes	No	62.56	85.56
M(T) with 24 holes and 0.05 in. MSD	Yes	No	65.4	86.66

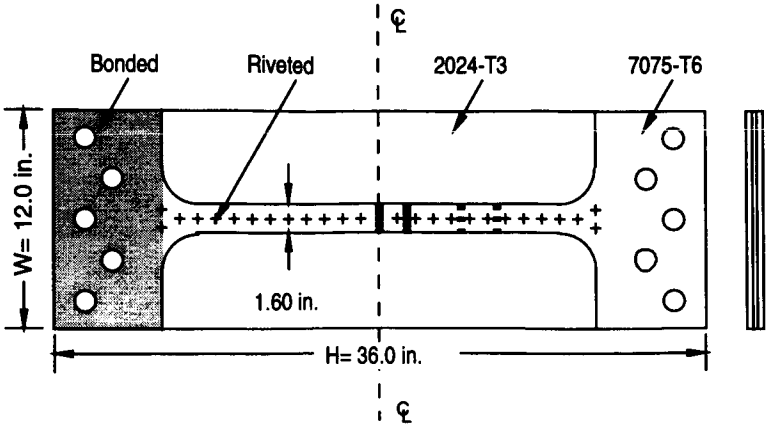

Figure 1. M(T) specimen with a single riveted stiffener.

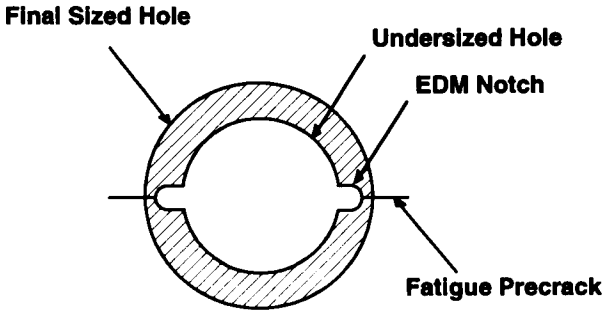

Figure 2. Schematic for precracking of hole with MSD cracks.

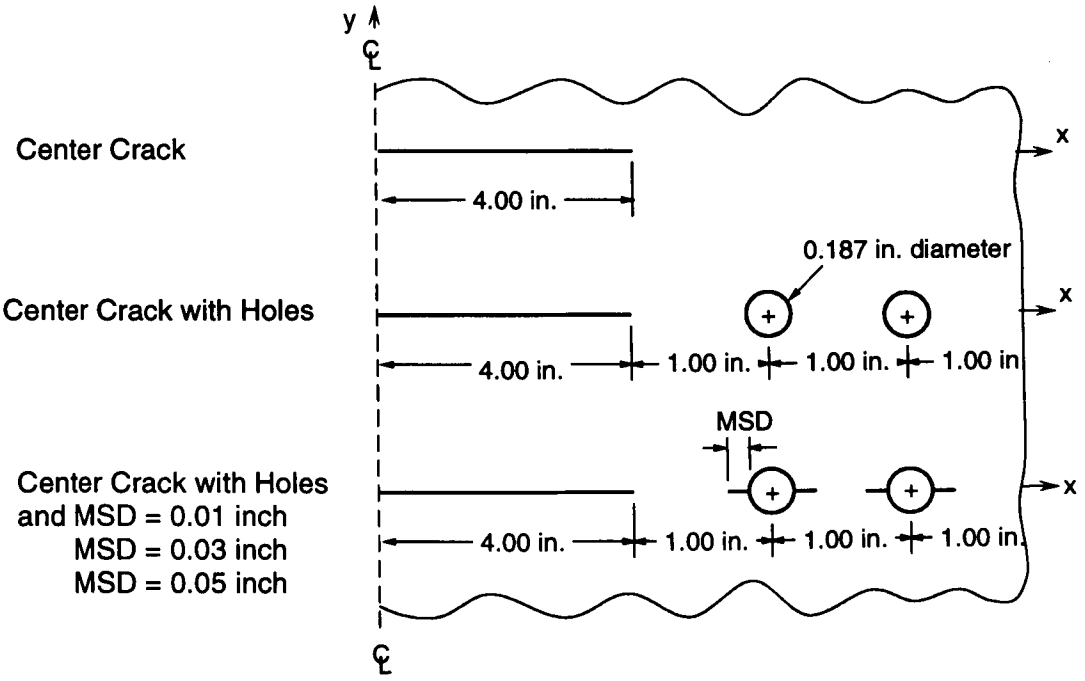

Figure 3. Details of the crack configurations.

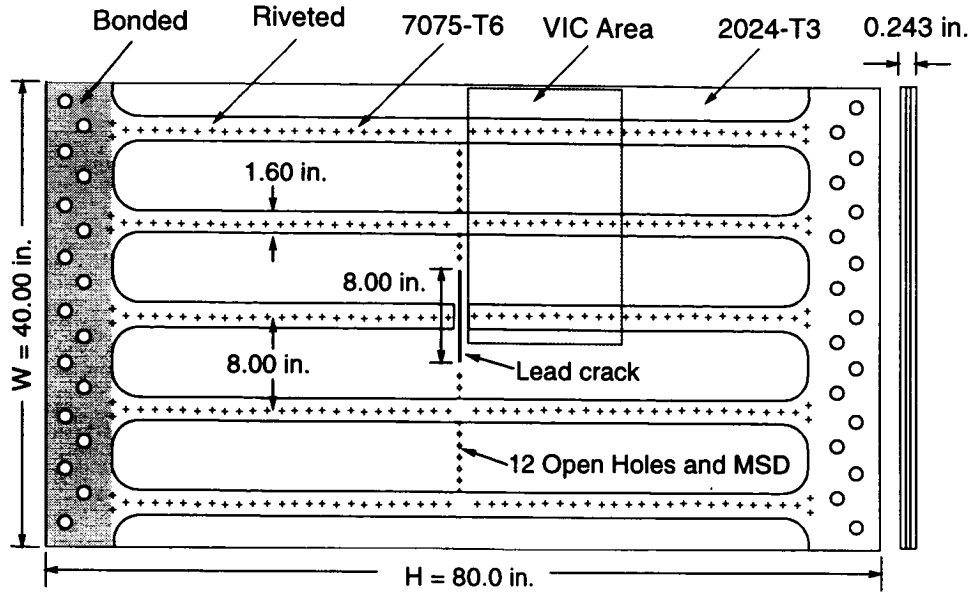

Figure 4. Schematic of the stiffened wide panels.

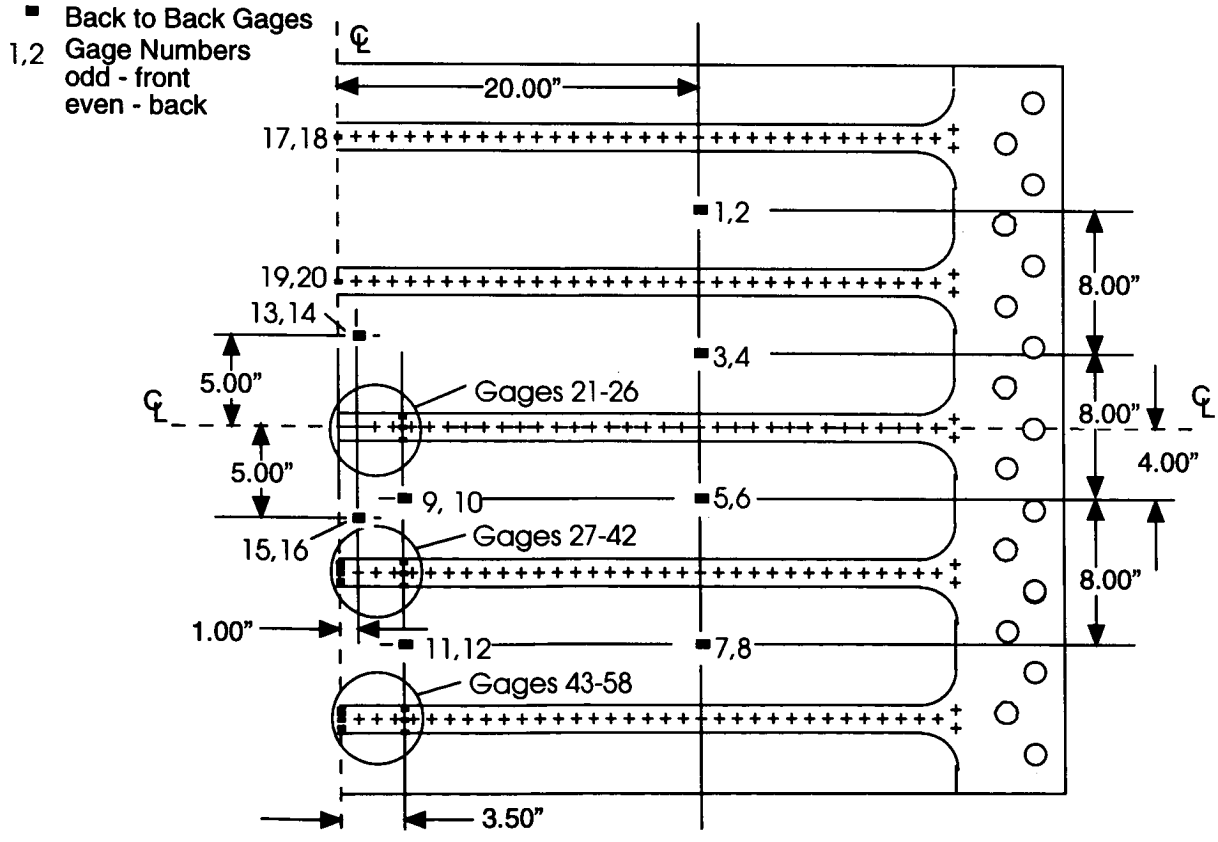

Figure 5. Strain gage locations on the stiffened wide panels.

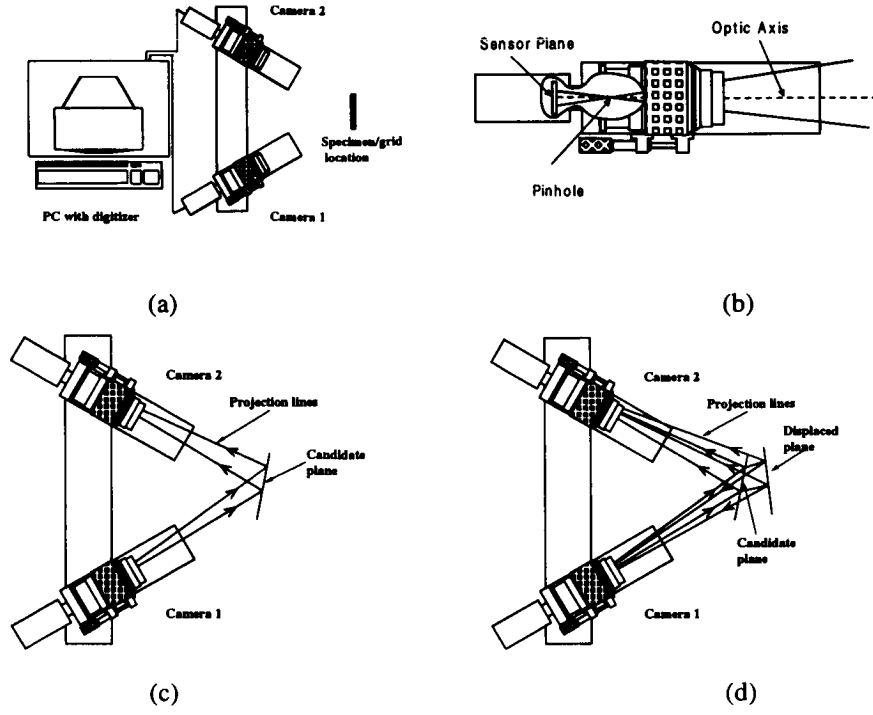

Figure 6. Video image correlation system.

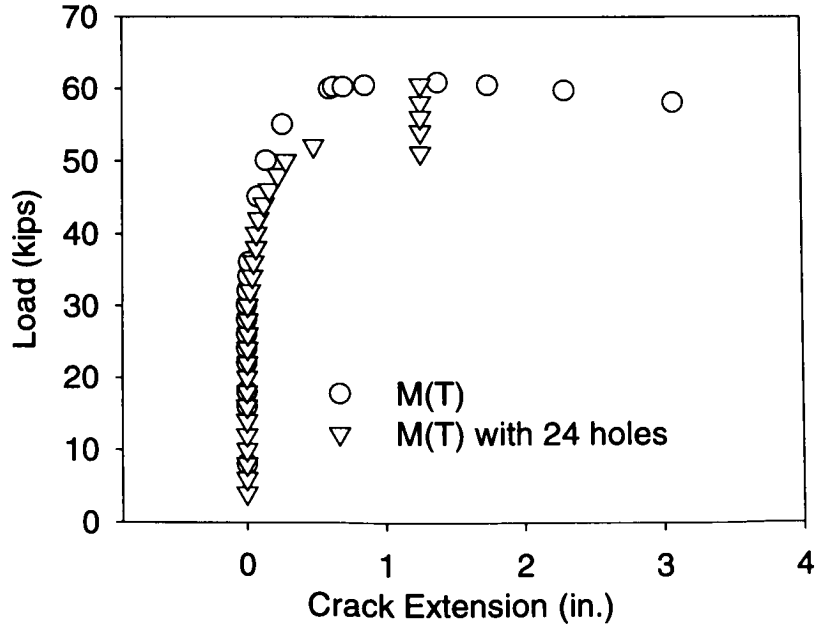

Figure 7. Load against crack extension data for unstiffened wide panels.

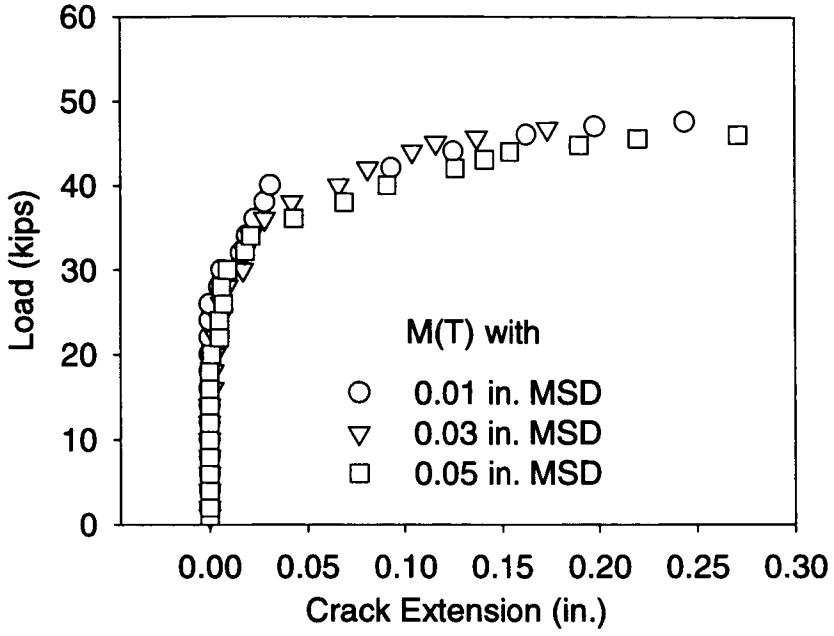

Figure 8. Load against crack extension data for unstiffened wide panels with MSD.

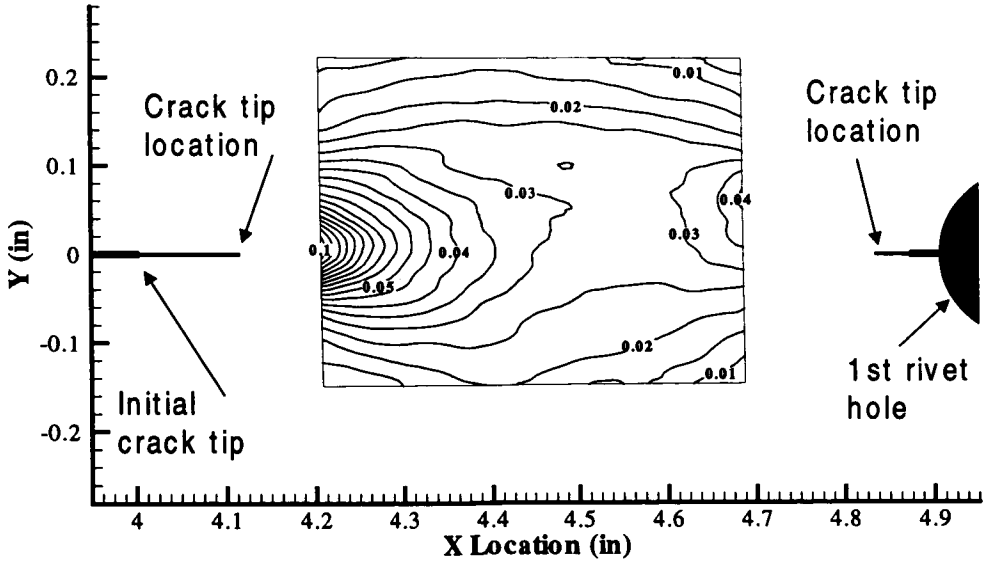

Figure 9. Local strain field for unstiffened wide panel with 0.05 in. MSD at peak load.

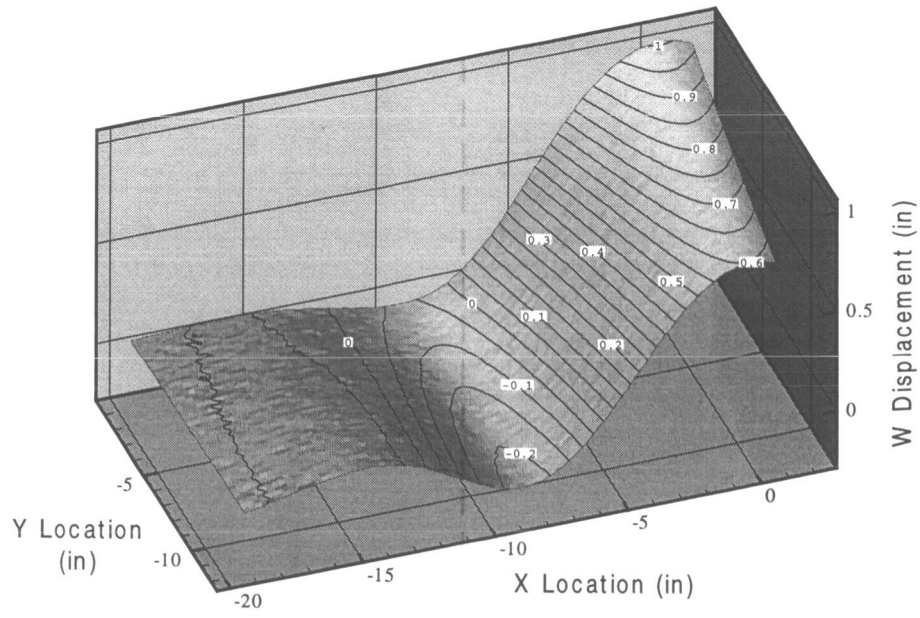

Figure 10. Out-of-plane displacement for the middle crack specimen.

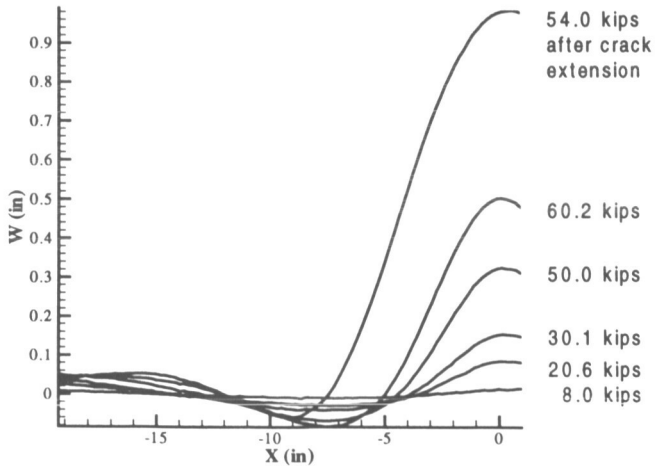

Figure 11. Out-of-plane displacement for the unstiffened wide specimen with the 8-inch center crack.

NOVEL NDE/I PROBE FOR THE DETECTION OF CORROSION IN AIRCRAFT METALLIC STRUCTURES BASED ON ELECTROCHEMICAL IMPEDANCE

Jinseong Kim, Anuncia Gonzalez, and Dalibor Hodko
Lynntech, Inc.
7610 Eastmark Dr., Suite 105, College Station, TX 77840
(409) 693-0017
(409) 764-7479 (fax)
lynntech@myriad.net

ABSTRACT

Lynntech has developed a prototype of a new NDE/I probe for the detection of corrosion in aircraft metallic structures. The NDE/I system is based on electrochemical impedance (EI) measurements. Lynntech's EI prototype probe uses a single characteristic frequency of the ac signal applied between the probe and the structure under testing. At the selected frequency, the impedance signal is highly sensitive to the degree of corrosion of the sample under study. Thus, real time, on-line evaluation of the corrosion process has been easily achieved.

The developed NDE/I probe is simple in design, portable, low in cost, and will not require trained personnel to operate. Another advantage of the probe design is that the use of aggressive electrolytes, a problem known in designing EI probes, is eliminated. The NDE/I probe has been fabricated in different sizes (from 2.3 to 182 cm^2), and is capable of detecting: (i) corroded areas as small as $5x10^{-4}$ cm^2 in painted surfaces, and, (ii) a damage area/probe size ratio as low as 0.0004%. The probe has been successfully tested to promptly screen large areas of aircraft structures, such as fuselage, including lap joints and rivets.

1. INTRODUCTION

In today's economic climate, the prospect of operating both the DoD, NASA, and commercial airline fleets (Federal Airline Administration (FAA)) for extended periods beyond their original designed life will depend on the ability to anticipate required adjustments in the inspection and maintenance activities to compensate for the aging aircraft. Aircraft metallic structures often suffer from corrosion during operation or storage, especially in humid, rainy, hot and seriously polluted areas. Corrosion may shorten the aircraft service life, increase maintenance costs, and cause structural failures. The development of inexpensive, practical, and user friendly nondestructive evaluation/inspection (NDE/I) techniques to detect corrosion with a high degree of accuracy, sensitivity and versatility is urgently needed.

Aircraft metallic structures may suffer from corrosion even when they are "protected" by primers, coatings, and paint. Hidden corrosion of aircraft metallic structures comprises a family of deterioration mechanisms, non-detectable by visual inspection, which may produce flaws of a destructive nature affecting the durability of aircraft. Most of the NDE methods currently in use are based on detection principles which involve measurements of macroscopic changes in aircraft

structures such as pits, crevices or cracks with sizable dimensions.[1] These NDE techniques are not capable of detecting early stages of corrosion initiation nor to alarm in advance about critical areas where possible severe corrosion could occur. In addition, existing NDE techniques for the detection of hidden corrosion present other practical limitations such as the need for highly trained personnel, cost, time, and the use of complicated and even hazardous instrumentation. Thus, the development of an inexpensive, user friendly, fast, and portable novel NDE system is highly desirable. At the same time, the new NDE system should be able to detect hidden corrosion in early stages so that both structural damage can be prevented and maintenance procedures can be minimized. Methods to both detect corrosion initiation of metallic structure and assess the amount and severity of damage are crucial not only to avoid failure and save cost, but also to assure the implementation of a systematic, cost effective approach to repair and/or replace the damaged structure.

Lynntech has developed a prototype of a new NDE/I probe for the detection of corrosion in aircraft metallic structures. The NDE/I system is based on electrochemical impedance (EI) measurements. The developed NDE/I probe is simple in design, portable, low in cost, highly sensitive to small defects, has an immediate time response, and will not require trained personnel to operate. Another advantage of the probe design is that the use of aggressive electrolytes, a problem known in designing EI probes, is eliminated. The EI-NDE/I probe is capable of: (i) detecting corrosion initiation at the surfaces of painted aluminum alloy substrates before any macroscopic damage has occurred, and (ii) predicting areas of where severe corrosion attack is most likely to occur. It is believed that the developed EI-NDE/I probe will address corrosion detection problems in the maintenance program of interest to DoD, NASA and FAA.

Advantages of the proposed EI-NDE system are summarized in TABLE 1.

TABLE 1. ADVANTAGES OF LYNNTECH'S EI-NDE SYSTEM FOR THE DETECTION OF CORROSION IN AIRCRAFT METALLIC STRUCTURES.

- Useful for a wide variety of inspections of aircraft metallic structures.
- Simple detection principle. Easy interpretation.
- User friendly. Highly skilled, trained inspectors will not be required.
- Corrosion detection of coated and non-coated metallic substrates.
- Sensitive to small defects. High resolution.
- Independent on flaw orientation.
- Fast. Real time response.
- It can be designed as a lightweight, portable, as well as a robotic NDE system.
- Low cost for development and low capital cost.
- Readily automated.
- Sensing probe and imaging system will be easily transferable to the industrial level.
- It can be adapted for use with artificial intelligence (i.e., pattern recognition).
- Elimination of need for paint removal.
- Reduction of operator fatigue.
- Surface preparation requirements will be, at the most, to a simple cleaning of the surface.

The approach used in EIS is to apply a small ac voltage perturbation (dV) across the interface under study and measure the perturbation in the current response (dI). The impedance of the system (i.e., dV/dI) is determined as a function of the frequency of the signal. The use of non-steady-state techniques with low amplitude perturbation signals (e.g., EIS) has become very attractive in corrosion research and testing, because it provides additional information on the kinetics of the corrosion processes without significantly affecting the system under study. Thus, corrosion studies and EIS are bound together, as documented by the large number of investigations using this technique.

The capabilities of EIS for the characterization of corrosion processes on Al, Al alloys and steel have been tested in the past. They include the characterization of: (i) pitting and crevice corrosion (e.g., [2,3,4,5,6,7,8]); (ii) estimation of the pitted area;[2,4] (iii) corrosion under a protective films, including delamination (e.g.,[2,9,10,11,12,13,14,15]); (iv) filiform corrosion; [16] and (v) stress corrosion.[3] The main features of EIS on localized corrosion arise from the frequency dependence of the *ac* current distribution between corrosion sites and the surrounding passive background.[3] In addition, the form of the spectra provides information on multistep dissolution, ionic migration through protective layer, relaxation effects, and the influence of corroding ions.[17]

Impedance methods have significant advantages over other methods to detect corrosion on coated and non-coated metals because EIS is: (i) best suited for high-impedance interfaces, (ii) particularly applicable for evaluating the deviation from purely capacitive behavior of organic coatings on metals, (iii) highly sensitive, (iv) a nondestructive technique, and (v) capable of providing spectrographic impedance data when a sufficient frequency bandwidth is used. EIS has been used by many researchers to measure the corrosion protection properties of organic coatings on metals, and proved to be a powerful technique for: (i) the early detection of the deviation of organic coatings from their initial capacitive behavior, and (ii) the evaluation of the performance and degradation of commonly used coating systems.[15]

Mansfeld et al. (e.g., [2,4,18,19]), Juttner et al., [20,21] Kending et al.,[22] and Scully et. al.[23], among others, have developed models to describe the events occurring on corroding metal surfaces (coated and non-coated). It is found that significant changes in EIS can be observed even when 0.01% of the area has been corroded.[23] Thus, EIS is a sensitive technique to detect hidden corrosion of coated and non-coated metallic surfaces.

Most of the EIS studies on the corrosion of coated metallic substrates measure the impedance response as a function of time during the exposure of the sample to a corrosive environment. The relatively steady values of capacitance during the early stages of immersion gives information about the properties of the film such as paint thickness and water absorption. A sharp increase in capacitance or fall in resistance indicates breakdown of the paint and the onset of corrosion.[24,25] Although this information is very useful, EIS would be impractical as an NDE/I technique for the detection of hidden corrosion because: (i) it will become time consuming, and (ii) it will accelerate the corrosion of the sample under test. However, we have developed a NDE/I prototype where EIS can be used to detect hidden corrosion instantly. This was achieved by selecting a single frequency which is highly sensitive to the corrosion stage of the sample under testing.[26,27] Another advantage of the probe design is that the use of aggressive electrolytes,[28] a problem known in designing EI probes, is eliminated.

2. RESULTS AND DISCUSSION

2.1 LYNNTECH'S EI-NDE/I PROTOTYPE PROBE

The development of Lynntech's prototype probe is described in two previous publication by our group.[26,27] Figure 1 shows a diagram of Lynntech's EI-NDE/I prototype probe. The probe is very simple. The probe consists of a counter electrode (CE), a membrane for contact between the CE and the surface under testing, and a spring loaded contact. Due to its simple design and flexibility, the probe can be fabricated in different sizes and shapes. We have constructed prototype probes with sizes ranging from 0.3 cm^2 to 147 cm^2.

Most of the work carried out by different groups on the detection of corrosion using EIS has involved the use of corrosive liquid electrolytes (e.g., NaCl and H_2SO_4). The use of these media in an EI-NDE probe may cause further problems to the samples due to acceleration of the corrosion process. Our probe avoids the use of aggressive liquid electrolytes. In addition, only environmentally benign materials are used during testing.

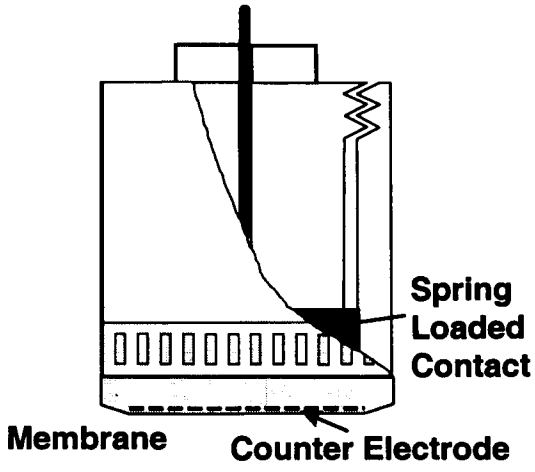

Figure 1. Diagram of Lynntech's EI-NDE/I prototype probe.

2.2 SCANNING TEST PARAMETERS

Some of the system operational parameters of Lynntech's EI-NDE/I probe used during testing are summarized in TABLE 2.

2.3 INSPECTION OF ANAl7075-T6 COUPON

Figure 2 shows the performance of the NDE/I on a 25,200 cm^2 painted Al7075-T6 coupon. The coupon was painted according to military specifications (i.e., primer MIL-C-83286; top coating MIL-C-83286). Three probes of different sizes were used: 154, 20, and 1.8 cm^2. The coupon had several

intentionally damaged sites. A single frequency was used for the inspection. The first step was to inspect the entire surface with the largest probe. When the impedance value was less than the reference value (i.e., the value of the impedance magnitude corresponding to a damaged-free surface), that area was identified as "damaged" (i.e., shadowed areas in Figure 2). Next, the "damaged" area was inspected with the medium size probe to further localize the flaw. These "damaged" sites were also identified as shadows (darker than before). Further localization of the flaws on the substrate was carried out by using the smallest probe. The damaged sites identified by the smallest probe are shown as the darkest shadows in Figure 2. In addition to the all intentionally damaged sites, few other damaged sites were also localized. This successive inspection with probes of different sizes reduces the time-labor to inspect a wide area of a substrate. Also, this procedure will save time and cost during the repair process, because repair will be limited to those sites were the flaws are localized with the smallest probe.

2.4 INSPECTION OF A SECTION OF ANAIRCRAFT FUSELAGE

Part of an aircraft fuselage containing lap joints and rivets was inspected using Lynntech's EI-NDE/I prototype probe. The part of a fuselage of a Boeing 727 aircraft after 30 years service was purchased from Tracor Comjet Services. The lap joint was fabricated by overlapping adjacent ca. 1 mm thick skin segments of the fuselage and then bonding and riveting the skin together. Rivets in the middle row were installed to a stringer. Figure 3 shows a diagram of the side skin (4 inches by 12 inches) of the fuselage containing lap joints and rivets. The diameter of one rivet was 0.625 cm. The outside of the lap joint was coated with paint.

TABLE 2. SOME OF THE SYSTEM OPERATIONAL PARAMETERS DETERMINED DURING THE DESIGN, FABRICATION, AND TEST OF LYNNTECH'S EI-NDE/I PROTOTYPE PROBE.

Prototype Probe Characteristics	**Data Measurement and Interpretation**	**Surface Pretreatment**
• For a surface with flaws, impedance magnitude is independent of: (i) the probe size, (ii) CE size and shape, (iii) relative position between CE and flaw, and (iv) flaw orientation. • For a surface with flaws, impedance magnitude is dependent on the damaged area. • There is not interference of flaws located *outside* the area inspected by the probe. • Aircraft metallic parts can be inspected by large probes. Once a damaged site has been detected, further location of the site is carried out using smaller probes. • Contact between probe and surface under test: ca. 0.1 Kg/cm^2. • Surface under test has to be moisturized (e.g., a few drops of water). • No corrosive electrolytes are used.	• Use of a single frequency. • One time determination of a "universal" reference point.	• Simple surface cleaning.

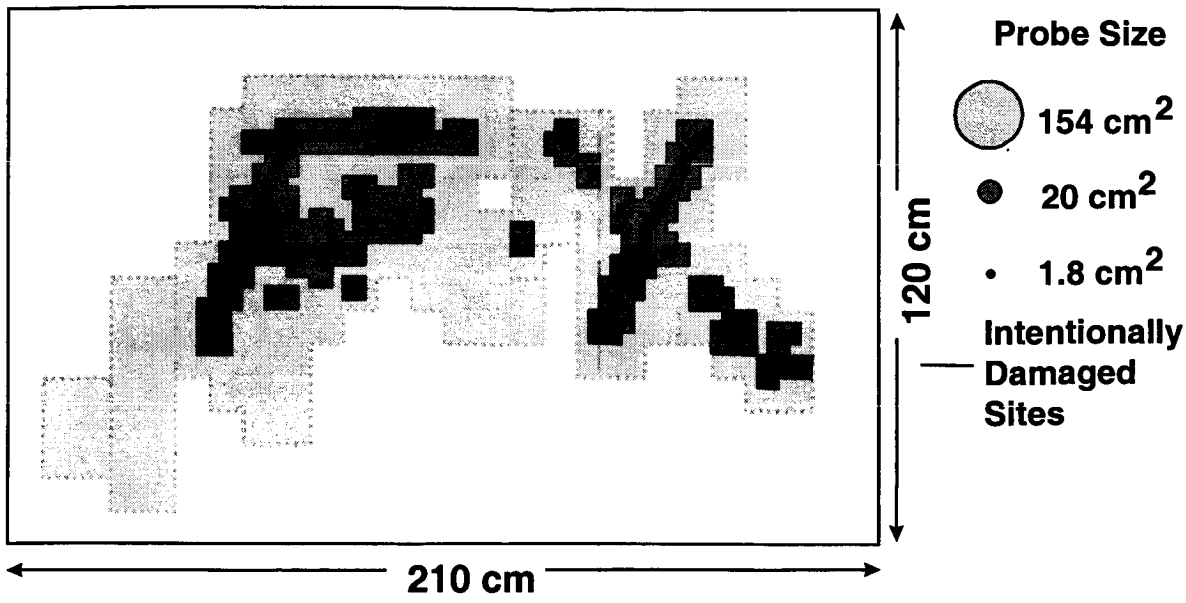

Figure 2. Scanning test of a 25,200 cm^2 painted Al7075-T6 coupon with three prototypes probes of different sizes: 154, 20, and 1.8 cm^2. Shadowed areas represent damaged sites, and were detected when either part or all of the intentionally damaged site was underneath the probe. Darker areas were detected with smaller probes. A couple of non-intentionally damaged sites were also detected.

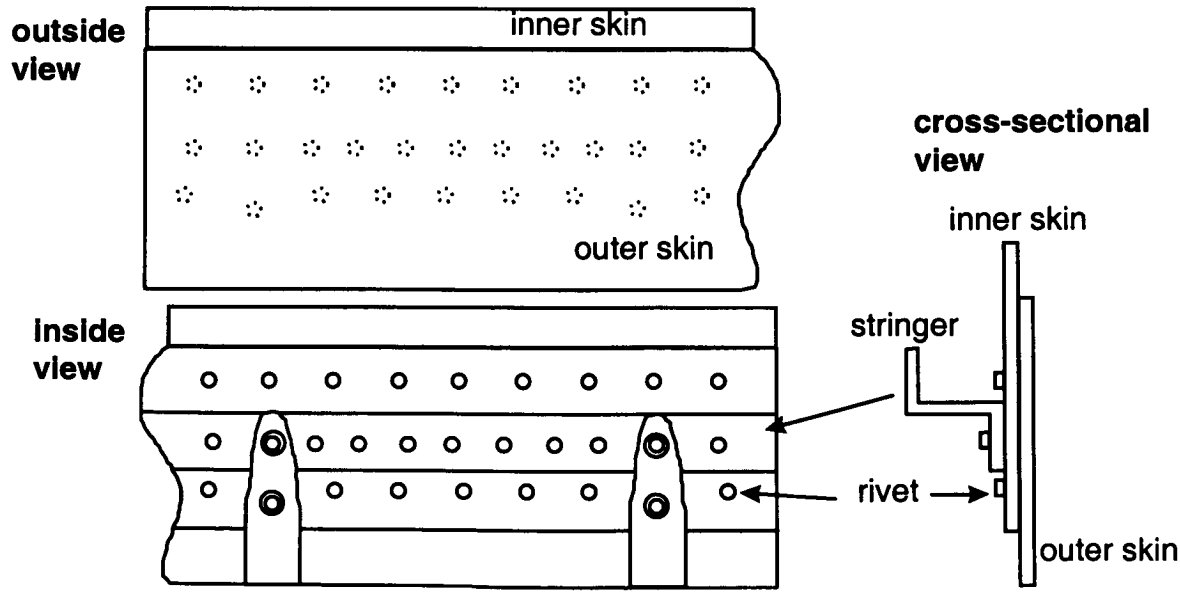

Figure 3. Diagram of the aircraft side fuselage showing lap joints and rivets.

Figure 4 shows the result of the NDE/I inspection on the aircraft part using two Lynntech's prototype probes of different sizes: 20 and 2.3 cm^2. The first step was inspecting the entire surface with the large probe. A single frequency was used. When the impedance value was less than the reference value (i.e., the value of the impedance magnitude corresponding to a damaged-free surface), the site was identified as "damaged" (i.e., shadowed areas in Figure 4a). Next, the "damaged" area was inspected with the small probe to further localize the damaged site. The "damaged" sites identified with the small probe are shown as dark shadows in Figure 4b. This successive inspection with probes of different sizes reduces the time-labor to inspect a wide area of a substrate. Also, this procedure will save time and cost during the repair process, because repair will be limited to those sites were the flaws are localized with the smallest probe. One remarkable achievement of Lynntech's EI- NDE/I prototype is that damaged rivets could be identified as shown as solid circles in Figure 4c. The painting on the damaged rivets included in the "damaged" areas or sites were found: (i) torn by vibration motion of the fuselage, and/or (ii) swollen by hidden corrosion.

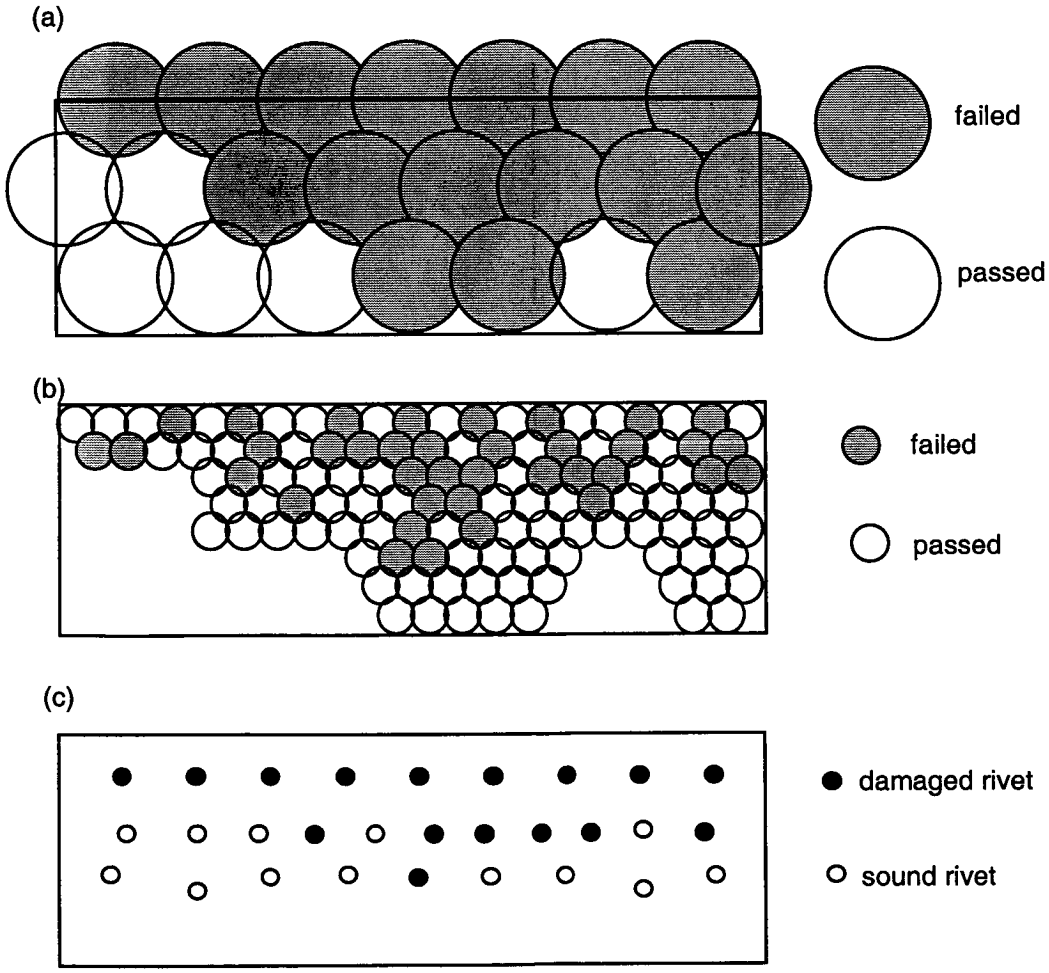

Figure 4. Scanning test of a side fuselage of a Boeing 727 aircraft with prototype probes of two different sizes: (a) 20 and (b) 2.3 cm^2. Shadowed areas represent damaged sites, and were detected when either part or all of the intentionally damaged site was underneath the probe. Defective rivets (solid circle) were also identified and differentiated from sound rivets (broken circle) in (c).

3. CONCLUSIONS

EIS is a powerful technique for the detection of the corrosion initiation of aircraft metallic materials.

A new NDE/I prototype probe based on EIS has been developed and characterized:

- It uses a single frequency. Real time testing.
- It is highly sensitive (smallest flaw size detected = 5 $x10^{-4}$ cm^2). Minimum ratio of flaw size to probe size was 0.0004% (damaged size=5 $x10^{-4}$ cm^2; probe size=154 cm^2).
- Impedance magnitude is dependent on the damaged area.
- Impedance magnitude is independent of the probe size and the CE size or shape.
- Impedance magnitude is reproducible in short and long term testing.
- Impedance magnitude is independent of the flaw orientation. Probe detects total damaged area, no matter the number of defects under the probe.
- It is applicable to a wide variety of inspections of aircraft metallic structures: clad and unclad; painted and bare metallic substrates; flat and curve surfaces.
- Probe can be fabricated in different sizes and shape.
- Surface preparation is limited to a simple cleaning of the surface.
- No corrosive electrolytes are used. Only environmentally benign materials are used during testing.
- Calibration of the probe is simple: it requires one time determination of the reference point, that can be stored in the memory of a hand held instrument.
- Low cost.
- Testing does not required skilled personnel.
- Readily automated.
- For aircraft testing, no removal of the aircraft paint is necessary.

4. ACKNOWLEDGMENT

This work was funded by the Air Force Office of Scientific Research through a grant # F49620-95-C-0050. The authors wish to thank Capt. Hugh C. De Long, the technical monitor for this Phase II SBIR project.

5. REFERENCES AND FOOTNOTES

1. G. Ansley et al., "Current Nondestructive Inspection Methods For Aging Aircraft, Report No. DOT/FAA/CT-91/5.
2. F. Mansfeld, S. Lin, K. Kim and H. Shih, Corr. Sci., **27** (1987) 997.
3. R. Oltra and M. Keddam, Corrosion Sci., **28** (1988) 1.
4. F. Mansfeld, S. Lin, S. Kim and H. Shih, J. Electrochem. Soc., **137** (1990) 78.
5. T.R. Beck, Electrochim. Acta, **33** (1988) 1321.
6. L. Tomcsanyi, K. Varga, I. Bartik, G. Horanyi and E. Maleczki, Electrochim. Acta, **34** (1989) 855.
7. S. Szklarska-Smialowska, Corros. Sci., **33** (1992) 1193.
8. C. Brett, Corros. Sci., **33** (1992) 203.
9. T. Nguyen, J.B. Hubbard and J.M. Pommersheim, J. of Coating Technol., **68** (April 1996) 45.
10. J. Hitzig, K. Juttner, W.J. Lorenz and W. Paatsch, J. Electrochem. Soc., **133** (1986) 887.

11. H. Leidheiser, Jr. And M.W. Kending, Corrosion, **32** (1976) 69.
12. E.P.M. van Westing, G.M. Ferrari and J.H.W. De Wit, Electrochim. Acta, **39** (1994)899.
13. F. Mansfeld, M.W. Kendig and S. Tsai, Corrosion, **38** (1982) 478.
14. F. Mansfeld, S.L. Jeanjaquet and M.W. Kendig, Corr. Sci., **26** (1986) 735.
15. C.H. Tsai and F. Mansfed, Corrosion, **49** (1993) 726.
16. H.J.W. Lenderink, M.V.D. Linden, J.H.W. De Wit, Electrochim. Acta, **38** (1993) 1989,
17. C.M.A. Brett, J. Appl. Electrochem., **20** (1990) 1000.
18. F. Mansfeld, Corrosion **44** (1988) 856.
19. F. Mansfeld, Electrochim. Acta, **38** (1993) 1891.
20. K. Juttner, Electrochim. Acta, **35** (1990) 1501.
21. K. Juttner, W.J. Lorenz and W. Paatsch, Corr. Sci., **29** (1989) 279.
22. M. Keding and J. Scully, Corrosion, **46** (1990) 22.
23. H.P. Hack and J.R. Scully, J. Electrochem. Soc., **138** (1991) 33.
24. G.W. Walter, Corr. Sci. **30** (1990) 617.
25. G.W. Walter, Corr. Sci., **32** (1991) 1059.
26. A. Gonzalez-Martin, J. Kim, D. Hodko, "New NDE/I Probe for the Detection of Early Stages of Corrosion in Aircraft:", in "The First Joint DOD/FAA/NASA Conference on Aging Aircraft", Utah, July 1997.
27. A. Gonzalez-Martin, J. Kim, D. Hodko, C. Salinas, U.S. Patent, *submitted.*
28. The use of aggressive electrolytes (e.g., NaCl and H_2SO_4) may cause further problems to the samples under testing due to the acceleration of the corrosion process.

IMPLEMENTATION OF FILMLESS RADIOGRAPHY FOR AEROSPACE APPLICATIONS

Timothy Kinsella
Liberty Technologies, Inc.
555 North Lane
Conshohocken PA 19428-2208
(610) 834-0330

Diana Carlin
Air Force Research Laboratory
Materials and Manufacturing Directorate
Manufacturing Technology Division
2977 P Street, Suite 6
Wright-Patterson AFB, OH 45433-7739

ABSTRACT

Storage phosphor (filmless) imaging technology provides the potential of utilizing all the advantages of digital imaging as well as eliminating the hazardous material issues related to film processing. This paper describes the efforts undertaken by Liberty Technologies, Inc. to evaluate, develop, and implement an effective, affordable, mobile system of filmless radiography. This program is entitled "Filmless Radiography for Aerospace Applications." Initially, the Air Force NDI Program Office conducted a Phase I SBIR project with Liberty Technologies to determine if filmless radiography is technically feasible and economically viable for the inspection of Air Force weapon systems in both the depot and field environments. Liberty's RADView filmless radiography system was evaluated at several bases and confirmed the system's potential. As a result, the Air Force Research Laboratory, Materials and Manufacturing Directorate, Manufacturing Technology Division then funded a program to enhance RADView's sensitivity and enlarge the image format to meet the needs of aircraft inspections. This paper provides a basic discussion of the technology and system operating specifications, and what they mean with reference to image quality, throughput, and overall costs.

1. INTRODUCTION

A latent film image is created when incident radiation causes the silver halide crystals to be converted to metallic silver. This process is related to the amount of incident radiation in a logarithmic fashion. In a phosphor imaging system, an imaging screen employing storage phosphor crystals instead of silver halide grains is used to capture the latent image. The phosphor grains are coated on a flexible substrate (Figure 1) and store the incident radiation energy in the form of trapped electrons - thus the name storage phosphor. Unlike film, however, the number of trapped electrons is *linearly* related to the input radiation intensity pattern.

The process by which electrons become trapped is shown in Figure 1; part of the incident radiation is absorbed by the storage phosphor and electrons from a luminescent center are excited into trapping sites.

Readout of the latent image can be accomplished by laser stimulation at an appropriate wavelength resulting in the emission of visible light (luminescence) from the phosphor grains; this process is referred to as *photo-stimulated luminescence*, or PSL, and is shown in Figure 2. The incident laser stimulates the trapped electrons back to the luminescent center. Eventually, the electrons settles to the ground state of the luminescent center and gives off visible light in the process.

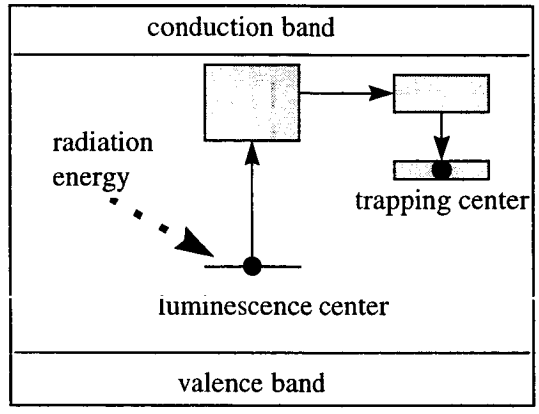

Figure 1. Energy Diagram

Since the luminescence is correlated to the latent image, it has the intensity pattern of the original radiation image. In this way, the storage phosphor acts as an energy transducer, converting the radiation pattern to a visible light pattern. Since the processes are completely reversible, the storage phosphor can undergo a vast number of cycles without noticeable degradation. That is, once the initial latent image has been read, any residual latent image can be subsequently erased and the imaging screen re-used. Tests have demonstrated that this expose/scan/erase cycle can be repeated over 500 times without degradation of image quality. The number of reuses is normally governed by mechanical wear and tear as opposed to any inherent degradation of the phosphor.

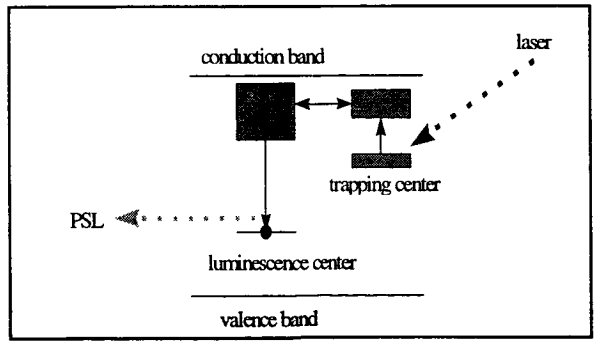

Figure 2. Energy Diagram Showing PSL Generation

1.1 SYSTEM CHARACTERISTICS

Readout of the information in a storage phosphor screen is best accomplished by scanning it with a laser beam having a wavelength tuned to the particular storage phosphor chemistry; the process is shown schematically in Figure 3. In the system described here, a 50 micrometer diameter near-infrared laser is employed to scan the screen. While the laser is scanned across the screen at a constant velocity, PSL is generated along this line. Each scan is along a stationary line, so the screen is also indexed at a constant

velocity normal to the scan line to achieve 2-dimensional readout. The scan and index velocities are accurately synchronized to minimize pixel errors and obtain a uniform scan.

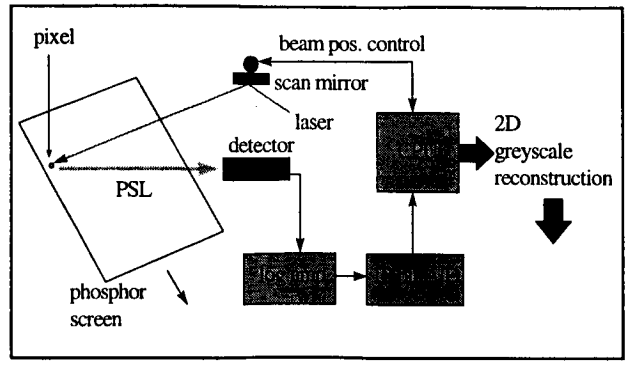

Figure 3. Schematic of Readout

Since a "flying-spot" laser is employed for PSL generation, the smallest detail which can be resolved will be equal to or larger than the laser spot size. This smallest resolvable element is referred to as a pixel and is defined by the product of laser scan velocity and the sampling period. For example, if the 50 micron diameter laser scan velocity (x-direction) is 1000 cm/second and the screen translation velocity (y-direction) is about 50 lines/second, the sampling period can be varied from $5x10^{-6}$ to $15x10^{-6}$ seconds/pixel to achieve a pixel pitch of 50 - 150 microns. Other readout systems are available which will scan at coarser resolutions. The key here is to note that the total readout time will vary with scan resolution. For example, a 14"x17" screen scanned at 100 microns will take roughly 80 seconds, whereas reducing the scan resolution to 200 microns can reduce the scan time to about 40 seconds. Therefore, it is best to first select the resolution needed to achieve a certain image quality. If the application requires a very fast scan rate, then it should be noted that resolution is being sacrificed. This is directly analogous to film, where a fast film generally produces low resolution.

Three additional considerations include the screen size which the readout device accommodates, screen flexibility, and the erase cycle. First, all commercial systems have some limits on the size of phosphor screen they can accommodate. In the system described here, screen widths between 2" to 14" can be accommodated, and the maximum length is limited only by the amount of system memory. Non-rectangular shapes within these boundaries can also be accommodated as shown in Figure 4. The second consideration is the flexibility of the screen and cassette, allowing them to be placed in small, curved areas as shown in the T-38 inlet in Figure 5. Though the scanning process removes some of the stored image information, it does not remove all of it; an erase step is required before the screen can be re-used. The erasure time varies with exposure conditions. Erasing can be performed as a separate step external to the scanning device where the user has control over the actual erase time. Systems also exist where scanning and erasing are performed in a closed-loop. The problem with a closed-loop cycle is that the proper erase time can vary depending on the type and amount of radiation exposure. This can result in ghost images in subsequent exposures. The optimum choice depends on the amount of flexibility desired, cost, and throughput requirements. In addition to resolution, the way in which PSL signal is processed and digitized will impact the contrast sensitivity and system latitude (or dynamic range). As shown in Figure 3, the PSL generated during scanning is captured in a light collector and propagated to a PMT where the light photons are converted to an electrical signal. But before the signal can be digitized, it has to be amplified to fit the input range of the analog-to-digital converter (ADC). A unique feature of the system described here is that a patented log-amplifier design (Lim, 1995) is employed to convert the linear PMT output to a logarithmic signal which is then digitized by a 12 bit ADC. Since the aim of radiographic inspection is to image small changes in object density, simply digitizing the linear output of

the PMT would result in uneven sampling of contrast changes. For example, with linear digitization a signal change of 1-10 is represented by 9 digital units and has equal weight as a signal change of 11-20. However, an object contrast change of 1-10 (an order of magnitude!) is equal to a ten-fold change and should have equal weight as a change from 10-100. By employing a log-amplifier, the digitized values equally represent relative changes in contrast the same as density values in film.

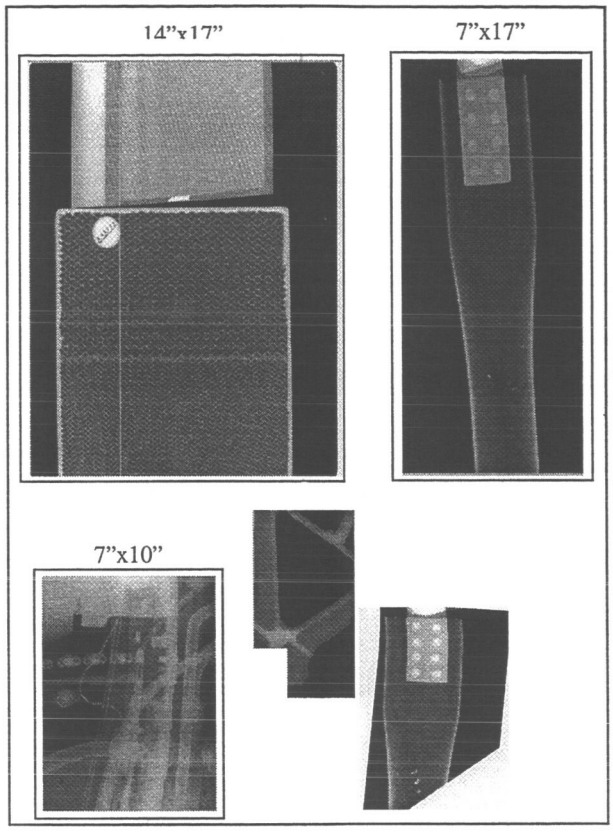

Figure 4. Size and Shape

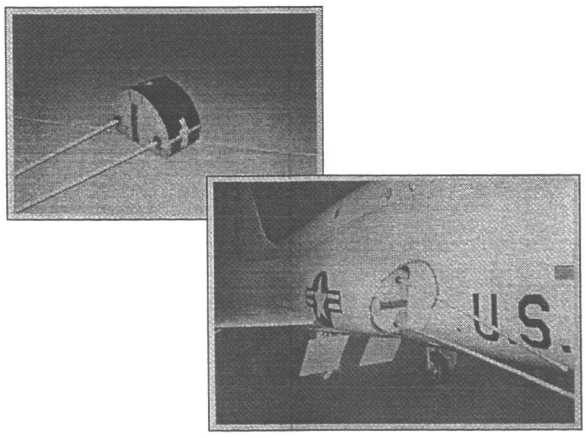

Figure 5. Flexibility

1.3 IMAGE PROCESSING

Because of the vast variety of aerospace and industrial applications, engineers will want to know what the raw data for an image looked like or want to reprocess it in other ways for further analysis. Also, saving and displaying the raw data allows the calculation of exposure adjustments, in much the same way as with film, to obtain specific image results.

It may also be desirable to have the raw data available for future reference and may, in fact be required by regulation. As a result, industrial systems should permit the storage and retrieval of the original image as well as the one that was processed or enhanced for acceptance and/or rejection of the inspection. The important point to note is that the system should provide raw data for primary archival. After this, a variety of image processing applications are possible depending on the particular need.

Image processing can be useful in two areas. One is to compensate or correct for readout artifacts; some commercial systems perform automatic corrections employing proprietary algorithms, whereas others do not. Though the use of such algorithms is not necessarily wrong, the user should have knowledge of how and when such corrections might be applied. The second type of processing involves enhancement of the image data. Image enhancement offers the possibility of sharper contrast, and improved visibility of edges, lines, details, and other features. While no information is added in the process, enhancement can make the information more easily viewed and more understandable. Furthermore, enhancement can be specified and controlled and thus offers an objective means of improving an image. Image processing should be employed under well defined conditions for very specific application requirement and be documented as a formal part of the radiographic technique employed.

Histogram equalization is a redistribution, or mapping, of digital image values so that all gray scale intervals will contain an equal number of pixels. AT first glance this seems trivial. One can imagine ordering the pixels by gray scale, then assigning them to the available bins in an equitable manner. However, there is a difficulty. Since indistinguishable levels must be combined, like gray values cannot be separated into different bins. If like gray levels were separated, this would add considerably to the noise without any real improvement in the signal. Thus, histograms usually end up far from having uniform distributions.

Statistical differencing is an approach in image processing analogous to automatic gain control in electronics. If the signal is too low, the gain is increased. If it is too high, then it is decreased. This approach has the effect of "flattening" the appearance so that minor changes appear as important as major changes. The details are emphasized and fine changes made more visible, although there is the risk of also increasing the noise to an unacceptable level.

Edge detection filters emphasize linear patterns such as cracks. These are generally gradient operators and are directionally oriented. There are many different such detectors and they can be combined to produce one gradient operator that is sensitive to all directions. The maximum response is automatically captured, no matter what the orientation of the crack.

While not adding information to an image, enhancement does present the information in a form more visible to the human investigator. Image enhancement is one of the benefits of working in the digital domain. However, it must be emphasized that while processing is advantageous, "raw" data must be preserved. In addition, any processing techniques employed must be fully documented and become an integral part of the radiographic technique, similar to source-to-film distance, energy, and exposure.

1.4 IMAGE ARCHIVING

Archiving requirements, i.e. file sizes and storage devices, must be carefully considered when developing techniques. For example, a radiograph for moisture or corrosion may employ a 14"x17" image area and, because of the low resolution required, use 200 micron (0.008") pixels. This would produce an image of 1,780 pixels horizontally and 2,160 pixels vertically for a total of 3.8 million pixels, or a 7.6 megabyte file size. If, on the other hand, one is looking for fatigue cracks and still wants to use a 14"x17" image area, then a 50 micron (0.002") pixel size would be more desirable. This would result in an image that is 7,000 x 8,500 pixels, or about 60 megapixels and a corresponding file size of 120 megabytes. This is equivalent to more than 80 floppy disks for a single image!

As can readily be seen, as image resolution increases, storage requirements, and therefore cost of storage, will increase as well. There are key capacity and performance tradeoffs which a user must evaluate and which will ultimately influence the cost and possibly the total throughput of the inspection process. Furthermore, recent advances have, and will continue to reduce drastically the long term cost of storage, while improving capacity and overall performance. Proper selection of storage media and a well planned archiving procedure will minimize any production delays such as having to wait for an acquired image to be written to, or recovered from, a storage device. Since this technology continues to evolve rapidly no attempt will be made to deal with it in any detail here.

1.5 DATA AND INFORMATION TRANSFER

In addition to the elimination of chemical processing, and improved image interpretation, implementation of digital imaging also enables the transmission of inspection information (data, images, reports, etc.) electronically. Inspections can be duplicated with no degradation in fidelity and transferred, either via land line or satellite, from remote locations to engineering or depot functions. The use of a digital NDT workstation also creates the possibility of integrating and managing the digital inspection data from a variety of sensor types (radiography, ultrasound, eddy current, borescope, thermography, etc.) for a particular aircraft or structure type.

1.6 APPLICATIONS

While there are fundamental differences between film and phosphor radiography, many of the practical technique principles can be applied to both. For example, the standard rules regarding the geometric factors in radiography also apply to both: viewing a dark image is generally better than viewing a light image, selection of a particular density in the area of interest as a judge of proper technique, and the use of penetrameters as one indicator of image quality. However, there are also additional parameters which are not normally measured in film radiography and can be important in phosphor imaging. For example, it is not standard practice to measure film resolution; in the case of phosphor however, it has been shown that resolution can impact a wide variety of implementation issues, including throughput and cost. Thus, resolution test patterns can be used to evaluate or demonstrate the resolution of a system. Similarly, since various phosphor imaging systems exhibit different response characteristics (i.e., different latitudes), a suitable step wedge is also useful in establishing the system dynamic range either during system evaluation, during set up, or as part of routine inspection.

Radiographic sensitivity depends on the combination of contrast (the density difference between a small detail and its surroundings) and definition (the sharpness of outline). The optimum combination of these two factors is not a constant and varies depending on the application. Since each of these factors is affected by a variety of controllable variables in the storage phosphor imaging process, some degree of technique development may be necessary to produce the most effective technique.

The scanning, or readout, process gives rise to one of the major differences between phosphor and film and that is the difference between optical and phosphor density. The phosphor images of the system being discussed are digitized at 12 bits, producing gray scale levels from 0 to 4095. For convenience sake, they are divided by 1000 resulting in PD values from 0 to 4, just like film. This similarity in density values is purely coincidental. As shown in Figure 6, optical density is a measure of the amount of light transmitted through the film. Phosphor density on the other hand, is a measure of the amount of light emitted from an imaging screen. There is therefore, no meaningful conversion between OD and PD.

There are similarities however, in the way these numbers can be used. For example, it can be stated that the measure of an acceptable radiograph is still determined by obtaining a specific phosphor density or density distribution for a particular application.

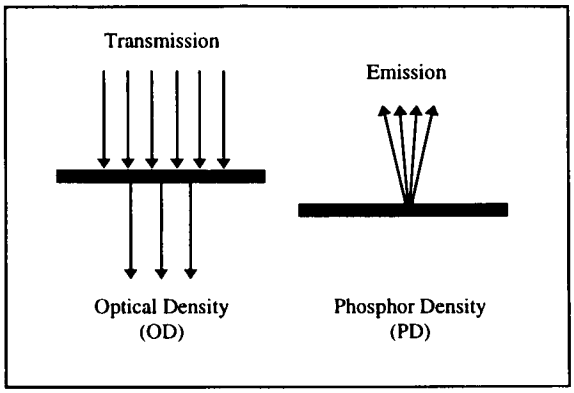

Figure 6. Optical vs. Phosphor Density

Since the storage phosphor interaction with radiation is linear over a much greater practical range than with film, it exhibits a wider exposure latitude than film, as shown by the representative characteristic curves in Figure 7. In many cases this can permit either shorter exposures or a much wider range of thicknesses to be imaged in a single exposure. This unique characteristic curve also makes for much more forgiving exposures. Because of the steep slope and narrow linear band of film characteristic curves, a relatively slight error in exposure will cause some portion of the image to be in the low contrast area of the curve; this would require another exposure to be made with corrections. With phosphor images on the other hand, considerable variation in exposure is possible while maintaining the same contrast.

Films of different speeds are selected to either increase the latitude covered (double loading two speeds), reduce exposure times (coarse grain films), or improve image quality (fine grain films). Because it has such wide latitude, a single phosphor screen can be exposed in such a way as to simulate the use of more than one film speed. For example, an image of moderate quality can be obtained in a short time to reduce exposure, while a longer exposure time could also be used with the same screen to produce an image with much higher quality. As can be seen, proper employment of phosphor screens requires considerably more than just the application of a new "R" factor.

Examples

The system described has been employed in the field and has proved capable of meeting a diverse range of applications, some of which are described below. Figure 8 illustrates the wide latitude achievable with phosphor imaging. The image on the left is a film image of a T-38 inlet structure. This structure typically requires the simultaneous exposure of two different speeds of film in order to image the entire range of densities.

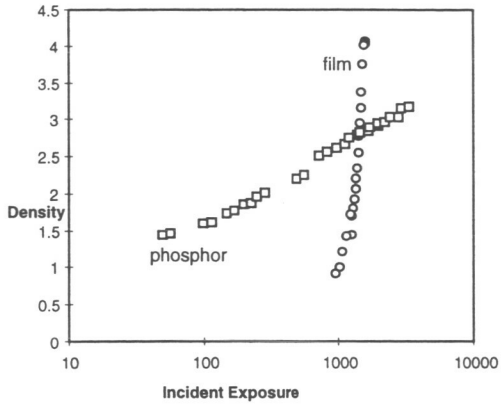

Figure 7. Response Characteristics of Film and Phosphor

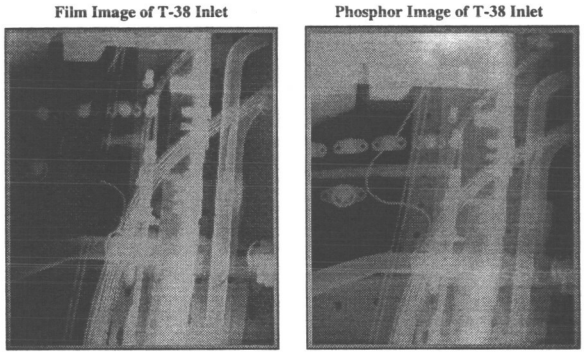

Figure 8. Phosphor Latitude (courtesy of USAF).

It can be seen however, that the phosphor image on the right displays a great deal more of the structure with a single exposure. An interesting side note is that a similar situation was encountered on another aircraft and, instead of imaging with phosphor, one of the films was digitized. Because of the ability to adjust the window and level (brightness and contrast), the entire structure was visible on this single film. Therefore, digitization of conventional film would also permit the elimination of one of the two double loaded films.

Figure 9 illustrates the contrast sensitivity possible with phosphor imaging. It shows a bonded honeycomb structure with areas of varying degrees of water entrapment. The square indication in lower center is a piece of masking tape that was used for registration. Figure 10 also shows good contrast sensitivity in detecting corrosion in an aluminum wing skin.

Figure 11 shows a pipe elbow with surrounding insulation that is held in place with a winding of wire. The image on the left is the original, and the one on the right shows the detail enhancement possible with histogram equalization.

Figure 12 is a small turbine blade (approximately 1" square) showing the structure of internal cooling passages. Image processing using statistical differencing greatly increases the definition of the passages making measurements or detection of internal inclusions easier. It will also be noted that noise is also increased, which illustrates that careful consideration must be given to the tradeoffs that accompany image processing.

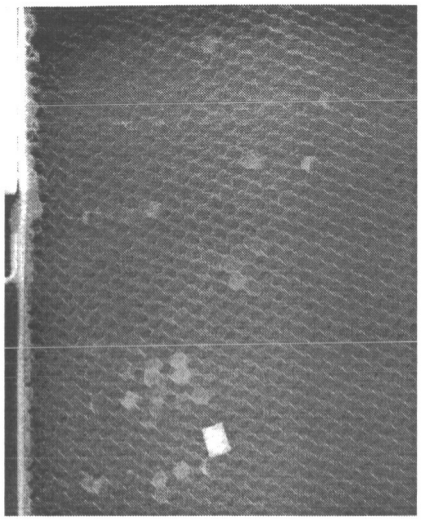

Figure 9. Honeycomb panel shot with phosphor employing 125 keV x-rays, 50 mA-sec (courtesy of USAF).

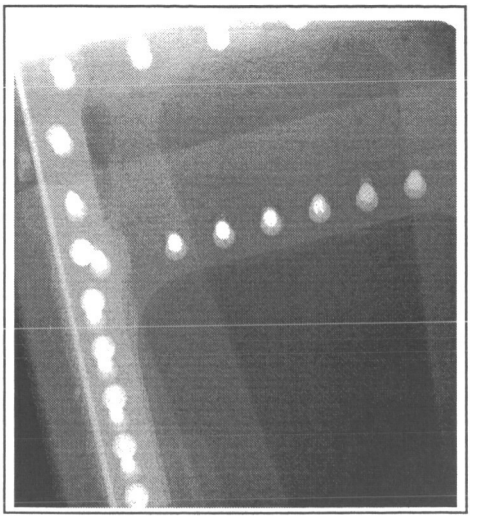

Figure 10. Corroded Aircraft Skin (courtesy of USAF).

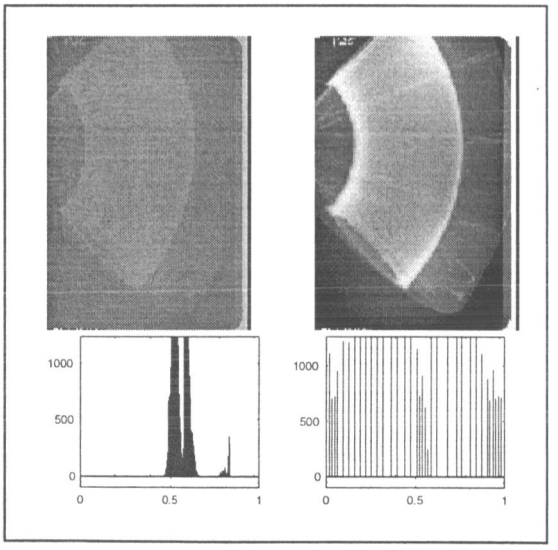

Figure 11. Histogram Equalization

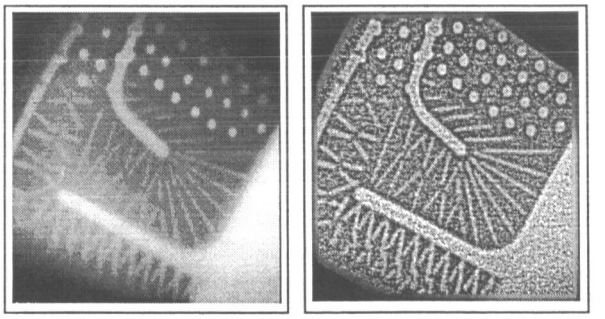

Figure 12. Turbine Blade with Statistical Differencing

Finally, Figure 13 illustrates a cracked aluminum aircraft structure. The crack extends completely between two fatener holes, but is only partially visible in the raw image displayed on the left. The application of a Kirsch edge detection filter on the right makes the entire length of the crack much more visible, even through a vertical stiffener obscures much of it (left to right in the bottom third of the image).

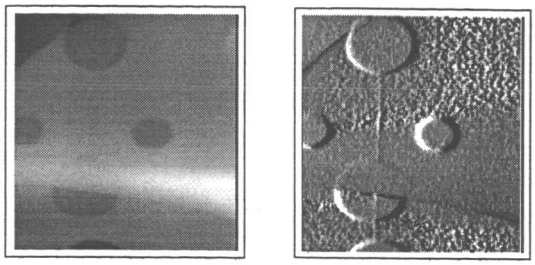

Figure 13. Crack with Kirsch Filter.

CONCLUSION

In radiography, as with other areas of NDT, no one method or technique will serve all situations or needs. There are a number of factors to be considered when evaluating a radiographic imaging system beginning with the size, shape, and flexibility of the sensor. The contrast sensitivity, or gray scale range (e.g. 8 bit versus 12 bit), and resolution (pixel size) are major factors in determining the imaging performance and scan speed. Finally, all these factors must be traded off against size, mobility, and cost.

There are available today a variety of radiographic inspection choices including conventional film, real or near-real time, CT, storage phosphor, etc. Each have their own advantages and disadvantages depending on the environment and flaws sought.

3D VISUALIZATION OF X-RAY BACKSCATTER IMAGES

W.Niemann, J. Kosanetzky, K.-H. Fischer
YXLON International X-Ray GmbH
Röntgenstrasse 24
D-22335 Hamburg, Germany

E. Siegel, S. Zahorodney
YXLON Inc.
5110 McGinnis Ferry Road
Alpharetta, GA 30202, USA

ABSTRACT

X-ray backscatter imaging has become a well-known technique for inspection of light materials. Due to its capability of measuring and displaying density differences it has found widespread applications in aircraft industry, such as corrosion inspection of aging aircraft. The commercial system ComScan 160 measures a 3D data-set consisting of 500 * 250 voxels in 22 layers. On a monitor, a set of up to 4 individual slices parallel to the surface of the specimen is displayed for visual inspection. Recently, we have developed new software tools which enable the operator to perform many new kinds of visualization. Various different slices (e.g. xy-, xz- and yz-slices) can be displayed, and furthermore, 3D presentations of the full data sets are possible. As an example, the object can be rotated and tilted. Other software functions enable the presentation of data on a homogenous 3D grey level, so local structures such as cracks, voids, corrosion effects etc. are enhanced and easier to find.
With these new tools, the operator has many new possibilities to display and analyze defects in aging aircraft. In problematic inspection cases, the tools enable a more reliable decision on the state of the inspection object.

1 GENERAL PRINCIPLES OF X-RAY BACKSCATTER IMAGING

Since the market introduction of the commercial system ComScan 160 X-ray backscatter imaging has become an established inspection technique in certain areas of nondestructive testing, e.g. corrosion inspection on aircrafts. The success of this technique is based on its unique strengths :

- The inspection needs only single-sided access, and it is nondestructive.
- Grey values in the images are proportional to the material density inside the object.
- Small cracks, voids and other defects such as corrosion are visible.

The ComScan 160 backscatter system is based on direct imaging by the pinhole camera principle. Out of the conical radiation field of a standard x-ray tube a specially designed rotating aperture is creating a flying pencil-beam which hits the object under inspection [1,2,3]. The irradiated area is imaged through imaging slits onto two detector array located parallel to the x-ray tube on the same side of the object (see Fig. 1 for explanation). Along the primary beampath inside the object scattered radiation which is detected through these imaging slits by the detector arrays. Each detector element looks at a different position in depth. Therefore the signals read out give depth-resolved information of the scatter intensity. The signal measured by a detector element of the X-ray backscatter system is directly proportional to

the density of the object in the selected volume element (voxel) and proportional to the intensity I(E) of the bremsstrahlung spectrum emitted by the X-ray tube. The signal will be attenuated by absorption of the incoming beam on its way to the voxel and by absorption of the scattered beam on its way to the detector. These absorption processes result in a decreasing detector signal with increasing material depth and thus give a natural limitation for the achievable information depth of this imaging technique. With a 160 kV X-ray tube and a short integration time of only a few ms per pixel, the information depth is limited to 20 to 50 mm, depending on the type of penetrated light material. For metals like Fe or Cu it is approx. 3 mm.
By simple x-y scanning - realized as a combination of a flying x-ray beam and a movement of the whole detection unit - a fully 3D data-set is generated build up of 22 parallel slices.

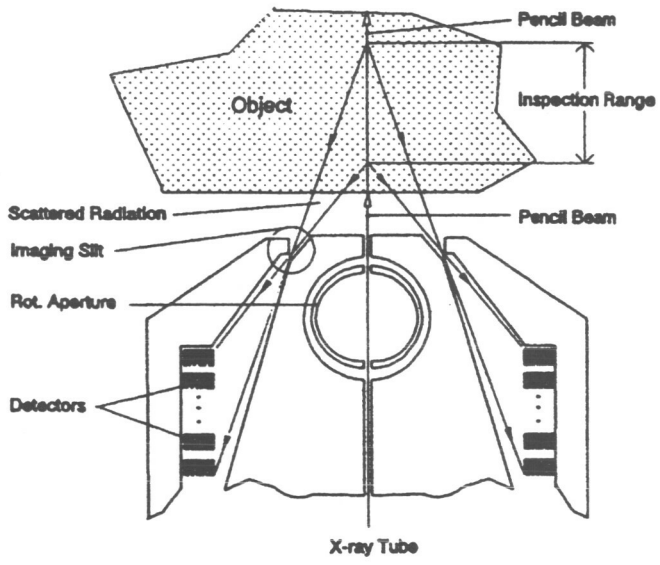

Fig. 1 : Imaging principle of the ComScan backscatter system

The achievable information depth depends on the kind of bremsstrahlung spectrum, i.e. on the voltage and power of the X-ray source. The higher the tube voltage, the larger will be the information depth. With a 450 kV tube, information depths of up to 20 cm are possible [4]. The final limitation is given by scatter processes inside the object. In addition to the single scattering , there are multiple scattering effects, the strength of which increases with increasing penetration depth. Above 20 cm the multiple scatter contribution to the total signal is hardly distinguishable from the total signal, resulting in poor contrasts.
The fact that the scantime per voxel T is related to the geometrical resolution L by the 7^{th} power of 1/L, i.e. $T \propto L^{-7}$ [5] gives a natural reason for the limited resolution in backscatter systems. For very high resolution, i.e. better than 0.2 mm; the required inspection time will be very long.

2 THE COMMERCIAL COMSCAN 160 SYSTEM

The commercial system ComScan 160 has been designed for the inspection of lightweight materials such as Aluminum, Honeycombs, carbon fiber structures etc. [6]. In this inspection system the X-ray beam is collimated in such a way that a resolution of 0.4 mm is achieved with the 10 mm aperture. By

using a 160 kV, 19 mA X-ray tube the acquisition of 500 x 250 x 22 voxels requires a typical scan time of a few minutes for the whole inspection volume. This means that for every individual voxel a measurement time of only 1 to 3 ms is used. The typical information depth is 10 mm; the maximum selectable aperture allows a 50 mm depth. In figure 2 the total system is shown, i.e. the scanner head together with high voltage generator, electronics etc., whereas in figure 3 the backscatter system can be seen during setup for a typical inspection of a wing.

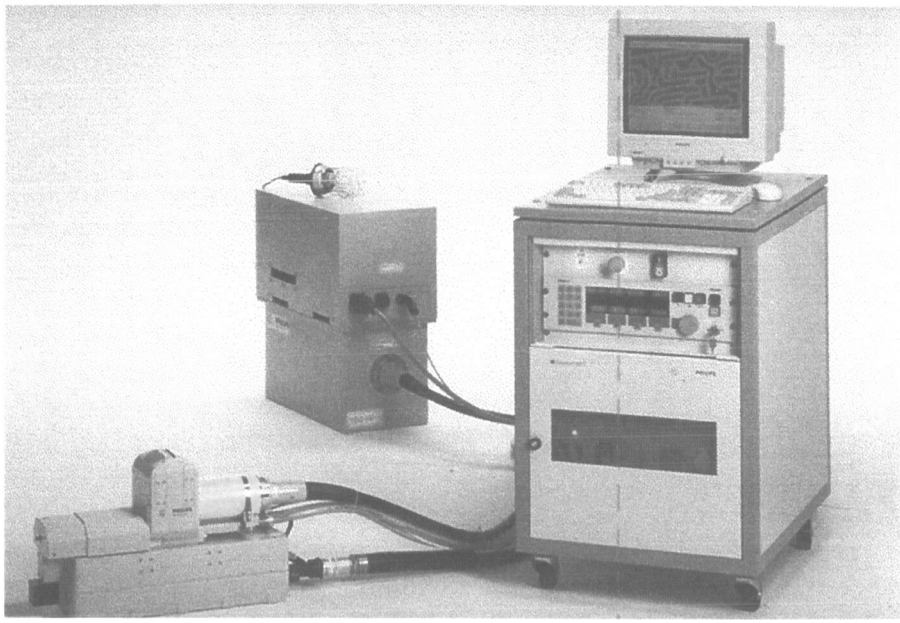

Fig. 2 : New generation ComScan 160 II

Fig. 3 : ComScan 160 setup for wing inspection
(courtesy of Jet Aviation, Basel airport, Switzerland).

2.1 COMSCAN 160 IMAGE PROCESSING

The ComScan 160 backscatter system is a direct tomographic technique which delivers three-dimensional data sets build up of 22 layer images with no need for reconstruction techniques. Nevertheless image processing is getting more and more involved. One reason is that the generated layer images must be corrected for absorption effects or system inaccuracies to increase the detectability of small details.

The ComScan 160 software contains internal correction procedures for gain and offset settings of every individual detector element. Furthermore, a flat-field correction (sometimes called shading correction) for every pixel on a line (corresponding to the flying beam) is included. The basis for this correction procedure is a calibration measurement with a homogenous calibration object. This can be an aluminum block or a water phantom or a similar well-suited object. In this way, small angular variations of X-ray flux and the depth-dependence of the measured signal are compensated for. The depth compensation of the signal clearly depends on a good choice of the calibration material. In reality, a certain depth dependence of the signal will be left due to differences in absorption properties of the calibration material and the object under inspection.

The visualization of images in the present commercial system is restricted to 2D layer images, where the layers are oriented parallel to the surface of the inspection object (more precise : parallel to the surface of the scanner head). With these basic image processing functions, high quality images of lightweight materials are routinely obtainable in a few minutes. As an example, 4 layers of a honeycomb structure with an impact damage are shown in figure 4. Measurements were done at 160 kV, 18 mA.

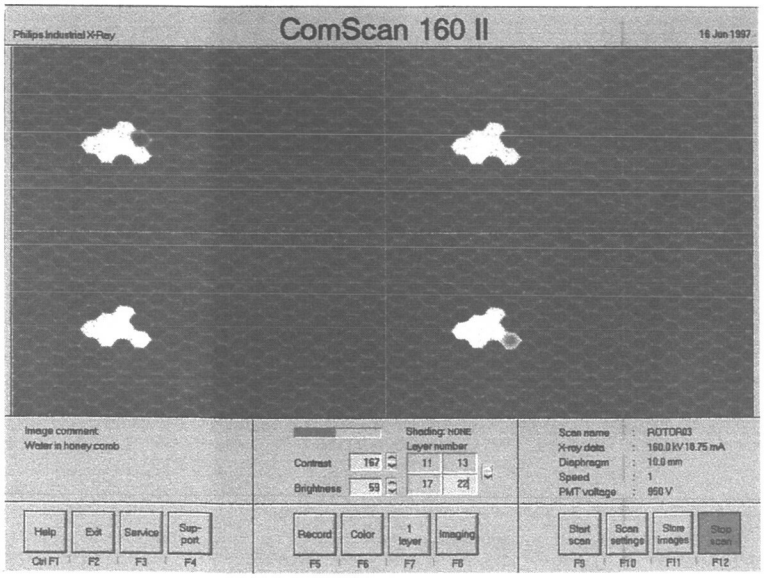

Fig. 4 : ComScan image of a honeycomb structure with impact

2.2 THE REDESIGNED COMSCAN 160 SCANNER

YXLON has redesigned the commercial product ComScan 160 scanner to the new ComScan 160 II based on customer requirements and technological progress (see figure 3 and [6]). The main changes and customer benefits are :

- Increased detector signal and reduced crosstalk due to tilting of the detector crystals.

- Improved signal-to-noise ration due to photon counting technique
- Faster exchange of apertures by new design
- Compact electronics and plug-in technology for enhanced mobility
- Industrial PC with OS/2 multi-task operating system
- Use of the .TIF data format for open communication
- Real time browsing through the various layer during the scanning process for faster diagnosis
- Storage of results on a CD-writer

Summing up, an increased image quality and a higher mobility have been achieved with the redesigned ComScan system. Furthermore the system throughput has been raised from approx. 50 scans per 8h-shift to approx. 80 scans by drastically improved data processing and handling.

The new system offers much better inspection results, e.g. for corrosion inspection on aircrafts or sonar domes. An example, the inner corrosion of an aircraft piece, is shown in figure 5.

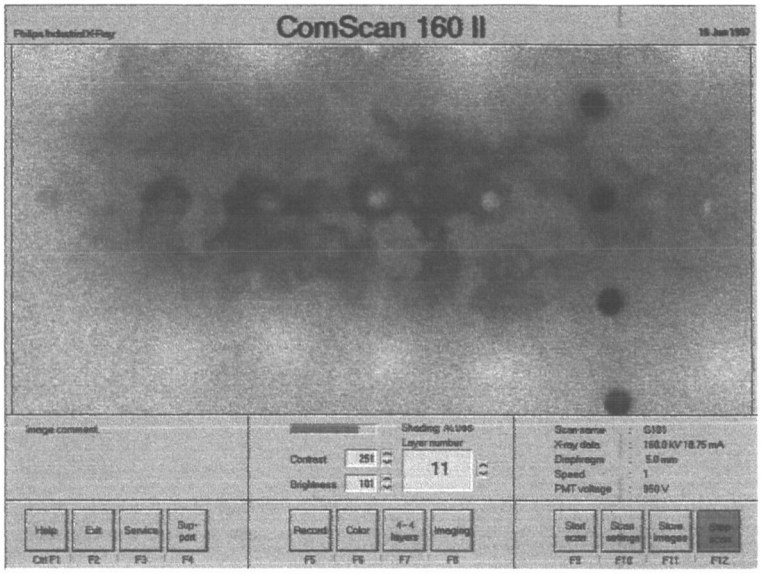

Fig. 5 : Corrosion in an aircraft piece. Corroded areas are darker than the non-corroded areas due to the reduced density of oxides compared to the metal.

3 2D AND 3D VISUALIZATION

Recently, we have developed new software tools for ComScan images offering the operator many new kinds of visualization. Slices can be displayed in various orientations (e.g. xy-, xz- and yz-slices) and in a combined view (ortho view). Furthermore, 3D presentations of the full data sets are possible (volume view). Every voxel has assigned values for the luminosity (scattering strength) and for the opacity (absorption). A careful definition of appropriate values for level and window for the two functions opacity and luminosity leads to a virtual 3D visualization of the inspected objects. The use of pseudo colors instead of grey values is another helpful feature. This is demonstrated in figure 6 for the case of the honeycomb structure.

Additionally, virtual manipulations of the inspection object are possible. For example, the object can be rotated, tilted or a different perspective can be chosen. Other software functions enable the presentation of data on a homogenous 3D grey level, i.e. depth-dependent grey value differences are compensated in

a predefined region of interest. Thus, local structures such as cracks, voids, corrosion effects etc. are enhanced and sometimes easier to find.
Original 2D ComScan data of a stringer with 4 layers shown in figure 7 are compared with a volume view of the whole inspection volume in figure 8.

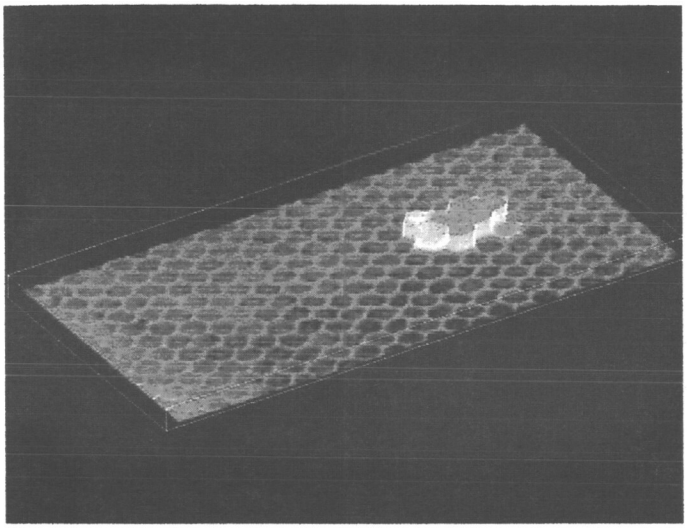

Fig. 6: Volume view of ComScan images of the honeycomb structure

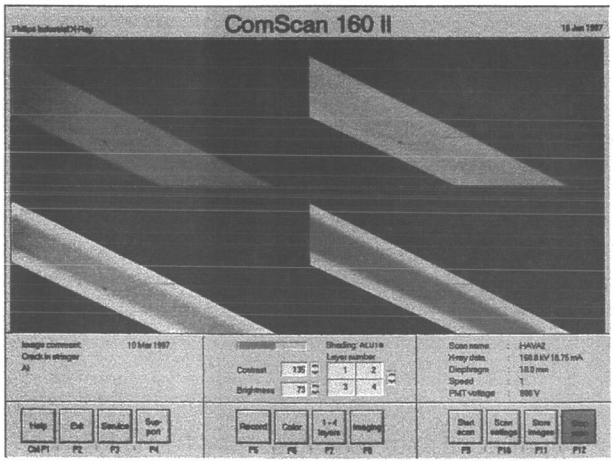

Fig. 7 : 2D view of the stringer
(4 layers, Nos. 1, 2, 3, and 4)

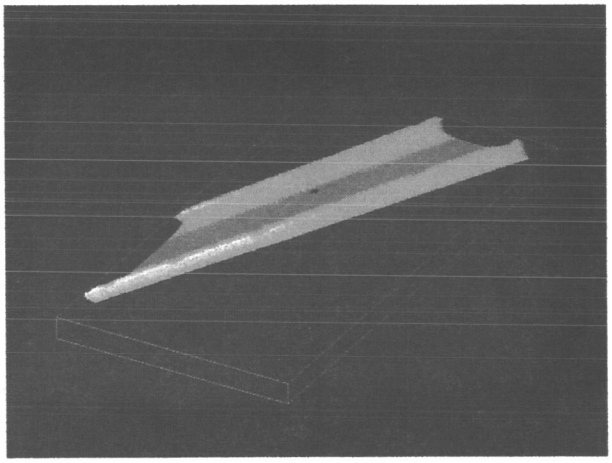

Fig. 8 : 3D view of the stringer

As a last example, a 3D volume view of the corrosion between Al plates (see fig. 5 for 2D) is displayed in figure 9.

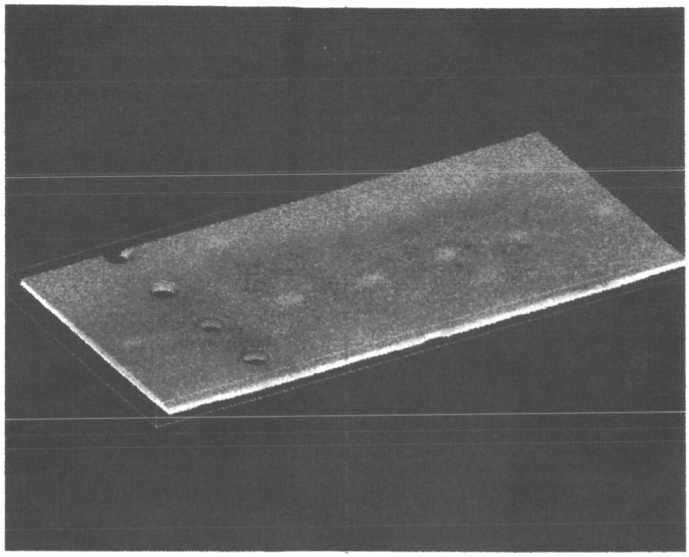

Fig. 9 : Volume view of corrosion between Al plates.

CONCLUSIONS

X-ray backscatter imaging is an inspection technique which is used for a lot of NDT applications such as corrosion inspection of aging aircraft or of sonar domes [7]. Sometimes fine details in the inspection object have to be found and explained. This requires high quality original measured data and a good correction for any kind of possible artifact. Several authors have tried to achieve a full understanding of the details of the backscatter images by computer simulations (see e.g. [8]). Although substantial progress has been made, published results still miss a full explanation of the small details. Therefore the best choice is to use sophisticated image processing software based on heuristic principles. Image processing of backscatter images based on software for 2D and 3D visualization is becoming more and more important. With these new tools, the operator has many new possibilities to display and analyze defects in aging aircraft. In problematic inspection cases, the tools enable a more reliable decision on the state of the inspection object. We have demonstrated the capabilities of the improved SW packages for displaying and analyzing results of objects scanned with the improved ComScan 160 II system.

ACKNOWLEDGMENTS

We gratefully acknowledge a substantial contribution to this work by our colleagues from Philips Research Labs at Hamburg.

REFERENCES

1. H.Strecker : *Scatter imaging of aluminum castings using an X-ray fan beam and a pinhole camera.* Materials evaluation 40, 1982.
2. J.-M. Kosanetzky, G.Harding, K.Fischer, A.Meyer: *Compton backscatter tomography of low atomic number materials with the ComScan system.* Philips Techn. Information Bulletin (1988).
3. G.Harding and J.Kosanetzky, *Scattered X-ray beam nondestructive testing*, Nucl. Instr. Meth. Phys. Res. A 280, p517 (1989)

4. W.Niemann and S.Zahorodny, *Status and Future Aspects of X-ray Backscatter Imaging.* Review of Progress in Quantitative Nondestructive Evaluation, Vol 17A, p. 379-385 (1997)
5. G.Harding: *Inelastic photon scattering : effects and applications in biomedical science and industry.* Radiation Physics and Chemistry 50, No.1 (1997).
6. *ComScan 160 II Compton X-Ray Backscatter Inspection System.* Data sheet YXLON International X-Ray GmbH, Hamburg.
7. E.C.Greenawald, Y.S.Ham and C.F.Poranski : *Application of backscatter tomography* . DGZfP Berichtsband 44, 354-361 (1994)
8. Y.S.Ham, C.F.Poranski, and E.C.Greenawald: *Monte Carlo simulation of X-ray back-scatter tomography using visual methods.* DGZfP Berichtsband 44, 346-353 (1994)

Multiple Initial Coldworking with the Split Mandrel System

Anthony Leon
West Coast Industries
14900 Whitman Avenue North
Seattle, Washington 98133
(P) 206/365-7513, (F) 206/365-7483
aleon@wcoastindustries.com

ABSTRACT
This paper describes a new coldworking procedure, Multiple Initial Coldworking, utilizing the split mandrel process. This procedure coldworks the hole initially three times with the same tooling, instead of the usual one time. An analytical and experimental program was developed to determine the feasibility of this innovative procedure. Computer analysis was performed to determine initial coldwork parameters. Static tests conducted on aluminum and titanium sheets analyzed the effect of the new process on various hole quality issues and applications. Fatigue tests compared the overall life enhancement of the new process over the basic process. Multiple Initial Coldworking produces a hole with greater overall hole quality and retained expansion than traditional single pass coldworking methods. Fatigue results indicate that three-passes at lower applied expansion levels produce fatigue results similar to nominal single pass coldworking. Future testing is also discussed.

1.0 INTRODUCTION

Fatigue-related issues take on an added importance as service life of airframes increase. Fastener holes are especially challenging, since flaws originating at these locations are a prevalent source of fatigue cracks that decrease the overall service life of the component. Coldworking these holes is a common method of improving the fatigue resistance of a metallic component. However, when repairing or reworking fastener holes, the hole is generally oversized, which may reduce the edge margin or hole spacing beyond acceptable limits. If these dimensions are too short, material damage could occur, resulting in a scrapped part. One solution to this has been to reduce the applied expansion, but with the drawback of less than nominal fatigue life improvement.

An improved coldworking procedure has been developed that produces the fatigue life benefits expected from coldworking with the reduced material upset provided by coldworking at a reduced applied expansion rate. The procedure consists of initially coldworking a hole multiple times with split mandrel tooling.

An experimental program was carried out to quantify the hole quality and fatigue life improvement of the new coldworking procedure. Holes were coldworked to analyze hole quality issues including material finish, axial ridge width and height, overall hole shape, and material upset around the hole. Fatigue tests were performed to compare the fatigue enhancement benefits of "multiple-pass" coldworking to single-pass coldworking in aluminum alloys.

2.0 COLDWORKING

Coldworking fastener holes is a mechanical method of strengthening metallic components by retarding crack growth around the hole. The most common method of coldworking involves pulling a tapered mandrel through a hole. This expands the hole diameter, creating a radial plastic flow of material, thereby producing a high residual compressive stress zone around the hole. [1,2]. The residual zone, depending upon variables such as material and applied expansion levels, will extend approximately one radius from the edge of the hole. This acts as a barrier to crack growth, thereby increasing the fatigue life of the component [3].

2.1 Considerations

The amount of expansion a hole experiences during coldworking can be expressed as either applied or retained expansion [4]. For split mandrel coldworking the applied expansion is stated as a ratio of the mandrel major diameter (correlating to the mandrel major diameter plus twice the sleeve thickness for the split sleeve process) and the start hole diameter. Retained expansion is defined as the resulting increase in hole diameter after coldworking. It is expressed as a percentage of the applied expansion. Retained expansion is proportional to the yield strength of the material being coldworked. In general, applied expansion levels for nominal coldworking ranges from between 4.0% to 5.5%. Nominal retained expansion values are 70 – 75% for 2000 series aluminum alloys, 60% for 7000 series aluminum alloys, and 50% for titanium and high strength steels [5].

Additional aspects of coldworking are the material upset phenomenon of hourglass shaped holes and volcanoing. Coldworked holes are generally larger at their ends than at the middle. Final sizing of the hole by reaming will eliminate the hourglass shape, resulting in a straight final hole. During the coldworking process the speed and shape of the mandrel causes material to be extruded to the surface of the component. This ridge of upset material is known as volcanoing for obvious reasons. The amount of volcanoing is proportional to the applied expansion rate of coldworking. For nominal applied expansion levels the volcanoing is removed when reaming the hole to its final diameter.

2.2 Split Mandrel Process

The Boeing Company developed the split mandrel system in the early 80's. This sleeveless coldworking operation has been used in the production of aluminum structures since 1982. The split mandrel process (Figure 1) uses an automatically lubricated, hollow, longitudinally slotted, and tapered oversized mandrel. The operation begins when the mandrel (which is collapsible, due to the longitudinal slots and hollow center) is inserted into the hole. When the coldworking cycle begins a pilot (a thin, solid, cylindrical tool that supports the mandrel during coldworking) is automatically inserted through the hollow portion of the mandrel, thereby expanding and solidifying the mandrel. The hole is coldworked as the mandrel's major diameter is drawn through the hole with the pilot extended.

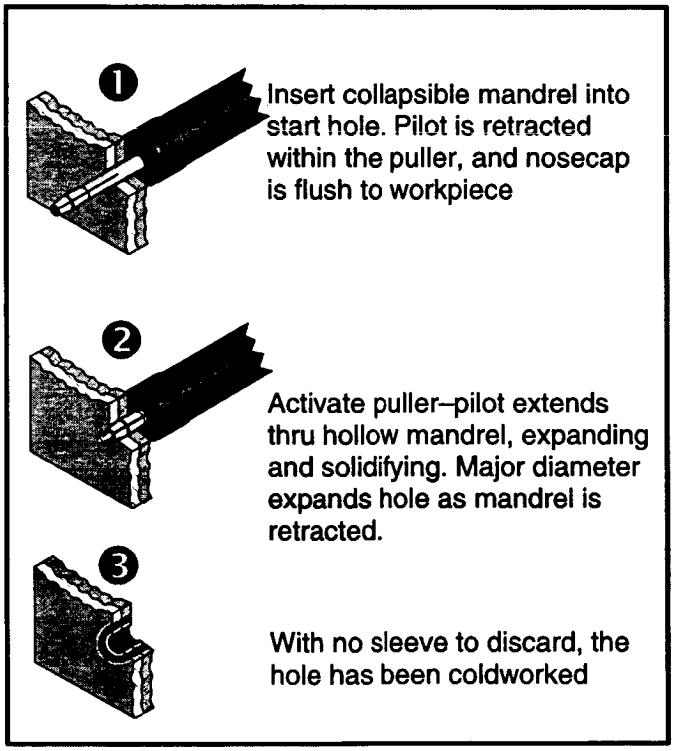

Figure 1, Split Mandrel Coldworking Process.

3.0 MULTIPLE INITIAL COLDWORKING

This program began with a simple question, "What would happen if a hole were coldworked several times with split mandrel tooling?" A preliminary inquiry was launched. Several holes were coldworked with both single-pass and multiple-pass coldworking. These results showed the multi-pass coldworked holes had increased retained expansion, greatly reduced the hourglass shape and axial ridge height, and produced an excellent hole finish. These initial results generated interest in Multiple Initial Coldworking, and a research program was initiated.

3.1 Program Development

The objective of the research program was to determine the feasibility of the Multiple Initial Coldworking process, as well as comparing the process to single-pass split mandrel process. Parameters for investigation include: (a) the amount of added retained expansion produced by the new process, (b) The resulting quality of the coldworked hole, (c) using the new process to coldwork high strength materials, (d) the effect of the material upset issues of volcanoing and hourglass shape, and (e) Comparing the life enhancement of the new process to single-pass coldworking.

3.2 Computer Analysis

The author has created a computer program that can accurately predict the applied and retained expansion, and post-coldwork hole diameter for single-pass coldworking. This program will be used to calculate the estimated applied and retained expansion as well as the post-coldwork hole diameter. For the initial analysis each coldwork pass was treated as a different hole. The results were then combined and analyzed against actual measurements.

3.3 Basic Static Tests

The program began with a series of 12 holes drilled in 6.5 mm (1/4 inch) aluminum plate. The holes were processed with existing split mandrel procedures using standard 10-0 split mandrel tooling. The hole tested correlated to an 8-mm (5/16-inch) final hole diameter. Diameter measurements were obtained for the top, middle, and bottom of groups of holes after each coldworking pass.

The approximate heights of axial ridges in the coldworked hole made by the slots of the mandrel were included in the measurements. The height of the ridges was determined by measuring the hole diameter with a two contact point ball gage set between axial ridges. This diameter was subtracted from the properly measured diameter, and resulting measurement represents the estimated height of two axial ridges. These results are tabulated in Table A in the appendix. Additional axial ridge measurements were made on a set of 25 holes. The holes correlate to a final hole diameter of 11-mm (7/16-inch). Test specimens were manufactured from 6.5-mm (1/4-inch) 2024-T3 and 7075-T6 aluminum plate. The holes were coldworked with either a nominal single- or triple-pass split mandrel coldwork process (approximate single-pass applied expansion level of 4.0%). Measurements of the post-coldworked hole and axial ridge measurements are included in Table B in the appendix.

An additional test was conducted to measure volcanoing. Test specimens containing 42 holes correlating to a nominal 11-mm (7/16-inch) final diameter were made out of 6.5-mm (1/4-inch) thick 2024-T3 aluminum plate. The start holes were varied to produce applied expansion levels between 2.0% and 4.5% in 0.5% increments. The holes were equally divided into two groups, and then coldworked with either a single- pass or three-passes using standard 14-0 split mandrel tooling. Measurements of the height of the volcano were taken in 0.25-mm (0.010-inch) increments from the edge of the hole to 4.57-mm (0.180 inch) with a CMM unit.

Static coldworking was also designed for 6Al-4V-titanium plate. The holes were coldworked three times using standard 10-0 tooling, correlating to a nominal 8-mm (5/16-inch) hole. The first set of holes did not follow the same pattern of the holes in the aluminum plate. The hole diameter did not change with, and thus there was no advantage to, additional coldworking passes. The decision was made to focus testing on aluminum alloys and to investigate high strength material at a later time in the project.

3.4 Fatigue Testing

The initial fatigue testing investigated the life enhancement properties of Multiple Initial Coldworking. Two multiple coldworking methods were compared to nominal single-pass split mandrel coldworking (applied

expansion of approximately 4.5%). The two new methods differ in the amount of applied expansion during their first coldwork pass. One method has a comparable applied expansion to the single-pass method, resulting in the largest retained expansion tested. The applied expansion level on other method has been reduced by approximately 1.0%. After three coldworking passes, the resulting retained expansion level should approximate the life enhancement results of the single pass coldworking group. The fatigue specimen coldworking matrix is summarized in Table 1 below.

Table 1 - Fatigue Specimen Coldworking Matrix

Coldwork	Applied Expansion		Retained Expansion	
Method	2024	7075	2024	7075
Nominal Single-Pass	4.8%	4.8%	3.8%	3.4%
Nominal Triple-Pass	4.8%	4.8%	4.0%	3.8%
Lower Triple-Pass	3.1%	3.2%	2.4%	2.3%

Constant amplitude fatigue testing was conducted in laboratory air at ambient temperature and humidity on servohydraulic test frames with digital-based electronic controls. The test machines and electronics are calibrated annually with standards traceable to the National Institute of Standards and Technology. Testing was conducted on zero-load transfer, open hole specimens of standard dogbone geometry. The tested hole corresponds to a nominal 9.5-mm (3/8-inch) final hole. Thirty specimens each were manufactured from 6.5-mm (1/4-inch) thick 2024-T3 and 7075-T6 aluminum plate. Specimens were evenly divided into the three coldworking groups, 20 specimens (10 per material) per group. Specimens were coldworked to the parameters listed in Table 1 using standard 12-0 split mandrel tooling. After coldworking the holes were reamed to a final diameter of 9.55-mm (0.376-inch). Testing was conducted at five maximum gross stresses (40-ksi, 35-ksi, 30-ksi, 28-ksi, and 25-ksi) at a stress ratio R = +0.10. Two specimens per material per coldwork group were tested at each stress level. At the completion of testing S/N curves will be generated from the fatigue data.

4.0 RESULTS AND DISCUSSION

4.1 Computer Analysis

Results from the computer analysis indicated that a Multiple Initial Coldworked hole diameter approximates the major diameter of the mandrel that coldworked it. After the third coldwork pass the estimated post-coldworked diameter was within 0.001-inch of the mandrel major diameter. These results were independent of hole diameter, initial applied expansion, and the material being coldworked.

Unfortunately the actual measurements did not correlate as expected with the analytical results. The post-coldworked diameter measurements, for both 2024 and 7075 aluminum alloys, were closest to the initial estimates. Diameter measurements differed a maximum of 0.003-inches from the expected results. The applied and retained expansion values had a larger degree of variability, depending on the material being coldworked. The applied expansion values for 2024 specimens varied up to 0.30% from the initial estimates, and 0.60% for the 7075 specimens. Retained expansion values for 2024 specimens varied from the initial estimates as much as 0.80%, and the values from 7075 specimens were as much as 1.20% different from initial estimates.

It is clear that WCI's singe-pass coldworking analysis program will not work for multiple-pass analysis. Previous coldworking passes are altering the properties of the material by working/hardening mechanisms. Additional research is needed to determine how to modify the program to accurately estimate multiple initial coldworking parameters

4.2 Basic Static Tests

The results of the basic static tests are tabulated in Table A in the Appendix. The initial static tests help quantify the mechanisms of each coldworking pass. During the first coldwork pass the hole has expanded an average of 1.27-mm (0.050-inch). In addition, the hole has developed an hourglass shape during coldworking. Diameter measurements at various points through the thickness of the hole vary between 0.02- and 0.10-mm (0.0006- and 0.0040-inch). The second coldworking pass expands the hole slightly, averaging just 0.15-mm (0.006-inch). The hole is also straightening out, the differences between point measurements ranges from 0.00- to 0.08-mm (0.0000- to 0.0032-inch) with an average of 0.04-mm (0.0015-inch). The final coldworking pass expands the hole less than 0.02-mm (0.001-inch) and continues to straighten out the hole. The difference in point measurements ranges from 0.00- to 0.05-mm (0.0000- to 0.0019-inch) averaging less than 0.02-mm (0.001-inch) difference in the diameter of the hole throughout the material. The results from the set of 25 holes (Table B) agree with the initial results. The diameter measurements of multiple coldworked holes follow the established pattern. The holes were larger in diameter with less variability between the top and bottom measurements.

The measurements of the estimated height of the axial ridge illustrate how Multiple Initial Coldworking almost eliminates the ridges from the hole. Axial ridge height measurements range from 0.03- to 0.008-mm (0.0012- to 0.0003-inch). The additional axial ridge measurements illustrate the reduction of axial ridge height. The measurements are included in Table B in the Appendix. The axial ridges in single-pass coldworked holes average 0.05- to 0.08-mm (0.002- to 0.003-inch) in height. The heights of the axial ridges were not measurable in the multiple coldworked holes.

The measurements of volcano height were somewhat unexpected. Samples of the overall results are included in Table C in the Appendix. According to these measurements there is minimal difference (0.02-mm (0.001-inch) or less) in volcano height between different applied expansion levels and comparing one-pass with three-passes. The reason for these similar results is unknown at this time.

4.3 Fatigue Tests

The initial fatigue results were promising. They help to confirm the hypothesis that three passes of lower applied expansion coldworking produces results similar to single-pass coldworking at a higher nominal applied expansion. The fatigue testing was not completed at the time this paper was drafted. The fatigue results, to date, are summarized in Graphs 1 and 2 in the Appendix.

The fatigue results illustrate an excellent agreement between the single-pass coldworking and three-pass lower applied expansion groups for both aluminum alloys tested. As expected the three-pass coldworked group with the larger retained expansion experiences the best life enhancement from coldworking.

5.0 FUTURE DIRECTIONS

The research detailed in this paper represents the start of an ongoing research program. The initial static and fatigue results indicate that the Multiple Initial Coldworking process may be feasible. Additional analysis, including detailed statistical analyses, will need to be conducted at the completion of this program to prove the feasibility of the new process.

Upcoming research areas in this program include the following:

5.1 Edge Margin Static Tests

How do the various coldworking processes effect the dimensional stability of the short ligament in short edge margin situations? This phase of testing will provide the preliminary data to answer that question.

The data will be used to quantify material upset issues (e.g., volcanoing, ligament buckling) for the three coldworking processes.

5.2 Edge Margin Fatigue Tests

After the results of the static tests are reviewed work will begin on the fatigue testing specimens with short edge margins. The fatigue testing will be similar to the initial multiple initial coldwork fatigue testing.

5.3 Multiple Initial Coldworking Analysis Tool

Can a computer program be created to predict the retained expansion for a multiple initial coldworked hole? Multiple initial coldworking has proven more complex than single-pass coldworking. Developing an effective analysis tool will increase the knowledge base, thereby providing the capability to optimize the process.

5.4 Maximum Retained Expansion

Is there a maximum retained expansion value for coldworking? The majority of testing on coldworking has measured it by applied expansion. Retained expansion values offer a more direct measurement for the multiple initial coldworking process. Additional static and fatigue tests will need to be conducted to evaluate the effect of high-retained expansion levels on life enhancement.

5.5 Coldwork Process Variables

How will the various mechanisms of the coldwork process affect the multiple initial coldworking process? The author has researched how various process mechanisms influence coldworking in various situations [6]. Research and analysis will need to be conducted to understand process variables, such as rate, pull force, and material thickness.

5.6 Other Applications

Short edge margin applications are just the first applications being reviewed for this new coldworking process. Other applications to be reviewed include maximizing retained expansion for fatigue critical areas, and coldworking to final hole dimensions among others.

6.0 CONCLUSION

Cost effective processes like fastener hole coldworking will be needed by the Aerospace Industry to help keep fatigue in check in both new and aging aircraft. The split mandrel process is an improvement over the well-known split sleeve system. Both processes offer similar life enhancement benefits; however, the split mandrel process offers additional benefits of simplicity, speed, and adaptability at a reduced cost.

Research to better understand the complexities of the coldwork process has led to possible new coldworking processes. Multiple Initial Coldworking is an example of these new processes. The new procedure appears to have applications unsuited for nominal one-pass coldworking processes. Utilizing standard split mandrel coldwork tooling and multiple initial coldworking passes coldworking can be optimized for new fatigue critical applications.

7.0 REFERENCES

1 Yanishevsky, M., Guellec, S. Le, "CF116 Main Lower Wing Skin Enhancement Coupon Test Program," Unpublished Provisional Copy, Department of National Defense, Canada.

2 Phillips Joseph, L., "Fatigue Improvement by Sleeve Coldworking," SAE Paper 730905, Society of Automotive Engineers, 1973.

3 Wieland, David H., Cutshall, Jon T., Burnside, O. Hal, Cardinal, Joseph W., "Analysis of Cold Worked Holes for Structural Life Extension," Presented at the FAA/NASA Symposium on May 6, 1994, Southwest Research Institute, San Antonio, Texas, 1994.

4 West Coast Industries "Split Mandrel Coldworking Holes (Aluminum)," Engineering Handout WCI-EH-9202-6.1, West Coast Industries, Seattle, Washington,

5 Class Notes, "Structural Integrity of New and Aging Metallic Aircraft – January 4 – 13, 1995," Engineering 839.60, Matthew Creager, Coordinator, University of California, Los Angeles, University Extension, Department of Engineering, Information Systems and Technical Management Short Course Program

6 Leon, A., "Benefits of Split Mandrel Coldworking," International Journal of Fatigue, vol. 20, no. 1, pp. 1-8, Elsevier Science Ltd., 1998.

8.0 APPENDIX

able A, Multiple Initial Coldwork Data

Hole I.D. #	Start Hole Dia. (in.)	First Pass Coldwork Diameter Top (in.)	Middle (in.)	Bottom (in.)	Average (in.)
1	0.2975	0.3050	0.3010	0.3020	0.3027
2	0.2978	0.3045	0.3005	0.3015	0.3022
3	0.2977	0.3043	0.3012	0.3018	0.3024
4	0.2976	0.3040	0.3005	0.3025	0.3023
5	0.2977				
6	0.2977				
7	0.2977				
8	0.2977				
9	0.2982				
10	0.2981				
11	0.2979				
12	0.2979				

Hole I.D. #	Second Pass Coldwork Diameter Top (in.)	Middle (in.)	Bottom (in.)	Average (in.)	Key Height (in.)
1	0.3085	0.3074	0.3074	0.3078	
2	0.3087	0.3076	0.3070	0.3078	
3	0.3086	0.3073	0.3073	0.3077	
4	0.3087	0.3075	0.3073	0.3078	
5	0.3087	0.3072	0.3085	0.3081	0.0003
6	0.3090	0.3062	0.3082	0.3076	0.0003
7	0.3089	0.3057	0.3074	0.3073	0.0012
8	0.3087	0.3055	.0.3080	0.3074	0.0005
9					
10					
11					
12					

Hole I.D. #	Third Pass Coldwork Diameter Top (in.)	Middle (in.)	Bottom (in.)	Average (in.)	Key Height (in.)
1	0.3090	0.3078	0.3081	0.3083	
2	0.3088	0.3076	0.3081	0.3082	
3	0.3087	0.3076	0.3081	0.3081	
4	0.3088	0.3078	0.3078	0.3081	
5	0.3094	0.3079	0.3079	0.3084	
6	0.3089	0.3078	0.3078	0.3082	
7	0.3094	0.3075	0.3078	0.3082	
8	0.3088	0.3074	0.3076	0.3079	
9	0.3083	0.3078	0.3075	0.3079	0.0008
10	0.3080	0.3079	0.3078	0.3079	0.0007
11	0.3085	0.3087	0.3075	0.3082	0.0008
12	0.3083	0.3080	0.3077	0.3080	0.0010

Table B, Additional Multiple Coldworked Hole Measurements

Specimen I.D. #	Hole I.D. #	Start Hole Dia. (in.)	Post-Cw Hole Dia. Top (in.)	Bottom (in.)	Avg. (in.)	Est. Key Height (in.)
One-Pass	1	0.4215	0.4301	0.4268	0.4285	0.0024
Nominal	2	0.2415	0.4301	0.4268	0.4285	0.0025
Coldwork	3	0.4215	0.4298	0.4268	0.4283	0.0021
7075	4	0.4215	0.4297	0.4269	0.4283	Note 1
	5	0.4214	0.4298	0.4281	0.4290	0.0011
	6	0.4215	0.4310	0.4314	0.4312	0.0032
One-Pass	1	0.4216	0.4310	0.4287	0.4299	0.0023
Nominal	2	0.4216	0.4313	0.4295	0.4304	0.0030
Coldwork	3	0.4218	0.4312	0.4293	0.4303	0.0023
2024	4	0.4216	0.4311	0.4294	0.4303	0.0027
	5	0.4216	0.4315	0.4304	0.4310	0.0030
	6	0.4218	0.4315	0.4313	0.4314	0.0028
Three-Pass	1	0.4216	0.4310	0.4282	0.4296	0.0000
Nominal	2	0.4215	0.4310	0.4281	0.4296	0.0000
Coldwork	3	0.4216	0.4310	0.4280	0.4295	0.0000
7075	4	0.4216	0.4300	0.4281	0.4291	0.0000
	5	0.4215	0.4310	0.4290	0.4300	0.0000
	6	0.4213	0.4321	0.4312	0.4317	0.0000
Three-Pass	1	0.4217	0.4320	0.4302	0.4311	0.0000
Nominal	2	0.4217	0.4320	0.4300	0.4310	0.0000
Coldwork	3	0.4216	0.4319	0.4300	0.4310	0.0000
2024	4	0.4216	0.4319	0.4301	0.4310	0.0000
	5	0.4219	0.4321	0.4314	0.4318	0.0000
	6	0.4216	0.4336	0.4340	0.4338	0.0000

Note 1: Key height measurement not taken

Table C, Volcano Height Measurements

Distance From Edge Of Hole (in.)	**1 Pass Nominal Coldworking – Volcano Height (in.) Applied Expansion**			**3 Pass Nominal Coldworking – Volcano Height (in.) Applied Expansion**		
	2.0%	**3.0%**	**4.0%**	**2.0%**	**3.0%**	**4.0%**
0.000	0.0642	0.0668	0.0677	0.0654	0.0689	0.0699
0.010	0.0647	0.0650	0.0656	0.0650	0.0668	0.0683
0.020	0.0637	0.0643	0.0641	0.0635	0.0656	0.0650
0.030	0.0630	0.0636	0.0636	0.0625	0.0643	0.0642
0.040	0.0623	0.0630	0.0632	0.0618	0.0635	0.0635
0.050	0.0618	0.0634	0.0627	0.0614	0.0628	0.0630
0.060	0.0612	0.0619	0.0623	0.0610	0.0622	0.0624
0.070	0.0608	0.0615	0.0620	0.0607	0.0618	0.0621
0.080	0.0605	0.0612	0.0618	0.0605	0.0613	0.0618
0.090	0.0604	0.0609	0.0615	0.0602	0.0611	0.0615
0.100	0.0602	0.0606	0.0612	0.0600	0.0607	0.0612
0.110	0.0600	0.0604	0.0610	0.0599	0.0605	0.0610
0.120	0.0599	0.0602	0.0608	0.0599	0.0603	0.0608
0.130	0.0598	0.0601	0.0606	0.0597	0.0601	0.0606
0.140	0.0597	0.0600	0.0605	0.0597	0.0600	0.0604
0.150	0.0598	0.0599	0.0604	0.0596	0.0599	0.0603
0.160	0.0596	0.0598	0.0604	0.0595	0.0598	0.0602
0.170	0.0595	0.0597	0.0602	0.0595	0.0597	0.0601
0.180	0.0594	0.0597	0.0601	0.0595	0.0597	0.0600

Graph 1, S/N Curve for 2024 Aluminum

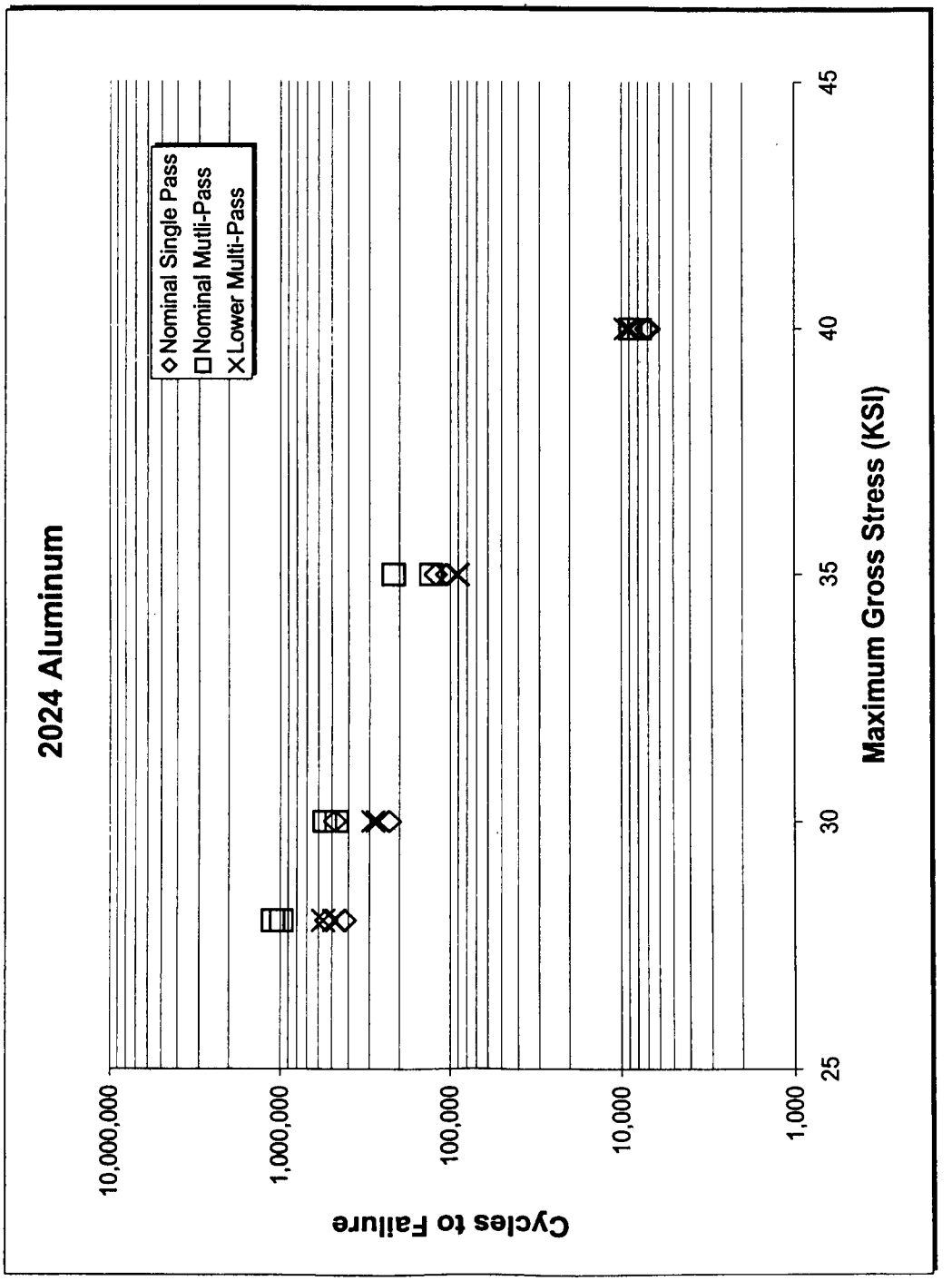

Graph 2, S/N Curve for 7075 Aluminum

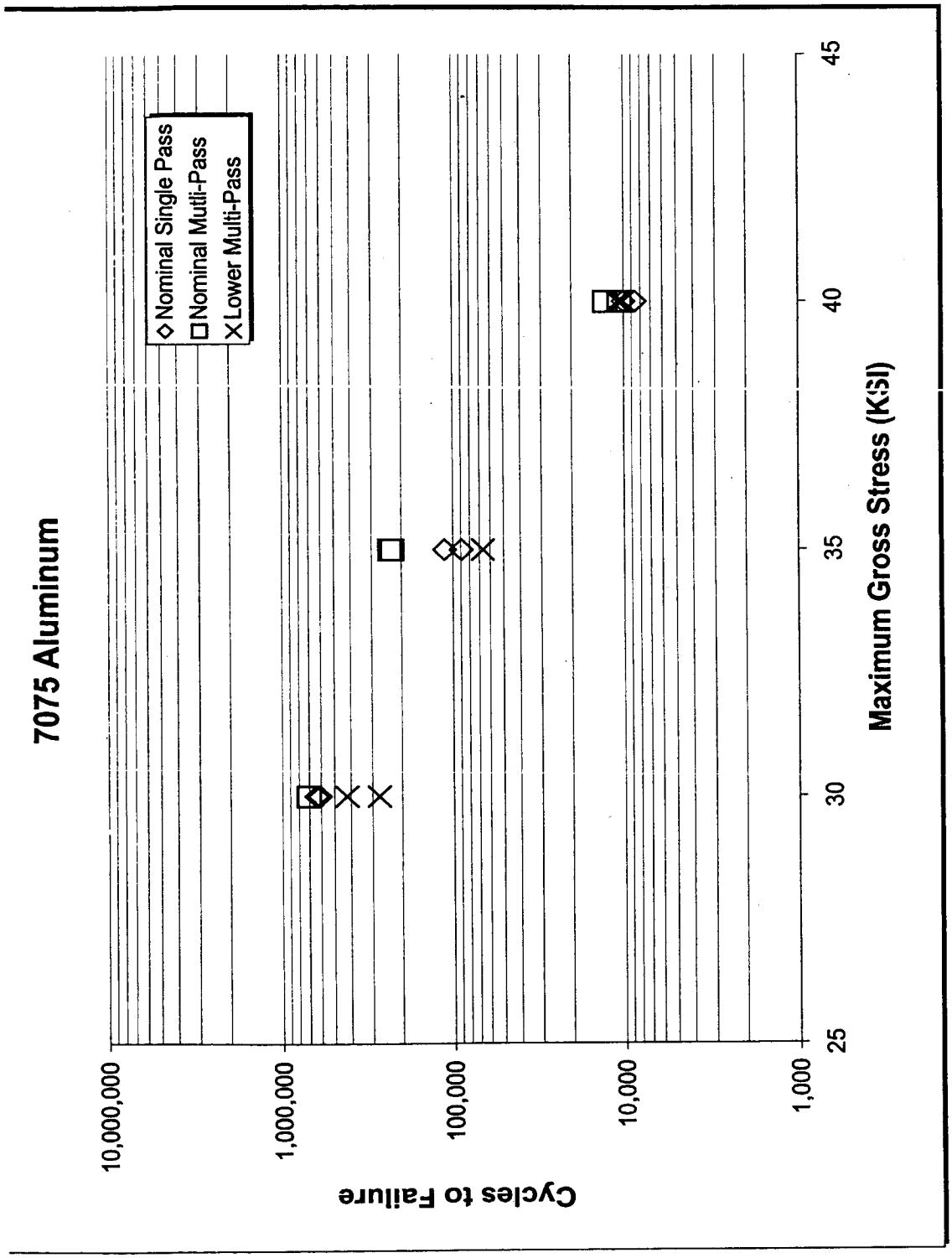

NASGRO 3.0 - A SOFTWARE FOR ANALYZING AGING AIRCRAFT

S. R. Mettu, V. Shivakumar, J. M. Beek, F. Yeh and L. C. Williams
Lockheed Martin Space Mission Systems & Services
Houston, Texas 77058

R. G. Forman and J. J. McMahon
NASA Johnson Space Center
Houston, Texas 77058

J. C. Newman, Jr.
NASA Langley Research Center
Hampton, Virginia 23681

ABSTRACT

Structural integrity analysis of aging aircraft is a critical necessity in view of the increasing numbers of such aircraft in general aviation, the airlines and the military. Efforts are in progress by NASA, the FAA and the DoD to focus attention on aging aircraft safety. The present paper describes the NASGRO software which is well-suited for effectively analyzing the behavior of defects that may be found in aging aircraft. The newly revised Version 3.0 has many features specifically implemented to suit the needs of the aircraft community. The fatigue crack growth computer program NASA/FLAGRO 2.0 was originally developed to analyze space hardware such as the Space Shuttle, the International Space Station and the associated payloads. Due to popular demand, the software was enhanced to suit the needs of the aircraft industry. Major improvements in Version 3.0 are the incorporation of the ability to read aircraft spectra of unlimited size, generation of common aircraft fatigue load blocks, and the incorporation of crack-growth models which include load-interaction effects such as retardation due to overloads and acceleration due to underloads. Five new crack-growth models, viz., generalized Willenborg, modified generalized Willenborg, constant closure model, Walker-Chang model and the deKoning-Newman strip-yield model, have been implemented. To facilitate easier input of geometry, material properties and load spectra, a Windows-style graphical user interface has been developed. Features to quickly change the input and rerun the problem as well as examine the output are incorporated. NASGRO has been organized into three modules, the crack-growth module being the primary one. The other two modules are the boundary element module and the material properties module. The boundary-element module provides the ability to model and analyze complex two-dimensional problems to obtain stresses and stress-intensity factors. The material properties module allows users to store and curve-fit fatigue-crack growth data. On-line help and documentation are provided for each of the modules. In addition to the popular PC windows version, a unix-based X-windows version of NASGRO is also available. A portable C++ class library called WxWindows was used to facilitate cross-platform availability of the software.

1. INTRODUCTION

Structural integrity analysis of aging aircraft is a critical necessity in view of the increasing numbers of such aircraft in general aviation, the airlines and the military. Damage tolerance analysis can be used to assess the remaining life of aircraft in service. It also provides a basis for setting up proper inspection intervals and a maintenance schedule for aging aircraft. The efforts of NASA, the FAA, the Department of Transportation and the Department of Defense to focus attention on problems related to aging aircraft are being coordinated to improve public safety.

The present paper describes the NASGRO 3.0 software which is well-suited for a comprehensive analysis of defects that may be found in aging aircraft. The predecessor of the current NASGRO computer program for fatigue crack growth analysis, called NASA/FLAGRO 2.0 [1] was originally developed to analyze space hardware such as the Space Shuttle, the International Space Station and the associated payloads. In the current version, the software was enhanced to suit the needs of the aircraft industry. Major improvements in Version 3.0 are the incorporation of the ability to input aircraft spectra of unlimited size, generation of common aircraft fatigue load blocks, and the incorporation of crack-growth models which include load-interaction effects such as retardation due to overloads and acceleration due to underloads. Five new crack-growth models, viz., generalized Willenborg, modified generalized Willenborg, Constant closure model, Walker-Chang model and the deKoning-Newman strip-yield model, have been implemented. To facilitate easier input of geometry, material properties and load spectra, a Windows-style graphical user interface has been developed. Features to quickly change the input and reanalyze the problem as well as examine the output are incorporated.

The software has been organized into three modules. The crack-growth module is the primary module which is used for crack growth analysis, stress intensity factor computation and critical crack size determination. The second module is based on boundary element analysis and provides the ability to model and analyze complex two-dimensional problems to obtain stresses and stress-intensity factors. The third module in NASGRO is designed to organize and process material data. It allows users to store and curve-fit fatigue-crack growth data. On-line help and documentation are provided for each of the modules. In addition to the popular PC windows version, a unix-based X-windows version of NASGRO is also available. A portable C++ class library called WxWindows was used to facilitate cross-platform availability of the software.

The NASA Fracture Control and Analytical Methodology Panel and the Interagency Working Group (IWG) are charged with guiding and monitoring the developments. The former panel consists of members from each of the NASA field centers and NASA Head Quarters. The latter group (IWG) is comprised of representatives from NASA, the Federal Aviation Administration, the US Air Force, the US Department of Transportation and experts from major aerospace companies such as Boeing, Lockheed Martin, United Technologies as well as specialists from research institutes such as the Southwest Research Institute and the University of Dayton Research Institute.

2. CRACK GROWTH MODELS

2.1 NON INTERACTION MODELS

There are three basic crack growth models in NASGRO for describing the growth behavior of cracks subjected to cyclic loads. They are: 1) NASGRO equation 2) Walker equation and 3) Tabular interpolation of da/DN vs ΔK. Using these three basic approaches, load interaction models such as the Willenborg, Modified Willenborg and the Strip Yield models were formulated.

2.1.1 NASGRO equation

Different elements of this equation were developed by Forman and Newman at NASA, de Koning at NLR and Henriksen at ESA and was first published in [2]. It is given by:

$$\frac{da}{dN} = C\left[\left(\frac{1-f}{1-R}\right)\Delta K\right]^n \frac{\left(1-\frac{\Delta K_{th}}{\Delta K}\right)^p}{\left(1-\frac{K_{max}}{K_c}\right)^q} \tag{1}$$

where N is the number of applied fatigue cycles, a is the crack length, R is the stress ratio, ΔK is the stress intensity factor range, and C, n, p, and q are empirically derived constants. Explanations of the crack opening function, f, the threshold stress intensity factor, ΔK_{th}, and the critical stress intensity factor, K_C are presented later. This equation provides a direct formulation of the stress-ratio effect. Also, the variations in K_C and ΔK_{th} values can have a reduced effect on the linear region of the curve (by a suitable choice of p,q), which produces a better fit to data. Figure 1 shows the curve fit for the A357 Cast Aluminum alloy along with the crack growth data. This material exhibits a rough fatigue surface unlike most materials. It was not easy to fit this data with the usual values of q - a much larger value of 2.0 was needed to enhance the effect of K_{max} on the crack growth rate thus achieving a reasonable fit. Also the value of C_{th} had to be somewhat larger. This indicates the ability of Eq. (1) to fit the crack growth data for a variety of materials.

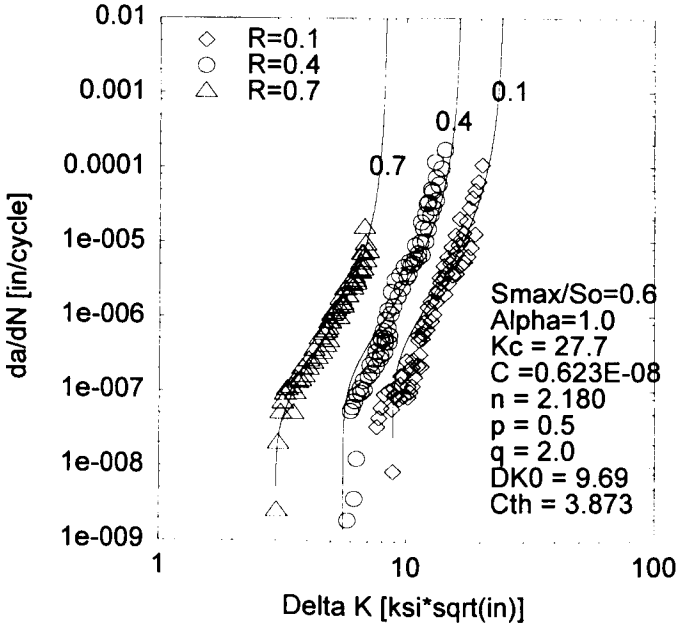

Figure 1 – Curve fit to Equation 1 for A357 Cast Aluminum

NASGRO incorporates fatigue crack closure analysis for calculating the effect of the stress ratio on crack growth rate under constant amplitude loading. The crack opening function, f, for plasticity-induced crack closure has been defined by Newman [3].

The threshold stress intensity factor range in Eq. (1), DK_{th}, is approximated as a function of the stress ratio, R, the Newman closure function f, the threshold stress intensity factor range at R = 0, DK_0, the crack length, a, and an intrinsic crack length, a_0, by the following empirical equation:

$$\Delta K_{th} = \Delta K_0 \left(\frac{a}{a + a_0} \right)^{1/2} \Big/ \left(\frac{1 - f}{(1 - A_0)(1 - R)} \right)^{(1 + C_{th} R)} . \tag{2}$$

This is a modification of the previous formula, involving the arctan function, that takes into consideration the small crack effect demonstrated by Tanaka, et al. [4]. The present form of the equation allows the spread for various R ratios to be controlled much better using the parameter C_{th}. Values of C_{th} and DK_0 are stored as constants in the NASGRO materials files, and a_0 has been assigned a fixed value of 0.0015 in. (0.0381 mm).

2.1.2 Walker-Chang Equation

The following equations define the basic Walker-Chang equation [5].
For $\Delta K > \Delta K_{th}$, $R \geq 0$

$$da / dN = C \left[\Delta K / (1 - \bar{R})^{1-m} \right]^n$$

$$R < R^+_{cut}, \ \bar{R} = R \tag{3}$$

$$R > R^+_{cut}, \ \bar{R} = R^+_{cut}$$

For $\Delta K > \Delta K_{th}$, $R < 0$

$$da / dN = C \left[(1 + \bar{R}^2)^q K_{\max} \right]^n$$

$$R \geq R^-_{cut}, \ \bar{R} = R \tag{4}$$

$$R < R^-_{cut}, \ \bar{R} = R^-_{cut}$$

For $\Delta K < \Delta K_{th}$,

$$da / dN = 0 \tag{5}$$

In the above equations, R^+_{cut}, R^-_{cut} are the cutoff values for positive and negative stress ratios. The threshold stress intensity factor range for this model is determined using

$$\Delta K_{th} = (1 - A\,R) \Delta K_o \tag{6}$$

A being a material constant.

2.1.3 Tabular Input

There are many material/environment combinations for which the fatigue crack growth rate data may not quite fit the above two models. In such cases, direct input of the tabular data for various stress ratios for

use in the crack growth routines will greatly increase the accuracy of predictions. NASGRO provides for 1-D tables which accept growth rate versus effective range of the stress intensity factor data and two types of 2-D table input. The first type requires that the da/dN values be identical for each of the R ratios whereas the second type of input allows independent values of da/dN vs Delta K for each R ratio. The latter table is internally converted to the former and used in the interpolation process. There is also an option in the windows interface to allow users to enter an arbitrary crack growth equation. A table is generated using such an equation and can be used in the crack growth computations.

2.2 LOAD INTERACTION MODELS

2.2.1 Generalized Willenborg Model

The Generalized Willenborg model, based on Gallagher's [6] generalization of Willenborg's [7] original development, was incorporated into NASGRO 3.0. This model deals with crack retardation effects only and the details of the formulation are given in [6].

The effect of current loading on crack growth is known to be influenced by the load history; the term "load interaction" describes the interplay of these influences. The Generalized Willenborg model, utilizes a residual stress intensity, K_R, which determines the effective stress ratio due to a load interaction which in turn is used in the crack growth equation and has the effect of retarding the crack growth. Since K_R depends on threshold which in turn depends on R_{eff}, an iterative scheme has been developed and used.

The retardation for a given applied cycle of loading depends on the loading and the extent of crack growth into the overload plastic zone. Details of the formulation may be found in [6, 7, 8]. The constraint factor used in computing the plastic zone size is taken from a fit developed by Newman [9].

2.2.2 Modified Generalized Willenborg Model

A load interaction model termed the Modified Generalized Willenborg (MGW) Model was developed by T. R. Brussat [10] of Lockheed Martin. Based on this, a computer model was developed and incorporated into NASGRO 3.0.

The MGW model extends the Generalized Willenborg load interaction model [6] by taking into account the reduction of retardation effects due to underloads. The MGW model (like the Generalized Willenborg), utilizes a residual stress intensity, K_R, which determines the effective maximum and minimum stress due to a load interaction. The equations are:

$$\begin{aligned} K_{\max}^{eff} &= K_{\max} - K_R \\ K_{\min}^{eff} &= Max\{(K_{\min} - K_R), 0\}, \quad for\ K_{\min} > 0 \\ &= K_{\min} \qquad\qquad\qquad for\ K_{\min} \le 0 \end{aligned} \tag{7}$$

These effective stress intensity factors are used instead of the actual $K_{\max}, K_{\min}$ within the crack growth equation and have the effect of retarding the crack growth. In addition, an underload (i.e., a compressive or tensile load that is lower than the previous minimum load subsequent to the last overload cycle) can reduce such retardation. The stress ratio R_U given by $S_{UL} / S_{\max}^{OL}$ (the ratio of current underload stress

to overload stress) is used to adjust the factor ϕ. The factor ϕ used to achieve the reduction in retardation is given by

$$\begin{aligned} \phi &= 2.523\phi_0 / (1.0 + 3.5(.25 - R_U)^{.6}), \quad R_U < 0.25 \\ &= 1.0 \qquad\qquad\qquad\qquad\quad , \quad R_U \geq 0.25 \end{aligned} \tag{8}$$

The parameter ϕ_0 is the value of ϕ for $R_U = 0$. Parameter ϕ_0 is a material dependent parameter that can be determined, ideally, by conducting a series of typical aircraft spectrum tests. The value of ϕ_0 ranges typically from 0.2 to 0.8.

2.2.3 Walker-Chang Willenborg Model

Another load interaction model implemented into NASGRO 3.0 is the Walker- Chang Willenborg model used in the B-1 program at Rockwell. Chang and Engle [5] developed a version of the Generalized Willenborg model which takes into account the acceleration due to negative loads. The formulation was computerized into a code named CRKGRO at Rockwell under contract from US Air Force. They use the Walker-Chang equations as given earlier(equations (3)-(6)). The retardation effects are modeled as in the case of Generalized Willenborg. Whenever the Willenborg load interaction model is invoked, the effective stress ratio R_{eff} is computed and used in the above equations.

2.2.4 Constant Closure Model

This crack growth model was originally developed at Northrop and was used on the B-2 program. It is a simplified closure model based on the observation that for some load spectra the closure stress does not deviate substantially from some stabilized value. This stabilized value is determined by assuming that the spectrum has a "controlling overload" and a "controlling underload" that occur often enough to keep the residual stresses in the crack wake constant, and thus the closure level constant. The closure level can be determined in three ways. Firstly, it can be calculated from a function that is an empirical fit of test data. The fit usually has three segments of which two are straight line segments joined in the middle by a relation using the Walker crack growth law. The user provides the fitting constants. Secondly, the closure level can be entered directly. Thirdly, Newman's closure function may also be used to calculate the closure level. This model is available for the NASGRO equation or a 1-D or a 2-D table look-up.

2.2.5 Strip Yield Model

A Strip Yield Model also has been incorporated in NASGRO 3.0. This model was created by the European Space Agency (ESA) and the National Aerospace Laboratory (NLR) in the Netherlands in cooperation with the NASA Langley Research Center and the NASA Johnson Space Center. The NLR report [11] contains details of the model and its implementation into NASGRO. Strip Yield is a mechanical model based on the assumption that a growing fatigue crack will propagate through the crack tip plastic region, and that this plastic deformation left in the wake of the crack will contribute to stress interaction effects such as stress-level dependence and crack growth rate acceleration and retardation.

3. CRACK GEOMETRY

An extensive library of crack geometries is provided in NASGRO. The crack cases are classified into through cracks, embedded crack, surface cracks, corner cracks, standard specimens and tabular inputs. Plates, cylinders and spheres are some of the configurations that can be modeled. The stress intensity factor solutions for these cases were obtained by various means and have been documented in reports and journal articles. In quite a few cases, detailed finite element models were used to obtain the solutions for the full range of geometric parameters. Such solutions have been built into NASGRO in the form of either fitted equations or tabular interpolation.

To analyze problems with combined loading, NASGRO allows up to four stress quantities. The stress intensity factor is expressed as:

$$K = \left[S_0 F_0 + S_1 F_1 + S_2 F_2 + S_3 F_3\right]\sqrt{\pi a} \tag{9}$$

The stress quantities S_0, S_1, S_2, and S_3 are usually the applied tension/compression, bending in the thickness and width directions, and pin bearing pressures respectively, F_0, F_1, F_2, F_3 being the corresponding geometry correction factors.

4. FATIGUE LOAD SPECTRA

The basic unit of fatigue loading in NASGRO is a schedule. The load schedule concept provides flexibility by allowing the user to repeat blocks and/or combine different blocks together. This is especially useful for analyses of parts that are subjected to both pre-flight testing and flight loads. In addition, the load schedule method provides a means for entering larger spectra. A load schedule is created by filling up to 9999 blocks with different block cases. Up to 20 different block cases can be combined, ordered, and/or repeated within these available blocks. Each distinct block case can contain up to 200 load steps when stored in the SCHDLE file, where a load step is defined as any number of cycles (up to 999,999,999.99) of stress alternating between two specified limits. For aircraft applications when each block is stored in a separate file either in standard NASGRO format or in sequential form, there is no restriction on the number of load steps.

The loading spectrum for payloads, which experience stresses associated with the launch and landing of the Space Shuttle, is provided in the SCHDLE file. This spectrum was developed at the Goddard Space Flight Center (hence the name GSFC) and is reported in reference [12]. It is used for analysis of primary, load-carrying payload structures in the Space Shuttle Orbiter payload bay.

5. BOUNDARY ELEMENT METHOD

This section describes the NASBEM (NASA Boundary Element Method) computer program, a tool for fracture mechanics and stress analysis of two-dimensional elastic bodies of arbitrary geometry and loading, with or without cracks, and multiple zones of different materials.

Although transparent to the user, NASBEM consists of three parts: a user-friendly data input interface, the boundary element method (BEM) computational engine which also contains the stress-intensity factor calculation code, and a post-processing stress analysis component with optional graphical output.

The boundary element computational engine was furnished by researchers at the University of Texas as part of their FADD (Fracture Analysis by Distributed Dislocations) computer code. In this BEM, cracks are modeled by point dislocations and any external and internal boundaries are modeled by conventional boundary elements [13].

The program may be used to compute stresses in bodies that are free of cracks. In the case of multiple zone bodies, stresses can be computed in any of the zones that are crack-free. Special means have been used to overcome the "boundary layer" effect [14], the decay in accuracy in stress and strain as the boundary is approached that is commonly experienced with boundary element techniques. The stress computing algorithms have been tested on several geometric shapes and found to yield acceptably accurate values at all locations within the bodies up to and including their boundaries.

The program allows the specification of points for computing stresses in one of three ways: (a) point by point, (b) straight (or parabolic) line, and (c) circular arc subtending any angle about any point. The output is presented in tabular form or plotted as a function of distance (or angle) along the line (or arc) of interest.

In developing expressions for stresses that are valid for all locations within a body, three regions have been considered: (a) the interior, (b) the boundary, and (c) a narrow boundary layer adjacent to the boundary elements. Different sets of stress expressions are employed for each of these regions. For a point in the boundary layer, stresses are obtained by interpolation between proximal boundary and interior points.

6. MATERIAL PROPERTIES

A major strength of the NASGRO software is its large database of fracture mechanics and fatigue crack growth properties, mainly for aerospace alloys and for some generally used metallic materials. The fracture mechanics data which have been curve fit for this release of NASGRO are contained in a database that includes approximately 6000 sets of fracture toughness data and about 3000 sets of crack propagation data [15]. The list of references for the fracture mechanics data includes Hudson's Compendium [16] and the Damage Tolerant Handbook [17]. The remaining references were taken from miscellaneous published reports and journal articles. Curve fit constants to Eq. (1) were generated for over 300 different material-environment conditions and have been entered into the NASGRO material files. For a complete description of the curve fitting methodology and a comparison of the curve fits with the crack growth data, see reference [18].

7. GRAPHICAL USER INTERFACES

New graphical user interfaces (GUI) have been built for each of the three modules to guide the users in a Windows environment to create batch files and to facilitate easy input of fatigue crack growth data. In the case of NASFLA module, a number of pull-down menus along with timely presentation of the figures of crack geometries makes the input very intuitive. Under windows 95, the user can directly proceed to execute, once the necessary data have been entered. The results of analysis presented in text and graphic form can also be viewed by using menu choices in the post-processing menu. The NASBEM and NASMAT modules also have suitable menu choices and dialog boxes to facilitate input.

8. FUTURE ENHANCEMENTS

Several enhancements are planned for the next version, NASGRO 4.0. Among these are: expanded and improved material properties, additional crack cases that will include weight functions for corner cracks and surface cracks, elastic-plastic fracture mechanics methods, environmentally assisted crack growth models and a comprehensive three-dimensional boundary element module. The 3-D boundary element module will include contact analysis, load redistribution due to crack growth and multiple site damage analysis. Advances in computer technology will also be utilized to make the software more user-friendly and efficient.

9. SUMMARY

A description of the NASGRO software for damage tolerance analysis of aging aircraft is presented. The newly revised Version 3.0 has many features specifically implemented to suit the needs of the aging aircraft community. NASGRO was originally developed to analyze space hardware such as the Space Shuttle, the International Space Station and the associated payloads. In the current version, the software was enhanced to suit the needs of the aircraft industry. Major improvements in Version 3.0 are the incorporation of the ability to read aircraft spectra of unlimited size, generation of common aircraft fatigue load blocks, and the incorporation of crack-growth models which include load-interaction effects such as retardation due to overloads and acceleration due to underloads. Five new crack-growth models, viz., generalized Willenborg, modified generalized Willenborg, Constant closure model, Walker-Chang model and the deKoning-Newman strip-yield model have been implemented. To facilitate easier input of geometry, material properties and load spectra, Windows-style graphical user interfaces have been developed for each of the three modules.

10. REFERENCES

1. Fatigue Crack Growth Computer Program NASGRO Version 3.00, NASA Report, JSC-22267A, NASA Johnson Space Center, Houston, Texas, March 1995.

2. Forman, R. G., and Mettu, S. R., "Behavior of Surface and Corner Cracks Subjected to Tensile and Bending Loads in Ti-6Al-4V Alloy," *Fracture Mechanics: Twenty-second Symposium, Vol. 1, ASTM STP 1131*, H. A. Ernst, A. Saxena, and D. L. McDowell, eds., American Society for Testing and Materials, Philadelphia, 1992, pp. 519-546.

3. Newman, Jr., J. C., "A Crack Opening Stress Equation for Fatigue Crack Growth," *International Journal of Fracture*, Vol. 24, No. 3, March 1984, pp. R131-R135.

4. Tanaka, K., Nakai, Y., and Yamashita, M., "Fatigue Growth Threshold of Small Cracks," *International Journal of Fracture*, Vol. 17, No. 5, October 1981, pp. 519-533.

5. Chang, J.B. and Engle, R.M. "Improved Damage-Tolerance Analysis Methodology," Journal of Aircraft, Vol. 21, 1984, pp. 722-730.

6. Gallagher, J.P.,., "A Generalized Development of Yield Zone Models," AFFDL-TM-74-28-FBR, Wright Patterson Air Force Laboratory, January 1974.

7. Willenborg, J., Engle, R.M. and Wood, H.A., "A Crack Growth Retardation Model Using an Effective Stress Concept," AFFDL-TM-71-1-FBR, Wright Patterson Air Force Laboratory, January 1971.

8. Gallagher, J.P., Hughes, T.F.., "Influence of Yield Strength on Overload Affected Fatigue Crack Growth Behavior in 4340 Steel," AFFDL-TR-74-27-FBR, Wright Patterson Air Force Laboratory, February 1974.

9. Newman, J.C. Jr., Private Communication, 1995.

10. Brussat, T. R., Private communication, May 1997.

11. Ten Hoeve, H.J. and de Koning, A.U., "Implementation of the Improved Strip Yield Model into NASGRO Software - Architecture and Detailed Design Document," National Aerospace Laboratory (NLR) Report: NLR CR 95312L, 1995.

12. Brodeur, S. J. and Basci, M. I., "Fracture Mechanics Loading Spectra for STS Payloads," AIAA-83-2655-CP, 1983.

13. Chungchu Chang, "A Boundary Element Method for Two Dimensional Linear Elastic Fracture Analysis", Ph.D. Dissertation, The University of Texas at Austin, December, 1993.

14. Ghosh, N., Rajiyah, H., Ghosh, S., and Mukherjee, S., 1986, "A New Boundary Element Method Formulation for Linear Elasticity", *Journal of Applied Mechanics*, Vol. 53, pp. 69-76.

15. Lawrence, V. B. and Forman, R. G., "Structure and Applications of the NASA Fracture Mechanics Database," *Computerization and Networking of Materials Databases: Third Volume, ASTM STP 1140*, American Society for Testing and Materials, Philadelphia, 1992.

16. Hudson, M. C. and Seward, S. K., "Compendium of Sources of Fracture Toughness and Fatigue Crack Growth Data for Metallic Alloys," *International Journal of Fracture*, Vol. 20, 1982, pp. R59-R117.

17. Gallagher, J., *Damage Tolerant Design Handbook*, University of Dayton Research Institute, prepared for Air Force Wright Aeronautical Laboratories, Wright-Patterson Air Force Base, Ohio, December 1983.

18. Henkener, J. A., Lawrence, V. B., Williams, L. C., and Forman, R. G., "Derivation of Crack Growth Properties of Materials for NASA/FLAGRO 2.0," JSC 26254, NASA Lyndon B. Johnson Space Center, Houston, Texas, June 1994.

AUTOMATIC ANALYSIS OF DATA DERIVED FROM SCANNING ACOUSTIC/LASER DOPPLER VELOCIMETER.

Jackie Mew and Robert G. Topp.
University of Portsmouth,
Portsmouth, Hampshire, PO1 2UP, UK.
Telephone: +44 (1705) 844077
Telefax: +44 (1705) 844006
E-Mail: mewjm@sis.port.ac.uk

John M. Webster and Thangeval Thevar.
Holographics Inc.
Long Island City, New York, 11101, USA.

ABSTRACT

Large quantities of data are collected from a non-contacting acoustic/Doppler system that has been developed to non destructively inspect composite materials. It is time-consuming, exhausting and error-prone for a person to sit at a computer screen and physically browse up to 2048 detailed images that are produced from the data. Amongst those images only a small number contain useful information; the majority can be discarded. The useful images are easy to miss if the operator loses concentration, but vital as they may contain information about a fault. Computers process large quantities of information accurately without losing concentration or becoming fatigued. Expert evaluation of data derived from non-destructively inspecting composite samples such as those found on aircraft, ceramics, or metal structures such as helicopter blades, has led to the identification of rules, which in turn has led to the development of a prototype algorithm that automatically detects pertinent data and presents the shape of a fault as a two dimensional image. This paper reports on the results of tests on this prototype software, presenting the rules and applying them specifically to the identification of faults in composite structures. It concludes with a discussion of the next stage, which is the development of software to address issues raised from these experiments.

1. INTRODUCTION.

This NDT technique employs a non-contacting customized scanning laser Doppler velocimeter working in conjunction with an impulse acoustic transducer. No piece of equipment comes into contact with the object undergoing non-destructive testing, nor is the surface of the object subjected to any form of treatment, such as heat or paint, before, during or after the interrogation. Data collected during the interrogation is subsequently analyzed by computer, and the results presented in a concise format, whilst retaining the rich data set collected, in readiness for an audit trail if so required. In order to check the analysis software, it has been tested in the laboratory against samples with known faults, and has now been blind tested in a hangar-situation on a ray-dome. This software reduces the time taken to analyze the results of Non-Destructive Testing (NDT) by scanning laser Doppler/acoustic transducer from two days to 5 minutes, and simplifies the procedure itself.

2. SCANNING LASER DOPPLER VIBROMETER.

Remote interrogation of the relaxation frequencies which are induced by an acoustic impulse upon the surface of the object undergoing non-destructive testing are accomplished with a customized scanning laser Doppler velocimeter. This device normally employs a 3 milli-watt He Ne laser to scan the surface of the object undergoing NDT with an array of up to 512 x 512 data acquisition points which may be deployed and shaped at the operators choice. Time domain data is received from each data point into the processing computer and immediately converted to a Fast Fourier Transform (FFT).

Data after processing to an FFT is stored in the computer as individual frequency bands over the pre-selected frequency range. Optionally a number of FFT frequency lines can be selected: for example 512, 1024 or 2048. The norm is 1024 lines. There is a roll off in sensitivity above 80%, thus the useable bands are 400, 800 and 1600 respectively. Information is stored at each frequency band together with fault and noise data. The information pertaining to the object's surface response is recorded for each frequency condition at a specific band in the recorded frequency spectrum.

3. THE SOFTWARE.

3.1 BACKGROUND TO THE SOFTWARE.

Approximately 800 of these images contain information regarding the structure of the sample undergoing NDT. The rest of the images may be discarded as they do not contain any useful information. For example, the lower frequencies contain bending modes, whereby the whole sample resonates at that particular frequency. Working with the remaining images, an expert will, over two days, painstakingly, visually inspect every image. The expert is looking for a particular pattern on the image, sustained over several (two or more) adjacent frequencies. To visually inspect these images is not only time-consuming but it is probably not the most effective use of the expert's time, given that the inspection can be automatically performed by a computer. Manual, visual inspection is also error-prone as it is easy to miss a fault through fatigue or lack of concentration.

In spotting a fault, the expert has to visually scan each image, looking for a fault developing, which is usually characterized by green or yellow on the screen. Two or more faults may be at different stages of development at any one frequency. When a fault is spotted, it must be tracked through the adjacent frequencies to confirm that it is really a fault, and not just noise. Noise characteristically appears just on one frequency. It requires careful, methodical inspection, by the expert who is working in three dimensions.

3.2 THE PRINCIPLES UNDERLYING THE SOFTWARE.

Numbers underlie these images, and it is these numbers that are used by the software to create the images. Each data point acquisition can be referred to in the x,y plane and this can be used to map the fault back to the sample undergoing NDT. The data is subjected to FFT analysis. This provides an elegant sort in the z (or frequency) plane. We are left with a three dimensional data structure (in much the same way as is the expert looking at the images.) This cube can be subjected to array handling, which is a standard data processing technique. All that remains is for the software to search for a particular pattern in the data.

By experimentation it was found that faults typically resonate at a velocity above the average velocity of the rest of the sample, for that frequency. A single point resonating on its own, without a cluster of other surrounding it may be disregarded as 'noise'. This single point may be assigned a nominal

value, calculated from data points immediately surrounding it. For a high velocity to be indicative of a fault, the adjacent amplitudes are inspected to see if there is a substantial cluster of high velocities centered around this point, in both the x,y plane and the frequency plane. Even if there is a cluster in the x,y plane, if it does not go through two or more frequency planes, then it must be discarded as noise. True faults develop and are sustained over two or more frequencies. If these conditions are met then a fault has been found; in experimentation this has always shown a true fault. Figure 1 outlines these rules as a flowchart.

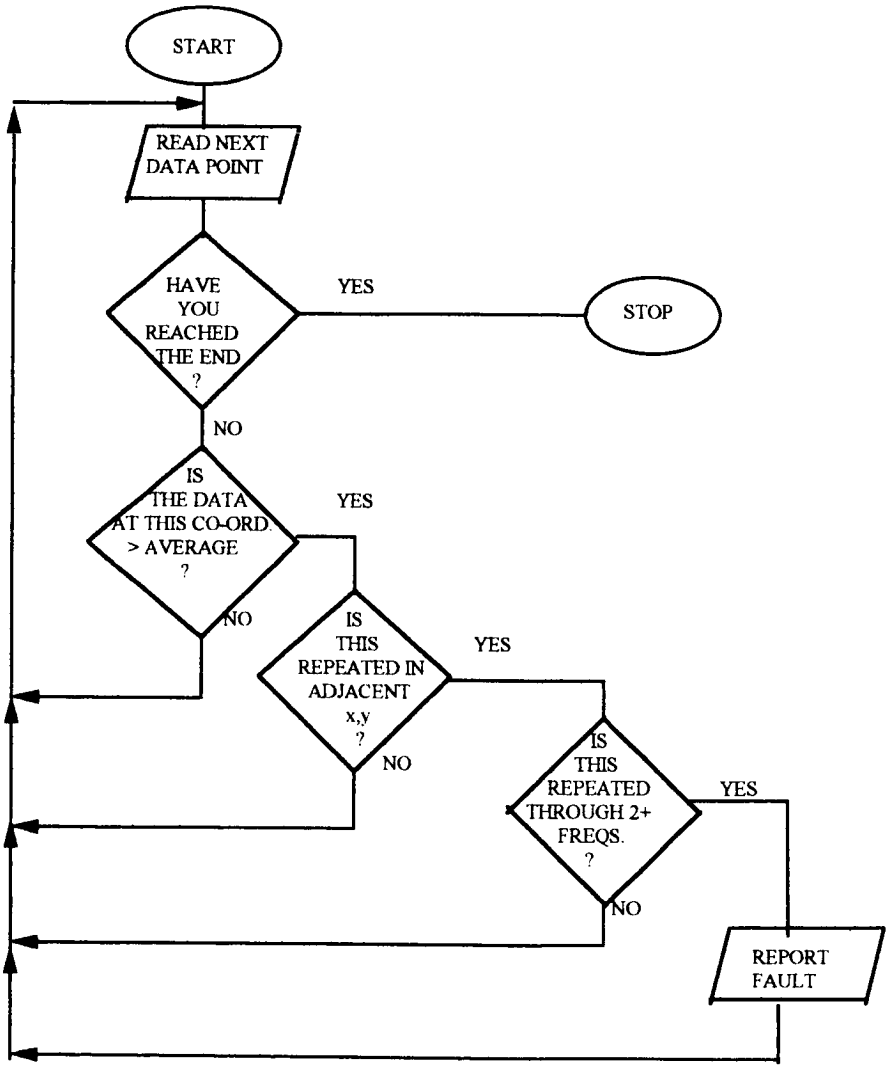

Figure 1. Flowchart of rules implemented by the software. The flowchart outlines the conditions to be met by the algorithm The initial algorithm is detailed in Mew and Webster (1998) and details of the actual software that produced these results will be presented at the 1998 Fall ASNT conference.

4. THE RESULTS OF EXPERIMENTS

4.1 DESCRIPTION OF EXPERIMENTS

It will have been noted that in the above narrative many of the statements are vague, e.g. "resonate at a velocity above the average velocity of the rest of the sample, for that frequency". For the purposes of the experimental software it is the task of the operator to set these parameters, as we are still learning about the relationship between the materials, faults and the parameters to be set. Figure 2 gives the parameters used to produce the results in figures 3 to 6. The software asks the operator to define:

a) the % above average of all frequencies to define a fault; typically between 125% and 200%.

b) the number of points in the x,y plane that defines a cluster; typically between 3 and 10.

c) the number of frequency planes needed to define a fault; typically 3. This parameter can never be less than 2 as then it is defined as 'noise'.

In addition the frequency range to be searched can be set. Normally it is set at between 2000 kHz. and 30,000 kHz. However care must be taken not to exclude, in error, faults manifesting at higher frequencies. For these experiments the maximum x,y points and maximum frequency planes were set arbitrarily high at 500 and 499 respectively. In time these settings may be useful to limit the size of the damage to be searched for.

PARAMETER	Figures 3&4	Figure 5	Figure 6
% above average	175	175	175
Min. x,y points	9	4	3
Max x,y points	500	500	500
Min. freq planes	8	8	8
Max. frequency planes	449	449	449
Min. FFT frequencies	3	3	3
Max. FFT frequencies	2,000	20,000	2,000
Min. number of points	30,000	30,000	30,000
Number of frequency bands	16	11	16

Figure 2. Table of parameters used to produce the images in figures 3 to 6.

4.2 DISCUSSION OF RESULTS.

Ideally the software selects between 7 and 15 frequency bands for production of images that can then be checked by an expert. This is an improvement on wading through 800 images, and the expert can be confident that these faults are sustained over several frequencies, or they would not have been selected. On each occasion faults found on the ray-dome were confirmed by a 'tap-test'. They have been included in the report back to ARINC.

Figure 3 is of a 'flat' part of the ray-dome. Because printing has been limited to black and white, we are looking for light, irregularly shaped areas, on a fairly dark background. In color this would be more striking as areas of yellow and green. The large white lines are markers, so that the results of the scan can be physically verified. Figure 3b shows a fault in the lower left-hand quadrant, which shows as a dark outline only in Figure 3a. This illustrates the way in which a fault is shown developing over different frequencies. Figure 3a is in the range 4750 kHz to 5187 kHz, whilst the fault is more striking at between 5125 to 5750 kHz. The software, presently, overlaps some frequencies.

Figure 4 shows the same test area, but a different fault, which is appearing at a very different frequency range: 14,000 kHz to 15,437 kHz.

Figure 5 is from an area more towards the bull-nose of the ray-dome. Here the fault in Figure 5a is shown as a light patch in the center of the test area. Immediately to the left is a black area. This appears again in Figure 5b. It is an interesting area. When the equipment was scanning this area, it could not pick up a signal. When 'tapped' it 'rang' as though it was very damaged. This will form part of the study of the relationship between frequencies and materials. At present, an area like this will always warrant further investigation.

This damage is confirmed in Figure 6. This is the bull-nose of the ray-dome. Note the fault just to right of center. Compare this to the black area on Figure 5. The damage is consistent across the boundary of the samples. Figure 5 is in the band 14062.5 to 14625 kHz and Figure 6 is between 14625 and 15625 kHz.

Occasionally on samples other than the ray-dome the software could not produce less than 100 images without losing information on faults. In order to improve this hit-rate by selecting fewer images, the relationship between parameters and material requires careful scrutiny and experimentation.

Plans for the future include:

a) automation of the selection of parameters using an expert system, based on an understanding of the relationship between materials and input parameters.

b) collation of images into one, showing all the faults in a particular area.

c) collation of images into a patchwork to show overall faults.

Both b) and c) will be part of a multi-media system, which will not only provide feedback on the inspection, but will also provide a record for when the part is next re-inspected.

ACKNOWLEDGMENTS

This work was sponsored by DARPA Phase II #DAAH01-95-C-R182 Contract "Development of an Optical/Acoustic Method for the Remote Non-Destructive Inspection of Large Area Composite Materials for Structural Defects". Approved for Public Release Distribution Unlimited.

ARINC, Oklahoma City, provided the hangar facility and ray-dome.

REFERENCES

Mew J., Webster J., The computerized analysis of data derived from scanning laser Doppler, the 9th Asia-Pacific conference on Non-Destructive Testing in conjunction with ASNT's 1998 Spring Conference and Seventh Annual Research Symposium "Transfer of emerging NDT technologies", March 23-27th, Anaheim, California, USA. pp. 350-353, ISBN 1-57117-026-x.

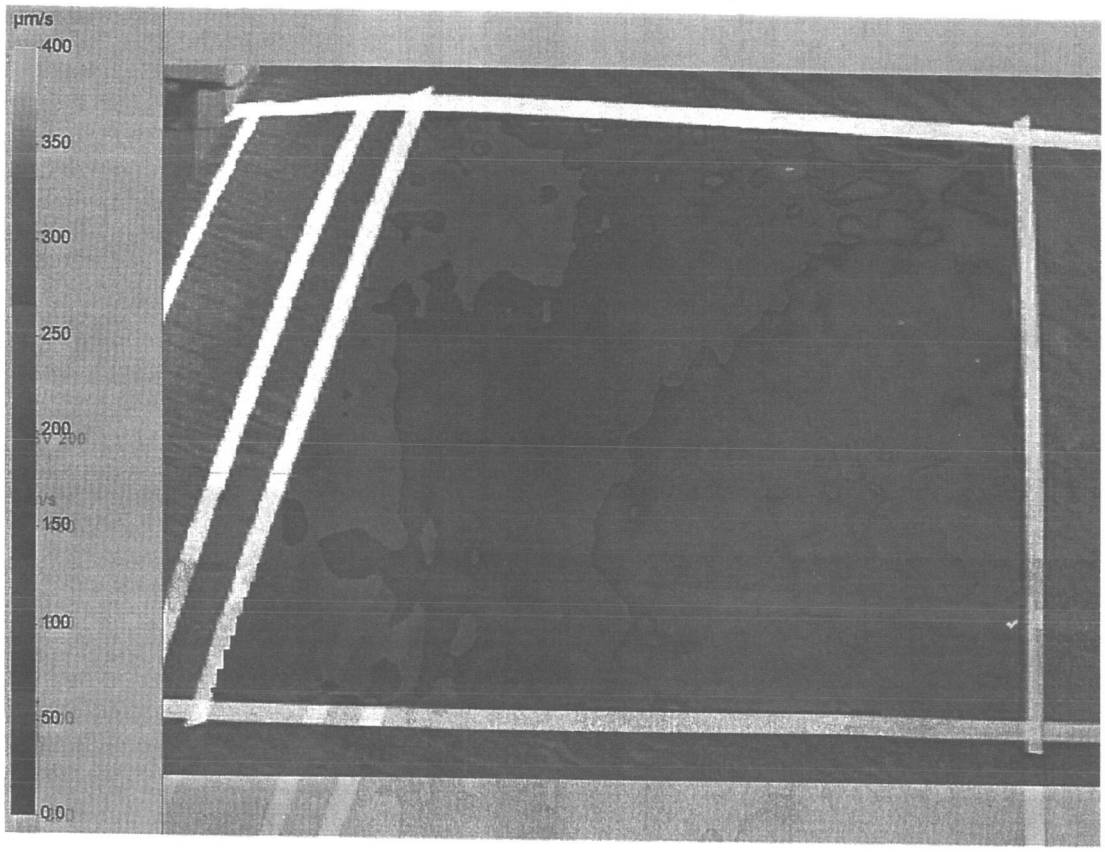

3a.

Figure 3. A 'flat' area of the ray-dome. This fault is showing at between 4750 and 5750 kHz.

3b.

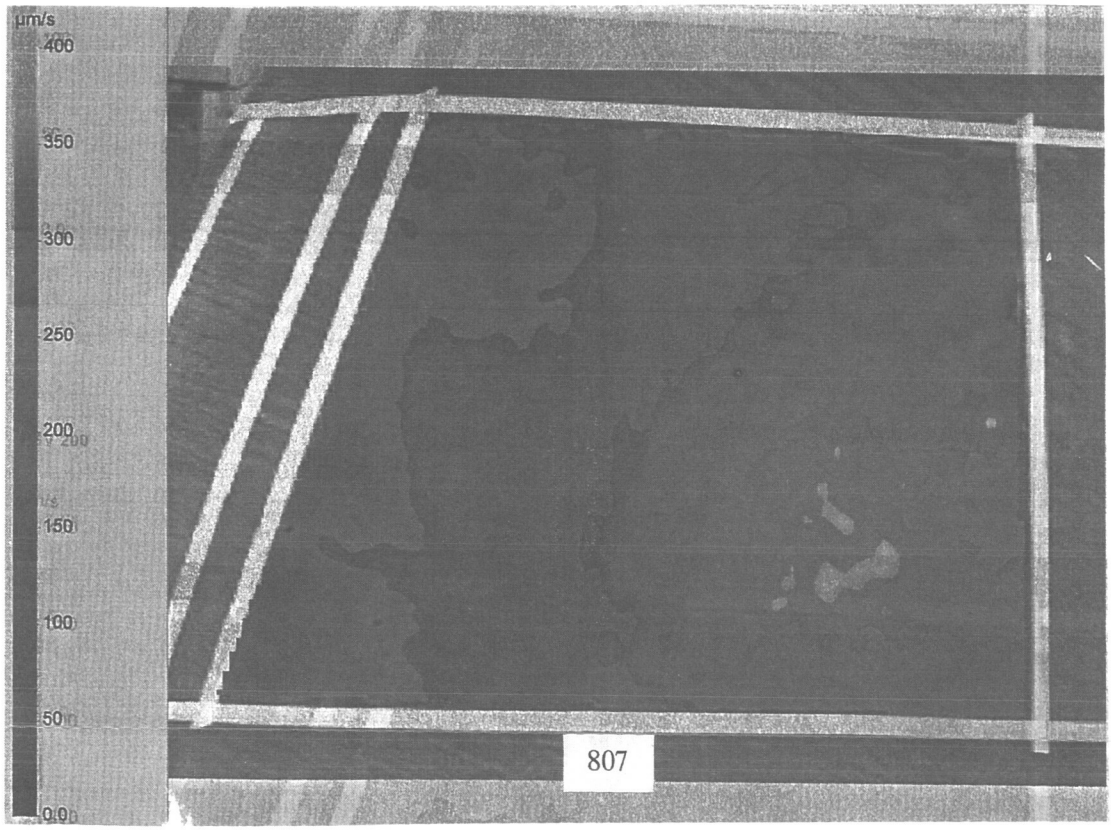

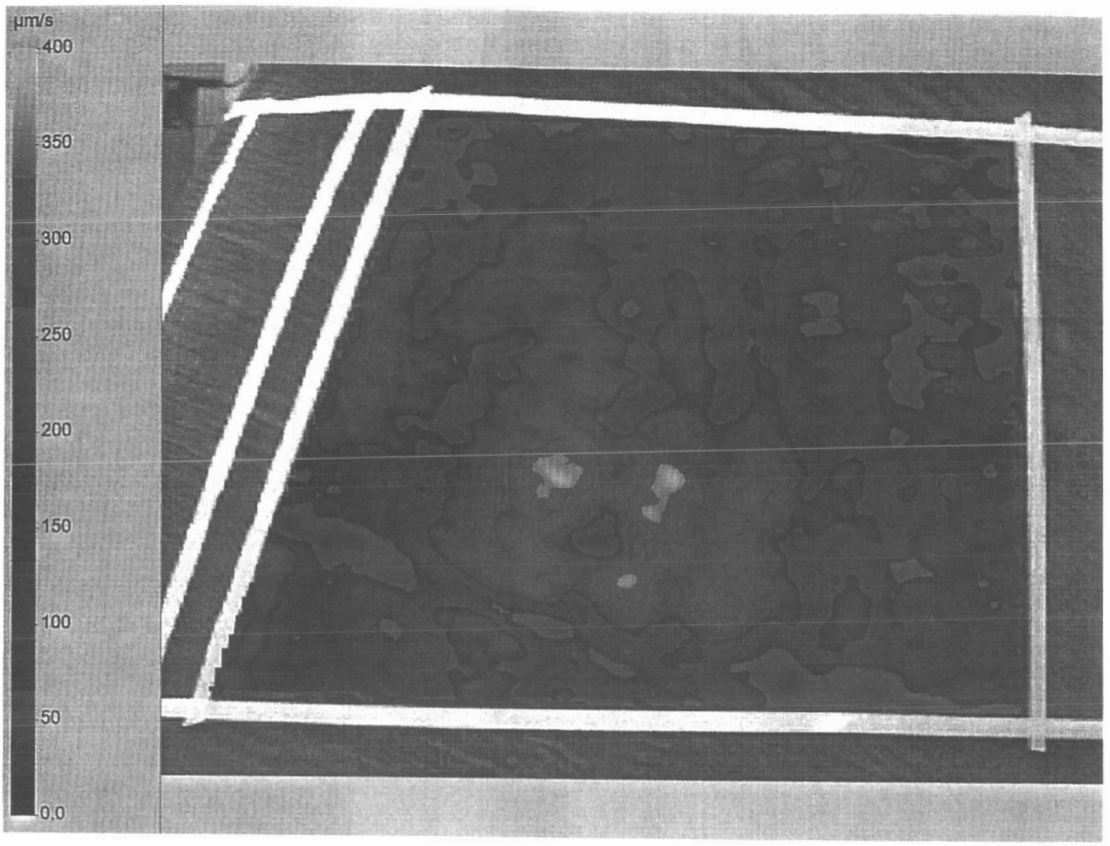

4a.

Figure 4. A 'flat' area of the ray-dome. This fault is showing at between 14,000 and 15,437 kHz.

4b.

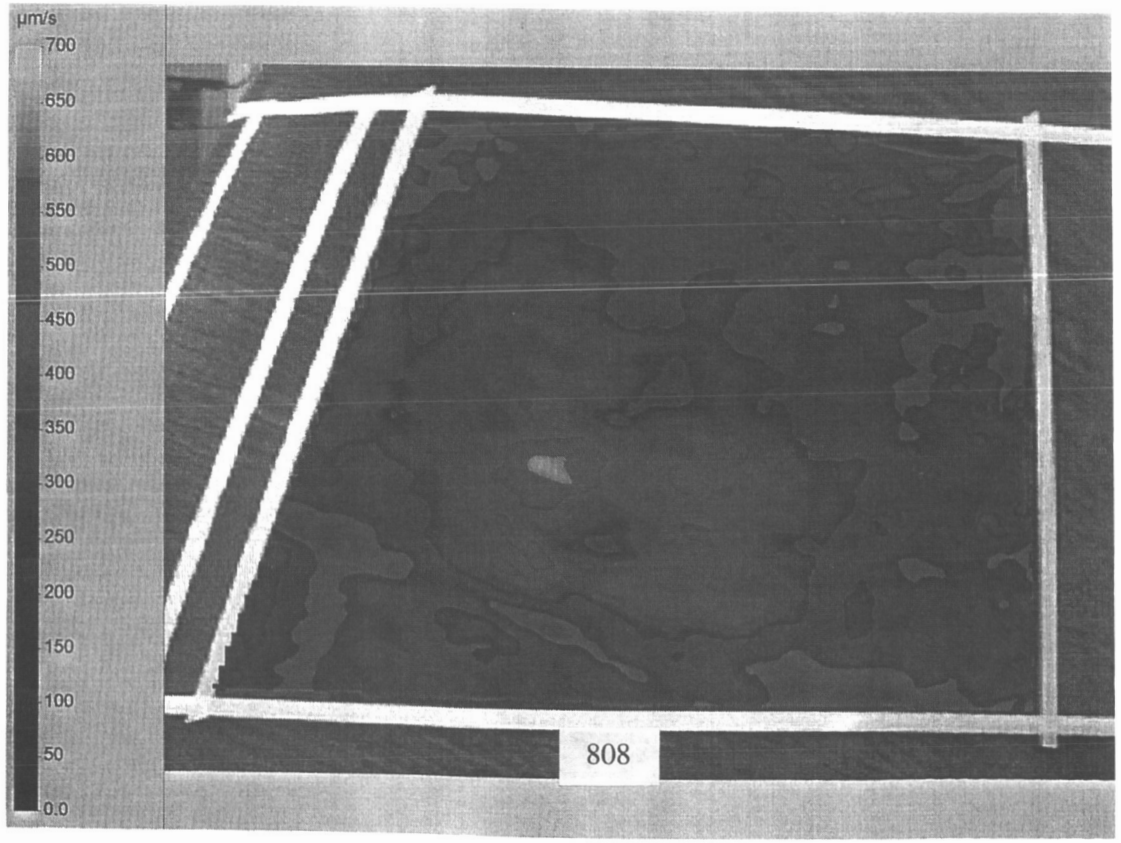

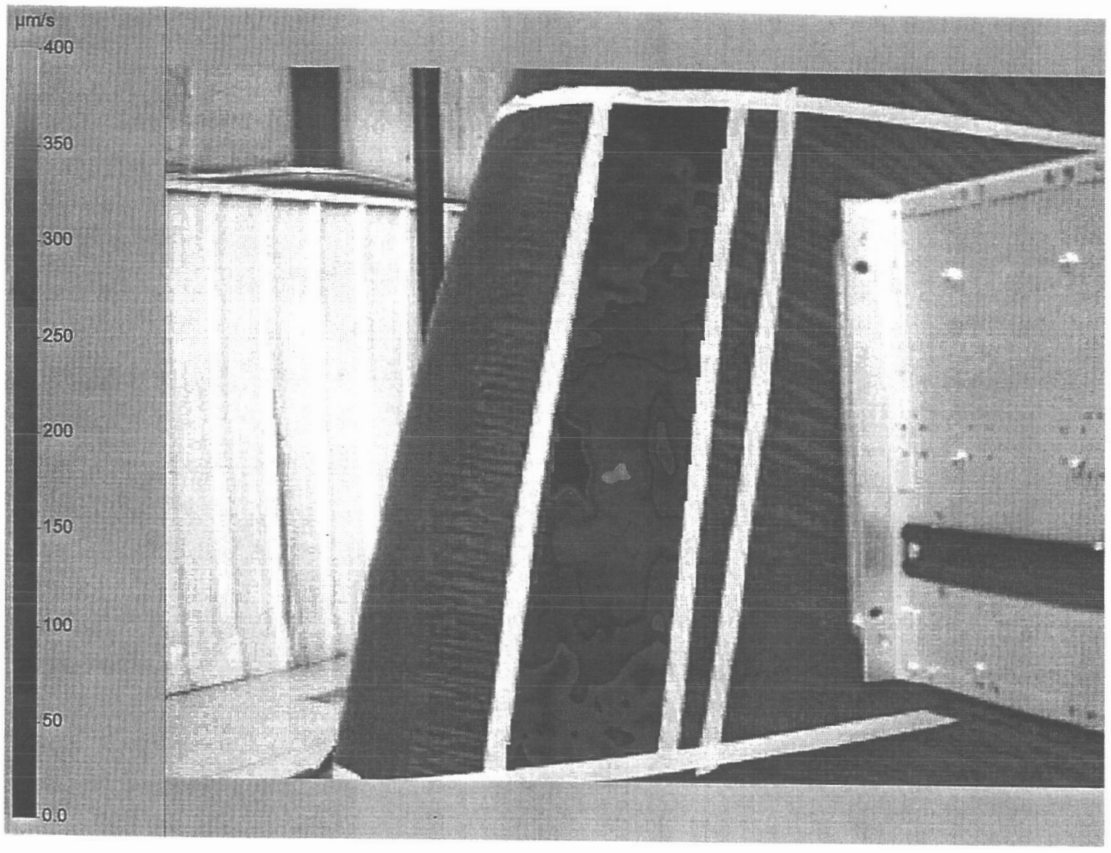

5a.
Figure 5. Towards the bull-nose of the ray-dome.
5b.

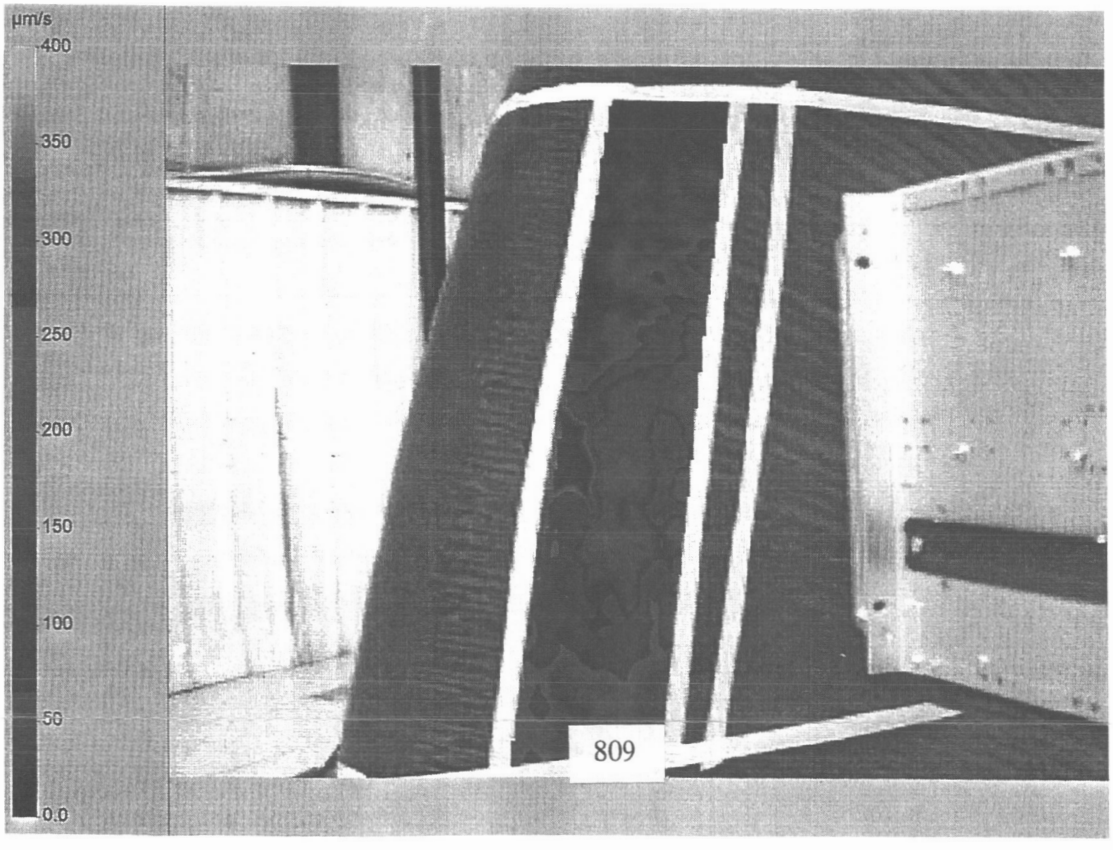

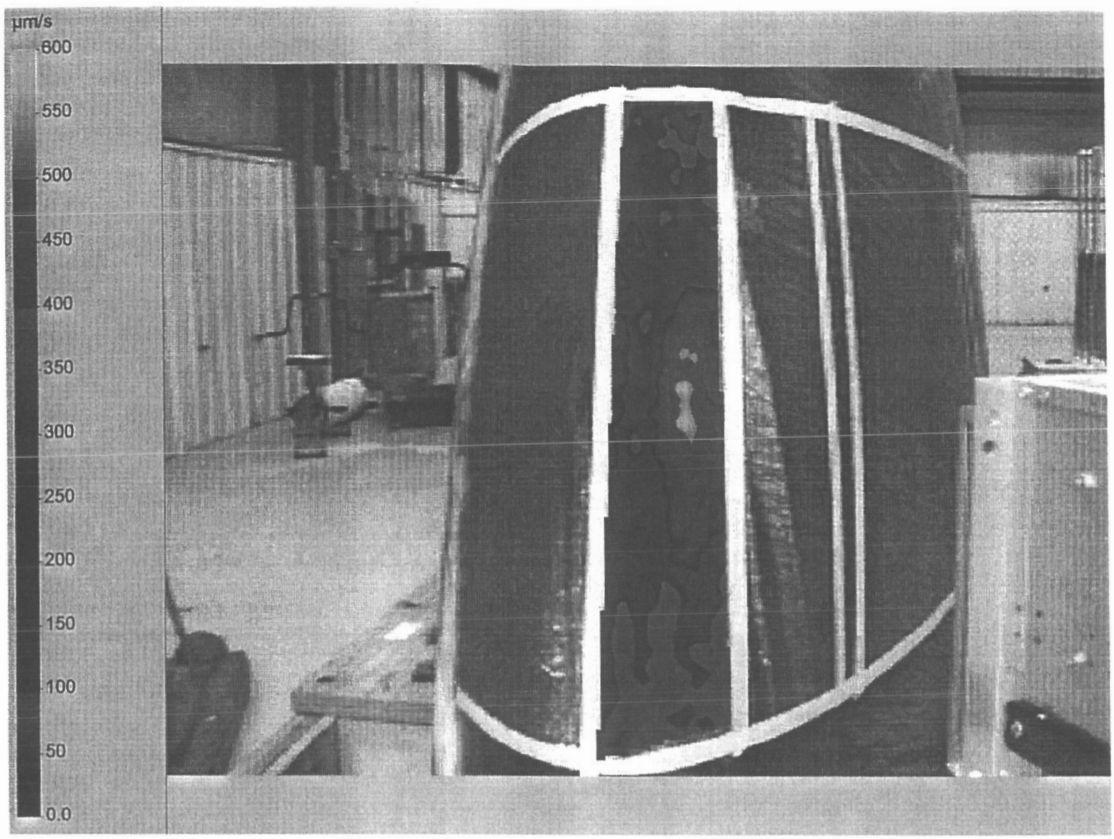

6a.
Figure 6. The bull-nose of the ray-dome.
6b.

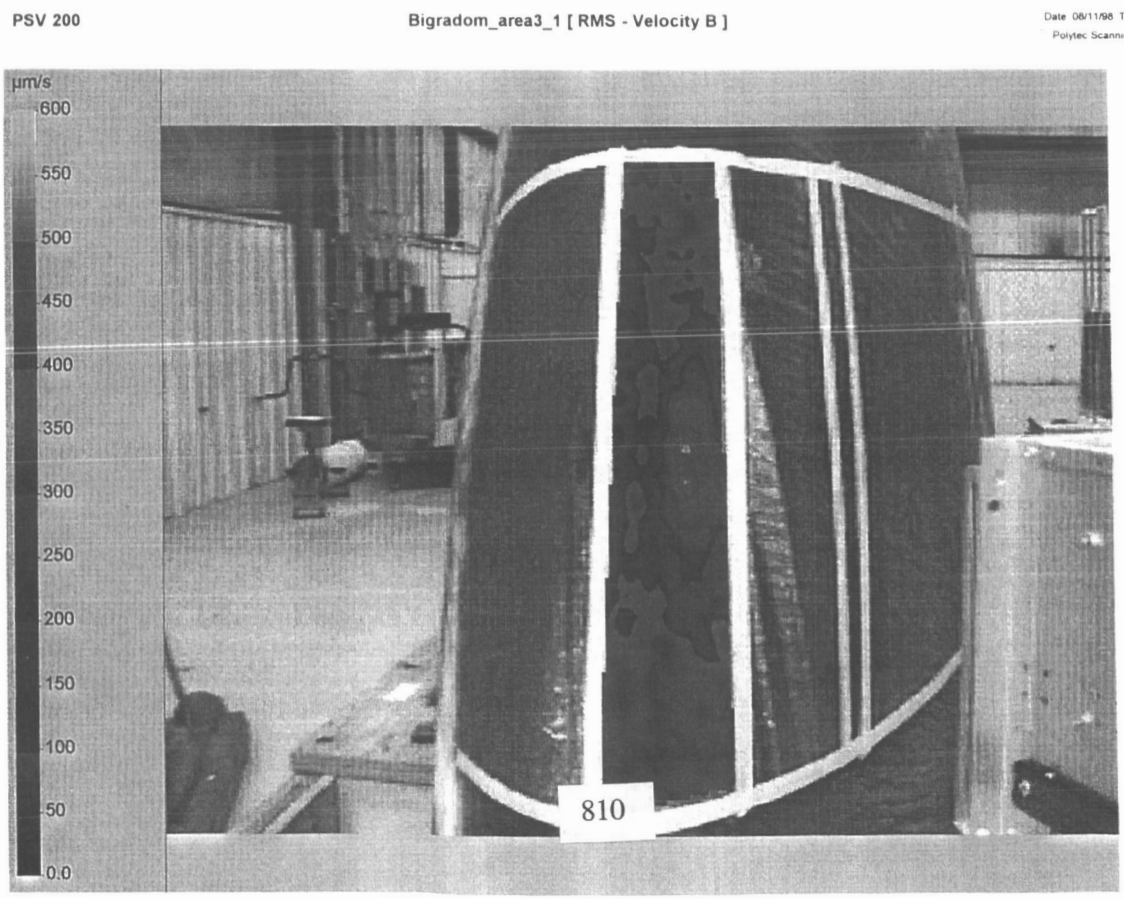

Experimental Flight Test Vibration Measurements and Nondestructive Inspection on a USCG HC-130H Aircraft

David G. Moore and Craig R. Jones
FAA Airworthiness Assurance NDI Validation Center (AANC)
Sandia National Laboratories, Albuquerque, NM 87185-0615

and

CDR Joseph E. Mihelic and ADC James D. Barnes
U.S. Coast Guard (USCG) Aircraft Repair and Supply Center (ARSC)
Elizabeth City, NC 27909-5001

ABSTRACT

This paper presents results of experimental flight test vibration measurements and structural inspections performed by the Federal Aviation Administration's Airworthiness Assurance NDI Validation Center (AANC) at Sandia National Laboratories and the U.S. Coast Guard Aircraft Repair and Supply Center (ARSC). Structural and aerodynamic changes induced by mounting a Forward Looking Infrared (FLIR) system on a USCG HC-130H aircraft are described. The FLIR adversely affected the air flow characteristics and structural vibration on the external skin of the aircraft's right main wheel well fairing. Upon initial discovery of skin cracking and visual observation of skin vibration in flight by the FLIR, a baseline flight without the FLIR was conducted and compared to other measurements with the FLIR installed. Nondestructive inspection procedures were developed to detect cracks in the skin and supporting structural elements and document the initial structural condition of the aircraft. Inspection results and flight test vibration data revealed that the FLIR created higher than expected flight loading and was the possible source of the skin cracking. The Coast Guard performed significant structural repair and enhancement on this aircraft, and additional in-flight vibration measurements were collected on the strengthened area both with and without the FLIR installed. After three months of further operational FLIR usage, the new aircraft skin with the enhanced structural modification was reinspected and found to be free of flaws. Additional U.S. Coast Guard HC-130H aircraft are now being similarly modified to accommodate this FLIR system. Measurements of in-flight vibration levels with and without the FLIR installed, and both before and after the structural enhancement and repair were conducted on the skin and supporting structure in the aircraft's right main wheel fairing. Inspection results and techniques developed to verify the aircraft's structural integrity are also discussed.

This work was supported by a reimbursable agreement between Sandia National Laboratories and the USCG Aircraft Repair and Supply Center. Sandia is a multiprogram laboratory operated by Sandia Corporation, a Lockheed Martin Company, for the United States Department of Energy under Contract DE-ACO4-94-AL85000.

INTRODUCTION

The USCG deploys the HC-130H 'Hercules' fixed-wing aircraft for long range surveillance and cargo transport to satisfy the needs of the maritime community. The USCG monitors radio coverage on distress frequency bands for recreational boats and commercial craft. When emergencies occur, the HC-130H is deployed to aid and assist in the search and rescue mission. Other aircraft are specifically outfitted to perform other unique functions such as drug interdiction and environmental compliance monitoring. The Aircraft Repair and Supply Center (ARSC) is the engineering center for all of the USCG fixed wing aircraft. One role of ARSC is to examine existing or impending problems for the HC-130H fleet, then seek solutions based upon scientific advancements in science and technology. ARSC has created an aggressive program of research and development in the area of nondestructive inspection to support appropriate advancements to the HC-130H maintenance program. To improve its mission effectiveness and efficiency, ARSC concentrates its engineering efforts where there is potential for high payoff to increase quality and productivity. Due to shrinking federal budgets, ARSC desired to maximize its engineering support activities. To this end, ARSC completed a Work-for-Others (WFO) agreement with Sandia National Laboratories – AANC. The mutually agreed upon Scope of Work specified that AANC would conduct inspections and engineering studies in conjunction with ASRC support activities that could help ARSC better use their assets to extend the service life of their HC-130H fleet.

PROBLEM HISTORY

A permanent universal FLIR system installation was proposed to be added to several U.S. Coast Guard HC-130H aircraft. A permanent universal FLIR mount was designed by Lockheed Martin and attaching hardware was installed on three HC-130H aircraft (See Figure 1). After 2.7 hours of flight operations with a FLIR system installed on aircraft S/N 1719, cracks were discovered in the skin and supporting stiffeners in the right main wheel well fairing near the new FLIR installation (See Figure 2). It was believed was that these cracks had developed in the main wheel well skin structure as a result of this new permanent FLIR installation. Air flow conditions, skin surface vibration and possible flutter were observed by the FLIR during initial flights with the FLIR prototype and after the Lockheed Martin permanent mount was installed. The overall structural integrity condition of this area of aircraft S/N 1719 was raised by ARSC, and an inspection to verify the structural integrity of this area of this aircraft was deemed prudent. In addition, an on-aircraft test was desired to measure and document the vibration environments in this area, and to determine if the new FLIR installation was the source of the recently discovered cracks in the wheel well skin and substructure of this HC-130H aircraft.

NONDESTRUCTIVE INSPECTION DEVELOPMENT

The HC-130H aircraft configuration originally had an outer skin thickness of 1.016 mm (0.040") and attached to 1.016 mm thick channel (forward to aft) or frame (inboard to outboard). The fasteners were button head configuration with an outside diameter of

8.128 mm (0.320"). Figures 3 and 4 display the inspection configuration. The inspection area on the HC-130H aircraft contains several square meters of aircraft skin and over one thousand fastener sites. Since the inspection technique must penetrate through the outer skin and fit over the raised fastener heads, it requires reducing the operating frequency and increasing coil probe inside diameter. Both conditions result in a larger detectable crack.

The probe selected to inspect the HC-130H structure is a low frequency, flat surface encircling 'ring' reflectance-type probe. It has an inside diameter of 7.62 mm (0.30"), an outside diameter of 19.56 mm (0.77") and operates at 2 kHz. The equipment selected for this inspection was an impedance plane instrument with test set-up storage capability. A reference standard was designed and manufactured using 2024 aluminum (See Figure 5). The ring probe and instrument is standardized over a raised fastener site containing no flaws. Probe lift-off is rotated to yield a nearly horizontal response on the screen. The probe is placed over each fastener site on the reference standard and the response is obtained. Figure 6 displays the signal response from the reference standard at positions A, B, C, and D. After calibration, the 'ring' probe is placed over each raised fastener and the inspector monitors the screen for crack indications.

INSPECTION RESULTS OF PROTOTYPE AND PERMANENT FLIR

Detailed eddy current measurements were performed on the right wheel well skin structure of HC-130H (S/N 1719) at the CGAS-Clearwater, Florida by Sandia on 26-28 Aug 97 (See Figure 2). No significant problems were encountered in accomplishing these inspections. Only relatively few small cracks were found and documented during the initial inspections (See Table 1).

Approximately 15 man-hours were required to perform these inspections using an impedance plane eddy current instrument that the Coast Guard has available. The aircraft was inspected with the FLIR hardware removed, and only minor additional disassembly was performed to allow better access to the upper portion of the FLIR mounting hardware.

FLIGHT TEST VIBRATION MEASUREMENTS

The structural area of interest was instrumented with 10 Wilcoxon Research Model 722 accelerometers. Four accelerometers were mounted directly on longerons and stiffeners, and several others were mounted to the internal surface of the right main landing gear pod skin using strain gauge cement. A tabulation of these accelerometers and their approximate locations is contained in Table 2. A photograph of some typical installations is shown in Figure 7. A flight of 2.0 hours duration was flown on 27 Aug 97 and vibration data recorded for a range of flight conditions. See Table 3 for a review of the flight profile and test conditions. A U.S. Coast Guard Rotor Analysis Diagnostic System - Advanced Technology (RADS-AT) data collection and analysis system was used to collect all accelerometer data during the flight testing.

Upon the end of the first flight, the accelerometer data were reviewed and determined to be valid and of good quality. All accelerometer installations except two hidden in difficult to access areas (on inner skin at FS 516 and 576 - BL 60) were inspected and found to be completely intact. These two accelerometers were still operational but did not remain rigidly bonded to the skin in this area after the engine ground runup of the test flight.

The FLIR was then installed on the aircraft. Two additional accelerometers were added at this time and a third was moved to the FLIR mount support plate to measure three-axis acceleration response of this structure (See Figure 8). A flight of 2.7 hours duration was flown on 28 Aug 97 and vibration data recorded for a range of flight conditions. The flight profile and test conditions for this flight were kept as close as possible to those on the previous flight. Approximately a third of the way through the second flight, data channels began to drop out or fail for no immediately explained reason. It was assumed that the flight vibration environments were becoming increasingly harsh at the higher indicated airspeeds and dynamic pressures, and the increased vibration levels being encountered were breaking the high strength cement bond causing the accelerometers to become detached.

Upon the end of the second flight, the data were reviewed and determined to be valid and of good quality. All accelerometer installations were inspected. Only four of the twelve accelerometers were found to have remained attached to the structure which it was intended to monitor. Three of these remaining four were those on the FLIR mounting plate and the other one was attached to the longeron at approximate FS 474 - BL 63. Upon the completion of this flight profile, it was concluded that significant structural modification was necessary to permit long term operation of this aircraft with the FLIR installed.

The aircraft was ferried to ARSC in Elizabeth City, NC where it underwent significant structural repair and modification. This repair and modification effort included replacing the entire lower skin panel of the right main wheel well fairing with a skin of a heavier gauge, 1.60 mm (0.063"), and adding additional stiffeners and longerons to further stiffen and strengthen this region of structure. These repairs and modifications were completed on 31 Oct 97. The aircraft was then instrumented with fourteen accelerometers in this area to as closely as possible repeat the locations that were instrumented in the earlier flight tests of 27-28 Aug 97. In a few cases, the exact locations were not repeated since new structure had been added at or very near the original locations. Two test flights were conducted on 1 Nov 97 to measure vibration environments in this structure to compare with the earlier environments measured on the original structure both with and without the FLIR installed. These test flight profiles were designed to duplicate the test conditions at which data were collected during the earlier series of flight tests. The following is an overview of the vibration results obtained after the structural repair and modification. These data were compared directly with those taken during the earlier flight tests to display the effects that the heavier gauge skin and additional internal stiffening members had on reducing the vibration environments in this area of the HC-130H aircraft.

FLIGHT TEST DATA REVIEW AND ANALYSIS

All data taken were plotted out in spectrum form, acceleration in g's vs. frequency from 0 to 1000 Hz in 2.5 Hz intervals. Selected conditions shown here are plotted as Maximum G's observed versus Flight Test Event Number for test cases where 'exact' flight test conditions were available for *both* baseline and FLIR attached configurations. A typical data graph (See Figure 9) allows for easy comparison between vibration environments at the same location for the baseline (without FLIR) and FLIR attached configurations and can be directly compared to the same locations (or nearly so) and conditions measured after the structural modifications and repairs.

Figures 10 and 11 (Maximum G's versus. Flight Event Number) show the loading experienced by right wheel well fairing structure throughout all phases of the test flight at one typical location. Generally, loading increased with increased airspeed and torque settings. Significant increased loading was observed with the FLIR installed. The stiffener shown here experienced an increase in loading by up to a factor of ten with the FLIR installed.

After the structural repairs, the vibration environments encountered by the skin structure and the MLG inner door with the FLIR attached are still high in some areas. FLIR video was also available during the second flight and confirmed that there was a significant reduction in visible skin panel vibration from that observed on a previous FLIR systems testing flight in August. Comparison plots directly showed that the vibration environments with the FLIR attached were almost always higher (sometimes significantly) than those measured during the first (baseline) flight and that the structural repairs and modifications were very effective in reducing vibration environments in this part of the HC-130H structure.

CONCLUSIONS

Accelerometer data from those attached to the FLIR mounting plate provide an overview of the vibration environments encountered at this location through a flight test profile of ground idle, ground engine runup, low speed level flight, climb and higher speed level flight conditions. The most severe vibration environments at this location appear to be during ground engine runup and at the higher indicated airspeed conditions, especially those with high torque settings. It should be noted that no significant loading of the FLIR mounting plate was encountered throughout any phase of flight during all of these flight tests.

This simple test demonstrated that the change in loading observed on the right wheel well fairing with the FLIR mount and FLIR installed has been substantially reduced by repairs and modifications done by ARSC. Further aerodynamic analysis is being performed to identify the cause of these high loading conditions so that appropriate additional modifications can be made to prevent further damage from occurring in the future to aircraft with the FLIR installed.

Subsequent NDI of this portion of new structure was performed after three months of flight operations with the FLIR installed and no cracks or other flaws were detected.

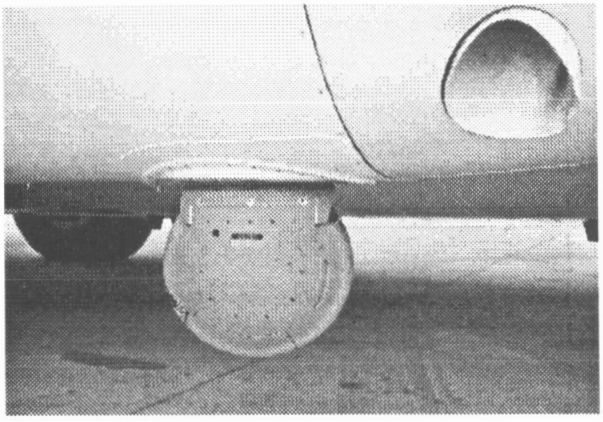

Figure 1: Permanent universal mount is Located internally and the FLIR Is mounted externally on HC-130H S/N 1719.

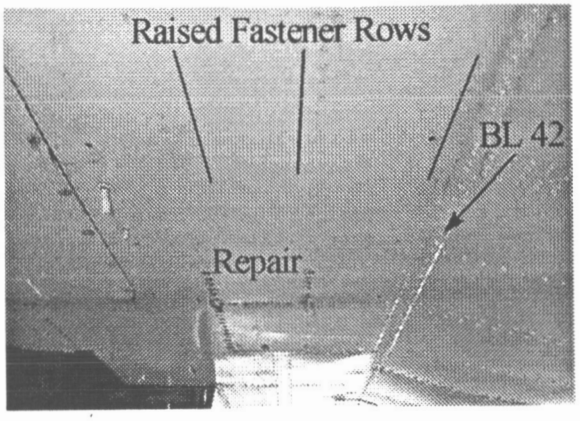

Figure 2: Inspection area (looking aft) of FLIR. Repair location is where Initial damage was detected.

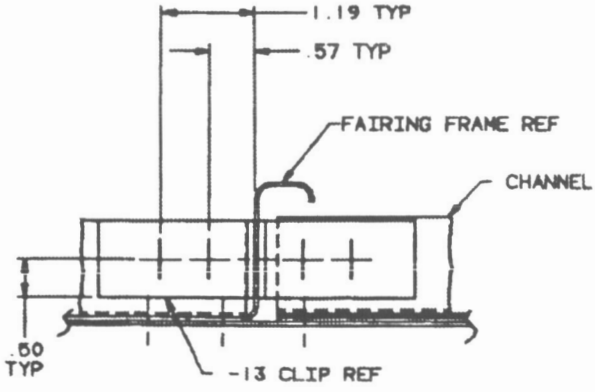

Figure 3: Sectional view of the wheel well Fairing. Button head fasteners are Not shown.

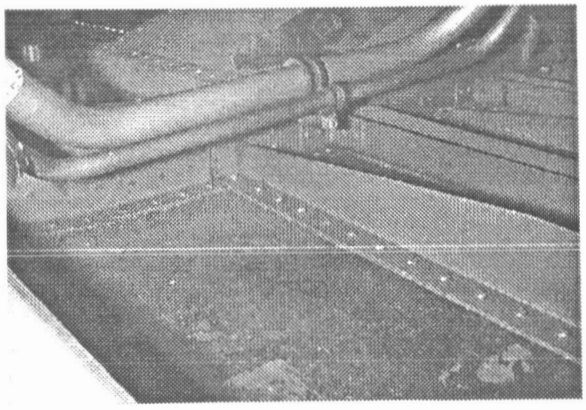

Figure 4: Inside view (looking aft) from the FLIR showing wheel well fairing skin and supporting structure.

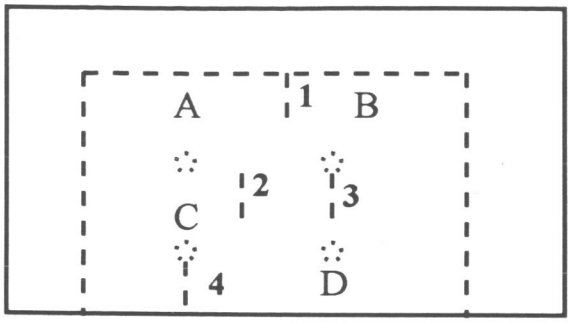

Figure 5: Reference standard used for calibration. Top plate 6.35 x 11.4 x 0.178 cm. Bottom plate 5.72 x 8.89 x 0.203 cm. EDM notches width 0.152 mm, Length 12.7 mm.

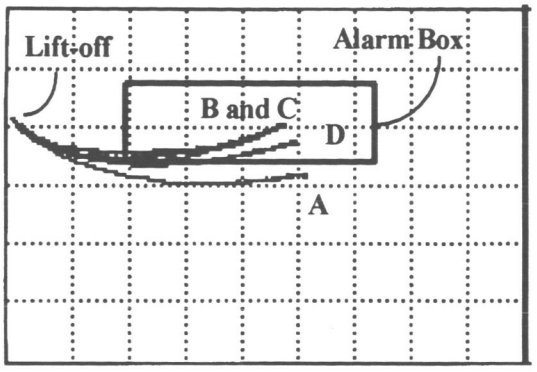

Figure 6: Signals produced on reference Standard at all four positions. Displayed is response from a Clear fastener & EDM notches 1.78 mm below the surface.

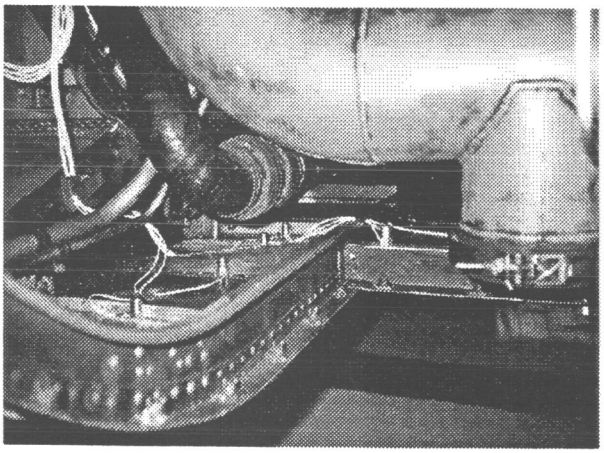

Figure 7: Accelerometer Mounting Detail (Note line of accelerometers at FS 485 and one on longeron at FS 474)

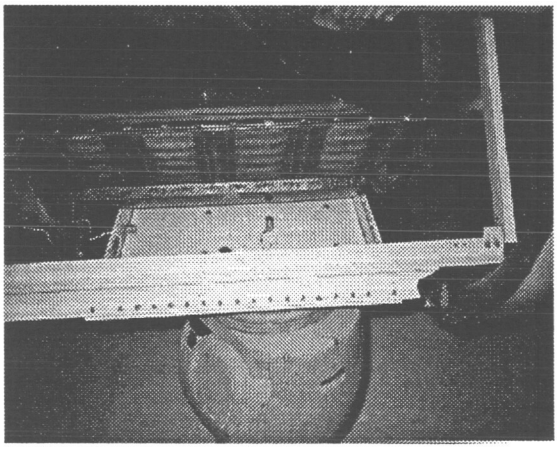

Figure 8: FLIR mounting structure with Accelerometers attached (Note X and Z accelerometers on FLIR Mounting Plate)

Figure 9: Accelerometer on Longeron, Before Structural Enhancement

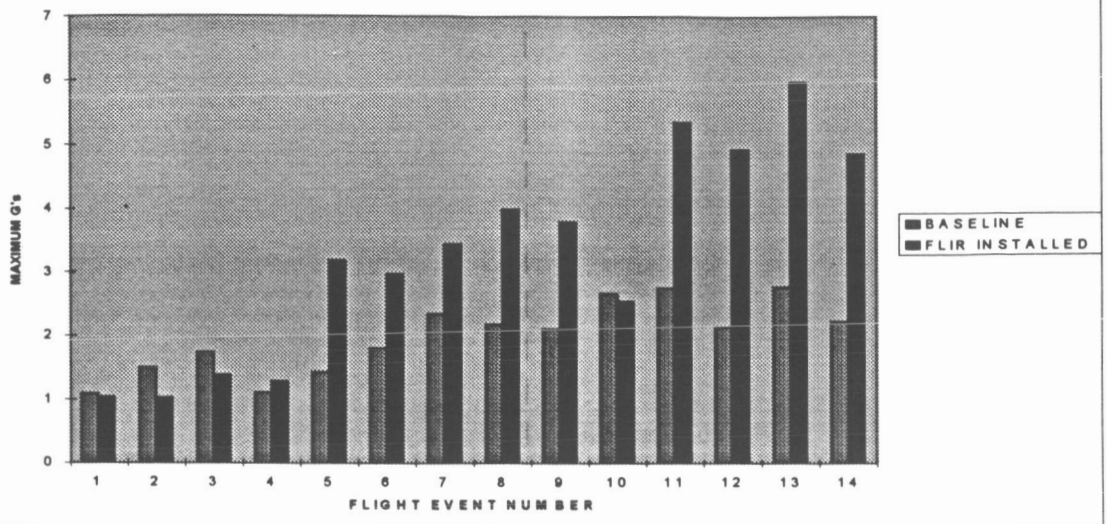

Figure 10: Accelerometer on Stiffener, Before Structural Enhancement

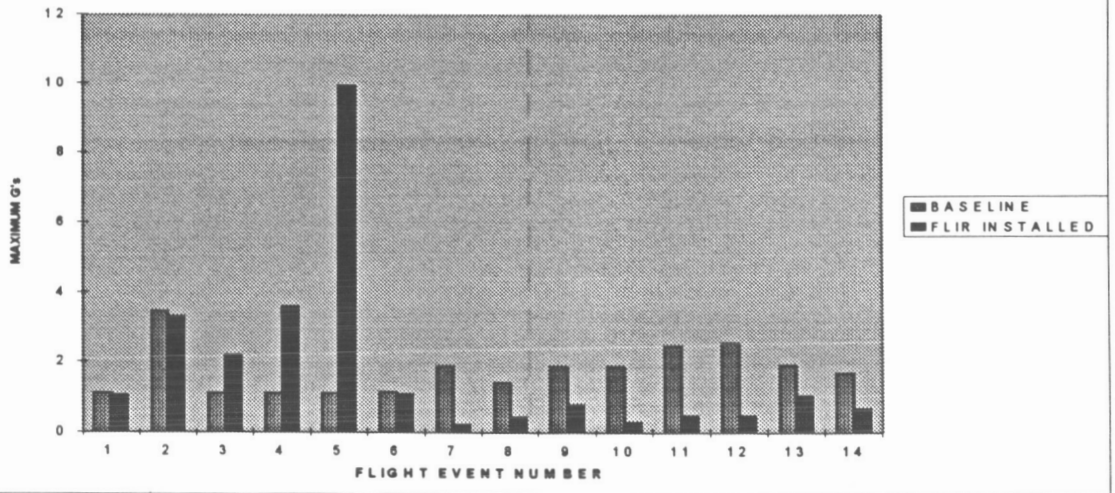

Figure 11: Accelerometer on Stiffener, After Structural Enhancement

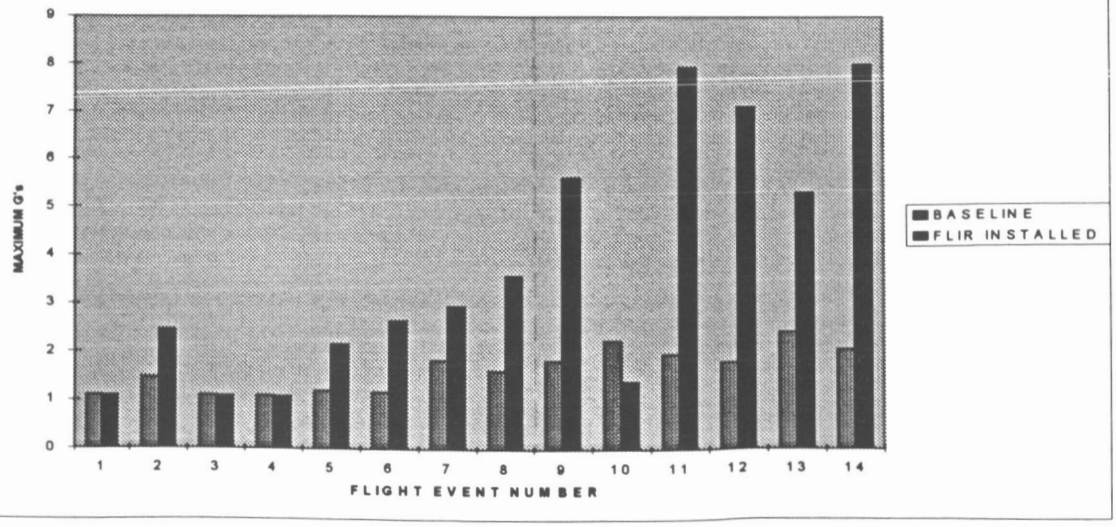

TABLE 1: HISTORICAL DAMAGE ON S/N 1719 WHEEL WELL FAIRING

DATE	DESCRIPTION OF DAMAGE
26 & 27 AUG 97	**EXTENSIVE (15 HRS) NDI OF RIGHT WHEEL WELL FAIRING CONDUCTED:**
	1) 21 SKIN ANOMALIES (CRACKS/CORROSION ORIGINATING FROM FASTENER HEADS IDENTIFIED AS FOLLOWS: A) 8 SKIN CRACKS AT FASTENERS AS NOTED IN ABOVE DISCREPANCY B) CRACKED SKIN ON FASTENER ROW FS 616.5 (THIRD FASTENER OUTBOARD OF FASTENER ROW BL 53.5) C) 2 CRACKS ON FASTENER ROW FS 607.5 (1 FASTENER INBOARD OF FASTENER ROW BL 52, 1 FASTENER OUTBOARD OF FASTENER ROW 42.5) D) 10 SKIN CRACKS ON FASTENER ROW BL 42.5 (9^{TH} AND 10^{TH} FASTENER FORWARD OF FASTENER ROW FS 607.5, 10^{TH}, 11^{TH} & 12^{TH} FASTENER FORWARD OF FASTENER ROW FS 587.5, 9^{TH} & 10^{TH} (CORROSION) FASTENER FORWARD OF FASTENER ROW FS 567.5, 11^{TH} & 12^{TH} FASTENER FORWARD OF FASTENER ROW FS 547.5 FASTENER AT INTERSECTION OF FASTENER ROW BL 42.5 & FASTENER ROW FS 457) 2) TWO ¼" CRACKS VISUALLY OBSERVED EMANATING FROM INBOARD CORNERS OF FORWARD, INBOARD SQUARE CUTOUT ON HAT SECTION ON NEWLY PROCURED FLIR MOUNT DOOR 3) APPROXIMATELY ½" CRACK ON SKIN PANEL AT CORNER INTERSECTION OF FS 491 AND BL 506
27 AUG 97	2.0 HR BASELINE FLIGHT FLOWN
28 AUG 97	2.7 HRS FLOWN WITH FLIR MOUNT AND FLIR INSTALLED. SUBSEQUENT VISUAL DAMAGE NOTED (DUE TO TIME CONSTRAINTS, AN NDI COULD NOT BE PERFORMED TO CHECK FOR INTERNAL DAMAGE): 1) 4 FASTENERS PULLED LOOSE ON FASTENER ROW BL 53.5 BETWEEN FS 491 AND 506 (1^{ST}, 2^{ND}, 3^{RD} & 4^{TH} FASTENER AFT OF FASTENER ROW FS 491.5) 2) 1 FASTENER PULLED LOOSE ON FASTENER ROW 52.0 (1^{ST} FASTENER AFT OF FASTENER ROW FS 491.5) 3) ¼" SKIN PANEL CRACK ON FASTENER ROW BL 52.0 (7^{TH} FASTENER AFT OF FASTENER ROW FS 491.5) REPLACED 5 FASTENERS/STOP DRILLED CRACK. AWAITING STRUCTURAL ENHANCEMENT.

NOTE: IT SHOULD NOT BE ASSUMED THAT THE DEFECTS DETECTED DURING THE INITIAL INSPECTIONS WERE CAUSE BY EARLIER FLIGHT OPERATIONS WITH THE FLIR INSTALLED.

TABLE 2: ACCELEROMETER LOCATIONS (FLIGHTS OF 27-28 AUGUST 97)

CHANNEL NUMBER	ACCEL S/N	LOCATION DESIGNATION	MOUNTING LOCATION TYPE	COMMENTS
1	331	FLIR SUPPORT BRACKET		FLIGHT 1 ONLY
1	331	FLIR - X-DIRECTION		FLIGHT 2 ONLY
2	260	472-55	SKIN (0.040")	
3	416	474-69	LONGERON	
4	395	485-50	SKIN (0.040")	
5	424	485-55	STIFFENER	
6	405	485-69	STIFFENER	
7	399	485-78	STIFFENER	
8	330	MLG INNER DOOR LEADING EDGE		
9	404	516-60	SKIN (0.032")	
10	259	576-60	SKIN (0.032")	
11		FLIR - Z-DIRECTION		FLIGHT 2 ONLY
12		FLIR - Y-DIRECTION		FLIGHT 2 ONLY

TABLE 3: TYPICAL TEST FLIGHT PROFILE

FLIGHT EVENT #	CONDITION	AIRSPEED (KIAS)	ALTITUDE (1000 FT)	COMMENTS
1	NORMAL GROUND IDLE	0	0	
2	GROUND RUNUP	0	0	
3	GEAR EXTENDED, FLAPS 50%	150	4	
4	GEAR UP, FLAPS 50%	150	4	
5	STRAIGHT/LEVEL	200	4	
6	STRAIGHT, 1 BALL OUT, RWD	200	8	RWD=RIGHT WING DOWN
7	STRAIGHT, 1 BALL OUT, LWD	200	8	LWD=LEFT WING DOWN
8	STRAIGHT/LEVEL	225	8	
9	STRAIGHT/LEVEL	250	8	
10	CLIMB	180-160	8-15	
11	MAXIMUM CRUISE	241-247	15	TIT: 1010° C
12	MAXIMUM CRUISE, STRAIGHT, 1 BALL OUT, RWD	245	15	TIT: 1010° C
13	MAXIMUM CRUISE, STRAIGHT, 1 BALL OUT, LWD	245	15	TIT: 1010° C
14	RGHT CONTINUOUS TURN, 30° AOB	250	11	

ACTIVE VERTICAL TAIL BUFFETING ALLEVIATION ON AN F/A-18 MODEL IN A WIND TUNNEL

Robert W. Moses
Aeroelasticity Branch, NASA Langley Research Center
Hampton, VA 23681, USA
757-864-7033
757-864-8678 (fax)
r.w.moses@larc.nasa.gov

ABSTRACT

A 1/6-scale F-18 wind-tunnel model was tested in the Transonic Dynamics Tunnel at the NASA Langley Research Center as part of the Actively Controlled Response Of Buffet-Affected Tails (ACROBAT) program to assess the use of active controls in reducing vertical tail buffeting. The starboard vertical tail was equipped with an active rudder and other aerodynamic devices, and the port vertical tail was equipped with piezoelectric actuators. The tunnel conditions were atmospheric air at a dynamic pressure of 14 psf. By using single-input-single-output control laws at gains well below the physical limits of the control effectors, the power spectral density of the root strains at the frequency of the first bending mode of the vertical tail was reduced by as much as 60 percent up to angles of attack of 37 degrees. Root mean square (RMS) values of root strain were reduced by as much as 19 percent. Stability margins indicate that a constant gain setting in the control law may be used throughout the range of angle of attack tested.

1. INTRODUCTION

Buffeting is an aeroelastic phenomenon which plagues high performance aircraft especially those with twin vertical tails. As shown in figure 1, for aircraft of this type at high angles of attack, vortices emanating from wing/fuselage leading edge extensions (LEX) burst, immersing the vertical tails in their wake. The resulting buffet loads on the vertical tails are a concern from fatigue and inspection points of view [1-4]. For example, for the McDonnell-Douglas F/A-18, special and costly 200-flight-hour inspections are required to check for structural damage due to buffet loads [4]. Inspections and repairs are high cost items to the military services.

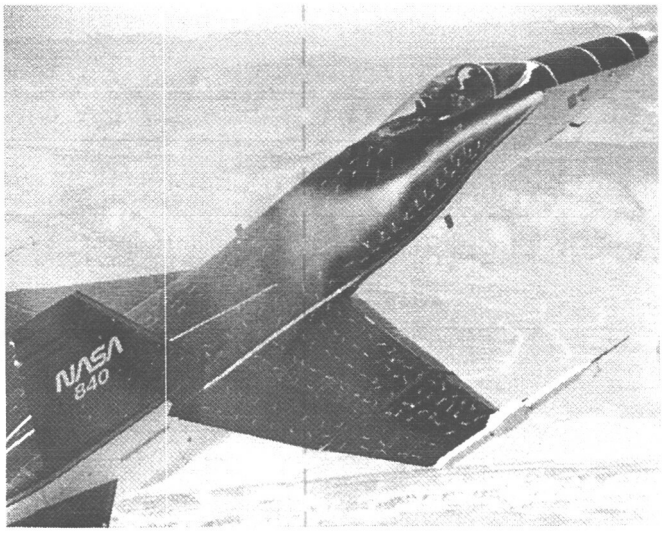

Figure 1. Flow Visualization of Leading Edge Extension (LEX) Vortex Burst, 30 degrees AOA

To reduce fatigue and thus increase the life of a vertical tail, the stresses caused by buffeting must be reduced. This reduction may be accomplished by 1) modifying the load-carrying structure within the tail, 2) reducing the buffet loads by altering the flowfield around the vertical tail, or 3) by reducing the buffeting response through active control of effectors on the tail. The success of a proposed fix to the buffeting problem has generally been measured by percentage reduction in the root mean square (RMS) of the strain at the root of the vertical tail.

For the purpose of understanding the buffeting problem, several programs have focused on quantifying the buffet loads by acquiring response measurements and surface pressures on the vertical tails of scaled models in a wind-tunnel and on an actual aircraft during flight[1-3, 5, 6]. In general, the results of these studies are published as spectra and pressure coefficients for the inboard and outboard surface of the tail.

Based on some of these studies, McDonnell-Douglas Aircraft (MDA) implemented an interim solution on the F-18 relying entirely upon structural modifications to the vertical tail in an attempt to reduce the dynamic stresses in critical areas[2]. Even with the structural enhancement, the dynamic stresses were still too severe. This led to the investigation of a LEX fence which reduced the peak accelerations in the first two modes of the vertical tail but also compromised the aircraft's high-alpha performance by reducing the unsteady lift and pitching moment of the aircraft[2]. Therefore, other options needed to be explored.
In 1992, the concept of an actively controlled rudder was proposed to alleviate vertical tail buffeting on an F-18 and an F-15 aircraft[7]. This analysis showed that an actively controlled rudder of an F-18 might be effective in adding damping to the vertical tail resulting in reductions in the RMS of the root bending moment.

In 1995, the use of actively controlled piezoelectric actuators on an F/A-18 vertical tail was analyzed[8]. This analysis showed that actively controlled piezoelectric actuators might increase damping greater than 60% in the first bending mode for less than an 8% increase in the weight of the vertical tail.

In 1995, vertical tail buffeting alleviation was achieved using piezoelectric actuators on a 5%-scale 76-/40-deg double delta wing wind-tunnel model with twin vertical tails that were not canted[9]. Over ranges of angle of attack from 20 to 55 degrees and dynamic pressure from 0.5 to 7 psf, peak response of the vertical tail was reduced by as much as 65% over the uncontolled response, using simple control algorithms employing collocated strain gauges.

In 1995, a wind-tunnel investigation at the Transonic Dynamics Tunnel (TDT) at the NASA Langley Research Center (LaRC) demonstrated that buffeting alleviation of the vertical tails on an F-18 can be achieved using active piezoelectric actuators or rudder [10]. The research objectives of the Actively Controlled Response Of Buffet-Affected Tails (ACROBAT) program are twofold: 1) to determine the spatial relationships of the differential pressures during open-loop and closed-loop conditions at various angles of attack; and, 2) to apply active controls technology, using a variety of force producers, to perform buffeting alleviation on twin vertical tails of a 1/6-scale F-18 wind-tunnel model. This investigation is the first experimental demonstration of active buffeting alleviation on a scaled F-18 wind-tunnel model using an active rudder and piezoelectric actuators.

The purpose of this paper is to present some open-loop and closed-loop wind-tunnel results using an active rudder or piezoelectric actuators to alleviate vertical tail buffeting. The results of the wind-tunnel tests presented herein demonstrate the feasibility of actively controlling vertical tail buffeting.

2. WIND-TUNNEL MODEL

An existing 1/6-scale, rigid, full-span model of the F/A-18 A/B aircraft was refurbished, and three flexible and two rigid vertical tails were fabricated. This model was then sting-mounted in the Transonic Dynamics Tunnel (TDT) at the NASA Langley Research Center, as shown in figure 2, where it underwent a series of tests to determine buffet flowfield characteristics and to demonstrate the alleviation of vertical tail buffeting.

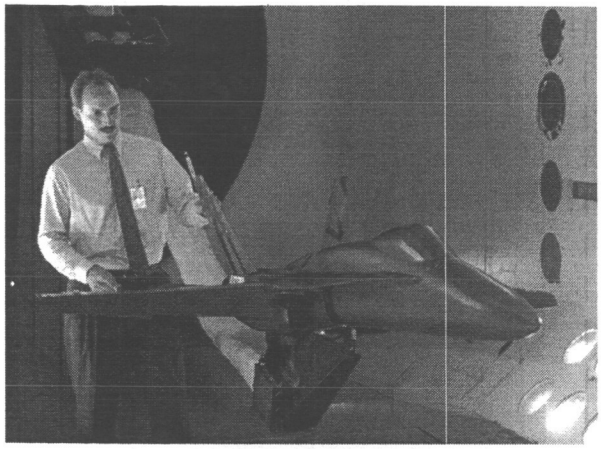

Figure 2. 1/6-Scale F/A-18 Model Mounted in the Transonic Dynamics Tunnel

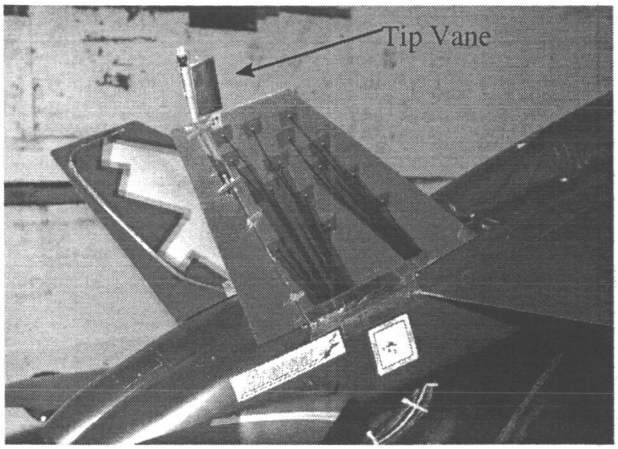

Figure 3: Side View of 1/6-Scale F/A-18 Model Mounted in the TDT

The three flexible tails were fabricated from a 1/8-inch thick aluminum plate and covered with balsa wood. The aluminum plate thickness was chosen such that the frequencies of the first three modes were close to those of the full-scale tail. Also, by using a frequency scaling near unity, the effects of actuator bandwidth could be compared directly between full-scale and reduced-scale results. All three flexible tails were instrumented with a root strain gauge aligned to measure bending moment and with two tip accelerometers near the leading and trailing edges. The two rigid tails (one port, one starboard) were fabricated from a block of aluminum and were geometrically identical to the flexible tails.

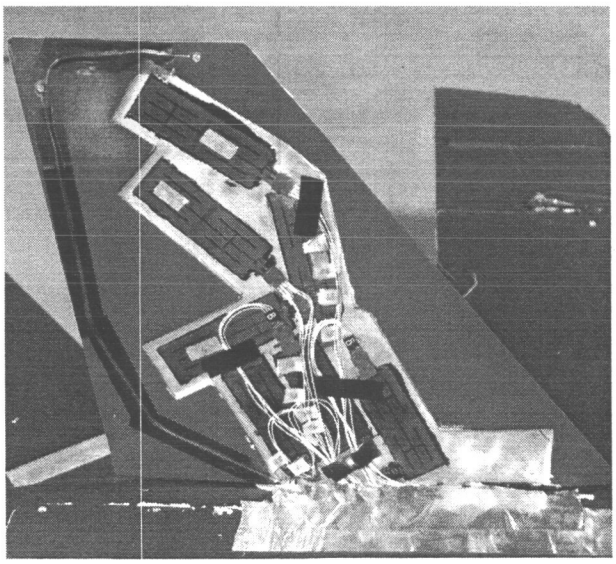

Figure 4. Piezoelectric Actuator Arrangement on Port Flexible Tail, Hatch Cover Removed

To investigate active buffeting alleviation, the flexible tails included the following control effectors: 1) a rudder surface; 2) a tip vane configuration containing a slotted cylinder; 3) piezoelectric actuation devices; or 4) an embedded slotted cylinder. The rudder, the tip vane, (shown in figure 3), and the embedded slotted cylinder were activated by clamping each of them (when necessary) to a drive shaft that was turned by a hydraulic actuator located below the root of the vertical tail. Each of the seven piezoelectric actuators consisted of two individual actuators that were commanded to strain in opposite directions simultaneously. By commanding the (pair of) actuators in this fashion, the tail could be bent. The piezoelectric actuators, whose individual actuators located on the inboard surface are shown in figure 4, were powered by

individual amplifiers located outside the test section of the TDT. Not counting bonding material, each individual piezoelectric actuator at the root of the vertical tail consisted of two stacks of four layers of encapsulated wafers. The individual actuators at other span locations consisted of two stacks of two layers of encapsulated wafers. Each individual actuator at the root had dimensions of 4.00"x1.50"x0.06" and weighed 1.02 ounces (2.1% of total vertical tail weight). Each individual actuator at other span locations had dimensions of 4.00"x1.50"x0.03" and weighed 0.51 ounces. There are a total of six individual actuators at the root and eight individual actuators elsewhere. For the port flexible tail with active piezoelectric actuators, the first bending mode is around 14 Hz (wind-off) and the first torsion mode is around 62 Hz (wind-off).

3. TEST CONDITIONS

For buffet, the Strouhal number is the primary scaling relationship used in determining tunnel conditions[1]. The Strouhal number, n, is a nondimensional frequency parameter that is proportional to reduced frequency, and is expressed as

$$n = \frac{f \cdot c}{U} \qquad (1)$$

where f is frequency in Hz, c is characteristic length, and U is velocity. Since active controls were a primary focus, comparisons of actuator bandwidths between model and flight were an issue. Therefore, to avoid any difficulties in scaling and defending any possible discrepancies, unity was chosen as the frequency ratio between model and aircraft structural modes and forcing function spectra.

4. GENERAL BUFFET AND BUFFETING CHARACTERISTICS OF THE WIND-TUNNEL MODEL

Typically, the buffet and buffeting are quantified by their dimensional or nondimensional power spectral density (PSD) functions. Since the results reported for this test are not being compared to other model or aircraft data, the dimensional form is used. For the1/6-scale F-18 model, the plots of the unsteady differential pressures of the buffet at angles of attack of 20 and 34 degrees are shown in figure 5. The differential pressures were computed from the pressure time histories acquired near the center of the planform of the starboard flexible tail. The buffet at 20 degrees AOA, in figure 5(a), appears broad band compared to the buffet at 34 degrees AOA, in figure 5(b). At 34 degrees AOA, an aerodynamic resonance around 25 Hz has emerged with a magnitude that is at least one order of magnitude larger than the levels at 20 degrees AOA. These trends of the pressures with angle of attack are consistent with other experimental data[1, 3].

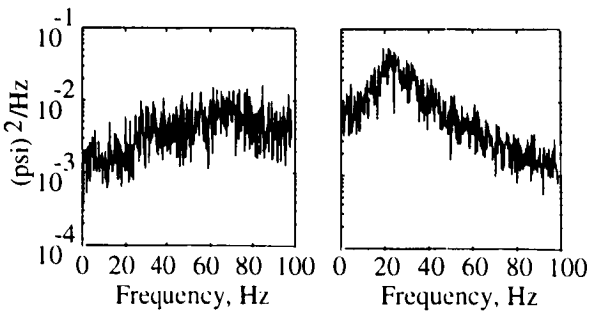

(a) 20 Degrees AOA (b) 34 Degrees AOA

Figure 5. PSDs of Differential Buffet Pressure, Midspan Midchord, Starboard Flexible Tail, 14 psf

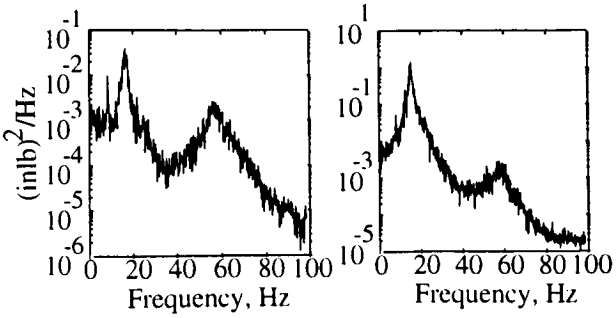

(a) 20 Degrees AOA (b) 34 Degrees AOA

Figure 6. PSDs of Root Bending Moment Buffeting Response, Starboard Flexible, 14 psf

The pressures, shown in figure 5 (a)-(b), created the buffeting, or structural response to the buffet, shown in figure 6 (a)-(b), respectively. At 34 degrees angle of attack, the buffeting shown in figure 6(b) around 14 Hz, which corresponds to the first bending mode of the vertical tail, has intensified by 1.5 orders of magnitude above the level at 20 degrees AOA, shown in figure 6(a). Since the buffet, or force input to the tail, around 25 Hz has grown with increased angle of attack, as indicated by figure 5, the vertical tail buffeting in the first bending mode has also grown with increased angle of attack, as indicated by comparing figures 6 (a) and 6 (b). The response in the mode around 58 Hz has not grown significantly with the increase in angle of attack because the magnitudes of the pressures in that portion of the spectrum have not increased with increased angle of attack, as seen in figure 5. Referred to as "open-loop" buffeting, the structural responses due to the buffet only (without a commanded signal to the rudder or piezoelectric actuators) peaked at an angle of attack of approximately 34 degrees for the 1/6-scale F-18 model. This peak at 34 degrees angle of attack agrees well with the results of other wind-tunnel tests[1, 3].

Another influence of the buffet on the vertical tail buffeting was seen by comparing the first bending frequency of the vertical tail as angle of attack was changed. The frequency of the first bending mode shifts to a lower value as angle of attack is increased (figure 7). This gradual shift in frequency with angle of attack was seen in the results of the wind-tunnel test reported on in Reference 1. If the vertical tail is considered a single degree-of-freedom system subject to the large perturbations in the flow due to the burst vortex, then this shift in frequency may be viewed as the result of increased aerodynamic damping of the first bending mode. During the ground vibration test of the starboard flexible tail, the structural damping was computed as approximately 1.8 percent for the wind-off damped first bending mode. Using the relationship between damped frequency and natural undamped frequency, the undamped natural frequency of the tail was calculated and used in estimating the total damping from the damped natural frequencies observed in the wind-tunnel at each angle of attack. The aerodynamic damping was calculated simply by subtracting the wind-off damping from the total damping. As seen in table 1, the aerodynamic damping reaches approximately 7 percent at 37 degrees angle of attack. This trend of aerodynamic damping with angle of attack was observed when comparing the frequency separation between half-power points on the power spectral density plots of the root bending moment at several angles of attack.

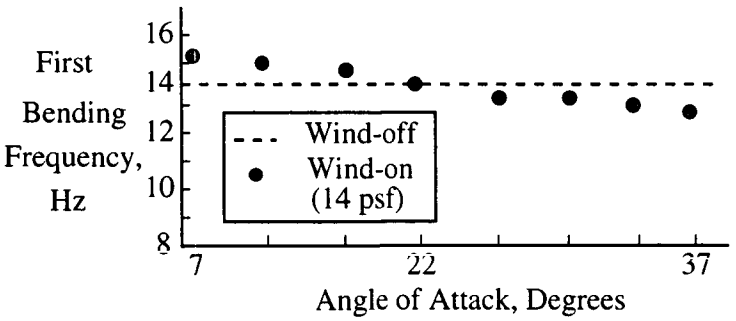

Figure 7. Variations of First Bending Frequency vs. Angle of Attack

Table 1. Estimates of Aerodynamic Damping Associated With Vertical Tail First Bending Mode

Angle of Attack, deg	Aerodynamic Damping, %
26	4.2
30	4.2
34	5.6
37	7.0

5. SYSTEM IDENTIFICATION OF THE WIND-TUNNEL MODEL IN PREPARATION FOR ACTIVE VERTICAL TAIL BUFFETING ALLEVIATION

The open-loop frequency response functions of the vertical tails due to the piezoelectric actuators were acquired experimentally by performing fast Fourier transforms[11] on the time histories of the responses of the commanded actuators and sensors located on the vertical tails. On-line capabilities at the TDT allowed quick computations of frequency response functions from time histories acquired just minutes earlier. No analytical predictions of the frequency response functions were made in advance of the wind-tunnel test because no analytical models of the aerodynamics associated with buffet were available at that time. The open-loop frequency response functions reported herein were obtained at a dynamic pressure of 14 psf in atmospheric air.

Several commands were sent separately to each actuator for determining the open-loop frequency response functions. To concentrate on the first bending mode around 15 Hz, a maximum frequency of 20 Hz was generally used in a linear frequency sweep. At times, linear sweeps up to 40 Hz were used to determine the influences of modes at frequencies higher than the frequency of the first bending mode of the vertical tail. In some cases, periodic pseudo noise (PPN) was used since this signal randomly selects the frequency content rather than sweeping through a mode which could result in damage to the wind-tunnel model. A matrix of transfer functions was obtained for all control effectors (as input) and the following outputs: strain at the root of the vertical tail, tip accelerations near the leading edge of the vertical tail, and tip accelerations near the trailing edge of the vertical tail.

The effectiveness of the seven piezoelectric actuator pairs were studied individually during tail buffeting. The three pairs of actuators at the root of the vertical tail were grouped together to boost actuator authority in the first bending mode. The remaining four pairs of actuators were abandoned because of their lack of authority in the higher tail modes. An open-loop frequency response function of the 3 pairs of piezoelectric actuators (grouped together as a single actuator) with respect to an accelerometer at the tip near the leading edge is shown in figure 8 for 24 degrees angle of attack. For comparison, an open-loop frequency response function of the rudder with respect to an accelerometer at the tip near the leading edge is shown in figure 9 for 26 degrees angle of attack. The hydraulic actuator resonance was around 24 Hz while the rudder-torque tube resonance was around 35 Hz, which contributed to the magnitude shown in figure 9.

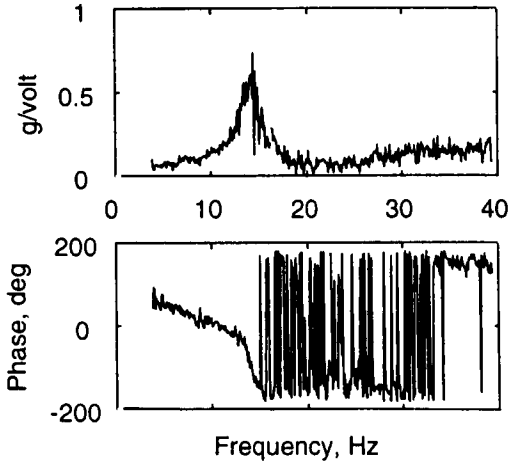

Figure 8. Open-Loop Frequency Response Functions Between Tip Acceleration and Piezo Actuator Command, 14 psf, 24 Deg AOA

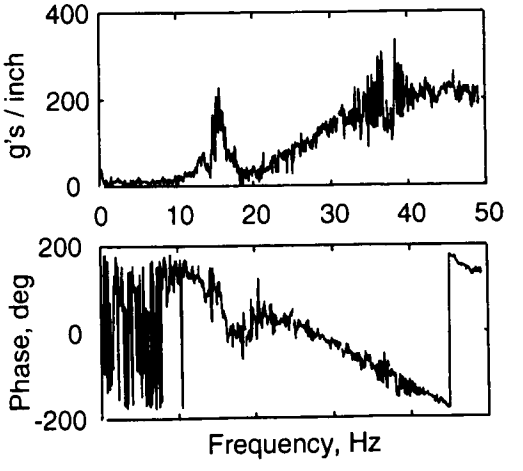

Figure 9. Open-Loop Frequency Response Functions Between Tip Acceleration and Rudder Command, 14 psf, 24 Deg AOA

Each open-loop frequency response function between actuator command and tip acceleration, shown in figures 8 and 9, is the input-output relationship of the forward loop of the active control system, shown in

figure 10. As shown in figure 10, buffet contributes to the response (output) of the vertical tail (accelerations for this case). For the purpose of computing open-loop transfer functions, the response (output) time histories obtained when the tail was buffeting will contain contributions from the unmeasured buffet (input) and the measured actuator responses (input). Therefore, some uncertainty will exist in the open-loop frequency response functions computed from these time histories because of the unmeasured buffet.

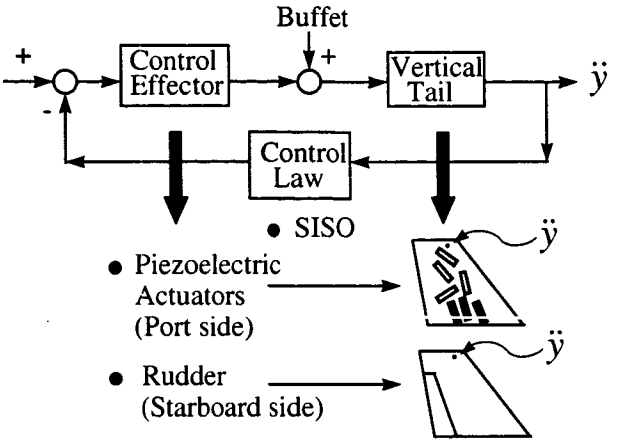

Figure 10. Active Control System

6. Control Law Design For The Buffeting Alleviation System

Using the open-loop frequency response functions obtained during the test, control laws were designed using frequency domain compensation methods[12]. These control laws were single-input, single-output control laws that utilized either a tip accelerometer or a root strain gage as the sensor to alleviate the response in the first bending mode. Because of some uncertainty in the measurement of the response created by the buffet, the control laws were designed based on the open-loop frequency response functions acquired at the lower angles of attack where the buffet, and the uncertainty in the plant, were much less. Since the buffeting of the vertical tail is maximum at 34 degrees, the feedback signal is maximum at 34 degrees. This maximum feedback signal was used in determining the constant gain setting of the control law.

The components of the active control system, shown in figure 10, include an analog-to-digital converter (A/D), a digital controller[13] in which the control law is implemented, and a digital-to-analog (D/A) converter. Since there were time delays associated with the digital controller and the actuator, the best approach to control law design was to take advantage of these phase lags. By lagging accelerations by ninety degrees of phase, the commanded motion of the actuator will provide damping to reduce the buffeting of the tail. For the rudder, the hydraulics and servo system were the major contributors to the phase lags. For the piezoelectric actuators, the digital controller was the major contributor to the phase lags. Because the frequency of the first bending mode was higher at the lower angles of attack, as shown in figure 7, the control law was designed to provide a total lag of 90 degrees at the frequency of the first bending mode expected at the higher angles of attack (see figure 7). In designing the control law, it was assumed that the phase relationship between tip accelerations and actuator command would not be a function of angle of attack. The resonance of the piezoelectric actuators was not encountered but was well above 100 Hz. Therefore, significant filtering was added to the control law to reduce its gain at frequencies above the first bending mode so that modes at higher frequencies were not affected. A notch filter around 35 Hz was used to prevent rudder motion near this frequency. Numerous levels of filtering in the control law were investigated analytically until arriving at the baseline control law for each actuator. The baseline control law design simply subtracted phase at the first bending mode so that the phase of the actuator lagged tip accelerations by ninety degrees at the frequency of the first bending mode.

7. ACTIVE BUFFETING ALLEVIATION RESULTS

In figures 11(a) and 11(b), the open-loop and closed-loop tip accelerations and root strains (bending moment), respectively, at 34 degrees angle of attack are overlayed on the same plot to illustrate the buffeting alleviation created by actively controlling the piezoelectric actuators. Similar buffeting alleviation results were achieved using the rudder, as shown in figure 12. The peak value of the PSD of the root bending moment at the frequency of the first bending mode has been reduced by approximately 60% while the RMS value of the total signal was reduced by approximately 19%.

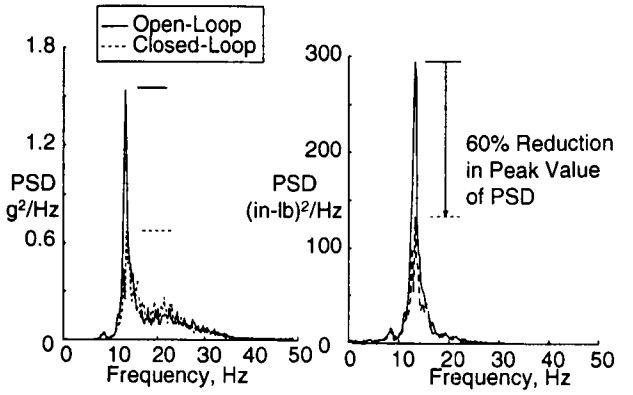

(a) Tip Acceleration (b) Root Bending Mom.

Figure 11. Comparison of Selected Responses for Open-Loop (Dotted Line) and Closed-Loop (Solid Line) Piezoelectric Actuators, 14 psf, 34 Degrees AOA

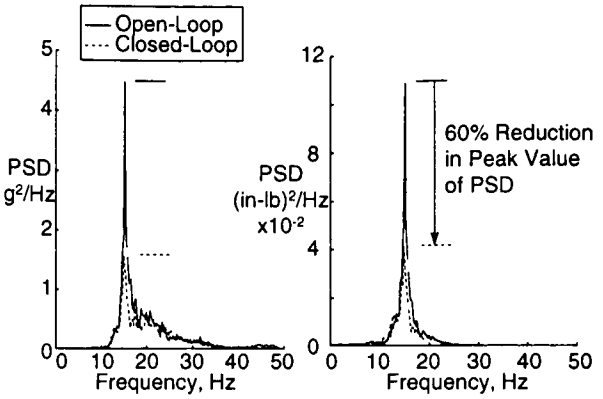

(a) Tip Acceleration (b) Root Bending Mom.

Figure 12. Comparison of Selected Responses for Open-Loop (Dotted Line) and Closed-Loop (Solid Line) Rudder, 14 psf, 34 Degrees AOA

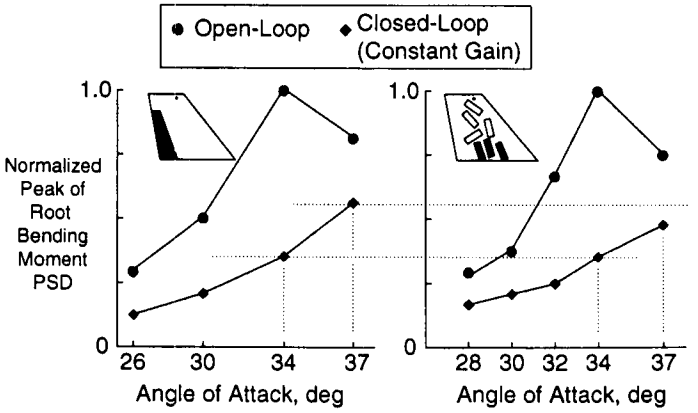

(a) Rudder Results (b) Piezo Results

Figure 13. Comparisons of the Peak Values of the PSD of the Root Bending Moment at the Frequency of the First Bending Mode for Open-Loop and Closed-Loop Conditions, At Various Angles of Attack, 14 psf

The actively controlled actuators provided damping to the tail for other angles of attack, as summarized in figure 13. The values reported in figure 13 are the (peak) value of the PSD curve of the root bending moment at the frequency of the first bending mode. Each value reported in figure 13 have been normalized to the maximum open-loop value which occurs at 34 degrees angle of attack. A constant gain setting was used for each actuator for all angles of attack values shown in figure 13. At 34 degrees angle of attack, 3 degrees (RMS) of the 20 degrees available and 2.4 volts (RMS) of the 10 volts available were used by the rudder and the piezoelectric actuators, respectively, to alleviate the vertical tail buffeting. The amount of buffeting alleviation obtained with the rudder is quite similar to that obtained with the

piezoelectric actuators. At 34 degrees angle of attack, the open-loop value of the PSD for root bending moment has been reduced by approximately 60 percent using either control effector (see figures 11 and 12 also). Therefore, for the gain selected during the test, the alleviation performance of each control effector are approximately identical.

For each baseline control law, stability calculations[14] were performed at numerous angles of attack prior to closing the loop. In figure 14, the stability gain margins (GM) illustrate that the baseline control law for the rudder, and for the piezoelectric actuators, with a constant gain setting will not cause any instabilities. For the rudder, the gain margin decreases initially with increases in angle of attack up to 30 degrees. Gain margin increases with increases in angle of attack after reaching 30 degrees. For the piezoelectric actuators, the gain margin decreases with increases in angle of attack after reaching 24 degrees.

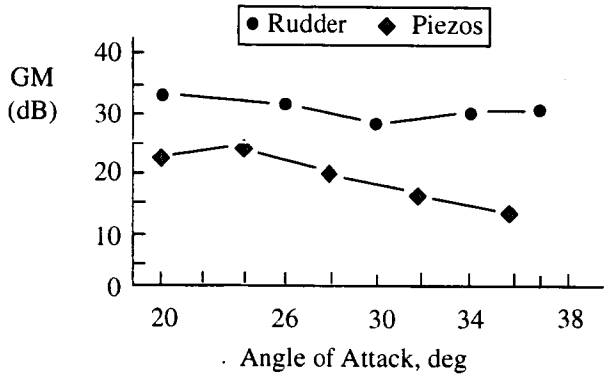

Figure 14. Gain Margins of the Baseline Control Laws For The Rudder and The Piezoelectric Actuators at Constant Gain, For Various Angles of Attack, 14 psf

Although the angle-of-attack trends of the gain margins vary between the two actuators, the gain margins remain greater than zero which indicates stability of the systems. Because the unmeasured buffet (input) is contributing to the magnitude of the frequency response function used in the stability calculations, the buffet may be the cause of the decrease in GM at the higher angles of attack. For the rudder at the higher angles of attack, a slight loss of force output will reduce the magnitude of the frequency response function slightly. This decrease in magnitude may be offsetting the increases from the buffet resulting in a relatively level gain margin curve, as shown in figure 14.

Setting the gain of the control law so that actuator performance was not exhausted at the worst case (34 degrees angle of attack) condition did not exclude the alleviation of buffeting at other angles of attack, as seen in figure 13. Based on the closed-loop and stability results in figures 13 and 14, respectively, it is anticipated that further improvement in the closed-loop response may be achieved by simply adjusting the gain in the control law to higher (still stable) values, thereby improving upon the percentage of total damping added to the system through the use of active controls.

8. CONCLUSIONS

During the wind-tunnel tests of the ACROBAT program's 1/6-scale F-18 model in the Transonic Dynamics Tunnel, reductions up to 60% in the peak value of the PSD of the root bending moment at the frequency of the first bending mode were observed when using actively controlled piezoelectric actuators or rudder at gains well below their physical limits. For the piezoelectric actuators, only 2.4 volts (RMS) were used of the 10 volts available to obtain the large reductions in root bending moment at 34 degrees angle of attack. At 34 degrees angle of attack, the rudder used only 3 degrees (RMS) of the 20 degrees available. For the gain settings tested in the wind-tunnel, the rudder and the piezoelectric actuators appeared equally

effective in adding damping to the vertical tail during buffeting. The stability margins of the system indicated that the gain of the control law may be increased without driving the first bending mode of the vertical tail unstable. Despite the changes in the structural dynamics of the vertical tail with angle of attack, a single-input-single-output control law was employed successfully at constant gain throughout the entire angle of attack range without requiring adaptations.

ACKNOWLEDGMENTS

The author would like to extend his gratitude to the test crews that conducted the investigation and reduced the pressure data to a useable format: Transonic Dynamics Tunnel at the NASA Langley Research Center and the Air Force Research Laboratory, Wright-Patterson Air Force Base. In addition, a special thanks is extended to Ms. Sherwood Hoadley and Ms. Carol Wieseman for the software used to compute and plot the results.

REFERENCES

1 Zimmerman, N. H., and Ferman, M. A., "Prediction of Tail Buffet Loads for Design Application," Vols. I and II, Rept. No. NADC-88043-60, July 1987.

2 Lee, B. H. K., Brown, D., Zgela, M., and Poirel, D., "Wind Tunnel Investigation and Flight Tests of Tail Buffet on the CF-18 Aircraft", in Aircraft Dynamic Loads Due to Flow Separation, AGARD-CP-483, NATO Advisory Group for Aerospace Research and Development, Sorrento, Italy, April 1990.

3 Pettit, C. L., Banford, M., Brown, D., and Pendleton, E., "Pressure Measurements on an F/A-18 Twin Vertical Tail in Buffeting Flow," Vols 1-4, United States Air Force, Wright Lab., TM-94-3039, Wright Patterson AFB, OH, August 1994.

4 White, E. V., "An Active Smart Material System for Buffet Load Alleviation: Functional Requirements Update and Maintenance Information," presented at the Active Buffet Suppression: Phase II Program Preliminary Design Review Meeting at Active Controls eXperts (ACX), August 4, 1995.

5 Meyn, L. A. and James, K. D., "Full-Scale Wind-Tunnel Studies of F/A-18 Tail Buffet," Journal of Aircraft, Vol. 33, No. 3, May-June 1996.

6 Moses, R. W. and Pendleton, E., "A Comparison of Pressure Measurements Between a Full-Scale and a 1/6-Scale F/A-18 Twin Tail During Buffet," presented at the 83rd Meeting of the Structures And Materials Panel (SMP) of the Advisory Group for Aerospace Research and Development (AGARD), Florence, Italy, September 2-6, 1996.

7 Ashley, H., Rock, S. M., Digumarthi, R., Chaney, K., and Eggers, A. J. Jr., "Active Control For Fin Buffet Alleviation," WL-TR-93-3099, January 1994.

8 Lazarus, K. B., Saarmaa, Erik, and Agnes, G. S., "An Active Smart Material System for Buffet Load Alleviation," SPIE Proceedings Vol. 2447, 1995, pp. 179-192.

9 Hauch, R. M., Jacobs, J. H., Dima, C., and Ravindra, K., "Reduction of Vertical Tail Buffet Response Using Active Control," Journal of Aircraft, Vol. 33, No. 3, May-June 1996.

10 Moses, R. W., "Vertical Tail Buffeting Alleviation Using Piezoelectric Actuators-Some Results of the Actively Controlled Response Of Buffet-Affected Tails (ACROBAT) Program," SPIE's 4th Annual Symposium on Smart Structures and Materials, Industrial and Commercial Applications of Smart Structures Technologies Conference 3044, Paper No. 3044-07, San Diego, CA, March 4-6, 1997.

11 Bendat, J. S. and Piersol, A. G., Engineering Applications of Correlation and Spectral Analysis, Second Edition, John Wiley & Sons, Inc., 1993.

12 Franklin, G. F., Powell, J. D., and Emami-Naeini, A., Feedback Control of Dynamic Systems, Addison-Wesley Publishing Co., Reading MA, 1986.

13 Hoadley, S. T. and McGraw, S. M., "Multiple-Function Digital Controller System for Active Flexible Wing Wind-Tunnel Model," Journal of Aircraft, Vol. 32, No. 1, January-February 1995, pp. 32-38.

14 Wieseman, C. D., Hoadley, S. T., and McGraw, S. M., "On-line Analysis Capabilities Developed to Support the Active Flexible Wing Wind-Tunnel Tests," Journal of Aircraft, Vol. 32, No. 1, January-February 1995, pp. 39-44.

CORROSION-FATIGUE CRACK INITIATION IN 7000-SERIES Al ALLOYS

Peter S. Pao, C.R. Jerry Feng, and Steven J. Gill
Naval Research Laboratory
Washington, DC 20375, USA
Tel: 202-767-0224
E-Mail: pao@anvil.nrl.navy.mil

ABSTRACT

The mechanisms of corrosion-fatigue crack initiation by pitting in high-strength 7000-series aluminum alloys were studied. The alloys used in this investigation were 7075-T7351 and 7050-T7451. Corrosion pits were formed in a 3.5% NaCl solution by the electrochemical reaction between the constituent particles and the surrounding matrix. Depending on whether these particles were cathodic (C-type) or anodic (A-type) relative to the alloy matrix, the pits formed as a consequence of matrix (around cathodic particles) or particle (for anodic particles) dissolution. In the 7075 alloy, both C-type and A-type particles were present. In the 7050 alloy, only C-type particles were present. The C-type particles were identified, using transmission electron microscopic techniques, as $Al_{23}CuFe_4$ in the 7075 alloy and Al_7Cu_2Fe in the 7050 alloy. Because these particles tend to cluster parallel to the rolling plane in the rolling direction, significant pit growth from pit coalescence was observed following prolonged exposure to a salt water environment.

The effect of pre-existing corrosion pits on fatigue crack initiation was investigated using blunt-notch fracture mechanics specimens oriented in the short-transverse direction to obtain cracks in the same orientation as those that grow from rivet holes. Results to date indicate that the presence of corrosion pits can significantly shorten the fatigue crack initiation life and decrease the threshold stress intensity of the alloy by as much as 50 percent. Post initiation analyses further confirmed that, when corrosion pits were present, fatigue cracks always initiated from these pits. In the absence of pits, fatigue cracks initiated from large inclusions. The identification of the constituent particles, the mechanism of pit formation and growth, and the analyses of fatigue crack initiation kinetics are discussed.

INTRODUCTION

7000-series aluminum alloys, such as 7075 and 7050, are extensively used in Navy aircraft. Because of the Navy's unique service requirements, these alloys are subjected to aggressive conditions like carrier deck take-off/landings and sea level flights where they often encounter salt water spray and/or salt fog environments. Since these commercial purity alloys contain numerous constituent particles that have different electrochemical potentials relative to the matrix, corrosion pits can readily develop at these particles [1-5]. Once corrosion pits are formed they can act as stress concentration sites and have the potential to significantly reduce the crack initiation time and overall fatigue life of the structure [2,5]. However, many of the previous studies used a smooth specimen geometry and results could not be easily applied to more complex aircraft structural configurations, such as rivet holes, where stress concentrations are prevalent. Thus, quantitative characterization of the influences of corrosion pits on the fatigue crack initiation kinetics in 7000-series alloys, in the presence of such structural discontinuities, is highly desirable and is essential for the development of life prediction methodology for aging aircraft.

Since constituent particles play important roles in corrosion pit formation, the present study started with the identification of these particles using analytical electron microscopy. Next, the pit formation sequence in 3.5 wt% NaCl solution was investigated, and the size and distribution of the active pits were determined. Finally, the influences of corrosion pits on the fatigue crack initiation kinetics

were studied using blunt-notch fracture mechanics type specimens that were designed to simulate the rivet hole geometry in aircraft structures.

MATERIALS AND EXPERIMENTAL PROCEDURES

The 7000-series aluminum alloys used in this investigation were 63.5 mm-thick rolled plates of overaged 7075-T7351 and 7050-T7451. The chemical compositions supplied by the vendor are shown in Table 1.

TABLE 1. CHEMICAL COMPOSITION (wt %)

Alloy	Zn	Mg	Cu	Cr	Mn	Ti	Si	Fe	Zr	Al
7075	5.70	2.52	1.59	.20	.05	.04	.09	.17		bal
7050	6.02	2.24	2.19	.02		.03	.05	.08	.10	bal

Thin foils of 7075 and 7050 for analytical electron microscopy studies were prepared by electrochemical jet polishing techniques. Both selected area diffraction (SAD) and converging beam electron diffraction (CBED) were employed for the identification of constituent particles.

For pit formation studies, 15.9-mm-diameter cylindrical 7075 and 7050 specimens were cut in the short transverse (S) direction. The specimen surfaces were mechanically polished with the final polishing step using 3 μm diamond paste. The polished specimens were then immersed in glass beakers each containing 200 ml of 3.5 wt% NaCl solution for predetermined lengths of time. For specimens that were immersed for more than few hours, thick layers of corrosion products were formed on the specimen surface, and, in these cases, a solution containing phosphoric acid and chromic trioxide was used to remove these layers before the pitted specimens were examined by scanning electron microscope (SEM). To avoid any possible beam/surface interactions, only newly pitted specimens were used for SEM examinations.

For fatigue crack initiation studies, 12.7 mm-thick blunt-notch wedge-opening-load (WOL) specimens with height H = 63 mm and width W = 64.8 mm were used. The specimen geometry and its relative orientation with respect to the rolled plate principal directions are shown schematically in Fig. 1. As shown in Fig. 1, the fatigue specimens were oriented in the ST-direction, which is the most problematic direction as it has the lowest resistance to stress-corrosion cracking and fatigue. The radius of the blunt-notch was 3.18 mm which resulted in a stress concentration factor K_t = 3.1. The blunt-notch surfaces were mechanically polished in the circumferential direction with the final

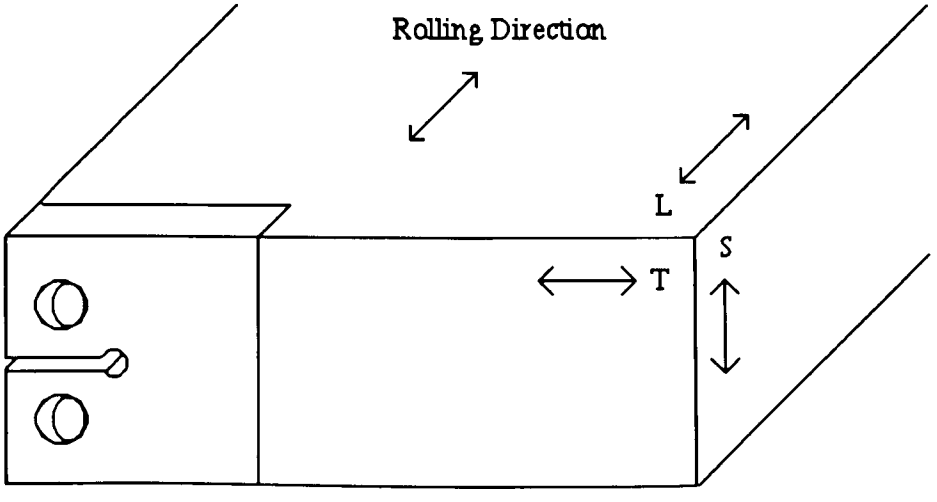

Figure 1. Blunt-notch type fatigue crack initiation specimen layout.

step using 3 μm diamond paste. Some of the blunt-notch WOL specimens were pitted by immersing the blunt notches in a 3.5 wt% NaCl solution for 336 hrs. They were then taken out of the solution, rinsed with distilled water, dried, and stored in a desiccator until used for fatigue crack initiation studies. Finally, since the bottom of the blunt-notch surface was parallel to the "S" surface, the corrosion pit size and density after 336 hrs immersion, which had been previously determined for the cylindrical specimens, were used for crack initiation analyses.

Fatigue crack initiation studies were carried out on as-polished and polished-and-pitted blunt-notch WOL specimens at various stress intensities to determine the fatigue crack initiation threshold. All fatigue tests were performed in ambient air at a stress ratio R = 0.10 and a frequency f = 5 Hz. Fatigue crack initiation was continuously monitored using a compliance technique. The initiation tests were automatically stopped and the number of cycles recorded when the normalized crack length, a/W, increased by 0.005, which corresponded to about 0.3 mm in crack extension. After initiation, specimens were examined by SEM to identify the microscopic features at the crack initiation sites.

RESULTS AND DISCUSSIONS

1. CONSTITUENT PARTICLES IN 7075 AND 7050

1A. 7075

In 7075, two major types of constituent particles are present. The first type is Fe-containing constituent particles which have irregular shapes and sizes ranging from a few μm to 30 μm. This type of particle has been identified by CBED and SAD techniques as $Al_{23}CuFe_4$, which has an orthorhombic structure with lattice spacings of a = 0.759, b = 0.6657, and c = 0.8840 nm. Because $Al_{23}CuFe_4$ particles have a higher electrochemical potential than the surrounding aluminum matrix and will act as cathodes in the presence of salt water, they are referred to as C-type particles in this study. About 80 % of the constituent particles seen in Al 7075 were C-type particles.

The other major type of constituent particles in Al 7075 is Cu-containing particles. Many of the Cu-containing constituent particles are spherical in shape with a size ranging from a few μm to less than 10 μm. Because these particles tend to be preferentially dissolved in the thin foil preparation processes, they cannot be positively identified by transmission electron microscopy techniques. Thus, SEM and energy dispersive x-ray spectroscopy (EDX) were used to study the chemical composition of these particles. The results indicate that these particles contain only Al and Cu and probably are of the Al_2Cu type. These Cu-containing constituent particles are anodic relative to the aluminum matrix and are referred to as A-type particles here.

Besides C- and A-type constituent particles, there are a few Si-containing particles in 7075. Their numbers are far less than those of the two major types of particles and they are electrochemically "neutral" relative to the aluminum matrix. These few Si-containing particles do not appear to play a significant role in the pitting process.

1B. 7050

Only one major type of constituent particle is found in 7050. This type has been identified by CBED and SAD techniques as tetragonal Al_7Cu_2Fe with lattice parameters a = 0.656 nm and c = 1.500 nm. These particles have irregular shapes and are cathodic relative to the aluminum matrix (C-type). A-type particles such as Cu-containing Al_2Cu are not present. As in 7075, there are a few Si-containing constituent particles in 7050.

2. PIT FORMATION

Figure 2 shows the constituent particle distribution in 7075. Because of the ingot processing, these constituent particles are lined up like strings in the rolling direction. Both C- and A-type constituent particles are present.

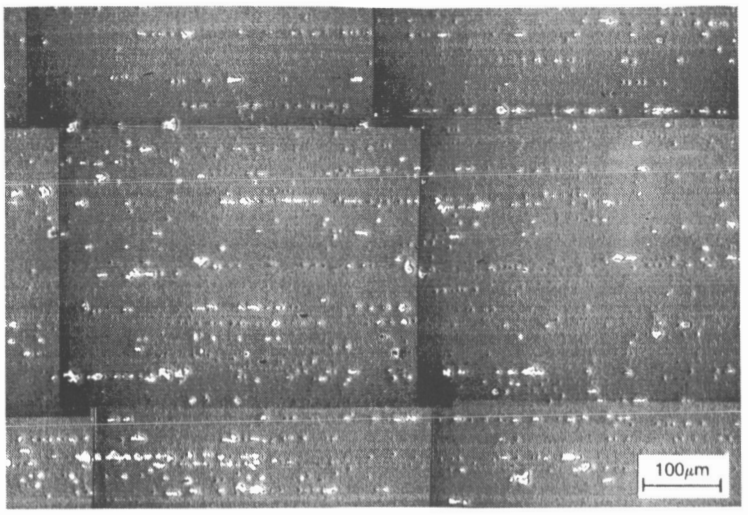

Figure 2. Constituent particles in 7075-T7351 as seen from the ST direction.

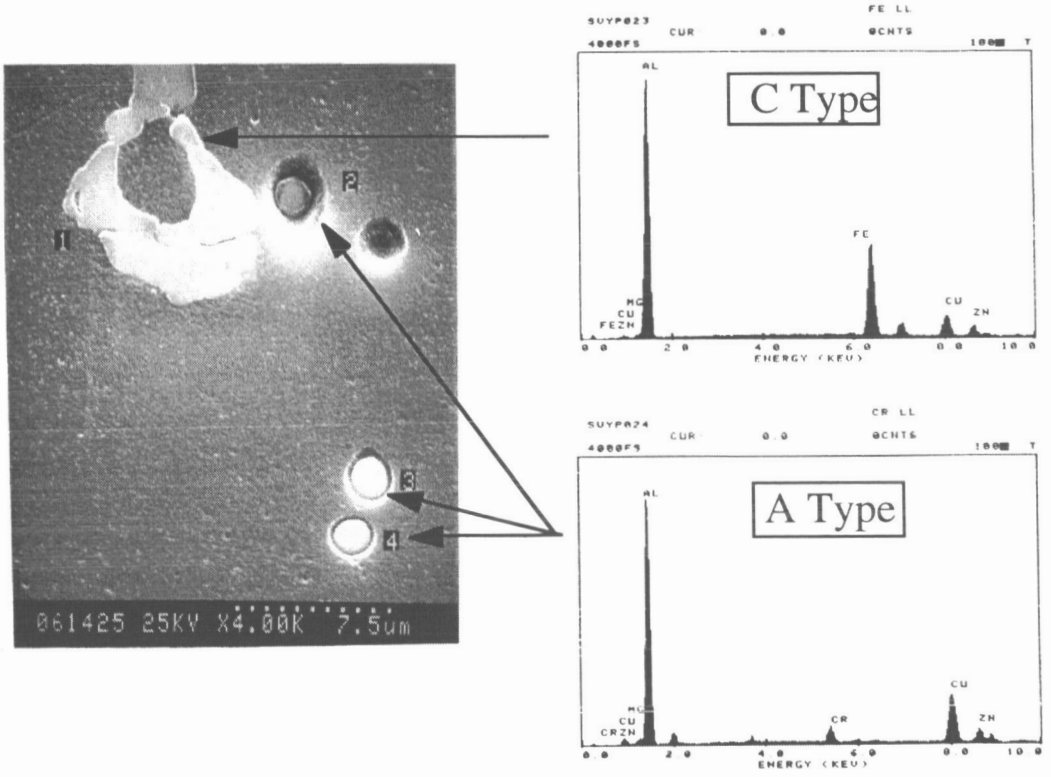

Figure 3. Surface morphology and EDX traces of constituent particles of 7075-T7351 after 3 hrs immersion in 3.5 wt% NaCl solution.

The typical surface morphology of the polished 7075 after 3 hrs immersion in 3.5 wt% NaCl solution is shown in Fig. 3. The large irregular-shaped particle (Particle 1) contains Fe and is probably $Al_{23}CuFe_4$ which is a C-type particle. The smaller round-shaped particles (Particles 2, 3, and 4) all contain Cu and are believed to be A-type Al_2Cu. The EDX traces for Particles 1 and 4 are also shown in Fig. 3. As shown in Fig. 3, after 3 hrs of continuous immersion, there is no appreciable attack on the matrix that surrounds Particle 1 even though Particle 1 is cathodic relative to the matrix. However, the A-type particles 2, 3, and 4 begin to dissolve following only 3 hrs immersion. This is due to the difference in electrochemical potential between these particles and the matrix. A-

type particles act like anodes and dissolve while the matrix and C-type particles act like cathodes. Particle 2 dissolved significantly faster than Particles 3 and 4, probably due to its close proximity to the C-type particle (Particle 1) and hence higher corrosion current and rate. The hole near Particle 2 probably contained an A-type particle which was either completely dissolved or pulled out during specimen preparation.

After continuous immersion in 3.5 wt% NaCl solution for 72 hrs, all A-type constituent particles that had been exposed on the specimen surface were dissolved and, as a result, left dimples in their places. The matrix around C-type particles, which was anodic relative to the particles, was attacked and formed shallow dimples as illustrated in Fig. 4. Thus, after 72 hrs of immersion, dimples were formed on all C- and previous A-type particle sites.

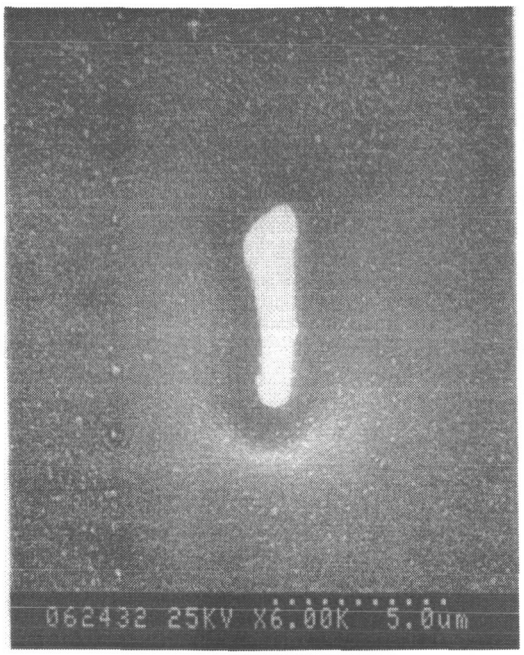

Figure 4. Matrix dissolution around a C-type particle in 7075-T7351 after 72 hrs in 3.5 wt% NaCl solution.

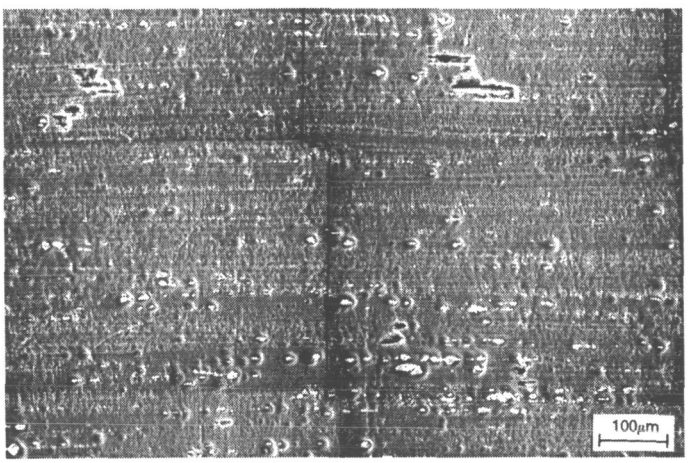

Figure 5. Corrosion pits in 7075-T7351 after 336 hrs in 3.5 wt% NaCl solution.

After immersion in 3.5 wt% NaCl solution for 336 hrs, pits were formed at some, but not all, dimpled sites. Figure 5 shows an example of the corrosion pits in 7075 after 336 hrs immersion. The pit sizes vary from as small as a few μm to larger than 50 μm. The average pit size and the two dimensional pit density in 7075-T7351 and 7050-T7451 following 336 hrs immersion were measured and tabulated in Table 2. As can be seen in Table 2, the average pit size and density for 7075 are larger than those for 7050. The pit depths and the pit widths beneath the surface, however, could be several times larger than those measured on the surface.

TABLE 2. CORROSION PIT SIZE AND DENSITY

Alloy	Exposure Time (h)	Mean Size (μm)	Density ($1/mm^2$)
7075-T7351	336	30	7.5
7050-T7451	336	25	6.7

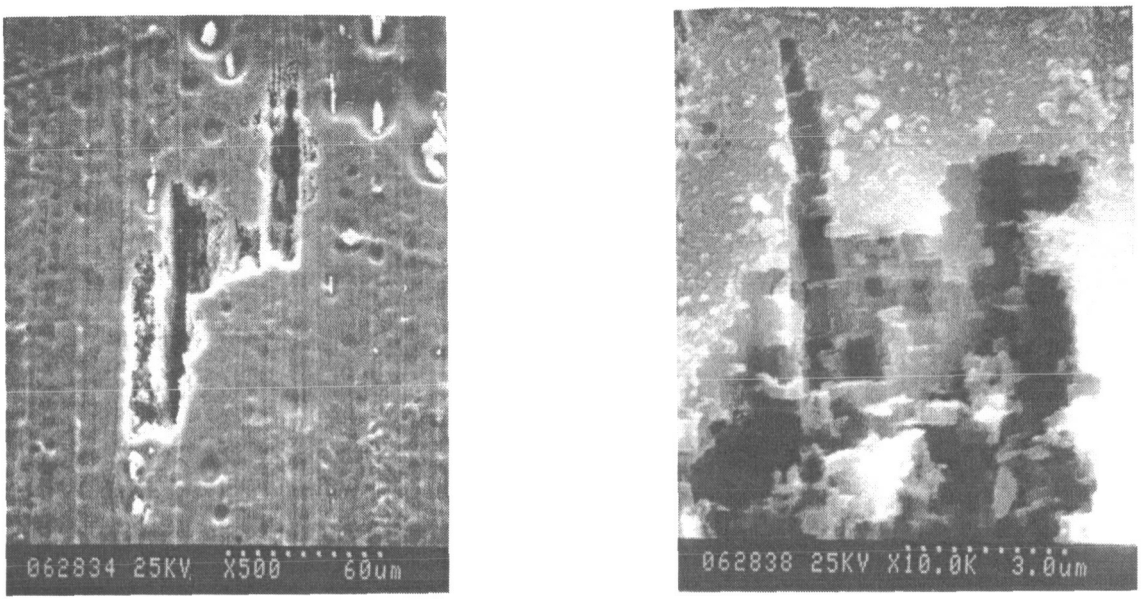

(A) (B)

Figure 6. Corrosion pit morphology in 7075-T7351 after 336 hrs in 3.5 wt% NaCl solution.

Figure 6 shows the pit morphologies of 7075 at higher magnifications. As shown in Fig. 6A, these corrosion pits not only grow along the rolling direction but also can coalesce with neighboring pits to form a larger one. At substantially higher magnification as in Fig. 6B, square pits much like etch pits can be seen at the forefront of the growing corrosion pit. The presence of these square pits suggests that the specimen surface is of the [100] type and the pitted region is highly acidic.

Pit formation in 7050 is similar to that in 7075 except that only C-type particles are present. The average pit size and the pit density are reported in Table 2.

3. FATIGUE CRACK INITIATION

3A. FATIGUE CRACK INITIATION KINETICS

Fatigue crack initiation in ambient air of as-polished and polished-and-pitted (by 336 hrs pre-exposure to 3.5 wt% NaCl solution) for 7075-T7351 specimens are compared in Fig. 7A. Since the surface at the root of blunt-notch in the specimens was parallel to the "S" surface of the rolled plate, the mean corrosion pit size and density following a 336 hrs immersion, therefore, should be approaching those reported in Table 2. For example, the mean pit size for 7075-T7351 as measured from the surface was about 30 μm. As shown in Fig. 7A, due to the presence of pits in specimens that had been pre-exposed to 3.5 wt% NaCl solution, the fatigue initiation lives, at comparable stress levels, are two to three times shorter than those of as-polished specimens which contained no pits. Additionally, the presence of corrosion pits reduces the fatigue crack initiation threshold stress by about 50 %. Because the present study is limited to only one pit size and density, a functional relation can not be developed to predict their influence on fatigue crack initiation thresholds and fatigue lives. Nevertheless, it is expected that a larger pit size, which would produce a greater stress concentration, and a higher pit density, and thus provide more initiation sites, would result in a lower fatigue crack initiation threshold and shorter fatigue life. As will be shown later in the post-initiation fractographic examinations, corrosion pits play an important role in facilitating fatigue crack initiation.

Fatigue crack initiation in ambient air of as-polished and polished-and-pitted (by 336 hrs pre-exposure to 3.5 wt% NaCl solution) 7050-T7451 specimens is compared to those of 7075-T7351 in Fig. 7B. As shown in Fig. 7B, the general responses of 7050 alloy are quite similar to those of 7075

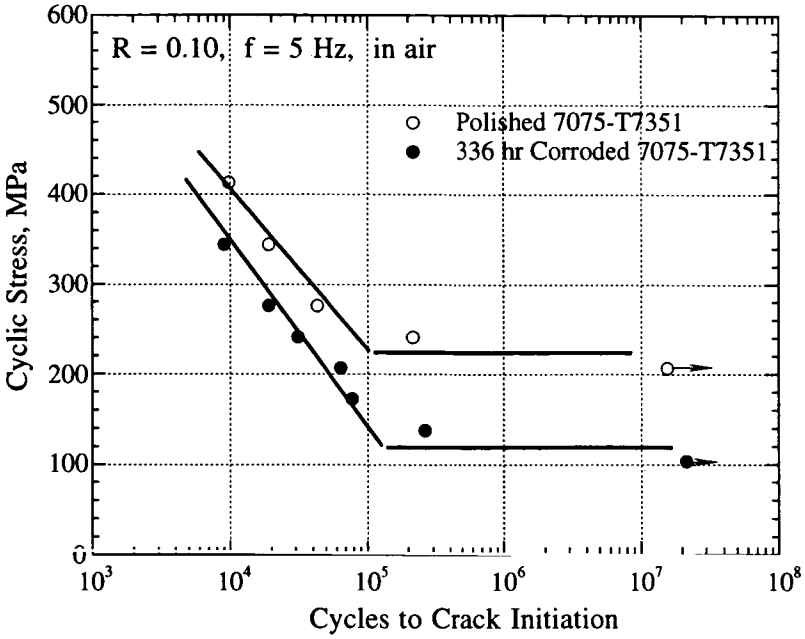

(A)

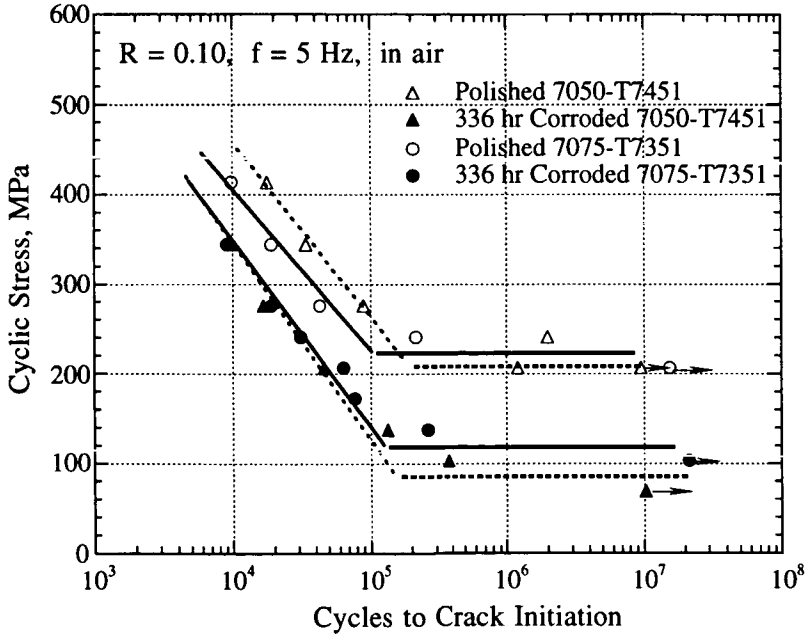

(B)

Figure 7. (A) Fatigue crack initiation kinetics of 7075-T7351. (B) Comparison of fatigue crack initiation kinetics between 7075-T7351 and 7050-T7451.

in that the presence of corrosion pits significantly reduces the fatigue initiation lives and the fatigue crack initiation threshold stresses. The difference between 7050-T7451 and 7075-T7351, in terms of fatigue crack initiation performance, is probably not significant even though the newer 7050 alloy has slightly smaller mean pit size and density than those of 7075.

3B. FRACTOGRAPHIC EXAMINATIONS

Fractographic examinations indicated that, for the polished specimens with no prior exposure to 3.5 wt% NaCl solution and hence containing no corrosion pits, fatigue cracks generally initiated from a few constituent particles that were on or near the free surface at the root of the blunt-notch where the local stresses were at their maximum. An example is shown in Fig. 8 for a polished 7075 specimen at a fatigue stress of 276 MPa. The dashed line in Fig. 8 indicates the fatigue crack region

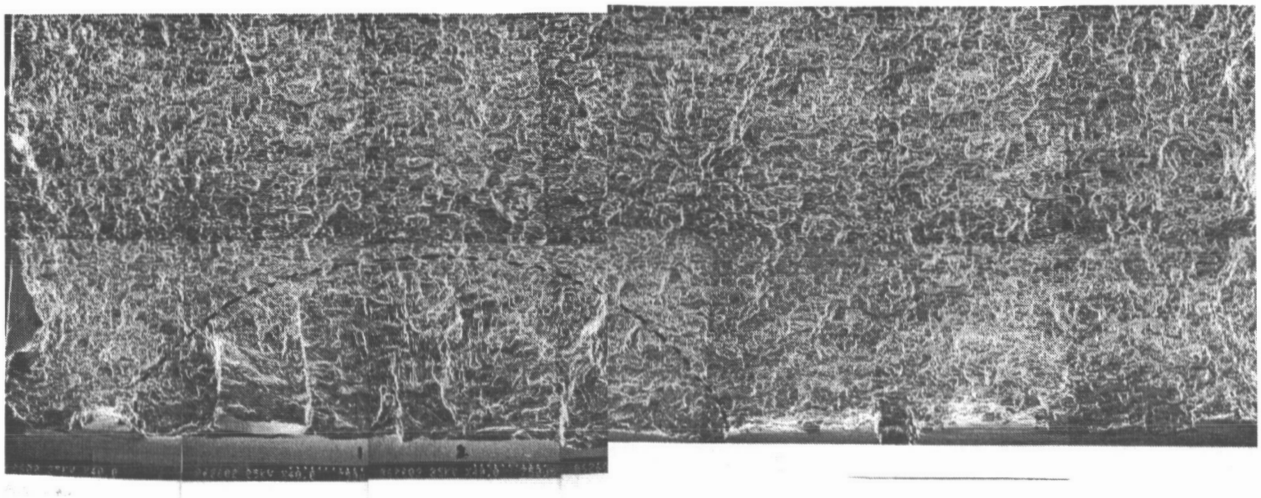

Figure 8. Fractograph of polished 7075-T7351 specimen fatigued at 276 MPa.

Figure 9. Fatigue crack initiation region of specimen shown in Fig. 8.

and, in this fatigue region, fatigue cracks were initiated from a couple of C-type constituent particles. The initiation region can be easily identified by the cleavage-like river lines emanating from the constituent particles shown at a higher magnification in Fig. 9. The 15-μm constituent particle at the free-surface shown in Fig. 9 acted as a stress concentration site that facilitated fatigue crack initiation after about 400,000 loading cycles.

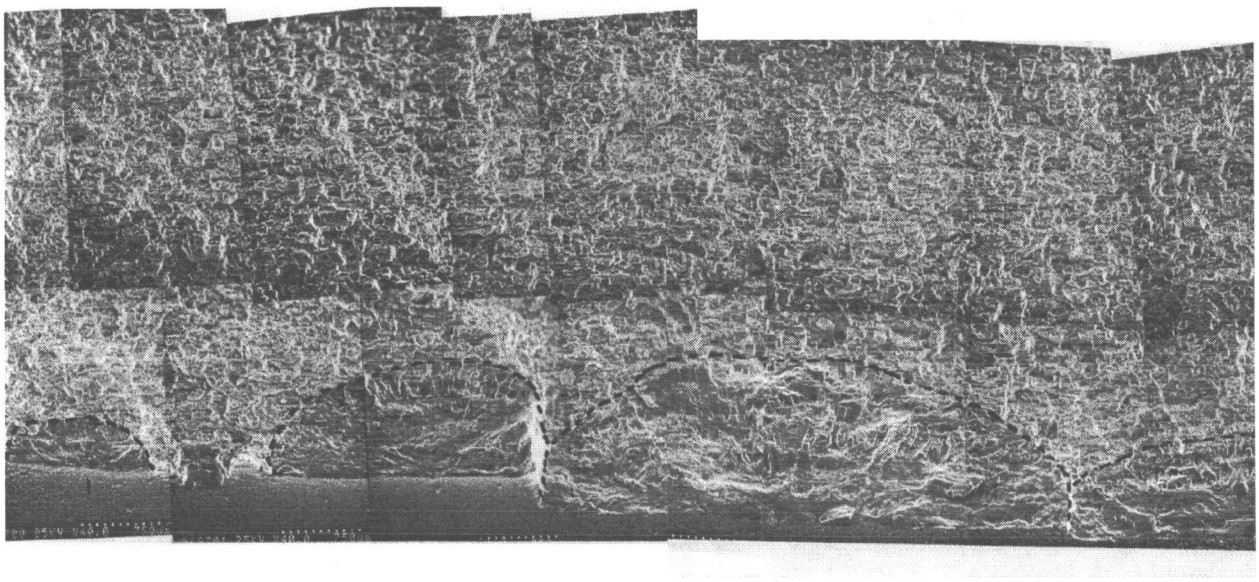

Figure 10. Fractograph of pre-corroded (336 hrs in 3.5 wt% NaCl solution) 7075-T7351 specimen fatigued at 276 MPa.

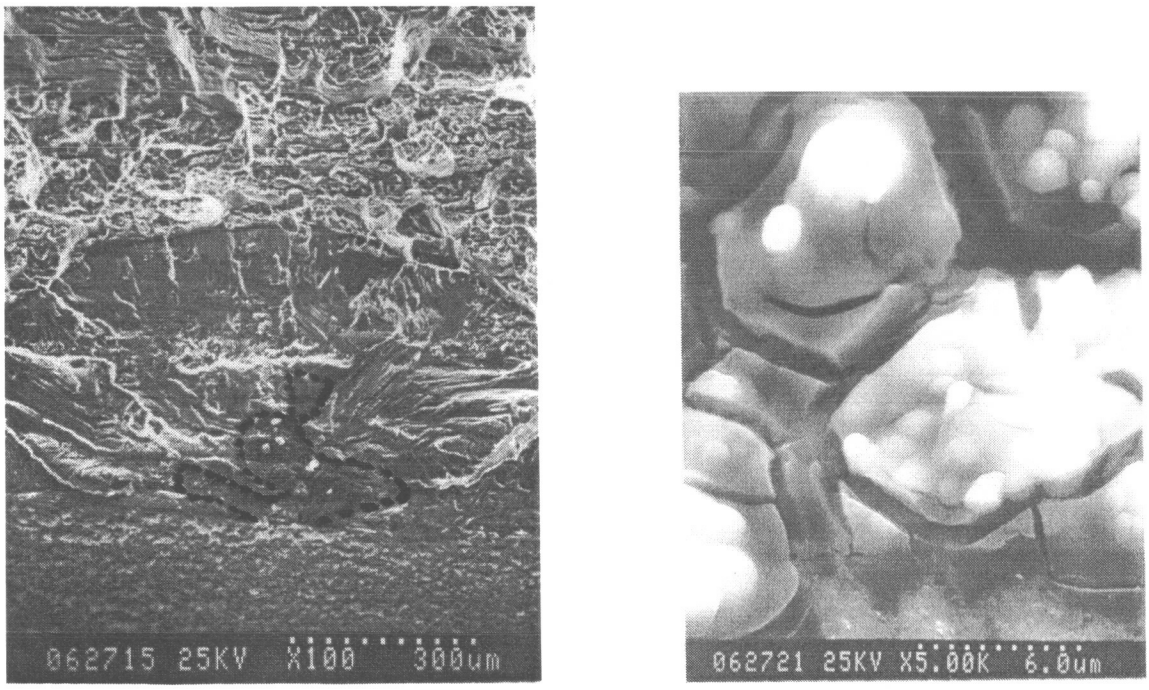

(A) (B)

Figure 11. Fatigue crack initiation region of specimen shown in Fig. 10.

For alloys that had been immersed in 3.5 wt% NaCl solution for 336 hrs and contained many deep corrosion pits on the free surface at the blunt-notch root, multiple fatigue cracks were always formed as shown for 7075 in Fig. 10. Here four fatigue cracks were initiated across the width of the specimen and each fatigue crack initiated from a corrosion pit. Fatigue crack initiation from a corrosion pit is better illustrated at higher magnification in Fig. 11.

Again, the relative flatness of the fatigue region can be readily distinguished from the fast overload fracture region. The river line pattern in the fatigue region was used to trace the crack initiation site which, in Fig. 11A, is a corrosion pit. At higher magnification, the corrosion pitted area has a unique "mud cake" corrosion product structure as shown in Fig. 11B and can be used to define the extent of the pitted region. The dashed line in Fig. 11A represents the boundary of the corrosion pit. It is important to note that while the width of the pit in Fig. 11A as measured from the root of blunt-notch surface is only about 60 μm, the interior depth and the width of this particular pit beneath the root surface are over 300 μm. Thus, the actual stress concentration from this pit would be significantly higher than those derived from analyses based on the surface pit dimensions and semicircular pit geometry. This observation also suggests that the pit size measurements from the surface such as those in Table 2 are of limited value for crack initiation and life prediction analyses. Instead, an average pit depth in the direction normal to the S plane, though very difficult to obtain, should be used.

CONCLUSIONS

Pit formation and fatigue crack initiation from corrosion pits and from constituent particles in 7075-T7351 and 7050-T7451 aluminum alloys were studied. 7075 contains both cathodic (C-type) $Al_{23}CuFe_4$ constituent particles and anodic (A-type) Al_2Cu particles while 7050 contains only the C-type Al_7Cu_2Fe constituent particles. In 3.5 wt% NaCl solution, corrosion pits were formed by the electrochemical reaction between the constituent particles and the surrounding matrix. Depending on whether these particles were cathodic or anodic relative to the alloy matrix, the pits formed as a consequence of matrix (around cathodic particles) or particle (for anodic particles) dissolution. Because these particles tend to cluster parallel to the rolling plane in the rolling direction, significant pit growth from pit coalescence was observed following prolonged exposure. The presence of these pre-existing corrosion pits significantly shortens the fatigue crack initiation life and decreases the threshold stress intensity of the alloy by as much as 50 percent. Post initiation analyses revealed that the actual pit depth is several times larger than that determined from the free surface and that multiple fatigue cracks always initiated from corrosion pits.

ACKNOWLEDGMENTS

The authors gratefully acknowledge many helpful discussions with Professor R.P. Wei of Lehigh University and Dr. Ming Gao of Mobil Corporation. This work was supported by the Office of Naval Research.

REFERENCES

1. D.G. Harlow and R.P. Wei, Eng. Fract. Mech., Vol. 59, 305(1998).
2. G.S. Chen, K.C. Wan, M. Gao, R.P. Wei, T.H. Flournoy, Mat. Sci. & Eng., A219, 126(1996).
3. M. A. Alodan and W. H. Smyrl, J. Electrochem. Soc., Vol. 144, L282(1997).
4. R.G. Buchheit Jr., J. P. Moran, and G.E. Stoner, Corrosion, Vol. 46, 610(1990).
5. K.K. Sankaran, B. Johnson, R. Perez, and K.V. Jata, Proc.1997 Tri-Service Conf. on Corrosion.

DETERMINATION OF THE CORROSIVE CONDITIONS PRESENT WITHIN AIRCRAFT LAP-SPLICE JOINTS

Karen S. Lewis and Robert G. Kelly
Center for Electrochemical Science and Engineering
University of Virginia
Charlottesville, VA 22903
phone: (804) 982-5790
fax: (804) 982-5799
KSL5F@virginia.edu

Robert S. Piascik
Mechanics and Materials Branch
NASA Langley Research Center
Hampton, VA 23681-0001

ABSTRACT

The complexity of airframe structure lends itself to damage resulting from crevice corrosion. Fuselage lap-splice joints are a particularly important structural detail in this regard because of the difficulty associated with detection and measurement of corrosion in these occluded regions. The objective of this work is to develop a laboratory corrosion test protocol to identify the chemistry to which lap joints are exposed and to develop a model of the corrosion within the joints.

A protocol for collecting and identifying the chemistry of airframe crevice corrosion has been developed. Capillary electrophoresis (CE) is used to identify the ionic species contained in corrosion product samples removed from fuselage lap splice joints. CE analysis has been performed on over sixty corrosion product samples removed from both civilian and military aircraft. Over twenty different ions have been detected. Measurements of pH of wetted corroded surfaces indicated an alkaline occluded solution. After determining the species present and their relative concentrations, the resultant solution was reproduced in bulk and electrochemical tests were performed to determine the corrosion rate. Electrochemical analyses of the behavior of AA2024-T3 in these solutions gave corrosion rates of up to 250 microns per year (10 mpy). Additional tests have determined the relative importance of each of the detected ions in model solutions used for future predictive tests. The statistically significant ions have been used to create a second generation solution.

Laboratory studies have also included exposure tests involving artificial lap joints exposed to various simulated bulk and crevice environments. The extent and morphology of the attack in artificial lap joints has been compared to studies of corroded samples from actual aircraft. Other effects, such as temperature and potential, as well as the impact of the environment on fatigue crack growth have also been studied.

1. INTRODUCTION

As the fleet of both commercial and military aircraft ages, damage caused by corrosion becomes a more pressing concern. The KC-135 is one aircraft for which life extension is an important issue. Built in the mid-1950s, these aircraft are now expected to continue flying until the year 2040. In 1990, Groner[1] estimated that corrosion maintenance was costing $185,000 per aircraft per year. With a fleet of over six hundred KC-135s still flying, this reaches over $110 million per year in repair costs. However, this is not

only a high cost issue, but also leads to a decrease in aircraft readiness because of the length of time aircraft spend in depots for repair and a possible loss of safety if the damage becomes severe.

Lap-splice joints are the regions of overlap on the fuselage of an aircraft where two pieces of aircraft skin are riveted together. This arrangement forms an occluded region in which detection of corrosion is especially difficult. Although much work is underway to improve non-destructive inspection, more information about the corrosion process is necessary to aid in setting reasonable inspection intervals which are currently based on calendar time. The current mentality when dealing with aircraft corrosion is "find it - fix it". This idea means that any time corrosion is found, it is either ground out or, if too severe, the panel of skin is removed or reinforced. Grinding out corrosion leads to concern about the decrease of skin thickness and resulting loss of strength. Although Scheuring[2] has shown that failure due to fatigue does not decrease if the corrosion is polished off of a sample, if the corrosion is not detected, Scheuring determined that the skins would fail in one-quarter of the expected number of cycles.

Most research addressing strength concerns is performed in 0.6 M sodium chloride solution. This research attempts to determine if this is a relevant environment for the testing of lap splice joints. In order to investigate the actual chemical environment present within these joints, corrosion product samples were dissolved and analyzed with capillary electrophoresis (CE). CE is a technique used extensively by the biological sciences and analytical chemists. There are several advantages to this technique. It can be used to analyze very small (< 30 μL) solution samples and can detect ions in concentrations as small as a few ppb. Depending on the electrolyte and run parameters chosen, CE can detect anions or cations. It is capable of both qualitative and quantitative analysis.

Development of a more relevant model environment aided in the determination of boundary conditions for future lifetime prediction models. Performing electrochemical and mechanical tests in the more relevant environment improved predictive ability. This work determined the chemical environment, the pH, the electrochemical environment, and the corrosion morphology found within aircraft lap-splice joints.

2. EXPERIMENTAL TECHNIQUES

2.1 SAMPLING METHODS

Two primary methods were used to obtain samples from aircraft for solution analysis. The scraping method was the field sampling method. When aircraft were undergoing repairs at an Air Logistics Center (ALC) or commercial aircraft refurbisher, small amounts (< 0.5 g) of corrosion product were removed from recently opened lap-splice joints. The product was removed by gently scraping it off using a new rubber policeman on a glass rod and it was collected in a clean Petri dish. It was important throughout this process that contamination was avoided because of the sensitive nature of the analysis technique. Upon arrival at the University of Virginia, the product was soaked in two milliliters of high purity water for twenty-four hours. The solution was then removed, filtered to remove any insoluble particles, and transferred to vials for ion analysis.

The second sampling method was a laboratory procedure which will be referred to as the microsampling method. Unopened aircraft doublers were sent to the University of Virginia where they were opened and exposed to a high humidity environment for twenty-four hours. Small amounts of solution (less than 5 μL) were removed using a microsyringe. These solutions were then diluted with 30 to 50 microliters of high purity water. This method allowed a better estimation of the dilution of the sample and easier control of contamination, but unopened aircraft skins are difficult to obtain.

2.2 ION ANALYSIS

Both sampling methods produced solutions that were analyzed with a Waters Quanta 4000 capillary electrophoresis system connected to a computer with Millennium 2.10 software. Capillaries were sixty centimeter long tubes of fused silica with an inner diameter of seventy-five micrometers and an effective length (from sample to detector) of fifty-two centimeters. Each capillary was prepared by purging for two minutes with 0.1 M KOH, followed by ten minutes with high purity water, and finally fifteen minutes with electrolyte. Four electrolytes were used to analyze each solution. For cations, UVCat1 and UVCat2 (Waters Corp. Milford, MA) were used and for anions, chromate and phosphate electrolytes were used.[3] Calibration curves with an R^2 value of 0.99 or greater were required for analysis using commercial standards from Analytical Products Group, Inc. (Belpre, OH). Sample injection was performed hydrostatically for thirty seconds at a ten centimeter elevation.

After analysis of sixty samples, a first generation solution was developed. This solution contained all of the ions detected by CE at their average concentrations. The solution was developed so that no additional ions were added except for H^+ and OH^- which were added as needed to maintain electroneutrality. The solution contained eighteen salts for a total of twenty-three ions. Through electrochemical testing, the ions which affected corrosion current density, corrosion potential, and corrosion morphology were determined. A final solution composition was thus determined. Only these ions were added to the final solution in the highest concentrations measured by CE. The highest concentration was used to observe the greatest effect possible in the electrochemical testing and was less than twenty millimolar for any ion.

2.3 ELECTROCHEMICAL TESTS

Electrochemical testing was used to determine any difference in the behavior of AA2024-T3 in CE-derived solutions versus sodium chloride. All tests were performed with a PAR Versastat (EG&G) connected to a computer with PAR M352 Softcorr II software. Testing was performed a flat cell with a one square centimeter working electrode of bare aluminum alloy 2024-T3 with 32 mil thickness. The coupons were wet polished by hand to a 600 grit finish with silicon carbide paper. Potentiodynamic tests were used to compare the open circuit potentials, pitting potentials, and passive behavior of 2024 in the first generation solution and 0.6 M sodium chloride.

A factorial design was used to develop two sets of experiments that could determine the statistically significant variables in control of important corrosion parameters. The first set of experiments studied six variables: chloride, nitrite, sulfate, bicarbonate, the pH, and "others". The "others" are all of the other anions detected by capillary electrophoresis added as a group. When a species was added to the solution (as determined by the factorial design), it was added in the highest concentration measured in the lap-joints by CE. The pH was either 3.5 or 9.0 with 9.0 chosen because it is the average ambient pH of our bulk analogue solutions and 3.5 chosen because it is the pH found in occluded regions on aluminum alloys with a boldly exposed cathode. Cyclic polarization scans were generated using a platinum counter electrode and a saturated calomel reference electrode. After testing, the samples were examined with optical microscopy to determine the presence of pits, the relative size and density of pits, and any changes in surface roughness. Changes in surface roughness were defined as the inability to see the scratches caused by the initial polishing. The results were analyzed using the statistical analysis program SPSS ver. 8.0 (Statistical Product and Service Solutions, Chicago, IL) to determine which species caused a statistically significant change (greater than 99% confidence level) in the parameters of interest. The second factorial investigated the ions that were in the "others" category in the first set of experiments. The variables were: fluoride, nitrate and phosphate, organics (formate, acetate, propionate, and butyrate), and the pH.

2.4 EXPOSURE TESTING

Model lap joints were constructed for tests to determine the corrosion morphology produced by exposure of 2024 to various solutions. The model lap joints were constructed from two sheets of AA2024-T3 cut to pieces one inch by three inches. The pieces were held together by two aluminum pop rivets. Studies were conducted for three months at three different temperatures in four solutions. The temperatures were room, 35, and 45 degrees Celsius. The solutions were the first generation solution, DI water, 0.6 M sodium chloride, and 1 mM hydrochloric acid and 4 mM $Cu(NO_3)_2$. Model joints were placed in solution so that the solution could wick into the joint by capillary action. Periodically, water was added to maintain a constant water level. After three months the bulk and occluded pH values were measured. The corrosion rate was calculated from weight loss data and corrosion morphology was examined with cross-sectional metallography. The model joints were cross-sections, mounted in epoxy, and polished to a one micron finish with diamond spray compounds. The samples were then etched with Keller's etch for 45 seconds before examination with an optical microscope.

Model joints were also used to determine the potential within a joint. Any area directly exposed to bulk solution was painted with XP-2000 Peelable Stop-off Laquer (Tolbar Products, Hope, AR) to force all electrochemical activity to occur within the joint. The same solutions were used as for the exposure tests. The tip of a saturated calomel reference electrode was contacted with solution at a marked spot and the potential was measured by contacting one lead of a voltmeter to the reference and the other to the model joint. This potential was measured weekly for three months.

2.5 EXPERIMENTAL pH

Coupons of 2024 were placed in four solutions and the pH was measured weekly for six months. The solutions used were DI water, 0.6 M sodium chloride, the first generation solution, and the first generation solution diluted one to ten. One hundred milliliters of each solution were used. Another experiment to show that a range of pH values could be measured using our techniques involved exposure of 1 mM HCl solution to a sheet of 2024. The pH of this solution was measured daily until no solution remained on the aluminum surface.

2.6 FATIGUE TESTING

A series of corrosion fatigue tests were conducted to study the effects of crevice environment on the growth of fatigue cracks in aluminum alloy 2024-T3 sheet. Constant amplitude fatigue crack growth tests were performed using the eccentrically-loaded single edge crack tension specimen (ESE(T) – formally the EC(T) specimen)[4]. The back-face strain compliance method was used to continuously monitor crack length and to verify closure free (intrinsic) crack growth. The constant cyclic stress intensity factor (ΔK) experiments were conducted using a computer controlled servohydraulic test machine that continuously adjusted the load to maintain the programmed ΔK at a constant stress ratio (R). The mid-half of the ESE(T) specimen (fatigue crack region) was encapsulated by a 1.5 liter O-ring sealed plastic chamber that contained the crevice solution at room temperature. Specimen electrochemical potential was potentiostatically controlled using a platinum counter and Ag/AgCl reference electrodes. A reservoir containing 20 liters of solution exposed to air was continuously circulated through the test chamber at a rate of 30 ml/min.

3. RESULTS AND DISCUSSION

3.1 ION ANALYSIS

In the sixty corrosion product samples analyzed to date, twenty-three ions have been detected. The result from analysis of a capillary electrophoresis sample is an electropherogram. The peaks represent the changes in UV absorbance that occur as the bands of each ion pass by the UV detector. Example electropherograms showing the common ions detected are shown in Figure 1. The commonly found anions were chloride, sulfate, nitrate, and bicarbonate. Aluminum, potassium, sodium, and magnesium were the commonly found cations. Common ions are those that are present in at least seventy-five percent of the sample solutions. It is important to note that the solution present within lap-splice joints is not simply sodium chloride, but is actually rather complicated. It is also not as concentrated as the standard 0.6 M sodium chloride solution. The sum of all of the highest ion concentrations is only 80 mM.

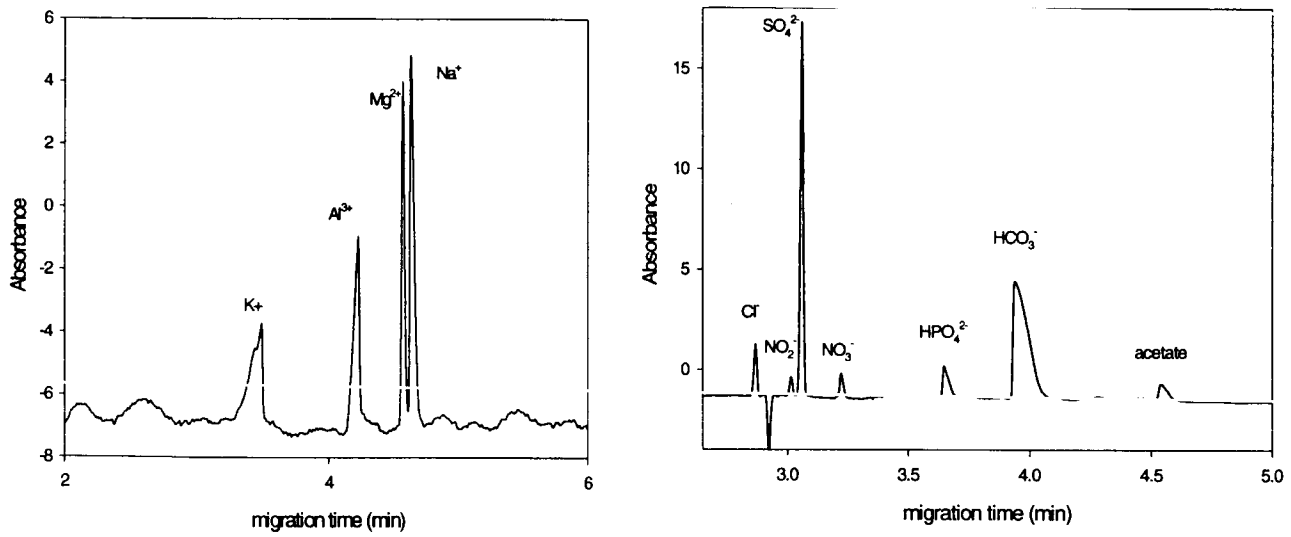

Figure 1: Example electropherograms showing common cations and anions

The ions present in the samples varied greatly even between samples from a single aircraft. Figure 2 shows two charts that illustrate the variability of the samples. The top chart shows the percentage of samples in which each anion is found. The range of concentrations also varies between samples. The lower chart shows the number of samples that contained a concentration of chloride in each range. Like ocean water, there is not a single solution that will have the exact ions and concentrations as every sample taken. Instead, our goal has been to develop a model solution that recreates the corrosion morphology and important electrochemical parameters that exist within actual lap-splice joints. A solution derived from the CE results better reproduced the corrosion environment found within these joints and so electrochemical and mechanical tests performed in this solution will better examine the conditions to which lap-splice joints are exposed.

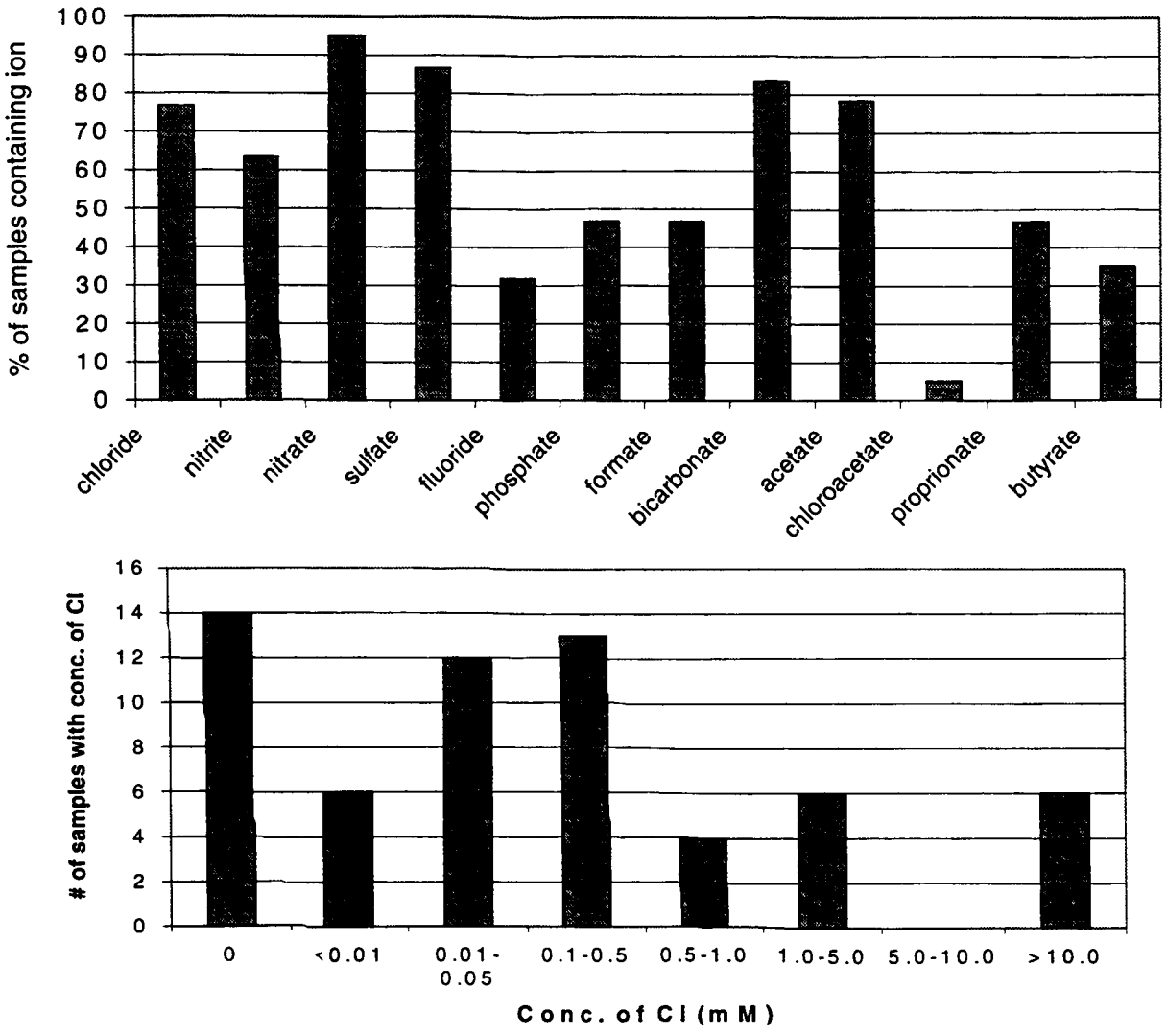

Figure 2: Variability of anions and concentrations detected by capillary electrophoresis

3.2 ELECTROCHEMICAL TESTING

The initial testing demonstrated that the electrochemical behavior of 2024-T3 in the first generation solution was very different from that in sodium chloride. As shown in Figure 3, the sample tested in 0.6 M sodium chloride did not passivate, but was immediately pitting while the sample run in the first generation solution has about an 600 mV passive region. This passive region give the sample in the first generation solution a higher pitting potential (about -0.2 V_{SCE}) than in the sodium chloride where the sample actively pits at all potentials above the open circuit (-0.6 V_{SCE}).

The results of the two factorial designs from the cyclic polarization scan data are shown in Table 1. The arrows indicate the direction in which the parameter was changed with the increase of that variable. The variable listed first for each parameter was the one that was found to be the most significant. All of the investigated pitting parameters (presence, size, and density) depended solely on the chloride concentration, but chloride was not a dominant factor in all of the studied parameters. This reinforces the idea that testing in sodium chloride solution is insufficient. This information allowed for the

determination of the recommended solution composition containing only the significant ions (20 mM chloride, 4 mM nitrite, 4 mM bicarbonate, and 2 mM fluoride at pH 9.0). The factorial also demonstrated that even in dilute solutions (<80 mM = total ionic concentration) the impact of individual ions on the corrosion rate, potential, and morphology could be observed.

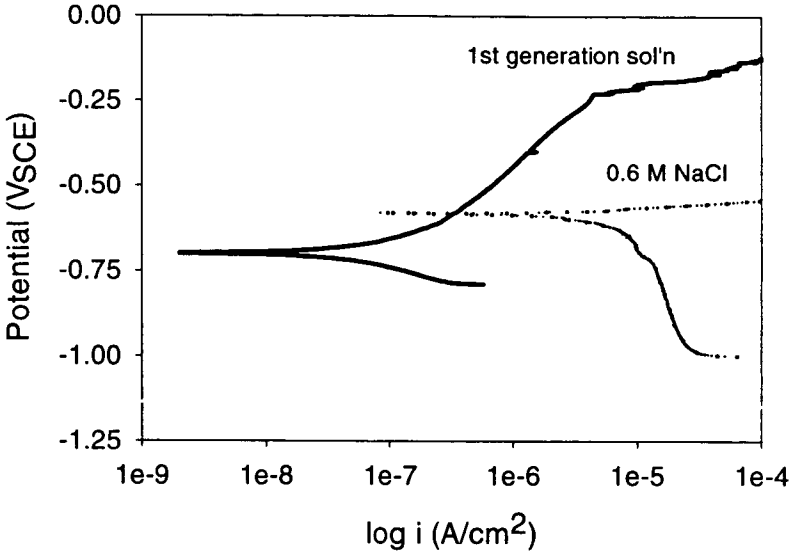

Figure 3. Comparison of electrochemical behavior of AA2024 in 0.6 M NaCl and the 1st generation solution

TABLE 1. Results from the factorial design analyses

Parameter	significant variables
i_{corr}	$pH\downarrow$, $F\uparrow$, $NO_2^-\uparrow$
E_{corr}	$Cl^-\downarrow$, $HCO_3^-\downarrow$, $NO_2^-\uparrow$
pitting during polarization scan	$Cl^-\uparrow$
increased surface roughness	$HCO_3^-\uparrow$, $pH\uparrow$

3.3 EXPOSURE TESTING

Exposure of model joints to the test solutions allowed for comparisons of the resulting corrosion morphology and calculated corrosion rates. Along with examination of corroded model lap joints, doubler samples were studied. Cross-sectional metallography determined that the most common corrosion morphology in the doubler samples is general corrosion. In about half of the doublers studied, the aluminum clad layer, a thin layer of pure aluminum used for corrosion prevention, was still visible. In one of the eleven doubler samples examined, pitting corrosion was found. Also on this doubler intergranular corrosion was evident near the spot welds. The morphology of models exposed to sodium chloride solution was well-defined pitting. Within models exposed to the first generation solution, uniform corrosion similar to that observed in the doubler samples was observed.

Both the bulk and occluded pH were measured at the end of the temperature study. The bulk pH was measured with a pH meter and glass electrode while the occluded pH was measured with pH paper. As can be seen in Table 2, the occluded pH in all solutions approached a value of 8.0. This agrees with pH measurements taken directly of wetted doublers that were corroded in the field and with the pH of our CE derived solutions which are also mildly alkaline. From the weight loss data, the corrosion rates were calculated. These rates are shown in Table 2 and indicate that corrosion rate does not increase significantly with temperature. Additional research is underway to investigate the dependence.

TABLE 2. Results from exposure test at three temperatures

solution	temperature	bulk pH	occluded pH	μm/yr (mpy)
DI water	room	7.2	8.0	177.0 (7.1)
1st generation	room	8.5	7.7	227.0 (9.1)
NaCl	room	7.3	8.0	256.3 (10.2)
HCl+Cu	room	2.5	7.7	286.7 (11.5)
DI water	35 C	7.5	7.7	217.2 (8.7)
1st generation	35 C	8.5	7.7	217.2 (8.7)
NaCl	35 C	7.6	8.0	294.3 (11.8)
DI water	45 C	7.2	8.0	196.6 (7.8)
1st generation	45 C	8.7	8.0	220.5 (8.8)

The potential within model lap joints was measured over thirty days. As shown in Figure 5, the occluded potential reached a value above the open circuit potential of AA2024 when boldly exposed to the same solution for five hours. The open circuit potentials of AA 2024-T3 in DI water is -0.4 Volts, in CE-derived solutions is -1.0 Volts, and in sodium chloride solution is -0.7 V_{SCE}. The occluded potentials of model joints that had wicked in these solutions were all above -0.3 Volts. The potentials have been used in fatigue crack growth experiments to simulate more complete environmental conditions.

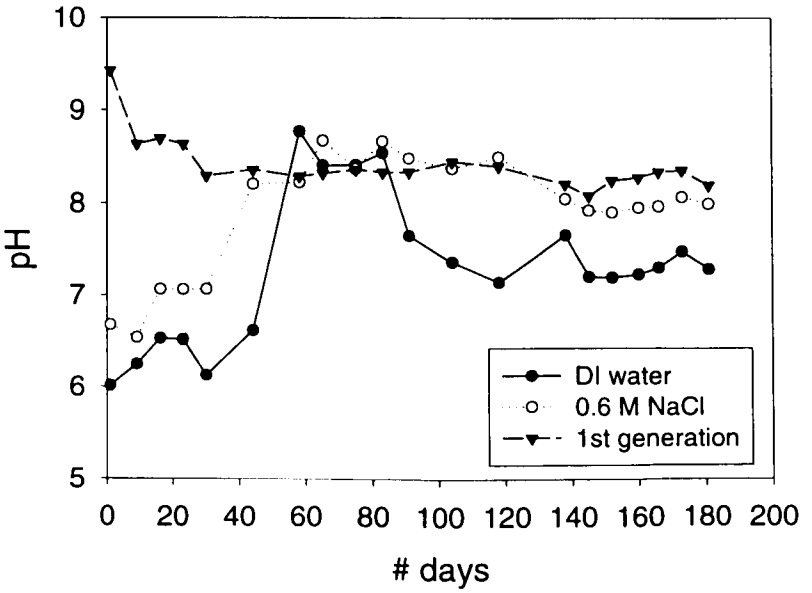

Figure 5. Occluded potentials of model joints over time

3.4 EVOLUTION OF pH

As shown in the exposure testing, the occluded pH of model joints approaches 8.0 after a three month exposure. The pH of similar solutions exposed to a piece of 2024 with ambient aeration, also approaches a mildly alkaline pH value. Figure 6 shows the pH evolution of these solutions over a 180 day exposure. All four solutions reached a pH of between 7.5 and 9.0. It is important to note that in both this set of experiments and the temperature study that not only did the lower pH solutions rise to a higher pH, but also the higher pH solutions also decreased to this mildly alkaline pH value.

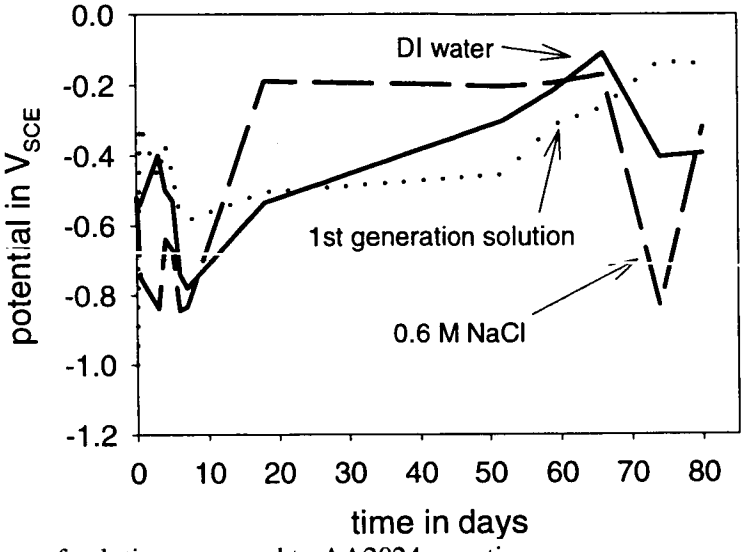

Figure 6. pH values of solutions exposed to AA2024 over time

When 0.5 mL of one millimolar hydrochloric acid was placed on a sheet of 2024-T3 and the pH was measured over time, the pH also increased with time as shown in Figure 7. This shows that a large range of pH can be measured with pH paper and again confirms the tendency of solutions to increase in pH when exposed to this alloy.

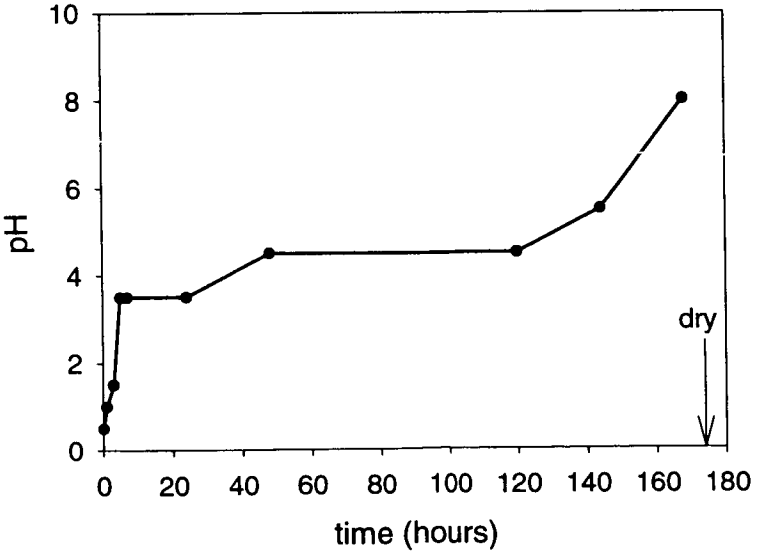

Figure 7. Values of pH over time of HCl solution on AA2024

3.5 FATIGUE TESTING

The objective of the first series of corrosion fatigue tests was to determine the cumulative affects of the compound groups listed in Table 3 on the fatigue crack growth (FCG) characteristics of alloy 2024. Eleven constant ΔK tests (5.5 MPa$\sqrt{m}$, R=0.5, f=2Hz) were performed in lab air followed by distilled water and nine solutions containing the additions listed in Table 3. A stress ratio of 0.5 was selected to limit the effects of crack-tip closure and thereby produce intrinsic environmental FCG rates. To study the effect of each compound group, changes in crack growth rate were monitored as each of the nine sets of compounds was added to the reservoir of distilled water (combined with the previously added compounds). The series of tests were designed to expose the crack to more benign environments (compounds) initially followed by increasingly more aggressive compounds. The test results shown in Table 3 reveal no difference in the intrinsic fatigue crack growth rate characteristics of alloy 2024 for air, distilled water, and eight of the nine compounds over a pH range of 5.5 to 10.5. A small decrease in FCG rate was observed after adding compound group 2 to the solution.

TABLE 3. TEST SERIES #1 ENVIRONMENTS

Group #	Compounds Added	pH	FCG rate (mm/cycle) $x10^5$
Air	----------	------	2.4
H_2O	----------	5.5	2.5
1	$Al(OH)_3$, $Ca(OH)_2$, KOH, NaOH	10.5	2.5
2	$SrCO_3$, $CuSO_4$, $MnCl_3 4H_2O$, $ZnC_2O_2H_3$, $MgCO_3 3H_2O$	10.1	1.5
3	$Al_2F_6 H_2O$, NaF, $NaC_3H_7CO_2$, $NaC_2H_5CO_2$	10.1	2.4
4	$AlCl_3 6H_2O$	9.8	2.6
5	KNO_3	9.7	2.8
6	$NaNO_2$	9.4	2.4
7	K_2SO_4	9.4	2.2
8	$K_2H_2PO_4$	7.8	2.3
9	$NaHCO_3$	8.1	2.2

The second series of constant ΔK tests determined the affect of electrochemical potential on the FCG rate in the crevice solution containing all the compound groups listed in Table 3. Thirteen fatigue crack growth tests were conducted; test #1 was performed in laboratory air and the remaining twelve crack growth tests were conducted in the crevice solution at different constant electrochemical potentials. The tests were conducted at potentials both cathodic to and anodic to the corrosion potential of -575 mV_{SCE}. Figure 8 is a summary of results for the constant ΔK test; here, a change the slope of the crack length versus load cycles plot represents a change in FCG rate. Figure 8a shows that similar intrinsic FCG rates were obtained for laboratory air and crevice environments at cathodic potentials of -1015 mV_{SCE}, -815 mV_{SCE}, -615 mV_{SCE} and an anodic potential of -415 mV_{SCE}. Figure 8b is an enlargement of Figure 8a showing the results of tests 6 - 13. As the potential was changed from -415 mV (test #6) to -215 mV (test #7), the FCG rate initially increased and then rapidly decreased. The rapid decease in FCG rate (region A in Figure 8b) corresponded to the observation of copious amounts of corrosion product along the outside surface of the fatigue crack and a corresponding increase in the measured level of crack closure. This behavior was reproduced at regions B and C in Figure 8b where the fatigue crack stopped growing when exposed to the same highly corrosive anodic (-215 mV) environment. Presumably, the initial increase in intrinsic (closure free) FCG resulted from the additional chemical crack-tip driving force produced by an increase in crack-tip corrosion at an anodic potential of -215 mV_{SCE}. The retardation in FCG rate at -215 mV_{SCE} was caused by the rapid buildup of corrosion products that

produced crack closure and a corresponding decrease in the mechanical crack-tip driving force. Figure 8b also shows that loading frequency influences the observed corrosion effects, possibly suggesting complex time dependent behavior.

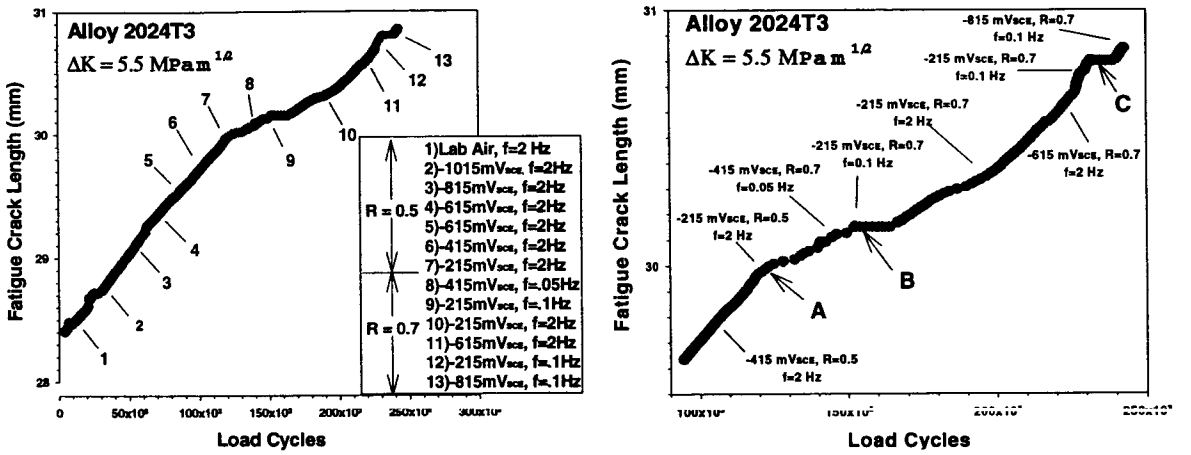

Figure 8. A summary of constant ΔK test results showing the effect of electrochemical potential on the fatigue crack growth characteristics of alloy 2024 exposed to a laboratory simulated crevice corrosion environment.

CONCLUSIONS

By collecting samples directly from field-exposed aircraft, the environment to which the interior of a lap-splice joint is exposed has been investigated. Analyses of the solutions formed by dissolving corrosion product sample have determined that the occluded solutions found within these aircraft joints are complicated, dilute, and mildly alkaline. They are complicated as over twenty different ions have been detected in the sample solutions. The total concentration of all ions is less than 80 mM which is significantly more dilute than 0.6 M sodium chloride that is typically used in such testing. By exposure testing and direct measurement of the surface of a corroded aircraft skin, the pH of the solution was found to be mildly alkaline. A bulk analogue solution with these characteristics has been developed using the information obtained by analyzing solutions derived from scraping samples with capillary electophoresis and used for electrochemical and exposure testing. Based on statistical analyses of the effects of each ion on corrosion current density, potential, and morphology, the first generation solution was simplified to a solution containing 20 mM chloride, 4 mM nitrite, 4 mM bicarbonate, and 2 mM fluoride at pH 9.0. Model lap joints were used to determine that the occluded potential within a lap joint is greater than the open circuit potential of 2024 exposed to the same solution. Potentiodynamic scans performed on AA2024 using CE-derived solution and 0.6 M sodium chloride had determined that the electrochemical behavior of 2024 is significantly different in the two solutions. There is also an important difference in the corrosion morphology of model lap joints exposed to the two solutions for three months. General corrosion occurs when model lap joints are exposed to CE-derived solutions, whereas pitting occurs when the model joints are exposed to 0.6 M NaCl. This difference is important because the observed corrosion morphology in skins obtained from actual aircraft is general corrosion. In fatigue testing, the observation that the occluded potential is above the open circuit potential of boldly exposed surfaces has proven to be important in producing corrosion product and leading to crack closure. All of these observations indicate that the CE-derived solutions are more relevant to the corrosion environment found within actual aircraft lap-splice joints and should be used for future electrochemical and mechanical testing.

ACKNOWLEDGMENTS

The authors would like to acknowledge Mr. Scott Willard who obtained all of the field samples of corrosion product for analysis. We would also like to thank Jim Krol of the Waters Corporation and EG&G for equipment support. The doubler samples and lap-splice joints provided by Don Neiser of Oklahoma City ALC, Mike Hahn of Northrop Grunman, and Steve Kaldron of NCI are also greatly appreciated.

REFERENCES

[1]Groner, D.J. and D.E. Neiser. "U.S. Air Force Aging Aircraft Corrosion". *Canadian Aeronautics and Space Journal.* Vol. 42, No. 2, June 1996 pp. 63-67.

[2]Scheuring, Jason N. and Alten F. Grandt. "An Evaluation of Aging Aircraft Material Properties". Presented at 1995 ASME International Mechanical Engineering Congress and Exposition. Nov. 1995.

[3]*Waters Quanta 4000 Capillary Electrophoresis Operator's Manual.* Manual number 250119. Millipore Corporation. Millford, MA. Revision 0, July 1990.

[4]Piascik, R.S., Newman, J.C., Jr., and Underwood, J.H., "The Extended Compact Tension Specimen", *Fatigue and Fract. Engng.. Mater. Struct.*, Vol. 20, No. 4, 1997, pp. 559-563.

DESIGN OF VISUALLY INSPECTABLE FUSELAGE SKIN REPAIRS

P. C. Chen and D. B. Roderick
Interpacific Technology, Inc.
Alameda, CA 94501 U.S.A.

ABSTRACT

A new approach which uses the concept of visually inspectable repairs has been employed to design fuselage skin repairs. A visually inspectable fuselage skin repair is one for which a crack emanating from the fastener hole with the largest fastener load in the skin is visually inspectable from the most accessible side of the skin, thus reducing the reliance on nondistructive inspection (NDI) techniques to detect cracks prior to catastrophic failure.

This paper presents the guidelines used in designing visually inspectable repairs for fuselage skins with different damage configurations, i.e., skin with a circular hole, skin with a rectangular cutout, and skin with a crack. It discusses why a skin repair is or is not visually inspectable, how a nonvisually inspectable skin repair can be made visually inspectable, and what guidelines need to be followed to design a visually inspectable fuselage skin repair.

INTRODUCTION

Fuselage skin repairs that are fastened to the skin have been designed based on equal or better static strength considerations. This repair design induces fastener loads and subsequent bearing stresses on the fastener holes in the skin. The bearing stress on the fastener holes reduces the fatigue life of the fuselage skin compared to that of the fuselage skin without repairs[1]. Any cracks which may occur hence will most likely occur at the fastener holes. The presence of cracks reduces the strength of the airframe. Since aircraft are designed to a given strength, it is essential that cracks which would reduce the strength below the design level be detected in time to prevent catastrophic failure.

Fuselage skin repairs commonly utilize either a single external doubler (Figure 1), two staggered external doublers (Figure 2), or an internal doubler and an external doubler that are the same length (Figure 3). The largest fastener load in the skin for these repairs will be in a fastener location that is usually not visually detectable from the most accessible side of the skin. This is because, in each of these repair cases, the fastener hole in the skin which experiences the largest fastener load is covered by the external doubler. As such, the potential crack at this fastener hole in the skin can propagate undetected until the crack emerges from under the external doubler. The existence of such a long crack may cause catastrophic failure of an airplane component if not detected in time. Of course, nondestructive inspection (NDI) techniques can be used to detect the cracks prior to catastrophic failure. However, such techniques are costly, and their

accuracy depends on the experience of the inspector. A new approach which uses the concept of visually inspectable repairs[1] has been employed to design fuselage skin repairs. A visually inspectable fuselage skin repair is one for which a crack emanating from the fastener hole with the largest fastener load in the skin is visually inspectable from the most accessible side of the skin (Figure 4), thus reducing the reliance on NDI techniques to detect cracks prior to catastrophic failure.

The key feature of a visually inspectable repair is to distribute fastener loads in the repair so that the critical fastener which applies the largest loads and applies the largest bearing stress to the fastener hole in the skin is in a visually inspectable position. Commonly used fuselage skin repairs do not meet this requirement and therefore are not visually inspectable.

GENERAL GUIDELINES FOR VISUALLY INSPECTABLE FUSELAGE SKIN REPAIRS

There are many design factors which affect the visual inspectability of a fuselage skin repair. However, no single factor will render a repair visually inspectable. Rather, it is a combination of factors in the repair design that result in a visually inspectable repair. The example repairs in Figure 5 illustrate the effects of these design factors, as given below. The fastener loads were determined using finite element analysis. The Case 1 repair of Figure 5 is the base repair case. Other repair cases highlight the uses of various design factors. Comparisons of the fastener loads of the base repair case to that of the other repair cases illustrate the effects of various design factors on designing visually inspectable repairs. For the repair cases in Figure 5, the fastener with the largest load is the critical fastener.

a. **Repair Member Thickness.** The thicker the repair member, the more load the member will carry, and the more load the critical fastener will carry. This effect is illustrated by comparing the fastener loads in Case 1 and Case 2 of Figure 5.

b. **Fastener Size.** The larger the diameter of a fastener, the more load the critical fastener will carry. This effect is illustrated by comparing the fastener loads in Case 1 and Case 3 of Figure 5.

c. **Fastener Spacing.** The larger the spacing between the leading fastener row and the second fastener row, the larger the load carried by the leading fastener. Also, the larger the spacing between fasteners in the leading fastener row, the larger the load that the leading fasteners will carry. Case 1 and Case 4 of Figure 5 illustrate the effects of fastener spacing on fastener loads.

d. **Number of Fasteners.** Increasing the number of fastener rows used in a repair decreases the loads in all of the fasteners. However, this causes the critical fastener of a repair with more fasteners to proportionally carry a larger load. This effect is illustrated by comparing the fastener loads in Case 1 and Case 5 of Figure 5

e. **Repair Configuration.** Different repair configurations have different fastener load distributions which change the locations of the critical fasteners. If the critical fastener

locations are not visually inspectable, the repair is not visually inspectable, as illustrated in Figure 6(a). This occurs because the fasteners that are in visually inspectable locations in the skin, indicated as the leading fasteners in Figure 6(a), are in single shear, whereas fasteners in nonvisually inspectable locations in the skin are in double shear. Since the fasteners in double shear usually carry more load than the fasteners in single shear, as is the case in Figure 6(a), the critical fastener location in the skin is hidden by the external doubler on the most accessible side of the skin. Therefore, the repair is not visually inspectable.

The repair design of Figure 6(b) is visually inspectable. This is because the leading fasteners are also the critical fasteners due to the fact that, by changing the repair configuration (adding an additional row of fasteners at the ends of the repair) the single shear loads of the leading fasteners are larger than the largest double shear loads in this repair.

VISUALLY INSPECTABLE FUSELAGE SKIN REPAIRS

Common fuselage skin repairs for skin with a circular hole, skin with a crack, and skin with a rectangular cutout are respectively shown in Figures 7, 9, and 11. These fuselage skin repairs are not visually inspectable because the leading fasteners, which for these repair configurations are also the critical fasteners, are not visually inspectable from the external, or most accessible, side of the skin. If cracks occur at these fastener holes, the cracks are not detectable by visual means until the cracks extend beyond the edges of the repair.

The above nonvisually inspectable fuselage skin repairs can be made visually inspectable by using different repair configurations as shown respectively in Figures 8, 10 and 12. These fuselage skin repairs are visually inspectable from the external side of the skin because once the cracks occur, they are visually inspectable.

It is seen from Figures 7 and 8, Figures 9 and 10, and Figures 11 and 12 that the differences in repair configurations between nonvisually inspectable and visually inspectable fuselage skin repairs are small, the efforts required to design these two types of repairs are about the same, and yet the visually inspectable repairs reduce the reliance on NDI techniques to detect cracks prior to catastrophic failure of the skin. The visually inspectable fuselage skin repairs are therefore more desirable and economical for maintaining aircraft safety.

REFERENCES

1. T. Swift, "Repairs to Damage Tolerant Aircraft," Structural Integrity of Aging Aircraft, eds. S. N. Alturi, S. G. Sampath, and P. Tang, Springer-Verlag, 1991.

ACKNOWLEDGMENTS

This work was sponsored under Contract No. DTFA03-94-C-00005 by the U.S. Federal Aviation Administration.

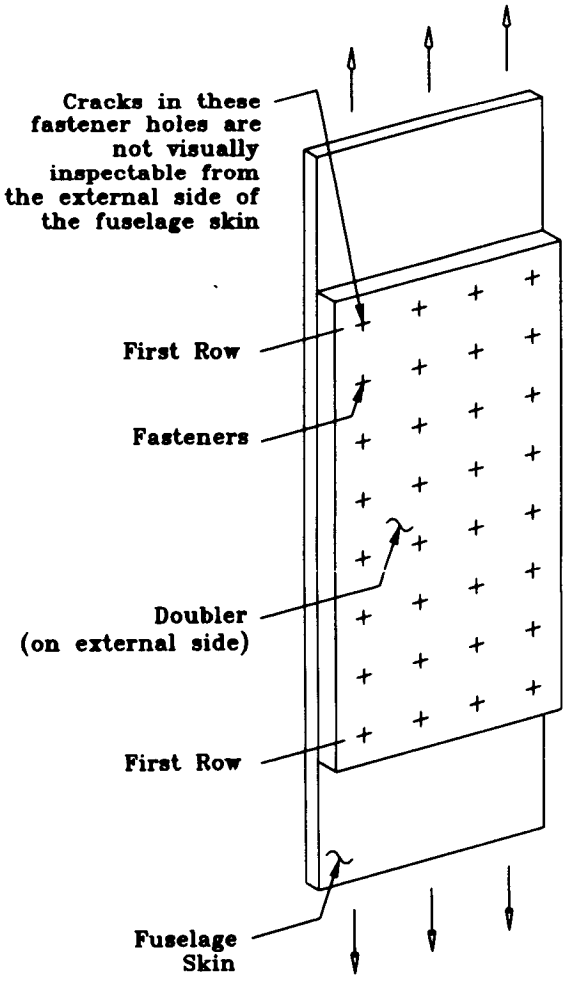

Figure 1. A Doubler on the External Side of the Fuselage Skin

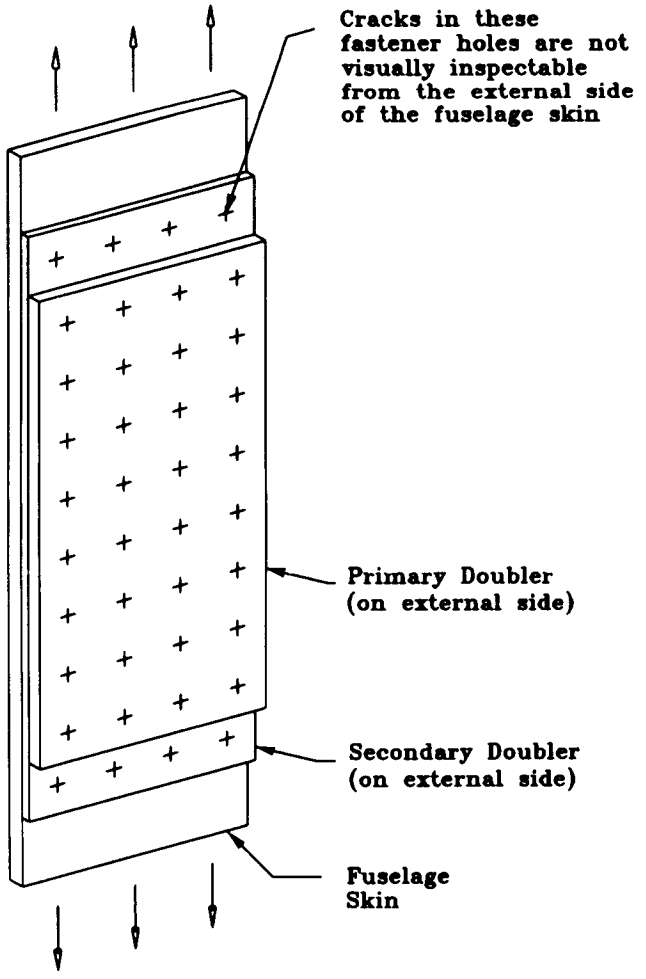

Figure 2. Two Staggered Doublers on the External Side of the Fuselage Skin

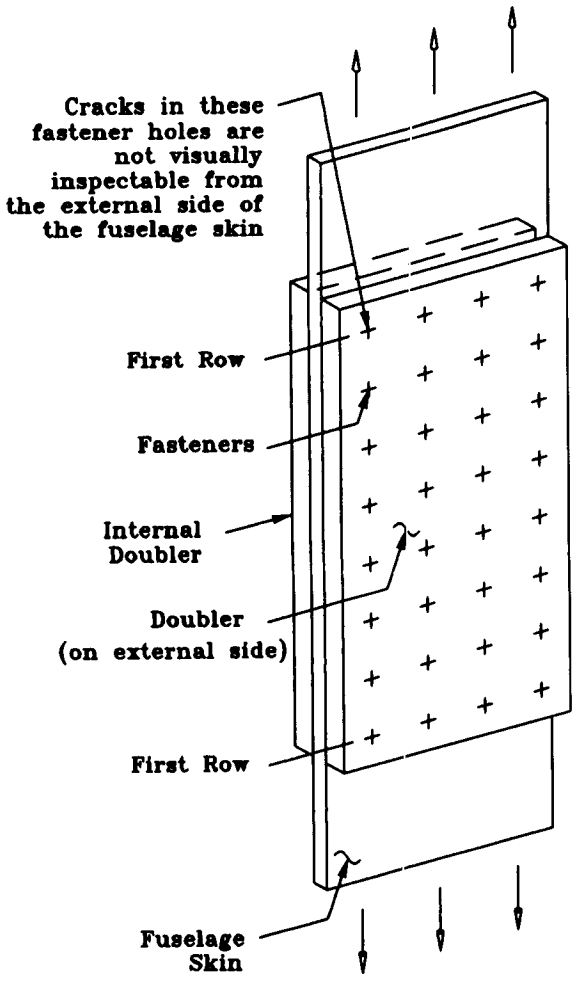

Figure 3. Internal and External Doublers of the Same Size

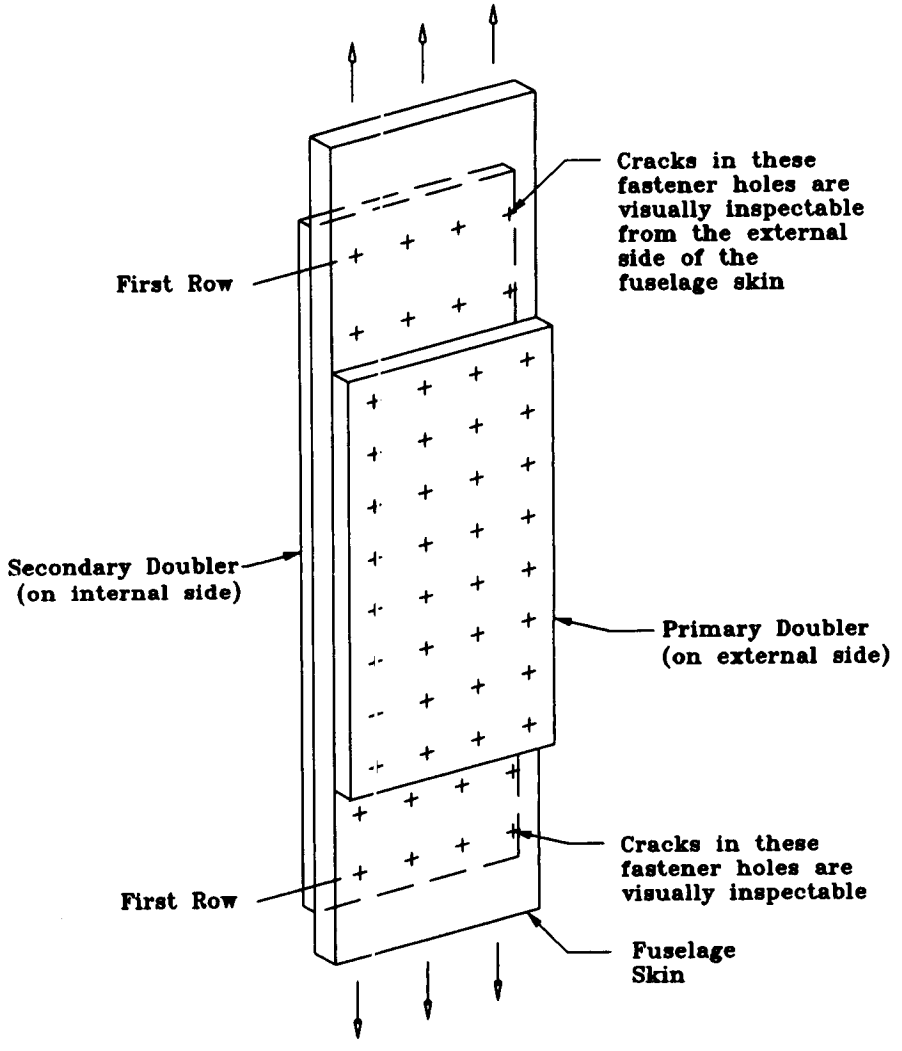

Figure 4. Visually Inspectable Fuselage Skin Repair

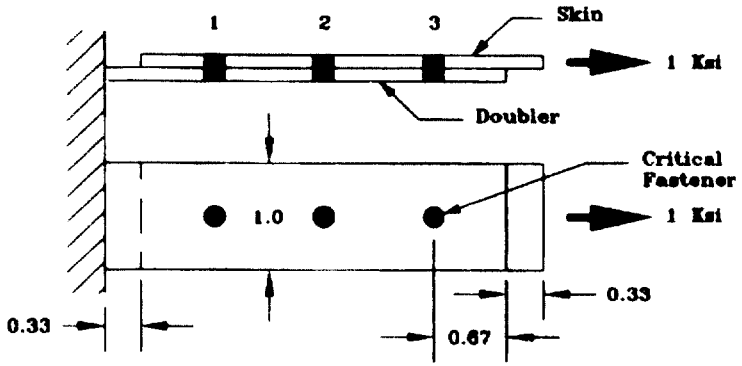

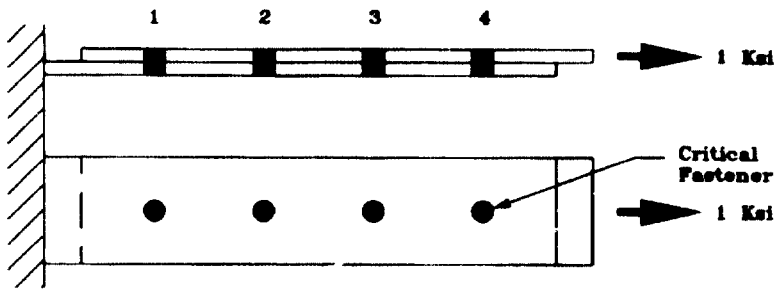

Note: Dimensions apply to Sketches (a) and (b)

Sketch (a) Sketch (b)

Description of Repair Cases					
Case	1	2	3	4	5
Repair Description	Base Repair	Thicker Doubler	Smaller Fasteners	Larger Fastener Spacing	One Additional Fastener
Applys to Sketch	(a)	(a)	(a)	(a)	(b)
Skin (in)	0.040	0.040	0.040	0.040	0.040
Doubler (in)	0.040	0.050	0.040	0.040	0.040
Fastener Diameter (in)	3/16	3/16	5/32	3/16	3/16
Fastener Spacing (in)	1.00	1.00	1.00	1.20	1.00
	Fastener Loads (Lbs)				
Fastener No. 1	14.147	13.456	14.112	14.278	11.767
Fastener No. 2	11.669	11.739	11.770	11.427	8.228
Fastener No. 3	14.154	14.805	14.118	14.296	8.234
Fastener No. 4	-	-	-	-	11.770
Total Loads (lbs)	39.97	40.00	40.00	40.00	39.99

Figure 5. Effect of Various Design Factors on Fastener Loads

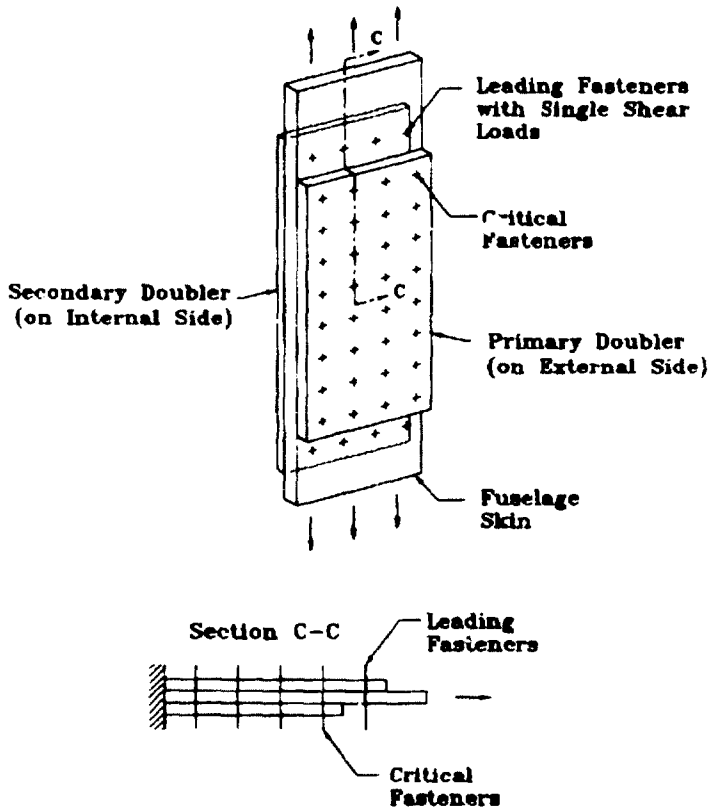

(a) Repair is not visually inspectable because the critical fasteners are not visually inspectable in the skin

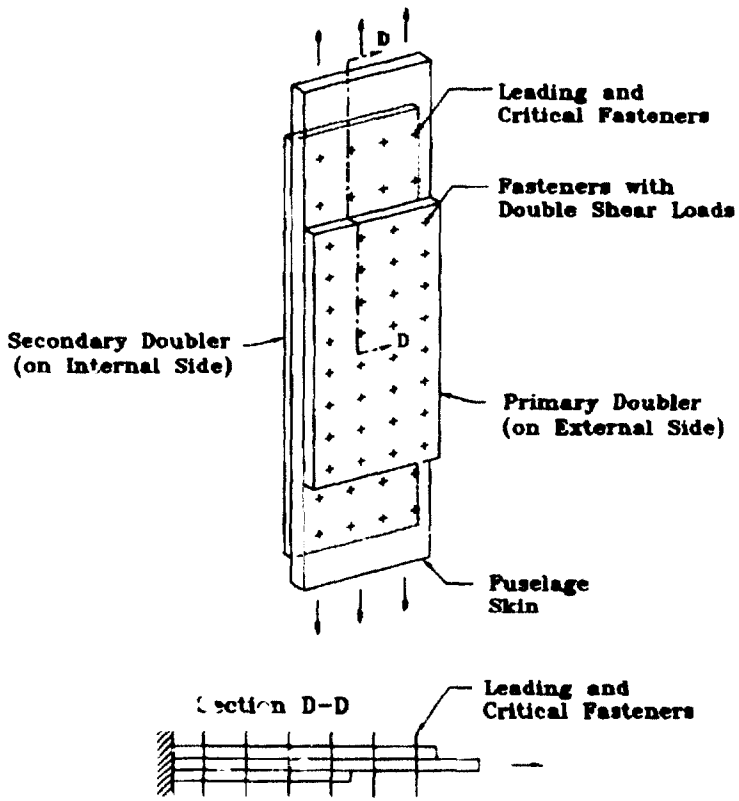

(b) Repair is visually inspectable because the critical fasteners are visually inspectable in the skin

Figure 6. Visual Inspectability of Different Repair Configurations

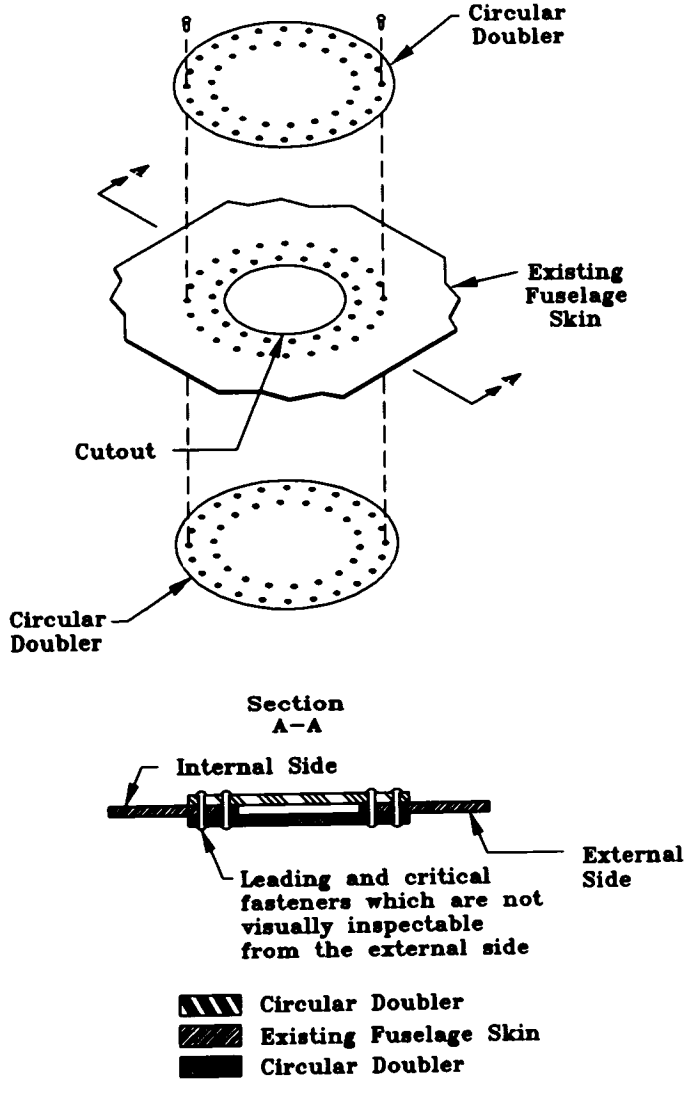

Figure 7. Nonvisually Inspectable Fuselage Skin Circular Cutout Repair

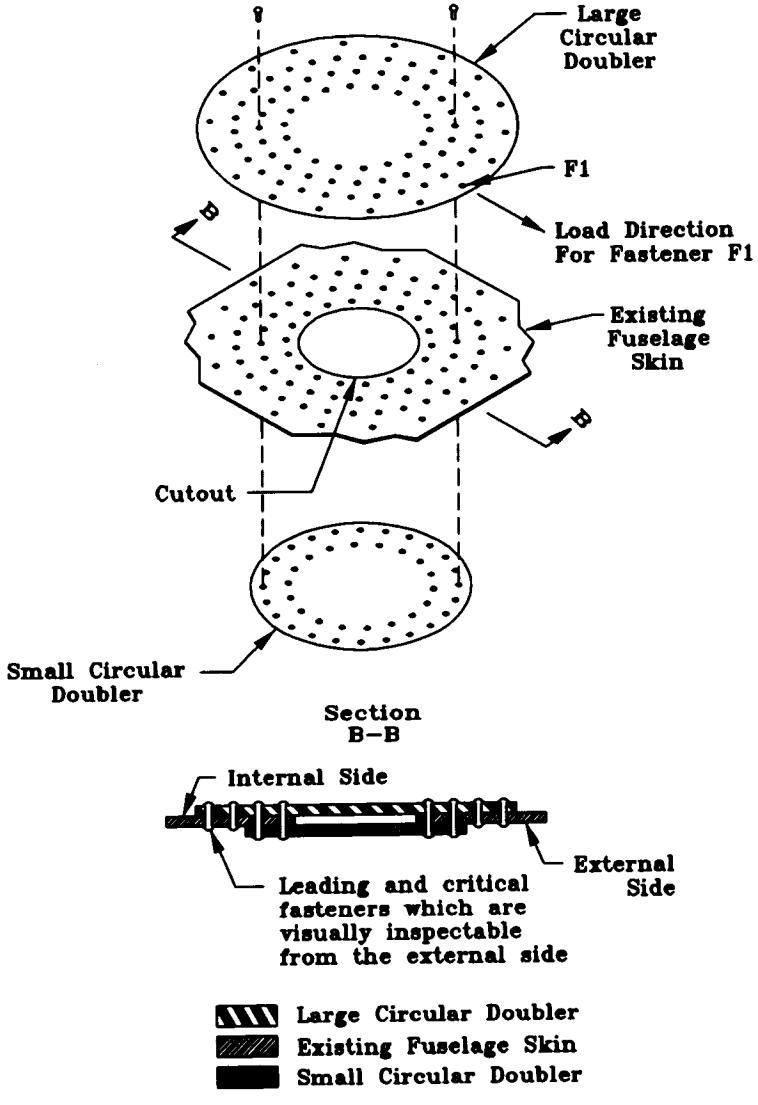

Figure 8. Visually Inspectable Fuselage Skin Circular Cutout Repair

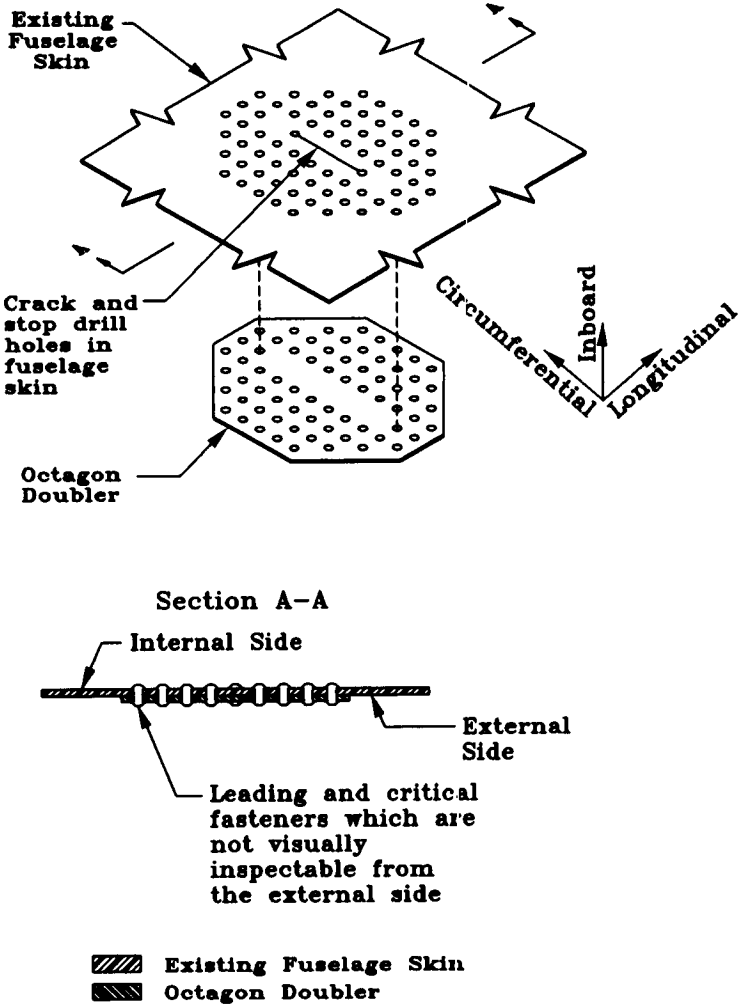

Figure 9. Nonvisually Inspectable Octagon Fuselage Skin Repair

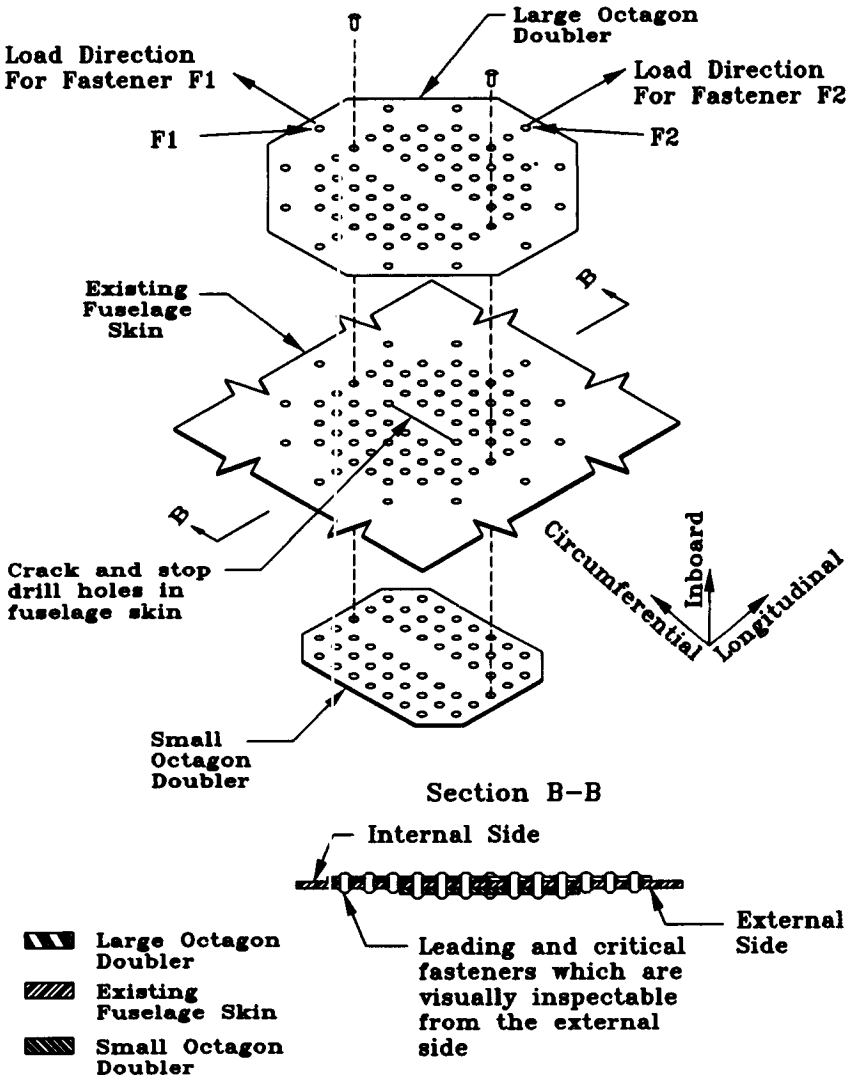

Figure 10. Visually Inspectable Octagon Fusleage Skin Repair

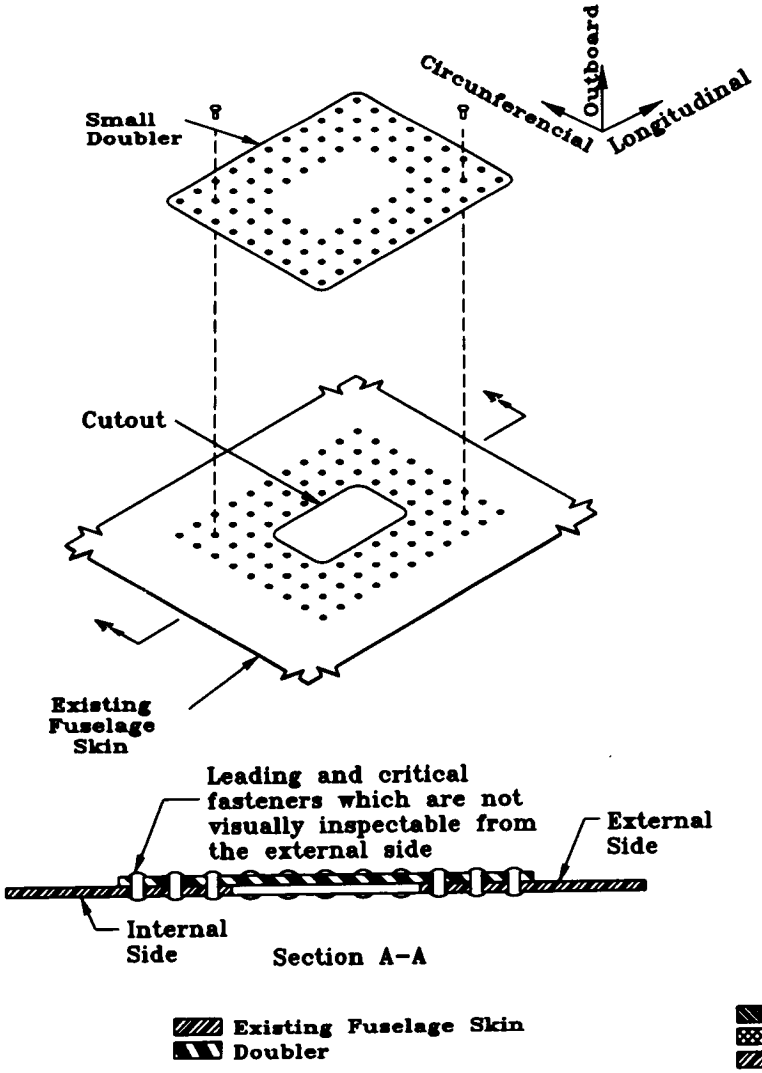

Figure 11. Nonvisually Inspectable Fuselage Skin Panel Repair

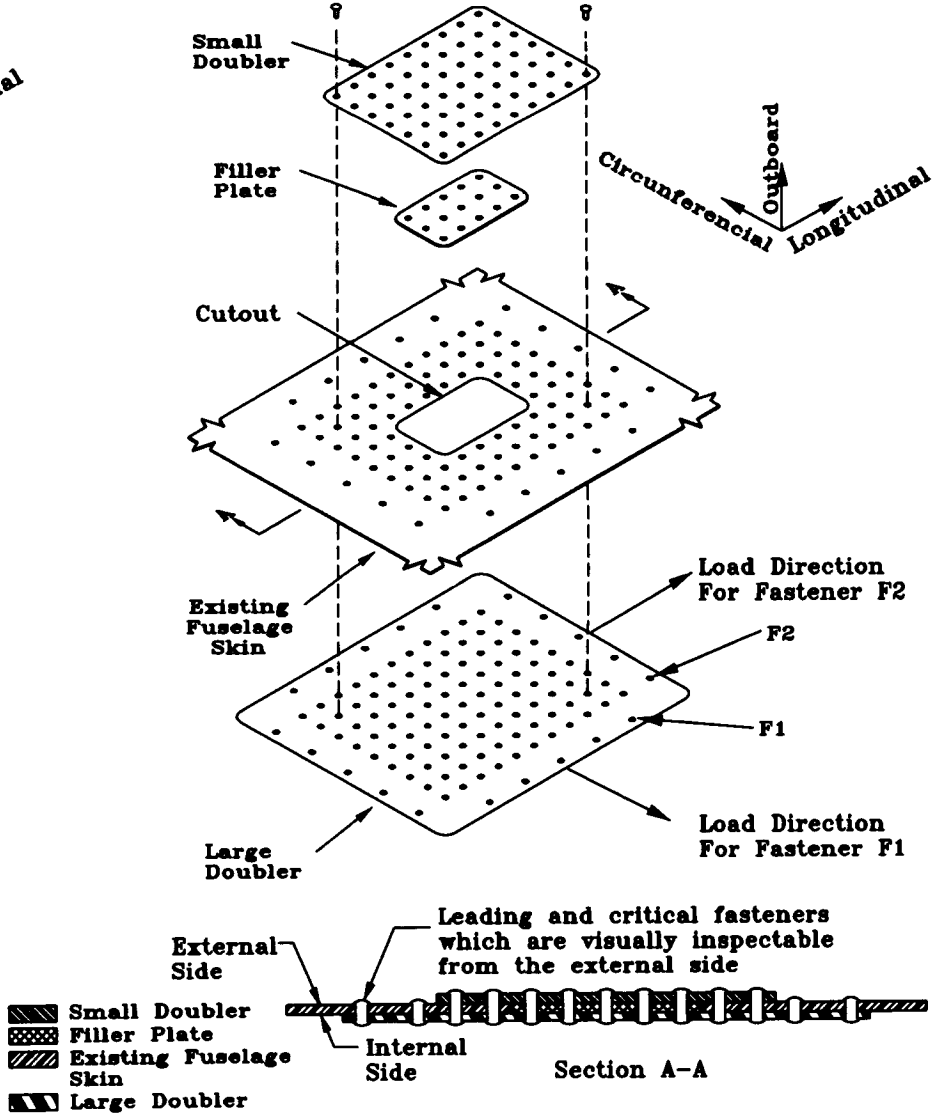

Figure 12. Visually Inspectable Fuselage Skin Panel Repair

PROGRAM FOR PROBABILISTIC STRESS SPECTRA GENERATION (PROSPECTRA)

Mary W. Schleider and Robert A. Babb
Mercer Engineering Research Center
Warner Robins, Georgia, 31088, USA
Ph: (912) 953-6800
Fax: (912) 953-6801
Email: mschleider@merc.mercer.edu

Randy Jansen
WR-ALC/TIEDD
Robins AFB, Georgia, 31098, USA

ABSTRACT

ProSpectra is a Windows-based PC program for developing probabilistic stress spectra for use in crack growth and fatigue analysis. ProSpectra incorporates a simulation methodology whereby the user defines pertinent variables, the relationships between them, and a sequence of events representing specific missions. This program processes discrete stress events, constant amplitude cyclic stresses, and power spectral density stress data to produce a stress spectrum. ProSpectra is a highly flexible tool which allows the definition of nonstandard missions, including those based on a non-certain probability of occurrence.

1. INTRODUCTION

Damage tolerance analysis requires the application of appropriate loads in the form of stress spectra. Generally, major airframe manufacturers have supplied the U.S. Air Force with computer programs which contain libraries of stress spectra. These libraries are weapon-system specific, based on missions anticipated at the time of the program development. Many features are internally coded, making changes difficult or impossible.

In light of the state of the existing tools which generate limited, weapon-specific stress spectra, an additional tool was needed. The tool developed was a PC-based program. The object of this program was to move to a simulation-based methodology wherein the user can define pertinent variables, the relationships between them, and the sequence of events based on data relevant to a specific problem. One of the objectives of the program was to develop a program flexible enough for the user to tailor it to the task at hand. The problem to solve could be as simple (constant amplitude or discrete event) or as complex (random, multivariable, probabilistic) as required. This approach allows engineers and analysts to generate stress spectra based on available data, such as detailed stresses from localized finite element models, load sources not included in the original design, usage which differs from the standard (including evaluating the effects of proposed mission changes before they are implemented), and probabilistic occurrence data. Even if the user is limited by the amount of usage data or test data accessible, the user employs whatever data is available along with any assumptions he chooses, and is

able to generate a reasonable spectrum, without being constrained or limited by rigid, aircraft-specific computer codes. This program also allows generation of stress spectra for systems which have no existing crack growth programs, such as ground vehicles and other support equipment for which the U.S. Air Force is responsible.

2. PROGRAM METHODOLOGY

The basis of the program starts with the setup of a simulation environment for the point of interest on the structure to be analyzed. Figure 1 provides a flowchart of the program overview. The simulation environment consists of the state of all of the affecting variables, load sources, times and lengths of occurrences of events, definition of missions, and the creation of the desired combination of missions. Random values and occurrences can be specified.

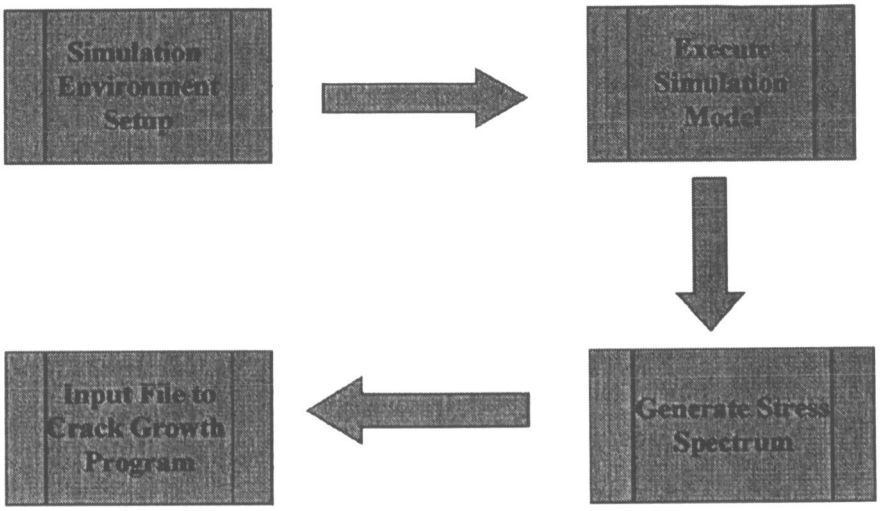

Figure 1. ProSpectra Program Overview

The execution of the simulation model consists of the processing of the provided data, keeping track of the values of environmental parameters throughout the simulation. Execution of the simulation model results in a raw stress spectrum. This raw stress spectrum is then simplified to a form appropriate for input to crack growth programs.

The probabilistic stress spectrum program described and developed is called ProSpectra. ProSpectra is based on parameters, events, segments, missions, and mission mixes. A parameter is one of many environmental conditions. Some examples of parameters are airspeed, altitude, cargo weight, and fuel weight. Events are typically stresses. Examples of events are lateral or vertical gusts or various maneuvers. Events may be defined as discrete stresses, power spectral density stress data (PSD), or constant amplitude cyclic stress data (CSD). Events may also be parameter changes, since these can alter stresses. Segments consist of one or more events, missions are built from one or more segments, and a mission mix is a combination of one or more missions.

Figure 2 provides the program methodology. For a new problem, the user defines parameters, such as altitude, airspeed, cargo weight, fuel weight, etc., for which the stress or loads of interest vary. The

user then defines events, segments, or other mission parameters. Quite often the user will provide the relationships using tables of data created outside of the program.

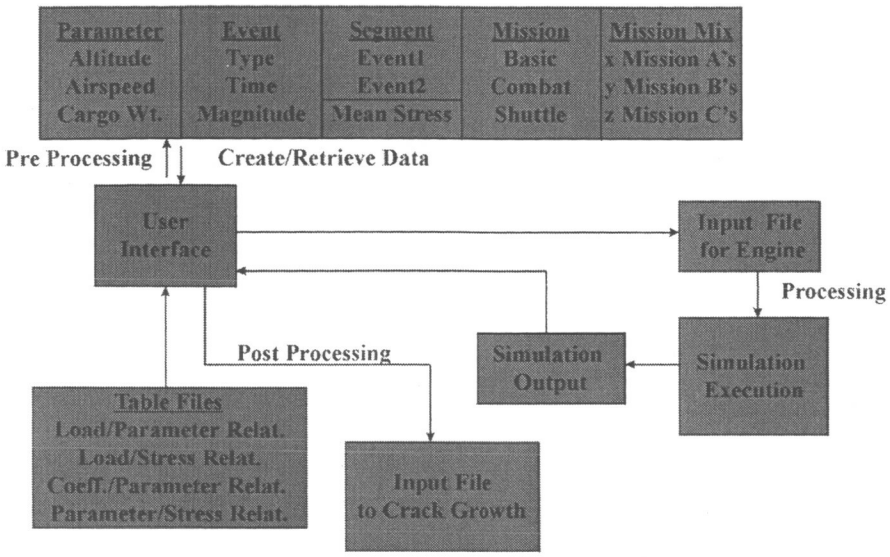

Figure 2. Program Methodology

The magnitude and duration of parameters and events can change at discrete times, regular intervals, or randomly based on a defined probability distribution, such as exponential or Poisson's distribution. The user then specifies events making up the segments and segments making up the missions. The simulation itself is based on a particular mission mix consisting of the combination of many missions. This mix represents some portion of the lifetime of the structure analyzed. Upon completion of the simulation execution, the user provides post-processing information to take a raw stress spectrum and tailor it to a refined list of stress cycle data.

3. PROGRAM ORGANIZATION

ProSpectra is divided into three major sections: the pre-processor, the processor, or "engine", and the post-processor. The pre-processor sets up the simulation. The processor simulates the environment defined by the user and produces a raw stress spectrum. The post-processor takes the raw stress spectrum and layers and orders it into a refined spectrum.

3.1 PRE-PROCESSOR

The pre-processor is the user-interface which allows the user to create and modify parameters, events, segments, missions, and mission mixes. Figure 3 displays the important features of the pre-processor. Table files are typically used for listing variable values and functions between parameters and events or equation coefficients. The user has the option of specifying magnitudes and timing with actual values or as random numbers or random distributions.

The inputs to the pre-processor are provided using a Windows environment. The entire setup of the simulation is saved in a database file structure. It is anticipated that much of the data describing the simulation environment will be in files set up in a tabular format outside of ProSpectra, using a word

processor or spreadsheet program. These table files are accessed from the ProSpectra program. All of the inputs such as occurrence distributions, mission definitions, etc., are saved to the database and are available for reuse in future simulations. Data is referenced such that it can be used by multiple variables. For example, if the user builds a table for duration of occurrence, that table can be referenced by several variables which have the same occurrence distribution. References can be nested to any level of complexity the user desires.

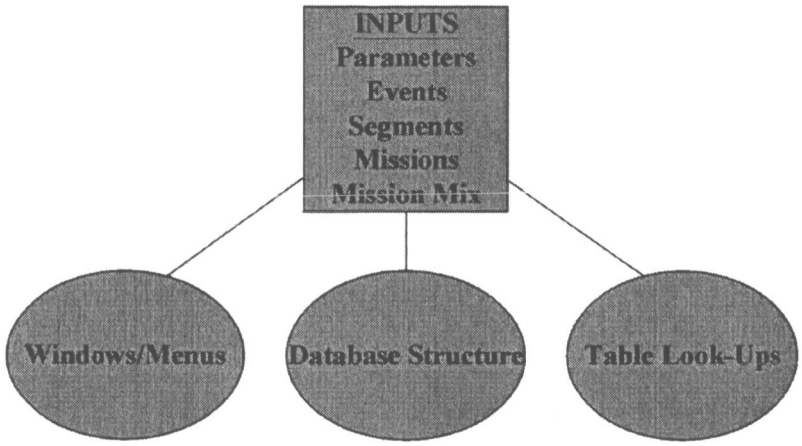

Figure 3. Pre-Processor Features

Figure 4 shows a typical ProSpectra pre-processor screen with various windows displayed. The menu conventions are common among other Windows application programs. This particular screen shows the creation and editing of segments, missions, and the active mix. The user builds and edits his simulation set, as required. The user can select from previously defined segments, missions, etc., and edit them to create similar, but new, segments or missions. One database can define numerous mission mixes. At each session the user designates an active mix for which the stress spectrum is developed.

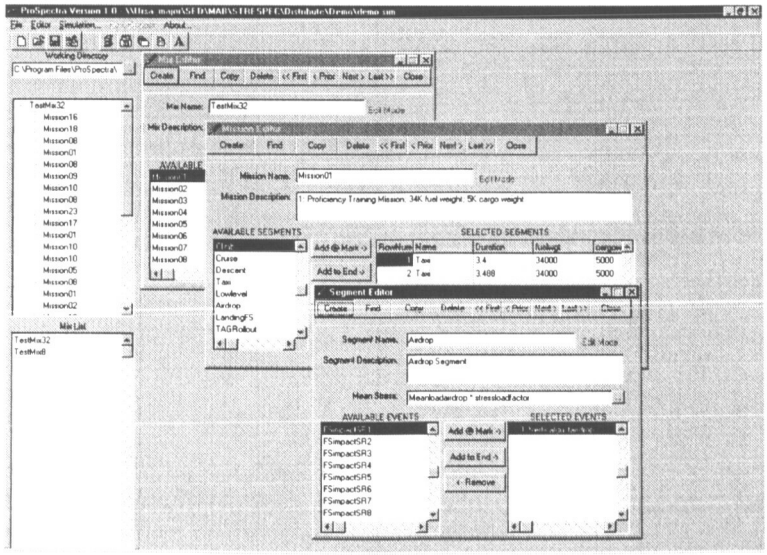

Figure 4. Editor Screens

Figure 5 shows a typical Events Editor menu. The current choices for event types are discrete, constant amplitude cyclic stress data (CSD), PSD stress, and parameter change event. Depending on the type of

event selected, the user is prompted to provide required values for variables. For example, the PSD type event shown in Figure 5 requires six values which are part of the equation shown. The PSD event is used to define stress due to random phenomenon such as turbulence.[1] The required values can be explicitly entered, random values, values from a table look-up, a function, or a variable name.

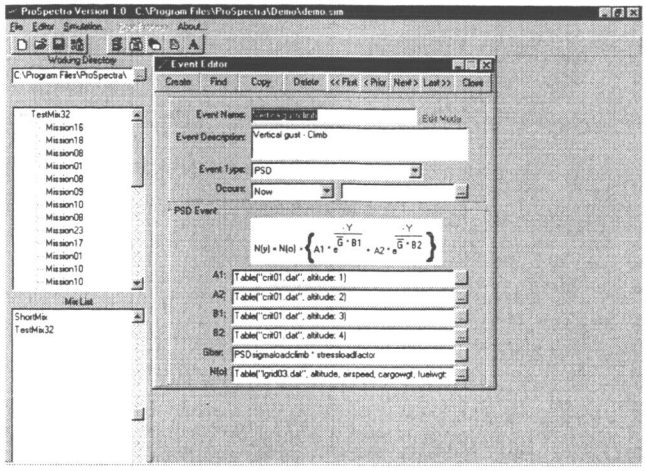

Figure 5. Event Editor

Figure 6 shows the window in which the setup file for ProSpectra is created. An initial user-specified random seed can be entered here if random variables are used in the simulation. The global environment variables of simulation clock starting value, if the starting time differs from zero, is also specified in this menu. This window is used to generate files required by the simulation processor, as well as to execute the simulation.

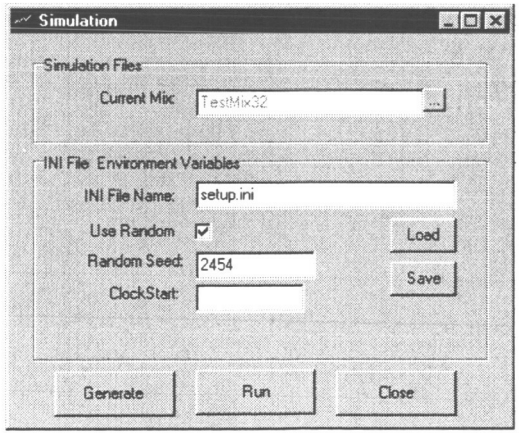

Figure 6. Simulation Setup Window

3.2 PROCESSOR

The processor, or engine, runs the simulation based on the input from the pre-processor. Figure 7 shows the main features of the processor. The processor receives the missions, mix, and global setup files from the pre-processor. Referenced tabular data is interpolated, as needed. The processor

includes built-in functions, including several pertaining to random number generation and distributions. The processor generates an event queue. The events are processed in a prioritized time order. The output of the processor is the raw stress spectrum based on processed events, without grouping or ordering. The output includes a listing of discrete stress data, CSD data with applicable mean stress, and PSD data.

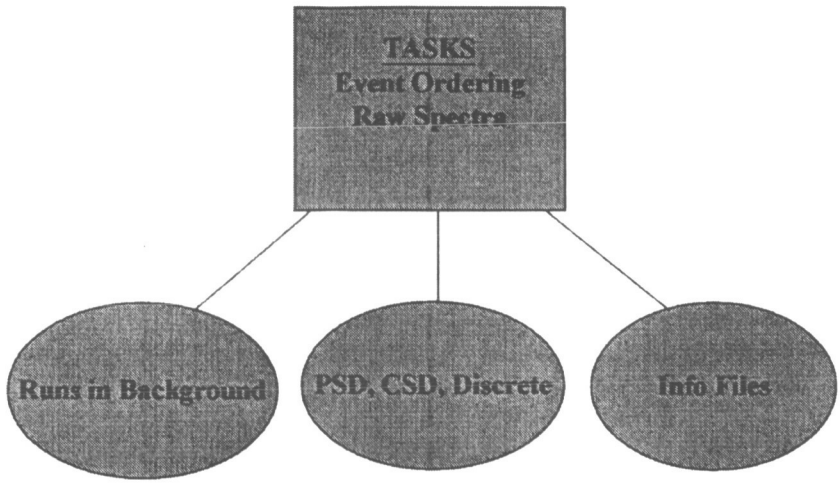

Figure 7. Processor Features

3.3 POST-PROCESSOR

The post-processor of ProSpectra uses the raw spectrum generated by the processor, or engine, and allows the user to generate a summarized stress spectrum. The post-processor uses windows and menus similar to the pre-processor. Tasks included in the post-processor include mission ordering, setup of stress layers, rainflow counting, and high and low level stress truncation. The post-processor summarizes the number of stress cycles according to user-specified stress layers. Mission stresses are ordered according to user specifications. Graphical displays of occurrences and exceedances are available. Figure 8 shows the main features of the post-processor.

Stresses are layered, or combined, by mean stress and delta stress values. Mean stress layers establish individual layers with upper and lower limits that permit mean stress data within these limits to be considered equal. Delta stress layering establishes the upper and lower limits of the stress ranges which are combined, or considered equal. All event types, that is, discrete, constant amplitude cyclic stress, and PSD, are merged in the delta stress layering. Both mean and delta stress layering are performed on the entire active mix.

Figure 9 displays a typical post-processing window. In this particular window, the user is prompted to provide the number and sizes of delta stress layers. After providing this data, the program shows the number of counts for each stress layer. Options for high and low level stress truncation are included in the post-processor.

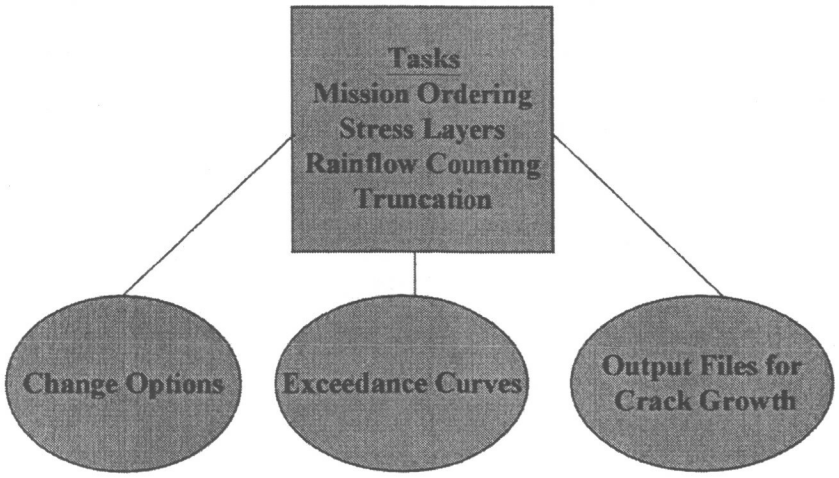

Figure 8. Post-Processor Features

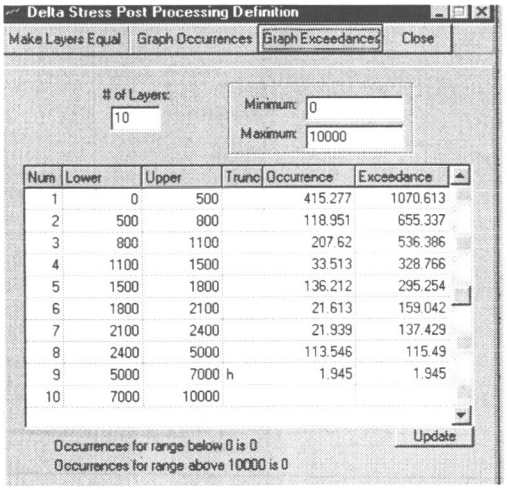

Figure 9. Delta Stress Layering

Truncation is an important feature of ProSpectra. High and low delta stress truncation is used to remove portions of the spectrum in order to perform conservative and efficient crack growth calculations. High stress truncation is intended to remove stress cycles above a specified level to minimize crack growth retardation effects. The number of cycles for high stress levels is typically small and high stress truncation results in totally excluding those cycles from the spectrum. Low stress truncation is applied to remove stress levels below a specified level to improve the efficiency of crack growth calculation. The number of cycles for low stress levels is typically large. Instead of totally removing the low stresses from the cycle counts, ProSpectra recalculates the cycles in the adjacent layer in order to approximate the effects of removing these low stress, high count, cycles.

After the user makes his decisions regarding stress layers and truncation, he is provided feedback as to how his decisions affect the occurrence and exceedance curves. If desired, the user can change his layering scheme and truncation options and very easily redo his choices. Figure 10 displays a typical exceedance curve.

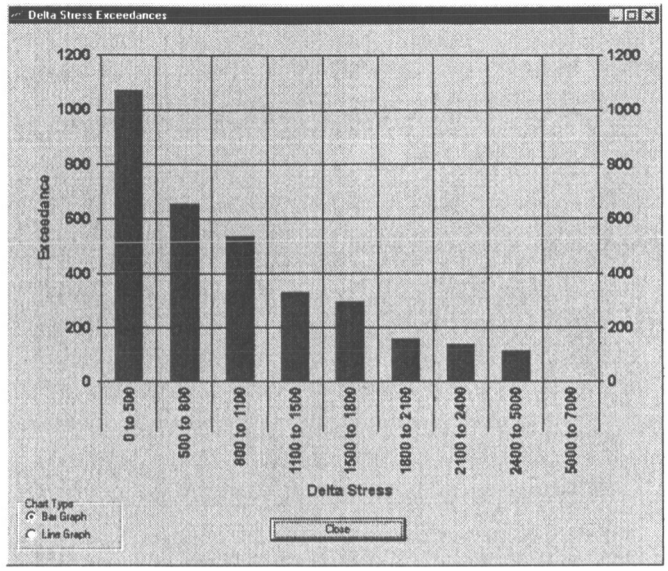

Figure 10. Exceedance Curve Graph

4. **Output**

The final product from ProSpectra is the stress spectrum. The user specifies his choice of mean and delta stress ordering in the summarized stress spectrum. Options of high-to-low stress, low-to-high stress, and random order are provided. The stress spectrum is ordered at the mission level. ASCII output files appropriate to crack growth programs are generated. At this time, two output format choices are provided. The first output format is that appropriate to AFGROW crack growth program, in which integer number of cycles are produced. The second option is similar in format, except partial cycles replace the integer number of cycles. A sample output file in AFGROW format is shown in Figure 11. Maximum stress, minimum stress, and number of cycles are written.

1	5	
2243.5	1743.5	2
3012.5	-487.5	2
2512.5	12.5	6
2012.5	512.5	12
1512.5	1012.5	18
2	5	
2243.5	1743.5	2
3012.5	-487.5	2
2512.5	12.5	6
2012.5	512.5	12
1512.5	1012.5	18

Figure 11. Excerpt of Sample Stress Spectrum

5. SYSTEM REQUIREMENTS

The following system requirements are the minimum recommended hardware and software requirements for installing and running ProSpectra. These configurations have been tested. Other configurations may be acceptable, but have not been tested.

- Pentium PC
- 64 MB RAM
- Windows 95 or Windows NT
- 20 MB free disk space

CONCLUSIONS

ProSpectra is a very flexible tool for simulating both deterministic and probabilistic events and generating stress spectra. ProSpectra has a broad range of applications across military and civil aircraft, as well as other ground transportation systems. ProSpectra allows the generation of stress spectra from probabilistic occurrence data, new load sources, and limited test data.

This was a pilot program to develop a highly flexible tool and prove a basic methodology. This methodology has been proven. As the program is being tested and validated, several additional features and capabilities to further improve the program are being identified for possible future versions of ProSpectra. Areas of recommended further research and development include the addition of a "smart" feature to aid the user in development of his simulation model, output file formats for additional crack growth programs, addition of standard truncating and clipping schemes, and direct translation from flight recording data to ProSpectra input files.

ACKNOWLEDGMENTS

Mercer Engineering Research Center acknowledges WR-ALC/TIED and AFRL for funding the development of this program, as well as providing monumental support throughout this program.

REFERENCES

[1]E.W. Turner, "An Exposition on Aircraft Response to Atmospheric Turbulence Using Power Spectral Density Analysis Techniques", AFFDL-TR-76-162, Air Force Flight Dynamics Laboratory, Air Force Systems Command, WPAFB, May 1977

ACOUSTIC DETECTION OF IN SITU CORROSION IN AGING AIRCRAFT

Jeffrey N. Schoess
Honeywell Technology Center
3660 Technology Dr., Minneapolis, MN 55418-1096
Telephone: (612) 951-7873
Telefax: (612) 951-7438
E-mail: schoess_jeff@htc.honeywell.com

ABSTRACT

Hidden and inaccessible corrosion in aircraft structures is the number-one logistics problem for the U.S. Air Force, with an estimated maintenance cost in excess of $1.0 billion per year in 1990-equivalent dollars. Reliable detection of hidden corrosion damage using conventional nondestructive inspection (NDI) techniques is a difficult task, requiring significant maintenance training and manpower to access damaged structural locations. This paper summarizes a novel in situ measurement approach using stress-wave acoustic emission (AE) technology to detect and quantify corrosion damage without removing structural panels. A summary problem statement, existing NDI methods, and their limitations, corrosion factors, design concept approach for using AE, and design implementation details are presented.

1. Introduction

Reliable inspection and detection of hidden and inaccessible corrosion in aging aircraft structures is a challenging and costly task.[1,2,3] The long-term Air Force goal to know which aircraft to inspect, where to inspect, when to inspect, and how to inspect them to reduce maintenance costs and improve fleet readiness is achievable. Fatigue crack inspections are typically localized to joints and high-stress locations on the fuselage structure. Hidden corrosion effects can occur, not only at such locations, but throughout the aircraft structure. Corrosion occurs in areas of the fuselage subject to excess moisture or wetted by other fluids. These areas include the bilge of the fuselage for military and commercial transport aircraft, around wing fastener holes (primary exfoliation), fuel shelf areas, wheel well shelves and backwalls in the F-16, and the structure surrounding all doors, including cargo access and landing gear doors.

For fixed- and rotary-wing applications, the external fuselage skins are especially vulnerable to corrosion attack. The external surfaces of magnesium alloy or aluminum alloy skins are particularly susceptible to corrosion along rivet lines, lap joint fasteners, frying surfaces, or where protective coatings have been damaged or neglected. A typical wing skin application involves corrosive electrolytes (i.e., water) entering the structure at unsealed skin edges and capillaries along the inner joint wall to fastener locations. A buildup of corrosion effects (i.e., intergranular and exfoliation) can cause a "pillowing" effect to occur between fastener sites and eventual buckling of the outer skin.

2. Background

The currently available NDI techniques for detecting and characterizing corrosion in hidden and inaccessible areas of aircraft and industrial control structures have specific limitation in terms of the types of corrosion they can detect, the ease of use (mobility), system cost, availability of corrosion NDI equipment, including the detection methods of visual inspection, tap testing, ultrasonic, eddy current, X-ray radiography, neutron radiography, acoustic emission, and magneto-optic eddy current (MRI). Each of these techniques uses sound, heat, electrical current, or X-rays to detect cracks in metal structures. However, they are generally less effective in detecting uniform hidden corrosion, and the accumulation of corrosion products in and around fatigue cracks can limit the effectiveness of these techniques even further.

3. Technical Approach

The system concept for detecting hidden corrosion is shown in Figure 1. An illustration of an aircraft wing is highlighted, with a specific section of the wing being instrumented with an array of in situ transducers. The transducers are configured to provide two types of functions: an AE transmitter and an AE receiver. The transducers would be integrated in the aircraft Hi-Lok fastener and installed as a normal maintenance repair activity during depot-level repair. The transmitter transducer will be configured to emit a high-frequency stress-wave AE event signal, which is then transmitted through the aircraft structure as a bulk wave to the damaged (i.e., corroded area of interest) site. The reflected and transmitted acoustic energy is then detected by an array of acoustic receiver transducers located in the vicinity of the damage site to convert the acoustic response into an equivalent electrical signal for processing and detailed analysis.

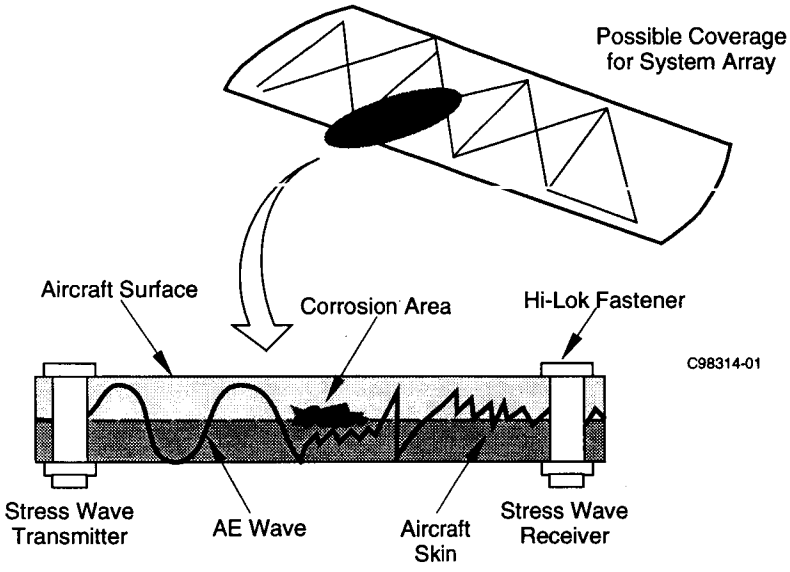

Figure 1. Stress-Wave Acoustic Emission System Concept

Figure 2 illustrates a detailed view of the acoustic transmitter. The figure shows a design implementation of an installed Hi-Lok fastener with a dedicated acoustic projector located at the end of the fastener body, a piezoelectric-based structural AE generator, which on command from a AE pulser emits an acoustic event with a frequency bandwidth of DC to 300 kHz. The projected AE energy is then reflected at the damage site to the receiver array. A ratio of transmitted to received energy could be used to quantify actual structural damage.

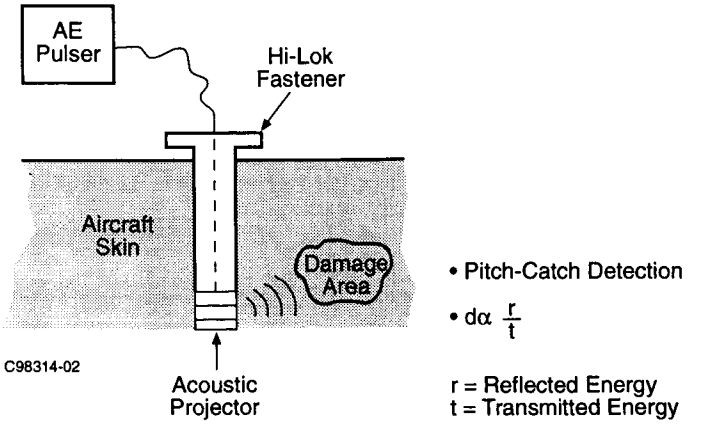

Figure 2. Detailed View of Acoustic Transmitter

CONCLUSIONS

A novel in situ corrosion detection concept has been presented using stress-wave acoustic emission technology. This approach offers the potential of dual-use NDI for fatigue monitoring and corrosion inspection in hidden and inaccessible structures.

REFERENCES

1. Schoess, J. 1995. "Smart Aircraft Fastener Technology for Aging Aircraft," 1995 SPIE Smart Structures and Materials Conference, No. 2444-15, February 26.

2. Schoess, J., and G. Seifert. 1996. "Smart Aircraft Fastener Evaluation System. A Condition-Based Corrosion Detection System for Aging Aircraft," 3rd Air Force Aging Aircraft Conference, Sept. 27.

3. Schoess, J., and G. Seifert. 1996. "SAFE: A Condition-Based Corrosion Detection System for Aging Aircraft, 1996 SPIE Smart Structures and Materials Symposium, No. 2718-21, February 27, San Diego.

MODELLING OF WEAK BONDS IN ADHESIVELY FASTENED JOINTS

Krishnakumar Shankar
School of Aerospace and Mechanical Engineering
University College, Australian Defence Force Academy
The University of New South Wales, Canberra, ACT 2600 Australia
Ph: 61-2-6268 8584, Fax: 61-2-6268 8276
E-Mail: k-shankar@adfa.edu.au

Dong Fei
School of Aerospace and Mechanical Engineering
University College, Australian Defence Force Academy
The University of New South Wales, Canberra, ACT 2600 Australia

ABSTRACT

A new conceptual model for the analysis of peel behaviour of weakly bonded adhesive joints is presented in this paper. The paper focuses on modelling weakness in adhesion caused by deterioration of the adhesive bondline, as opposed to weakness in cohesion. For the purposes of analysis the bondline interface in a perfectly bonded adhesive joint is assumed to have the same material properties as the adhesive material, and modelled as such. The degradation of the bondline interface in a weak joint is modelled by considering reduced properties for the bondline interface. Finite element analysis of bonded doubler joints and double lap joints are carried out to study the peel deformation on the surface of the outer adherends. It is shown that when a doubler or a double lap joint has a good bond on one side and weak one on the other, the reduction in the strength of the bondline on the weak side causes an unsymmetric distribution of the load transferred by the outer adherends, resulting in bending. The bending deformation accentuates the peel deformation on one side while diminishing that on the other, resulting in a considerable difference in the distribution of out of plane displacements on the two sides. Measurement of the differences in the distribution of out of plane displacements using sensitive optical methods such as holographic interferometry enables the detection of weak adhesive bonds by non-destructive inspection.

1. INTRODUCTION

Adhesively bonded joints are being increasingly utilised in aircraft construction as well as repair of airframe structures due to their many advantages over mechanically fastened joints such as reduction in stress concentrations, higher fatigue resilience, better sealing, lower part count, lesser weight, and so on. However adhesive joints have drawbacks of their own, the most serious of which is the difficulty in inspecting them non-destructively, particularly for weaknesses in the bondline integrity. Weakness in adhesively bonded joints can either be due to reduced strength and/or stiffness in the adhesive, which causes a reduction in the cohesive strength of the bond, or a weakness in the bondline interface, which causes a reduction in the adhesive strength of the bond[1-2]. Weakness in cohesion may exist immediately upon manufacture, mainly due to the use of poor quality materials or improper curing, or may set in with the passage of time, due to environmental effects such as absorption of moisture. In either case, weakness in cohesion is more easily detectable, and has been the subject of many theoretical and experimental investigations[3-7]. This paper deals exclusively with weakness associated adhesion or reduction in strength in the adhesive bondline. Adhesion is also affected by environmental factors, such as ingress of moisture, which, over a period of time, causes

deterioration in the strength of the bondline. However, durability of adhesion is extremely sensitive to the surface preparation techniques employed during the manufacture of the bond, which primarily dictate the influence that environmental factors will have on the bondline integrity[7-9].

Previous studies have shown that weakness in cohesive strength defects can be measured with a reasonable degree of confidence and be monitored by a number of nondestructive methods such as normal incidence ultrasonics, ultrasonic spectroscopy, and leaky Lamb waves[4]. Finite element modelling for prediction of environmental degradation of cohesive strength in bonded structures as well as experimental validation has also been reported previously[5-6]. On the other hand, several NDI techniques such as ultrasonics and thermography[4] are applicable for detection of total loss of adhesion between the adherends or disbonds, and are commonly employed by the aircraft industry, both in manufacturing and maintenance. However, to date there do not appear to be any standard or accepted non-destructive technique for the detection of weakness in adhesion, although techniques using high frequency oblique incidence ultrasonics and interface waves have been proposed as promising possibilities[4].

The difficulty in inspecting for weakly bonded joints arises from the fact that weak bonds are as effective as strong bonds at low loads, but when the load increases beyond a certain value, they fail abruptly. Thus the lack of integrity of a weak bond is manifested only when the bond fails, ie. at the point of destruction. If the reduction in adhesive strength caused by bondline degradation is accompanied by a reduction in the stiffness of the joint, then one may employ techniques of monitoring stiffness to identify adhesive weakness in the joint. However, whether bondline strength reduction is accompanied by a bondline stiffness reduction is an issue that has yet to be resolved. Many experts in the field find the concept of stiffness of the bondline unpalatable, considering it somewhat antithetical to the very notion of "bondline", since it implies a finite variation in a finite thickness of the bondline.

1.1 EXPERIMENTAL EVIDENCE

While the concept of bondline stiffness remains controversial, it is a fact that experiments in the recent past at the Australian Defence Force Academy using the Portable Holographic Interferometric Testing System (PHITS) appear to indicate that weakness in the bondline may be detectable through measurement of peel deformations[10-12]. PHITS is an off-table double exposure holographic interferometric technique which produces fringes that are contours of out of plane displacement with a sensitivity of about 0.3 μm per fringe. Measurement using the PHITS system on a double lap joint with a simulated weak bond on one side and a good bond on the other has reportedly indicated a difference of about 60% in the magnitudes of the out of plane displacements of the two sides, with the weaker side producing less number of fringes. Based on this experimental evidence, a spring system model has been developed in accompanying literature, in which the effective peel stiffness of the joint is obtained by considering the adherends, the adhesive layers and the bondline interfaces as springs with finite values of spring constant. According to this model, a joint with a weak interface will have lower peel stiffness and hence higher out of plane deformations than a joint of the same geometry with a perfect bond under the same load. Thus PHITS is proposed as an effective NDI tool for the detection of weak bonds in adhesively bonded joints.

1.2 BASIS OF THE PRESENT MODEL

The experimental evidence cited in the foregoing section indicates that in adhesively bonded double lap joints and doubler joints with unsymmetrical bondline strengths, the out of plane deformations of adherends with good and weak bonds are distinctly different, raising the possibility of surface measurement techniques such as holographic interferometry to be employed as a reliable tools for

detection and monitoring of weak bonds. Other researchers have contended that since weakness in adhesion affects only the interface between the adhesive and the adherend and not the properties of the adhesive, the effective peel stiffness of a weakly bonded joint should be no different from that of a joint with good bonds. Even if one accepts the hypothesis of variations in transverse stiffness of the bondline due to loss of adhesion, any effect of such variations in the total peel deformation between the adherends will be negligible, due to the negligible thickness of the bondline (less than 10 μm) in comparison to the thickness of the adhesive layer, which is a few hundred microns.

In this paper an attempt is made to develop a new conceptual model to explain the observed difference in out of plane displacements between the good and weak sides of an adhesively bonded doubler or double lap joint, without resorting to the controversial issue of peel stiffness of the bondline. The model is based on the more acceptable concept that weakness in adhesion is equivalent to a reduction in the *strength* of the bondline, which may have arisen from a failure of some of the inter-molecular bonds between the outermost layer of the adherend and that of the adhesive. A reduction in bondline strength implies a local reduction in the load transfer capability of the interfacial layer, so that when the applied axial load is sufficiently high in a doubler joint or a double lap joint with unsymmetric bondline strengths, more load is transferred to the outer adherend with the stronger bond than the outer adherend with the weaker bond.

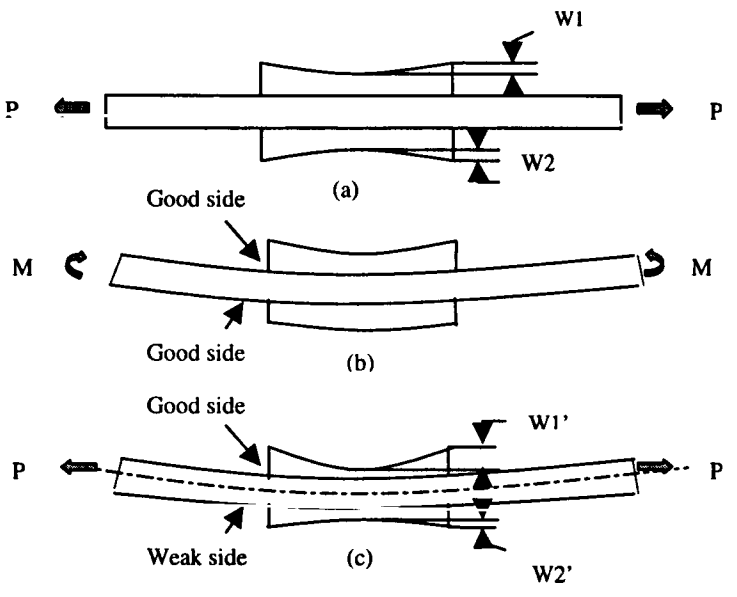

Fig 1. Effect of bending on peel deformation

The effect of the unequal distribution of the load transferred to the outer adherends in a doubler joint with unsymmetric bond strength is depicted schematically in Figure 1. The unsymmetric distribution of the load transferred to the outer adherends results in an overall bending of the whole joint, in addition to the local internal bending moments which produce peel deformations concentrated at the ends of the adherends even in a symmetrically loaded double lap joint. The latter peel deformations are symmetric in nature with respect to the mid-plane of the joint as shown in Figure 1(a), whereas the out of plane deformations caused by overall bending is antisymmetric in nature (see Figure 1(b)). Thus the out of plane displacements due to bending adds to the peel deformation on one side of the joint, while it decreases the peel deformation on the other side, resulting in an appreciable measurable difference in magnitude in the total out of plane displacements of the two sides, as shown in Figure 1(c). Thus mapping of the out of plane displacements using a system such as the PHITS provides a means of distinguishing between the strong and the weak interfaces, as well as a measure of the relative strengths of the two bondlines.

The remainder of this paper explores this hypothesis using the finite element method. The essence of the finite element analysis is the modelling of the interfacial layers between the adhesive and the adherends separately from the adhesive, employing, for lack of any other available data, the same material properties for the interface as those of the adhesive for good bonds, and similar properties with reduced magnitudes for the bondline at the weak interface. The finite element modelling necessitates assuming a finite thickness for the bondline, which is arbitrarily taken to be 2 microns. But the results are fairly insensitive to the thickness of the bondline, as long as it remains small in comparison to the thickness of the adhesive layer.

2. DESCRIPTION OF THE MODELS

Figure 2 shows schematic representations of the doubler joint and the double lap joint employed in the finite element study. The joints are balanced and symmetric in geometry about their mid-plane, with a thickness t = 1.6 mm for the outer adherends and 3.2 mm for the inner adherends. The length of the overlap in each case is "2a" with values of being 12.7 mm and 13.9 mm respectively for the doubler joint and the double lap joint. The inset in Figure 3 shows an magnified view of the section of the joints. The thickness of the adhesive is "t_a" is equal to 190 μm, while the bondline thicknesses "t_i" at the interfaces was taken to be 2 μm.

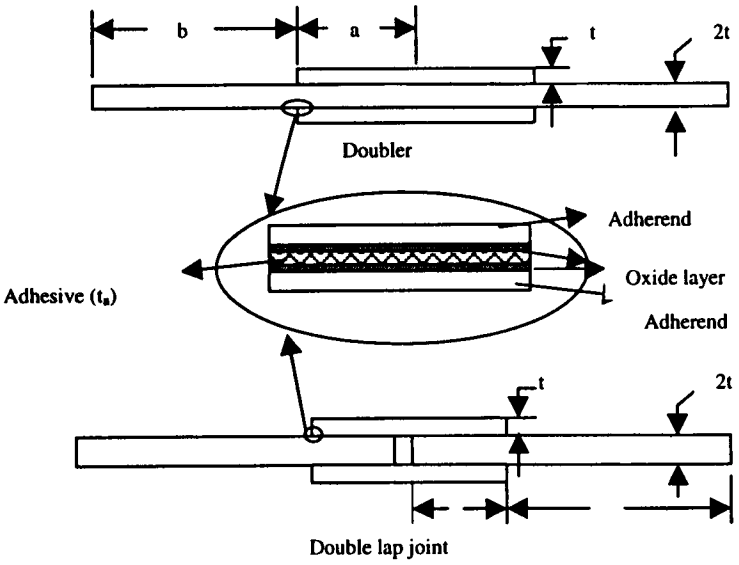

Fig 2. Adhesively bonded joints geometry

2.1 MATERIAL PROPERTIES

The material considered for the adherends is aluminium alloy 2024-T3 and that for the adhesive is FM300, whose properties are shown in Table 1 below. Both materials are taken to be elasto-plastic material and modelled in the FE analysis using multi-linear isotropic relationships. The values of the stresses and strains at the intersections between the various linear segments are tabulated as σ_i, ε_i, with "i" varying from 1 to 4 for the adhesive and 1 to 3 for the adherend materials. It is to be noted that the material properties of the interfacial layer is taken to be the same as that of the adhesive (FM300) for the perfectly bonded interface as indicated by the upper curve in Figure 3. The lower curve in the figure indicates the reduced properties assumed for the weakly bonded interface. In the present study, the values for this curve were taken to be 50% of those of the perfect interfacial layer, representing a reduction in strength of 50%. The Von Mises failure criterion was employed for determining the limiting values for the stresses at each point in the FE analysis.

TABLE 1 Material properties

Property	Adhesive	Adherend	Interface layer (good bond)
Young's modulus(GPa)	2.9	70	2.9
Poisson's ratio	0.34	0.3	0.34
σ_1 (MPa)	38	338	38
ε_1	0.013	0.0048	0.013
σ_2 (MPa)	49	355	49
ε_2	0.02	0.006	0.02
σ_3 (MPa)	55	362	55
ε_3	0.024	0.0098	0.024
σ_4 (MPa)	60		60
ε_4	0.031		0.031

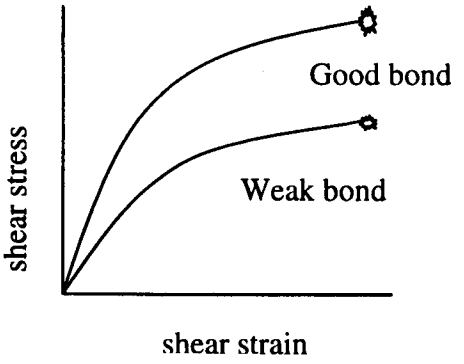

Fig.2 Interface property

2.2 MODEL SPECIFICATIONS

The finite element software package ANSYS 5.4 was employed to perform two dimensional analysis of the doubler joint and the double lap joint., with 8 node quadrilateral plane strain elements (PLANE82) with mid-side nodes. Figure 4 shows schematic representations of the meshes generated in ANSYS for the doubler joint and the double lap joint (top and bottom respectively). The mesh sizes in the figure are representative only, since the actual meshes employed in the models are too dense to be shown with clarity. The outer adherent, adhesive layer and the inner adherend were respectively modelled with 4, 5 and 8 elements across the thickness. The 2 μm thick bondline interface was modelled with a single row of elements across the thickness. The mesh density was varied along the length of the joint to obtain greater accuracy in regions of high stress concentrations. The regions at the ends of the overlap were modelled with a fine mesh having a density of about 40 elements per mm over a length of about 5 mm. The mid-section of the double lap joint was also modelled with a similar fine mesh. Due to symmetry, it was necessary to model only one quarter of the symmetrically bonded joints, whereas for the specimens with different bond strengths on the two sides, it was required to model the full

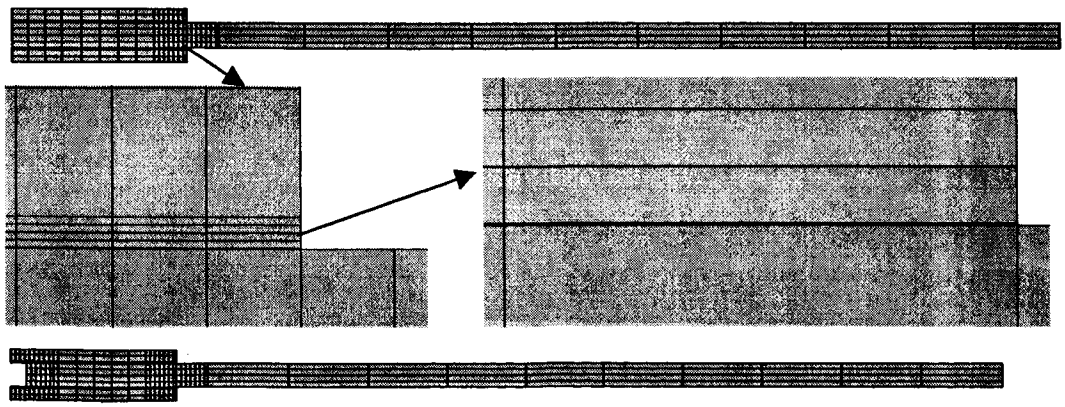

Fig.4 Finite element mesh

thickness along one half of the length of the joint. The half model joints in the latter case has a total of approximately 12000 elements with a total number of about 74,000 degrees of freedom.

3. RESULTS OF FINITE ELEMENT MODELLING

Each joint was analysed with three different models. The first two models are symmetric, with perfect or full strength bonds on either side of the joint in one case, and bondlines with only 50% strength on either side in the second. The third model is unsymmetric, with the bond on one side being 100% strong and the bond on the other side only 50% strong.

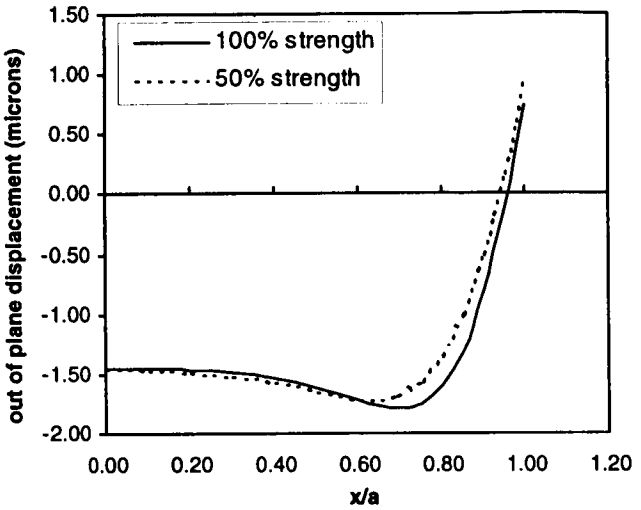

Fig. 5 Comparison of Out of Plane Displacements of Doubler Joints

Figure 5 shows a comparison of the out of plane displacement distributions along the half-length of the overlap in the perfectly bonded and the 50% weak symmetric doubler joints subjected to an axial stress of 150 MPa. The displacement distributions in the two cases are quite close, with a maximum difference of less than 10% in magnitude. The out of plane displacement distributions obtained from the FE analysis were used to compute locations of "fringes" or contours of out of plane displacement similar to those produced by PHITS. The simulated fringe patterns as well as the plots of out of plane displacements for the 100% strong and the 50% strong symmetric doubler joints are shown in Figures 6(a) and 6(b) respectively. Each fringe in these figures represent a change in transverse displacement of the order of 0.3 μm. The displacements plotted in Figures 6(a) and 6(b) are relative to the location of the mid-point of the doublers, since it is this relative displacement that produces fringes. Similar results obtained from the finite element analysis of symmetric double lap joints with 100% and 50% bond strengths in their respective interfacial layers and subjected to an axial stress of 100 MPa, are presented in Figures 7(a) and 7(b), respectively. It is interesting to note that, while in the case of the doubler joint, the weaker specimen has a higher number of fringes indicating a larger deflection, it is the stronger model that has higher number of fringes in the case of the double lap joint.

It is seen that for both joints, while there is a difference of one or two in the total numbers of fringes seen on the strong and weak models, there is hardly any recognisable difference in the density of the fringes in the two patterns. Considering the sensitivity of the PHITS system and the numerous possible sources of experimental error, the small difference in fringe numbers between the two patterns is hardly be sufficient to distinguish between a weakly bonded joint and a strong joint (even with a strength reduction of 50%) were the weakness not known beforehand.

The results of the finite element analysis of a doubler joint with a perfect bond along one side and imperfect bond with only 50% strength along the other, are presented in Figures 8 and 9. The out of plane displacements computed for the outer surfaces of the doublers on either side are compared in Figure 8. The difference in displacements indicates a Poisson's contraction of about 3 mm at the

section of the joint, about the same as that of the symmetric doubler joints in the foregoing section, whose half value is seen to be 1.5 microns in Figure 5. The mean value of the displacement, indicative of the lateral deflection of the mid-plane, is about 28 microns at the mid-section, which indicates that whole joint suffers from a relatively high degree of bending.

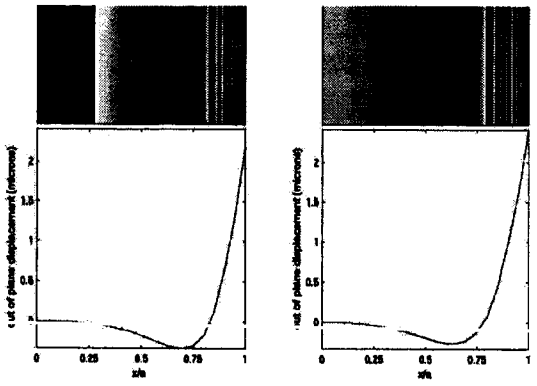

Fig. 6 Fringe Patterns in Symmetric Doubler Joints with (a) 100% (b) 50% Bond Strength

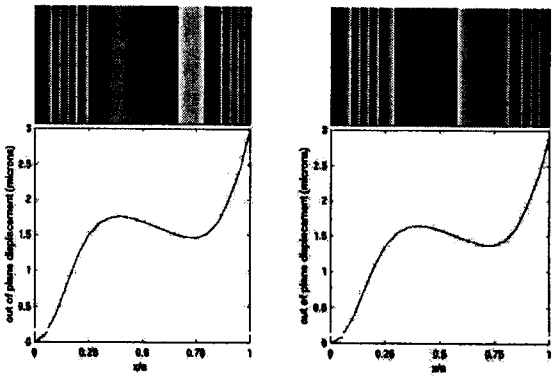

Fig.7 Fringe Patterns in Symmetric Double Lap Joints with (a) 100% (b) 50% Bond Strength

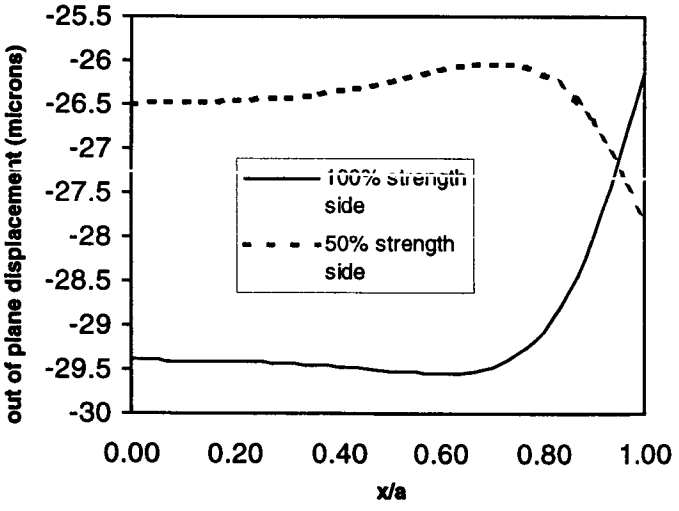

Fig. 8 Comparison of Out of Plane Displacements between Strong and Weak Sides of Doubler Joints

The simulated fringe patterns as well as the plots of the relative out of plane displacements on the good side and the weak side of the unsymmetrical doubler joint are shown in Figures 9(a) and 9(b) respectively. It may be noted the displacement at the ends of the doubler on the good side is about twice as much as that of the ends of the weaker side. Further, the fringe density at the end of the overlap is much higher on the strong side than on the weak side. The variations in the fringe density and fringe number is even more conspicuous when the axial stress applied on the unsymmetrical joint is increased from 150 MPa to 200 MPa as shown in Figures 10(a) and 10(b). At this higher load, the bending produced by the difference in the loads carried by the two doublers is so high that both of them deform towards the same side. The displacement plots and the fringe patterns on the good and weak sides of a double lap joint with bond strengths of 100% and 50% are shown in Figure 11 in which the load were 100MPa. The maximum displacement on the good side in this case is seen to be about 1.5 times of that on the weak side. The high density of the fringes at the mid-section and at the end of the overlap of the good joint makes it obviously different from the coarser set of fringes on the weak side, indicating once again that the relative difference in bond strengths is identifiable by a surface mapping technique such as holography.

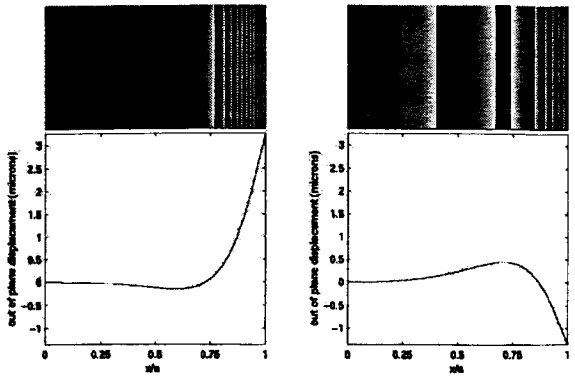

Fig. 9 Fringe Patterns in Unsymmetric Doubler Joint at 150MPa (a) Good Side (b) Weak Side

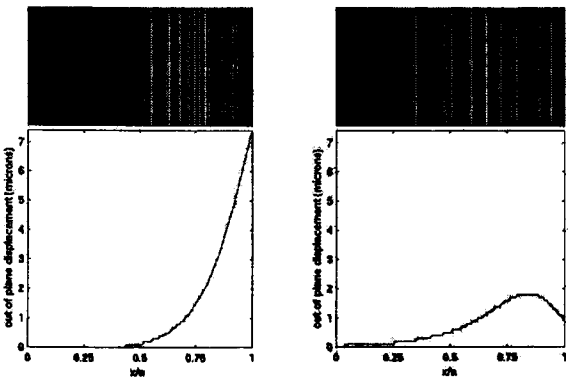

Fig.10 Fringe Patterns in Unsymmetric Doubler Joint at 200MPa (a) Good Side (b) Weak Side

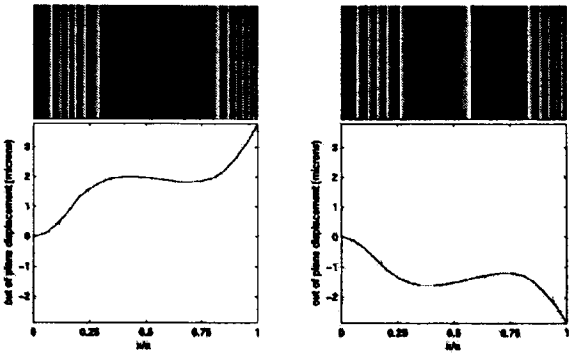

Fig. 11 Fringe Patterns in Unsymmetric Double Lap Joint at 100MPa (a) Good Side (b) Weak Side

4. CONCLUSION

In this paper a phenomenological model is developed to explain the apparent difference in peel behaviour that was observed in earlier experiments between the good side and the weak side of a double lap joint with unsymmetrical bond strengths. It is shown that the reduction in bond strength on the weaker side produces a difference in the load transferred to the doublers on either side, resulting in a bending of the mid-plane of the whole joint under axial tensile loading. The bending deformation accentuates the peel deformations on the strong side and reduces those on the weaker side, producing an appreciable

difference in the magnitudes of the relative out of plane displacements between the mid-sections and the ends of the doublers. Furthermore, the lateral displacements are more evenly distributed on the weaker side than on the strong side of the joint so that fringe patterns representing displacement contours on the two surfaces have sufficient contrast to be easily distinguishable. The same phenomenon occurs in a double lap joint with unsymmetric bond strengths, so that surface monitoring techniques such as PHITS can be employed to detect a relative change in adhesive bond strength between the two sides of an apparently symmetric joint. The results, however, show that if

both sides of the joint are equally weak then they may not be distinguishable from a symmetric joint with perfect bonds on both sides.

The work presented herein was aimed at exploring how the hypothesis applies to unsymmetrical peel deformations occurring in a geometrically symmetric double lap joint with unsymmetric bond strengths. Experimental work to develop quantitative correlations between observed differences in fringe patterns and reduction in bond strength on the weaker side of the joint is currently being undertaken. These tests involve destructive and non-destructive testing of double lap and doubler joints with varying degrees of bond strength produced with different types of surface preparation.

While the current work indicates that techniques such as PHITS may be applicable to detecting weak bonds in symmetrically bonded joints, one of the major practical applications of such an NDI technique will be for monitoring the integrity of bonded patch repairs, which are not symmetrical in nature. The applicability of surface measurement techniques to asymmetric joints of the nature of single lap joints and bonded patch repairs is currently being investigated through finite element modelling.

REFERENCES

1. Arnott, David, *Surface preparation:obvious requirement to emphysis on design variables and design philosophy. Workshop on practical adhesive bonding for performance and durability:standards and standardisation*, ICCM-11, Brisbane, 11 July 1997
2. Davis, Max, *The state of play: existing regulations, what goes wrong, why and how much it cost, Workshop on practical adhesive bonding for performance and durability:standards and standardisation*, ICCM-11, Brisbane, 11 July 1997
3. Newman,W.John, *Shearographic inspection of aircraft structure, Materials Evaluation*, September,1991
4. Adams, R. D. and Drinkwater, B. W., *Nondestructive Testing of Adhesive-Bonded Joints, NDT & E International*, Vol.30,No.2,pp.93-98, 1997
5. Crocombe, A. D., *Durability Modelling Concepts and tools for the Cohesive Environmental Degradation of Bonded Structures, International Journal of Adhesion and Adhesives*, Vol.17, pp.229-238, 1997.
6. John, S. J., Kinlock, A. J., and Mathews, F. L., *Measuring and Predicting the Durability of Bonded Carbon Fibre/Epoxy Composite Joints, Composites*, Vol.22, No.2, March 1991.
7. Armstrong, K. B., *Long-term durability in water of aluminium alloy adhesive joints bonded with epoxy adhesives, Int.J.Adhesion and Adhesives*, vol. 17, pp89-105, 1997.
8. Davis, M. J., *The role of materials and processes in defective aircraft bonded structural repairs, 41st International SAMPE Symposium*, Mar 24-28, 1996
9. Arnott, D. R., Wilson, A. R., Rider, A. N., Olsson-Jacques, C. L., Lambrianidis, L. T., and Pearce, P. J., Davis, M. J., and Swan, G., *Research underpinning the adherend surface*

preparation aspects of the RAAF Engineering Standard C5033, The International Aerospace Congress (IAC97), pp27-39,1997

10. Heslehurst, R. B. and Baird, J. P., *Holographic interferometry application to composite and bonded aircraft structural repairs, Composite repair engineering development program,* St.Louis,MO,USA, 11-13 May 1993
11. Heslehurst, R. B., Baird, J. P., and Williamson, H. M., *The effect on adhesion stiffness due to bonded surface contamination, Journal of advanced materials,* ,pp.11-15, April 1995
12. Heslehurst, R. B., Baird, J. P., Williamson, H. M. and Clark, R., *Can aging adhesively bonded joints be found?, 41st International SAMPE Symposium,* Mar 24-28, 1996

METHODS FOR RELATING FRACTURE SURFACE TOPOGRAPHY TO LOAD SPECTRA

The Second Joint NASA/FAA/DoD Conference on Aging Aircraft

Donald A. Shockey and Takao Kobayashi
SRI International
Menlo Park, California, 94025, U.S.A.

A key objective in performing failure analysis of aircraft components subjected to cyclic loads is to determine the load spectra that produced the fracture. SRI International is developing methods to extract this information from the fracture surfaces.

One method, fracture surface topography analysis (FRASTA), characterizes the topography of conjugate fracture surfaces with a confocal optics scanning laser microscope, inverts and superimposes one topograph over the other, compares the conjugate topographies with an aid of a computer, and reconstructs the details of the fracture process. A key result is the relationship of the fractured area increase rate with conjugate surface spacing. The increment of conjugate surface spacing increase measured from a base linear line is a parameter representing the inelastic deformation that occurred at the crack tip and thus may be useful in assessing the load spectrum that operated at a specific location on the fracture surface.

Another method is to consider the fracture surface profile as a wave composed of different wavelengths and determine the weighting of the component waves by applying fast Fourier transform algorithms. The resulting elevation power spectrum density curves appear to reflect the sequence of load spectrum changes and, thus, can be used to evaluate the load spectra.

A third method is to obtain the characteristics of specific fracture surface features using wavelet analysis. The density of dimples, for example, may reflect load magnitudes and we are experimenting to determine if wavelets can identify where changes in load spectrum occurred and if the surface produced by a specific load spectrum has a unique signature.

The results obtained by applying these methods to aluminum alloy specimens fractured under several fatigue conditions are presented.

ACCIDENT ANALYSIS

TO DETERMINE THE CAUSE OF STRUCTURAL FAILURES, FAILURE ANALYSTS OFTEN WOULD LIKE TO KNOW

- When the crack initiated
- The crack growth rate
- Crack growth fluctuations (accelerations, decelerations, dwell periods)
- Load conditions (K_{MAX}, ΔK, R, overloads)
- Environment conditions (temperature, atmosphere)

THE PROBLEM	THE QUESTIONS
This information is not usually available.	Do fracture surfaces contain it? Can it be extracted?

CAN WE

- Get nucleation time and growth history of a crack?

- Get loading and environmental conditions under which the crack occurred?

From microdeformation features on fracture surfaces.

EVIDENCE

That Quantitative Information Can Be Extracted From Fracture Surfaces

On crack growth history:

- **Fatigue striations—but not always 1 striation per cycle**
- **FRASTA— correlate crack face displacement with component displacement rate**

On load parameters

- **ΔK—from striations via Paris Eq**
- **R—from striation height-to-spacing ratio**
- **K_{max} and K_{min}—from combining ΔK and R**
- **Overloads—from FRASTA combined with computations**

Also, Fourier transforms of fracture surface elevation data distinguished specimens broken under different loading and environmental conditions.

Fracture Surface of Fatigued Aluminum Fuselage Skin

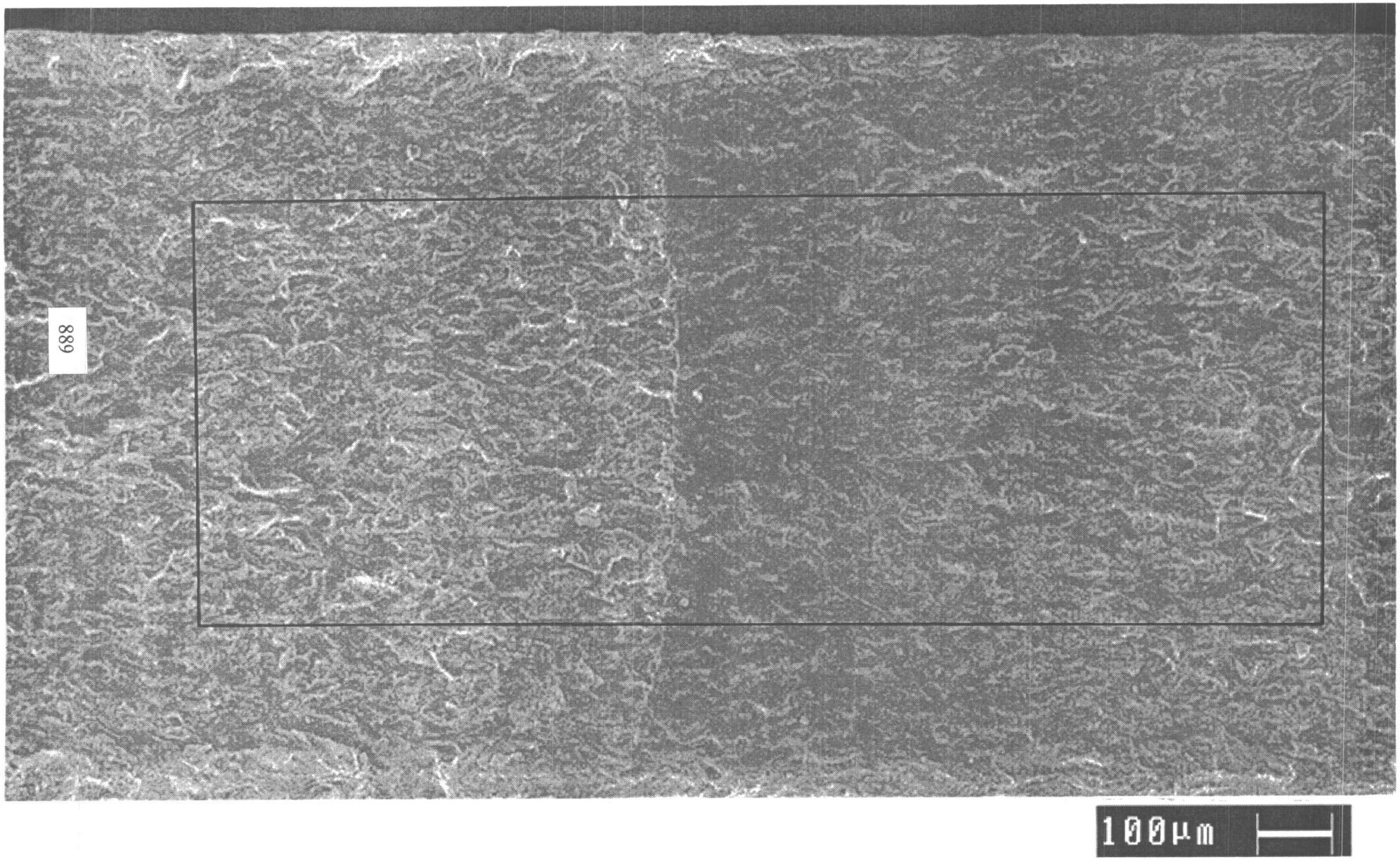

The FRASTAscope: A Computer-controlled Confocal Optics Scanning Laser Microscope with X, Y, θ Stage, Acquires, Stores, Manipulates, and Displays Topographic Data from Fracture Surfaces

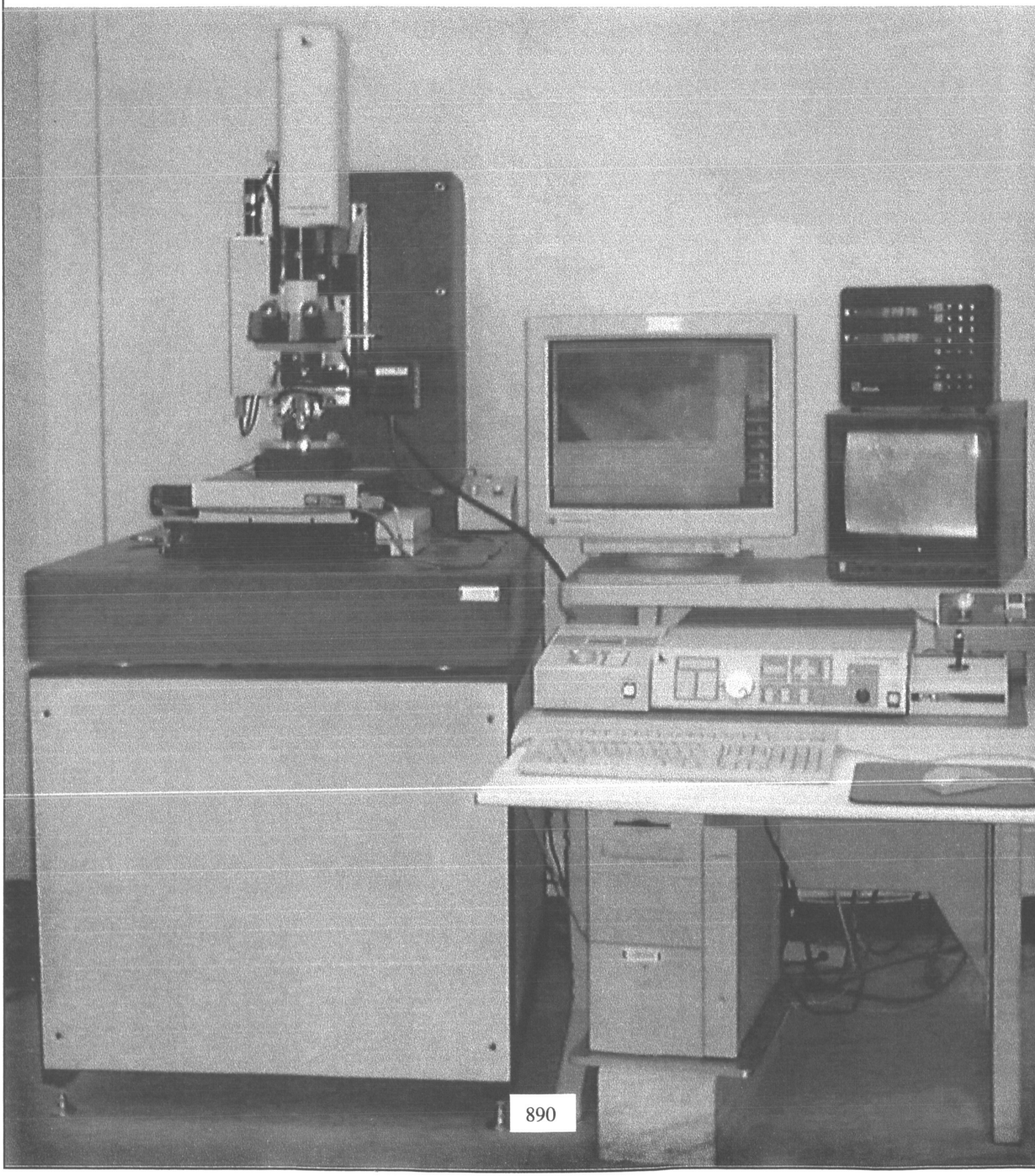

Topographic Maps of Conjugate Fracture Surfaces

Presented as Gray-scale Images

(Lighter Areas are Higher; Darker Areas are Lower)

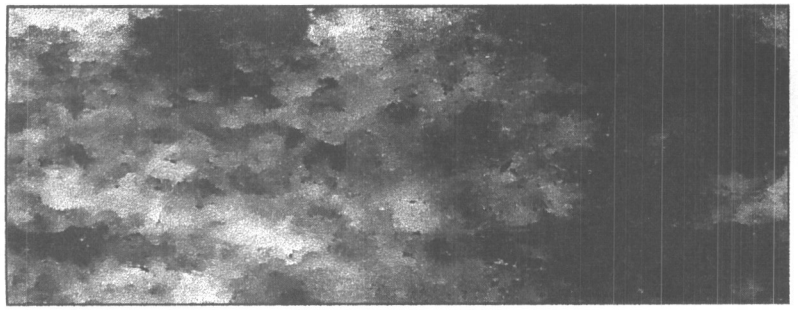

(a) Surface A

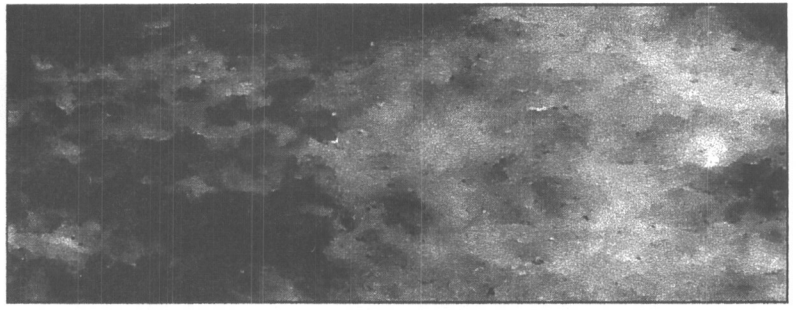

(b) Surface B

Presented as Isometric Images

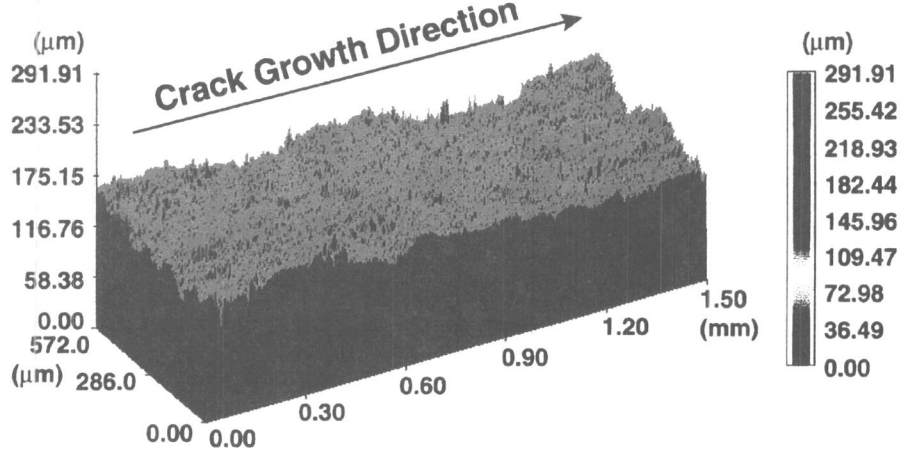

Surface A

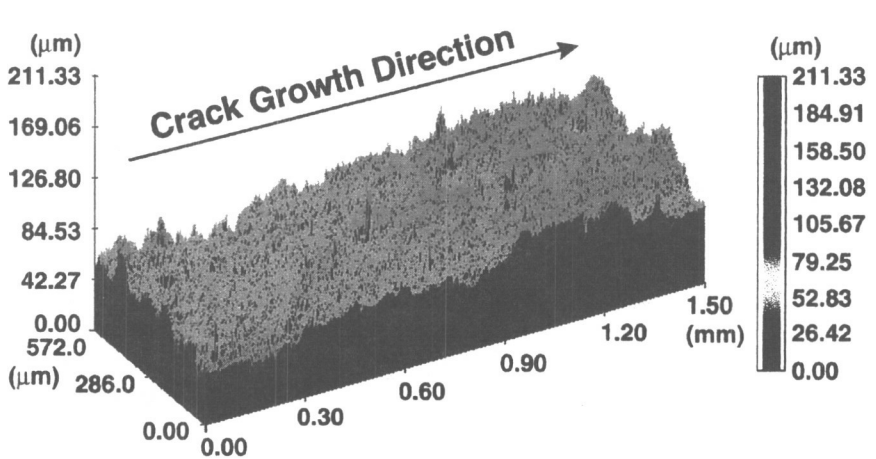

Surface B

The FRASTA Concept—Aligning Conjugate Topographs and Examining the Fit at Different Displacements

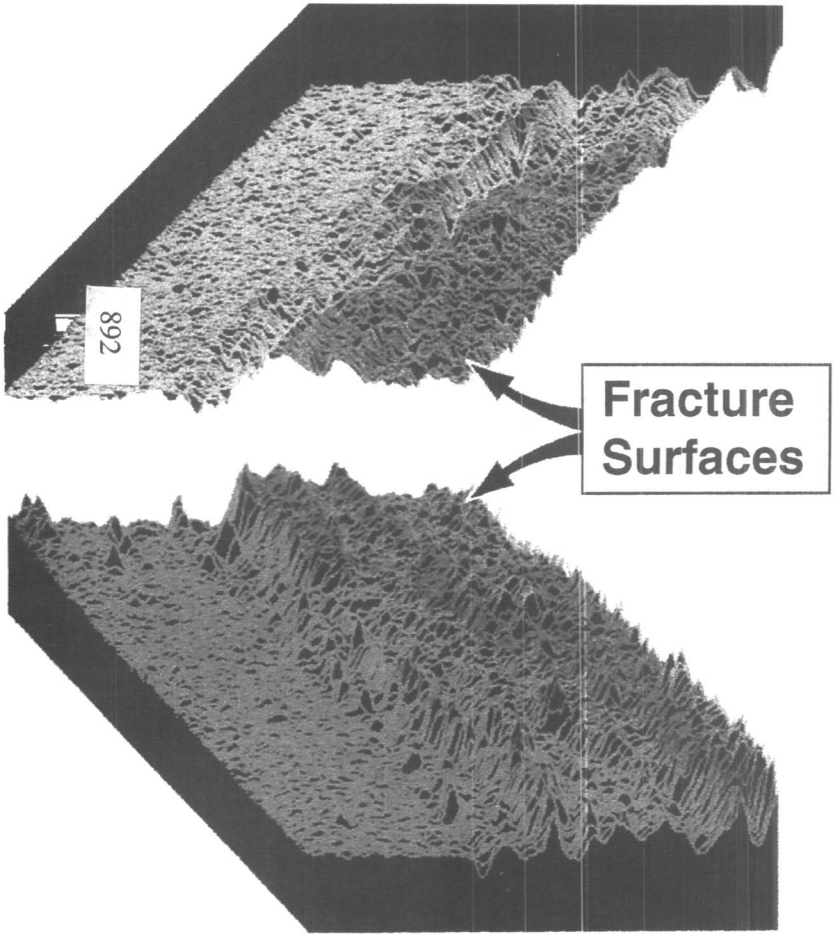

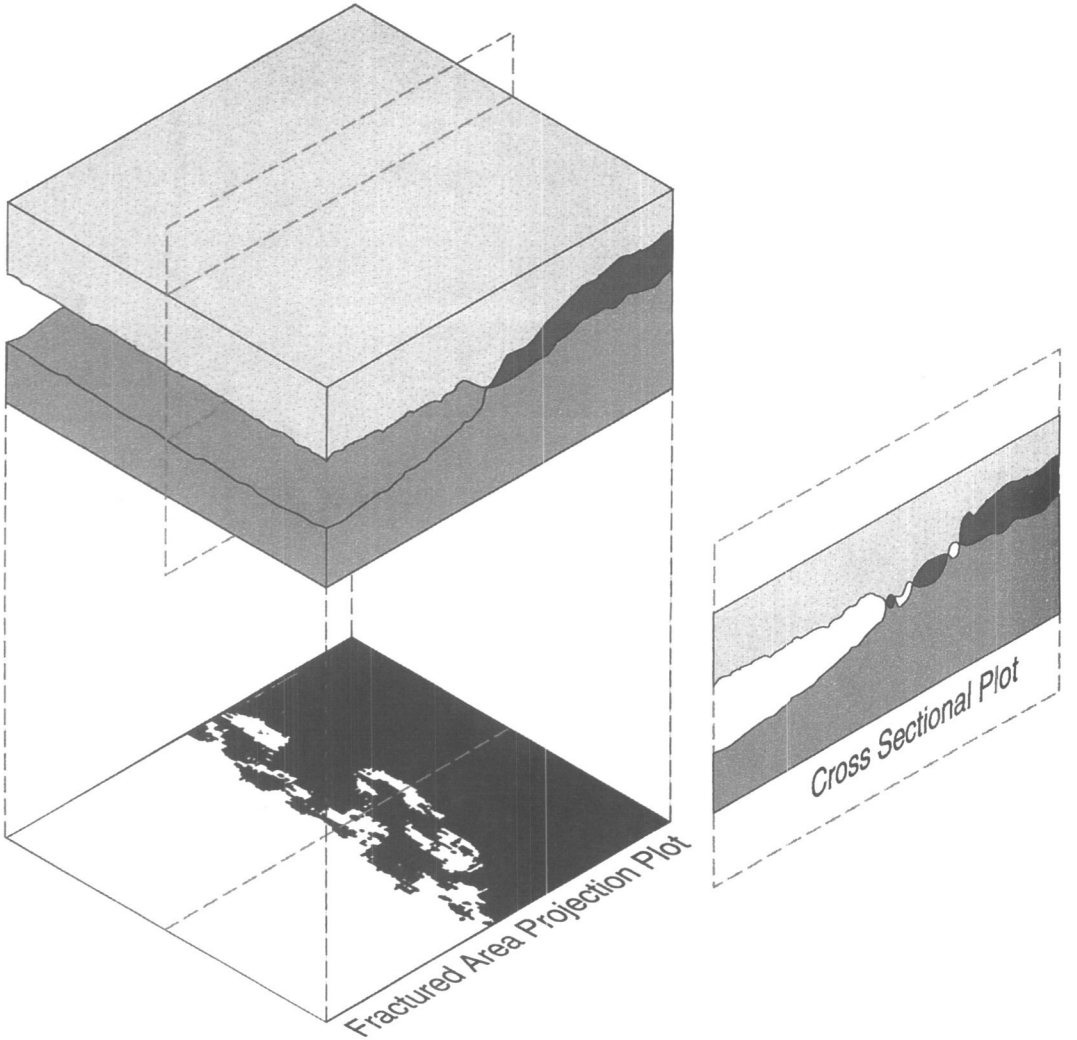

Cross-sectional Views of Crack at Several Topograph Displacements Showing Crack Progress

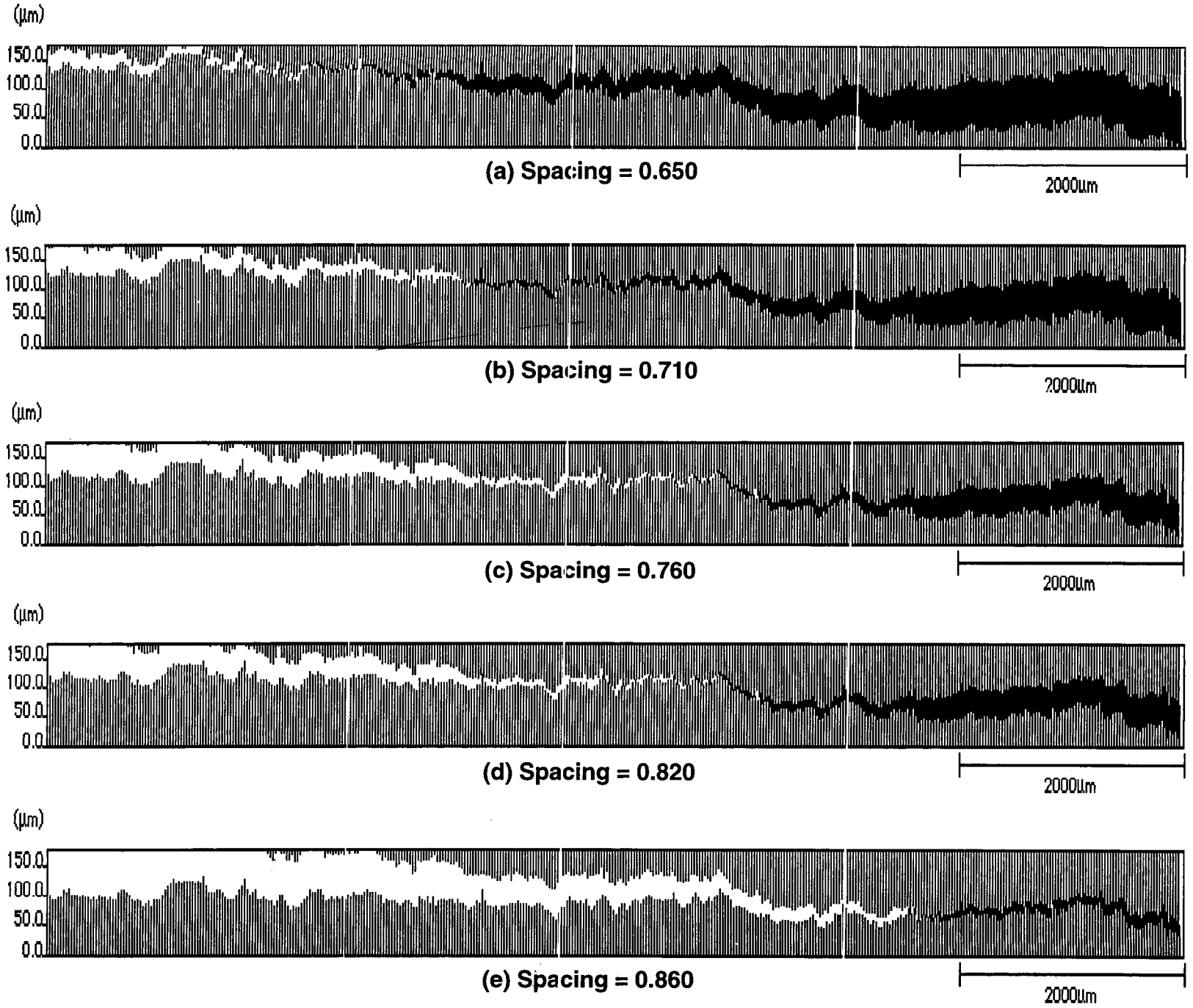

(a) Spacing = 0.650

(b) Spacing = 0.710

(c) Spacing = 0.760

(d) Spacing = 0.820

(e) Spacing = 0.860

Projections of Fractured Area at Several Topograph Displacements Showing Crack Progress

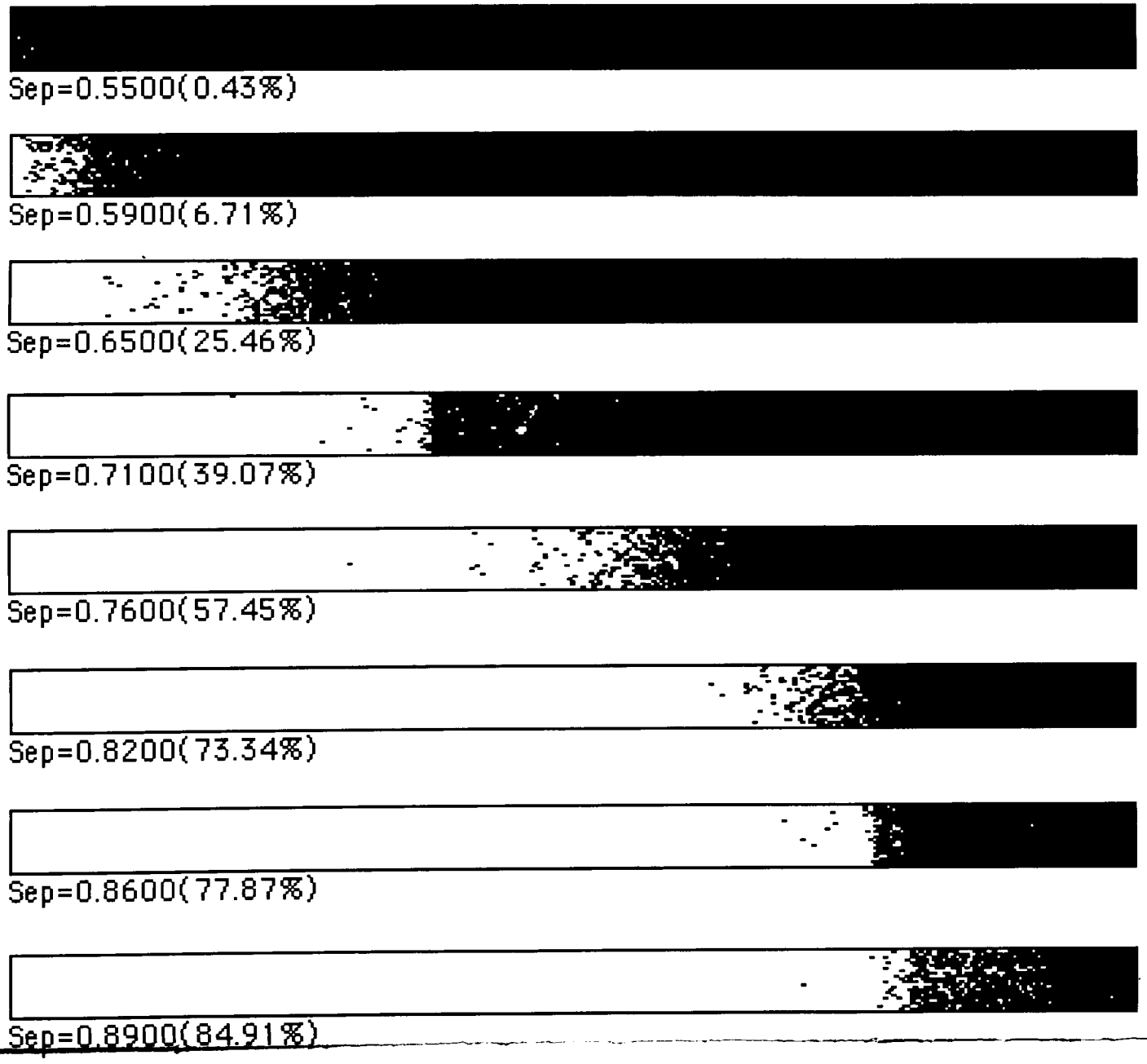

Center-Cracked Panel and Fatigue/Overload History

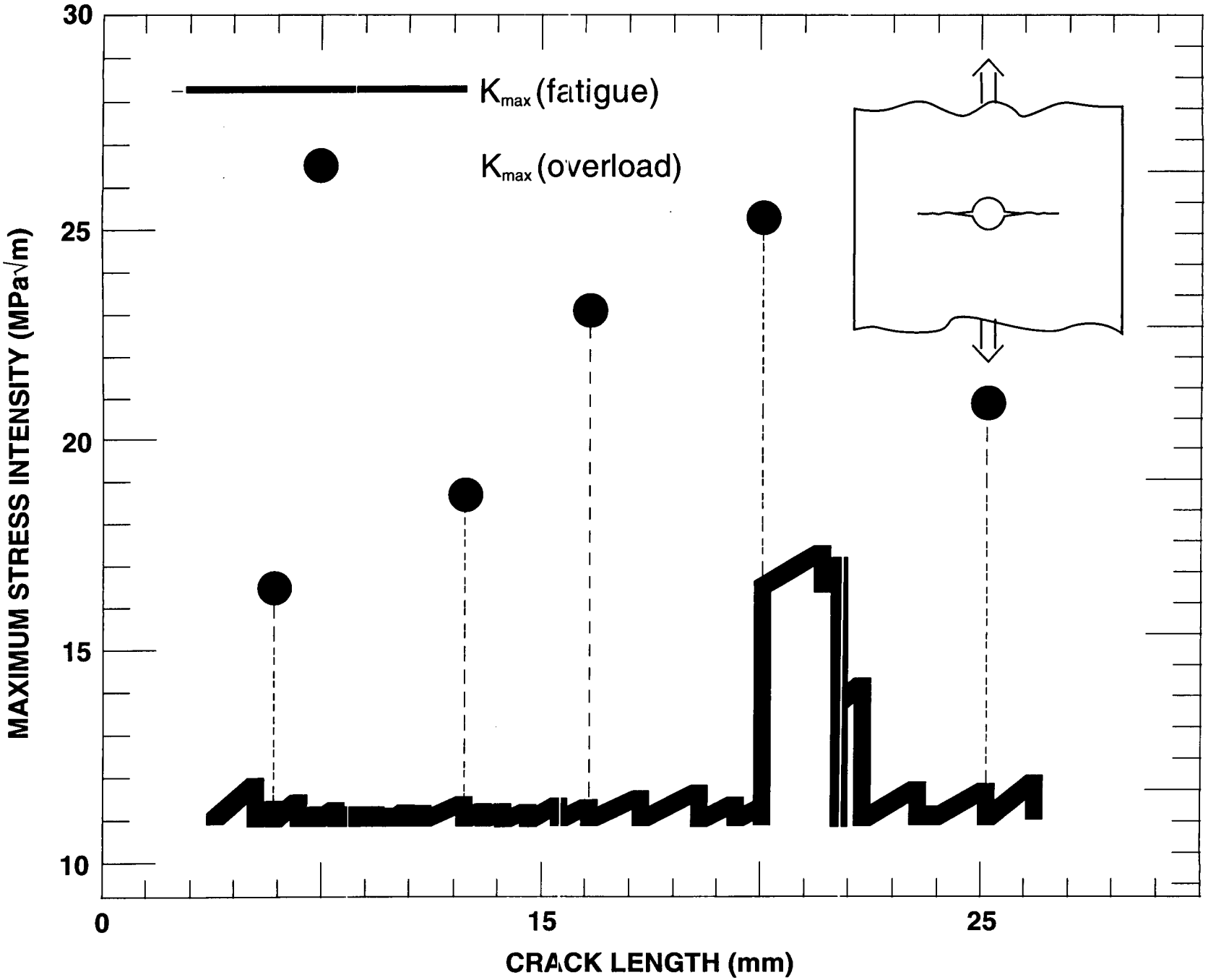

Fracture Progression Curve with Baseline

Inflections Indicate Changes in Crack Growth Rate

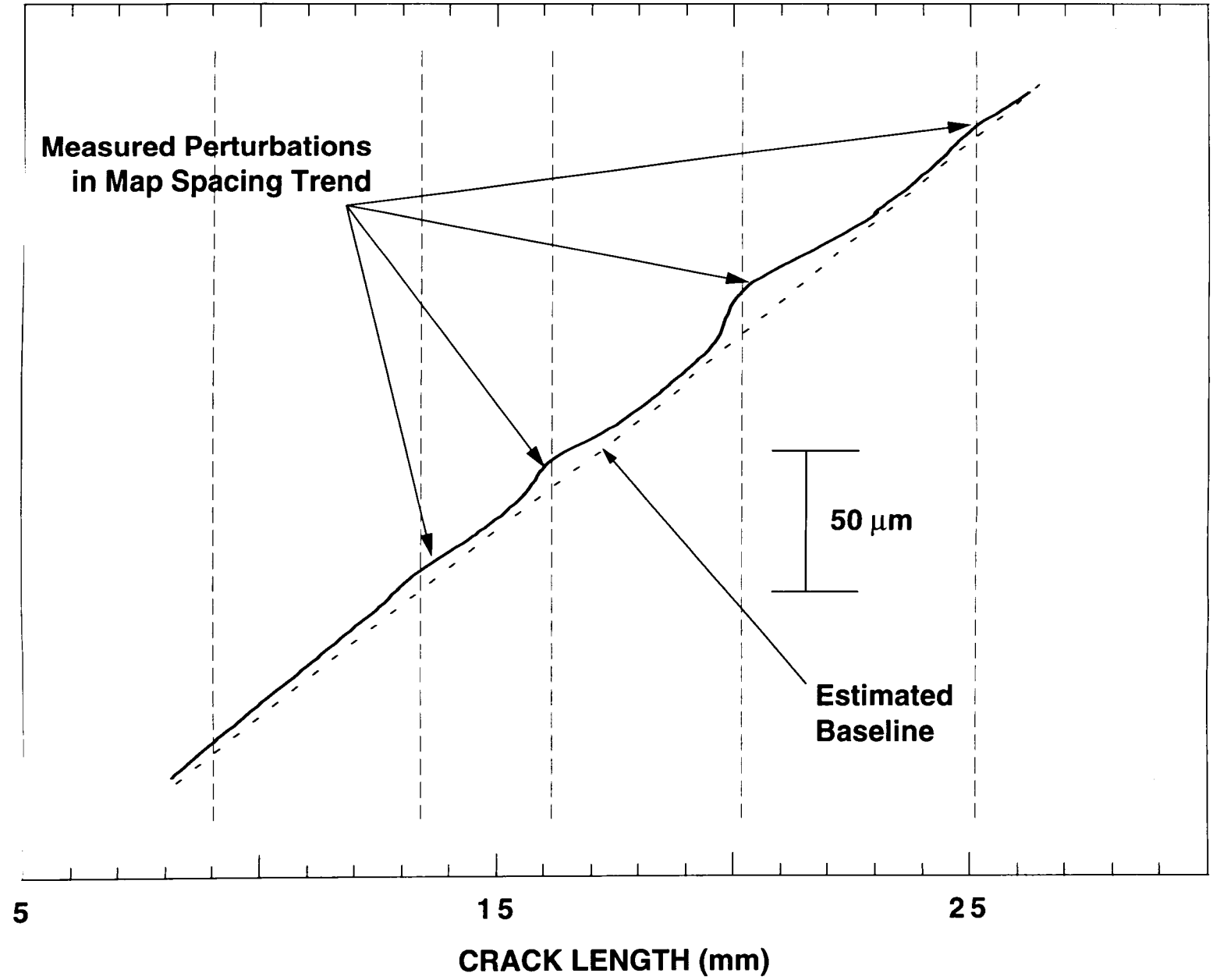

Perturbations of FPC from Baseline and Comparison with Overloads

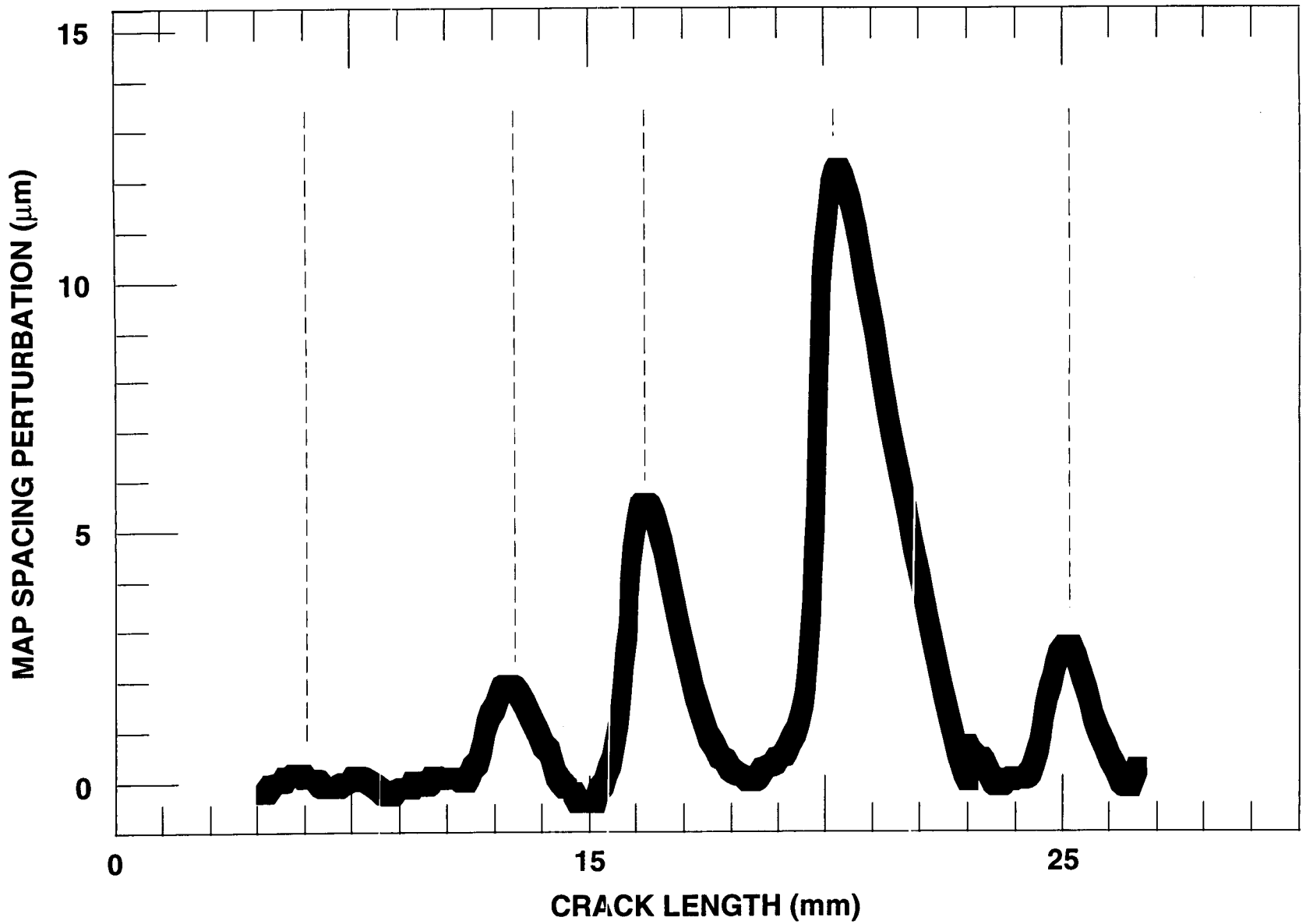

Effect of Overload Level on Deformation Step on Fracture Surface

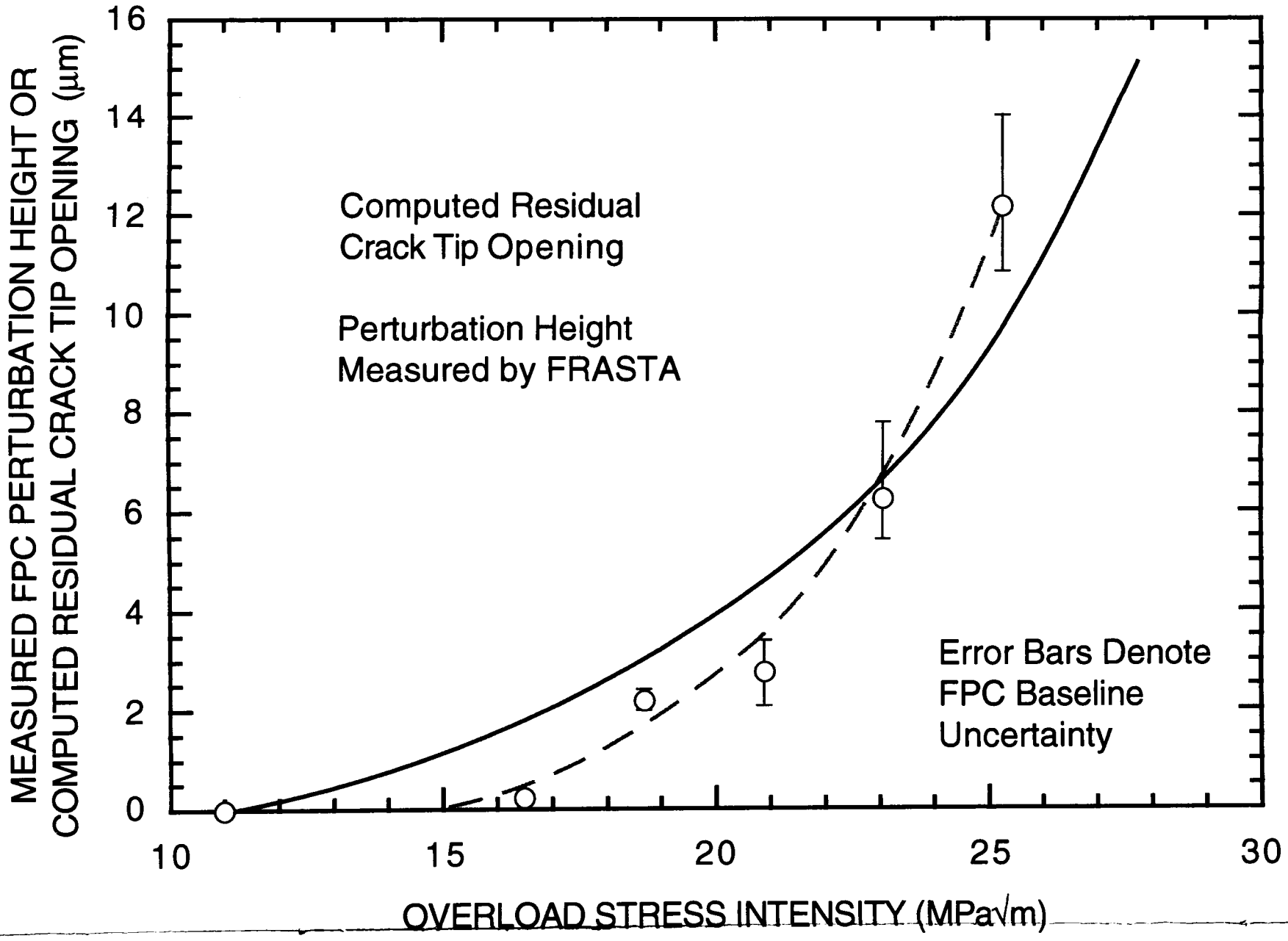

Fourier Analysis of Elevation Data

Differentiates Failure Surfaces Produced Under Different Load Spectra

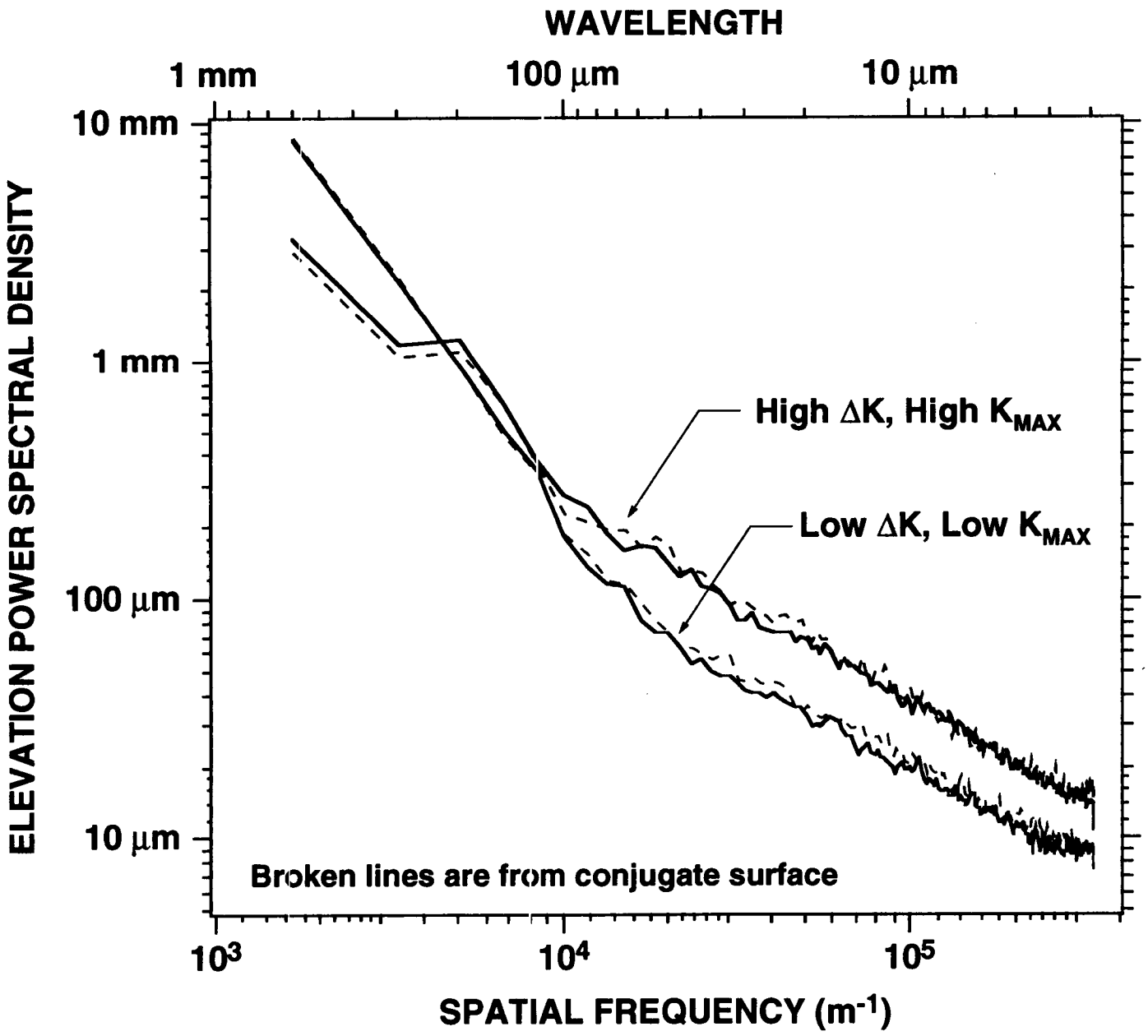

Daubechies Wavelet Transform Coefficient

From Fracture Surfaces Produced Under Different Loading Conditions

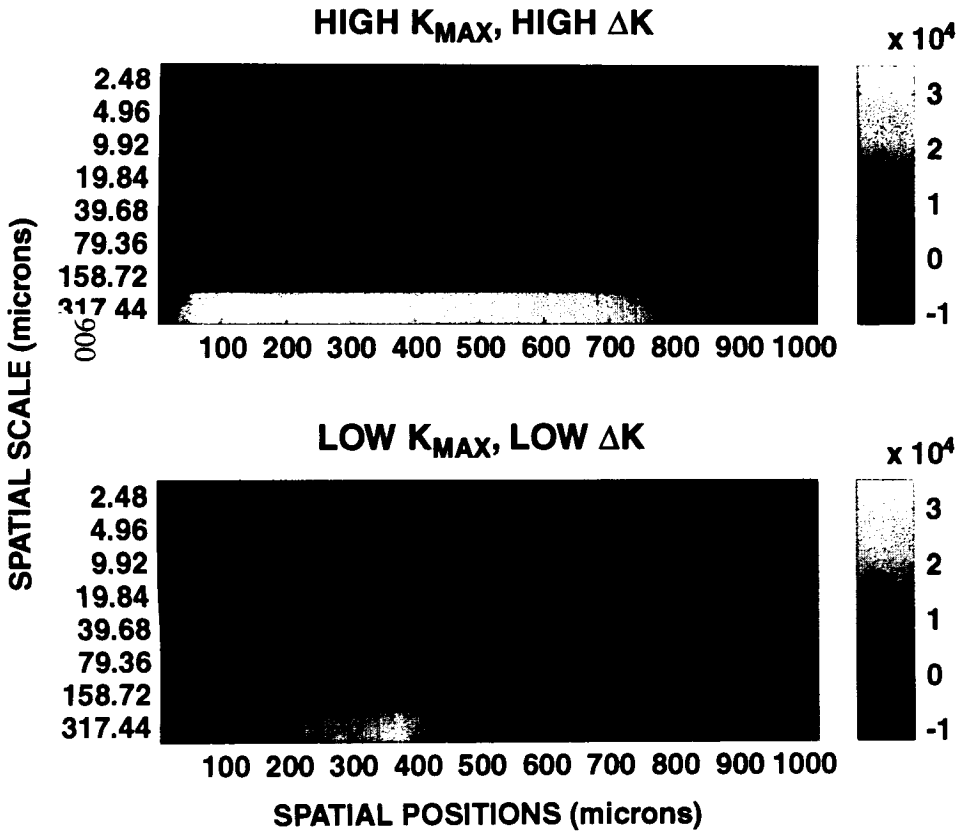

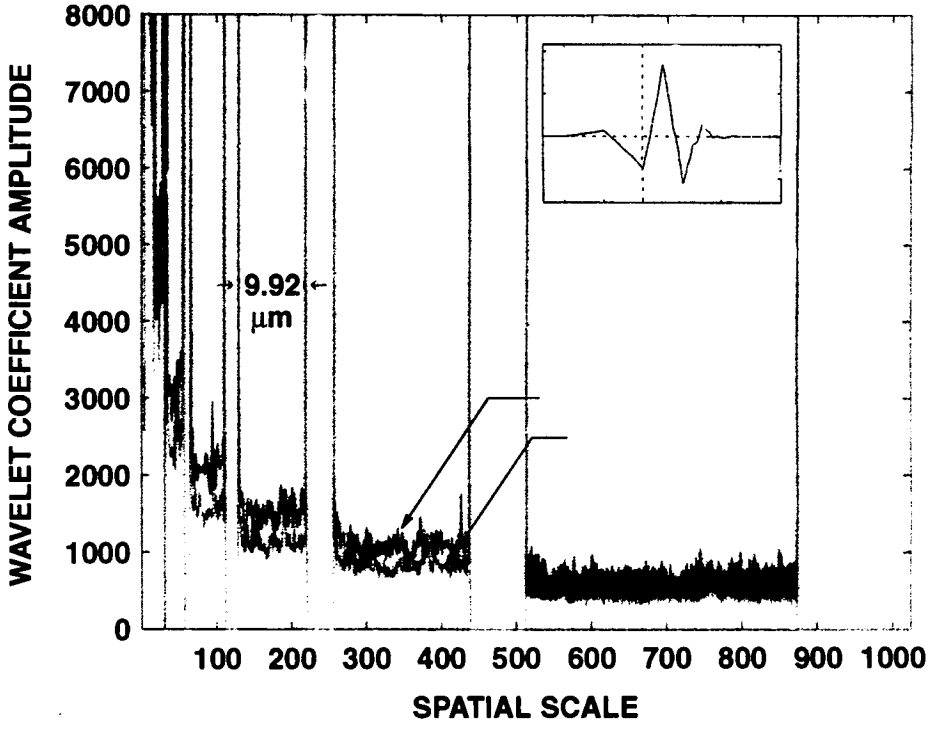

CONCLUSIONS

- Important but previously unobtainable information regarding the conditions that produced fatigue failures can likely be obtained from fracture surfaces.
- Keys to extracting this information are a fast and accurate method for characterizing fracture surface topography and a three-dimensional analysis of the data.
- Comparison of conjugate fracture surface topographs may detect and estimate magnitudes of the overload spectrum experienced by a component that failed in fatigue.
- Shapes of striations may be quantifiable by stereoscopy or COSLM and provide a means to determine maximum and minimum values of the cyclic load spectrum.
- Fourier or wavelet analyses of fracture surface topography data may provide the basis for a library of reference curves useful in determining the load spectrum and environmental conditions that caused a service failure.
- These promising findings should be explored further to seek advances in failure analysis technology.

ACKNOWLEDGMENTS

This work was supported by the Federal Aviation Administration
under Grant No. 93-G-065.

The authors thank A. K. Vasudevan, J. T. Cammett, and C. L. Brooks for bringing the problem of load spectrum determination to our attention at the Fatigue Structural Reliability Workshop on 20-22 September 1995 at West Dennis, MA. We are also indebted to Y. Chuman and M. Yamauchi of Mitsubishi Heavy Industries, ltd. for suggesting the use of Fourier analysis to characterize fracture surfaces.

TITLE:

AIRCRAFT CORROSION INSPECTION AND EVALUATION TECHNIQUE USING SCANNING ULTRASONIC METHODS

AUTHORS/AFFILIATIONS:

T. P. SIVAM and CARL M. OCHOA

Raytheon E-Systems - Waco
7500 Maehr Road
Waco, Texas 76705 USA

Vista Engineering Services, Inc.
1301 Barthelow Drive, Suite 4A
College Station, Texas 77840
USA

(In Collaboration with Texas A & M University, College Station, Texas, USA)

903

ABSTRACT

The present work is based upon the collection and evaluation of scanned ultrasonic data from corroded coupon test specimens. The ultimate purpose is to support an approach for a rating scale that can be used to monitor and evaluate quantitatively the effect of detected corrosion in aircraft upon service life for safety evaluation and for the planning of maintenance. Even though the results are preliminary, they indicate the utility of the methodology for aircraft maintenance purposes for some structural materials. For the present effort, representative structural thickness (.063 in.) of 2024 T3 aluminum coupons were corroded by exposure to sea salt water immersion as a simulation of aircraft skin corrosion. These coupons were subsequently examined using scanning ultrasonics and used to identify correlations between the corrosion mass loss and the residual strength and cyclic fatigue life of the coupons. The results indicate that for the corrosion mechanisms considered, it is likely that an accurate and useful field assessment of corrosion may be made at the aircraft maintenance facility level, and that a rating scale is a realistic approach. The rating scale can be used in conjunction with ultrasound data collected from an aircraft and design and service history information to make projections of maintenance intervals and useful service life. Future efforts will address other structural materials such as 7075 T6 aluminum, and will focus upon quantifying intergranular effects in terms of their detection and their contribution to the structural degradation process during corrosion.

NEED FOR "QUANTIFYING" CORROSION

Many U. S. Military Aircraft that have been in service for a long time, including C/KC-135s, C-130s, C-141s and C-5s, have been exposed to adverse atmospheric conditions and contaminants. The effect of resulting corrosion damage on structural integrity is not readily quantifiable or predictable. There is a need for developing more reliable techniques to detect and quantify corrosion damage to estimate the residual safe life of aircraft structures. Further understanding of corrosion phenomena, corrosion prevention, and corrosion repairs will enhance the safety and effective use of aging military and commercial aircraft.

METHODOLOGY

1. **Among the most commonly used high-strength aluminum alloys for the construction of modern aircraft, 2024-T3 alloy was selected for this "corrosion" program, because of its favorable combination of mechanical properties and relatively simpler chemical process in comparison to 7075-T6 alloys.**
2. **Dog-bone shaped test samples of size 3" x 12" x 0.063" thick, were corroded in the center gage area of 1.8" wide by 2.3" long, while the rest of the surface areas were painted with epoxy primer to avoid corrosion in areas other than the gage area. Fig 1 shows typical Dog-bone shaped test sample with the center gage area for corrosion.**
3. **906 he test specimens were corroded using "instant ocean" salt water-electrolyte, powered by Kepco model no. ATE 36-8M 1533 power supply with 800mV between the graphite and the test specimens. Fig 2 shows the "corrosion" set-up for various mass loss of test samples due to corrosion.**
4. **The test samples were corroded at various levels of mass losses resulting approximately 10%, 20%, 30%, and 40%. The mass loss measurements of test samples were monitored using control samples of 2"x2"x0.063" corroded simultaneously with the actual test samples. There were a total of 56 test samples corroded with allocation of 14 samples for each of the four (4) sets of mass loss of corrosion levels given above.**

METHODOLOGY (Continued)

5. All corroded test samples were precisely monitored and weighed for mass loss comparison, before and after corrosion and again after cleaning the corrosion products deposited in the gage area. The samples were cleaned per ASTM G 1 or equivalent procedure, so that no metal was removed during cleaning. Fig 3 shows an un-corroded test sample, while Fig 4 shows typical samples after "corrosion" materials were cleaned off at the gage area.
6. All samples were subjected to scanning ultrasonic inspections using a grid size of 0.01"x0.01" and covered 200x250 points in measuring the remaining thickness due to corrosion at the gage area, and mass losses were also computed using ultrasound data. The samples were also photographed using digital camera with1280x960 pixel resolution. Also, some samples were selectively taken photomicrographs to show details of corroded surfaces under various levels of corrosion and mass loss.
7. The photomicrographs shown for a test sample with low mass loss of 7.1% in Fig. 5 (sample ID# 2B-F-0-03) and for another sample with high mass loss of 16% in Fig. 6 (sample ID# 2B-F-40-02) can be compared. For low mass loss due to corrosion, there is still some metal surface left un-corroded and relatively there are fewer number of smaller size pits (see Fig. 5) as compared to many number of larger size pits (see Fig. 6) as distributed on the corroded gage area.

METHODOLOGY (Continued)

8. Fig. 7a shows a typical digital camera picture of a corroded sample (ID #7) with 6.5% mass loss, while Fig. 7b shows the same sample (ID #7) with 6.5% mass loss obtained from ultrasonic data. The digitized ultrasonic data were correlated to the digitized photographic data for most of the test samples. Fig. 7 shows a typical correlation between the digitized ultrasonic and photographic data for the sample ID #7 with 6.5% mass loss due to corrosion. The ultrasonic data presented are related to thickness reduction. The photographic data are related to the light intensity reflected off the corroded surface, which is determined by the size and distribution of corrosion-induced pits. Since thickness reduction due to corrosion as letected through ultrasound is not directly related to the reflected light ntensity off the corroded surface pictured by the digital camera, the computed correlation coefficient "r" is very low (r = 0.26). We are currently extending the processing of ultrasound data to quantify pit size and distribution of corrosion-induced pits to improve the correlation between the digitized ultrasound and optical data. The correlation computations and picture plots for sample ID#7 as shown in Fig. 7 were performed using an advanced state-of-the-art IDL5.0 statistical software package.

9. All corroded samples of various percent mass loss were tested for the residual static strength and fatigue cycles at 10Hz, 16ksi, with R=0.1. There were a total of seven dog-bone samples tested for static as well as fatigue cycles under each of the four (4) sets of percent mass loss.

10. The number of test samples were increased by twenty (20) more and they were corroded to yield mass loss between the range of 4% - 13%. Ten samples for each of the static and fatigue tests were chosen with mass loss distributed between 4% - 13% for both tests.
11. In order to assess the residual strength and fatigue life of corroded samples, as compared to un-corroded samples, seven samples for each of the static and fatigue conditions were tested without corrosion.
12. There were a total of ninety (90) samples of which 14 un-corroded, 76 corroded conditions tested for both the static and fatigue tests with the number of samples and range of percent mass loss of samples equally divided between the two tests. The test matrix is shown in Table-I.
13. All un-corroded samples survived the fatigue cycles up to 3 million cycles. A typical shear failure at 45 degrees to the load axis of an un-corroded sample tested for static strength is shown in Fig. 8a. The static fracture of a corroded sample is shown in Fig. 8b, while the fatigue fracture of a corroded sample is shown in Fig. 8c.
14. The results of the residual static strength vs. percent mass loss are plotted and shown in Fig. 9 and the residual fatigue life vs. percent mass loss is shown in Fig. 10.
15. Current work involves in the corrosion of 7075-T6 aluminum alloy in collaboration with Texas Tech University, Lubbock, Texas. A rating scale development is underway for both 2024-T3 and 7075-T6 aluminum alloys.

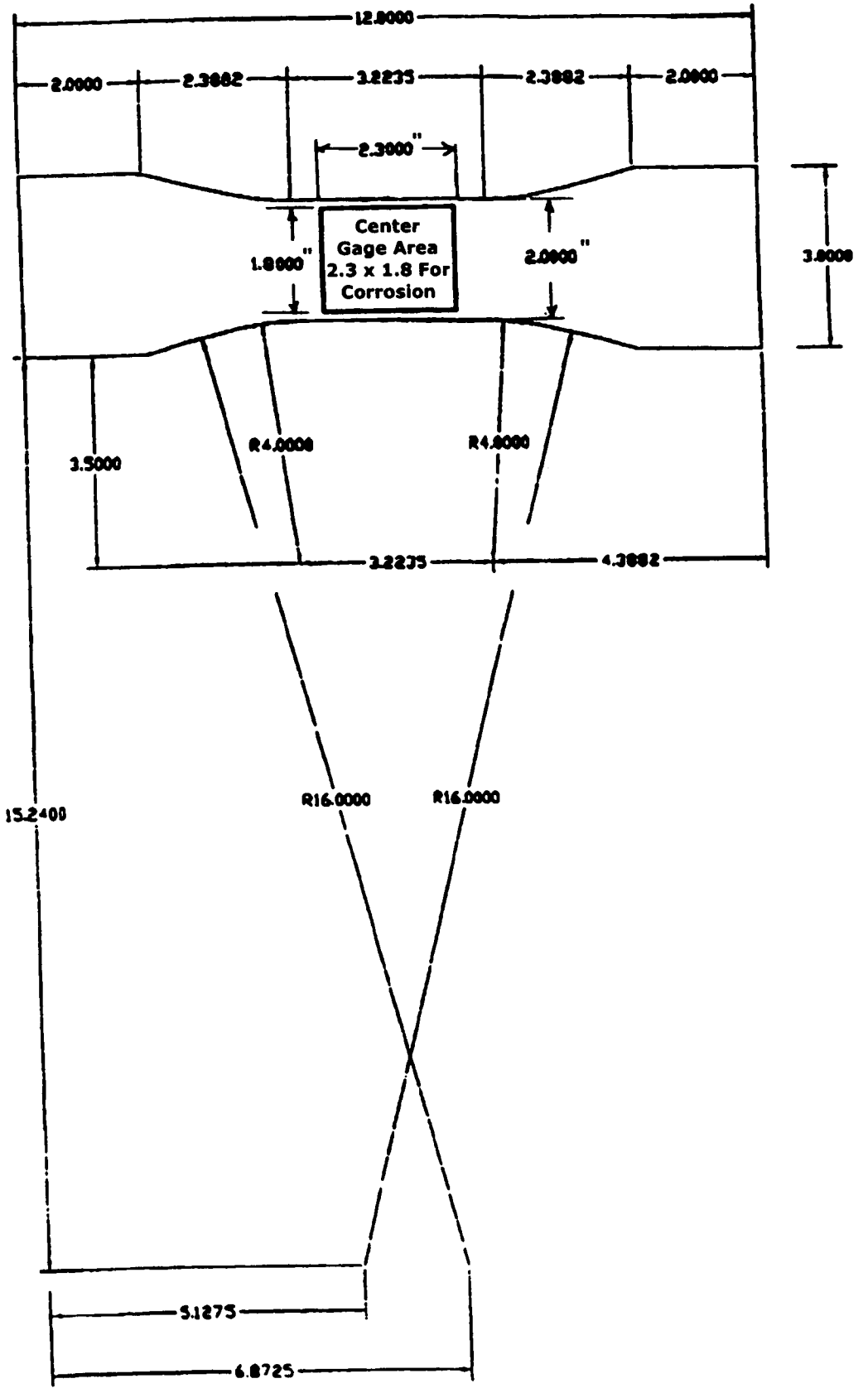

Figure 1. Typical Dimensional Sketch for the Dog-Bone Test Sample With Center Gage Area for Corrosion on One Side Marked-Up

Figure 2. Corrosion Set-Up Showing Four (4) Levels of Mass Loss for Various Test Samples

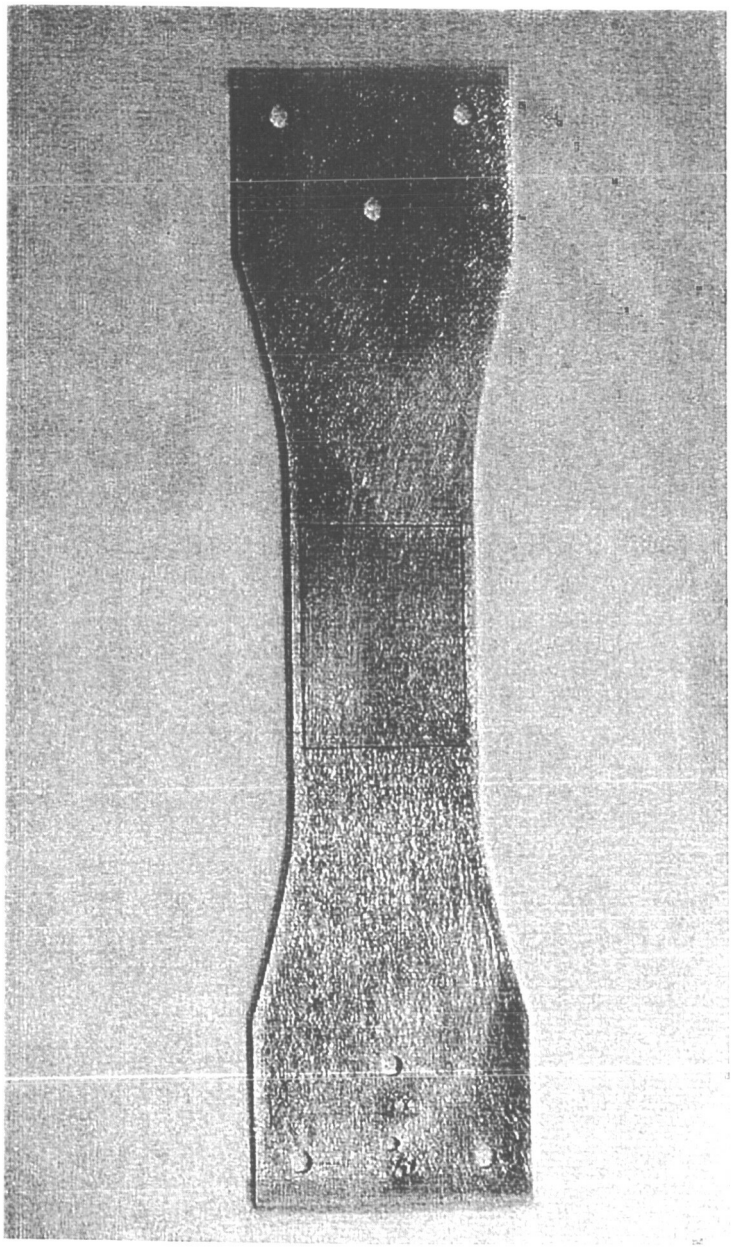

Figure 3. Typical Dog-Bone Test Sample Fabricated with the Center Gage Area for Corrosion Marked Up

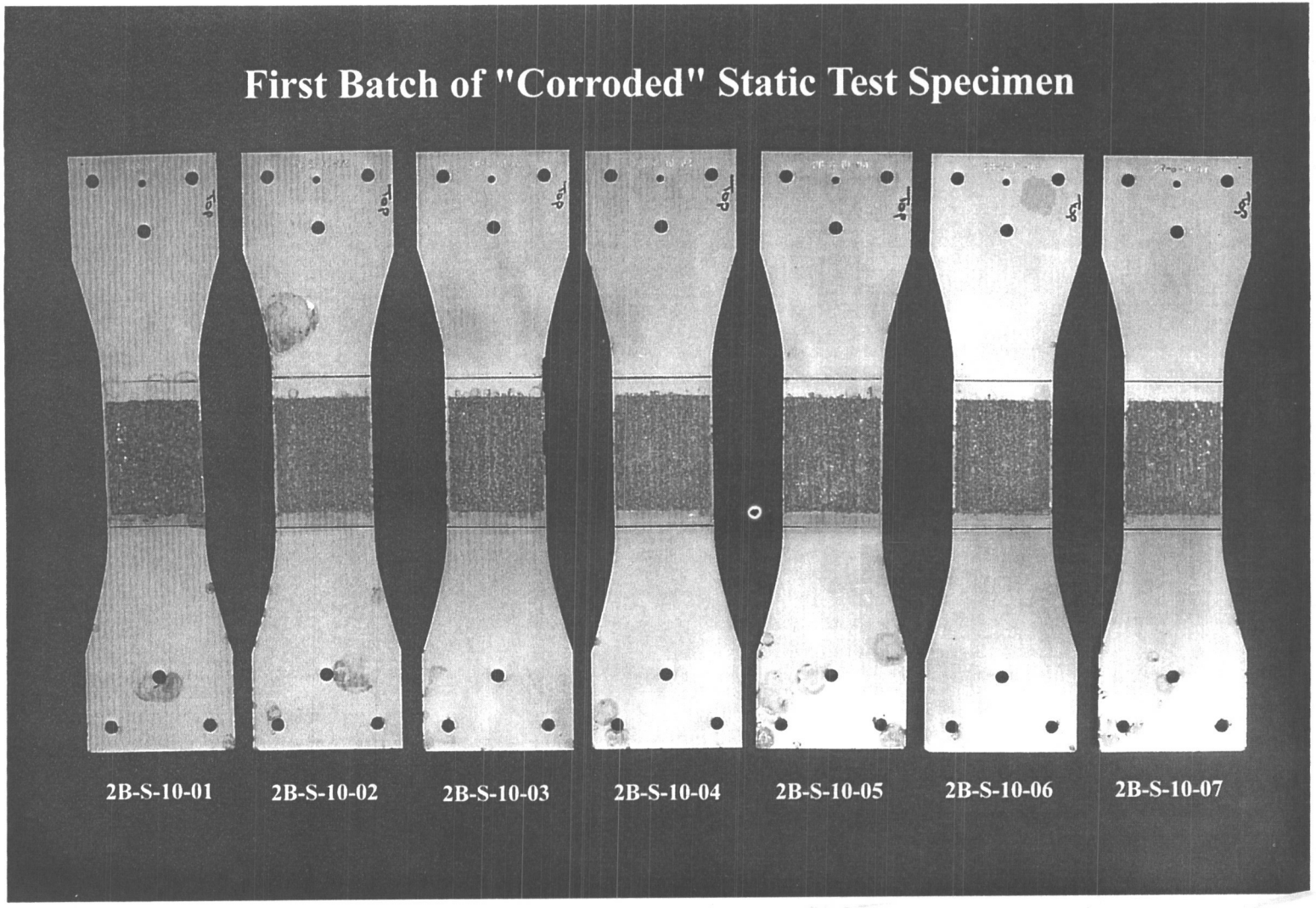

Figure 4. A Set of Seven Test Samples Corroded to Approximately 10% Mass Loss and Cleaned Before Testing

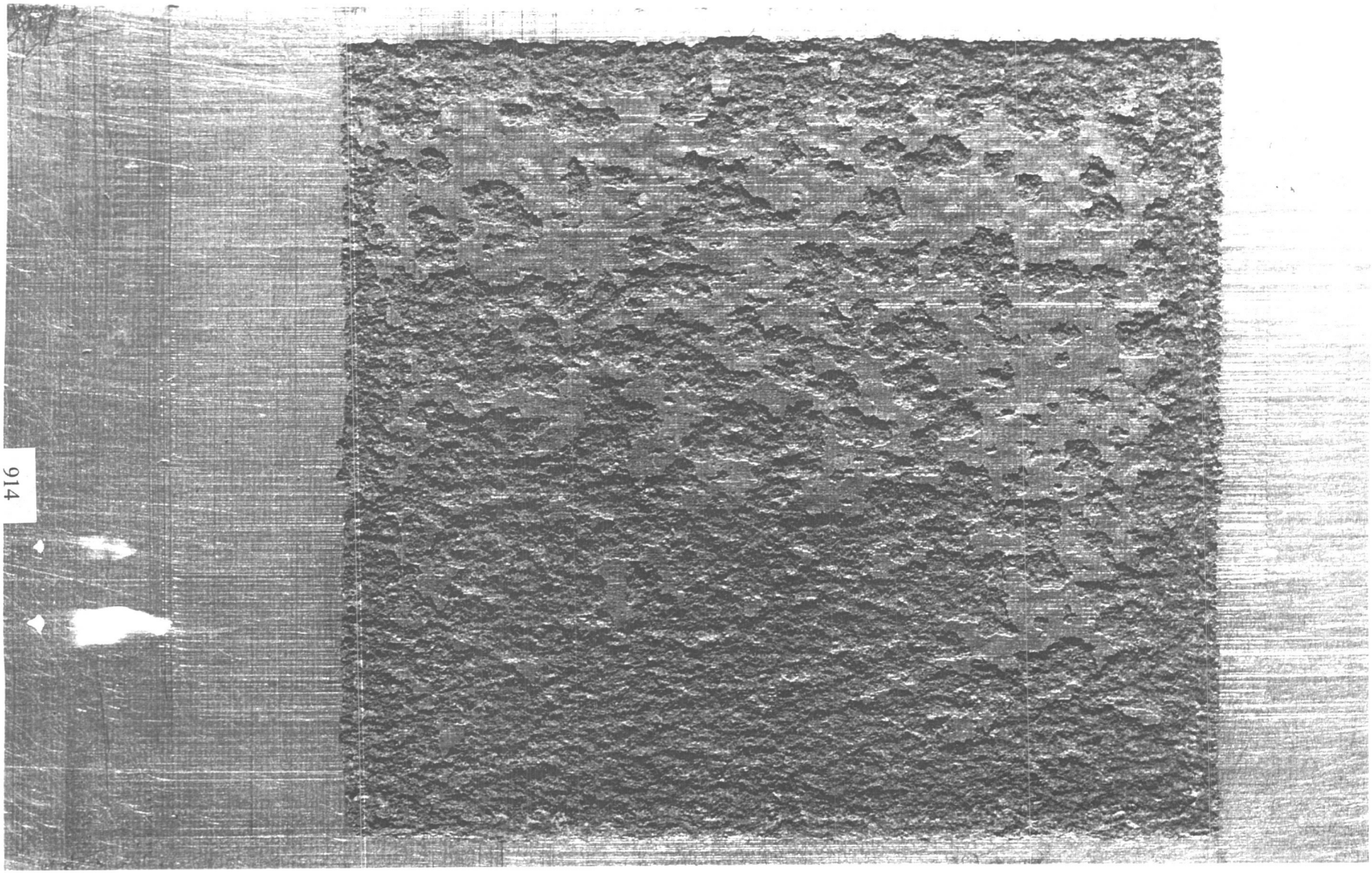

Figure 5. Typical Photomicrograph of a Low (7.1%) Mass Loss Corroded Sample of 2024-T3 Aluminum Alloy

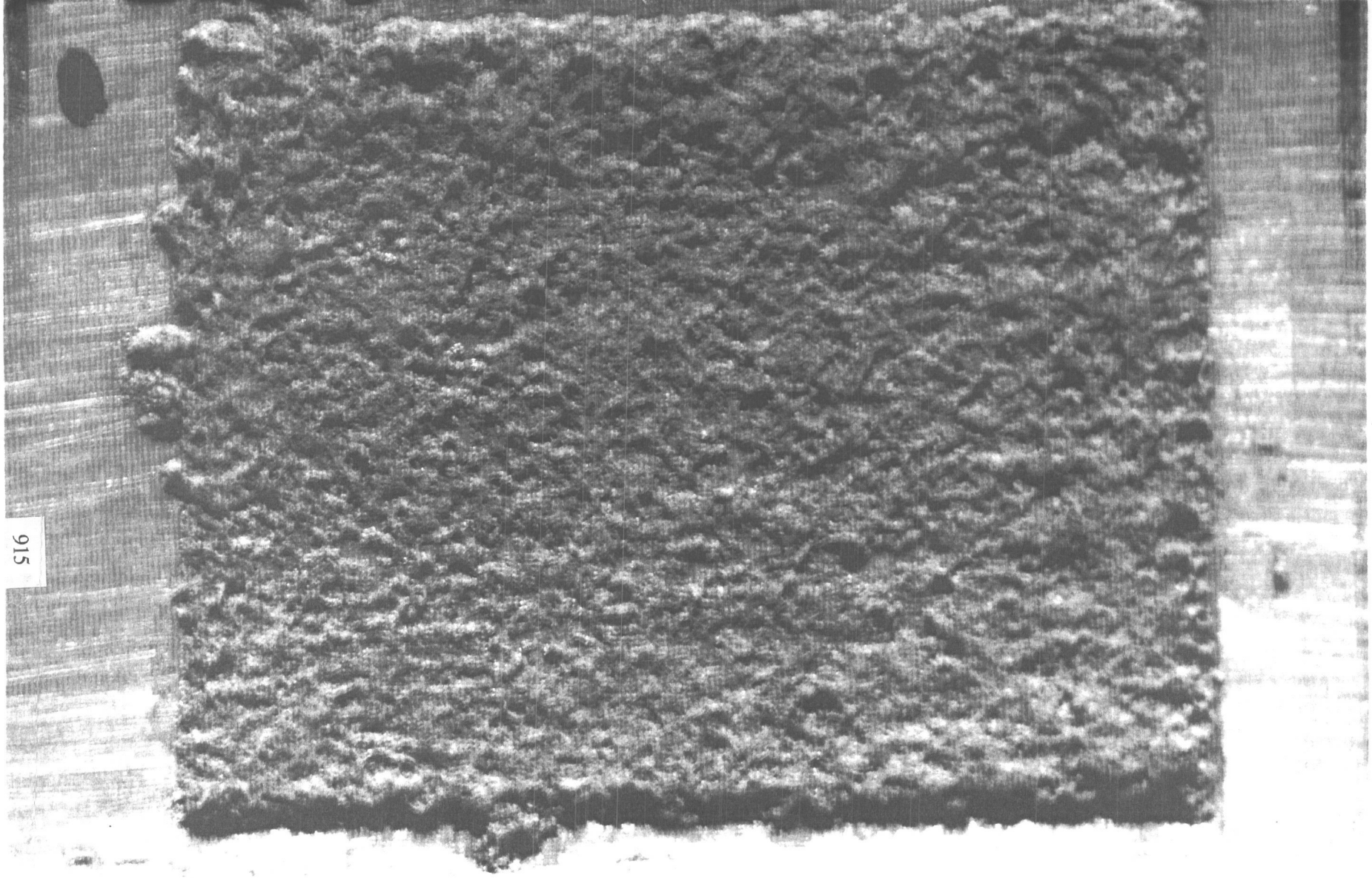

915

Figure 6. Typical Photomicrograph of a High (16%) Mass Loss Corroded Sample of 2024-T3 Aluminum Alloy

(a) Digital Camera Image

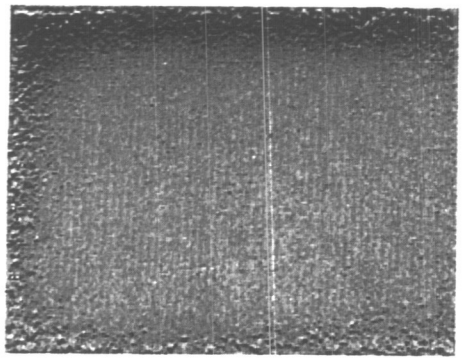

(b) Ultrasonic TOF Image

(c) Image of Absolute Difference

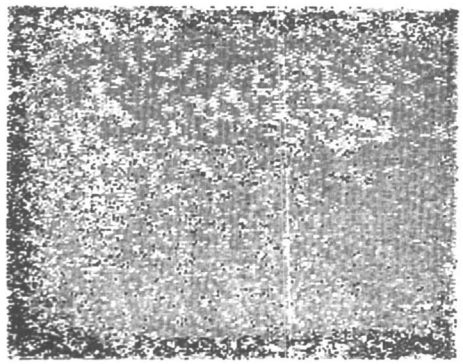

Statictics	
Camera Data	
Mean:	61.6081
Variance:	189.257
Skewness:	−0.294545
Kurtosis:	0.442039
Mean ABS.Dev.:	10.7182
Standard Deviation:	13.7571
Ultrasonic Data	
Mean:	205.540
Variance:	3637.08
Skewness:	−1.66791
Kurtosis:	1.76188
Mean ABS.Dev.:	45.4569
Standard Deviation:	60.3082
Pearson Correlation Coefficient	
Correlation Coefficient:	0.264479

Figure 7. Correlation of Digitized Data Between Digital Camera and Ultrasonic Images of a Typical Corroded Sample of 2024-T3 Aluminum Alloy

TABLE-I TEST MATRIX FOR 2024-T3

TEST CONDITION	STATIC TEST	FATIGUE TEST	REMARKS
NO CORROSION	7	7	0% CORROSION
SALT SOL'N IMMERSE, TIME 1	7	7	APP 10% CORROSION
SALT SOL'N IMMERSE, TIME 2	7	7	APP 20% CORROSION
SALT SOL'N IMMERSE, TIME 3	7	7	APP 30% CORROSION
SALT SOL'N IMMERSE, TIME 4	7	7	APP 40% CORROSION
SALT SOL'N IMMERSE, TIME 5 (VARIED)	10	10	APP 4% TO 13% CORROSION
TOTAL NUMBER OF SAMPLES	45	45	90 TOTAL

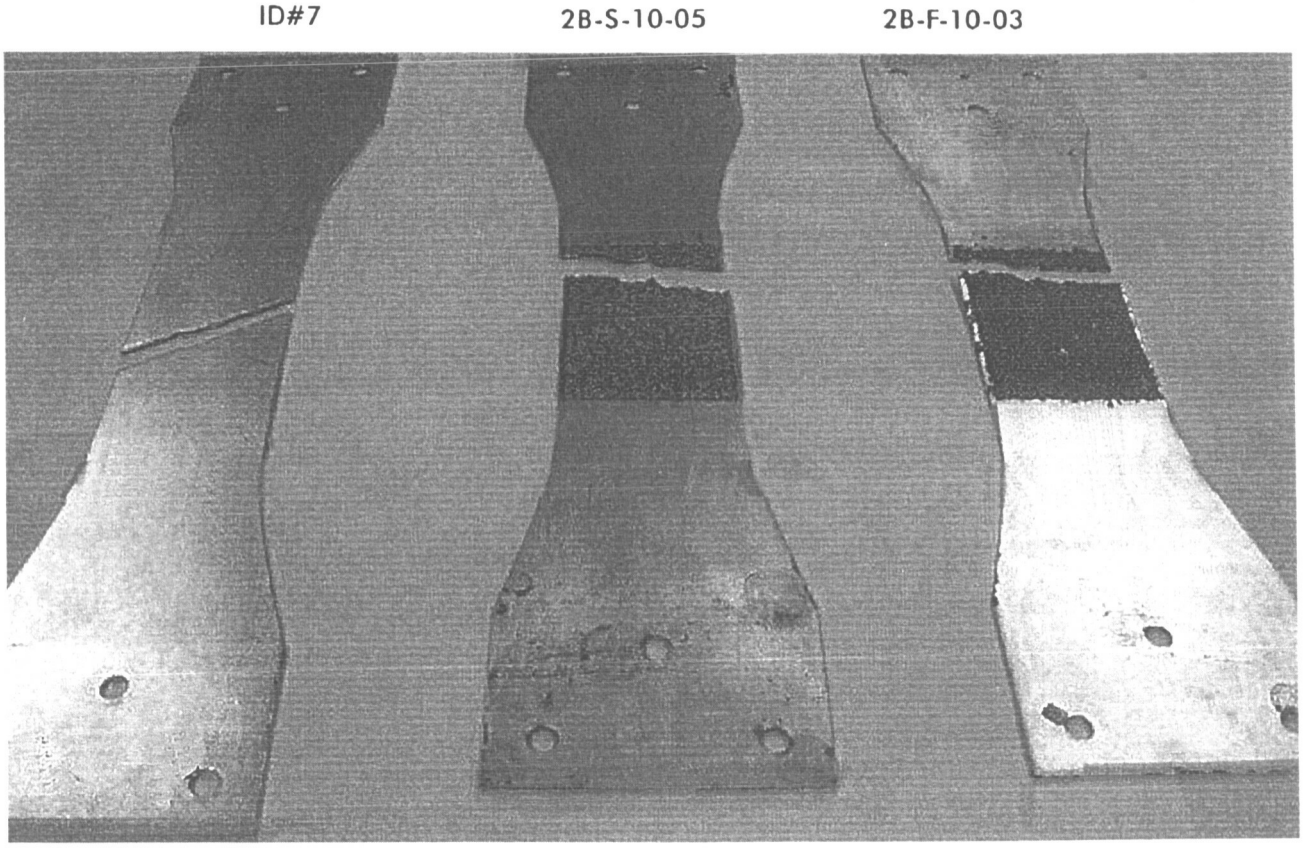

Figure 8. (a) Typical Shear Failure of Un-Corroded 2024-T3 Aluminum Alloy Test Sample in Static Loading

(b) Typical Net-Section Failure of Corroded 2024-T3 Aluminum Alloy Test Sample in Static-Loading

(c) Typical Net-Section Fatigue Fracture of Corroded 2024-T3 Aluminum Alloy Test Sample in Fatigue Loading

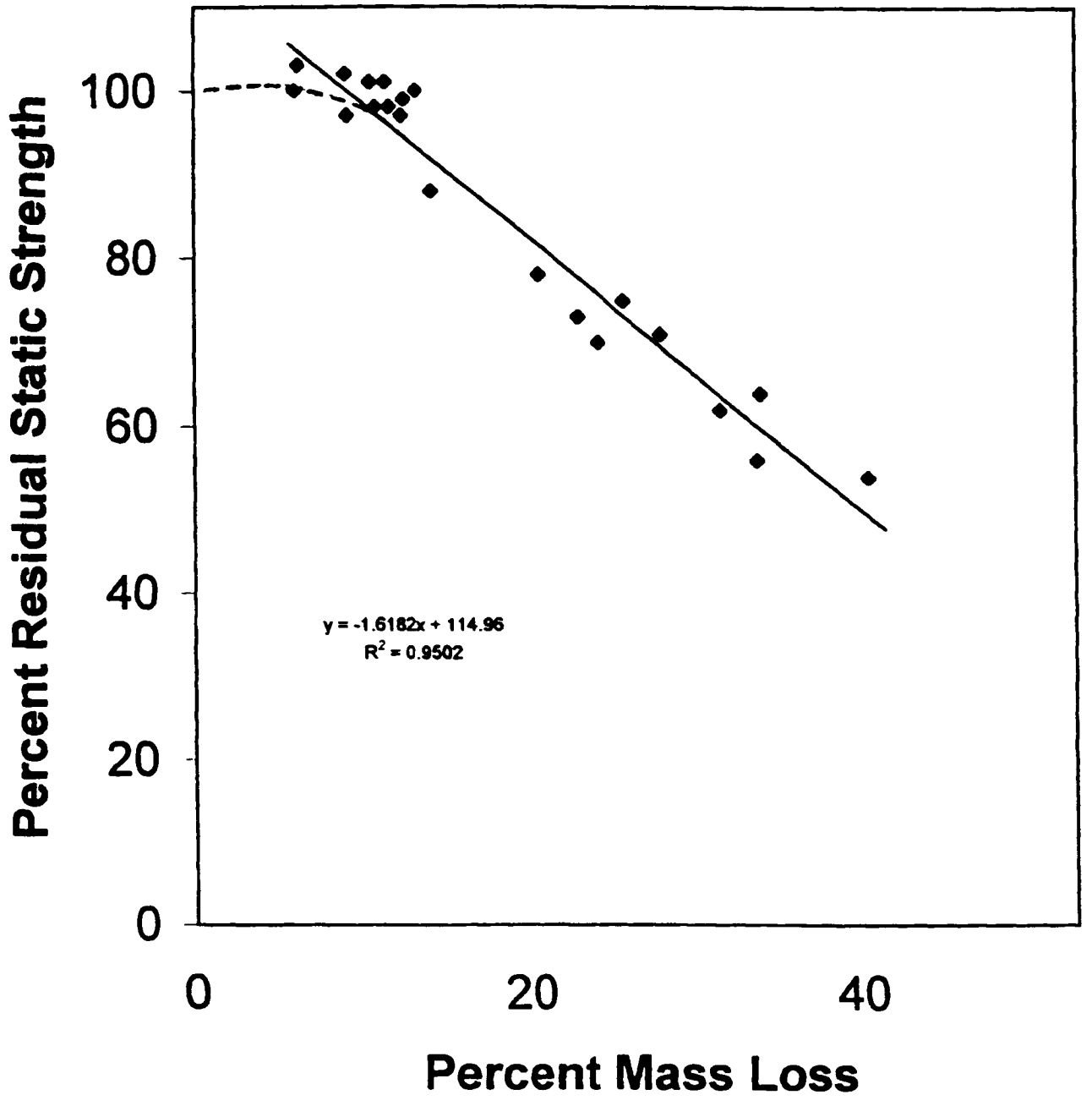

Figure 9. Correlation of Static 919 **ıgth with Percent Mass Loss**

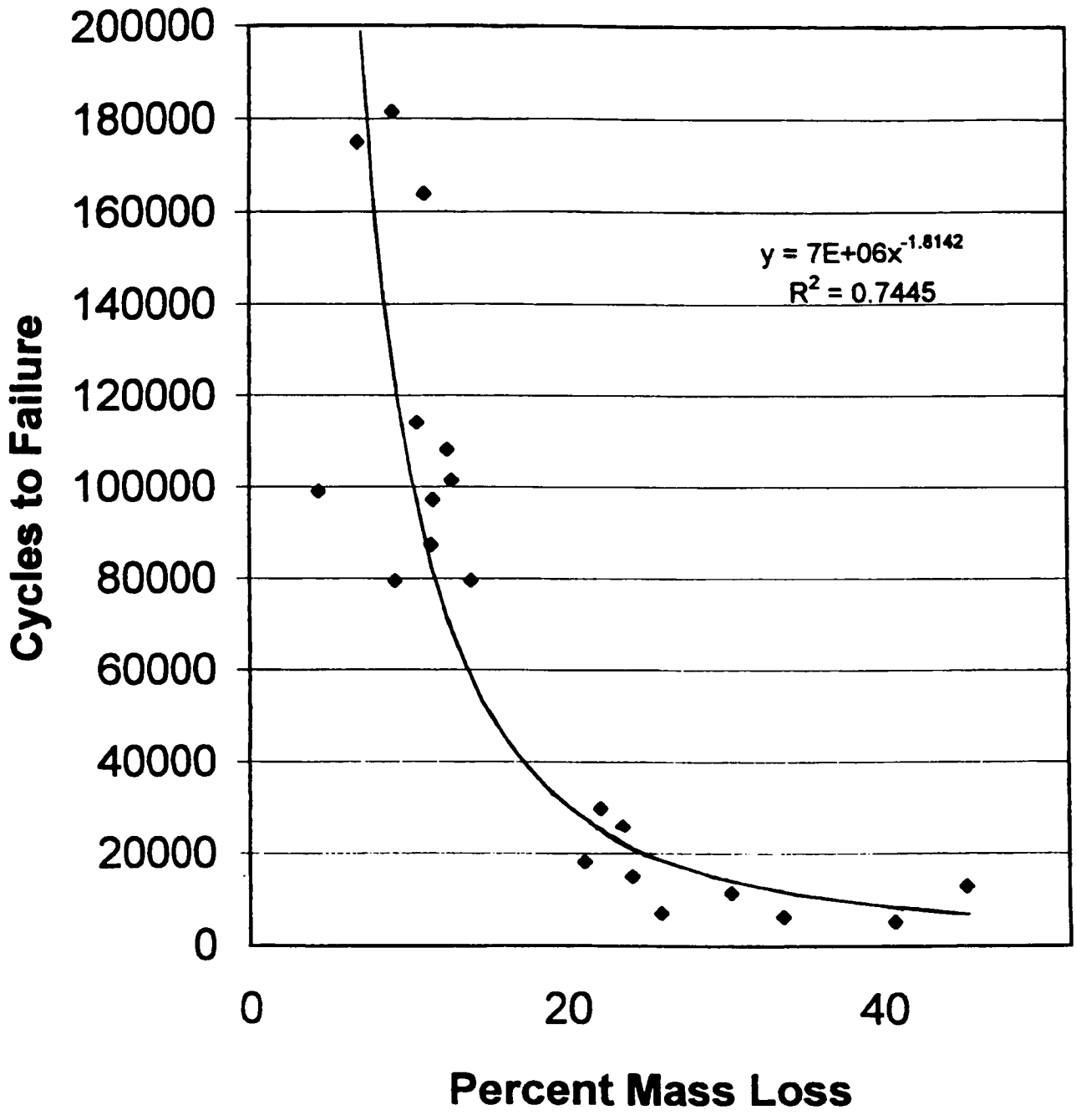

Figure 10. Correlation of Resid[920] Life with Percent Mass Loss

CONCLUSION

- **Residual strength and fatigue life data have been generated for 0.063" thick 2024-T3 aluminum alloy samples. A rating scale development is underway to quantify the effect of corrosion induced damage for 0% - 40% mass loss on the residual strength and fatigue life, so that improved inspection, repair, and maintenance may be implemented.**

- **Scanning Electron Microscope (SEM) Examination of the cross-section of the fractured sample(s) is planned to quantify the effects of corrosion-induced reduction of strength and fatigue life in terms of size, distribution, and location of PITS.**

AIRCRAFT STRUCTURAL INTEGRITY MONITORING SYSTEM DEVELOPMENT – REVIEW OF THE AIR FORCE/NAVY SMART METALLIC STRUCTURES PROGRAM

Craig B. Van Way and Jay N. Kudva
Northrop Grumman Corporation
One Northrop Avenue MS 9B71/63, Hawthorne, CA 90250
(310) 332-9639,
vanwacr@mail.northgrum.com

Mark N. West
Mission Research Corporation
17150 Newhope, Unit 516, Fountain Valley, CA 92708

Dr. Steve M. Ziola
Digital Wave Corporation
11234A East Cayley Avenue, Englewood, CO 80110

Capt. V. Scott May and Michael N. Zeigler
Advanced Development Branch, AFRL/VASA
Wright Patterson Air Force Base, OH 45433

Dr. James M. Alper
Naval Air Warfare Center
Patuxent River, MD

ABSTRACT

Structural health monitoring (SHM) technologies, the concept of populating an airframe with an array of sensors for damage detection and loads monitoring, have the potential to revolutionize current methods of aircraft tracking. An automated health monitoring system capable of remote damage detection and comprehensive usage monitoring can significantly add to the established success of the US Air Force's aircraft structural integrity program (ASIP), and corresponding US Navy NASIP. Recent advances in sensing systems and data processing hardware have made it possible to greatly expand the type and amount of information used to assess the status of a structure.

The objective of one recent investigation into structural health monitoring technologies, the joint Air Force/Navy Smart Metallic Structures (SMS) [1] program, conducted by the Northrop Grumman Corporation, was to demonstrate a prototype structural health monitoring system incorporating crack growth detection, strain recording, and integrity assessment. The recently concluded final test of this program, a full-scale fatigue test of a wing carry through bulkhead from a modern fighter aircraft, was conducted at the Air Force Research Laboratory, Wright Patterson Air Force Base (WPAFB) during April and May of 1997, and was successful in detecting fatigue crack growth and recording strain history on the bulkhead for the duration of the test. Eighteen acoustic emission sensors and twelve fiber optic strain sensors were distributed in five fatigue critical zones on the test article for health monitoring. Fatigue crack acoustic emissions were detected from a series of crack initiations that eventually led to the catastrophic failure of the bulkhead in one of the critical zones.

This paper will first present an overview of ASIP and its relationship to structural health monitoring (SHM), followed by a brief review of SHM requirements (a more detailed discussion of ASIP and SHM

can be found in Reference 3). The bulk of the paper consists of a review of the SMS program, focusing on the health monitoring system architecture (specifically the sensors, processors, and analysis algorithms contained therein), the testing performed under the program, and the lessons learned. Health monitoring implementation payoffs are briefly discussed, and finally, conclusions and a preview of future programs are given.

1. INTRODUCTION

The principles governing aircraft life cycle monitoring in the United States can be invariably traced back to the Air Force's Aircraft Structural Integrity Program (ASIP) [2]. ASIP, since its implementation in the late fifties, has had unparalleled success at increasing fleet readiness and reducing aircraft down time through the prediction, identification and containment of structural degradation. The ASIP ideal is to field a structure which never develops unanticipated flaws. The reality, of course, is there will always be unexpected problems during the life of a structure. And all of this success has been accomplished with, in some cases, relatively rudimentary technologies, such as manual flight logs, counting accelerometers, and limited strain gage applications.

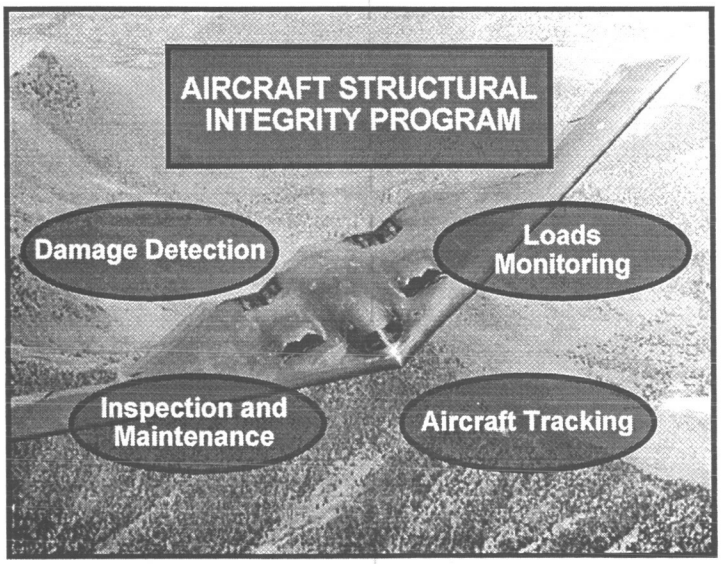

Figure 1. ASIP functional tasks.

In recent years there has been a concerted effort from the research and development community [3-9] aimed at further improving the ASIP paradigm by making use of new sensors and data processing techniques to modernize and enhance current tracking methodologies with the ultimate goal of "condition based maintenance". Put simply, aircraft structural inspections and maintenance will be performed only when there is an indication of damage, unlike the current schedule driven system, when costly inspections often find no defects.

Structural health monitoring, the concept of populating an aircraft structure with an array of sensors, remote data collection units, and a central processing and analysis unit for the purpose of providing damage detection and loads monitoring, has benefited in recent years from significant advances in sensors, data acquisition, electronic miniaturization, and sensor system integration. It is now possible to create a system which can handle both the severe processing demands of modern damage detection techniques, and the huge database management tasks associated with maintaining an entire fleet of aircraft at peak readiness.

Recent work at the Northrop Grumman Corporation on the joint US Air Force/Navy Smart Metallic Structures (SMS) program [1] has successfully demonstrated a laboratory prototype structural health monitoring system (SHMS), combining acoustic emission (AE) crack detection, fiber optic strain recording, and aircraft parameter collection with an innovative distributed hierarchical data acquisition and analysis system, to provide a structural integrity assessment capability for an instrumented structure.

2. SMART METALLIC STRUCTURES PROGRAM

Utilizing advanced monitoring and data processing technologies to design, develop, and test a prototype SHMS on a large aircraft component is the primary objective of the SMS program. A highly sophisticated data acquisition network was created to support the sensor array by collecting and storing the generated data, and a series of algorithms were incorporated to perform fatigue damage location, crack growth analysis, and data reduction.

2.1 SENSORS

AE and fiber optic sensors have been used extensively in health monitoring applications. AE based sensors provide the only established technique capable of remote damage sensing, i.e., they do not have to be located in the immediate vicinity of the damage [10, 11]. Fiber optic sensors exhibit high strain sensitivity, excellent strain resolution, and multiplexing capability [12]. Foil strain gages and accelerometers are commonly used in existing aircraft tracking programs, and thus are an important consideration in the overall design of an aircraft SHMS.

2.2 SYSTEM ARCHITECTURE

Figure 2 shows a schematic of the SHMS architecture. It consists of a network of AE transducers, strain gages, accelerometers, and crack gages controlled by two different remote hosts, the acoustic emission smart sensor (AESS), which monitors the AE sensors, and the utility smart sensor (USS), which

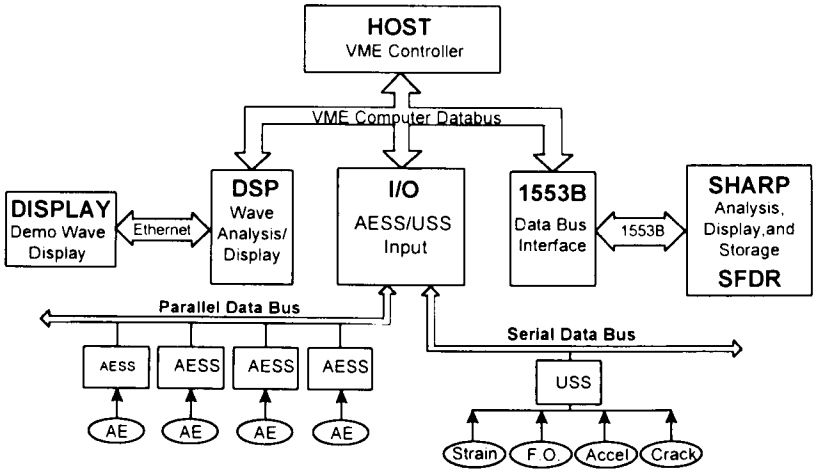

Figure 2. SHMS system architecture.

measures structural loads and aircraft environment via the accelerometers, strain, and crack gages(Figure 3). The central computer, which consists of a host processor, the input/output (I/O) controller, and a digital signal processor (DSP), is connected to the sensor controllers via two separate high speed data buses, and performs the functions of data collection, analysis, and storage (Figure 4). The Mil-Std-1553B board interfaces with the analysis and display software contained in the structural health

assessment and review program (SHARP) [13], and would, in an aircraft implementation, provide communications with the flight computer and the standard flight data recorder (SFDR). Raw sensor data is collected from each of the monitored zones and passed to the local processors (AESS, USS), and the central unit interrogates each of the local processors in turn to extract the sensor data.

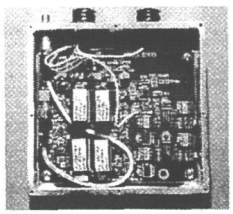

(a) AESS (4 in. x 4 in.)

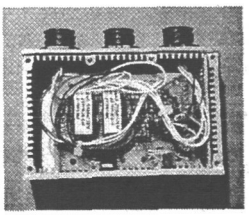

(b) USS (3 in. x 2 in.)

Figure 3. Remote hosts.

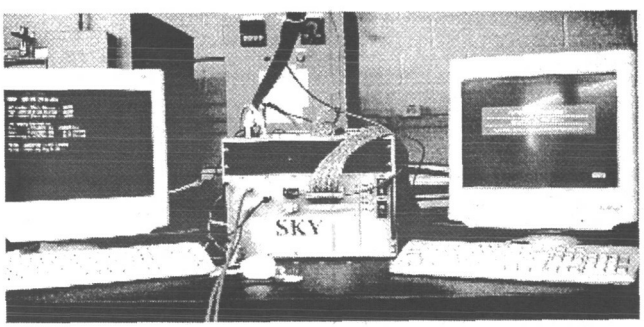

Figure 4. Central computer.

2.3 SUB-ELEMENT TESTING

The system was initially tested on sub-elements, shown in Figures 5 (a) and (b), which verified both the ability of the AE system to identify flaws and of the fiber optic system to monitor strain in complex structures. However, while the system was successful in finding cracks, the tests identified the difficulties in detecting a propagating acoustic signal. Namely, the signals can be easily detected in a simple geometry like a wing spar web, but in more complex geometric configurations, such as the stiffeners between the bays in a machined bulkhead, or in the rows of fasteners of a built-up wing spar, the crack signals are much more difficult to sense. The fiber optic sensors performed flawlessly in both tests, demonstrating excellent fidelity. These tests are discussed in detail in References 14 and 15.

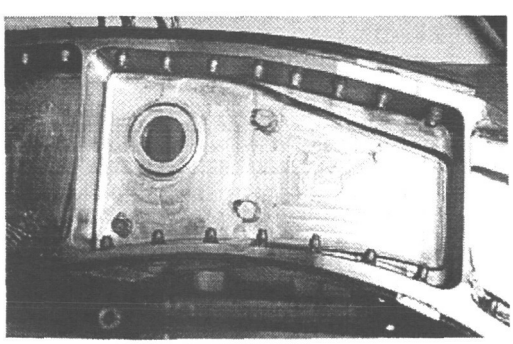

(a) Multiple Bay Specimen.

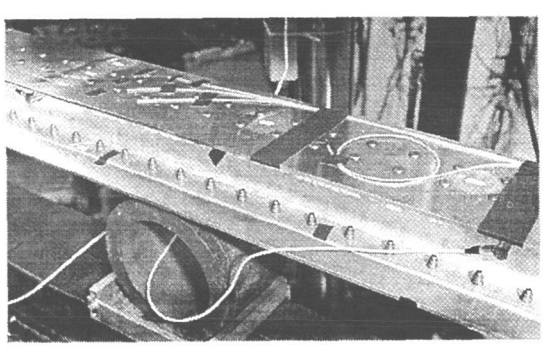

(b) Wing Spar Specimen.

Figure 5. Sub-element test articles.

2.4 COMPONENT TESTING

The next program test was used to evaluate the integrated operation of the SHMS hardware and software components, including the USS, AESS, central processor, storage units, and data communication. This test had two goals: 1) integrate the independently developed damage and loads monitoring modules, and 2) utilize the system to monitor a complex structure. The test article, representative of a fighter aircraft bulkhead, was a machined specimen consisting of four bays separated by stiffeners, with access holes in two of the bays (Figure 6). Crack initiations were placed at the 9 o'clock position of both access holes.

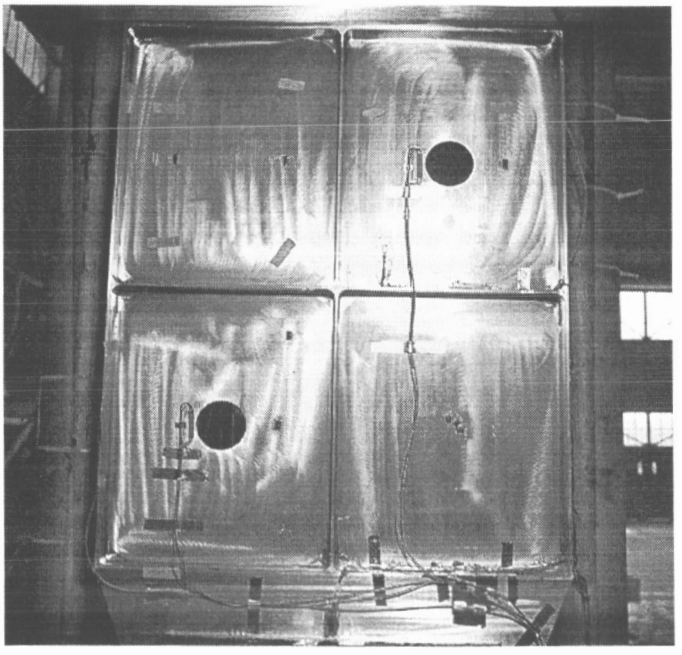

Figure 6. Component test article.

Figure 7 shows a typical crack waveform and its corresponding frequency content (Fourier transform). It can be seen that the signal has a well defined time of arrival at each of the sensors (at roughly 40 ms) and contains significant frequency content from 200 kHz up to 1.5 MHz, both strong indicators of a crack.

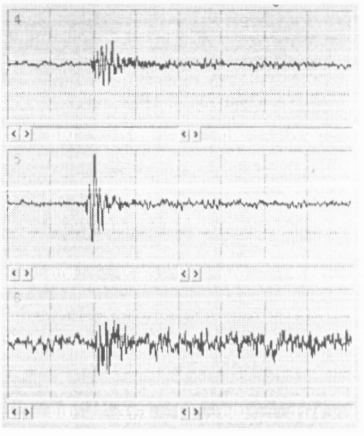

(a) Time vs. Amplitude
(Time/Div. = 20.48 ms)

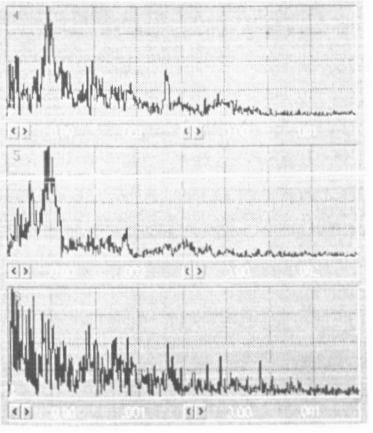

(b) Frequency vs. amplitude
(Freq./Div. = 390.6 kHz)

Figure 7. Task 3 test crack acoustic emission.

Additionally, a waveform generated by a fatigue crack typically has a low pre-trigger energy content, defined as the area below the curve in the first 25% of the signal. Clearly, this particular event meets this criteria. (In the next section a comparison of a crack and a structural noise event is made showing these distinguishing characteristics even more clearly.)

2.5 FINAL DEMONSTRATION TEST

The final test of the SMS program was conducted at the Wright Patterson Air Force Base Structural Test Facility, Dayton, Ohio, USA, from April 15 to June 15, 1997. The final demonstration article, a fighter aircraft wing attach bulkhead (Figure 8), was subjected to static and fatigue loading. During the test, approximately 9,000 equivalent spectrum flight hours were applied to the bulkhead, leading to a catastrophic fatigue failure in the region between the left-hand inlet duct hole and the adjacent wheel well cutout on the bulkhead (Figure 9).

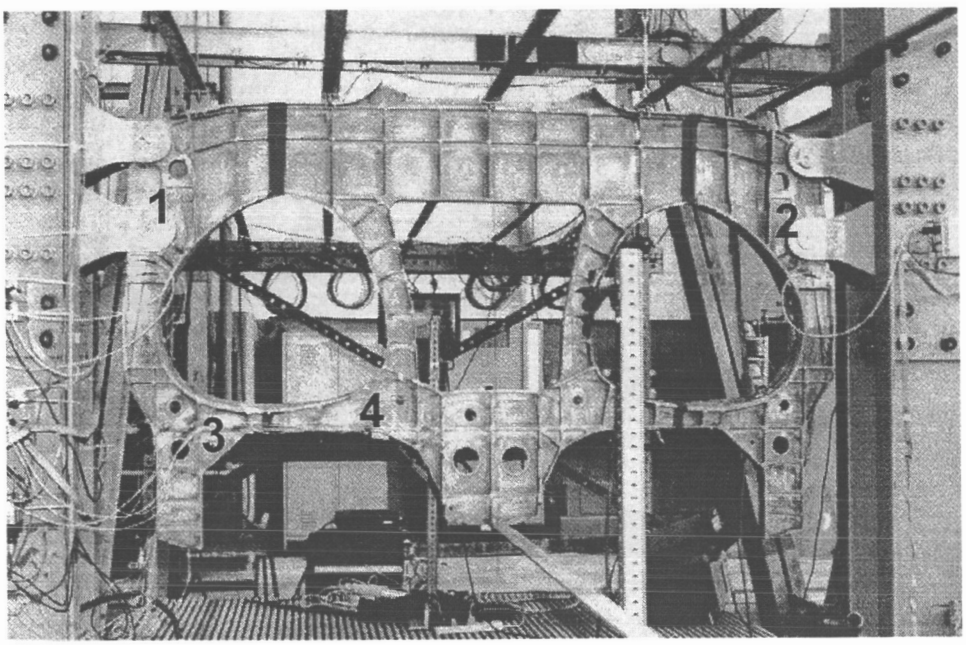

Figure 8. Test article mounted in test frame (numbers indicate monitoring zones).

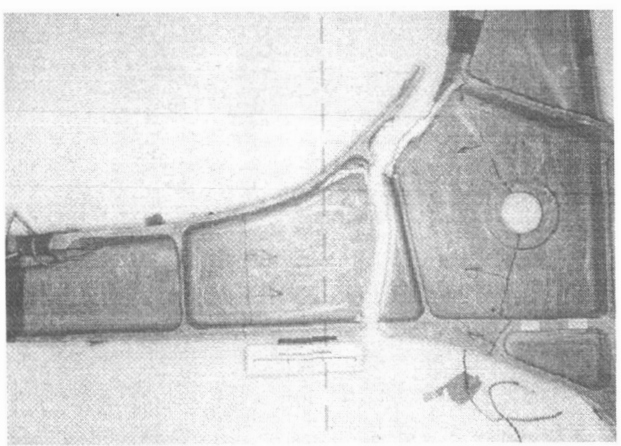

Figure 9. Catastrophic fatigue failure of bulkhead.

Eighteen AE sensors were used to monitor four locations on the bulkhead: zones 1 and 2 are the wing attach lug areas on both sides of the bulkhead, zone 3 contains the two access holes in the lower left hand

region of the bulkhead, and zone 4 is the inboard wheel well radius on the left hand side. Based on historical data, the anticipated failure site was either of the wing attach lug areas (zones 1 and 2), and thus these areas received the highest sensor coverage. The failure, however, occurred in the wheel well radius (zone 4, Figure 8), which had been identified as a high stress area and selected as a monitoring zone based on finite element model results. No crack indications were found during a scheduled eddy current inspection of the area after 6,000 flight hours. The failure came just prior to the 9,000 hour inspection, indicating the cracks initiated and grew to failure during this 3,000 hour interval.

Crack signals were first detected by the SHMS at approximately 7,000 spectrum flight hours. Figure 10 shows the sensor arrangement in the wheel well zone, and Figures 11 and 12 show time versus amplitude and frequency versus amplitude plots for a structural noise event (Figure 11) and a crack event (Figure 12). Inspection of the noise signal in Figure 11 reveals no distinct arrival time, and the corresponding frequency plot indicates most of the event energy is below 200 kHz. As stated earlier, both of these characteristics indicate that the recorded event is not related to crack growth. Furthermore, the pre-trigger energy content of this waveform is quite high, another strong indicator that it is not a crack event.

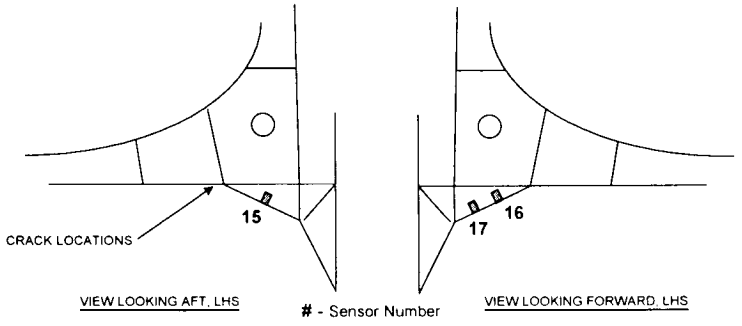

Figure 10. Wheel well radius sensor locations.

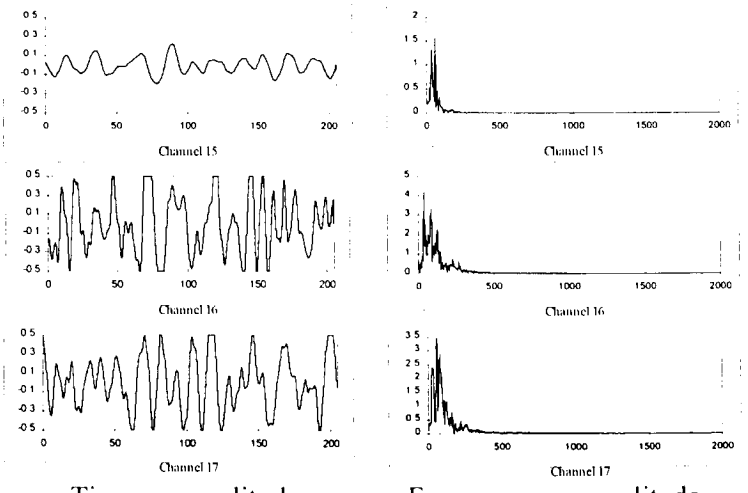

Time vs. amplitude. Frequency vs. amplitude

Figure 11. Structural noise event.

However, the event shown in Figure 12 displays all of the characteristic features of crack growth. In the time domain, the signal has a distinct time of arrival at channels 16 and 17 (sensor 15 had come loose during this portion of the test). Additionally, it can be seen that this event contains significant energy in the higher frequencies. Numerous similar events were present in the data leading up to the failure.

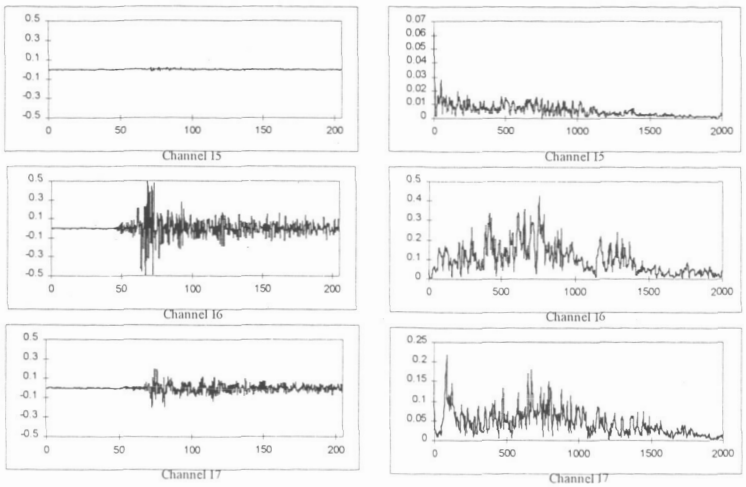

Time vs. amplitude Frequency vs. amplitude

Figure 12. Crack growth event.

Post test analysis of the failure site revealed numerous fatigue initiation sites (Figure 13). The catastrophic failure of the bulkhead occurred at a load point measuring 98% of the maximum spectrum load. Except for the crack initiations shown in Figure 13, the failure was a ductile overload type fracture. The fracture surface contains 43 separate crack initiations (Figure 14). The largest of the initiation sites on the fracture surface, shown at point A in Figure 13, measured 0.168 inches at its deepest penetration (Figure 15). In the right-hand picture, the fatigue striations in the initiation can be seen.

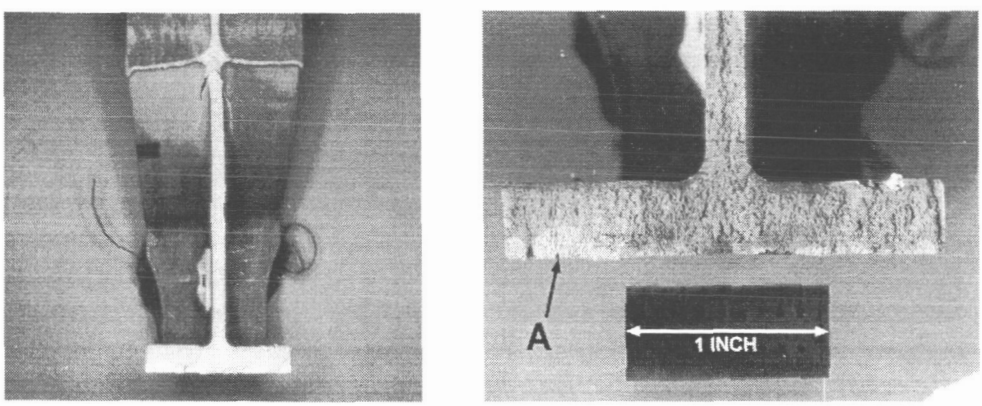

Figure 13. Fracture surface.

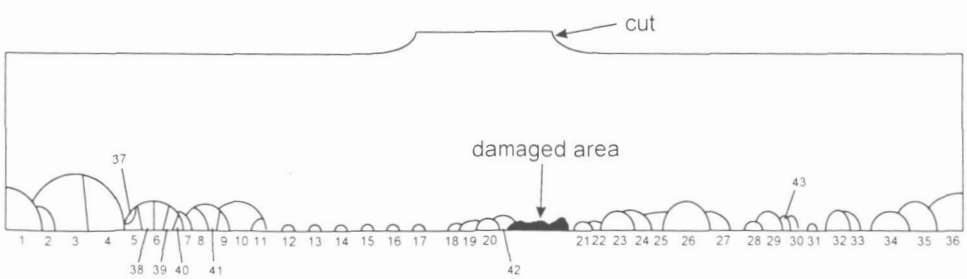

Figure 14. Crack initiation sites.

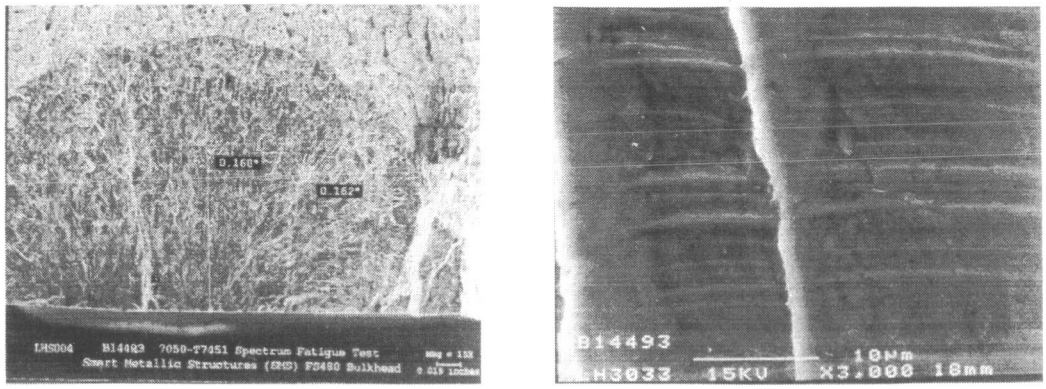

Figure 15. Primary crack initiation site.

Continuous strain data was recorded during the test with both foil and fiber optic strain gages. The five foil strain sensors being monitored by the USS controller units were collocated with the AE sensor groups to record continuous strain traces as well as instantaneous strain levels during acoustic events for use in the AE analysis. An additional eleven fiber optic strain gages were distributed over the bulkhead to monitor and record strain levels in critical regions. One of the fiber optic gages used during the test is shown in the center of the picture in Figure 16. A significant result of the test was that the foil gages began to fail in fatigue as early as 2,000 spectrum flight hours, whereas the fiber optic gages survived the entire test with no signal degradation.

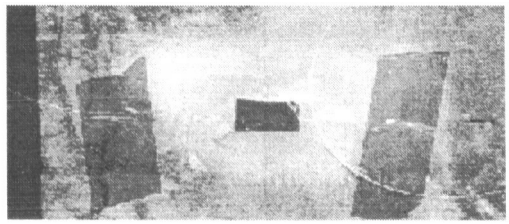

Figure 16. SHMS fiber optic strain gage.

Overall, the test can be seen to be a successful demonstration of the prototype SHMS. Each of the program objectives were met or exceeded: 1) metallic fatigue events were detected and located using AE, 2) strain was monitored continuously using fiber optic sensors, 3) data from multiple sensor types was collected and stored, and 4) a full scale aircraft component was monitored under fatigue cycling. The only shortfall of this test, which is currently being addressed, was the fact that the damage detection algorithms were run post-test. That is, the AE source location calculations had to be run off-line. Thus, there was no way to predict beforehand when the bulkhead would fail, only to see that the crack signals were present just prior to failure. Automation of the crack location algorithms so that sources can be identified in real time is the most important future development for the damage detection system.

3. SYSTEM BENEFITS AND PAYOFFS

The long-term goal of health monitoring is to create an aircraft with a 'condition based maintenance' system, i.e., replace analytical flaw tracking with automated structural damage detection and evaluation. While ideal performance capabilities have yet to be attained, health monitoring applications could enhance current methods of analytic flaw tracking. Payoffs include fewer special inspection requirements at repaired or known critical locations as well as improved mission readiness. In addition, initial steps to automate the data collection and transmission procedures can improve data validity and reduce turnaround times.

CONCLUSIONS

The next critical step in the development of an aircraft health monitoring system will be the creation of a flight qualified system. Significant hardware and software development will be required before a system can be installed and flown on an applicable test bed. And while the sensor technologies for monitoring local areas (i.e. hot spots) are fairly mature, a great deal of work will be demanded to automate the process of collecting and analyzing the sensor data, particularly in the acoustic emission damage detection arena. Additionally, one of the largest gaps in current research efforts is the consideration of damage detection and loads monitoring schemes for composite materials. Addressing these issues and continuing current research effort will collectively pave the way towards the development of a completely automated SHMS providing total aircraft coverage and resulting in unprecedented levels of fleet readiness, flight safety, and life cycle cost reduction.

ACKNOWLEDGMENTS

The work documented in this paper was performed under a government contract to a team lead by Northrop Grumman Corporation entitled "Smart Metallic Structures (SMS)," F33615-92-C-3203. The contract monitors are Capt. V. Scott May and Mr. Michael Ziegler of the Air Force Wright Laboratories and Dr. James Alper of the Naval Air Warfare Center.

The members of the multidisciplinary SMS team include Honeywell Corporation (system hardware development), Digital Wave Corporation (acoustic emission monitoring), Mission Research Corporation (system software), and Fiber & Sensors Technologies (fiber optic sensing system) and the support provided by these organizations is greatly appreciated.

REFERENCES

1. Van Way, C. B., et. al., "Development of an Automated Aircraft Structural Integrity Monitoring System–Overview Of The Air Force/Navy Smart Metallic Structures Program," 37th AIAA/ASME/ASCE/AHS/ASC Structures, Structural Dynamics, and Materials Conference, Salt Lake City, Utah, April 15-17, 1996.
2. MIL-STD-1530A, Aircraft Structural Integrity Program, Airplane Requirements, December 1975.
3. Kudva, J.N., et. al., "Structural Health Monitoring of Aircraft Components," Paper No. 9, AGARD-LS-205, 79th Meeting of the AGARD Structures and Materials Panel, Paris, France, Nov., 1996.
4. Schmidt, W., and Boller, C., "Smart Structures - A Technology for the Next Generation Aircraft", Paper No. 1 AGARD-CP-531, Presented at the 75th Meeting of the AGARD Structures and Materials Panel, Lindau, Germany, Oct. 1992.
5. Boller, C., Dilger, R., "In-flight Aircraft Structures Health Monitoring Based on Smart Structures Technology", Paper No. 17, AGARD-CP-531, Presented at the 75th Meeting of the AGARD Structures and Materials Panel, Lindau, Germany, Oct. 1992.
6. Hickman, G. A., Gerardi, A., "Application of Smart Structures to Aircraft Health Monitoring", Journal of Intelligent Material Systems and Structures, Vol. 1, pp. 411 - 430, July 1991.
7. Gentry, J. D., et al., "The Impact of Smart Structures on Aircraft Structural Integrity Programs", 1992 USAF ASIP Conference, San Antonio, TX, December 1992.
8. Appels, A. J., Capt., "The cost effectiveness of aircraft structural integrity programs", 1993 USAF ASIP Conference, San Antonio, TX, December 1993.
9. Van Way, C. B., et al., "Integration of smart structures concepts for improved structural integrity monitoring of the T-38 aircraft," 1993 USAF ASIP Conference, San Antonio, TX, December 1993.

10. McBride, S. L., et al., "Acoustic Emission Determination of Crack Presence and Crack Advance During Flight", Journal of Acoustic Emission, Nov. 8, pp. 4 - 7, 1989.

11. Gorman, M. R., "Acoustic emission for the 1990s," Proceedings of the IEEE: Ultrasonics, Ferroelectrics and Frequency Control, 1992.

12. Murphy, K. A., et al., "Elliptical-core, two-mode optical fiber sensor implementation methods," Journal of Lightwave Technologies, November 1992.

13. Gentry, J. D., et al., "Structural health assessment and review program (SHARP) - prototype of an on-board structural health monitoring system," 1993 SPIE Smart Structures Conference, Albuquerque, NM, February 1993.

14. Van Way, C. B., et al., "Aircraft structural health monitoring system development – overview of the Air Force/Navy Smart Metallic Structures program," 1995 SPIE Smart Structures and Materials Conference, San Diego, CA, February, 1995, Paper No. 2443-30.

15. Van Way, C. B., et. al., "Development of an Automated Aircraft Structural Integrity Monitoring System-Overview of the Air Force/Navy Smart Metallic Structures Program," AIAA-96-1615-CP, paper presented at the 37th AIAA SDM Conference, Salt Lake City, UT, April 1996.

- AUTHOR INDEX -

- PARTICIPANTS -

-A-

Mr. William H. **Abbott**
Battelle Columbus Operations
505 King Avenue
Columbus, OH 43201
Tel: 614/424-4198
E-mail: abbott@battelle.com

Mr. Jim **Abel**
National Technical Systems, Inc.
1800 Interstate Drive
Norman, OK 73072
Tel: 405/290-1292

Prof. Jan D. **Achenbach**
Northwestern University
Center for Quality Engineering and
Failure Prevention
2137 Sheridan Road
Evanston, IL 60208
Tel: 847/491-5527
E-mail: achenbach@nwu.edu

Mr. Steven F. **Adams**
WR-ALC/TIEDD
420 2nd Street, Suite 100
Robins AFB, GA 31089-1640
Tel: 912/926-4228
E-mail: sadams@ti.robins.af.mil

Mr. Janiel **Adan**
Bombardier Services
10,000 Cargo A-4 Street
Montreal International Airport - Mirabel
Mirabel Quebec, J7N 1H3 Canada
Tel: 450/476-4879
E-mail: paul.londei@services.bombardier.com

Dr. Robert A. **Adey**
Computational Mechanics, Inc.
25 Bridge Street
Billerica, MA 01821
Tel: 978/667-5841
E-mail: r.adey@beasy.com

Dr. Vinod S. **Agarwala**
Naval Air Warfare Center Aircraft Division
Building 2187, Suite 3356
48110 Shaw Road
Patuxent River, MD 20670-1906
Tel: 301/342-8002
E-mail: vinod_agarwala@alum.mit.edu

Mr. Aydin **Akdeniz**
Boeing Commercial Airplane Group
P.O. Box 3707, MS 2J-56
Seattle, WA 98124-2207
Tel: 206/544-8541
E-mail: aydin.akdeniz@boeing.com

Dr. Santgerma **Alain**
Aerospatiale Aeronautique
Dept A/BTE/CC/CM
Route de Bayonne, 316
Toulouse, 31060, France
Tel: 33561938205
E-mail: alain.sntgerma@avions.aerospatiale.fr

Mr. Andrew **Albright**
Emery World Wide Airlines
303 Corporate Drive Center
Vandilia, OH
Tel: 937/264-2682

Mr. Russell E. **Alford**
WR-ALC/LJLEA
270 Ocmulgee Court
Robins AFB, GA 31098-1646
Tel: 912/926-9146
E-mail: alfordre@c141.robins.af.mil

Mr. Glenn **Andrew**
SAIC Ultra Image International
Two Shaw's Cove, Suite 101
New London, CT 06320
Tel: 860/442-0100
E-mail: glenn.a.andrew@cpmx.saic.com

Mr. Robert J. **Andrews**
University of Dayton Research Institute
300 College Park
Dayton, OH 45469-0120
Tel: 937/229-4417
E-mail: andrewrj@udri.udayton.edu

Mrs. Tanya **Andrews**
Panametrics, Inc.
221 Crescent Street
Waltham, MA 02154
Tel: 781/899-2719
E-mail: ndt@panametrics.com

Mr. Robert W. **Arden**
Westar Corporation
4505 Mellowlight Drive
St. Louis, MO 63129
Tel: 314/298-8748
E-mail: arden@westar.com

Mr. Kemal **Arin**
US/DOT Volpe Center
DTS-74
55 Broadway
Cambridge, MA 02142-1093
Tel: 617/494-2066

Dr. Fred E. **Arnold**
NAVAIR 4.3.4.3
Naval Air Warfare Center
Aircraft Division
Patuxent River, MD 20670
Tel: 301/342-8123
E-mail: arnoldfe%am7@mr.nawcad.navy.mil

Mr. Terrence **Arthur**
Raytheon System Company
7500 Maerh Road, M/S 1261
Waco, TX 76705
Tel: 254/867-2595
E-mail: terry_arthur@readwo.com

Mr. Dennis M. **Ashbaugh**
AANC/SAIC
3260 University Boulevard SE
Access Road B
Albuquerque, NM 87106
Tel: 505/843-8722

1Lt Jason **Avram**
AFRL/MLSA
5626 Benjamin Court
Huber Heights, OH 45424
Tel: 937/656-6010
avranjb@ml.wpafb.af.mil

Mr. Didier **Avril**
Air-France / ACSDCA
B2 7
93352 Le Bourget Cedex, France
Tel: 33143348342
E-mail: acsdca.af1@wanadoo.fr

-B-

Mr. Chuck **Babish**
WPAFB (C-17 SPO)
ASC/YC (AV/AF)
Bldg 558
2590 Loop Road W
Wright-Patterson AFB, OH 45433-7142
Tel: 937/255-1035
E-mail: babishea@c17mis.wpafb.af.mil

Mr. Robert M. **Bader**
Consultant
1613 Kingsway Drive
Xenia, OH 45385-9589
Tel: 937/426-4871
E-mail: baderm@msr.com

Dr. Behnam **Bahr**
Wichita State University
1845 Fairmount Street
Wichita, KS 67260-0133
Tel: 316/978-6319
E-mail: bahr@me.twsu.edu

Mr. Asad M. **Baig**
SPAR Aerospace Limited
SPAR Aviation Services
P.O. Box 9864
Edmonton International Airport
Edmonton, Alberta, Canada
Tel: 403/890-6503
E-mail: baiga@telusplanet.net

Ms. Deborah A. **Bailey**
Aging Aircraft Program Office
Aging Aircraft & Systems Office
2145 Monahan Way
Wright-Patterson AFB, OH 45433-7017
Tel: 937/255-6053
E-mail: baileyda@ntnotes2.ascsm.wpafb.af.mil

Dr. Alan A. **Baker**
Defence Science and Technology
Organisation (Australia)
Aeronautical and Maritime Research Lab
506 Lorimer Street, Fishermans Bend
Melbourne, Victoria 3207, Australia
Tel: 610396267495
E-mail: alan.baker@dsto.defence.gov.au

LCDR Joe T. **Baker**
U.S. Coast Guard
Aircraft Repair and Supply Center
Building 78
Elizabeth City, NC 27909
Tel: 252/335-6631
E-mail: jbaker@arsc.uscg.mil

Dr. John G. **Bakuckas**
FAA William J. Hughes Technical Center
AAR-431
Atlantic City International Airport, NJ 08405
Tel: 609/485-4784
E-mail: john_bakuckas@admin.tc.faa.gov

Dr. David **Baldwin**
University of Oklahoma
865 ASP Avenue, Room 212
Norman, OK 73109
Tel: 405/325-1090
E-mail: baldwin@ou.edu

Mr. Dale L. **Ball**
Lockheed Martin Tactical Aircraft System
P.O. Box 748
MZ 2846
Fort Worth, TX 76101
Tel: 817/777-3760
E-mail: dale.l.ball@lmco.com

Mr. Brent **Bandley**
Federal Aviation Administration
3960 Paramount Boulevard
Lakewood, CA 90712-4137
Tel: 562/627-5237

Mr. Martin R. **Bare**
NAVAIRSYSCOM 3.6.3.1
47038 McLeod Road
Patuxent River, MD 20670-1626
Tel: 301/757-3083
E-mail: baremr.jfk@navair.navy.mil

Mr. Gene **Barndt**
Naval Air Systems Command
Code 4.3.3.2
Building 2187, Suite 2340
NAWGAD - 48110 Shaw Road
Patuxent River, MD 20570-1161
Tel: 301/342-0302

Mr. **Barnier**
Dassault Aviation
Zone Aeronautique Louis Breguet
BP12
78141 Velizy Villacoublay, France
Tel: 33140832246

Mr. David P. **Barrera**
SA/ALC-TIELM
512 Shop Lane
Building 318
Kelly AFB, TX 78241
Tel: 210/925-0971

Major Nelson B. **Barrett**
Canadian Forces
Aerospace & Maritime Research Laboratory
P.O. Box 4331
Melbourne, Victoria 3207, Australia
Tel: 61396267228
E-mail: nelson.barrett@dsto.defence.gov.au

Dr. Feldon D. **Bartlett, Jr.**
U.S. Army Research Laboratory
NASA Langley Research Center
MS 266
Hampton, VA 23681
Tel: 757/864-3952
E-mail: f.d.bartlett@larc.nasa.gov

Dr. Michael L. **Basehore**
Federal Aviation Administration
NASA Langley Research Center
MS 229
Hampton, VA 23681
Tel: 757/864-8951
E-mail: ml.basehore@larc.nasa.gov

Mr. George **Bauer**
Sikorsky Aircraft
Mail Stop S313A2
6900 Main Street
Stratford, CT 06497
Tel: 203/386-7139
E-mail: gbauer@sikorsky.com

Mr. O. Alois **Baumann**
German Air Force
Material Office III A1
Heidestrasse 245,
51140 Cologne, Germany
Tel: 022036022416

Mr. Bill **Baumeister**
Cessna Aircraft Company
1234 Hickory Creek Court
Wichita, KS 67235
Tel: 316/941-8212
E-mail: bbaumeister@cessna.textron.com

Mr. Jean-Yves **Beaufils**
Aerospatiale Aeronautique
Dept A/BTE/CC/CM
Route de Bayonne, 316
Toulouse, 31060 Cedex 03, France
Tel: 33561937629
E-mail: jean-yves.beaufils@avions.aerospatiale.fr

Ms. Laurel T. **Beckman**
Naval Air Systems Command
Code 4.3.3.4
Bldg 2187, Ste 2320A
48110 Shaw Road, Unit 5
Patuxent River, MD 20670-1906
Tel: 301/342-9350
E: beckman_laurel%pax5a@mr.nawcad.navy.mil

Dr. Theodor **Beier**
Boeing Phantom Works
P.O. Box 516, MS 1022147
St. Louis, MO 63166
Tel: 314/232-0634
E-mail: theodor.h.beier@boeing.com

Mr. Robert P. **Bell**
Lockheed Martin Aeronautical Systems
86 South Cobb Drive
Marietta, GA 30063-0160
Tel: 770/494-2166
E-mail: bell@c1410.mar.lmco.com

Mr. Nicholas C. **Bellinger**
National Research Council Canada
IAR-SMPL
Building M-14, Montreal Road
Ottawa, Ontario K1A 0R6, Canada
Tel: 613/993-2410
E-mail: nick.bellinger@nrc.ca

Mr. Richard **Bentz**
Mitre Corporation
Burlington Road
Bedford, MA 01730
Tel: 781/271-5246
E-mail: rbentz@mitre.org

Mr. Hugh P. **Bergeron**
FAA R&D Field Office
NASA Langley Research Center
MS 250
Hampton, VA 23681-2199
Tel: 757/864-1905
E-mail: h.p.bergeron@larc.nasa.gov

Mr. William E. **Berner**
AFRL/MLS
2179 12th Street, Room 122
Wright-Patterson AFB, OH 45433-7718
Tel: 937/656-6054
E-mail:.bernewe@ml.wpafb.af.mil

Mr. Henry K. **Berry**
Berry Engineering
11712 C Jefferson Avenue
Newport News, VA 23602
Tel: 757/596-4146
E-mail: hberry@visi.net

Mr. Paul **Berry**
ARINC
6205 S. Sooner Road
Oklahoma City, OK 73135
Tel: 405/739-0939
E-mail: pberry@arinc.com

Mr. Robert F. **Berry**, Jr.
NASA Langley Research Center
MS 397
Hampton, VA 23681
Tel: 757/864-4095
E-mail: r.f.berry@larc.nasa.gov

Dr. Catherine **Bigelow**
FAA William J. Hughes Technical Center
AAR-431
Atlantic City International Airport, NJ 08405
Tel: 609/485-6662
E-mail: cathy_bigelow_at_ct27@admin.tc.faa.gov

Mr. Rick **Binder**
Boeing North American
M/C SL15
PO Box 3644
2600 Westminster Blvd
Seal Beach, CA 90740-7644
Tel: 562/797-2730
E-mail: richard.a.binder@boeing.com

Mr. Ken **Bishop**
MATEC Instruments
56 Hudson Street
Northboro, MA 01532
Tel: 508/393-0155
E-mail: kbishop@matec.com

Mrs. Mary **Bishop**
OO-ALC/CD-2
7981 Georgia Street
Hill Air Force Base, UT 84056-5824
Tel: 801/777-5999
E-mail: bishopm@hill.wpos.hill.af.mil

Dr. Kay Y. **Blohowiak**
The Boeing Company
Phantom Works
P.O. Box 3999, MS 82-32
Seattle, WA 98124-2499
Tel: 253/773-2055
E-mail: kay.y.blohowiak@boeing.com

Mr. James F. **Bockman**
SAIC
2810 Shorehan Drive
Richmond, VA 23235
Tel: 757/825-0001

Mr. Frank D. **Boensch**
FDB Associates
6025 Oak Hill Lane
Centerville, OH 45459
Tel: 937/435-2870
E-mail: edbassociates@compuserve.com

Mr. Jeffrey S. **Boghosian**
The College of William and Mary
Physics Department
P.O. Box 8795
Williamsburg, VA 23187
Tel: 757/221-1988
E-mail: jsbogh@physics.wm.edu

Ms. Loren D. **Bolstridge**
ARINC, Inc.
2551 Riva Road
Annapolis, MD 21401
Tel: 410/266-4784
E-mail: lbolstri@arinc.com

Dr. David **Bond**
Royal Australian Air Force
ASI-DGTA
RAAF Williams
Laverton Victoria, 8027 AUSTRALIA
Tel: 61392563491
E-mail: dabond1@raaf.defenc.gov.au

Dr. Leonard J. **Bond**
Battelle
Pacific Northwest National Laboratory
P.O. Box 999
MSIN K5-25
Richland, WA 99352
Tel: 509/375-4486
E-mail: leonard.bond@pnl.gov

Mr. Richard **Boor**
Zimac Laboratories, Inc.
1241 Cascades Street
Chateaugauy, Quebec J6J 4Z2, Canada
Tel: 450/691-5607
E-mail: zimac.labs@sympatico.ca

Mr. Michael P. **Bouchard**
University of Dayton Research Institute
300 College Park
Dayton, OH 45469-0110
Tel: 937/229-3030
E-mail: bouchard@udri.udayton.edu

Mr. David **Boyer**
Wyle Laboratories
Technical Support Services
4200 Col Glenn Hgy, Ste 900
Dayton, OH 45431-1663
Tel: 937/426-0252

Ms. Lisa **Brasche**
Iowa State University
Center for Aviation Systems Reliability
185 ASCII
Ames, IA 50011
Tel: 515/294-5227
E-mail: lbrasche@cnde.lastate.edu

Mr. John L. **Bratton**
TASC, Inc.
872 W. Heritage Park Blvd, Suite 220
Layton, UT 84041
Tel: 801/775-9577
E-mail: jlbratton@tasc.com

Mr. Brad J. **Braun**
Systems & Electronics, Inc.
190 Gordon Street
Elk Grove, IL 60007-1120
Tel: 847/228-0985
E-mail: sysei@msn.com

Mr. Andrew T. **Brindisi**
Pratt & Whitney
400 Main Street
M/S 102-26
East Hartford, CT 06108
Tel: 860/565-5600

Dr. John **Bristow**
Civil Aviation Authority
Aviation House
South Area Gatwick Airport
W Sussex RH60YR, United Kingdom
Tel: 441293573531

Ms. Vicki **Britt**
Gulfstream Aerospace Corporation
115 Bluebill Drive
Savannah, GA 31419
Tel: 912/965-5861

Capt. Jean **Brosseau**
Director of Technical Airworthiness
National Defence Headquarters
Department of National Defence, Canada
MGen George R. Pearkes Building
Ottawa, Ontario K1A 0K2, Canada
Tel: 613/990-5871

Dr. Alfred L. **Broz**
Federal Aviation Administration
ANE-105N
FAA New England Region
12 New England Executive park
Burlington, MA 01803-5213
Tel: 781/238-7105
E-mail: alfred.broz@faa.dot.gov

Mr. Albert G. **Bruetsch**
U.S. Air Force
Sacramento Air Logistics Center
5020 Dudley Boulevard
McClellan AFB, CA 95652-1391
Tel: 916/643-5300
E-mail: bruetschal@fasn1.mcclellan.af.mil

Mr. Frederick W. **Brust**
Battelle Memorial Institute
505 King Avenue
Columbus, OH 43201-2693
Tel: 614/424-5034
E-mail: brust@battelle.org

Mr. Ernest C. **Bryan**
Technical Oversight Group
for Aging Aircraft (TOGAA)
256 Tequesta Circle
Tequesta, FL 33469
Tel: 561/747-0569
E-mail: ecbryan@worldnet.att.net

Dr. Cliff **Bueno**
GE R&D Center
KWD 246
P.O. Box 8
Schenectedy, NY 12031
Tel: 518/387-5543
E-mail: bueno@crd.ge.com

Dr. Robert J. **Bucci**
Aluminum Company of America
Alcoa Technical Center
100 Technical Drive
Alcoa Center, PA 15069-0001
Tel: 724/337-2671
E-mail: robert.bucci@alcoa.com

Mr. Jerry **Burke**
Applied Fiberoptics, Inc.
64 Technology Park Road
Sturbridge, MA 01566
Tel: 508/347-5100

Mr. George **Burkhardt**
SA-ALC/TIEM
Kelly AFB, TX 78241
Tel: 210/925-7391

Mr. David A. **Burton**
Boeing
BCAG Structures Post-Production
P.O. Box 3707
MS 2T-20
Seattle, WA 98124-2207
Tel: 206/544-5535
E-mail: david.a.burton@pss.boeing.com

Major Lawrence M. **Butkus**
ASC/ENFS
Structures Branch, Engineering Dir.
2530 Loop Road West
Building 560
Wright-Patterson AFB, OH 45433-7101
Tel: 937/255-7138
E-mail: butkuslm@asc-en.wpafb.af.mil

CDR Mark E. **Butt**
U.S. Coast Guard
Aircraft Repair and Supply Center
Building 78
Elizabeth City, NC 27909
Tel: 252/335-6039
E-mail: mbutt@arsc.uscg.mil

Mr. Charles F. **Buynak**
USAF AFRL
2230 10th Street, Suite 1
Wright-Patterson AFB, OH 45433-7817
Tel: 937/255-9807
E-mail: buynakcf@ml.wpafb.af.mil

-C-

Mr. Joseph W. **Cardinal**
Southwest Research Institute
6220 Culebra Road
San Antonio, TX 78238-5166
Tel: 210/522-3323
E-mail: jcardinal@swri.org

LCDR Mark S. **Carmel**
U.S. Coast Guard
Aircraft Repair and Supply Center, Building 79
Elizabeth City, NC 27909
Tel: 252/335-6556
E-mail: mcarmel@arsc.uscg.mil

Mr. Douglas P. **Carmody**
Northrop Grumman
2000 NASA Boulevard
Melbourne, FL 32902
Tel: 407/726-7821
E-mail: carmodo@mail.northgrum.com

Mr. Aubrey E. **Carter**
Delta Air Lines, Inc.
Engineering Department 553
Technical Operations Center
Hartsfield Atlanta International Airport
Atlanta, GA 30320-6001
Tel: 404/714-0051
E-mail: aubrey.carter@mailport.delta-air.com

Mr. Michael L. **Carter**
Naval Aviation Deport Jacksonville
Code 4.3
6255 Lake Gray Blvd, Suite 5
Jacksonville, FL 32244-5894
Tel: 904/779-3541

Prof. David T. **Cartwright**
Bucknell University
Department of Mechanical Engineering
Lewisburg, PA 17837
Tel: 717/524-3193
E-mail: dcartwri@bucknell.edu

Dr. Louis G. **Casagrande**
Northrop Grumman AS&T
M/S A01-26
Bethpage, NY 11714-3581
Tel: 516/346-6379
E-mail: lou-casagrande@atdc.northgrum.com

Mr. Dale J. **Casper**
USAF
OO-ALC/LFSS
6080 Gum Lane
Hill AFB, UT 84056
Tel: 801/775-4899
E-mail: casperda@lfmail.hill.ae.mil

Mr. Frank W. **Cazier**
NASA Langley Research Center
MS 254
Hampton, VA 23681
Tel: 757/864-2860
E-mail: f.w.cazier@larc.nasa.gov

Dr. Jim C.I. **Chang**
Air Force Office of Scientific Research
110 Duncan Avenue
Suite B115
Bolling AFB, DC 20332-8050
Tel: 202/767-4987
E-mail: jim.chang@afosr.af.mil

Mr. Chun C. **Chen**
The Boeing Company
2401 E Wardlow Road
MC C078-0209
Long Beach, CA 90807-5309
Tel: 562/593-2385
E-mail: chun.c.chen@boeing.com

Mr. John **Christiansen**
MTS Systems Corporation
14000 Technology Drive
Eden Prairie, MN 55344
Tel: 612/937-4865

Mr. David **Coddington**
Fatigue Technology, Inc.
100 Anclover Park W.
Seattle, WA 98188
Tel: 206/246-2010
E-mail: dcoddington@fatiguetech.com

Capt. Mario **Colavita**
Italian Air Force
DASRS-RCT
Aeroporto M. De Bernardi
Pratica Di Mare
00040 Pomezia (Roma), Italy
Tel: +39 6 91292809

Mr. Elias **Collas**
Gulfstream Aerospace Corporation
MS G-07
PO Box 2206
Savannah, GA 31402-2206
Tel: 912/965-4027
E-mail: emc5133@yahoo.com

Mr. Don **Collier**
Air Transport Association
1301 Pennsylvania Avenue, NW, Suite 1100
Washington, DC 20004-1707
Tel: 202/626-4017
E-mail: dcollier@air-transport.org

Mr. Richard A. **Collins**
British Aerospace Airbus
New Filton House
Filton, Bristol B599 1AR, United Kingdom
Tel: 441179365847

Major Dale K. **Colter**
HQ AMC USAF
HQAMC/LGBE
402 Scott Drive, Unit 2A2
Scott AFB, IL 62225-5308
Tel: 618/256-3151
E-mail: colterd@hqamclg.scott.af.mil

Dr. Jeffrey A. **Colwell**
Battelle
505 King Avenue
Columbus, OH 43201
Tel: 614/424-4528
E-mail: colwell@battelle.org

Mr. Chuck **Compton**
Litton/TASC
2555 University Boulevard
Fairborn, OH 45324
Tel: 937/426-1040
E-mail: cccompton@tasc.com

CDR Doug **Connor**
U.S. Coast Guard
Aircraft Repair and Supply Center, Building 78
Elizabeth City, NC 27909
Tel: 919/335-6240
E-mail: d.connor/arsceng@maillant.uscg.mil

Ms. Zayna **Connor**
Northwestern University
225 N. Campus Drive
MLSF #1004
Evanston, IL 60208
Tel: 847/491-3689
E-mail: z-connor@nwu.edu

Mr. Garth R. **Cooke**
NCI Information Systems, Inc.
3150 Presidential Drive
Fairborn, OH 45324
Tel: 937/427-0252
E-mail: coog@nciinc.com

Mr. Eric G. **Cooper**
NASA Langley Research Center
MS 152D
Hampton, VA 23681
Tel: 757/864-6674
E-mail: e.g.cooper@larc.nasa.gov

Mr. Thomas D. **Cooper**
Universal Technology Corporation
1270 N. Fairfield Road
Dayton, OH 45432-2600
Tel: 937/426-8530
E-mail: tcooper@utcdayton.com

Mr. Dale **Cope**
Boeing ISDS Post-Production/
Derivative Aircraft
P.O. Box 7730
MS K86-81
Wichita, KS 67277
Tel: 316/526-9873
E-mail: dale.a.cope@boeing.com

Mr. Alan J. **Copeland**
Northrop Grumman Corporation
1 Northrop Avenue
Dept 9B74/63
Hawthorne, CA 90250
Tel: 310/332-9401
E-mail: alan_copeland@mail.northgrum.com

Mr. Leo **Corbeil**
Zimac Laboratories, Inc.
1241 Cascades Street
Chateauguay, Quebec J6J 4Z2, CANADA
Tel: 514/691-5607
E-mail: zimac.labs@sympatico.ca

Mr. Tobey M. **Cordell**
AFRL/MLLP
Building 655
2977 P Street, Suite 1
Wright-Patterson AFB, OH 45433-7734
Tel: 937/255-9802
E-mail: cordeltm@ml.wpafb.af.mil

Ms. Brandy **Corley**
Naval Aviation Depot North Island
PO Box 180742
Coronado, CA 92178
Tel: 619/545-4763
E-mail: corley-b@A1.nadepni

Mr. William B. **Corwin**
Oak Ridge National Laboratory
P.O. Box 2008
4500S, MS 6161
Oak Ridge, TN 37831-6161
Tel: 423/574-4648
E-mail: corwinwr@ornl.gov

Mr. Thomas **Courbe**
French ROD/DGA/DSA/SPAe
26 France
Tel: 33145524083

Mr. MichaelBritt **Covington**
U.S. Air Force Safety Center
HQ AFSC/SEFE
9700 G Avenue SE, Suite 250C
Kirtland AFB, NM 87117-5670
Tel: 505/846-0990
E-mail: covingtb@kafb.saia.af.mil

Mr. Michael A. **Cox**
Defense Logistics Information Service
Attn: DRMS-UMW
74 Washington Avenue N
Battle Creek, MI 49017-3092
Tel: 616/961-7065

Mr. Bryan D. **Cramer**
University of Dayton Research Institute
300 College Park
Dayton, OH 45469-0138
Tel: 937/656-6011

Mr. K. Elliot **Cramer**
NASA Langley Research Center
MS 231
Hampton, VA 23681
Tel: 757/864-7945
E-mail: k.e.cramer@larc.nasa.gov

Dr. Matthew **Creager**
Structural Integrity Engineering
9509 Vassar Avenue
Chatsworth, CA 91311
Tel: 818/718-2195

-D-

GEN John R. **Dailey**
Acting Deputy Administrator
National Aeronautics and
Space Administration
Washington, DC

Dr. Claudio Dalle **Donne**
German Aerospace Cente DLR
Institute of Materials Research
Linder Mohe
D-51170 Cologne, Germany
Tel: 4922036014608
E-mail: claudio.dalle-donne@dlr.de

Mr. James **Daly**
Metal Improvement Company
10 Forest Avenue
Paramus, NJ 07652
Tel: 201/843-7800
E-mail: metalimp@ix.netcom.com

Mr. Donald **Damm**
JENTEK Sensors, Inc.
200 Dexter Avenue
Watertown, MA 02472
Tel: 617/926-8422
E-mail: jentek@shore.net

Mr. Frank V. **Daniels**
Boeing North American
System Safety & Product Assurance
12214 Lakewood Boulevard
Mail Code AD60
Downey, CA 90242-2693
Tel: 562/922-5126
E-mail: frank.v.daniels@boeing.com

Dr. Steve **Daniewicz**
Mississippi State University
Department of Mechanical Engineering
P.O. Box ME
Mississippi State, MS 39762
Tel: 601/325-7322
E-mail: daniewicz@me.msstate.edu

Dr. David S. **Dawicke**
NASA Langley Research Center
MS 188E
Hampton, VA 23681
Tel: 757/864-3477
E-mail: d.s.dawicke@larc.nasa.gov

Prof. Xiaomin **Deng**
University of South Carolina
Department of Mechanical Engineering
Columbia, SC 29208-0000
Tel: 803/777-7144
E-mail: deng@engr.sc.edu

Mr. David E. **Denman**
University of Oklahoma
865 Asp Avenue
Felgar Hall, Rm 212
Norman, OK 73019
Tel: 405/325-1090
E-mail: denman@ou.edu

Mr. J. Ronald **Denney**
FABRICO/FANA Dry Storage Systems
4222 S. Pulasky Road
Chicago, IL 60632
Tel: 773/890-5350

Mr. Anthony **Denyer**
Boeing North American
M/C SL15
PO Box 3644
2600 Westminster Blvd
Seal Beach, CA 90740-7644
Tel: 562/797-2825
E-mail: anthony.g.denyer@boeing.com

CDR Kurt **Devoe**
U.S. Coast Guard
Aircraft Repair and Supply Center
Building 78
Elizabeth City, NC 27909
Tel: 252/335-6011

Dr. Don **Dickson**
Texas A&M University
Texas Center for Applied Technology
214 Wisenbaker Engineering Research Center
College Station, TX 77843-3407
Tel: 409/862-3272
E-mail: don-dickson@tamu.edu

Dr. B. Boro **Djordjevic**
Johns Hopkins University
102 Maryland Hall/CNDE
3400 N Charles Street
Baltimore, MD 21218
Tel: 410/516-5215

Dr. Evan J. **Dolley, Jr.**
Lehigh University
Department of Mechanical
Engineering and Mechanics
Sinclair Lab, 7 Asa Drive
Bethlehem, PA 18015-3085
Tel: 610/758-5622
E-mail: ejd2@lehigh.edu

Mr. David **Douglas**
ARINC, Inc.
2551 Riva Road
Annapolis, MD 21403
Tel: 410/266-4432
E-mail: ddouglas@arinc.com

Mr. Mike **Dubberly**
Fatigue Technology, Inc.
100 Anclover Park W.
Seattle, WA 98188
Tel: 206/246-2010

Dr. Gregory L. **Dunn**
Federal Aviation Administration
Transport Directorate
1601 Lind Avenue SW
Renton, WA 98055
Tel: 425/227-2799
E-mail: gregory.dunn@faa.dot.gov

LCDR Patrick J. **Dwyer**
U.S. Coast Guard
Aircraft Repair and Supply Center
Building 79
Elizabeth City, NC 27909
Tel: 252/335-6129

-E-

Mr. Robert G. **Eastin**
Federal Aviation Administration
3960 Paramount Boulevard
Lakewood, CA 90712
Tel: 562/627-5205
E-mail: robert.eastin@faa.dot.gov

Dr. Hans **Eberhard**
German Air Force
Air Material Office
Postbox 902500/503
D-51140 Koln, Germany
Tel: 4922036022217
E-mail: nesoft@t.-online.de

COL David W. **Eidsaune**
SAF/AQQ
1060 Air Force, Pentagon
Wasington, DC 20330-1060
Tel: 703/588-7756
E-mail: eidsauned@af.pentagon.mil

Mr. Randall **Elliott**
Boeing Aging Fleet Group
P.O. Box 3707
MS 2T-20
Seattle, WA 98124-2207
Tel: 206/544-5535
E-mail: randall.i.elliott@boeing.com

Mr. William R. **Elliott**
Chief, Structures Technology Branch
WR-ALC/TIED
255 2nd Street, Suite 122
Robins AFB, GA 31098-1637
Tel: 912/926-9835
E-mail: welliott@ti.robins.af.mil

Mr. Thomas G. **Ellis**
NAVAIRSYSCOM 3.6.3.1
47038 McLeod Road, Building 448, Unit 8
Patuxent River, MD 20670-1626
Tel: 301/757-3098
E: ellis_thomas%pax8b@mr.nawcad.navy.mil

Ms. Jennifer **Elmore**
Naval Air Warfare Center
Aircraft Division
48110 Shaw Road, Unit 5
Patuxent River, MD 20670-1906
Tel: 301/342-9354
E: elmore_jennifer%pax5a@mr.nawcad.navy.mil

Ms. Jennifer L. **Elster**
F&S, Inc.
PO Box 11704
Blacksburg, VA 24062-1704
Tel: 540/961-4074
E-mail: jelster@f-s.com

Mrs. Ann M. **Embrey**
FAA (AVN-347)
6500 S MacArthur Blvd
Oklahoma City, OK 73125
Tel: 405/954-8713
E-mail: ann.embrey@faa.dot.gov

Mr. Steven M. **Enloe**
Boeing Information
Space and Defense Systens
P.O. Box 7730
MC K84-47
Wichita, KS 67277-7730
Tel: 316/523-2150
E-mail: mike.enloe@wichita.boeing.com

Mr. Gavin **Evans**
BIB ASIP
OC-ALC/LABEF
Tinker AFB, OK 73145-3006
Tel: 405/736-7264
E-mail: evans.gavin@b1b.tinker.af.mil

-F-

Mr. Timothy **Fallon**
NAVAIRSYSCOM
Structures Division
Bldg 2187, Suite 2320A
48110 Shaw Road, Unit 5
Patuxent River, MD 20678
Tel: 301/342-9325
E-mail: fallon-tim%pax5a@mr.nawcad.navy.mil

Mr. Michael **Falugi**
AFRL/VASA
Building 45
2130 Eighth Street, Suite 1
Wright-Patterson AFB, OH 45433-7542
Tel: 937/255-6639
E-mail: michael.falugi@va.afrl.af.mil

Dr. Lawrence D. **Favro**
Wayne State University
Insitute for Manufacturing Research
and Department of Physics
Detroit, MI 48202
Tel: 313/577-2727
E-mail: skip@thermal.physics.wayne.edu

Capt. Scott A. **Fawaz**
Air Force Research Laboratory / VASE
2790 D Street, Room 504
Wright-Patterson AFB, OH 45433-7402
Tel: 937/255-6104
E-mail: fawazsa@paula.flight.wpafb.af.mil

Dr. Jiri **Fidransky**
Aero Vodochody a.s.
250 70 Odolena Voda
CZECH REPUBLIC
Tel: 42026858041
E-mail: jiri.fidransky@aero.cz

Mr. Jay W. **Fiebig**
WR-ALC/TIEDD
420 Second Street
Suite 100
Robins AFB, GA 31098-1640
Tel: 912/926-4228
E-mail: jfiebig@tl.robins.af.mil

Mr. David V. **Finch**
Consultant
12 Rectory Close
Windsor, Berkshire SL4 5ER, United Kingdom
Tel: 44 1753 866819

Mr. Richard **Finlayson**
Physical Acoustics Corporation
P.O. Box 3135
Princeton, NJ 08543

Dr. Jay L. **Fisher**
Southwest Research Institute
6220 Culebra Road
San Antonio, TX 78238
Tel: 210/522-2028
E-mail: jfisher@swri.edu

Mr. Dennis A. **Flath**
Galaxy Scientific Corporation
2500 English Creek Avenue
Building "C"
Egg Harbor Township, NJ 08234-5562
Tel: 609/645-0900
E-mail: dennis.flath@galaxyscientific.com

Dr. Thomas **Fleischer**
IMA Materialforschung und
Anwendungstechnik GbmH
Hermann-Reicheit-Strabe (am Flughafen)
D-01109 Dresden, Germany
Tel: 493518837423
E-mail: ima@ima-dresden.de

Mr. John T. **Flood**
The Boeing Company
PO Box 516
St. Louis, MO 63166
Tel: 314/232-7623
E-mail: john.t.flood@boeing.com

Dr. Tom **Flournoy**
FAA W.J. Hughes Technical Center
AAR 430
Atlantic City Int'l Airport, NY 08405
Tel: 609/485-5327
E-mail: flournot@admin.tc.faa.gov

Mr. Sylvain **Forgues**
Bombardier Services
10,000 Cargo A-4 Street
Montreal International Airport - Mirabel
Mirabel Quebec, J7N 1H3 Canada
Tel: 450/476-4620

Mr. Donald M. **Forney**
Universal Technology Corporation
1270 N. Fairfield Road
Dayton, OH 45432-2600
Tel: 937/426-8530
E-mail: dforney@utcdayton.com

Mr. Scott C. **Forth**
United Technologies Research Center
MS 129-73
411 Silver Lane
East Hartford, CT 06108
Tel: 757/864-8937
E-mail: s.c.forth@larc.nasa.gov

Mr. James **Foucault**
United Parcel Service
1400 N. Hurstbourne Pkwy
Louisville, KY 40223
Tel: 502/329-6662
E-mail: air2jxf@air.ups.com

Mr. Yvan **Francoeur**
Bombardier Services
10,000 Cargo A-4 Street
Montreal International Airport - Mirabel
Mirabel Quebec, J7N 1H3 Canada
Tel: 450/476-4584
Email: yvan.francoeur@services.bombardier.com

Major Robert **Fredell**
European office of Aerospace R&D (AFOSR)
PSC 802 Box 14
FPO AE, 09499-0200
Tel: 44 171 5144505
E-mail: rfredell@eoard.af.mil

Mr. Carl A. **French**
Boeing
2601 Liberty Parkway
Midwest City, OK 73110
Tel: 405/7391410

-G-

Mr. Jean-Michel **Gaillardon**
Airbus Industrie
1, Rond Point Maurice Bellonte
31707 Blagnac Cedex, France
Tel: 33561933518

Mr. Dave **Galella**
FAA W.J. Hughes Technical Center
AAR-433
Atlantic City International Airport, NJ 08405
Tel: 609/485-5784
E-mail: galellad@admin.tc.faa.gov

Mr. Jack **Gallagher**
SYMTECH Corporation
21694 Great Mills Road
Lexington Park, MD 20653
Tel: 301/866-0330
E-mail: gallagjp@wl.wpafb.f.mil

Dr. Joseph P. **Gallagher**
AFRL/ML
Building 45
2130 Eighth Street, Suite 1
Wright-Patterson AFB, OH 45433-7542
Tel: 937/255-9696
E-mail: gallagjp@wl.wpafb.af.mil

Mr. Todd A. **Gallagher**
Naval Air Pacific Repair Activity DET Naples
PSC 817 Box 28
FPO AC 09622,
Tel: 390815685497
E-mail: tgallagh@naples.navy.mil

Mr. Bruce **Garbett**
Airbus Industrie (Toulouse)
Rond Point
Maurice Bellonte
31700 Blagnac Cedex, France
Tel: 33561933569
E-mail: bruce.garbett@airbus.fr

Ms. Jane **Garvey**
Federal Aviation Administration
Office of the Administrator
800 Independence Avenue, SW
Washington, DC 20591

Ms. Georgette B. **Gaskin**
Naval Air Warfare Center
Aircraft Division
Patuxent River, MD 20670-1545
Tel: 301/342-8091

Dr. Jean **Gebman**
RAND
1700 Main Street
Santa Monica, CA 90402
Tel: 310/393-0411

Mr. Mark **Gehlen**
UniWest Corporation
330 W. Clark Street
Pasco, WA 99301
Tel: 509/544-0720
E-mail: uniwest@owt.com

Dr. Edward R. **Generazio**
Nasa Langley Research Center
MS 231
Hampton, VA 23681
Tel: 757/864-4970
E-mail: e.r.generazio@nasa.larc.gov

Mr. Tony **Gerardi**
APR Consultants, Inc.
27 Oaklawn Avenue
Medway, OH 45341
Tel: 937/849-6795
E-mail: apr@erinet.com

Mr. Johnny **Gibson**
Liberty Technologies, Inc.
555 North Lane
Conshohocken, PA 19428
Tel: 610/834-0330
E-mail: jgibson@libtech.attmail.com

Mr. Robert **Giese**
OO-ALC/LACM
6064 Dogwood Avenue
Hill Air Force Base, UT 54056-5816
Tel: 801/777-5292
E-mail: giesero@hillwpos.hill.af.mil

Dr. Neil J. **Goldfine**
JENTEK Sensors, Inc.
200 Dexter Avenue
Watertown, MA 02172
Tel: 617/926-8422
E-mail: jentek@shore.net

Dr. Matthew J. **Golis**
Advanced Quality Concepts
PO Box 141388
Columbus, OH 43214
Tel: 614/268-0518
E-mail: golismj@earthlink.net

Dr. Anuncia **Gonzalez-Martin**
Lynntech, Inc.
7610 Eastmark Drive, Suite 202
College Station, TX 77840
Tel: 409/693-0017
E-mail: anuncia@ix.netcom.com

Mr. Dan **Goodyear**
ALCOA
Atlanta, GA
Tel: 770/421-0188

Mr. David **Graham**
DSTO - Aeronatucial & Marine Research Lab
506 Lorimer Street
Fishermens Bend, Victoria 3207, Australia

Mr. Alten F. **Grandt**
School of Aeronautics & Astronautics
Purdue University
1282 Grissom Hall
W Lafayette, IN 47907-1282
Tel: 765/494-5141
E-mail: grandt@ecn.purdue.edu

Mr. Jonathan **Greene**
F&S, Inc.
2801 Commerce Street
Blacksburg, VA 24060
Tel: 540/953-4269
E-mail: jag@f-s.com

Major James M. **Greer, Jr.**
HQ, United States Air Force Academy
Department of Engineering Mechanics
2354 Fairchild Drive, Suite 6H2
USAF Academy, CO 80840-6240
Tel: 719/333-3618
E-mail: greerjm.dfem@usafa.af.mil

Mr. Ron **Grendahl**
Cessna Aircraft Company
One Cessna Boulevard
Wichita, KS 67215
Tel: 316/941-7161

Mr. Kenneth E. **Griffin**
Southwest Research Institute
6220 Culebra Road
San Antonio, TX 78238-5166
Tel: 210/522-6873
E-mail: kgriffin@swri.org

Mr. Robert **Grills**
SAIC Ultra Image International
Two Shaw's Cove, Suite 101
New London, CT 06320
Tel: 860/442-0100
E-mail: robert.h.grills@cpmx.saic.com

Mr. Frank **Grimsley**
ASC/YC
Wright-Patterson AFB, OH 45433-7142
Tel: 937/255-1049
E-mail: babishea@c17mis.wpafb.af.mil

Capt. Daniel J. **Groner**
Technology Insertion Program
Aging Aircraft & Systems Office
2145 Monahan Way
Wright-Patterson AFB, OH 45433-7017
Tel: 937/255-6053
E-mail: gronerdj@ntnotes2.ascsm.wpafb.af.mil

Mr. Allan **Gunderson**
Universal Technology Corporation
1270 N. Fairfield Road
Dayton, OH 45432-2600
Tel: 937/426-8530
E-mail: agunderson@utcdayton.com

Mr. Allan **Gunderson**
Universal Technology Corporation
1270 N. Fairfield Road
Dayton, OH 45432-2600
Tel: 937/426-8530
E-mail: agunderson@utcdayton.com

Mr. Cornelis **Guyt**
USAF Academy
HQ USAFA/DFEM
2354 Fairchild Drive, Suite 6H2
USAF Academy, CO 80840-6240
Tel: 719/333-3043
E-mail: guytcb.dfem@usafa.af.mil

-H-

Mr. Richard N. **Hadcock**
RNH Associates, Inc.
6 Sue Circle
Huntington, NY 11743-1979
Tel: 516/271-7037
E-mail: rhadcock@li.net

Mr. Donald **Hagemaier**
Boeing
2401 E. Wardlow Road
MC C071-0013
Long Beach, CA 90807
Tel: 562/593-7304
E-mail: donald.j.hagemaier@boeing.com

Mr. Dennis S. **Hager**
U.S. Air Force
AFRL/MLSS
2179 12th Street, Rm 122
Wright-Patterson AFB, OH 45433-7718
Tel: 937/255-3480
E-mail: hagerds@ml.wpafb.af.mil

MG Dennis G. **Haines**
Director of Logistics
HQ, Air Combat Command
Langley AFB, VA 23681

Mr. Bradley L. **Hallock**
Naval Aviation Depot
NAS North Island
San Diego, CA 92145
Tel: 619/545-3933

Prof. Xiaoyan **Han**
Wayne State University
Insitute for Manufacturing Research
and Department of Physics
666 W. Hancock
Detroit, MI 48202
Tel: 313/577-2792
E-mail: han@thermal.physics.wayne.edu

LCDR Paul E. **Hansen**
USCG Aircraft Repair & Supply Center
Weeksville Road
Elizabeth City, NC 27909
Tel: 252/335-6597
E-mail: phansen@arsc.useg.mil

Mr. Keith **Hardman**
Lockheed Martin - Aeronautical Systems
Dept 66-15, Zone 0555
86 S Cobb Drive
Marietta, GA 30063-0555
Tel: 770/494-8079
E-mail: keith.hardman@lmco.com

Prof. D. Gary **Hariow**
Lehigh University
Department of Mechanical
Enginering and Mechanics
19 Memorial Drive West
Bethlehem, PA 18015-3085
Tel: 610/758-4127
E-mail: dgh0@lehigh.edu

Dr. Charles E. **Harris**
NASA Langley Research Center
Mail Stop 188M
Hampton, VA 23681
Tel: 757/864-3447
E-mail: c.e.harrs@larc.nasa.gov

Mr. James R. **Harrison**
Metal Improvement Compamy, Inc.
1618 Ida
Wichita, KS 67211
Tel: 316/267-8201
E-mail: metalimp@ix.netcom.com

Mr. James A. **Harter**
AFRL/VASE
2790 D Street, Building 65, Area B
Wright-Patterson AFB, OH 45429
Tel: 937/255-6104
E-mail: jim@fibecin5.flight.wpafb.af.mil

Mr. Paul **Hauwiller**
Anteon Corporation
5100 Springfield Pike, Suite 509
Dayton, OH 45431-1264
Tel: 937/254-7950
E-mail: phauwill@dayton.anteon.com

Mr. Richard **Hazard**
The Boeing Company
3855 Lakewood Blvd, MS D046-0046
Long Beach, CA 90846
Tel: 562/982-6320
E-mail: richard.s.hazard@boeing.com

Mr. Iain G. **Hebden**
British Aerospace Military
Aircraft and Aerostructures
Warthon Aerodrome
Preston, Lancashire PR4 1AX, United Kingdom
Tel: 441772855420
E-mail: iain.hebden@bae.co.uk

Major Burkhard **Heesing**
German Air Force Support Command
Department of Air Armament
P.O. Box 902 500/502/09
D 51140 Cologne, GERMANY
Tel: 4922032352

Mr. James **Helbling**
Northrop Grumman Corporation
F 5/T 38 Engineering
One Hornet Way
El Segundo, CA 90245-2804
Tel: 310/332-6004
E-mail: james_helbling@mail.norhgrum.com

Mr. Jeffrey D. **Helm**
University of South Carolina
Department of Mechanical Engineering
300 Main Street
Columbia, SC 29208
Tel: 803/777-7617

Mr. Grant D. **Herring**
OO-ALC/LACM
6064 Dogwood Avenue
Hill Air Force Base, UT 84056
Tel: 801/777-7346
E-mail: herringg@hillwpos.hill.af.mil

Mr. Erwin **Hess**
NASA Dryden Flight Research Center
PO Box 273
MS 1049
Edwards, CA 93523-0273
Tel: 805/258-7470

Mr. Thomas E. **Hess**
Naval Air Systems Command
Building 2187 Suite 2340A
48110 Shaw Road, Unit 5
Patuxent River, MD 20670
Tel: 301/342-9363
E-mail: hess_tom%pax5a@mr.nawcad.navy.mil

Mr. Richard **Heusser**
West Coast Industries
14900 Whitman Avenue North
Seattle, WA 98133-6532
Tel: 206/365-7513

Mr. Richard **Heusser**
West Coast Industries
14900 Whitman Avenue, N.
Seattle, WA 98133
Tel: 206/365-7513
E-mail: rheusser@wcoastindustries.com

Dr. Joseph S. **Heyman**
NASA Langley Research Center
MS 118
Hampton, VA 23681
Tel: 757/864-6006
E-mail: j.s.heyman@larc.nasa.gov

Dr. Mark K. **Hinders**
Applied Science Department
The College of William & Mary
P.O. Box 8795
Williamsburg, VA 23187-8795
Tel: 757/221-1519
E-mail: hinders@as.wm.edu

Dr. Bruce **Hinton**
Defense Science and Technology Organisation
Aeronautical and Maritime Research Laboratory
506 Lorimer St, Fishermens Bend
Victoria 3207, Australia
Tel: 61396267535
E-mail: bruce.hinton@dsto.defence.gov.edu

Mr. Michael **Hitchcock**
U.S. Air Force
AFRL/MLSA
2179 12th Street
Wright-Patterson AFB, OH 45433-7718
Tel: 937/656-9262
E-mail: hitchcmf@ml.wpafb.af.mil

LtCol Tom **Hixon**
HQ USAF/ILMY
1030 Air Force Pentagon
Washington, DC 20330-1030
Tel: 703/697-9231

Dr. Margery E. **Hoffman**
Naval Air Systems Command
ATTN: Code 4.3.3.4
Building 2187, Suite 2320
48110 Shan Road Unit 5
Patuxent River, MD 20670
Tel: 301/342-9344
hoffman_margery%pax5a@mr.nawcad.navy.mil

Dr. Paul C. **Hoffman**
NAVAIR 4.3.3
Structures Division
Building 2187, Suite 2340A
48110 Shaw Road, Unit 5
Patuxent River, MD 20670-1906
Tel: 301/342-9361
hoffman_paul%pax5a@mr.nawcad.navy.mil

Mr. Amos W. **Hoggard, Jr.**
Boeing Commercial Airplane Group
Douglas Products Division
D801-0037
3855 Lakewood Boulevard
Long Beach, CA 90846
Tel: 562/593-1843
E-mail: amos.w.hoggard-jr@boeing.com

Mr. Bert **Hoogeland**
KLM Royal Duthch Airlines
PO Box 7700
U17 2L Schiphol Airport, The Netherlands
Tel: 31206495866
E-mail: klm11715@to.klm.nl

Mr. Wally C. **Hoppe**
University of Dayton Research Institute
300 College Park Avenue
Dayton, OH 45469-0120
Tel: 937/229-3711
E-mail: hoppe@udri.udayton.edu

Mr. Cornelius O. **Horgan**
Department of Civil Engineering
University of Virginia
Thornton Hall
Charlottesville, VA 22903
Tel: 804/924-7230
E-mail: coh8p@virginina.edu

Dr. Peter **Horst**
Instit fuer Flugzeugbau und Leichtbau
TU Braunchweig
Langer Kamp 19
38106 Braunschweig, Germany
Tel: 495313912694
E-mail: p.horst@tu-bs.de

Dr. Peter W. **Hovey**
U.S. Air Force
AFRL/VASE
Building 65
2790 D Street
Wright-Patterson AFB, OH 45433-7402
Tel: 937/255-6104
E-mail: peter.hovey@va.afrl.af.mil

Ms. Daniele **Hovington**
Bombardier Services
10,000 Cargo A-4 Street
Montreal International Airport - Mirabel
Mirabel Quebec, J7N 1H3 Canada
Tel: 450/476-4620
E-mail: paul.londei@services.bombardier.com

Mr. Michael A. **Howard**
ARINC, Inc.
2551 Riva Road
MS1-203
Annapolis, MD 21401
Tel: 410/266-4725

Mr. Dave **Howell**
Oak Ridge National Laboratory
P.O. Box 2009, Mail Stop 8050
Oak Ridge, TN 37831-8050
Tel: 423/576-8283
E-mail: howelld1@ornl.gov

Mr. Chris **Hoyle**
British Aerospace M.A. and A
Greengate, Middleton
Manchester M24 1SA, United Kingdom
Tel: 1619558744

Mr. Ching-long **Hsu**
The Boeing Company
2401 E Wardlow Road
Long Beach, CA 90807-5309
Tel: 562/593-3779

Mr. Gerardo M. **Hueto**
Alaska Airlines - Engineering
PO Box 68900 - SEAME
Seattle, WA 98168-0900
Tel: 206/431-5518
E-mail: gerardo.hueto@alaskaair.com

Mr. James **Hunt**
Naval Aviation Depot
P.O. Box 357058
San Diego, CA 92135-7058
Tel: 619/545-4982
E-mail: hunt_j@al.nadepni.navy.mil

Mr. Kipplan D. **Hunter**
Boeing Company
P.O. Box 516
M/S 102-2147
St. Louis, MO 63166-0516
Tel: 314/234-4162
E-mail: kipplan.d.hunter@boeing.com

-I-

Dr. Roy **Ikegami**
Boeing Company
Information, Space, & Defense Systems
P.O. Box 3999
MS 82-97
Seattle, WA 98124-2499
Tel: 253/773-5876
E-mail: roy.ikegami@boeing.com

Mr. J. Ed **Ingram**
Lockheed Martin Aeronautical Systems
86 South Cobb Drive
Marietta, GA 30063
Tel: 770/494-8172
E-mail: ed.ingram@lmco.com

Mr. Deryl W. **Israel**
WR-ALC/LJ
270 Ocmulgee Court
Robins AFB, GA 31098-1646
Tel: 912/926-6491
E-mail: disrael@wrdissl.robins.af.mil

-J-

LtCol Joachim **Jacker**
NATO Liaison Officer at the OC-ALC
408 Buckboard Lane
Midwest City, OK 73130
Tel: 405/736-3108
E-mail: laki-nato@worldnet.att.net

Dr. Michael R. **James**
Rockwell Science Center
1049 Camino Dos Rios
Thousand Oaks, CA 91360
Tel: 805/373-4230
E-mail: mrjames@rsc.rockwell.com

Mr. Navin **Jaunky**
Old Dominion University
1039 Rockbridge Avenue, #185
Norfolk, VA 23508
Tel: 757/865-4849

Dr. David Y. **Jeong**
U.S. Department of Transportation
Volpe National Transportation Systems Center
Kendall Square
Cambridge, MA 02142
Tel: 617/494-3654
E-mail: jeong@volpe.dot.gov

Ms. Melody W. **Jiran**
Gulfstream Aerospace Corporation
MS G-07, P.O. Box 2206
Savannah, GA 31402-2206
Tel: 912/965-3561

Mr. John B. **Johns**
Commander
U.S. Army Aviation and Missile Command
AMSAM-AR-ZS
Redstone Arsenal, AL 35898-5000
Tel: 256/313-1737
E-mail: johns-jb@redstone.army.mil

Mr. David H. **Johnson**
Air Force Research Laboratory
AFRL/MLSA
Building 652
2179 Twelfth Street, Suite 1
Wright-Patterson AFB, OH 45433-7718
Tel: 937/656-9163

Mr. Ronald T. **Johnson**
Raytheon Systems Company Greenville
502 Turtle Creek
Greenville, TX 75402
Tel: 903/457-5690
E-mail: johnsonrt@grl.esys.com

Capt. Thomas N. **Johnson**
U.S. Air Force OO-ALC/LACM
6064 Dogwood Avenue
Hill AFB, UT 84056-5816
Tel: 801/775-4749
E-mail: johnstho@hillwpos.hill.af.mil

Dr. Patrick H. **Johnston**
NASA Langley Research Center
MS 231
Hampton, VA 23681
Tel: 757/864-4966
E-mail: p.h.johnston@larc.nasa.gov

Mr. William M. **Johnston**
Analytical Services & Materials, Inc.
107 Research Drive
Hampton, VA 23666
Tel: 757/864-3472
E-mail: w.m.johnston@larc.nasa.gov

Mr. Craig R. **Jones**
Sandia National Laboratories
MS 0615
Albuquerque, NM 87185-0615
Tel: 505/843-8722
E-mail: criones@sandia.gov

Mr. Victor **Juarez**
Damage Tolerant Structures Engineers, Inc
P.O. Box 460873
San Antonio, TX 78246
Tel: 210/863-8347
E-mail: vicj@swbell.net

Mr. Alan **Julier**
Krautkramer Branson
50 Industrial Park Road
Lewistown, PA 17044
Tel: 717/242-0327
E-mail: ajulier@krautkramer.com

-K-

Mr. David **Karmel**
Orbital Science Corporation
Fairchild Defense
20301 Country Blvd
Germantown, MD 20874
Tel: 301/428-6639

Prof. Noriko **Katsube**
The Ohio State University
Applied Mechanics Boyd Laboratory
155 W. Woodruff Avenue
Columbus, OH 43210
Tel: 614/292-0971
E-mail: katsube.1@osu.edu

Dr. James C. **Kennedy**
Battelle
505 King Avenue
Columbus, OH 43201
Tel: 614/424-4831

LT Thomas **Kennedy**
VQ-4
VQ-4 7791 Mercury Road
Tinker AFB, OK 73145
Tel: 405/739-3672
E-mail: kennedy@tacamo.navy.mil

Mr. Trent **Kerbs**
U.S. Navy
1601 NE 4th Street
Moore, OK 73160
Tel: 405/739-4593
E-mail: kerbs@tacamo.navy.mil

Mr. Alan **Kerr**
Advanced Repair Technology International
6500 West Freeway
Office 314
Fort Worth, TX 76116
Tel: 817/737-1656

Major Klaus W. **Kessler**
NATO - E-3A (A WACS)
LWFC
52511 Jeilen Kirchen, Germany
Tel: 492451633600

Dr. Jinseong **Kim**
Lynntech, Inc.
7610 Eastmark Drive, Suite 202
College Station, TX 77840
Tel: 409/693-0017
E-mail: lynntech@myriad.net

Mr. Jon **Kimmel**
AO-ALC/LAKRA
3001 Staff Drive
Suite 2AH110
Tinker AFB, OK 73071

Mr. Brian **Kinkade**
U.S. Air Force
7278 4th Street, Building 100 N
Hill AFB, UT 84056
Tel: 801/777-1709
E-mail: kinkaded@software.hill.af.mil

Mr. Richard **Kinzie**
AF Corrosion Program Office
325 2nd Street
Robins AFB, GA 31098
Tel: 912/926-3284
E-mail: rkinzie@wrdiss1.robins.af.mil

Ms. Diane **Kirts**
OC-ALC/LCPM
3001 Staff Drive
Suite 2AH190
Tinker AFB, OK 73145-5019
Tel: 405/736-4499
E-mail: dlkirts@tinker.af.mil

Ms. Mindy **Klement**
Everest Imaging
11500 Metric Boulevard
Building 210
Austin, TX 78758
Tel: 512/833-9408
E-mail: klementm@everestimaging.com

Mr. Phillip C. **Kloos**
MTS Systems Corporation
14000 Technology Drive, MS 231
Eden Prairie, MN 55344
Tel: 612/937-4854
E-mail: phil.kloos@mts.com

Dr. Edward T. **Knobbe**
Environmental Institute
201 CITD Building
Stillwater, OK 74078-3011
Tel: 405/744-9994
E-mail: knobbe@okway.okstate.edu

Mr. Ray T. **Ko**
Veridian
2700 Indian Ripple Road
Dayton, OH 45440
Tel: 937/476-2830
E-mail: rko@cytn.veridian.com

Mr. Gerhardus H. **Koch**
CC Technologies Laboratories, Inc.
6141 Avery Road
Dublin, OH 43016
Tel: 614/761-1214
E-mail: kochg@cctlabs.com

Mr. Jerzy P. **Komorowski**
National Research Council Canada
Montreal Road M-14
Ottawa, Ontario K1A 0R6, Canada
Tel: 613/993-3999

Dr. Igor **Komsky**
Northwestern University
Center for Quality Engineering
and Failure Prevention
2137 N. Sheridan Road
Evanston, IL 60208
Tel: 847/491-5579
E-mail: ikomsky@nwu.edu

Mr. Keijo **Koski**
VTT Manufacturing Technology
P.O. Box 1705
FIN-02044 VTT, Finland
Tel: 35894566549
E-mail: keijokoski@vtt.fi

Dr. Victor **Kowalenko**
Aerostructures Australia
Level 14
222 Kingsway
South Melbourne Victoria 3250, Australia
Tel: 61346941016

Mr. Steven R. **Kramer**
Raytheon Systems Company
FM1564 Majors Field
P.O. Box 6056, CBN 170
Greenville, TX 75403-6056
Tel: 903/457-7096

Mr. Srinivas **Krishnan**
AS&M
107 Research Drive
Hampton, VA 23666
Tel: 757/865-7093
E-mail: krish@asmobj.larc.nasa.gov

Mr. Michael **Kulak**
ALCOA Technical Center
100 Technical Drive
Alcoa Center, PA 10568
Tel: 724/337-5874

Dr. Robert E. **Kurth**
Battelle Memorial Institute
505 W. King Avenue
Columbus, OH 43201
Tel: 614/424-7151
E-mail: kurth@battelle.org

Mr. Joseph **Kuzniar**
AFRL/ML
Building 45, Room 203
2130 Eighth Street, Suite 1
Wright-Patterson AFB, OH 45433-7542
Tel: 937/255-9696
E-mail: joseph.kuzniar@wl.wpafb.af.mil

-L-

Ms. Diane **Lafferman**
The Boeing Company
1200 Wilson Boulevard
Arlington, VA 22209
Tel: 703/465-3428
E-mail: diane.lafferman@boeing.com

Mr. Lawrence M. **Landall**
Federal Aviation Administration
DER for Aircraft Structural Certification Co
872 Leopard Trail
Winter Springs, FL 32708
Tel: 407/699-5114
E-mail: llandall@earthlink.net

Mr. Stephen **Langheim**
British Airways
B4, TBA, 5343
P.O. Box 10
Heathrow Airport
Hounslow Middlesex TW6 2JA, United Kingdom
Tel: 441815123652
E-mail: stephen.1.langheim@british-airways.com

Mr. Ken L. **Langille**
Directorate of Technical Airworthiness
National Defence Headquarters
Department of National Defence, Canada
MGen George R. Pearkes Building
Ottawa, Ontario K1A 0K2, Canada
Tel: 613/990-5871
E-mail: ken.langille@dsto.defence.gov.au

Mr. Bob **Lasser**
Imperium, Inc.
2092 Gaither Road, Suite 220F
Rockville, MD 20850
Tel: 301/330-7179
E-mail: blasser@po.mctec.com

Dr. Marvin **Lasser**
Imperium, Inc.
2092 Gaither Road, Suite 220F
Rockville, MD 20850
Tel: 301/330-7179
E-mail: blasser@po.mctec.com

Mr. Harvey M. **Leake**
DCMC Lockheed Martin
36 S Cobb Drive
Marietta, GA 30063-0260
Tel: 770/494-1051
E-mail: hleake@dcmde.dla.mil

Mr. Randall E. **Lefler**
U.S. Navy
Naval Air System Command
48110 Shaw Road, Unit 5
Patuxent River, MD 20670-1906
Tel: 301/342-9376
E-mail: leflerr.ntrprs@navair.navy.mil

Mr. Klamen I. **Leikach**
Naval Air Systems Command
Building 2187, Suite 2343, CST 5
48110 Shaw Road
Patuxent River, MD 20670-1906
Tel: 301/342-9362
E-mail: leikachki.ntrprs@navair.navy.mil

Mr. Anthony **Leon**
West Coast Industries
14900 Whitman Avenue, N.
Seattle, WA 98133
Tel: 425/745-0553

Mr. Jess **Lewis**
Regulatory Support Division
Federal Aviation Administration
Airworthiness Program
Branch (AFS-610)
P.O. Box 25082
Oklahoma City, OK 73125
Tel: 405/954-7044
E-mail: jess.lewis@faa.dot.gov

Ms. Karen S. **Lewis**
University of Virginia
Department of Materials Science, Thornton Hall
Charlottesville, VA 22903
Tel: 804/982-5790
E-mail: ksl5f@virginia.edu

Major Ralf **Liesenfeld**
German Air Force
Air Materiel Office
Postfach 902500-50/13
51140 Koln, Germany
Tel: 4922036024679

Mr. Gus **Liggon**
Defense Supply Center Richmond
8000 Jefferson Davis Highway
Richmond, VA 23297-5000
Tel: 804/279-5940
E-mail: gliggon@dscr.dla.mil

Dr. John W. **Lincoln**
United States Air Force Air Materiel Command
ASC/EN
2530 Loop Road West
Wright-Patterson AFB, OH 45433-7101
Tel: 937/255-5312
E-mail: lincoljw@asc-en.wpafb.af.mil

Mr. Alexander **Litvinov**
AS&M
2790 D Street
Building 65, Area B
Wright-Patterson AFB, OH 45429
Tel: 937/255-0434
E-mail: alex@fibecin6.flight.wpafb.af.mil

Mr. Ko-Wei **Liu**
Boeing Company
Boeing Airlift and Tanker
2401 E. Wardlow Road
M/C C052-0660
Long Beach, CA 90807-4418
Tel: 562/982-5422
E-mail: ko-wei@boeing.com

Mr. Rex R. **Liu**
The Boeing Company
5000 E McDowell Road
Mesa, AZ 85215-9797
Tel: 602/891-0297

Mr. James G. **Lo**
The Boeing Company
2401 E Wardlow Road
MC C078-0209
Long Beach, CA 90807-5309
Tel: 562/593-2129
E-mail: james.g.lo@boeing.com

Mr. Don **Locke**
Karta Technologies, Inc.
1892 Grandstand
San Antonio, TX 78238
Tel: 210/681-9382
E-mail: dlocke@karta.com

Mr. Domenico **Lombardo**
Defence Science and Technology Organisation
P.O. Box 4331
Melbourne, Victoria 3001, Australia
Tel: 61396267560
E-mail: domenico.lombardo@dsto.defence.gov.au

Mr. Robert **Lomardo**
Fuji NDT Systems
911 Hope Street
P.O. Box 4960
Stampford, CT 06907
Tel: 800/431-1850
E-mail: bobl@fujimed.com

Mr. David **Lotterer**
Regional Airline Association
1200 19th Street, NW, Suite 300
Washington, DC 20036
Tel: 202/857-1140
E-mail: david_lotterer@dc.sba.com

Mr. John J. **Lundeen**
Naval Air Warfare Center
48060 Shaw Road, Building 2188
Patuxent River, MD 20670
Tel: 301/342-8017

Mr. Joe **Luzar**
Boeing Information, Space and Missile Systems
P.O. Box 7730
MS K86-71
Wichita, KS 67277-7730
Tel: 316/523-5408
E-mail: joe.luzar@wichita.boeing.com

Mr. Robert R. **Lynn**
TOGAA
4305 Hidden Valley Court
Colleyville, TX 76034
Tel: 817/788-2458
E-mail: rrlynn@aol.com

-M-

Ms. Susan **MacPherson**
Foster-Miller, Inc.
350 Second Avenue
Waltham, MA 02451
Tel: 781/684-4434
E-mail: smacpherson@foster-miller.com

Dr. Eric I. **Madaras**
NASA Langley Research Center
MS 231
Hampton, VA 23681
Tel: 757/864-4993
E-mail: e.i.madaras@larc.nasa.gov

Mr. James E. **Malinak**
Boeing Information Space and Defense Systems
2600 Paramount, Suite 400
Fairborn, OH 45324
Tel: 937/427-1767

Mr. Malte **Malmbo**
Teknikinfu I Krukom AB
Box 58
S-83125 Krokom, Sweden
Tel: 4664016970

Mr. Scott **Mangrum**
WR-ALC/LRAA
750 Third Street
Robins AFB, GA
Tel: 912/926-3466
E-mail: scott_mangrum@lr.robins.af.mil

Mr. James W. **Mar**
TOGAA
905 Jewell Ave
Pacific Grove, CA 93950
Tel: 831/373-3850
E-mail: agingprof@aol.com

Mr. Larry **Marable**
O-ALC/TISMD
Building 100, Bay N
7278 4th Street
Hill AFB, UT 84056-5205
Tel: 801/777-1709
E-mail: marablel@software.hill.af.mil

Mr. Danny N. **Marks**
AlliedSignal ALS Repair & Overhaul
3520 Westmoor Street
South Bend, IN 46628-1373
Tel: 219/231-2579

Mr. James **Martin**
Bell Helicopter Textron, Inc.
P.O. Box 482
Fort Worth, TX 76101
Tel: 817/280-3517
E-mail: jmartin@bellhelicopter.textron.com

Mr. Thomas **Martin**
MATEC Instruments
RD#1, Box 169-4
Woodcliff Circle
Seven Valleys, PA 17360
Tel: 717/792-3455

Mr. John C. **Mason**
Naval Air Pacific Repair Activity NAPRA
PSC 477 Box 35
FPO AP 96306
Tel: 81467763771
E-mail: mason@shogun.ndo.navy.mil

Mr. Allen W. **Maxin**
Aerospace Rivet Manufacturers Corp.
8535 Dice Road
Santa Fe Springs, CA 90670
Tel: 562/945-5456

Capt. V. Scott **May**
AFRL/VASA
2130 Eighth Street, Suite 1
Wright-Patterson AFB, OH 45433
Tel: 937/255-5664
E-mail: mayvs@wl.wpafb.af.mil

Mr. James J. **Mazza**
U.S. Air Force Research Laboratory
AFRL/MLSA
2179 12th Street, Room 122
Wright-Patterson AFB, OH 45433-7718
Tel: 937/255-7778
E-mail: mazzajj@ml.wpafb.af.mil

Dr. Stuart L. **McBride**
AEMS Acoustic Emission Monitoring Services
120 Clarence Street, Suite 274
Kingston, Ontario K7L 1X4, Canada
Tel: 613/544-6792
E-mail: aems@kos.NET

Mr. Mickey **McCabe**
UDRI
300 College Park
Dayton, OH 45469-0101
Tel: 937/229-2113

Mr. John **McCoury**
Raytheon System Company
7500 Maerh Road
M/S 1261
Waco, TX 76705
Tel: 254/867-4254
E-mail: john_mjccoury@readwo.com

Mr. Daniel **McCray**
University of Dayton Research Institute
300 College Park
Dayton, OH 45469-0138
Tel: 937/656-6009
E-mail: mccraydb@ml.wpafb.af.mil

2LT Scott **McCumsey**
Air Force NDI Office
485 Quentin Roosevelt, Suite 7
Kelly AFB, TX 78241-6426
Tel: 210/925-6408
E-mail: msmccumsey@ldgate1.kelly.af.mil

Ms. Michelle **McDevitt**
JENTEK Sensors, Inc.
200 Dexter Avenue
Watertown, MA 02472
Tel: 619/926-8422

Mr. Joseph H. **McGarvey**
FAA Chicago Aircraft Certifiction Office
2300 E Devon Avenue
Des Plaines, IL 60018
Tel: 847/294-7136

Mr. John J. **McGrath**
Galaxy Scientific Corporation
2500 English Creek Avenue, Building C
Egg Harbor, NJ 08234-5562
Tel: 609/645-0900
E-mail: john.mcgrath@galaxyscientific.com

Mr. Jack F. **McGuire**
Boeing Commercial Airplane Group
P.O. Box 3707
M/C 67-UT
Seattle, WA 98124-2207
Tel: 425/234-9991

Dr. Peter C. **McKeighan**
Southwest Research Institute
6220 Culebra Road
San Antonio, TX 78238
Tel: 210/522-3617
E-mail: pmckeighan@swri.org

Mr. Don **McMillian**
NADEP Jacksonville FLA, Norfolk DET
639 Aguila Drive
Chesapeake, VA 23322
Tel: 757/444-8282
E-mail: dmac104@aol.com

Mr. Ken **McRae**
Department of Naval Defence Canada
Mgen George R. Pearkes Building
Ottowa, K1A OK2 Canada
Tel: 613/991-6908
E-mail: ken.mcrae@nrc.ca

Prof. Mark E. **Mear**
The University of Texas at Austin
Department of Aerospace Engineering
Austin, TX 78712
Tel: 512/471-4212
E-mail: mmear@max.ae.utexas.edu

Mr. Paul **Mehrkam**
Naval Air Systems Command
AIR-4343, Building 2188
22541 Shaw Road, Unit 5
Patuxent River, MD 20670-1908
Tel: 301/342-8064
E: mehrkam_paul%pax5@mr.nawcad.navy.mil

LDCR Charles W. **Mello**
U.S. Coast Guard
Aircraft Repair and Supply Center
Building 78
Elizabeth City, VA 27909
Tel: 252/335-6887

Mr. Randy **Merrill**
Northrop Grumman
P.O. Box 655907
Dallas, TX 75265-5907
Tel: 972/946-0771
E-mail: randy_merrill@mail.northgrum.com

Mr. Sambi R. **Mettu**
Lockheed Martin Space Mission
Systems & Services
2400 NASA Road 1
Mail Code CB2
Houston, TX 77058
Tel: 281/483-3960
E-mail: smettu@ems.jsc.nasa.gov

Ms. Jackie **Mew**
Portsmouth University
Computer Science Building, Locksway Road
Milson, Southsea, Hants P048JF, United Kingdom
Tel: 441705844077
E-mail: mewjm@sis.port.ac.uk

Mr. George H. **Miller**
Boeing
3801 S. Oliver
M/C K86-97
Wichita, KS 67210
Tel: 316/526-6533
E-mail: george.h.miller2@boeing.com

Dr. Ronnie K. **Miller**
Physical Acoustics Corporation
195 Clarksville Road
Lawrencevill, NJ 08648
Tel: 608/716-4000
E-mail: esi@pacndt.com

Mr. William J. **Miller**
Transport Canada
Place De Ville, Tower C
330 Sparks Street, 2nd Floor
Ottawa, Ontario K1A 0N8, CANADA
Tel: 613/952-4388

Mr. Richard **Mills**
Northrop Grumman Commercial Aircraft Division
1801 SE Airport Road
Stuart, FL 34995
Tel: 561/220-5730

Mr. Howard F. **Miner**
Naval Air Systems Command AIR-6.3.4.2.3
47038 McLeod Road, Unit 8
Naval Air Station
Patuxent River, MD 20670-1626
Tel: 301/757-3064

Mr. Merrill L. **Minges**
Air Force Aging Aircraft Office
2130 8th Street
Wright-Patterson AFB, OH 45433-7542
Tel: 937/255-9696
E-mail: mingesml@wl.wpafb.af.mil

Mr. W. Craig **Mitchell**
U.S. Air Force
OO-ALC/LACI
6089 Wardleigh Road
Hill AFB, UT 84056
Tel: 801/777-9859
E-mail: mitchelc@1fmail.hill.af.mil

Mr. James M. **Moll**
U.S. Air Force
913th AW
5 Gough Avenue
Ivyland, PA 18974
Tel: 215/443-1241
E-mail: jmoll@nxx.afres.af.mil

Mr. David G. **Moore**
Sandia National Laboratories
PO Box 5800-0615
Albuquerque, NM 87185-0615
Tel: 505/844-7095
E-mail: dgmoore@sandia.gov

Mr. James **Montgomery**
U.S. Coast Guard
Comandant (6-SEA)
2100 2nd Street S.W.
Washington, DC 20593
Tel: 202/267-1641
E-mail: jmontgomery@comdt.uscg.mil

Mr. Montgomery **Morgan**
Boeing - BCAG Sturctures Post-Production
P.O. Box 3707, MS 2T-20
Seattle, WA 98124-2207
Tel: 206/544-5535
E-mail: montgomery.h.morgan@boeing.com

Dr. Robert W. **Moses**
NASA Langley Research Center
MS 340
Hampton, VA 23681-0001
Tel: 757/864-7033
E-mail: r.w.moses@larc.nasa.gov

Mr. Joseph R. **Mosher**
Aging Aircraft & Systems Office
2145 Monahan Way
Wright-Patterson AFB, OH 45433-7017
Tel: 937/255-6053
E-mail: mosherjr@ntnotes2.ascsm.wpafb.af.mil

Mr. Edwin G. **Mullin**
Naval Aviation Depot
North Island
P.O. Box 357058
San Diego, CA 92135-7058
Tel: 619/545-0745
E-mail: mullin_e@a1.nadepni.navy.mil

-N-

Dr. Min **Namkung**
NASA Langley Research Center
MS 231
Hampton, VA 23681
Tel: 757/864-4962
E-mail: m.namkung@larc.nasa.gov

Mr. John **Nanasi**
Krautkramer Branson
50 Industrial Park Road
Lewistown, PA 17044
Tel: 717/242-0327
E-mail: jnanasi@krautkramer.com

Dr. Arnold **Nathan**
Israel Aircraft Industries
Department 4441 - Engineering Division
Commercial Aircraft Group
Ben Gurion Internation Airport 70100, Israel
Tel: 97239353868
E-mail: nathanfam@netmedia.net.il

Ms. Kelly R. **Navarra**
AFRL/PRTF
1950 Fifth Street, Building 18D
Wright-Patterson AFB, OH 45433-7251
Tel: 937/255-2734

Mr. George W. **Neat**
Volpe Center / US DOT
Kendall Square
Cambridge, MA 02142
Tel: 617/494-2679
E-mail: neat@volpe.dot.gov

Mr. David **Nelson**
Mechanical Dynamics Ltd
400 Carlingview Drive
Etobicoke, Ontario M9W 5X9,
Tel: 416/674-2144
E-mail: dnels@adams.com

Prof. Grigory I. **Nesterenko**
Central Aerohydrodynamics Institute
JsAGI
1 Lhukovsky str.
Lhukovsky, Moscow region, 140160, Russia
Tel: 0955564002

Dr. James C. **Newman**, Jr.
NASA Langley Research Center
MS 188E
Hampton, VA 23681
Tel: 757/864-3487
E-mail: j.c.newman.jr@larc.nasa.gov

Dr. Crystal H. **Newton**
University of Delaware
Center for Composite Materials
201 CMSL
Newark, DE 19716
Tel: 302/831-4941
E-mail: newton@ccm.udel.edu

Dr. Karl-Fredrik **Nilsson**
The Aeronautical Research Institute of Sweden
P.O. Box 110 21
S-1161 11 Bromma, Sweden
Tel: 46863412
E-mail: nnk@ffa.se

Mr. J.E. **Norkyke**
The Nordam Group - Texas
5101 Blue Bound
Fort Worth, TX 76106
Tel: 817/740-6116

-O-

Mr. Thomas **O'Brien**
Federal Aviation Administration
William J. Hughes Technical Center
AAR-400
Atlantic City International Airport, NJ 084095
Tel: 609/485-6085

Mr. Ray **O'Connor**
Lockheed Martin Aeronautical Systems
86 S. Cobb Drive
Marietta, GA 30063
Tel: 770/494-4294
E-mail: thoas.r.oconnor@lmco.com

Mr. Tom **O'Connor**
Advanced Repair Technology International
6500 West Freeway, Office 314
Fort Worth, TX 76116
Tel: 817/737-1655

Mr. Sten **Oberg**
Swedish Civil Aviation Administration (LFV)
Aviation Safety Dept, Airworthiness Section
SE-601 79 Norrkoeping, Sweden
Tel: 4611192067
E-mail: sten.oberg@fltsafety.lfv.se

Mr. Per **Obrelius**
Celsius Applied Composites AB
P.O. Box 13070
S-58013 Linkoping, Sweden
Tel: 4613209700
E-mail: per.obrelius@celsius.acab.se

Mr. Robert Kirk **Odian**
Structural Integrity Engineering
9509 Vassar Avenue
Chatsworth, CA 91311
Tel: 818/718-2195

Mr. Scott C. **Olson**
West Coast Industries
14900 Whitman Avenue, N.
Seattle, WA 98133
Tel: 206/365-7513

Dr. L.R. (Wally) **Orisamolu**
MARTEC Limited
1888 Brunswick Street, Suite 400
Halifax, Nova Scotia B3J 3J8,
Tel: 902/425-5101
E-mail: wally@martec.com

Mr. Jack **Orms**
SA-ALC/TIEM
Kelly AFB, TX 78214
Tel: 210/925-7393

-P-

Ms. Patricia L. **Pahlavani**
NASA Langley Research Center
Hampton, VA 23681

Mr. Mathew J. **Palakal**
Department of Computer & Information Science
Purdue School of Science, IUPUI
723 W. Michigan Street
Indianapolis, IN 46202
Tel: 317/274-9735
E-mail: mpalakal@indyvax.iupui.edu

Mr. Ron **Palchinsky**
NAWCAD 4.3.4.2
48066 Shaw Road MS 5
Patuxent River, MD 20670
Tel: 301/342-3581

Mr. Donald D. **Palmer, Jr.**
The Boeing Company
MC S102 1322
PO Box 516
St. Louis, MO 63166
Tel: 314/233-8321
E-mail: donald.d.palmer-jr@boeing.com

Mr. Charles **Pan**
SAIC Ultra Image International
Two Shaw's Cove, Suite 101
New London, CT 06320
Tel: 860/442-0100
E-mail: cpan@cpva.saic.com

Dr. Peter S. **Pao**
Naval Research Laboratory
Code 6312
Washington, DC 20375
Tel: 202/767-0224
E-mail: pao@anvil.nrl.navy.mil

Capt. James E. **Pappas**, Jr.
OC-ALC/LCRA
C/KC-135 Program Management Directorate
3001 Staff Drive, Suite 2AH 190
Tinker AFB, OK 73145-3019
Tel: 405/736-3832
E-mail: jepappas@exchange.tinker.af.mil

Mr. Clare A. **Paul**
AFRL/VASE
2790 DST
Wright-Patterson AFB, OH 45433-7402
Tel: 937/255-6104
E-mail: claire.paul@va.afrl.af.mil

Mr. Michael **Paulk**
Air Force NDI Office
485 Quenton Roosevelt Road, Suite 7
Kelly AFB, TX 78241-6426
Tel: 210/925-6408
E-mail: mpaulk@ldgate1.kelly.af.mil

Mr. Pal-Ove **Pedersen**
Lehigh University
226 E Sinclair Laboratory, 7 Asa Drive
Bethlehem, PA 18015
Tel: 610/758-5622
E-mail: pop2@lehigh.edu

Dr. Deborah T. **Peeler**
AFRL/MLSA
Wright-Patterson AFB, OH 45433-7251
Tel: 937/255-4150
E-mail: peelerdt@ml.wpafb.af.mil

Dr. Airan J. **Perez**
Naval Air Warfare Center
Code 4.3.4.1.
Building 2188, Unit 5
48066 Shaw Road
Patuxent River, MD 20678
Tel: 301/342-8098

Dr. Ignacio **Perez**
Naval Air Warfare Center
Code 4.3.4.2
Unit 5, Building 2188
Patuxent River, MD 20670-5304
Tel: 301/342-8074

Mr. Richard L. **Perry**
Sandia National Laboratories
P.O. Box 5800
MS 0615
Albuquerque, NM 81185-0615
Tel: 505/284-4296
E-mail: perry@sandia.gov

Mr. Don E. **Pettit**
Lockheed Martin Aero Systems
D 73-51, MZ 0484
86 South Cobb Drive
Marietta, GA 30063-0484
E-mail: don.e.pettit@lmco.com

Dr. Andrew W. **Phelps**
University of Dayton RI
300 College Park
Dayton, OH 45469-0130
Tel: 937/229-2793
E-mail: phelps@saber.udayton.edu

Mr. Neal **Phelps**
U.S. Air Force
Ogden Air Logistics Center
80-ALC/LFSS
680 Gum Lane, Building 1212
Hill Air Force Base, UT 84056-5825
Tel: 801/775-4892
E-mail: phelpsn@lfmail.hill.af.mil

Dr. Robert S. **Piascik**
NASA Langley Research Center
MS 188E
Hampton, VA 23681-0001
Tel: 757/864-1236
E-mail: r.s.piascik@larc.nasa.gov

Dr. Ramana M. **Pidaparti**
Department of Mechanical Engineering
Purdue School of Engineering Technology, IUPUI
723 W. Michigan Street
Indianapolis, IN 46202-5132
Tel: 317/274-6796
E-mail: ramana@engr.iupui.edu

Mr. Yves **Pilon**
Sino Swearingen Aircraft Company
1770 Sky Place Blvd
San Antonio, TX 78216
Tel: 210/258-3941

Mr. Robert W. **Plummer**
STI Technologies
1800 Brighton-Henrietta Townline Road
Rochester, NY 14623
Tel: 716/424-2010
E-mail: rplummer@sti-tech.com

Mr. Donald **Polakovics**
Naval Air Systems Command
43971 White Cedar Lane
California, MD 20619
Tel: 301/342-0283

Dr. Peter **Poole**
Defence Evaluation and Research Agency
AT Building
Farnborough, Hants Gulb OLX, United Kingdom
Tel: 44252395004
E-mail: ppoole@dear.gov.uk

Mr. Jerry **Porter**
Lockheed Martin Aeronautical Systems
D 73-71, Z 0303
86 South Cobb Drive
Marietta, GA 30063-0303
Tel: 770/494-7799
E-mail: jerry.porter@lmco.com

Mr. Jan **Potts**
Boeing
5000 E. McDowell Road
Mesa, AZ 85215-9797
Tel: 602/891-4883
E-mail: jan.potts@boeing.com

Mr. Robert **Prause**
Battelle
505 King Avenue
Columbus, OH 43201
Tel: 614/424-3294
E-mail: prause@battelle.org

Mr. Adarsh **Pun**
Universal Analysis, Inc.
3625 Del Amo Boulevard, Suite 370
Torrance, CA 90503
Tel: 310/216-2922

-R-

Dr. Anisur **Rahman**
Drexel University
FMRC, ME, 32nd and Chestnut Streets
Philadelphia, PA 19104
Tel: 215/895-2382
E-mail: anisur.rahman@drexel.edu

Prof. Veniamin L. **Raikher**
Central Aerohydrodynamics Institute TsAGI
140160, Zhukorsky, Moscow region, Russia
Tel: 70955564454

Dr. Ivatury S. **Raju**
NASA Langley Research Center
MS 188E
Hampton, VA 23681
Tel: 757/864-3449
E-mail: i.s.raju@larc.nasa.gov

Dr. Charles C. **Rankin**
Lockheed Martin Misiles & Space
B250/0 HI-6l
3251 Hanover Street
Palo Alto, CA 94304
Tel: 650/424-3240

Mr. Ramon A. **Raoux**
Transport Canada
Place De Ville, Tower C
330 Sparks Street, 2nd Floor
Ottowa, Ontario K1A 0N8, Canada
Tel: 613/952-4365
E-mail: raouxr@tc.gc.ca

Dr. Mohan **Ratwani**
R-Tec
4 Latigo Lane
Rolling Hills Estates, CA 90247-1520
Tel: 310/378-9236
E-mail: mohanr@aol.com

Mr. Tom **Reep**
ZETEC, Inc.
1370 NW Mall Street
PO Box 140
Issaquah, WA 98027
Tel: 425/392-5316

Mr. David A. **Rees**
Aerostructures Australia
Level 14, 222 Kingsway
South Melbourne, Victoria, Australia
Tel: 61396941013
E-mail: david.rees@aerostructures.com.au

Mr. Len **Reid**
Fatigue Technology, Inc.
100 Andover Park West
Seattle, WA 98188
Tel: 206/246-2010
E-mail: engineering@fatiguetech.com

Ms. Susan **Reilly**
University of Dayton Research Institute
300 College Park
Dayton, OH 45469-0102
Tel: 937/229-3051
E-mail: s.reilly@udri.udayton.edu

Mr. Robert **Rennell**
ARINC, Inc.
6205 S. Sooner Road
Oklahoma City, OK 73135
Tel: 405/739-0939
E-mail: rrennell@arinc.com

Mr. Martin **Renshaw**
British Aerospace M.A. and A
Greengate, Middleton
Manchester M24 1SA, United Kingdom
Tel: 1619558618

Mr. Jude **Restis**
Fatigue Technology, Inc.
100 Andover Park West
Seattle, WA 98188
Tel: 206/246-2010
E-mail: jrestis@fatiguetech.com

Mr. Richard C. **Rise**
Battelle
505 King Avenue
Columbus, OH 43201
Tel: 614/424-4433
E-mail: ricerc@battelle.org

Mr. Luc **Richardson**
Bombardier Services
10,000 Cargo A-4 Street
Montreal International Airport - Mirabel
Mirabel Quebec, J7N 1H3 Canada
Tel: 450/476-4590
E-mail: luc.richardson@services.bombardier.com

Dr. Melissa M. **Rieger**
School of Chemical Eng'r & Material Sci.
University of Oklahoma
T335 Sarkeys Energy Center
100 E Boyd Street
Norman, OK 73019
Tel: 405/325-2268
E-mail: rieger@mailhost.ecn.ou.edu

Mr. Ron **Rise**
National Technical Systems
401 Rockburn Court
Purceville, VA 20132
Tel: 540/338-4549

Mr. Steven R. **Rives**
OO-ALC/CD-2
7981 Georgia Street
Hill Air Force Base, UT 84056-5824
Tel: 801/775-6532
E-mail: rivess@hill.wpos.hill.af.mil

Mr. Dennis **Roach**
Sandia National Laboratories
Box 5800, MS-0615
Albuquerque, NM 87185
Tel: 505/844-6078
E-mail: dproach@sandia.gov

Mr. Jay **Roberts**
Nicolet Technologies
5225-4 Verona Road
Madison, WI 53711
Tel: 608/276-6302

Major David **Robertson**
AFRL/MLS-OL
325 Second Street
Robins AFB, GA 31098-1639
Tel: 912/926-3284
E-mail: darobert@wrdigg1.robins.af.mil

Mr. Gerald W. **Robertson**
Boeing Information, Space & Defense Systems
P.O. Box 3999
Seattle, WA 98124-2499
Tel: 253/657-3824
E-mail: gerald.w.robertson@boeing.com

Mr. David B. **Roderick**
Inerpacific Technology, Inc.
2150 Mariner Square Drive, Suite 200
Alameda, CA 94501
Tel: 510/523-2662
E-mail: interpac@amer.net

Dr. Lynn **Rogers**
CSA Engineering, Inc.
3945 N. Lake Shore Drive
Jamestown, OH 45335-1119
Tel: 937/255-4402

Mr. Ted **Roman**
Liberty Technologies, Inc.
555 North Lane
Conshohocken, PA 19428
Tel: 610/834-0330
E-mail: troman@libtech.attmail.com

Mr. Dennis J. **Romano**
NADEP North Island
302 Diablo Creek Court
Clayton, CA 94517
Tel: 619/545-0626
E-mail: roano_d@a1.nadepni.navy.mil

Dr. Cheryl A. **Rose**
NASA Langley Research Center
MS 190
Hampton, VA 23681
Tel: 757/864-5419
E-mail: c.a.rose@nasa.larc.gov

Dr. L.R. Francis **Rose**
Aeronautical and Maritime Research Lab
P.O. Box 4331
Melbourne, Victoria 3001, Australia
Tel: 61396267517
E-mail: francis.rose@dsto.defence.gov.au

Mr. Bruce A. **Rosenberg**
Avibank Manufacturing, Inc.
96 Tulip Road
Holland, PA 18966-2442
Tel: 215/364-6130
E-mail: bar96@mcione.com

Mr. Edwin L. **Rosenzweig**
Office of Naval Research
Ballston Centre Tower One (Room 804)
800 North Quincy Street
Arlington, VA 22217-5660
Tel: 703/696-7646
E-mail: rosenze@onr.navy.mil

Mr. Wayne **Rosholt**
Battelle
5100 Springfield Pike
Suite 210
Dayton, OH 45431-1231
Tel: 937/258-6708
E-mail: rosholtv@battelle.org

Mr. Stefan **Ross**
Saab Sircraft AB
SE-58188 Linkoping Sweden
Tel: 4613185286
E-mail: stefan.ross@saab.sc

Dr. Kevin **Rotenberger**
Division Chief, Structures & Materials
U.S. Army Aviation and Missile Command
Redstone Arsenal, AL 35898-5000

CDR Christopher **Roum**
Asst CDR for Log & Indust Ops
NAVAIRSYSCOM (AIR-3.0/6.0)
47033 McLeod Road, Unit 8
Patuxent River, MD 20670-1625
Tel: 301/757-8440

TSgt Nicholas W. **Roussel**
U.S. Air Force
913 AW/LGMFN
2184 Langley Street (WGARS)
Willow Grove, PA 19090-5201
Tel: 215/443-1136
E-mail: droussel@nxx.ae.mil

-S-

Mr. Sven-Ingemae **Sandstroem**
Defence Materiel Administration
S-11588 Stockholm, Sweden
Tel: 4687824728

Dr. Alain **Santgerma**
Aerospatiale Aeronautique
Dept A/BTE/CC/CM
Route de Bayonne, 316
Toulouse, 31060 France

Dr. Davood **Sarchamy**
BAe Airbus
Test & Development Engineering
Filton, Bristol BS99 7AR, United Kingdom
Tel: 79362793

Mr. Gilles **Sarrazin**
Bombardier Services
10,000 Cargo A-4 Street
Montreal International Airport - Mirabel
Mirabel Quebec, J7N 1H3 Canada
Tel: 450/476-4655
E-mail: gilles.sarrazin@services.bombardier.com

SQNLDR Terry **Saunder**
Royal Australian Air Force
ASI-DGTA
RAAF Williams
Laverton Victoria, 8027 Australia
Tel: 61392563496
E-mail: tjsaunde@raaf.defenc.gov.au

Mr. Charles **Saye**
Naval Air Systems Command
48298 Shaw Road, Unit 4
Patuxent River, MD 20670-1900
Tel: 301/342-0842
E-mail: sayecs@navair.navy.mil

Ms. Mary **Schleider**
Mercer Engineerig Research Center
135 Osigian Boulevard
Warner Robins, GA 31088
Tel: 912/953-6800
E-mail: mschleider@mercer.edu

Mr. Hans-Juergen **Schmidt**
Daimler-Benz Aerospace Airbus
Department EMF
Kreetslag 10
D21129 Hamburg, Germany
Tel: 494074372252

Ms. Bianka **Schmidt-Brandecker**
Daimler-Benz Aerospace Airbus
Department EMF
Kreetslag 10
D21129 Hamburg, Germany
Tel: 494074375883

Mr. Jeffrey N. **Schoess**
Honeywell Technology Center
3660 Technology Drive
Mineapolis, MN 55418-1096
Tel: 612/951-7873
E-mail: schoess_jeff@htc.honeywell.com

Major Joel J. **Schubbe**
AFRL/XPA
4375 Chidlaw Road, Suite 6
Wright-Patterson AFB, OH 45433-5006
Tel: 937/257-4191
E-mail: schubbej@afrl.af.mil

Mr. Chris C. **Seher**
Federal Aviation Administration
William J. Hughes Technical Center
AAR-400
Atlantic City International Airport, NJ 08405
Tel: 609/485-6085
E-mail: chris_seher_at_ct27@admin.tc.faa.gov

Mr. Vlad **Semiga**
Bombarier Aerospace
123 Garrat Blvd (N51-39)
Downsview, Ontario M3K 1Y5, Canada
Tel: 416/375-3894

Mr. Banavara R. **Seshadri**
NASA Langley Research Center
MS 188E
Hampton, VA 23681-2199
Tel: 757/864-3487
E-mail: b.r.seshadri@larc.nasa.gov

Mr. Bobby **Sexton**
Federal Aviation Administration
ACE-102
601 E 12th Street
Kansas City, MO 64106
Tel: 816/426-3241
E-mail: bob.sexton@faa.dot.gov

Mr. Surendra **Shah**
Lockheed Martin Aeronautical Systems
Dept. 73-25, B1-Mezz Zone 0160
86 South Cobb Drive
Marietta, GA 30063-0160
Tel: 770/494-2391

Mr. Tom **Shahood**
Textron
201 Lowell Street
Wilmington, MA 01887
Tel: 978/657-2958
E-mail: tshamood@systems.textron.com

Dr. Krishnakumar **Shankar**
School of Aerospace and
Mechanical Engineering
Australian Defence Force Academy
University of New South Wales
Australian Defence Force Academy
Northcott Drive Canberra 2600, Australia
Tel: 61262688584
E-mail: k-shankar@adfa.oz.au

Mr. Jim **Sheedy**
Panametrics
221 Crescent Street
Waltham, MA 02453-3497
Tel: 781/899-2719
E-mail: ndt@panametrics.com

Mr. Tony **Shen**
The Boeing Company
5000 E McDowell Road
Mesa, AZ 85215-9797
Tel: 602/891-0330

Dr. Chi-Yu **Shiao**
Galaxy Scientific Corporation
2500 English Creek Avenue
Building C
Egg Harbor, NJ 08234-5562
Tel: 609/485-6638

Dr. W.C.L. **Shih**
PRI Instrumentation, Inc.
25500 Hawthorne Boulevard
Suite 2300
Torrance, CA 90505
Tel: 310/791-1774
E-mail: physres@earthlink.net

Dr. Donald A. **Shockey**
SRI International
333 Ravenswood Avenue
Room AA279
Menlo Park, CA 94025-3493
Tel: 650/859-2587
E-mail: dshockey@unix.sri.com

Dr. William **Shurtleff**
Iowa State University - FAA
Airworthiness Assurance Ctr Excellence
Applied Sciences Complex II
1915 School Road, Room 115C
Ames, IA 50011-3042
Tel: 515/294-5274
E-mail: wwshurt@cnde.iastate.edu

Mr. Eric **Siegel**
Yxlon International, Inc.
11300 Johns Creek Parkway
Duluth, GA 30097-1539
Tel: 770/497-4528
E-mail: esiegel@atl.yxlon.com

Dr. Aslak **Siljander**
VTT Manufacturing Technology
P.O. Box 1705
FIN-02044 VTT, Finland
Tel: 35894565857
E-mail: aslak.siljander@vtt.fi

Prof. J.G. **Simmonds**
Department of Civil Engineering
University of Virginia
Thornton Hall
Charlottesville, VA 22903
Tel: 804/924-1041
E-mail: jgs@virginia.edu

Ms. Sandra **Simms**
PRI Instrumentation, Inc.
25500 Hawthorne Boulevard
Suite 2300
Torrance, CA 90505
Tel: 310/791-1774
E-mail: physres@earthlink.net

Mr. David **Simpson**
National Reserach Council of Canada
Montreal Road, M-14
Ottowa, Ontario K1A 0R6, Canada
Tel: 613/993-0899

Mr. John W. **Simpson**
NASA Langley Research Center
(NESB) LEMS
MS 231
Hampton, VA 23681
Tel: 757/864-4716
E-mail: j.w.simpson@larc.nasa.gov

Dr. Ripudaman **Singh**
Karta Technologies, Inc.
1892 Grandstand
San Antonio, TX 78238
Tel: 210/681-9102
E-mail: rsingh@karta.com

Dr. T.P. **Sivam**
Raytheon E-Systems - Waco
P.O. Box 154580, MS 1143
7500 Maehr Road
Waco, TX 76705
Tel: 254/867-4282
E-mail: sivam_sivam@readwo.com

Dr. Henry **Sklyut**
ALCOA
ALCOA Technical Center
Alcoa Center, PA 15069
Tel: 724/337-2713
E-mail: henry.sklyut@alcoa.com

Mr. Charles J. **Slade**
Boeing
St. Louis Automated Systems
P.O. Box 516
MS 1021111
St. Louis, MO 63166
Tel: 314/234-9000
E-mail: cj.slade@boeing.com

Prof. Bert L. **Smith**
Wichita State University
Aerospace Engineering Department
Wichita, KS 67260-0044
Tel: 316/978-5938
E-mail: bsmith@ae.twsu.edu

Dr. Christopher **Smith**
FAA W.J. Hughes Technical Center
Atlantic City International Airport
Pomona, NJ 08405
Tel: 609/485-5221
E-mail: smithc@admin.tc.faa.gov

Mr. Kevin D. **Smith**
Pratt & Whitney
P.O. Box 109600
MS 70721
West Palm Beach, FL 33478
Tel: 561/796-6536
E-mail: smithkev@pwfl.com

Ms. Marty **Smith**
Advanced Repair Technology International
6500 West Freeway, Office 314
Fort Worth, TX 76116
Tel: 817/737-1655
E-mail: smithm@dyncorp.com

Mr. Robert A. **Smith**
Defence Evaluation and Research Agency
Structural Materials Centre
Griffith Building A7
DERA, Farnborough GU14 0LX, United Kingdom
Tel: 441252395655
E-mail: rasmith@dera.gov.uk

Mr. O. Lester **Smithers**, Jr.
Aeronautical Systems Center (ASC/EN)
2530 Loop Road West
Wright-Patterson AFB, OH 45433-7101
Tel: 937/255-3208
E-mail: smitheol@asc-en.wpafb.af.mil

Mr. Fred **Sobeck**
Federal Aviation Administration
800 Independence Avenue
Washington, DC 20591
Tel: 202/267-7355

Mr. Flynn **Spears**
ZETEC, Inc.
1370 NW Mall Street
PO Box 140
Issaquah, WA 98027
Tel: 415/392-5316

Dr. James H. **Starnes**, Jr.
NASA Langley Research Center
MS 190
Hampton, VA 23681-0001
Tel: 757/864-3168
E-mail: j.h.starnes@larc.nasa.gov

Mr. Warren A. **Stauffer**
FAA - TOGAA
2501 S. El Camino Ral, Suite 108
San Clemente, CA 92672
Tel: 949/498-2917
E-mail: wstouffer@home

Mr. David **Steadman**
Delta Air Lines
Department 572
P.O. Box 20706
Atlanta, GA 30320-6001
Tel: 404/714-0057
E-mail: david.steadman@delta-air.com

RADM Craig E.**Steidle**
Vice Commander
Naval Air Systems Command Headquarters
Patuxent River, MD 20670

Mr. Todd **Steyer**
Northrop Grumman
8900 E Washington Blvd
MS 9B61/GK
Pico Rivera, CA 90660-3737
Tel: 562/948-9641

Mr. Barry K. **Sturgis**
NAVAIRSYSCOM
Structures Division
Building 2187, Suite 2540A
48110 Shaw Road, Unit 5
Patuxent River, MD 20670
Tel: 301/342-9381
E-mail: sturgisbk.ntrprs@navair.navy.mil

Mr. Tom **Swift**
Fatigue Technology, Inc.
100 Anclover Park W.
Seattle, WA 98188
Tel: 206/246-2010

-T-

Mr. Richard D. **Tabery**
Technical Oversight Group Aging Aircraft
51 Oak Valley Road
San Meteo, CA 94402
Tel: 650/347-8979

Dr. Paul W. **Tan**
Federal Aviation Administration
William J. Hughes Technical Center
Atlantic City International Airport, NJ 08405
Tel: 609/485-6665

Mr. Brian M. **Taylor**
University of Oklahoma
865 Asp Avenue
Felgar Hall, Rm 212
Norman, OK 73019
Tel: 405/325-1090
E-mail: bmtaylor@ou.edu

Mr. Drew **Taylor**
USAF ASC/XR
2275 D Street, Suite 10
Wright-Patterson AFB, OH 45433-7227
Tel: 937/255-3264
E-mail: drew.taylor@ascxr.wpafb.af.mil

Mr. Martin W. **Taylor**
TOGAA (FAA)
521 Golf Links Lane
Longboat Key, FL 34228
Tel: 941/383-7776
E-mail: mwtjbt@aol.com

SQLDR Wayne **Taylor**
Royal Australian Air Force
WR ALC/FM-AT
480 Second Street, Suite 200
Robins AFB, GA 31098-1640
Tel: 912/926-2580
E-mail: raaf_wralc@msn.com

Mr. Richard J. **Tello**
MITRE Corporation
202 Burlington Road
Bedford, MA 01730-1420
Tel: 781/377-9919
E-mail: rtello2mitre.org

Mr. Robert L. **Temucin**
Naval Aviation Depot
PSC Box 8021
Cherry Point, NC 28533
Tel: 252/464-7332
E-mail: temucinrl@engrz.nadepcd.navy.mil

Mr. Yves **Theriault**
Bombardier Aerospace
400 Cote-Vertu W.
Dorjal, Quebec, H42 1Y9 Canada
Tel: 514/855-5001

Mrs. Brigham **Thomas**
Oak Ridge National Lab
P.O. Box 2009
Oak Ridge, TN 37831-8050
Tel: 423/576-0515

Prof. Robert L. **Thomas**
Wayne State University
Insitute for Manufacturing Research
and Department of Physics
666 W. Hancock
Detroit, MI 48202
Tel: 313/577-2970
E-mail: bob@thermal.physics.wayne.edu

Mr. Art **Thompson**
GE Aircraft Engines
1 Neumann Way
MD 0-65
Cincinnati, OH 45215
Tel: 513/552-4627
E-mail: art.thompson@ae.ge.com

Flt Sgt Nigel **Thorpe**
Royal Air Force
NDT Sqn, RAF St. Althan
Barry, Vale of Glamorgan CF62 4WA
United Kingdom
Tel: 441446797290

Mr. James S. **Tira**
AlliedSignal Federal Manufacturing
and Technologies
Department 833, Mail Stop 2C43
2000 East 95th Street
Kansas City, MO 64141
Tel: 816/997-2563
E-mail: jtira@kcp.com

Mr. Peter N. **Toivonen**
Boeing
MailCode 0644500
P.O. Box 516
St. Louis, MO 63166
Tel: 314/233-3066
E-mail: ptoivonen1@mdc.com

Mr. Walter **Tomczykowski**
ARINC, Inc.
2551 Riva Road
Annapolis, MD 21401
Tel: 410/266-4535
E-mail: wtomczyk@arinc.com

Mr. Chris **Tonthat**
Continental Airlines
3663 N Sam Houston Parkway E, Suite 200
Houston, TX 77032
Tel: 281/985-1196
E-mail: ctonth@coair.com

Dr. Milton J. **Torres**
Florida International University
Industrial Energy Department
University Park, ECS 119
Miami, FL 33199
Tel: 305/348-3148

Mr. J. Douglas **Trader**
Naval Aviation Depot, Jacksonville FL
Code 4.3.3.
Building 2
Jacksonville, FL 322212
Tel: 304/542-2631

Dr. Angela **Trego**
Boeing ISDS
P.O. Box 3999
MS 82-97
Seattle, WA 98124-2499
Tel: 253/773-9556
E-mail: angela.trego@boeing.com

Mr. Donald E. **Triest**
Naval Aviation Deport Jacksonville
Code 4.3.3
6255 Lake Gray Blvd, Suite 5
Jacksonville, FL 32244-5894
Tel: 904/779-3541

Mr. Doug E. **Tritsch**
University of Dayton Research Institute
300 College Park
Dayton, OH 45469-0120
Tel: 937/229-4482
E-mail: tritsch@udri.udayton.edu

Mr. Michael **Troller**
Everest Imaging
11500 Metric Boulevard
Austin, TX 78758
Tel: 512/833-9400
E-mail: www.everestimaging.com

Mr. Billy R. **Trussell**
WR-ALC/LFEFS
296 Cochran Street
Robins AFB, GA 31098-1622
Tel: 912/926-5482
E-mail: billy.tussell@lf.robins.af.mil

Mr. Jim **Tucker**
Southern Research Institute
757 Tom Martin Drive
Birmingham, AL 35211
Tel: 205/581-2526
E-mail: tuckerj@sri.org

-U-

Ms. Penelope **Ulander**
Naval Aviation Depot North Island
1242 23rd Street
San Diego, CA 92102
Tel: 619/545-3935
E-mail: ulanders_p@al.nedepni.navy.mil

LT Volker **Ulrich**
German Air Force
Material Office III A1
Heidestrasse 245
51140 Cologne, Germany
Tel: 022036024924

-V-

Mr. Ray **Valeika**
Technical Operations Center
Delta Air Lines, Inc.
Atlanta, GA 30320
Tel: 404/714-0350

Dr. Mike **Valley**
Sandia National Laboratories
FAA/AANC
3260 University Boulevard SE
Access Road B
Albuquerque, NM 87106
Tel: 505/843-8722
E-mail: mtvalle@sandia.com

Mr. Craig B. **Van Way**
Northrop Grumman Corporation
Advanced Structural Technologies
One Hornet Way 9B71/63
El Segundo, CA 90245
Tel: 310/332-9639
E-mail: vanwacr@mail.northgrum.com

Mr. Michael **VanDerwerken**
GE Corporate R&D Center
One Research Circle, KW C260
Schenectady, NY 12309
Tel: 518/387-6141

Mr. Bill **Via**
ZETEC, Inc.
1370 NW Mall Street
PO Box 140
Issaquah, WA 98027
Tel: 425/392-5316

Mr. Christophe **Vuillot**
French Military of Defense/DGA/SPAe
26 Boulevard Victor, 00460
Armees, France
Tel: 33145524373
E-mail: cvuillot@cedocar.fr

-W-

Mr. Michael **Waddell**
Air Force Research Laboratory / MLMP
2977 P Street, Suite 6, Building 653
Wright-Patterson AFB, OH 45433-7739
Tel: 937/255-7277
E-mail: waddelmd@ml.wpafb.af.mil

Mr. Anders **Wahlstrom**
Celsius Applied Composites AB
P.O. Box 13070
S-58013 Linkoping, Sweden
Tel: 4613209700
E-mail: anders.wahlstrom@celsius.acab.sc

Mr. Kevin **Walker**
Aeronautical and Maritime Research
Laboratory (AMRL), DSTO, Australia
C/-LMTAS
P.O. Box 748, Mail Zone 6465
Fort Worth, TX 76101
Tel: 817/777-2423
E-mail: kevin.walker.itar@lmtas.com

Mr. Markus **Wallin**
Helsinki University of Technology
Laboratory of Lightweight Structures
PO Box 4300
FIN-02015 HUT, Finland
Tel: +358-9-451-3437
E-mail: markus.wallin@hut.fi

Mr. Douglas C. **Walling**
Naval Aviation Depot
PSC Box 8021
Cherry Point, NC 28533
Tel: 252/464-8517
E-mail: wallingdc@elis.nadepcp.navy.mil

Mr. Ralph T. **Ward, Jr.**
Boeing
2601 Liberty Parkway
MS RM-00
Midwest City, OK 73110
Tel: 405/779-1488

Mr. Charles J. **Warren**
Aluminum Company of America
Alcoa Technical Center
100 Technical Drive
Alcoa Center, PA 15069-0001
Tel: 724/337-5417

Mr. Roy T. **Watanabe**
Structures Technology Support
Boeing Commerical Airline Group
PO Box 3707, MC 67-FF
Seattle, WA 98124-2207
Tel: 425/237-4720
E-mail: roy.watanabe@pss.boeing.com

Ms. Patricia **Watts**
Federal Aviation Administration
William J. Hughes Technical Center
Atlantic City International Airport
Atlantic City, NJ 08405
Tel: 609/485-5043
E-mail: patricia.watts@faa.dot.gov

Dr. Paul A. **Wawrzynek**
The Cornell University Fracture Group
Cornell University
638 Rhodes Hall
Ithaca, NY 14853
Tel: 607/255-5894
E-mail: wash@stout.cfg.cornell.eu

Mr. Woody **Weaver**
MTS Systems Corporation
7400 Browns Farm Road
Spotsylvania, VA 22553
Tel: 540/786-6585

Mr. Hans J. **Weber**
Weber Technology Applications
7916 Laurelridge Road
San Diego, CA 92120
Tel: 619/286-6660

Dr. John M. **Webster**
Holographics, Inc.
44-01 11th Street
Long Island City, NY 11101
Tel: 718/268-3465
E-mail: john_webster@compuserve.com

Dr. Robert P. **Wei**
Dept of Mechanical En'r & Mechanics
Lehigh University
327 Sinclair Laboratory, 7 Asa Drive
Bethlehem, PA 18015
Tel: 610/758-3587
E-mail: rpwo@lehigh.edu

Mr. Donald F. **Welch**
Oak Ridge National Laboratory
P.O. Box 2009
MS 6066
Oak Ridge, TN 37831-8066
Tel: 423/576-6563
E-mail: wel@ornl.gov

Mr. Kevin M. **Welch**
Lockheed Martin
Tactical Aircraft Systems (LMTAS)
P.O. Box 748
Mail Zone 6242
Fort Worth, TX 76101
Tel: 817/777-4807
E-mail: kevin.m.welch@lmco.com

Mr. David **White**
Aerostructures, Inc.
1725 Jefferson Davis Highway
Suite 701
Arlington, VA 22202
Tel: 703/413-1600

Mr. Tommy N. **White**
Naval Aviation Depot North Island
P.O. Box 357058
San Diego, CA 92135-7058
Tel: 619/545-3922
E-mail: white_t@ai.nadepni.navy.mil

Mr. Andy **Wilkinson**
Department of the Navy
Naval Aviation Depot
PSC Box 8021
Cherry Point, NC 28533-0021
Tel: 252/464-8383

Mr. Scott **Willard**
Lockheed-Martin
NASA Langley Research Center
Bldg 1205, MS 188E
Hampton, VA 23681
Tel: 757/864-3469
E-mail: s.a.willard@larc.nasa.gov

Mr. John R. **Williamson**
Anteon Corporation
5100 Springfield Pike, Suite 509
Dayton, OH 45431
Tel: 937/254-7950
E-mail: jwilliam@dayton.anteon.com

Mr. Marvin W. **Wilson**
GE Reuter Stokes, Inc.
8499 Darrow Road
Twinsburg, OH 44087
Tel: 530/963-2448
E-mail: wilsonm@rscpo1.wilm.ge.com

Mr. Russell A. **Wincheski**
NASA Langley Research Center
MS 231
Hampton, VA 23681
Tel: 757/864-4798
E-mail: r.a.wincheski@larc.nasa.gov

Dr. William P. **Winfree**
NASA Langley Research Center
MS 231
Hampton, VA 23681
Tel: 757/864-4963
E-mail: w.p.winfree@larc.nasa.gov

Mr. Billy S. **Wood**
Fuji NDT Systems
1055 Stevenson CT, Building 105
Roselle, IL 60172-2300
Tel: 770/985-8951

Ms. Nancy **Wood**
The Boeing Company
Mail Code 1111
PO Box 516
St. Louis, MO 63166
Tel: 314/234-9028

Mr. Richard **Wood**
Naval Aviation Depot
Code 4.3.4.2
PSC Box 8021
Cherry Point, NC 28533-021
Tel: 252/464-7157

Mr. James H. **Workley**
Foerster Instruments Inc.
140 Industry Drive
Pittsburgh, PA 15275-1028
Tel: 412/788-8976
E-mail: jworkley@aol.com

Mr. Dan **Wysnewski**
Liberty Technologies, Inc.
555 North Lane
Conshohocken, PA 19428
Tel: 864/234-9746

-Y-

Dr. Hsing C. **Yeh**
Aeronautical Systems Center (USAF)
ASC/ENFS
Building 560
2530 Loop Road West
Wright-Patterson AFB, OH 45433-7101
Tel: 937/255-8547

Dr. H. Thomas **Yolken**
Texas Research Institute / Austin, Inc.
1815 N. Fort Myer Drive
Suite 509
Arlington, VA 22209
Tel: 703/243-0889
E-mail: yolken.tri@erols.com

Mr. Jess W. **Young**
OO-ALC-LACM
6064 Dogwood Avenue
Hill ABF, UT 84056-5815
Tel: 801/777-5291
E-mail: youngs@hillwpos.hill.af.mil

Mr. R.W. **Young**
British Aerospace
Military Aircraft & Aerostructures
Skillings Lane
Brough, East Yorkshire HU15 1EQ, England
Tel: 441482663709
E-mail: bobwyoung@aol.com

Dr. Richard D. **Young**
NASA Langley Research Center
MS 190
Hampton, VA 23681-2199
Tel: 757/864-2894
E-mail: r.d.young@larc.nasa.gov

-Z-

Prof. Alan T. **Zehnder**
Cornell University
Department of Theoretical and Applied Mechanics
Kimball Hall
Ithaca, NY 14853
Tel: 607/255-9181
E-mail: atz@msc.cornell.edu

Mr. H. Lewis **Zion**
GTRI Aerospace Laboratory
Building 2, Suite 111
7220 Richardson Road
Smyrna, GA 30080
Tel: 770/528-4906
E-mail: lew.zion@gtri.gatech.edu

Mr. Dennis **Zwigart**
Krautkramer Branson
50 Industrial Park Road
Lewistown, PA 17044
Tel: 717/242-0327

REPORT DOCUMENTATION

Form Approved
OMB No. 0704-0188

Public reporting burden for this collection of information is estimated to average 1 hour per response, including the time for reviewing instructions, searching existing data sources, gathering and maintaining the data needed, and completing and reviewing the collection of information. Send comments regarding this burden estimate or any other aspect of this collection of information, including suggestions for reducing this burden, to Washington Headquarters Services, Directorate for Information Operations and Reports, 1215 Jefferson Davis Highway, Suite 1204, Arlington, VA 22202-4302, and to the Office of Management and Budget, Paperwork Reduction Project (0704-0188), Washington, DC 20503.

1. AGENCY USE ONLY (*Leave blank*)	2. REPORT DATE	3. REPORT TYPE AND DATES COVERED
	January 1999	Conference Publication

4. TITLE AND SUBTITLE
The Second Joint NASA/FAA/DoD Conference on Aging Aircraft

5. FUNDING NUMBERS
WU-538-10

6. AUTHOR(S)
Charles E. Harris, Editor

7. PERFORMING ORGANIZATION NAME(S) AND ADDRESS(ES)
NASA Langley Research Center
Hampton, VA 23681-2199

8. PERFORMING ORGANIZATION REPORT NUMBER
L-17819B

9. SPONSORING / MONITORING AGENCY NAME(S) AND ADDRESS(ES)
National Aeronautics and Space Administration
Washington, DC 20546-0001

10. SPONSORING / MONITORING AGENCY REPORT NUMBER
NASA CP-1999/208982/PART2

11. SUPPLEMENTARY NOTES

12a. DISTRIBUTION / AVAILABILITY STATEMENT
Unclassified-Unlimited
Subject Category: 39
Distribution: Standard
Availability: NASA CASI (301) 621-0390

12b. DISTRIBUTION CODE

13. ABSTRACT (*Maximum 200 words*)

The purpose of the Conference was to bring together world leaders in aviation safety research, aircraft design and manufacturing, fleet operation and aviation maintenance to disseminate information on current practices and advanced technologies that will assure the continued airworthiness of the aging aircraft in the military and commercial fleets. The Conference included reviews of current industry practices, assessments of future technology requirements, and status of aviation safety research. The Conference provided an opportunity for interactions among the key personnel in the research and technology development community, the original equipment manufacturers, commercial airline operators, military fleet operators, aviation maintenance, and aircraft certification and regulatory authorities. Conference participation was unrestricted and open to the international aviation community. Appendix B contains the name and addresses of the 623 participants in the Conference.

14. SUBJECT TERMS
fatigue, fracture, corrosion, structural integrity, aircraft, NDE, NDI nondestructive evaluation, inspection, aging aircraft, fleet management

15. NUMBER OF PAGES
611

16. PRICE CODE
A99

17. SECURITY CLASSIFICATION OF REPORT	18. SECURITY CLASSIFICATION OF THIS PAGE	19. SECURITY CLASSIFICATION OF ABSTRACT	20. LIMITATION OF ABSTRACT
Unclassified	Unclassified	Unclassified	UL